UNIVERSITÉ DE PARIS 7 - Denis DIDEROT

Mémoire d'habilitation à diriger des recherches

DU FOND COSMOLOGIQUE AU CIEL MILLIMÉTRIQUE : OBSERVATIONS ET ANALYSE DE DONNÉES

Jacques DELABROUILLE

CNRS, Laboratoire APC
F-75205 Paris Cedex 13

Habilitation soutenue le 06/04/2011 devant le jury composé de :

Pierre	BINÉTRUY	Examinateur
François	BOUCHET	Examinateur
Gianfranco	DE ZOTTI	Rapporteur
Isabelle	GRENIER	Rapporteur
Yannick	MELLIER	Rapporteur

Table des matières

Remerciements

Les travaux présentés ici doivent beaucoup à plusieurs personnes, que je me dois de remercier ici. En tout premier lieu, je tiens à remercier Edward 'Rocky' Kolb et David N. Schramm. C'est en assistant, pendant l'été 1991, à un séminaire de Rocky Kolb au Fermilab que j'ai découvert la cosmologie, et en discutant plus avant avec lui que j'ai décidé de faire les études nécessaires pour pouvoir travailler dans ce domaine. David Schramm, à Chicago, m'a toujours apporté son soutien enthousiaste et indéfectible en toutes circonstances. Si j'ai la chance de travailler aujourd'hui en cosmologie, c'est, pour beaucoup, grâce à lui. Son décès dans un tragique accident d'avion en décembre 1997 m'a profondément marqué.

Sans faire une liste exhaustive de mes collaborateurs, je tiens à remercier aussi les personnes avec qui j'ai travaillé le plus étroitement pour le travail présenté ici. Un grand merci donc à Xavier Désert et Alain Benoît pour m'avoir permis de participer aux expériences Diabolo et Archeops, à Jean-Baptiste Melin, que j'ai eu le plaisir d'encadrer pendant sa thèse, et qui est maintenant ma référence sur les amas de galaxies, à Jean-Loup Puget, François Bouchet, et Jean-Michel Lamarre, avec qui j'ai interagi sur à peu près tous les aspects concernant la mission Planck. Une pensée spéciale pour Richard Gispert, qui nous a quittés bien trop tôt.

Je remercie Yannick Giraud-Héraud, qui m'a accueilli dans le groupe de cosmologie du laboratoire PCC après ma thèse, et Benoît Revenu, Cyrille Rosset, et aussi et surtout Jean Kaplan, avec qui j'ai étroitement travaillé pendant plusieurs années sur le problème de la mesure de polarisation avec l'instrument HFI.

Je dois beaucoup à Jean-François Cardoso, qui a été mon collaborateur privilégié sur la "séparation de sources", notamment pour le développement de SMICA. Merci également à Guillaume Patanchon, qui m'a fait confiance pour l'encadrement de sa thèse sur ce sujet, et à Mathieu Remazeilles et Soumen Basak, qui effectuent actuellement un postdoc avec moi sur la séparation de composantes. Plusieurs publications jointes en annexe de ce mémoire ont été écrites avec Mathieu, et Soumen a contribué à la préparation de la réponse à l'appel d'offre COrE au programme Cosmic Vision de l'ESA.

L'analyse multi-résolution à l'aide de needlets sphériques tient une part importante dans les méthodes d'analyse présentées dans ce mémoire. Pour leur contribution au développement de ces outils, je tiens à remercier Gilles Faÿ, Frédéric Guilloux, Gérard Kerkyacharian et Dominique Picard.

Le développement du PSM doit beaucoup à un grand nombre de personnes. Merci particulièrement à Joaquin Gonzalez-Nuevo, Jean-Baptiste Melin, et Marc-Antoine Miville-Deschênes, qui ont assuré l'essentiel des développements relevant des simulations de l'émission de sources non résolues, de l'effet SZ, et de l'émission galactique respectivement. Merci aussi à Marc Betoule, qui a assemblé la première version du PSM, et à Guillaume Castex, qui effectue actuellement sa thèse avec moi sur ce sujet.

Merci également à tous mes collègues de l'équipe ADAMIS, avec une mention particulière pour Maude Le Jeune pour tout le travail qu'elle y a effectué avec moi, et pour Radek Stompor, qui a accepté de prendre la relève et d'assurer la coordination de l'équipe à partir de mai 2010. La création de cette équipe à l'APC a mobilisé une part importante de mon énergie de 2004 à 2010, et je tiens à remercier Pierre Binétruy, directeur du laboratoire APC, de m'avoir fait confiance pour cette responsabilité.

J'espère que l'équipe fonctionnera avec succès pendant bien des années encore.

Merci enfin à tous les membres du jury, Pierre Binétruy, François Bouchet, Gianfranco de Zotti, Isabelle Grenier et Yannick Mellier, qui ont accepté de lire ces quelques pages et de me donner leur avis sur le travail qui y est présenté.

Avant-propos

L'essentiel du travail présenté dans ce mémoire relève de l'observation du ciel millimétrique. Mon intérêt pour le sujet, à l'origine, concernait exclusivement le fond diffus cosmologique, et tout ce que son observation détaillée avec une mission spatiale comme Planck pouvait nous apporter d'information sur le modèle du Big-Bang, sur l'univers primordial, et sur les lois fondamentales de la physique.

Malgré les quelques détours que j'ai pu faire par d'autres expériences, d'autres thèmes de recherche, des incursions multidisciplinaires en collaboration avec des experts de sciences et techniques de l'information et de la communication ou de mathématiques appliquées, le lecteur notera que toute mon activité ou presque, depuis le début de ma thèse en 1994 jusqu'à aujourd'hui, est fortement liée à la préparation de l'analyse des données de la mission Planck, qui en constitue le fil directeur. Au fil des opportunités, je me suis toutefois impliqué ponctuellement sur d'autres projets, dont tous ne sont pas exposés dans ce mémoire.

Après une introduction générale permettant de placer le travail effectué dans son contexte, qui fait l'objet du chapitre 1, les chapitres qui suivent sont présentés de façon chronologique, selon la période pendant laquelle le sujet abordé a occupé la majeure partie de mon activité.

Ainsi, cet exposé de mes travaux commence par les observations et l'étude de l'effet Sunyaev Zel'dovich dans les amas de galaxies, dont il est question au chapitre 2. Dans la première année qui a suivi ma thèse, j'ai participé à l'analyse d'observations que nous avons prises au télescope de 30 mètres de l'IRAM avec l'instrument Diabolo. Pour faire suite à ces observations, l'encadrement d'un stage de DEA, puis d'une thèse sur l'effet SZ et sa mesure, m'ont donné l'occasion d'approfondir ce sujet, notamment les aspects liés à la modélisation et la simulation de l'effet SZ, au problème de la détection des amas dans des observations multifréquence, et à l'analyse des observations WMAP et Planck pour en extraire la signature de l'interaction des photons du fond cosmologique avec le gaz chaud d'électrons présent dans les amas de galaxies.

J'ai continué, en tâche de fond, le travail nécessaire à la préparation de la mission Planck, avec notamment une forte implication sur la thématique de la polarisation du fond cosmologique. J'ai ainsi participé à la définition de l'instrument HFI pour effectuer cette mesure de polarisation, et coordonné les activités relatives à l'estimation et à la minimisation des effets systématiques qui y sont liés. Dans la même optique, j'ai coordonné les activités relevant de la définition de la chaîne de traitement de données polarisées, avant que la mesure de polarisation avec Planck ne soit suffisamment définie pour être intégrée, comme il se doit, à l'ensemble des activités de la collaboration. J'ai également continué le travail commencé durant ma thèse, avec l'extension à la polarisation de la méthode de déstriage qui permet avec Planck une mesure en puissance totale, et la poursuite des études sur les problèmes de lumière parasite. Ces différents travaux sont exposés au chapitre 3 du présent mémoire.

J'ai participé, à partir de 1999, à la formidable aventure de l'expérience Archeops, à laquelle je consacre le chapitre 4. Cela a été une occasion très appréciable de travailler sur de vraies données, suffisamment sensibles pour mesurer le spectre Cl du fond cosmologique, suffisamment compétitives pour mériter l'attention de toute la communauté des cosmologues, suffisamment complexes pour m'in-

citer à développer ma connaissance des méthodes et techniques de traitement et d'analyse de données multifréquences.

A partir de 2001, avec le financement d'un projet jeune chercheur par le ministère de la recherche, le projet ACI-CMB, j'ai commencé à m'intéresser sérieusement au développement de thèmes de recherche interdisciplinaire pour l'analyse de données, notamment pour la séparation de composantes. Deux autres projets qui ont fait suite, Astro-Map et Cosmostat, ont donné un élan supplémentaire à cette activité, qui m'a permis de créer au laboratoire APC le groupe thématique ADAMIS. Cette équipe est conçue comme un lieu de convergence interdisciplinaire, où se conjuguent les compétences d'astrophysiciens, de mathématiciens, de spécialistes du traitement statistique de l'information et d'ingénieurs informaticiens, pour résoudre par des méthodes novatrices les problèmes les plus complexes auxquels se heurte l'analyse de données dans les domaines de l'astrophysique et de l'astroparticule. Dans le cadre des thématiques sur lesquelles je me suis plus particulièrement impliqué, cette interdisciplinarité a abouti au développement de méthodes de séparation de composantes, d'outils logiciels de traitement de données, et d'outils mathématiques d'analyse multi-résolution sur la sphère. Le chapitre 5 est consacré à la présentation d'une partie de ces travaux.

Dans une perspective future, le succès de la mission Planck se prolonge naturellement par la définition d'une mission spatiale de quatrième génération, dédiée à la mesure de la polarisation du fond cosmologique avec une précision suffisante pour aborder la compréhension de la physique encore spéculative à l'oeuvre dans l'univers primordial, et notamment pour contraindre les modèles d'inflation. La séparation des émissions de différentes origines astrophysiques est un des aspects cruciaux pour le succès d'une telle mission. Mon travail pour évaluer l'impact de la contamination par les avants-plans astrophysiques sur la mesure de la polarisation d'origine inflationnaire est présenté à la fin du même chapitre 5.

Je présente au chapitre 6 le développement d'un modèle de l'émission du ciel millimétrique, le "Planck Sky Model" ou PSM, qui permet d'en prédire l'émission multicomposantes, et de simuler des cartes et des catalogues en température et polarisation. Ces simulations permettent de développer et de valider, sur données synthétiques, les méthodes d'analyse développées et utilisées pour exploiter scientifiquement les observations du ciel avec WMAP, avec Planck, et avec les instruments actuellement en cours de conception. Le développement de ce modèle, et sa mise à jour sur la base des observations de la mission Planck, constitue mon projet de recherche principal pour les quelques années à venir.

Enfin, une brève mise en perspective des différents thèmes abordés dans le mémoire se trouve au chapitre 7, dans lequel je mentionne également les pistes pour la continuation de mes activités de recherche. Ce sont, bien sûr, des thématiques susceptibles de s'adapter aux découvertes à venir et à l'évolution du contexte scientifique au cours de ces prochaines années.

La rédaction de ce document a été l'occasion de faire un bilan de mes contributions dans le domaine de l'observation du ciel millimétrique. J'ai, au cours de ces années passées à préparer la mission Planck, appris à connaître, notamment par mon activité de coordination du groupe de séparation de composantes, les autres émissions du ciel, et ce suffisamment pour m'y intéresser non plus comme à des avant-plans à rejeter, mais comme à une source inépuisable de sujets de recherche passionnants, auxquels j'ai bien l'intention de consacrer une partie de mes activités dans le cadre de l'analyse des données de la mission Planck. Ceci justifie le titre que j'ai choisi pour ce mémoire d'habilitation à diriger les recherches.

Chapitre 1

Introduction

1.1 Le modèle du Big-Bang

Le modèle cosmologique du Big-Bang, maintenant bien établi, offre un contexte standard pour étudier le contenu et l'évolution de notre Univers. Ce modèle est suffisamment abouti pour être décrit dans plusieurs livres de cours destinés aux étudiants de physique et d'astrophysique de premier et second cycle universitaire (voir par exemple Kolb & Turner 1990; Peebles 1993; Peacock 1999; Harrison 2000; Liddle & Lyth 2000; Coles & Lucchin 2002; Narlikar 2002; Dodelson 2003; Liddle 2003; Weinberg 2008; Rich 2010, ...).

Il serait hors de propos de décrire ici en détail l'ensemble du modèle, et nous nous contentons de donner les éléments qui permettent de placer le présent mémoire dans son contexte.

1.1.1 Cadre général

Le modèle standard du Big-Bang s'appuie sur quelques observations majeures :
- l'expansion de l'Univers, mise en évidence par la récession des galaxies (Hubble 1929; Hubble & Humason 1931) ;
- la mesure de l'abondance des éléments légers, qui s'explique par la nucléosynthèse primordiale à $t \sim 3$ min (Alpher et al. 1948; Wagoner et al. 1967) ;
- l'existence d'un fond diffus cosmologique (Dicke et al. 1965), rayonnement fossile émis lorsque les électrons se sont combinés aux noyaux à $t \sim 380\,000$ ans, dont la détection au niveau attendu (Penzias & Wilson 1965) et la loi d'émission de corps noir (Fixsen et al. 1996) étayent l'hypothèse d'un big band chaud ;
- l'existence, au delà de l'anisotropie dipolaire essentiellement due au déplacement de l'observateur par rapport au flot de Hubble, de fluctuations de température de ce fond cosmologique au niveau de $\delta T/T \simeq 10^{-4}$ (Smoot et al. 1992), et de fluctuations de polarisation (Kovac et al. 2002) corrélées avec les anisotropies de températures (Page et al. 2007).

Le modèle du Big-Bang s'appuie également sur l'hypothèse que l'Univers est homogène et isotrope à grande échelle. Cette hypothèse est étayée par la quasi isotropie du fond de rayonnement cosmologique, et par l'observation de la distribution des galaxies, qui tend vers l'uniformité à grande échelle (Peacock & Dodds 1994).

Dans le cadre du modèle, la géométrie de l'univers observable est au premier ordre celle d'un espace homogène et isotrope en expansion au cours du temps. La métrique de l'espace-temps (métrique de Friedmann-Robertson Walker, ou FRW) fait intervenir un paramètre k qui détermine la courbure moyenne de l'espace, et une fonction $a(t)$, le facteur d'échelle, qui peut être interprété comme une

description de l'expansion des coordonnées d'espace au cours du temps (la coordonnée t mesure le temps propre d'observateurs comobiles). Par convention, la valeur du facteur d'échelle aujourd'hui est $a_0 = a(t_0) = 1$.

L'équation d'Einstein relie cette métrique au contenu de l'univers en énergie sous différentes formes : matière non relativiste (sans pression), rayonnement (pour lequel $p = \rho/3$), autres types d'énergie (distingués par leur équation d'état $p = w\rho$). L'effet d'une constante cosmologique non nulle Λ est équivalent à celui d'une énergie du vide, d'équation d'état $p = -\rho$.

La mesure du taux d'expansion au cours du temps (mesure de la constante de Hubble $H_0 = \dot{a}(t_0)$ (Freedman et al. 2001), mesure de l'accélération de l'expansion avec la luminosité apparente des supernovae de type Ia à différents décalages spectraux (Perlmutter et al. 1999; Astier et al. 2006)) implique des contraintes sur la densité d'énergie sous ces différentes formes. Les meilleures mesures actuelles sont interprétables en supposant que 95% environ de la densité dans l'Univers est sous forme de matière invisible et d'énergie de nature inconnue, la matière noire et l'énergie noire. Sans que ceci soit réellement choquant (l'histoire de la physique est parsemée de découvertes de nouvelles formes de particules et d'énergie), ce n'est pas non plus entièrement satisfaisant tant que matière noire et énergie noire n'auront pas été détectées directement (autrement que par un effet gravitationnel issu d'un ajustement un peu *ad hoc*) et tant que leur nature n'aura pas été identifiée. Toute observation susceptible d'apporter des contraintes supplémentaires, permettant de valider indépendamment ou de falsifier cette interprétation, est importante pour affiner notre compréhension du modèle et de ses paramètres.

1.1.2 Matière noire et énergie noire

Il semble que la première indication de l'existence de matière noire remonte à 1933. Compte tenu de la dispersion de vitesses des galaxies, pour être gravitationnellement liés, les amas doivent avoir une masse totale nettement supérieure à la masse visible (Zwicky 1933). Aujourd'hui, il existe beaucoup d'autres preuves plus ou moins directes de l'existence de matière noire, à la fois baryonique et non baryonique.

Matière noire baryonique

L'explication de la formation des éléments légers par la nucléosynthèse primordiale (BBN) est un grand succès du modèle du Big-Bang. La mesure précise de l'abondance du Deutérium, de l'Hélium 3 et 4, du Lithium 7, donne une mesure du nombre de photons primordiaux par baryon (voir Iocco et al. 2009, pour un article de synthèse récent). On obtient $\eta = n_b/n_\gamma \sim 6.1 \times 10^{-10}$ (contrainte provenant essentiellement du Deutérium). Compte tenu du nombre de photons primordiaux, déduit directement de la température du fond cosmologique, on obtient une contrainte sur la densité de baryons dans l'univers, $\Omega_b h^2 = 0.021 \pm 0.003$. La densité baryonique inférée est environ dix fois supérieure à la densité de baryons directement observables sous forme d'étoiles, de gaz émissif, et de galaxies. Il existe donc de la matière noire baryonique.

Par ailleurs, l'étude des courbes de rotation des galaxies (notamment des galaxies spirales) met en évidence une vitesse de rotation nettement trop élevée à la périphérie, incompatible avec la gravitation classique de Newton ou d'Einstein si seule la matière visible sous forme d'étoiles et de gaz est à l'origine du potentiel gravitationnel (Volders 1959; Rubin et al. 1980; Sofue & Rubin 2001). Pour expliquer les courbes, il faut invoquer l'existence d'un halo sombre de matière, de masse environ dix fois supérieure à la masse visible. Il est intéressant de noter que ce rapport masse visible sur masse invisible est compatible avec l'hypothèse que le halo pourrait être entièrement constitué de baryons, la densité totale en baryons étant alors compatible avec les contraintes issues de la nucléosynthèse primordiale.

La recherche de cette matière noire sous la forme d'objets sombres compacts, résidus stellaires ou étoiles avortées (Paczynski 1986) ayant donné un résultat allant de mitigé à négatif (Palanque-Delabrouille et al. 1998; Alcock et al. 1998; Lasserre et al. 2000; Alcock et al. 2000), il est plausible que la matière noire baryonique se trouve essentiellement sous forme de gaz, soit associé aux galaxies, soit dans la matière extragalactique. Des simulations numériques permettent de prédire la forme et la localisation de ces baryons invisibles (Cen & Ostriker 1999). Les baryons associés aux galaxies pourraient se trouver sous la forme de nuages froids et ténus d'hydrogène et d'hélium neutre, ou de gaz moléculaire froid. Le gaz extragalactique pourrait être du gaz chaud ionisé autour des filaments de la toile cosmique (Combes 2002). Dans les deux cas, ce gaz est assez difficile à détecter.

La mesure du spectre C_ℓ des anisotropies du fond diffus cosmologique permet également de contraindre la densité de l'univers sous forme de baryons. L'interprétation des données issues de cinq années d'observation de l'expérience WMAP (Hinshaw et al. 2009; Dunkley et al. 2009b) implique $\Omega_b h^2 = 0.0227 \pm 0.0006$, en accord avec la contrainte issue de la nucléosynthèse primordiale. Cette contrainte n'a pas changé notablement avec l'analyse de sept années de données (Komatsu et al. 2010).

Matière noire non-baryonique

L'évaluation de la fraction de gaz dans les amas de galaxies indique une fois de plus, de façon assez directe, la présence de matière noire. La masse totale des amas (qui peut être inférée à la fois par dispersion de vitesse des galaxies, par lentille gravitationnelle, ou par mesure de la température du gaz dans le cas d'un modèle hydrostatique), comparée à la masse de baryons (qui peut être mesurée par son émission X ou SZ), indique la présence de matière noire non-baryonique, e.g. un rapport de masse $M_b/M_{\rm tot} \simeq 0.015+0.08h^{-3/2}$, où M_b est la masse baryonique (dont on suppose ici qu'elle est sous forme de gaz chaud essentiellement) et $M_{\rm tot}$ la masse totale. Avec $h \simeq 0.7$, on obtient une fraction de gaz de 15%. Si la teneur en baryons des amas riches est représentative de la teneur en baryons moyenne dans l'univers, on en déduit $\Omega_b/\Omega_m \simeq 0.15$. Avec $\Omega_b \simeq 0.045$, on obtient $\Omega_m \simeq 0.3$. S'il existe une quantité significative de baryons non détectés dans les amas (i.e. de matière noire baryonique n'émettant pas en X), alors $\Omega_b/\Omega_m \geq 0.15$ et $\Omega_m \leq 0.3$ (White et al. 1993). Toutefois, l'interprétation de la mesure de la fraction de baryons de cette façon nécessite une bonne compréhension de la distribution et de l'étendue du gaz dans les amas (voir Sadat & Blanchard 2001). A cet égard, l'effet SZ permet de mesurer de façon indépendante la fraction de gaz de différents amas. Les mesures que nous avons effectuées avec l'instrument Diabolo, présentées au chapitre 2 de ce mémoire, nous ont permis de déterminer la masse de gaz de plusieurs amas à différents décalages spectraux (avec, toutefois, une précision assez modeste).

Un autre argument en faveur de l'existence de matière noire non baryonique est apporté par la formation des structures, difficile, dans le cadre du modèle du Big-Bang, sans invoquer la présence de matière noire non-collisionnelle qui a pu commencer son effondrement gravitationnel avant le découplage photons-baryons. Cette matière noire doit être *froide* (d'énergie cinétique négligeable devant son énergie de masse) pour permettre la formation hiérarchique – petites structures se formant en premier, et fusionnant pour donner les plus grands amas et super-amas observables aujourd'hui.

Ces observations et considérations ont conduit au modèle standard avec matière noire froide (voir Bertone et al. (2005) et références incluses). Bien que non détectée de façon directe aujourd'hui, la matière noire froide pourrait être constituée de particules massives interagissant uniquement faiblement et gravitationnellement, les WIMPs (Weakly Interacting Massive Particles), dont le candidat le plus en vogue est le neutralino. Cette particule est susceptible d'exister s'il existe une famille de particules venant compléter le modèle standard dans le cadre de la supersymétrie, et serait la moins massive des particules supersymétriques (ou LSP, Lightest Supersymmetric Particle), dans la plupart des modèles de supersymétrie. Une autre particule, l'axion (voir Sikivie (2008) pour un article de synthèse récent), dont l'existence a été postulée pour résoudre le problème de la conservation de la symétrie CP dans les

interactions fortes (Peccei & Quinn 1977; Weinberg 1978), a été proposée pour constituer la matière noire non baryonique (Preskill et al. 1983).

Bien que l'existence de ces candidats plausibles soit de nature à conforter l'hypothèse de l'existence de matière noire froide, la détection directe de ces particules, la détermination de leurs masses et sections efficaces de production et d'annihilation, et le calcul de leur abondance et de leur densité dans le cadre du modèle du Big-Bang, sont attendus avec impatience pour confirmer la validité du modèle. Le LHC au CERN, qui vient de redémarrer fin 2009, devrait apporter des éléments de réponse dans cette direction, en mettant en évidence la production de WIMPs à haute énergie. De même, plusieurs projets tentent de mettre en évidence expérimentalement l'existence d'axions, par exemple par leur couplage avec les photons, qui changerait légèrement l'état de polarisation d'un faisceau laser se propageant dans un champ magnétique (Maiani et al. 1986; Andriamonje et al. 2007; Zavattini et al. 2008).

Il convient malgré tout de noter que même si l'existence de ces particules était mise en évidence, il resterait à démontrer qu'elles sont bien les constituants de la matière noire. Dans cette optique, un programme de recherche très actif ambitionne de détecter directement des particules de matière noire supersymétriques (Ahmed et al. 2003; Akerib et al. 2005; Alner et al. 2005; EDELWEISS Collaboration 2009). Les performances de ces 'détecteurs de WIMPs', commencent aujourd'hui à atteindre la zone de sensibilité où l'on peut attendre des détections, selon les modèles les plus raisonnablement optimistes. Les expériences DAMA (Bernabei et al. 2000) et CDMS (The CDMS Collaboration 2009) ont annoncé des détections de signaux compatibles avec l'observation de WIMPs. Toutefois, la détection DAMA n'est (toujours) pas confirmée par les autres expériences (Savage et al. 2009), et la 'détection' CDMS est très marginale (le signal observé pouvant être interprété par le fond de bruit avec une probabilité de 23%). Du côté des axions, L'expérience ADMX tente, pour l'instant sans succès, de détecter directement d'hypothétiques axions de matière noire par le biais de leur transmutation en photons en présence d'un fort champ magnétique (Asztalos et al. 2010).

L'expansion accélérée et l'énergie noire

En supposant correcte la représentation de l'espace-temps par la métrique de FRW, et si la relativité générale décrit correctement la gravitation jusqu'à l'échelle du Gpc, il est possible, à partir de mesures de l'accélération de l'expansion, de déduire l'évolution au cours du temps de la densité d'énergie. Ceci fournit une possibilité pour déterminer la proportion des différents types d'énergie dans l'univers, ou plus précisément, pour ajuster le taux d'expansion avec un modèle faisant intervenir un mélange de différents types d'énergie.

Aujourd'hui, ce sont les supernovae de type Ia qui permettent de mesurer le plus précisément l'expansion (de façon directe), à partir de diagrammes distance de luminosité – décalage spectral. La mesure du taux d'expansion, jusqu'à un décalage spectral de 1 depuis le sol au CFHT et 1,7 depuis l'espace avec le télescope Hubble, permet de mettre en évidence une accélération de l'expansion, interprétée comme une manifestation de la présence d'une énergie dont le paramètre w (dans l'équation d'état $p = w\rho$) est négatif – ou par une constante cosmologique de valeur finie *ad hoc*, déterminée expérimentalement par ces mesures (Astier et al. 2006; Guy et al. 2010).

Notons que l'interprétation des observations des supernovae suppose que celles-ci sont des chandelles 'standardisables' (à défaut d'être parfaitement standard). Les résultats récents de l'expérience SNLS (Guy et al. 2010) sont obtenus avec une analyse très rigoureuse des effets systématiques susceptibles de biaiser la mesure, mais se basent toujours sur une standardisation empirique. Une confirmation indépendante de la mesure de géométrie reste donc très importante pour consolider ces résultats. Une telle confirmation est possible par exemple, avec le test proposé par Alcock & Paczynski (1979), basé sur la recherche d'une asymétrie apparente, dépendente du décalage spectral, de 'sphères standard'.

Dans l'attente d'une telle confirmation, la concordance des différentes mesures actuelles (supernovae, grandes structures, et fond cosmologique), constitue toutefois un élément de nature à conforter l'interprétation en vigueur.

Bilan sur la matière et l'énergie noire

Il est donc établi que si le modèle du Big-Bang est correct dans ses grandes lignes (et notamment, si les effets de la gravitation à grande échelle sont bien décrits par la relativité générale avec une métrique FRW), alors il est impossible d'expliquer les observations sans évoquer l'existence

- de matière noire baryonique, selon les contraintes établies par l'abondance des éléments légers, expliquées par la nucléosynthèse primordiale ;
- de matière noire non collisionnelle (ou peu collisionnelle), structurée, mise en évidence (entre autres) par la fraction de gaz dans les amas (voir section 1.1.4) et par les anisotropies du fond cosmologique (voir sections 1.1.4 et 1.2) ;
- d'une autre forme d'énergie, l'énergie noire, d'équation d'état $p = w\rho$ avec $w < 0$, qui pourrait être l'énergie du vide (ou de façon équivalente une constante cosmologique).

Les interprétations de l'observation des anisotropies du fond diffus cosmologique, dont il sera question tout au long de ce mémoire, se feront dans le cadre d'un modèle qui contient une part inconnue de baryons, de matière noire non baryonique, et d'énergie noire.

1.1.3 Structuration

Au second ordre, l'univers n'est pas complètement homogène et isotrope, comme en témoigne l'existence de structures de tailles diverses : planètes, étoiles, amas d'étoiles, galaxies, amas de galaxies... Ces structures peuvent se former par effondrement gravitationnel de petites inhomogénéités initiales. Dans l'univers primordial, la métrique peut s'écrire :

$$g_{\mu\nu} \simeq g_{\mu\nu}^{FRW} + h_{\mu\nu} \tag{1.1}$$

où $h_{\mu\nu}$ est une correction à la métrique de FRW (petites perturbations). L'étude de la formation des grandes structures (LSS, pour Large Scale Structure) en régime linéaire conduit à résoudre les équations pour les petites perturbations $h_{\mu\nu}$ dans un univers dont l'expansion est gouvernée par l'évolution du facteur d'échelle $a(t)$, et contenant un mélange de matière, de rayonnement, et d'énergie du vide en proportion fixée par le modèle.

De façon générale, les perturbations de la métrique peuvent s'écrire comme la somme de perturbations de type scalaire, de type vecteur, et de type tenseur. Seules les perturbations scalaires et tenseur sont importantes pour l'origine de structures. Les modèles les plus classiques, basés sur une origine inflationnaire des fluctuations de métrique initiales, supposent que les perturbations sont des réalisations de champs aléatoires gaussiens quasi-invariants d'échelle. Les propriétés statistiques de ces champs sont entièrement décrites par leur spectre de puissance. Une description paramétrique de ces spectres de puissance fait apparaître des paramètres d'amplitude ${\Delta_S}^2$ et ${\Delta_T}^2$, des indices spectraux n_S et n_T, et éventuellement des paramètres de correction, e.g. une courbure ou 'running'.

Aux temps récents, le contraste de densité $\delta\rho/\bar{\rho}$ est important, ce qui ne permet plus de résoudre les équations de la gravitation en relativité linéarisée. On suppose néanmoins que le contraste de densité n'induit que des modifications locales de la métrique (qui conserve donc à grande échelle une forme FRW), et donc que l'expansion obéit toujours, à grande échelle, aux équations établies ci-dessus dans le cas d'un univers homogène et isotrope. C'est toutefois là un point qui mérite d'être réexaminé à la lumière des observations de l'expansion accélérée (voir par exemple Kolb et al. 2006; Alnes et al. 2006; Buchert 2008).

1.1.4 Paramètres cosmologiques

La détermination des principaux paramètres du modèle du Big-Bang est l'un des objectifs des travaux présentés dans les chapitres suivants. Le principaux paramètres globaux, dans le cadre du modèle "standard" de Big-Bang inflationnaire, sont :

- paramètres géométriques : constante de Hubble H_0, et son évolution dans le temps $H(t) = \dot{a}/a$, courbure spatiale k (ou de façon équivalente paramètre Ω_k) ;
- constante cosmologique Λ (ou de façon équivalente paramètre de densité d'énergie du vide Ω_Λ) ;
- paramètres de densité : Ω_b, Ω_m, ...
- paramètres "inflationaires" n_S, n_T, $r = {\Delta_T}^2/{\Delta_S}^2$, ou jeu plus complet de paramètres décrivant la statistique des perturbations primordiales ;
- normalisation du contraste de densité σ_8 ;
- paramètres de réionisation : pour un modèle simple à un paramètre, soit la profondeur optique $\tau_{\rm reion}$ ou (pour une réionisation instantanée) décalage spectral de la réionisation $z_{\rm reion}$.

Ces paramètres peuvent être mesurés ou contraints de diverses façons. Nous citons rapidement les principales observations permettant de les contraindre.

Les paramètres géométriques peuvent être mesurés directement par une mesure de distance en fonction du décalage spectral (mesure directe de H_0, $a(t)$, et de la courbure spatiale k), ce qui impose des contraintes sur les paramètres de densité d'énergie sous différentes formes. Ces mesures doivent utiliser soit des objets de taille connue, auquel cas la mesure d'un angle sous-tendu et du décalage spectral donne la distance angulaire $D_A(z)$, soit des objets de luminosité connue, auquel cas la mesure du flux reçu donne la distance de luminosité $D_L(z)$. Des comptages d'objets (galaxies, amas de galaxies) en fonction du décalage spectral donnent une mesure de $D_A(z)$, en supposant que l'on ait un modèle sur l'évolution de la densité d'objets en fonction de z, et que l'on sache gérer les biais dus à la fonction de sélection (e.g. biais de Malmquist). Une discussion sur la constitution d'un catalogue d'amas et son exploitation se trouve au chapitre 2 du présent mémoire.

Certains paramètres de densité peuvent être mesurés ou évalués directement. C'est le cas de la densité de matière visible, $\Omega_{\rm vis}$, de la densité de rayonnement Ω_γ, de la densité de baryons Ω_b (par la nucléosynthèse primordiale), de la quantité de matière totale (par mesure de fraction de gaz dans les structures via leur dynamique). Comme mentionné plus haut (section 1.1), une contrainte sur les différentes formes d'énergie est obtenue par interprétation (via les lois de la gravitation) de la mesure des paramètres géométriques k et $a(t)$ (qui imposent un contenu énergétique compatible avec le géométrie). A défaut de contraintes plausibles sur la valeur de Λ qui proviendraient des prédictions d'énergie du vide en théorie des champs quantiques, la constante cosmologique est un paramètre libre du modèle, dont la valeur est obtenue par la contrainte du paramètre Ω_Λ, à partir de la mesure du taux d'expansion au cours du temps et de son impact sur la formation des structures.

La mesure des paramètres inflationnaires n_S, n_T, $r = {\Delta_T}^2/{\Delta_S}^2$ n'est pas directement possible, puisque l'on ne peut pas observer directement les perturbations à l'issue de l'inflation. Leur détermination nécessite donc d'interpréter des observations 'tardives' (fond diffus cosmologique et grandes structures). Les paramètres n_S, r et éventuellement n_T peuvent être contraints à partir de l'observation du fond cosmologique (Knox 1995). La normalisation du contraste de densité, σ_8, est quant-à-elle mesurable à partir de relevés de galaxies, de l'observation du spectre de puissance de l'effet SZ thermique, ou encore par l'interprétation de la mesure des anisotropies du fond cosmologique.

Enfin, l'historique de réionisation est possible soit par l'observation directe d'absorption par l'hydrogène neutre dans le spectre de quasars lointains (Gunn & Peterson 1965), soit par la mesure de la polarisation du fond cosmologique à grande échelle (Zaldarriaga 1997).

De façon générale, la mesure du spectre d'anisotropies du fond cosmologique C_ℓ permet de contraindre fortement les paramètres cosmologiques dans le cadre du modèle de Big-Bang inflation-

naire “standard” (Jungman et al. 1996). Ceci est l'un des objectifs majeurs de la mission spatiale Planck, dont il est question au chapitre 3. La section 1.2 décrit la physique du CMB et donne un état des lieux sur le plan théorique et observationnel.

Pour conclure cette section, mentionnons pour référence que les données issues de sept années d'observation du fond cosmologique avec la mission WMAP, en tenant compte des contraintes indépendantes apportées par différentes mesures astrophysiques, sont compatibles avec un modèle de Big-Bang inflationnaire ‘de concordance’, dont les principaux paramètres ont les valeurs suivantes : $h = 0.704^{+0.013}_{-0.014}$, $0.013 < 1 - n_s < 0.061$ (à 95% de niveau de confiance), $\Omega_b = 0.0456 \pm 0.0016$, $\Omega_c = 0.227 \pm 0.014$, $\Omega_\Lambda = 0.728^{+0.015}_{-0.016}$, $\tau = 0.087 \pm 0.014$, $\sigma_8 = 0.809 \pm 0.024$.

WMAP place une limite assez peu contraignante sur le rapport $r = T/S$, de $r \leq 0.36$ (à 95% de niveau de confiance, pour un modèle avec un seul indice spectral n_s ne dépendant pas de l'échelle, c'est à dire sans ‘running’).

1.2 Le fond de rayonnement cosmologique

Si l'on suppose correct le modèle général du Big-Bang, il a existé, par le passé, une phase chaude et dense pendant laquelle l'univers était ionisé. La transition au cours de laquelle la matière est passée de l'état plasma à l'état gazeux (hydrogène et hélium neutre essentiellement) s'est accompagnée de l'émission des photons primordiaux qui constituent aujourd'hui le rayonnement fossile. Avant cette ‘recombinaison’ des noyaux avec les électrons, l'Univers ionisé était opaque au rayonnement. Fortement couplés aux baryons, les photons s'opposaient à l'effondrement gravitationnel des structures, par pression de radiation. Au moment de la recombinaison, le libre parcours moyen des photons devient plus grand que l'horizon de l'univers observable. Les photons deviennent libres de se propager, nous apportant avec eux une image de l'univers au moment de la recombinaison. Sans la pression radiative pour s'opposer à l'effondrement gravitationnel, les structures de matière baryonique deviennent libres de se former dans les puits de potentiel formés par les petites inhomogénéités de densité. Ces inhomogénéités présentes au moment du découplage induisent des fluctuations de la brillance du fond cosmologique (Sachs & Wolfe 1967; Silk 1968; Peebles & Yu 1970), dont l'observation et l'analyse font l'objet de l'essentiel des travaux exposés dans ce mémoire.

1.2.1 Formation des perturbations

Anisotropies primaires

La formation des anisotropies primaires suppose l'existence de perturbations initiales de la métrique (voir section 1.1.3). De telles perturbations sont prédites dans le contexte des modèles de Big-Bang avec une phase d'inflation, pour lesquelles on postule l'existence d'une phase d'expansion accélérée dans l'univers primordial (voir par exemple Liddle & Lyth 2000). Les fluctuations quantiques amplifiées par l'expansion rapide durant la phase inflationnaire constituent les perturbations initiales à l'origine des structures. Pour la grande classe générique de modèles d'inflation à roulement lent (slow roll) à un champ scalaire unique ϕ décrit par un potentiel $V(\phi)$, on définit deux paramètres de roulement lent, ϵ et η :

$$\epsilon = \frac{m_{\rm Pl}^2}{16\pi} \left(\frac{V'}{V}\right)^2 \tag{1.2}$$

$$\eta = \frac{m_{\rm Pl}^2}{8\pi} \frac{V''}{V} \tag{1.3}$$

où V' et V'' sont respectivement la dérivée première et la dérivée seconde du potentiel par rapport à ϕ. L'hypothèse de roulement lent correspond à une variation lente de V avec ϕ, et donc à de petites valeurs de ϵ et η. Dans le cadre de ces modèles, les indices spectraux scalaires et tenseur n_S et n_T, ainsi que le rapport scalaire sur tenseur r, sont donnés par

$$n_S = 1 - 6\epsilon + 2\eta \tag{1.4}$$

$$n_T = -2\epsilon \tag{1.5}$$

$$r \simeq 12\epsilon \tag{1.6}$$

La détermination observationnelle des paramètres n_S, n_T et r permet de valider (ou d'invalider) ce type de scénario en vérifiant la quasi-invariance d'échelle des perturbations scalaires ($n_S \simeq 1$), l'existence de perturbations de type tenseur (i.e. d'ondes gravitationnelles primordiales) si $r \neq 0$, et en vérifiant la relation de consistence $r \simeq -6n_T$. Si n_S peut être mesuré précisément à partir de la mesure du spectre de température des anisotropies (Knox 1995), éventuellement complétée par la mesure du spectre des fluctuations de densité des grandes structures, obtenu à partir des grands relevés de galaxies ou à partir de l'observation de la 'forêt Lyman alpha', la mesure de la polarisation du fond cosmologique offre probablement les meilleures perspectives pour contraindre r, et éventuellement contraindre n_T. Ceci, toutefois, constitue un gros défi observationnel, notamment en présence d'émissions polarisées d'avant plan. La mesure de r à partir de l'observation de la polarisation du fond cosmologique, et la séparation de composantes polarisées, font l'objet de travaux présentés à la fin du chapitre 5.

Les perturbations scalaires évoluent au cours du temps. Les détails de cette évolution dépendent de la nature (de la composition) des perturbations. Dans un scénario standard, on suppose que les perturbations initiales sont adiabatiques (rapport de densité constant entre les différentes espèces). Les perturbations évoluent, entre la fin de l'inflation et le découplage, sous l'action combinée de l'attraction gravitationnelle et de la pression de radiation. Ceci engendre des oscillations acoustiques dans le plasma, dont la période dépend de la taille physique des perturbations, et dont l'amplitude dépend du rapport baryons/photons et de l'amplitude des puits de potentiel de matière noire. La relation entre le spectre des perturbations au moment du découplage et le spectre initial est donnée par la fonction de transfert T_k, qui peut être calculée pour différents types de perturbations (e.g. adiabatique, isocourbure).

Au moment du découplage, les anisotropies de température primaires découlent de la combinaison de trois effets :

- la température intrinsèque de la zone d'émission, qui dépend de la densité au point émetteur ;
- un décalage Sachs-Wolfe, décalage gravitationnel de la fréquence des photons émis ;
- un décalage Doppler, dû à la vitesse particulière de la zone émettrice.

Des codes numériques comme COSMICS (Bertschinger 1995), CMBFAST (Seljak & Zaldarriaga 1996), CAMB (Lewis et al. 2000) et CMBEASY (Doran 2005) permettent de résoudre les équations gouvernant l'évolution des structures dans l'univers primordial, puis de calculer l'effet géométrique de leur observation. Ces codes permettent de calculer avec une précision de l'ordre d'une fraction de pour cent le spectre des anisotropies, en température et en polarisation, pour un jeu de paramètres cosmologiques donné. La précision du calcul de l'observable (ici spectre de puissance des anisotropies) en fonction des paramètres d'intérêt (paramètres cosmologiques) est cruciale pour résoudre le problème inverse (détermination des paramètres d'intérêt à partir des observations). Toutefois, les codes de Boltzmann ne permettent de simuler qu'un aspect des observations. En réalité, l'observable est l'émission du ciel (incluant les émissions d'avant plan) telle qu'observée par un instrument. Dans l'optique d'intégrer ces aspects à l'analyse des données, il convient tout d'abord de pouvoir modéliser toutes les émissions du ciel. C'est là l'objectif du Planck Sky Model (PSM), dont il est question au chapitre 6. La simulation de certains aspects de l'observation du ciel avec la mission spatiale Planck fait l'objet d'une partie du travail présenté au chapitre 3.

Anisotropies secondaires

Si l'on fait exception du décalage spectral lié à l'expansion, les photons du fond cosmologique interagissent peu lors de leur parcours depuis le découplage. Les exceptions les plus notables sont l'effet Sachs-Wolfe intégré (ISW), les lentilles gravitationnelles, l'effet Sunyaev-Zel'dovich (SZ), et la rediffusion des photons suite à la réionisation.

L'effet Sachs-Wolfe intégré est le décalage spectral subi par les photons du fond cosmologique par effet gravitationnel lors de leur trajet depuis la dernière diffusion, en présence de structures dont le potentiel gravitationnel varie (assez rapidement) au cours du temps (Sachs & Wolfe 1967; Rees & Sciama 1968; Kofman & Starobinskii 1985). Un effet significatif est attendu dans le cas de très grandes structures pour lesquelles l'expansion accélérée l'emporte sur l'effondrement gravitationnel, ce qui engendre un décalage spectral vers les hautes fréquences, i.e. une fluctuation de température $\Delta T > 0$ (Crittenden & Turok 1996).

Les structures plus petites (à l'échelle des amas de galaxies) perturbent la trajectoire des photons, en provenance de la surface de dernière diffusion, par effet de lentille gravitationnelle (Seljak 1996). Le champ de cisaillement perturbe le fond cosmologique aux petites échelles, en température et polarisation. De même, la présence d'éventuels défauts topologiques dans l'univers est susceptible de générer des anisotropies en température (Kaiser & Stebbins 1984; Crittenden & Turok 1995) et en polarisation (Garcia-Bellido et al. 2010), même s'il est désormais établi, par la gaussianité des fluctuations de température du fond cosmologique et la forme du spectre C_ℓ, que les défauts topologiques ne peuvent être à l'origine de l'essentiel des anisotropies observées (Bevis et al. 2004).

L'effet Sunyaev Zel'dovich (Sunyaev & Zeldovich 1972), diffusion Compton inverse des photons du fond cosmologique sur le gaz chaud d'électrons présent notamment au coeur des amas de galaxies, fait l'objet des travaux présentés au chapitre 2.

Enfin, la réionisation du gaz par le rayonnement des premières étoiles a pour effet premier de rediffuser partiellement, à bas décalage spectral ($z \leq 10$), les photons primordiaux. Ceci a pour effet de lisser les anisotropies de température aux petites échelles, et de générer notamment ainsi une anisotropie de polarisation à grande échelle (Sugiyama et al. 1993; Kaplinghat et al. 2003).

1.2.2 Description et statistique

Le couplage fort matière-rayonnement dans l'univers primordial implique l'équilibre thermodynamique local. Ceci permet la définition, en tout point $\boldsymbol{x}$ de l'espace au moment du découplage, d'une température $T(\boldsymbol{x})$. L'intensité spécifique du rayonnement en provenance de ce point suit, à l'émission, une loi de corps noir à la température $T(\boldsymbol{x})$. Pour un univers homogène à grande échelle, $T(\boldsymbol{x})$ varie peu en fonction de $\boldsymbol{x}$. La température moyenne au moment de la dernière diffusion est de l'ordre de 3000 K.

Lors de la propagation du rayonnement dans l'univers en expansion, la distribution des photons reste celle d'une loi de Planck, mais la température décroît proportionnellement à l'inverse du facteur d'échelle $a(t)$. Le fond cosmologique est observé à une température moyenne de $T_0 = 2,725\,\mathrm{K}$ (Mather et al. 1999). En un point du ciel donné, repéré par des coordonnées (θ, ϕ), on observe une température $T(\theta, \phi) = T_0 + \Delta T(\theta, \phi)$.

Les propriétés statistiques de $\Delta T(\theta, \phi)$ sont une mine d'information pour la cosmologie, puisqu'elles dépendent fortement des paramètres du modèle. On peut décomposer un champ ΔT en harmoniques sphériques :

$$\Delta T(\theta, \phi) = \sum_{\ell=0}^{\infty} \sum_{m=-\ell}^{\ell} a_{\ell m} Y_{\ell m}(\theta, \phi) \tag{1.7}$$

Les harmoniques sphériques $Y_{\ell m}$ sont les fonctions de base de cette décomposition, qui est unique. Si l'on considère ΔT comme un champ aléatoire, les moments d'ordre 2 des coefficients a_{lm} définissent le spectre de puissance C_ℓ du champ ΔT. Pour un champ gaussien, stationnaire, le spectre de puissance décrit de façon exhaustive la statistique des fluctuations. On a :

$$\mathrm{E}(a_{\ell m} a^*_{\ell' m'}) = C_\ell \, \delta_{\ell\ell'} \, \delta_{mm'} \tag{1.8}$$

où E(.) dénote l'espérance mathématique. A noter que le spectre C_ℓ correspond à une moyenne d'ensemble (et non pas à une moyenne à ℓ donné des $|a_{\ell m}|^2$ du ciel observé, qui n'en est qu'un estimateur). Les codes CMBFAST et CAMB donnent la forme du spectre C_ℓ en fonction des paramètres cosmologiques (H_0, Ω_b, Ω_{cdm}, Ω_k, Λ, n_S, n_T, r, ...). La comparaison du modèle avec le spectre estimé à partir des observations permet de contraindre ces paramètres. En pratique, il est possible de construire des estimateurs du spectre à partir de l'observation d'une réalisation (un ciel unique) en faisant des hypothèses d'isotropie (C_ℓ ne dépend pas de m), et éventuellement de continuité et régularité de la courbe des C_ℓ. Ces estimateurs, toutefois, sont nécessairement entachés d'erreurs en raison de la taille finie de l'échantillon analysé. La mesure du spectre C_ℓ du fond diffus en présence de bruit inhomogène et de couverture partielle fait l'objet d'une section du chapitre 5.

Les harmoniques sphériques sont bien adaptées à la représentation d'un champ aléatoire gaussien stationnaire. Dans le cadre du modèle de Big-Bang standard, l'isotropie de l'univers à grande échelle implique la stationnarité du champ, et l'origine inflationnaire des perturbations implique la gaussianité des fluctuations de température. L'observation du CMB, toutefois, implique des bruits et de contaminations astrophysiques qui ne sont pas nécessairement stationnaires. L'analyse des observations, pour cette raison, doit être localisée sur la sphère pour être optimisée.

Il est possible de décomposer un champ sphérique sur d'autres systèmes de fonctions que les harmoniques sphériques. Au chapitre 5, nous considérons pour la séparation de composante et pour l'estimation spectrale la décomposition de cartes sphériques sur un frame tendu d'ondelettes. La représentation par frame est redondante, ce qui présente potentiellement aussi un intérêt pour le débruitage. Elle est localisée dans l'espace des pixels, ce qui est bien adapté au traitement des problèmes liés à la présence d'émissions d'avant plan localisées dans le plan de la galaxie. Elle est localisée dans l'espace harmonique, ce qui est adapté à l'estimation d'un spectre de puissance qui varie lentement en fonction de ℓ.

Notons enfin qu'avec la mesure de plus en plus précise du spectre des anisotropies, l'attention se tourne vers la recherche de (petites) signatures non-gaussiennes, susceptibles de permettre la distinction entre différents modèles inflationnaires (voir Komatsu et al. (2005) et références incluses).

1.2.3 Polarisation

Le fond diffus cosmologique acquiert une polarisation par diffusion Compton. La section efficace Compton étant proportionnelle au carré du produit scalaire des champs incident et diffusé, une (petite) anisotropie quadrupolaire de l'intensité du rayonnement incident au niveau de la région de diffusion engendre une (petite) polarisation linéaire du rayonnement diffusé.

La description d'une polarisation linéaire se fait au moyen des paramètres de Stokes I, Q, U. Il n'est pas fait état, dans le présent mémoire, de polarisation circulaire (paramètre de Stokes V), pour deux raisons : d'une part ce type de polarisation n'est pas créé lors de la dernière diffusion ; d'autre part, les détecteurs utilisés pour l'observation du CMB avec Archeops et Planck ne sont pas sensibles à une polarisation circulaire.

Le champ de polarisation sur la sphère se comporte comme un champ de spin 2 (une rotation des axes d'un angle θ correspond à une rotation d'un angle 2θ des composantes Q et U de la polarisation).

L'analyse de la polarisation en harmoniques sphériques du champ de polarisation se fait avec des harmoniques sphériques de spin 2. Cette analyse fait apparaître deux champs distincts, le champ de polarisation E (champ de parité paire), et le champ de polarisation B (champ de parité impaire), décrits chacun par son spectre de puissance. Les modes primordiaux de type scalaire et tenseur contribuent aux anisotropies de température et à la polarisation de type E, et donc aux spectres C_ℓ^{TT} et C_ℓ^{EE}. Seuls les modes tenseurs contribuent au spectre de puissance C_ℓ^{BB}.

La préparation de la mesure de polarisation avec la mission Planck fait l'objet d'une partie des travaux exposés au chapitre 3.

1.2.4 Observation des anisotropies

Principales expériences

La recherche, puis l'observation de plus en plus précise, des anisotropies du fond cosmologique, a fait l'objet d'un effort observationnel très conséquent au cours des quarante dernières années. Parmi les expériences les plus marquantes, on note trois missions spatiales (COBE, WMAP et Planck), plusieurs ballons stratosphériques (notamment Archeops, Boomerang, et MAXIMA), plusieurs interféromètres (CBI, VSA), et des expériences bolométriques au sol (ACBAR, ACT, QUaD, SPT). Les expériences Planck et Archeops font l'objet d'une partie des travaux présentés dans ce mémoire (chapitres 3 et 4 respectivement).

Émissions d'avant-plan

Le maximum d'émission des fluctuations de température du fond se trouve à 143 GHz (longueur d'onde de 2 mm environ). C'est donc dans le domaine millimétrique que se font les observations – typiquement entre 1 mm et 1 cm. A ces longueurs d'onde, d'autres processus d'émission contribuent à l'émission totale du ciel. Le milieu interstellaire diffus, notamment, émet par l'intermédiaire de plusieurs processus d'émission. La séparation des différentes émissions est un des problèmes les plus cruciaux pour l'exploitation des observations. Pour cela, les expériences récentes utilisent des stratégies d'observation et d'analyse s'appuyant sur des données multifréquence, et exploitant la diversité des lois d'émission correspondant aux différents processus mis en jeu. Le chapitre 5 est consacré à ce problème et à différentes méthodes pour séparer les différentes composantes contribuant à l'émission totale du ciel.

Projets actuels et futurs

La mission Planck a déjà achevé son programme nominal de 14 mois d'observation. Le satellite continue à prendre des données jusqu'à l'épuisement de l'hélium 3 servant au refroidissement des détecteurs de l'expérience HFI. Simultanément, plusieurs programmes observationnels ambitionnent de pousser plus loin les limites de notre connaissance du fond cosmologique selon deux axes principaux : haute résolution angulaire, et polarisation. Dans les deux cas, les instruments comprennent un grand nombre de détecteurs ultra-sensibles, ceci représentant un saut de technologie très significatif par rapport aux expériences de génération précédente, où le nombre de détecteurs est plutôt de quelques dizaines.

Sur le plan de la haute résolution angulaire, les instruments les plus performants aujourd'hui sont SPT, installé au pôle sud (Ruhl et al. 2004; Carlstrom et al. 2009), et ACT, dans le désert de l'Atacama au Chili (Kosowsky 2003; Swetz et al. 2010). Ceux-ci observent le ciel avec un à plusieurs milliers de détecteurs bolométriques 'Transition Edge' dans quelques bandes de fréquence centrées sur les fenêtres

de transmission atmosphérique (150 et 220 pour SPT, 148, 218 et 277 GHz pour ACT). La résolution typique des observations est de 0,5 à 1 minute d'arc pour SPT, et environ 1 à 1,5 minutes d'arc pour ACT. Les caractéristiques de ces expériences les destinent non seulement à la mesure du spectre C_ℓ à petite échelle, mais aussi aux anisotropies secondaires (effet SZ) et à l'observation à basse fréquence de sources compactes radio et infrarouge, ainsi que des anisotropies du fond de rayonnement infrarouge émis par les premières galaxies.

En ce qui concerne la polarisation, l'objectif principal sera la recherche, aux plus grandes échelles, du spectre des modes B. Ceci fait l'objet d'une discussion succincte au Chapitre 5, et fait partie des perspectives dont il est fait mention au Chapitre 7. En attendant une future mission spatiale, plusieurs expériences sol ou ballon mesurent les modes E de polarisation, et ambitionnent de mettre des limites sur les modes B d'origine primordiale. Les mesures récentes des spectres de polarisation avec les instrument QUaD (Hinderks et al. 2009; Brown et al. 2009) et BICEP (Chiang et al. 2009) sont compatibles avec le modèle de cosmologie standard.

Parmi les instruments dont on attend les observations pour un futur proche, outre la mission Planck, notons les projets ballon EBEX (Reichborn-Kjennerud et al. 2010), PIPER (Chuss et al. 2010), SPIDER (Crill et al. 2008), qui visent la détection des modes B primordiaux d'origine tensorielle. A haute résolution angulaire, des versions polarisées de ACT (Niemack et al. 2010) et de SPT (McMahon et al. 2009) sont en cours de développement. Ces dernières expériences sont notamment appropriées pour mesurer les modes B de polarisation d'origine scalaire, dus à l'effet de lentille gravitationnelle sur les modes primordiaux de type E.

Le laboratoire APC est plus ou moins impliqué dans la plupart de ces expériences dédiées à la mesure de la polarisation du fond cosmologique. Il prend également une part active dans le développement de l'interféromètre bolométrique QUBIC (The QUBIC collaboration et al. 2010) et dans la conception et la proposition d'une mission spatiale de quatrième génération.

Chapitre 2

Amas de galaxies et effet SZ

2.1 L'effet Sunyaev-Zel'dovich

L'effet Sunyaev-Zel'dovich (Sunyaev & Zeldovich 1972), interaction des photons du fond cosmologique avec un gaz d'électrons, est une redistribution de la fréquence des photons du CMB par interaction Compton inverse. On distingue classiquement deux effets principaux : l'effet thermique, qui correspond à l'interaction avec un gaz d'électrons thermalisé et chaud, et l'effet cinétique, dû à l'interaction des photons du CMB avec un gaz d'électrons en mouvement par rapport au flot de Hubble. A ces deux effets viennent s'ajouter des effets polarisés, d'amplitude typique notablement plus faible.

2.1.1 Effet SZ thermique

Dans le cas thermique, la population d'électrons est caractérisée par une distribution de Fermi à une température électronique T_e nettement supérieure à la température du fond cosmologique. De telles conditions se trouvent notamment au sein des amas de galaxies, pour lesquels la température du gaz peut atteindre 1-10 keV. L'effet s'écrit, pour des électrons non relativistes (ou faiblement relativistes) :

$$\delta I_\nu = y\, f(\nu)\, B_\nu(T_{\rm CMB}) \tag{2.1}$$

où $B_\nu(T_{\rm CMB})$ est la loi de corps noir du fond diffus cosmologique, $f(\nu)$ une fonction de la fréquence qui ne dépend pas des paramètres physiques de la population d'électrons (donc de l'amas de galaxies), et y, paramètre de Comptonisation, est proportionnel à l'intégrale le long de la ligne de visée de la densité électronique n_e multipliée par la température du gaz d'électrons :

$$y = \int \frac{kT_e}{m_e c^2}\, n_e \sigma_T\, dl \tag{2.2}$$

Pour un amas typique détectable en SZ avec les instruments actuels, $T_e \simeq 5$ keV, $\tau \simeq 10^{-2}$, $y \simeq 10^{-4}$, et le paramètre de Comptonisation SZ intégré, $Y_{\rm SZ}$, est de l'ordre de 10^{-4} arcmin^2 pour un amas de taille angulaire typique 1 minute d'arc.

2.1.2 Effet SZ cinétique

Dans le cas cinétique, les photons du CMB interagissent avec un gaz d'électrons (chaud ou non) en déplacement. Cette interaction a pour effet de décaler spectralement la distribution des photons

vus par un observateur terrestre :

$$\delta I_\nu = -\beta_r \tau \left[\frac{\partial B_\nu(T)}{\partial T}\right]_{T=T_{\rm CMB}} \tag{2.3}$$

où $\tau = \int n_e \sigma_T \, dl$ est l'épaisseur optique du gaz. Les deux effets sont visibles préférentiellement dans la même gamme de longueur d'onde que le fond diffus, du centimétrique au submillimétrique. Les vitesses particulières typiques sont de l'ordre de 300 km/s ($\beta_r \simeq 10^{-3}$), ce qui implique, pour $\tau \simeq 10^{-2}$, un effet SZ cinétique de $\Delta T/T \sim 10^{-5}$.

2.1.3 Intérêt pour l'étude des amas et la cosmologie

L'observation de l'effet Sunyaev-Zel'dovich dans les amas de galaxies présente un intérêt scientifique à plusieurs titres. Du point de vue de la cosmologie, cette observation confirme la présence du rayonnement de corps noir dans les amas de galaxies lointains, en accord avec le modèle du Big-Bang et l'origine cosmologique du rayonnement. Du point de vue de l'étude des amas, la mesure de l'effet SZ thermique offre une évaluation quasi directe de la masse totale de gaz, puisque le paramètre y est directement proportionnel à la densité électronique n_e. Par comparaison, l'émission X du gaz, qui est un rayonnement de freinage des électrons sur les noyaux présents dans le gaz ionisé, est proportionnelle au produit de la densité en électrons et de la densité en ions, donc de n_e^2. La mesure de la masse de gaz en X nécessite donc de modéliser la distribution des électrons dans l'amas. Elle est sensible, notamment à la présence d'inhomogénéités ou de sous-structures.

L'effet SZ cinétique, dont l'amplitude est directement proportionnelle à la vitesse radiale de l'amas par rapport à l'observateur, est probablement la meilleure observable pour mesurer la vitesse particulière des amas de galaxies par rapport au flot de Hubble, et donc déterminer les propriétés du champ des vitesses à grande échelle. La contamination des mesures de SZ cinétique par le CMB primordial, de même loi d'émission, constitue toutefois une difficulté majeure pour la réalisation de ces observations. Pour une mission comme Planck, la résolution de 5 minutes d'arc ne permet pas de bien distinguer les amas. Des observations avec une sensibilité de l'ordre du μK, et une résolution suffisante pour résoudre les amas de petite taille angulaire (i.e. une résolution inférieure à la minute d'arc), seraient nécessaire pour tirer parti de cette possibilité, un filtrage spatial permettant alors d'isoler assez efficacement le SZ cinétique des anisotropies primaires, fortement atténuées à ces échelles.

En adjoignant aux observations SZ un suivi optique et/ou X, il est possible
- de mesurer la fraction de gaz de l'amas, et de contraindre Ω_b/Ω_m ; compte tenu des contraintes sur Ω_b issues de la mesure de l'abondance des éléments légers, interprétée au moyen de la nucléosynthèse primordiale, on en déduit la valeur de Ω_m ; si l'on suppose que l'univers est spatialement plat ($k = 0$), on en déduit que celui-ci ne peut pas être constitué exclusivement de matière ;
- de mesurer la distance diamètre-angulaire de l'amas ; il est nécessaire pour cela de mesurer le profil de densité (en supposant une symétrie sphérique pour un amas relaxé), et donc de résoudre l'amas ; en déduisant n_e et T_e des observations SZ (et éventuellement X), on peut déduire la longueur de la ligne de visée à travers l'amas, ce qui donne la distance diamètre-angulaire en comparant à la taille apparente de l'amas ;
- d'obtenir, en combinant la mesure de distance diamètre-angulaire à une mesure du décalage spectral z (par suivi optique), des contraintes sur le taux d'expansion en fonction de z, et donc sur H_0, mais aussi Ω_m et Λ.

Plusieurs contraintes sur H_0 ont été obtenues de cette façon dans les 20 dernières années (Birkinshaw et al. 1984, 1991; Jones et al. 1993; Grainge et al. 1993; Birkinshaw & Hughes 1994; Herbig et al. 1995; Carlstrom et al. 1996; Tsuboi et al. 1998; Reese et al. 2000; Grainge et al. 2002). Ces mesures

ne sont toutefois pas, pour l'instant, compétitives avec les autres contraintes de H_0, notamment la mesure directe avec le télescope Hubble (Freedman et al. 2001). Elles offrent, toutefois, une bonne opportunité de vérifier la cohérence des observations et de leur interprétation dans le cadre du modèle cosmologique standard.

Par ailleurs, le nombre d'amas de masse M au décalage spectral z dépend du scénario de formation de structures, qui dépend lui-même des paramètres cosmologiques. La constitution d'un catalogue d'amas permet donc de contraindre notamment les paramètres σ_8, Ω_m, Ω_Λ. Les ingrédients nécessaires pour l'interprétation du catalogue sont :

- une fonction de masse $dN(M,z)/dMdz$, qui modélise le nombre d'amas attendus en fonction de la cosmologie, et qui peut être obtenue soit à partir de la statistique des pics de densité d'un champ gaussien (à trois dimensions) représentant les perturbations de densité à grande échelle (Press & Schechter 1974; Sheth et al. 2001), soit à partir de simulations numériques (Jenkins et al. 2001) ;
- la fonction de sélection de l'instrument (et de la méthode d'extraction des amas), dont il est question plus amplement section 2.3 et dans la publication reproduite page 81.

L'une des difficultés du comptage d'amas en fonction de la masse et du décalage spectral réside en la difficulté d'accéder à la masse totale M d'un amas. La section 2.4 discute de cette question, et contribue à établir la correspondance qui relie les paramètres directement observables (dont le paramètre de comptonisation intégré $Y_{\rm SZ}$ à la masse de l'amas observé).

Les comptages d'amas sur le ciel dépendent par ailleurs de la conversion volume comobile $\rightarrow$ $d\Omega dz$, qui dépend de la distance diamètre-angulaire $D_A(z)$ et du paramètre d'échelle $a(z)$. Au final, le comptage d'amas, toutefois, ne fournit pas des contraintes équivalentes à une mesure de distance-diamètre angulaire, puisque les comptages dépendent aussi de l'historique de la formation des amas (d'autant plus efficace, donc rapide, que Ω_m est grand).

2.2 Observations avec Diabolo

Diabolo est (ou plutôt, était, puisqu'il n'est plus opérationnel aujourd'hui dans la mesure où les instruments récents dédiés à la même physique sont désormais bien plus performants) un petit instrument à deux voies bolométriques, dédié à l'observation du fond diffus cosmologique, et notamment des anisotropies secondaires engendrées par effet SZ. Diabolo observe le ciel dans deux longueurs d'onde centrées autour de 1.2 et 2.1 mm (soit 250 et 143 GHz), longueurs d'onde correspondant à deux fenêtres de transmission atmosphérique. Entre 1995 et 1997, Diabolo a été installé consécutivement au téléscope MITO en Italie (Benoît et al. 2000), au télescope POM 2 sur le plateau de Bure, et au foyer de l'antenne de 30 m de l'IRAM située au pico Veleta en Espagne.

A l'antenne de 30 m, l'instrument permet des observations avec une résolution de 20 à 30 secondes d'arc. Si la résolution est remarquable, la sensibilité est assez modeste – de l'ordre de 25 et 12 mK.s$^{1/2}$ pour les observations effectuées en 1995, à comparer avec la sensibilité d'Archeops, dont il est question au chapitre 4 (220, 190 et 740 μK.Hz$^{-1/2}$, c'est à dire 0.15, 0.13, et 0.52 mK.s$^{1/2}$, respectivement pour les canaux à 143, 217, et 545 GHz, selon les mesure prises lors du vol test à Trapani (Benoît et al. 2002)). Pour cette raison, Diabolo n'est pas très performant pour la mesure d'anisotropies primaires. Par contre, il est adapté à l'observation d'amas dont la taille typique correspond à la résolution de l'instrument (i.e. de l'ordre de 30 secondes d'arc), et a permis des mesures compétitives de l'effet SZ en direction de quelques amas de galaxies.

J'ai participé à deux campagnes d'observations effectuées à l'antenne de 30m de l'IRAM en Espagne entre 1996 et 1998. Deux publications, décrivant les résultats obtenus à partir des mesures effectuées, sont reproduites en annexe A, page 61 et page 77.

Au moment où nous avons collecté et analysé ces données, relativement peu de détections SZ étaient disponibles. Les plus sensibles étaient obtenues par interférométrie radio, l'interférométrie permettant une excellente résolution spatiale, et les mesures étant assez peu contaminées par l'émission atmosphérique.

En ce qui concerne les observations bolométriques, l'expérience SuZie (Holzapfel et al. 1997b) avait observé l'amas A2163, et déduit une contrainte (assez modeste) sur H_0 en combinant cette mesure à la mesure X du satellite *ROSAT* : $H_0 = 78^{+60}_{-40}$ km s^{-1} Mpc^{-1} (Holzapfel et al. 1997a). L'une des difficultés pour la mesure du SZ avec des bolomètres au sol est la nécessité d'une atmosphère à faible teneur en vapeur d'eau, afin de minimiser le bruit d'origine atmosphérique. Ce bruit atmosphérique provient des fluctuations du niveau d'émission de l'atmosphère, qui proviennent elles-mêmes d'inhomogénéités de composition et/ou de température, et éventuellement de colonne densité totale, le long de la ligne de visée au cours des observations. Ces fluctuations peuvent être, à l'origine, des instabilités atmosphériques (fluctuations en fonction du temps, par exemple en raison de nuages poussés par le vent), ou des inhomogénéités stables dans le temps, mais dépendant de la ligne de visée, et donc du temps pour des observations dans lesquelles le pointage varie au cours du temps.

Par ailleurs, les erreurs d'estimation de H_0 avec un amas unique doivent tenir compte d'incertitudes dans la modélisation et les propriétés spécifiques de l'amas (asphéricité, structuration du gaz, confusion, effet SZ cinétique).

2.2.1 Mesure de l'effet SZ de A665, A2163 and CL0016+16

La première des publications jointes en annexe, *Observations of the Sunyaev-Zel'dovich effect at high angular resolution towards the galaxy clusters A665, A2163 and CL0016+16*, parue dans New Astronomy en 1998 et reproduite ici page 61, présente l'observation de trois amas massifs connus (et une limite supérieure pour un quatrième amas, A2218). En supposant les amas isothermes (de température T_e), la mesure de $Y_{\rm SZ}$ avec Diabolo permet de contraindre la masse de gaz de chacun de ces amas indépendamment des estimées obtenues par des mesures de flux en X (par contre, le spectre ROSAT-ASCA est utilisé pour obtenir une estimation de la température électronique). Mon rôle dans ce travail a consisté à participer à la sélection des amas observés, à la préparation de demande de temps, à la prise de données sur site, et à la rédaction de la publication présentant les résultats de l'analyse.

La mesure de $Y_{\rm SZ}$ avec Diabolo est de sensibilité modeste (détections au niveau de 3-4 σ), et la contrainte sur la masse de gaz dépend par ailleurs des paramètres cosmologiques (la masse de gaz est proportionnelle au carré du diamètre distance angulaire $D_A(z)$). Nos observations, qui datent d'avant 1998, sont interprétées en supposant $k = 0$ (univers spatialement plat), $h = 0.5$, $\Omega_m = 1$ et $\Lambda = 0$. Pour une valeur actuelle des paramètres cosmologiques, $h = 0.72$, $\Omega_m = 0.3$ et $\Omega_\Lambda = 0.7$, compte tenu des décalages spectraux des amas, les masses de gaz inférées doivent être divisées par des facteurs de 1,41 pour CL0016+16, 1,73 pour A2163, et 1,76 pour A665.

L'estimation de la masse de gaz obtenue suppose par ailleurs les amas isothermes. Cette approximation semble confirmée pour CL0016+16 (Worrall & Birkinshaw 2003), avec toutefois une température (mesurée avec EPIC sur XMM-Newton) de 9.13 ± 0.23, au lieu de 8.22 comme supposé dans la publication jointe. La correction que cela implique est faible (division de la masse de gaz par un facteur 1.11). Par contre, l'observation de A665 et A2163 avec le satellite Chandra montre de fortes inhomogénéités de la température électronique, interprétées comme un signe de chocs lié à des fusions récentes (Markevitch & Vikhlinin 2001). Ceci rend plus délicate la conversion du flux SZ mesuré en masse de gaz, puisqu'il faut tenir compte de la structure de l'amas étudié. Ceci montre l'importance de la résolution angulaire pour l'étude des amas de galaxies.

Aujourd'hui, compte tenu de la précision sur les paramètres cosmologiques inférés des observations du CMB, l'intérêt premier de l'observation d'amas SZ est surtout l'étude de la physique des amas (dynamique, évolution, lois d'échelle), plutôt que la contrainte de la cosmologie (paramètres H_0, fraction de gaz...). Toutefois, en présence du problème de la matière et de l'énergie noire, les contraintes directes (et non géométriques) sur les paramètres de densité conservent un intérêt réel. L'interprétation des mesures SZ pour contraindre finement les paramètres cosmologiques doit alors prendre en compte une modélisation plus aboutie des amas (notamment, de leur structure en densité et en température). Ceci nécessite d'exploiter les diverses observations des amas pour en comprendre la structure et la dynamique. Les observations de la mission Planck, combinées aux données X de XMM-Newton et aux observations optiques (observation des galaxies de l'amas avec SDSS, détermination de décalage spectral par spectrométrie X, détermination éventuelle d'un profil de masse par lentille gravitationnelle), offrent d'excellentes perspectives pour l'exploitation cosmologique d'un catalogue d'amas SZ, le grand nombre d'amas observés palliant, par moyennage des propriétés physique des amas sur l'échantillon observé, le handicap de la résolution angulaire insuffisante pour les modéliser individuellement.

2.2.2 Carte SZ de RXJ1347-1145

La seconde publication concernant Diabolo reproduite en annexe, *A Sunyaev-Zeldovich Map of the Massive Core in the Luminous X-Ray Cluster RX J1347-1145* (page 77), parue dans The Astrophysical Journal en 1999, décrit les résultats obtenus à partir des observations effectuées en 1997 en direction d'un amas extrêmement brillant, RXJ1347-1145. Une carte du coeur de l'amas, avec une résolution de 23 secondes d'arc, est produite. Cette carte permet de tenter de contraindre les paramètres de l'amas, dans le contexte d'un désaccord entre la masse inférée par les observations X et par effet de lentille gravitationnelle. En combinant la mesure Diabolo avec les observations X obtenues avec *ROSAT* (Schindler et al. 1997), nous déduisons une température de $16,2 \pm 3,8$ keV, une masse de $1.0 \pm 0.3 \times 10^{15}$ masse solaire, et une fraction de gaz de l'ordre de 20%. A noter toutefois que ces résultats sont obtenus en supposant, là encore, $H_0 = 50$ km/s/Mpc, $\Omega_0 = 1$, et $\Lambda = 0$.

Les observations récentes de ce même amas, en SZ (Kitayama et al. 2004; Mason et al. 2009) et en X (Allen et al. 2002; Gitti & Schindler 2004), ont mis en évidence une structure complexe, avec une température variant de 6 à 20 keV. Une région chaude ($T_e \simeq 20$ keV) au sud-est du maximum d'émission correspond probablement à une fusion violente. Cet amas est donc un mauvais candidat pour une exploitation cosmologique, mais présente un intérêt évident pour la compréhension des processus physiques se produisant dans les amas en formation.

Ma participation à ce travail se résume à la participation aux demandes de temps et aux observations sur site, l'essentiel de l'analyse ayant été fait par Étienne Pointecouteau au CESR.

2.3 Analyse de données pour la détection d'amas SZ

Le signal SZ (thermique ou cinétique) étant faible, sa détection et sa caractérisation dans des données bruitées, en présence d'autres sources d'émission astrophysiques, est un problème délicat.

La problématique de l'extraction de l'effet SZ de cartes observationnelles se présente sous différents aspects, en fonction des objectifs scientifiques visés, parmi lesquels on citera notamment :

- la recherche aveugle (i.e. détection) d'amas inconnus dans une carte du ciel (ou dans plusieurs cartes, obtenues à différentes fréquences) ;
- la mesure du flux SZ thermique d'un amas connu (et dont la taille est éventuellement connue, ou modélisée) ;
- la mesure de paramètres statistiques liés aux amas SZ (e.g. comptage $dN/dYd\theta$ du nombre

d'amas en fonction du paramètre de Comptonisation intégré $Y = \int y d\Omega$ et de la taille angulaire typique θ) ;
– la construction d'une carte d'émission SZ thermique, incluant éventuellement un fond diffus de SZ lié aux grandes structures (par exemple, de filaments de la toile cosmique).

La mesure du flux SZ d'un amas brillant de position connue peut se faire avec une mesure monofréquence, par comparaison du signal en direction de la source (position *on*), et du signal à côté de l'amas (position *off*). Toutefois, ce type de mesure est sujet à la contamination par des signaux d'origine astrophysique (notamment anisotropies du CMB, sources radio ou infrarouges au sein de l'amas). Si l'on dispose d'une carte de la région centrée sur l'amas, il est possible d'estimer le flux par filtrage adapté. Avec plusieurs cartes, correspondant chacune à une observation à une fréquence différente, il est possible d'implémenter un filtrage adapté multifréquence, qui prend en compte la connaissance *a priori* de la loi d'émission du SZ thermique. Dans les deux cas, le filtrage adapté utilise spécifiquement la connaissance de la forme de l'amas.

Dans le contexte actuel, la recherche aveugle d'amas par effet SZ thermique, et l'assemblage d'un catalogue d'amas, présente un grand intérêt scientifique, notamment dans le cadre de la mission Planck. Un catalogue peut être obtenu par détection directe dans des observations multifréquence (Herranz et al. 2002, 2005). D'un autre côté, des méthodes de séparation de composantes diffuses, s'appuyant sur la loi d'émission du SZ, permettent d'obtenir des cartes de SZ dans lesquelles il est possible de faire une détection d'amas par filtrage spatial, ou en utilisant des outils classiques comme SExtractor (Bertin & Arnouts 1996). Deux publications décrivant nos travaux pour la détection d'amas SZ et la construction d'un catalogue d'amas sont présentées en annexe (pages 81 et page 91). Ces travaux constituent une partie du travail de thèse de Jean-Baptiste Melin, effectué sous la direction conjointe de James Bartlett et moi-même. Je me suis surtout investi sur les aspects relevant de la simulation de cartes, de la détection des amas par filtrage, et de validation des méthodes sur simulations.

2.3.1 La fonction de sélection

La première de ces publications, *The selection function of SZ cluster surveys* (Melin et al. 2005), aborde le problème de la caractérisation d'un catalogue d'amas. Dans la mesure où l'exploitation scientifique d'un tel catalogue implique, en particulier, la comparaison du nombre observé d'amas à un nombre attendu d'amas en fonction d'un modèle et de paramètres cosmologiques, il est indispensable de pouvoir caractériser la fonction de sélection des amas, qui permet d'inférer, en fonction des comptages d'amas dans un espace de paramètres mesurés (par exemple, en fonction de masse et décalage spectral, ou en fonction de flux SZ et de taille angulaire), le nombre réel d'amas en fonction de paramètres vrais. Nous étudions ici cette fonction de sélection dans le cas particulier d'observations monofréquence, en présence de bruit, de sources ponctuelles, et de fluctuations primordiales de température du CMB, et concluons que la fonction de sélection ne se résume pas à une simple coupure en flux. Cette étude peut être généralisée à des observations multifréquence, avec des bruits inhomogènes et/ou corrélés, et en présence de contamination par une population plus complexe de sources et de contamination galactique. La fonction de sélection devient alors une fonction de la position des amas sur le ciel. Une étude complète sera indispensable pour l'exploitation du catalogue d'amas observé par Planck. La présente publication pose les bases méthodologiques de cet aspect de l'analyse des observations.

2.3.2 Extraction d'un catalogue SZ

La seconde publication jointe à ce mémoire et relative à la préparation de la mesure d'un catalogue d'amas SZ, *Catalog extraction in SZ cluster surveys : a matched filter approach* (Melin et al. 2006), présente une méthode pour la détection d'amas SZ, et la mesure du flux SZ intégré des amas détectés. Les performances de la méthode sont évaluées sur des simulations pour trois types d'expériences :

- une expérience sol monofréquence à haute résolution utilisant une technologie d'interférométrie radio, semblable à l'expérience AMI (Zwart et al. 2008) ;
- une expérience sol multifréquence utilisant des bolomètres au foyer d'un télescope de grande taille, telle l'expérience SPT (Ruhl et al. 2004) ;
- une expérience spatiale multifréquence, sensible mais de résolution moindre (instrument Planck HFI).

Il s'agit, là encore, d'un travail méthodologique qui vise à préparer l'exploitation scientifique de données à venir.

2.3.3 Challenge SZ

Dans le cadre de la préparation de la mission Planck, les groupes de travail WG5 et WG2 ont organisé conjointement un *data challenge* pour la constitution d'un catalogue d'amas à partir de données Planck simulées avec le Planck Sky Model (décrit au chapitre 6). Cet exercice, qui a permis de comparer les performances de plusieurs méthodes de détection d'amas, fait l'objet d'une publication en préparation. Dans le cadre de ce data challenge, nous avons utilisé une adaptation récente de la méthode ILC needlets faisant l'objet de la publication jointe page 259 pour obtenir une carte d'effet SZ thermique. La détection des amas se fait alors avec SExtractor ou à l'aide d'un filtre adapté monofréquence sur la carte ainsi obtenue. Cette méthode a été développée et implémentée sous ma responsabilité avec une participation significative de Maude le Jeune et Jean-François Cardoso (pour l'ILC needlets) et de Jean-Baptiste Melin (pour le filtrage adapté et la sétection d'amas avec SExtractor). Elle a permis d'obtenir, en terme de taux de détection pour un niveau de contamination donné du catalogue, les meilleures performances pour la détection d'amas SZ dans le cadre du data challenge. La continuation de ce travail fait l'objet d'une partie du travail post-doctoral de Mathieu Remazeilles, sous ma responsabilité (voir notamment à ce sujet la publication de Remazeilles et al. (2010), décrite plus en détail au chapitre 5 et jointe à ce mémoire page 295).

2.4 Lois d'échelle des amas de galaxies

Avec la mission Planck, avec les expériences ACT et SPT, il est possible d'envisager la mesure précise de l'effet SZ sur un nombre significatif d'amas de galaxies, et notamment la constitution d'un catalogue d'amas compétitif (en nombre d'objets détectés) avec ceux obtenus à partir d'observations X. Ceci ouvre la voie à la constitution de catalogues d'amas sélectionnés par leur masse de gaz, et donc potentiellement à la contrainte de la fonction de masse $dN/dMdz$.

Pour cela toutefois, il est nécessaire, après la détection des amas SZ, d'estimer leur masse M et leur décalage spectral z. Si la mesure de ce dernier est possible *a posteriori*, soit en identifiant les galaxies de l'amas détecté dans un catalogue de galaxies tel SDSS (Abazajian et al. 2009) et en déterminant un décalage spectral photométrique, soit directement à partir d'un spectre, la détermination de la masse de tous les amas d'un catalogue est une tâche ardue. Les méthodes basées sur les lentilles gravitationnelles sont prohibitives en temps d'observation. Il faut donc établir des lois qui permettent, à partir des observables SZ (et X), d'estimer directement et de façon non biaisée la masse des amas détectés.

Dans le cas spécifique des mesures X, une loi d'échelle reliant la luminosité X à la masse totale a été obtenue par Pratt et al. (2009), à partir d'un échantillon de 31 amas observés en détail avec le satellite XMM. Pour cet échantillon a été établie une loi reliant $L_{\rm X}$ et $Y_{\rm X}$ (produit de la température X et de la masse de gaz). La correspondance entre $Y_{\rm X}$ et M (nécessaire pour obtenir la relation $L_{\rm X} - M$) est établie par des travaux antérieurs qui proposent un 'profil de masse universel' pour les amas de

galaxies, et normalisent les paramètres de ce modèlent à partir de la comparaison des observations X et de simulations numériques (Pointecouteau et al. 2005; Arnaud et al. 2007).

Dans la mesure où ces travaux établissent que le paramètre $Y_{\rm X}$ permet une meilleure estimation de la masse d'un amas que la luminosité ou la température X, et puisque le paramètre $Y_{\rm X}$, produit de la température et de la masse de gaz, mimique l'observable naturelle SZ, il est intéressant d'établir les relations entre le paramètre de Comptonisation $Y_{\rm SZ}$ des amas de galaxies et la masse de ces mêmes amas. Ce travail fait l'objet d'une publication, *The galaxy cluster Ysz-Lx and Ysz-M relations from the WMAP 5-yr data* (Melin et al. 2010), reproduite en annexe page 103. Ma contribution à ce travail concerne essentiellement le traitement des données de WMAP pour extraire les amas et en mesurer le paramètre de Comptonisation, l'estimation des erreurs de mesure, et la validation des résultats sur simulations.

Les données WMAP, bien qu'intrinsèquement trop bruitées pour permettre la détection 'aveugle' d'amas de galaxie, offrent la possibilité d'une telle étude en empilant les mesures SZ centrées sur un grand nombre d'amas connus. Nous utilisons pour cela un catalogue de 893 amas sélectionnés en X, obtenus par la fusion des catalogues NORAS (Böhringer et al. 2000) et REFLEX (Böhringer et al. 2004) tous deux issus des observations du satellite ROSAT. Ces amas peuvent être groupés en fonction de leur luminosité X ou en fonction de leur masse. Pour chaque sous-ensemble d'amas ainsi différenciés, nous mesurons le paramètre $Y_{\rm SZ}$ intégré.

Grâce à cette technique d'empilement, et en utilisant sur les données WMAP le filtre adapté que nous avons mis au point (Melin et al. 2006), nous mesurons pour les amas des catalogues NORAS et REFLEX un paramètre de Comptonisation $Y_{\rm SZ}$ intégré compatible avec le modèle de profil de pression proposé par Arnaud et al. (2010). Nous montrons par ailleurs que l'émission SZ thermique dans les données WMAP est au niveau attendu. Cette confirmation participe à un débat ouvert par Lieu et al. (2006), qui annoncent au contraire ne détecter dans les données WMAP qu'un quart du signal SZ espéré.

Notre travail ouvre la voie pour effectuer le même type d'analyse, avec une précision bien meilleure, en utilisant les données de la mission Planck qui fit l'objet du chapitre qui suit.

Chapitre 3

Préparation de la mission Planck

L'observation précise des anisotropies de température et de polarisation du fond cosmologique, et leur interprétation dans le contexte du modèle de Big Bang chaud avec des fluctuations initiales d'origine inflationnaire, offre une opportunité de tester dans le détail les prédictions du modèle cosmologique 'standard'. Les quelques paramètres globaux du modèle ont tous un impact mesurable sur les spectres de puissance des anisotropies, en température et en polarisation. Ceci motive une observation précise de ces spectres. C'est là l'objectif premier de la mission Planck (Tauber et al. 2010), initialement présentée à l'ESA sous le nom de COBRAS/SAMBA.

Depuis 1994, j'ai travaillé sur de nombreux aspects de la mission Planck, depuis la définition de la mission jusqu'à l'analyse scientifique des données. Les points clefs de ma contribution sont les suivants :

- Validation du concept de mesure en puissance totale avec fabrication de cartes par déstriage ;
- Calcul des effets de lumière parasite par signal de lobe lointain, identification d'une méthode pour s'affranchir de ces effets, et validation des niveaux de réjection assurés par la définition de l'optique et des écrans ;
- Définition d'une géométrie de détecteurs pour la mesure de la polarisation du fond cosmologique avec des bolomètres sensibles à la polarisation ;
- Études d'effets systématiques polarisés (différences de réponses des détecteurs, dépolarisation), et coordination du groupe de travail sur ce sujet ;
- Participation à la définition de la chaîne de traitement des données de polarisation avec Planck, et coordination du groupe de travail correspondant dans le "Data Processing Center" de l'instrument HFI ;
- Coordination des activités du groupe "séparation de composantes", développement des méthodes SMICA et ILC needlets (voir également chapitre 5) ;
- Mise en place de l'outil de simulation de l'émission du ciel "Planck Sky Model" (voir également chapitre 6.

Les deux premiers points ont fait l'objet d'une partie de mon travail de thèse, et de développements nouveaux depuis 1998. Les autres points ont fait l'objet d'une part très significative de mon activité depuis 1998.

3.1 Le concept

3.1.1 Sensibilité

La mission est conçue avec l'idée d'obtenir une sensibilité 'ultime' de mesure, limitée essentiellement par le bruit de photons du rayonnement incident sur les détecteurs (idéalement, le fond de rayonnement

cosmologique à 2,725 K). En pratique, l'instrument lui même contribue un peu à la charge radiative, pour une fraction comparable au fond de ciel (dans les canaux 'cosmologiques'), mais ceci ne dégrade la sensibilité des détecteurs que d'un facteur de l'ordre de $\sqrt{2}$. Ainsi, la sensibilité de Planck n'est plus limitée par la sensibilité des détecteurs individuels, mais par le nombre de détecteurs, et éventuellement par la confusion astrophysique due aux émissions d'avant plan. La sensibilité intégrée est de l'ordre de 5 μK thermodynamique par pixel de 5 minutes d'arc sur le ciel, environ 30 fois mieux que WMAP en sensibilité par degré carré (voir Lamarre et al. (2010) pour une description des performances de l'instrument le plus sensible, l'instrument HFI).

3.1.2 Bandes de fréquence

Le fond diffus est observable essentiellement dans la gamme de fréquence 30 GHz - 300 GHz (longueurs d'onde entre 1 mm et 1 cm). Aux fréquences moindres, l'émission synchrotron d'origine galactique contamine les observations sur une grande fraction du ciel. Aux fréquences plus élevées, ce sont les émissions thermiques des poussières de la voie Lactée qui dominent. Ces deux types d'émissions d'avant-plan sont à la fois présents dans notre propre galaxie, et dans d'autres galaxies.

Pour cette raison, la fréquence optimale d'observation pour minimiser la contamination d'avant plan se trouve aux alentours de 70-100 GHz, où deux technologies de détecteurs, radiomètres et bolomètres, permettent d'observer le ciel. Les radiomètres sont surtout performants aux basses fréquences, car l'amplification d'un signal à haute fréquence présente des difficultés techniques, ce qui limite la largeur de bande de détection. Les bolomètres fonctionnent sur le principe de l'échauffement d'un cristal de faible capacité calorifique par le rayonnement incident. Ils sont surtout sensibles aux fréquences élevées, où ils peuvent intégrer l'énergie d'une large bande spectrale dans un domaine de fréquence où le rayonnement est assez énergétique pour chauffer les absorbeurs. Leur fonctionnement nécessite de refroidir les détecteurs à une température de quelques dizaines à quelques centaines de mK, ce qui impose un système cryogénique complexe avec plusieurs étages de refroidissement, une technologie difficile à mettre en oeuvre dans l'espace.

En pratique, même entre 70 et 100 GHz, l'émission totale du ciel est un mélange d'émissions d'origines diverses (voir chapitre 6). Pour identifier le fond diffus sans ambiguïté, il faut observer le ciel à plusieurs fréquences. La question du choix des bandes d'observation a fortement mobilisé l'équipe Planck pendant la définition de la mission (Tegmark & Efstathiou 1996; Hobson et al. 1998; Bouchet & Gispert 1999; Bouchet et al. 1999). Les observations basse fréquence permettent de 'tracer' l'émission des avant plans basse fréquence (synchrotron, free-free, poussières en rotation), et les observations haute fréquence permettent de 'tracer' l'émission thermique des poussières. La mission Planck observe le ciel dans 9 bandes de fréquence centrées entre 30 et 850 GHz, ce qui permet de séparer les différentes contributions à l'émission totale (voir chapitre 5). Pour obtenir cette couverture en longueur d'onde, Planck utilise conjointement deux instruments, le LFI (Low frequency Instrument) et le HFI (High Frequency Instrument), utilisant les deux technologies de détecteurs.

3.1.3 Résolution

L'exploitation optimisée de la mesure des spectres d'anisotropie de température et de polarisation nécessite une bonne résolution angulaire. Une résolution de quelques minutes d'arc suffit pour mesurer toute la gamme d'échelles utiles pour l'étude des anisotropies primaires, mais une résolution meilleure serait souhaitable pour résoudre l'essentiel des amas de galaxies et, de façon générale, pour une meilleure détection et séparation des sources ponctuelles et compactes.

En pratique, ce sont des contraintes extérieures qui fixent la résolution de l'instrument, la taille du miroir primaire étant limitée par la coiffe du lanceur, ce qui limite la résolution (par diffraction). Pour

un miroir de 2,5 m à 100 GHz, la résolution théorique est de 5 minutes d'arc environ, mais la nécessité de sous-illuminer le miroir primaire pour éviter le rayonnement de débordement source de signal de lobes lointains, ne permet pas d'atteindre cette limite. La résolution finale résulte d'un compromis, qui a motivé le travail que j'ai effectué sur le problème des lobes secondaires, présenté succinctement section 3.3.

3.1.4 Orbite et pointage

Le refroidissement des détecteurs, et la minimisation de la charge radiative sur les détecteurs, nécessite un premier étage de refroidissement passif de la charge utile. Ceci est obtenu en plaçant le satellite en orbite au point de Lagrange L2 du système Terre-Soleil, la charge utile étant en permanence orientée côté espace froid. Ceci permet aussi de garder le Soleil, la Terre et la Lune loin de l'axe d'observation du ciel. Ce choix limite les options de balayage du ciel. Dans ce contexte, j'ai étudié l'optimisation de cette stratégie de balayage, travail qui est décrit dans la section 3.2.

La stratégie de balayage prévoit un contrôle précis des systématiques par des redondances de mesure à différentes échelles de temps : la fraction de seconde, par la disposition des détecteurs dans le plan focal de façon à ce que leurs faisceaux sur le ciel se suivent le long d'une trajectoire commune ; la minute, par la rotation du satellite avec une période d'une minute ; 6 mois environ, correspondant au temps de couverture d'un ciel complet.

3.2 Bruit basse fréquence et stratégie de balayage

La stratégie d'observation de Planck, par balayage du ciel le long de cercles plus ou moins entrelacés couvrant la totalité de la sphère, implique la mise au point d'une méthode qui permet de reconstruire une carte à partir des flots temporels de données ainsi obtenus. La présence de bruit basse fréquence, de dérives temporelles des paramètres instrumentaux, et d'effets systématiques divers, ne permet pas cette reconstruction par simple moyennage, pour chaque pixel, de l'ensemble des données acquises dans sa direction.

Avant la conception de Planck, l'impact de ces instabilités de la mesure dans les observations du fond cosmologique était minimisé par le biais de mesures différentielles, pour lesquelles les flots temporels de données sont constitués de différences entre l'émission de deux directions du ciel. Ces différences peuvent être obtenues soit par l'utilisation de deux systèmes imageurs, comme pour les expériences COBE-DMR et WMAP, soit par une stratégie d'observation à direction de pointage modulée rapidement, de type *on-off*.

Pour une mission comme Planck, doubler l'instrument et l'optique engendrerait un surplus de complexité quasi-rédhibitoire. Nous avons donc étudié la faisabilité d'une mesure en puissance totale. J'ai pour cela mis au point un logiciel permettant de simuler des flots de données temporels semblables à ceux de la mission, comprenant le signal du ciel, des dérives basse-fréquence additives, et un certain nombre d'effets systématiques instrumentaux. Une première version de ce logiciel, LAMBADA (Logiciel pour l'Analyse et la Minimisation des Bruits Altérant la Détection des Anisotropies), a été utilisé (pendant ma thèse) pour la démonstration de faisabilité de la mesure lors de l'étude de phase A de la mission.

L'une des premières utilisations de ce logiciel a concerné la reconstruction de cartes du ciel en présence de bruit basse fréquence. J'ai mis au point une méthode de déstriage utilisant la spécificité d'une stratégie de balayage basée sur l'observation de cercles sur le ciel, telle que conçue pour Planck. J'ai montré qu'une méthode exploitant les redondances permet de fabriquer des cartes du ciel sans résidu important des dérives basse-fréquence, validant ainsi le concept de mesure en puissance totale.

Cette stratégie de déstriage est basée sur l'ajustement de quelques paramètres par cercle, représentant la contribution du bruit basse fréquence, et exploite la possibilité de séparer la fabrication de cartes en deux étapes : la fabrication de cercles associés à une période pendant laquelle l'axe de rotation du satellite reste fixe sur le ciel (Delabrouille et al. 1998a), puis la fabrication de cartes à partir des cercles en utilisant leurs croisements (Delabrouille 1998a). Les publications correspondantes sont jointes à ce manuscrit (page 115 et page 121 respectivement).

Cette étude a également abouti d'une part à la définition de l'angle d'ouverture de 85° entre l'axe de spin du satellite et l'axe optique, et d'autre part à la définition d'une stratégie de balayage avec précession et un axe de spin non strictement anti-solaire (Delabrouille et al. 1998b). Ceci permet une redondance des observations suffisante pour assurer la fabrication de cartes d'anisotropies. A posteriori, ces choix s'avèrent importants également, par exemple, pour l'étalonnage de paramètres liés à la polarisation en observant la région du Crabe (Tau-A) avec des orientations différentes à différents temps de la mission, mais aussi pour mieux contraindre les paramètres instrumentaux sources d'effets systématiques dans les données. La figure 3.1 illustre la géométrie des redondances pour différentes stratégies de balayage.

J'ai ensuite proposé d'étendre cette méthode de fabrication de carte par 'déstriage' à la mesure de la polarisation. En collaboration avec Jean Kaplan au laboratoire PCC du collège de France, nous avons défini le problème et la méthode pour le résoudre, par une extension assez directe de la méthode que j'ai mis au point pendant ma thèse. Nous avons co-encadré une partie du travail de thèse de Benoît Revenu sur ce sujet, qui a abouti à une publication (Revenu et al. 2000) jointe à ce manuscrit, page 135. Cet algorithme a par la suite été implémenté dans le Data Processing Center de Planck HFI, mais je ne me suis pas impliqué directement dans cette implémentation.

Ces travaux sur la fabrication de cartes avec la mission Planck ont par la suite été repris par nombre d'auteurs, et ont fait l'objet de développements supplémentaires qui appellent plusieurs commentaires.

Le problème de la fabrication de cartes (en température, par souci de simplification de l'exposé), en effet, *peut, mais ne doit pas forcément* se formuler de la façon suivante. Un détecteur (ou jeu de détecteurs) observe une fonction linéaire de l'émission du ciel, i.e.

$$y_t = A_{tp} T_p + n_t \tag{3.1}$$

où A est une matrice de pointage qui indique le point (i.e. pixel) p observé au temps t, T_p dénote le signal d'intérêt (la température du ciel dans le pixel p), et n_t le bruit. C'est le modèle (simplifié) que j'ai adopté dans mon travail original (Delabrouille 1998a), et également le modèle que nous avons utilisé dans l'extension à la polarisation (Revenu et al. 2000)

Les travaux faisant l'objet de publication récentes améliorent les aspects numériques de l'étude, avec des implémentations sur des données plus volumineuses (Sutton et al. 2009a,b), et/ou implémentent une solution de moindre carrés 'optimale' dans le cas où le bruit est gaussien stationnaire (Natoli et al. 2001; Cantalupo et al. 2009), et/ou modélisent le bruit avec une paramétrisation différente (Keihänen et al. 2005, 2009), et/ou implémentent des solutions différentes pour résoudre le système linéaire (Challinor et al. 2002; Stompor et al. 2002; Sbarra et al. 2003; Yvon & Mayet 2005), et/ou envisagent la possibilité que les bruits de différents détecteurs soient corrélés (Patanchon et al. 2008; Sutton et al. 2009b). Plusieurs travaux comparent différentes méthodes, sur le plan conceptuel, en terme de performance sur des problèmes simplifiés, et en terme de coût calcul (Tegmark 1997; Keihänen et al. 2004; Poutanen et al. 2006; Ashdown et al. 2007).

Si ces travaux sont utiles pour faire avancer les aspects numériques (gestion de flots temporels de grande taille, implémentation parallèle, etc.) et comprendre le fonctionnement de ces codes de fabrication de cartes, toutes les méthodes restent conceptuellement assez semblables sur le plan de la modélisation du problème. Notamment, tous les algorithmes utilisent le modèle de données de

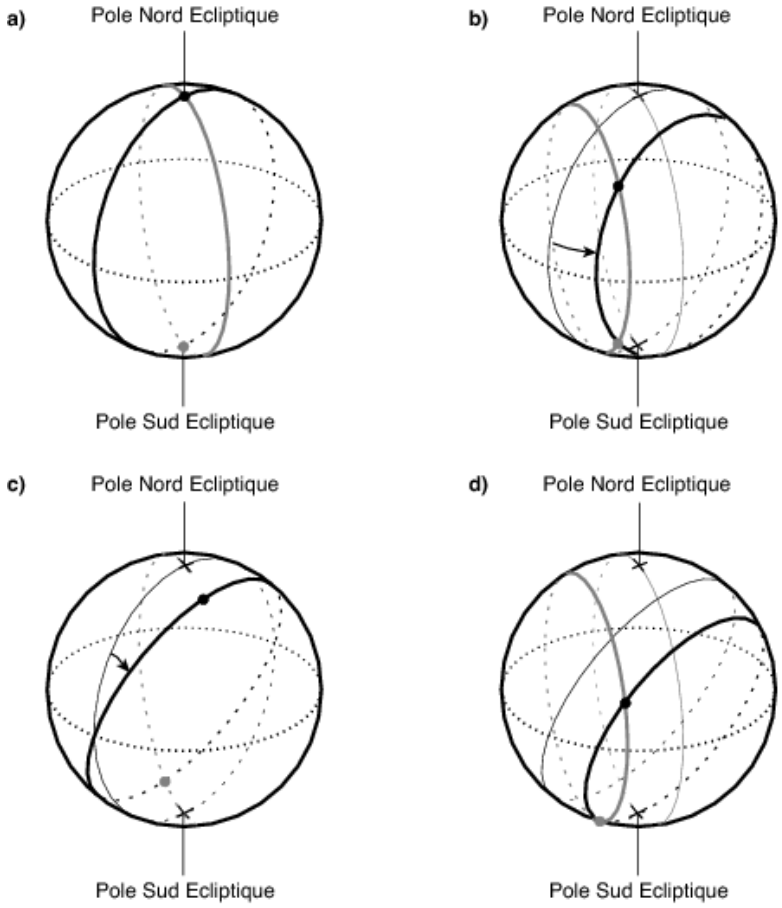

Figure 3.1 – Figure adaptée de Delabrouille et al. (1998b). Options pour la stratégie de balayage de la mission Planck. a) Angle d'ouverture de 90 degrés, axe de spin anti-solaire : tous les cercles se croisent aux pôles écliptiques, chaque pixel éloigné des pôles est observé avec seulement deux géométries, avec un intervalle de temps de 6 mois. b) Angle d'ouverture inférieur à 90 degrés, axe de spin anti-solaire : les points de croisement sont distribués sur le ciel, mais les pôles écliptiques ne sont pas couverts. c) Angle d'ouverture de 90 degrés, axe de spin mobile par rapport à l'anti-solaire : les points de croisement sont distribués sur le ciel, et dépendent de la trajectoire de l'axe de spin. d) Angle d'ouverture inférieur à 90 degrés, axe de spin mobile par rapport à l'anti-solaire : cette stratégie permet la stratégie b) comme repli si la mobilité de l'axe de spin est cause d'effets systématiques gênants, tout en permettant une certaine flexibilité pour la distribution des redondances. C'est la stratégie adoptée pour Planck, avec un angle d'ouverture de 85 degrés.

l'équation 3.1, basé sur une représentation pixélisée du ciel. Dans une telle implémentation, deux mesures qui 'tombent dans le même pixel' sont supposées égales, fournissant une contrainte pour l'inversion du système linéaire, et deux mesures tombant dans deux pixels différents sont supposées différentes (et n'apportent aucune contrainte).

En réalité, l'émission du ciel est une fonction continue. Planck n'a pas de fortes redondances, i.e. un pixel de la taille du lobe est observé peu de fois, notamment pour les canaux haute fréquence. Les performances de la fabrication de carte dépendent du choix de pixélisation. Si les pixels sont trop petits, il n'y a pas assez de redondances, ce qui conduit à des résidus de striage importants (et éventuellement des trous dans les cartes). Si les pixels sont trop grands, il y a perte de résolution, la pixélisation n'obéit pas au critères d'échantillonage (ce qui induit un repliement de spectre) et la variabilité du signal dans les pixels nuit à la performance de la fabrication de cartes, puisque sont supposées égales (car tombant dans le même pixel) des mesures en réalité différentes (car le signal du ciel est inhomogène dans le pixel). Si ce problème a été identifié et étudié par plusieurs auteurs (Maino et al. 2002; Kurki-Suonio et al. 2009), il n'a pas été résolu de façon satisfaisante à ce jour. Il est à noter que la plupart des expériences autres que Planck ne souffrent pas de ce problème de la même façon, les mesures étant très fortement redondantes (beaucoup d'échantillons par pixel, même pour des petits pixels). Une solution de type Wiener peut résoudre partiellement ce problème en utilisant la connaissance a priori de la corrélation à deux points du ciel, qui apporte des contraintes supplémentaires susceptible de régulariser l'inversion dans le cas où la redondance des observations est marginalement suffisante, i.e. lorsque la carte est fabriquée en utilisant une représentation pixélisée finement (Dupac & Giard 2002).

Malgré tous ces travaux, la fabrication de carte pour Planck mériterait peut-être d'être repensée, et ce même si les codes existants fournissent des solutions satisfaisantes au premier ordre. Toutefois, un tel travail ne saurait avoir de sens sans raffiner simultanément le modèle de la mesure, en prenant en compte les effets systématiques instrumentaux susceptibles de conduire à des erreurs du même ordre : différences de lobe (y compris les constantes de temps des détecteurs), différences de bande spectrale, erreurs de pointage, dérive des gains, lobes secondaires. Des travaux récents du groupe CTP de la collaboration Planck évaluent l'effet de certaines de ces complications pour le cas du canal à 30 GHz de Planck, sans toutefois tenter de corriger l'impact de ces effets (Ashdown et al. 2009).

3.3 Lumière parasite, lobes lointains

LAMBADA a permis également d'étudier l'impact sur les données de la lumière parasite observée dans les lobes lointains de la réponse du système optique de Planck. Celui-ci ne permet pas de rejeter complètement le rayonnement incident en provenance du ciel dans toutes les directions (voir figure 3.2). Les réjections typiques dans les lobes lointains du diagramme d'antenne étant typiquement dans la gamme 10^{-6} à 10^{-12} (voir figure 3.3), la présence de corps célestes émissifs, même modérément étendus, dont le signal est modulé par les lobes secondaires du diagramme d'antenne au cours du balayage du ciel, est susceptible de générer des signaux parasites d'amplitude supérieure à la sensibilité de Planck.

L'amplitude et les caractéristiques de l'effet peuvent être évalués à partir d'un modèle de diagramme de rayonnement des détecteurs de Planck, d'un modèle de l'émission du ciel, et d'un code permettant de calculer l'intégrale de l'émission du ciel dans le diagramme d'antenne en fonction de la stratégie de balayage, en séparant éventuellement les différentes contributions. Le diagramme de rayonnement est calculé à l'aide d'un logiciel commercial adapté, GRASP (figure 3.3). L'émission du ciel aux fréquences de Planck HFI est l'objet du chapitre 6 du présent mémoire. LAMBADA permet le calcul de la 'convolution', i.e. de l'intégrale d'une carte du ciel 4π dans un diagramme d'antenne 4π. La même fonctionnalité, étendue à la polarisation, est disponible dans le package 'Level S', un outil de simulation développé au sein de la collaboration Planck (Wandelt & Górski 2001; Reinecke et al. 2006).

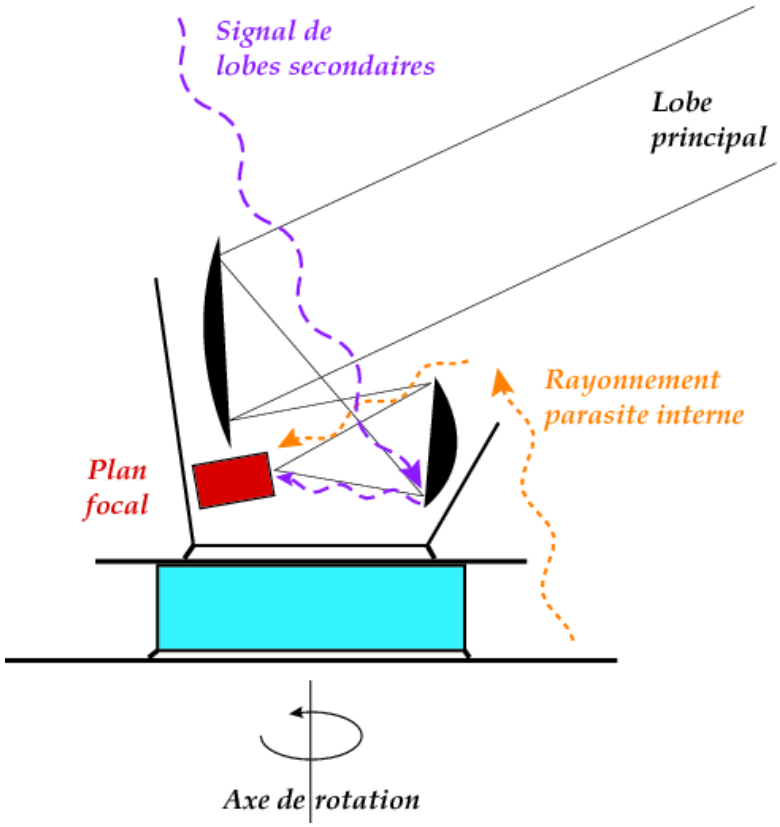

Figure 3.2 – Figure adaptée de Delabrouille (2001). Illustration de l'origine de la lumière parasite pour la mission Planck. On distingue le signal de lobes secondaires, en provenance du ciel, de la lumière parasite 'interne', due aux fluctuations d'émissions originaires du satellite lui-même.

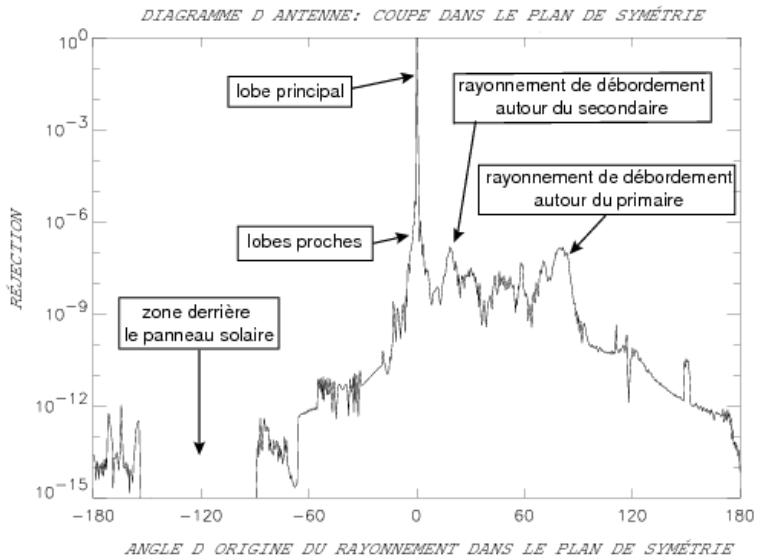

Figure 3.3 – Figure adaptée de Delabrouille (2001). Coupe dans un diagramme de rayonnement typique pour un détecteur de Planck, selon les études préliminaires effectuées lors de la définition de la mission (la forme exacte dépend de la configuration optique retenue, de la position du détecteur, des propriétés du cornet).

La figure 3.4 illustre le signal (sous formes de cercles Planck, non re-projetés sur le ciel) issu de l'intégrale de l'émission du ciel dans le diagramme d'antenne représenté figure 3.3, calculé avec LAMBADA pour une stratégie de balayage avec un axe de spin anti-solaire, et en négligeant la contribution de l'anisotropie dipolaire du fond cosmologique. On note que l'amplitude totale du signal est assez faible (inférieure à 1 μK), mais comme ce signal est très corrélé, il resterait au dessus de la sensibilité de Planck aux grandes échelles.

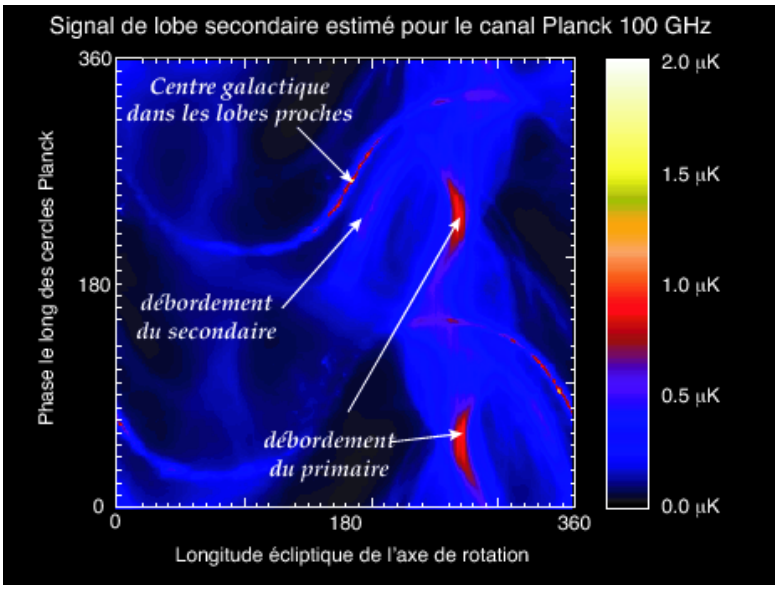

Figure 3.4 – Figure adaptée de Delabrouille (2001). Signal typique de lobes secondaire pour un détecteur de Planck, calculé avec LAMBADA en utilisant le diagramme de rayonnement présenté figure 3.3, pour une stratégie de balayage 'anti-solaire'. On distingue bien les contributions des différents lobes forts du diagramme d'antenne : lobes proches, rayonnement de débordement autour du secondaire, rayonnement de débordement autour du primaire.

Il est possible de tenter de corriger le signal de l'effet systématique engendré par les lobes secondaires. Ceci peut être réalisé de façon non paramétrique, par une technique identique à celle utilisée pour le déstriage, en notant simplement que le signal de lobes lointains est essentiellement basse fréquence. Alternativement, il est possible de modéliser le signal à partir d'une version pixélisée du diagramme d'antenne. Le problème se pose alors de la façon suivante : on dispose de mesures

$$y_t = A_{tpq}(\bar{B}_q + \Delta B_q)(\bar{T}_p + \Delta T_p) + n_t$$

où $\bar{B}_q$ est un lobe principal supposé connu (e.g. mesuré sur les planètes), ΔB_q représente le diagramme d'antenne hors lobe principal (et, éventuellement, des corrections au lobe principal), $\bar{T}_p$ représente le ciel au premier ordre, par exemple modélisé avec le PSM, ou encore mesuré lors d'une première itération 'naïve' de la fabrication de carte, et ΔT_p les (petites) fluctuations de cette émission (le signal d'intérêt qui doit être mesuré avec Planck). Le terme n_t est un bruit de mesure additif. On suppose la sommation sur les indices p (pixel de la carte du ciel) et q (pixel de la carte du diagramme de rayonnement d'antenne). Compte tenu des ordres de grandeur en jeu, le signal peut être linéarisé, ce qui donne, après soustraction de la partie connue au premier ordre,

$$y_t - A_{tpq}\bar{B}_q\bar{T}_p \simeq A_{tpq}\bar{T}_p\Delta B_q + A_{tpq}\bar{B}_q\Delta T_p + n_t$$

En notant $y'_t = y_t - A_{tpq}\bar{B}_q\bar{T}_p$, et

$$\begin{aligned} S_{tq} &= A_{tpq}\bar{T}_p \\ L_{tp} &= A_{tpq}\bar{B}_q, \end{aligned}$$

on obtient :

$$y'_t \simeq S_{tq}\Delta B_q + L_{tp}\Delta T_p + n_t \tag{3.2}$$

On retrouve un problème classique de fabrication de carte, i.e. une inversion au sens des moindres carrés d'un système linéaire dont les inconnues sont ΔB_q et ΔT_p, que l'on peut résoudre si le système n'est pas dégénéré. J'ai montré, pour l'étude de phase A de Planck, que cette équation pouvait être résolue de façon itérative pour un modèle simple du ciel et du diagramme de rayonnement, et pour une stratégie de balayage typique offrant suffisamment de redondances, en l'absence de dérives basses fréquence. Une étude ultérieure de fabrication de carte avec déconvolution, publiée en 2004 (Armitage & Wandelt 2004), ne considère pas le problème complet de la déconvolution des effets de lobes lointains, le diagramme d'antenne étant supposé connu. Il reste donc à implémenter une solution en vraie grandeur au problème de déconvolution tel que présenté dans l'équation 3.2, mais ceci nécessite de prendre en considération simultanément les autres effets systématiques du même ordre de grandeur, et reste assez lourd du point de vue numérique.

3.4 Mesure de la polarisation

La mission COBRAS/SAMBA telle que présentée à l'issue de l'étude de phase A ne propose pas la mesure de la polarisation du CMB. Toutefois, la sélection en 1996 de la mission MAP (à présent WMAP), moins ambitieuse et prévue pour un lancement en 2001, change le contexte international. De plus, l'échec du vol Ariane 501 le 4 juin 1996 implique un retard inévitable pour Planck. Il devient alors raisonnable de considérer Planck comme une mission de troisième génération, pour laquelle il semble incontournable que l'instrument le plus sensible (le HFI) soit capable de mesurer la polarisation.

3.4.1 Configuration de détecteurs de Planck

Les bolomètres ne sont pas naturellement sensibles à la polarisation. La sélection d'une polarisation dans le rayonnement incident nécessite la mise en place de polariseurs, et la mesure des trois paramètres de Stokes utiles I, Q et U (le paramètre V, mesurant une polarisation circulaire, étant supposé nul) nécessite au moins trois directions d'observation indépendantes pour chaque pixel du ciel. L'optimisation de l'instrument nous a conduits à étudier les différentes configurations possibles de polariseurs, la sensibilité dans les différentes configurations, et les redondances. Nous avons proposé des *configurations optimisées* pour lesquelles un ensemble de n détecteurs d'égale sensibilité permettent la mesure avec un bruit minimal (Couchot et al. 1999). La publication issue de cette étude est jointe au présent mémoire (page 147). De telles configurations à 4 ou 8 détecteurs ont été adoptées pour les différents canaux polarisés de Planck HFI (Delabrouille & Kaplan 2002). Cette disposition des directions de polarisation utilise également les propriétés des détecteurs PSB (Polarisation Sensitive Bolometers), pour lesquels la sélection de la direction de polarisation se fait par la géométrie des absorbeurs de deux bolomètres appariés dans un même pixel du plan focal. Partageant les mêmes cornets et les mêmes filtres, les réponses spatiales et fréquentielles des deux bolomètres appariés sont censées être semblables, ce qui est important pour éviter des fuites du signal de température dans la mesure de polarisation. La figure 3.5 illustre l'utilisation de deux paires de bolomètres, disposés en une configuration optimisée à 4 détecteurs, pour mesurer la polarisation avec Planck.

3.4.2 Effets systématiques en polarisation

Malheureusement, les détecteurs ne sont pas parfaits. Une petite différence des réponses de différents détecteurs polarisés est une source d'effets systématiques gênants pour la mesure, et particulièrement dommageables pour la mesure des modes B de polarisation. J'ai participé à plusieurs

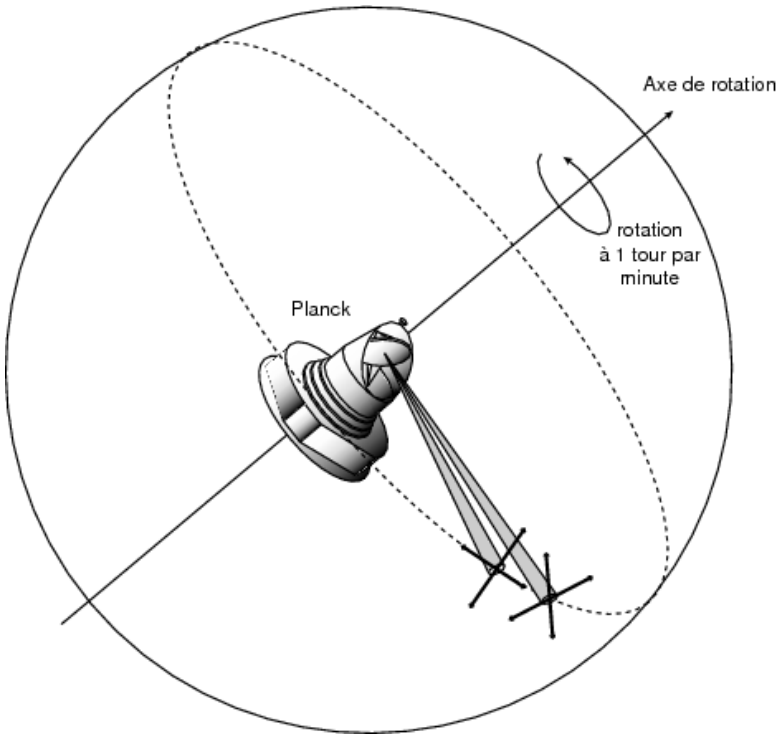

Figure 3.5 – Figure adaptée de Delabrouille & Kaplan (2002). L'observation de la polarisation avec Planck utilisée des configurations optimisées de 4 détecteurs polarisés, avec deux paires de PSB, dont les trajectoires sur le ciel se suivent.

études qui évaluent ces effets systématiques et proposent des méthodes de traitement de données permettant d'en minimiser l'impact sur la mesure (Kaplan & Delabrouille 2002). Nous montrons également comment une correction au premier ordre avec une itération lors de la fabrication de carte polarisée permet de corriger l'essentiel de la fuite de polarisation de type E en polarisation de type B lorsque les lobes des différents détecteurs polarisés ne sont pas exactement identiques (Rosset et al. 2007). La publication correspondante est jointe à ce mémoire (page 153).

Chapitre 4

Archeops

La mission Archeops, qui a observé le fond cosmologique sur une large fraction du ciel avec une résolution supérieure à 10 minutes d'arc, est un grand succès de la recherche française dans le domaine de l'observation du fond cosmologique. Outre ses résultats scientifiques, cette mission a eu un rôle important pour la préparation de Planck HFI. Elle a tenu une place très significative dans mon activité de recherche entre 1998 et 2003. J'ai participé aux campagnes d'observation à Trapani en 1999, à Kiruna en 2001 et 2002-2003, et travaillé sur plusieurs aspects du traitement des données (organisation du dépôt CVS des logiciels de traitement, participation au développement de logiciels de traitement, séparation de composantes et estimation du spectre de puissance des anisotropies avec la méthode SMICA). J'ai également, en 2000 et 2001, participé avec les équipes russes à la récupération (dans des conditions climatiques et logistiques assez difficiles) de la nacelle de l'expérience Archeops en Russie.

4.1 Contexte et concept du ballon Archeops

Au moment de la sélection de la mission WMAP par la NASA en 1996, juste avant la sélection de COBRAS/SAMBA, il apparait clairement qu'une partie du programme scientifique de Planck, et notamment la mesure précise du spectre de puissance C_ℓ à grande échelle, serait faite avant le lancement de Planck. Par ailleurs, le retard prévisible de la mission spatiale implique que les équipes travaillant sur Planck n'auraient pas accès à de vraies données avant une petite dizaine d'années. La mise au point d'une mission ballon s'appuyant sur les études menées dans le cadre de la mission spatiale s'impose donc naturellement à plusieurs titres. Tout d'abord, la mise au point de cette expérience intermédiaire permet de conserver une compétitivité et une visibilité internationale importante pour la communauté française, en valorisant l'investissement fourni pour préparer Planck HFI. Elle permet aussi de tester et valider certaines des options choisies pour la mission spatiale (et notamment le système de dilution, la stratégie de balayage en puissance totale, l'optique, et une partie de l'électronique de lecture). Elle fournit une possibilité à notre équipe d'acquérir l'expérience de données semblables à celles de Planck HFI. Enfin, elle offre une possibilité de mesurer avec précision, avant WMAP, le spectre de puissance C_ℓ depuis les échelles mesurées par COBE jusqu'au second pic acoustique (résolution d'une dizaine de minutes d'arc), contraignant ainsi, notamment, la courbure spatiale Ω_k (conjointement avec les expériences BOOMERanG, DASI et MAXIMA, sensibles surtout aux plus petites échelles, à partir du sommet du premier pic acoustique). Archeops est présenté dans une publication parue dans Astroparticle Physics (Benoît et al. 2002) (voir également Delabrouille & Filliatre (2004) pour une présentation plus récente et plus concise, incluant la description de l'instrument pour le principal vol scientifique, la chaîne de traitement, et les principaux résultats).

Archeops

Si l'expérience Archeops présente de nombreuses similitudes avec Planck HFI, elle présente aussi quelques différences notables.

Tout d'abord, le fait que l'instrument est porté par un ballon stratosphérique ne permet pas de concevoir un balayage du ciel exactement semblable à celui retenu pour Planck. La dérive continue du ballon avec les vents et le balancement de la nacelle ne permettent pas une stratégie d'observation utilisant des grands cercles observés quelques dizaines de fois avec une superposition précise, séparés par des repointages par décalage discret de l'axe de rotation. Ceci a pour conséquence que la stratégie de fabrication de cartes par déstriage décrite au chapitre 3 (Delabrouille 1998a; Revenu et al. 2000) ne sera pas adaptée pour fabriquer les cartes pour Archeops, et ce d'autant moins que le bruit basse fréquence d'Archeops contient des contributions dues à l'émission atmosphérique et aux dérives de température de l'instrument à des fréquences nettement supérieures à la fréquence de rotation de la nacelle. L'angle d'ouverture, enfin, sera plus petit, afin d'éviter d'observer à élévation trop basse.

En second lieu, l'état de disponibilité des détecteurs (bolomètres, filtres, cornets) au moment des campagnes d'observation et les fenêtres de transmission atmosphérique ne permettent pas une couverture spectrale aussi complète que pour la mission spatiale. Archeops observe à 4 fréquences seulement (au lieu de 6 pour HFI et 9 pour Planck), et doit gérer, outre la contamination par les avant-plans galactiques (poussière), la contamination par l'émission atmosphérique, ce qui complique très notablement la séparation des composantes.

L'étalonnage de l'expérience est délicat car le dipôle cosmologique est mal mesuré, en raison de dérives basse fréquence fortes dans les données. Il faudra utiliser, pour étalonner, une combinaison de mesures impliquant le dipôle, le signal des planètes (éventuellement mal échantillonné, et dont l'émission absolue dans les bandes Archeops est entachée d'incertitudes), et un modèle galactique pour les détecteurs haute fréquence. La précision relative ultime obtenue sera de l'ordre de 4-5% en déviation standard pour les meilleurs bolomètres (erreur fortement corrélée entre les bolomètres).

Enfin, la sensibilité de la mission ballon est très inférieure à celle attendue pour Planck. Tout d'abord, une grande partie du bruit présent dans les signaux des détecteurs vient d'émissions parasites et d'effets systématiques instrumentaux liés à l'environnement terrestre. De plus, le temps d'observation est de quelques heures uniquement, au lieu de plusieurs années.

4.2 Observations et analyse de données

Après un premier vol test en été 1999 depuis Trapani en Sicile, le ballon Archeops a été lancé plusieurs fois en hiver depuis la base suédoise d'Esrange, près de Kiruna, au nord du cercle polaire, ce qui permet des observations de nuit, dans de bonnes conditions (notamment, en évitant les effets thermiques et la lumière parasite due à la présence du soleil). La table 4.1 donne les principales caractéristiques des trois vols réussis. Le principal vol scientifique (vol KS3) a eu lieu le 7 février 2002, et a permis d'accumuler une douzaine d'heures de données utiles. Les données des autres vols, dont l'analyse jointe avec les données du vol KS3 aurait permis une meilleure couverture du ciel et un meilleur contrôle des systématiques en utilisant les redondances fournies par les croisements des scans du vol T99 avec les deux autres, n'ont pu être pleinement exploitées en raison du calendrier très serré imposé par la concurrence avec l'expérience spatiale WMAP, et de la complexité de l'analyse en présence de systématiques mal compris. Ces données sont désormais rendues obsolètes par les observations de la mission Planck, qui couvrent toutes les fréquences Archeops avec des perfomances bien meilleures. Pour citer Enrico Fermi, 'If your experiment needs statistics, then you ought to have done a better experiment'. C'est maintenant chose faite.

La chaîne de traitement des données d'Archeops (Macías-Pérez et al. 2007) est organisée comme une succession de traitements quasi indépendants :

Table 4.1 – Performance et principales caractéristiques des données recueillies lors des trois vols principaux de la mission Archeops. Pour chaque vol, les sensibilités sont des valeurs moyennes estimées après soustractions des dérives basse fréquence, et en supposant une répartition homogène du temps d'intégration sur la zone observée.

vol	fréquence	# canaux	lobe	μK.deg^{-1}	$f_{\rm ciel}$
Trapani T99	143 GHz	2	11'	110	19%
Trapani T99	217 GHz	1	12'	96	19%
Trapani T99	353 GHz	1	10'	374	19%
Kiruna KS1	143 GHz	6	10'	57	23%
Kiruna KS1	217 GHz	5	10'	51	23%
Kiruna KS1	353 GHz	5	10'	384	23%
Kiruna KS1	545 GHz	2	10'	8337	23%
Kiruna KS3	143 GHz	6	10'	33	30%
Kiruna KS3	217 GHz	7	10'	48	30%
Kiruna KS3	353 GHz	6	10'	437	30%
Kiruna KS3	545 GHz	1	10'	3417	30%

- Reconstruction du pointage à partir des données du senseur stellaire et de la mesure de la géométrie du plan focal lors de l'observation des planètes ;
- Pré–traitement des données : soustraction des pics dus aux cosmiques (ou 'glitches'), corrections de non-linéarités, correction des dérives corrélées aux mesures de température des éléments optiques, déconvolution des constantes de temps ;
- Étalonnage photométrique en utilisant le dipôle, les planètes, et les spectres FIRAS d'émission galactique ;
- Fabrication de cartes ;
- Séparation de composantes et/ou masquage des zones fortement contaminées par les émissions d'avant plan ;
- Estimation du spectre C_ℓ des anisotropies.

Une première analyse, rapide, mais non-optimisée, a permis d'obtenir une première mesure du spectre C_ℓ avant la première publication des résultats de WMAP (Benoît et al. 2003a). Cette analyse a été ensuite améliorée pour obtenir les résultats définitifs de l'expérience pour le CMB (Tristram et al. 2005). La seconde analyse a utilisé, entre autres, la méthode SMICA présentée au chapitre 5 pour améliorer l'intercalibration des détecteurs, et séparer le CMB des avant-plans astrophysiques. Les deux publications correspondantes sont jointes à ce mémoire (pages 165 et 171 respectivement).

4.3 Principaux résultats

Le premier résultat majeur d'Archeops est une mesure du spectre C_ℓ au niveau du premier pic acoustique (Benoît et al. 2003a). La figure 4.1, tirée de la publication précitée, illustre ce résultat.

Cette mesure du spectre permet de contraindre tout d'abord la position, et la largeur du premier pic acoustique, avec une précision meilleure que les expériences précédentes. La figure 4.2, montre les contours de vraisemblance d'un ajustement de la hauteur, la position, et la largeur du pic à partir des spectres mesurés par Archeops, BOOMERanG, DASI et MAXIMA. La figure (adaptée de Benoît et al. (2003b)) a été modifiée ici de façon à faire apparaître les valeurs déduites à partir du pic correspondant au modèle ajusté sur les mesures récentes par WMAP (croix vertes). Si l'amplitude du pic est en deçà de la mesure actuelle en raison des difficultés d'étalonnage mentionnées plus haut, la position et la largeur mesurées par Archeops sont en parfait accord avec les résultats récents.

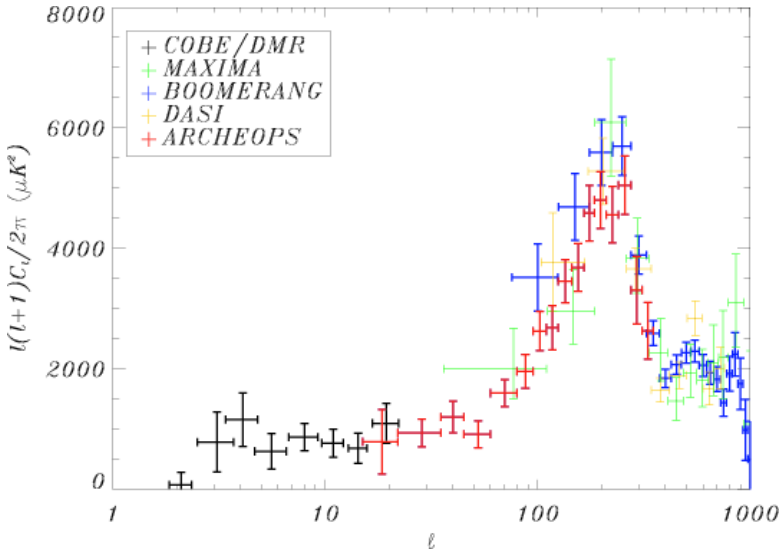

Figure 4.1 – Figure issue de Benoît et al. (2003a). Spectre d'anisotropies C_ℓ obtenu après la première analyse des données du vol KS3. L'ensemble des expériences Archeops, BOOMERanG, COBE, DASI, et MAXIMA offre une bonne mesure des premiers pics acoustiques. Noter, toutefois, un léger défaut de puissance du spectre Archeops par rapport aux autres mesures au niveau du premier pic, imputable aux erreurs d'étalonnage.

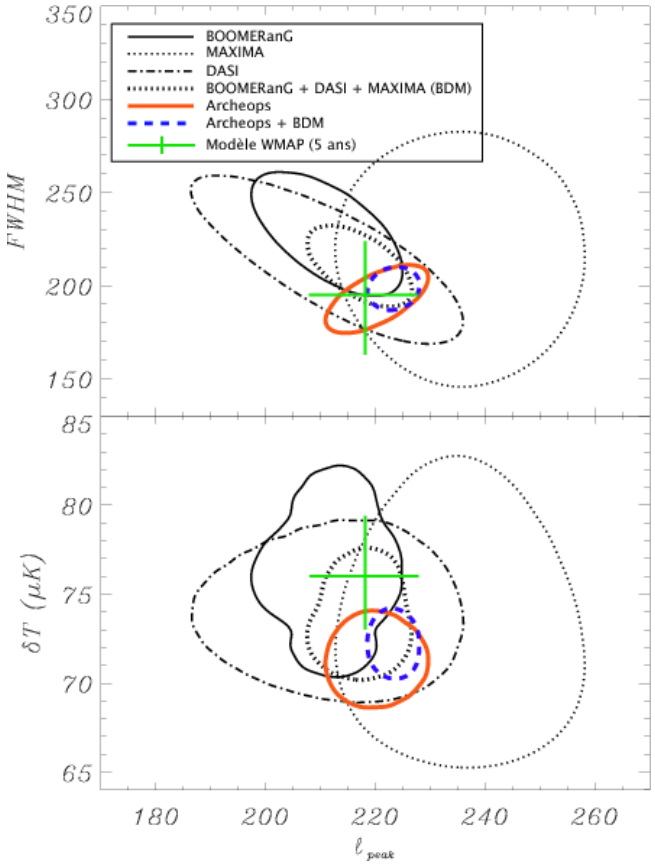

Figure 4.2 – Figure adaptée de Benoît et al. (2003b). Mesure de la position, de l'amplitude et de la largeur du premier pic acoustique à partir de combinaisons des spectres mesurés par Archeops, BOOMERanG, DASI, et MAXIMA.

Dans le cadre du modèle standard du Big-Bang, la mesure du spectre C_ℓ permet de contraindre la valeur des paramètres cosmologiques. En utilisant conjointement les meilleures mesures disponibles au moment de la publication du spectre d'Archeops, nous avons été en mesure de contraindre significativement 6 paramètres, dont certains avec précision si l'on prend en compte les contraintes issues d'autres mesures (mesure de h avec le télescope spatial Hubble, contraintes issues de l'observation des supernovae de type Ia). Les détails sont exposés dans la publication jointe à ce mémoire page 185 (Benoît et al. 2003b), parue en même temps que la première détermination du spectre Archeops, avant la publication des données de la première année d'observation de la mission WMAP et leur interprétation. Cette publication donne les principales contraintes cosmologiques obtenues avec Archeops, ainsi qu'avec une analyse jointe du spectre Archeops et d'autres observations.

Enfin, au delà de l'observation du CMB, il convient de noter qu'Archeops a également apporté des résultats intéressants scientifiquement sur la physique des avant-plans. La mesure de polarisation à 353 GHz a permis de contraindre le taux de polarisation de l'émission thermique des poussières, avec des conséquences sur l'efficacité de l'alignement des grains dans le champ magnétique galactique (Benoît et al. 2004; Ponthieu et al. 2005). Ces mesures sont utilisées pour la modélisation de l'émission polarisée des poussières, dans le cadre du Planck Sky Model (chapitre 6 du présent mémoire). Enfin, la recherche de sources compactes dans les données Archeops a mis en évidence une population nombreuse de sources galactiques froides, non détectées au préalable par les observations du satellite IRAS (Désert et al. 2008). Les données de Planck permettront de poursuivre le recensement de ces zones d'émission compactes au coeur de notre galaxie.

Chapitre 5

Séparation de composantes et estimation spectrale

5.1 Problématique, stratégies d'analyse multi-composantes

La contamination des observations du CMB par les émissions d'avant plan est une source potentielle d'erreur lors de l'observation des anisotropies de température ou de polarisation du fond cosmologique. Les premières observations du CMB sont marquées du questionnement récurrent de l'origine des anisotropies observées : anisotropies primordiales, ou émission d'avant-plan ?

En effet, le milieu interstellaire de notre galaxie et des galaxies externes émet par émission synchrotron, par émission bremstrahlung (ou free-free), par émission thermique des poussières, par des transitions atomiques et moléculaires (raies d'émission moléculaires), par émission dipolaire de grains de poussières en rotation. L'émission de notre propre galaxie par ces processus conduit à la présence d'un fond diffus de rayonnement dont l'amplitude moyenne dépend de la latitude galactique, et dont les fluctuations dépendent de la structure du milieu interstellaire. Ces mêmes processus d'émission, dans d'autres galaxies plus ou moins distantes, font apparaître des sources compactes qui contaminent l'observation du fond diffus cosmologique sur la totalité du ciel. A ces processus d'émission s'ajoutent l'effet SZ décrit au chapitre précédent, la lumière zodiacale des poussières de notre système solaire, et éventuellement d'autres processus comme une émission d'annihilation de WIMPs au coeur de notre galaxie. Le fond cosmologique se distingue par une signature spectrale connue, sa loi d'émission étant celle d'une dérivée de corps noir par rapport à la température.

Si elle a marqué les premières mesures, l'évaluation de l'impact des avants-plans est aussi le problème ultime auxquelles les observations du fond cosmologiques sont confrontées, puisque s'il est toujours possible d'augmenter la sensibilité d'un instrument, nous ne disposons que d'un ciel à observer, dont il n'est pas possible de modifier les processus d'émission.

Les observations multi-fréquence de COBE, de Boomerang, de WMAP, ont permis de vérifier que les fluctuations de température observées à haute latitude galactique avaient bien un spectre d'émission de CMB, la dérivée (par rapport à la température) d'une loi de corps noir à 2,725 K. Ainsi, le CMB est à l'origine de l'essentiel des fluctuations de l'émission de fond de ciel autour de 100 GHz (3 mm) à haute latitude galactique.

Pour l'objectif scientifique consistant à mesurer le spectre de puissance des anisotropies de température, la stratégie la plus simple et la plus efficace pour s'affranchir de la contamination des observations par les avant-plans consiste dès-lors à observer dans des régions où ceux-ci restent peu gênants. Les régions les moins contaminées, où sont réalisées et analysées les observations du ciel,

sont identifiées à partir de traceurs annexes d'émission galactique : raies moléculaires, observations de l'instrument DIRBE et du satellite IRAS, observations du synchrotron à 408 MHz, et de l'émission Hα du milieu interstellaire ionisé.

Lorsque l'on souhaite augmenter la couverture du ciel pour une meilleure contrainte des premiers modes harmoniques du spectre C_ℓ de fluctuations du fond, et lorsque le bruit instrumental devient sous-dominant dans le budget des erreurs, l'interprétation des observations nécessite l'identification et la séparation des différentes composantes qui contribuent au signal observé. Cette activité de 'séparation de composantes' est, par ailleurs, une nécessité lorsque l'on s'intéresse à l'ensemble des émissions du ciel, et non au seul fond diffus cosmologique. C'est également une nécessité absolue pour la mesure précise de la polarisation du fond diffus (voir section 5.4).

En traitement de signal ou d'image, le problème de 'séparation de sources' (à comprendre comme 'sources distinctes de signal') fait l'objet d'un champ d'investigations riche en applications, appelé Analyse en Composantes Indépendantes (ACI en français, ou ICA en anglais). Ce nom fait apparaître le point crucial de la séparation de composantes : la définition même des composantes à partir de leur indépendance statistique. En traitement de signal, les 'sources' seront des processus ayant des origines physiques distinctes, et qui sont donc supposées indépendantes dans la mesure où chacune émet sa propre partie indépendamment des autres.

Comme nous le verrons plus loin, pour les applications astrophysiques, cette façon de définir les composantes ne convient pas vraiment. L'astrophysicien s'intéresse à des émissions définies soit comme ayant pour origine des phénomènes physiques distincts (émission synchrotron par opposition à émission free-free, par exemple, ou émission thermique des poussières par opposition à émission non thermique des grains de poussière en rotation), soit comme provenant de régions ou d'objets différents (notre galaxie, par opposition à d'autres galaxies, ou à la surface de dernière diffusion ; la poussière galactique, par opposition au synchrotron galactique...). Ainsi, la séparation de composantes en astrophysique se basera sur une modélisation des émissions, contrairement aux méthodes d'analyse en composantes indépendantes classiques qui laissent, en général, exclusivement 'parler les données'.

Par ailleurs, contrairement aux applications traditionnelles de séparation de sources pour l'imagerie médicale ou le traitement d'enregistrements sonores pour lesquels la validité de la séparation se fait sur des critères qualitatifs (le signal est il reconnaissable à un observateur humain), la séparation de sources en astrophysique nécessite une évaluation quantitative des erreurs : erreurs statistiques, et erreurs de modélisation. C'est ce qui fait de ce champ d'investigation en astronomie une discipline particulièrement intéressante et complexe.

Un article de revue assez complet sur la séparation des composantes diffuses (Delabrouille & Cardoso 2009), qui fait suite à un cours donné sur le sujet à l'école d'été 'Analyse de données en cosmologie' tenue à Valence en Espagne en septembre 2004, est annexé à ce mémoire en page 191. Parmi les méthodes présentées, deux ont fait l'objet d'une partie importante de mon activité de recherche depuis 2001. La première, SMICA (Spectral Matching Independent Component Analysis), modélise les observations comme un mélange linéaire de composantes statistiquement indépendantes, et estime des modèles paramétriques des matrices de covariance spectrale des composantes pour les séparer par filtrage de Wiener. La deuxième, la méthode ILC (Internal Linear Combination), estime une composante unique (par exemple le CMB ou le SZ), dans l'hypothèse de séparabilité de sa loi d'émission (i.e. $x_c(\nu, p)$ pour cette composante peut s'écrire comme le produit d'une fonction de ν seulement supposée connue, et d'une fonction de p seulement à estimer, $x_c(\nu, p) = a(\nu)s(p)$). L'estimation de $s(p)$ se fait par formation de la combinaison linaire des données qui reconstruit $s(p)$ avec un gain de 1 en minimisant la variance de la carte reconstruite.

5.1.1 Composantes

Le milieu interstellaire diffus et ionisé de notre galaxie émet par rayonnement synchrotron et/ou par rayonnement de freinage (free-free). Les condensations de matière plus froide, nuages moléculaires et grains de poussière microscopiques, émettent par d'autres processus : raies d'émission des molécules et des atomes, rayonnement thermique des poussières. Enfin, il semble de plus en plus évident que la poussière galactique émet également un rayonnement non thermique aux alentours de 10 GHz (voir chapitre 6).

A ces émissions diffuses viennent se superposer les émissions de sources plus localisées, que ce soient des régions localisées de notre galaxie (nuages moléculaires denses, résidu stellaires, régions de formation d'étoiles, régions H-II), ou des objets extragalactiques (radio-sources, galaxies, amas de galaxies).

L'émission totale du ciel comprend donc à la fois une superposition d'émissions diffuses (CMB, composantes galactiques), et la contribution d'objets compacts (point sources, amas SZ). La détection des points sources dans les cartes se base essentiellement sur des méthodes de filtrage spatial, alors que la séparation de composantes diffuses fait appel à des méthodes multifréquence basées sur une modélisation paramétrique plus ou moins physique des émissions.

L'approche la plus classique de la séparation de composantes distingue ainsi deux types de traitements.

1. Détection des objets compacts (sources compactes et amas de galaxies) par des méthodes de filtrage spatial, et soustraction de l'émission des sources ainsi détectées (ou masquage des pixels concernés) ;
2. Séparation des composantes diffuses, supposées contenir essentiellement du CMB, l'émission du milieu interstellaire, et un résidu d'émission de sources compactes non détectées individuellement.

La séparation de composantes nécessite la mise en place d'une chaîne d'analyse comprenant différents traitements, itérant entre ces deux types de filtrages pour en optimiser l'efficacité, et permettant de caractériser les erreurs de reconstruction des différents processus d'émission.

La détection des amas SZ par filtrage spatial a été présentée au chapitre 2. Nous discutons ici la séparation de composantes diffuses par des méthodes multifréquence exploitant les lois d'émission des composantes, ainsi que certaines de leurs propriétés statistiques.

5.1.2 Position du problème

De façon générale, l'observation du ciel dans une collection de N_i bandes de fréquence $b_i(\nu)$ indexées par i, sur une collection de pixels indexés par p, peut s'écrire comme un mélange linéaire d'émissions $s_c(\nu, p)$, correspondant à N_c composantes indexées par c.

$$x_i(p) = \sum_c \int_\nu b_i(\nu) s_c(\nu, p) d\nu + n_i(p) \tag{5.1}$$

$$= \sum_c s_{ci}(p) + n_i(p) \tag{5.2}$$

En l'absence de toute hypothèse supplémentaire, le problème de séparer les différentes composantes, i.e. estimer les différentes émissions $s_c(\nu, p)$, ou même leurs version intégrées dans les bandes d'observations, $s_{ci}(p)$, ne peut être résolu. Les différentes méthodes de séparation de composantes vont s'appuyer sur différents types d'hypothèses, qui modélisent de façon plus ou moins précise les différentes émissions astrophysiques, les effets liés à la réponse de l'instrument, et le bruit de mesure.

J'ai travaillé particulièrement sur le développement et l'utilisation de deux méthodes, l'ILC et SMICA, présentées respectivement dans les sections 5.2 et 5.3.

5.1.3 Planck Working Group 2

Dans le cadre de la mission Planck, les activités relevant de la séparation de composantes sont intimement liées à la problématique de la définition des composantes, à leur représentation (sur la base de paramètres physiques ou à partir de propriétés d'ordre statistique), et à la modélisation de l'émission du ciel décrite au chapitre 6. L'ensemble de ces activités font l'objet d'un groupe de travail, le groupe WG2, dont j'assure la coordination pour l'instrument HFI. Le groupe de travail a notamment organisé plusieurs data challenges, qui ont permis de comparer, sur un même jeu de données simulées, les performances des différentes méthodes de séparation de composantes développées au sein de la collaboration. Le travail d'extraction des composantes, effectué en aveugle dans un premier temps, puis finalisé après mise à disposition des différentes composantes entrant dans les simulations, a permis de mettre en évidence les limitations des différents codes, et d'en comparer les performances de façon objective.

Une publication reproduite en annexe en page 239 (Leach et al. 2008) donne les principales conclusions de cette comparaison dans le cadre d'un *data challenge* visant à extraire le meilleur CMB possibles de données simulées à l'aide du Planck Sky Model. La publication compare les résultats obtenus avec 9 méthodes différentes. Parmi celles-ci, la méthode SMICA, dont il est question section 5.3, se compare très favorablement aux méthodes concurrentes en terme d'erreurs résiduelles. Aux échelles inférieures à quelques degrés ($\ell = 50 - 100$, en fonction de la zone considérée) SMICA offre la meilleure reconstruction. A plus bas ℓ, la comparaison est plus mitigée, et il semble que la méthode SMICA est moins performante que certaines de ses concurrentes. Il est plausible que ceci soit dû au manque de statistique pour l'ajustement spectral aux grandes échelles. Notons toutefois que, dans l'objectif de la mesure du spectre C_ℓ de température du fond cosmologique, la variance cosmique est de toute façon la source principale d'erreur.

5.2 ILC et applications

L'utilisation d'un modèle complet des différentes émissions afin de les séparer pose nécessairement le problème de la pertinence du modèle. La méthode 'ILC' (Internal Linear Combination) évite cet écueil en n'utilisant que des hypothèses minimalistes. L'ILC sépare les composantes uniquement sur la base de considérations d'ordre statistique (décorrélation de la composante d'intérêt et des composantes de contamination). Ceci pose problème pour des jeux de données de taille insuffisante pour que les statistiques soient estimées sur les données de façon précise (voir section 5.2.2).

Considérons le problème d'extraire, d'une collection d'observations du ciel à différentes fréquences, une composante unique (la plupart du temps, le fond diffus cosmologique) dont on suppose :

- que son émission s'écrit $x(\nu, p) = a(\nu)s(p)$ (séparabilité d'une loi d'émission $a(\nu)$ est d'une carte d'intensité $s(p)$) ;
- qu'elle est décorrélée des autres émissions et du bruit dans chaque canal.

Les observations, à une série de fréquences ν_i, s'écrivent alors sous la forme :

$$x_i(p) = a_i s(p) + n_i(p) \tag{5.3}$$

Ici, $s(p)$ est la carte d'intensité de la composante astrophysique d'intérêt, et les coefficients a_i sont supposés connus (ils sont entièrement déterminés par la loi d'émission de la composante et les bandes instrumentales). La contamination de l'observation, représentée par le terme n_i, contient les émissions de tous les autres processus astrophysiques, ainsi que la contribution du bruit de mesure.

On recherche une estimée $\widehat{s}(p)$ de $s(p)$ sous la forme d'une combinaison linéaire des observations :

$$\widehat{s}(p) = \sum w_i x_i(p) = \boldsymbol{w}^t \boldsymbol{x} \tag{5.4}$$

Si l'on impose la contrainte $w.a = 1$, qui garantit une réponse unité à la composante d'intérêt, et si $s(p)$ et $n_i(p)$ sont décorrélés pour tout i, alors la combinaison linéaire qui minimise l'erreur de reconstruction au sens des moindres carrés s'écrit comme ci-dessus, avec :

$$[\boldsymbol{w}_{\rm ILC}]^t = \frac{\boldsymbol{a}^t \widehat{\mathbf{R}}_x^{-1}}{\boldsymbol{a}^t \widehat{\mathbf{R}}_x^{-1} \boldsymbol{a}} \tag{5.5}$$

où $\widehat{\mathbf{R}}_x$ est la matrice de corrélation empirique des observations. C'est la solution ILC.

5.2.1 ILC sur une décomposition en ondelettes

Pour une application particulière, la combinaison linéaire optimale dépend de la région observée, ou de l'échelle angulaire. Ceci appelle à réaliser le filtrage ILC de façon localisée, soit dans l'espace harmonique, soit dans l'espace des pixels, soit dans ces deux espaces, en utilisant des formes d'ondelettes. Nous avons développé une implémentation de l'ILC utilisant une décomposition des données sur un type particulier d'ondelettes, les *needlets*. Cette méthode a été appliquée à l'analyse des données 5 ans de l'expérience WMAP, pour estimer une carte complète du CMB à partir des données publiques de la mission spatiale (Delabrouille et al. 2009). La publication décrivant ce travail sur les données WMAP est jointe en annexe au présent mémoire (page 259).

Une part importante de la publication est consacrée à comparer cette carte aux cartes précédentes. Nous montrons notamment que la carte NILC (Needlet ILC) est sensiblement moins contaminée que les autres dans le plan galactique d'une part, et à petite échelle angulaire d'autre part, où la carte obtenue est très compétitive. La localisation dans les deux espaces (pixel et harmoniques sphériques) permet en effet d'adapter les poids de l'ILC aux conditions locales de contamination par les avant-plans et le bruit non-stationnaire.

Aux grandes échelles, la situation est moins claire. Les biais de l'ILC, dont il est question section 5.2.2, sont susceptibles de dégrader la qualité du filtre, et nous n'avons pas de moyen direct d'évaluer l'impact exact de ces biais, sinon par des simulations numériques nécessairement partiellement dépendantes des détails du modèle supposé dans la simulation. Le manque de statistique aux grandes échelles est clairement un handicap pour les méthodes de séparation aveugles, qui présupposent le strict minimum sur les sources de contamination astrophysique et instrumentale des observations.

Nous avons également appliqué une méthode d'ILC dans l'espace des needlets pour l'extraction d'une carte d'effet SZ de données simulées de la mission Planck. Le SZ (dans son approximation non-relativiste) se prête bien à l'utilisation d'une méthode d'ILC, puisque l'émission est séparable comme le produit d'une carte de paramètre de comptonisation y, et d'une loi d'émission universelle connue. L'ILC needlets a été utilisée pour le 'Challenge SZ' co-organisé par les groupes WG2 (séparation de composantes) et WG5 (anisotropies secondaires) de Planck. Une post-détection des amas sur la carte de SZ obtenue par notre méthode a permis l'obtention des meilleurs catalogues d'amas (en terme de complétude à taux de contamination fixe) parmi 9 méthodes participantes au 'data challenge'. Une publication résumant les résultats de cette comparaison est en phase de finalisation pour soumission à A&A.

5.2.2 Biais de l'ILC

Il convient de noter que l'application de l'ILC à de petits jeux de données conduit en général à un biais, dont l'origine est expliquée en détail dans notre travail sur les données WMAP. L'existence de

ce biais, engendré par la corrélation empirique de l'émission d'intérêt avec les contaminants lorsque la statistique est limitée, a été réalisée (probablement plus ou moins indépendamment) par différents auteurs au cours des dernières années (Hinshaw et al. 2007; Saha et al. 2008; Delabrouille & Cardoso 2009). Notre article (Delabrouille et al. 2009) est à ce jour le seul, à notre connaissance, qui discute ce premier biais de façon assez exhaustive (voir publication jointe page 259).

Qualitativement, ce premier biais peut s'expliquer de la façon suivante. Dans la mesure ou le filtre ILC (équation 5.5) est la combinaison linéaire des données qui minimise la variance de la carte reconstruite (et non directement de l'erreur de reconstruction), tout mode de fond cosmologique qui se trouverait être corrélé au bruit ou aux avants-plans peut être annulé par une combinaison linéaire appropriée de ces bruits et avants-plans. La puissance de fond cosmologique ainsi annulée est proportionnelle à la covariance empirique de la carte d'intérêt et des contaminants.

Dans le même esprit, nous avons montré par ailleurs que l'ILC était susceptible d'être à l'origine d'erreurs grossières de reconstruction en présence d'erreurs de calibration (Dick et al. 2010). Ce second biais est dû au fait qu'en présence d'erreurs sur la connaissance des coefficients a_i, le critère de minimisation de l'ILC (minimisation de la variance totale de la carte reconstruite, sous contrainte de réponse unité au fond cosmologique) pousse la solution à annuler une partie de la composante d'intérêt, ce qui est possible en raison de l'erreur sur la contrainte. Paradoxalement, ces erreurs de calibration induisent des erreurs de reconstruction d'autant plus fortes que le rapport signal à bruit est grand. Le bruit permet, en quelque sorte, de régulariser le comportement de l'ILC. La publication décrivant ce travail est jointe à ce mémoire page 283.

Ainsi, la méthode ILC, si elle présente l'énorme avantage d'être très simple d'implémentation et de ne faire aucune hypothèse sur les avants-plans, doit toujours être utilisée avec circonspection, et ce d'autant plus que le rapport signal sur bruit est élevé, puisque les biais deviennent alors la source dominante d'erreur.

5.2.3 Optimalité de l'ILC

Notons que dans le cas où l'estimée $\widehat{R}_x$ de la matrice de covariance des observations est parfaite ($\widehat{R}_x = R_x$), si la composante d'intérêt est de loi d'émission connue (colonne a de la matrice de mélange connue), et si la composante d'intérêt n'est pas corrélée avec les autres composantes, alors la solution ILC est strictement équivalente à la solution de moindre carré :

$$[\boldsymbol{w}_{\chi^2}]^t = \frac{\boldsymbol{a}^t \mathbf{R}_n^{-1}}{\boldsymbol{a}^t \mathbf{R}_n^{-1} \boldsymbol{a}} \tag{5.6}$$

où $\mathbf{R}_n$ est la matrice de corrélation du 'bruit' (qui comprend le bruit instrumental et le 'bruit' d'avant-plan astrophysique). En effet, on a alors

$$\begin{aligned}
\boldsymbol{a}^t \widehat{\mathbf{R}}_x^{-1} &= \boldsymbol{a}^t \mathbf{R}_x^{-1} && (5.7)\\
&= \boldsymbol{a}^t \left[\mathbf{R}_n + \sigma^2 \boldsymbol{a}\boldsymbol{a}^t\right]^{-1} && (5.8)\\
&= \boldsymbol{a}^t \left[\mathbf{R}_n^{-1} - \sigma^2 \frac{\mathbf{R}_n^{-1}\boldsymbol{a}\boldsymbol{a}^t\mathbf{R}_n^{-1}}{1+\sigma^2 \boldsymbol{a}^t \mathbf{R}_n^{-1}\boldsymbol{a}}\right] && (5.9)\\
&\propto \boldsymbol{a}^t \mathbf{R}_n^{-1} && (5.10)
\end{aligned}$$

et donc $\boldsymbol{w}_{\rm ILC} = \boldsymbol{w}_{\chi^2}$. L'ILC peut donc être vue comme une solution approchée de la solution 'optimale' des moindres carrés, dans la limite asymptotique où les matrices de covariance sont bien estimées (i.e. quand, par limite centrale, un grand nombre de modes indépendants sont disponibles pour les estimer).

5.2.4 Extensions de l'ILC

L'ILC telle que présentée ci-dessus s'applique pour la reconstruction d'une composante unique. Dans nos travaux récents (Remazeilles et al. 2010), nous montrons que l'ILC peut être étendue à la reconstruction de plusieurs composantes de lois d'émission connue non corrélées entre elles, avec contamination nulle de l'une dans les autres. La publication correspondante, *CMB and SZ effect separation with constrained Internal Linear Combinations*, est annexée à ce mémoire en page 295. Nous montrons également qu'il est possible d'étendre la méthode à la reconstruction d'une composante 'multidimensionnelle', dont l'émission $s_i(p)$ en fonction du canal de fréquence (indexé par i) peut s'écrire comme un mélange de composantes $u_j(p)$ éventuellement corrélées, $s_i(p) = \sum_j A_{ij} u_j(p)$.

5.3 SMICA

La méthode SMICA (pour Spectral Matching Component Separation Analysis), est une méthode aveugle de séparation de composantes et d'estimation spectrale. Il s'agit d'une méthode très souple permettant d'ajuster aux données un modèle paramétrique des émissions astrophysiques et du bruit. Contrairement à l'ILC, elle ne nécessite de connaître *a priori* aucune des lois d'émission des différentes composantes présentes dans les données.

La justification du développement de cette méthode, à l'origine, part de la constatation que la séparation de composantes, dans le cas de mélanges linéaires, utilise la matrice de corrélation du bruit, des composantes, et des coefficients du mélange. Un mélange linéaire de composantes dont l'émission est parfaitement séparable en une carte d'amplitude $s(p)$ multipliée par un spectre d'émission s'écrit :

$$\boldsymbol{x}(p) = \mathbf{A}\boldsymbol{s}(p) + \boldsymbol{n}(p) \tag{5.11}$$

où $x(p)$ est le vecteur des observation (n cartes $x_i(p)$, pour $i = 1...n$), $\boldsymbol{s}(p)$ est le vecteur des composantes (m cartes indexées par j, pour $j = 1...m$), et la matrice $\mathbf{A}$ de dimension $n \times m$ est appelée matrice de mélange. La propriété critique de ce modèle des composantes est que la matrice $\mathbf{A}$ ne dépend pas du pixel p (ni du mode harmonique ℓ, m).

Pour un tel mélange, la séparation des composantes par filtrage de Wiener par exemple (méthode optimale pour des composantes représentées par des champs stationnaires gaussiens), s'écrit :

$$\widehat{\boldsymbol{s}}(p) = \left[\mathbf{A}^t \mathbf{R}_n^{-1} \mathbf{A} + \mathbf{R}_s^{-1}\right]^{-1} \mathbf{A}^t \mathbf{R}_n^{-1} \boldsymbol{x}(p) \tag{5.12}$$

Les cartes $\widehat{s}_i(p)$ sont des estimées des cartes d'émissions des composantes $s_i(p)$.

L'implémentation de cette solution nécessite la connaissance de la matrice de mélange $\mathbf{A}$, et des matrices de corrélation des signaux astrophysiques, $\mathbf{R}_s$, et du bruit $\mathbf{R}_n$.

Dans le cas qui nous intéresse, l'objectif premier des expériences est précisément la mesure de la matrice de corrélation $\mathbf{R}_s$ du CMB (ou, de façon équivalente, du spectre de puissance angulaire C_ℓ). Par ailleurs, la matrice $\mathbf{A}$ reflète les lois d'émission des différentes composantes, qui ne sont pas forcément parfaitement connues, et présentent dans certains cas elles-mêmes un intérêt scientifique (par exemple, dans le cas du synchrotron ou de l'émission des poussières). Il n'est pas très satisfaisant d'utiliser, tôt dans la chaîne d'analyse, une connaissance *a priori* des paramètres que l'on cherche à mesurer.

SMICA offre une solution élégante à ce problème, en permettant d'estimer les spectres de puissance des différents processus, ainsi que la matrice de mélange, directement à partir des observations. Cette solution consiste à ajuster, sur les matrices de covariance empiriques $\widehat{\mathbf{R}}_x(\ell, m)$, un modèle de covariance de la forme $\mathbf{A}\mathbf{R}_s(\ell, m)\mathbf{A}^t + \mathbf{R}_n(\ell, m)$. Pour une implémentation dans l'espace harmonique dans

des domaines moyennes en m, le terme diagonal de $\mathbf{R}_s$ correspondant à la composante du fond cosmologique est directement une mesure du spectre C_ℓ. La méthode SMICA est donc, avant même d'être une méthode de séparation de composantes, une méthode d'estimation spectrale multi-composantes.

Le papier fondateur de la méthode (Delabrouille et al. 2003a) est reproduit en annexe page 303. Par la suite, nous avons assoupli le modèle de covariance, qui peut désormais comprendre des composantes corrélées entre elles, comprendre conjointement les spectres de température et de polarisation, ou dépendre directement et explicitement des paramètres cosmologiques (Cardoso et al. 2008; Betoule et al. 2009). Par ailleurs, ce modèle peut être contraint (certains paramètres peuvent être fixés).

Comme nous l'avons vu au chapitre 4, la méthode SMICA a été utilisée pour l'analyse des données Archeops (Tristram et al. 2005). Elle a également été utilisée sur les données WMAP (publication de Patanchon et al. (2005) jointe en annexe de ce manuscrit, page 317). Elle a été utilisée dans les différents "data challenges" organisés par le Working Group 2 de Planck, pour la préparation d'une future mission de mesure de polarisation (voir section 5.4). Enfin, elle est utilisée actuellement pour l'analyse en cours des données de Planck.

5.4 Séparation de composantes polarisées

La question de la séparation de composantes en polarisation est une question cruciale pour Planck et pour une future mission dédiée à la détection des modes B primordiaux d'origine tensorielle, qui serait une suite naturelle aux observations précédentes par les missions spatiales COBE, puis WMAP, puis Planck.

La séparation de composantes en polarisation se différencie de la séparation de composantes en température par plusieurs aspects. Le premier est le caractère particulier du champ de polarisation sur la sphère, qui nécessite son analyse en harmoniques sphériques de spin 2. Toutefois, une fois cette analyse faite, les coefficients $a^E_{\ell m}$ et $a^B_{\ell m}$ peuvent être utilisés pour reconstruire, par simple transformée en harmoniques sphériques inverse, des champs scalaires non spinnés, dont les cartes d'émissions sont les cartes de E et de B.

Il est possible dès-lors d'appliquer à chacune de ces cartes (ou de ces jeux de cartes multi-fréquence), les mêmes types d'outils d'analyse que ceux utilisés pour la séparation de composantes en température. Toutefois, pour l'analyse d'observations telles celles de WMAP et Planck, nous ne disposons à l'heure actuelle ni de modèle fiable de l'émission polarisée, ni de cartes "externes" qui permettraient de marquer le niveau d'émission des avant-plans, ou pourrait être utilisée pour nettoyer les observations du fond cosmologique par décorrélation d'une carte externe de l'émission. Les méthodes aveugles que nous avons développées, telles SMICA ou l'ILC sur des domaines de needlets, prennent alors tout leur sens.

Une adaptation de la méthode SMICA pour contraindre le rapport tenseur-scalaire à l'aide des modes B de la polarisation du fond cosmologique a fait l'objet d'une partie du travail de thèse de Marc Betoule sous ma direction (Betoule et al. 2009). Pour Planck en particulier, nous montrons que la principale source d'erreur pour cette mesure provient de la sensibilité limitée de la mission. La publication correspondante est jointe à ce mémoire en page 327. Ce travail a également été intégré dans une publication de synthèse de l'état de l'art en séparation de composantes polarisée pour la préparation d'une future mission spatiale dédiée à ces mesures (Dunkley et al. 2009a).

Plus récemment, dans le cadre de la préparation d'une réponse à un appel d'offre de l'ESA pour une mission moyenne, nous avons proposé la mission COrE, pour laquelle Soumen Basak et moi-même avons implémenté une mesure du spectre des modes B de polarisation par ILC sur des domaines de needlets. Pour cette mission, j'ai proposé une configuration utilisant 15 bandes de fréquence réparties

entre 45 et 795 GHz, qui a été retenue pour la réponse à l'appel d'offre. Le grand nombre de canaux offre d'excellentes perspectives pour différencier l'émission du fond cosmologique des avant-plans polarisés, sans avoir besoin de former d'hypothèse particulière sur la structure de ceux-ci. La figure 5.1 montre les résultats obtenus lors de cette étude de séparation de composantes, qui démontrent une réjection des avant-plans permettant de mesurer $r \simeq 10^{-3}$.

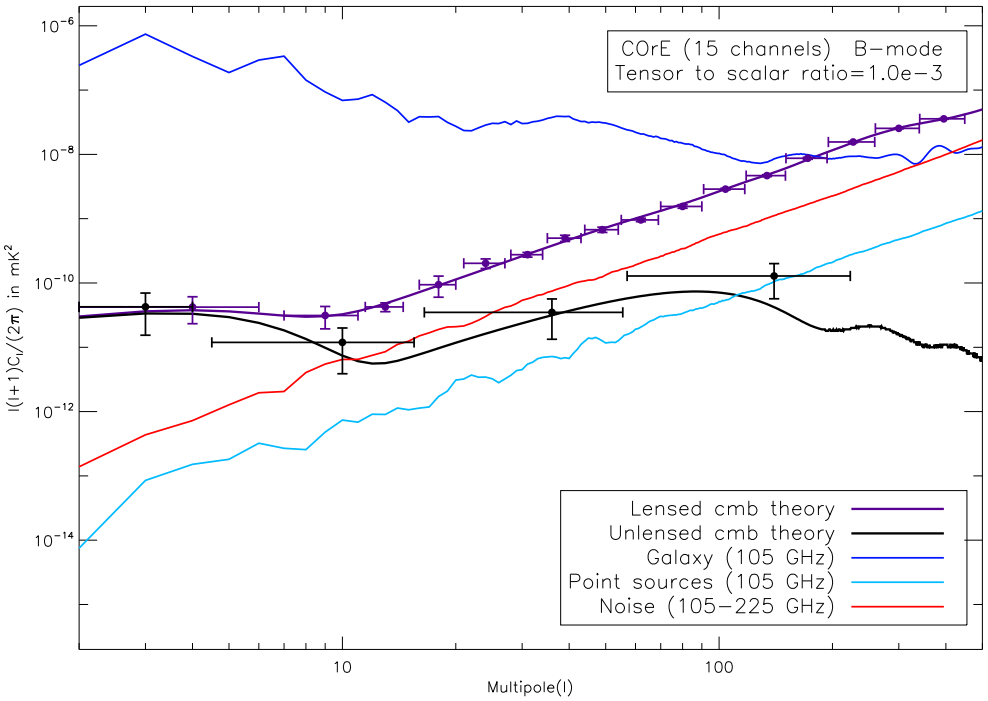

Figure 5.1 – Séparation de composantes polarisées pour la mesure du spectre C_ℓ^{BB}. Les courbes bleu foncé et bleu clair correspondent à la contamination par les avant-plans à 105 GHz, après avoir coupé les sources les plus fortes (flux supérieur à 100 mJy à 20 GHz et 500 mJy à 100 microns). La courbe violette correspond au spectre des modes B (primordiaux et dus aux effets de lentille gravitationnelle), et la courbe noire la contribution d'origine tensorielle à ce spectre de modes B. les points de même couleur correspondent à la mesure obtenue après séparation de composantes.

5.5 Estimation spectrale

5.5.1 Needlets

Si l'observation de petits régions du ciel peut se faire en approximation plane, l'analyse des observations d'expériences comme WMAP et Planck implique le traitement de données de géométrie sphérique.

Ainsi, tous les outils classiques de traitement d'images échantillonnées sur un pavé du plan ne peuvent pas être directement utilisés sur la sphère. Certes, il est possible de découper celle-ci en petites cartes constitutives d'un atlas. Ceci, toutefois, est source de complications : effets de bord, problèmes de continuité.

Par ailleurs, les spectres de puissance du fond cosmologique se calculent à partir de la décomposition en harmoniques sphériques des champs de température et de polarisation sur la sphère. Le développement de la librairie logicielle HEALPix (Górski et al. 2005), qui implémente à différentes

résolutions des pavages de la sphère en pixels de surface identique et les transformées en harmoniques sphériques associées, permet l'équivalent sur la sphère de ce qu'est la transformée de Fourier discrète en traitement classique d'images sur le plan.

La deuxième moitié du XXe siècle a vu l'émergence de l'analyse en ondelettes. La décomposition d'une image sur une base d'ondelettes permet de l'analyser simultanément dans l'espace des pixels et dans l'espace de Fourier. Ceci permet de prendre en compte à la fois la localisation des propriétés de l'image dans l'espace des pixels et dans l'espace des fréquences.

On s'attend, dans le cadre du modèle cosmologique inflationnaire standard, à ce que les anisotropies du fond de rayonnement cosmologique soient parfaitement décrites par un champ gaussien stationnaire (les corrections non gaussiennes et non stationnarités étant au mieux de second ordre). Ainsi, les harmoniques sphériques semblent parfaitement adaptées à l'analyse des propriétés statistiques de ce champ. Par contre, l'émission des avant-plans n'est pas stationnaire. Une analyse en harmoniques sphériques présente l'inconvénient de sommer, dans un unique coefficient de la décomposition, les contributions de régions du ciel fortement contaminées par les avant-plans galactiques, et celles de régions très éloignées du plan de la galaxie.

En réalité, aucune des émissions du ciel, à l'exception du fond cosmologique, n'est parfaitement stationnaire. Le bruit instrumental n'est pas non plus, en général, un champ stationnaire. Ceci appelle à la location des traitements dans l'espace des pixels et dans l'espace des harmoniques sphériques, et donc à l'utilisation d'ondelettes pour analyser les observations sur la sphère.

Pour cette raison, nous avons développé une méthode d'estimation spectrale basée sur les needlets, qui permet d'estimer le spectre C_ℓ du ciel à partir d'un ensemble de cartes mesurées chacune avec un niveau de sensibilité et une résolution qui lui est propre, et couvrant éventuellement chacune une fraction du ciel. La publication correspondante, *CMB power spectrum estimation using wavelets*, parue en 2009 dans Physical Review D, est jointe à ce mémoire page 347.

Chapitre 6

Un modèle d'émission du ciel millimétrique

Le développement d'une mission spatiale comme Planck nécessite, pour son optimisation, une chaîne de simulation. La première brique consiste en un modèle d'émission du ciel, qui permet de prédire ou de simuler une émission du ciel plausible, et de tester l'adéquation de l'expérience pour tirer de 'l'observation' de ces cartes simulées l'information recherchée.

A cette fin, nous avons décidé de développer un outil de prédiction et simulation du ciel millimétrique, le Planck Sky Model (PSM). Le PSM est l'outil de référence utilisé pour les simulations dans le cadre de la mission Planck. Il est également utilisé dans la communauté scientifique plus large. J'ai défini la stratégie d'ensemble de son développement, coordonné les activités, et participé activement à l'écriture d'une grande partie du code.

6.1 Le concept du PSM

La constitution d'un modèle d'émission du ciel millimétrique, et la possibilité d'en simuler l'émission multi-composantes en température et en polarisation, répond en effet à un besoin crucial pour la planification d'observations du fond cosmologique, pour la mise en place de méthodes d'analyse (notamment pour la séparation des composantes) et pour l'interprétation d'observations telles celles des satellites WMAP et Planck.

En témoignent les efforts effectués en ce sens par nombre d'auteurs ou d'équipes de recherche. Un premier modèle d'émission du ciel pour la préparation de la mission Planck a été créé par Bouchet & Gispert (1999). Ce modèle a été par la suite amélioré par Tegmark et al. (2000), avec l'introduction de variations d'indice spectral des différentes composantes galactiques. Plus récemment, de Oliveira-Costa et al. (2008) ont construit un modèle de l'émission du ciel entre 10 MHz et 100 GHz, basé sur l'interpolation et l'extrapolation d'un grand nombre d'observations du ciel dans cette gamme de fréquence. Enfin, Sehgal et al. (2010) ont modélisé l'émission du ciel micro-ondes à 30 secondes d'arc de résolution pour tester le pipeline d'analyse de l'expérience ACT.

De même, plusieurs 'data challenges' ont été organisés sur la base d'observations simulées du ciel millimétrique (Jaffe et al. 1999; Leach et al. 2008).

Le rayonnement électromagnétique perceptible lors d'observations du ciel millimétrique provient essentiellement de quelques processus physiques distincts. Dans le domaine millimétrique, on distingue habituellement le fond diffus cosmologique, les émissions du milieu interstellaire dans notre galaxie (au nombre de trois, ou quatre), les sources extragalactiques (qui se répartissent en plusieurs populations

plus ou moins bien définies), et l'effet Sunyaev Zel'dovich dont il a été question au chapitre 2.

Le PSM présenté ici n'est pas un outil de simulation de la physique de ces processus d'émission. Il se distingue ainsi des grandes simulations cosmologiques de formation de structures (Katz et al. 1996; Kravtsov et al. 1997; Springel et al. 2001; Teyssier 2002) ou de défauts topologiques, des simulations hydrodynamiques ou magnéto-hydrodynamiques d'amas de galaxies (Navarro et al. 1995; Knight & Ponman 1997; Quilis et al. 2001; da Silva et al. 2004; Springel et al. 2005; Norman 2010), des simulations physiques du milieu interstellaire (Waelkens et al. 2009) ou des processus d'émission d'astres compacts. C'est un modèle phénoménologique, dont l'objectif premier est décrire l'émission du ciel par un modèle paramétrique cohérent, justifié par la physique et les observations, et permettant de produire des cartes représentant au mieux l'émission effective qui peut être observée dans tout le domaine de fréquences situé entre 3 GHz et 3 THz (entre 10 cm et 100 μm).

6.1.1 Le logiciel

Le logiciel du PSM est écrit essentiellement en langage IDL. Le logiciel dans sa version 1.7 est constitué de près de 500 fonctions et procédures IDL, qui représentent un peu plus de 20000 lignes de code (en excluant environ 10000 lignes de commentaires). Il fait appel à quelques librairies externes (principalement astron, HEALPix, CAMB, et MPFIT), et utilise un nombre de fichiers de données annexes, correspondant soit à des données (observations, simulations) faisant partie du domaine public, soit à des données préparées spécifiquement pour le PSM.

Le logiciel est conçu de façon a pouvoir être appelé aisément au sein d'un pipeline de simulation incluant, en aval, outre une observation plus ou moins sophistiquée du ciel ainsi simulé, une chaîne de traitement et d'analyse de ces observations. Ceci est censé permettre, à terme, la réalisation de simulations Monte Carlo dont la simulation du ciel avec le PSM ne constituera que l'une des parties.

6.1.2 Simulation du ciel et observation par un modèle d'instrument

Un 'run' du PSM comprend typiquement deux tâches principales : une phase de simulation de l'émission du ciel (modélisation et réalisation des différentes composantes d'émission), et une phase d'observation (sommaire) de ce modèle du ciel avec un ou plusieurs instruments.

Du point de vue de l'utilisateur, le modèle du ciel est spécifié par une liste de paramètres cosmologiques, puis une liste de paramètres spécifiques à chacune des émissions (dipôle, anisotropies du fond cosmologique, galaxie, effet SZ, sources non résolues...). Le ciel modélisé peut être polarisé ou non, et si besoin ne comprendre qu'une sous-liste de composantes spécifiée par l'utilisateur. Le modèle est créé à une résolution unique (correspondant à une réponse angulaire gaussienne de largeur à mi-hauteur spécifiée par l'utilisateur), ce qui permet d'assurer un échantillonnage approprié pour toutes les cartes produites.

La représentation de l'émission d'une composante dans le PSM se base sur la notion centrale de loi d'émission. Dans le PSM, chaque loi d'émission est une fonction paramétrique de la fréquence ν. Les paramètres peuvent être la température, l'indice spectral, ou tout jeu de paramètres nécessaires pour décrire la loi d'émission. Une composante diffuse est représentée par un ensemble de cartes de lois d'émissions (ce qui nécessite autant de cartes différentes qu'il y a de paramètres au total. La composante représentant le fond cosmologique, par exemple, est décrite par une carte unique d'anisotropie de température, paramètre de la loi d'émission correspondant à la dérivée d'une loi de corps noir. Le modèle par défaut de poussière thermique la représente par deux lois d'émission (deux corps gris), avec des indices spectraux de 1,5 et 2,6 respectivement, et chacune spécifiée par une carte d'amplitude et une carte de température.

Les instruments sont représentés chacun par une liste de détecteurs, caractérisés chacun par une bande spectrale ('band'), une réponse angulaire ('beam'), des unités, et d'autres paramètres spécifiant les niveaux de bruit, la pixélisation, et éventuellement la stratégie d'observation (stratégie de balayage, polarisation des détecteurs).

Les paragraphes qui suivent décrivent les fonctionnalités développées dans le cadre de la distribution version 1.7 du PSM.

6.2 Le fond cosmologique

L'émission $I_\nu(p)$ du fond cosmologique en fonction de la fréquence ν et de la direction p est représentée par le produit d'une loi d'émission en fréquence $A_{\rm CMB}(\nu)$ connue, et d'une carte d'amplitude $\Delta T(p)$. La loi d'émission $A_{\rm CMB}(\nu)$ est la dérivée d'un corps noir à $T = T_{\rm CMB} = 2.725$ K environ, et $\Delta T(p)$ est la carte des anisotropies de température.

Les propriétés statistiques des cartes de température et de polarisation du fond cosmologique sont essentiellement caractérisées par les spectres de puissance C_ℓ^{TT}, C_ℓ^{TE}, C_ℓ^{EE} et C_ℓ^{BB}. Toutefois, la recherche et la mesure de propriétés non-standard (non-gaussianité), ou de corrections de second ordre (effet de lentille gravitationnelle du fond) nécessite de pouvoir simuler, avec le PSM, un fond de rayonnement cosmologique au delà du simple modèle gaussien.

Enfin, les paramètres cosmologiques qui déterminent le spectre de puissance angulaire du CMB ont aussi un impact sur la formation des structures et sur les comptages d'amas et de sources. Le PSM doit donc, autant que possible, gérer ces paramètres de façon cohérente entre les différentes composantes.

6.2.1 Dipôle

Le PSM permet de simuler un dipôle, qui peut être soit une prédiction (le dipôle est fixé, entièrement défini par un axe et une amplitude tels que mesurés aujourd'hui), soit une réalisation contrainte par les barres d'erreur actuelles. On utilise par défaut $A_{\rm dip} = 3,355 \pm 0,008$, $l_{\rm dip} = 263,99 \pm 0,14$, $b_{\rm dip} = 48,26 \pm 0,03$, en accord avec les mesures obtenues par Jarosik et al. (2010).

Les directions et amplitudes du dipôle peuvent également être fixées par l'utilisateur. Cette flexibilité permet d'évaluer la qualité de la mesure du dipôle avec un instrument donné, et d'évaluer l'impact des incertitudes sur la direction et l'amplitude du dipôle sur l'étalonnage d'un instrument à partir de ses données.

6.2.2 Anisotropies

Le mode de base pour la simulation d'un CMB (modèle Gaussien) consiste à réaliser un tirage aléatoire des modes $a_{\ell m}$ du fond cosmologique à partir de la spécification des spectres de puissance C_ℓ (température et éventuellement polarisation). Ces spectres peuvent être obtenus soit à partir d'un modèle fixe correspondant au meilleur ajustement actuel des observations existantes, soit à partir de la définition par l'utilisateur des paramètres cosmologiques de son choix, qui sont ensuite utilisés pour appeler le logiciel CAMB. Les spectres obtenus par CAMB sont utilisés pour générer un CMB simulé.

Il est possible de contraindre la réalisation du fond cosmologique de façon à ce qu'elle soit compatible avec une carte observée de fluctuations de température, caractérisée par une température mesurée $\Delta T(\theta, \phi)$, une réponse angulaire supposée symétrique et stationnaire, caractérisée par un filtrage b_ℓ indépendant de m dans l'espace des harmoniques sphériques, et un bruit caractérisé par un spectre

de bruit N_ℓ. La réalisation du CMB est alors obtenue par tirage aléatoire selon le spectre théorique d'entrée, sous contrainte de l'observation spécifiée.

Il est possible également de modéliser les anisotropies du fond cosmologique à partir d'une simulation non-gaussienne obtenue par ailleurs (Liguori et al. 2003; Elsner & Wandelt 2009). Les modèles disponibles actuellement sont des modèles avec une correction quadratique aux perturbations initiales, paramétrisée par un coefficient non-linéaire $F_{\rm NL}$ qui peut être fixé par l'utilisateur.

Enfin, une carte de fond cosmologique déformée (au niveau de la carte) par l'effet de lentille gravitationnelle selon l'implémentation de Basak et al. (2009) peut être utilisée pour simuler le fond cosmologique avec le PSM.

6.3 Les émissions du milieu interstellaire dans notre galaxie

Le milieu interstellaire de notre galaxie est constitué de matière diffuse sous différentes formes. La distribution et les propriétés des nuages de matière interstellaire, dont la densité, la température, et la composition chimique sont fortement hétérogènes, sont étroitement liés au cycle de vie des étoiles, qui naissent à partir de condensations du milieu interstellaire, le chauffent par rayonnement au cours de leur vie, et l'enrichissent en éléments lourds par nucléosynthèse stellaire (Ferrière 2001).

Les émissions du milieu interstellaire se distinguent par les processus physiques mis en oeuvre. Ces processus dépendent des conditions locales du milieu émissif, et sont ainsi localisés dans des régions plus ou moins clairement identifiées.

Le rayonnement synchrotron est émis par les électrons relativistes qui spiralent dans le champ magnétique galactique. Les électrons moins énergétiques, dans les régions ionisées 'tièdes' (à des températures de quelques milliers de K), émettent par rayonnement de freinage (free-free). Les poussières galactiques froides émettent par rayonnement thermique (de corps gris) dans le domaine millimétrique et submillimétrique, et sont susceptibles d'émettre également par d'autres mécanismes.

Contrairement à celle du fond cosmologique, les lois d'émission du milieu interstellaire ne sont pas parfaitement séparables sous la forme du produit d'une loi d'émission, indépendante de la position du ciel, et d'une carte d'amplitude fixe. Les spectres d'émission dépendent en effet des propriétés physiques du milieu émissif, qui varient d'un nuage de milieu interstellaire à l'autre. Ces propriétés varient dans l'espace tri-dimensionnel occupé par le milieu interstellaire, mais seules les intégrales des émissions le long de la ligne de visée sont accessibles à l'observateur.

La modélisation de l'émission galactique dans le PSM se base sur cinq composantes distinctes, décrite chacune par des cartes d'intensité et de paramètres de leurs lois d'émission. Ces cartes sont établies à partir d'observations prises avec divers instruments, mises à disposition de la communauté scientifique. Les cinq émissions actuellement inclues dans le PSM sont le synchrotron, le free-free, l'émission thermique des poussières, l'émission de poussières en rotation, et l'émission de raies moléculaires du CO. De ces émissions, seules le synchrotron et l'émission thermique des poussières sont supposées polarisées. La modélisation par défaut de toutes les émissions galactiques à l'exception du CO se base sur le travail de Miville-Deschênes et al. (2008).

6.3.1 Synchrotron

L'émission synchrotron domine à basse fréquence (en dessous de quelques GHz). Pour chaque point p du ciel, l'émission totale $I_\nu(p)$, moyenne des émissions d'une population d'électrons répartis selon un spectre en énergie, s'écrit :

$$I_\nu(p) \simeq \nu^\alpha \Delta T(p) \tag{6.1}$$

La loi d'émission en fréquence $A_{\rm sync}(\nu) \propto \nu^{\alpha}$ est de la forme d'une loi de puissance, l'indice spectral α se situant typiquement autour de $\alpha \simeq -1 \pm 0.3$ pour un flux exprimé en brillance ($\alpha \simeq -3 \pm 0.3$ pour un flux exprimé en température Rayleigh-Jeans). L'émission synchrotron est fortement polarisée (jusqu'à 75%, bien que la dépolarisation par intégration le long de la ligne de visée tende à faire décroitre le taux de polarisation moyen, qui se trouve plutôt aux alentours de 10-15% en moyenne).

La modélisation de l'émission synchrotron se base en premier lieu sur la carte d'émission à 408 MHz de Haslam et al. (1981, 1982). Le PSM utilise la carte mise à disposition sur le site de la 'Legacy Archive for Microwave Data Analysis' (LAMBDA) [1]. L'extrapolation en fréquence de cette carte d'émission nécessite une carte d'indice spectral.

A partir de la mesure de la polarisation par WMAP à 23 GHz (supposée ne comprendre que de l'émission synchrotron), Miville-Deschênes et al. (2008) obtiennent une carte d'intensité d'émission synchrotron à 23 GHz sur la base d'une modélsation du champ magnétique galactique, qui permet de prédire le degré de polarisation de l'émission synchrotron. La carte d'instensité synchrotron ainsi obtenue, utilisée conjointement à la carte de Haslam et al. (1981, 1982), permet d'obtenir une carte d'indice spectral synchrotron. Le reste de l'émission à 23 GHz est essentiellement attribué au free-free et à l'émission de poussières en rotation (voir ci-dessous).

Les cartes d'intensité et d'indice spectral obtenues ainsi sont à une résolution limitée à environ 1 degré. Elles permettent d'extrapoler l'intensité synchrotron à des fréquences plus élevées, éventuellement en supposant un raidissement du spectre. La polarisation est extrapolée avec la même loi que l'intensité.

6.3.2 Free-free

L'émission free-free, bien comprise théoriquement, mais mal observée car sous-dominante par rapport au synchrotron et à l'émission des poussières, a une loi d'émission contrainte assez précisément :

$$I_{\nu}(p) \simeq \nu^{\alpha} \Delta T(p) \tag{6.2}$$

avec un indice spectral $\alpha \simeq -0,15$ en brillance, et $\alpha \simeq -2,15$ en température Rayleigh-Jeans. Elle n'est pas polarisée au premier ordre, même si la diffusion Thomson pourrait induire de faibles polarisations en périphérie de nuages denses.

Il n'existe pas à l'heure actuelle d'observation qui donne directement l'intensité de l'émission free-free car celle-ci ne domine vraiment à aucune fréquence. Deux approches ont été privilégiées pour obtenir une telle carte. La première solution (Dickinson et al. 2003) consiste à partir d'une carte d'émission Hα, qui trace l'hydrogène ionisé, à corriger cette carte de l'extinction par la poussière galactique, et à convertir l'émission Hα ainsi obtenue en émission radio. Cette première approche présente l'inconvénient d'une correction approximative de l'extinction par les poussières. La seconde solution, qui consiste à tenter une séparation des composantes galactiques dans les données WMAP, a été implémentée par Bennett et al. (2003) sur les données de la première année d'observation du satellite WMAP, puis mise à jour par Hinshaw et al. (2007) sur 3 années de données et Gold et al. (2010) sur 7 années de données. La séparation de composantes utilisée, basée sur la méthode MEM (Hobson et al. 1998; Stolyarov et al. 2005), utilise la carte Hα comme information *a priori*.

La loi d'émission du free-free dépend assez faiblement de la température électronique (voir Dickinson et al. (2003)). Cette loi d'émission est utilisée dans le PSM pour extrapoler en fréquence une carte d'intensité d'émission. L'implémentation du free-free peut être facilement mise à jour en changeant la carte d'intensité d'émission. Pour l'instant, le modèle suppose une température électronique uniforme

1. http ://lambda.gsfc.nasa.gov/

de 7000K. Ceci peut également être modifié, et éventuellement remplacé par une carte de température variable sur le ciel.

Comme la carte d'émission synchrotron, la carte d'intensité d'émission free-free est obtenue à une résolution limitée : de l'ordre de 1° pour la carte MEM de WMAP (solution par défaut dans la version 1.7 du PSM), de l'ordre de 6 minutes d'arc pour une carte obtenue à partir de la carte composite d'émission Hα de Finkbeiner (2003).

6.3.3 Émission thermique des poussières

L'émission thermique des poussières est l'émission dominante à haute fréquence (au dessus de 300 GHz) sur une grande fraction du ciel. La poussière est constituée de différents types de grains, dont la distribution est à l'origine de l'émission observée (Désert et al. 1990). La dépendance en fréquence de l'émission moyenne pour chaque point du ciel est assez bien modélisée par une ou plusieurs émissions de corps gris (Finkbeiner et al. 1999) :

$$I_\nu(p) \simeq \nu^\alpha B_\nu(T_{\rm dust})\Delta T(p) \tag{6.3}$$

ou l'indice spectral α se situe entre 1,7 et 2, et la température $T_{\rm dust}$ apparaissant dans la fonction de Planck se situe typiquement entre 10 et 20 K. Les températures et indices spectraux semblent dépendre de façon significative de la direction d'observation. L'émission des poussières est polarisée au niveau de quelques pour cent (Benoît et al. 2004).

La modélisation de l'émission thermique des poussières se base sur les données d'IRAS et DIRBE à 100 microns, et sur les lois d'émissions observées par FIRAS qui permettent des les extrapoler à plus basse fréquence. Le modèle adapté par défaut est le modèle 7 de Finkbeiner et al. (1999), où la poussière est modélisée par la somme de deux corps gris, définis chacun par une carte d'intensité d'émission à 100 microns, une carte de température, et un indice spectral. Les indices spectraux des deux lois démission sont respectivement 1,5 et 2,6. Ce modèle est essentiellement un ajustement empirique des données.

L'émission en polarisation des poussières se base sur le même modèle de champ magnétique que le synchrotron, décrit par Miville-Deschênes et al. (2008). La direction de polarisation est perpendiculaire au champ magnétique en raison de l'alignement des grains de poussière allongés erpendiculairement au champ magnétique (Davis & Greenstein 1951). L'amplitude de la polarisation adoptée pour le PSM est ajustée pour coïncider avec les observations effectuées avec Archeops (Benoît et al. 2004). Ce modèle, bien que plausible, est assez peu contraint par les données observationnelles, et devra être mis à jour avec l'analyse des observations de la mission Planck.

6.3.4 Poussières en rotation

Les observations récentes de la poussière interstellaire indiquent un excès d'émission à basse fréquence (de Oliveira-Costa et al. 1999; Finkbeiner et al. 2002, 2004; Watson et al. 2005; Dobler & Finkbeiner 2008; Tibbs et al. 2010), en accord avec le modèle d'émission par rayonnement dipolaire électrique de grains de poussière en rotation proposé par Draine & Lazarian (1998), et récemment raffiné par Hoang et al. (2010).

Cette loi d'émission 'anormale' des poussières reste à caractériser plus précisément, par l'analyse jointe des différentes cartes disponibles dans la gamme de fréquences entre 1 et 1000 GHz (les plus basses fréquences mesurant cette émission, tandis que les plus hautes fréquences permettent de tracer de façon précise les régions d'émission de poussières dans le domaine millimétrique).

L'émission des poussières en rotation est décrite dans le PSM par une carte unique d'intensité à 23 GHz, obtenue à partir de la séparation de l'observation WMAP à 23 GHz en ses différentes composantes. Cette carte suppose, pour séparer synchrotron et poussière en rotation, le modèle de polarisation décrit plus haut.

La carte est extrapolée en fréquence à partir d'une loi d'émission dérivée de Draine & Lazarian (1998). Cette loi suppose un mélange de composantes du milieu interstellaire, décrit par l'émissivité de diverses phases du milieu interstellaire : Milieu froid neutre (CNM, pour 'Cold Neutral Medium'), milieu chaud neutre (WNM), milieu chaud ionisé (WIM), etc. Ces émissivités sont des paramètres de la loi d'émission de la poussière en rotation, qui utilise par ailleurs des cartes de colonne densité de H_2, H-I et H-II pour obtenir un spectre moyen.

6.3.5 Petites échelles angulaires

Les cartes d'émission utilisées pour la modélisation de l'émission galactique sont pour la plupart à résolution limitée (de 6 minutes d'arc à 1 degré). Une simulation du ciel qui se baserait sur ces cartes uniquement ne verrait, à petite échelle angulaire, aucune contamination du fond cosmologique par les avant-plans galactiques. Cette situation très optimiste pourrait falsifier l'évaluation des différentes méthodes de séparation de composantes mises au point sur les simulations. Le PSM offre donc la possibilité de générer des fluctuations à petite échelle, qui viennent se superposer au modèle à grande échelle. L'amplitude de ces petites échelles est ajustée de façon dépendante du niveau moyen local d'émission.

6.3.6 Commentaires

Le modèle de l'émission galactique, bien que cohérent et globalement en accord avec les niveaux d'émission mesurés par WMAP et Archéops, reste assez incertain. Le modèle d'émission en intensité se base sur une séparation de la carte WMAP à 23 GHz en la somme de quatre composantes : fond cosmologique (obtenu à partir de l'ILC de l'équipe WMAP, à 1 degré de résolution), free-free (obtenu à partir de la séparation MEM de l'équipe WMAP), synchrotron (obtenu à partir de la polarisation observée par WMAP et d'un modèle de champ magnétique galactique), et poussière en rotation (le reste de l'émission, corrélé avec la poussière thermique du modèle de Finkbeiner et al. (1999)).

La cohérence du modèle est testée soit en vérifiant que le modèle de champ magnétique et la fraction de polarisation du synchrotron qui en découlent donnent un indice spectral synchrotron cohérent avec les niveaux attendus (de l'ordre de -3, pour des émissions exprimées en température Rayleigh-Jeans), et que la carte résiduelle de poussière en rotation à 23 GHz est bien corrélée avec l'émission thermique des poussières (carte d'extinction).

Ce modèle est donc une interprétation cohérente des données, qui laisse toutefois clairement place à des incertitudes... Une mise à jour du modèle sera basée sur l'analyse des données de la mission Planck.

6.4 L'effet Sunyaev Zel'dovich

L'origine et les propriétés de l'effet SZ sont décrits au chapitre 2 (voir également les articles de revue de Birkinshaw (1999) et Carlstrom et al. (2002)).

Si l'on exclut les corrections relativistes, qui ne sont significatives que pour les amas les plus chauds (Fabbri 1981; Challinor & Lasenby 1998; Pointecouteau et al. 1998; Diego et al. 2003), la loi d'émission

du SZ thermique est parfaitement connue et indépendante des propriétés physiques de l'amas concerné. Ceci permet, au premier ordre, de modéliser l'émission SZ thermique à l'aide d'une carte unique et d'une loi d'émission universelle. Il en est de même pour le SZ cinétique, qui a la même loi d'émission que le fond cosmologique primordial. L'objectif primaire de la simulation de l'effet SZ dans le PSM est de fournir des cartes d'effet SZ thermique et cinétique, et un catalogue associé d'amas qui fournit les grandeurs physiques d'intérêt de chacun d'eux (position, masse, décalage spectral, paramètre de Comptonisation intégré Y, étendue angulaire...).

Enfin, le SZ polarisé (Sunyaev & Zeldovich 1980; Audit & Simmons 1999; Sazonov & Sunyaev 1999; Cooray & Baumann 2003; Shimon et al. 2009), dont l'amplitude attendue est extrêmement faible, n'est probablement pas détectable par la génération actuelle d'instruments. Il est engendré par diffusion Thomson du rayonnement quadrupolaire incident sur le gaz chaud intra-amas. Ce rayonnement quadruplaire a plusieurs origines : quadrupôle intrinsèque du fond cosmologique à l'emplacement de l'amas, quadrupôle cinétique engendré par le déplacement de l'amas (vitesse particulière par rapport au fond cosmologique), quadrupôle engendré par l'émission SZ de l'amas lui-même (double diffusion). Les filaments de la toile cosmique sont également susceptibles d'engendrer de la polarisation par diffusion (Liu et al. 2005). La modélisation de ces effets présente un intérêt pour préparer les futurs instruments qui chercheront à le détecter.

La simulation de l'effet SZ dans le PSM peut se faire de plusieurs manières différentes. La solution par défaut se base sur un modèle de comptage d'amas $dN/dMdz$, comme décrit dans Delabrouille et al. (2002). Pour un modèle cosmologique donné, plusieurs fonctions de masse sont disponibles, selon qu'elles sont obtenues analytiquement (Press & Schechter 1974) ou à partir de simulations numériques (Jenkins et al. 2001). L'espace (z, M) est divisé en cellules, pour chacune desquelles est tiré un nombre d'amas simulés. Ceci permet d'obtenir un catalogue d'objets, de masses situées au dessus d'une masse minimum spécifiée par l'utilisateur du PSM.

Dans le cadre de simulations sur le ciel entier, les positions des amas sont tirées aléatoirement avec une densité de probabilité uniforme sur la sphère (chaque cellule de l'espace (z, M) est une coquille sphérique d'épaisseur dz), et leurs vitesses particulières sont tirées aléatoirement selon une distribution Gaussienne centrée, dont la variance est entièrement déterminée par le décalage spectral z de l'amas considéré. Le catalogue peut être modifié pour contenir spécifiquement environ 900 amas observés par le satellite ROSAT (obtenus par fusion des catalogues NORAS et REFLEX), qui viennent remplacer dans le catalogue des amas de masse et décalage spectral équivalents.

Alternativement, le PSM peut utiliser des cartes simulées d'effet SZ, obtenues à partir de simulations N-corps et simulations hydrodynamiques.

6.5 Les sources non résolues

Les sources galactiques et extragalactiques non résolues, improprement appelées 'sources ponctuelles' (ou, encore pire, 'points sources'), constituent la dernière grande classe de sources d'émission dans le domaine de longueur d'onde du centimétrique au submillimétrique. Les sources non résolues sont de natures diverses. Elles comprennent toute la panoplie d'objets astrophysiques galactiques ou extragalactiques qui émettent dans les domaines radio, millimétrique, submillimétrique et infrarouge.

Les sources infrarouges extragalactiques sont principalement des galaxies à forte émission de poussières, et des galaxies à haut décalage spectral. Comme chaque source a sa propre loi d'émission, éventuellement décalée spectralement, l'ensemble des sources non résolues constitue un fond d'émission semblable à un bruit partiellement corrélé de bande à bande. Ce fond comprend quelques milliers de sources brillantes détectables individuellement par une mission comme Planck, et un fond de rayonnement d° à l'ensemble des sources trop faibles pour être détectées de façon individuelle (voir par

exemple Lagache et al. (2005) pour un article de synthèse). En particulier, le fond d'émission provenant de l'ensemble des premières galaxies infrarouges constitue le CIB (Cosmic Infrared Background), mis en évidence dans les observations du satellite COBE (Puget et al. 1996).

Ce fond extragalactique est caractérisé par un spectre angulaire dominé, à petite échelle, par la statistique poissonienne. Il se distingue également par la stationnarité du champ sur le ciel (au moins au premier ordre), une propriété que doivent avoir les simulations d'un population de sources extragalactiques sur le ciel.

Les sources radio comprennent toutes les galaxies et noyaux de galaxies émettant dans le domaine radio (AGN, quasars, blazars, galaxies de Seyfert, BL-Lac, etc...). Si l'on fait abstraction de cette distinction pour partie d'origine historique, ces sources peuvent être classées phénoménologiquement, dans le domaine radio, en deux catégories, sources 'flat' (de spectre d'émission plat) et sources 'steep' (dont l'émission décroît fortement avec la fréquence), en fonction de leur loi d'émission spectrale. Cette distinction sera utilisée pour la modélisation de l'émission des sources radio dans le PSM.

Enfin, notre Voie lactée elle-même comprend un grand nombre de sources compactes (non résolues par un instrument du type de Planck) qui émettent en radio et/ou en infrarouge. Ces sources sont concentrées dans les régions de basse latitude galactique, avec une forte concentration dans les régions centrales de la galaxie. Ces sources sont de types divers : microquasars, restes de supernovae, condensations de poussière froide, régions H-II...

La simulation des sources compactes dans le PSM se base sur des catalogues de sources réelles, observées soit dans le domaine radio, soit dans l'infrarouge lointain. Les observations radio utilisées sont les catalogues NVSS (Condon et al. 1998), SUMSS (Mauch et al. 2003), GB6 (Gregory et al. 1996), et PMN (Gregory et al. 1994), ainsi que le catalogue de sources de WMAP (Wright et al. 2009). Le catalogue de sources infrarouges est basé sur les observations effectuées par le satellite IRAS (Joint Iras Science 1994).

La simulation génère plusieurs catalogues de modèles de sources, auxquels s'ajoute la simulation d'une carte de fluctuations d'un fond de sources non résolues. Le fond est généré par tirage aléatoire de fluctuations de comptage de sources, suivant une fonction de corrélation à deux points (ou de façon équivalente, un spectre $P(k)$) compatible avec les observations actuelles (voir González-Nuevo et al. (2005) pour une discussion complète de la méthode de simulation et des données utilisées pour fixer la fonction de corrélation).

Les catalogues de sources sont au nombre de quatre : sources radio, sources WMAP, sources infrarouge, régions HII ultracompactes.

6.5.1 Catalogue radio

Chaque source du catalogue radio est modélisée par quatre lois de puissance, limitées par les fréquences 4,85, 20 et 100 GHz. La loi d'émission pour $\nu \leq 4.85$ GHz est établie à partir des catalogues de sources radio, directement à partir des mesures pour les sources observées à deux fréquences (4,85 et soit 0.84, soit 1.4). Pour les sources observées à une seule fréquence, leur loi d'émission est tirée aléatoirement parmi les indices spectraux des sources observées à deux fréquences.

L'extrapolation des flux à plus haute fréquence se fait de façon probabiliste, en classant les sources en deux catégories : plates ('flat') et raides ('steep'). Pour chacune de ces sous-catégories, des corrections de l'indice spectral sont tirées aléatoirement, avec une moyenne de -0,45 pour les sources à spectre raide, et de -0,24 pour les sources à spectre plat. Dans les deux cas le tirage se fait selon une gaussienne d'écart-type 0,3. Ces chiffres sont tirés des travaux de Ricci et al. (2004) et Ricci et al. (2006).

A plus haute fréquence encore ($\nu \geq 100\,\mathrm{GHz}$), un nouvel indice spectral est attribué pour les sources trop raides ou inversées, afin d'éviter que les valeurs extrêmes d'indice spectral entre 20 et 100 GHz ne conduisent à des flux extrêmes aux hautes fréquences de modélisation par le PSM. Toutes les sources dont l'indice spectral est en dehors de l'intervalle $-2,5\sigma < (\alpha - \bar{\alpha}) < 2,5\sigma$ se voient affecter l'indice spectral moyen $\bar{\alpha}$.

6.5.2 Sources WMAP

Les sources observées par WMAP, bien qu'elles soient des radiosources comme celles dont il vient d'être question, font l'objet d'un traitement particulier afin de prendre en compte les mesures dans les cinq bandes de WMAP. Elles sont modélisées avec 7 lois de puissance, limitées par les fréquences de mesure (5, 23, 33, 41, 61, et 94 GHz), le flux à 5 GHz étant tiré du catalogue de sources radio établi précédemment. Ces sources sont ôtées du catalogue de sources radio lorsque une correspondance a pu être trouvée.

6.5.3 Sources infrarouges

Les sources infrarouges du PSM sont basées sur le catalogue d'IRAS (Joint Iras Science 1994). Leur lois d'émission sont modélisées par des corps gris. La couverture est homogénéisée (notamment pour couvrir le trou de couverture du satellite IRAS, mais aussi pour compenser les inhomogénéités de sensibilité) par génération aléatoire de sources additionnelles dans les régions où elles font défaut.

6.5.4 Régions H-II ultracompactes

Un petit nombre de sources identifiées comme des régions H-II galactiques non résolues font l'objet d'un traitement particulier. Chacune d'entre elles est modélisée par la somme d'une loi d'émission de corps gris et d'une loi d'émission de poussières.

6.6 La lumière zodiacale

En dernier lieu, l'émission du ciel submillimétrique comprend une émission zodiacale, provenant du disque de poussières, d'astéroïdes et de divers objets constitutifs du système solaire. Cette émission est variable sur le ciel en fonction du temps, en raison de la rotation annuelle de la Terre autour du Soleil. Pour cette raison, elle n'est pas modélisée actuellement dans le PSM, tout comme ne sont pas modélisées non plus les émissions des planètes, ni les émissions des petits corps du système solaire.

6.7 Observation du ciel

Le PSM comprend les outils logiciels permettant l'intégration dans des bandes spectrales des différentes lois d'émission implémentées dans le PSM. Les bandes spectrales peuvent être monochromatiques, de forme carrée, ou tabulées. Ceci permet de générer des cartes d'émission du ciel intégrées dans les bandes spectrales d'un instrument, défini dans le PSM par un modèle simple.

Chapitre 7

Conclusion et perspectives scientifiques

La mission Planck a terminé sa phase nominale de prise de données. L'analyse des observations est organisée en deux grandes étapes. La première est la production, à partir des données brutes, de jeux de données mis en forme et directement exploitables pour des analyses scientifiques (les "data products" officiels de Planck, qui seront mis à la disposition de la communauté scientifique deux ans après la fin de la mission nominale de 14 mois). La seconde consiste à interpréter les observations pour extraire, de ces données pré-traitées, l'information scientifique pertinente.

7.1 Traitement des données de la mission Planck

La production des données "publiables" de la mission est la responsabilité des "Data Processing Centers". Elle comprend des tâches de caractérisation de l'instrument, de pré-traitement des flots de données ordonnés en temps, de fabrication des cartes, et de séparation de composantes. Une partie des travaux exposés dans ce mémoire participent à ce traitement de données. Notamment, les méthodes de fabrication de cartes et de séparation de composantes sélectionnées pour le traitement nominal des données de l'instrument HFI sont, à l'heure actuelle, basées sur certains des travaux présentés en annexe. Si ces méthodes donnent satisfaction au premier ordre, il reste encore une marge d'amélioration.

La méthode de fabrication de cartes implémentée dans la chaîne de traitement des données de l'instrument HFI, PolkaPix, est basée sur la méthode de déstriage faisant l'objet des publications jointes en annexe pages 121 et 135 (Delabrouille 1998a; Revenu et al. 2000). Cette méthode permet d'obtenir des cartes satisfaisantes, malgré plusieurs défauts dont il est fait état au chapitre 3. Pour améliorer cette fabrication de cartes, il serait utile (pour Planck) de l'affranchir de la pixélisation utilisée au final pour la reprojection des données. Il serait souhaitable également d'étendre le modèle de la mesure pour représenter de façon adéquate les effets systématiques qui doivent être pris en compte simultanément à la fabrication de cartes, notamment les asymétries de réponses angulaires du système optique, certains bruits additifs, et les différences de bandes spectrales. C'est l'un de mes projets pour la suite de l'analyse de ces données. Compte-tenu cependant de contraintes de temps et d'organisation pour la publication des "data products", il n'est pas clair qu'une véritable optimisation de cette fabrication sera possible d'ici-là, auquel cas un tel traitement amélioré, s'il s'avère indispensable, pourra intervenir dans une phase ultérieure.

La séparation de composantes utilisée pour soustraire le fond cosmologique des cartes utilisées pour les premières publications de la collaboration Planck est une implémentation de la méthode de l'ILC needlets exposée au chapitre 5 et jointe en annexe page 251. Cette méthode, toutefois, ne résout pas non plus tous les problèmes à la fois. Elle n'est bonne que si le critère d'optimisation est la minimisation (au sens des moindres carrés) de l'erreur sur la carte reconstruite, si le choix des

domaines de needlets utilisés pour le calcul des covariances empiriques des cartes fait l'objet d'une optimisation compte tenu du biais de l'ILC, et si l'étalonnage de l'instrument est suffisamment précis pour que l'effet décrit dans la publication jointe page 283 soit une source négligeable d'erreur. Le développement de chaînes de séparation de composantes optimisées selon différents critères reste un sujet d'actualité pour l'analyse finale des données de la mission. Les différentes publications associées au chapitre 5, jointes à ce mémoire en annexe section A, relèvent de cette activité.

7.2 Exploitation scientifique des données de Planck

Il serait illusoire de penser qu'il existe une méthode de séparation de composantes universelle qui pourrait produire des cartes de composantes parfaitement nettoyées de toutes les sources d'erreur. En réalité, les cartes sont nécessairement imparfaites, et le critère d'optimisation à utiliser pour la séparation de composantes (afin de minimiser l'impact de ces imperfections) dépend de l'objectif scientifique de l'analyse à faire sur les cartes ainsi obtenues. La séparation de composantes, donc, n'est pas seulement un traitement à appliquer pour extraire des données les "data products". C'est aussi l'un des aspects cruciaux de l'analyse scientifique des données.

La mission Planck est riche d'objectifs scientifiques variés : pour ne citer que les sujets liés au fond cosmologique, on peut s'intéresser au spectre C_ℓ des anisotropies (en température et polarisation), aux statistiques d'ordre supérieur, à la recherche de non-gaussianité, à la mesure de l'effet de lentille gravitationnelle, à la recherche de l'effet Sachs-Wolfe intégré grâce à la statistique jointe de la carte de fond diffus et de relevés de grandes structures (galaxies, ou amas de galaxies), à la topologie de l'univers... Pour chacun de ces objectifs, on peut concevoir une séparation de composantes basée sur un critère d'optimisation qui lui est propre. J'aborderai, dans la suite de mon activité, certaines de ces questions (en fonction des opportunités qu'apportent les collaborations, ou le recrutement d'étudiants ou de post-doctorants pour travailler sur ces sujets avec moi).

Au delà de la science liée au fond cosmologique, la mission Planck produit un jeu de données extraordinaire pour étudier les émissions millimétriques de notre cosmos. Du système solaire au fond cosmologique, en passant par le milieu interstellaire de notre Voie lactée, par les autres galaxies et les amas de galaxies, tout l'univers froid émet dans le domaine de longueur d'onde couvert par la mission Planck. La séparation de composantes est au coeur de l'analyse de ces données. L'interprétation des observations au sein d'un modèle cohérent, le "Planck Sky Model", permettra de synthétiser notre connaissance de toutes ces émissions. C'est là mon projet principal pour les quelques années à venir.

7.3 Une mission spatiale pour la polarisation du fond cosmologique

La mission Planck n'est pas la mission ultime pour l'observation du ciel millimétrique. En particulier, elle n'a pas été conçue, à l'origine, comme une mission pour mesurer la polarisation, même si cette capacité a été ajoutée après sa sélection en 1996, ainsi qu'il en a été fait état au chapitre 3.

L'un des objectifs les plus ambitieux de la mesure de polarisation est l'observation des modes B primordiaux d'origine tensorielle. Ces modes de polarisation, en effet, permettraient de contraindre de façon non ambigüe l'amplitude des modes tenseurs des perturbations initiales de la métrique, une mesure susceptible de contraindre les modèles d'inflation.

Pour un modèle d'inflation à roulement lent, on attend une relation qui lie le niveau des modes tenseurs (le paramètre $r = {\Delta_T}^2/{\Delta_S}^2$) à l'indice spectral scalaire n_S des perturbations primordiales de densité. De même, on s'attend à ce que la déviation de l'indice spectral scalaire à 1 donne l'ordre de grandeur de r. Compte tenu de la mesure actuelle de n_S ($0{,}013 < 1 - n_S < 0{,}061$ à 95% de niveau

de confiance), il est alors plausible que $r \sim$ quelques 10^{-2}. Ceci est l'ordre de grandeur du niveau de sensibilité attendu avec la mission Planck...

Ainsi, il est vraisemblable que Planck ne pourra pas détecter sans ambiguïté les modes tenseurs. L'indice spectral tenseur, quant-à lui, semble hors de portée de Planck pour des raisons de sensibilité. Ceci justifie la poursuite de la mesure de polarisation du fond cosmologique avec une mission spatiale de quatrième génération, par exemple la mission COrE proposée dans le cadre du programme "Cosmic Vision" de l'Agence Spatiale Européenne [1]. La préparation de cette mission, si elle est sélectionnée, constituera le sujet principal de mon programme de recherche une fois terminée l'analyse des données de Planck.

1. http ://oberon.roma.infn.it/core/

Annexe A

Publications choisies

Effet Sunyaev-Zel'dovich

- Observations of the Sunyaev-Zel'dovich effect at high angular resolution towards the galaxy clusters A665, A2163 and CL0016+16 (p. 61)
- A Sunyaev-Zeldovich Map of the Massive Core in the Luminous X-Ray Cluster RX J1347-1145 (p. 77)
- The selection function of SZ cluster surveys (p. 81)
- Catalog extraction in SZ cluster surveys : a matched filter approach (p. 91)
- The galaxy cluster Ysz-Lx and Ysz-M relations from the WMAP 5-yr data (p. 103)

Préparation de la mission Planck

- Circular scans for CMB anisotropy observation and analysis (p. 115)
- Analysis of the accuracy of a destriping method for future Cosmic Microwave Background mapping with the Planck Surveyor Satellite (p. 121)
- Destriping of polarized data in a CMB mission with a circular scanning strategy (p. 135)
- Optimised polarimeter configurations for measuring the Stokes parameters of the Cosmic Microwave Background Radiation (p. 147)
- Beam mismatch effects in Cosmic Microwave Background polarization measurements (p. 153)

Archeops

- The Cosmic Microwave Background anisotropy power spectrum measured by Archeops (p. 165)
- The CMB temperature power spectrum from an improved analysis of the Archeops data (p. 171)
- Cosmological constraints from Archeops (p. 185)

Séparation de composantes et estimation spectrale

- Diffuse source separation in CMB observations (p. 191)
- Component separation methods for the PLANCK mission (p. 239)
- A full sky, low foreground, high resolution CMB map from WMAP (p. 259)
- Impact of calibration errors on CMB component separation using FastICA and ILC (p. 283)
- CMB and SZ effect separation with constrained Internal Linear Combinations (p. 295)
- Multidetector multicomponent spectral matching and applications for cosmic microwave background data analysis (p. 303)

Publications choisies

- Cosmic microwave background and foregrounds in Wilkinson Microwave Anisotropy Probe first-year data (p. 317)
- Measuring the tensor to scalar ratio from CMB B-modes in the presence of foregrounds (p. 327)
- CMB power spectrum estimation using wavelets (p. 347)

ELSEVIER

New Astronomy 3 (1998) 655–669

New Astronomy

Observations of the Sunyaev–Zel'dovich effect at high angular resolution towards the galaxy clusters A665, A2163 and CL0016+16

F.-X. Désert[a,b,1], A. Benoit[c,2], S. Gaertner[e,3], J.-P. Bernard[b,4], N. Coron[b,5], J. Delabrouille[b,f,6], P. de Marcillac[b,7], M. Giard[e,8], J.-M. Lamarre[b,9], B. Lefloch[d,10], J.-L. Puget[b,11], A. Sirbi[c,12]

[a]*Laboratoire d'Astrophysique de l'Observatoire de Grenoble, 414 rue de la Piscine, BP 53, F-38041 Grenoble Cedex 9, France*
[b]*Institut d'Astrophysique Spatiale, Bât. 121, Université Paris XI, F-91405 Orsay Cedex, France*
[c]*Centre de Recherche sur les Très Basses Températures, 25 Avenue des Martyrs BP166, F-38042 Grenoble Cedex 9, France*
[d]*IRAM, avd Divina Pastora 7 Nucleo Central 18012, Granada Spain*
[e]*Centre d'Études Spatiales sur les Rayonnements, 9 Avenue du Colonel Roche, BP 4346, F-31029 Toulouse Cedex, France*
[f] *Enrico Fermi Institute, University of Chicago, 5460 South Ellis Avenue, Chicago, IL 60637, USA*

Received 22 June 1998; accepted 24 August 1998
Communicated by Francesco Melchiorri

Abstract

We report on the first observation of the Sunyaev–Zel'dovich (SZ) effect, a distortion of the Cosmic Microwave Background radiation (CMB) by hot electrons in clusters of galaxies, with the Diabolo experiment at the IRAM 30 m telescope. Diabolo is a dual-channel 0.1 K bolometer photometer dedicated to the observation of CMB anisotropies at 2.1 and 1.2 mm. A significant brightness decrement in the 2.1 mm channel is detected in the direction of three clusters (Abell 665, Abell 2163 and CL0016+16). With a 30 arcsec beam and 3 arcmin beamthrow, this is the highest angular resolution observation to date of the SZ effect. Interleaving integrations on targets and on nearby blank fields have been performed in order to check and correct for systematic effects. Gas masses can be directly inferred from these observations.

PACS: 95.55; 98.80; 98.65; 95.85.B
Keywords: Instrumentation: photometers; Cosmology: observations; Galaxies: clusters: individual: Abell 665; Galaxies: clusters: individual: Abell 2163; Galaxies: clusters: individual: CL0016+16; Radio continuum: general

[1]E-mail: Francois-Xavier.Desert@obs.ujf-grenoble.fr
[2]E-mail: benoit@polycnrs-gre.fr
[3]E-mail: gaertner@cesr.fr
[4]E-mail: bernard@ias.fr
[5]E-mail: coron@ias.fr
[6]E-mail: jacques@ias.fr
[7]E-mail: demarcillac@ias.fr
[8]E-mail: giard@cesr.fr
[9]E-mail: lamarre@ias.fr
[10]E-mail: lefloch@astro.iem.csic.es
[11]E-mail: puget@ias.fr
[12]E-mail: sirbi@polycnrs-gre.fr

1384-1076/98/$ – see front matter
PII: S1384-1076(98)00032-3

1. Introduction

After the discovery of the Cosmic Microwave Background (CMB) radiation by Penzias & Wilson (1965), and the observation of hot ionised gas in clusters of galaxies through its X-ray emission (Lea et al., 1973), Sunyaev & Zel'dovich (1970) soon realised that the scattering of the CMB photons by the hot electrons of the intracluster medium (ICM) should generate a distinctive spectral distortion of the CMB blackbody spectrum in the (sub)millimetre and radio domain. Several millimetre and radio detections towards a dozen of clusters have recently been obtained using various techniques (Birkinshaw, 1991a,b; Carlstrom et al., 1996; Grainge et al., 1993; Jones et al., 1993; Wilbanks et al., 1994; Herbig et al., 1995; Pizzo et al., 1995; Saunders, 1995; Andreani et al., 1996). These results, which are compatible with the expected brightness decrement, constitute a direct evidence for the SZ effect and have profound cosmological importance:

- They are a strong confirmation of the cosmological origin of the CMB radiation.
- The mass of the ionised gas in clusters of galaxies can be obtained from SZ measurements, even for unresolved clusters (De Luca et al., 1995). If hydrostatic equilibrium is assumed, the total mass can also be deduced from the SZ profile, and compared with cluster mass estimates by other methods (gravitational lensing, velocity fields) for consistency. This, together with cluster number counts, yields an estimate of Ω at cluster scales.
- The detection via the SZ effect of very distant clusters ($z \simeq 1$ and above) would put severe constraints on Ω, as only in a low-density Universe could structures form so early (e.g., Barbosa et al., 1996).
- The angular diameter distance to a cluster can be estimated from the CMB intensity change due to the SZ effect combined with the observed X-ray surface brightness. For low redshift clusters, the combination of SZ and X-ray data thus allows estimating the Hubble constant H_0 (Birkinshaw, 1979; Cavaliere et al., 1979; Silk & White, 1978). For high redshift clusters, because of the additional dependence of the angular diameter distance on the deceleration parameter q_0 (Silk & White, 1978), it is also possible, in principle, to constrain Ω and Λ (see Kobayashi et al., 1996) for an application of the method to available SZ measurements).
- The measurement of the kinetic SZ effect on many clusters using an optimal filtering technique would make a measurement of very large scale velocity flows possible (Haehnelt, 1996; Aghanim et al., 1997).
- The SZ effect is the strongest ''contamination'' source for the measurement of the primary CMB anisotropies at high angular resolution and in the millimetre spectral window, and therefore deserves careful studies (one's noise is the other's signal), especially in the light of the preparation to the Planck mission (Bersanelli et al., 1996).

In an effort to detect the SZ effect in clusters at high redshift, we installed the Diabolo photometer at the focus of the IRAM 30 m millimetre radiotelescope (MRT). This photometer saw its first light (Benoît et al., 1998) at the Millimetre Infrared Testa Grigia Observatory (MITO) in Italy on a 2.6 m telescope. The task of detecting a signal which is a part in a million of the background is very challenging but at a wavelength around 2 mm, the confusion by other astrophysical sources (dust, point sources, CMB anisotropies (Franceschini et al., 1991; Fischer & Lange, 1993)) is minimal. In addition, the high angular resolution achieved with the 30 m facility (about 30 arcsec for the two Diabolo channels) reduces the beam dilution on distant clusters. Owing to major improvements in bolometer and cooling technology, this task can now be achieved in a reasonable integration time (a few hours). The observations and data reduction method are described in Section 2, and the results are presented and discussed in Section 3.

2. Observations at the IRAM 30 m telescope

The Diabolo experiment is a dual-channel photometer of which the innovative cooling system, bolometers and readout electronics are prototypes for space submillimetre astronomical applications (the ESA Planck Surveyor mission, Bersanelli et al., 1996) and FIRST cornerstone (Pillbratt, 1997)). It is

a cryostat with two bolometers observing around 1.2 and 2.1 mm, cooled to 0.1 K by a ^{3}He–^{4}He compact dilution fridge. The two bands matching the atmospheric windows are obtained with low pass filters common to the two channels and free-standing bandpass meshes after the light is selected by a dichroic beam splitter. The bolometer at 1.2 mm provides a constant monitoring of the so-called atmospheric noise in a co-aligned and co-extensive beam with respect to the 2.1 mm ''astrophysical'' bolometer channel. The instrument, described in length by Benoît et al. (1998), has been modified as follows for the present observations:

- Only one bandpass filter is used for the 2.1 mm channel, instead of two, in order to increase the detection efficiency. We checked that the small spectral leaks that appeared at high frequency have no influence on the SZ measurements.
- New readout electronics, now fully digital, have been used. Each bolometer is AC square-wave modulated in opposition in a Winston bridge with a stable capacity. The out-of-equilibrium voltage is amplified by a cold FET and warm amplifiers, AD converted, and then numerically demodulated after the electrical transients have been blanked. The digital signal is proportional to the total power received by the bolometer up to an arbitrary offset constant. A complete discussion of the readout electronics scheme can be found in Gaertner et al. (1997).
- A NbSi thermometer has been installed on the dilution fridge to monitor the 100 mK cold base plate temperature. Another resistance used as a heater now allows an active regulation of this base plate temperature within about 30 μK. This is especially useful for skydips (see Section 2.1.4) and to avoid changes in the responsivity.
- A warm polyethylene lens (90% transmission) has been installed in front of the cryostat to match the *f*-ratio of the telescope (about ten) with that of the instrument (about five).

The photometer has been installed at the Nasmyth focus of the telescope for a test run from November 10th to November 14th 1995, when the precipitable water vapor was too large (typically 5 to 9 mm) for sensitive measurements. The sensitivity and calibration of the instrument could nevertheless be measured on bright sources. Some 100 hours of observing time were allocated from December 1st to 4th from which the following results have been obtained. These observations were complemented with a few more hours in December 1996.

2.1. Calibration

2.1.1. Alignment

The alignment of the cryostat with respect to the telescope axes was achieved using a movable hot load situated between the entrance of the cryostat and the secondary. The recording of the signal in total power mode gives the beam direction and the appropriate corrections to be done for the cryostat optical axis to be pointed at the center of the secondary, which is crucial for straylight minimisation.

2.1.2. Pointing

Pointing corrections were made every two hours, using data obtained by scanning across a strong (several Jy) source (planet, quasar) situated near the target. The signal was modulated by the wobbling secondary at about 1 Hz. Fig. 1 shows the demodulated signal as a function of telescope direction along lines of constant elevation and constant azimuth. A Gaussian fit is made to determine pointing corrections if necessary.

2.1.3. The beam pattern

The beam pattern has been measured on Saturn in the November 95 test run with a simple azimuth-elevation mapping technique. It is shown in Fig. 2 for the two wavelengths. The beam centers (as defined by Gaussian one-dimensional fits) are within less than 2 seconds of arc from each other, confirming the accuracy of optical positioning of the two bolometers with respect to the system optical axis inside the cryostat. Fig. 3 shows the two integrated beam profiles as defined by the function of the angular radius θ starting from the center of the beam:

$$B(\theta) = \int_0^{\theta} \mathrm{d}\theta' \, \theta' \int_0^{2\pi} \mathrm{d}\phi \frac{S(\theta',\phi)}{S(0,0)}, \quad (1)$$

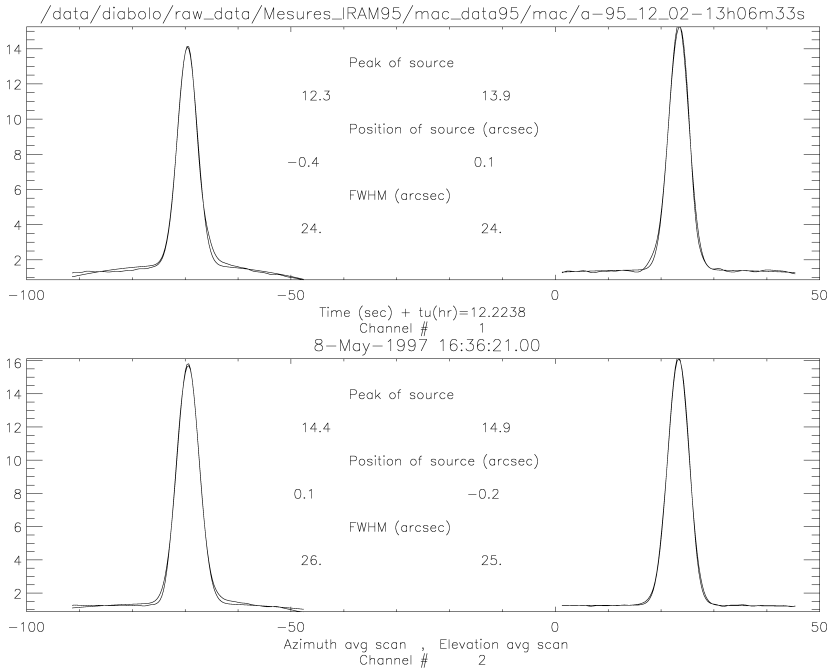

Fig. 1. The average demodulated signal from back and forth scans across Mars. The top and bottom panels are for the 1.2 mm and 2.1 mm channels respectively. For both panels, the left plot corresponds to a constant elevation scan, the right one to a constant azimuth scan. The X axis is in arcsec, the Y axis is in μV. A Gaussian fit is superposed to the data. Parameters of the fit are written on each panel. The precision on the center and FWHM is about 2 and 3 arcsec respectively.

where the measured signal S is in cylindrical coordinates and where an offset, estimated in the outskirts of the beam ($\theta > 45$ arcsec) has been taken out. B has units of a solid angle and represents the integrated beam efficiency which levels off at large θ. The beams for the two channels are much alike, except that the longer wavelength channel one is slightly more extended because of diffraction effects.

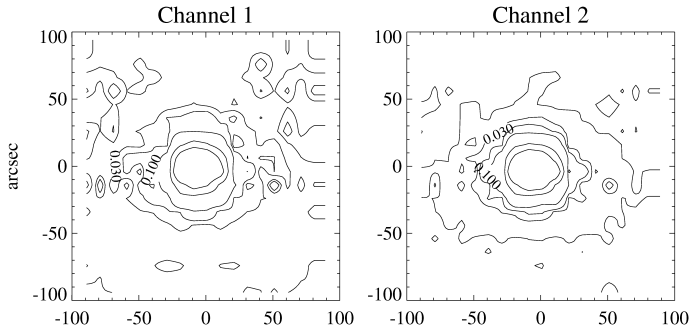

Fig. 2. Contour map of the two beams observed by mapping Saturn. Contour levels are at 0, 1, 3, 5, 10, 30, and 50% of peak value.

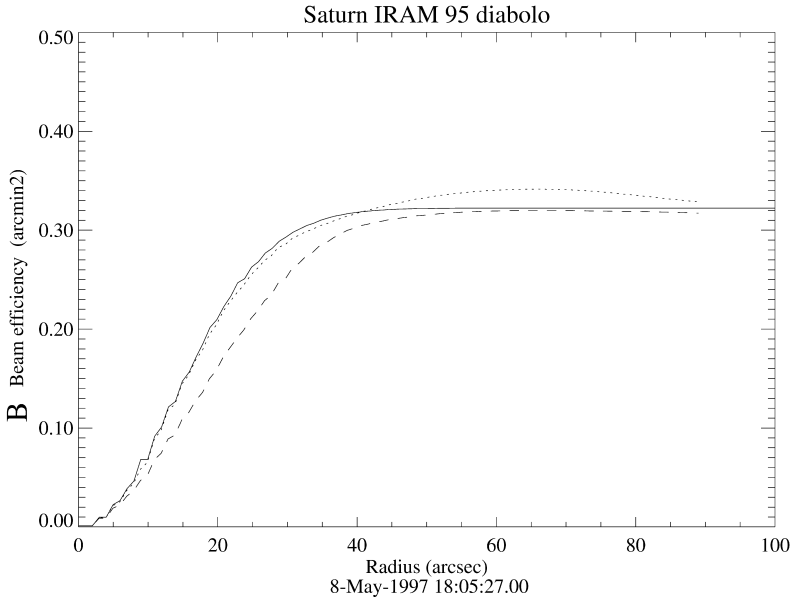

Fig. 3. Integrated beam efficiency as observed with Saturn. The function $B(\theta)$ defined by Eq. (1) is plotted for the two wavelengths (dotted line for 1.2 mm and dashed line for 2.1 mm) against the angular radius θ. The simulated integrated beam of a 2-dimensional Gaussian of FWHM 34 arcsec convolved with the Saturn 17 arcsec disk is shown as a plain line.

Saturn is not point-like (17 arcsec diameter) and slightly distorts the real beams. The integrated beamwidth, calculated from the integrated beam solid angle $\Omega_{\rm mb}$ as $\theta = \sqrt{4\Omega_{\rm mb}/\pi}$ is larger than the one-dimensional Gaussian FWHM (34 instead of 25 arcsec), because of near-sidelobe wings.

2.1.4. Skydips

Skydips must be performed in order to compare fluxes measured at different elevations β. If the optical depth at the zenith $\tau_0(\lambda)$ is known, all the measurements F can be put on the same scale ''outside'' the atmosphere, yielding corrected measurements F_c. Assuming a plane-parallel geometry, this can be written as:

$$F_c(\lambda) = F(\lambda)\exp\left(\frac{\tau_0(\lambda)}{\sin\beta}\right). \quad (2)$$

Skydips were done in total power mode without any modulation, by having a scan of the whole telescope at constant azimuth through 10 steps of elevation with a constant cosecant increment. The skydip technique has been pioneered by Chini et al. (1986) at the IRAM 30 m telescope. Here, we did not need a chopper for reference. The signal S_i in a given channel and at elevation β_i, for an average atmospheric temperature $T_{\rm atm}$, can be written as:

$$S_i = C + B_f T_{\rm atm}\left(1 - \exp\left(-\frac{\tau_0}{\sin\beta_i}\right)\right). \quad (3)$$

At each wavelength (1.2 and 2.1 mm), the constant C represents an arbitrary zero level. The forward beam efficiency $B_f = {\rm d}S/{\rm d}T$ is compared to the main beam efficiency B_m (see below Section 2.1.5). Before formula Eq. (3) can be applied, one has to correct for the drifts of the 100 mK base plate temperature $T_{\rm bath}$, induced by the increasing heat load that occurs with the skydip. The NbSi thermometer gives a sufficiently sensitive measurement of $T_{\rm bath}$. With a simple linear correlation technique, the coefficients of which are established independently of the skydip, the contribution ${\rm d}S/{\rm d}T_{\rm bath} \times T_{\rm bath}$ can be subtracted. Fig. 4 shows the non-linear

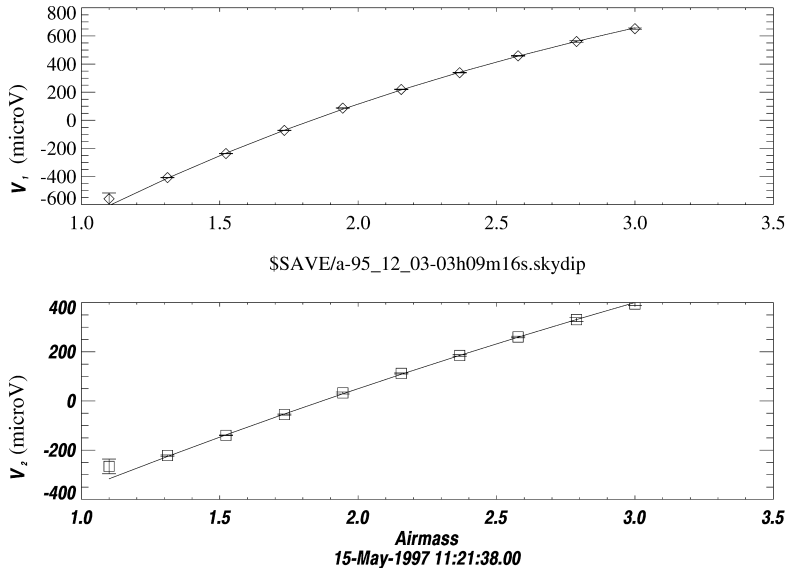

Fig. 4. Total power skydip measurements for the 2 channels. The average signal output in μV as a function of airmass is fitted using the model of Eq. (3).

fit of the data based on formula Eq. (3). The correction which is applied to the data via Eq. (2) is deduced by interpolating between the two observed skydip values of τ_0 (1.2 mm) closest in time to the observation. It is found to be only of the order of 30% or less at 2.1 mm where the SZ effect is expected. During the December 95 observations, the zenith optical depths at 1.2 mm varied between 0.1 and 0.3, which corresponds to 2–4 mm of precipitable water vapour. This definitely is an acceptable range of opacity values for SZ measurements.

2.1.5. Sensitivity

The calibration is done with planets which partially fill the beam. Mars (angular diameter 4.1 arcsec), Saturn (16.7 arcsec) and Jupiter (30.5 arcsec) have been used for the present observations assuming a blackbody emission with temperatures of respectively 214, 150, and 170 K. After correcting for atmospheric opacity effects (Eq. (2)), and taking into account the beam dilution, the responsivity of each bolometer $B_{mc}(\lambda) = \mathrm{d}S/\mathrm{d}T$ is deduced. It represents the response of the bolometer to 1 Rayleigh-Jeans Kelvin filling the main beam. The noise level is measured on blank fields. The instrument noise on the sky was found to be above the bolometer noise (as measured in the laboratory) by a factor of 3. The additional noise is likely related to an imperfect isolation from vibrations in the Nasmyth cabin, which generates noise of microphonic origin by optical modulation of straylight.

The final sensitivities are given in Table 1, when

Table 1
Best sensitivities obtained with Diabolo at the IRAM 30 m telescope in 1995

Channel	FWHM arcsec	$\sqrt{\frac{4\Omega_{\mathrm{mb}}}{\pi}}$ arcsec	mK · s$^{1/2}$	MJy sr^{-1} · s$^{1/2}$	mJy · s$^{1/2}$
1.2 mm	24±3	34±2	25	50	900
2.1 mm	27±3	34±2	13(11)	8(7)	170(140)

Sensitivities in parentheses are for the 2.1 mm channel after spectral decorrelation of the atmospheric noise (see text).

the sky noise is minimal and the zenith opacity is 0.1 at 1.2 mm. FWHM is given by the point source profile Gaussian fit and $\Omega_{\rm mb}$ is the integrated beam solid angle up a 45 arcsec radius. Brightness sensitivities are for a filled beam, and flux sensitivities are for a point source on axis. These best performances are degraded whenever the source is not at the zenith, the sky is less transparent or the sky is more noisy. The overall noise degradation can be by as much as a factor of 3 at 1.2 mm, but rarely exceeds fifty percent at 2.1 mm. In all cases, sky noise can be reduced by a decorrelation technique (see Section 3). The corresponding noise levels are given in parentheses in Table 1. For the observation technique described in Section 2.2, the effective sensitivity is worse than in Table 1 by a factor of 2.

The ratio between the corrected main beam efficiency $B_{mc}(\lambda)$ (obtained from mapping planets) and the forward beam efficiency $B_f(\lambda)$ (obtained from skydips: Eq. (3)) is only 25%±5 (50%±5) at 1.2 (resp. 2.1) mm. These values are in agreement with the telescope efficiencies measured by Garcia-Burillo et al. (1993). The far sidelobe pattern implied by these results can be troublesome for the observation of weak sources. This question is addressed in the discussion of Section 3.

2.2. Observing strategy

Four types of modulation were simultaneously used in order to limit the various low-frequency noises and monitor systematics.

1. The electronic AC modulation, referred to in the beginning of this section, avoids using electronics at frequencies below 10 Hz (the typical $1/f$ knee frequency). Here we modulate the bolometers at 36 Hz and the readout electronics deliver one sample per bolometer at the rate of 72 Hz.
2. The wobbling secondary provides the second modulation at the typical frequency of 1 Hz and with a beamthrow of 3 arc minutes. This allows the slowly varying background emission (sky and telescope) to be subtracted from the comparison of the on-axis measurement with that from an offset position at the same elevation.
3. The whole telescope is nodded in azimuth every 20 seconds with an amplitude of 3 arcmin in an ABBA cycle which is repeated 4 times to form one scan. This permits to compensate for any imbalance between the two beams provided by the wobbling. Each scan obtained in this way lasts about 2 minutes (repointing overheads included).
4. Each scan above is done consecutively on a reference field offset from the target by a lag of a few minutes of time in RA (R at coordinates $(\alpha - \text{lag},\delta)$), on target twice ($T$ and T' at coordinates (α,δ)), and on a second reference field offset by the same number of minutes of time in RA in the other direction (R' at coordinates $(\alpha + \text{lag},\delta)$). With this method, the reference fields are followed in the same way as the target in local coordinates. This ensures that sidelobe effects (ground pickup), if any, are subtracted. This technique has been used by Herbig et al. (1995) for single-dish measurements of very weak sources with proper baseline subtraction.

2.3. Reduction procedure

The data reduction proceeds as follows.

1. Cosmic ray hits are removed by interpolation from the data flow by a running median algorithm. Typical time constants are 10 milliseconds and the glitch rate is less than one hit per bolometer every 10 seconds, so that few samples are affected. The particles which deposit their energy into the bolometer are thought to mainly be muons, more abundant at the telescope site than in the laboratory.
2. The data are then synchronously demodulated with the help of the wobbler position (which is recorded along with the bolometer signals). The mean and dispersion values are computed for each position of the nodding cycle *ABBA*. Typical offsets (the imbalance between the positive and negative wobbler positions) are of the order of 0.2 K.
3. A complete scan is reduced by averaging the differences of values between the two nodding positions: $v = \sum_1^N (v_A - v_B)/(2N)$. The noise on the final value is obtained from the dispersion of the individual differences. The sensitivity quoted in Table 1 corresponds to the best noise figure

obtained after a scan and corrected for the square root of the scan integration time.

4. The third channel, which is a thermometer measuring the base plate temperature $v_3 = T_{\rm bath}$, is treated the same way as the two others in order to check for a possible systematic effect or additional noise possibly induced by drifts of the thermal bath temperature. None have been found.
5. A linear combination of the first two bolometers, $v_4 = v_2 - rv_1$ is calculated. The ratio r is chosen so as to minimise the noise of v_4. It can be shown that r can be deduced from a simple linear correlation between v_1 and v_2 even if both measurements are noisy, and r is always smaller than the color of the sky emission. This procedure is intended to specifically work at removing sky noise from the second channel when little or no signal is expected from the first one (in particular, in case of the SZ effect). An histogram of the values of r during the December observations is shown in Fig. 5. The correlation coefficient C tells us by how much we can reduce the initial noise of v_2 to that of v_4: $\sigma_4 = \sigma_2\sqrt{1-C}$. The typical correlation coefficient C of 0.4 leads to a small improvement in the signal to noise ratio of weak sources. On the other hand the statistical distribution which is obtained with the corrected v_4 is much closer to Gaussian than that of the data for the original channels, v_1 and v_2 (see Section 3.1).
6. For each channel, an elementary block of data, made of 4 scans (R, T, T', R'), is reduced by computing an average signal $s = (v_T + v_{T'} - v_R - v_{R'})/2$ and a difference signal $d = (v_{T'} - v_T - v_R + v_{R'})$ with associated errors.

Four rich clusters of galaxies (A665, A2163, A2218 and CL0016+16) have been selected for observations due to their small angular core radius (less than 2 arcmin), adapted to a large millimetre antenna. In addition to the 1995 data, we gathered a few more hours of observation towards two of these

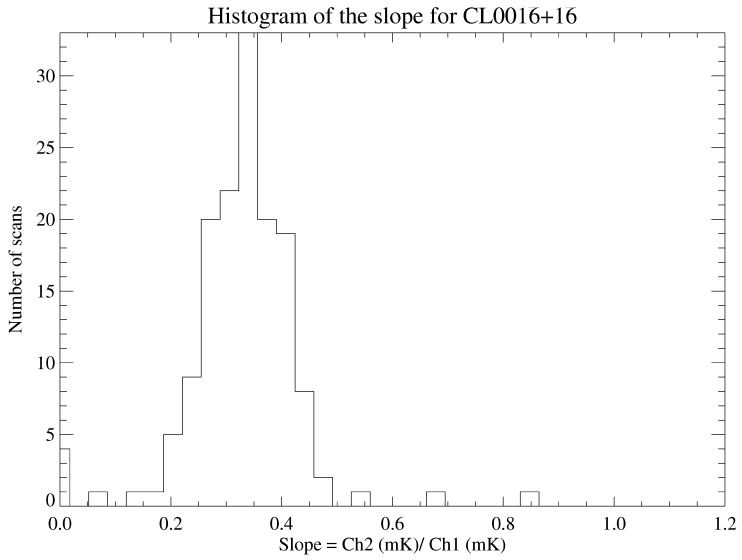

Fig. 5. Histogram of the values r, the slope between channel 2 against channel 1 in units of a temperature brightness ratio. A value of 0.3 is expected from the fluctuations of water vapour and the photometric model of the instrument. Sky noise seems indeed to be the source of extra noise seen in the bolometers.

clusters (A2163 and CL0016+16) in 1996. The observation and data reduction schemes were very different, in an attempt to measure SZ profiles.

3. Tentative detections of the SZ effect

3.1. Results

The parameters of the observations towards the four clusters are given in Table 2, and the full results are summarised in Table 3 (antenna Rayleigh-Jeans equivalent temperature in μK, corrected for atmospheric absorption). Rayleigh-Jeans temperature differences (the corrected signal s see Section 2.3) for all cycles of measurements are plotted in Figs. 6–9.

For the 1995 data, the final result for each cluster has been obtained by averaging the measurements obtained from each cycle of four scans, weighted proportionally to the inverse square of the noise for the individual sets. For each measurement, we compare the internal error obtained with this optimal averaging by using the internal noise value, and the external error obtained from the dispersion between the scan values. The square of the ratio between the two is the reduced χ^2. The values listed in Table 3 show the internal consistency of the measurement and its estimated noise, except for the first channel where the χ^2 value is systematically larger than unity. This discrepancy can be explained by the statistics of the atmospheric noise, which is not Gaussian and affects more the 1.2 mm channel than the 2.1 mm one. To first order, it should not affect much the decorrelated channel, as observed.

For the 1996 data, which use a different scanning technique, results have been obtained from the difference between the average of the signal from the scans on 30 arcsec centered on the target source and the average value of the signal at more than 40 arcsec of the target.

A significant negative signal is detected in the 2.1 mm decorrelated channel for the three clusters A665, A2163 and CL0016+16. This detection is particularly significant for the latter cluster.

If we interpret those measurements as due to the Sunyaev-Zel'dovich effect, one can convert the obtained value from antenna temperature to the y parameter (see Sunyaev & Zel'dovich, 1970, 1980), neglecting the spectral dependency on the cluster gas temperature (Rephaeli, 1995; Giard, 1995). The final results (1995, 1996, and combination of the two years) are given in Table 4.

The correction η for the 1995 beam dilution is calculated by convolving the measured beam profile obtained on Saturn (modulated at 3 arcmin) with a theoretical SZ profile using core parameters from X-ray measurements.

We do not detect any significant signal in the

Table 2
Observation logbook summary

Cluster	RA (1950)	Dec (1950)	Offset (arcsec)	Int. time 95 (96)
A665 source	08.26.25.0	+66.01.21.	0.	13.1 hours
A665 ref1	08.25.29.2	+66.01.21.	− 340.	
A665 ref2	08.27.20.8	+66.01.21.	+ 340.	
A2163 source	16.13.05.8	− 06.01.29.	0.	5.7 (3.2)
A2163 ref1	16.13.05.8	− 06.01.29.	− 340.	
A2163 ref2	16.13.05.8	− 06.01.29.	+ 340.	
A2218 source	16.35.35.0	+66.18.50.	0.	3.1
A2218 ref1	16.29.50.8	+66.18.50.	− 2074.	
A2218 ref2	16.41.19.2	+66.18.50.	+ 2074.	
CL0016+16 source	00.15.58.3	+16.09.37.	0.	15.7 (9.8)
CL0016+16 ref1	00.15.34.7	+16.09.37.	− 340.	
CL0016+16 ref2	00.16.21.9	+16.09.37.	+ 340.	
CL0016+16 ref1p	00.10.18.2	+16.09.37.	− 4900.	
CL0016+16 ref2p	00.21.38.4	+16.09.37.	+ 4900.	

Table 3
Observation results

	Channel	λ (mm)	Signal (μK) (noise)	χ^2 (df)	Prob %
A665	source – ref (microK RJ):				
	1	1.2 mm	193. (235. 277.)	41.6 (30)	7.7
	2	2.1 mm	− 224. (115. 129.)	37.7 (30)	15.9
	4	2.1 mm corr	− 253. (110. 106.)	33.7 (30)	29.3
	ref2 – ref1 (microK RJ):				
	1	1.2 mm	− 439. (470. 685.)	63.8 (30)	0.0
	2	2.1 mm	− 80. (231. 298.)	50.0 (30)	1.2
	4	2.1 mm corr	303. (200. 265.)	52.8 (30)	0.6
A2163	source – ref (microK RJ):				
	1	1.2 mm	− 451. (398. 656.)	32.6 (12)	0.1
	2	2.1 mm	− 695. (247. 246.)	11.9 (12)	45.4
	4	2.1 mm corr	− 476. (188. 203.)	14.1 (12)	29.6
	ref2 – ref1 (microK RJ):				
	1	1.2 mm	− 1388. (797. 1282.)	31.1 (12)	0.2
	2	2.1 mm	961. (494. 657.)	21.2 (12)	4.7
	4	2.1 mm corr	636. (376. 405.)	13.9 (12)	30.6
A2218	source – ref (microK RJ):				
	1	1.2 mm	1151. (712. 971.)	11.2 (6)	8.4
	2	2.1 mm	80. (299. 342.)	7.9 (6)	24.8
	4	2.1 mm corr	39. (234. 207.)	4.7 (6)	58.1
	ref2 – ref1 (microK RJ):				
	1	1.2 mm	3504. (1423. 2485.)	18.3 (6)	0.6
	2	2.1 mm	2. (598. 480.)	3.9 (6)	69.5
	4	2.1 mm corr	− 429. (467. 544.)	8.2 (6)	22.7
CL0016+16	source – ref (microK RJ):				
	1	1.2 mm	1. (172. 200.)	47.2 (35)	8.1
	2	2.1 mm	− 233. (118. 122.)	37.8 (35)	34.2
	4	2.1 mm corr	− 384. (104. 109.)	38.2 (35)	32.5
	ref2 – ref1 (microK RJ):				
	1	1.2 mm	243. (344. 464.)	63.6 (35)	0.2
	2	2.1 mm	176. (235. 240.)	36.4 (35)	40.5
	4	2.1 mm corr	− 51. (209. 210.)	35.5 (35)	44.7

blank field positions ($v_R + v_{R'}$): in contrast to cm radio observations, no systematic signal is seen in the blank field measurements. Indeed, we find that the average signal obtained by keeping only the on-source component ($v_T + v_{T'}$) is about $\sqrt{2}$ more significant than that shown in Table 3. This gives us confidence in the final results for the y parameters of Table 4. Moreover, for A2163 and CL0016+16, the 1995 and 1996 results are compatible with each other.

An additional outcome of the observations are temperature differences from blank field measurements (d: see Section 2.3). No signal is detected in any of the 4 differences (around the 4 observed clusters) at the $\Delta T/T = 2 \times 10^{-4}$ level (1σ). If this result were improved by repeated measurements on a larger number of clusters, it could yield interesting constraints on the level of CMB anisotropies at small angular scales (30 arcsec to few arcmin) in a wavelength range where the smallest contamination from radio and infrared galaxies (Franceschini et al., 1991) is expected.

All clusters show no signal at 1.2 mm within the observational errors. In principle, both the thermal and kinetic SZ effect could contribute to this channel, but the upper limit that we can put on cluster radial velocities is not stringent enough to be relevant. No galactic dust emission is detected either.

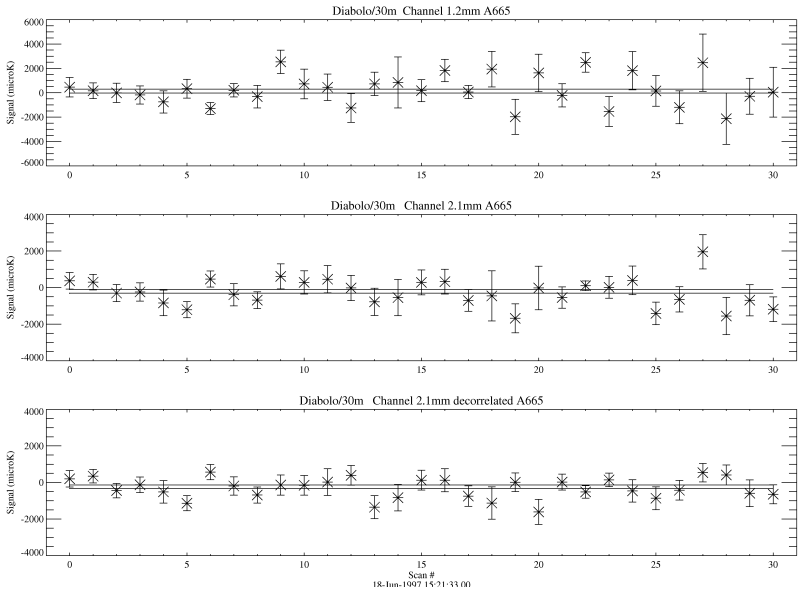

Fig. 6. Antenna temperature observed for cluster A665. The two upper plots show the two independent diabolo channel measurements and the lower plot is the the second channel corrected for atmospheric noise (see text). The 2 lines show $\pm 1\sigma$ from the final optimally averaged value.

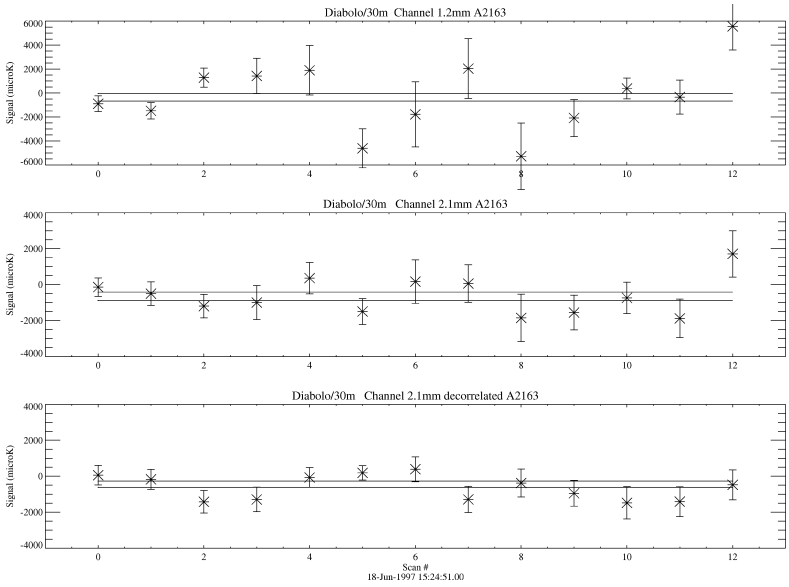

Fig. 7. Antenna temperature for the cluster A2163.

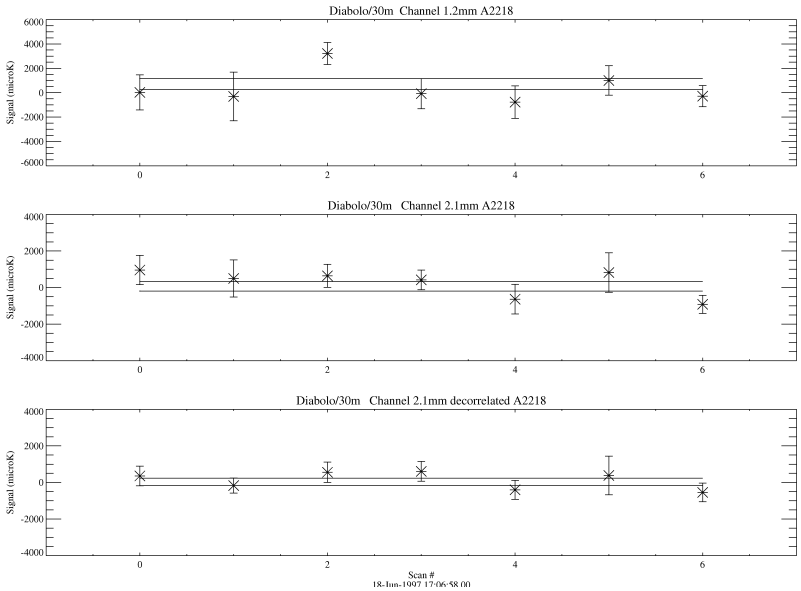

Fig. 8. Antenna temperature for the cluster A2218.

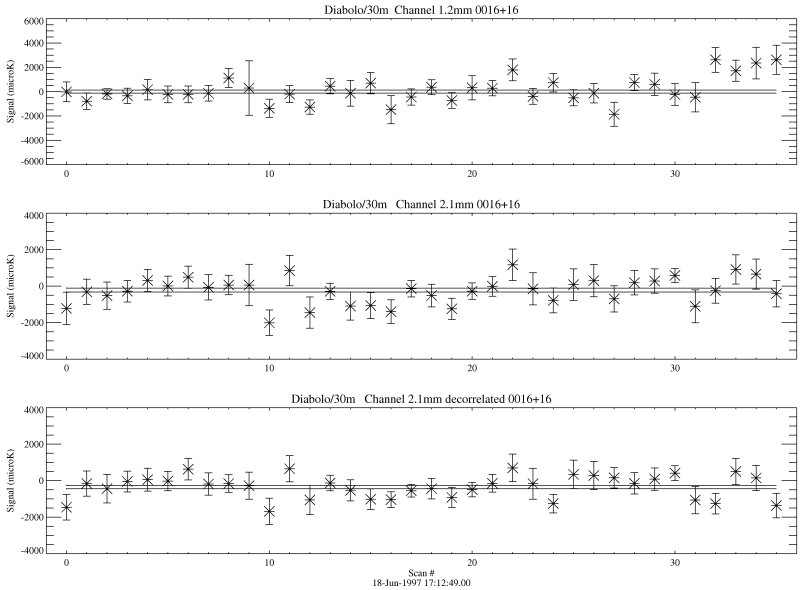

Fig. 9. Antenna temperature for the cluster CL0016+16.

Table 4
Final calibrated results

Cluster	η	$y_0/10^{-4}$			S/N
		1995	1996	all	
A665	0.498	2.92±1.15		2.92±1.15	2.5
A2163	0.548	4.99±1.97	4.60±2.00	4.80±1.40	3.4
A2218	0.607	−0.37±2.21		−0.37±2.21	0.2
CL0016+16	0.668	3.30±0.90	2.90±1.60	3.20±0.78	4.1

3.2. Interpretation

The mass of hot gas can be directly deduced from these observations by using:

$$M_g = 8.2\times10^{14}\,M_\odot \times\left(\frac{h}{0.5}\right)^{-2}\left(\frac{Y}{10^{-4}\,\mathrm{arcmin}^2}\right)\left(\frac{kT_e}{10\,\mathrm{keV}}\right)^{-1} \times\frac{(\sqrt{1+z}-1)^2}{(1+z)^3}, \quad (4)$$

a formula derived by De Luca et al. (1995). Here we have assumed $\Omega_0 = 1$ and $h = H_0/(100\,\mathrm{km/s/Mpc})$, and the measurement y_0 has been converted into $Y = \int y d\Omega = y_0\Omega_{\mathrm{eff}}$. The effective solid angle Ω_{eff} is calculated with

$$\frac{\Omega_{\mathrm{eff}}}{\theta_c^2} = f_{\mathrm{geom}} = 2\pi\int x\mathrm{d}x(1+x^2)^{\frac{(1-3\beta)}{2}}, \quad (5)$$

and $x = \theta/\theta_c$, assuming a King profile with an angular core radius of θ_c. The resulting masses are given in Table 5. Parameters for the clusters, θ_c, β, and T_e, have been taken from recent ROSAT X-ray measurements. These estimated masses do not depend on the absolute X-ray fluxes.

Our result for A2163, $y_0 = 4.8\pm1.4\times10^{-4}$ is in agreement with the determination by Wilbanks et al. (1994) of $y_0 = (3.78^{+0.74}_{-0.65})\times10^{-4}$ and that of Holzapfel et al. (1997) of $y_0 = (3.73^{+0.47}_{-0.61})\times10^{-4}$, both obtained at the same wavelength (2.1 mm) as the present measurements with the 1.4' beam (2' throw) of the SuZie experiment. It is also in agreement with the submillimeter detection by the SPM photometer onboard the PRONAOS balloon (with a 3.7' beam and 6' beamthrow). A detailed discussion of the combined bolometer results for A2163 is given by Lamarre et al. (1998). The gas mass we deduce is $14.6\pm4.2\times10^{14}\,M_\odot$, very close to the X-ray determined gas mass (Elbaz et al., 1995) $14.3\pm0.5\times10^{14}\,M_\odot$.

Our most significant detection (at the 4σ level) concerns the distant cluster CL0016+16 at a redshift of 0.541. This cluster is the highest redshift object detected with the SZ effect in the millimetric domain. Our result of $y_0 = 3.20\pm0.78\times10^{-4}$ is larger than but compatible with the central parameter $y_0 = 2.18\times10^{-4}(h/0.5)^{-1/2}$ predicted by Birkinshaw (1998) using ROSAT X-ray data (within 1.3σ). It is in agreement with the SZ radio determination of Hughes & Birkinshaw (1998) with a larger beam (1.8' with a 7' beam throw) of $y_0 = 2.20\pm0.37\times10^{-4}$ (see also Birkinshaw, 1991a), and more marginally with the SZ map of the interferometer experiment of Carlstrom et al. (1996) of $y_0 = 1.31\pm0.12\times10^{-4}$, which spans 1 to 10' angular scales. Our gas

Table 5
Physical parameters of the observed clusters

Cluster	z	T_e (keV)	θ_c arcmin	β	Y (10^{-4} arcmin^2)	$M_g/10^{14}\,M_\odot$
A665	0.182	8.2	1.60	0.66	439	20.2±8.0
A2163	0.201	14.6	1.20	0.62	491	14.6±4.2
A2218	0.171	6.72	1.00	0.65	<408	<20.9 (3σ)
CL0016+16	0.541	8.22	0.64	0.68	70	11.1±2.7

Parameters taken from Birkinshaw et al. (1991b), Elbaz et al. (1995), Birkinshaw & Hughes (1994), Neumann & Böhringer (1997), Hughes et al. (1995). The total gas mass is computed from the present measurements. Uncertainties are statistical only.

mass estimate of $M_g = 11.1 \pm 2.7 \times 10^{14} M_\odot$ is twice as large as the X-ray gas mass deduced by Neumann & Böhringer (1997) but still within errors.

For A665, the observations were centered on the IPC X-ray center as given by Birkinshaw et al. (1991b), which is offset by 2' from the nominal Abell center. Although less significant, the measured central brightness decrement $y_0 = 2.92 \pm 1.15 \times 10^{-4}$ is in agreement with the more accurate value $1.69 \pm 0.15 \times 10^{-4}$ determined by Birkinshaw et al. (1991b), albeit in the radio domain.

The integration time was clearly insufficient for A2218 to reach a significant noise level for that cluster. The upper limit that we get is compatible with the radio measurements that were previously reported (Birkinshaw, 1991a; Jones et al., 1993).

3.3. Perspective

We have reported here the highest angular resolution (30'') observations of the SZ effect on at least 2 clusters. These observations could be achieved thanks to the large millimetre Pico Veleta antenna and a total on source integration time of fifty hours. It is clear that SZ profiles or even maps of rich clusters can be measured with the Diabolo instrument, with sufficient winter integration time, when improvements in the overall efficiency are made (these are currently underway). These observations are complementary to X-ray measurements in the sense that they directly sample the gas pressure with similar angular resolution (the future XMM and AXAF will have few arcsecond resolutions). High resolution SZ observations in the millimeter atmospheric windows will also grow in importance after the unbiased survey of SZ clusters from the Planck Surveyor satellite. For resolved clusters the amplitude of the SZ distortion is independent of distance, and thus high-redshift clusters are adequate targets for millimetre observations of the SZ effect, whereas X-ray measurements of gas masses are more difficult.

Acknowledgements

We wish to thank the IRAM staff especially for their help during the setup of the instrument, Bernard Fouilleux for his help during the observations, and Bernard Lazareff for his support of the mission. We thank the whole Diabolo team for the continuous improvements brought to the instrument, with a special attention to Jean-Pierre Crussaire, Gerard Dambier, Jacques Leblanc, Bernadette Leriche, and Marco De Petris along with the Testa Grigia MITO team for a previous test of the instrument. INSU, IAS, CESR, CRTBT, and the GdR Cosmologie contributed financially to this instrument.

References

Aghanim, N., De Luca, A., Bouchet, F.R., Gispert, R., & Puget, J.-L., 1997, A&A, 325, 9.
Andreani, P., Pizzo, L., Dall'Oglio, G., et al., 1996, ApJL, 459, L49.
Barbosa, D., Bartlett, J.G., Blanchard, A., & Oukbir, J., 1996, A&A, 314, 13.
Benoît, A., Zagury, F., Coron, N., et al., 1998, A&ASS, to be submitted.
Bersanelli, M. et al., 1996, COBRAS/SAMBA: Report on the Phase A Study, ESA report D/SCI(96)3.
Birkinshaw, M., 1979, MNRAS, 187, 847.
Birkinshaw, M., 1991a, in: Proc. Physical Cosmology, ed. J. Trân Than (Editions Frontières, Gif-sur-Yvette).
Birkinshaw, M., Hughes, J.P., & Arnaud, K.A., 1991b, ApJ, 379, 466.
Birkinshaw, M. & Hughes, J.P., 1994, ApJ, 420, 33.
Birkinshaw, M., 1998, PhR, in press.
Cavaliere, A., Danese, L., & De Zotti, G., 1979, A&A, 75, 322.
Carlstrom, J.E., Joy, M., & Grego, L., 1996, ApJL, 456, L75.
Chini, R., Kreysa, E., Mezger, P.G., & Gemuend, H.-P., 1986, A&A, 154, L8.
De Luca, A., Désert, F.-X., & Puget, J.-L., 1995, A&A, 300, 335.
Elbaz, D., Arnaud, M., & Böhringer, H., 1995, A&A, 293, 337.
Fischer, M.L. & Lange, A.E., 1993, ApJ, 419, 433.
Franceschini, A., De Zotti, G., Toffolatti, L., et al., 1991, A&AS, 89, 285.
Gaertner, S., Benoit, A., Lamarre, J.-M., et al., 1997, A&AS, 126, 151.
Garcia-Burillo, O. S., Guelin, M., & Cernicharo, J., 1993, A&A, 274, 123.
Giard, M., 1995, Proc XVth Moriond Astrophysics Meeting, ed. J. Tran Thanh Van (Editions Frontières, Gif-sur-Yvette).
Grainge, K., Jones, M., Pooley, G., Saunders, R., & Edge, A., 1993, MNRAS, 265, L57.
Haehnelt, M., 1996, in: Proc. XVIth Moriond Astrophysics Meeting, eds. F.R. Bouchet, R. Gispert, B. Guiderdoni, & J. Tran Thanh Van (Editions Frontières, Gif-sur-Yvette).
Herbig, T., Lawrence, C.R., Readhead, A.C.S., & Gulkis, S., 1995, ApJL, 449, L5.

Hughes, J.P., Birkinshaw, M., & Huchra, J.P., 1995, ApJ, 448, L93.
Hughes, J.P. & Birkinshaw, M., 1998, ApJ, 501, 1.
Holzapfel, W., Arnaud, M., Ade, P.A.R., et al., 1997, ApJ, 480, 449.
Jones, M., Saunders, R., Alexander, P., et al., 1993, Natur, 365, 320.
Kobayashi, S., Sasaki, S., & Suto, Y., 1996, PASJ, 48, L107.
Lamarre, J.-M., Giard, M., Pointecouteau, E., et al., 1998, ApJL, in press.
Lea, S.M., Silk, J., Kellogg, E., & Murray, S., 1973, ApJ, 184, L105.
Neumann, D.M. & Böhringer, H., 1997, MNRAS, 289, 123.
Penzias, A.A. & Wilson, R.W., 1965, ApJ, 142, 419.
Pillbratt, G., 1997, in: Proc. ESA Symp. on The Far Infrared and Submillimetre Universe, ESA SP-401, p. 7.
Pizzo, L., Andreani, P., Dall'Oglio, G., et al., 1995, ExA, 6, 249.
Rephaeli, Y., 1995, ARA&A, 33, 541.
Saunders, R., 1995, ApL, 32, 339.
Silk, J. & White, S., 1978, ApJ, 226, L103.
Sunyaev, R.A. & Zel'dovich, Ya.B., 1970, Ap&SS, 7, 3.
Sunyaev, R.A. & Zel'dovich, Ya.B., 1980, MNRAS, 190, 413.
Wilbanks, T.M., Ade, P.A.R., Fischer, M.L., Holzapfel, W.L., & Lange, A.E., 1994, ApJL, 427, L75.

THE ASTROPHYSICAL JOURNAL, 519:L115–L118, 1999 July 10

A SUNYAEV-ZELDOVICH MAP OF THE MASSIVE CORE IN THE LUMINOUS X-RAY CLUSTER RX J1347−1145

E. POINTECOUTEAU,[1] M. GIARD,[1] A. BENOIT,[2] F. X. DÉSERT,[3] N. AGHANIM,[4]
N. CORON,[4] J. M. LAMARRE,[4] AND J. DELABROUILLE[5]
Received 1999 March 8; accepted 1999 May 11; published 1999 June 10

ABSTRACT

We have mapped the Sunyaev-Zeldovich (SZ) decrement in the direction of the most luminous X-ray cluster known to date, RX J1347−1145, at $z = 0.451$. This has been achieved with an angular resolution of about 23″ using the Diabolo photometer running on the IRAM 30 m radio telescope. We present here a map of the cluster central region at 2.1 mm. The Comptonization parameter toward the cluster center, $y_c = (12.7^{+2.9}_{-3.1}) \times 10^{-4}$, corresponds to the deepest SZ decrement ever observed. Using the gas density distribution derived from X-ray data, this measurement implies a gas temperature of $T_e = 16.2 \pm 3.8$ keV. The resulting total mass of the cluster is, under hydrostatic equilibrium, $M(r < 1 \text{ Mpc}) = (1.0 \pm 0.3) \times 10^{15}\ M_\odot$ for a corresponding gas fraction $f_{\rm gas}(r < 1 \text{ Mpc}) = 19.5\% \pm 5.8\%$.

Subject headings: cosmic microwave background — cosmology: observations — galaxies: clusters: individual (RX J1347−1145) — intergalactic medium

1. INTRODUCTION

The hot intergalactic gas (10^6–10^8 K) is, with the galaxies themselves and the gravitational effects on background objects, one of the tools used to derive mass distributions within clusters of galaxies. It can be detected at X-ray wavelengths via its bremsstrahlung emission. From submillimeter to centimeter wavelengths, the cosmic microwave background (CMB) blackbody spectrum is distorted in the direction of the cluster by the so-called Sunyaev-Zeldovich (SZ) effect (Sunyaev & Zeldovich 1972). This characteristic distortion is due to the inverse Compton scattering of the CMB photons by the intracluster electrons (see Birkinshaw 1999 for a detailed review on the SZ effect).

In this Letter, we report the SZ measurement of the X-ray cluster RX J1347−1145 with the ground-based Diabolo millimeter instrument. This cluster has been observed with the *ROSAT* PSPC and HRI instruments by Schindler et al. (1995, 1997). At a redshift of $z = 0.451$, it appears as the most luminous X-ray cluster ($L_{\rm Bol} = 21 \times 10^{45}$ ergs s^{-1}) and, so far, one of the most massive [$M_{\rm tot}^{\rm X\text{-}ray}(r < 1 \text{ Mpc}) = 5.8 \times 10^{14}\ M_\odot$]. It is also a relatively hot and very dense cluster (temperature: $T_e = 9.3 \pm 1$ keV, central density: $n_0 = 0.094 \pm 0.004$ cm^{-3}). Optical studies of the gravitational lensing effects toward RX J1347−1145 have also been performed by Fischer & Tyson (1997) and Sahu et al. (1998). The results have pointed out a discrepancy between the total mass obtained from the optical and the X-ray data, with a surface lensing mass toward the core ($r < 240$ kpc) being 1–3 times higher than the X-ray mass estimates. Because the SZ effect also directly probes the projected gas mass, which is not the case for X-ray masses, the comparison with SZ measurements might help to discriminate between the optical and the X-ray determination.

In § 2, we describe the Diabolo instrument and our observations of RX J1347−1145. The data reduction is explained in § 3. The map of the cluster core is presented in § 4. The physical parameter values are extracted from the data analysis in § 5.

2. OBSERVATIONS

Diabolo is a millimeter photometer that provides an angular resolution of about 23″ when installed at the focus of the IRAM 30 m radio telescope at Pico Veleta, Spain. It uses two wavelengths channels centered at about 1.2 and 2.1 mm. The detectors are bolometers cooled at 0.1 K with an open cycle ^{4}He-^{3}He dilution refrigerator (Benoit et al. 1999). Two thermometers associated to a heater and a proportional-integral-derivative (PID) digital control system are used to regulate the temperature of the 0.1 K plate. There are three adjacent bolometers per channel, arranged in an equilateral triangle at the focus of the telescope. For a given channel, each bolometer is co-aligned with one bolometer of the second channel, both looking toward the same sky direction. Detections of the SZ effect have already been achieved with Diabolo on nearby clusters (A2163, 0016+16, and A665) with a single, large throughput bolometer per channel at 30″ resolution. The experimental setup is described in Désert et al. (1998). The only difference between the present configuration and the one described in Désert et al. is the increase in the number of bolometers per wavelength channel and the slight decrease of the beam FWHM from 30″ to 23″. With three bolometers at the focus of the telescope, there is no longer just one detector on the central optical axis. With the 30 m telescope focus being of Nasmyth type, the rotation of the field has to be taken into account in the reconstruction of the sky maps.

RX J1347−1145 has been observed in 1997 December. Our observations are pointed on the *ROSAT* HRI X-ray emission center reported by Schindler et al. (1997): $\alpha_{2000} = 13^{\rm h}47^{\rm m}31^{\rm s}$, $\delta_{2000} = -11°45'11''$. The observations have been performed using the wobbling secondary mirror of the IRAM telescope at a frequency of 1 Hz and with a modulation amplitude of 150″. An elementary observation sequence is a 120″ × 55″ map in right ascension, declination coordinates for a duration of 277 s each. This is obtained using the right ascension drift provided by the Earth rotation so that the telescope

[1] Centre d'Etude Spatiale des Rayonnements, 9 Avenue du Colonel Roche, BP 4346, Toulouse Cedex 4, F-31028, France; pointeco@cesr.fr.
[2] Centre de Recherche des Très Basses Températures, 25 Avenue des Martyrs, BP 166, Grenoble Cedex 9, F-38042, France.
[3] Laboratoire d'Astrophysique de l'Observatoire de Grenoble, 414 Rue de La Piscine, Grenoble Cedex 9, F-38041, France.
[4] Institut d'Astrophysique Spatiale, Bâtiment 121, CNRS Université Paris 11, Orsay Cedex, 91405, France.
[5] Collège de France, 11 Place Marcelin Berthelot, Paris Cedex 5, F-75231, France.

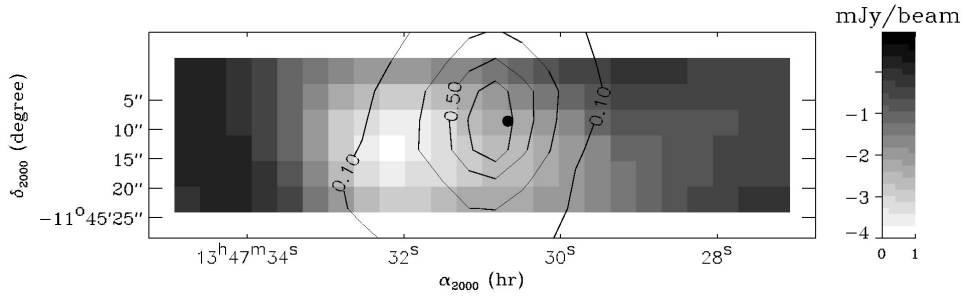

FIG. 1.—A 2.1 mm map of the RX J1347−1145 central region obtained with Diabolo. The map has been smoothed with a 25″ FWHM Gaussian filter. The 1 σ noise is about 1 mJy beam^{-1}. The X-ray contours have been overplotted. The filled circle indicates the radio source position.

could be kept fixed during the measurement. This was done to minimize microphonic noises and electromagnetic influences from the motors driving the IRAM 30 m antenna. The map of the cluster is obtained by stepping in declination between two consecutive lines. The line length is 120″ with a step of 5″. The wobbling is horizontal, and thus it is not aligned with the scan direction. However, the wobbling amplitude is large enough for the reference field to be always farther out of the cluster. In order to remove systematic signal drifts that are produced by the antenna environment, we used, alternatively, the positive and negative beam to map the cluster. We performed 208 such individual maps on the cluster, for a total duration of 16 hr.

Another target of Diabolo's 1997 run was the direction of the decrement detected at 8.44 GHz by Richards et al. (1997). We refer to this source as VLA 1312+4237 in the following. Richards et al. (1997) measured a flux decrement of -13.9 ± 3.3 μJy in a 30″ beam. The presence of two quasars in this direction led them to claim the possible existence of a cluster at a redshift of $z = 2.56$. Campos et al. (1999) have reported the detection of a concentration of Lyα-emitting candidates around the quasars. They argued that the probability for such a clustering to be random is 5×10^{-5}. Our pointing direction was $\alpha = 13^{h}12^{m}17^{s}$, $\delta = 42°37'30''$. We performed 287 individual maps on this target for a total time of about 20 hr.

3. DATA REDUCTION AND CALIBRATION

The reduction procedure includes the following main steps: (1) We remove cosmic-ray impacts. (2) A synchronous demodulation algorithm is applied, taking into account the wobbling secondary frequency and amplitude. (3) We remove from the 2.1 mm bolometer time line the signal that is correlated with the 1.2 mm bolometer that is looking at the same sky pixel. This correlated signal is mainly due to the atmospheric emission whose spectral color is very different from the SZ effect. (4) Correction for opacity is done from the bolometer total power measurements and its calibration by sky dips. (5) To eliminate the low-frequency detector noises, a baseline is subtracted from each line of the map. The baseline is a 1° polynomial. It is fitted to 60% of the data points: 30% at each end of the line. (6) Each map is then resampled on a regular right ascension/declination grid, taking into account the field rotation in the Nasmyth focal plane. (7) An average map is computed for each bolometer. Since the weather conditions were not permanently ideal, the noise quality of the individual maps is not homogeneous, particularly at 1.2 mm. We thus exclude from the average the maps in which the rms pixel-to-pixel fluctuation is larger than 1.5 times the median rms value of all the individual maps. (8) A single map is then produced for each channel (1.2 and 2.1 mm) by the co-addition of the three bolometer average maps.

During the run, pointing verifications and the mapping of reference sources have been performed. We have used the planet Mars as a calibration target. The apparent angular diameter of Mars was 5″, so that we can consider it as a point source with respect to Diabolo's beam. The accuracy of the absolute calibration obtained is on the order of 25% at 1.2 mm and 15% at 2.1 mm. Mars observations are also used for the characterization of Diabolo's beams. The measured FWHMs are 24″ and 22″ at 1.2 and 2.1 mm, respectively. Mars has been observed in an azimuth-elevation mapping mode with a scanning speed that is slower than the natural drift speed of the cluster observation mode. This later speed is fast enough compared with the wobbler period to spread the signal in the scanning direction (i.e., right ascension) significantly. The resulting beam FWHM for the cluster mode along this direction is 28″. It has been experimentally determined by the observation of a quasar lying at about the same declination as the cluster.

4. RESULTS

The final map of RX J1347−1145 at 2.1 mm is shown on Figure 1. The X-ray contours have been overplotted. The average right ascension profile at 2.1 mm is plotted in Figure 2. The profile obtained for the VLA 1312+4237 direction, using the same data processing, has been overplotted. The map and the profiles have been smoothed with a Gaussian filter of 25″ FWHM to maximize the signal-to-noise ratio. The 2.1 mm RX J1347−1145 map presents a very strong decrement. For a thermal SZ effect, this corresponds to a Comptonization parameter on the order of 10^{-3}. The decrement that we measure is not centered on the cluster X-ray maximum. We will show in the analysis that this effect can be explained by the superposition of the SZ decrement from the intracluster gas and a positive emission from a known radio source slightly shifted west off the cluster center.

We have no detection for the direction of VLA 1312+4237. Our 3 σ upper limit is $y < 1.5 \times 10^{-4}$. This is actually compatible with the decrement measured by Richards et al. (1997) that translates into a central Comptonization parameter on the

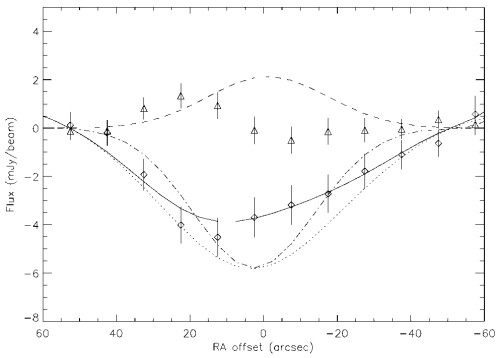

FIG. 2.—A 2.1 mm right ascension profile of RX J1347−1145 (data smoothed with a 25″ FWHM Gaussian). The data points have been plotted (*diamonds*) with their 1 σ error bars. The best-fit model (*solid line*) combines an SZ component (*dotted line*) with a point-source component (*dashed line*). The dot-dashed line draws a point-source profile with the same amplitude as the SZ effect. It shows that the decrement we observed is more extended than a point source. The VLA 1312+4237 average profile (no detection; see text) is shown with triangles.

order of 7×10^{-5} for a thermal SZ effect. If this decrement is in fact due to a kinetic SZ effect, then we expect a signal at 2.1 mm that is equivalent to a thermal SZ effect of $y_c = 1.4 \times 10^{-4}$, still within our 3 σ limit.

Actually, we have used the VLA 1312+4237 data set to obtain a reliable assessment of the error bars on RX J1347−1145. The individual maps have been averaged over increasing durations in order to evaluate the effective scatter of the average signal over independent data sets. The maximum duration that could be checked with this method is about 5 hr, corresponding to an average of 64 individual maps. We have checked that for all bolometers, the rms pixel noise scales as the square root of the integration time. The error bars extrapolated from this analysis to longer integration times are consistent with the error bars derived from the internal scatter of the data averaged for RX J1347−1145. The typical sensitivity reached in the 2.1 mm channel is on the order of 1 mJy in a 25″ beam.

5. DATA ANALYSIS

In the following, we have used for the intracluster gas density a spherical β-model with the parameter values derived from the X-ray analysis of Schindler et al. (1997): core radius $r_c = 8\farcs4$ (57 kpc), $\beta = 0.56$, central density $n_0 = 0.094$ cm^{-3}, and temperature $T_e = 9.3$ keV. We choose to cut off this distribution at a radial distance of $r_{\rm cut} = 15r_c$. We assume the same cosmological parameters too, $H_0 = 50$ km s^{-1} Mpc^{-1} and $\Omega_0 = 1$ ($\Lambda = 0$). With such a model, the measured SZ skymap reads

$$I(\bar{\nu}, \mathbf{\Omega}) = y_c \int \tau(\nu) \mathrm{SZ}(\nu, T_e) d\nu \int P(\mathbf{\Omega}) L(\mathbf{\Omega} - \mathbf{\Omega}') d\mathbf{\Omega}', \quad (1)$$

where $y_c = (k/m_e c^2)\, \sigma_{\rm T} \int T_e n_e(r) dl$ is the Comptonization parameter toward the cluster center; $n_e(r) = n_0[1 + (r/r_c)^2]^{-3\beta/2}$ is the β-radial distribution of the gas density; $\tau(\nu)$ is the normalized Diabolo band spectral efficiency (given in Désert et al. 1998); and $\mathrm{SZ}(\nu, T_e)$ is the spectral density of the thermal SZ distortion for a unit Comptonization parameter, including the relativistic weak dependence on T_e (see Pointecouteau, Giard, & Barret 1998). In fact, for a 9.3 keV cluster, the use of relativistic spectra avoids making errors on the SZ flux estimations of 45% and 10% at 1.2 and 2.1 mm, respectively. We did not include any kinetic SZ contribution, which is generally weak (Birkinshaw 1999); k, m_e, c, and $\sigma_{\rm T}$ are, respectively, the Boltzmann constant, the electron mass, the speed of light, and the Thomson cross section. $P(\mathbf{\Omega})$ and $L(\mathbf{\Omega})$ are the normalized angular distributions of the cluster and the experimental beam, respectively. $P(\mathbf{\Omega})$ has no analytical expression; it is numerically computed by the integration of the gas density β-profile on the line of sight.

Two radio sources are known from the NRAO VLA Sky Survey in the neighborhood of the cluster (Condon et al. 1998). One, at (α, δ) = ($13^{\rm h}47^{\rm m}30\fs67$, $-11°45'8\farcs6$), is very close to the cluster center and is likely to correspond to the central Cd galaxy. Komatsu et al. (1999) have compiled observations of this radio source at 1.4, 28.5, and 105 GHz. They have derived the following power law for the radio source spectrum: $F_\nu(\mathrm{band}) = (55.7 \pm 1.0)\,(\nu/1\ \mathrm{GHz})^{-0.47 \pm 0.02}$ mJy. So the extrapolated millimeter flux should be $F_\nu(1.2\ \mathrm{mm}) = 3.7 \pm 0.4$ mJy beam^{-1} and $F_\nu(2.1\ \mathrm{mm}) = 4.9 \pm 0.5$ mJy beam^{-1}.

To analyze the data properly, we have performed a realistic simulation of the Diabolo observations on the skymap of the SZ model (eq. [1]). The whole set of observed individual maps has been simulated by taking into account the 150″ wobbling amplitude and the proper sky rotation at the Nasmyth focus. The simulated data have been processed through the same pipeline as the observed data set in order to obtain averaged model maps.

Finally, using this simulated data set, we have simultaneously fitted the SZ decrement amplitude and the point-source flux on the 2.1 mm profile with y_c and $F_\nu(2.1\ \mathrm{mm})$ as free parameters. The best-fit parameters are $y_c = (12.7^{+2.9}_{-3.1}) \times 10^{-4}$ and $F_\nu(2.1\ \mathrm{mm}) = 6.1^{+4.3}_{-4.8}$ mJy beam^{-1} with a reduced χ^2 of 1.3. Results are given at a 68% confidence level. The absolute calibration error, 25% and 15% at 1.2 and 2.1 mm, respectively, is not included. $F_\nu(2.1\ \mathrm{mm})$ is compatible with the value expected from radio observations. The best fit is overplotted on the data (see Fig. 2). It reproduces the asymmetric profile. This asymmetry is due to the point-source contribution that fills part of the SZ decrement.

During a second time, we fixed the radio point-source flux at the expected value deduced from Komatsu et al. (1999), $F_\nu(2.1\ \mathrm{mm}) = 4.9$ mJy beam^{-1}, and we fitted with a maximum likelihood method both the central Comptonization parameter y_c, and the angular core radius θ_c. We have found $y_c = (13.2^{+0.2}_{-2.6}) \times 10^{-4}$ and $\theta_c = 7.2^{+7.3}_{-7.2}$ arcsec with a reduced χ^2 of 1.2. The Comptonization parameter value is consistent with the previous one. The angular core radius is consistent with the X-ray value within the 68% confidence level.

6. CONCLUSION

We confirm through our SZ detection that RX J1347−1145 is an extremely massive and hot cluster. We have measured the deepest SZ effect ever observed. It corresponds to a very large Comptonization parameter, $y_c = (12.7^{+2.9}_{-3.1}) \times 10^{-4}$. This is almost twice the value expected from the X-ray data: $y_{\text{X-ray}} = (7.3 \pm 0.7) \times 10^{-4}$ if we use the cluster gas parameters derived by Schindler et al. (1997). Although our result points to a mass higher than the X-ray mass, as is the case for gravitational lens measurements, the uncertainties do not allow us to conclude

firmly that there is a discrepancy. The X-ray flux toward the cluster center is actually dominated by the very strong cooling flow in the core. The average temperature of the gas that contributes to the SZ effect is thus likely to be higher than the temperature derived from the X-ray data, $T_e = 9.3 \pm 1$ keV. The gas temperature that is needed to produce the thermal SZ effect that we have observed is $T_e = 16.2 \pm 3.8$ keV, assuming all other parameters are kept unchanged. In a reanalysis that takes into account the heterogeneity of the cluster, Allen & Fabian (1998) have actually derived for this cluster a very high gas temperature: $T_e = 26.4^{+7.8}_{-12.3}$ keV, which is indeed consistent with our measurement. Under the hypothesis of hydrostatic equilibrium, a higher gas temperature implies a higher total cluster mass, thus decreasing the gas fraction if all other cluster parameters are kept unchanged. For $T_e = 16.2 \pm 3.8$ keV, the total mass of RX J1347−1145 within 1 Mpc is considerable, $M_{\rm tot}(r < 1\ {\rm Mpc}) = (1.0 \pm 0.3) \times 10^{15}\ M_\odot$, and the corresponding gas fraction is $f_{\rm gas}(r < 1\ {\rm Mpc}) = 19.5\% \pm 5.8\%$.

We are very grateful to the IRAM staff at Pico Veleta for their help during observations. We thank Laurent Ravera for very useful comments during the data analysis phase. Diabolo is supported by the Programme National de Cosmologie, Institut National pour les Sciences de l'Univers, Ministère de l'Education Nationale de l'Enseignement Supérieur et de la Recherche, CESR, CRTBT, IAS-Orsay, and LAOG. We thank the anonymous referee for numerous comments and corrections that allowed us to improve the Letter considerably.

REFERENCES

Allen, S. W., & Fabian, A. C. 1998, MNRAS, 297, L57
Benoit, A., et al. 1999, A&AS, submitted
Birkinshaw, M. 1999, Phys. Rep., 1999, 310, 97
Campos, A., Yahil, A., Windhorst, R. A., Richards, E. A., Pascarelle, S., Impey, C., & Petry, C. 1999, ApJ, 511, L1
Condon, J. J., Cotton, W. D., Greisen, E. W., Yin, Q. F., Perley, R. A., Taylor, G. B., & Broderick, J. J. 1998, AJ, 115, 1693
Désert, F. X., et al. 1998, NewA, 3(8), 655
Fischer, P., & Tyson, J. A. 1997, AJ, 114, 14
Komatsu, E., Kitayama, T., Suto, Y., Hattori, M., Kawabe, R., Matsuo, H., Schindler, S., & Yoshikawa, K. 1999, ApJ, 516, L1
Pointecouteau, E., Giard, M., & Barret, D. 1998, A&A, 336, 44
Richards, E. A., Fomalont, E. B., Kellermann, K. I., Partridge, R. B., & Windhorst, R. A. 1997, AJ, 113, 1475
Sahu, K. C., et al. 1998, ApJ, 492, L125
Schindler, S., et al. 1995, A&A, 299, L9
Schindler, S., Hattori, M., Neumann, D. M., & Böhringer, H. 1997, A&A, 317, 646
Sunyaev, R., & Zeldovich, Y. 1972, Comments Astrophys. Space Phys., 4, 173

A&A 429, 417–426 (2005)
DOI: 10.1051/0004-6361:20048093

Astronomy & Astrophysics

The selection function of SZ cluster surveys

J.-B. Melin, J. G. Bartlett, and J. Delabrouille

APC – Université Paris 7, 75005 Paris, France
PCC – Collège de France, 75005 Paris, France
e-mail: [melin;bartlett;delabrouille]@cdf.in2p3.fr

Received 15 April 2004 / Accepted 11 September 2004

Abstract. We study the nature of cluster selection in Sunyaev-Zel'dovich (SZ) surveys, focusing on single frequency observations and using Monte Carlo simulations incorporating instrumental effects, primary cosmic microwave background (CMB) anisotropies and extragalactic point sources. Clusters are extracted from simulated maps with an optimal, multi-scale matched filter. We introduce a general definition for the survey selection function that provides a useful link between an observational catalog and theoretical predictions. The selection function defined over the observed quantities of flux and angular size is independent of cluster physics and cosmology, and thus provides a useful characterization of a survey. Selection expressed in terms of cluster mass and redshift, on the other hand, depends on both cosmology and cluster physics. We demonstrate that SZ catalogs are not simply flux limited, and illustrate how incorrect modeling of the selection function leads to biased estimates of cosmological parameters. The fact that SZ catalogs are not flux limited complicates survey "calibration" by requiring more detailed information on the relation between cluster observables and cluster mass.

Key words. cosmology: large-scale structure of Universe – galaxies: clusters: general

1. Introduction

Galaxy cluster surveys are important tools for measuring key cosmological quantities and for understanding the process of structure formation in the universe (Bahcall et al. 1999; Rosati et al. 2002). Surveying for clusters using the Sunyaev-Zel'dovich (SZ) effect (Sunyaev & Zeldovich 1970; Sunyaev & Zeldovich 1972; for recent reviews, see Birkinshaw 1999; and Carlstrom et al. 2002) offers a number of advantages over more traditional methods based on X-ray or optical imaging. These advantages include good detection efficiency at high-redshift; a selection based on the thermal energy of the intracluster medium, a robust quantity relative to any thermal structure in the gas; and an almost constant mass detection limit with redshift (Holder et al. 2000; Bartlett 2000; Bartlett 2001). A new generation of optimized, dedicated instruments, both large bolometer arrays (Masi et al. 2003; Runyan et al. 2003; Kosowsky 2004) and interferometers (Lo et al. 2000; Jones 2002), will soon perform such SZ cluster surveys, and we may look forward to the large and essentially full-sky SZ catalog expected from the Planck mission[1]. In anticipation, many authors have studied the nature and use of SZ cluster catalogs and made predictions for the number of objects expected from various proposed surveys (Holder et al. 2000; Kneissl et al. 2001). A good example of the potential of an SZ survey is the use of its redshift distribution to examine structure formation at high redshift and to thereby constrain cosmological parameters, such as the density parameter $\Omega_{\rm M}$ (Barbosa et al. 1996), and the dark energy equation-of-state ω (Haiman et al. 2001).

An astronomical survey is fundamentally characterized by its selection function, which identifies the subclass of objects detected among all those actually present in the survey area. It is a function of cluster properties and survey conditions. Depending on the nature of the observations, relevant cluster properties may include: mass, redshift, luminosity, morphology, etc., while key descriptors of the survey would be sensitivity, angular resolution, spectral coverage, etc. The selection function will also depend on the the detection algorithm used to find clusters in the survey data. Understanding of the selection function is a prerequisite to any statistical application of the survey catalog; otherwise, one has no idea how representative the catalog is of the parent population actually out in the universe.

Selection function issues for SZ surveys have been touched on recently by several authors (Bartlett 2001; Schulz & White 2003; White 2003), while most previous studies of the potential use of SZ surveys have not examined this point in detail. For example, predictions of the redshift distribution of SZ-detected clusters usually assume that they are point sources, simply selected on their total flux[2]. We shall see below that this is not necessarily the case, and an analysis of cosmological

[1] A list of web pages describing a number of experiments is given in the reference section.

[2] The term *flux* does not really apply in the case of SZ observations, as the effect is measured relative to the unperturbed background and may be negative. We shall nevertheless use it throughout for simplicity.

parameters based on such an assumption would significantly bias the results.

Understanding a survey selection function is difficult. By its very nature and purpose, the selection function is supposed to tell us about objects that we *don't see* in the survey! Realistic simulations of a survey are central to determining its selection function (e.g., Adami et al. 2001). One knows which objects are put into the simulation and can then compare them to the subset of objects detected by the mock observations. In practice, of course, understanding of a selection function comes only from a combination of such simulations and diverse observations taken under different conditions and/or in different wavebands; full understanding thus comes slowly.

There are really two distinct issues connected to the selection function: object detection, or *survey completeness*, and object measurement, which we shall refer to as *photometry*; as a separate issue, one must also determine the contamination function. One would like to characterize each detected cluster by determining, for example, its total flux, angular size, etc. As practitioners are well aware, photometry of extended objects faces many difficulties that introduce additional uncertainty and, in particular, potential bias into the survey catalog. The selection function must correct for bias induced by both the detection and photometric procedures. The two are, however, distinct steps in catalog construction, and the selection function (see below) should reflect this fact.

The object of the present work is to begin a study of SZ selection functions for the host of SZ surveys that are being planned, and to propose a formalism for their characterization. To this end, we have developed a rapid Monte Carlo simulation tool (Delabrouille et al. 2002) that produces mock images of the SZ sky, including various clustering and velocity effects, primary cosmic microwave background (CMB) anisotropies, radio point sources and instrumental effects. The main goals of such studies, in this period before actual surveying has begun, are to improve understanding of the expected scientific return of a given survey and to help optimize observing strategies.

Our specific aim in the present work is to study selection effects in SZ surveys by focusing on single frequency observations, such as will be performed by up-coming interferometers. Most bolometer cameras propose surveys at several frequencies, although not necessarily simultaneously; the present considerations are therefore applicable to the first data sets from these instruments. This work builds on that of Bartlett (2000) by adding the effects of primary CMB anisotropies, point sources and photometric errors, and by the use of an optimized cluster detection algorithm (Melin et al. 2004).

General considerations concerning the selection function are given in the next section and used to motivate our definition given in Eq. (1). We then briefly describe (Sect. 3) our simulations, based on a Monte Carlo approach incorporating cluster correlations and velocities, as well as our cluster detection and photometry algorithms built on an optimized spatial filter (details will be given elsewhere, Melin et al. 2004). A discussion of cluster selection with this method follows (Sect. 4), where with a simple analytic argument, we show how cluster detection depends on *both* total flux and angular size. Our main conclusion is that SZ surveys will not be simply flux limited. Our simulations support the analytical expectations, and they also highlight the difficulty of performing accurate photometry on detected clusters.

We close with a discussion (Sect. 5) of some implications for upcoming surveys. The most important is that the redshift distribution of observed clusters differs from that of a pure flux-limited catalog; assuming pure flux selection will therefore lead to biased estimates of cosmological parameters. In this same section, we give an explicit example of biased parameter estimation caused by the presence of incorrectly modeled excess primary CMB power on cluster scales, as suggested by the CBI experiment (Mason et al. 2001). We note that non-trivial cluster selection complicates survey "calibration" (Bartelmann 2001; Hu 2003; Majumdar & Mohr 2003; Lima & Hu 2004) because a *size-mass* relation must be obtained in addition to a *flux-mass* relation. Photometric errors will further increase the difficulty by augmenting scatter in the mass-observable relations.

2. Selection function: General considerations

To motivate our definition, we first consider some general properties desired of a survey selection function. Fundamentally, it relates observed catalog properties (e.g., flux and size) to relevant intrinsic characteristics of the source population under study. In particular, we want it to tell us about the *completeness* of the survey catalog as a function of source properties, which is a measure of the selection bias. In addition, we also wish for it to reflect the effects of statistical (e.g., photometric) errors. Notice, on the other hand, that the selection function will not tell us anything about *contamination* of the catalog by false detections; this is another function of observed quantities that must be separately evaluated.

Consider the example of a flux-limited catalog of point sources. Neglecting photometric measurement errors, the probability that a source at redshift z will find its way into the survey catalog is simply given by the fraction of sources brighter than the flux limit, which may be calculated as an integral over the luminosity function at z (e.g., Peebles 1993). Extended objects complicate the situation, for their detection will in general depend on morphology. One must then define appropriate source descriptors other than just a total flux; and even the definition of total flux, conceptually simple, becomes problematic (fixed aperture flux, isophotal flux, integrated flux with a fitted profile, etc.). The choice of descriptors is clearly important and the selection function will depend on it. They must encode relevant observational information on the sources and represent observables with as little measurement error as possible.

The simplest characterization for extended SZ sources would employ a total observed flux, Y_o, and a representative angular size, which we take to be the core radius θ_{co}. By total flux, we mean the flux density integrated over the entire cluster profile, out to the virial radius, and we express it in a frequency independent manner as the integrated Compton-y parameter. We limit ourselves to these two descriptors in the ensuing discussion, although clearly many others describing cluster morphology are of course possible (ellipticity, for example...). How the observed quantities are actually measured is crucial –

measurement errors and the selection function will both depend on the technique used.

Our detected clusters will then populate the observed parameter space according to some distribution $\mathrm{d}N_\mathrm{o}/\mathrm{d}Y_\mathrm{o}\mathrm{d}\theta_\mathrm{co}$. What we really seek, however, is the true cluster distribution, $\mathrm{d}N/\mathrm{d}Y\mathrm{d}\theta_\mathrm{c}$, over the intrinsic cluster parameters Y and θ_c. Measurement errors and catalog incompleteness both contribute to the difference between these two distributions. In addition, the catalog will suffer from contamination by false detections.

These general considerations motivate us to define the *selection function* as the *joint distribution of* Y_o *and* θ_co, as a function of (i.e., given) Y and θ_c. There are many other factors that influence the selection function, such as instrument characteristics, observation conditions and analysis methods, so in general we write

$$\Phi\left[Y_\mathrm{o}, \theta_\mathrm{co}|Y, \theta_\mathrm{c}, \sigma_\mathrm{N}, \theta_\mathrm{fwhm}, ...\right] \quad (1)$$

where θ_fwhm is the *FWHM* of an assumed Gaussian beam and σ_N^2 is the map noise variance. We illustrate our main points throughout this discussion with simple uniform Gaussian white noise. The dots represent other possible influences on the selection function, such as the detection and photometry algorithms employed to construct the catalog.

Several useful properties follow from this definition. For example, the selection function relates the observed counts from a survey to their theoretical value by

$$\frac{\mathrm{d}N_\mathrm{o}}{\mathrm{d}Y_\mathrm{o}\mathrm{d}\theta_\mathrm{co}}(Y_\mathrm{o}, \theta_\mathrm{co}) = \int_0^\infty \mathrm{d}Y \int_0^\infty \mathrm{d}\theta_\mathrm{c}\ \Phi(Y_\mathrm{o}, \theta_\mathrm{co}|Y, \theta_\mathrm{c}) \times \frac{\mathrm{d}N}{\mathrm{d}Y\mathrm{d}\theta_\mathrm{c}}(Y, \theta_\mathrm{c})\,. \quad (2)$$

A similar relation can be established between the observed counts and cluster mass and redshift:

$$\frac{\mathrm{d}N_\mathrm{o}}{\mathrm{d}Y_\mathrm{o}\mathrm{d}\theta_\mathrm{co}}(Y_\mathrm{o}, \theta_\mathrm{co}) = \int_0^\infty \mathrm{d}z \int_0^\infty \mathrm{d}M\ \Psi(Y_\mathrm{o}, \theta_\mathrm{co}|z, M) \times \frac{\mathrm{d}N}{\mathrm{d}z\mathrm{d}M}(z, M) \quad (3)$$

where $\mathrm{d}N/\mathrm{d}z\mathrm{d}M$ is the mass function and Ψ incorporates the intrinsic and observational scatter in the relation between $(Y_\mathrm{o}, \theta_\mathrm{co})$ and (z, M) (mass-observable relations). This is made more explicit by

$$\Psi(Y_\mathrm{o}, \theta_\mathrm{co}|z, M) = \int_0^\infty \mathrm{d}Y \int_0^\infty \mathrm{d}\theta_\mathrm{c}\Phi(Y_\mathrm{o}, \theta_\mathrm{co}|Y, \theta_\mathrm{c}) \times T(Y, \theta_\mathrm{c}|z, M) \quad (4)$$

where the function T represents the intrinsic scatter in the relation between actual flux Y and core radius θ_c, and cluster mass and redshift.

In general, we may separate the selection function into two parts, one related to detection and the other to photometry:

$$\Phi(Y_\mathrm{o}, \theta_\mathrm{co}|Y, \theta_\mathrm{c}) = \chi(Y, \theta_\mathrm{c})F(Y_\mathrm{o}, \theta_\mathrm{co}|Y, \theta_\mathrm{c}). \quad (5)$$

The first factor represents survey completeness and is simply the ratio of detected to actual clusters as a function of true cluster parameters. The second factor quantifies photometric errors with a distribution function F normalized to unity:

$$\int \mathrm{d}Y_\mathrm{o}\mathrm{d}\theta_\mathrm{co}\ F(Y_\mathrm{o}, \theta_\mathrm{co}|Y, \theta_\mathrm{c}) = 1$$

In the absence of measurement errors we would have

$$\Phi(Y_\mathrm{o}, \theta_\mathrm{co}|Y, \theta_\mathrm{c}) = \chi(Y_\mathrm{o}, \theta_\mathrm{co})\delta(Y_\mathrm{o} - Y)\delta(\theta_\mathrm{co} - \theta_\mathrm{c})$$

in which case the observed counts become

$$\frac{\mathrm{d}N_\mathrm{o}}{\mathrm{d}Y_\mathrm{o}\mathrm{d}\theta_\mathrm{co}}(Y_\mathrm{o}, \theta_\mathrm{co}) = \chi(Y_\mathrm{o}, \theta_\mathrm{co})\frac{\mathrm{d}N}{\mathrm{d}Y\mathrm{d}\theta_\mathrm{c}}(Y, \theta_\mathrm{c})\,. \quad (6)$$

The importance of the selection function for cosmological studies lies in Eq. (3) which relates the cosmologically sensitive mass function to the observed catalog distribution. Accurate knowledge of Ψ is required in order to obtain constraints on cosmological parameters, such as the density parameter or the dark energy equation-of-state.

3. Simulations

Detailed study of SZ selection issues requires realistic simulations of proposed surveys. Although analytic arguments do provide significant insight, certain effects, such as cluster-cluster blending and confusion, can only be fully modeled with simulations. To this end, we have developed a rapid Monte Carlo-based simulation tool that allows us to generate a large number of realizations of a given survey. This is essential in order to obtain good measures of the selection function that are not limited by insufficient statistics. In this section we briefly outline our simulation method and our cluster detection algorithm, leaving details to Delabrouille et al. (2002) and Melin et al. (2004).

Unless explicitly stated, the simulations used in this work are for a flat concordance model (Spergel et al. 2003) with $\Omega_\mathrm{M} = 0.3 = 1 - \Omega_\Lambda$, Hubble constant of $H_0 = 70\ \mathrm{km\,s^{-1}\,Mpc^{-1}}$ Freedman et al. 2001) and a power spectrum normalization $\sigma_8 = 0.98$. The normalization of the $M - T$ relation is chosen to reproduce the local abundance of X-ray clusters with this value of σ_8 (Pierpaoli et al. 2001). Finally, we fix the gas mass fraction at $f_\mathrm{gas} = 0.12$ (e.g., Mohr et al. 1999).

3.1. Method

Our simulations produce sky maps at different frequencies and include galaxy clusters, primary CMB anisotropies, point sources and instrumental properties (beam smoothing and noise). In this work, we do not consider diffuse Galactic foregrounds, such as dust and synchrotron emission, as we are interested in more rudimentary factors influencing the selection function; we leave foreground issues to a future work (as general references, see Bouchet & Gispert 1999; Tegmark et al. 2000; Delabrouille et al. 2003).

We model the cluster population using the Jenkins et al. (2001) mass function and self-similar, isothermal β-profiles for the SZ emission. A realization of the linear density field $\delta\rho/\rho$ within a comoving 3D box, with the observer placed at one

end, is used to construct the cluster spatial distribution and velocity field. We scale the density field by the linear growth factor over a set of redshift slices (or bins) along the past light-cone of the observer; a set of mass bins is defined within each redshift slice. We then construct a random cluster catalog by drawing the number of clusters in each bin of mass and redshift according to a Poisson distribution with mean given by the mass function integrated over the bin. Within each redshift slice, we spatially distribute these clusters with a probability proportional to $1 + b\frac{\delta\rho}{\rho}$, where b is the linear bias given by Mo & White (1996). Comparison of the resulting spatial and velocity 2-point functions of the mock catalog with results from the VIRGO consortium's N-body simulations shows that this method faithfully reproduces the correlations down to scales of order of 10 h^{-1} Mpc.

Individual clusters are assigned a temperature using a $M - T$ relation consistent with the chosen value of σ_8 (Pierpaoli et al. 2001)

$$\frac{M}{10^{15}\, h^{-1}\, M_\odot} = \left(\frac{T}{\beta_p}\right)^{\frac{3}{2}} \left(\Delta_c E^2\right)^{-\frac{1}{2}} \tag{7}$$

with $\beta_p = 1.3 \pm 0.13 \pm 0.13$ keV. Here, Δ_c is the mean density contrast for virialization (weakly dependent on the cosmology) and $E(z) = H(z)/H_0$. As mentioned, we distribute the cluster gas with an isothermal β-model:

$$n_e(r) = n_e(0)\left[1 + \left(\frac{r}{r_c}\right)^2\right]^{\frac{-3\beta}{2}} \tag{8}$$

where we fix $\beta = 2/3$ and the core radius is taken to be $r_c = 0.1\, r_v$, with the virial radius given by

$$r_v = 1.69\, h^{-2/3} \left(\frac{M}{10^{15}\, M_\odot}\right)^{1/3} \left(\frac{\Delta_c}{178}\right)^{-1/3} E^{-2/3}\ \text{Mpc}. \tag{9}$$

The central electron density is determined by the gas mass fraction $f_{\rm gas}$. For the present work, we ignore any intrinsic scatter in these scaling relations.

In this way we produce a 3×3 degree map of the SZ sky. Primary CMB anisotropies are added as a Gaussian random field by drawing Fourier modes according to a Gaussian distribution with zero mean and variance given by the power spectrum as calculated with CMBFAST (Seljak & Zaldarriaga 1996). We then populate the maps with radio and infrared point sources, using the counts summarized in Bennett et al. (2003) and fitted by Knox et al. (2003), and the counts from SCUBA (Borys et al. 2003). Finally, the map is smoothed with a Gaussian beam and white Gaussian noise is added to model instrumental effects.

3.2. Detection algorithm

We have developed (Melin et al. 2004) a rapid detection routine incorporating a deblending algorithm that is based on matched filtering (Haehnelt & Tegmark 1996), for single frequency surveys, and matched multi-filtering (Herranz et al. 2002), for multi-frequency surveys. Recall that in this work we only examine single frequency surveys. The matched filter, on a scale θ_c, is defined to yield the best linear estimate of the amplitude of the SZ signal from a cluster with (matched) core radius θ_c. It depends on both the beam-smoothed cluster profile τ_c and the noise power spectrum $P(k)$. In Fourier space it is given by

$$\hat{F}(\boldsymbol{k}) = \left[\int \frac{|\hat{\tau}_c(\boldsymbol{k}')|^2}{P(k')} \frac{\mathrm{d}^2 k'}{(2\pi)^2}\right]^{-1} \frac{\hat{\tau}_c^*(\boldsymbol{k})}{P(k)} \tag{10}$$

where $P = (P_{\rm cmb} + P_{\rm sources})|\hat{B}|^2 + P_{\rm ins}$, $\hat{\tau}_c$ is the Fourier transform of the beam-smoothed cluster profile τ_c, $\hat{B}$ is that of the instrumental beam (a Gaussian), and $P_{\rm cmb}$, $P_{\rm sources}$ and $P_{\rm ins}$ represent the power spectra of the primary CMB anisotropies, residual point sources and instrumental noise, respectively. We denote the standard deviation of the noise (including primary CMB and residual points sources) passed through the filter at scale θ_c by σ_{θ_c}, and give its expression for future reference:

$$\sigma_{\theta_c} = \left[\int \frac{|\hat{\tau}_c(\boldsymbol{k})|^2}{P(k)} \frac{\mathrm{d}^2 k}{(2\pi)^2}\right]^{-\frac{1}{2}}. \tag{11}$$

This is the fluctuation amplitude of the filtered signal in the absence of any cluster signal.

We can summarize the detection algorithm in three steps:

- filter the observed map with matched filters on different scales θ_c in order to identify clusters of different sizes. This produces a set of filtered maps;
- in each filtered map, find the pixels that satisfy $\frac{S}{N} > threshold$ (e.g. 3 or 5). Define cluster candidates as local maxima among these pixels. At this point, each cluster candidate – in each map – has a position, size (that of the filter that produced the map), and a SZ flux given by the signal through the matched filter;
- identify cluster candidates across the different filtered maps using a tree structure (the same cluster can obviously be detected in several filtered maps) and eliminate multiple detections by keeping only cluster properties corresponding to the highest *S/N* map for each candidate.

4. Selection function for single frequency SZ surveys

We consider a single frequency SZ survey with characteristics representative of upcoming interferometers (e.g., the *Arcminute MicroKelvin Imager* being constructed in Cambridge[3]): a 15 GHz observation frequency, 2 arcmin *FWHM* (synthesized) beam and a noise level of 5 μK/beam. Note that, for simplicity and generality, we model the observations as a fully sampled sky map instead of actual visibilities. This approximation should be reasonably accurate given the good sampling expected in the Fourier plane; it will, however, miss important details of the selection function that will require adequate modeling when the time comes. In the same spirit, we also model the noise as a white Gaussian random variable with zero mean and the given variance.

During the course of the discussion, we will often compare the following observational cases: 1) no instrumental

[3] http://www.mrao.cam.ac.uk/telescopes/ami/index.html

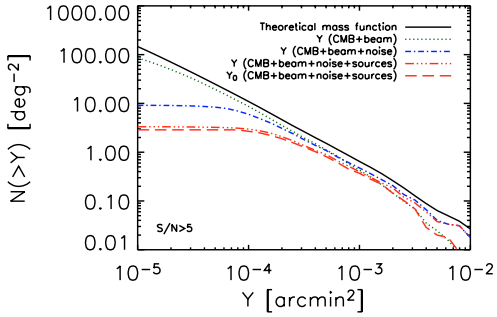

Fig. 1. Cluster counts in terms of integrated Y for the input concordance model (black solid line) and for detected clusters: the green dotted line gives the counts neglecting the effects of instrumental noise and point sources (CMB + beam = 2 arcmin *FWHM*); the blue dash-dotted line includes instrumental noise (5 μK/beam); the red dash-triple-dotted line further includes the effects of residual point sources after explicit subtraction of all sources with flux greater than 100 μJy (see text). These are all plotted as functions of the *true* total flux Y. The red dashed line shows the observed counts for the latter case in terms of the *observed* flux Y_o.

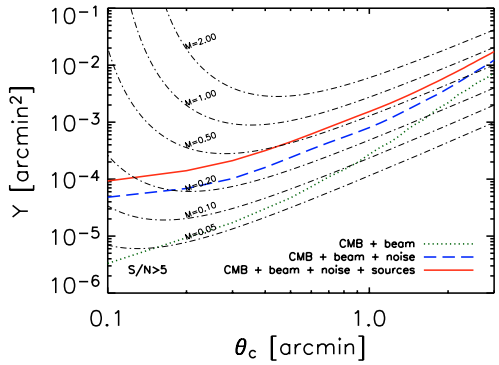

Fig. 2. Selection in the parameter plane of total flux Y and core radius θ_c. The three curves correspond to the different simulated cases, as indicated in the legend; all correspond to a cut at signal-to-noise of 5. The dot-dashed lines in the background give contours of constant mass in this plane; each is parameterized by redshift z. Note that cluster selection does not follow a simple flux cut, which would be a horizontal line, nor a simple mass cut. Photometric errors are neglected in this plot, meaning that observed cluster parameters Y_o and θ_c equal the true values Y and θ_c.

noise (CMB+beam[4]); 2) the former plus instrumental noise at 5 μK/beam; and 3) the previous plus point sources below a flux limit of 100 μJy at 15 GHz. In this last case, we are assuming that all sources brighter than the flux limit are explicitly subtracted; for example, both AMI and the SZA[5] plan long baseline observations for point source removal.

Integrated source counts in terms of total cluster flux Y (measured in arcmin^2) are shown in Fig. 1. The theoretical counts for the fiducial model are given by the solid black line, while the other curves give the counts from our simulated observations. They are plotted in terms of *true* flux Y, except for the red dashed curve that gives the counts as a function of *observed* flux Y_o, as would actually be observed in a survey. Differences between the detected cluster counts and the theoretical prediction (black solid line) reflect catalog incompleteness; the nature of this incompleteness is the focus of our discussion. The influence of photometric errors is illustrated by the difference between the observed counts as a function of observed flux (red dashed curve) and the detected-cluster counts given as a function of true flux.

4.1. Catalog completeness

It is important to understand the exact nature of the incompleteness evident in Fig. 1, and we shall now demonstrate that it is not simply a function of total flux. Our detection algorithm operates as a cut at fixed signal-to-noise, which leads to the following constraint on (true) cluster parameters Y and θ_c:

$$Y = y_{\rm est} \int {\rm d}\Omega\ \tau_c(\hat{n}) \geq \left(\frac{S}{N}\right)\sigma_{\theta_c} \int {\rm d}\Omega\ \tau_c(\hat{n}) \qquad (12)$$

[4] Note that in this case of no noise, the beam can be perfectly deconvolved.

[5] `http://astro.uchicago.edu/sze`

where $y_{\rm est}$ is the central Compton parameter estimated by the filter matched to a cluster of core radius θ_c, and the filter noise on this scale is given by Eq. (11). Figure 2 shows the resulting selection curves for our three cases in the $Y - \theta_c$ plane at $S/N \geq 5$. Note that we are speaking in terms of true cluster parameters, leaving the effects of photometric errors aside for the moment.

It is clear from this figure that cluster selection does not correspond to a simple flux cut – it depends rather on a combination of both source flux and angular extent. The exact form of this dependence is dictated by the noise power spectrum, which must be understood to include primary CMB anisotropy. That this latter dominates on the larger scales can be seen from the fact that the three curves approach each other at large core radii. For smaller objects, on the other hand, instrumental noise and residual point source contamination "pull" the curve towards higher fluxes relative to the ideal case that includes only CMB anisotropies (dotted line).

For the solid red curve, we calculate the flux variance induced by residual point sources at the given filter scale and then add the equivalent Gaussian noise term to the instrumental noise and CMB contributions. One may well ask why the source fluctuations should be Gaussian given the shallow slope of the radio source counts that would normally lead to very non-Gaussian statistics. The fluctuations are in fact Gaussian, as we have verified with the simulations, essentially because the source subtraction is performed at higher angular resolution than the smallest filter scale; in effect, we have cleaned "below" the filter confusion limit, so that the number of sources/filter beam is large and we approach the Gaussian limit. This realistically reflects what will actually be done with interferometers using long baseline observations for source subtraction.

The dot-dashed lines in the background of the figure represent contours of constant cluster mass $M(Y, \theta_c)$. They result

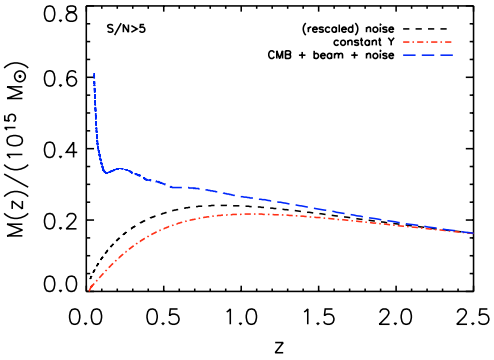

Fig. 3. Detection mass as a function of redshift. The blue long-dashed line shows the result for the case CMB + noise (blue long-dashed line in Fig. 2). The rise at low redshift is due confusion with primary CMB fluctuations that is more important for nearby clusters with large angular extent. The red dot-dashed line gives the result for a pure flux-limited catalog (see text), and the black short dashed line that for observations without CMB confusion (e.g., multi-frequency). Relative to a pure flux-limited catalog, both observed catalogs loose clusters over a range of redshifts.

from inversion of the $Y(M,z)$ and $\theta_c(M,z)$ relations, where we associate cluster core radius with filter scale. Note that redshift varies along each contour, and that we have assumed zero scatter in the relations so that the inversion is one-to-one. In reality, of course, they contain intrinsic scatter, due to cluster physics, as well as observational scatter induced by photometric errors. The position of these mass contours depends on both cluster physics and the underlying cosmology; we may, for example, displace the contours by changing the gas-mass fraction. The selection curves, in contrast, are independent of cosmology and cluster physics, being based on purely observational quantities.

Observed clusters populate this plane according to the distribution $\mathrm{d}N_o/\mathrm{d}Y_o\mathrm{d}\theta_{co}$, which depends on cluster physics, cosmology and photometry; Eq. (3) gives it in terms of the key theoretical quantity, the mass function. If photometric errors are assumed to be unimportant, then Eq. (6) applies and we see that the function $\chi(Y,\theta_c)$ is a step function taking the value of unity above the selection curves, and zero below; photometric errors simply "smooth" the selection function Φ as manifest by Eq. (5). Completeness expressed in terms of the function χ is therefore *independent* of cluster physics and cosmology. A more common way to express completeness is by the ratio of detected to actual clusters as a function of total flux (or angular scale). At a given flux, for example, this ratio is the fraction of clusters falling above the selection curve. Clearly, it depends on the distribution of clusters over the plane and is, hence, *dependent* on cluster physics, cosmology and photometry. We conclude that the function χ is a more useful description of a survey.

Figure 2 provides a concise and instructive view of cluster selection over the observational plane. We are of course ultimately interested in the kinds of objects that can be detected as a function of redshift, and to this end it is useful to study the *detection mass* shown in Fig. 3. This is defined as the smallest mass cluster detectable at each redshift given the detection criteria. For the figure, we assume that there is no scatter in the $Y_o(M,z)$ and $\theta_{co}(M,z)$ relations so that a selection curve in the observational plane uniquely defines the function $M_{det}(z)$. Note that, as emphasized above, these detection mass curves depend on the assumed cosmology.

We compare three situations in the figure. The blue long-dashed line gives the detection mass for the case CMB + noise (single frequency experiment), while the red dot-dashed line shows the result for a pure flux-limited catalog. The chosen flux cut corresponds to the left-most point on the blue long-dashed selection curve in Fig. 2 (CMB+noise). Finally, the black short-dashed line gives the detection mass for a case with just instrumental noise (with the same beam as the previous cases) and no primary CMB; this approximates the situation for a multi-frequency experiment which eliminates CMB confusion. The noise level has been adjusted such that the selection curve in the (Y,θ_c)-plane matches the previous two cases on the smallest scales. With this choice, all three detection mass curves overlap at high z as seen in Fig. 3.

We see that that the observed catalog (blue long-dashed curve) looses clusters (i.e., has a higher detection mass) over a broad range of redshifts relative to the pure flux-limited catalog (red dot-dashed line); the effect is most severe for nearby objects, whose large angular size submerges them in the primary CMB anisotropies, but it remains significant out to redshifts of order unity. This is also reflected in the redshift distribution of Fig. 5 to be discussed below. We note in addition that even multi-frequency experiments loose clusters over a rather broad range of redshifts, as indicated by the difference between the lower two curves.

Simulations are needed to evaluate the importance of factors not easily incorporated into the simple analytic calculation of the cluster selection curve; these include source blending and morphology, other filtering during data analysis, etc. Using our simulations, we find that cluster detection in mock observations closely follows the analytic predictions, thus indicating that blending does not significantly change the above conclusions, at least for the case under study – a 2 arcmin beam with noise at a level of 5 μK/beam – representative of planned interferometer arrays. As our current simulations only employ spherical beta model profiles, they only test for the importance of blending effects; future work will include more realistic profiles taken, for example, from hydrodynamical N-body simulations. The simulations are also crucial for correctly evaluating the photometric precision of the survey catalog. Contrary to the situation for cluster detection, we find that blending greatly affects photometric measurements: photometric scatter from the simulations is significantly larger than expected based on the S/N ratio, whether the threshold is taken at $S/N = 5$ or 3.

4.2. Catalog contamination

Contamination by false detections is a separate function that can only be given in terms of observed flux and angular (or filter) scale; once again, simulations are crucial for evaluating effects such as blending and confusion. Figure 4 shows

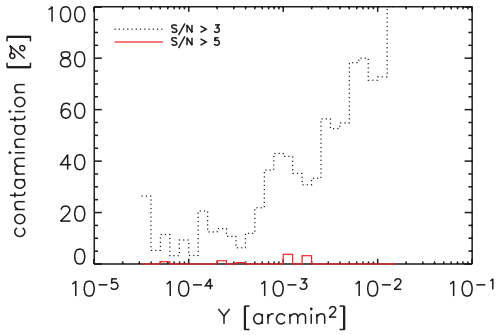

Fig. 4. Contamination rate for a single frequency survey as a function of total flux for two different detection thresholds. The histograms give the percentage of sources that are false detections in catalogs extracted from our simulations.

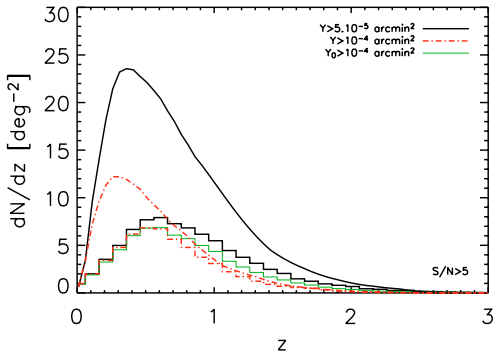

Fig. 5. Redshift distribution of SZ clusters (case 2 – without residual point source noise). The black solid and red dashed curves give the theoretically predicted counts at the two indicated flux limits. Corresponding distributions for the simulated recovered counts, with the same two flux cuts on the true Y, are shown by the black and red, dashed histograms; the small difference between the two reflects the flat observed counts in Fig. 1. The lighter, green histogram shows the simulated counts cut at an *observed* flux of $Y_o > 10^{-4}$ arcmin^2.

the contamination level in our extracted catalogs as a function of total flux Y. The level is significantly higher than expected from the S/N ratio, indicating that confusion and blending effects are clearly important. This is most obvious for the case with $S/N = 3$, where contamination rises towards the high flux end due to confusion with primary CMB fluctuations that are more prevalent on larger angular scales. Even at relatively low flux levels around 10^{-4} arcmin^2, we see that the contamination rate remains near or above 10% for the $S/N = 3$ case. This quantifies the the expectation that single frequency surveys will contend with a non-negligible level of contamination.

4.3. The redshift distribution

The example of extracting cosmological constraints from the redshift distribution of SZ detected clusters affords a good illustration of the importance of understanding the selection function. These constraints arise from the shape of the cluster redshift distribution, which is affected by such parameters as the matter density (Oukbir & Blanchard 1997) and the dark energy equation-of-state (Wang & Steinhardt 1998); this is in fact one of the primary motivations for performing SZ cluster surveys (Haiman et al. 2001). The important point is that the redshift distribution expected in a given cosmological model also depends on the catalog selection function. In the following discussion, we assume that the $Y(M, z)$ and $\theta_c(M, z)$ relations are perfectly known.

Consider the redshift distributions shown in Fig. 5 for an observation where residual point source contamination has been reduced to a negligible level (case 2). The black line represents the theoretical distribution for clusters with total flux $Y > 5 \times 10^{-5}$ arcmin^2, which corresponds to the point source detection limit on the smallest filter scale (leftmost point on the dashed blue curve in Fig. 2). This predicted distribution is very different from the actual distribution of clusters shown as the black histogram. It is clearly impossible to deduce the correct cosmological parameters by fitting a flux-limited theoretical curve to the observed distribution. This demonstrates that the point-source flux limit cannot be used to model the catalog redshift distribution, which is already clear from the fact that the counts in Fig. 1 have already turned over and the catalog is clearly incomplete.

One can try to cut the catalog at a higher flux limit of $Y > 10^{-4}$ arcmin^2, where the observed counts just begin to flatten out and incompleteness is not yet severe. Comparison of the dashed red line – theoretically predicted counts at this flux limit – with the red dashed histogram shows that the observed distribution still differs significantly from the predicted flux-limited redshift distribution. Modeling the observed catalog as a pure flux cut would again lead to incorrect cosmological constraints. In order to extract unbiased parameter estimates, one must adequately incorporate the full catalog selection criteria.

We may illustrate this point by considering the effect of an un-modeled CMB power excess at high l, such as suggested by the CBI experiment (Mason et al. 2001). As we have seen in Fig. 2, the primary CMB fluctuations influence the exact form of the selection curve in the (Y, θ_c) plane; their power on cluster scales must therefore be accurately known to correctly model the cluster selection function. The black curve and black histogram in Fig. 6 repeat the results of Fig. 5 for a cut at $Y > 5 \times 10^{-5}$ arcmin^2. In particular, the black histogram gives the redshift distribution of clusters extracted from simulations including a CMB power spectrum corresponding to the concordance model. The blue (lower) histogram shows the redshift distribution for clusters extracted from simulations in which additional CMB power has been added at high l – a constant power of $l(l+1)C_l/2\pi = 20\ \mu$K was smoothly joined to the concordance model CMB spectrum (just below $l = 2000$) and continuing out to $l = 3000$. Instead of plunging towards zero, as expected of the primary CMB fluctuations in the concordance model, this second model levels off at a constant power level on cluster scales. This has an important effect on cluster detection, as clearly evinced in the figure.

We now examine the effect of ignoring this excess power in an analysis aimed at constraining cosmological parameters.

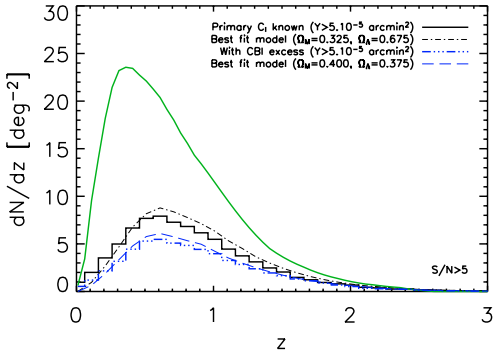

Fig. 6. Effect of incorrect modeling of the selection function. The black continuous curve and black (upper) histogram repeat the results of Fig. 5 for catalogs cut at a flux of $Y = 5 \times 10^{-5}$ arcmin^2 – the former for a pure flux-limited catalog, the latter for the clusters extracted from our concordance model simulations with the expected primary CMB power spectrum $[(\Omega_M, \Omega_\Lambda) = (0.3, 0.7)]$; note that the histogram is calculated as the average over 50 simulations of a 3×3 square degree survey field. The light black, dot-dashed curve is the best-fit model to the redshift distribution from a single such simulation; the constraints from for this fit are shown in Fig. 7. The lower (blue) histogram shows the distribution of clusters extracted from the same 50 simulations, but with excess primary CMB power added at high l (see text); once again, the histrogram is the average over the ensemble of simulations. The blue dashed curve shows the best-fit for the same realization as before – but now with the excess – *when ignoring the excess in the fitting* (incorrect selection function modeling). Corresponding constraints are shown in Fig. 7. Both fits are statistically acceptable (see text).

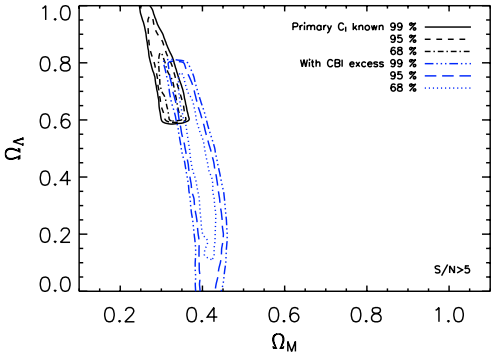

Fig. 7. Confidence contours for the fits discussed in Fig. 6, shown for a survey covering 3 × 3 sq. degrees. The upper (black) contours correspond to the case where the selection function is correctly modeled (no excess CMB power at high l); the best-fit parameters are $(\Omega_M, \Omega_\Lambda) = (0.325, 0.675)$ and 1σ contours fully enclose the true (simulation input) cosmological values of $(0.3, 0.7)$. The larger (blue) contours represent the situation when the CMB excess is not properly accounted for by the selection function model. The best-fit parameter values are significantly biased – $(0.4, 0.375)$ – and the true parameter values, lie outside the 99% contour. In both cases the fits are acceptable (see text).

This means that we ignore the excess both in the construction of the matched filter and in the selection function model needed for the fit. The former has only a relatively minor effect on the catalog extraction and observed histogram. The second effect is much more serious, as we now demonstrate.

Consider constraints on the parameter pair $(\Omega_M, \Omega_\Lambda)$ by fitting models to the redshift distribution of a 3×3 square degree survey. Note that the histograms shown in the figures are in fact averages taken over an ensemble of 50 such simulations, to avoid confusing statistical fluctuations. For the present example, however, we fit models to the redshift distribution from a single simulation. During the fit, we fix the Hubble parameter to its standard value ($H_0 = 70$ km s^{-1} Mpc^{-1}) and adjust the power spectrum normalization σ_8 to maintain the observed present-day cluster abundance (following Pierpaoli et al. 2001). For our simplified case of zero-scatter relations between (Y_o, θ_{co}) and (M, z), both the selection function Φ and the intrinsic scatter function T contain Dirac delta functions that collapse the various integrals in Eqs. (3) and (4). We then obtain the following expression for the redshift distribution of observed clusters brighter than a flux of Y_o:

$$\frac{dN_o}{dz}(>Y_o) = \int_{M(Y_o,z)}^{\infty} dM\, \chi\,[Y(M,z), \theta_c(M,z)]\, \frac{dN}{dz dM} \qquad (13)$$

where $M(Y, z)$ is the zero-scatter relation between flux and mass and redshift. All selection effects are encapsulated in the completeness function χ, whose dependence on the primary CMB power is the focus of our present discussion.

We consider two cases: the first with the expected concordance primary CMB power spectrum, the second with the CBI-like excess power. In the first case, we adopt the true power spectrum for catalog construction and modeling of χ – the selection function is properly modeled. In the second situation, we ignore the excess in both catalog construction and in fitting – the selection function is incorreclty modeled. When correctly modeling the selection function, we find best-fit values of $(\Omega_M, \Omega_\Lambda) = (0.325, 0.675)$. The light black dot-dashed curve in Fig. 6 shows that this model reasonably reproduces the predicted redshift distribution (black solid histogram), and the 1σ contours in Fig. 7 enclose the true (simulation input) values. The fit is good with a reduced $\chi^2 = 0.94$ (34 degrees-of-freedom). When incorrectly modeling the selection function, on the other hand, we find biased best-fit values of $(0.4, 0.375)$, and, as shown in Fig. 7, the true parameter values fall outside the 99% confidence contours. Furthermore, this biased fit is acceptable with a reduced $\chi^2 = 1.17$ (31 degrees-of-freedom), giving no indication of its incorrectness. The redshift distribution of this model is shown as the light dashed (blue) curve in Fig. 6, faithfully reproducing the (averaged) histogram for this case. This is a particularly telling example of the importance of the selection function, because the primary CMB power on cluster scales is at present not well known. It will have to be constrained by the same experiments performing SZ cluster surveys; cosmological constraints will be correspondingly degraded, a subject we return to in a future work.

For another example of incorrect modeling of the selection function, consider that β and θ_c of real clusters may not behave as we assume when constructing the matched filter.

This will bias flux measurments and displace the selection curve in the (Y, θ_c) plane relative to our expectations, leading to an incorrect selection function model. As above, this will yield biased parameter estimates.

As a final note, and returning to Fig. 5, we show the distribution of detected clusters at the higher flux cut as a function of *observed* flux with the lighter, green histogram. The difference with respect to the corresponding distribution in terms of true flux (the red, dashed histogram) reflects statistical photometric errors; note that in fact this tends to falsely increase the number of objects seen at the higher redshifts. Although in this case photometric errors are of secondary importance to the observed redshift distribution (completeness effects dominate), they must also be fully accounted for in any cosmological analysis.

5. Discussion and conclusions

Our aim as been to emphasize the importance of understanding the SZ cluster selection function, as for any astronomical survey. We proposed a general definition of the selection function that can be used to directly relate theoretical cluster distributions to observed ones, and which has the nice property of clearly separating the influence of catalog incompleteness and photometric errors. It is a function of both observing conditions and of the detection and photometry algorithms used to construct the survey catalog. Defined over the (true) total flux-angular size plane, however, the selection function is independent of cosmology and cluster physics; its connection to theoretical cluster descriptors, such as mass and redshift, on the other hand, depends on both. A common way of quoting incompleteness in terms of total flux is similarly sensitive to cluster physics and underlying cosmology.

Using a matched spatial filter (Melin et al. 2004), we studied the selection function for single frequency SZ surveys, such as will be performed with upcoming interferometers[6]. Our main result is that a SZ catalog is not simply flux limited, and this has implications for cosmological studies. A simple analytic argument shows the exact manner in which catalog selection depends on both cluster flux and angular size; simulated observations indicate that this simple estimate is quite accurate and little affected by blending, although future work needs to take into account more realistic cluster profiles. We also noted that noise induced by residual point sources tends to be Gaussian, because subtraction of the brightest sources will be done at higher angular resolution than the smallest filter scale in the SZ maps.

The implications for cosmological studies were illustrated with the redshift distribution, which will serve to constrain cosmological parameters in future surveys. Theoretical redshift distributions based on a simple flux limit cannot fit observed distributions; at best they would lead to biased estimates of cosmological parameters. One must incorporate the complete selection criteria depending on both flux and angular extent, and hence have a good understanding of the catalog selection function. This understanding depends on a number of astrophysical factors in addition to instrumental parameters. Our example of an unmodeled primary CMB power excess (relative to the adopted concordance model) on small angular scales ($l \geq 2000$) highlights the point: we obtained biased parameter estimates because the selection function was incorrectly modeled; note that the false fit was in fact a good fit to the data, according to the χ^2. Other factors, for example, cluster morphology and its potential evolution, will also play a role. In the particular case of the CMB power excess, we note that accurate knowledge of the primary CMB power on cluster scales will come from the same experiments performing the cluster surveys. It will be necessary to constrain the primary CMB power at the same time as cluster extraction, a point we return to in a future work.

An issue currently receiving attention in the literature concerns SZ survey "calibration", by which is meant the empirical Establishment of the $Y(M, z)$ relation. This is clearly essential for any cosmological study. The fact that SZ catalog selection depends not only on total flux but also on angular size complicates the question of survey calibration, for it implies that one must additionally establish a $\theta_c(M, z)$ relation, or its equivalent with some other angular size measure. In fact, since the dispersion on Y and θ_c will in general be correlated, we need the full joint distribution for these observables as a function of mass and redshift. Photometric errors, which we find can be significant, further complicate the issue by increasing scatter in observed relations and hence making them more difficult to obtain.

Although in this work we have focused our detailed study on single frequency surveys, the general conclusions should carry over to multiple frequency observations. In closing we note that the selection function obviously has equally important implications for other studies based on SZ-detected cluster catalogs, such as spatial clustering, etc. For many of these studies, photometric errors, which we have only briefly touched on here, will take on even greater importance.

Acknowledgements. J.-B. Melin and J. G. Bartlett thank the France Berkeley Fund (grant "Precision Cosmology from CMB analysis") and the Lawrence Berkeley Laboratory for financial assistance and hospitality for a visit during which part of this work was completed. We also thank our anonymous referee for helpful and thoughfull comments.

[6] Although we have not here modeled the actual data taking in the visibility plane.

References

Adami, C., Ulmer, M. P., Romer, A. K., et al. 2001, ApJS, 131, 391
Bahcall, N. A., Ostriker, J. P., Perlmutter, S., & Steinhardt, P. J. 1999, Science, 284, 1481
Barbosa, D., Bartlett, J. G., & Blanchard, A. 1996, A&A, 314, 13
Bartelmann, M. 2001, A&A, 370, 754
Bartlett, J. G. 2000 [arXiv:astro-ph/0001267]
Bartlett, J. G. 2001, Review in Tracing cosmic evolution with galaxy clusters, Sesto Pusteria 3–6 July 2001, ASP Conf. Ser., in press [arXiv:astro-ph/0111211]
Bennett, C. L., Hill, R. S., Hinshaw, G., et al. 2003, ApJS, 148, 97
Birkinshaw, M. 1999, Proc. 3K Cosmology, American Institute of Physics, Woodbury, 476, 298

Borys, C., Chapman, S., Halpern, M., & Scott, D. 2003, MNRAS, 344, 385
Bouchet, F. R., & Gispert, R. 1999, New Astron., 4, 443
Carlstrom, J. E., Holder, G. P., & Reese, E. D. 2002, ARA&A, 40, 643
Delabrouille, J., Melin, J.-B., & Bartlett, J. G. 2002, in AMiBA 2001: High-Z Clusters, Missing Baryons, and CMB Polarization, ASP Conf. Proc. [arXiv:astro-ph/0109186]
Delabrouille, J., Cardoso, J.-F., & Patanchon, G. 2003, MNRAS, 346, 1089
Freedman, W. L., Madore, B. F., Gibson, B. K., et al. 2001, ApJ, 553, 47
Haehnelt, M. G., & Tegmark, M. 1996, MNRAS, 279, 545
Haiman, Z., Mohr, J. J., & Holder, G. 2001, ApJ, 553, 545
Herranz, D., Sanz, J. L., Hobson, M. P., et al. 2002, MNRAS, 336, 1057
Holder, G. P., Mohr, J. J., Carlstrom, J. E., Evrard, A. E., & Leitch, E. M. 2000, ApJ, 544, 629
Hu, W. 2003, Phys. Rev. D., 67, 081304
Jenkins, A., Frenk, C. S., White, S. D. M., et al. 2001, MNRAS, 321, 372
Jones, M. E., in AMiBA 2001: High-Z Clusters, Missing Baryons, and CMB Polarization, ASP Conf. Proc. [arXiv:astro-ph/0109351]
Kneissl, R., Jones, M. E., Saunders, R., et al. 2001, MNRAS, 328, 783
Knox, L., Holder, G. P., & Church, S. E. 2003 [arXiv:astro-ph/0309643]
Kosowsky, A. 2004 [arXiv:astro-ph/0402234]
Lima, M., & Hu, W. 2004 [arXiv:astro-ph/0401559]
Lo, K. Y., Chiueh, T. H., Martin, R. N., et al. 2000 [arXiv:astro-ph/0012282]
Majumdar, S., & Mohr, J. J. 2003 [arXiv:astro-ph/0305341]
Masi, S., Ade, P., de Bernardis, P., et al. 2003, Memorie della Societa Astronomica Italiana, 74, 96
Mason, B. S., Myers, S. T., & Readhead, A. C. S. 2001, ApJ, 555, L11
Melin, J.-B., et al. 2004, in preparation
Mo, H. J., & White, S. D. M. 1996, MNRAS, 282, 347
Mohr, J. J., Mathiesen, B., & Evrard, A. E. 1999, ApJ, 517, 627
Oukbir, J., & Blanchard, A. 1997, A&A, 317, 1
Peebles, P. J. E. 1993, Principles of Physical Cosmology, Princeton Series in Physics (New Jersey, Princeton: Princeton University Press)
Pierpaoli, E., Scott, D., & White, M. 2001, MNRAS, 325, 77
Rosati, P., Borgani, S., & Norman, C. 2002, ARA&A, 40, 539
Runyan, M. C., Ade, P. A. R., Bhatia, R. S., et al. 2003, ApJS, 149, 265
Schulz, A. E., & White, M. 2003, ApJ, 586, 723
Seljak, U., & Zaldarriaga, M. 1996, ApJ, 469, 437, www.cmbfast.org
Sunyaev, R. A., & Zel'dovich, Ya. B. 1970, Comments Astrophys. Space Phys., 2, 66
Sunyaev, R. A., & Zel'dovich, Ya. B. 1972, Comments Astrophys. Space Phys., 4, 173
Spergel, D. N., Verde, L., Peiris, H. V., et al. 2003, ApJS, 148, 175
Tegmark, M., Eisenstein, D. J., Hu, W., & Oliveira-Costa, A. 2000, ApJ, 530, 133
Wang, L., & Steinhardt, P. J. 1998, ApJ, 508, 483
White, M. 2003, ApJ, 597, 650

Web pages of various SZ experiments:

- ACBAR http://cosmology.berkeley.edu/group/swlh/acbar/
- ACT http://www.hep.upenn.edu/~angelica/act/act.html
- AMI http://www.mrao.cam.ac.uk/telescopes/ami/index.html
- AMiBA http://www.asiaa.sinica.edu.tw/amiba
- APEX http://bolo.berkeley.edu/apexsz
- BOLOCAM http://astro.caltech.edu/~lgg/bolocam_front.htm
- SPT http://astro.uchicago.edu/spt/
- SZA http://astro.uchicago.edu/sze
- Planck http://astro.estec.esa.nl/Planck/

A&A 459, 341–352 (2006)
DOI: 10.1051/0004-6361:20065034

Astronomy & Astrophysics

Catalog extraction in SZ cluster surveys: a matched filter approach

J.-B. Melin[1,2,⋆], J. G. Bartlett[1], and J. Delabrouille[1]

[1] APC, 11 pl. Marcelin Berthelot, 75231 Paris Cedex 05, France
(UMR 7164 – CNRS, Université Paris 7, CEA, Observatoire de Paris)
e-mail: jean-baptiste.melin@cea.fr, [bartlett;delabrouille]@apc.univ-paris7.fr
[2] Department of Physics, University of California Davis, One Shields Avenue, Davis, CA, 95616, USA

Received 16 February 2006 / Accepted 30 June 2006

ABSTRACT

We present a method based on matched multifrequency filters for extracting cluster catalogs from Sunyaev-Zel'dovich (SZ) surveys. We evaluate its performance in terms of completeness, contamination rate and photometric recovery for three representative types of SZ survey: a high resolution single frequency radio survey (AMI), a high resolution ground-based multiband survey (SPT), and the Planck all-sky survey. These surveys are not purely flux limited, and they loose completeness significantly before their point-source detection thresholds. Contamination remains relatively low at <5% (less than 30%) for a detection threshold set at $S/N = 5$ ($S/N = 3$). We identify photometric recovery as an important source of catalog uncertainty: dispersion in recovered flux from multiband surveys is larger than the intrinsic scatter in the $Y - M$ relation predicted from hydrodynamical simulations, while photometry in the single frequency survey is seriously compromised by confusion with primary cosmic microwave background anisotropy. The latter effect implies that follow-up observations in other wavebands (e.g., 90 GHz, X-ray) of single frequency surveys will be required. Cluster morphology can cause a bias in the recovered $Y - M$ relation, but has little effect on the scatter; the bias would be removed during calibration of the relation. Point source confusion only slightly decreases multiband survey completeness; single frequency survey completeness could be significantly reduced by radio point source confusion, but this remains highly uncertain because we do not know the radio counts at the relevant flux levels.

Key words. large-scale structure of Universe – galaxies: clusters: general – methods: data analysis

1. Introduction

Galaxy cluster catalogs play an important role in cosmology by furnishing unique information on the matter distribution and its evolution. Cluster catalogs, for example, efficiently trace large-scale features, such as the recently detected baryon oscillations (Eisenstein et al. 2005; Cole et al. 2005; Angulo et al. 2005; Huetsi 2006), and provide a sensitive gauge of structure growth back to high redshifts (Oukbir & Blanchard 1992; Rosati et al. 2002; Voit 2004, and references therein). This motivates a number of ambitious projects proposing to use large, deep catalogs to constrain both galaxy evolution models and the cosmological parameters, most notably the dark energy abundance and equation-of-state (Haiman et al. 2000; Weller & Battye 2003; Wang et al. 2004). Among the most promising are surveys based on the Sunyaev-Zel'dovich (SZ) effect (Sunyaev & Zeldovich 1970; Sunyaev & Zeldovich 1972; and see Birkinshaw 1999; Carlstrom et al. 2002 for reviews), because it does not suffer from surface brightness dimming and because we expect the observed SZ signal to tightly correlate to cluster mass (Bartlett 2001; Motl et al. 2005). Many authors have investigated the scientific potential of SZ surveys to constrain cosmology (e.g., Barbosa et al. 1996; Colafrancesco et al. 1997; Holder et al. 2000; Kneissl et al. 2001; Benson et al. 2002), emphasizing the advantages intrinsic to observing the SZ signal.

Cosmological studies demand statistically pure catalogs with well understood selection criteria. As just said, SZ surveys are intrinsically good in this light; however, many other factors – related, for example, to instrumental properties, observing conditions, astrophysical foregrounds and data reduction algorithms – influence the selection criteria. This has prompted some authors to begin more careful scrutiny of SZ survey selection functions in anticipation of future observations (Bartlett 2001; Schulz & White 2003; White 2003; Vale & White 2006; Melin et al. 2005; Juin et al. 2005).

In Melin et al. (2005), we presented a general formalism for the SZ selection function together with some preliminary applications using a matched-filter cluster detection method. In this paper we give a thorough presentation of our cluster detection method and evaluate its performance in terms of catalog completeness, contamination and photometric recovery. We focus on three types of SZ survey: single frequency radio surveys like the Arcminute MicroKelvin Imager (AMI interferometer) survey[1], multi-band ground-based bolometric surveys such as the South Pole Telescope (SPT) survey[2], and the space-based Planck survey[3]. In each case, we quantify the selection function using the formalism of Melin et al. (2005).

We draw particular attention to the oft-neglected issue of photometry. Even if the SZ flux–mass relation is intrinsically tight, what matters in practice is the relation between the *observed* SZ flux and the mass. Photometric errors introduce both

⋆ *New address*: CEA Saclay, DAPNIA/SPP, 91191 Gif-sur-Yvette, France.

[1] http://www.mrao.cam.ac.uk/telescopes/ami/
[2] http://astro.uchicago.edu/spt/
[3] http://astro.estec.esa.nl/Planck/

bias and additional scatter in the observed relation. Calibration of the $Y - M$ relation will in principal remove the bias; calibration precision, however, depends crucially on the scatter in the observed relation. Good photometry is therefore very important. As we will see, observational uncertainty dominates the predicted intrinsic scatter in this relation in all cases studied.

We proceed as follows. In Sect. 2, we discuss cluster detection techniques and present the matched filter formalism. We describe our detection algorithm in Sect. 3. Using Monte Carlo simulations of the three types of survey, we discuss catalog completeness, contamination and photometry. This is done in Sect. 4 under the ideal situation where the filter perfectly matches the simulated clusters and in the absence of point sources. In Sect. 5 we examine effects caused by cluster morphology, using N-body simulations, and then the effect of point sources. We close with a final discussion and conclusions in Sect. 6.

2. Detecting clusters

The detection and photometry of extended sources presents a complexity well appreciated in Astronomy. Many powerful algorithms, such as *SExtractor* (Bertin & Arnouts 1996), have been developed to extract extended sources superimposed on an unwanted background. They typically estimate the local background level and group pixels brighter than this level into individual objects. Searching for clusters at millimeter wavelengths poses a particular challenge to this approach, because the clusters are embedded in the highly variable background of the primary CMB anisotropies and Galactic emission. Realizing the importance of this issue, several authors have proposed specialized techniques for SZ cluster detection. Before detailing our own method, we first briefly summarize some of this work in order to motivate our own approach and place it in context.

2.1. Existing algorithms

Diego et al. (2002) developed a method designed for the Planck mission that is based on application of *SExtractor* to SZ signal maps constructed by combining different frequency channels. It makes no assumption about the frequency dependance of the different astrophysical signals, nor the cluster SZ emission profile. The method, however, requires many low-noise maps over a broad range of frequencies in order to construct the SZ map to be processed by *SExtractor*. Although they will benefit from higher resolution, planned ground-based surveys will have fewer frequencies and higher noise levels, making application of this method difficult.

In another approach, Herranz et al. (2002a,b; see also López-Caniego et al. 2005 for point-source applications) developed an ingenious filter (*Scale Adaptive Filter*) that simultaneously extracts cluster size and flux. Defined as the optimal filter for a map containing a single cluster, it does not account for source blending. Cluster-cluster blending could be an important source of confusion in future ground-based experiments, with as a consequence poorly estimated source size and flux.

Hobson & McLachlan (2003) recently proposed a powerful Bayesian detection method using a Monte Carlo Markov Chain. The method simultaneously solves for the position, size, flux and morphology of clusters in a given map. Its complexity and runtime, however, rapidly increase with the number of sources.

More recently, Schäfer et al. (2006) generalized scale adaptive and matched filters to the sphere for the Planck all-sky SZ survey. Pierpaoli et al. (2005) propose a method based on wavelet filtering, studying clusters with complex shapes. Vale & White (2006) examine cluster detection using different filters (matched, wavelets, mexican hat), comparing completeness and contamination levels.

Finally, Pires et al. (2006) introduced an independent component analysis on simulated multi-band data to separate the SZ signal, followed by non-linear wavelet filtering and application of SExtractor.

Our aim is here is two-fold: to present and extensively evaluate our own SZ cluster catalog extraction method, and to use it in a comprehensive study of SZ survey selection effects. The two are in fact inseparable. First of all, selection effects are specific to a particular catalog extraction method. Secondly, we require a robust, rapid algorithm that we can run over a large number of simulated data sets in order to accurately quantify the selection effets. This important consideration conditions the kind of extraction algorithm that we can use. With this in mind, we have developed a fast catalog construction algorithm based on matched filters for both single and multiple frequency surveys. It is based on the approach first proposed by Herranz et al., but accounts for source blending.

After describing the method, we apply the formalism given in Melin et al. (2005) to quantify the selection function and contamination level in up-coming SZ surveys. We take as representative survey configurations AMI, SPT and Planck, and Monte Carlo simulate the entire catalog extraction process from a large ensemble of realizations for each configuration. By comparing to the simulated input catalogs, we evaluate the extracted catalogs in terms of their completeness, contamination and photometric accuracy/precision. We will place particular emphasis on the importance of the latter, something which has received little attention in most studies of this kind.

2.2. Matched filters

The SZ effect is caused by the hot gas ($T \sim 1{-}10$ keV) contained in galaxy clusters known as the intracluster medium (ICM); electrons in this gas up-scatter CMB photons and create a unique spectral distortion that is negative at radio wavelengths and positive in the submillimeter, with a zero-crossing near 220 GHz. The form of this distortion is universal (in the non-relativistic limit applicable to most clusters), while the amplitude is given by the Compton y parameter, an integral of the gas pressure along the line-of-sight. In a SZ survey, clusters will appear as sources extended over arcminute scales (apart from the very nearby objects, which are already known) with brightness profile

$$\Delta i_\nu(\boldsymbol{x}) = y(\boldsymbol{x})\, j_\nu \tag{1}$$

relative to the mean CMB brightness. Here $y(\boldsymbol{x})$ is the Compton y parameter at position $\boldsymbol{x}$ (a 2D vector on the sky) and j_ν is the SZ spectral function evaluated at the observation frequency ν.

Matched filters for SZ observations were first proposed by Haehnelt & Tegmark (1996) as a tool to estimate cluster peculiar velocities from the kinetic effect, and Herranz et al. (2002a,b) later showed how to use them to detect clusters via the thermal SZ effect. They are designed to maximally enhance the signal-to-noise for a SZ cluster source by optimally (in the least square sense) filtering the data, which in our case is a sky map or set of maps at different frequencies. They do so by incorporating prior knowledge of the cluster signal, such as its spatial and spectral characteristics. The unique and universal frequency spectrum of the thermal SZ effect (in the non-relativistic regime) is hence well suited for a matched-filter approach.

Less clear is the choice of the spatial profile $T_{\theta_c}(\boldsymbol{x})$ to adopt for cluster SZ emission. One aims to choose a spatial template that represents as well as possible the average SZ emission profile. In other words, we want $T_{\theta_c}(\boldsymbol{x}) = \langle y(\boldsymbol{x})/y_o\rangle_C$, where the average is over many clusters of size θ_c. In the following, we choose to describe clusters with a projected spherical β-profile:

$$y(\boldsymbol{x}) = y_o(1 + |\boldsymbol{x}|^2/\theta_c^2)^{-(3\beta-1)/2} \quad (2)$$

with $\beta = 2/3$ (with one exception, shown for comparison in Fig. 2). The spatial template is therefore described by a single parameter, the core radius θ_c; in our calculations, we truncate the profile at $10\theta_c$. This is a reasonable choice, given X-ray observations (Arnaud 2005) of the intracluster medium and the resolution of planned SZ surveys.

In reality, of course, we know neither this average profile precisely nor the dispersion of individual clusters around it beforehand. This is an important point, because our choice for the template will affect both the detection efficiency and photometric accuracy. Detection efficiency will be reduced if the template does not well represent the average profile and, as will become clear below, the photometry will be biased. In general, *the survey selection function unavoidably suffers from uncertainty induced by unknown source astrophysics* (in addition to other sources of uncertainty).

In the following, we first study (Sect. 4) the ideal case where the filters perfectly match the cluster profiles, i.e., we use the β-model for both our simulations and as the detection template. In a later section (5), we examine the effects caused by nontrivial cluster morphology, as well as by point source confusion.

Consider a cluster with core radius θ_c and central y-value y_o positioned at an arbitrary point $\boldsymbol{x}_o$ on the sky. For generality, suppose that the region is covered by several maps $M_i(\boldsymbol{x})$ at N different frequencies ν_i ($i = 1, ..., N$). We arrange the survey maps into a column vector $\boldsymbol{M}(\boldsymbol{x})$ whose ith component is the map at frequency ν_i; this vector reduces to a scalar map in the case of a single frequency survey. Our maps contain the cluster SZ signal plus noise:

$$\boldsymbol{M}(\boldsymbol{x}) = y_o \boldsymbol{j}_\nu T_{\theta_c}(\boldsymbol{x} - \boldsymbol{x}_o) + \boldsymbol{N}(\boldsymbol{x}) \quad (3)$$

where $\boldsymbol{N}$ is the noise vector (whose components are noise maps at the different observation frequencies) and $\boldsymbol{j}_\nu$ is a vector with components given by the SZ spectral function j_ν evaluated at each frequency. Noise in this context refers to both instrumental noise as well as all signals other than the cluster thermal SZ effect; it thus also comprises astrophysical foregrounds, for example, the primary CMB anisotropy, diffuse Galactic emission and extragalactic point sources.

We now build a filter $\boldsymbol{\Psi}_{\boldsymbol{\theta_c}}(\boldsymbol{x})$ (in general, a column vector in frequency space) that returns an estimate, $\hat{y_o}$, of y_o when centered on the cluster:

$$\hat{y_o} = \int \mathrm{d}^2x\, \boldsymbol{\Psi}_{\boldsymbol{\theta_c}}{}^t(\boldsymbol{x} - \boldsymbol{x}_o) \cdot \boldsymbol{M}(\boldsymbol{x}) \quad (4)$$

where superscript t indicates a transpose (with complex conjugation when necessary). This is just a linear combination of the maps, each convolved with its frequency-specific filter $(\Psi_{\theta_c})_i$. We require an unbiased estimate of the central y value, so that $\langle\hat{y_o}\rangle = y_o$, where the average here is over both total noise and cluster (of core radius θ_c) ensembles. Building the filter with the known SZ spectral form and adopted spatial template optimizes the signal-to-noise of the estimate; in other words, the filter is *matched* to the prior information. The filter is now uniquely specified by demanding a minimum variance estimate. The result expressed in Fourier space (the flat sky approximation is reasonable on cluster angular scales) is (Haehnelt & Tegmark 1996; Herranz et al. 2002a; Melin et al. 2005):

$$\boldsymbol{\Psi}_{\boldsymbol{\theta_c}}(\boldsymbol{k}) = \sigma^2_{\theta_c} \boldsymbol{P}^{-1}(\boldsymbol{k}) \cdot \boldsymbol{F}_{\boldsymbol{\theta_c}}(\boldsymbol{k}) \quad (5)$$

where

$$\boldsymbol{F}_{\boldsymbol{\theta_c}}(\boldsymbol{k}) \equiv \boldsymbol{j}_\nu T_{\theta_c}(\boldsymbol{k}) \quad (6)$$

$$\sigma_{\theta_c} \equiv \left[\int \mathrm{d}^2k\, \boldsymbol{F}_{\boldsymbol{\theta_c}}{}^t(\boldsymbol{k}) \cdot \boldsymbol{P}^{-1} \cdot \boldsymbol{F}_{\boldsymbol{\theta_c}}(\boldsymbol{k})\right]^{-1/2} \quad (7)$$

with $\boldsymbol{P}(\boldsymbol{k})$ being the noise power spectrum, a matrix in frequency space with components P_{ij} defined by $\langle N_i(\boldsymbol{k}) N_j^*(\boldsymbol{k}')\rangle_N = P_{ij}(\boldsymbol{k})\delta(\boldsymbol{k} - \boldsymbol{k}')$. The quantity σ_{θ_c} gives the total noise variance through the filter. When we speak of the signal-to-noise of a detection, we refer to $\hat{y_o}/\sigma_{\theta_c}$.

We write the noise power spectrum as a sum $P_{ij} = P_i^{\mathrm{noise}}\delta_{ij} + B_i(\boldsymbol{k})B_j^*(\boldsymbol{k})P_{ij}^{\mathrm{sky}}$, where P_i^{noise} represents the instrumental noise power in band i, $B(\boldsymbol{k})$ the observational beam and P_{ij}^{sky} gives the foreground power (non-SZ signal) between channels i and j. As explicitly written, we assume uncorrelated instrumental noise between observation frequencies. Note that we treat the astrophysical foregrounds as isotropic, stationary random fields with zero mean. The zero mode is, in any case, removed from each of the maps, and the model certainly applies to the primary CMB anisotropy. It should also be a reasonable model for fluctuations of other foregrounds about their mean, at least over cluster scales[4].

Two examples of the matched filter for $\theta_c = 1$ arcmin are shown in Fig. 1, one for an AMI-like single frequency survey with a 1.5 arcmin beam (left-hand panel) and the other for a SPT-like 3-band filter (right-hand panel); see Table 1 for the experimental characteristics. The filters are circularly symmetric, with the figures giving their radial profiles, because we have chosen a spherical cluster model. We clearly see the spatial weighting used by the single frequency filter to optimally extract the cluster from the noise and CMB backgrounds. The multiple frequency filter $\boldsymbol{\Psi}_{\boldsymbol{\theta_c}}$ is a 3-element column vector containing filters for each individual frequency. In this case, the filter employs both spectral and spatial weighting to optimally extract the cluster signal.

Figure 2 shows the filter noise as a function of template core radius θ_c. We plot the filter noise expressed in terms of an equivalent noise $\sigma_Y \equiv \sigma_{\theta_c} \int T_{\theta_c}(\boldsymbol{x})\, \mathrm{d}\boldsymbol{x}$ on the integrated SZ flux Y. The dashed-triple-dotted red curve with $\beta = 0.6$ is shown for comparison to gauge the impact of changing this parameter, otherwise fixed at $\beta = 2/3$ throughout this work. Melin et al. (2005) use the information in this figure to construct survey completeness functions. At fixed signal-to-noise q, the completeness of a survey rapidly increases to unity in the region above the curve $q\sigma_Y$. The figure shows that high angular resolution ground-based surveys (e.g., AMI, SPT) are not purely flux limited, because their noise level rises significantly with core radius. The lower resolution of the Planck survey, on the other hand, results in more nearly flux limited sample.

[4] We make no assumption about the Gaussianity of the fields; the estimator remains unbiased even if they are not Gaussian, although optimality must be redefined in this case.

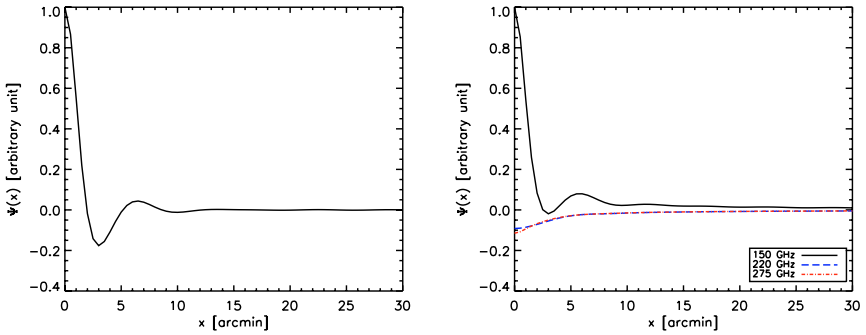

Fig. 1. Two examples of the matched filter for $\theta_c = 1$ arcmin. The curves give the radial profiles of the filters, which are symmetric because we have chosen a symmetric cluster template. *Left*: filter for a single frequency survey with a $\theta_{FWHM} = 1.5$ arcmin beam and 8 μK instrumental noise/beam (AMI-like, see Table 1). The undulating form of the filter maximizes the cluster signal while reducing contamination from primary CMB anisotropy. *Right*: the three components of the 3-band filter for a SPT-like experiment (Table 1). The filter is arbitrarily normalized to unity at 150 GHz. The filter uses both spatial and frequency weighting to optimally extract the cluster signal from the CMB and instrument noise. Although in this figure the filters continue to large radii, in practice we truncate them at $10\theta_c$.

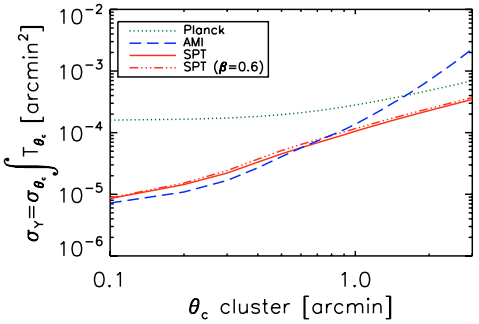

Fig. 2. Filter noise expressed in terms of integrated SZ flux $Y - \sigma_Y = \sigma_{\theta_c} \int T_{\theta_c}(\boldsymbol{x})\, \mathrm{d}\boldsymbol{x}$ – as a function of template core radius θ_c for the three experiments listed in Table 1. A cluster with $Y = \sigma_Y$ would be detected at a signal-to-noise ratio $q = 1$. At a fixed detection threshold q (e.g., 3 or 5), the completeness of a survey rapidly increases from zero to unity in the region above its corresponding curve $q\sigma_Y(\theta_c)$ (Melin et al. 2005). All the curves adopt our fiducial value of $\beta = 2/3$, except the dashed-triple-dotted red curve, shown for comparison, which corresponds to the SPT case with $\beta = 0.6$; this curve is systematically higher by (2.5 to 13)%, depending on θ_c.

3. Catalog extraction

Catalog construction proceeds in three steps, the last two of which are repeated[5]:

1. Convolution of the frequency map(s) with matched filters corresponding to different cluster sizes;
2. Identification of candidate clusters as objects with signal-to-noise $\hat{y_o}/\sigma_{\theta_c} > q$, where q is our fixed detection threshold, followed by photometry of the brightest remaining cluster candidate, which is then added to the final cluster catalog;
3. Removal of this object from the set of filtered maps using the photometric parameters (e.g., y_o and θ_c) from the previous step.

We loop over the last two steps until there are no remaining candidates above the detection threshold. The following sections detail each step.

[5] Note that we have made some changes in the two last steps compared to the description given in Melin et al. (2005). We no longer sort candidates in a tree structure for de-blending; instead, we identify and then remove candidates one by one from the filtered maps. This has only a small impact on the completeness of the detection algorithm, leaving the conclusions of our previous paper intact. The changes, however, greatly improve photometry and lower contamination.

Table 1. Characteristics of the three types of experiments considered. We run our extraction method on 100 sky patches of 3×3 square degrees (for AMI and SPT) and 12 × 12 square degrees (for Planck).

Type	Frequencies [GHz]	Res. *FWHM* [arcmin]	Inst. noise [μK/beam]	Area [deg^2]
AMI	15	1.5	8	10
SPT	150	1	10	
	220	0.7	60	4000
	275	0.6	100	
Planck	143	7.1	6	
	217	5	13	41253
	353	5	40	

3.1. Map filtering

In the first step, we convolve the observed map(s) with matched filters covering the expected range of core radii. For AMI and SPT, for example, we vary θ_c from 0.1 to 3 arcmin in 0.1 steps (i.e., $\theta_c = 0.1, 0.2, ..., 2.9, 3$ arcmin) and add three values for the largest clusters: 4, 5, 6 arcmin. We thus filter the map(s) n_{θ_c} times ($n_{\theta_c} = 33$ for AMI and SPT) to obtain $2\,n_{\theta_c}$ filtered maps, J_{θ_c} et L_{θ_c}. The n_{θ_c} maps J_{θ_c} give the SZ amplitude (obtained using Ψ_{θ_c}), while the n_{θ_c} maps L_{θ_c} give the signal-to-noise ratio: $L_{\theta_c} = J_{\theta_c}/\sigma_{\theta_c}$). We set a detection threshold at fixed signal-to-noise q and identify candidates at each filter scale θ_c as pixels with $L_{\theta_c} > q$. Common values for the threshold are $q = 3$ and $q = 5$; the choice is a tradeoff between detection and contamination rates (see below).

3.2. Cluster parameter estimation: photometry

We begin the second step by looking for the brightest candidate pixel in the set of maps L_{θ_c}. The candidate cluster is

assigned the spatial coordinates (x, y) of this pixel, and its core radius is defined as the filter scale of the map containing the pixel: $\theta_c = \theta_f$. We then calculate the total integrated flux using $Y = \hat{y_o} \int T_{\theta_c}(\boldsymbol{x})\, \mathrm{d}\boldsymbol{x}$, where $\hat{y_o}$ is taken from the map J_{θ_c} at the same filter scale. We refer to this step as the photometric step, and the parameters $\hat{y_o}$, θ_c and Y as photometric parameters. Note that measurement error on Y comes from errors on both $\hat{y_o}$ and θ_c (we return to this in greater detail in Sect. 4.4).

3.3. Catalog construction

The candidate cluster is now added to the final cluster catalog, and we proceed by removing it from the set of filtered maps J_{θ_c} and $Ł_{\theta_c}$ before returning to step 2. To this end, we construct beforehand a 2D array (library) of un-normalized, filtered cluster templates (postage–stamp maps)

$$\mathcal{T}_{\theta_c,\theta_f}(\boldsymbol{x}) = \int \mathrm{d}^2x'\ \Psi_{\theta_f}(\boldsymbol{x}' - \boldsymbol{x}) T_{\theta_c}(\boldsymbol{x}') \tag{8}$$

with the cluster centered in the map. Note that θ_c runs over core radius and θ_f over filter scale. At each filter scale θ_f, we place the normalized template $\hat{y_o}\mathcal{T}_{\theta_c,\theta_f}$ on the cluster position (x, y) and subtract it from the map. The library of filtered templates allows us to perform this step rapidly.

We then return to step 2 and repeat the process until there are no remaining candidate pixels. Thus, clusters are added to the catalog while being subtracted from the maps one at a time, thereby de-blending the sources. By pulling off the brightest clusters first, we aim to minimize uncertainty in the catalog photometric parameters. Nevertheless, it must be emphasized that the entire procedure relies heavily on the use of templates and that real clusters need not conform to the chosen profiles. We return to the effects of cluster morphology below.

In the end, we have a cluster catalog with positions (x, y), central Compton y parameters, sizes θ_c and fluxes Y.

4. Cluster recovery

We tested our catalog construction method on simulated observations of the three representative types of SZ survey specified in Table 1. The simulations include SZ emission, primary CMB anisotropy and instrumental noise and beam smearing. We do not include diffuse Galactic foregrounds in this study. We begin in this section with the ideal case where the filter perfectly matches the simulated clusters (spherical β-model profiles) and in the absence of extragalactic point sources. We return to the additional effects of cluster morphology and point source confusion in Sect. 5.

The simulated maps are generated by Monte Carlo. We first create a realization of the linear matter distribution in a large box using the matter power spectrum. Clusters are then distributed according to their expected number density, given by the mass function, and bias as a function of mass and redshift. We also give each cluster a peculiar velocity consistent with the matter distribution according to linear theory. The simulations thus featuring cluster spatial and velocity correlations accurate first order, which is a reasonable approximation on cluster scales. In this paper, we use these simulations but we do not study the impact of the correlations on the detection method, leaving this issue to forthcoming work.

The cluster gas is modeled by a spherical isothermal β-profile with $\beta = 2/3$ and $\theta_c/\theta_v = 0.1$, where θ_v is the angular projection of the virial radius and which varies with cluster mass and redshift following a self-similar relationship. We choose an $M-T$ relation consistent with the local abundance of X-ray clusters and our value of σ_8, given below (Pierpaoli et al. 2005). Finally, we fix the gas mass fraction at $f_{\rm gas} = 0.12$ (e.g., Mohr et al. 1999). The input catalog consists of clusters with total mass $M > 10^{14}\ M_\odot$, which is sufficient given the experimental characteristics listed in Table 1. Delabrouille et al. (2002) describe the simulation method in more detail.

Table 2. Extracted counts/sq. deg. from simulations of the three types of survey. The numbers in parenthesis give the counts predicted by our analytic cluster model; the difference is due to cluster overlap confusion (see text).

deg^{-2}	$S/N > 3$	$S/N > 5$
AMI	44	20
	(38)	(16)
SPT	35	12
	(27)	(11)
Planck	1.00	0.38
	(0.84)	(0.35)

We generate primary CMB anisotropies using the power spectrum calculated by CMBFAST[6] (Seljak & Zaldarriaga 1996) for a flat concordance model with $\Omega_M = 0.3 = 1 - \Omega_\Lambda$ (Spergel et al. 2003), Hubble constant $H_o = 70\ \mathrm{km\,s^{-1}\,Mpc^{-1}}$ (Freedman et al. 2001) and a power spectrum normalization $\sigma_8 = 0.98$. As a last step we smooth the map with a Gaussian beam and add Gaussian white noise to model instrumental effects[7].

We simulate maps that would be obtained from the proposed surveys listed in Table 1. The first is an AMI[8]-like experiment (Jones et al. 2005), a single frequency, high resolution interferometer; the sensitivity corresponds to a one-month integration time per 0.1 square degree (Kneissl et al. 2001). The SPT[9]-like experiment (Ruhl et al. 2004) is a high resolution, multi-band bolometer array. We calculate the noise levels assuming an integration time of 1 hour per square degree, and a split of 2/3, 1/6, 1/6 of the 150, 220, 275 GHz channels for the 1000 detectors in the focal plane array (Ruhl et al. 2004). Finally, we consider the space-based Planck[10]-like experiment, with a nominal sensitivity for a 14 month mission. For the AMI and SPT maps we use pixels[11] of 30 arcsec, while for Planck the pixels are 2.5 arcmin.

We simulate 100 sky patches of 3×3 square degrees for both AMI and SPT, and of 12×12 square degrees for Planck. This is appropriate given the masses of detected clusters in each experiment. In practice, AMI will cover a few square degrees, similar to the simulated patch, while SPT will cover 4000 square degrees and Planck will observe the entire sky. Thus, the surveys decrease in sensitivity while increasing sky coverage from top to bottom in Table 2 (see also Table 1).

[6] http://cmbfast.org/

[7] The 3-year WMAP results, published after the work presented here was finished, favor a significantly lower value of σ_8 (Spergel et al. 2006). This could lower the total number of clusters in our simulations by up to a factor of ∼2. As we are interested here in catalog recovery, where we compare output to input catalogs, this change should only cause relatively minor changes to our final results.

[8] http://www.mrao.cam.ac.uk/telescopes/ami/index.html

[9] http://astro.uchicago.edu/spt/

[10] http://www.rssd.esa.int/index.php?project=PLANCK

[11] Pixel sizes are at least 2 times smaller than the best channel of each experiment.

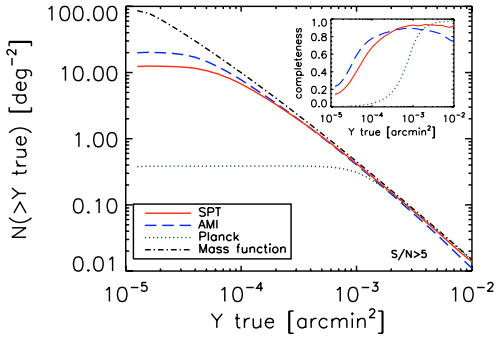

Fig. 3. Cluster counts $N(>Y)$ per square degree as a function of true SZ flux Y for a threshold of $S/N > 5$. The dash-dotted black line gives the cluster counts from the mass function (Jenkins et al. 2001). The dashed blue line gives the recovered cluster counts for AMI, the red solid line for SPT and the dotted green line for Planck. The inset shows the completeness ratio (relative to the mass function prediction) for each survey. All the surveys are significantly incomplete at their point-source sensitivities (5 times the y-intercept in Fig. 2).

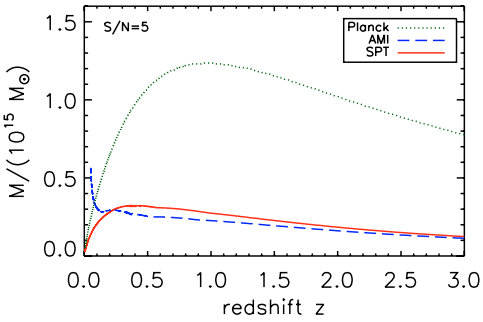

Fig. 4. Mininum detectable cluster mass as a function of redshift, $M(z)$, corresponding to $S/N = 5$ for the three experiments discussed in the text. The rise at low redshift for the single-frequency (AMI) curve is caused by confusion with primary CMB anisotropy.

4.1. Association criteria

An important issue for catalog evaluation is the association between a detected object (candidate cluster) with a cluster from the simulation input catalog (real cluster); in other words, a candidate corresponds to which, if any, real cluster. Any association method will be imprecise, and estimates of catalog completeness, contamination and photometric accuracy will unavoidably depend on the choice of association criteria.

We proceed as follows: for each detection, we look at all input clusters with centers positioned within a distance $r = \sqrt{8} \times d$, where d is the pixel size ($d = 30$ arcsec for AMI and SPT, $d = 2.5$ arcmin for Planck); this covers the neighboring 24 pixels. If there is no input cluster, then we have a false detection; otherwise, we identify the candidate with the cluster whose flux is closest to that of the detection. After running through all the candidates in this fashion, we may find that different candidates are associated with the same input cluster. In this case, we only keep the candidate whose flux is closest to the common input cluster, and we flag the other candidates as false detections (multiple detections).

At this stage, some associations may nevertheless be chance alignments. We therefore employ a second parameter, $Y_{\rm cut}$: a candidate associated with a real cluster of flux $Y < Y_{\rm cut}$ is flagged as a false detection. We indicate these false detections as diamonds in Figs. 7, 8, 9 and 11. The idea is that such clusters are too faint to have been detected and the association is therefore by chance. In the following, we take $Y_{\rm cut} = 1.5 \times 10^{-5}$ arcmin^2 for AMI and SPT, respectively, and $Y_{\rm cut} = 3 \times 10^{-4}$ arcmin^2 for Planck. Note that these numbers are well below the point-source sensitivity (at $S/N = 5$) in each case (see below and Fig. 2).

4.2. Completeness

Figure 3 shows completeness for the three experiments in terms of *true* integrated Y, while Table 2 summarizes the counts. In Fig. 4 we give the corresponding limiting mass as a function of redshift. Given our cluster model, AMI, SPT and Planck should find, respectively, about 16, 11 and 0.35 clusters/deg.^{2} at a $S/N > 5$; these are the numbers given in parentheses in Table 2. Cluster overlap confusion accounts for the fact that the actual counts extracted from the simulated surveys are higher: some clusters that would not otherwise pass the detection cut enter the catalog because the filter adds in flux from close neighbors.

A detection threshold of $S/N = 5$ corresponds to a point-source sensitivity of just below $Y = 5 \times 10^{-5}$ arcmin^2 for both AMI and SPT, as can be read off the left-hand-side of Fig. 2. The surveys approach a high level of completeness only at $Y > 10^{-4}$ arcmin^2, however, due to the rise of the selection cut with core radius seen in Fig. 2. For these high resolution surveys, point-source sensitivity gives a false idea of the survey completeness flux limit.

At the same signal-to-noise threshold, Planck is essentially complete above $Y \sim 10^{-3}$ arcmin^2 and should detect about 0.4 clusters per square degree. Since most clusters are unresolved by Planck, the survey reaches a high completeness level near the point-source sensitivity. We also see this from the small slope of the Planck selection cut in Fig. 2.

We emphasize that the surveys (in particular, the high resolution surveys) are not flux limited for any value of q, because increasing q simply translates the curve in Fig. 2 along the y axis. However, one can approach a flux-limited catalog by selecting clusters at $S/N > q$ and then cutting the resulting catalog at $Y_o > Y_{\rm limit} \equiv Q\sigma_Y(\theta_{\rm c} = 0.1$ arcmin), where the constant $Q > q$. As Q increases we tend towards a catalog for which $Y \sim Y_o > Y_{\rm limit}$. In the case of SPT with $q = 3$, for example, we find that large values of Q (>10) are required to approach a reasonable flux-limited catalog; this construction, however, throws away a very large number of detected clusters.

Although the AMI (single frequency) and SPT (multi-band) survey maps have comparable depth, SPT will cover ~4000 sq. degrees, compared to AMI's ~10 sq. degrees. Planck will only find the brightest clusters, but with full sky coverage. Predictions for the counts suffer from cluster modeling uncertainties, but the comparison between experiments is robust and of primary interest here.

4.3. Contamination

Figure 5 shows the contamination level at $S/N > 5$ for each survey type as a function of *recovered* flux $Y_{\rm o}$. The multiband experiments (SPT and Planck) benefit from low contamination at all fluxes. Single frequency surveys (e.g., AMI), on the other hand, experience a slightly higher contamination level at large

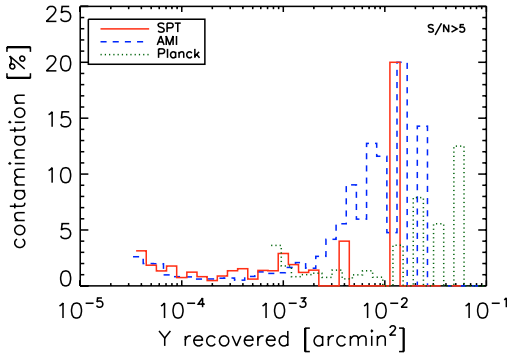

Fig. 5. Contamination as a function of the core radius θ_c for the three experiments and for $S/N > 5$.

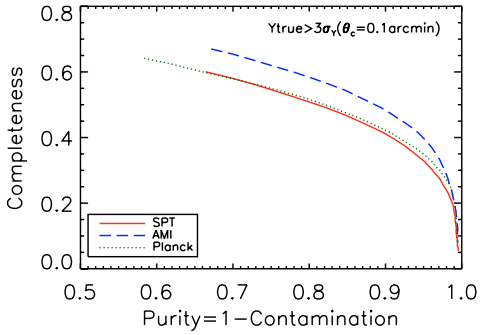

Fig. 6. Completeness-Purity plot. For each curve, q varies from 3 (*top-left*) to 10 (*bottom-right*). For each experiment, the input catalog contains clusters with true flux greater than three times the point source sensitivity ($Y_{\rm true} > 2.2\times10^{-5}$ arcmin^2 for AMI, $Y_{\rm true} > 2.6\times10^{-5}$ arcmin^2 for SPT and $Y_{\rm true} > 4.8\times10^{-4}$ arcmin^2 for Planck). See text for details.

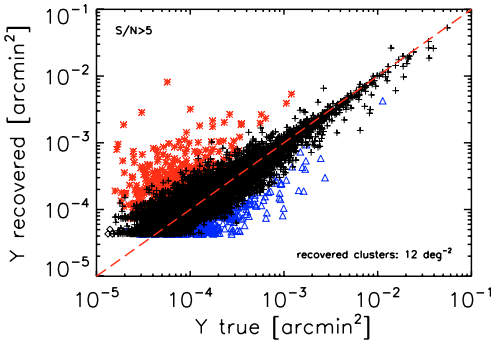

Fig. 7. Recovered vs. true flux for SPT clusters extracted at $S/N > 5$ from 100 survey simulations. The diamonds indicate cluster detections with $Y < Y_{\rm cut}$, which we take as false detections. The mean trend $Y_o(Y)$ has a slight bias (see text) and a roughly constant scatter of $\sigma_{\log Y_o} = 0.17$ over the interval in true Y from 10^{-4} arcmin^2 to 4×10^{-3} arcmin^2. The clusters which have their core radii overestimated by a factor of 2 are plotted as red crosses and the clusters which have their core radii underestimated by a factor of 2 are plotted as blue triangles.

flux due to confusion from primary CMB anisotropy. This confusion also degrades the photometry, as we discuss below.

At $S/N > 5$, the AMI, SPT and Planck catalogs have less than 2% total contamination rate. These numbers increase to ~23, 20 and 27 percent, respectively, for AMI, SPT and Planck at a detection threshold of $S/N > 3$. Note that the total contamination rate is an average over the histogram of Fig. 5 weighted by the number of objects in each bin; thus, the higher contamination at large flux is down-weighted in the total rate.

In all cases, the contamination rate is higher than expected from pure Gaussian noise fluctuations; there is an important contribution from cluster-cluster confusion (residuals from cluster subtraction and overlaps). We expect even higher contamination rates in practice, because of variations in cluster morphology around the filter templates. We quantify this latter effect below.

A useful summary of these results is a completeness-purity plot, as shown in Fig. 6. Proper comparison of the different experiments requires an appropriate choice of input catalog used to define the completeness in this plot. Here, we take the input catalog as all clusters with (true) flux geater than three times the point source sensitivity for each experiment. If the clusters were point sources and the detection method perfect (i.e. not affected by confusion), the completeness would be 1 for $q = 3$ in the top-left corner. These curves summarize the efficiency of our cluster detection method; however, they give no information on the photometric capabilities of the experiments.

4.4. Photometry

We now turn to the important, but often neglected issue of cluster SZ photometry. The ability of a SZ survey to constrain cosmology relies on application of the $Y - M$ relation. As mentioned, we expect the *intrinsic* (or *true*) flux to tightly correlate with cluster mass (Bartlett 2001), as indeed borne out by numerical simulations (da Silva et al. 2004; Motl et al. 2005; Nagai 2005). Nevertheless, unknown cluster physics could affect the exact form and normalization of the relation, pointing up the necessity of an empirical calibration (referred to as survey *calibration*), either with the survey data itself (self-calibration; Hu 2003; Majumdar & Mohr 2003; Lima & Hu 2004; Lima & Hu 2005) or using external data, such as lensing mass estimates (Bartelmann 2001) (although the latter will be limited to relatively low redshifts).

Photometric measurement accuracy and precision is as important as cluster physics in this context: what matters in practice is the relation between *recovered* SZ flux Y_o and cluster mass M. Biased SZ photometry (bias in the $Y - Y_o$) relation will change the form and normalization of the $Y_o - M$ relation and noise will increase the scatter. One potentially important source of photometric error for the matched filter comes from cluster morphology, i.e., the fact that cluster profiles do not exactly follow the filter shape (see Sect. 5).

Survey calibration will help remove the bias, but with an ease that depends on the photometric scatter: large scatter will increase calibration uncertainty and/or necessitate a larger amount of external data. In addition, scatter will degrade the final cosmological constraints (e.g., Lima & Hu 2005). Photometry should therefore be considered an important evaluation criteria for cluster catalog extraction methods.

Consider, first, SPT photometry. Figure 7 shows the relation between observed (or recovered) flux Y_o and true flux Y for a detection threshold of $S/N > 5$. Fitting for the average trend of Y_o as a function of Y, we obtain

$$\log Y_o = 0.96 \log Y - 0.15$$

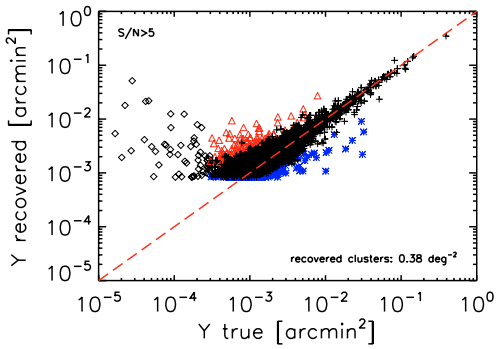

Fig. 8. Recovered vs. true flux for Planck clusters extracted at $S/N > 5$ from 100 survey simulations. The diamonds indicate cluster detections with $Y < Y_{\rm cut}$, which we take as false detections. The mean trend $Y_{\rm o}(Y)$ has a slight bias (see text) and a roughly constant scatter of $\sigma_{\log Y_{\rm o}} = 0.13$ over the interval in true Y from 2×10^{-3} arcmin^2 to 2×10^{-2} arcmin^2. The clusters which have their core radii overestimated by a factor of 2 are plotted as red crosses and the clusters which have their core radii underestimated by a factor of 2 are plotted as blue triangles.

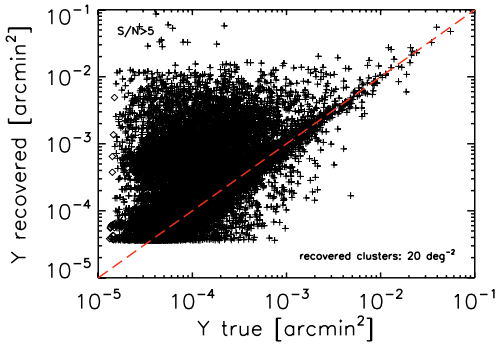

Fig. 9. Recovered vs. true flux for AMI clusters extracted at $S/N > 5$ from 100 survey simulations. The diamonds indicate cluster detections with $Y < Y_{\rm cut}$, which we take as false detections. The extremely large dispersion in recovered flux results from a bimodal distribution caused by an inability to determine the core radius of detected clusters. This inability is due to confusion from primary CMB anisotropy, as demonstrated in Fig. 10. Figure 11 shows that reasonable photometry is possible if the core radius can be accurately determined. This problem is specific to single-frequency surveys that are unable to spectrally remove primary CMB anisotropy.

over the interval 10^{-4} arcmin^2 $< Y < 4 \times 10^{-3}$ arcmin^2, with $Y_{\rm o}$ and Y measured in arcmin^2. There is a slight bias in that the fit deviates somewhat from the equality line, but the effect is minor. Below this flux interval, the fit curls upward in a form of Malmquist bias caused by the S/N cut (seen as the sharp lower edge on $Y_{\rm o}$). The lack of any significant bias is understandable in this ideal case where the filter perfectly matches the cluster SZ profile. Cluster morphology, by which we mean a mismatch between the cluster SZ profile and the matched filter template), can induce bias; we return to this issue in Sect. 5.

The scatter about the fit is consistent with a Gaussian distribution with a roughly constant standard deviation of $\sigma_{\log Y_{\rm o}} = 0.17$ over the entire interval.

The scatter is a factor of 10 larger than expected from instrumental noise alone, which is given by the selection curve in

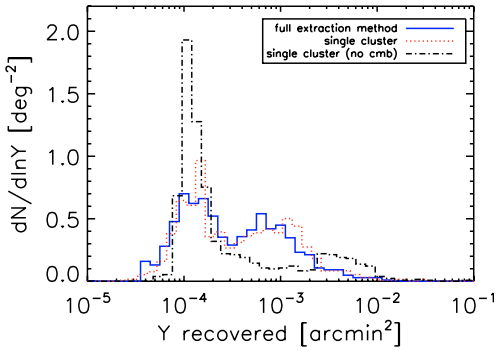

Fig. 10. The full blue histogram gives the cluster counts from Fig. 9 in the bin ($10^{-4} < Y < 2.10^{-4}$, $0.25 < \theta_c < 0.35$). We have added the cluster counts obtained from the size and flux estimation of a single cluster ($Y = 1.5 \times 10^{-4}$, $\theta_c = 0.3$) at a known position through 1000 simulations. SZ cluster background maps and the instrumental beam and noise are included. Two cases are considered : with primary CMB (dotted red histogram) and without primary CMB (dash-dotted black line). The double bump in Y recovery is visible when the primary CMB is present and disappears when it's removed showing that the primary CMB power spectrum is the cause of the double bump.

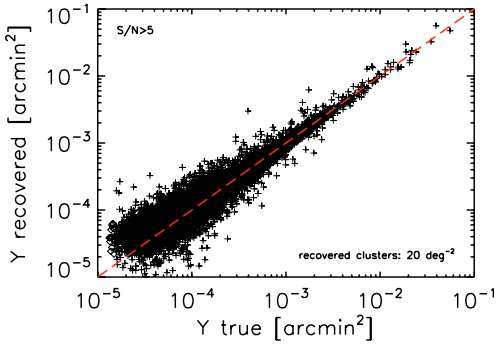

Fig. 11. Single-frequency photometry when we artificially set the core radii of detected clusters to their true values from the input catalog. The dispersion decreases dramatically, demonstrating that the inability to recover the core radius is the origin of the bad photometry seen in Fig. 9.

Fig. 2. Uncertainty in the recovered cluster position, core radius and effects from cluster-cluster confusion all strongly influence the scatter. Photometry precision, therefore, cannot be predicted from instrumental noise properties alone, but only with simulations accounting for these other, more important effects.

Figure 8 shows the photometry for the Planck survey. Apart from some catastrophic cases (the diamonds), the photometry is good and fit by

$$\log Y_{\rm o} = 0.98 \log Y - 0.07$$

over the interval 2×10^{-3} arcmin^2 $< Y < 2 \times 10^{-2}$ arcmin^2 ($Y_{\rm o}$, Y measured in arcmin^2). The dispersion is $\sigma_{\log Y_{\rm o}} = 0.13$, roughly constant over the same interval. For unresolved clusters, this scatter is ~5 times larger than the expected instrumental-induced scatter. The brightest diamonds in the Figure correspond to real clusters with positional error larger than the association criteria r. As a consequence, the candidates are falsely

associated with a small, nearby cluster, unrelated to the actual detected object.

We emphasize that the observational scatter in the $Y_o - Y$ relation for both SPT and Planck dominates the intrinsic scatter of less than 5% seen in the $Y - M$ relation from numerical simulations (da Silva et al. 2004; Motl et al. 2005).

We now turn to single frequency surveys, which Fig. 9 shows to have seriously compromised photometry. The distribution at a given true flux Y is in fact bimodal, as illustrated by the solid blue histogram in Fig. 10 that gives the distribution of the recovered flux Y_o for clusters with true flux and core radius in a bin centered on $Y = 1.5 \times 10^{-4}$ arcmin^2 and $\theta_c = 0.3$ arcmin. We have traced this effect to an inability to accurately determine the core radius of the candidate clusters. We demonstrate this in Fig. 11 by artificially setting the candidate core radius to its true value taken from the associated input cluster; the photometry now cleanly scatters about the mean trend.

This inability to determine the core radius mainly arises from confusion with primary CMB anisotropy, as we now show using Fig. 10. We performed 1000 simulations of a single cluster ($Y = 1.5 \times 10^{-4}$ arcmin^2, $\theta_c = 0.3$ arcmin) placed at the middle of a beam-convolved map containing background SZ clusters (from our general simulations), primary CMB anisotropy and instrumental noise. We then estimate its core radius and flux with our matched filters centered on the known position (to avoid any positional uncertainty) and trace the histogram of resulting measured flux. This is the red dot-dashed histogram in the figure, which displays a bi-modality similar to that of the blue solid histogram. We then follow the same procedure after first removing the primary CMB anisotropy from the simulated map. The resulting histogram of recovered flux is given by the black dot-dashed line with much less pronounced bimodality. The remaining tail reaching towards high flux is caused by cluster–cluster confusion.

With their additional spectral information, multiband surveys remove the primary CMB signal, thereby avoiding this source of confusion. *The result suggests that follow-up observations of detected clusters at a second frequency will be required for proper photometry*; without such follow-up, the scientific power of a single frequency survey may be seriously compromised, as can be appreciated from inspection of Fig. 9.

5. Additional effects

As emphasized, our previous results follow for a filter that perfectly matches the (spherical) clusters in our simulations and in the absence of any point sources. In this section we examine the effects of both cluster morphology and point sources.

We find that cluster morphology has little effect on catalog completeness, but that it does increase contamination. More importantly, it can bias photometric recovery, although it does not significantly increase the scatter. This bias changes the observed $Y - M$ relation from its intrinsic form, adding to the modeling uncertainty already caused by cluster gas physics. For this reason, the relation must be calibrated in order to use the SZ catalog for any cosmological study. The observational bias would be removed during this calibration step.

Completeness is the most affected by point source confusion, decreasing somewhat for the multi-band surveys in the presence of IR point sources. The level of confusion for the single frequency survey remains highly uncertain due to the unknown point source counts at low flux densities. Contamination and photometry are essentially unaffected.

5.1. Cluster morphology

To assess the influence of cluster morphology, we ran our catalog extraction algorithm on maps constructed from numerical simulations. We use the simulations presented by Schulz & White (Schulz & White 2003) and kindly provided to us by M. White. Their simulations follow dark matter clustering with a N-body code in a flat concordance cosmology, and model cluster gas physics with semi-analytical techniques by distributing an isothermal gas of mass fraction Ω_B/Ω_M according to the halo dark matter distribution. For details, see Schulz & White. In the following, we refer to these simulations as the "N-body" simulations.

We proceed by comparing catalogs extracted from the N-body map to those from a corresponding simulation made with spherical clusters. The latter is constructed by applying our spherical β-model gas distribution to the cluster halos taken from the N-body simulation and using them as input to our Monte Carlo sky maps. In the process, we renormalize our $Y - M$ relation to the one used in the N-body SZ maps. We thus obtain two SZ maps containing the same cluster halos, one with spherical clusters (referred to hereafter as the "β-model" maps) and the other with more complex cluster morphology (the N-body maps). Comparison of the catalogs extracted from the two different types of simulated map gives us an indication of the sensitivity of our method to cluster morphology. We make this comparative study only for the SPT and Planck like surveys.

Catalog completeness is essentially unaffected by cluster morphology; the integrated counts, for example, follow the same curves shown in Fig. 3 with very little deviation, the only difference being a very small decrease in the Planck counts at the lowest fluxes. The effect, for example, is smaller than that displayed in Fig. 13 due to point source confusion (and discussed below).

Non-trivial cluster morphology, however, does significantly increase the catalog contamination rate; for example, in the SPT survey the global contamination rises from less than 2% to 13% at $S/N = 5$ for the N-body simulations. We trace this to residual flux left in the maps after cluster extraction: cluster SZ signal that deviates from the assumed spherical β-model filter profile remains in the map and is picked up later as new cluster candidates. Masking those regions where a cluster has been previously extracted (i.e., forbidding any cluster detection) drops the contamination to 4% (SPT case), but causes a decrease of 2.8 clusters per square degree in the recovered counts; this technique would also have important consequences for clustering studies.

From Fig. 12, we clearly see that cluster morphology induces a bias in the photometry. This arises from the fact that the actual cluster SZ profiles differ from the template adopted for the filter. The differences are of two types: an overall difference in the form of radial profile and local deviations about the average radial profile due to cluster substructure. It is the former that is primarily responsible for the bias. In our case, the N-body simulations have much more centrally peaked SZ emission than the filter templates, which causes the filter to systematically underestimate the total SZ flux. Cluster substructure will increase the scatter about the mean $Y_o - Y$ relation. This latter effect is not large, at least for the N-body simulations used here, as can be seen by comparing the scatter in Figs. 12 and 7.

We emphasize, however, that the quantitative effects on photometry depend on the intrinsic cluster profile, and hence are subject to modeling uncertainty. The simulations used here do not include gas physics and simply assume that the gas follows the dark matter. The real bias will depend on unknown cluster physics, thus adding to the modeling uncertainty in the

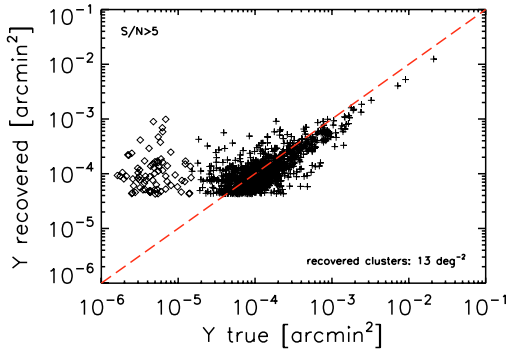

Fig. 12. Photometry for the SPT catalog from the *N*-body simulations. Cluster morphology (mismatch between the filter profile and the actual cluster SZ profile) clearly induces a bias between the recovered and true SZ flux. The scatter, on the other hand, is not very affected, as can be seen in comparing with Fig. 7.

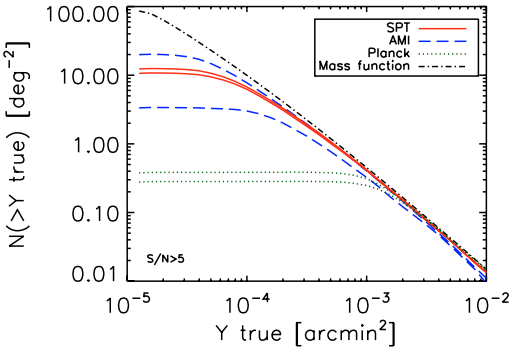

Fig. 13. Integrated cluster counts for the three types of survey. The upper curve in each pair reproduces the results of Fig. 3, while the lower curve shows the effect of point source confusion. Despite the large IR point source population, multiband surveys efficiently eliminate confusion. The AMI-like survey is, on the other hand, strongly affected. This latter effect remains uncertain due to a lack of information on the faint end of the radio point source counts (see text).

$Y - M$ relation. This uncertainty, due to both cluster physics and the photometric uncertainty discussed here, must be dealt with by empirically calibrating the relation, either with external data (lensing) and/or internally (self-calibration).

5.2. Point sources

We next examine the effect of point sources. In a previous paper (Bartlett & Melin 2005, hereafter BM) we studied their influence on survey detection sensitivity. We extend this work to our present study in this section.

Low frequency surveys, such as our AMI example, contend with an important radio source population, while higher frequency bolometer surveys face a large population of IR sources. Radio source counts down to the sub-mJy flux levels relevant for SZ surveys are unfortunately poorly known. The IR counts are somewhat better constrained at fluxes dominating the fluctuations in the IR background, although at higher frequencies (850 microns) than those used in SZ surveys; an uncertain extrapolation in frequency is thus necessary.

For the present study, we use the radio counts fit by Knox et al. (2004) to a combination of data from CBI, DASI, VSA and WMAP (see also Eq. (6) in BM), and IR counts fit to blank-field SCUBA observations at 850 microns by Borys et al. (2003) (and given by Eq. (8) in BM). We further assume that all radio sources brighter than 100 μJy have been subtracted from our maps at 15 GHz (AMI case); this is the target sensitivity of the long baseline Ryle Telescope observations that will perform the source subtraction for AMI. No such explicit point source subtraction is readily available for the higher frequency bolometer surveys; they must rely solely on their frequency coverage to reduce point source confusion. We therefore include all IR sources in our simulations, and fix their effective spectral index $\alpha = 3$ with no dispersion[12]. We refer the reader to BM for details of our point source model. Note that for this study we use the spherical cluster model for direct comparison to our fiducial results.

Figure 13 compares the integrated counts from Fig. 3 (upper curve in each case) to those extracted from the simulations including point sources (lower curves). We see that point source confusion only slightly decreases the completeness of the multiband surveys, but greatly affects the single frequency survey.

In the case of SPT, this is because point source confusion remains modest compared to the noise: the two are comparable at 150 GHz, but the noise power rises more quickly with frequency than the confusion power (see BM for details) – in other words, the noise is bluer than the confusion. This is an important consideration when looking for the optimal allocation of detectors to the observation bands.

For Planck, confusion power dominates at all frequencies, but the spectral coverage provides sufficient leverage to control it. In this light, it must be emphasized that we only include three astrophysical signals (SZ, CMB & point sources) in these simulations, so that three observation bands are sufficient. In reality, one will have to deal with other foregrounds, e.g., diffuse Galactic emission, which will require the use of additional observation bands.

The single frequency observations, on the other hand, are strongly affected. This is consistent with the estimate in BM (Eq. (15)) placing confusion noise well above instrumental noise for the chosen point source model and source subtraction threshold. We emphasize the uncertainty in this estimate, however: in BM we showed, for example, that a model with flattening counts has much lower source confusion while remaining consistent with the observed counts at high flux densities. The actual confusion level remains to be determined from deeper counts at CMB frequencies (see Waldram et al. 2003; Waldram et al. 2004 for recent deep counts at 15 GHz).

Contamination in the multiband surveys is practically unaffected by point source confusion. For AMI we actually find a lower contamination rate, an apparent gain explained by the fact that the catalog now contains only the brighter SZ sources, due to the lowered sensitivity caused by point source confusion.

The photometry of the multiband surveys also shows little effect from the point sources. Fits to the recovered flux vs. true flux relation do not differ significantly from the no-source case, and the dispersion remains essentially the same. This is consistent with the idea that point source confusion is either modest compared to the noise (SPT) or controlled by multiband observations (Planck).

[12] As discussed in BM, any dispersion has only a small effect on survey sensitivity.

6. Discussion and conclusion

We have described a simple, rapid method based on matched multi-frequency filters for extracting cluster catalogs from SZ surveys. We assessed its performance when applied to the three kinds of survey listed in Table 1. The rapidity of the method allows us to run many simulations of each survey to accurately quantify selection effects and observational uncertainties. We specifically examined catalog completeness, contamination rate and photometric precision.

Figure 2 shows the cluster selection criteria in terms of total SZ flux and source size. It clearly demonstrates that SZ surveys, in particular high resolution ground-bases surveys, will not be purely flux limited, something which must be correctly accounted for when interpreting catalog statistics (Melin et al. 2005).

Figure 3 and Table 2 summarize the expected yield for each survey. The counts roll off at the faint end well before the point-source flux limit (intercept of the curves in Fig. 2 multiplied by the S/N limit) even at the high detection threshold of $S/N = 5$; the surveys loose completeness precisely because they are not purely flux-limited. These yields depend on the underlying cluster model and are hence subject to non-negligible uncertainty. They are nonetheless indicative, and in this work we focus on the nature of observational selection effects for which the exact yields are of secondary importance.

At our fiducial $S/N = 5$ detection threshold, overall catalog contamination remains below 5%, with some dependence on SZ flux for the single frequency survey (see Fig. 5). The overall contamination rises to between 20% and 30% at $S/N > 3$. We note that the contamination rate is always larger than expected from pure instrumental noise, pointing to the influence of astrophysical confusion.

We pay particular attention to photometric precision, an issue often neglected in discussions of the scientific potential of SZ surveys. Scatter plots for the recovered flux for each survey type are given in Figs. 7–9. In the two multiband surveys, the recovered SZ flux is slightly biased, due to the flux cut, with a dispersion of $\sigma_{\log Y_o} = 0.17$ and $\sigma_{\log Y_o} = 0.13$ for SPT and Planck, respectively. This observational dispersion is significantly larger than the intrinsic dispersion in the $Y - M$ relation predicted by hydrodynamical simulations. This uncertainty must be properly accounted for in scientific interpretation of SZ catalogs; specifically, it will degrade survey calibration and cosmological constraints.

Even more importantly, we found that astrophysical confusion seriously compromises the photometry of the single frequency survey (Fig. 9). The histogram in Fig. 10 shows that the recovered flux has in fact a bimodal distribution. We traced the effect to an inability to determine source core radii in the presence of primary CMB anisotropy. If cluster core radius could be accurately measured, e.g., with X-ray follow-up, then we would obtain photometric precision comparable to the multiband surveys (see Fig. 11). This confusion can also be removed by follow-up of detected sources at a second radio frequency (e.g., 90 GHz). Photometric uncertainty will therefore be key limiting factor in single frequency SZ surveys.

All these results apply to the ideal case where the filter exactly matches the (simulated) cluster profiles. We then examined the potential impact of cluster morphology and point sources on these conclusions.

Using N-body simulations, we found that cluster morphology has little effect on catalog completeness, but that it does increase the contamination rate and bias the photometry. The increased contamination is caused by deviations from a smooth radial SZ profile that appear as residual flux in the maps after source extraction. More importantly, the photometry is biased by the mismatch between the filter template and the actual cluster profile. This observational bias adds to the modeling uncertainty in the $Y - M$ relation, which will have to be empirically determined in order to use the catalog for cosmology studies.

As shown by Fig. 13, point sources decrease survey completeness. The multiband surveys effectively reduce IR point source confusion and suffer only a small decrease. Radio source confusion, on the other hand, greatly decreased the completeness of the single frequency survey. This is consistent with the expectation that, for our adopted radio point source model and source subtraction threshold, point source confusion dominates instrumental noise. Modeling uncertainty here is, however, very large: radio source counts are not constrained at relevant fluxes ($\sim$100 μJy), which requires us to extrapolate counts from mJy levels (see BM for a more detailed discussion).

Surveys based on the SZ effect will open a new window onto the high redshift universe. They inherit their strong scientific potential from the unique characteristics of the SZ signal. Full realization of this potential, however, requires understanding of observational selection effects and uncertainties. Overall, multiband surveys appear robust in this light, while single frequency surveys will most likely require additional observational effort, e.g., follow-up in other wavebands, to overcome large photometric errors caused by astrophysical confusion with primary CMB anisotropy.

Acknowledgements. We thank T. Crawford for useful comments on matched filters and information about SPT, and A. Schulz and M. White for kindly providing us with their N-body simulations. We are also grateful to the anonymous referee for helpful and insightful comments. JBM wishes to thank L. Knox, the Berkeley Astrophysics group and E. Pierpaoli for discussions on the detection method, and D. Herranz and the Santander group for discussions on matched filters. JBM was supported at UC Davis by the National Science Foundation under Grant No. 0307961 and NASA under Grant No. NAG5–11098.

References

Angulo, R., Baugh, C. M., Frenk, C. S., et al. 2005, MNRAS, 362, L25
Arnaud, M. [arXiv:astro-ph/0508159]
Barbosa, D., Bartlett, J. G., & Blanchard, A. 1996, A&A, 314, 13
Bartelmann, M. 2001, A&A, 370, 754
Birkinshaw, M. 1999, Proc. 3K Cosmology, 476, American Institute of Physics, Woodbury, 298
Blanchard, A., & Bartlett, J. G. 1998, A&A, 332, L49
Bartlett, J. G. 2001, review in Tracing cosmic evolution with galaxy clusters (Sesto Pusteria 3–6 July 2001), ASP Conf. Ser., in press [arXiv:astro-ph/0111211]
Bartlett, J. G., & Melin, J.-B. 2005, submitted
Benson, A. J., Reichardt, C., & Kamionkowski, M. 2002, MNRAS, 331, 71
Bertin, E., & Arnouts, S. 1996, A&A, 117, 393
Borys, C., Chapman, S., Halpern, M., & Scott, D. 2003, MNRAS, 344, 385
Carlstrom, J. E., Holder, G. P., & Reese, E. D. 2002, ARA&A, 40, 643
Colafrancesco, S., Mazzotta, P., & Vittorio, N. 1997, ApJ, 488, 566
Cole, S., Percival, W. J., Peacock, J. A., et al. 2005, MNRAS, 362, 505
Delabrouille, J., Melin, J.-B., & Bartlett, J. G. 2002, in AMiBA 2001: High-Z Clusters, Missing Baryons, and CMB Polarization, ASP Conf. Proc. [arXiv:astro-ph/0109186]
da Silva, A. C., Kay, S. T., Liddle, A. R., & Thomas, P. A. 2004, MNRAS, 348, 1401
Diego, J. M., Vielva, P., Martínez-González, E., Silk, J., & Sanz, J. L. 2002, MNRAS, 336, 1351
Eisenstein, D. J., Zehavi, I., Hogg, D. W., et al. 2005, ApJ, 633, 560
Eke, V. R., Cole, S., Frenk, C. S., & Patrick Henry, P. J. 1998, MNRAS, 298 1145
Freedman, W. L., Madore, B. F., Gibson, B. K., et al. 2001, ApJ, 553, 47
Haehnelt, M. G., & Tegmark, M. 1996, MNRAS, 279, 545
Haiman, Z., Mohr, J. J., & Holder, G. P. 2000, ApJ, 553, 545

Herranz, D., Sanz, J. L., Barreiro, R. B., & Martínez-González, E. 2002, ApJ, 580, 610
Herranz, D., Sanz, J. L., Hobson, M. P., Barreiro, R. B., et al. 2002, MNRAS, 336, 1057
Hobson, M. P., & McLachlan, C. 2003, MNRAS, 338, 765
Holder, G. P., Mohr, J. J., Carlstrom, J. E., Evrard, A. E., & Leitch, E. M. 2000, ApJ, 544, 629
Hu, W. 2003, Phys. Rev. D, 67, 081304
Huetsi, G. 2006, A&A, 446, 43
Jenkins, A., Frenk, C. S., White, S. D. M., et al. 2001, MNRAS, 321, 372
Jones, M. E., Edge, A. C., Grainge, K., et al. 2005, MNRAS, 357, 518
Juin, J. B., Yvon, D., Refregier, A., & Yeche, C. 2005 [arXiv:astro-ph/0512378]
Kneissl, R., Jones, M. E., Saunders, R., et al. 2001, MNRAS, 328, 783
Knox, L., Holder, G. P., & Church, S. E. 2004, ApJ, 612, 96
Lima, M., & Hu, W. 2004, Phys. Rev. D, 70, 043504
Lima, M., & Hu, W. 2005, Phys. Rev. D, 72, 043006
López-Caniego, M., Herranz, D., Sanz, J. L., & Barreiro, R. B. 2005 [arXiv:astro-ph/0503149]
Majumdar, S., & Mohr, J. J. 2004, ApJ, 613, 41
Melin, J.-B., Bartlett, J. G., & Delabrouille, J. 2005, A&A, 429, 417
Mohr, J. J., Mathiesen, B., & Evrard, A. E. 1999, ApJ, 517, 627
Motl, P. M., Hallman, E. J., Burns, J. O., & Norman, M. L. 2005, ApJ, 623, L63
Nagai, D. 2005 [arXiv:astro-ph/0512208]
Oukbir, J., & Blanchard, A. 1992, A&A, 262, L21
Pierpaoli, E., Anthoine, S., Huffenberger, K., & Daubechies, I. 2005, MNRAS, 359, 261
Pires, S., Juin, J. B., Yvon, D., et al. 2006, A&A, 455, 741
Rosati, P., Borgani, S., & Norman, C. 2002, ARA&A, 40, 539
Ruhl, J. E., et al. 2004 [arXiv:astro-ph/0411122]
Schäfer, B. M., Pfrommer, C., Hell, R. M., & Bartelmann, M. 2006, MNRAS, 370, 1713
Schulz, A. E., & White, M. 2003, ApJ, 586, 723
Seljak, U., & Zaldarriaga, M. 1996, ApJ, 469, 437, www.cmbfast.org
Spergel, D. N., Verde, L., Peiris, H. V., et al. 2003, ApJS, 148, 175
Spergel, D. N., Bean, R., Dore, O., et al. 2006 [arXiv:astro-ph/0603449]
Sunyaev, R. A., & Zel'dovich, Ya. B. 1970, Comments Astrophys. Space Phys., 2, 66
Sunyaev, R. A., & Zel'dovich, Ya. B. 1972, Comments Astrophys. Space Phys., 4, 173
Vale, C., & White, M. 2006, New Astron., 11, 207
Voit, G. M. 2004 [arXiv:astro-ph/0410173]
Waldram, E. M., & Pooley, G. G. 2004 [arXiv:astro-ph/0407422]
Waldram, E. M., Pooley, G. G., Grainge, K., et al. 2003, MNRAS, 342, 915
Wang, S., Khoury, J., Haiman, Z., & May, M. 2004, Phys. Rev. D, 70, 12300
Weller, J., & Battye, R. A. 2003, NewAR, 47, 775
White, M. 2003, ApJ, 597, 650

A&A 525, A139 (2011)
DOI: 10.1051/0004-6361/201013999

Astronomy & Astrophysics

The galaxy cluster Y_{SZ}–L_X and Y_{SZ}–M relations from the WMAP 5-yr data

J.-B. Melin[1], J. G. Bartlett[2], J. Delabrouille[3], M. Arnaud[4], R. Piffaretti[4], and G. W. Pratt[4]

[1] DSM/Irfu/SPP, CEA/Saclay, 91191 Gif-sur-Yvette Cedex, France
e-mail: jean-baptiste.melin@cea.fr
[2] APC – Université Paris Diderot, 10 rue Alice Domon et Léonie Duquet, 75205 Paris Cedex 13, France
e-mail: bartlett@apc.univ-paris7.fr
[3] APC – CNRS, 10 rue Alice Domon et Léonie Duquet, 75205 Paris Cedex 13, France
e-mail: delabrouille@apc.univ-paris7.fr
[4] DSM/Irfu/SAp, CEA/Saclay, 91191 Gif-sur-Yvette Cedex
e-mail: [monique.arnaud;rocco.piffaretti;gabriel.pratt]@cea.fr

Received 6 January 2010 / Accepted 21 October 2010

ABSTRACT

We use multifrequency matched filters to estimate, in the WMAP 5-year data, the Sunyaev-Zel'dovich (SZ) fluxes of 893 ROSAT NORAS/REFLEX clusters spanning the luminosity range $L_{X,[0.1-2.4]\,keV} = 2\times10^{41}-3.5\times10^{45}$ erg s^{-1}. The filters are spatially optimised by using the universal pressure profile recently obtained from combining XMM-Newton observations of the REXCESSsample and numerical simulations. Although the clusters are individually only marginally detected, we are able to firmly measure the SZ signal ($>10\sigma$) when averaging the data in luminosity/mass bins. The comparison between the bin-averaged SZ signal versus luminosity and X-ray model predictions shows excellent agreement, implying that there is no deficit in SZ signal strength relative to expectations from the X-ray properties of clusters. Using the individual cluster SZ flux measurements, we directly constrain the Y_{500}–L_X and Y_{500}–M_{500} relations, where Y_{500} is the Compton y-parameter integrated over a sphere of radius r_{500}. The Y_{500}–M_{500} relation, derived for the first time in such a wide mass range, has a normalisation $Y^*_{500} = [1.60 \pm 0.19] \times 10^{-3}$ arcmin^2 at $M_{500} = 3 \times 10^{14}\,h^{-1}\,M_\odot$, in excellent agreement with the X-ray prediction of 1.54×10^{-3} arcmin^2, and a mass exponent of $\alpha = 1.79 \pm 0.17$, consistent with the self-similar expectation of 5/3. Constraints on the redshift exponent are weak due to the limited redshift range of the sample, although they are compatible with self-similar evolution.

Key words. cosmology: observations – galaxies: clusters: general – galaxies: clusters: intracluster medium – cosmic background radiation – X-rays: galaxies: clusters

1. Introduction

Capability to observe the Sunyaev-Zel'dovich (SZ) effect has improved immensely in recent years. Dedicated instruments now produce high resolution images of single objects (e.g. Kitayama et al. 2004; Halverson et al. 2009; Nord et al. 2009) and moderately large samples of high-quality SZ measurements of previously-known clusters (e.g., Mroczkowski et al. 2009; Plagge et al. 2010). In addition, large-scale surveys for clusters using the SZ effect are underway, both from space with the Planck mission (Valenziano et al. 2007; Lamarre et al. 2003) and from the ground with several dedicated telescopes, such as the South Pole Telescope (Carlstrom et al. 2009) leading to the first discoveries of clusters solely through their SZ signal (Staniszewski et al. 2009). These results open the way for a better understanding of the SZ-Mass relation and, ultimately, for cosmological studies with large SZ cluster catalogues.

The SZ effect probes the hot gas in the intracluster medium (ICM). Inverse Compton scattering of cosmic microwave background (CMB) photons by free electrons in the ICM creates a unique spectral distortion (Sunyaev & Zeldovich 1970, 1972) seen as a frequency-dependent change in the CMB surface brightness in the direction of galaxy clusters that can be written as $\Delta i_\nu(\hat{n}) = y(\hat{n})\, j_\nu(x)$, where j_ν is a universal function of the dimensionless frequency $x = h\nu/kT_{\rm cmb}$. The Compton y-parameter is given by the integral of the electron pressure along the line-of-sight in the direction $\hat{n}$,

$$y = \int_{\hat{n}} \frac{kT_{\rm e}}{m_{\rm e}c^2} n_{\rm e}\sigma_{\rm T}{\rm d}l, \qquad (1)$$

where $\sigma_{\rm T}$ is the Thomson cross section.

Most notably, the integrated SZ flux from a cluster directly measures the total thermal energy of the gas. Expressing this flux in terms of the integrated Compton y-parameter $Y_{\rm SZ}$ – defined by $\int {\rm d}\Omega\, \Delta i_\nu(\hat{n}) = Y_{\rm SZ} j_\nu(x)$ – we see that $Y_{\rm SZ} \propto \int {\rm d}\Omega\, {\rm d}l n_{\rm e} T_{\rm e} \propto \int n_{\rm e} T_{\rm e} {\rm d}V$. For this reason, we expect $Y_{\rm SZ}$ to closely correlate with total cluster mass, M, and to provide a low-scatter mass proxy.

This expectation, borne out by both numerical simulations (e.g., da Silva et al. 2004; Motl et al. 2005; Kravtsov et al. 2006) and indirectly from X-ray observations using $Y_{\rm X}$, the product of the gas mass and mean temperature (Nagai et al. 2007; Arnaud et al. 2007; Vikhlinin et al. 2009), strongly motivates the use of SZ cluster surveys as cosmological probes. Theory predicts the cluster abundance and its evolution – the mass function – in terms of M and the cosmological parameters. With a good mass proxy, we can measure the mass function and its evolution and hence constrain the cosmological model, including the properties of dark energy. In this context the relationship between the

integrated SZ flux and total mass, $Y_{SZ}-M$, is fundamental as the required link between theory and observation. Unfortunately, despite its importance, we are only beginning to observationally constrain the relation (Bonamente et al. 2008; Marrone et al. 2009).

Several authors have extracted the cluster SZ signal from WMAP data (Bennett et al. 2003; Hinshaw et al. 2007, 2009). However, the latter are not ideal for SZ observations: the instrument having been designed to measure primary CMB anisotropies on scales larger than galaxy clusters, the spatial resolution and sensitivity of the sky maps render cluster detection difficult. Nevertheless, these authors extracted the cluster SZ signal by either cross-correlating with the general galaxy distribution (Fosalba et al. 2003; Myers et al. 2004; Hernández-Monteagudo et al. 2004, 2006) or "stacking" existing cluster catalogues in the optical or X-ray (Lieu et al. 2006; Afshordi et al. 2007; Atrio-Barandela et al. 2008; Bielby & Shanks 2007; Diego & Partridge 2009). These analyses indicate that an isothermal β-model is not a good description of the SZ profile, and some suggest that the SZ signal strength is lower than expected from the X-ray properties of the clusters (Lieu et al. 2006; Bielby & Shanks 2007).

Recent in-depth X-ray studies of the ICM pressure profile demonstrate regularity in shape and simple scaling with cluster mass. Combining these observations with numerical simulations leads to a universal pressure profile (Nagai et al. 2007; Arnaud et al. 2010) that is best fit by a modified NFW profile. The isothermal β-model, on the other hand, does not provide an adequate fit. From this newly determined X-ray pressure profile, we can infer the expected SZ profile, $y(r)$, and the $Y_{SZ}-M$ relation at low redshift (Arnaud et al. 2010).

It is in light of this recent progress from X-ray observations that we present a new analysis of the SZ effect in WMAP with the aim of constraining the SZ scaling laws. We build a multifrequency matched filter (Herranz et al. 2002; Melin et al. 2006) based on the known spectral shape of the thermal SZ effect and the shape of the universal pressure profile of Arnaud et al. (2010). This profile was derived from REXCESS (Böhringer et al. 2007), a sample expressly designed to measure the structural and scaling properties of the local X-ray cluster population by means of an unbiased, representative sampling in luminosity. Using the multifrequency matched filter, we search for the SZ effect in WMAP from a catalogue of 893 clusters detected by ROSAT, maximising the signal-to-noise by adapting the filter scale to the expected characteristic size of each cluster. The size is estimated through the luminosity-mass relation derived from the REXCESS sample by Pratt et al. (2009).

We then use our SZ measurements to directly determine the $Y_{SZ}-L_X$ and $Y_{SZ}-M$ relations and compare to expectations based on the universal X-ray pressure profile. As compared to the previous analyses of Bonamente et al. (2008) and Marrone et al. (2009), the large number of systems in our WMAP/ROSAT sample allows us to constrain both the normalisation and slope of the $Y_{SZ}-L_X$ and $Y_{SZ}-M$ relations over a wider mass range and in the larger aperture of r_{500}. In addition, the analysis is based on a more realistic pressure profile than in these analyses, which were based on an isothermal β-model. Besides providing a direct constraint on these relations, the good agreement with X-ray predictions implies that there is in fact no deficit in SZ signal strength relative to expectations from the X-ray properties of these clusters.

The discussion proceeds as follows. We first present the WMAP 5-year data and the ROSAT cluster sample used, a combination of the REFLEX and NORAS catalogues. We then present the SZ model based on the X-ray-measured pressure profile (Sect. 3). In Sect. 4, we discuss our SZ measurements, after first describing how we extract the signal using the matched filter. Section 5 details the error budget. We compare our measured scaling laws to the X-ray predictions in Sects. 6 and 7 and then conclude in Sect. 8. Finally, we collect useful SZ definitions and unit conversions in the Appendices.

Throughout this paper, we use the WMAP5-only cosmological parameters set as our "fiducial cosmology", i.e. $h = 0.719$, $\Omega_M = 0.26$, $\Omega_\Lambda = 0.74$, where h is the Hubble parameter at redshift $z = 0$ in units of 100 km s^{-1}/Mpc. We note $h_{70} = h/0.7$ and $E(z)$ is the Hubble parameter at redshift z normalised to its present value. M_{500} is defined as the mass within the radius r_{500} at which the mean mass density is 500 times the critical density, $\rho_{crit}(z)$, of the universe at the cluster redshift: $M_{500} = \frac{4}{3}\pi\rho_{crit}(z)\,500\,r_{500}^3$.

2. The WMAP-5yr data and the NORAS/REFLEX cluster sample

2.1. The WMAP-5 yr data

We work with the WMAP full resolution coadded five year sky temperature maps at each frequency channel (downloaded from the LAMBDA archive[1]). There are five full sky maps corresponding to frequencies 23, 33, 41, 61, 94 GHz (bands K, Ka, Q, V, W respectively). The corresponding beam full widths at half maximum are approximately 52.8, 39.6, 30.6 21.0 and 13.2 arcmins. The maps are originally at HEALPix[2] resolution nside = 512 (pixel = 6.87 arcmin). Although this is reasonably adequate to sample WMAP data, it is not adapted to the multifrequency matched filter algorithm we use to extract the cluster fluxes. We oversample the original data, to obtain nside = 2048 maps, by zero-padding in harmonic space. In detail, this is performed by computing the harmonic transform of the original maps, and then performing the back transform towards a map with nside = 2048, with a maximum value of ℓ of $\ell_{max} = 750, 850, 1100, 1500, 2000$ for the K, Ka, Q, V, W bands respectively. The upgraded maps are smooth and do not show pixel edges as we would have obtained using the HEALPix upgrading software, based on the tree structure of the HEALPix pixelisation scheme. This smooth upgrading scheme is important as the high spatial frequency content induced by pixel edges would have been amplified through the multifrequency matched filters implemented in harmonic space.

In practice, the multifrequency matched filters are implemented locally on small, flat patches (gnomonic projection on tangential maps), which permits adaptation of the filter to the local conditions of noise and foreground contamination. We divide the sphere into 504 square tangential overlapping patches (100 deg^2 each, pixel = 1.72 arcmin). All of the following analysis is done on these sky patches.

The implementation of the matched filter requires knowledge of the WMAP beams. In this work, we assume symmetric beams, for which the transfer function b_ℓ is computed, in each frequency channel, from the noise-weighted average of the transfer functions of individual differential assemblies (a similar approach was used in Delabrouille et al. 2009).

[1] http://lambda.gsfc.nasa.gov/
[2] http://healpix.jpl.nasa.gov

Table 1. Values for the parameters of the $L_X - M$ relation derived from REXCESS data (Pratt et al. 2009; Arnaud et al. 2010).

Corrected for MB	$\log\left(\frac{C_M}{10^{44}\ h_{70}^{-2}\ [\mathrm{ergs}^{-1}]}\right)$	α_M	$\sigma_{\log L-\log M}$
no	0.295	1.50	0.183
yes	0.215	1.61	0.199

2.2. The NORAS/REFLEX cluster sample and derived X-ray properties

We construct our cluster sample from the largest published X-ray catalogues: NORAS (Böhringer et al. 2000) and REFLEX (Böhringer et al. 2004), both constructed from the ROSAT All-Sky Survey. We merge the cluster lists given in Tables 1, 6 and 8 from Böhringer et al. (2000) and Table 6 from Böhringer et al. (2004) and since the luminosities of the NORAS clusters are given in a standard cold dark matter (SCDM) cosmology ($h = 0.5$, $\Omega_M = 1$), we converted them to the WMAP5 cosmology. We also convert the luminosities of REFLEX clusters from the basic ΛCDM cosmology ($h = 0.7$, $\Omega_M = 0.3$, $\Omega_\Lambda = 0.7$) to the more precise WMAP5 cosmology. Removing clusters appearing in both catalogues leaves 921 objects, of which 893 have measured redshifts. We use these 893 clusters in the analysis detailed in the next section.

The NORAS/REFLEX luminosities L_X, measured in the soft [0.1–2.4] keV energy band, are given within various apertures depending on the cluster. We convert the luminosities L_X to L_{500}, the luminosities within r_{500}, using an iterative scheme. This scheme is based on the mean electron density profile of the REXCESS cluster sample (Croston et al. 2008), which allows conversion of the luminosity between various apertures, and the REXCESS L_{500}–M_{500} relation (Pratt et al. 2009), which implicitly relates r_{500} and L_{500}. The procedure thus simultaneously yields an estimate of the cluster mass, M_{500}, and the corresponding angular extent $\theta_{500} = r_{500}/D_{ang}(z)$, where $D_{ang}(z)$ is the angular distance at redshift z. In the following we consider values derived from relations both corrected and uncorrected for Malmquist bias. The relations are described by the following power law models[3]:

$$E(z)^{-7/3}\, L_{500} = C_M \left(\frac{M_{500}}{3\times10^{14}\ h_{70}^{-1}\ M_\odot}\right)^{\alpha_M} \quad (2)$$

where the normalisation C_M, the exponent α_M and the dispersion (nearly constant with mass) are given in Table 1. The L_{500}–M_{500} relation was derived in the mass range $[10^{14}$–$10^{15}]$ $M_\odot$. These limits are shown in Fig. 1. Note that we assume the relation is valid for lower masses.

The final catalogue of 893 objects contains the position of the clusters (longitude and latitude), the measured redshift z, the derived X-ray luminosity L_{500}, the mass M_{500} and the angular extent θ_{500}. The clusters uniformly cover the celestial sphere at Galactic latitudes above $|b| > 20$ deg. Their luminosities L_{500} range from 0.002 to 35.0×10^{44} erg/s, and their redshifts from 0.003 to 0.460. Figure 1 shows the masses M_{500} as a function of redshift z for the cluster sample (red crosses). The corresponding corrected luminosities L_{500} can be read on the right axis. The typical luminosity correction from measured L_X to L_{500} is about 10%. The progressive mass cut-off with redshift (only the most massive clusters are present at high z) reflects the flux limited nature of the sample.

[3] Since we consider a standard self-similar model, we used the power law relations given in Appendix B of Arnaud et al. (2010). They are derived as in Pratt et al. (2009) with the same luminosity data but for masses derived from a standard slope M_{500}–Y_X relation.

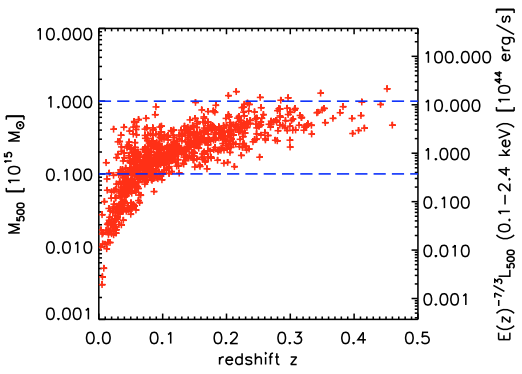

Fig. 1. Inferred masses for the 893 NORAS/REFLEX clusters as a function of redshift. The cluster sample is flux limited. The right vertical axis gives the corresponding X-ray luminosities scaled by $E(z)^{-7/3}$. The dashed blue lines delineate the mass range over which the L_{500}–M_{500} relation from Pratt et al. (2009) was derived.

3. The cluster SZ model

In this section we describe the cluster SZ model, based on X-ray observations of the REXCESS sample combined with numerical simulations, as presented in Arnaud et al. (2010). We use the standard self-similar model presented in their Appendix B. Given a cluster mass M_{500} and redshift z, the model predicts the electronic pressure profile. This gives both the SZ profile shape and Y_{500}, the SZ flux integrated in a sphere of radius r_{500}.

3.1. Cluster shape

The dimensionless universal pressure profile is taken from Eqs. (B1) and (B2) of Arnaud et al. (2010):

$$\frac{P(r)}{P_{500}} = \frac{P_0}{x^\gamma (1+x^\alpha)^{(\beta-\gamma)/\alpha}} \quad (3)$$

where $x = r/r_s$ with $r_s = r_{500}/c_{500}$ and $c_{500} = 1.156$, $\alpha = 1.0620$, $\beta = 5.4807$, $\gamma = 0.3292$ and with P_{500} defined in Eq. (4) below.

This profile shape is used to optimise the SZ signal detection. As described below in Sect. 4, we extract the Y_{SZ} flux from WMAP data for each ROSAT system fixing c_{500}, α, β, γ to the above values, but leaving the normalisation free.

3.2. Normalisation

The model allows us to compute the physical pressure profile as a function of mass and z, thus the Y_{SZ}–M_{500} relation by integration of $P(r)$ to r_{500}. For the shape parameters given above, the normalisation parameter $P_0 = 8.130\, h_{70}^{3/2} = 7.810$ and the self-similar definition of P_{500} (Arnaud et al. 2010, Eq. (5) and Eq. (B2)),

$$P_{500} = 1.65\times10^{-3} E(z)^{8/3} \left(\frac{M_{500}}{3\times10^{14}\ h_{70}^{-1}\ M_\odot}\right)^{2/3} h_{70}^2\ \mathrm{keV\ cm^{-3}}, \quad (4)$$

one obtains:

$$Y_{500}\,[\mathrm{arcmin}^2] = Y^*_{500}\left(\frac{M_{500}}{3\times10^{14}\,h^{-1}\,M_\odot}\right)^{5/3} \times E(z)^{2/3}\left(\frac{D_{\mathrm{ang}}(z)}{500\ \mathrm{Mpc}}\right)^{-2}, \quad (5)$$

where $Y^*_{500} = 1.54\times10^{-3}\left(\frac{h}{0.719}\right)^{-5/2}$ arcmin^2. Equivalently, one can write:

$$Y_{500}\,[\mathrm{Mpc}^2] = Y^*_{500}\left(\frac{M_{500}}{3\times10^{14}\,h^{-1}\,M_\odot}\right)^{5/3} E(z)^{2/3} \quad (6)$$

where $Y^*_{500} = 3.27\times10^{-5}\left(\frac{h}{0.719}\right)^{-5/2}$ Mpc^2. Details of unit conversions are given in Appendix B. The mass dependence ($M_{500}^{5/3}$) and the redshift dependence ($E(z)^{2/3}$) of the relation are self-similar by construction. This model is used to predict the Y_{500} value for each cluster. These predictions are compared to the WMAP-measured values in Figs. 3–6.

4. Extraction of the SZ flux

4.1. Multifrequency matched filters

We use multifrequency matched filters to estimate cluster fluxes from the WMAP frequency maps. By incorporating prior knowledge of the cluster signal, i.e., its spatial and spectral characteristics, the method maximally enhances the signal-to-noise of a SZ cluster source by optimally filtering the data. The universal profile shape described in Sect. 3 is assumed, and we evaluate the effects of uncertainty in this profile as outlined in Sect. 5 where we discuss our overall error budget. We fix the position and the characteristic radius θ_s of each cluster and estimate only its flux. The position is taken from the NORAS/REFLEX catalogue and $\theta_s = \theta_{500}/c_{500}$ with θ_{500} derived from X-ray data as described in Sect. 2.2. Below, we recall the main features of the multifrequency matched filters. More details can be found in Herranz et al. (2002) or Melin et al. (2006).

Consider a cluster with known radius θ_s and unknown central y-value y_o positioned at a known point x_o on the sky. The region is covered by the five WMAP maps $M_i(x)$ at frequencies ν_i = 23, 33, 41, 61, 94 GHz ($i = 1,...,5$). We arrange the survey maps into a column vector $\boldsymbol{M}(x)$ whose ith component is the map at frequency ν_i. The maps contain the cluster SZ signal plus noise:

$$\boldsymbol{M}(x) = y_o \boldsymbol{j_\nu} T_{\theta_s}(x - x_o) + \boldsymbol{N}(x) \quad (7)$$

where $\boldsymbol{N}$ is the noise vector (whose components are noise maps at the different observation frequencies) and $\boldsymbol{j_\nu}$ is a vector with components given by the SZ spectral function j_ν evaluated at each frequency. Noise in this context refers to both instrumental noise as well as all signals other than the cluster thermal SZ effect; it thus also comprises astrophysical foregrounds, for example, the primary CMB anisotropy, diffuse Galactic emission and extragalactic point sources. $T_{\theta_s}(x - x_o)$ is the SZ template, taking into account the WMAP beam, at projected distance $(x - x_o)$ from the cluster centre, normalised to a central value of unity before convolution. It is computed by integrating along the line-of-sight and normalising the universal pressure profile (Eq. (3)). The profile is truncated at $5\times r_{500}$ (i.e. beyond the virial radius) so that what is actually measured is the flux within a cylinder of aperture radius $5\times r_{500}$.

X-ray observations are typically well-constrained out to r_{500}. Our decision to integrate out to $5\times r_{500}$ is motivated by the fact that for the majority of clusters the radius r_{500} is of order the Healpix pixel size (nside = 512, pixel = 6.87 arcmin). Integrating only out to r_{500} would have required taking into account that only a fraction of the flux of some pixels contributes to the true SZ flux in a cylinder of aperture radius r_{500}. We thus obtain the total SZ flux of each cluster by integrating out to $5\times r_{500}$, and then convert this to the value in a sphere of radius r_{500} for direct comparison with the X-ray prediction.

The multifrequency matched filters $\boldsymbol{\Psi}_{\boldsymbol{\theta_s}}(x)$ return a minimum variance unbiased estimate, $\hat{y_o}$, of y_o when centered on the cluster:

$$\hat{y_o} = \int \mathrm{d}^2x\ \boldsymbol{\Psi}_{\boldsymbol{\theta_s}}{}^t(x - x_o)\cdot\boldsymbol{M}(x) \quad (8)$$

where superscript t indicates a transpose (with complex conjugation when necessary). This is just a linear combination of the maps, each convolved with its frequency-specific filter $(\Psi_{\theta_s})_i$. The result expressed in Fourier space is:

$$\boldsymbol{\Psi}_{\boldsymbol{\theta_s}}(k) = \sigma^2_{\theta_s}\boldsymbol{P}^{-1}(k)\cdot\boldsymbol{F}_{\boldsymbol{\theta_s}}(k) \quad (9)$$

where

$$\boldsymbol{F}_{\boldsymbol{\theta_s}}(k) \equiv \boldsymbol{j_\nu} T_{\theta_s}(k) \quad (10)$$

$$\sigma_{\theta_s} \equiv \left[\int \mathrm{d}^2k\ \boldsymbol{F}_{\boldsymbol{\theta_s}}{}^t(k)\cdot\boldsymbol{P}^{-1}\cdot\boldsymbol{F}_{\boldsymbol{\theta_s}}(k)\right]^{-1/2} \quad (11)$$

with $\boldsymbol{P}(k)$ being the noise power spectrum, a matrix in frequency space with components P_{ij} defined by $\langle N_i(k)N_j^*(k')\rangle_N = P_{ij}(k)\delta(k - k')$. The quantity σ_{θ_s} gives the total noise variance through the filter, corresponding to the statistical errors quoted in this paper. The other uncertainties are estimated separately as described in Sect. 5.1. The noise power spectrum $\boldsymbol{P}(k)$ is directly estimated from the maps: since the SZ signal is subdominant at each frequency, we assume $\boldsymbol{N}(x) \approx \boldsymbol{M}(x)$ to do this calculation. We undertake the Fourier transform of the maps and average their cross-spectra in annuli with width $\Delta l = 180$.

4.2. Measurements of the SZ flux

The derived total WMAP flux from a cylinder of aperture radius $5\times r_{500}$ (Y^{cyl}_{5r500}) for the 893 individual NORAS/REFLEX clusters is shown as a function of the measured X-ray luminosity L_{500} in the left-hand panel of Fig. 2. The clusters are barely detected individually. The average signal-to-noise ratio (S/N) of the total population is 0.26 and only 29 clusters are detected at $S/N > 2$, the highest detection being at 4.2. However, one can distinguish the deviation towards positive flux at the very high luminosity end.

In the right-hand panel of Fig. 2, we average the 893 measurements in four logarithmically-spaced luminosity bins (red diamonds plotted at bin center). The number of clusters are 7, 150, 657, 79 from the lowest to the highest luminosity bin. Here and in the following, the bin average is defined as the weighted mean of the SZ flux in the bin (weight of $1/\sigma^2_{\theta_s}$). The thick error bars correspond to the statistical uncertainties on the WMAP data only, while the thin bar gives the total errors as discussed in Sect. 5.1. The SZ signal is clearly detected in the two highest luminosity bins (at 6.0 and 5.4σ, respectively). As a demonstrative check, we have undertaken the analysis a second time using random cluster positions. The result is shown by the green triangles in Fig. 2 and is consistent with no SZ signal, as expected.

In the following sections, we study both the relation between the SZ signal and the X-ray luminosity and that with the mass

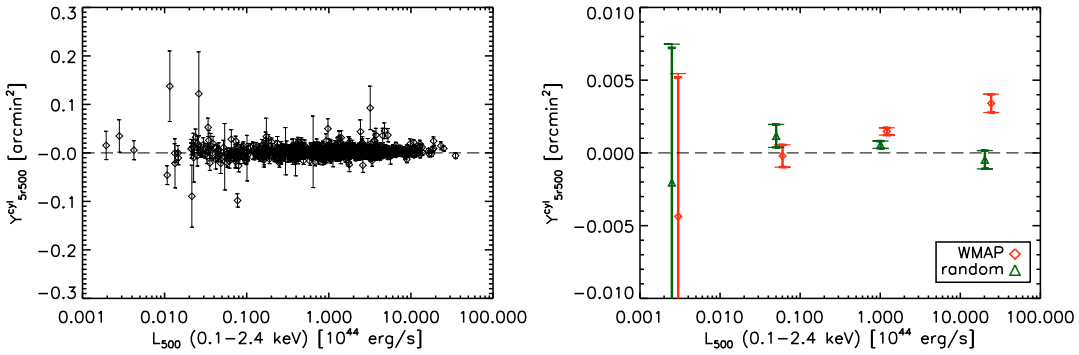

Fig. 2. *Left*: estimated SZ flux from a cylinder of aperture radius $5 \times r_{500}$ (Y^{cyl}_{5r500}) as a function of the X-ray luminosity in an aperture of r_{500} (L_{500}), for the 893 NORAS/REFLEX clusters. The individual clusters are barely detected. The bars give the total 1σ error. *Right:* Red diamonds are the weighted average signal in 4 logarithmically-spaced luminosity bins. The two high luminosity bins exhibit significant SZ cluster flux. Note that we have divided the vertical scale by 30 between Fig. left and right. The thick and thin bars give the 1σ statistical and total errors, respectively. Green triangles (shifted up by 20% with respect to diamonds for clarity) show the result of the same analysis when the fluxes of the clusters are estimated at random positions instead of true cluster positions.

M_{500}. We consider Y_{500}, the SZ flux from a sphere of radius r_{500}, converting the measured Y^{cyl}_{5r500} into Y_{500} as described in Appendix A. This allows a more direct comparison with the model derived from X-ray observations (Sect. 3). Before presenting the results, we first discuss the overall error budget.

5. Overall error budget

5.1. Error due to dispersion in X-ray properties

The error σ_{θ_s} on Y_{500} given by the multifrequency matched filter only includes the statistical SZ measurement error, due to the instrument (beam, noise) and to the astrophysical contaminants (primary CMB, Galaxy, point sources). However, we must also take into account: 1) uncertainties on the cluster mass estimation from the X-ray luminosities via the $L_{500} - M_{500}$ relation, 2) uncertainties on the cluster profile parameters. These are sources of error on individual Y_{500} estimates (actual parameters for each individual cluster may deviate somewhat from the average cluster model). These deviations from the mean, however, induce additional *random* uncertainties on statistical quantities derived from Y_{500}, i.e. bin averaged Y_{500} values and the $Y_{500}-L_{500}$ scaling relation parameters. Their impact on the $Y_{500}-M_{500}$ relation, which depends directly on the M_{500} estimates, is also an additional random uncertainty.

The uncertainty on M_{500} is dominated by the intrinsic dispersion in the $L_{500}-M_{500}$ relation. Its effect is estimated by a Monte Carlo (MC) analysis of 100 realisations. We use the dispersion at $z = 0$ as estimated by Pratt et al. (2009), given in Table 1. For each realisation, we draw a random mass $\log M_{500}$ for each cluster from a Gaussian distribution with mean given by the $L_{500}-M_{500}$ relation and standard deviation $\sigma_{\log L-\log M}/\alpha_M$. We then redo the full analysis (up to the fitting of the Y_{SZ} scaling relations) with the new values of M_{500} (thus θ_s).

The second uncertainty is due to the observed dispersion in the cluster profile shape, which depends on radius as shown in Arnaud et al. (2010, $\sigma_{\log P} \sim 0.10$ beyond the core). Using new 100 MC realisations, we estimate this error by drawing a cluster profile in the log-log plane from a Gaussian distribution with mean given by Eq. (3) and standard deviation depending on the cluster radius as shown in the lower panel of Fig. 2 in Arnaud et al. (2010).

The total error on Y_{500} and on the scaling law parameters is calculated from the quadratic sum of the standard deviation of both the above MC realisations and the error due to the SZ measurement uncertainty.

5.2. The Malmquist bias

The NORAS/REFLEX sample is flux limited and is thus subject to the Malmquist bias (MB). This is a source of systematic error. Ideally we should use a $L_{500}-M_{500}$ relation which takes into account the specific bias of the sample, i.e. computed from the true $L_{500}-M_{500}$ relation, with dispersion and bias according to each survey selection function. We have an estimate of the true, ie MB corrected, $L_{500}-M_{500}$ relation, from the published analysis of REXCESS data (Table 1). However, while the REFLEX selection function is known and available, this is not the case for the NORAS sample. This means that we cannot perform a fully consistent analysis. In order to estimate the impact of the Malmquist Bias we thus present, in the following, results for two cases.

In the first case, we use the published $L_{500}-M_{500}$ relation derived directly from the REXCESS data, i.e. not corrected for the REXCESS MB (hereafter the REXCESS $L_{500}-M_{500}$ relation). Note that the REXCESS is a sub-sample of REFLEX. Using this relation should result in correct masses if the Malmquist bias for the NORAS/REFLEX sample is the same as that for the REXCESS. The $Y_{500}-M_{500}$ relation derived in this case would also be correct and could be consistently compared with the X-ray predicted relation. We recall that this relation was derived from pressure and mass measurements that are not sensitive to the Malmquist bias. However L_{500} would remain uncorrected so that the $Y_{500}-L_{500}$ relation derived in this case should be viewed as a relation uncorrected for the Malmquist bias. In the second case, we use the MB corrected $L_{500}-M_{500}$ relation (hereafter the intrinsic $L_{500}-M_{500}$ relation). This reduces to assuming that the Malmquist bias is negligible for the NORAS/REFLEX sample.

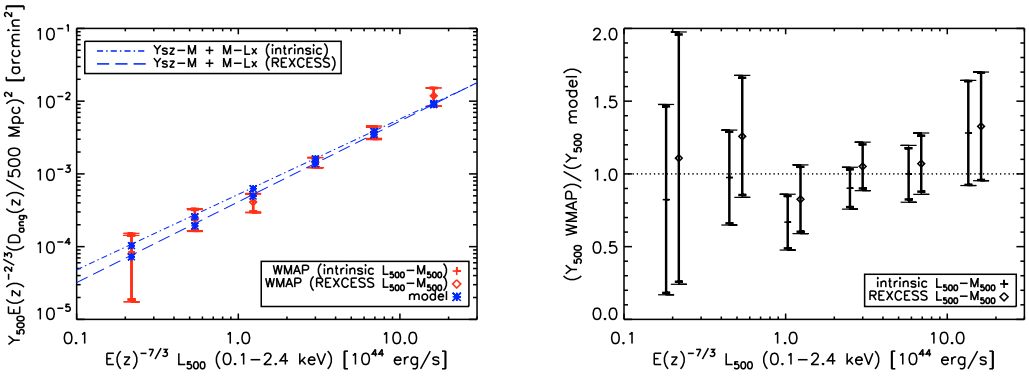

Fig. 3. *Left*: bin averaged SZ flux from a sphere of radius r_{500} (Y_{500}) as a function of X-ray luminosity in a aperture of r_{500} (L_{500}). The WMAP data (red diamonds and crosses), the SZ cluster signal expected from the X-ray based model (blue stars) and the combination of the Y_{500}−M_{500} and L_{500}−M_{500} relations (dash and dotted dashed lines) are given for two analyses, using respectively the intrinsic L_{500}−M_{500} and the REXCESS L_{500}−M_{500} relations. As expected, the data points do not change significantly from one case to the other showing that the Y_{500}-L_{500} relation is rather insensitive to the finer details of the underlying L_{500}−M_{500} relation. *Right*: ratio of data points to model for the two analysis. The points for the analysis undertaken with the intrinsic L_{500}−M_{500} are shifted to lower luminosities by 20% for clarity.

The comparison of the two analyses provides an estimate of the direction and amplitude of the effect of the Malmquist bias on our results. The REXCESS L_{500}−M_{500} relation is expected to be closer to the L_{500}−M_{500} relation for the NORAS/REFLEX sample than the intrinsic relation. The discussions and figures correspond to the results obtained when using the former, unless explicitly specified.

The choice of the L_{500}−M_{500} relation has an effect both on the estimated L_{500}, M_{500} and Y_{500} values and on the expectation for the SZ signal from the NORAS/REFLEX clusters. However, for a cluster of given luminosity measured a given aperture, L_{500} depends weakly on the exact value of r_{500} due to the steep drop of X-ray emission with radius. As a result, and although L_{500} and M_{500} (or equivalently r_{500}) are determined jointly in the iterative procedure described in Sect. 2.2, changing the underlying L_{500}−M_{500} relation mostly impacts the M_{500} estimate: L_{500} is essentially unchanged (median difference of ∼0.8%) and the difference in M_{500} simply reflects the difference between the relations at fixed luminosity. This has an impact on the measured Y_{500} via the value of r_{500} (the profile shape being fixed) but the effect is also small (<1%). This is due to the rapidly converging nature of the Y_{SZ} flux (see Fig. 11 of Arnaud et al. 2010). On the other hand, all results that depend directly on M_{500}, namely the derived Y_{500}−M_{500} relation or the model value for each cluster, that varies as $M_{500}^{5/3}$ (Eq. (5)), depend sensitively on the L_{500}−M_{500} relation. M_{500} derived from the intrinsic relation is higher, an effect increasing with decreasing cluster luminosity (see Fig. B2 of Pratt et al. 2009).

5.3. Other possible sources of uncertainty

The analysis presented in this paper has been performed on the entire NORAS/REFLEX cluster sample without removal of clusters hosting radio point sources. To investigate the impact of the point sources on our result, we have cross-correlated the NVSS (Condon et al. 1998) and SUMMS (Mauch et al. 2003) catalogues with our cluster catalogue. We conservatively removed from the analysis all the clusters hosting a total radio flux greater than 1 Jy within $5 \times r_{500}$. This leaves 328 clusters in the catalogue, removing the measurements with large uncertainties visible in Fig. 2 left. We then performed the full analysis on these 328 objects up to the fitting of the scaling laws, finding that the impact on the fitted values is marginal. For example, for the REXCESS case, the normalisation of the Y_{500}−M_{500} relation decreases from 1.60 to 1.37 (1.6 statistical σ) and the slope changes from 1.79 to 1.64 (1 statistical σ). The statistical errors on these parameters decrease respectively from 0.14 to 0.30 and from 0.15 to 0.40 due to the smaller number of remaining clusters in the sample.

The detection method does not take into account superposition effects along the line of sight, a drawback that is inherent to any SZ observation. Thus we cannot fully rule out that our flux estimates are not partially contaminated by low mass systems surrounding the clusters of our sample. Numerical simulations give a possible estimate of the contamination: Hallman et al. (2007) suggest that low-mass systems and unbound gas may contribute up to $16.3\%^{+7\%}_{-6.4\%}$ of the SZ signal. This would lower our estimated cluster fluxes by $\sim 1.5\sigma$.

6. The Y_{SZ}–L_{500} relation

6.1. WMAP SZ measurements vs. X-ray model

We first consider bin averaged data, focusing on the luminosity range $L_{500} \gtrsim 10^{43}$ ergs/s where the SZ signal is significantly detected (Fig. 2 right). The left panel of Fig. 3 shows Y_{500} from a sphere of radius r_{500} as a function of L_{500}, averaging the data in six equally-spaced logarithmic bins in X-ray luminosity. Both quantities are scaled according to their expected redshift dependence. The results are presented for the analyses based on the REXCESS (red diamonds) and intrinsic (red crosses) L_{500}−M_{500} relations. For the reasons discussed in Sect. 5.2, the derived data points do not differ significantly between the two analyses (Fig. 3 left), confirming that the measured Y_{500}−L_{500} relation is insensitive to the finer details of the underlying L_{500}−M_{500} relation.

We also apply the same averaging procedure to the model Y_{500} values derived for each cluster in Sect. 3. The expected values for the same luminosity bins are plotted as stars in the

Table 2. Fitted parameters for the observed Y_{SZ}–L_{500} relation.

L_{500}–M_{500}	Y^{*L}_{500} [10^{-3} $(h/0.719)^{-2}$ arcmin^2]	α^L_Y	β^L_Y
REXCESS	0.92 ± 0.08 stat [±0.10 tot]	1.11 (fixed)	2/3 (fixed)
	0.88 ± 0.10 stat [±0.12 tot]	1.19 ± 0.10 stat [±0.10 tot]	2/3 (fixed)
	0.90 ± 0.13 stat [±0.16 tot]	1.11 (fixed)	1.05 ± 2.18 stat [±2.25 tot]
Intrinsic	0.95 ± 0.09 stat [±0.11 tot]	1.04 (fixed)	2/3 (fixed)
	0.89 ± 0.10 stat [±0.12 tot]	1.19 ± 0.10 stat [±0.10 tot]	2/3 (fixed)
	0.89 ± 0.13 stat [±0.16 tot]	1.04 (fixed)	2.06 ± 2.14 stat [±2.21 tot]

Notes. The X-ray based model gives $Y^{*L}_{500} = 0.89|1.07 \times 10^{-3}$ $(h/0.719)^{-5/2}$ arcmin^2, $\alpha^L_Y = 1.11|1.04$ and $\beta^L_Y = 2/3$ for the REXCESS and intrinsic L_{500}–M_{500} relation, respectively.

left-hand hand panel of Fig. 3. The Y_{500}–L_{500} relation expected from the combination of the Y_{500}–M_{500} (Eq. (5)) and L_{500}–M_{500} (Eq. (2)) relations is superimposed to guide the eye. The right-hand panel of Fig. 3 shows the ratio between the measured data points and those expected from the model. As discussed in Sect. 5.2, the model values depend on the assumed L_{500}–M_{500} relation. The difference is maximum in the lowest luminosity bin where the intrinsic relation yields ∼40% higher value than the REXCESS relation (Fig. 3 left panel). The SZ model prediction and the data are in good agreement, but the agreement is better when the REXCESS L_{500}–M_{500} is used in the analysis (Fig. 3 right panel). This is expected if indeed the agreement is real and the effective Malmquist bias for the NORAS/REFLEX sample is not negligible and is similar to that of the REXCESS.

6.2. Y_{500}–L_{500} relation fit

Working now with the individual flux measurements, Y_{500}, and L_{500} values, we fit an Y_{500}–L_{500} relation of the form:

$$Y_{500} = Y^{*L}_{500} \left(\frac{E(z)^{-7/3} L_{500}}{10^{44} h^{-2} \mathrm{erg/s}} \right)^{\alpha^L_Y} E(z)^{\beta^L_Y} \left(\frac{D_{\mathrm{ang}}(z)}{500\ \mathrm{Mpc}} \right)^{-2} \quad (12)$$

using the statistical error on Y_{500} given by the multifrequency matched filter. The total error is estimated by Monte Carlo (see Sect. 5.1) but is dominated by the statistical error. The results are presented in Table 2. As already stated in Sect. 6.1, the fitted values depend only weakly on the choice of L_{500}–M_{500} relation.

7. The Y_{SZ}–M_{500} relation and its evolution

In this section, we study the mass and redshift dependence of the SZ signal and check it against the X-ray based model. Furthermore, we fit the Y_{500}–M_{500} relation and compare it with the X-ray predictions.

7.1. Mass dependence and redshift evolution

Figure 4 shows the bin averaged SZ flux measurement as a function of mass compared to the X-ray based model prediction. As expected, the SZ cluster flux increases as a function of mass and is compatible with the model. In order to study the behaviour of the SZ flux with redshift, we subdivide each of the four mass bins into three redshift bins corresponding to the following ranges: $z < 0.08$, $0.08 < z < 0.18$, $z > 0.18$. The result is shown in the left panel of Fig. 5. In a given mass bin the SZ flux decreases with redshift, tracing the $D_{\mathrm{ang}}(z)^{-2}$ dependence of the flux. In particular, in the highest mass bin (10^{15} $M_\odot$), the SZ flux decreases from 0.007 to 0.001 arcmin^2 while the redshift varies

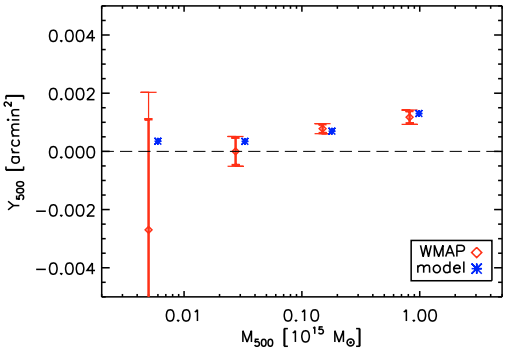

Fig. 4. Estimated SZ flux Y_{500} (in a sphere of radius r_{500}) as a function of the mass M_{500} averaged in 4 mass bins. Red diamonds are the WMAP data. Blue stars correspond to the X-ray based model predictions and are shifted to higher masses by 20% for clarity. The model is in very good agreement with the data.

from $z < 0.08$ to $z > 0.18$. The mass and the redshift dependence are in good agreement with the model (stars) described in Sect. 3.

Since the $D_{\mathrm{ang}}(z)^{-2}$ dependence is the dominant effect in the redshift evolution, we multiply Y_{500} by $D_{\mathrm{ang}}(z)^2$ and divide it by the self-similar mass dependence $M^{5/3}_{500}$. The expected self-similar behaviour of the new quantity $Y_{500} D_{\mathrm{ang}}(z)^2 / M^{5/3}_{500}$ as a function of redshift is $E(z)^{2/3}$ (see Eq. (5)). The right panel of Fig. 5 shows $Y_{500} D_{\mathrm{ang}}(z)^2 / M^{5/3}_{500}$ as a function of redshift for the three redshift bins $z < 0.08$, $0.08 < z < 0.18$, $z > 0.18$. The points have been centered at the average value of the cluster redshifts in each bin. The model is displayed as blue stars. Since the model has a self-similar redshift dependence and $E(z)^{2/3}$ increases only by a factor of 5% over the studied redshift range, the model stays nearly constant. The blue dotted line is plotted through the model and varies as $E(z)^{2/3}$. The data points are in good agreement with the model, but clearly, the redshift leverage of the sample is insufficient to put strong constraints on the evolution of the scaling laws.

We now focus on the mass dependence of the relation. We scale the SZ flux with the expected redshift dependence and plot it as a function of mass. The result is shown in Fig. 6 for the high mass end. The figure shows a very good agreement between the data points and the model, which is confirmed by fitting the relation to the individual SZ flux measurements (see next section).

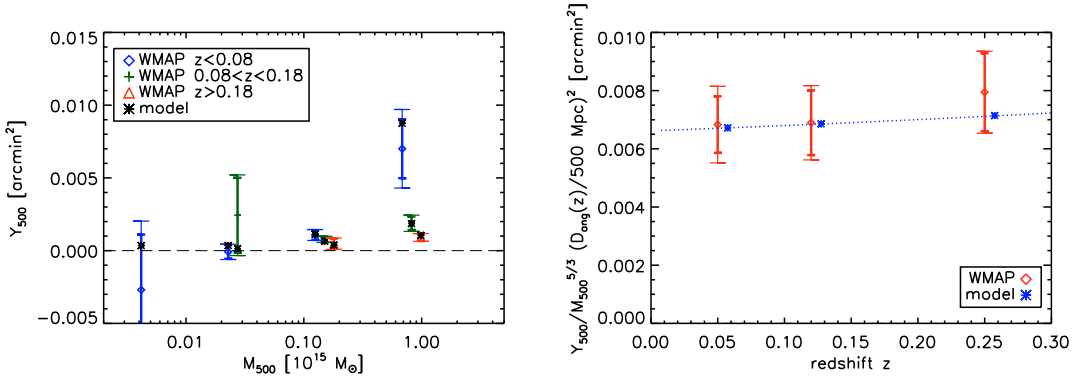

Fig. 5. Evolution of the Y_{500}-M_{500} relation. *Left*: the WMAP data from Fig. 4 are divided into three redshift bins: $z < 0.08$ (blue diamonds), $0.08 < z < 0.18$ (green crosses), $z > 0.18$ (red triangles). We observe the expected trend: at fixed mass, Y_{500} decreases with redshift. This redshift dependence is mainly due to the angular distance ($Y_{500} \propto D_{\rm ang}(z)^{-2}$). The stars give the prediction of the model. *Right*: we divide Y_{500} by $M_{500}^{5/3} D_{\rm ang}(z)^{-2}$ and plot it as a function of z to search for evidence of evolution in the Y_{500}–M_{500} relation. The thick bars give the 1σ statistical errors from WMAP data. The thin bars give the total 1 sigma errors.

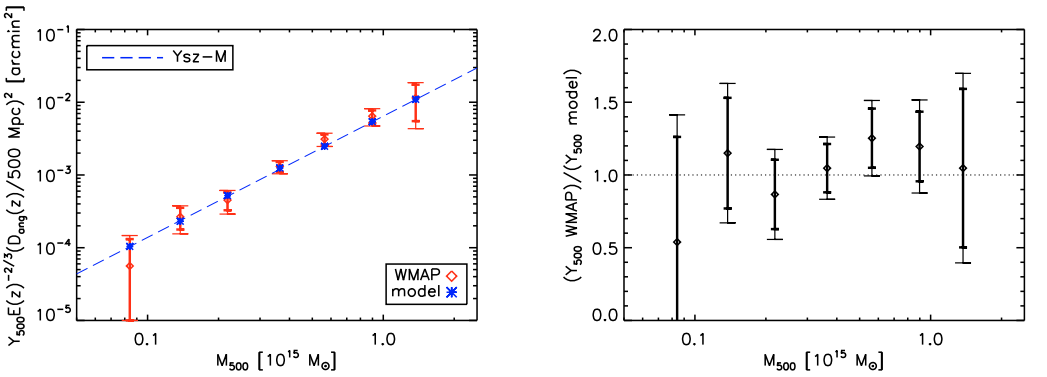

Fig. 6. *Left*: zoom on the $>5 \times 10^{13}\ M_\odot$ mass range of the Y_{500}–M_{500} relation shown in Fig. 4. The data points and model stars are now scaled with the expected redshift dependence and are placed at the mean mass of the clusters in each bin. *Right*: ratio between data and model.

7.2. Y_{500}–M_{500} relation fit

Using the individual Y_{500} measurements and M_{500} estimated from the X-ray luminosity, we fit a relation of the form:

$$Y_{500} = Y_{500}^{*} \left(\frac{M_{500}}{3 \times 10^{14} h^{-1} M_\odot} \right)^{\alpha_Y} E(z)^{\beta_Y} \left(\frac{D_{\rm ang}(z)}{500\ {\rm Mpc}} \right)^{-2}. \quad (13)$$

The results are presented in Table 3 for the analysis undertaken using the REXCESS and that using the intrinsic L_{500}–M_{500} relation. The pivot mass $3{\times}10^{14}h^{-1}\ M_\odot$, close to that used by Arnaud et al. (2010), is slightly larger than the average mass of the sample ($2.8|2.5 \times 10^{14}\ M_\odot$ for the REXCESS|intrinsic L_{500}–M_{500} relation, respectively). We use a non-linear least-squares fit built on a gradient-expansion algorithm (IDL curvefit function). In the fitting procedure, only the statistical errors given by the matched multifilter ($\sigma_{Y_{500}}$) are taken into account. The total errors on the final fitted parameters, taking into account uncertainties in X-ray properties, are estimated by Monte Carlo as described in Sect. 5.

We first discuss the results obtained using the REXCESS L_{500}–M_{500} relation, which is expected to be close to the optimal case (see discussion in Sect. 5.2). First, we keep the mass and redshift dependence fixed to the self-similar expectation ($\alpha_Y = 5/3, \beta_Y = 2/3$) and we fit only the normalisation. We obtain $Y_{500}^{*} = 1.60 \times 10^{-3}\ (h/0.719)^{-2}$ arcmin^2, in agreement with the X-ray prediction $Y_{500}^{*} = 1.54 \times 10^{-3}\ (h/0.719)^{-5/2}$ arcmin^2 (at 0.4σ). Then, we relax the constraint on α_Y and fit the normalisation and mass dependence at the same time. We obtain a value for $\alpha_Y = 1.79$, slightly greater than the self-similar expectation (5/3) by 0.8σ. To study the redshift dependence of the effect, we fix the mass dependence to $\alpha_Y = 5/3$ and fit Y_{500}^{*} and β_Y at the same time. We obtain a somewhat stronger evolution $\beta_Y = 1.05$ than the self-similar expectation (2/3). The difference, however, is not significant (0.2σ). As already mentioned above (see also Fig. 5 right), the redshift leverage is too small to get interesting constraints on β_Y.

As cluster mass estimates depend on the assumption of the underlying L_{500}–M_{500} relation, so does the derived Y_{500}–M_{500}

Table 3. Fitted parameters for the observed Y_{SZ}–M_{500} relation.

L_{500}–M_{500} relation	Y^*_{500} [10^{-3} $(h/0.719)^{-2}$ arcmin^2]	α_Y	β_Y
REXCESS	1.60 ± 0.14 stat [±0.19 tot]	5/3 (fixed)	2/3 (fixed)
	1.60 ± 0.15 stat [±0.19 tot]	1.79 ± 0.15 stat [±0.17 tot]	2/3 (fixed)
	1.57 ± 0.23 stat [±0.29 tot]	5/3 (fixed)	1.05 ± 2.18 stat [±2.52 tot]
intrinsic	1.37 ± 0.12 stat [±0.17 tot]	5/3 (fixed)	2/3 (fixed)
	1.36 ± 0.13 stat [±0.17 tot]	1.91 ± 0.16 stat [±0.18 tot]	2/3 (fixed)
	1.28 ± 0.19 stat [±0.24 tot]	5/3 (fixed)	2.06 ± 2.14 stat [±2.48 tot]

Notes. The X-ray based model gives $Y^*_{500} = 1.54 \times 10^{-3}$ $(h/0.719)^{-5/2}$ arcmin^2, $\alpha_Y = 5/3$ and $\beta_Y = 2/3$.

relation as well. However, the effect is small. The normalisation is shifted from (1.60 ± 0.14 stat [±0.19 tot]) 10^{-3} arcmin^2 to (1.37 ± 0.12 stat [±0.17 tot]) 10^{-3} arcmin^2 when using the intrinsic L_{500}–M_{500} relation. The difference is less than two statistical sigmas, and for the mass exponent, it is less than one.

8. Discussion and conclusions

In this paper we have investigated the SZ effect and its scaling with mass and X-ray luminosity using WMAP 5-year data of the largest published X-ray-selected cluster catalogue to date, derived from the combined NORAS and REFLEX samples. Cluster SZ flux estimates were made using an optimised multifrequency matched filter. Filter optimisation was achieved through priors on the pressure distribution (i.e., cluster shape) and the integration aperture (i.e., cluster size). The pressure distribution is assumed to follow the universal pressure profile of Arnaud et al. (2010), derived from X-ray observations of the representative local REXCESS sample. This profile is the most realistic available for the general population at this time, and has been shown to be in good agreement with recent high-quality SZ observations from SPT (Plagge et al. 2010). Furthermore, our analysis takes into account the dispersion in the pressure distribution. The integration aperture is estimated from the L_{500}–M_{500} relation of the same REXCESS sample. We emphasise that these two priors determine only the input spatial distribution of the SZ flux for use by the multifrequency matched filters; the priors give no information on the amplitude of the measurement. As the analysis uses minimal X-ray data input, the measured and X-ray predicted SZ fluxes are essentially independent.

We studied the Y_{SZ}–L_X relation using both bin averaged analyses and individual flux measurements. The fits using individual flux measurements give quantitative results for calibrating the scaling laws. The bin averaged analyses allow a direct quantitative check of SZ flux measurements versus X-ray model predictions based on the universal pressure profile derived by Arnaud et al. (2010) from REXCESS. An excellent agreement is found.

Using WMAP 3-year data, both Lieu et al. (2006) and Bielby & Shanks (2007) found that the SZ signal strength is lower than predicted given expectations from the X-ray properties of their clusters, concluding that that there is some missing hot gas in the intra-cluster medium. The excellent agreement between the SZ and X-ray properties of the clusters in our sample shows that there is in fact no deficit in SZ signal strength relative to expectations from X-ray observations. Due to the large size and homogeneous nature of our sample, and the internal consistency of our baseline cluster model, we believe our results to be robust in this respect. We note that there is some confusion in the literature regarding the phrase "missing baryons". The "missing baryons" mentioned by Afshordi et al. (2007) in the WMAP 3-year data are missing with respect to the universal baryon fraction, but not with respect to the expectations from X-ray measurements. Afshordi et al. (2007) actually found good agreement between the strength of the SZ signal and the X-ray properties of their cluster sample, a conclusion that agrees with our results. This good convergence between SZ direct measurements and X-ray data is an encouraging step forward for the prediction and interpretation of SZ surveys.

Using L_{500} as a mass proxy, we also calibrated the Y_{500}–M_{500} relation, finding a normalisation in excellent agreement with X-ray predictions based on the universal pressure profile, and a slope consistent with self-similar expectations. However, there is some indication that the slope may be steeper, as also indicated from the REXCESS analysis when using the best fitting empirical M_{500}-Y_X relation (Arnaud et al. 2010). M_{500} depends on the assumed L_{500}–M_{500} relation, making the derived Y_{500}–M_{500} relation sensitive to Malmquist bias which we cannot fully account for in our analysis. However, we have shown that the effect of Malmquist bias on the present results is less than 2σ (statistical).

Regarding evolution, we have shown observationally that the SZ flux is indeed sensitive to the angular size of the cluster through the diameter distance effect. For a given mass, a low redshift cluster has a bigger integrated SZ flux than a similar system at high redshift, and the redshift dependence of the integrated SZ flux is dominated by the angular diameter distance ($\propto D^2_{ang}(z)$). However, the redshift leverage of the present cluster sample is too small to put strong contraints on the evolution of the Y_{500}–L_{500} and Y_{500}–M_{500} relations. We have nevertheless checked that the observed evolution is indeed compatible with the self-similar prediction.

In this analysis, we have compensated for the poor sensitivity and resolution of the WMAP experiment (regarding SZ science) with the large number of known ROSAT clusters, leading to self-consistent and robust results. We expect further progress using upcoming Planck all-sky data. While Planck will offer the possibility of detecting the clusters used in this analysis to higher precision, thus significantly reducing the uncertainty on individual measurements, the question of evolution will not be answered with the present RASS sample due to its limited redshift range. A complementary approach will thus be to obtain new high sensitivity SZ observations of a smaller sample. The sample must be representative, cover a wide mass range, and extend to higher z (e.g., XMM-Newton follow-up of samples drawn from Planck and ground based SZ surveys). This would deliver efficient constraints not only on the normalisation and slope of the Y_{SZ}–L_X and Y_{SZ}–M relations, but also their evolution, opening the way for the use of SZ surveys for precision cosmology.

Acknowledgements. The authors wish to thank the anonymous referee for useful comments. J.-B. Melin thanks R. Battye for suggesting introduction of the h dependance into the presentation of the results. The authors also acknowledge the use of the HEALPix package (Górski et al. 2005) and of the Legacy Archive for Microwave Background Data Analysis (LAMBDA). Support for LAMBDA is provided by the NASA Office of Space Science. We also acknowledge use of the Planck Sky Model, developed by the Component Separation Working Group (WG2) of the Planck Collaboration, for the estimation of the radio source flux in the clusters and for the development of the matched multifilter, although the model was not directly used in the present work.

Appendix A: SZ flux definitions

In this Appendix, we give the definitions of SZ fluxes we used. Table A.1 gives the equivalence between them. In this paper, we mainly use Y_{500} as the definition of the SZ flux. This flux is the integrated SZ flux from a sphere of radius r_{500}. It can be related to Y_{nr500}, the flux from a sphere of radius $n \times r_{500}$ by integrating over the cluster profile:

$$Y_{nr500} = Y_{500} \frac{\int_0^{nr_{500}} \mathrm{d}r P(r) 4\pi r^2}{\int_0^{r_{500}} \mathrm{d}r P(r) 4\pi r^2} \tag{A.1}$$

where $P(r)$ is given by Eq. (3). The ratio Y_{nr500}/Y_{500} is given in Table A.1 for $n = 1, 2, 3, 5, 10$.

In practice, an experiment does not directly measure Y_{500} but the SZ signal of a cluster integrated along the line of sight and within an angular aperture. This corresponds to the Compton parameter integrated over a cylindrical volume. In Sect. 4, we estimate Y^{cyl}_{5r500}, the flux from a cylinder of aperture radius $5 \times r_{500}$ using the matched multifilter. Given the cluster profile, we can derive Y_{nr500} from Y^{cyl}_{nr500}:

$$Y^{\mathrm{cyl}}_{nr500} = Y_{nr500} \frac{\int_0^{\infty} \mathrm{d}r \int_{r \sin\theta < nr_{500}} d\theta\, P(r) 2\pi r^2}{\int_0^{nr_{500}} \mathrm{d}r P(r) 4\pi r^2} \cdot \tag{A.2}$$

The ratio $Y_{nr500}/Y^{\mathrm{cyl}}_{nr500}$ is given in Table A.1 for $n = 1, 2, 3, 5, 10$. In the paper, we calculate Y_{500} from $Y_{500} = 0.986/1.814 \times Y^{\mathrm{cyl}}_{5r500}$.

Table A.1. Equivalence of SZ flux definitions

n	1	2	3	5	10
Y_{nr500}/Y_{500}	1	1.505	1.690	1.814	1.873
$Y_{nr500}/Y^{\mathrm{cyl}}_{nr500}$	0.827	0.930	0.963	0.986	0.997

Appendix B: SZ units conversion

In this Appendix, we provide the numerical factor needed for the SZ flux units conversion and derive the relation between the recently introduced Y_{X} parameter and the SZ flux Y_{SZ}. The latter will allow readers to easily convert between SZ fluxes given in this paper and those reported in other publications.

Given the definition of SZ flux:

$$Y^{\mathrm{cyl}}_{nr500} = \int_{\Omega_{nr500}} \mathrm{d}\Omega\, y \tag{B.1}$$

where Ω_{nr500} is the solid angle covered by $n \times r_{500}$, and the fact that the Compton parameter y is unitless, the observational units for the SZ flux are those of a solid angle and usually given in arcmin^2.

The SZ flux can be also computed in units of Mpc^2 and the conversion is given by

$$\begin{aligned} Y_{\mathrm{SZ}}[\mathrm{Mpc}^2] &= 60^{-2} \left(\frac{\pi}{180}\right)^2 Y_{\mathrm{SZ}}[\mathrm{arcmin}^2] \left(\frac{D_{\mathrm{ang}}(z)}{1\ \mathrm{Mpc}}\right)^2 \\ &= 8.46 \times 10^{-8}\, Y_{\mathrm{SZ}}[\mathrm{arcmin}^2] \left(\frac{D_{\mathrm{ang}}(z)}{1\ \mathrm{Mpc}}\right)^2 \end{aligned} \tag{B.2}$$

where $D_{\mathrm{ang}}(z)$ is the angular distance to the cluster.

The X-ray analogue of the integrated SZ Comptonisation parameter is $Y_{\mathrm{X}} = M_{\mathrm{gas},500} T_{\mathrm{X}}$ whose natural units are $M_\odot$ keV, where $M_{\mathrm{gas},500}$ is the gas mass in r_{500} and T_{X} is the *spectroscopic* temperature excluding the central $0.15\, r_{500}$ region (Kravtsov et al. 2006). To convert between Y_{SZ} and Y_{X}, we first have

$$Y_{\mathrm{SZ}}[\mathrm{Mpc}^2] = \int_0^{r_{500}} \mathrm{d}r\, \sigma_{\mathrm{T}} \frac{T_{\mathrm{e}}(r)}{m_{\mathrm{e}}c^2} n_{\mathrm{e}}(r) 4\pi r^2 \tag{B.3}$$

where σ_{T} is the Thomson cross section (in Mpc^2), $m_{\mathrm{e}}c^2$ the electron mass (in keV), $T_{\mathrm{e}}(r)$ the electronic temperature (in keV) and $n_{\mathrm{e}}(r)$ the electronic density. By assuming that the gas temperature $T_{\mathrm{g}}(r)$ is equal to the electronic temperature $T_{\mathrm{e}}(r)$ and writing the gas density as $\rho_{\mathrm{g}}(r) = \mu_{\mathrm{e}} m_p n_{\mathrm{e}}(r)$, where m_p is the proton mass and $\mu_{\mathrm{e}} = 1.14$ the mean molecular weight per free electron, one obtains:

$$\begin{aligned} Y_{\mathrm{SZ}}[\mathrm{Mpc}^2] &= \frac{\sigma_T}{m_{\mathrm{e}}c^2} \frac{1}{\mu_{\mathrm{e}} m_p} \int_0^{r_{500}} \mathrm{d}r\, \rho_{\mathrm{g}}(r)\, T_{\mathrm{g}}(r) 4\pi r^2 \\ &= C_{\mathrm{XSZ}}\, M_{\mathrm{gas},500}\, T_{\mathrm{MW}} = A\, C_{\mathrm{XSZ}}\, Y_{\mathrm{X}} \end{aligned} \tag{B.4}$$

where, as in Arnaud et al. (2010), we defined

$$C_{\mathrm{XSZ}} = \frac{\sigma_T}{m_{\mathrm{e}}c^2} \frac{1}{\mu_{\mathrm{e}} m_p} = 1.416 \times 10^{-19} \frac{\mathrm{Mpc}^2}{M_\odot\ \mathrm{keV}} \cdot \tag{B.5}$$

The *mass weighted* temperature is defined as:

$$T_{\mathrm{MW}} = \frac{\int_0^{r_{500}} \mathrm{d}r\, \rho_{\mathrm{g}}(r)\, T_{\mathrm{g}}(r) 4\pi r^2}{\int_0^{r_{500}} \mathrm{d}r\, \rho_{\mathrm{g}}(r) 4\pi r^2} \tag{B.6}$$

and the factor $A = T_{\mathrm{MW}}/T_{\mathrm{X}}$ takes into account for the difference between mass weighted and spectroscopic average temperatures. Arnaud et al. (2010) find $A \sim 0.924$.

References

Afshordi, N., Lin, Y.-T., Nagai, D., & Sanderson, A. J. R. 2007, MNRAS, 378, 293
Arnaud, M., Pointecouteau, E., & Pratt, G. W. 2007, A&A, 474, L37
Arnaud, M., Pratt, G. W., Piffaretti, R., et al. 2010, A&A, 517, A92
Atrio-Barandela, F., Kashlinsky, A., Kocevski, D., & Ebeling, H. 2008, ApJ, 675, L57
Bennett, C. L., Halpern, M., Hinshaw, G., et al. 2003, ApJS, 148, 1
Bielby, R. M., & Shanks, T. 2007, MNRAS, 382, 1196
Böhringer, H., Voges, W., Huchra, J. P., et al. 2000, ApJS, 129, 435
Böhringer, H., Schuecker, P., Guzzo, L., et al. 2004, A&A, 425, 367
Böhringer, H., Schuecker, P., Pratt, G. W., et al. 2007, A&A, 469, 363
Bonamente, M., Joy, M., LaRoque, S. J., et al. 2008, ApJ, 675, 106
Carlstrom, J. E., Ade, P. A. R., Aird, K. A., et al. 2009, PASP, submitted [arXiv:0907.4445]
Condon, J. J., Cotton, W. D., Greisen, E. W., et al. 1998, AJ, 115, 1693
Croston, J. H., Pratt, G. W., Böhringer, H., et al. 2008, A&A, 487, 431
da Silva, A. C., Kay, S. T., Liddle, A. R., & Thomas, P. A. 2004, MNRAS, 348, 1401
Delabrouille, J., Cardoso, J.-F., Le Jeune, M., et al. 2009, A&A, 493, 835

Diego, J. M., & Partridge, B. 2009, MNRAS, 1927
Fosalba, P., Gaztañaga, E., & Castander, F. J. 2003, ApJ, 597, L89
Górski, K. M., Hivon, E., Banday, A. J., et al. 2005, ApJ, 622, 759
Hallman, E. J., O'Shea, B. W., Burns, J. O., et al. 2007, ApJ, 671, 27
Halverson, N. W., Lanting, T., Ade, P. A. R., et al. 2009, ApJ, 701, 42
Hernández-Monteagudo, C., Genova-Santos, R., & Atrio-Barandela, F. 2004, ApJ, 613, L89
Hernández-Monteagudo, C., Macías-Pérez, J. F., Tristram, M., & Désert, F.-X. 2006, A&A, 449, 41
Herranz, D., Sanz, J. L., et al. 2002, MNRAS, 336, 1057
Hinshaw, G., Nolta, M. R., Bennett, C. L., et al. 2007, ApJS, 170, 288
Hinshaw, G., Weiland, J. L., Hill, R. S., et al. 2009, ApJS, 180, 225
Kitayama, T., Komatsu, E., Ota, N., et al. 2004, PASJ, 56, 17
Kravtsov, A. V., Vikhlinin, A., & Nagai, D. 2006, ApJ, 650, 128
Lieu, R., Mittaz, J. P. D., & Zhang, S.-N. 2006, ApJ, 648, 176
Lamarre, J. M., Puget, J. L., Bouchet, F.., et al. 2003, New Astron. Rev., 47, 1017
Marrone, D. P., Smith, G. P., Richard, J., et al. 2009, ApJ, 701, L114
Mauch, T., Murphy, T., Buttery, H. J., et al. 2003, MNRAS, 342, 1117
Melin, J.-B., Bartlett, J. G., & Delabrouille, J. 2006, A&A, 459, 341
Motl, P. M., Hallman, E. J., Burns, J. O., & Normal, M. L. 2005, ApJ, 623, L63
Mroczkowski, T., Bonamente, M., Carlstrom, J., et al. 2009, ApJ, 694, 1034
Myers, A. D., Shanks, T., Outram, P. J., Frith, W. J., & Wolfendale, A. W. 2004, MNRAS, 347, L67
Nagai, D., Kravtsov, A. V., & Vikhlinin, A. 2007, ApJ, 668, 1
Nord, M., Basu, K., Pacaud, F., et al. 2009, A&A, 506, 623
Plagge, T., Benson, B., Ade, P. A. R., et al. 2010, ApJ, 716, 1118
Pratt, G. W., Croston, J. H., Arnaud, M., Böhringer, H. 2009, A&A, 498, 361
Staniszewski, Z., Ade, P. A. R., Aird, K. A., et al. 2009, ApJ, 701, 32
Sunyaev, R. A., & Zel'dovich, Ya. B. 1970, Comments Astrophys. Space Phys., ComAp, 2, 66
Sunyaev, R. A., & Zel'dovich, Ya. B. 1972, Comments Astrophys. Space Phys., 4, 173
Valenziano, L., et al. 2007, New Astron. Rev., 51, 287
Vikhlinin, A., Burenin, R., Ebeling, H., et al. 2009, ApJ, 692, 1033

Mon. Not. R. Astron. Soc. **298,** 445–450 (1998)

Circular scans for cosmic microwave background anisotropy observation and analysis

J. Delabrouille,[1,2] K. M. Górski[3,4] and E. Hivon[3]

[1]*Institut d'Astrophysique Spatiale, CNRS & Université Paris XI, bât 121, 91405 Orsay Cedex, France*
[2]*Enrico Fermi Institute, University of Chicago, 5460 South Ellis Avenue, Chicago, ILL 60637, USA*
[3]*Theoretical Astrophysics Center, Juliane Maries Vej 30, DK-2100, Copenhagen, Denmark*
[4]*On leave from Warsaw University Observatory, Warsaw, Poland*

Accepted 1998 March 11. Received 1998 February 19; in original form 1997 November 10

ABSTRACT

A number of experiments for measuring anisotropies of the cosmic microwave background (CMB) use scanning strategies in which temperature fluctuations are measured along circular scans on the sky. It is possible, from a large number of such intersecting circular scans, to build two-dimensional sky maps for subsequent analysis. However, since instrumental effects – especially the excess low-frequency $1/f$ noise – project on to such two-dimensional maps in a non-trivial way, we discuss the analysis approach which focuses on information contained in the individual circular scans. This natural way of looking at CMB data from experiments scanning on the circles combines the advantages of elegant simplicity of Fourier series for the computation of statistics useful for constraining cosmological scenarios, and superior efficiency in analysing and quantifying most of the crucial instrumental effects.

Key words: methods: data analysis – methods: observational – cosmic microwave background cosmology: theory.

1 INTRODUCTION

The exploration of the cosmic microwave background (CMB) is undergoing a boom in both theoretical and experimental directions. The planning of two ambitious space missions, *MAP* and *PLANCK*, to be launched in the beginning of the 21st century, is one of the sources of stimulus for research in this field. In addition, several long duration balloon-borne experiments are scheduled for operation within the next few years time.

Many of the future CMB anisotropy experiments will perform circular scans on the sky. *MAP*,[1] *PLANCK*[2] (Bersanelli et al. 1996), and the balloon-borne experiments TopHat[3] and BEAST (Lubin, private communication), will collect data from a large number of intersecting circles, which will then be merged into two-dimensional sky maps. Smaller ground-based experiments as DIABOLO (Benoît et al., in preparation) may scan on only a few circles. In winter of 1997 for instance, a one-ring observation of anisotropies was carried out at the POM2 telescope in the French alps with the DIABOLO instrument.

A common problem in the analysis of the data obtained by performing one-dimensional sky scans is that all instrumental effects (other than smoothing by the beam) occur in the monotonic time domain of the data stream, but need to be projected onto the often complicated geometry of directions of observation, which is essential for the interpretation of the results.

In the following, we explore the relation between the Fourier spectrum of temperature fluctuations measured on a circle and spherical harmonic expansion coefficients on the sphere, with associated uncertainties in the framework of Gaussian statistics, and investigate how circular scans permit to analyse naturally both the signal of cosmological origin and some of the effects coming from the instrument.

2 CMB ANISOTROPIES ON CIRCULAR SCANS

2.1 Fourier spectra

The usual expansion in spherical harmonics of the statistically isotropic CMB temperature fluctuations on the sky observed with a symmetric beam reads:

$$T(\boldsymbol{n}) = \sum_{\ell=1}^{\infty} \sum_{m=-\ell}^{\ell} a_{\ell m} B_\ell Y_{\ell m}(\boldsymbol{n}). \quad (1)$$

Here, the coefficients $a_{\ell m}$ are assumed to be zero-mean Gaussian deviates with variances given by $\langle |a_{\ell m}|^2 \rangle = C_\ell$ (on assumption of statistical isotropy of the CMB temperature perturbations, here

[1]*MAP* home page: http://map.gsfc.nasa.gov/
[2]*PLANCK* home page: http://astro.estec.esa.nl/SA-general/ Projects/ Cobras/cobras.html
[3]MSAM/TopHat home page: http://cobi.gsfc.nasa.gov/msam-tophat.html

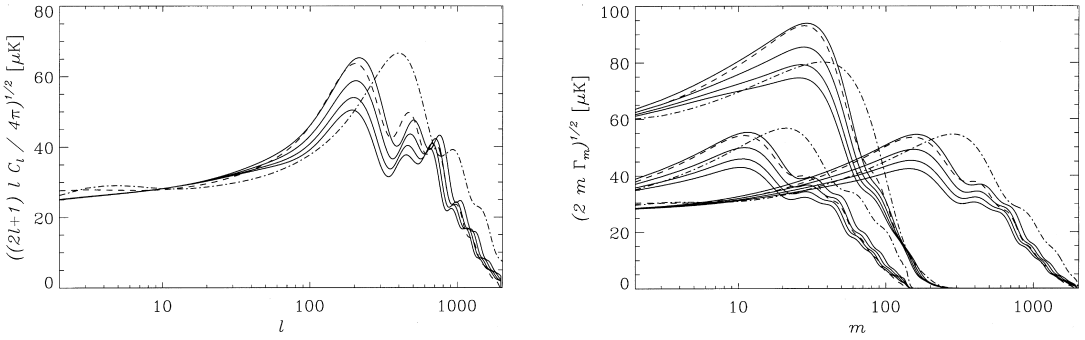

Figure 1. Left panel: full-sky power spectra C_ℓ of CMB anisotropy, smoothed with a Gaussian beam of FWHM = 7 arcmin, in various CDM cosmological models normalised roughly to match the CMB anisotropy detected by *COBE*-DMR. All models obey the primordial nucleosynthesis constraint $\Omega_b h^2 = 0.015$. Solid lines (top to bottom) correspond to flat, matter dominated models with Hubble constant $h = 0.5$, 0.6, 0.7, and 0.8. The dashed line shows a cosmological constant dominated model with $\lambda = 0.7$ and $h = 0.8$, and the dot–dashed line shows an open model with $\Omega_0 = 0.3$ and $h = 0.65$. Right panel: one-dimensional power spectra of CMB anisotropy on circular scans computed for the same models as shown in the left panel. Three groups of curves as viewed from left to right correspond to different specifications (by the angular radius of the circle, Θ and the FWHM of the beam) of the geometry of observations: the left group corresponds to a small ring of $\Theta = 4°$, FWHM = 5 arcmin; the middle group (amplitudes multiplied by 2 to avoid overlap with the other curves) corresponds to an intermediate size ring of $\Theta = 12°$, FWHM = 20 arcmin; finally, the right group corresponds to a large ring of $\Theta = 80°$, FWHM = 7 arcmin. Both the left and the right panels show the CMB anisotropy rms amplitude per logarithmic increment of the relevant index ℓ or m, taking into account the number of degrees of freedom per mode [factors $(2\ell + 1)\ell$ and $2m$, respectively].

expressed via the ensemble averaging), B_ℓ is the beam response function (we have assumed for simplicity that the beam is symmetric), and a unit vector $\boldsymbol{n}$ defines the position on the sphere. The functions $Y_{\ell m}(\boldsymbol{n}) = Y_{\ell m}(\theta, \phi)$ are the orthonormal spherical harmonics, defined, for $-\ell \le m \le \ell$, as

$$Y_{\ell m}(\theta, \phi) = \mathcal{P}_{\ell m}(\theta)\, \mathrm{e}^{\mathrm{i}m\phi}, \tag{2}$$

with

$$\mathcal{P}_{\ell m}(\theta) = \sqrt{\frac{2\ell+1}{4\pi}\frac{(\ell-m)!}{(\ell+m)!}}\, P_{\ell m}(\cos\theta), \quad \text{for } m \ge 0,$$

$$= (-1)^{|m|}\mathcal{P}_{\ell|m|}(\theta), \quad \text{for } m < 0,$$

where $P_{\ell m}$ are the associated Legendre polynomials. This definition of the $Y_{\ell m}$, together with the fact that the temperature is real, implies $a_{\ell m} = (-1)^m a^*_{\ell -m}$.

If only one ring of angular radius Θ on the sky is being scanned, it is convenient to use coordinates such that the observed circle is the set of points of the sphere at constant colatitude Θ. The CMB temperature on this circle, $T(\Theta, \phi)$, can be decomposed uniquely in the form of a Fourier series

$$\alpha_m = \frac{1}{2\pi}\int_0^{2\pi} \mathrm{d}\phi\; T(\Theta, \phi)\, \mathrm{e}^{-\mathrm{i}m\phi} = \sum_{\ell=|m|}^{\infty} a_{\ell m}\, B_\ell\, \mathcal{P}_{\ell m}(\Theta). \tag{3}$$

If $a_{\ell m}$ are uncorrelated Gaussian random variables, as expected in an inflationary scenario (Bardeen et al. 1986), the same is the case also for the ring mode amplitudes α_m. The corresponding Fourier spectrum, the components of which we shall denote as Γ_m, is the one-dimensional analogue of the C_ℓ spectrum on the sky. The anisotropy Fourier spectrum Γ_m is obtained from the C_ℓ spectrum by:

$$\langle \alpha_m \alpha^*_{m'} \rangle = \Gamma_m \delta_{mm'}, \tag{4}$$

and

$$\Gamma_m = \sum_{\ell=|m|}^{\infty} C_\ell\, B_\ell^2\, \mathcal{P}_{\ell m}^2(\Theta). \tag{5}$$

This last equation allows a straightforward computation of the ring anisotropy power spectrum Γ_m given the instrumental specifications (Θ and B_ℓ) and the cosmological model (C_ℓ spectrum as a function of the relevant parameters).

Fig. 1 illustrates some properties of the ring spectrum Γ_m as compared to the usual full sky spectrum C_ℓ. Observational configurations chosen for the plot correspond to (1) a single ring scan of the *PLANCK* satellite observing with the High Frequency Instrument (the large ring), (2) a single ring of the TopHat balloon experiment (the intermediate ring), and (3) a hypothetical small ring and a narrow beam configuration. One should note that the ring anisotropy power spectra preserve the dependence on cosmological parameters observed by the C_ℓ curves, and, if the resolution of the instrument is good enough and the ring size sufficiently large, display clearly the array of adiabatic peaks. This promotes the strategy of observing the CMB anisotropy on the rings to a very interesting status. Clearly one should be able to conduct a well-guided analysis of such a data with the aid of a simple statistic, Γ_m, which, owing to the natural geometric reduction from the whole sky to the circle, captures all those features of theoretical CMB anisotropy predictions – direct reflection of physical processes that perturb CMB temperature in the shape of power spectrum, and the traceable dependence on cosmological parameters – which created high level of expectations for the full sky CMB mapping missions.

Ring power spectrum coefficients Γ_m can be viewed as the estimators of the spectrum C_ℓ integrated over ℓ with a certain m-dependent window function, the coefficients of which are simply

$$W_\ell^{(m)} = \mathcal{P}_{\ell m}{}^2(\Theta) B_\ell{}^2. \tag{6}$$

A number of such window functions $W_\ell^{(m)}$, corresponding to the ring configurations used in Fig. 1, are displayed in Fig. 2. Window functions similar to ours have been computed independently for polarization measurements on a ring by Zaldarriaga (Zaldarriaga 1997).

An important, if simple, property of these window functions, and, hence, the Γ_m coefficients, is that the power at mode m is

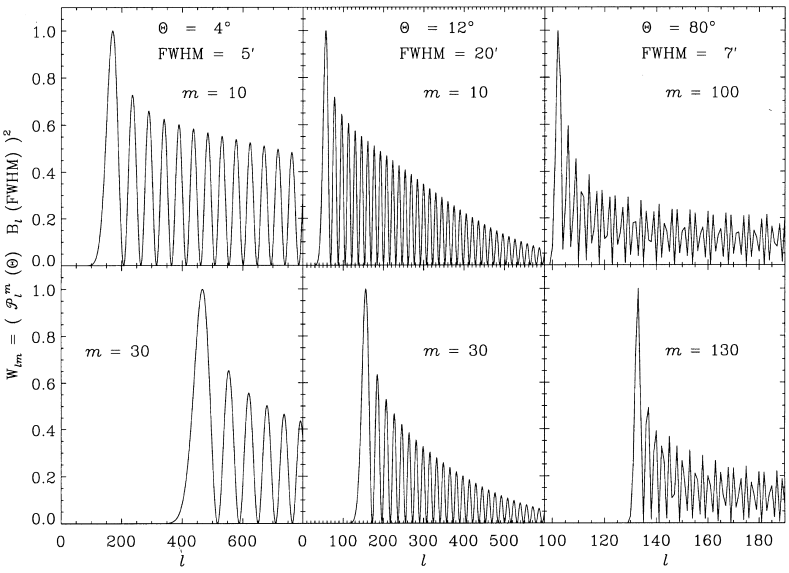

Figure 2. Window functions for computation of the CMB anisotropy ring power spectrum Γ_m, see equations (5) and (6), normalized to unity at their maxima.

generated by only those components of sky anisotropy for which $\ell \geq m$. This is rather important for the sub-orbital attempts to measure the CMB anisotropy, which have to cope with the atmospheric effects. It has been the case for a long time that owing to the variation from zenith to horizon of the length of path through the Earth's atmosphere, and the associated systematic effects in the measurements of CMB temperature, the preferred scanning strategy in CMB experiments was usually along the lines of constant elevation. Can one, in a sub-orbital experiment, afford to scan on any other circle than that at constant elevation? If the atmospheric temperature gradient is predominantly large-scale compared to the size of the observing ring, its contaminating effects will be confined to low-m modes of the ring anisotropy spectrum, and high-m modes will be algebraically decoupled from such a source of spurious anisotropy.

To what extent would a measurement of CMB anisotropy on the ring allow us to estimate the parameters of cosmological model used to describe the data? To be able to answer this question we need first to clarify the statistical properties of circular modes of CMB anisotropy, and the properties of instrumental noise as projected on the ring geometry of observations. We shall see momentarily that the estimation of uncertainties in measurements of α_m arising from white noise, excess low-frequency noise, or instrumental systematic effects is simpler and more secure in the case of ring anisotropy than in the case of two-dimensional maps used in C_ℓ estimation.

2.2 Statistics of Fourier transforms of CMB anisotropy measurements on the rings

Here we address the issue of cosmic variance of the ring modes of the CMB anisotropy. Fourier coefficients of temperature fluctuations measured on the circle, α_ms, are linear combinations of $a_{\ell m}$s, whose statistical properties they hence inherit. Specifically, Gaussian distribution of $a_{\ell m}$s renders Gaussian distribution of α_ms. Statistical isotropy of the model CMB anisotropy field results in a very special property of the m-independence of variance – $\langle |a_{\ell m}|^2 \rangle = C_\ell$, which makes the C_ℓ spectral coefficients $\chi^2_{(2\ell+1)}$ distributed. In the case of Fourier coefficients of the ring data the number of degrees of freedom associated with a specific m value is reduced to only two – $\pm m$ waves have identical variance. Hence, the cosmic variance on the Γ_m coefficients is described by the χ^2_2 probability distribution, independent of the value of m.

In Fig. 3 we illustrate the statistical properties of ring Fourier coefficients of CMB anisotropy. The plot shows a few features of probability distribution of the rms power in mode m. It is clear that the cosmic variance in the ring Fourier coefficients is large, and, unlike in the case of full sky measurements of CMB anisotropy, when available at small enough angular scales, the statistics of power at high m do not improve compared to those in low-m modes, as the ring configuration allows just two degrees of freedom per mode, independent of m. It is clear that the only opportunity for improvement of statistics of the measurements of ring modes of CMB anisotropy rests with repeating the observations on many rings. The essential issues of assessing the ring to ring covariance of the Fourier modes of CMB anisotropy will be addressed in detail in a separate paper (Górski, Delabrouille & Hivon, in preparation).

3 NOISE ON CIRCULAR SCANS

Now we turn to the estimation of the projection of instrumental noise onto a ring of data. Noise, unlike the CMB temperature anisotropies, is a time-dependent process that is independent (to first order) of the position on the sky. The same is true of many instrumental effects in the measured signal (system impulse response, sampling...), but we first limit our discussion to a simple Gaussian noise as an illustration of the connection between the measured data stream and the signal re-projected on the ring.

Let us assume that data is collected by a total-power experiment as *PLANCK*, TopHat, BEAST or DIABOLO, and that a circle on the

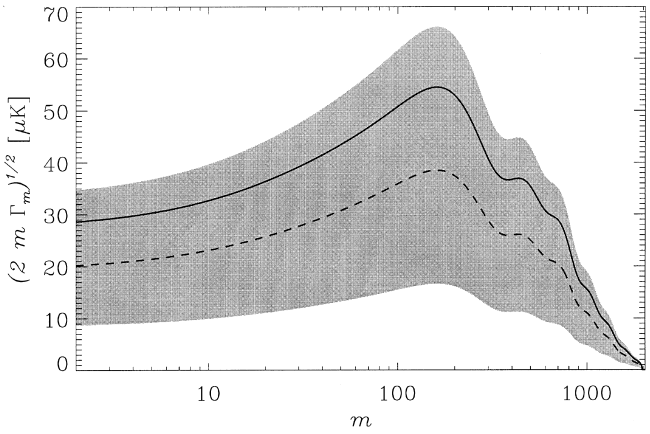

Figure 3. Statistics of the rms power of the CMB anisotropy measured on the ring. Grey band covers the 68 per cent confidence range for each rms power coefficient and scales identically at each value of m in terms of the variance, which is shown by solid line. Dashed line shows the loci of the most probable values of the rms power, illustrating the skewness of the distribution.

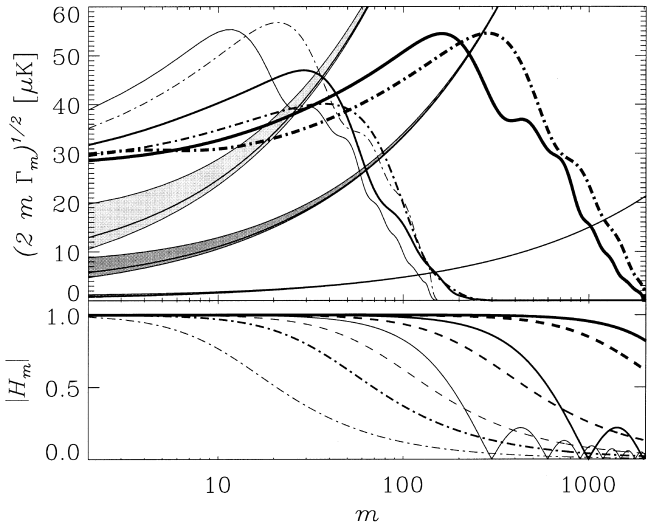

Figure 4. Top panel: power spectra Γ_m of signal and noise for the following set-ups of CMB anisotropy measurements: (1) the ring radius of $\Theta = 4^\circ$ and FWHM = 5 arcmin – light lines, (2) $\Theta = 12^\circ$ and FWHM = 20 arcmin – medium-width lines, and (3) $\Theta = 80^\circ$ and FWHM = 7 arcmin – heavy lines. Solid lines show the predictions of standard CDM model, and dot–dashed lines those of an $\Omega_0 = 0.3$ open model, both normalized to *COBE*-DMR. Three grey bands show the range of rms values of instrumental noise contributions. Bottom edges of the grey bands correspond to pure white noise behaviour of the detector. Solid lines inside the bands illustrate the noise enhancement arising from the $1/f$ component when the knee frequency is equal to the spin frequency on the ring scan. The upper edges of the grey bands correspond to $f_{\rm knee}/f_{\rm spin} = 5$ (excess low frequency noise grows with $f_{\rm knee}/f_{\rm spin}$). The assumed (white noise) detector performance is characterised by sensitivity of 1 mK$\sqrt{s}$ and total integration time of 20 and 100 h for the upper two bands (light and medium grey respectively), while the third, narrow, dark grey noise band corresponds to a sensitivity of 20 μK$\sqrt{s}$ and integration time of 2 h. Bottom panel: illustration of the effects of sampling and bolometer time constant (see text). Heavy lines correspond to spin period of 1 min, and illustrate the effect of sampling at 10 ms – solid line, and bolometer time constant of 6 ms – dashed line. Medium-width and light curves correspond to spin period of 10 and 3 s, respectively. For these two spin rates the solid lines illustrate the effect of sampling at 10 ms, and the dashed and dot–dashed lines show the effect of bolometer time constant of 6 and 40 ms, respectively.

sky is scanned continuously N times, with a spinning frequency $f_{\rm spin}$ (spinning period $T_{\rm spin}$). The output of each detector is a signal $s(t)$, the value as a function of time of which can be written as

$$s(t) = u[\phi(t)] + n(t). \qquad (7)$$

In this equation, $\phi(t) = 2\pi f_{\rm spin} t$ is the longitude angle on the circle. The way it depends upon time reflects the scanning strategy. $u(\phi) = T(\Theta, \phi)$ is the useful signal from the sky, i. e. the temperature anisotropy smoothed with the beam. It is a 2π-periodic function of ϕ for fixed Θ. If anisotropies are correctly represented

by a Gaussian random field, the Fourier components u_m of the Fourier series decomposition of $u(\phi)$ are realizations of the random variables α_m defined in the previous section. The noise $n(t)$ is assumed to be a realization of a Gaussian stationary random process with zero mean and a bilateral spectrum $S_n(f)$ which, over a large range of frequencies, can be typically of the form:

$$S_n(f) = a\left[1 + \left(\frac{f_{\rm knee}}{|f|}\right)\right] \tag{8}$$

This is the simple case of the so-called $1/f$ noise.

Given the signal time-line as defined in equation (7), the estimation of the Fourier components of anisotropy on the ring can be done by computing the integral

$$\begin{aligned} s_m &= \frac{1}{NT_{\rm spin}}\int_0^{NT_{\rm spin}} s(t)\exp\left(-\frac{2{\rm i}\pi mt}{T_{\rm spin}}\right){\rm d}t \\ &= u_m + \frac{1}{NT_{\rm spin}}\int_0^{NT_{\rm spin}} n(t)\exp\left(-\frac{2{\rm i}\pi mt}{T_{\rm spin}}\right){\rm d}t. \end{aligned} \tag{9}$$

Under the present hypotheses (no foregrounds, uncorrelated Gaussian noise), this quantity s_m is an unbiased estimator of α_m, which variance originates in only two sources of uncertainty. First, there is the theoretical 'cosmic' or 'sample' variance owing to the fact that u_m is just one realization of α_m, as discussed in Section 2.2. Secondly, there is the uncertainty as a result of the detection process [i.e. owing to the noise $n(t)$]. Let us denote as n_m the quantity

$$n_m = \frac{1}{NT_{\rm spin}}\int_0^{NT_{\rm spin}} n(t)\exp\left(-\frac{2{\rm i}\pi mt}{T_{\rm spin}}\right){\rm d}t. \tag{10}$$

Each of the n_m-s can be viewed as a realization of a Gaussian random variable. They obey the correlation statistics

$$\langle n_m n^*_{m'}\rangle = \int_{-\infty}^{\infty} S_n(f)H_m(f)H^*_{m'}(f)\,{\rm d}f \tag{11}$$

where $H_m(f)$ is given by

$$H_m(f) = {\rm e}^{[{\rm i}\pi N(f/f_{\rm spin}-m)]}\times\frac{\sin[\pi N(f/f_{\rm spin}-m)]}{\pi N(f/f_{\rm spin}-m)}. \tag{12}$$

Interestingly, but not surprisingly, there may be some correlations between Fourier amplitudes of the noise re-projected on the ring, depending on the nature of the noise spectrum $S_n(f)$. However, if the number N of scans on a circle is large and the noise spectrum S_n is not too steep ($1/f$ is fine), the expectation value of $n_m n^*_m$ becomes:

$$\langle n_m n^*_{m'}\rangle \simeq \frac{S_n(mf_{\rm spin})}{NT_{\rm spin}}\delta_{mm'}. \tag{13}$$

Thus, for each individual m value, the uncertainty in $s_m s^*_m$ induced by noise depends on $f_{\rm spin}$ through the noise spectrum value $S_n(mf_{\rm spin})$, and upon the total integration time $NT_{\rm spin}$. For a given experiment, the spinning frequency and total integration time should be optimized by comparing the level of the noise spectrum to the expected spectrum of the signal of astrophysical origin. Usually, the noise spectrum decreases with increasing f, and thus the minimization of $n_m n^*_m$ requires to spin fast, up to a compromise which depends on other experimental considerations.

If the number of scans on a circle, N, is large, and the noise spectrum S_n is not too steep, the expectation value of $s_m s^*_m$ averaged over sky realizations of the CMB *and* noise realizations is

$$\langle s_{m'} s^*_m\rangle \simeq \left[\Gamma_m + \frac{S_n(mf_{\rm spin})}{NT_{\rm spin}}\right]\delta_{mm'}. \tag{14}$$

Thus a direct comparison of the signal and noise spectra for typical next-generation experiments is quite straightforward in the ring formalism and is presented here in Fig. 4.

In the top panel of Fig. 4, we have plotted together the rms values of Γ_m for three different experiments and two different cosmological models, and the noise-induced sensitivity limits to individual Γ_m components. Experimental parameters chosen for the plot are representative of the next generation balloon-borne or satellite experiments. The pure white noise contribution, proportional to $m^{1/2}$, has the shape of an exponential because of the logarithmic scale for m. $1/f$ noise alone would appear on the plot as an horizontal line, with amplitude equal to that of the white noise at $m = m_{\rm knee} = f_{\rm knee}/f_{\rm spin}$. As long as $m_{\rm knee}$ is smaller than a few, the excess $1/f$ noise induces a slight flattening of the noise curve for low m, with negligible total additional noise power.

4 OTHER SYSTEMATICS AND INSTRUMENTAL EFFECTS

Apart from noise, there are a few effects of instrumental origin that can be understood much easier on time-lines than on maps of the sky. Some of these effects can be described as those of filters with a known impulse response, $h(t)$. The Fourier transform of the impulse response, $H(f)$, is known in signal processing as the transfer function of the filter. For such filters, the filtering theorem states that if a signal $u(t)$ has a spectrum $S_u(t)$, the corresponding filtered signal, $u_F(t) = u(t)\star h(t)$, has spectrum $S_u(t)|H(f)|^2$. Two important instrumental effects can be addressed with this formalism.

4.1 Time constant of bolometers

A typical bolometer for CMB anisotropy observations is a temperature-sensitive resistor heated by incoming radiation and cooled by a heat-conducting connection to a sub-Kelvin thermal bath. The response of such a system to an impulse of incident power is

$$h(t) = \frac{1}{\tau}\exp(-t/\tau). \tag{15}$$

The constant τ is known as the time constant of the bolometer. It is set by physical characteristics of the bolometer ($\tau = C/G$, where C is the heat capacity of the bolometer and G the effective conductivity of the link to the thermal bath). However, other bolometer characteristics, and in particular the sensitivity of the bolometer, depend on the same parameters. Thus, it is crucial, for bolometer optimization, to understand the effect of the time constant of the bolometers on the spectrum of the useful astrophysical (and especially cosmological) signal.

The transfer function $H(f)$ corresponding to the impulse response of equation 15 is

$$H(f) = \frac{1}{1 + 2{\rm i}\pi f\tau}. \tag{16}$$

Using the relation between m and frequencies of the signal, $m = f/f_{\rm spin}$, the attenuation function A_m on the Γ_m corresponding to the effect of the time constant of the bolometers is

$$A_m = |H_m|^2 = \frac{1}{1 + (2\pi f_{\rm spin}\tau)^2 m^2} \tag{17}$$

and instead of measuring the quantities Γ_m, the instrument measures $A_m\Gamma_m$.

4.2 Effect of the sampling frequency

Another instrumental parameter which needs to be set carefully

by designers of CMB experiments is the sampling frequency. It should be high enough in order to avoid aliasing, but making it unnecessarily high results in a very large set of data, with the associated problems of data storage and telemetry, especially for satellite or long duration ballooning experiments.

Again, the effect of the sampling rate can be understood very simply as that of a filter. If sampling is modelled by a perfect integrator over a period T_0 (which is the inverse of the sampling rate) for obtaining each sample, the corresponding impulse response is

$$h(t) = \frac{1}{T_0}\mathrm{rect}(T_0), \tag{18}$$

where $\mathrm{rect}(T_0)$ is the function whose value is 1 between $t - T_0/2$ and $t + T_0/2$, and 0 elsewhere. The corresponding transfer function is

$$H(f) = \frac{\sin(\pi f T_0)}{\pi f T_0} \tag{19}$$

and the corresponding attenuation function A_m on the $\mathbf{\Gamma}_m$ is:

$$A_m = |H_m|^2 = \frac{\sin^2(\pi m f_{\mathrm{spin}} T_0)}{(\pi m f_{\mathrm{spin}} T_0)^2} \tag{20}$$

Attenuation functions for these two effects are plotted in the bottom panel of Fig. 4.

5 CONCLUSION

In this paper, we presented the formalism to project the CMB anisotropy predictions and instrumental noise effects on the rings of data. Because of the feasibility of experimental setup for CMB observations with circular scans, and simplicity of the data analysis on such scans, we believe that collecting CMB anisotropy data in this format is an interesting option for the next generation of anisotropy experiments. It provides a natural frame for studying the statistics of CMB anisotropies, in which many instrumental effects can be modelled and analysed under the most natural connection between the time stream of data and the spatial distribution of the directions of measurements. We attempted to illustrate this point comprehensively in our Fig. 4. Given that this comparative plot allows to present simultaneously a natural rendition of a number of factors that affect the attempts to measure the CMB anisotropy on the celestial rings, we believe that Fig. 4 should provide significant insights on optimization of experimental setup for future CMB experiments.

For the most ambitious CMB programmes such as *PLANCK*, many such scans will have to be merged into two-dimensional maps. The reduction of the data set from time-lines to a set of rings via the circular scan method described in this paper is a non destructive compression of the data (by two orders of magnitude in the case of *PLANCK*), and a useful intermediate step in the analysis of such data in the global analysis of CMB anisotropies on the celestial sphere. An additional advantage of this step is that the effect of any filter on the time-lines (such as those owing to the electronics, the time constant of bolometers...) can be quantified in an exact way on the rings.

ACKNOWLEDGMENTS

Original inspiration for KMG to consider the circular scanning came from discussions of the UCSB HACME experiment with P. Lubin and M. Seiffert, whereas JD's interest in the subject was stimulated by discussions with François-Xavier Désert and Jean-Loup Puget over the choice of an optimal scanning strategy for the DIABOLO 1997 observations. JD would like to thank Eric Aubourg, Nathalie Palanque-Delabrouille and Simon Prunet for help and suggestions in numerical computations of $\mathbf{\Gamma}_m$s for the first draft of this paper. CMB anisotropy power spectra in the flat CDM models were computed using the code CMBFAST (Seljak & Zaldarriaga 1996). JD was supported by a PhD research grant from CNES, the French national space agency. KMG and EH were supported in part by the Danish National Research Foundation through its establishment of the Theoretical Astrophysics Center.

REFERENCES

Bardeen J. M. et al., 1986, ApJ, 304, 15
Bersanelli et al., 1996, *COBRAS/SAMBA*: Report on the Phase A Study
Seljak U., Zaldarriaga M., 1996, ApJ, 469, 437
Zaldarriaga M., 1997, ApJ, in press (astro-ph/9709271)

This paper has been typeset from a TEX/LATEX file prepared by the author.

ASTRONOMY & ASTROPHYSICS
SUPPLEMENT SERIES

FEBRUARY I **1998**, PAGE 555

Astron. Astrophys. Suppl. Ser. **127,** 555-567 (1998)

Analysis of the accuracy of a destriping method for future cosmic microwave background mapping with the PLANCK SURVEYOR satellite

J. Delabrouille[1,2]

[1] Institut d'Astrophysique Spatiale, CNRS & Université Paris XI, Bât. 121, 91405 Orsay Cedex, France
[2] Enrico Fermi Institute, University of Chicago, 5460 South Ellis Avenue, Chicago, IL 60510, U.S.A.

Received March 20; accepted May 9, 1997

Abstract. A major problem in cosmic microwave background radiation (CMBR) anisotropy measurements is the presence of low-frequency noise in the data streams. This noise arises from thermal instabilities of optical elements or of the thermal bath, gain instabilities and $1/f$ noise in the electronics, and other poorly understood processes. If improperly monitored or processed, this excess low-frequency noise might lead to striping in the maps, compromising the success of the experiment. In this paper, we show that a simple destriping method will clean the maps obtained with the High Frequency Instrument of the PLANCK SURVEYOR mission of any significant additional noise from low-frequency drifts, provided that the knee frequency of the low frequency noise is less than the spinning frequency of the satellite, i.e. $f_{\rm knee} \leq 0.017$ Hz. For the High Frequency Instrument of PLANCK, the nominal knee frequency of the noise is $f_{\rm knee} \simeq 0.01$ Hz or less, and thus no significant striping nor increase of the noise rms is expected due to low-frequency drifts. In addition, we show that even if the knee frequency of the low frequency noise were somewhat higher than the spinning frequency of the satellite one could estimate and remove the striping with a excellent accuracy.

Key words: methods: data analysis — cosmology: cosmic microwave background — space vehicles

1. Introduction

After the encouraging results of the DMR experiment on the COBE satellite (Smoot 1992), there has been a burst of renewed interest in the anisotropies of the Cosmic Microwave Background Radiation (CMBR), both on the experimental side and on the theoretical side. While theorists refined calculations to evaluate how individual parameters of the theories affect the expected properties of the tiny fluctuations of the CMBR, experimenters, in answer to announcements of opportunities by several space agencies, proposed sophisticated new generation satellites to map the anisotropies of the CMBR with a sensitivity and angular resolution an order of magnitude better than those of COBE. Of these, the Microwave Anisotropy Probe (MAP) experiment has been selected by NASA as one of the next medium-size explorer, or midex, and the PLANCK satellite (formerly COBRAS/SAMBA) has been selected by ESA as the next medium-size mission M3.

The accuracy with which the useful cosmological information can be deduced from the data of such a mission depends on the global characteristics of the instrument and on the observing strategy: sensitivity of the detectors, spectral coverage, resolution, susceptibility to systematics, scanning strategy... the optimal solution is often a trade-off between several marginally compatible constraints, and very different strategies can be adopted.

Because a large telescope is necessary in order to achieve the high angular resolution that is mandatory to distinguish between cosmological models, the option of differential measurements implies complicated optics. Fortunately, the availability of space-qualified cryogenic devices (Benoit et al. 1994) and the development of new readout electronics (Gaertner et al. 1997) now permits to use in space bolometers cooled to 0.1 K. These are much more sensitive than available radiometers at the frequencies most interesting for cosmology, and so much more stable that for the PLANCK bolometer instrument (HFI, for High Frequency Instrument), the conservative differential approach has been abandoned in favour of total-power measurements.

In the case of the nominal PLANCK mission, the scanning of the sky is performed very simply, by rotating the

Send offprint requests to: J. Delabrouille (jacques@ias.fr)

satellite at 1 rpm around a spin axis which position on the sky is roughly anti-solar (to first order the spin axis remains in the ecliptic plane, and its position is shifted by $\sim 5'$ every 2 hours). There is some flexibility as to the direction of the spin axis, however, so that the scanning strategy can be adapted for optimal sky coverage or rejection of systematics within technical constraints (the thermal stability of the payload puts a limit on the solar aspect angle of 15°, and the telemetry rate a limit on the earth aspect angle of 15° during the dumping of the data).

The beam axis makes an angle of 70° with the spin axis, and thus scans 140° diameter circles on the sky. The PLANCK orbit is a Lissajous orbit around the sun-earth Lagrange point L2. More details on PLANCK can be found in the COBRAS/SAMBA report on the phase A study (1996).

For this observing strategy, there are several important characteristic time-scales. One scan corresponding to one complete rotation of the satellite around itself is performed in a time $T_{\rm spin} = 1$ minute. Data circles are obtained by averaging 120 such scans, and correspond to a period of two hours. Each of these data circles crosses in two points all other data circles obtained less than about 20 weeks before or after. Thus, they share a common area on the sky of at least two pixels (and more for circles that are tangent or nearly tangent). Finally, data circles corresponding to measurements separated by a 1 year period coincide on the sky. Figure 1 shows four PLANCK SURVEYOR circles on a sinusoidal projection of the sky in ecliptic coordinates.

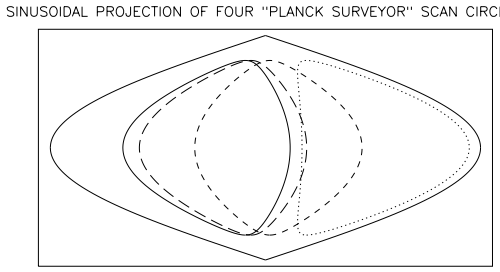

Fig. 1. Sinusoidal projection of four scans for the nominal PLANCK SURVEYOR scanning strategy. The second, third and fourth scans from the left (long-dashed, short-dashed, and dotted line) are obtained 2 weeks, 2 months, and 5 months respectively after the first (plain line). Because these circles have 140° diameters, intersections are distributed everywhere along circles, not only at ecliptic poles as for great circles. Not all pairs of circles intersect: here for instance the first and last circles, separated by a period of 5 months, have no pixel in common

All these redundancies at very different time-scales make it possible to minimise low-frequency noise effects by comparing the values the signal takes at times where the useful astrophysical signal is supposed to be the same (because the antenna is pointed at the same place on the sky) and thus estimating and correcting for low-frequency drifts.

It has recently been suggested that the scanning strategy and destriping method adopted for PLANCK might lead to striping on the maps due to excess low-frequency noise even if there were no intrinsic low frequency noise in the measurements (Wright 1996).

In that paper, the author argues correctly that relying on no more than a pixel or two per scan (namely, ecliptic poles) to readjust relative offsets might cause striping in the maps. However, when suggesting that for this reason the PLANCK maps will be striped, he seems to disregard completely two essential characteristics of the PLANCK SURVEYOR scanning strategy, which are the 15° freedom of motion of the spin axis and the 70° off-axis spin angle, any of which characteristics modifies completely the way circles on the sky intersect each other. Thus, his suggested conclusions should be regarded with extreme caution.

In the following, we investigate how well a simple destriping technique can remove the striping in the maps in the context of the PLANCK SURVEYOR mission.

2. Analysis of the "noise processing"

It is in general a reasonably good assumption that the total noise (excluding systematics that might be scan-synchronous or correlated to the signal), be a Gaussian process that can be described by a Power Spectral Density (PSD, in Volts^2 of electrical signal per Hz) typically of the form:

$$\mathcal{S}_{\rm n}(f) = a\left(1 + \left(\frac{f_{\rm knee}}{f}\right)^{\alpha}\right) \cdot \tag{1}$$

Here $f_{\rm knee}$ is a "knee frequency" at which low-frequency noise and white noise contributions to the power spectral density are statistically equal, and α is a spectral index, typically between 1.0 and 2.5, depending on the dominant physical process which generates low frequency noise. It is a good approximation to assume that $\mathcal{S}_{\rm n}(f)$ vanishes for $f < f_{\rm min}$ and $f > f_{\rm max}$, with $f_{\rm min} \sim 1/T_{\rm total}$ and $f_{\rm max} \sim 1/2T_{\rm sampling}$.

In an experiment for which the scanning strategy consists in scanning repeatedly the same circle of the sky, the sky signal for any given pixel is calculated by averaging the "samples" corresponding to this pixel. When the white noise contribution dominates the total noise, i.e. when $f_{\rm knee}$ and α are such that

$$f_{\rm max} - f_{\rm min} \gg \int_{f_{\rm min}}^{f_{\rm max}} \left(\frac{f_{\rm knee}}{f}\right)^{\alpha} {\rm d}f, \tag{2}$$

which can be simplified to $f_{\rm max}/f_{\rm knee} \gg \ln\left(f_{\rm max}/f_{\rm min}\right)$ if $\alpha = 1$, and $f_{\rm min} \ll f_{\rm max}$, or to $f_{\rm min}/f_{\rm max} \ll (\alpha - 1) \times (f_{\rm min}/f_{\rm knee})^{\alpha}$ if $\alpha > 1$ and $f_{\rm min} \ll f_{\rm max}$, then the rms

of the final noise on one scan circle obtained by averaging N consecutive scans is just the rms of the original noise divided by $\sqrt{N}$. This is not the case when the noise is significantly coloured (i.e. not white), since averaging consecutive scans actually reduces the bandwidth of the signal in such a way that most of the low-frequency noise contribution at frequencies $f < 1/T_{\rm spin}$ is filtered out. In Fourier space, the spinning and averaging process keeps all components of the signal that are harmonics of the spinning frequency, and cuts other components (this is only an approximation, but good enough for this discussion). In our case, the low-frequency contribution to the standard deviation will be much larger on a 2-hour data stream than on the corresponding circle of data obtained by averaging.

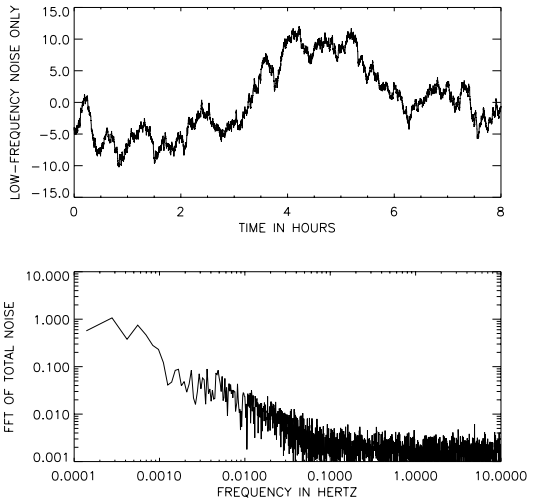

Fig. 2. Example of 8 consecutive hours of simulated low-frequency noise, with $\alpha = 2.0$ and $f_{\rm knee} = 0.10$ Hz. These values are typical for ground-based experiments which suffer from thermal fluctuations and atmospheric noise (for the PLANCK HFI, due to the extremely favourable observing conditions, we expect the low-frequency drifts to be dominated by electronics noise, i.e. $\alpha \simeq 1.0$ and $f_{\rm knee} \leq 0.01$ Hz instead). The top panel shows drifts due to the low-frequency part of the noise only, with a spectrum of the form $S(f) = a \times (f_{\rm knee}/f)^2$. The effect of adding the white noise contribution (which has a standard deviation of 1.00) would be a strong broadening of the line. The bottom panel shows the absolute value of the FFT of the total noise. The knee frequency of 0.10 Hz is clearly visible

The top plot of Fig. 2 is a plot of 8 hours of the low-frequency part of a noise with a spectrum of the form of Eq. (1), with $\alpha = 2.0$ and $f_{\rm knee} = 0.10$ Hz (which is extremely pessimistic for the PLANCK HFI, but illustrates our point better than more realistic noise: drifts on the scale of 8 hours are almost imperceptible for $\alpha = 1.0$ and $f_{\rm knee} = 0.01$ Hz unless the noise is significantly smoothed to filter high frequency components). Such figures for the noise are quite typical for ground-based CMB experiments. Only the low-frequency component is represented in the top panel of Fig. 2 (which corresponds thus to a spectrum or PSD of $S_{\rm n}(f) = (f_{\rm knee}/f)^2$). Units for noise generation have been normalised so that the rms of the white part of the noise per sample is 1.00 (and the rms per resolution element on a data circle, obtained from averaging the 120 consecutive scans of one 2-hour period for one detector, would be $1/\sqrt{120} = 0.091$ if there were no low frequency noise). In this simulation, the sampling frequency is 2034 samples per minute, which for PLANCK corresponds to one sample per 10 arcminute pixel. The bottom plot of Fig. 2 is the absolute value of the Fast Fourier Transform of the noise realization with white noise included as well as the low-frequency part. The knee frequency of about 0.10 Hz is clearly visible.

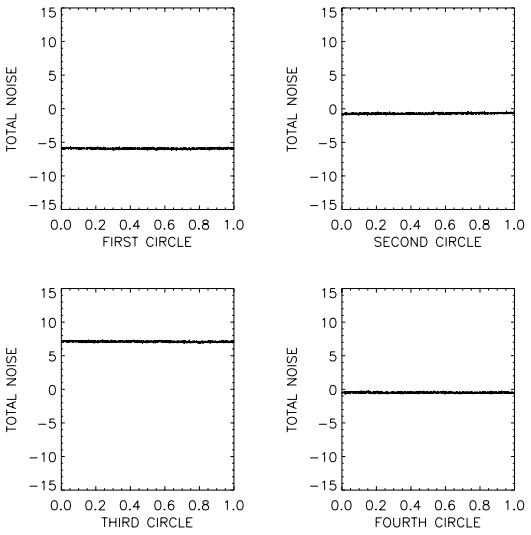

Fig. 3. Residual total noise on 4 consecutive circles, each obtained by averaging 120 consecutive 1 minute scans of the 8-hour sample of the simulated low-frequency noise plotted in Fig. 2. The data for each circle looks flat at this scale, but each circle has a very different offset

Low frequency drifts with an amplitude of a few (whereas the rms of the white part of the noise only is 1.00) are obvious in Fig. 2. The standard deviation of the total 8-hour noise (white + low-frequency) is about 2.49, that of the low-frequency part is 2.28, and that of the white part is 1.00. However, what actually happens on

circles after 120 consecutive scans have been averaged is shown in Fig. 3, where the data corresponding to the four circles obtained from this 8-hour signal are plotted with the same units on the vertical axis. Here, the white noise component has been included. The variance on each individual circle is much smaller than that of the original signal, because each circle is obtained by averaging 120 scans as explained above. Also, it is impressive to notice that almost all the power of low frequency noise now appears in the form of a different "offset" A_i for each circle i. The average level of all the circles is not the same, but low frequency drifts on each circle are much smaller than on the original time sequence.

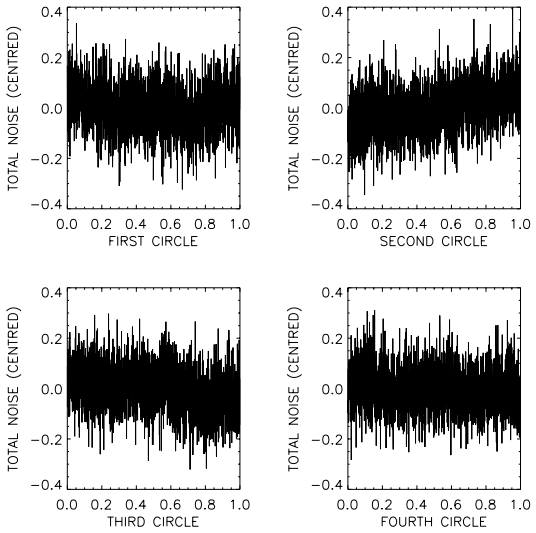

Fig. 4. Here we show the centred signal for each of the circles of Fig. 3. Note the scale compared to that of Fig. 2 and Fig. 3. Even for the very pessimistic assumed values for α and $f_{\rm knee}$, low frequency drifts are barely visible in the white noise

It is important to check whether the low frequency noise will have any effect other than to add a different offset to the data corresponding to each circle. Figure 4 shows the centred noise for each of the above 4 circles. Even with the very pessimistic values of α and $f_{\rm knee}$ used here, low-frequency drifts are almost too low to be distinguished in the dominating white noise. If however we remove the white part of the noise and look at the four circles (Fig. 5), we see clearly that some low frequency drifts are still there, which would appear if a drastic smoothing of the data were performed.

A crude estimate of the increase of the standard deviation of the noise on a circle (compared to the standard deviation of white noise only) can be obtained by integrating the PSD between $f_{\rm min} \sim f_{\rm spinning} \simeq 1/60$ Hz and $f_{\rm max} \simeq f_{\rm sampling}/2$. This method underestimates slightly the rms increase because drifts at frequencies lower than the spinning frequency are not totally cut out by the spin-chopping. The steeper the noise spectrum, the less accurate this method is. A rigorous calculation can be found in (Janssen et al. 1996) for the special case of $\alpha = 1$.

Although this additional noise power is quite low, it is at low frequency only, and the effect on the accuracy of the measurement of interesting cosmological quantities (e.g., the power spectrum of the fluctuations) should be investigated. For instance, it should be kept in mind that when the resolution of maps is degraded by smoothing, the standard deviation of pure white noise scales as the inverse of the size of the pixel, whereas the standard deviation of parallel stripes scales roughly as the square root of the size of the pixel. Quantifying the effect of striping on sophisticated statistical tests or pattern recognition methods is even harder, and may require the help of numerical simulations of two-dimensional noise maps.

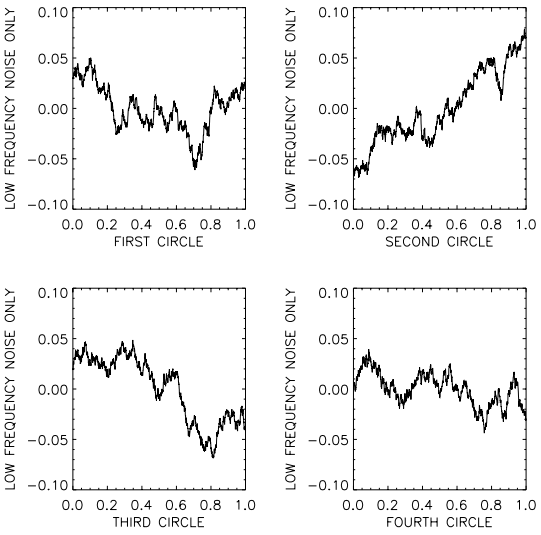

Fig. 5. Residual of low frequency component of the noise only for each of the circles of Fig. 4. These structures, which can barely be distinguished in Fig. 4, would appear more and more clearly if the data were smoothed

3. From scan circles to sky maps

What is the effect of reprojecting data circles as those of Fig. 3 on sky maps? The answer depends on the statistical properties of the noise along the "data circles", on the scanning strategy, and on the way that the relative

"offsets" of the data circles are readjusted with respect to one another.

3.1. Readjusting the offsets of the circles

It is clear from looking at Fig. 3 and from the above discussion that we should first find a way to adjust the relative values of the offsets A_i of the different data circles before reprojecting on the sky. Even for very low values of the knee frequency, there is no hope to keep the signal from diverging on time-scales of a few months. Just setting the average level of each circle to zero is not good enough, since there is no reason the average level of the useful signal on each circle should be the same, and the only measurement we have access to is signal+noise.

For PLANCK, the observing strategy ensures that, in addition to the short term redundancy provided by "spin-chopping", there is also redundancy at long periods. In particular, as each data circle (obtained from 120 superimposed scans) crosses 3360 other such circles in two spots for a 1 year mission, it is quite natural, as a first order method for suppressing low-frequency noise effects, to try to readjust the average relative offset of the data circles by imposing that all the differences between signal over the same sky pixels but observed with different rotation axis of the satellite (at different times) are minimised. One key requirement on the scanning strategy for this method to work properly is that any given circle do not cut all the other circles in just a small number of pixels, in which case the adjusted value for the offset of that circle would depend drastically on the realization of the (white part of the) noise on the pixels used for the adjustment. For PLANCK, the scanning strategy is such that all the pixels of a circle are seen by at least one other circle, and thus all of them are used for the readjustment.

This method allows one to estimate the drifts due to low-frequency noise independently of the useful signal from the sky, since only differences of the total (signal+noise) at times where the beam is pointing on the same direction of the sky are used.

What should the accuracy of this method be? For a simple scanning strategy where the spin axis of the satellite is kept in the ecliptic, all circles play the same role (total symmetry), and thus $\sigma_{\rm stripes}(i)$, the rms of the error on readjusting the offset for circle i, should be the same for all circles. If we denote by $\sigma_{\rm n}$ the rms of the noise per pixel on a single circle obtained by averaging 120 scans, the accuracy of the determination of the offsets will be of the order of $\sigma_{\rm n}/\sqrt{N_j}$, where N_j is the number of independent pixels per circle.

It would be possible to optimise the scanning so that there be no preferred direction for this residual striping (which is anyway small, as for the PLANCK HFI N_j is about 2000 to 4500, depending on the channel), but it does not seem worth compromising the monitoring of other systematics and noise in the process.

Note that if we could build an ideal experiment with no low-frequency noise, the value for $\sigma_{\rm stripes}$ that we would estimate *just from sample variance on a circle of N_j pixels* would be ${\sigma_{\rm stripes}}^2 = {\sigma_{\rm n}}^2/N_j$, and thus no significant additional striping should be added by this inversion.

In order to check the above assertions about the accuracy of offset readjusting, and to evaluate the effect of low frequency noise on PLANCK maps, a low-resolution version of the expected PLANCK data has been simulated. For the moment, the simulation of the complete data stream for one detector at the actual PLANCK resolution is out of reach of our computers. However, the conclusions obtained with a degraded resolution can be scaled to the actual resolution.

In this simulation, a vector of spin-axis positions on the sky corresponding to a scanning strategy of PLANCK is generated. Each position of the spin-axis is distant from the previous one by a step equal to the resolution at which the simulation is performed, and for each such position, a vector of beam positions on a circle of radius 70° on the sky is generated. For each beam position, a single one degree by one degree pixel on a simulated map of the sky is selected. A two-dimensional set of data corresponding to these beam positions is generated. Here we assume that the knee frequency of the low frequency noise is small enough that there be no significant low-frequency contribution to the noise along individual data circles. We simulate the effect of low frequency drifts by adding to each data circle some offset A_i.

The actual data taking process is such that the zero level of the measurements is frequently readjusted, in order to avoid the saturation of the detectors due to slow drifts in the signal. In the end, the average value of the signal on each circle is not known precisely, but certainly does not drift by more than a couple orders of magnitude (extremely conservative assumption!).

The actual inversion is performed by the following least mean square method. The linear system of equations on the constants A_i to be determined is obtained by requiring a function $S(A_1, ..., A_n)$ to be minimal. Here we take:

$$S(A_i) = \sum_{p\in{\rm sky}} \sum_{i_1=2}^{n(p)} \sum_{i_2=1}^{i_1-1} w_{i_1,i_2} \times (\delta(i_1,i_2) - A_{i_1} + A_{i_2})^2 \qquad (3)$$

where $\delta(i_1, i_2)$ is the estimated difference of offsets obtained by comparing the measurements of circle i_2 and circle i_1 on pixel p, $n(p)$ is the number of times pixel p is seen by the experiment, and w_{i_1,i_2} is a weight attributed to measurement $\delta(i_1, i_2)$. Since pixel p contributes $n(p) \times (n(p)-1)/2$ terms in the sum, we set $w_{i_1,i_2} = 2/(n(p)-1)$ (the total weight of the contribution of the $n(p)$ measurements at pixel p is thus proportional to $n(p)$).

We get the linear system to be inverted by writing that all partial derivatives of S with respect to all constants A_i should vanish. This system is degenerated, since if a set of constants $A_1, ..., A_n$ is solution, the same set with

a constant K added to all the A_i is also solution. This degeneracy is lifted by adding the requirement that the mean of the constants A_i vanish.

We first use the nominal scanning strategy of PLANCK, with a spin axis kept rigorously anti-solar, and check that the accuracy of the inversion does not depend on the input offsets for the circles, but does improve with the resolution. For each simulation, the data of the mission are stored as a table of N_i scan circles of N_j samples each. For a simulation with a 1 degree resolution, $N_i = 421$ and $N_j = 339$ for a 14 month mission and a 140° scan diameter. We evaluate the amount of striping by calculating the mean value of the signal on each scan circle, and computing the square root of the variance of the collection of N_i numbers so obtained. This is denoted as $\sigma_{\rm stripes}$.

For a 1° resolution simulation, we generate a 421×339 element table of Gaussian random numbers with rms 1. This simulates the white noise of the mission. To this noise we add offsets which simulate the low frequency drifts. Various types of offsets were considered: a) no offset, in order to test that the method does not add striping where there is none; b) a linear drift of $100i/N_i$, where i is the index of the circle and N_i the number of circles; c) a sinusoidal drift of $100\sin(2\pi i/N_i)$; d) a sequence of random offsets with an rms of 100 (hundred times the rms of the noise); e) a random walk of rms 10 per step; f) in order to check the intrinsic precision of the inversion, we try to recover the offsets of the random walk without adding any white noise.

In order to be able to compare the performance of the method in all cases above, let us consider one specific realization of the white part of the noise here, and add to it the offsets described above to get five different "noise signals". In all cases a) through e), the value of $\sigma_{\rm stripes}$ after the inversion is 0.0412, which proves that the accuracy does not depend on the offsets to be corrected for to any significant level. It is interesting to realize also that if there is no offset, the expected value of $\sigma_{\rm stripes}$ before any inversion *just from sample variance* is 0.0543 (and on the particular noise realization we used here it happened to be 0.0522), so that the method does not only remove the striping due to drifts in the offsets due to low-frequency noise if any, but does even readjust to some extent the variations in the average level of the circles due to the sample variance of the average of the N_j points on a circle. This is anecdotic, of course, but does show that no additional noise or bias is generated in the readjusting process - in fact, for a 14 month mission the method partly suppresses low frequency components of the white noise itself. It is worth stressing that the success of the method is due for a large part to the fact that all the points of any circle contribute to the evaluation of the value of its offset, and not only two points at the North and South ecliptic poles. The precision of the inversion (performed in double-precision) is evaluated from the results of case f) above, for which we get a totally negligible residual striping of $3.83\ 10^{-7}$.

In order to check that the accuracy does indeed depend on the resolution, we repeat the simulation of a) through e) for resolutions of 2° and 5°. In these cases, the value of $\sigma_{\rm stripes}$ after the inversion is 0.0549 and 0.0800 respectively, independent of the original stripes again, and below the value we get from sample variance on the original data. Note that the weight given to each term in the least-square sum above is critical to reach this accuracy. For instance, if we put the same weight to each term, too much importance is given to points on the circles that are close to the north and south ecliptic poles (because they are "seen" by many more circles than the ones in the ecliptic), and some residual striping of the order of magnitude of the white noise per pixel remains, because the value of the offset recovered depends most on the realization of the white noise at points near the poles.

We tried this inversion scheme with all kinds of offsets, with various kinds of scanning strategy and different mission durations (from 3 to 14 months). In all cases the inversion works extremely well. To be a little more illustrative, we show images of a noise generated according to method e) above, for a 1 year mission, at the resolution of 1°, reprojected on the sky, with no destriping treatment (Fig. 6) and after destriping (Fig. 7). For this simulation we used a scanning strategy for which the spin axis has been made to oscillate sinusoidally out of the ecliptic with an amplitude of 15° and a frequency of 8 oscillations per year, in order to maximise the sky coverage. Note the different scales for the amplitude of the structures that can be seen. No striping whatsoever remains on the map after the treatment.

3.2. Improving the method

3.2.1. Modelization of nominal PLANCK HFI noise

Whereas it has been made clear that our method is satisfactory to remove the striping due to low-frequency noise off maps obtained by PLANCK in the case where the knee frequency of the noise is low enough that all significant low-frequency noise appears in the form of different offsets for different circles on the sky, it is worth mentioning that if there is significant low-frequency noise power at frequencies higher than the spinning frequency then the method above may not be sufficient anymore: After relative offsets are readjusted, the next effect of low-frequency noise is to add very low level drifts along individual circles, as shown in Fig. 4 and Fig. 5, and one should investigate whether or not these fluctuations may cause a problem.

It is not easy to generate degraded resolution maps that preserve exactly both the visual aspect (i.e. do we see striping or not) and the statistical properties of the noise for real 1/f noise on all scales. For instance, the rms amplitude of low-frequency noise relative to white noise depends on the sampling frequency (the variance of white noise is proportional to the sampling frequency, and the

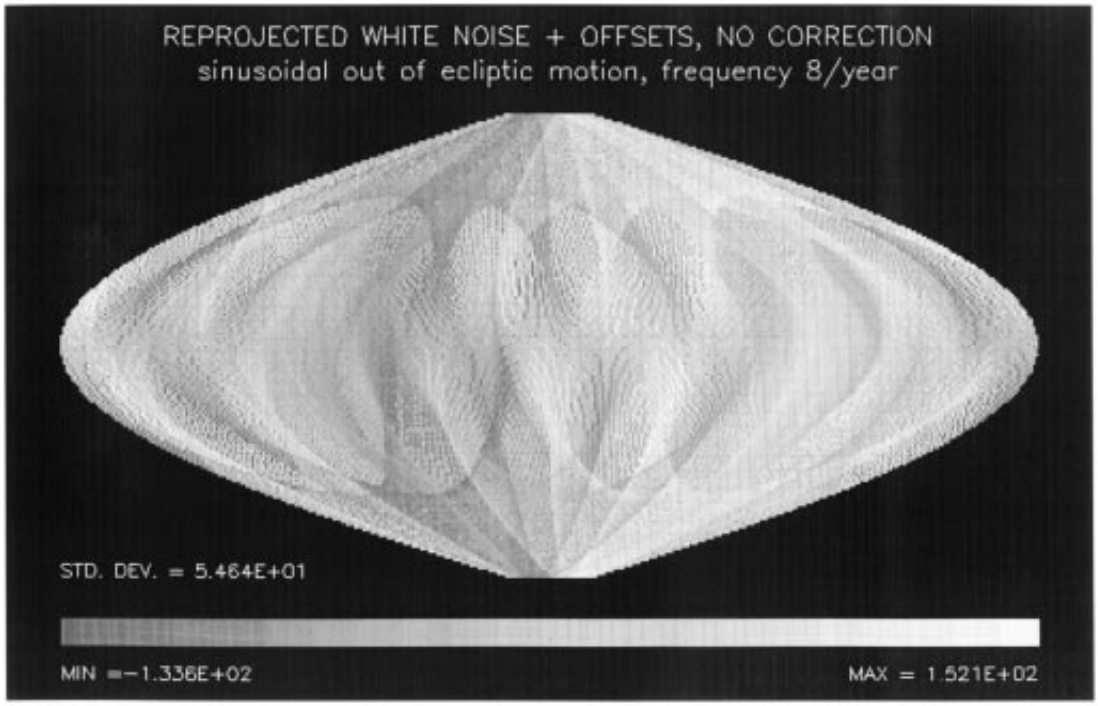

Fig. 6. Map of reprojected noise and offsets if no processing of the signal is done. The map is heavily striped. This should not be interpreted as a noise map for PLANCK, as at least some offset readjustment can be made before reprojecting. For this data set, the average level of circles has been left to drift some hundred sigma away!

variance of 1/f noise diverges proportionnaly to the logarithm of the sampling frequency). For these simulations, we decide to scale both the white noise and low frequency noise rms to their rms values for 10 arcminute pixels, independently of the size of the pixel of the simulation (here 1 square degree pixels). The next problem is that for 1 degree resolution simulations, instead of one circle every two hours, we generate one circle every day. However, we wish to preserve the possible correlations between consecutive circles of the simulation. Thus, we have to face the problem that either the correlations between consecutive circles is right, or the relative value of the offset between circles taken at a 1 day time interval is right. As the paragraph above demonstrates that relative levels of the circles do not play a role in the accuracy of the readjustment of the offsets, and as offsets will not drift too far away because they will be readjusted by the instrument anyway, I decided, in this next part of the simulations, to preserve the correlation between consecutive circles rather than their relative offsets.

Thus, a time sequence for the noise is generated by the following method: for a 1 year mission at a 1 degree resolution, we need 361 circles (so as to re-observe the first circle at the end of the mission) of 339 points each. Each of these circles is obtained from averaging 120 scans, and thus we need to generate a noise of almost 15 million data points. We wish that these data points preserve the relative rms amplitudes of low-frequency noise to white noise of the full 10 arcminute resolution maps, i.e. we do not smooth the noise down to the lower resolution, but rather affect to each 1 degree by 1 degree pixel the noise of its "central" 10 arcminute by 10 arcminute pixel, which corresponds to reprojecting on a 1 degree resolution map a subset of the 10 arcminute resolution pixels. This method preserves best the relative rms of the low-frequency residual noise and the white noise part of true full resolution maps.

Generating a 15 million sample dataset with a "true" 1/f spectrum is out of the reach of the computer I used. In order to generate the 1/f noise, an under-sampled (by a factor 32) white noise with a unit variance was

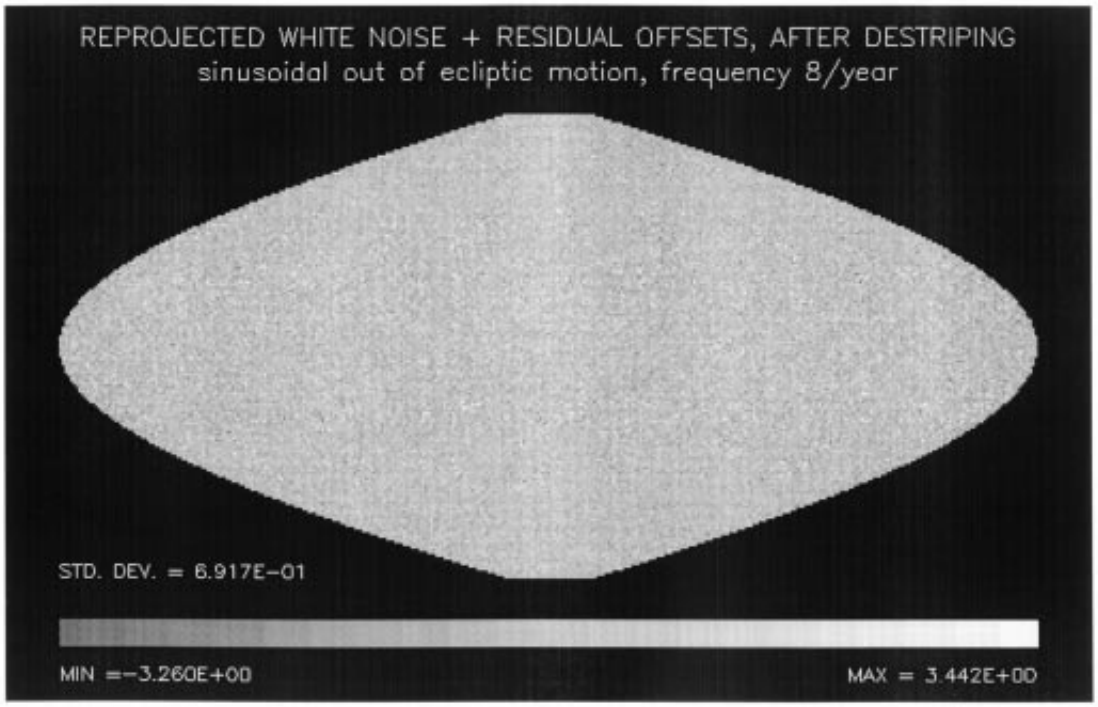

Fig. 7. Map of reprojected noise and offsets after signal-preserving destriping (see text). Compare with Fig. 6 (note the different colour scale!)

generated, converted to Fourier space (by FFT) where it was multiplied by $(f_{\rm knee}/f)^{\alpha/2}$ (with the appropriate rescaling to take into account the effect of undersampling). Then we compute the inverse FFT and interpolate between the samples, add consecutive circles by packs of 120 to get a 361×339 array of data points (corresponding to 361 circles), and add to it a randomly generated array of 361×339 data points with a Gaussian statistic and a rms of $1/\sqrt{120}$. We then re-scale everything conveniently by multiplying by $\sqrt{120}$. We check that the relative rms values and the visual aspect of the circles obtained in this way are correct by comparing with circles obtained from fully fast-sampled simulated low frequency noise of a few circles only.

First, let us generate such a noise for nominal low-frequency noise parameters for the PLANCK SURVEYOR High Frequency Instrument, i.e. $f_{\rm knee} = 0.01$ Hz and $\alpha = 1$, and readjust the offsets by the method of the previous sub-section. Again we use the scanning strategy for which the spin axis has been made to oscillate sinusoidally out of the ecliptic with an amplitude of 15° and a frequency of 8 oscillations per year. The resulting output noise map is shown in Fig. 8. No striping whatsoever is apparent on the map, and the increase of the rms of the noise is about 0.47%. In order to check the effect of the out-of-ecliptic motion, we do the simulation with the same realization of the noise but with a nominal anti-solar spin axis. In this case the increase in the rms of the noise is 0.49% (no significant difference). Repeated simulations with different noise realizations show that the small difference is always in favour of sinusoidal out-of-ecliptic motion.

In their 1996 paper, Janssen et al. computed the maximum noise increase along a scan circle. Adapted to our notations, their formula can be written as

$$F_{\rm max} \simeq \left(1 + \frac{T_{\rm spin} f_{\rm knee}}{m}(2\ln m + 0.743)\right)^{1/2} \qquad (4)$$

where m is the number of independent data points along one circle. For PLANCK, $m = 2034$ for a 10 arcminute resolution, $T_{\rm spin} = 60$ sec., $f_{\rm knee} = 0.01$ Hz, and we get $F_{\rm max} \simeq 1.01$. The average additional noise that we find by simulations is about half the maximum noise increase along one circle they predict (for diametrically opposed pixels), so our result is fully consistent with theirs. This

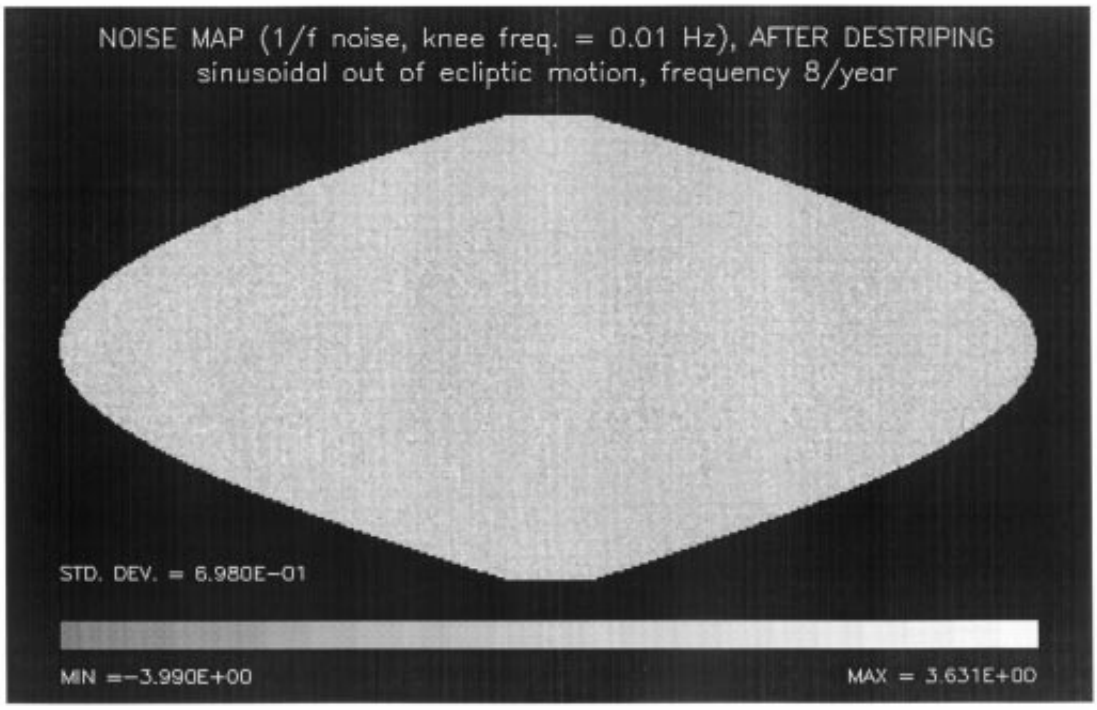

Fig. 8. Map of reprojected simulated 1/f noise, $f_{\rm knee} = 0.01$ Hz, $\alpha = 1.0$, after correction by simple offset readjustment. The very-low level residual striping can not be distinguished by eye. This is a 1-degree resolution projection of what the processed PLANCK all-sky noise could look like. The relative standard deviations of reprojected white noise and reprojected residual striping are those of a 10 arcminute resolution mission (see text)

is consistent with most of the additional noise being due to small drifts along individual circles.

In order to give an estimate of the order of magnitude of striping and the statistical properties of the noise, we show, in Fig. 9, plots of cuts through the noise map of Fig. 8. On both panels of Fig. 9, total noise is represented with diamonds, and the component of noise due to residual low-frequency drifts (obtained by computing the difference between the output map of Fig. 8 and the map obtained by simple reprojection on the sky of the white part of the noise used for the simulation only) as a plain line. In these plots, although one point only is plotted per degree, the spread in represented points is typical of what we would get in a 10 arcminute resolution map, not a smoothed map with a 1 degree resolution. The top panel corresponds to a vertical cut in the middle of the map, and the bottom panel to an horizontal cut in the middle of the map (thus perpendicular to the expected striping, if any). In both cases the total contribution of striping to the total noise is very small. The structure of residual low-frequency noise is not similar in both directions, which can be understood from the direction of scans. The small structure on the plot of residual low-frequency noise in the middle of the top panel is characteristic of very-low level striping. Finally, it is obvious from the distribution of the total noise that some regions of the sky are integrated more than others (as the region around ecliptic longitude $\lambda = 0°$ and ecliptic latitude $\beta = -45°$).

3.2.2. Monitoring unforeseen instabilities

Now we want to investigate what would happen if the low frequency noise were much worse than expected. The purpose of the following simulations, using parameters that are unrealistically pessimistic for the PLANCK HFI, is to show that the conclusions of the previous paragraphs do not depend drastically on noise assumptions, and that even unforeseen instabilities can be monitored quite well with PLANCK. Here we assume that some unwanted temperature fluctuations (for instance) generate low frequency noise with the parameters of $f_{\rm knee} = 0.1$ Hz (ten times the nominal!) and $\alpha = 2.0$ (same parameters as were used

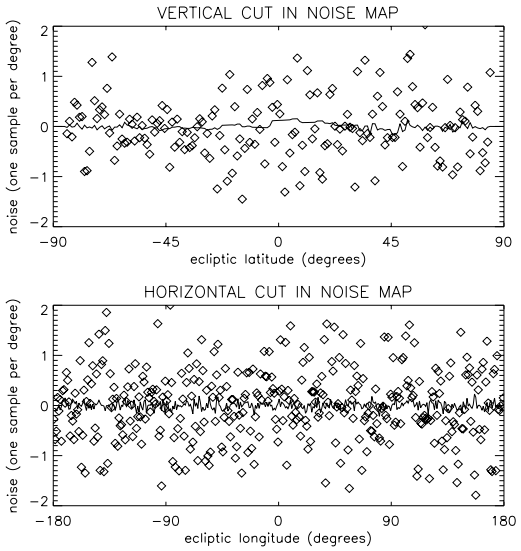

Fig. 9. Cuts through the noise map of Fig. 8. The top panel is a vertical cut at 0° ecliptic longitude, and the bottom panel an horizontal cut along the ecliptic plane. The plain line represents residual striping, obtained by computing the difference between the map of reprojected total noise after inversion, and the map of reprojected white part of the noise only. Diamonds correspond to the total reprojected noise. The structure due to striping is very small compared to the total noise, and the noise r.m.s. increase due to this residual striping is 0.47% on a 10 arcminute resolution map of the sky

to generate the plots of Figs. 2-5). The resulting increase in the noise standard deviation of the map (scaled to 10 arcminute pixel size as explained above) is 7.5%. This is not much, but it is significantly larger than the value of 0.5% obtained with nominal HFI noise. Because the excess power is not white, it could be distinguished on the maps, especially at degraded resolution. For instance, within the framework of standard assumptions of physical cosmology this could cause trouble for the estimation of the properties of primordial supra-horizon fluctuations, which are important for constraining the models of inflation. It could also be annoying in pattern recognition methods looking for discontinuities generated by cosmic strings. Finally, some optimal foreground separation methods rely on statistical methods which use prior knowledge of the spectrum (as a function of scale) of the various astrophysical components (i.e. cirrus clouds, primary CMB, free-free, synchrotron, etc...).

In order to get rid of this residual striping, we can try a more sophisticated treatment. The idea again is to find a method which does not depend on the real signal, and thus estimates low-frequency components by using signal differences on common pixels. To do so, we can adapt the above method: instead of fitting just one constant for each data circle, we fit a function with more parameters, so that along a scan circle i we may write

$$n_i(j) \sim \sum_k A_{ik} f_k(j). \quad (5)$$

In the equation above, j indexes the samples along the data circle, and the functions $f_k(j)$ are vectors of a basis of functions on which to decompose the noise $n_i(j)$. Typically, the set of functions f_k can be sines and cosines (Fourier modes), or polynomials, or other well-chosen functions. The sum we want then to minimise is:

$$S(A_{ik}) = \sum_{p \in sky} \sum_{i_1=2}^{n(p)} \sum_{i_2=1}^{i_1-1} w_{i_1,i_2} \times (\delta(i_1,i_2) - F_1 + F_2)^2 \quad (6)$$

where

$$F_1(i_1, j_1) = \sum_k A_{i_1 k} f_k(j_1(p)) \quad (7)$$

and

$$F_2(i_2, j_2) = \sum_k A_{i_2 k} f_k(j_2(p)) \quad (8)$$

where $j_1(p)$ and $j_2(p)$ index the samples on circles i_1 and i_2 respectively for which pixel p on the sky is observed.

In this framework, for instance, we can take advantage of the fact that the most interesting property of low-frequency noise is that it does not have significant high frequency power. Because of that, low frequency noise itself can be estimated by sampling it at a much lower sampling frequency than the true signal. Thus, it seems to be a good idea to use as a basis of functions for noise estimation along one circle a set of a few "top-hat" functions, corresponding each to a constant on a fraction of a circle only.

Using the same realization of low-frequency and white noise, we inverted the data set by adjusting more than one constant for each circle. We do it for two constants (i.e. one for each half-circle), three constants (one for each third of a circle), and four constants (one for each fourth of a circle). We performed the inversion also using $1^{\rm st}$ through $3^{\rm rd}$ degree polynomials.

Table 1 gives the noise rms increase on maps in all the cases discussed above. Maps, too numerous to be shown here, can be provided by the author upon request. It is clear that the residual striping can be reduced substantially by this method (and the more so at high resolution, as more points are available to estimate individual parameters of the fitting functions f_k, whereas no more functions are needed at high resolution than at low resolution to estimate low-frequency structures in the noise). 4 constants per circle instead of one is the best that could be done because of computational limitations. For full-resolution

data sets, with a good computer, going to 10 constants or so should be possible and should improve the fit significantly. This method, used on very pessimistic noise here for illustrative purposes, could also be applied to destripe further full-resolution maps obtained with nominal PLANCK HFI noise, if one wished to do so.

Table 1. Increment of noise rms from residual striping for very pessimistic low-frequency drifts (assumed knee frequency $f_{\rm knee} = 0.1$ Hz and spectral index $\alpha = 2.0$). Different sets of fitting functions have been used to remove striping effects (see text). Polynomials seem to perform better up to 3 constants per circle (second degree polynomial). This can be understood from looking at the shape of drifts along circles (Fig. 5). A polynomial of degree 3 is worse as far as reducing the rms of the noise is concerned for 1 degree resolution simulations. This is due to insufficient constraints and to the fact that the weighting of the terms in the least square sum is not adapted to such functions, but to step functions. In fact the 3$^{\rm rd}$ degree polynomial induces a dipole on the sky, which can be understood as high degree polynomial fits have a known tendency to oscillate between the data points that carry the most weight. Most of the additional power comes from this dipole, although it is much lower in amplitude than the "real" physical (cosmological or Doppler-induced!) dipole. Maps can be made available by the author upon request

FIT	steps	polynomials
1 constant	+ 7.5%	+ 7.5%
2 constants	+ 3.3%	+ 2.9%
3 constants	+ 3.2%	+ 2.3%
4 constants	+ 2.9%	+ 6.3%

For each noise spectrum there must be an optimal set of functions f_k to use. For instance, a 1$^{\rm st}$ degree polynomial is better than two constants per circle for very steep noise spectra, as most of the low-frequency noise contribution comes from very low frequencies. For each noise spectrum, there is also an optimal number of functions f_k to use, as the more functions one uses, the less constraints one gets on each of the functions. These optimal solutions are yet to be found.

4. Discussion and comments

4.1. Finding an optimal scanning strategy?

It is clear that for the methods discussed above to work there must be some optimal way of scanning the sky. The scanning strategy sets the position of the points of intersection of the different circles described by the main beam of PLANCK SURVEYOR.

For instance, scanning the sky with great circles while the spin axis is kept rigorously anti-solar insures that every circle crosses every other circle in exactly two points, namely the North and South ecliptic poles. For this scanning strategy, pixels close to the ecliptic are seen by only one circle (obtained from adding together a great number of scans, 120 scans for PLANCK) every 6 months.

If instead of great circles the main beam scans 140 degree diameter circles while keeping the spin axis anti-solar, as for the nominal PLANCK mission, there is no common "reference" pixel seen by all circles. Circles cross each other on points that are spread out all over their length. Circles observed within a small time difference cross at high ecliptic latitudes. Circles observed at a time interval of about 140 days cross near the ecliptic plane, as shown in Fig. 1. For readjusting offsets, this scanning strategy should be superior, as all the pixels along one circle contribute to the evaluation of the offset of that circle.

This is not the case for great circles, and as emphasised by Wright (1996), the estimated offset for a great circle that crosses reference circles in only two points will depend on the realization of the noise at these two points. Of course, one could rely on more than two points, by using also points along the scan close to the pole which overlap substantially (and thus compare measurements in more extended "polar caps"). Some significant improvement can probably be obtained in this way, as after all consecutive great circles have a significant area in common, but one may have to worry about high spatial frequency signals on the sky (especially point sources) for fields of view that do not exactly coincide. Iterative correction of oversampled maps could be a solution, but this may lead to complications. Finally, this scanning strategy using great circles with anti-solar spin axis does not allow the natural improvement of the method where the low-frequency noise realization along each circle is fitted by sampling it at its own Nyquist frequency, as there are points of the circle (near the ecliptic plane) which are not seen by any other circle (here we talk about circles obtained by adding consecutive scans, not about individual scans).

In both cases, the destriping method can be improved by allowing the spin axis to move away from the anti-solar. This is especially true if great circles are used to scan the sky, as then circles would not cross other circles in two points only. A small displacement of the spin axis of a circle along the ecliptic makes it cross other circles near the ecliptic poles, and a small displacement of the spin axis perpendicular to the ecliptic makes the circle cross nearby circles near the ecliptic plane. Thus, in order to insure that all points along a circle have other circles to be compared to, a reasonable solution *as far as destriping is concerned* could be to move the spin axis on circles around the anti-solar. This has the additional characteristic that the sun aspect angle is kept constant, which may help monitoring the thermal stability of the payload if the satellite is reasonably symmetric around its spin axis. Sinusoidal or tooth-saw motion out of the ecliptic while the spin axis turns around the ecliptic are also possible solutions.

It has been argued by some authors (Wright et al. 1996) that based on the inherent difficulty of stabilising the sensitivity of an instrument to enough precision, it is desirable for the raw data to be collected in differential form. However, we would like to stress that even differential measurements can potentially suffer from low-frequency noise, because any asymmetric source of fluctuations (as for instance thermal fluctuations of optical elements which are not commonly shared) generates low-frequency instabilities in the measurements. Differential measurements are not just desirable: in a way or another they are, on short time scales, a necessity for radiometers, less stable than bolometers by orders of magnitude for CMB applications. These authors proved that it is possible to invert megapixel differential data. This task may be much harder if in addition some unforeseen low-frequency drifts contribute to the data stream.

Finally, whereas the method works better if the spin-axis is not kept rigorously anti-solar, it should be kept in mind than moving the spin axis could generate increased thermal instabilities of the payload or increased sidelobe contamination. For PLANCK, it has been shown that thermal specifications could be fulfilled if this angle does not exceed 15 degrees, which is sufficient for destriping and for sky integration time optimisation if desired. The freedom to move the spin axis also allows one to readjust the scanning strategy after the preliminary analysis of the first few days or weeks of data if necessary. This flexibility is a powerful tool for monitoring systematic effects.

4.2. Comments on the method

Our method has the very nice property that the correction of low frequency drifts does not require the inversion of a huge matrix, contrarily to methods which try to make a least square fit of both the signal on all pixels of the sky and all additional parameters as those which allow for the correction of low-frequency drifts. A (relatively!) small matrix of a few thousands by a few thousands needs to be inverted, which is an easy task for modern computers.

However, the method relies heavily on the assumption that different measurements on the same pixel of the sky should generate the same "useful" signal, apart from different contributions of low-frequency drifts. If this is not the case, it is still possible to fit the noise in much the same way, but this will require the inversion of huge matrices of typically a few million by a few million entries. Iterative methods make this task possible if there are not too many non-vanishing elements. Potential sources of trouble include far sidelobe straylight, which depends on the orientation of the satellite and on the position of bright sources in the sky, polarisation (for detectors sensitive to polarisation, because again what is measured on a given pixel with a polarisation-sensitive detector depends on the orientation of the satellite, as shown in Fig. 10), and all other potential systematic effects. The remark about the complications induced by the measurement of polarised light is also true when one wants to invert differential data (e.g. Wright et al. 1996). These authors' method for inverting the differential signal expected from the MAP satellite also relies on the assumption that the useful signal from a given pixel is independent of satellite orientation. This assumption is not correct for polarisation sensitive measurements, obviously, and again this can make the inversion significantly harder than expected.

Bolometers are not sensitive to polarisation unless one places a polariser in front of them.

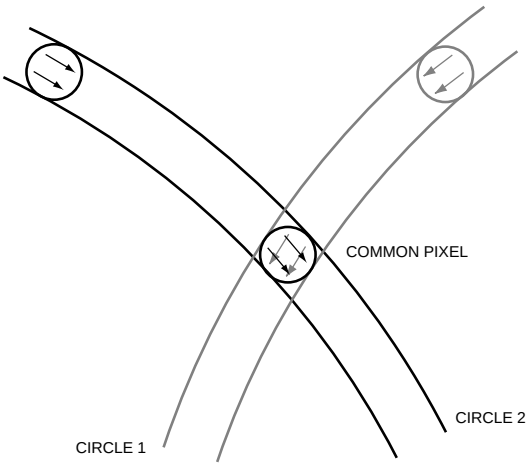

Fig. 10. Representation of the effect of polarisation-sensitive measurements on the comparison of relative measured signal on different scans. Small circles with arrows inside represent different fields of view of the instrument (main beam). On the common pixel in the middle of the figure, measurements on different scans do not see the same polarised light, as indicated by the arrows. This may complicate attempts to measure polarisation and/or the inversion of polarised differential data

5. Conclusion

In this paper, some aspects of the expected statistical properties of the noise for the future PLANCK satellite, both on data streams and on output maps, have been analysed. It has been shown that for the bolometer instrument of PLANCK, no significant striping on the maps is expected due to low-frequency noise only for the nominal knee frequency of the noise of 0.01 Hz, as a simple destriping method can remove low-frequency noise effects on maps. For the PLANCK HFI the increase in the noise rms on destriped maps is expected to be less than half a percent. Even if the low-frequency noise were much worse

than expected, correction for its effects are possible with the scanning strategy of PLANCK, contrarily to what has been suggested by Wright (Wright 1996).

However, we believe that testing the extraction of cosmological information using simulated noise maps is probably one of the best way to quantify the exact consequences of instrumental effects such as striping, and continuing efforts should be made towards simulating realistic noise maps in the future.

An optimised scanning strategy must be devised by including simulations of most foreseen systematics. We believe that this optimum can be found within the orbit specifications for PLANCK, which minimise most of the potentially harmful systematic effects.

Acknowledgements. Valuable comments from G. Smoot and helpful discussions with F.-X. Désert, R. Gispert, J.-M. Lamarre and J.-L. Puget are gratefully acknowledged. This work was supported by a PhD research grant from CNES, the French national space agency.

References

Benoit A., et al., SAE Technical Paper Series 941276

COBRAS/SAMBA report on the phase A study: this report summarises the results of the scientific and technical study activities of the COBRAS/SAMBA phase A; copies can be obtained from J. Tauber or O. Pace, both at ESTEC, Keplerlaan 1, P.O. Box 299, 2200 AG Noordwijk, The Netherlands, or from S. Volonté, Programme Coordination and Planning Office, ESA HQ, D/SCI, 8-10, rue Mario Nikis, 75738 Paris Cedex 15, France

Gaertner S., et al., 1997 (accepted for publication in A&A)

Janssen M.A., et al., 1996 (submitted to ApJ) (astro-ph 9602009)

Smoot G.F., 1992, ApJ 396, L1

Wright E., paper presented 22 November 1996 at the IAS CMB Data Analysis Workshop (astro-ph 9612006)

Wright E.L., Hinshaw G., Bennett C.L., 1996, ApJ 458, L53

ASTRONOMY & ASTROPHYSICS
SUPPLEMENT SERIES

MARCH II **2000**, PAGE 499

Astron. Astrophys. Suppl. Ser. **142**, 499–509 (2000)

Destriping of polarized data in a CMB mission with a circular scanning strategy

B. Revenu[1], A. Kim[1], R. Ansari[2], F. Couchot[2], J. Delabrouille[1], and J. Kaplan[1]

[1] Physique Corpusculaire et Cosmologie, Collège de France, 11 place Marcelin Berthelot, F-75231 Paris Cedex 05, France
[2] Laboratoire de l'Accélérateur Linéaire, IN2P3 CNRS, Université Paris Sud, F-91405 Orsay, France

Received May 28; accepted December 16, 1999

Abstract. A major problem in Cosmic Microwave Background (CMB) anisotropy mapping, especially in a total-power mode, is the presence of low-frequency noise in the data streams. If unproperly processed, such low-frequency noise leads to striping in the maps. To deal with this problem, solutions have already been found for mapping the CMB temperature fluctuations but no solution has yet been proposed for the measurement of CMB polarization. Complications arise due to the scan-dependent orientation of the measured polarization. In this paper, we investigate a method for building temperature and polarization maps with minimal striping effects in the case of a circular scanning strategy mission such as the PLANCK mission.

Key words: methods: data analysis; cosmology: cosmic microwave background; polarization

1. Introduction

Theoretical studies of the CMB have shown that the accurate measurement of the CMB anisotropy spectrum C_ℓ^T with future space missions such as PLANCK will allow for tests of cosmological scenarios and the determination of cosmological parameters with unprecedented accuracy. Nevertheless, some near degeneracies between sets of cosmological parameters yield very similar CMB temperature anisotropy spectra. The measurement of the CMB polarization and the computation of its power spectrum (Seljak 1996; Zaldarriaga 1998) may lift to some extent some of these degeneracies. It will also provide additional information on the reionization epoch and on the presence of tensor perturbations, and may also help in the identification and removal of polarized astrophysical foregrounds (Kinney 1998; Kamionkowski 1998; Prunet & Lazarian 1999).

A successful measurement of the CMB polarization stands as an observational challenge; the expected polarization level is of the order of 10% of the level of temperature fluctuations ($\Delta T/T \simeq 10^{-5}$). Efforts have thus gone into developing techniques to reduce or eliminate spurious non-astronomical signals and instrumental noise which could otherwise easily wipe out real polarization signals. In a previous paper (Couchot et al. 1999), we have shown how to configure the polarimeters in the focal plane in order to minimize the errors on the measurement of the Stokes parameters. In this paper, we address the problem of low frequency noise.

Low frequency noise in the data streams can arise due to a wide range of physical processes connected to the detection of radiation. $1/f$ noise in the electronics, gain instabilities, and temperature fluctuations of instrument parts radiatively coupled to the detectors, all produce low frequency drifts of the detector outputs. The spectrum of the total noise can be modeled as a superposition of white noise and components behaving like $1/f^\alpha$ where $\alpha \geq 1$, as shown in Fig. 1.

This noise generates stripes after reprojection on maps, whose exact form depends on the scanning strategy. If not properly subtracted, the effect of such stripes is to degrade considerably the sensitivity of an experiment. The elimination of this "striping" may be achieved using redundancies in the measurement, which are essentially of two types for the case of PLANCK:

- each individual detector's field of view scans the sky on large circles, each of which is covered consecutively many times (~ 60) at a rate of about $f_{\rm spin} \sim 1$ rpm. This permits a filtering out of non scan-synchronous fluctuations in the circle constructed from averaging the consecutive scans.
- a survey of the whole sky (or a part of it) involves many such circles that intersect each other (see Fig. 2); the exact number of intersections depends on the scanning

Send offprint requests to: B. Revenu
e-mail: revenu@cdf.in2p3.fr

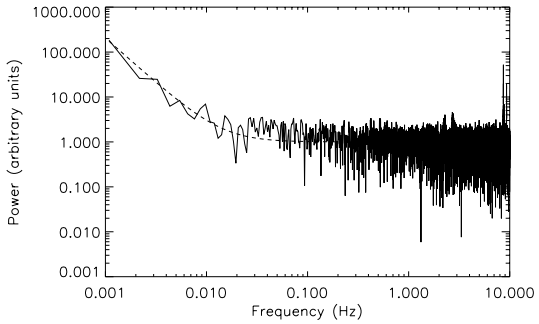

Fig. 1. The power spectrum of the K34 bolometer from Caltech, the same type of bolometer planned to be used on the PLANCK mission. The measurement was performed at the SYMBOL test bench at I.A.S., Orsay (supplied by Michel Piat). The knee frequency of this spectrum is ~ 0.014 Hz and the planned spin frequency for PLANCK is 0.016 Hz. We can model the spectrum as the function $S(f) = 1 + \left(\frac{1.43\ 10^{-2}}{f}\right)^2$ (dashed line)

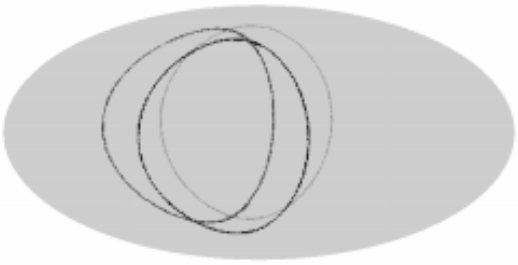

Fig. 2. The Mollweide projection of 3 intersecting circles. For clarity, the scan angle between the spin axis and the main beam axis is set to 60° for this figure

strategy but is of the order of 10^8 for the PLANCK mission: this will allow to constrain the noise at the intersection points.

One of us (Delabrouille 1998) has proposed to remove low frequency drifts for unpolarized data in the framework of the PLANCK mission by requiring that all measurements of a single point, from all the circles intersecting that point, share a common sky temperature signal. The problem is more complicated in the case of polarized measurements since the orientation of a polarimeter with respect to the sky depends on the scanning circle. Thus, a given polarimeter crossing a given point in the sky along two different circles will not measure the same signal, as illustrated in Fig. 3.

The rest of the paper is organized as follows: in Sect. 2, we explain how we model the noise and how low frequency drifts transform into offsets when considering the circles instead of individual scans. In Sect. 3, we explain how polarization is measured. The details of the algorithm for removing low-frequency drifts are given in Sect. 4. We present the results of our simulations in Sect. 5 and give our conclusions in Sect. 6.

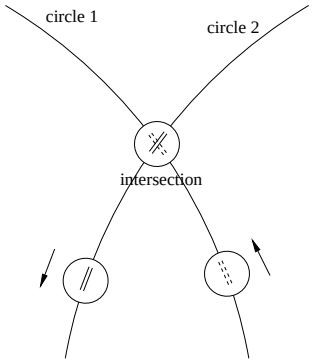

Fig. 3. The orientation of polarimeters at an intersection point. This point is seen by two different circles corresponding to two different orientations of the polarimeters in the focal plane. For clarity, we have just represented one polarimeter

2. Averaging noise to offsets on circles

As shown in Fig. 1, the typical noise spectrum expected for the PLANCK High Frequency Instrument (HFI) features a drastic increase of noise power at low frequencies $f \leq 0.01$ Hz. We model this noise spectrum as:

$$S(f) = \sigma^2 \times \left(1 + \sum_i \left(\frac{f_i}{f}\right)^{\alpha_i}\right). \quad (1)$$

The knee frequency $f_{\rm knee}$ is defined as the frequency at which the power spectrum due to low frequency contributions equals that of the white noise. The noise behaves as pure white noise with variance σ^2 at high frequencies. The spectral index of each component of the low-frequency noise, α_i, is typically between 1 and 2, depending on the physical process generating the noise.

The Fourier spectrum of the noise on the circle obtained by combining N consecutive scans depends on the exact method used. The simplest method, setting the circle equal to the average of all its scans, efficiently filters out all frequencies save the harmonics of the spinning frequency (Delabrouille et al. 1998b). Since the noise power mainly resides at low frequencies (see Fig. 1), the averaging transforms – to first order – low frequency drifts into constant offsets different for each circle and for each polarimeter. This is illustrated in the comparison between Figs. 4 and 5. More sophisticated methods for recombining the data streams into circles can be used, as χ^2 minimization, Wiener filtering, or any map-making method

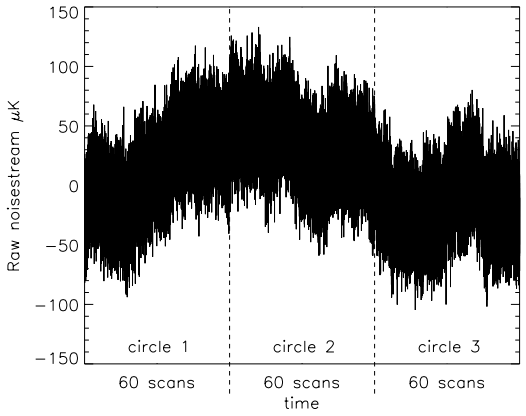

Fig. 4. Typical $1/f^2$ low frequency noise stream. Here, $f_{\rm knee} = f_{\rm spin} = 0.016$ Hz, $\alpha = 2$ and $\sigma = 21$ μK (see Eq. 1). This noise stream corresponds to 180 scans or 3 circles (60 scans per circle) or a duration of 3 hours

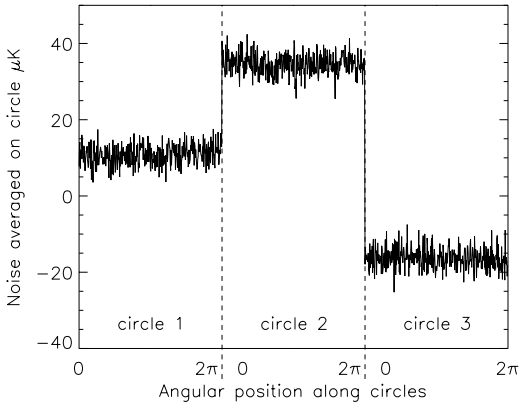

Fig. 5. The residual noise on the 3 circles after averaging. To first approximation, low frequency drifts are transformed into offsets, different for each circle and each polarimeter. Note the expanded scale on the y-axis as compared to that of Fig. 4

projecting about 6 10^5 samples onto a circle of about 5 10^3 points. For simplicity, we will work in the following with the circles obtained by simple averaging of all its consecutive scans.

We thus model the effect of low frequency drifts as a constant offset for each polarimeter and each circle. This approximation is excellent for $f_{\rm knee} \leq f_{\rm spin}$. The remaining white noise of the h polarimeters is described by one constant $h \times h$ matrix.

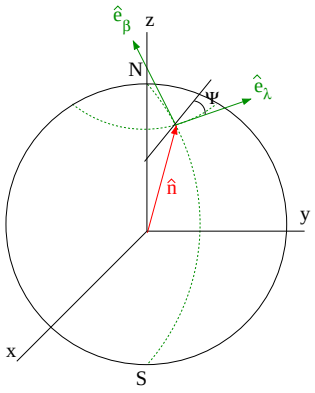

Fig. 6. The reference frame used to define the Stokes parameters and angular position Ψ of a polarimeter. Ψ lies in the plane $(\hat{e}_\lambda, \hat{e}_\beta)$

3. The measurement of sky polarization

3.1. Observational method

The measurement with one polarimeter of the linear polarization of a wave coming from a direction $\hat{\boldsymbol{n}}$ on the sky, requires at least three measurements with different polarimeter orientations. Since the Stokes parameters Q and U are not invariant under rotations, we define them at each point $\hat{\boldsymbol{n}}$ with respect to a reference frame of tangential vectors $(\hat{e}_\lambda, \hat{e}_\beta)$. The output signal given by a polarimeter looking at point $\hat{\boldsymbol{n}}$ is:

$$M_{\rm polar} = \frac{1}{2}(I + Q\cos 2\Psi + U \sin 2\Psi) \qquad (2)$$

where Ψ is the angle between the polarimeter and $\hat{e}_\lambda$[1]. In the following, we choose the longitude-latitude reference frame as the fixed reference frame on the sky (see Fig. 6).

3.2. Destriping method

The destriping method consists in using redundancies at the intersections between circle pairs to estimate, for each circle i and each polarimeter p, the offsets O_i^p on polarimeter measurements. For each circle intersection, we require that all three Stokes parameters *in a fixed reference frame* in that direction of the sky, as measured on each of the intersecting circles, be the same. A χ^2 minimization leads to a linear system whose solution gives the offsets. By subtracting these offsets, we can recover the Stokes parameters corrected for low-frequency noise.

[1] We do not consider the V Stokes parameter since no net circular polarization is expected through Thomson scattering.

3.3. Formalism

We consider a mission involving n circles. The set of all circles that intercept circle i is denoted by $\mathcal{I}(i)$ and contains $N_{\mathcal{I}(i)}$ circles. For any pair of circles i and j, we denote the two points where these two circles intersect (if any) by $\{i,j,\delta\}$. In this notation i is the circle currently scanned, j the intersecting circle in set $\mathcal{I}(i)$, and δ indexes the two intersections ($\delta = 1(-1)$ indexes the first (second) point encountered from the northernmost point on the circle) so that the points $\{j,i,-\delta\}$ and $\{i,j,\delta\}$ on the sky are identical.

The Stokes parameters at point $\{i,j,\delta\}$, with respect to a fixed global reference system, are denoted by a $3-$vector $\boldsymbol{S}_{i,j,\delta}$, with

$$\boldsymbol{S}_{i,j,\delta} = \boldsymbol{S}_{j,i,-\delta} = \begin{pmatrix} I \\ Q \\ U \end{pmatrix} (\hat{\boldsymbol{n}} \equiv \{i,j,\delta\}). \tag{3}$$

At intersection $\{i,j,\delta\}$, the set of measurements by h polarimeters travelling along the scanning circle i is a $h-$vector denoted by $\boldsymbol{M}_{i,j,\delta}$, and is related to the Stokes parameters at this point by (see Eq. 2):

$$\boldsymbol{M}_{i,j,\delta} = \boldsymbol{\mathcal{A}}_{i,j,\delta}\boldsymbol{S}_{i,j,\delta} \tag{4}$$

where $\boldsymbol{\mathcal{A}}_{i,j,\delta}$ is the $h \times 3$ matrix:

$$\boldsymbol{\mathcal{A}}_{i,j,\delta} = \frac{1}{2}\begin{pmatrix} 1 & \cos 2\Psi_1(i,j,\delta) & \sin 2\Psi_1(i,j,\delta) \\ \vdots & \vdots & \vdots \\ 1 & \cos 2\Psi_p(i,j,\delta) & \sin 2\Psi_p(i,j,\delta) \\ \vdots & \vdots & \vdots \\ 1 & \cos 2\Psi_h(i,j,\delta) & \sin 2\Psi_h(i,j,\delta) \end{pmatrix}.$$

$\Psi_p(i,j,\delta) \in [0,\pi]$ is the angle between the orientation of polarimeter p and the reference axis in the fixed global reference frame (see Fig. 6). The matrix $\boldsymbol{\mathcal{A}}_{i,j,\delta}$ can be factorised as

$$\boldsymbol{\mathcal{A}}_{i,j,\delta} = \boldsymbol{\mathcal{A}}\boldsymbol{R}_{i,j,\delta}. \tag{5}$$

The constant $h\times 3$ matrix $\boldsymbol{\mathcal{A}}$ characterizes the geometrical setup of the h polarimeters in the focal reference frame:

$$\boldsymbol{\mathcal{A}} = \frac{1}{2}\begin{pmatrix} 1 & 1 & 0 \\ \vdots & \vdots & \vdots \\ 1 & \cos 2\Delta_p & \sin 2\Delta_p \\ \vdots & \vdots & \vdots \\ 1 & \cos 2\Delta_h & \sin 2\Delta_h \end{pmatrix} \tag{6}$$

where Δ_p is the angle between the orientations of polarimeters p and 1, so we have $\Psi_p = \Psi_1 + \Delta_p$ and $\Delta_1 = 0$. The rotation matrix $\boldsymbol{R}_{i,j,\delta}$ brings the focal plane to its position at intersection $\{i,j,\delta\}$ when scanning along circle i:

$$\boldsymbol{R}_{i,j,\delta} = \begin{pmatrix} 1 & 0 & 0 \\ 0 & \cos 2\Psi_1(i,j,\delta) & \sin 2\Psi_1(i,j,\delta) \\ 0 & -\sin 2\Psi_1(i,j,\delta) & \cos 2\Psi_1(i,j,\delta) \end{pmatrix}. \tag{7}$$

4. The algorithm

4.1. The general case

To extract the offsets from the measurements, we use a χ^2 minimization. This χ^2 relates the measurements $\boldsymbol{M}_{i,j,\delta}$ to the offsets $\boldsymbol{O}_i$ and the Stokes parameters $\boldsymbol{S}_{i,j,\delta}$, using the redundancy condition (3). In order to take into account the two contributions of the noise (see Sect. 2) and of the Stokes parameters (see Eq. 4), we model the measurement as:

$$\boldsymbol{M}_{i,j,\delta} = \boldsymbol{\mathcal{A}}\boldsymbol{R}_{i,j,\delta}\,\boldsymbol{S}_{i,j,\delta} + \boldsymbol{O}_i + \text{white noise}. \tag{8}$$

so that we write

$$\chi^2 = \sum_{i,j\in\mathcal{I}(i),\delta=\pm1} (\boldsymbol{M}_{i,j,\delta} - \boldsymbol{O}_i - \boldsymbol{\mathcal{A}}\boldsymbol{R}_{i,j,\delta}\,\boldsymbol{S}_{i,j,\delta})^T \times {\boldsymbol{N}_i}^{-1} (\boldsymbol{M}_{i,j,\delta} - \boldsymbol{O}_i - \boldsymbol{\mathcal{A}}\boldsymbol{R}_{i,j,\delta}\,\boldsymbol{S}_{i,j,\delta}). \tag{9}$$

where $\boldsymbol{N}_i$ is the $h\times h$ matrix of noise correlation between the h polarimeters.

Minimization with respect to $\boldsymbol{O}_i$ and $\boldsymbol{S}_{i,j,\delta}$ yields the following equations:

$${\boldsymbol{N}_i}^{-1} \sum_{j\in\mathcal{I}(i),\delta=\pm1} (\boldsymbol{M}_{i,j,\delta} - \boldsymbol{O}_i - \boldsymbol{\mathcal{A}}\boldsymbol{R}_{i,j,\delta}\,\boldsymbol{S}_{i,j,\delta}) = 0, \tag{10}$$

and

$$\boldsymbol{R}^{-1}_{i,j,\delta}\,\boldsymbol{\mathcal{A}}^T\,{\boldsymbol{N}_i}^{-1}\,(\boldsymbol{M}_{i,j,\delta} - \boldsymbol{O}_i - \boldsymbol{\mathcal{A}}\boldsymbol{R}_{i,j,\delta}\,\boldsymbol{S}_{i,j,\delta}) + \boldsymbol{R}^{-1}_{j,i,-\delta}\boldsymbol{\mathcal{A}}^T{\boldsymbol{N}_j}^{-1}\,(\boldsymbol{M}_{j,i,-\delta} - \boldsymbol{O}_j - \boldsymbol{\mathcal{A}}\boldsymbol{R}_{j,i,-\delta}\,\boldsymbol{S}_{i,j,\delta}) = 0. \tag{11}$$

We can work with a reduced set of transformed measurements and offsets which can be viewed as the Stokes parameters in the focal reference frame and the associated offsets which are the 3 dimensional vectors:

$$\begin{aligned} &\mathcal{S}_{i,j,\delta} = {\boldsymbol{X}_i}^{-1}\,\boldsymbol{\mathcal{A}}^T\,{\boldsymbol{N}_i}^{-1}\boldsymbol{M}_{i,j,\delta} \quad \text{and} \\ &\boldsymbol{\Delta}_i = {\boldsymbol{X}_i}^{-1}\,\boldsymbol{\mathcal{A}}^T\,{\boldsymbol{N}_i}^{-1}\boldsymbol{O}_i, \\ &\text{where } \boldsymbol{X}_i = \boldsymbol{\mathcal{A}}^T\,{\boldsymbol{N}_i}^{-1}\,\boldsymbol{\mathcal{A}}. \end{aligned} \tag{12}$$

Equations (10) and (11) then simplify to:

$$\sum_{j\in\mathcal{I}(i),\,\delta=\pm1} (\mathcal{S}_{i,j,\delta} - \boldsymbol{\Delta}_i - \boldsymbol{R}_{i,j,\delta}\,\boldsymbol{S}_{i,j,\delta}) = 0, \tag{13}$$

and

$$\boldsymbol{R}^{-1}_{i,j,\delta}\,\boldsymbol{X}_i\;(\mathcal{S}_{i,j,\delta} - \boldsymbol{\Delta}_i - \boldsymbol{R}_{i,j,\delta}\,\boldsymbol{S}_{i,j,\delta}) + \boldsymbol{R}^{-1}_{j,i,-\delta}\,\boldsymbol{X}_j\;(\mathcal{S}_{j,i,-\delta} - \boldsymbol{\Delta}_j - \boldsymbol{R}_{j,i,-\delta}\,\boldsymbol{S}_{i,j,\delta}) = 0. \tag{14}$$

$\boldsymbol{R}_{i,j,\delta}\,\boldsymbol{S}_{i,j,\delta}$ in Eq. (14) can be solved for and the result inserted in Eq. (13). After a few algebraic manipulations,

one gets the following linear system for the offsets $\boldsymbol{\Delta}_i$ as functions of the data $\mathcal{S}_{i,j,\delta}$:

$$\sum_{j\in\mathcal{I}(i),\delta=\pm1}\left[\mathbb{1}+\widetilde{\boldsymbol{R}}(i,j,\delta)\,{\boldsymbol{X}_j}^{-1}\,\widetilde{\boldsymbol{R}}(i,j,\delta)^{-1}\,\boldsymbol{X}_i\right]^{-1}\times$$
$$\left[\boldsymbol{\Delta}_i-\widetilde{\boldsymbol{R}}(i,j,\delta)\,\boldsymbol{\Delta}_j-\mathcal{S}_{i,j,\delta}+\widetilde{\boldsymbol{R}}(i,j,\delta)\,\mathcal{S}_{j,i,-\delta}\right]=0, \quad (15)$$

where the rotation

$$\widetilde{\boldsymbol{R}}(i,j,\delta)=\boldsymbol{R}_{i,j,\delta}\,\boldsymbol{R}^{-1}_{j,i,-\delta} \quad (16)$$

brings the focal reference frame from its position along scan j at intersection $\{i,j,\delta\}$ to its position along scan i at the same intersection (remember that $\{i,j,\delta\}=\{j,i,-\delta\}$). Note that $\widetilde{\boldsymbol{R}}(i,j,\delta)=\widetilde{\boldsymbol{R}}(j,i,-\delta)^{-1}$. In this linear system, we need to know the measurements of the polarimeters at the points $\{i,j,\delta\}$ and $\{j,i,-\delta\}$. These two points on circles i and j respectively will unlikely correspond to a sample along these circles. So we have linearly interpolated the value of the intersection points from the values measured at sampled points. For a fixed circle i, this is a $3\times N_{\mathcal{I}(i)}$ linear system. In Eq. (15), i runs from 1 to n, therefore the total matrix to be inverted has dimension $3n\times 3n$. However, because the rotation matrices are in fact two dimensional (see Eq. 7), the intensity components Δ^I_i of the offsets only enter Eq. (15) through their differences $\Delta^I_i-\Delta^I_j$ so that the linear system is not invertible: the rank of the system is $3n-1$. In order to compute the offsets, we can fix the intensity offset on one particular scanning circle or add the additionnal constraint that the length of the solution vector is minimized.

Once the offsets $\boldsymbol{\Delta}_i$ are known, the Stokes parameters in the global reference frame $(\hat{e}_\lambda,\hat{e}_\beta)$ at a generic sampling k of the circle i, labeled by $\{i,k\}$ are estimated as

$$\boldsymbol{S}_{i,k}=\boldsymbol{R}^{-1}_{i,k}\left(\mathcal{S}_{i,k}-\boldsymbol{\Delta}_i\right), \quad (17)$$

where $\boldsymbol{R}_{i,k}$ is the rotation matrix which transforms the focal frame Stokes parameters into those of the global reference frame.

The quantities $\mathcal{S}_{i,k}$ are the Stokes parameters measured in the focal frame of reference at this point and are simply given in terms of the measurements $\boldsymbol{M}_{i,k}$ (see Eq. 12) by:

$$\mathcal{S}_{i,k}={\boldsymbol{X}_i}^{-1}\,\boldsymbol{\mathcal{A}}^T\,{\boldsymbol{N}_i}^{-1}\boldsymbol{M}_{i,k}. \quad (18)$$

The matrix

$$\boldsymbol{N}_i^{\rm Stokes}=\left(\boldsymbol{\mathcal{A}}^T\,\boldsymbol{N}_i^{-1}\,\boldsymbol{\mathcal{A}}\right)^{-1} \quad (19)$$

is the variance matrix of the Stokes parameters on circle i. Note that this algorithm is totally independent of the pixelization chosen which only enters when reprojecting the Stokes parameters on the sphere.

4.2. Uncorrelated polarimeters, with identical noise

When the polarimeters are uncorrelated with identical noise, the variance matrix reduces to $\boldsymbol{N}_i=\mathbb{1}/{\sigma_i}^2$ and the matrices $\boldsymbol{X}_i$ can all be written as

$$\boldsymbol{X}_i=\frac{1}{{\sigma_i}^2}\,\boldsymbol{X} \text{ with } \boldsymbol{X}=\boldsymbol{\mathcal{A}}^T\boldsymbol{\mathcal{A}}.$$

Case of "Optimized Configurations"

We have shown (Couchot et al. 1999) that the polarimeters can be arranged in "Optimized Configurations", where the h polarimeters are separated by angles of π/h. If the noise level of each of the h polarimeters is the same and if there are no correlation between detector noise, then the errors of the Stokes parameters are also decorrelated and the matrix $\boldsymbol{X}$ has the simple form:

$$\boldsymbol{X}=\frac{n}{8}\begin{pmatrix}2&0&0\\0&1&0\\0&0&1\end{pmatrix}. \quad (20)$$

Because this matrix commutes with all rotation matrices $\widetilde{\boldsymbol{R}}(i,j,\delta)$, Eq. (15) simplifies further to

$$\frac{N_{\mathcal{I}(i)}}{\sigma^2_{\mathcal{I}(i)}}\boldsymbol{\Delta}_i-\sum_{m\in\mathcal{I}(i)}\frac{1}{\sigma_i^2+\sigma_j^2}\left(\widetilde{\boldsymbol{R}}(i,j,1)+\widetilde{\boldsymbol{R}}(i,j,-1)\right)\boldsymbol{\Delta}_j$$
$$=\sum_{j\in\mathcal{I}(i),\delta=\pm1}\frac{1}{\sigma_i^2+\sigma_j^2}\left(\mathcal{S}_{i,j,\delta}-\widetilde{\boldsymbol{R}}(i,j,\delta)\,\mathcal{S}_{j,i,-\delta}\right), \quad (21)$$

where the sum over δ is explicit on the left side of the equation and we have defined an average error $\sigma_{\mathcal{I}(i)}$ along circle i by

$$\frac{N_{\mathcal{I}(i)}}{\sigma^2_{\mathcal{I}(i)}}=\sum_{j\in\mathcal{I}(i)}\frac{2}{\sigma_i^2+\sigma_j^2},$$

and where the rotation matrix $\widetilde{\boldsymbol{R}}(i,j,\delta)$ is defined by Eq. (16). Rotations $\widetilde{\boldsymbol{R}}(i,j,\delta)$ and $\widetilde{\boldsymbol{R}}(i,j,-\delta)=\widetilde{\boldsymbol{R}}(j,i,\delta)^{-1}$ correspond to the two intersections between circles i and j. Equation (21) can be simplified further. We can separate the $\boldsymbol{\Delta}_i$ and the $\mathcal{S}_{i,j,\delta}$ into scalar components related to the intensity: Δ^I_i, $\mathcal{S}^I_{i,j,\delta}$ and 2-vectors components related to the polarization: $\boldsymbol{\Delta}^P_i$, $\mathcal{S}^P_{i,j,\delta}$. We obtain then two separate equations, one for the intensity offsets Δ^I_i, which is exactly the same as in the unpolarized case (see Appendix A):

$$\sum_{j\in\mathcal{I}(i)}\frac{2}{\sigma_i^2+\sigma_j^2}\left(\Delta^I_i-\Delta^I_j\right)=$$
$$\sum_{j\in\mathcal{I}(i),\delta=\pm1}\frac{1}{\sigma_i^2+\sigma_j^2}\left(\mathcal{S}^I_{i,j,\delta}-\mathcal{S}^I_{j,i,-\delta}\right), \quad (22)$$

and one for the polarization offsets $\mathbf{\Delta}_i^P$:

$$\frac{N_{\mathcal{I}(i)}}{\sigma^2_{\mathcal{I}(i)}}\,\mathbf{\Delta}_i^P - \sum_{j\in\mathcal{I}(i)} \frac{2}{\sigma_i^2+\sigma_j^2}\,\cos(2\Psi_{ij})\;\mathbf{\Delta}_j^P = \sum_{j\in\mathcal{I}(i),\delta=\pm1} \frac{1}{\sigma_i^2+\sigma_j^2}\left(\mathbb{S}^P_{i,j,\delta} - \boldsymbol{\mathcal{R}}(i,j,\delta)\,\mathbb{S}^P_{j,i,-\delta}\right), \quad (23)$$

where $\Psi_{ij} = \Psi_1(i,j,\delta) - \Psi_1(j,i,-\delta)$ is the angle of the rotation that brings the focal reference frame along scan j on the focal reference frame along scan i at intersection $\{i,j,\delta\}$. The two dimensional matrix $\boldsymbol{\mathcal{R}}(i,j,\delta)$ is the rotation sub-matrix contained in $\widetilde{\boldsymbol{R}}(i,j,\delta)$ (see Eq. 16). Note that all mixing between polarization components have disappeared from the left side of Eq. (23)). Therefore we are left with two different $n\times n$ matrices to invert in order to solve for the offsets $\mathbf{\Delta}_i$, instead of one $3n\times 3n$ matrix.

As in Eq. (15), the linear system in Eq. (22) involves differences between the offsets Δ_i^I, the matrix is not invertible, and we find the solution in the same way as in the general case. On the other hand, for the polarized offsets Δ_i^P, the underlying matrix of Eq. (23) is regular as expected.

5. Simulations and test of the algorithm

5.1. Methods

We now discuss how we test the method using numerical simulations. For each simulated mission, we produce several maps. The first, which we use as the standard "reference" of comparison, is a projected map of a mission with only white noise, $f_{\rm knee} = 0$. The remaining maps include $1/f$ plus white noise streams with $f_{\rm knee} = \eta f_{\rm spin}$, $\eta \in \{1,2,5,10\}$. The first of these is an "untreated" image which is projected with no attempt to remove striping affects. In the second "zero-averaged" map, we attempt a crude destriping by subtracting its average to each circle. The final "destriped" map is constructed using the algorithm in this paper. We subtract the input maps (I, Q and U) from the final maps in order to get maps of noise residuals. Note that in case of a zero signal sky, setting the average of each circle to zero is better than destriping by nature because the offsets are only due to the noise. With a real sky, both signal and noise contribute to the average so that zeroing circle not only removes the noise but also the signal. Giard et al. (1999) have attempted to refine their method by fitting templates of the dipole and of the galaxy before subtracting a baseline from each circle. They concluded that an additional destriping (they used the algorithm of Delabrouille 1998) is needed.

5.2. Simulated missions

In order to test its efficiency, the destriping algorithm has been applied to raw data streams generated from simulated observations using various circular scanning strategies representative of a satellite mission as Planck, different "Optimized Configurations", and various noise parameters. The resulting maps were then compared with input and untreated maps to test the quality of the destriping.

The input temperature (I) maps are the sum of galaxy, dipole, and a randomly generated standard CDM anisotropy map (we used HEALPIX[2] and CMBfast[3]). Similarly, the polarization maps Q and U are the sum of the galaxy and CMB polarizations. The CMB polarization maps are randomly generated assuming a standard CDM scenario. For the galactic polarization maps, we constructed a random, continuous and correlated vector field defined on the 2-sphere with a correlation length of 5° and a maximum polarization rate of 20% (100% gave similar results). Given the temperature map of the sky (not including CMB contribution), we can thus construct two polarization maps for Q and U.

5.3. Results

We first consider the case of destriping pure white noise and check that the destriping algorithm does not introduce spurious structure. Once this is verified, we apply the destriping algorithm to low frequency noise. We find that the quality of the destriping is significantly dependent on η only. To demonstrate visually the quality of the destriping, we produce projected sky maps with the input galaxy, dipole and CMB signal subtracted.

For temperature maps, we can compare Figs. 7, 8 and 9. The eye is not able to see any differences between the white noise map and the noise residual on the destriped map. We will see in the following how to quantify the presence of structures. For the "zero-averaged circles" map, the level of the structure is very high and make it impossible to compute the power spectrum of the CMB (see Fig. 13).

For the Q Stokes parameter, Fig. 10 shows the white noise map, Fig. 11 shows the destriped map for $\eta = 1$. Figure 12 shows a map where the offsets are calculated as the average of each circle. The maps for U are very similar. As for the I maps, the destriped map is very similar to the white noise map. There exist some residual structure on the "zero-averaged circles" map. To assess quantitatively the efficiency of the destriping algorithm, we have first studied the power spectra C_ℓ^T, C_ℓ^E, C_ℓ^B, C_ℓ^{TE} and C_ℓ^{TB} calculated from the I, Q and U maps (Zaldarriaga & Seljak 1997; Kamionkowski et al. 1997).

The reference sensitivity of our simulated mission is evaluated by computing the average spectra of 1000 maps of reprojected mission white noise. This reference sensitivity falls, within sample variance, between the two dotted

[2] http://www.tac.dk/~healpix/
[3] http://www.sns.ias.edu/~matiasz/CMBFAST/cmbfast.html

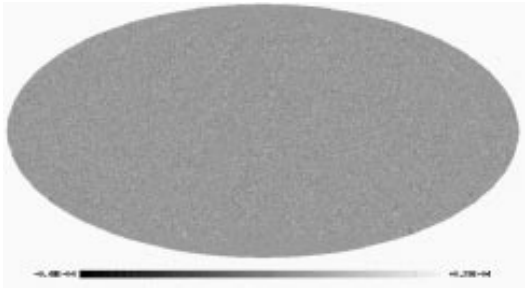

Fig. 7. The Mollweide projection of the residuals of the $I-$Stokes parameter for a white noise mission. The scale is in Kelvins. The parameters of the simulation leading to this map are described in Appendix B

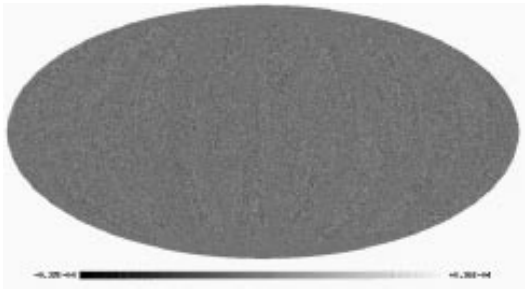

Fig. 8. The Mollweide projection of the residuals of the $I-$Stokes parameter after zeroing the average of the circles, for $1/f$ noise plus white noise with $\eta = 1$

Fig. 9. The Mollweide projection of the residuals of the $Q-$Stokes parameter for a white noise mission

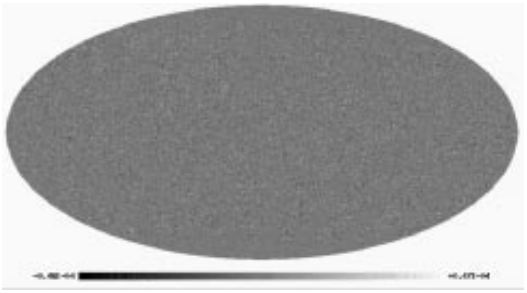

Fig. 10. The Mollweide projection of the residuals of the $Q-$Stokes parameter after zeroing the average of the circles, for $1/f$ noise plus white noise with $\eta = 1$. Although the remaining structures seem small, they are responsible for the excess of power in C_ℓ^E, see Fig. 15

lines represented in Figs. 13, 14, 15 and 16 and below the dotted line in Figs. 17 and 18. Figures 13 and 14 show the spectra C_ℓ^T corresponding to $f_{\rm knee}/f_{\rm spin} = 1$ and 5 respectively, for the T field. Similarly, Figs. 15 and 16 are the spectra C_ℓ^E. The B field is not represented because it is very similar to E. Figures 17 and 18 represent the correlation between E and T: C_ℓ^{ET}. For $f_{\rm knee}/f_{\rm spin} = 1$, we see that we are able to remove very efficiently low frequency drifts in the noise stream: the destriped spectra obtained are compatible with the white spectrum (within sample variance). Similar quality destriping is achieved for any superposition of $1/f$, $1/f^2$ and white noise, provided that the knee frequency is lower than or equal to the spin frequency. In the case of $f_{\rm knee}/f_{\rm spin} = 5$, the method as implemented here leaves some striping noise on the maps at low values of ℓ. Modeling the noise as an offset is no longer adequate and a better model of the averaged low-frequency noise is required (superposition of sine and cosine functions for instance), or a more sophisticated method for constructing one circle from 60 scans. We again note that the value of the ratio $f_{\rm knee}/f_{\rm spin}$ for both Planck HFI and LFI is likely to be very close to unity (in Fig. 1, $f_{\rm knee}^{\rm measured} \sim 0.014$ Hz and $f_{\rm spin} = 0.016$ Hz).

To quantify the presence of stripes in the maps of residuals, we can compute the value of the "striping" estimator $\mathrm{rms}\left(a_{\ell\ell}^{T,E,B}\right)/\mathrm{rms}\left(a_{\ell 0}^{T,E,B}\right)$, because stripes tend to appear as structure grossly parallel to the iso-longitude circles. In the case of pure white noise with a uniform sky coverage, this value is 1. Here, because of the scanning strategy, the sky coverage is not uniform and the value of this estimator is greater than 1, showing that it is not specific of the striping. In order to get rid of the effect of non-uniform sky coverage, we express the estimator $\mathrm{rms}\left(a_{\ell\ell}^{T,E,B}\right)/\mathrm{rms}\left(a_{\ell 0}^{T,E,B}\right)$ in units of $\mathrm{rms}\left(a_{\ell\ell}^{T,E,B}\right)/\mathrm{rms}\left(a_{\ell 0}^{T,E,B}\right)$ for the white noise. This new estimator is specific to the striping. The results in Table 1 show the improvement achieved by the destriping algorithm although the result is still not perfect.

6. Discussions and conclusions

Comparison with other methods. Although no other method has yet been developped specifically for destriping polarized data, many methods exist for destriping

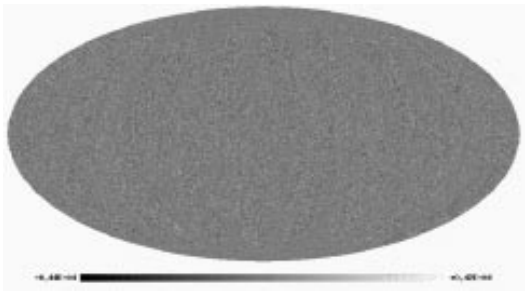

Fig. 11. The Mollweide projection of the residuals of the $Q-$Stokes parameter after destriping of $1/f$ noise plus white noise with $\eta = 1$

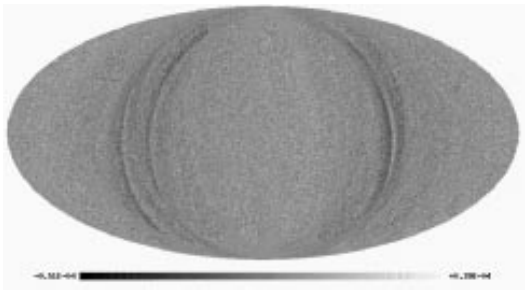

Fig. 12. The Mollweide projection of the residuals of the $Q-$Stokes parameter after zeroing the average of the circles, for $1/f$ noise plus white noise with $\eta = 1$. Although the remaining structures seem small, they are responsible for the excess of power in C_ℓ^E, see Fig. 15

Table 1. Values of rms $\left(a_{\ell\ell}^{T,E,B}\right)$ /rms $\left(a_{\ell 0}^{T,E,B}\right)$ as a function of $\eta = f_{\rm knee}/f_{\rm spin}$ in units of rms $\left(a_{\ell\ell}^{T,E,B}({\rm WN})\right)$ /rms $\left(a_{\ell 0}^{T,E,B}({\rm WN})\right)$ We have checked that the systematic difference between the zero-averaged E and B fields is randomly in favor of E and B depending on the particular sky simulation

Method	$f_{\rm knee}/f_{\rm spin}$	T	E	B
white noise	0	1	1	1
destriped	**0.5**	**1.19**	**1.05**	**1.03**
zero-averaged	0.5	51.9	9.23	3.64
undestriped	0.5	6.98	7.04	15.2
destriped	**1**	**1.24**	**1.12**	**1.19**
zero-averaged	1	52.2	9.91	3.95
undestriped	1	10.7	10.9	7.51
destriped	**2**	**1.26**	**1.32**	**1.23**
zero-averaged	2	49.5	10.2	3.85
undestriped	2	6.41	9.97	8.18
destriped	**5**	**1.35**	**1.39**	**1.38**
zero-averaged	5	49.8	10.4	3.99
undestriped	5	11.3	8.24	12.4

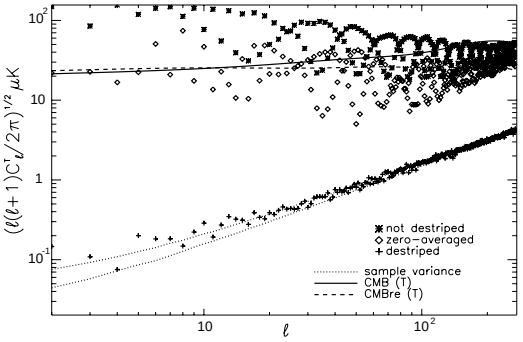

Fig. 13. Efficiency of destriping for the T field with $f_{\rm knee}/f_{\rm spin} = 1$. The sample variance associated to a pure white noise mission is plotted as the dotted lines. The "destriped spectrum" is very close to the white noise spectrum (within the limits due to the sample variance). The zero-averaged and the "not destriped" spectra are a couple of orders of magnitude above. The solid line represents a standard CDM temperature spectrum and the dashed line represents a CDM temperature spectrum with reionization

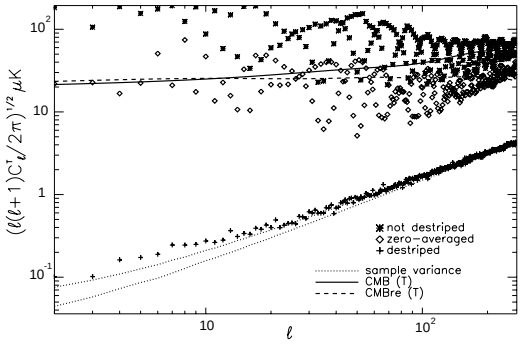

Fig. 14. Efficiency of destriping for the T field with $f_{\rm knee}/f_{\rm spin} = 5$. The modelling of low-frequency noise with an offset is no longer sufficient and the destriping leaves some power at low values of ℓ. Nevertheless, it remains a very good way to significantly reduce the effect of low-frequency noise

unpolarized CMB data, which could be adapted to polarized data as well.

We first comment on the classical method which consists in modelling the measurement as

$$m_{\rm t} = A_{\rm tp} T_{\rm p} + n_{\rm t} \tag{24}$$

where A is the so-called "pointing matrix", T a vector of temperatures in pixels of the sky, $m_{\rm t}$ the data and $n_{\rm t}$

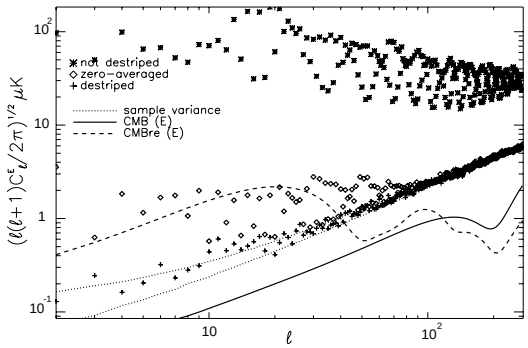

Fig. 15. Efficiency of destriping for the E field for $f_{\rm knee}/f_{\rm spin} = 1$. The zero-averaged spectrum is not as bad as for T but the residual striping we can see in Fig. 12 leads to some excess of power for low values of ℓ (up to $\ell \sim 100$). We do not see such effect in the destriped spectrum (and maps). The spectra for the B fields are very similar. The solid line represents a standard CDM E spectrum and the dashed line represents a CDM E spectrum with reionization

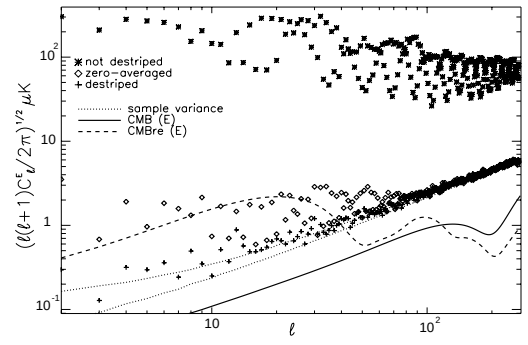

Fig. 16. Same as Fig. 15 but for $f_{\rm knee}/f_{\rm spin} = 5$. The spectra for the B fields are very similar

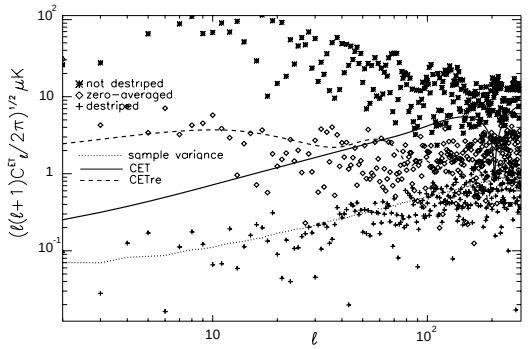

Fig. 17. Same as Fig. 15 for the ET-correlation for $f_{\rm knee}/f_{\rm spin} = 1$

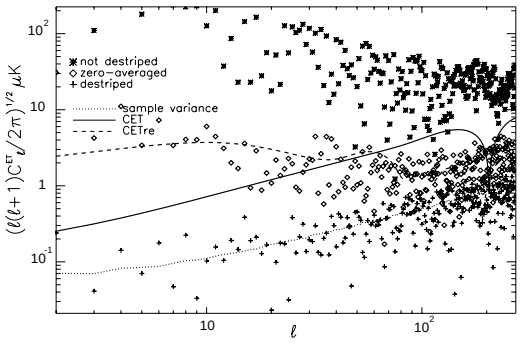

Fig. 18. Same as Fig. 17 but for $f_{\rm knee}/f_{\rm spin} = 5$

the noise. The problem is solved by inversion, yielding an estimator of the signal:

$$\tilde{T_{\rm p}} = [A^{\rm t} N^{-1} A]^{-1} A^{\rm t} N^{-1}\, m, \tag{25}$$

where $N = \langle n n^{\rm t} \rangle$ is the noise correlation matrix and $A^{\rm t}$ is the transposed matrix of A.

This method can be extended straightforwardly to polarized measurements, at the price of extending by a factor of $3 \times h$ the size of the matrix $A_{\rm tp}$, by 3 that of vector $T_{\rm p}$ (replaced by $(I_{\rm p}, Q_{\rm p}, U_{\rm p})$), and by h that of the data stream (remember that h is the number of polarimeters). The implementation of this formally simple solution may turn into a formidable problem when megapixel maps are to be produced. Numerical methods have been proposed by a variety of authors (Wright 1996; Tegmark 1997), that use properties of the noise correlation matrix (symmetry, band-diagonality) and of the pointing matrix (sparseness). Such methods, however, rely critically on the assumption that the noise is a Gaussian, stationary random process, which has been a reasonable assumption for CMB mission as COBE where the largest part of the uncertainty comes from detector noise, but is probably not so for sensitive missions such as Planck. Our method requires only inverting a $3n \times 3n$ matrix where n is the number of circles involved, and does not assume anything on the statistical properties of low frequency drifts. It just assumes a limit frequency (the knee frequency) above which the noise can be considered as a white Gaussian random process.

Another interesting method is the one that has been used by Ganga in the analysis of FIRS data (Ganga 1994), which is itself adapted from a method developed originally by Cottingham (1987). In that method, coefficients for splines fitting the low temperature drifts are obtained by minimising the dispersion of measurements on the pixels of the map. Such a method, very similar in spirit to ours, could be adapted to polarization. Splines are natural candidates to replace our offsets in refined implementations of our algorithm.

Here, we have assumed that the averaged noise can be modeled as circle offsets plus white noise (Eq. 8), i.e. that the noise between different measurements from the same bolometer is uncorrelated after removal of the offset. This allowed us to simplify the χ^2 to that shown in Eq. (9). In reality, the circular offsets do not completely remove the low frequency noise and there does remain some correlation between the measurements. The amount of correlation is directly related to the value of $f_{\rm knee}/f_{\rm spin}$; the smaller $f_{\rm knee}/f_{\rm spin}$ the smaller the remaining correlation. Figures 13-18 already contain the errors induced from the fact that we did not include these correlations in the covariance matrix, and thus demonstrate that the effect is small for $f_{\rm knee}/f_{\rm spin} \sim 1$.

Conclusion. The destriping as implemented in this paper removes low frequency drifts up to the white noise level provided that $f_{\rm knee}/f_{\rm spin} \leq 1$. For larger $f_{\rm knee}$, the simple offset model for the averaged noise could be replaced with a more accurate higher-order model that destripes to better precision provided the scan strategy allows to do so, as discussed in Delabrouille et al. (1998a). We are currently working on improving our algorithm to account for these effects. However, despite the shortcomings of our model, it still appears to be robust for small $f_{\rm knee}$ and can serve as a first order analysis tool for real missions. In particular, our technique cannot only be used for the Planck HFI and LFI, but can also be adopted for other CMB missions with circular scanning strategies, such as COSMOSOMAS for instance (Rebolo et al. 1999).

Acknowledgements. We would like to acknowledge our referee's very useful suggestions.

Appendix A: Destriping of unpolarized data

We give here the formulæ for the simpler case of destriping temperature measurements with bolometers. The assumptions are the same as in the polarized case and we adopt the same notation for the common quantities. Instead of polarimeters, we have h bolometers. Since the measurement is no longer dependent on the orientation of the bolometer, the model of the measurement is given by:

$$\boldsymbol{M}_{i,j,\delta} = \boldsymbol{O}_i + I_{i,j,\delta}\ \boldsymbol{u} \quad \text{with} \quad \boldsymbol{u} = \begin{pmatrix} 1 \\ \vdots \\ 1 \end{pmatrix} \tag{A1}$$

where $\boldsymbol{M}_{i,j,\delta}$ is the $h-$vector made of measurements by the h bolometers, $\boldsymbol{O}_i$ is an $h-$vector containing the offsets for the i'th circle and $I_{i,j,\delta}$ is the temperature in the direction of the intersection point labeled by $\{i,j,\delta\}$. $\boldsymbol{u}$ is an h-vector, corresponding to the $\boldsymbol{\mathcal{A}}$ matrix of the polarized case. The χ^2 can be written as:

$$\chi^2 = \sum_{i,j\in\mathcal{I}(i),\delta=\pm1} (\boldsymbol{M}_{i,j,\delta} - \boldsymbol{O}_i - I_{i,j,\delta}\ \boldsymbol{u})^T \times \boldsymbol{N}_i{}^{-1}\,(\boldsymbol{M}_{i,j,\delta} - \boldsymbol{O}_i - I_{i,j,\delta}\ \boldsymbol{u})\,. \tag{A2}$$

In this case, the physical quantity uniquely defined at an intersection point is the temperature of the sky at this point. The constraint used here for removing low-frequency noise is then:

$$I_{i,j,\delta} = I_{j,i,-\delta}. \tag{A3}$$

Given this relation, the minimization of the χ^2 with respect to $\boldsymbol{O}_i$ and $I_{i,j,\delta}$ leads to the linear system:

$$\sum_{j\in\mathcal{I}(i)} \frac{x_j}{x_i+x_j}\,(\Delta_i - \Delta_j) = \frac{1}{2}\sum_{j\in\mathcal{I}(i),\delta=\pm1} \frac{x_j}{x_i+x_j}\,(\mathfrak{I}_{i,j,\delta} - \mathfrak{I}_{j,i,-\delta}) \tag{A4}$$

where

$$x_i = \boldsymbol{u}^{\boldsymbol{T}}\,\boldsymbol{N}_i^{-1}\,\boldsymbol{u} \tag{A5}$$

corresponds to the $\boldsymbol{X}_i$ matrix of the polarized case,

$$\mathfrak{I}_{i,j,\delta} = \frac{1}{x_i}\,\boldsymbol{u}^{\boldsymbol{T}}\,\boldsymbol{N}_i^{-1}\,\boldsymbol{M}_{i,j,\delta} \tag{A6}$$

corresponds to the $\mathcal{S}_{i,j,\delta}$ local Stokes parameters of the polarized case and the scalar

$$\Delta_i = \frac{1}{x_i}\,\boldsymbol{u}^{\boldsymbol{T}}\,\boldsymbol{N}_i^{-1}\,\boldsymbol{O}_i \tag{A7}$$

corresponds to the 3-vector Δ_i of the polarized case.

Temperature offsets appear through their differences $\Delta_i - \Delta_j$ so this linear system is not invertible and we can use the same methods to invert the system than in the polarized case. The size of the matrix to invert is $n \times n$.

After evaluation of the offsets Δ_i, one can recover the value of temperature for any sample k along circle i:

$$I_{i,k} = \mathfrak{I}_{i,k} - \Delta_i. \tag{A8}$$

Appendix B: Details of the simulations

The results presented in this paper correspond to the "Optimized Configuration" involving 3 polarimeters and to an angular step of $18'$: the angle between two consecutive samples along a circle is $18'$ and there is one circle every $18'$.

In this case, the number of circles is $n_{\rm c} = 1200$ and the number of samples on each circle is $n_{\rm s} = 1195$. The spin axis has a sinusoidal motion around the ecliptic plane with an amplitude of $8°$ and with 8 cycles during the mission.

The aperture angle of the circles is 85°. The simulated noise has $f_{\rm knee} = \eta f_{\rm spin}$ with $\eta = 1$ and 5.

The white noise variance is calculated based on the expected sensitivity on Q and U (3.7 μK/K) of the (arbitrarily selected) 143 GHz polarized channel of the PLANCK mission.

All the maps (CMB, dipole, galaxy, simulation) are HEALPIX maps with 196 608 pixels of 27.48′. Only 12 pixels (0.006% of the map) are not seen by the mission: their values are set to the average of the map. The signal maps have been smoothed by a gaussian beam with a FWHM set to $2.5 \times 18'$.

We have run other simulations with "Optimized Configuration" involving 3 or 4 polarimeters, and with cycloidal, sinusoidal or anti-solar spin axis trajectories (see Bersanelli et al. 1996, and the PLANCK web page[4] for additionnal information about proposed scanning strategies). The aperture angle of the circles have been taken in $[70°, 75°, 80°, 85°, 90°]$. In all these cases, the results are similar for $f_{\rm knee}/f_{\rm spin} \sim 1$. For more pessimistic noise cases, the choice of the scanning strategy may have a strong impact on the quality of the final maps. A quantitative study of this point is deffered to a forthcoming publication.

References

Bersanelli M., et al., 1996, Report on the phase A study, Technical report, ESA, D/SCI(96)3

Cottingham D., 1987, Ph.D. Thesis. Princeton University

Couchot F., Delabrouille J., Kaplan J., Revenu B., 1999, A&AS 135, 579

Delabrouille J., 1998, A&AS 127, 555

Delabrouille J., Gispert R., Puget J.-L., Lamarre J., 1998a, astro-ph/9810478

Delabrouille J., Górski K.M., Hivon E., 1998b, MNRAS 298, 445

Ganga K., 1994, Ph.D. Thesis, http://spider.ipac.caltech.edu/staff/kmg/

Giard M., Hivon E., Nguyen C., Gispert R., Górski K., Lange A., 1999, astro-ph/9907208

Kamionkowski M., 1998, astro-ph/9803168

Kamionkowski M., Kosowsky A., Stebbins A., 1997, Phys. Rev. D 55, 7368

Kinney W., 1998, astro-ph/9806259

Prunet S., Lazarian A., 1999, astro-ph/9902314

Rebolo R., Gutiérrez C., Watson R., Gallegos J., 1999, in Proceedings of the Workshop "The CMB and the Planck Mission" held in Santander (to appear in Astrophysical Letters and Communications)

Seljak U., 1996, astro-ph/9608131

Tegmark M., 1997, Phys. Rev. D 56, 4514

Wright E.L., 1996, astro-ph/9612006

Zaldarriaga M., 1998, Ph.D. Thesis, astro-ph/9806122

Zaldarriaga M., Seljak U., 1997, Phys. Rev. D 55, 1830

[4] `http://astro.estec.esa.nl/SA-general/Projects/Planck/report/report.html`

ASTRONOMY & ASTROPHYSICS
SUPPLEMENT SERIES

MARCH II **1999**, PAGE 579

Astron. Astrophys. Suppl. Ser. **135**, 579–584 (1999)

Optimised polarimeter configurations for measuring the Stokes parameters of the cosmic microwave background radiation

F. Couchot[1], **J. Delabrouille**[2], **J. Kaplan**[3], **and B. Revenu**[3]

[1] Laboratoire de l'Accélérateur Linéaire, IN2P3 CNRS, Université Paris Sud, 91405 Orsay, France
[2] Institut d'Astrophysique Spatiale, CNRS & Université Paris XI, Bât. 121, 91405 Orsay Cedex, France, and University of Chicago, Dept. of Astronomy and Astrophysics, 5640 South Ellis Avenue, Chicago, IL 60637, U.S.A.
[3] Physique Corpusculaire et Cosmologie, Collège de France, 11 place Marcelin Berthelot, 75231 Paris Cedex 05, France

Received July 10; accepted October 27, 1998

Abstract. We present configurations of polarimeters which measure the three Stokes parameters I, Q and U of the Cosmic Microwave Background Radiation with a nearly diagonal error matrix, independent of the global orientation of the polarimeters in the focal plane. These configurations also provide the smallest possible error box volume.

Key words: cosmic microwave background — cosmology: observations — instrumentation: polarimeters — methods: observational — polarisation

1. Introduction

This paper originates from preparatory studies for the Planck satellite mission. This Cosmic Microwave Background (CMB) mapping satellite is designed to be able to measure the polarisation of the CMB in several frequency channels with the sensitivity needed to extract the expected cosmological signal. Several authors (see for instance Rees 1968; Bond & Efstathiou 1987; Melchiorri & Vittorio 1996; Hu & White 1997; Seljak & Zaldarriaga 1998), have pointed out that measurements of the polarisation of the CMB will help to discriminate between cosmological models and to separate the foregrounds. In the theoretical analyses of the polarised power spectra, it is in general assumed (explicitly or implicitly) that the errors are uncorrelated between the three Stokes parameters I, Q and U[1] in the reference frame used to build the polarised multipoles (Zaldarriaga & Seljak 1997; Ng & Liu 1997). However, the errors in the three Stokes parameters will in general be correlated, even if the noise of the three or more measuring polarimeters are not, unless the layout of the polarimeters is adequately chosen. In this paper we construct configurations of the relative orientations of the polarimeters, hereafter called "Optimised Configurations" (OC), such that, if the noise in all polarised bolometers have the same variance and are not correlated, the measurement errors in the Stokes parameters I, Q and U are independent of the direction of the focal plane and decorrelated. Moreover, the volume of the error box is minimised. The properties of decorrelation and minimum error are maintained when one combines redundant measurements of the same point of the sky, even when the orientation of the focal plane is changed between successive measurements. Finally, when combining unpolarised and data from OC's, the resulting errors retain their optimised properties.

In general, the various polarimeters will not have the same levels of noise and will be slightly cross-correlated. Assuming that these imbalances and cross-correlations are small, we show that for OC's the resulting correlations between the errors on I, Q and U are also small and easily calculated to first order. This remains true when one combines several measurements of the same point of the sky, the correlations get averaged but do not cumulate.

Finally, we calculate the error matrix between E and B multipolar amplitudes and show that it is also simpler in OC's.

1.1. General considerations

In the reference frame where the Stokes parameters I, Q, and U are defined, the intensity detected by a polarimeter rotated by an angle α with respect to the x axis is:

$$I_\alpha = \frac{1}{2}(I + Q\cos 2\alpha + U\sin 2\alpha). \quad (1)$$

Send offprint requests to: J. Kaplan (kaplan@cdf.in2p3.fr)

[1] For a definition of the Stokes parameters, see for instance Born & Wolf (1980) page 554, where I, Q, U are noted s_0, s_1, s_2 respectively.

Because polarimeters only measure intensities, angle α can be kept between 0 and π. To be able to separate the 3 Stokes parameters, at least 3 polarised detectors are needed (or 1 unpolarised and 2 polarised), with angular separations different from multiples of $\pi/2$. If one uses $n \geq 3$ polarimeters with orientations $\alpha_p,\ 1 \leq p \leq n$ for a given line of sight, the Stokes parameters will be estimated by minimising the χ^2:

$$\chi^2 = (\mathbf{M} - \mathbf{AS})^T\ \mathbf{N^{-1}}\ (\mathbf{M} - \mathbf{AS}) \tag{2}$$

where $\mathbf{M} = \begin{pmatrix} m_1 \\ \vdots \\ m_p \\ \vdots \\ m_n \end{pmatrix}$ is the vector of measurements, and $\mathbf{N}$ is their $n \times n$ noise autocorrelation matrix. The $n \times 3$ matrix

$$\mathbf{A} = \frac{1}{2} \begin{pmatrix} 1 & \cos 2\alpha_1 & \sin 2\alpha_1 \\ \vdots & \vdots & \vdots \\ 1 & \cos 2\alpha_p & \sin 2\alpha_p \\ \vdots & \vdots & \vdots \\ 1 & \cos 2\alpha_n & \sin 2\alpha_n \end{pmatrix} \tag{3}$$

relates the results of the n measurements to the vector of the Stokes parameters $\mathbf{s} = \begin{pmatrix} I \\ Q \\ U \end{pmatrix}$ in a given reference frame, for instance a reference frame fixed with respect to the focal instrument. If one looks in the same direction of the sky, but with the instrument rotated by an angle ψ in the focal plane, the matrix A is simply transformed with a rotation matrix of angle $2\,\psi$:

$$\mathbf{A} \rightarrow \mathbf{A}\ \mathbf{R}(\psi),\ \text{with}\ \mathbf{R}(\psi) = \begin{pmatrix} 1 & 0 & 0 \\ 0 & \cos 2\psi & \sin 2\psi \\ 0 & -\sin 2\psi & \cos 2\psi \end{pmatrix}. \tag{4}$$

As is well known, the resulting estimation for the Stokes parameters and their variance matrix $\mathbf{V}$ are:

$$\mathbf{S} = \left(\mathbf{A}^T\,\mathbf{N}^{-1}\,\mathbf{A}\right)^{-1}\ \mathbf{A}^T\mathbf{N}^{-1}\mathbf{M},$$

and

$$\mathbf{V} = \left(\mathbf{A}^T\,\mathbf{N}^{-1}\,\mathbf{A}\right)^{-1}. \tag{5}$$

2. Optimised configurations

2.1. The ideal case

If we assume that the measurements m_p $(1 \leq p \leq n)$ have identical and decorrelated errors ($\mathbf{N}_{pq} =< \delta m_p\ \delta m_q >= \sigma_0^2\,\delta_{pq}$), the χ^2 is simply:

$$\chi^2 = \frac{1}{\sigma^2} \sum_{p=1}^{n} \left[m_p - \frac{1}{2}(I + Q\,\cos 2\alpha_p + U\,\sin 2\alpha_p) \right]^2, \tag{6}$$

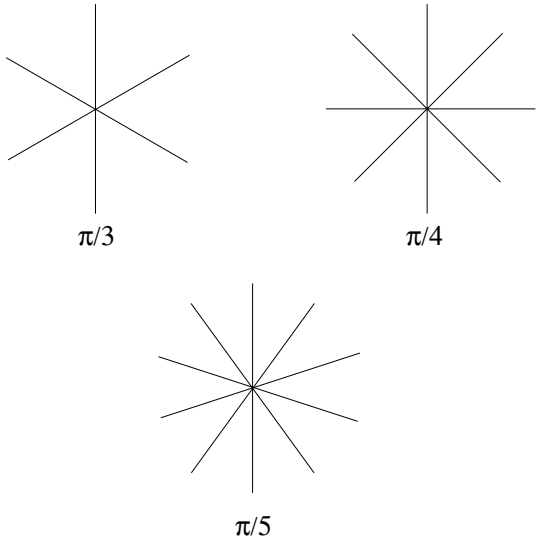

Fig. 1. The relative orientations of polarimeters in "Optimised Configurations" with 3, 4 and 5 detectors

and the inverse of the covariance matrix of the Stokes parameters is given by:

$$\mathbf{V}^{-1} = \frac{1}{\sigma^2}\,\mathbf{X}, \qquad \mathbf{X} = \mathbf{A}^T\mathbf{A} = \frac{1}{4}\ \times \tag{7}$$

$$\begin{pmatrix} n & \sum_1^n \cos 2\alpha_p & \sum_1^n \sin 2\alpha_p \\ \sum_1^n \cos 2\alpha_p & \frac{1}{2}(n + \sum_1^n \cos 4\alpha_p) & \frac{1}{2}\sum_1^n \sin 4\alpha_p \\ \sum_1^n \sin 2\alpha_p & \frac{1}{2}\sum_1^n \sin 4\alpha_p & \frac{1}{2}(n - \sum_1^n \cos 4\alpha_p) \end{pmatrix}.$$

It is shown in the appendix that, if the orientations of the polarimeters are evenly distributed on 180°:

$$\alpha_p = \alpha_1 + (p-1)\,\frac{\pi}{n},\ p = 1...\ n,\ \text{with}\ n \geq 3, \tag{8}$$

the matrix $\mathbf{V}$ takes the very simple diagonal form:

$$\mathbf{V}_0 = \sigma^2 {\mathbf{X}_0}^{-1},\ \text{with}\ {\mathbf{X}_0}^{-1} = \frac{4}{n} \begin{pmatrix} 1 & 0 & 0 \\ 0 & 2 & 0 \\ 0 & 0 & 2 \end{pmatrix}, \tag{9}$$

independent of the orientation of the focal plane, while its determinant is minimised. In other words, at the same time, the errors on the Stokes parameters get decorrelated, their error matrix becomes independent of the orientation of the focal plane and the volume of the error ellipsoid takes its smallest possible value: $\frac{\pi}{3}\left(\frac{4\sigma}{\sqrt{n}}\right)^3$.

The "Optimised Configurations" (OC) are the sets of polarimeters which satisfy condition (8), (see Fig. 1). They are hereafter referred to by the subscript 0 as in Eq. (9). The smallest OC involves three polarimeters with relative angle $\pi/3$. With 4 polarimeters, the angular separation must be $\pi/4$, and so on. Note that a configuration

with one unpolarised detector and 2 polarised detectors can never measure the Stokes parameters with uncorrelated errors, because this would require polarimeters oriented 90° apart from each other, which would not allow the breaking of the degeneracy between Q and U.

If one combines several OC's with several unpolarised detectors, all uncorrelated with each other, the resulting covariance matrix for the Stokes parameters remains diagonal and independent of the orientation of the various OC's. More precisely, when combining the measurements of n_T unpolarised detectors (temperature measurements), with n_P polarised detectors arranged in OC's, the covariance matrix of the Stokes parameters reads:

$$\mathbf{V} = \frac{4\,\sigma_P^2}{n_P} \begin{pmatrix} \left(1 + 4\,\frac{n_T}{n_P}\left(\frac{\sigma_P}{\sigma_T}\right)^2\right)^{-1} & 0 & 0 \\ 0 & 2 & 0 \\ 0 & 0 & 2 \end{pmatrix}, \tag{10}$$

where we have introduced inverse average noise levels, σ_T and σ_P, for the unpolarised and polarised detectors respectively:

$$\frac{1}{{\sigma_T}^2} = \left\langle \frac{1}{\sigma^2_{\rm unpolarised}} \right\rangle, \text{ and } \frac{1}{{\sigma_P}^2} = \left\langle \frac{1}{\sigma^2_{\rm polarised}} \right\rangle. \tag{11}$$

Note that the levels of noise can be different from one OC to the other and from those of the unpolarised detectors.

2.2. A more realistic description of the measurements

In general one expects that there will be some slight imbalance and cross-correlation between the noise of the detectors. The noise matrix of the measurements will in general take the form:

$$\mathbf{N} = \sigma^2(\mathbb{1} + \hat{\beta} + \hat{\gamma}), \tag{12}$$

where the imbalance $\hat{\beta}$ and cross-correlation $\hat{\gamma}$ matrices

$$\hat{\beta} = \begin{pmatrix} \beta_{1\,1} & 0 & 0 & \dots \\ 0 & \beta_{2\,2} & 0 & \dots \\ 0 & 0 & \beta_{3\,3} & \dots \\ \vdots & \vdots & \vdots & \ddots \end{pmatrix}, \ \mathrm{Tr}(\hat{\beta}) = 0, \text{ and}$$
$$\hat{\gamma} = \begin{pmatrix} 0 & \gamma_{1\,2} & \gamma_{1\,3} & \dots \\ \gamma_{1\,2} & 0 & \gamma_{2\,3} & \dots \\ \gamma_{1\,3} & \gamma_{2\,3} & 0 & \dots \\ \vdots & \vdots & \vdots & \ddots \end{pmatrix}, \tag{13}$$

are "small", that is will be treated as first order perturbations in the following, and therefore

$$\mathbf{N}^{-1} = \frac{1}{\sigma^2}\,(\mathbb{1} - \hat{\beta} - \hat{\gamma}).$$

To this order, the variance matrix of the Stokes parameters is easily obtained from Eq. (5):

$$\mathbf{V} = \sigma^2 \left[\mathbf{X}^{-1} + \hat{\mathcal{B}} + \hat{\mathcal{G}}\right], \tag{14}$$

where the matrix $\mathbf{X}$ is given by Eq. (7) and the first order corrections to $\mathbf{V}$, matrices $\hat{\mathcal{B}}$ and $\hat{\mathcal{G}}$, read:

$$\begin{pmatrix} \hat{\mathcal{B}} \\ \hat{\mathcal{G}} \end{pmatrix} = \mathbf{X}^{-1}\ \mathbf{A}^T \begin{pmatrix} \hat{\beta} \\ \hat{\gamma} \end{pmatrix} \mathbf{A}\ \mathbf{X}^{-1}. \tag{15}$$

In an OC, the matrix $\mathbf{X}^{-1}$ takes the simple diagonal form ${\mathbf{X_0}}^{-1}$ of Eq. (9), and the non diagonal parts, $\hat{\mathcal{B}}$ and $\hat{\mathcal{G}}$ remain of order 1 in $\hat{\beta}$ and $\hat{\gamma}$. For instance, if we consider an OC with 3 polarimeters, and polarimeter number 1 is oriented in the x direction,

$$\hat{\mathcal{B}} = \frac{4}{3} \begin{pmatrix} 0 & \beta_{1\,1} & \frac{\beta_{2\,2}-\beta_{3\,3}}{\sqrt{3}} \\ \beta_{1\,1} & \beta_{1\,1} & \frac{\beta_{3\,3}-\beta_{2\,2}}{\sqrt{3}} \\ \frac{\beta_{2\,2}-\beta_{3\,3}}{\sqrt{3}} & \frac{\beta_{3\,3}-\beta_{2\,2}}{\sqrt{3}} & -\beta_{1\,1} \end{pmatrix},$$

where $\beta_{2\,2} + \beta_{3\,3} = -\beta_{1\,1}$, and

$$\hat{\mathcal{G}} = \frac{4}{3} \times \begin{pmatrix} \frac{2(\gamma_{1\,2}+\gamma_{1\,3}+\gamma_{2\,3})}{3} & \frac{\gamma_{1\,2}+\gamma_{1\,3}-2\gamma_{2\,3}}{3} & \frac{\gamma_{1\,2}-\gamma_{1\,3}}{\sqrt{3}} \\ \frac{\gamma_{1\,2}+\gamma_{1\,3}-2\gamma_{2\,3}}{3} & \frac{2(\gamma_{2\,3}-2\gamma_{1\,2}-2\gamma_{1\,3})}{3} & \frac{2(\gamma_{1\,2}-\gamma_{1\,3})}{\sqrt{3}} \\ \frac{\gamma_{1\,2}-\gamma_{1\,3}}{\sqrt{3}} & \frac{2(\gamma_{1\,2}-\gamma_{1\,3})}{\sqrt{3}} & -2\,\gamma_{2\,3} \end{pmatrix}.$$

Note that $\hat{\mathcal{B}}$ and $\hat{\mathcal{G}}$ transform under a rotation of the focal plane by a rotation $\mathbf{R}(\psi)$:

$$\begin{pmatrix} \hat{\mathcal{B}} \\ \hat{\mathcal{G}} \end{pmatrix} \rightarrow \mathbf{R}(\psi)^{-1} \begin{pmatrix} \hat{\mathcal{B}} \\ \hat{\mathcal{G}} \end{pmatrix} \mathbf{R}(\psi). \tag{16}$$

Because $\mathbf{V_0}$ is invariant, as long as $\hat{\beta}$ and $\hat{\gamma}$ are small the dependence of $\mathbf{V}$ on the orientation of the focal plane remains weak.

3. Co-adding measurements

The planned scanning strategy of Planck goes stepwise: at each step the satellite will spin about 100 times around a fixed axis, covering the same circular scan, then the spin axis of the satellite will be moved by a few arc-minutes, and so on. This provides two types of redundancy: every pixel along each circle will be scanned about 100 times, and some pixels will be seen by several circles, with different orientations of the focal plane. In this section we show, assuming a perfect white noise along each scan, that the properties of the error matrix of the Stokes parameters coming from OC's are kept if all data are simply co-added at each pixel, whatever the orientations of the focal plane. The redundancy provided by intersecting circles can be used to remove the stripes induced on maps by low-frequency noise in the data streams. An extension adapted to polarised measurements of the method proposed by Delabrouille (1998) for the de-striping of Planck maps is studied in Revenu et al. (1999).

Here we assume that the noise is not correlated between different scans and can thus be described by one matrix $\mathbf{N}_l$ for each scan, indexed by l, passing through the pixel. The χ^2 is then the sum of the χ^2_l over the L scans that cross the pixel:

$$\chi^2 = \sum_{l=1}^{L} (\mathbf{M}_l - \mathbf{A}_l\,\mathbf{S})^T {\mathbf{N}_l}^{-1} (\mathbf{M}_l - \mathbf{A}_l\,\mathbf{S}). \quad (17)$$

The estimator of the Stokes parameters stemming from this χ^2 is

$$\mathbf{S} = \left(\sum_{l=1}^{L} \mathbf{A}_l^T\,\mathbf{N}_l^{-1}\,\mathbf{A}_l \right)^{-1} \sum_{l=1}^{L} \mathbf{A}_l^T\,\mathbf{N}_l^{-1}\,\mathbf{M}_l, \quad (18)$$

with variance matrix:

$$\mathbf{V} = \left(\sum_{l=1}^{L} \mathbf{A}_l^T\,\mathbf{N}_l^{-1}\,\mathbf{A}_l \right)^{-1}. \quad (19)$$

In the ideal case, for a given scan, the noise (assumed to be white on each scan) has the same variance for all bolometers with no correlation between them, although it can vary from one scan to the other:

$$\mathbf{N}_l = {\sigma_l}^2 \mathbb{1}, \quad (20)$$

and one can write the resulting variance combining the L scans:

$$\mathbf{V}_L = \left(\sum_{l=1}^{L} \frac{\mathbf{X}_l}{{\sigma_l}^2} \right)^{-1} = \left(\sum_{l=1}^{L} \frac{1}{{\sigma_l}^2} \mathbf{R}^{-1}(\psi_l)\,\mathbf{X}_1\,\mathbf{R}(\psi_l) \right)^{-1}, \quad (21)$$

where $\mathbf{X}_l = \mathbf{A}_l^T\,\mathbf{A}_l$, and we have written explicitly the rotation matrices which connect the orientation of the focal plane along scan l with that along scan 1. Note that these matrices are dependent of the position along the scan through angle ψ_l.

If the observing setup is in an OC, all orientation dependence drops out and the expression of the covariance matrix becomes diagonal as for a single measurement (Eq. 9):

$$\mathbf{V}_{0\,L} = \frac{4\,{\sigma_L}^2}{n\,L} \begin{pmatrix} 1 & 0 & 0 \\ 0 & 2 & 0 \\ 0 & 0 & 2 \end{pmatrix} = \frac{{\sigma_L}^2}{L}\,{\mathbf{X}_0}^{-1}, \quad (22)$$

where ${\mathbf{X}_0}^{-1}$ is defined in Eq. (9) and the average noise level σ_L is defined as:

$$\frac{1}{{\sigma_L}^2} = \left\langle \frac{1}{{\sigma_l}^2} \right\rangle. \quad (23)$$

Of course one recovers the fact that, with L measurements, the errors on the Stokes parameters are reduced by a factor $\sqrt{L}$.

More realistically, we expect that the noise matrices will take a form similar to Eq. (12):

$$\mathbf{N}_l = {\sigma_l}^2 \left(\mathbb{1} + \hat{\beta}_l + \hat{\gamma}_l \right). \quad (24)$$

If $\hat{\beta}_l$ and $\hat{\gamma}_l$ are small, first order inversion allows to calculate $\mathbf{V}$ ($\mathbf{V}_L$ is given by Eq. (21)):

$$\mathbf{V} = \mathbf{V}_L + \mathbf{V}_L \sum_{l=1}^{L} \mathbf{A}_l^T \frac{\hat{\beta}_l + \hat{\gamma}_l}{{\sigma_l}^2} \mathbf{A}_l \mathbf{V}_L. \quad (25)$$

If the focal plane is in an OC, this expression simplifies to

$$\mathbf{V}_L = \frac{{\sigma_L}^2}{L} \left({\mathbf{X}_0}^{-1} + \frac{{\sigma_L}^2}{L} \sum_{l=1}^{L} \frac{\hat{\mathcal{B}}_l + \hat{\mathcal{G}}_l}{{\sigma_l}^2} \right), \quad (26)$$

where

$$\begin{pmatrix} \hat{\mathcal{B}}_l \\ \hat{\mathcal{G}}_l \end{pmatrix} = \mathbf{R}^{-1}(\psi_l) {\mathbf{X}_0}^{-1}\,\mathbf{A}_1^T \begin{pmatrix} \hat{\beta}_l \\ \hat{\gamma}_l \end{pmatrix} \mathbf{A}_1\,{\mathbf{X}_0}^{-1} \mathbf{R}(\psi_l). \quad (27)$$

The $1/L$ factor inside the parenthesis in equation (26) implies that the cross-correlations and the dependence on on the orientation ψ_l of the focal plan remain weak when one cumulates measurements of the same pixel.

4. The error covariance matrix of the scalar E and B parameters

Scalar polarisation parameters, denoted E and B, have been introduced, which do not depend on the reference frame (Newman & Penrose 1966; Zaldarriaga & Seljak 1997). However, the properties of OCs do not propagate simply to the error matrix of the E and B parameters because their definition is non local in terms of the Stokes parameters.

Nevertheless, if the measurements errors are not correlated between different points of the sky (or if the correlation has been efficiently suppressed by the data treatment) then the elements of the error matrix of the multipolar coefficients $a_{E,lm}$ and $a_{B,lm}$ can be written in a simple form which is given in Appendix B for a general configuration.

For an OC, the error matrix simplifies further and its elements reduce to:

$$\begin{aligned} &< \delta a_{\substack{E\\B},lm}\,\delta a_{\substack{E\\B},l'm'}{}^{*} > = \frac{1}{2} \left(\frac{4\,\pi}{N_{pix}} \right)^2 \sum_{\hat{\mathbf{n}}_k} \sigma^2_{\rm Stokes}(\hat{\mathbf{n}}_k) \\ &\quad \times \left[{}_2Y_{lm}(\hat{\mathbf{n}}_k)^*\,{}_2Y_{l'm'}(\hat{\mathbf{n}}_k) + {}_{-2}Y_{lm}(\hat{\mathbf{n}}_k)^*\,{}_{-2}Y_{l'm'}(\hat{\mathbf{n}}_k) \right] \\ &< \delta a_{E,lm}\,\delta a_{B,l'm'}{}^{*} > = \frac{i}{2} \left(\frac{4\,\pi}{N_{pix}} \right)^2 \sum_{\hat{\mathbf{n}}_k} \sigma^2_{\rm Stokes}(\hat{\mathbf{n}}_k) \\ &\quad \times \left[{}_2Y_{lm}(\hat{\mathbf{n}}_k)^*\,{}_2Y_{l'm'}(\hat{\mathbf{n}}_k) - {}_{-2}Y_{lm}(\hat{\mathbf{n}}_k)^*\,{}_{-2}Y_{l'm'}(\hat{\mathbf{n}}_k) \right]. \end{aligned}$$

where N_{pix} is the total number of pixels in the sky, $\sigma_{\rm Stokes}$ is the common r.m.s. error on the Q and U Stokes parameters, $\hat{\mathbf{n}}_k$ is the direction of pixel k and functions ${}_{\pm2}Y_{lm}(\hat{\mathbf{n}}_k)$ are the spin 2 spherical harmonics. If $\sigma_{\rm Stokes}$ does not depend on the direction in the sky, a highly improbable situation, then the orthonormality of the spin weighted spherical harmonics makes the error matrix fully diagonal in the limit of a large number of pixels:

$$\begin{pmatrix} < \delta a_{E,lm}\,\delta a_{E,l'm'}{}^{*} > & < \delta a_{E,lm}\,\delta a_{B,l'm'}{}^{*} > \\ < \delta a_{B,lm}\,\delta a_{E,l'm'}{}^{*} > & < \delta a_{B,lm}\,\delta a_{B,l'm'}{}^{*} > \end{pmatrix} = \mathbb{1}\,\frac{4\,\pi}{N_{pix}}\,\sigma^2_{\rm Stokes}\,\delta_{ll'}\delta_{mm'}.$$

Note that, even for unpolarised data, the error matrix between multipolar amplitude is not diagonal unless the r.m.s. error is constant over the whole sky (see for instance Oh, Spergel & Hinshaw 1998).

In the same conditions, the noise matrix of fields E and B is also fully diagonal:

$$\begin{pmatrix} \langle \delta E(\hat{\mathbf{n}})\, \delta E(\hat{\mathbf{n}}')\rangle & \langle \delta E(\hat{\mathbf{n}})\, \delta B(\hat{\mathbf{n}}')\rangle \\ \langle \delta B(\hat{\mathbf{n}})\, \delta E(\hat{\mathbf{n}}')\rangle & \langle \delta B(\hat{\mathbf{n}})\, \delta B(\hat{\mathbf{n}}')\rangle \end{pmatrix} = \mathbb{1}\, \sigma^2_{\rm Stokes}\, \delta_{\hat{\mathbf{n}}\,\hat{\mathbf{n}}'}.$$

5. Conclusion

In this paper we have shown that, if the noise of the polarimeters have nearly equal levels and are approximately uncorrelated, these detectors can be set up in "Optimised Configurations". These configurations are optimised in two respects: first the volume of the error ellipsoid is minimised, and second the error matrix of the inferred Stokes parameters is approximately diagonal in all reference frames. This remains true even if one combines information from numerous measurements along different scanning circles. Such "Optimised Configurations", with 3 and 4 polarimeters, have been proposed by the Planck High Frequency Instrument consortium (HFI Consortium, 1998) for the three channels where it is intended to measure the CMB polarisation.

Appendix A: The conditions for an OC

In this appendix, we show that conditions (8) diagonalise the error matrix $\mathbf{V}$ of the Stokes parameters and minimise its determinant, if the noises in the n polarimeters have identical levels and are not correlated.
We use the notation:

$$S_k = \sum_{p=1}^{n} \mathrm{e}^{i\,k\,\alpha_p} = |S_k|\,\mathrm{e}^{i\,\theta_k},\ k = 2, 4.$$

It can be seen from Eq. (7) that requiring that the error on I be decorrelated from the errors on Q and U is equivalent to the condition:

$$S_2 = 0. \tag{A1}$$

This condition can easily be fulfilled in a configuration where the angles $\alpha_{\rm p}$ are regularly distributed:

$$\alpha_p = \alpha_1 + (p-1)\,\delta\alpha,\ p = 1...\ n, \tag{A2}$$
$$\text{with}\ \ n \geq 3,\ 0 < \delta\alpha < \pi,\ \delta\alpha \neq \pi/2\ \ \text{(see text)}.$$

In such configurations, Eq. (A1) becomes:

$$S_2 = \mathrm{e}^{i\,2\,\alpha_1}\frac{\mathrm{e}^{i\,2\,n\,\delta\alpha} - 1}{\mathrm{e}^{i\,2\,\delta\alpha} - 1} = 0. \tag{A3}$$

The solutions of Eq. (A3) under conditions (A2) reduce to:

$$\delta\alpha = \frac{\pi}{n},\ \text{with}\ n \geq 3. \tag{A4}$$

It is easily seen that conditions (A4) also automatically ensure that $S_4 = 0$ and therefore that $\mathbf{X}$ becomes diagonal and assumes the very simple form:

$$\mathbf{X}_0 = \frac{n}{4}\begin{pmatrix} 1 & 0 & 0 \\ 0 & 1/2 & 0 \\ 0 & 0 & 1/2 \end{pmatrix} \tag{A5}$$

independent of the orientation of the focal plane. Equation (9) is the consequence of (A5).

The error volume is proportional to the determinant of the error matrix $\mathbf{V}$. Therefore, it is minimum when the determinant of $\mathbf{X}$ (Eq. (7)) is maximum. This determinant can be written as:

$$\mathrm{Det}(\mathbf{X}) = \frac{1}{64}\left[n^3 - n\,|S_4|^2 - 2\,|S_2|^2(n - |S_4|\,\cos(\theta_4 - 2\,\theta_2))\right]. \tag{A6}$$

Because the S_k's are sums of n complex numbers with modulus 1, $|S_k| < n$, and it is clear from Eq. (A6) that

$$\mathrm{Det}(\mathbf{X}) \leq \frac{n^3}{64},$$

and that the upper bound is reached if and only if

$$S_2 = S_4 = 0. \tag{A7}$$

Conditions (A2) and (A4) have been shown above to imply (A7), and therefore ensure that the determinant of the covariance matrix $\mathbf{V}$ is minimum.

Appendix B: The general error matrix of the E and B multipolar coefficients

Assuming that the data treatment has removed all correlation between different directions in the sky, the matrix elements of the error matrix of the E and B multipolar coefficients are:

$$< \delta a_{\substack{E\\B},lm}\, \delta a_{\substack{E\\B},l'm'}{}^{*} >= \frac{1}{4}\left(\frac{4\,\pi}{N_{pix}}\right)^2 \sum_{\hat{\mathbf{n}}_k}$$
$$(\mathbf{N_{QQ}} + \mathbf{N_{UU}})(\hat{\mathbf{n}}_k)[{}_2Y_{lm}{}^{*}\,{}_2Y_{l'm'} + {}_{-2}Y_{lm}{}^{*}\,{}_{-2}Y_{l'm'}](\hat{\mathbf{n}}_k)$$
$$\pm\,(\mathbf{N_{QQ}} - \mathbf{N_{UU}})(\hat{\mathbf{n}}_k)[{}_2Y_{lm}{}^{*}\,{}_{-2}Y_{l'm'} + {}_{-2}Y_{lm}{}^{*}\,{}_2Y_{l'm'}](\hat{\mathbf{n}}_k)$$
$$\pm\,2i\,\mathbf{N_{QU}}(\hat{\mathbf{n}}_k)[{}_2Y_{lm}{}^{*}\,{}_{-2}Y_{l'm'} - {}_{-2}Y_{lm}{}^{*}\,{}_2Y_{l'm'}](\hat{\mathbf{n}}_k),$$

$$< \delta a_{E,lm}\, \delta a_{B,l'm'}{}^{*} >= \frac{i}{4}\left(\frac{4\,\pi}{N_{pix}}\right)^2 \sum_{\hat{\mathbf{n}}_k}$$
$$(\mathbf{N_{QQ}} + \mathbf{N_{UU}})(\hat{\mathbf{n}}_k)[{}_2Y_{lm}{}^{*}\,{}_2Y_{l'm'} - {}_{-2}Y_{lm}{}^{*}\,{}_{-2}Y_{l'm'}](\hat{\mathbf{n}}_k)$$
$$-\,(\mathbf{N_{QQ}} - \mathbf{N_{UU}})(\hat{\mathbf{n}}_k)[{}_2Y_{lm}{}^{*}\,{}_{-2}Y_{l'm'} - {}_{-2}Y_{lm}{}^{*}\,{}_2Y_{l'm'}](\hat{\mathbf{n}}_k)$$
$$-\,2i\,\mathbf{N_{QU}}(\hat{\mathbf{n}}_k)[{}_2Y_{lm}{}^{*}\,{}_{-2}Y_{l'm'} + {}_{-2}Y_{lm}{}^{*}\,{}_2Y_{l'm'}](\hat{\mathbf{n}}_k),$$

where $\mathbf{N}(\hat{\mathbf{n}}_\mathbf{k})$ is the noise matrix of the Stokes parameters Q and U in the direction $\hat{\mathbf{n}}_k$ of pixel k.

Acknowledgements. We thank Alex Kim for useful suggestions and for reading the manuscript, and the referee, Uroš Seljak, who suggested to consider the implications on the E and B scalar parameters.

References

Bond J.R., Efstathiou G., 1987, MNRAS 226, 655
Born M., Wolf E., 1980, Principles of Optics, sixth edition. Pergamon Press
Delabrouille J., 1998, A&AS 127, 555
HFI Consortium, 1998, High Frequency Instrument for the Planck Mission (submitted in response to the ESA Announcement of Opportunity)
Hu W., White M., 1997, New Astron. 2, 323
Melchiorri A., Vittorio N., 1996, proceedings of NATO Advanced Study Institute 1996 on the "Cosmic Background Radiation", astro-ph/961002
Newman E., Penrose R., 1966, J. Math. Phys. 7, 863
Ng K., Liu G., 1997, Correlation Functions of CMB Anisotropy and Polarization, astro-ph/9710012
Oh S.P., Spergel D.N., Hinshaw G., 1998, An Efficient Technique to Determine the Power Spectrum from Cosmic Microwave Background Sky Maps, astro-ph/9710012 (to appear in ApJ)
Rees M., 1968, ApJ 153, L1
Revenu B., Ansari R., Couchot F., Delabrouille J., Kaplan J., Kim A., 1999 (in preparation)
Seljak U., Zaldarriaga M., 1998, "Fundamental Parameters in Cosmology," proceedings of the XXXIIIrd Rencontres de Moriond 1998, Trân Thanh Vân et al. (ed.) Éditions Frontières, Paris, astro-ph/9805010
Zaldarriaga M., Seljak U., 1997, Phys. Rev. D 55, 1830

A&A 464, 405–415 (2007)
DOI: 10.1051/0004-6361:20042230

Astronomy & Astrophysics

Beam mismatch effects in cosmic microwave background polarization measurements

C. Rosset[1,4], V. B. Yurchenko[2], J. Delabrouille[1], J. Kaplan[1], Y. Giraud-Héraud[1], J.-M. Lamarre[3], and J. A. Murphy[2]

[1] APC, Université Paris 7, CNRS/IN2P3, 10 rue Alice Domon et Léonie Duquet, 75205 Paris Cedex 13, France
e-mail: [delabrouille;kaplan;ygh]@apc.univ-paris7.fr
[2] Experimental Physics Department, National University of Ireland, Maynooth, Co. Kildare, Ireland
e-mail: [amurphy;v.yurchenko]@may.ie
[3] LERMA, Observatoire de Paris, 61 Av. de l'Observatoire, 75014 Paris, France
e-mail: jean-michel.lamarre@obspm.fr
[4] LAL, Université Paris-Sud 11, CNRS/IN2P3, BP 34, 91898 Orsay Cedex, France
e-mail: rosset@lal.in2p3.fr

Received 22 October 2004 / Accepted 6 December 2006

ABSTRACT

Measurement of cosmic microwave background polarization is today a major goal of observational cosmology. The level of the signal to measure, however, makes it very sensitive to various systematic effects. In the case of Planck, which measures polarization by combining data from various detectors, the beam asymmetry can induce a conversion of temperature signals to polarization signals or a polarization mode mixing. In this paper, we investigate this effect using realistic simulated beams and propose a first-order method to correct the polarization power spectra for the induced systematic effect.

Key words. cosmology: cosmic microwave background – polarization

1. Introduction

After the success of *COBE* (Smoot et al. 1992) and *WMAP* (Bennett et al. 2003, the Planck mission, to be launched by ESA in early 2007, is the third generation space mission dedicated to the measurement of the properties of the Cosmic Microwave Background (CMB). About 20 times more sensitive than *WMAP*, Planck will observe the full sky in the millimeter and sub-millimeter domain in nine frequency channels centered around frequencies ranging from 30 to 70 Ghz (for the Low Frequncy Instrument, or LFI) and from 100 to 850 GHz (for the High Frequency Instrument or HFI). Of these channels, the seven at lowest frequencies – from 30 to 350 GHz, are polarization sensitive.

Temperature anisotropies have been detected by many experiments now, the most recent of which detect a series of acoustic peaks in the CMB spatial power spectrum (de Bernardis et al. 2000; Hanany et al. 2000; Benoît et al. 2003a; Hinshaw et al. 2003), confirm the Gaussianity of observable CMB fluctuations (Komatsu et al. 2003, though wavelet methods have detected presence of non-Gaussianity in *WMAP* data; Vielva et al. 2004); and demonstrate the spatial flatness of the Universe (Netterfield et al. 2002; Lee et al. 2001; Benoît et al. 2003b; Spergel et al. 2003; Spergel et al. 2006). This provides compelling evidence that the primordial perturbations indeed have been generated during an inflationary period in the very early Universe. The next challenge now is the precise measurement of polarization anisotropies and, in particular, the detection of the pseudo-scalar part of the polarization field (the *B* modes of CMB polarization) which are expected to carry the unambiguous signature of the energy scale of inflation and of the potential of the inflationary field. The Planck mission will be the first experiment able to constrain significantly these *B* modes over the full sky and hence to measure them on very large scales.

The first detection of CMB polarization at one degree angular scale of resolution, at a level compatible with predictions of the standard cosmological scenario, has been announced by Kovac et al. (2002; see also Leitch et al. 2004). Since then, CBI and CAPMAP have also obtained significant detection of CMB E-mode polarization (Readhead et al. 2004; and Barkats et al. 2005). More recently, the *B*oomerang (Piacentini et al. 2005; Montroy et al. 2005) and *WMAP* (Kogut et al. 2003; Page et al. 2006) teams have obtained a measurement of the temperature-polarization correlation and E-mode spectrum compatible with cosmological model. No significant constraint on B-mode at degree angular scales exist today.

While the measurement of the temperature and polarization auto and cross power spectra of the CMB carries a wealth of information about cosmological parameters and about scenarios for the generation of the seeds for structure formation, some near-degeneracies exist which require extremely precise measurements. In particular, a very precise control of systematic errors is required to constrain parameters which impact these anisotropies and polarization fields at a very low level.

Many sources of systematic errors are potentially a problem for polarization measurements. In particular, the shape of the beams of the instrument need to be known with extreme precision. In addition, when the measurements of several detectors are combined to obtain polarization signals, it is required that the responses of these detectors be matched precisely in terms of cross-calibration, beam shape, spectral response, etc.

Measurements of Planck telescope beams in the actual operation conditions are not to be made on ground. Also, there are no polarized astrophysical sources for the in-flight beam

calibration. Therefore, one should rely on numerical simulations of the beams and self-correcting algorithms of data processing that should allow efficient elimination of systematic errors. In polarization measurements, a significant systematic error would arise due to elliptical shapes of telescope beams which appear, mainly, due to ellipsoidal shape of telescope mirrors introducing astigmatic aberrations and other beam imperfections even with the otherwise ideal mirror surfaces.

In this paper, we investigate the impact of beam imperfections on the measurement of polarization power spectra. We then discuss a method for first-order correction of the effect of these imperfections. To illustrate this method, we apply it to the case of Planck HFI polarization measurement.

The remainder of this paper is organized as follows. In Sect. 2, we discuss the issue of beam shape mismatch for the detection of CMB polarization. Section 3 is dedicated to the computation of simulated readouts using the realistic beams described in Sect. 2 and the reconstruction of polarized power spectra. In Sect. 4, we present a method to correct for the systematic bias in the B mode power spectrum induced by the asymmetry of the beams. Finally, Sect. 5 draws the conclusions.

2. The beam-mismatch problem in polarization measurements

The HFI polarimeters employ Polarization Sensitive Bolometers (PSB) cooled down to the temperature of 100 mK by a space ^{3}He–^{4}He dilution fridge. These devices, also used on Boomerang (though at 300 mK), are presently the most sensitive operational detectors for CMB polarization measurements (Jones et al. 2003; Montroy et al. 2003). Each PSB measures the power of the CMB field component along one linear direction specified by the PSB orientation (Turner et al. 2001).

Ideally, the PSBs are combined in pairs, each pair placed at the rear side of respective HFI horn, with the two PSB of the pair, a and b, being oriented at 90° of relative angle and receiving the radiation from the same point on the sky. The ideal polarimeters produce the measured signals (readouts):

$$s_a = \frac{1}{2}(I + Q\cos 2\alpha + U\sin 2\alpha) \tag{1}$$

$$s_b = \frac{1}{2}(I - Q\cos 2\alpha - U\sin 2\alpha) \tag{2}$$

where I, Q, U are the Stokes parameters of incoming radiation (see e.g. Born & Wolf 1997, for the definition of Stokes parameters) and α is the angle between the orientation of the first (a) of two PSBs and the first (x) of two orthogonal axes of the frame chosen for the representation of Stokes parameters. The V Stokes parameter does not enter Eqs. (1), (2) since the PSBs are designed to be, ideally, insensitive to V and, besides, V is extremely small for the CMB radiation.

In practice, the detectors produce beam–integrated signals so that Eq. (1) is modified to (Kraus 1986)

$$s_a = \frac{1}{2}\int_{\rm beam} {\rm d}\Omega \int_{\rm band} {\rm d}\nu \left(\widetilde{I}_a I + \widetilde{Q}_a Q + \widetilde{U}_a U + \widetilde{V}_a V\right) \tag{3}$$

and similarly for s_b where the PSB responses $\widetilde{I}_a(\boldsymbol{x}, \nu)$ etc are the telescope beam patterns of Stokes parameters computed in transmitting mode and normalized to unity at maximum, functions of both the radiation frequency ν and the observation point $\boldsymbol{x}$ (the V term is neglected in most of the following discussion). The responses of different polarimeters (a and b) should be adjusted as much as possible (both in frequency and in angular pattern on the sky) so that, ideally, one should have

$$\widetilde{I}_a = \widetilde{I}_b \tag{4}$$

$$\widetilde{Q}_a = \widetilde{I}_a\cos 2\alpha, \quad \widetilde{U}_a = \widetilde{I}_a\sin 2\alpha, \tag{5}$$

$$\widetilde{Q}_b = -\widetilde{I}_b\cos 2\alpha, \quad \widetilde{U}_b = -\widetilde{I}_b\sin 2\alpha \tag{6}$$

$$\widetilde{V}_a = \widetilde{V}_b = 0 \tag{7}$$

where α, similarly to the definition above, is the angle of nominal orientation of polarimeter a on the sky with respect to the reference axis chosen for the definition of Q and U. In this case, with $\widetilde{I}_a = \widetilde{I}_b$, Eq. (3) is reduced to the form similar to Eqs. (1) and (2).

For simplicity, we approximate the PSB response as averaged over the frequency band of the particular channel, thus introducing the band-averaged beam patterns defined as

$$\widetilde{I}(\boldsymbol{x}) = \int_{\rm band} {\rm d}\nu\, \widetilde{I}(\boldsymbol{x}, \nu) \tag{8}$$

and similarly for $\widetilde{Q}$ and $\widetilde{U}$ (for radiation independent on ν on the beam width scale, this generates an exact readout).

Ideally, the beam patterns on the sky $\widetilde{I}(\boldsymbol{x})$ should be as close as possible to a perfect Gaussian. Unfortunately, design and construction imperfections, telescope aberrations, and optical misalignment all generate small differences in the beam patterns, the impact of which must be investigated accurately, especially for very sensitive CMB polarization measurements.

Measuring polarization, i.e. measuring the I, Q and U Stokes parameters, indeed involves combining several such measurements with different angles α to separate the I, Q and U contributions. The Planck HFI detector set-up is such that the beams of two horns with complementary pairs of PSB oriented at 45° one pair with respect to the other follow each other on circular scan paths on the sky as shown in Figs. 1 and 2 (see Appendix A for further detail and notations). Then, in a system where reference axes for defining Q and U are along the scan path (x) and orthogonal to it (y), the four readouts s_α of this set of PSB ($\alpha = 0°, 45°, 90°, 135°$) allow the direct measurement of I, Q and U as

$$\begin{aligned} I &= s_{0°} + s_{90°} = s_{45°} + s_{135°} \\ Q &= s_{0°} - s_{90°} \\ U &= s_{45°} - s_{135°}. \end{aligned} \tag{9}$$

In practice, when the responses $\widetilde{I}_{0°}$ and $\widetilde{I}_{90°}$ are not perfectly equal, there is a small residual of I in the estimate $\widehat{Q}$ of Q:

$$\widehat{Q} = Q + \frac{1}{2}\int_{\rm beam} {\rm d}\Omega \left(\widetilde{I}_{0°} - \widetilde{I}_{90°}\right) I. \tag{10}$$

Similarly, there may be a small leakage of each Stokes component into the others. These errors are a source of trouble for measuring B mode especially, as they result in the leakages of I into E and B (possibly significant) and of E into B because $I \gg E \gg B$ on most scales.

This source of systematic effects for polarization measurements is not specific to Planck. Any instrument measuring polarization in a similar way, where signals proportional to I need to be eliminated from the measurements in order to obtain polarization data, may suffer from this.

The quantitative investigation of the impact of such effects requires a realistic estimate of mismatch between the companion beams, the simulation of signal data using these beams, the

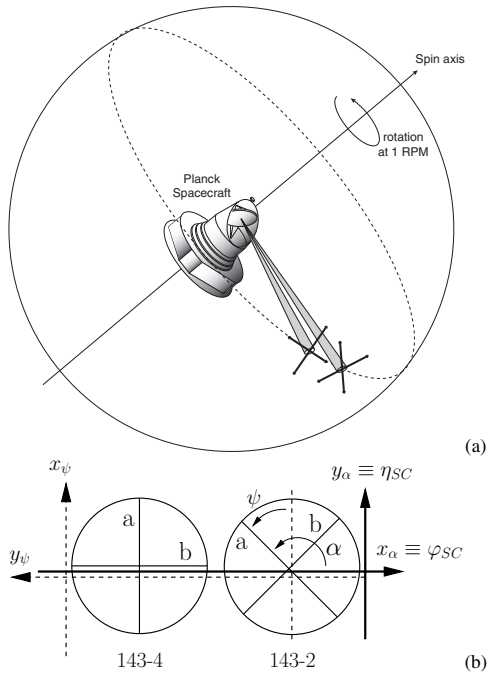

Fig. 1. a) The scanning of the polarized detectors provides the measurements of intensity of the CMB field components along four directions at each point on the scan path. **b)** Definition of axis specifying the Stokes parameters reference frame as seen from the sky. The detector pair on the left (e.g. 143-4) measures the Q Stokes parameter, while the pair on the right (e.g. 143-2) measures U when Q and U are defined with respect to the (x_α, y_α) frame (see Appendix A for further detail on reference axis).

reconstruction of maps and of power spectra using these simulated data, and the investigation of the correction of the effect by data processing methods.

The computation of the Planck HFI beams is discussed in Appendix A and in Yurchenko et al. (2004b). Here, we will describe their main characteristics relevant for the following sections. Because of telescope aberrations, the shape of the intensity beams is essentially Gaussian elliptic (down to nearly –30 dB) with the major axis around 10% longer than the minor axis (see Fig. 3). Thanks to the use of PSB, the intensity beams of an orthogonal pair of detectors within one horn are very close to each other: the difference is at most 0.6%. On the other hand, the difference between beams of detectors in two different horns can be up to 7%: this difference is mainly due to the different orientation of the beam ellipses. As emphasized in Appendix A, relaxing the assumptions of perfect conductors and perfect alignment is not expected to strongly modify the general shape of the beams. In the next sections, we will refer to these computer-simulated beams as "realistic beams".

3. Effect of beams on polarization power spectra

The main goal of this section is to study the systematic effect induced on the power spectra estimation by realistic beams described in the previous section, knowing that this effect will depend also on the scanning strategy. As the Planck mission will

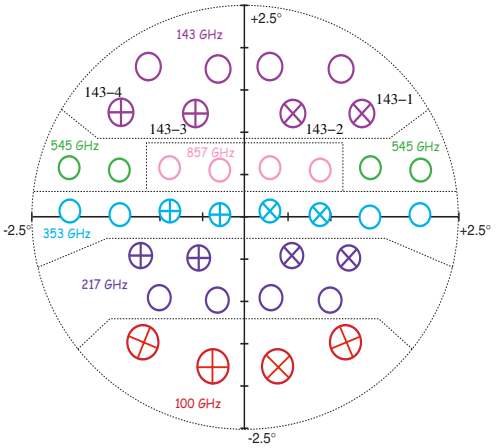

Fig. 2. Planck focal plane unit (FPU) with polarization sensitive bolometers as seen from the sky. Complementary pairs of PSB detectors are arranged in two horns following each other while scanning the sky so that four detectors are in an optimized configuration for polarization measurement.

scan the sky along large opening angle circles, resulting in large parts of the sky where the scans are mostly parallel, we have focused the study to the observation of a $15° \times 15°$ region of the sky scanned only along parallel directions. This restriction does not spoil the interest of the study as the small scale distortion of the beams are expected to affect mainly the small angular scales of the power spectra. In addition, other experiments scanning only a fraction of the sky are affected by the similar systematic effects. This restriction also offers a practical advantage: the computation of the effects of tiny beam mismatches on sub-beam scales requires a map resolution better than the beam size. For the Planck HFI 143 GHz channel, the resolution of about 7 arcmin justifies models at sub-arcminute scales. We have thus chosen to work on maps of 2048×2048 pixels of about 30 arcsec each.

The following paragraphs describe the generation of CMB polarization maps from power spectra, and the simulation of instrument signals.

3.1. Generation of CMB polarization maps

Simulated square maps of CMB intensity and polarization are generated using the approximate relation between the power spectra in flat ($C(k)$) and spherical (C_l) coordinates: $k^2C(k) \simeq l(l+1)C_l|_{l=k}$ (see, for example, White et al. 1999). The three maps of T, E and B are then computed from three independent realizations of Gaussian white noise $D^1(\mathbf{k})$, $D^2(\mathbf{k})$ and $D^3(\mathbf{k})$ as:

$$a^{T,B}(\mathbf{k}) = D^{1,3}(\mathbf{k}) \sqrt{C_l^{T,B}}$$

and

$$a^E(\mathbf{k}) = D^1(\mathbf{k}) \frac{C_l^{TE}}{\sqrt{C_l^T}} + D^2(\mathbf{k}) \left(C_l^E - \frac{\left(C_l^{TE}\right)^2}{C_l^T} \right)^{1/2}$$

so that the correlation between the T and E maps is taken into account. C_l's are the usual spectra describing the CMB temperature and polarization. For our simulations, we used the cosmological parameters from the *WMAP* best fit model, except that

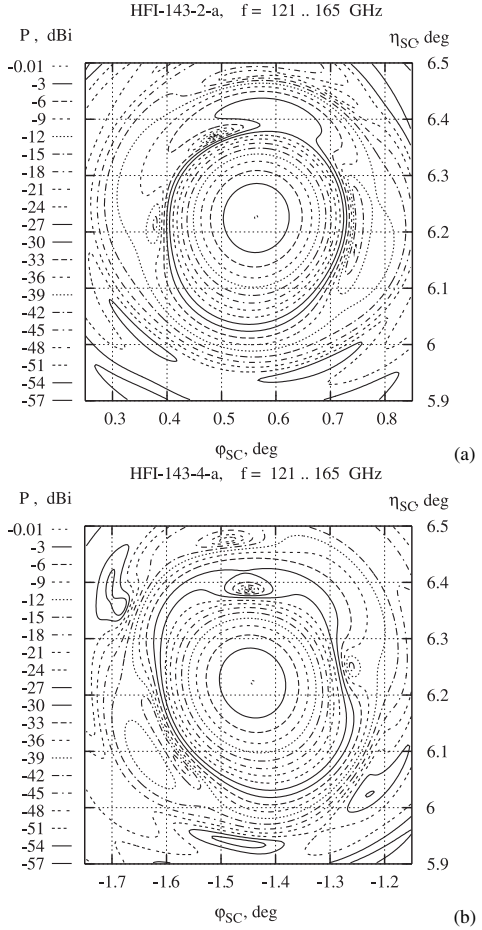

Fig. 3. Broad-band power patterns ($\widetilde{I}$ responses) of the telescope beams to be superimposed on the sky for polarization measurements, **a)** HFI-143-2a and **b)** HFI-143-4a, in SC spherical frame on the sky, with the spin axis of telescope as a pole (isolevels are shown from the maximum down to −60 dB with a step of −3 dB).

we imposed a tensor to scalar ratio of 0.1. The simulated maps include the Gaussian part of the gravitational lensing effect of the E mode.

3.2. Simulation of instrument readouts

The readouts must be computed from the I, Q and U Stokes parameters. We thus need to convert the E and B maps to Q and U using relations (38) in Zaldarriaga & Seljak (1997):

$$a^Q(\mathbf{k}) = a^E(\mathbf{k}) \cos 2\phi_{\mathbf{k}} - a^B(\mathbf{k}) \sin 2\phi_{\mathbf{k}} \quad (11)$$

$$a^U(\mathbf{k}) = a^E(\mathbf{k}) \sin 2\phi_{\mathbf{k}} + a^B(\mathbf{k}) \cos 2\phi_{\mathbf{k}} \quad (12)$$

where $k_x + \mathrm{i}k_y = k\mathrm{e}^{\mathrm{i}\phi_{\mathbf{k}}}$. The readout from one detector is then obtained by convolving its $\widetilde{I}$, $\widetilde{Q}$ and $\widetilde{U}$ beams with the I, Q and U maps from the sky and summing as in Eq. (3). In the case of the parallel scanning strategy we used, the convolution can be easily done, once for all directions of observation, by multiplication in Fourier space. Thus, we obtain four maps of readout signals, one for each polarization channel, s_{0°, s_{90°, s_{45° and s_{135°, with polarization angles $\alpha = 0^\circ$, 90°, 45° and 135° with respect to the x-axis of the map. With account of established focal plane unit (FPU) notation of channels (see Appendix A), they correspond, e.g., to the PSB channels 4b, 4a, 2b, and 2a, respectively, of two horns HFI-143-4 and HFI-143-2 where x-axis is the φ_{SC}-axis of spacecraft (SC, see Appendix A) frame viewed from the sky (Fig. 1b).

Since the goal of this work is to study only the systematic bias induced on polarization power spectra, we do not add any white or low-frequency noise to the signal, neither any other systematic effects (Kaplan & Delabrouille 2002). These other systematic effects will be studied in detail in a forthcoming paper. In particular, we assume here that the time constant of bolometers, which induce an elongation of the beams in the scanning direction, has been corrected for.

3.3. Reconstruction of the power spectra

The parallel scanning strategy allows us to reconstruct the I, Q and U maps from the readout maps using Eqs. (9). The reconstructed E and B maps can be obtained from Q and U using the reciprocal transformation of Eqs. (11) and (12). The power spectra are then estimated directly from the Fourier transform of the reconstructed $\widehat{I}$, $\widehat{E}$ and $\widehat{B}$ maps, by averaging the $\widehat{a}^X(\mathbf{k})\widehat{a}^{Y*}(\mathbf{k})$ in bins of width $\Delta k = \Delta l = 20$ (with $X, Y \in \{I, E, B\}$). The recovered power spectra are then corrected for the smoothing effect due to the beams, which can be approximated in Fourier space by a factor $\exp[-l(l+1)\sigma^2]$. However, because of the pixelization of the maps, this approximation is not good enough. Instead, we have corrected the power spectra using the power spectrum of the intensity beam, $B(k) = \left\langle |\widehat{a}^I(\mathbf{k})|^2 \right\rangle$, where $\widehat{a}^I(\mathbf{k})$ is the average of the intensity beams of the four detectors. This is exact if the beams are axially symmetric and identical, and otherwise provides a way to symmetrize the beams in Fourier space. We have used this correction in all the power spectra shown hereafter.

The B mode power spectrum reconstructed by using an ideal circular Gaussian beam in both the readout and reconstruction computations (assuming Eqs. (5) and (6)) is shown in Fig. 4a. The points shown are the average of 450 simulations and the error bars represent the dispersion. The relative error is shown in Fig. 4b, demonstrating that the statistical error on the power spectrum reconstruction averaged over 450 simulations is less than 2%. Finally, Fig. 5 presents the histogram of the bias divided by the dispersion, which is well fitted by a Gaussian with unit dispersion as expected for the ideal case. Identical results are obtained with other power spectra (T, E and T-E correlation).

We can now use this tool to estimate the bias induced on the power spectra reconstruction by the realistic beam shapes described in Sect. 2.

3.4. Effects of beams on polarization power spectra

We apply our algorithm (both the readout simulation and C_l reconstruction) using the realistic beam patterns $\tilde{I}$, $\tilde{Q}$ and $\tilde{U}$ presented in Sect. 2. The output power spectra shown in Figs. 6 and 7 are averaged over 450 simulations. The temperature power spectrum is perfectly recovered, while we can distinguish a small but systematic excess in the E power spectrum at $l > 2000$ and a systematic loss in the T-E correlation for $l > 1000$. The B mode

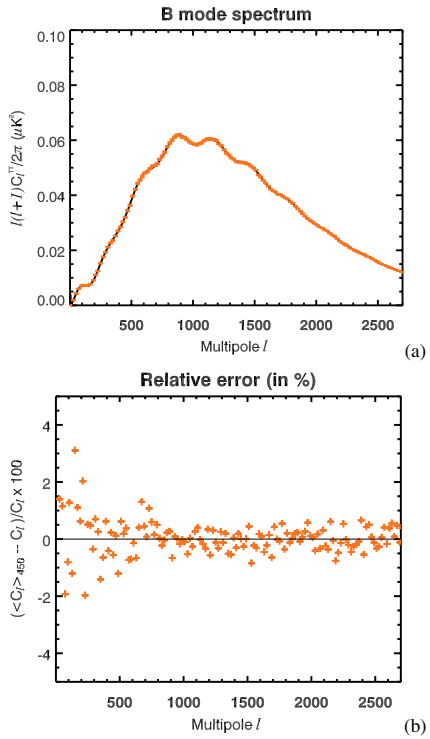

Fig. 4. a) Input and recovered B mode power spectrum with an ideal instrument, i.e. when four identical and axially symmetric Gaussian beams are used for both the readout generation and the C_l reconstruction. The small peak at $l \sim 100$ is produced by the gravitational waves (the tensor to scalar ratio is $r = 0.1$), while the main pattern peaking at $l \sim 1000$ is due to the lensing effect. The error bars are smaller than the thickness of the black solid line showing the input model. **b)** The relative error between the recovered and the initial power spectrum; the recovered power spectrum is the average of 450 simultations: the statistical error is less than 2%, thus allowing the detection, in non ideal cases, of biases higher than 2%. Identical figures are obtained for T, E and T-E correlation power spectra.

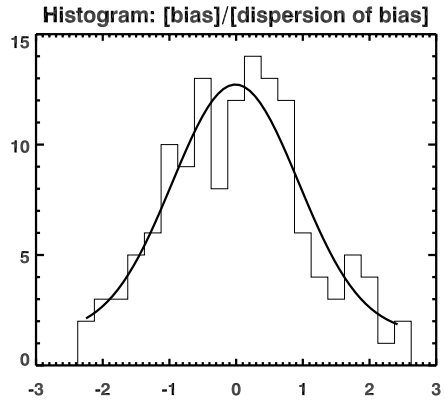

Fig. 5. Histogram of the biases divided by the statistical dispersion for all multipole bins shown in Fig. 4. As expected, the histogram is well fitted by a Gaussian of unit variance, showing that the dispersion on 450 simulations gives a good estimate of the errors.

is strongly affected after the peak of the lensing signal at $l \sim 900$, with a bias of up to 50% of the signal at $l \sim 1500$, and about 10% around the lensing signal peak at $l \sim 1000$.

The spurious B mode may come from leakage of either the temperature or the E mode. In order to separate the two possible origins, we have done the same simulation using the realistic beams $\tilde{I}$, $\tilde{Q}$ and $\tilde{U}$ when computing both the readouts and C_l reconstruction but with no input E mode (and no T-E correlation). The results for T-E, E and B power spectra are shown on Fig. 9 (the temperature power spectrum is not modified). We observe that the spurious B mode is about three times smaller in this case, indicating that about 2/3 of the spurious B seen with realistic input E mode came from E leakage. On the other hand, the level of the E mode is much higher than would be expected if it came from a mixing from B modes into E modes.

In order to check this, we made a simulation with elliptic Gaussian beams identical for detectors within the same horn, but with different ellipse directions for different horns. We have assumed Eqs. (5) and 6 to represent the ideal polarization sensitivity of the channels, so that there is no total intensity leakage into polarization signal due to beam difference, and, again, used no input E mode. In this situation, the recovered E mode is a small fraction of the input B mode signal, i.e. much smaller than the recovered E mode in the previous test. This means that the E mode recovered in the previous test (using realistic beams) was not due to a leakage from B modes to E modes, but rather from a leakage from T to E. We conclude that, both the E mode and the spurious B mode found with realistic simulated beams when there is no E mode in the readout simulation, come from a temperature leakage due to the differences in the beam patterns between detectors within the same horn, which is up to 0.9% (Fig. A.1a).

We thus see that two different effects produce the observed spurious B mode. First, there is a mixing between the two polarization modes, essentially from E to B as $E \gg B$ on all scales, due to the beam mismatch between the two different horns. Second, there is a temperature leakage, this time due to the beam mismatch between the PSB within the same horn.

As seen in Fig. 7, the beam asymmetry affects mainly the high-l part of the power spectra (typically $l > 500$). However, it is not negligible at low l, where the gravitational waves lie. Figure 8 shows the recovered power spectra when there is no initial B mode in the simulation compared to the expected B mode signal from gravitational for various tensor-to-scalar ratios. The leakage from T and E mode to B mode power spectrum becomes greater than the gravitational wave B mode signal for $T/S \lesssim 10^{-5}$.

3.5. Link with previous work

Various studies have been done on the systematic effects on CMB polarization measurements, in particular the exhaustive work by Hu et al. (2002, referred to as HHZ hereafter). This paper tries to estimate analytically the systematic effects on B mode power spectrum, using a second order expansion and relating the terms of the expansion to beam defects such as, for example, pointing error, ellipticity, monopole leakage or calibration. The different systematic effects are assumed to be described by a statistically isotropic field, with a power spectrum of the form:

$$C_l \propto \exp(-l(l+1)\alpha^2), \quad (13)$$

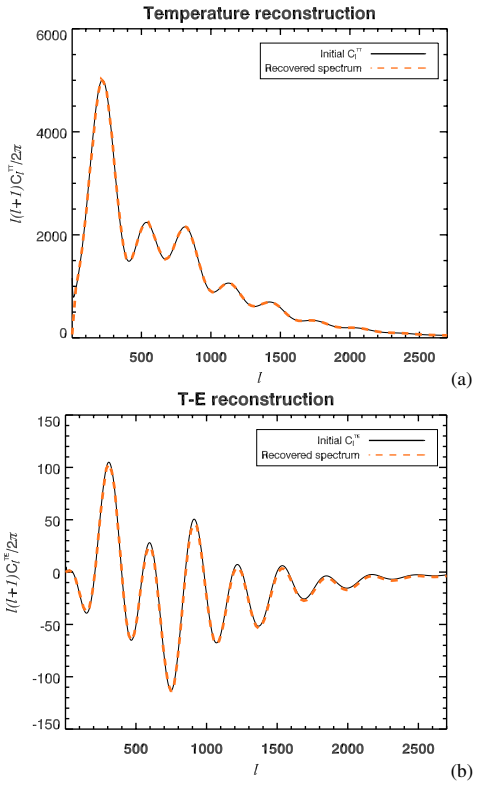

Fig. 6. Input and recovered power spectra of **a)** temperature and **b)** T-E correlation signals, using the simulated beams of Sect. 2 for the readout simulation and the C_l reconstruction. The recovered power spectra are corrected for an average symmetric beam effect by multiplying them by the power spectrum of the average beam map.

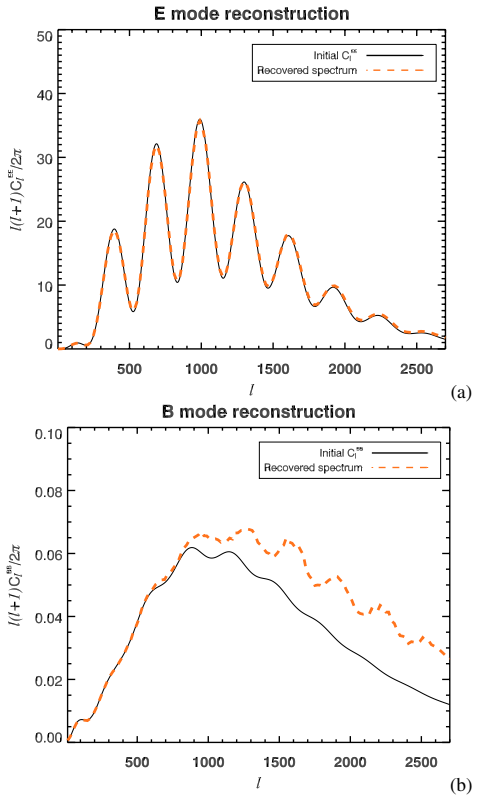

Fig. 7. Input and recovered power spectra of **a)** E mode and **b)** B mode signals, using the simulated beams of Sect. 2 for the readout simulation and the C_l reconstruction. The recovered power spectra are corrected for an average symmetric beam effect by multiplying them by the power spectrum of the average beam map.

so that the leakage from T or E to B can be written as a convolution between EE or TT and systematic effect power spectra (Eqs. (30) and (34) in HHZ).

In our approach, the I, Q and U maps are given through the signals of four detectors (Eqs. (9)). In the quasi-ideal case of all Q and U beams defined by Eqs. (5) and (6), but with intensity beams different between the two horns, it can be shown that the error on the B mode power spectrum is given by:

$$\delta C_l^{BB} = \frac{\left\langle \left|\Delta\widetilde{I}_{13}(\mathbf{l})\right|^2 \cos^2(2\phi_l)\sin^2(2\phi_l)\right\rangle_{\phi_l}}{B_l} C_l^{EE}(\sigma) \qquad (14)$$

where $\Delta\widetilde{I}_{13} = \widetilde{I}_1 - \widetilde{I}_3$ is the beam difference, B_l is the average beam power spectrum and $C_l^{EE}(\sigma)$ is the power spectrum of the E map convolved with the average beam. This form is a particular case of the one given by HHZ, and describes completely the systematic effects on the B mode power spectrum due to the beam mismatch between horns. Note however that there is no mixing between different l of the power spectra. The major difference with HHZ estimate is in the shape of the beam difference power spectrum (first factor in Eq. (14)) which can be fitted by $C_l^{\delta I} \propto l^4$ in the interval $l \in \{1, \ldots, 3000\}$, very different from HHZ assumption, Eq. (13).

In the particular case we consider (beam mismatch) our approach gives more realistic results, as we use accurate simulations of the beams. Moreover, the power spectrum of the defect due to beam mismatch we compute from these beams is very different to HHZ assumption, leading to a different estimate of the size of the effect.

4. Correction of polarization spectra for systematic errors

We shall now propose a simple way to correct for the spurious B mode deduced from the observations of the previous section. The idea is to assume that temperature and E mode maps are recovered well enough to estimate the T and E to B mode leakage, if we know the beam patterns. We will discuss three cases of C_l correction, depending on the knowledge of the beams. In all three cases, the initial readouts are generated with the realistic $\tilde{I}$, $\tilde{Q}$ and $\tilde{U}$ beam patterns of Sect. 2.

4.1. Perfect knowledge of the intensity beam pattern

In order to have an idea of the ability of the method to remove the spurious B mode, we have tested it in the case of a perfect

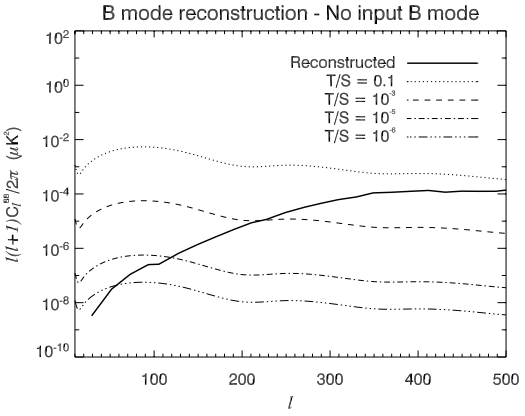

Fig. 8. Recovered B mode power spectrum in a simulation with no initial B mode. The theoretical B mode power spectra due to primordial gravitational waves are also shown for different values of the tensor-to-scalar ratio: 0.1, 10^{-3}, 10^{-5} and 10^{-6} from top to bottom.

knowledge of the intensity beam patterns. However, because of the lack of polarized point sources with known polarization characteristic, we assumed that only the intensity beam patterns $\widetilde{I}$ were perfectly measured while the $\tilde{Q}$ and $\tilde{U}$ needed for the C_l correction are computed using relations (5) and (6) with the relevant $\tilde{I}$ in all the three cases considered.

The method is as follows. By a quick analysis of the data, we would find maps and their corresponding power spectra similar to the ones shown in Figs. 6 and 7. Since the T and E mode power spectra are recovered with a very good approximation, we may assume that the recovered maps are good as well. Starting with the temperature and the E mode maps, assuming no initial B mode and using a precise knowledge of the beams, we could then simulate the instrument signals. From the previous consideration, we expect to find, from these simulated signals, a spurious B mode polarization coming both from a temperature leakage and a polarization mode mixing. The B mode power spectrum of this simulated signal should be an estimate of the spurious B mode.

The result for the B mode correction, using exact $\tilde{I}_a$ and $\tilde{I}_b$ and assuming relations (5) and (6) for the leakage estimation, is shown in Fig. 10. The correction allows us to reduce the bias down to less than 1% of the lensing signal in the interval $2 < l < 1500$.

4.2. Assuming identical beams within the same horn

In a second case, we supposed that, in order to increase the signal to noise ratio, we need to use the signal from both detectors within one horn to measure the beam patterns. With this method, we would find as beam pattern the average of the beams of the two detectors within one horn, i.e. the average error on the beams is about 0.5% of the beam maximum.

The result obtained for the B mode correction is presented in Fig. 11. This time, there is still some bias left in the corrected power spectrum, around 3% at $l \sim 1000$ and up to 13% for $l \sim 2100$.

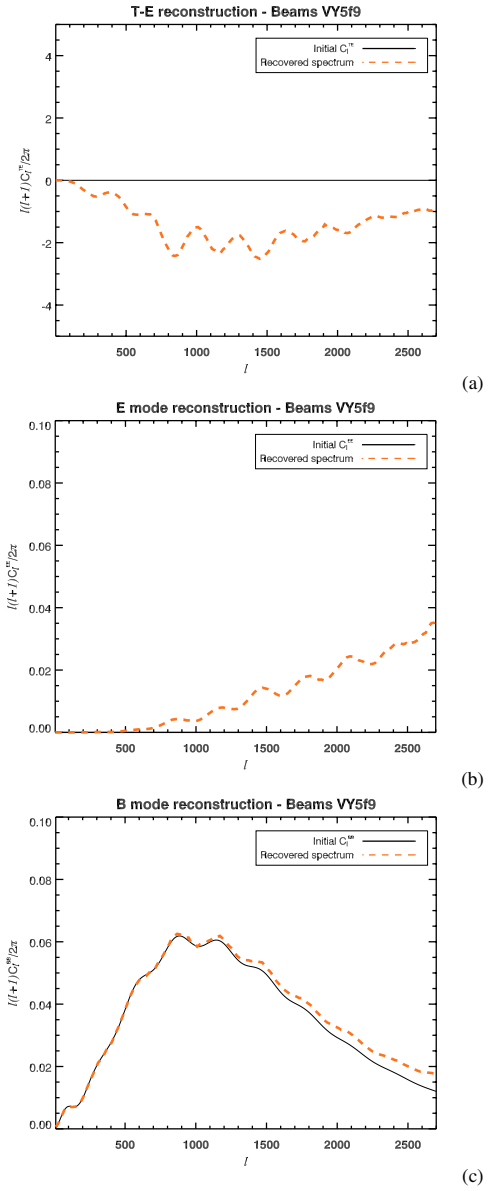

Fig. 9. Spurious generation of E and B modes from temperature signals using simulated beams of Sect. 2 for the readout simulation and the C_l reconstruction, but with no initial E mode.

4.3. Fitting the beams with elliptic Gaussians

If we have only few point sources or low signal-to-noise ratio on signal, we may want to parametrize the beam patterns with a function requiring a small number of parameters. As an example, we have fitted the four intensity beam patterns by elliptic Gaussian. The error of the fit is around 2% of the maximum of the beam.

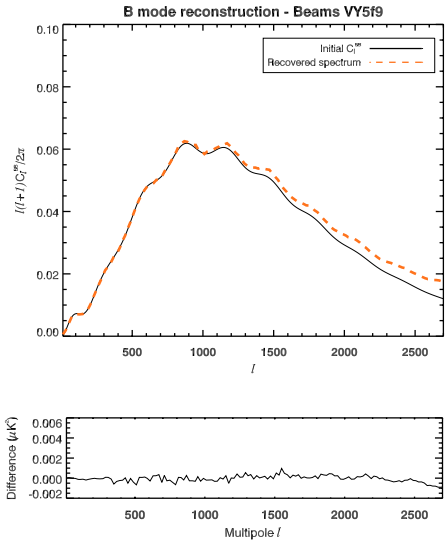

Fig. 10. Recovered B mode power spectrum before (red, dashed line) and after (green, dot-and-dashed line) correction. The power spectrum is corrected by subtracting the estimated leakage (blue dotted line) assuming knowledge of the exact beams (see text). *Bottom*: difference between corrected and initial power spectra.

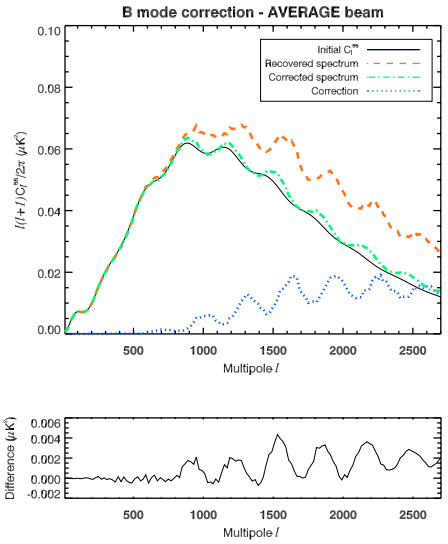

Fig. 11. Recovered B mode power spectrum before (red, dashed line) and after (green, dot-and-dashed line) correction. The power spectrum is corrected by subtracting the estimated leakage (blue dotted line) using beams averaged within one horn (0.5% error, see text). *Bottom*: difference between corrected and initial power spectra.

The result is shown in Fig. 12, together with the difference between the corrected and initial B mode power spectra. The result is very similar to that of Fig. 11 (using horn-averaged beams), though the remaining bias is slightly higher.

This simple method thus seems efficient to recover the right height of the lensing effect peak at $l \sim 1000$. Though it is applied here in the case of a simple scanning strategy (parallel scans), it should be applicable to any scan strategy, as soon as the bias estimation is done using the beams as precise as possible and the same scanning strategy as the real one.

5. Conclusions

In this paper, we have shown the effect of asymmetric telescope beams on the bolometric measurements of polarization of incoming radiation by considering the case of the Planck satellite mission. We have used electromagnetic simulation of the optical system (including telescope and horns) to compute the main beam shapes of the different detectors of Planck. These beams are roughly Gaussian elliptical, with a major axis 10% larger than the minor axis and with essentially different orientations of the beam ellipses for the two horns to be combined to measure the full set of Stokes parameters, I, Q and U.

By simulating the scan of a patch of the sky by Planck with these realistic, simulated beams, we have estimated the bias induced on the E and B mode polarization spectra due to their asymmetric shapes. We first remark that the E mode power spectrum is very well recovered (once corrected for an effective symmetric beam), the bias being around 0.1% of the signal in the multipole range $300 < l < 2000$, where lies the most interesting part of the signal. On the other hand, the B mode is affected by a bias around 10% at the peak of the lensing signal ($l \sim 1000$) and increasing for higher l, up to 100% of the signal at $l \sim 2500$.

This bias has two origins. First, it is produced by the difference of beam patterns of two different horns combined to measure Q and U. This difference induces mainly an error on the polarization angle, which turns to a mixing of E and B modes. Since, in general, $E \gg B$, we observe finally a leakage from E to B. The second origin of the bias is the minor difference of beam patterns of two PSB channels with orthogonal polarizations within the same horn, which induces a temperature to polarization leakage.

Finally, we have proposed a way to correct the B mode power spectrum from the above bias in a one-step correction which uses the measured T and E maps to compute the expected leakage into B when they are observed with a model of the instrument's beams. The efficiency of this correction depends on the precision of the beam knowledge: for example, using elliptical Gaussian fits of the actual beams allows us to reduce the bias from 10% to 3% at the lensing signal peak, $l \sim 1000$. In all cases, this first order correction has been shown to reduce significantly B mode contamination. More refined treatments, currently being investigated, are expected to be yet more efficient if needed.

Acknowledgements. The authors would like to thank Ken Ganga for fruitful discussions. We also want to thank the referee for interesting remarks which helped us to improve the manuscript. This work was supported by the Ulysses 2002 and 2003 Research Visit Grants paid by the Enterprise Ireland and CNRS France.

Appendix A: Simulation of the Planck HFI telescope beams

It will not be possible to measure HFI beams on ground. The HFI bolometers indeed work only at 100 mK and are designed for the thermal load of a few Kelvin environment in space. Whereas the instrument can be put in a large vacuum tank cooled to 4 K, it is not possible to perform far field measurements of the full

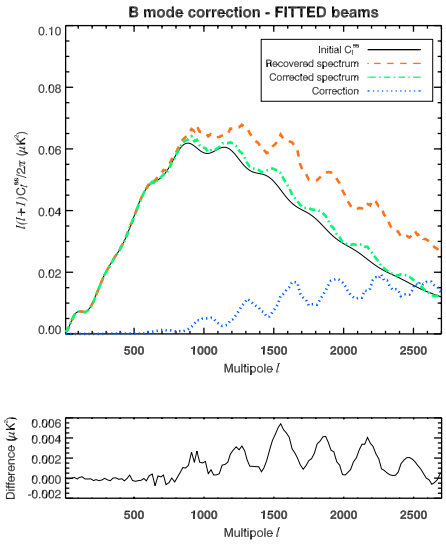

Fig. 12. Recovered B mode power spectrum before (red, dashed line) and after (green, dot-and-dashed line) correction. The power spectrum is corrected by subtracting the estimated leakage (blue dotted line) using elliptic Gaussian beams fitted on the exact beams (2% error, see text). *Bottom*: difference between corrected and initial power spectra.

system, which would require placing a source hundreds of meters away from the instrument. Hence, responses can only be measured at subsystem level (e.g. bolometers + horns) and must be associated to a physical model of the telescope to predict the beam shape of the complete integrated optical system.

In this paper, for the investigation of beam mismatch effects, we use computer-simulated Planck HFI beams. We consider four HFI-143 beams comprising eight PSB channels used for the polarization measurements in the band centered at the frequency $\nu = 143$ GHz. The polarization direction of each PSB is specified by the polarization angle ψ on the sky and labeled by the relevant index of the channel (ψ_{1a}, ψ_{1b} etc.) as shown in Fig. 1b.

In the design of the focal plane unit (FPU), the polarization angles $\psi_{i\alpha}$ notifying the channels are measured from the upward direction of local meridian of the spherical frame of spacecraft (SC) having the geometrical spin axis of telescope as a pole and counting the angles Ψ, as viewed from telescope, clockwise toward the direction of maximum polarization sensitivity of the channel. Similarly, we define the polarization angle ψ at each observation point $\boldsymbol{x}$ in the beam pattern. The direction of maximum polarization sensitivity is the major axis of polarization ellipse at point $\boldsymbol{x}$; for the angles $\psi_{i\alpha}$ notifying the channels, $\boldsymbol{x}$ is the beam axis defined as the point of maximum intensity $\widetilde{I}$ (at this point, the beam field is linearly polarized).

Following this definition, we consider eight PSB channels of the HFI-143 beams which are sensitive to the linearly polarized radiation with polarization angles on the sky $\psi_{1a} = \psi_{2a} = 45°$, $\psi_{1b} = \psi_{2b} = 135°$, $\psi_{3a} = \psi_{4a} = 0°$, and $\psi_{3b} = \psi_{4b} = 90°$. The four beams are arranged in two pairs (1 and 3, 2 and 4), with two beams of each pair scanning the sky along the same scan path as shown in Figs. 1 and 2. In each pair of beams, the angles $\psi_{i\alpha}$ correspond to a full set of four PSB detectors for polarization measurements with optimized polarimeter configuration (Couchot et al. 1999).

The power patterns of two beams tracing the same scan path, HFI-143-2-a/b and HFI-143-4-a/b, are shown in Fig. 3 as projected on the sky in the spherical frame SC with coordinates $\varphi_{\rm SC}, \theta_{\rm SC}$ ($\eta_{\rm SC} = 90° - \theta_{\rm SC}$) where the azimuthal angle $\varphi_{\rm SC}$ is counted to the right from the optical axis of telescope as viewed from the sky and the polar angle $\theta_{\rm SC}$ is measured from the upward direction of nominal spin axis (the optical axis of the telescope corresponds to $\varphi_{\rm SC} = 0°$ and $\eta_{\rm SC} = 5°$).

Notice that both the a, b labels of channels and polarization angles ψ are conventionally defined with respect to meridians (verticals) of the SC frame viewed from telescope, as accepted by the FPU design. In the meantime, because of the scanning strategy, the reference axes for the Stokes parameters on the CMB maps are usually parallels (horizontals) of the SC frame viewed from the sky to the telescope.

To reconcile these definitions, we continue to use the polarization angles ψ and the established notations a, b for the PSB channels. In the same time, for processing the readouts according to Eqs. (1)–(3), we define beam responses $\widetilde{I}$, $\widetilde{Q}$, $\widetilde{U}$, $\widetilde{V}$ in SC frame viewed from sky, with the first and the second reference axes being the azimuth $\varphi_{\rm SC}$ and the elevation $\eta_{\rm SC}$, respectively (they constitute the right-hand frame xy for defining Stokes parameters on the sky as viewed from sky to telescope). With these definitions, the polarization angle in xy frame is the angle α in Eqs. (1), (2) where $\alpha = \psi + 90°$.

The beams in Fig. 3 are computed with an extended version of the fast physical optics code (Yurchenko et al. 2001) developed specifically for the efficient simulations of the Planck HFI beams. The extended code allows us to propagate via the telescope the aperture field of the HFI horns mode-by-mode at various frequencies. The aperture field is generated by the PSB bolometers considered as polarized black-body radiators (in the transmitting mode) located at the rear side of the horns. In this way, we obtain the band-averaged far-field patterns of Stokes parameter responses $\widetilde{I}$, $\widetilde{Q}$, $\widetilde{U}$, $\widetilde{V}$ of the broad-band telescope beams as produced by the actual corrugated horns (Yurchenko et al. 2002) rather than by simplified model feeds.

Rigorous computations of beams require scattering matrix simulations of horns (Murphy et al. 2002). In this approach, the effective modes of the electric field at the horn aperture, E_{nm}, are represented via the canonical TE, TM modes $\mathcal{E}_{nj}$ of a cylindrical waveguide as follows

$$E_{nm}(\rho, \varphi) = \sum_{j=1}^{2M} S_{nmj} \mathcal{E}_{nj}(\rho, \varphi) \qquad \text{(A.1)}$$

where S_{nmj} is the scattering matrix computed by Murphy et al. (2002) for each horn at various frequencies, $n = 0, 1, ..., N$ is the azimuthal index and $m, j = 1, 2, ..., 2M$ are the radial indices accounting for both the TE ($m, j = 1, ..., M$) and TM ($m, j = M + 1, ..., 2M$) modes.

Recent simulations of the HFI-143 beams (Yurchenko et al. 2004a) were performed with the scattering matrices of size 20×20 ($M = 10$, $N = 1$) using nine sampling frequencies spanning the band $\nu = 123$–163 GHz. Although the power patterns of these beams only slightly differ from those computed earlier (Yurchenko et al. 2002) with matrices 10×10 and five sampling frequencies ($\Delta P < 0.1$ dB at $P = -3$ dB and $\Delta P < 1.5$ dB at $P = -30$ dB), the effect on the difference between the beams of different polarization and on the fine polarization properties of beams is noticeable. This suggests that the latter parameters could be sensitive to other features of the model as well.

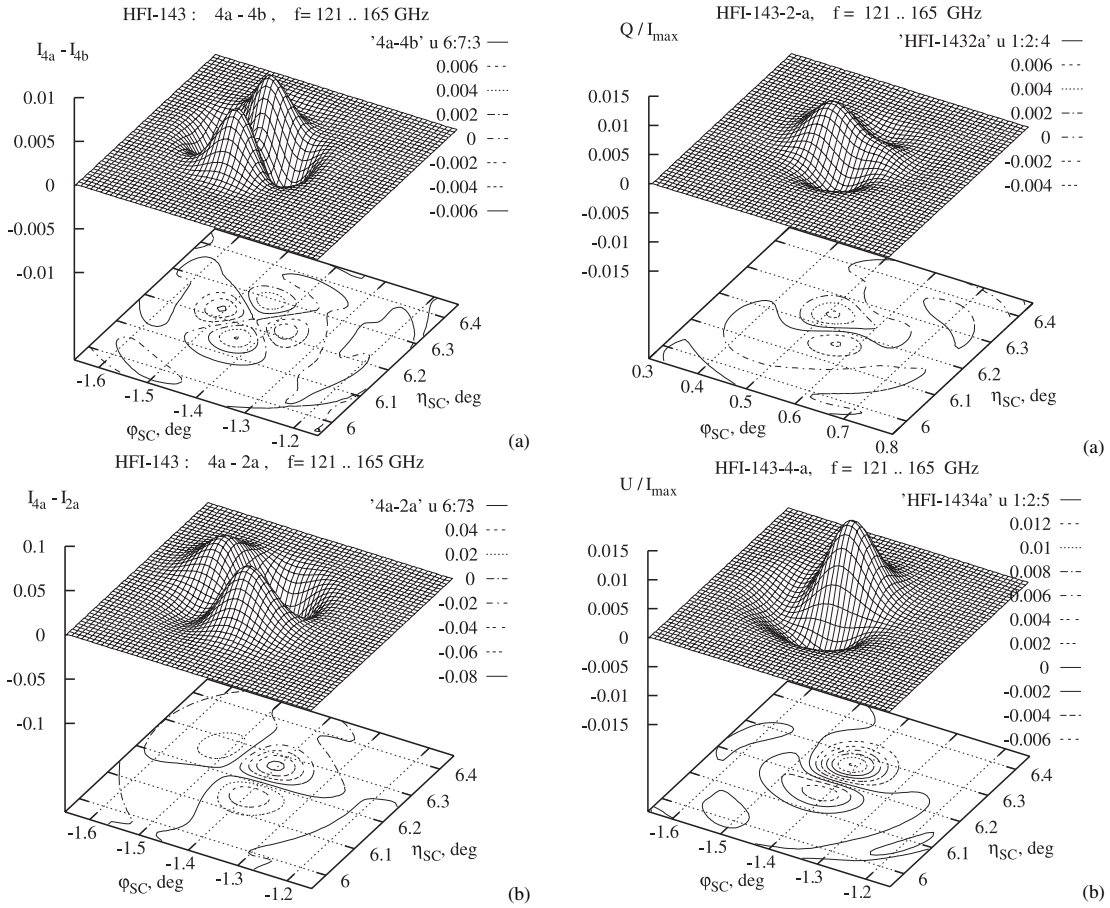

Fig. A.1. Relative difference of power patterns **a)** $\widetilde{I}_{4a} - \widetilde{I}_{4b}$ of two orthogonal channels of the same beam HFI-143-4 ($\psi = 0°$ and $\psi = 90°$, respectively) and **b)** $\widetilde{I}_{4a} - \widetilde{I}_{2a}$ of the channels HFI-143-4a and HFI-143-2a ($\psi = 0°$ and $\psi = 45°$, respectively) when superimposed by spinning the telescope about the geometrical spin axis.

Fig. A.2. The $\widetilde{Q}$ and $\widetilde{U}$ Stokes parameters responses: **a)** $\widetilde{Q}$ of the beam HFI-143-2a and **b)** $\widetilde{U}$ of the beam HFI-143-4a (ideally, both $\widetilde{Q}$ and $\widetilde{U}$ should be zero in the beams of these polarizations for the selected reference axes).

In this paper, the HFI-143 beams are computed with two essential updates compared to (Yurchenko et al. 2004a): the horn design is slightly altered so that the horns are now slightly elongated compared to those used earlier, and the horn positions are now the final ones, being defined by the parameter $R_C = 1.2$ mm that specifies the refocus of the horn aperture with respect to the geometrical focus of telescope for each beam.

The horn positions were optimized to achieve the best resolution (the minimum beam width) of the broadband beams (this also maximizes the gain) so that the value $R_C = 1.2$ mm is close to the optimal horn positioning. We use updated scattering matrices of size 20×20 for representing the horn field and nine sampling frequencies for spanning the frequency band $\nu = 121$–165 GHz which is characteristic of the updated horns.

At this stage, we assume smooth telescope mirrors with ideal elliptical shape, perfect electrical conductivity of their reflective surfaces, and with ideal positioning of both the mirrors and horn antennas. The convergence accuracy of computations was better than 0.1% relative to the maximum of the beam intensity pattern $\widetilde{I}(\varphi, \eta)$ (for comparison, the difference of the broadband power pattern and the pattern computed at the central frequency is about 1%).

To be perfectly representative of what the actual beams may be, one should take into account possible misalignments of the optics, tilts and deformations of the mirrors, etc. In principle, however, tolerances on the alignment of mirrors and positioning of horns are such that the modifications they induce on the beams are supposed to be small, and we neglect this last issue for the present work.

To minimize the beam mismatch between the channels of orthogonal polarizations, the PSB bolometers of each pair of channels, *a* and *b*, are placed in the same cavity in the rear side of the respective horn and share the same optics – waveguides, filters, horns, telescope. Because of this design, the difference of power patterns of orthogonal polarizations of the same beam on the sky is really small (Fig. A.1a), with the peak value for all the broadband beams being about $\delta\widetilde{I}_{4a4b} = \max(\widetilde{I}_{4a} - \widetilde{I}_{4b})/\widetilde{I}_{\max} = 0.6\%$

(at the central frequency $f = 143$ GHz, the typical difference is $\delta\widetilde{I}_{4a4b} = 0.9\%$).

A small difference of this kind arises for two reasons: (a) due to minor axial asymmetry of polarized modes that appears on the horn aperture when the PSB radiation (in the transmitting mode) propagates through the horn (the difference varies in sign and magnitude with frequency, though being well balanced over the band) and (b) due to some difference in the propagation of different polarizations along the same path via the telescope (all the differences are computed with the patterns normalized to the unit total power of the beams).

The mismatch of power patterns of different beams is about 10 times more significant (Fig. A.1b). It depends essentially on the location of horns in the focal plane of telescope. For the pair of beams HFI-143-2 and HFI-143-4, when superimposed on the sky by spinning the telescope until the coincidence of azimuths of beam axes, the peak difference of the relative power across the pattern varies from 7.0% to 8.2% depending on the polarizations being compared. Notice that the statistical difference of 5% is already rather crucial for the reliable reconstruction of the CMB polarization map (Kaplan et al. 2002).

Figure A.2 shows the patterns of $\widetilde{Q}$ and $\widetilde{U}$ Stokes parameter responses of the HFI-143-2a and HFI-143-4a beams, respectively. The peak values of these parameters are $\widetilde{Q}_{2a} = 0.6\%$ and $\widetilde{U}_{4a} = 1.2\%$ (ideally, $\widetilde{Q}$ and $\widetilde{U}$ should be zero in these polarizations). For comparison, the peak values of $\widetilde{V}$ are 3.7% and 4.2%, respectively. The positive and negative values of $\widetilde{Q}$ and $\widetilde{U}$ (as well as $\widetilde{V}$) are well balanced over the beam patterns and the average is very close to zero. It proves that the chosen directions of polarization of the horn aperture field as found by optimizing on-axis beam polarization directions (Yurchenko 2002) are pretty good, even though the beam patterns are not quite symmetrical due to aberrations.

The analysis of different contributions to non-zero values of $\widetilde{Q}_{2a}$, $\widetilde{U}_{4a}$ and $\widetilde{V}$ shows that $\widetilde{V}$ arises mainly because of the field propagation via the telescope ($\widetilde{V}_{\max}$ on the horn aperture is only 0.5%). On the contrary, both $\widetilde{Q}_{2a} = 0.6\%$ and $\widetilde{U}_{4a} = 1.2\%$ given above and the power differences between the orthogonal channels of the same beams, $\delta\widetilde{I}_{2a2b} = \delta\widetilde{I}_{4a4b} = 0.6\%$, are essentially due to the horn effects ($\widetilde{U} = 0.4\%$ and $\delta\widetilde{I}_{ab} = 0.8\%$ on the horn aperture). The telescope contribution, though non-additive, is still important, as the propagation of the axially symmetric quasi-Gaussian source field shows (in this case, $\delta\widetilde{I}_{2a2b} = 0.9\%$ and $\delta\widetilde{I}_{4a4b} = 1.0\%$ in the beams on the sky, being zero in the source field).

Finally, in the cross-beam power differences $\delta\widetilde{I}_{2\alpha4\beta}$, both the horn and the telescope effects are significant (e.g., $\delta\widetilde{I}_{2\alpha4\beta}$ depends, to some extent, on polarizations being compared), although the telescope effect dominates (for the quasi-Gaussian source field, $\delta\widetilde{I}_{2\alpha4\beta}$ varies from 5.7% to 6.7% in a way consistent with the variations in the beams from the actual corrugated horns of respective polarizations).

References

Barkats, D. Bischoff, C., Farese, P., et al. 2005, ApJ 619 L127
Bennett, C. L. Halpern, M., Hinshaw, G., et al. 2003, ApJS 148, 1
Benoît, A., Ade, P., Amblard, A., et al. 2003a, A&A, 399, L19
Benoît, A., Ade, P., Amblard, A., et al. 2003b, A&A, 399, L25
de Bernardis, P., Ade, P. A. R., Bock, J. J., et al. 2000, Nature, 404, 95
Born, M., & Wolf, E. 1997, Principles of Optics
Couchot, F., Delabrouille, J., Kaplan, J., & Revenu, B. 1999, A&A, 135, 579
Hanany, S., Ade, P., Balbi, A., et al. 2000, ApJ, 545, L5
Hinshaw, G., Spergel, D. N., Verde, L., et al. 2003, ApJS, 148, 135
Jones, W. C., Bhatia, R., Bock, J., & Lange, A. E. 2003, Proc. SPIE, 4855, 227
Kaplan, J., & Delabrouille, J. 2002, in Astrophysical Polarized Backgrounds, AIP Conf. Proc., 609, 209
Komatsu, E., Kogut, A., Nolta, M., et al. 2003, ApJS, 148, 119
Kogut, A., Spergel, D. N., Barnes, C., et al. 2003, ApJS, 148, 161
Kovac, J., Leitch, E. M., Pryke, C., et al. 2002, Nature, 420, 772
Hu, W, Hedman, M. M., & Zaldarriaga, M. 2003, Phys. Rev. D, 67, 4, 043004
Kraus, J. D. 1986, Radioastronomy
Lee, A. T., Ade, P., Balbi, A., et al. 2001, ApJ, 561, L1
Leitch, E. M., Kovac, J. M., Halverson, N.W., et al. 2004, ApJ, submitted [arXiv:astro-ph/0409357]
Miller, A. D., Caldwell, R., Devlin, M. J., et al. 1999, ApJ, 524, L15
Montroy, T., Ade, P. A. R., Balbi, A., et al. 2003, New Astron. Revi., 47, 11–12, 1057
Montroy, T. E., Ade P. A. R., Bock J. J., et al. 2005, [arXiv:astro-ph/0507514], submitted
Murphy, J. A., Gleeson, E., Maffei, B., & Wylde, R. J. 2002, in 25th ESA Antenna Workshop on Satellite Antenna Technology, ed. K. van 't Klooster, & L. Fanchi, (The Netherlands: ESTEC, Noordwijk), 649
Netterfield, C. B., Ade, P. A. R, Bock, J. J., et al. 2002, ApJ, 571, 604
Page, L., Hinshaw, G., Komatsu, E., et al. 2006, [arXiv:astro-ph/0603450]
Piacentini, F., Jones W. C., Ade P., et al. 2005, [arXiv:astro-ph/0507494]
Readhead, A. C. S., Myers, S. T., Pearson, T. J., et al. 2004, Science, 306, 836
Smoot, G. F., Bennett, C. L., Kogut, A., et al. 1992, ApJ, 396, L1
Spergel, D. N., Verde, L., Peiris, H. V., et al. 2003, ApJS, 148, 175
Spergel, D. N., Bean, R., Doré, O., et al. 2006, submitted
Turner, A. D., Bock, J. J., Beeman, J. W., et al. 2001, Appl. Opt., 40, 4921
Vielva, P., Martínez-González, E., Bareiro, R. B., et al. 2004 ApJ, 609, 22
White, M., Carlstrom, J. E., Dragovan, M., & Holzapfel, W. L. 1999, Astrophys. J., 514, 12
Yurchenko, V. B. 2002, in Experimental Cosmology at Millimetre Wavelengths, ed. M. De Petris, P. A. Moro, & M. Gervasi, AIP Conf. Proc., 616, 234
Yurchenko, V. B., Murphy, J. A., & Lamarre, J.-M. 2001, Int. J. Infrared & Millimeter Waves, 22, 173
Yurchenko, V. B., Murphy, J. A., & Lamarre, J.-M. 2002, in 25th ESA Antenna Workshop on Satellite Antenna Technology, ed. K. van 't Klooster, & L. Fanchi (The Netherlands: ESTEC, Noordwijk), 281
Yurchenko, V. B., Murphy, J. A., Lamarre, J.-M., & Brossard, J. 2004a, Int. J. Infrared & Millimeter Waves, 25, 601
Yurchenko, V. B., Murphy, J. A., & Lamarre, J.-M. 2004b, Proc. SPIE Int. Soc. Opt. Eng. 5487, 542
Zaldarriaga, M., & Seljak, U 1997, Phys. Rev. D, 55, 1830

A&A 399, L19–L23 (2003)
DOI: 10.1051/0004-6361:20021850

Astronomy & Astrophysics

The cosmic microwave background anisotropy power spectrum measured by Archeops

A. Benoît[1], P. Ade[2], A. Amblard[3,24], R. Ansari[4], É. Aubourg[5,24], S. Bargot[4], J. G. Bartlett[3,24], J.–Ph. Bernard[7,16], R. S. Bhatia[8], A. Blanchard[6], J. J. Bock[8,9], A. Boscaleri[10], F. R. Bouchet[11], A. Bourrachot[4], P. Camus[1], F. Couchot[4], P. de Bernardis[12], J. Delabrouille[3,24], F.–X. Désert[13], O. Doré[11], M. Douspis[6,14], L. Dumoulin[15], X. Dupac[16], P. Filliatre[17], P. Fosalba[11], K. Ganga[18], F. Gannaway[2], B. Gautier[1], M. Giard[16], Y. Giraud–Héraud[3,24], R. Gispert[7†⋆], L. Guglielmi[3,24], J.–Ch. Hamilton[3,17], S. Hanany[19], S. Henrot–Versillé[4], J. Kaplan[3,24], G. Lagache[7], J.–M. Lamarre[7,25], A. E. Lange[8], J. F. Macías–Pérez[17], K. Madet[1], B. Maffei[2], Ch. Magneville[5,24], D. P. Marrone[19], S. Masi[12], F. Mayet[5], A. Murphy[20], F. Naraghi[17], F. Nati[12], G. Patanchon[3,24], G. Perrin[17], M. Piat[7], N. Ponthieu[17], S. Prunet[11], J.–L. Puget[7], C. Renault[17], C. Rosset[3,24], D. Santos[17], A. Starobinsky[21], I. Strukov[22], R. V. Sudiwala[2], R. Teyssier[11,23], M. Tristram[17], C. Tucker[2], J.–C. Vanel[3,24], D. Vibert[11], E. Wakui[2], and D. Yvon[5,24]

[1] Centre de Recherche sur les Très Basses Températures, BP 166, 38042 Grenoble Cedex 9, France
[2] Cardiff University, Physics Department, PO Box 913, 5 The Parade, Cardiff, CF24 3YB, UK
[3] Physique Corpusculaire et Cosmologie, Collège de France, 11 Pl. M. Berthelot, 75231 Paris Cedex 5, France
[4] Laboratoire de l'Accélérateur Linéaire, BP 34, Campus Orsay, 91898 Orsay Cedex, France
[5] CEA-CE Saclay, DAPNIA, Service de Physique des Particules, Bât. 141, 91191 Gif sur Yvette Cedex, France
[6] Laboratoire d'Astrophysique de l'Obs. Midi-Pyrénées, 14 avenue E. Belin, 31400 Toulouse, France
[7] Institut d'Astrophysique Spatiale, Bât. 121, Université Paris XI, 91405 Orsay Cedex, France
[8] California Institute of Technology, 105-24 Caltech, 1201 East California Blvd, Pasadena CA 91125, USA
[9] Jet Propulsion Laboratory, 4800 Oak Grove Drive, Pasadena, California 91109, USA
[10] IROE–CNR, via Panciatichi, 64, 50127 Firenze, Italy
[11] Institut d'Astrophysique de Paris, 98bis boulevard Arago, 75014 Paris, France
[12] Gruppo di Cosmologia Sperimentale, Dipart. di Fisica, Univ. "La Sapienza", P. A. Moro, 2, 00185 Roma, Italy
[13] Laboratoire d'Astrophysique, Obs. de Grenoble, BP 53, 38041 Grenoble Cedex 9, France
[14] Nuclear and Astrophysics Laboratory, Keble Road, Oxford, OX1 3RH, UK
[15] CSNSM–IN2P3, Bât. 108, Campus Orsay, 91405 Orsay Cedex, France
[16] Centre d'Étude Spatiale des Rayonnements, BP 4346, 31028 Toulouse Cedex 4, France
[17] Institut des Sciences Nucléaires, 53 avenue des Martyrs, 38026 Grenoble Cedex, France
[18] Infrared Processing and Analysis Center, Caltech, 770 South Wilson Avenue, Pasadena, CA 91125, USA
[19] School of Physics and Astronomy, 116 Church St. S.E., University of Minnesota, Minneapolis MN 55455, USA
[20] Experimental Physics, National University of Ireland, Maynooth, Ireland
[21] Landau Institute for Theoretical Physics, 119334 Moscow, Russia
[22] Space Research Institute, Profsoyuznaya St. 84/32, Moscow, Russia
[23] CEA-CE Saclay, DAPNIA, Service d'Astrophysique, Bât. 709, 91191 Gif sur Yvette Cedex, France
[24] Fédération de Recherche APC, Université Paris 7, Paris, France
[25] LERMA, Observatoire de Paris, 61 Av. de l'Observatoire, 75014 Paris, France

Received 16 October 2002 / Accepted 15 December 2002

Send offprint requests to: A. Benoît,
e-mail: benoit@grenoble.cnrs.fr

⋆ Richard Gispert passed away few weeks after his return from the early mission to Trapani.

Letter to the Editor

Abstract. We present a determination by the Archeops experiment of the angular power spectrum of the cosmic microwave background anisotropy in 16 bins over the multipole range $\ell = 15-350$. Archeops was conceived as a precursor of the Planck HFI instrument by using the same optical design and the same technology for the detectors and their cooling. Archeops is a balloon–borne instrument consisting of a 1.5 m aperture diameter telescope and an array of 21 photometers maintained at ~100 mK that are operating in 4 frequency bands centered at 143, 217, 353 and 545 GHz. The data were taken during the Arctic night of February 7, 2002 after the instrument was launched by CNES from Esrange base (Sweden). The entire data cover ~30% of the sky. This first analysis was obtained with a small subset of the dataset using the most sensitive photometer in each CMB band (143 and 217 GHz) and 12.6% of the sky at galactic latitudes above 30 degrees where the foreground contamination is measured to be negligible. The large sky coverage and medium resolution (better than 15 arcmin) provide for the first time a high signal-to-noise ratio determination of the power spectrum over angular scales that include both the first acoustic peak and scales probed by COBE/DMR. With a binning of $\Delta\ell = 7$ to 25 the error bars are dominated by sample variance for ℓ below 200. A companion paper details the cosmological implications.

Key words. cosmic microwave background – cosmology: observations – submillimeter

1. Introduction

Observations of the Cosmic Microwave Background (CMB) temperature anisotropies have provided answers to fundamental questions in cosmology. The observational determination of the CMB angular power spectrum has already led to important insights on the structure and evolution of the universe. Most notable are the conclusions that the geometry of space is essentially flat (Miller et al. 1999; de Bernardis et al. 2000; Hanany et al. 2000) and that the measurements are consistent with the inflationary paradigm (Netterfield et al. 2002; Lee et al. 2001; Halverson et al. 2002; Sievers et al. 2002; Rubiño-Martin et al. 2002). Since the first detection of CMB anisotropy with COBE/DMR (Smoot et al. 1992), a host of experiments have measured the spectrum down to sub–degree scales, but measurements at large angular scales remain difficult, due to the large sky coverage required to access these modes. This difficulty will be overcome by the future full–sky space missions MAP and Planck.

This paper presents the first results from Archeops, an experiment designed to obtain large sky coverage in a single balloon flight. A detailed description of the instrument inflight performance will be given in Benoît et al. (2003b); here we provide only essential information. Archeops[1] is a balloon–borne experiment with a 1.5 m off–axis Gregorian telescope and a bolometric array of 21 photometers operating at frequency bands centered at 143 GHz (8 bolometers), 217 GHz (6), 353 GHz (6 = 3 polarized pairs) and 545 GHz (1). The focal plane is maintained at a temperature of ~100 mK using a ^{3}He–^{4}He dilution cryostat. Observations are carried out by turning the payload at 2 rpm producing circular scans at a fixed elevation of ~41 deg. Observations of a single night cover a large fraction of the sky as the circular scans drift across the sky due to the rotation of the Earth.

2. Observations and processing of the data

The experiment was launched on February 7, 2002 by the CNES[2] from the Swedish balloon base in Esrange, near Kiruna, Sweden, 68°N, 20°E. It reached a float altitude of ~34 km and landed 21.5 hours later in Siberia near Noril'sk, where it was recovered by a Franco–Russian team. The night–time scientific observations span 11.7 hours of integration from 15.3 UT to 3.0 UT the next day. Figure 1 shows the Northern galactic part of the sky observed during the flight.

A detailed description of the data processing pipeline will be given in Benoît et al. (2003c). Pointing reconstruction, good to 1 arcmin, is performed using data from a bore–sight mounted optical star sensor aligned to each photometer using Jupiter observations. The raw Time Ordered Information (TOI), sampled at 153 Hz, are preprocessed to account for the readout electronics and response variations. Corrupted data (including glitches), representing less than 1.5%, are flagged. Low frequency drifts correlated to various templates (altitude, attitude, temperatures, CMB dipole) are removed from the data. To remove residual dust and atmospheric signal, the data are decorrelated with the high frequency photometers and a synthetic dust timeline (Schlegel et al. 1998).

The CMB dipole is the prime calibrator of the instrument. The absolute calibration error against the dipole measured by COBE/DMR (Fixsen et al. 1994) is estimated to be less than 4% (resp. 8%) in temperature at 143 GHz (resp. 217 GHz). Two other independent calibration methods, both with intrinsic uncertainty of ~10%, give responsivities relative to the dipole calibration at 143 (resp. 217 GHz) of −5 (resp. +6%) on Jupiter and −20 (resp. −5%) with COBE–FIRAS Galactic Plane emission.

The beam shapes of the photometers measured on Jupiter are moderately elliptical, having a ratio of the major to minor axis of 1.2 (resp. 1.5) at 143 GHz (resp. 217 GHz), and have an equivalent *FWHM* of 11 arcmin (resp. 13). The error in beam size is less than 10%. The effective beam transfer function for each photometer, determined with simulations, is taken into account in the analysis and is in excellent agreement with analytical estimates (Fosalba et al. 2002).

3. Analysis

In this paper, we use data from only a single detector at each of the CMB frequencies, 143 and 217 GHz, with a sensitivity of 90 and 150 $\mu K_{CMB}.s^{1/2}$ respectively. To avoid the necessity of detailed modelling of Galactic foregrounds, we restrict the sky coverage to $b > +30$ deg, giving a total of ~100 000 15 arcmin pixels (HEALPIX nside = 256) covering 12.6% of the sky (see Fig. 1). To extract the CMB power spectrum, we use the MASTER analysis methodology (Hivon et al. 2002),

[1] See http://www.archeops.org

[2] Centre National d'Études Spatiales, the French national space agency.

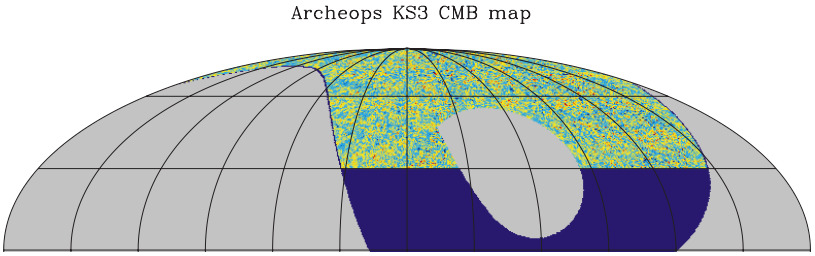

Fig. 1. Archeops CMB map (Galactic coordinates, centered on the Galactic anticenter, Northern hemisphere) in HEALPIX pixelisation (Gorski et al. 1998) with 15 arcmin pixels and a 15 arcmin Gaussian smoothing. The map is a two–photometers coaddition. The dark blue region is not included in the present analysis because of possible contamination by dust. The colors in the map range from -500 to 500 μK_{CMB}.

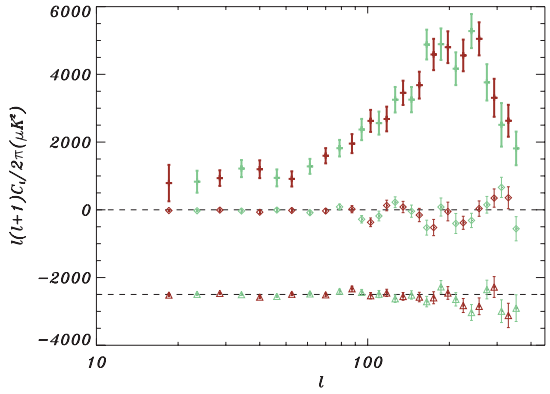

Fig. 2. The Archeops CMB power spectrum for the combination of the two photometers. Green and red data points correspond to two overlapping binnings and are therefore not independent. The light open diamonds show the null test resulting from the self difference (*SD*) of both photometers and the light open triangles correspond to the difference (*D*) of both photometers (shifted by $-2500\ \mu K^2$ for clarity) as described in Sect. 4 and shown in Table 1.

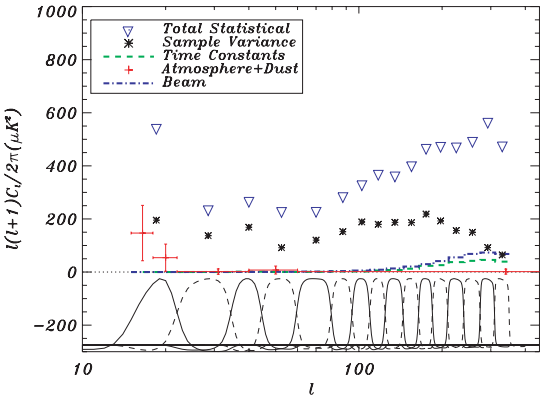

Fig. 3. Contamination by systematics: the Archeops CMB power spectrum statistical error bars (including noise and sample variance) are shown as the blue triangles. The large error bar in the first bin mainly comes from the high–pass filtering. A conservative upper–limit to contamination by dust and atmospheric signal is shown in red crosses, with a ℓ different binning to enhance the low ℓ side. Beam and time constants uncertainties are shown in dot–dashed blue and dashed green (see text). The 7% temperature calibration uncertainty is not shown here. The window functions are shown at the bottom of the figure.

which achieves speed by employing sub–optimal (but unbiased) map–making and spectral determinations.

First, the Fourier noise power spectrum is estimated for each photometer. Signal contamination is avoided by subtracting the data projected onto a map (and then re–read with the scanning strategy) from the initial TOI. This raw noise power spectrum is then corrected for two important effects (Benoît et al. 2003d): (i) pixelisation of the Galactic signal that leads to an overestimate of the noise power spectrum: sub–pixel frequencies of the signal are not subtracted from the inital TOI leaving extra signal at high frequency; (ii) due to the finite number of samples per pixel, noise remains in the map and is subtracted from the initial TOI, inducing an underestimation of the actual noise in the final TOI (Ferreira & Jaffe 2000; Stompor et al. 2002). Simulations, including realistic noise, Galactic dust and CMB anisotropies, indicate that both corrections are independent of the shape of the true noise power spectrum, and thus permit an unbiased estimate of the latter with an accuracy better than 1% at all frequencies. The corresponding uncertainty in the noise power spectrum estimation is included in the error bars of the C_ℓ spectrum.

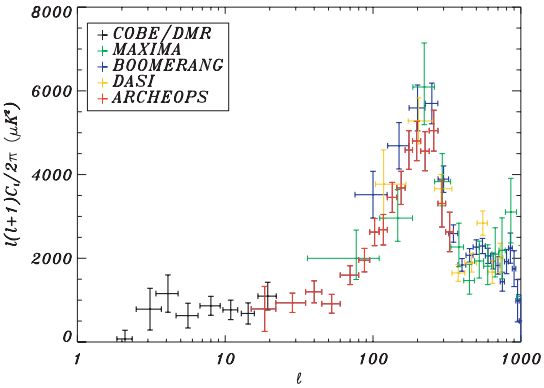

Fig. 4. The Archeops power spectrum compared with results of COBE, Boomerang, Dasi, Maxima (Tegmark 1996; Netterfield et al. 2002; Lee et al. 2001; Halverson et al. 2002).

We construct maps by bandpassing the data between 0.3 and 45 Hz, corresponding to about 30 deg and 15 arcmin scales, respectively. The high–pass filter removes remaining atmospheric and galactic contamination, the low–pass filter suppresses non–stationary high frequency noise. The filtering is done in such a way that ringing effects of the signal on bright compact sources (mainly the Galactic plane) are smaller than $\sim 36\,\mu\mathrm{K}^2$ on the CMB power spectrum in the very first ℓ–bin, and negligible for larger multipoles. Filtered TOI of each absolutely calibrated detector are co–added on the sky to form detector maps. The bias of the CMB power spectrum due to filtering is accounted for in the MASTER process through the transfer function. The map shown in Fig. 1 is obtained by combining the maps of each of the photometers. A $1/\sigma^2$ weighting of the data was done in each pixel, where σ^2 is the variance of the data in that pixel. This map shows significant extra variance compared to the difference map on degree angular scales which is attributed to sky–stationary signal.

We estimate the CMB power spectrum in 16 bins ranging from $\ell = 15$ to $\ell = 350$. The window functions derived from the multipole binning and renormalized to equal amplitude for clarity are shown at the bottom of Fig. 3. They are nearly top–hat functions due to the large sky coverage. The bins can therefore be approximated as independent: off–diagonal terms in the covariance matrix are less than ∼12%. For the purpose of estimating the power spectrum we made a map that combines the data of the two photometers using two different weighting techniques. Up to $\ell = 310$ the data of each photometer has equal weight and at larger ℓ values the data is noise weighted. This is valid because the multipole bins are nearly independent. It is also advantageous because it minimizes the overall statistical noise over the entire ℓ spectrum; equal weighting gives smaller error bars at small ℓ and noise weighting gives smaller error bars at large ℓ.

4. Results and consistency tests

The Archeops power spectrum is presented in Fig. 2 and in Table 1. Two different binnings corresponding to overlapping, shifted window functions (therefore not independent) were used. Archeops provides the highest ℓ resolution up to $\ell = 200$ ($\Delta\ell$ from 7 to 25) and most precise measurement of the angular power spectrum for $15 < \ell < 300$ to date. Sample–variance contributes 50% or more of the total statistical error up to $\ell \sim 200$.

The Archeops scanning strategy (large circles on the sky) provides a robust test of systematic errors and data analysis procedures: by changing the sign of the filtered TOIs every other circle, a TOI that should not contain any signal is obtained once it is projected on the sky. This TOI has the same noise power spectrum as the original one. This null test is referred to as the self–difference (*SD*) test. The angular power spectrum of such a dataset should be consistent with zero at all multipoles because successive circles largely overlap. This test has been performed with the two photometers independently. The spectra are consistent with zero at all modes: χ^2/ndf of 21/16 (resp. 27/16) at 143 GHz (resp. 217 GHz). Performed on the two–photometers co–added map, the same test gives a power spectrum consistent with zero, with a χ^2/ndf of 25/16 (see Fig. 2). These results show that there is no significant correlated noise among the two photometers and that the noise model is correct. They limit the magnitude of non–sky–stationary signals to a small fraction of the sky–stationary signal detected in the maps.

Table 1. The Archeops CMB power spectrum for the best two photometers (third column). Data points given in this table correspond to the red points in Fig. 2. The fourth column shows the power spectrum for the self difference (*SD*) of the two photometers as described in Sect. 4. The fifth column shows the power spectrum for the difference (*D*) between the two photometers.

$\ell_{\min}$	$\ell_{\max}$	$\frac{\ell(\ell+1)C_\ell}{(2\pi)}$ $(\mu\mathrm{K})^2$	$SD\,(\mu\mathrm{K})^2$	$D\,(\mu\mathrm{K})^2$
15	22	789 ± 537	−21 ± 34	−14 ± 34
22	35	936 ± 230	−6 ± 25	34 ± 21
35	45	1198 ± 262	−69 ± 45	−75 ± 35
45	60	912 ± 224	−18 ± 50	9 ± 37
60	80	1596 ± 224	−33 ± 63	−8 ± 44
80	95	1954 ± 280	17 ±105	169 ± 75
95	110	2625 ± 325	−368 ±128	−35 ± 92
110	125	2681 ± 364	127 ±156	46 ± 107
125	145	3454 ± 358	82 ±166	−57 ± 114
145	165	3681 ± 396	−154 ±196	−75 ± 140
165	185	4586 ± 462	−523 ±239	−97 ± 177
185	210	4801 ± 469	−50 ±276	44 ± 187
210	240	4559 ± 467	−382 ±192	−326 ± 206
240	275	5049 ± 488	35 ±226	−349 ± 247
275	310	3307 ± 560	346 ±269	220 ± 306
310	350	2629 ± 471	356 ±323	−619 ± 358

A series of Jack–knife tests shows agreement between the first and second halves of the flight (the difference of the power spectra has $\chi^2/\mathrm{ndf} = 21/16$), left and right halves of the map obtained with a cut in Galactic longitude ($\chi^2/\mathrm{ndf} = 15/16$). Individual power spectra of the two photometers agree once absolute calibration uncertainties are taken into account. The power spectrum measured on the differences (*D*) between the two photometers is consistent with zero with a χ^2/ndf of 22/16 (Fig. 2) showing that the electromagnetic spectrum of the sky–stationary signal is consistent with that of the CMB. The measured CMB power spectrum depends neither on the Galactic cut (20, 30 and 40 degrees north from the Galactic plane), nor on the resolution of the maps (27, 14 and 7′ pixel size) nor on the TOI high–pass filtering frequencies (0.3, 1 and 2 Hz).

Several systematic effects have been estimated and are summarized in Fig. 3, along with the statistical errors (blue triangles). The high frequency photometer (545 GHz) is only sensitive to dust and atmospheric emission, and thus offers a way to estimate the effect of any residual Galactic or atmospheric emission. Extrapolation of its power spectrum using a Rayleigh–Jeans spectrum times a ν^2 emissivity law between 545 and 217 GHz and as ν^0 between 217 and 143 GHz gives an upper–limit on the possible contamination by atmosphere (dominant) and dust. The combination of both is assumed to be much less than 50% of the initial contamination after the decorrelation process. The subsequent conservative upper–limit for dust and atmosphere contamination is shown in red crosses in Fig. 3. The contamination appears negligible in all bins but the first one ($\ell = 15$ to 22). High frequency spectral

leaks in the filters at 143 and 217 GHz were measured to give a contribution less than half of the above contamination. In the region used to estimate the CMB power spectrum there are 651 extragalactic sources in the Parkes–MIT–NRAO catalog. These sources are mainly AGN, and their flux decreases with frequency. We have estimated their contribution to the power spectrum using the WOMBAT tools (Sokasian et al. 2001). At 143 (resp. 217) GHz this is less than 2 (resp. 1) percent of the measured power spectrum at $\ell \sim 350$. The beam and photometer time constant uncertainties were obtained through a simultaneous fit on Jupiter crossings. Their effect is shown as the dot–dashed blue and green–dashed lines in Fig. 3. The beam uncertainty includes the imperfect knowledge of the beam transfer function for each photometer's elliptical beam. Beam and time constants uncertainties act as a global multiplicative factor, but in the figure we show the 1σ effect on a theoretical power spectrum that has a good fit to the data. After the coaddition of the two photometers, the absolute calibration uncertainty (not represented in Fig. 3) is estimated as 7% (in CMB temperature units) with Monte–Carlo simulations.

As a final consistency test, the Archeops C_ℓ are computed using two additional independent methods. The first is based on noise estimation with an iterative multi–grid method, MAPCUMBA (Doré et al. 2001), simple map–making and C_ℓ estimation using SpICE (Szapudi et al. 2001) which corrects for mask effects and noise ponderation through a correlation function analysis. The second is based on MIRAGE iterative map–making (Yvon et al. 2003) followed by multi–component spectral matching (Cardoso et al. 2002; Patanchon et al. 2003; Delabrouille et al. 2002). All methods use a different map–making and C_ℓ estimation. Results between the three methods agree within less than one σ. This gives confidence in both the C_ℓ and in the upper–limits for possible systematic errors. Table 1 provides the angular power spectrum which is used for cosmological parameter extraction (Benoît et al. 2003a).

A comparison of the present results with other recent experiment and COBE/DMR is shown in Fig. 4. There is good agreement with other experiments, given calibration uncertainties, and particularly with the power COBE/DMR measures at low ℓ and the location of the first acoustic peak. Work is in progress to improve the intercalibration of the photometers, the accuracy and the ℓ range of the power spectrum: the low ℓ range will be improved increasing the effective sky area for CMB (which requires an efficient control of dust contamination), the high ℓ range will be improved by including more photometer pixels in the analysis.

5. Conclusions

The Archeops experiment has observed a large portion of the sky. Maps from the two highest sensitivity detectors at 143 and 217 GHz show consistent, sky–stationary anisotropy signal that appears inconsistent with any known astrophysical source other than CMB anisotropy. The angular power spectrum of this signal at multipoles between $\ell = 15$ and $\ell = 350$ shows a clear peak at $\ell \simeq 200$. These results are consistent with predictions by inflationary–motivated cosmologies. Archeops provides the highest signal–to–noise ratio mapping of the first acoustic peak and its low–ℓ side of any experiment to date and covers the largest number of decades in ℓ. It has been obtained with a limited integration time (half a day) using a technology similar to that of the Planck HFI experiment. An extensive set of tests limits the contribution of systematic errors to a small fraction of the statistical and overall calibration errors in the experiment. More data reduction is under way to increase the accuracy and ℓ range of the power spectrum. The determination of cosmological parameters are discussed in a companion paper (Benoît et al. 2003a).

Acknowledgements. The authors would like to thank the following institutes for funding and balloon launching capabilities: CNES (French space agency), PNC (French Cosmology Program), ASI (Italian Space Agency), PPARC, NASA, the University of Minnesota, the American Astronomical Society and a CMBNet Research Fellowship from the European Commission. Healpix package was used throughout the data analysis (1998).

References

Benoît, A., Ade, P., Amblard, A., et al. 2002a, Astropart. Phys., 17, 101
Benoît, A., Ade, P., Amblard, A., et al. 2003a, A&A, 399, L25
Benoît, A., Ade, P., Amblard, A., et al. 2003b, in preparation
Benoît, A., Ade, P., Amblard, A., et al. 2003c, in preparation
Benoît, A., Ade, P., Amblard, A., et al. 2003d, in preparation
de Bernardis, P., Ade, P. A. R., Bock, J. J., et al. 2000, Nature, 404, 955
Cardoso, J. F., Snoussi, H., Delabrouille, J., & Patanchon, G. 2002, Proc. EUSIPCO02 Conf., Toulouse, Sep. 2002 [astro-ph/0209466]
Delabrouille, J., Cardoso, J. F., & Patanchon, G. 2002, MNRAS, submitted [astro-ph/0211504]
Doré, O., Teyssier, R., Bouchet, F. R., Vibert, D., & Prunet, S. 2001, A&A, 374, 358
Ferreira, P. G., & Jaffe, A. H. 2000, MNRAS, 312, 89
Fixsen, P. J., Cheng, E. S., Cottingham, D. A., et al. 1994, ApJ, 420, 445
Fosalba, P., Doré, O., & Bouchet, F. R. 2002, Phys. Rev. D, 65, 63003
Gorski, K. M., Hivon, E., & Wandelt, B. D. 1998, Proc. of the MPA/ESO Conf. on Evolution of Large-Scale Structure: from Recombination to Garching, 2–7 August 1998, ed. A. J. Banday, R. K. Sheth, & L. Da Costa [astro-ph/9812350]
Halverson, N. W., Leitch, E. M., Pryke, C., et al. 2002, ApJ, 568, 38
Hanany, S., Ade, P., Balbi, A., et al. 2000, ApJ, 545, L5
Hivon, E., Gorski, K. M., Netterfield, C. B., et al. 2002, ApJ, 567, 2
Lee, A. T., Ade, P., Balbi, A., et al. 2001, ApJ, 561, L1
Miller, A. D., Caldwell, R., Devlin, M. J., et al. 1999, ApJ, 524, L1
Netterfield, C. B., Ade, P. A. R., Bock, J. J., et al. 2002, ApJ, 571, 604
Patanchon, G., Snoussi, H., Cardoso, J.-F., & Delabrouille, J. 2003, Proc. of the PSIP03 Conf., Grenoble, January 2003 [astro-ph/0302078]
Rubiño-Martin, J. A., Rebolo, R., Carreira, P., et al. 2002, MNRAS, submitted [astro-ph/0205367]
Schlegel, D., Finkbeiner, D., & Davis, M. 1998, ApJ, 500, 525
Sievers, J. L., Bond, J. R., Cartwright, J. K., et al. 2002, ApJ, submitted [astro-ph/0205387]
Smoot, G. F., Bennett, C. L., Kogut, A., et al. 1992, ApJ, 396, L1
Sokasian, A., Gawiser, E., & Smoot, G. F. 2001, ApJ, 562, L88
Stompor, R., Balbi, A., Borrill, J. D., et al. 2002, Phys. Rev. D, 65, 022003
Szapudi, I., Prunet, S., Pogosyan, D., Szalay, A. S., Bond, J. R., et al. 2001, ApJ, 548, L115
Tegmark, M. 1996, ApJ, 464, L35
Yvon, D., et al. 2003, in preparation

A&A 436, 785–797 (2005)
DOI: 10.1051/0004-6361:20042416

Astronomy & Astrophysics

The CMB temperature power spectrum from an improved analysis of the Archeops data

M. Tristram[1], G. Patanchon[2], J. F. Macías-Pérez[1], P. Ade[3], A. Amblard[4], R. Ansari[5], É. Aubourg[6,7], A. Benoît[8], J.-Ph. Bernard[9], A. Blanchard[10], J. J. Bock[11,12], F. R. Bouchet[13], A. Bourrachot[5], P. Camus[8], J.-F. Cardoso[14], F. Couchot[5], P. de Bernardis[15], J. Delabrouille[7], F.-X. Désert[16], M. Douspis[10], L. Dumoulin[17], Ph. Filliatre[18,7], P. Fosalba[19], M. Giard[9], Y. Giraud-Héraud[7], R. Gispert[20,†,⋆], L. Guglielmi[7], J.-Ch. Hamilton[21], S. Hanany[22], S. Henrot-Versillé[5], J. Kaplan[7], G. Lagache[20], J.-M. Lamarre[23], A. E. Lange[11], K. Madet[8], B. Maffei[3], Ch. Magneville[6,7], S. Masi[15], F. Mayet[1], F. Nati[15], O. Perdereau[5], S. Plaszczynski[5], M. Piat[7], N. Ponthieu[20], S. Prunet[13], C. Renault[1], C. Rosset[7], D. Santos[1], D. Vibert[13], and D. Yvon[6]

[1] Laboratoire de Physique Subatomique et de Cosmologie, 53 avenue des Martyrs, 38026 Grenoble Cedex, France
e-mail: reprints@archeops.org;tristram@lpsc.in2p3.fr
[2] Department of Physics & Astronomy, University of British Columbia, Vancouver, Canada
[3] Cardiff University, Physics Department, PO Box 913, 5, The Parade, Cardiff, CF24 3YB, UK
[4] University of California, Berkeley, Dept. of Astronomy, 601 Campbell Hall, Berkeley, CA 94720-3411, USA
[5] Laboratoire de l'Accélérateur Linéaire, BP 34, Campus Orsay, 91898 Orsay Cedex, France
[6] CEA-CE Saclay, DAPNIA, Service de Physique des Particules, Bât. 141, 91191 Gif-sur-Yvette Cedex, France
[7] APC, 11 Pl. M. Berthelot, 75231 Paris Cedex 5, France
[8] Centre de Recherche sur les Très Basses Températures, BP 166, 38042 Grenoble Cedex 9, France
[9] Centre d'Étude Spatiale des Rayonnements, BP 4346, 31028 Toulouse Cedex 4, France
[10] Laboratoire d'Astrophysique de Tarbes Toulouse, 14 avenue E. Belin, 31400 Toulouse, France
[11] California Institute of Technology, 105-24 Caltech, 1201 East California Blvd, Pasadena CA 91125, USA
[12] Jet Propulsion Laboratory, 4800 Oak Grove Drive, Pasadena, California 91109, USA
[13] Institut d'Astrophysique de Paris, 98bis boulevard Arago, 75014 Paris, France
[14] CNRS-ENST, 46 rue Barrault, 75634 Paris, France
[15] Gruppo di Cosmologia Sperimentale, Dipart. di Fisica, Univ. "La Sapienza", PA Moro, 2, 00185 Roma, Italy
[16] Laboratoire d'Astrophysique, Obs. de Grenoble, BP 53, 38041 Grenoble Cedex 9, France
[17] CSNSM-IN2P3, Bât. 108, 91405 Orsay Campus, France
[18] CEA-CE Saclay, DAPNIA, Service d'Astrophysique, Bât. 709, 91191 Gif-sur-Yvette Cedex, France
[19] Institute for Astronomy, University of Hawaii, 2680 Woodlawn Dr, Honolulu, HI 96822, USA
[20] Institut d'Astrophysique Spatiale, Bât. 121, Université Paris XI, 91405 Orsay Cedex, France
[21] LPNHE, Universités Paris VI et Paris VII, 4 place Jussieu, Tour 33, 75252 Paris Cedex 05, France
[22] School of Physics and Astronomy, 116 Church St. SE, University of Minnesota, Minneapolis MN 55455, USA
[23] LERMA, Observatoire de Paris, 61 Av. de l'Observatoire, 75014 Paris, France

Received 23 November 2004 / Accepted 16 February 2005

Abstract. We present improved results on the measurement of the angular power spectrum of the Cosmic Microwave Background (CMB) temperature anisotropies using the data from the last ARCHEOPS flight. This refined analysis is obtained by using the 6 most sensitive photometric pixels in the CMB bands centered at 143 and 217 GHz and 20% of the sky, mostly clear of foregrounds. Using two different cross-correlation methods, we obtain very similar results for the angular power spectrum. Consistency checks are performed to test the robustness of these results paying particular attention to the foreground contamination level which remains well below the statistical uncertainties. The multipole range from $\ell = 10$ to $\ell = 700$ is covered with 25 bins, confirming strong evidence for a plateau at large angular scales (the Sachs-Wolfe plateau) followed by two acoustic peaks centered around $\ell = 220$ and $\ell = 550$ respectively. These data provide an independent confirmation, obtained at different frequencies, of the WMAP first year results.

Key words. cosmology: cosmic microwave background – cosmology: observations – methodes: data analysis

1. Introduction

Observations of the Cosmic Microwave Background (CMB) temperature anisotropies provide answers to fundamental

⋆ Richard Gispert passed away few weeks after his return from the early mission to Trapani.

questions in cosmology. The experimental determination of the CMB temperature angular power spectrum (Netterfield et al. 1997; Miller et al. 1999; de Bernardis et al. 2000; Hanany et al. 2000; Lee et al. 2001; Netterfield et al. 2002; Halverson et al. 2002; Sievers et al. 2003; Rubino-Martin et al. 2003; Benoît et al. 2003a; Hinshaw et al. 2003; Barkats et al. 2005; Readhead et al. 2004; Leitch et al. 2004) leads to important insights into the composition and evolution of the Universe. Most notable are the conclusions that the geometry of space is essentially flat, the measurements are consistent with the inflationary paradigm and the Universe is dominated by unknown forms of dark energy and dark matter (Lineweaver et al. 1997; Macías-Pérez et al. 2000; Benoît et al. 2003b; Douspis et al. 2003; Spergel et al. 2003).

ARCHEOPS[1] was designed to obtain a large sky coverage of CMB temperature anisotropies in a single balloon flight at millimeter and submillimeter wavelengths. ARCHEOPS is a precursor to the PLANCK HFI instrument (Lamarre et al. 2003), using the same optical design and the same technology for the detectors, spider-web bolometers, and their cooling, 0.1 K dilution fridge. The instrument consists of a 1.5 m aperture diameter telescope and an array of 21 photometric pixels operating at 4 frequency bands centered at 143, 217, 353 and 545 GHz. The data were taken during the Arctic night of February 7, 2002 after the instrument was launched by CNES from the Esrange base near Kiruna (Sweden). The entire data set covers ∼30% of the sky.

The ARCHEOPS initial analysis (Benoît et al. 2003a) – hereafter Paper I – presented for the first time measurements from large angular scales to beyond the first acoustic peak (ℓ = 15−350). A few months later, the first year WMAP results (Bennett et al. 2003) confirmed the previous measurements and significantly reduced the error bars on scales down to the second acoustic peak.

This paper presents a second and more refined analysis of the ARCHEOPS data. With respect to Paper I, major improvements on the timeline processing, the map-making, the beam modeling and the foreground removal were achieved. Further, new power spectrum estimation methods based mainly on the cross power spectra between different detectors maps are used to reduce the contribution from correlated noise and systematic effects. This essentially allows us to increase the number of detectors considered (from two for Paper I to six for this analysis) and to cover a larger fraction of clean sky (12% in Paper I, 20% in this paper). These developments lead to a better sampling and a larger range in multipole space with an improved accuracy.

The paper is organized as follows: Sect. 2 summarizes the processing on the TOIs (Time Ordered Information) with an emphasis on changes and improvements with respect to Paper I. Section 3 describes the methods, Xspect and SMICA, used for the estimation of the CMB angular power spectrum from observed emission maps. The estimation of the ARCHEOPS CMB angular power spectrum is presented in Sect. 4. Consistency checks on the data and the contribution from systematics to the ARCHEOPS CMB angular power spectrum are discussed in Sect. 5. A simple comparison with the best-fit cosmological model provided by the WMAP team (Spergel et al. 2003) is shown at the power spectrum level. However, we postpone to a forthcoming paper the comparison of this dataset to the WMAP data and other datasets at the map level.

[1] See `http://www.archeops.org`

2. Observations and data processing

The ARCHEOPS experiment is described in details in companion papers. Instrument and data processing are detailed in (Macías-Pérez et al. 2005) while the in-flight performances are summarized in Madet et al. (2004). In the following subsections, only key points on the data processing are summarized and we then focus on refinements implemented for the present analysis, as compared to Paper I.

2.1. Observations and standard data processing

The instrument contains a bolometric array of 21 photometric pixels, each one being made of cold optics consisting of an assembly of back-to-back horns, filters and lenses, and of a 100 mK bolometer, which operate at frequency bands centered at 143 GHz (8 pixels), 217 GHz (6), 353 GHz (6 = 3 polarized pairs) and 545 GHz (1). The two low frequencies are dedicated to CMB studies while high frequency bands are sensitive essentially to interstellar dust and atmospheric emission. The focal plane is made of 21 spider-web bolometers and some thermometers and is maintained at a temperature of ∼95 mK by a ^{3}He–^{4}He open-circuit dilution cryostat. Observations are carried out by spinning the payload around its vertical axis at 2 rpm. Thus the telescope produces circular scans at a fixed elevation of ∼41 deg. Observations of a single night cover a large fraction of the sky as the circular scans drift across the sky due to the rotation of the Earth and the gondola trajectory.

The ARCHEOPS experiment was launched on February 7, 2002 by the CNES[2] from the balloon base in Esrange, near Kiruna, Sweden, 68°N, 20°E. The night-time scientific observations span 11 hours of integration. The pointing reconstruction, with rms error better than 1 arcmin, is performed using data from a bore-sight mounted optical star sensor. Each photometric pixel offset is deduced from Jupiter observations.

Corrupted data (including glitches) in the Time Ordered Information (TOI), representing less than 1.5% of the full data set, are flagged. Low frequency drifts on the data generally correlated to house-keeping data (altitude, attitude, temperatures, CMB dipole) are removed using the latter as templates. Furthermore, a high frequency decorrelation is performed in few chosen time frequency intervals of ∼1 Hz width to remove some bursts of non-stationary high-frequency noise localised in time and in frequency. The corrected timelines are then deconvolved from the bolometer time constant and the flagged corrupted data are replaced by a realization of noise (which is not projected onto the maps in the map-making step). Finally, low time frequency atmospheric residuals are subtracted using a destriping procedure which slightly filters out the sky signal

[2] Centre National d'Études Spatiales, the French national space agency.

to a maximum of 5% (see the red curve in Fig. 4). This effect is corrected for when computing the CMB angular power spectrum as discussed in Sect. 3.2.

The CMB dipole is the prime calibrator of the instrument. The absolute calibration error against the dipole as measured by COBE/DMR (Fixsen et al. 1994) and confirmed by WMAP (Bennett et al. 2003) is estimated to be 4% and 8% in temperature at 143 GHz and 217 GHz respectively. These errors are dominated by systematic effects.

As Jupiter is a point-source at the ARCHEOPS resolution, local maps of Jupiter allow us to estimate the time constant of the bolometers and the main beam shape. This is performed using the two Jupiter observation windows. While the 143 GHz detector beams are mostly elliptical, the 217 GHz ones are rather irregular (multi-mode horns). The typical *FWHM* of the beams is about 12 arcmin. Two Saturn crossings allowed cross-checks on the time constants and beams.

2.2. Removal of Galactic and atmospheric foreground emissions

The ARCHEOPS cleaned TOIs at 143 and 217 GHz are contaminated by atmospheric residuals coming mostly from the inhomogeneous ozone emission. This contributes mainly at frequencies lower than 2 Hz in the timeline and follows approximatively a ν^2 law in antenna temperature. Therefore atmospheric emission is much more important at the high ARCHEOPS frequencies (353 and 545 GHz). In the same way, at the ARCHEOPS CMB frequencies (143 and 217 GHz) the Galactic dust emission also contaminates the estimation of the CMB angular power spectrum even at intermediate Galactic latitudes. Dust emission, which presents a modified blackbody spectrum at about 17 K with an emissivity of about ν^2, dominates the CMB at high frequencies and therefore the 353 and 545 GHz channels can be used to monitor it. To suppress both residual dust and atmospheric signals, the data are decorrelated using a linear combination of the high frequency photometric pixels (353 and 545 GHz) and of synthetic dust timelines. These are constructed from the extrapolation of IRAS and COBE observations in the far infrared domain (Schlegel et al. 1998; Finkbeiner et al. 1999) to the ARCHEOPS frequencies. We actually construct a synthetic dust template for the considered CMB bolometers and also for the high frequency bolometers so that we can take into account simultaneously in such a model both types of frequency behaviors.

As the decorrelation is not perfect in the Galactic plane, a Galactic mask is then applied to the ARCHEOPS maps for determination of the CMB power spectrum. This mask is deduced from a Galactic dust emission model (Schlegel et al. 1998; Finkbeiner et al. 1999) at 353 GHz. The Galactic plane and the Taurus region are efficiently masked by considering only regions with a brightness <0.5 MJy sr^{-1}. Applying this mask, the CMB maps derived from the ARCHEOPS data cover 20% of the sky sampled by ~100 000 pixels of 7 arcmin (HEALPix *nside* = 512). Figure 1 presents the ARCHEOPS coverage to which we have superimposed the Galactic mask. Only the Northern part above 30 degree was used in Paper I.

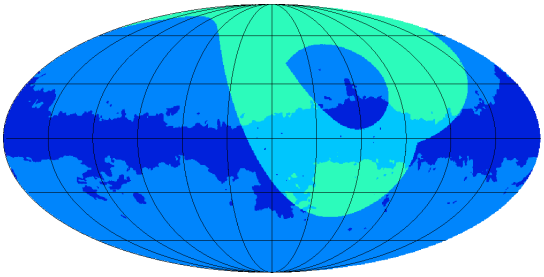

Fig. 1. Galactic mask (dark blue lane) applied to the ARCHEOPS coverage (annular green region). The CMB mask is obtained by requesting the SFD brightness at 353 GHz to be <0.5 MJy sr^{-1}. The Mollweide projection of the celestial sphere is in Galactic coordinates centered on the Galactic anti-center. Gridding on the full sky map is by 30 degree steps. The CMB analysis includes 20% of the sky (dark green area) while ARCHEOPS covers ~30% of the sky. The previous analysis only covered 12% of the sky above the 30 degree Northern parallel.

2.3. Map-making

The noise power spectrum of the ARCHEOPS TOIs is nearly flat with increasing power at very low time frequencies due to residuals from atmospheric noise, and at very high time frequencies due to the deconvolution from the bolometer time constants. To cope with these two features on the ARCHEOPS noise we have used an optimal (i.e. it achieves least square error on pixelised map) procedure called MIRAGE (Yvon & Mayet 2004) to produce maps for each of the detectors.

MIRAGE is based on a two-phase iterative algorithm, involving optimal map-making together with low frequency drift removal and Butterworth high-pass filtering. A conjugate gradient method is used for resolving the linear system. A very convenient feature of MIRAGE is that it handles classic experimental issues, such as corrupted samples in the data stream, bright sources and Galaxy ringing effects in the filtering and in the calculation of the noise correlation matrix.

Maps are computed with 7 arcmin pixels (HEALPix *nside* = 512) for each absolutely calibrated detector with their data time band-passed between 0.1 and 38 Hz. This corresponds to about 90 deg and 20 arcmin scales, respectively. The high-pass filter removes remaining atmospheric and Galactic contamination. The low-pass filter suppresses non-stationary high frequency noise.

About two thirds of the ARCHEOPS sky are observed with ~20 to 60 samples per bolometer and per square degree and one third with a higher redundancy, about 75 samples per bolometer and per square degree. For illustration, Fig. 2 shows a map obtained from a weighted linear combination of the maps of each of the six most sensitive ARCHEOPS detectors. This map is smoothed with a 30 arcmin Gaussian beam and has a typical rms noise of 50 μK per 30 arcmin pixel.

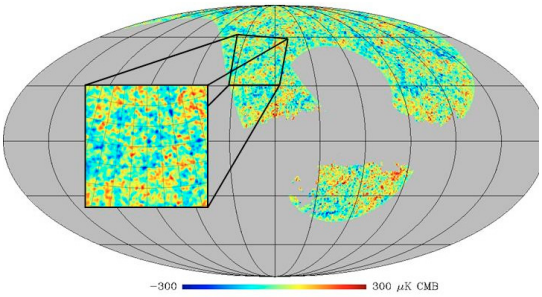

Fig. 2. ARCHEOPS map of the CMB sky in Galactic coordinates centered on the Galactic anti-center after smoothing with a 30 arcmin Gaussian. A patch of the sky of 30 × 30 deg, with high redundancy and centered on $(l, b) = (195, 45)$ degrees is zoomed up. Gridding on the full sky map is by 30 degree steps, gridding on the zoomed patch is 5 deg. The Galaxy is masked as described above.

3. Power spectrum estimation

In this section, we present three methods, Xspect (Tristram et al. 2005), SMICA (Patanchon 2003) and power spectrum on the rings (Γ_m hereafter) (Ansari et al. 2003) used for the determination of the angular power spectrum of the CMB temperature anisotropies with the ARCHEOPS data. Beforehand we detail the procedure we use to correct from beam smoothing and filtering effects as well as from inhomogeneous coverage.

We have thoroughly probed Xspect and SMICA with simulations which are described below. Results from both methods are included in this paper to cross validate the final results. The Γ_m method is provided here to illustrate its potential in the estimation of the angular power spectrum directly from ring data and is more suitable to Planck-like data.

Xspect and SMICA are based on the so-called "pseudo-C_ℓ"s estimators (Peebles 1973; Szapudi et al. 2001; Hivon et al. 2002) which directly compute the pseudo power spectrum from the spherical harmonics decomposition of the maps. These spectra are then corrected from the sky coverage, beam smoothing, data filtering, pixel weighting and noise biases.

A pseudo power spectrum D_ℓ is linked to the true power spectrum C_ℓ by

$$\widehat{D_\ell} = \sum_{\ell'} M_{\ell\ell'} p^2_{\ell'} B^2_{\ell'} T_{\ell'} \langle C_{\ell'} \rangle + \langle N_\ell \rangle, \quad (1)$$

where $M_{\ell\ell'}$ is the mode-mode coupling matrix, B_ℓ is the beam transfer function describing the beam smoothing effect, p_ℓ is the transfer function of the pixelization scheme of the map describing the effect of smoothing due to the finite pixel size and geometry, T_ℓ is an effective transfer function that represents any filtering applied to the time ordered data, and $\langle N_\ell \rangle$ is the noise power spectrum.

In the following, the $M_{\ell\ell'}$ matrix describes the mode-mode coupling resulting from the incomplete sky coverage and the weighting applied to the sky maps. We take into account the p_ℓ pixel transfer function due to the smoothing effect induced by the finite size of the map pixels. This function is provided in the HEALPix package (Gorski et al. 1999).

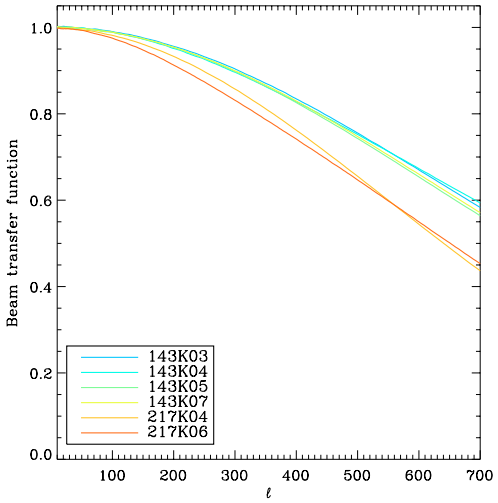

Fig. 3. Beam transfer functions of the six most sensitive ARCHEOPS detectors computed using the *Asymfast* beam description.

3.1. Beam smoothing effect

Most of the beams of the ARCHEOPS detectors have been measured on Jupiter to be elliptical. A few of them are irregular. Therefore, the effective beam transfer function must be carefully estimated for each bolometer. The beam transfer functions are computed from simulations using the *Asymfast* method detailed in Tristam et al. (2004). This method is based on the decomposition of the beam into a sum of Gaussians for which convolution is easy in the spherical harmonic space (up to 12 Gaussians are used here). This allows us to deal with asymmetric beam patterns using the scanning strategy of the instrument. Figure 3 shows the beam transfer function for each of the ARCHEOPS detectors used in this analysis. They are estimated with a Monte-Carlo of 100 *Asymfast* simulations per bolometer. The beam transfer functions for the 143 GHz detectors are very similar and close to circular Gaussian. The 217 GHz detector beams are larger and more irregular, and smear-out more the high multipoles.

The Asymfast method produces negligible (<0.1%) statistical uncertainties on the B_ℓ estimation. However, as the beam patterns have been measured on Jupiter maps they may differ from the effective beams on the CMB anisotropies. This comes mainly from uncertainties on the electromagnetic spectral dependence, far-side lobes, baseline subtraction and time constants, each of which estimated to be lower than 5%. For such systematics it is difficult to estimate their impact on the beam transfer function. As an illustration, we give conservative upper limits on the B_ℓ uncertainties by taking, as 1-sigma level error, a third of the difference between resulting transfer function from elliptical beams (Fosalba et al. 2002) and that from

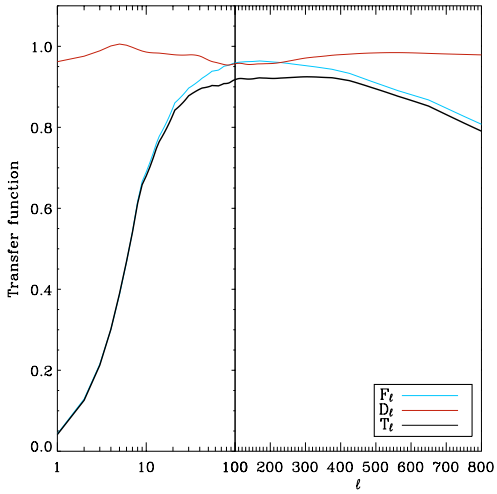

Fig. 4. ARCHEOPS transfer functions: F_ℓ filter function (in blue), D_ℓ destriping transfer function (in red) and T_ℓ total ARCHEOPS transfer function (in black).

the Asymfast decomposition in multiple Gaussians. Figure 6 shows the uncertainties on the C_ℓs due to the beam transfer function uncertainties. They are well below the statistical error bars.

3.2. Filtering and inhomogeneous coverage effects

Filtering leads to a preferred direction on the sky (the scanning direction) and so the assumption of isotropic temperature fluctuations implicitly done in Eq. (1) is not valid any more. However, to a first approximation, the bias on the CMB power spectrum due to the filtering of the time ordered data can be accounted for in the spherical harmonic space through the T_ℓ transfer function.

For this analysis we have performed two types of filtering associated with the destriping of the data discussed in Sect. 2.1 and with the band-pass filter applied to the data on the map making procedure.

The band-pass filter function F_ℓ is computed from 100 simulations of the CMB sky. The simulated maps are converted into timelines using ARCHEOPS pointing. These timelines are then filtered as the ARCHEOPS data. Subsequently, they are projected onto maps and the power spectrum of those is compared to the power spectrum obtained from maps of the same but unfiltered timelines.

Figure 4 shows in blue the band-pass filter function. It reaches 65% at $\ell = 10$ and remains above 85% in the multipole range [25–700]. In our analysis, all bolometers are identically filtered and the difference between their pointing vectors is very small as these bolometers are distributed onto two rows separated by only ∼30 arcmin in the focal plane. We therefore assume an identical F_ℓ function for all detectors. Uncertainties on the estimation of the F_ℓ function are derived from the dispersion of the simulations.

The transfer function associated with the destriping, D_ℓ, has been computed using simulations and is shown in red in Fig. 4. The accurate determination of this function is difficult because the destriping procedure is non linear and CPU intensive. Thus, in order to be very conservative, we choose to take a third of the estimate of the function itself as the systematic error for it.

The total transfer function used for the ARCHEOPS pipeline $T_\ell = F_\ell \times D_\ell$ is plotted in black in Fig. 4. The uncertainties on the final power spectrum due to the errors on the T_ℓ function are represented in Fig. 6.

3.3. Xspect

The ARCHEOPS angular power spectrum has been computed using an extension of the "pseudo-C_ℓ" method to cross power spectra called Xspect (Tristram et al. 2005). Assuming no noise cross-correlation between different detectors, the noise term in Eq. (1) vanishes and each cross power spectrum, $A \neq B$, is an unbiased estimate of the C_ℓs. Pseudo cross power spectra can be easily corrected from inhomogeneous sky coverage, beam smoothing and filtering effects by extending Eq. (1) into:

$$\widehat{D_\ell^{AB}} = \sum_{\ell'} M_{\ell\ell'}^{AB} p_{\ell'}^2 B_{\ell'}^A B_{\ell'}^B T_\ell \left\langle C_{\ell'}^{AB} \right\rangle \quad (2)$$

where the beam transfer functions B_ℓ for each bolometer and the transfert function T_ℓ are those previously described. The mode-mode coupling kernel $M_{\ell\ell'}^{AB}$ is computed for each cross power spectra from the cross-power spectrum of the weighted masks. For the noise weighting scheme we consider a different noise weighted mask for each ARCHEOPS detector. This mask is constructed by multiplying the mask in Fig. 1 by the inverse of the noise variance on each pixel and is convolved by a 30 arcmin Gaussian.

After correction, all cross power spectra $\left\langle C_{\ell'}^{AB} \right\rangle$ are combined into a single estimate of the power spectrum, $\widetilde{C_\ell}$, by weighted averaging assuming the correlation between multipoles to be negligible. This last assumption is not completely true, as we can see some correlation at low multipoles in Fig. 7. Thus the estimate is not completely optimal but no measurable bias has been found in tests of Xspect on realistic simulations of Archeops data sets. Analytical estimates of the covariance matrix and of the error bars in the power spectrum are also given.

Xspect is designed to estimate both the angular power spectrum and its error bars even with incomplete sky coverage and mask inhomogeneities, as is the case with the present ARCHEOPS data. The approach has been validated with simulations including realistic noise and CMB temperature anisotropies. The noise timelines are simulated from an estimation of the Fourier power spectrum of the noise (Amblard & Hamilton 2004) for each of the photometric pixels. The CMB signal is simulated using the HEALPix software from the ARCHEOPS best-fit ΛCDM model (Benoît et al. 2003b) convolved by the beam transfer function. Signal and noise are added into a single timeline which is filtered as the ARCHEOPS data and projected on the sky using the ARCHEOPS pointing.

Three sets of 1000 simulations have been computed for sky maps with HEALPix resolution $nside = 512$: a first one using an uniform weighting, a second one using a noise weighting scheme, and a third one with no noise added. Simulations were performed using the same optimal map-making method (Yvon & Mayet 2004) as the one used for the data.

From these simulations we have found that there is no bias at the 1% level in the estimation of the power spectrum. The analytical error bars provided by Xspect are also found to be above the standard deviation in the simulations by less than 10% and with a rms of 7%. Moreover, the noise contribution to the error bars on the simulated data and the ARCHEOPS data are in agreement within 5%. Hereafter, we will use the analytical estimates provided by Xspect for the error bars of the ARCHEOPS angular power spectrum excluding the sample variance contribution. The latter is computed from the dispersion of the simulations without noise and is added up to obtain the final error bars on the CMB angular power spectrum. Therefore, the sample variance contribution to the error bars is given by the best-fit ARCHEOPS model described in Benoît et al. (2003b).

As mentioned ealier, an improvement of about 10% on the error bars is obtained by using uniform weighting at low multipoles and a noise weighting scheme at high multipoles. Thus, in the following all power spectra presented are computed using uniform weighting up to $\ell < 260$ and using a noise weighting scheme for $\ell \geq 260$.

3.4. SMICA

Using the filtering and beam transfer functions as well as the masks described in Sects. 3.1 and 3.2, we process the Archeops maps with a different estimation method of the CMB angular power spectrum: SMICA (Spectral Matching Independent Component Analysis) (Patanchon 2003).

A specificity of SMICA is its ability to estimate jointly the power spectra of several underlying components (including noise) assuming that the observed sky is a linear combination of components. In spherical harmonic space and in a matrix form, the model is :

$$\boldsymbol{x}_{\ell m} = A\, \boldsymbol{s}_{\ell m} + \boldsymbol{n}_{\ell m} \tag{3}$$

where $\boldsymbol{x}_{\ell m}$ is a vector of spherical harmonics coefficients of the observed maps for each of the considered detectors; A is the $N_{\rm d}$ (number of detectors) $\times\, N_{\rm c}$ (number of components) mixing matrix which defines the amplitude of the different components in each observed map. The coefficients of A are related to the electromagnetic spectra of the components and to the relative calibration between detectors. The spherical harmonic coefficients of the components and noise are stored in vectors $\boldsymbol{s}_{\ell m}$ and $\boldsymbol{n}_{\ell m}$.

SMICA is based on matching empirical auto- and cross spectra to their expected forms, as predicted by model (Eq. (3)) and by the statistical assumption of decorrelation between components. The mismatch is measured by a measure of divergence between the measured and modeled spectra which stems from the likelihood of a Gaussian stationary model. The adjustable parameters are: the power spectrum of each of the components (including CMB and noise) as well as the mixing matrix A. A complete description of SMICA is given in Delabrouille et al. (2003); Cardoso et al. (2002); Patanchon (2003).

In the specific case of Archeops, spectral statistics are formed as follows. The spherical harmonic coefficients $x_{\ell m}$ are computed on the sky region which is common to all detectors using two different weighting schemes. For $\ell < 260$, pixels are uniformly weighted. For $\ell \geq 260$, pixels are weighted proportionally to the number of data samples per pixel for the best detector. Band-averaged pseudo auto- and cross-power spectra are formed from these $x_{\ell m}$ and corrected for beam smoothing. If Q bands are used, we obtain in this manner a set of Q spectral matrices $\widehat{R}_q$ ($q = 1, \ldots, Q$), each of size $N_{\rm d} \times N_{\rm d}$. Next, we choose which parameters should be estimated (power spectra for CMB and possibly other components, all or parts of the coefficients, noise levels), collect all these parameters into a vector θ and denote $R_q(\theta) = \left\langle \widehat{R}_q \right\rangle$ the expected value of the spectral matrices for a given value of θ (this is easily computed from model (3)). The SMICA algorithm estimates the unknown parameters by minimizing the spectral mismatch

$$\phi(\theta) = \sum_q w_q K(\widehat{R}_q, R_q(\theta)) \tag{4}$$

where w_q is the number of independent a_{lm} in the qth spectral band and where the mismatch measure $K(\cdot,\cdot)$ between two positive matrices is defined as $K(M_a, M_b) = \frac{1}{2}\left(\mathrm{trace}(M_a M_b^{-1}) - \log\det M_a M_b^{-1} - N_{\rm d}\right)$ (with this choice, the estimated parameter $\widehat{\theta} = \arg\min \phi(\theta)$ is a maximum likelihood estimate as shown in Delabrouille et al. 2003). The resulting estimated power spectra are then corrected from partial coverage and filtering effects using the MASTER formalism described in Sect. 3.2.

In order to evaluate error bars and possible biases, we have performed 500 realistic simulations of ARCHEOPS data. The data model includes synthetic CMB emission (observed with the same scanning strategy as used by ARCHEOPS) and noise for each detector. Application of SMICA to these simulated data has not shown any measurable bias.

Error bars for the estimated power spectra can also be obtained analytically from the Fisher information matrix. They have been compared to the dispersion found in the Monte-Carlo simulations. Analytic error bars on the CMB power spectrum are found to be slightly underestimated (about 10% on average). In the following, we use the analytic error bars corrected from the factor measured in the simulations.

3.5. CMB power spectrum on the rings

A third approach based on one-dimensional properties of the CMB inhomogeneities on rings has been performed on ARCHEOPS data (Ansari et al. 2003; Plaszczynski & Couchot 2003). It has been made possible by the ARCHEOPS sky scanning strategy, which scans quasi circles on the sky. The fact that we directly use TOI information with no requirement of projection on maps of the sky makes this method complementary to the two previous ones.

Table 1. ARCHEOPS CMB power spectrum and statistical error bars (total, instrumental and sample variance) in $(\mu K_{\rm CMB})^2$ computed with Xspect and SMICA (with two components) for the best six photometric pixels.

			XSPECT			SMICA			
bin	$\ell_{\rm min}$	$\ell_{\rm max}$	$\frac{\ell(\ell+1)}{2\pi}C_\ell$	Total error	Instrumental error	$\frac{\ell(\ell+1)}{2\pi}C_\ell$	Total error	Instrumental error	Sample variance
1	10	16	774	251	45	899	217	11	206
2	17	24	998	167	12	1027	170	15	155
3	25	34	1043	168	41	999	149	22	127
4	35	49	1487	144	39	1486	131	26	105
5	50	59	1217	185	51	1081	173	39	134
6	60	69	1537	195	54	1561	189	48	141
7	70	79	1613	227	78	1619	206	57	149
8	80	89	2038	234	78	1978	223	67	156
9	90	99	2275	258	93	2451	242	77	165
10	100	119	2586	204	74	2639	201	71	130
11	120	139	3193	238	90	3221	232	84	148
12	140	159	3148	273	110	3234	274	111	163
13	160	179	4225	312	138	4358	312	138	174
14	180	199	4941	339	159	5050	356	176	180
15	200	219	4589	369	189	4506	377	197	180
16	220	239	5085	392	219	5183	388	215	173
17	240	259	4258	421	263	4340	402	244	158
18	260	279	4356	374	235	4538	365	226	139
19	280	309	3174	325	233	3385	302	210	92
20	310	349	2325	302	247	2351	298	243	55
21	350	399	1960	322	292	1862	309	279	30
22	400	449	1832	418	394	1825	399	375	24
23	450	524	2569	507	483	2487	465	441	24
24	525	599	2394	799	774	2649	676	651	25
25	600	699	1885	1183	1168	1595	1124	1109	15

Γ_m is defined as the Fourier power spectrum of the signal on a sky ring. For a ring of colatitude Θ, the relation between $\Gamma_m(\Theta)$ and the C_ℓ (Delabrouille et al. 1998) follows:

$$\Gamma_m(\Theta) = \sum_{\ell=|m|}^{\infty} C_\ell T_\ell B_\ell^2 (\mathcal{P})^2_{\ell m}(\Theta), \quad (5)$$

where T_ℓ is the transfer function for the destriping and filtering, B_ℓ is the beam transfer function and $(\mathcal{P})_{\ell m}$ are the Legendre polynomials.

Rings are built for each bolometer from the TOIs by using the pointing information. They are then analysed by pairs. For each ring pair $(i-1, i)$, whenever measurements taken at the same angular phase ϕ are separated on the sky by less than 0.1 degree, we define a "signal" $S_i(\phi)$ and a "noise" $N_i(\phi)$ as respectively the half sum and half difference of the measurements from each ring.

Once these quantities are computed ring per ring, we analyse S and N in two ways. On the first hand, we compute the difference of the mean values of their Fourier spectra (that we call the Γ_m analysis). On the other hand, the average of the autocorrelation functions for each pair is computed and then Fourier transformed to obtain the Γ_m power spectrum. In both cases a Galactic mask similar to that described in Sect. 2.2 is applied. In addition since the autocorrelation approach needs all the low frequency drifts to be properly removed, we apply a cross-scan destriping (Bourrachot 2004). Since the noise directly pops-up from the data themselves, no simulation is needed in these approaches.

The error bars on the Γ_m power spectrum are computed from the dispersion on the Fourier transform across rings and then propagated to obtain the uncertainties on the angular power spectrum.

4. Main results

The analysis presented in this paper uses the six most sensitive ARCHEOPS bolometers, four at 143 GHz and two at 217 GHz with instantaneous sensitivities ranging from 93 to 207 $\mu K_{\rm CMB}\, s^{\frac{1}{2}}$. Note that those instantaneous sensitivities are better, by a factor of at least five, than those of the WMAP satellite mission detectors (Bennett et al. 2003) and a factor 2 to 4 worse than the nominal ones expected for the PLANCK-HFI instrument. We consider 20% of the sky by applying the Galactic mask presented in Sect. 2.2.

Table 1 presents the angular power spectrum measured by ARCHEOPS. Results for the Xspect and SMICA methods are both given as they are based on different assumptions on the data model.

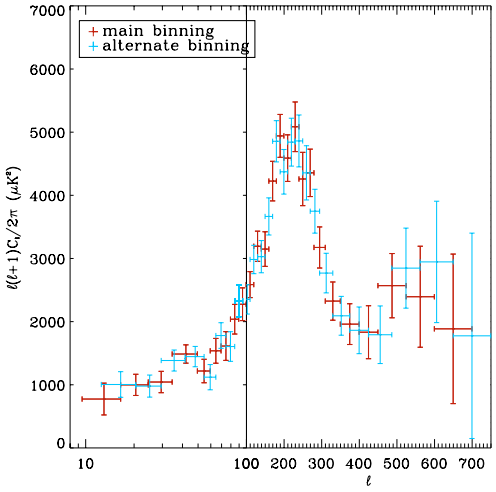

Fig. 5. ARCHEOPS temperature angular power spectrum obtained using the Xspect method. A mixing of log-linear scales is presented to improve the readibility of the figure both on the Sachs-Wolfe plateau and on the acoustic peaks regions. Two intertwined and therefore not independent binnings (red and blue) are represented.

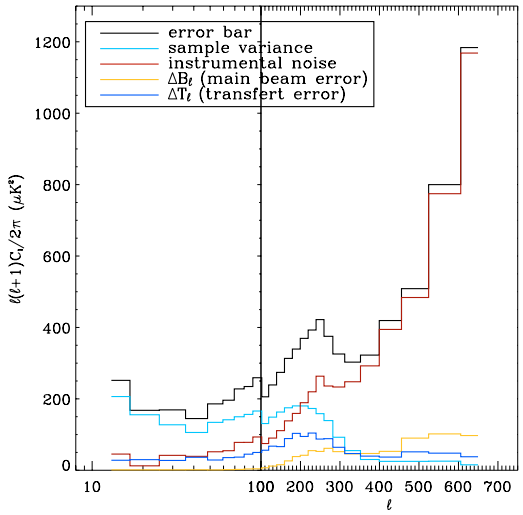

Fig. 6. Detailed description of the statistical error bars (in black) on the ARCHEOPS angular power spectrum obtained with Xspect in terms of sample variance (in cyan) and instrumental noise (in red). In addition, systematic errors on the angular power spectrum estimation due to uncertainties on the filter (in blue) and beam smoothing function (in yellow) are shown (see Sect. 3).

4.1. ARCHEOPS temperature angular power spectrum using Xspect

Figure 5 shows the ARCHEOPS CMB angular power spectrum obtained using the Xspect method for two intertwined binnings (blue and red). These binnings correspond to two sets of overlapping and shifted window functions which lead to two non-independent estimates of the CMB angular power spectrum. A mix of logarithmic and linear scales in multipole space is presented to improve the readibility of the figure both on the Sachs-Wolfe plateau and on the first two acoustic-peaks clearly detected by ARCHEOPS. Two different weighting schemes are combined to produce the smallest error bars. At low ℓ multipoles a uniform weighting is preferred whereas for high ℓs the sky maps for each detector are noise weighted by using $w_{p,d} = 1/\sigma^2_{p,d}$ where $\sigma^2_{p,d}$ is the variance of the pixel p of the sky map from the detector d. The two schemes yield identical results around the mixing point, $\ell \simeq 260$ and they are joined in order to minimize the final error bars.

Figure 6 shows a detailed description of the statistical error bars (in black) on the ARCHEOPS angular power spectrum in terms of sample variance (in cyan) and instrumental noise (in red). Sample variance is deduced from the set of simulation without noise. It corresponds to the uncertainty on the model that is induced by the fact that we can only look at a part of one realisation of the sky. Sample variance dominates for $\ell < 100$ and contributes to 50% or more of the total statistical error up to $\ell \sim 200$. Systematic errors due to uncertainties on the filter (in blue) and beam smoothing function (in yellow), which were computed as discussed in Sect. 3, are well below the statistical errors.

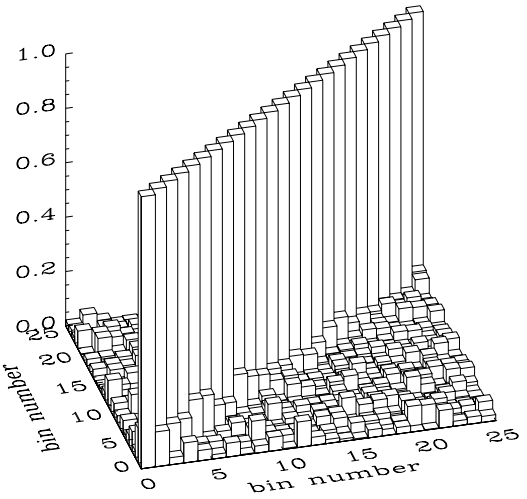

Fig. 7. Error covariance matrix of the ARCHEOPS angular power spectrum computed using the Xspect method. The correspondence between bin number and multipole range is indicated in Table 1. The off-diagonal terms are less than 12%.

Figure 7 shows the absolute value of the normalised error covariance matrix of the ARCHEOPS angular power spectrum for the binning shown in red in Fig. 5. The correspondence between bin number and multipole range is indicated in Table 1. This matrix was computed using the simulations described in Sect. 3.3 and provides the absolute correlation between

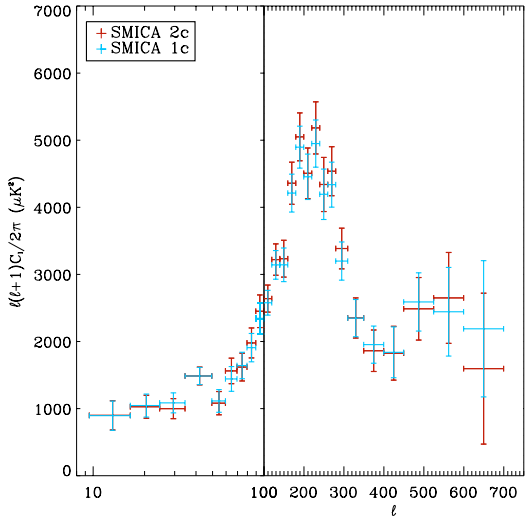

Fig. 8. ARCHEOPS temperature angular power spectrum obtained using the SMICA method for one (in red) and two (in blue) components. A mixing of log-linear scales is presented to improve the readibility of the figure both on the Sachs-Wolfe plateau and on the acoustic peaks regions.

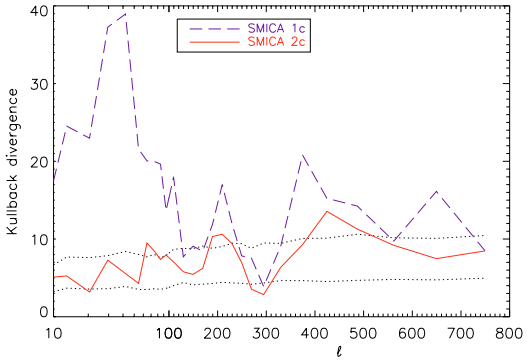

Fig. 9. Rescaled spectral fit as function of the multipole. The dashed line is the fit for 1 component, the solid line curve is for 2 components. The dotted lines are the bounds of the 68% confidence interval estimated in simulations of the two-component model. Note how a two-component model brings the spectral mismatch within the statistical error bounds, showing that in addition to the CMB anisotropies a second component is required by the data mainly at low spatial frequency ($\ell < 100$).

multipole bins. The off-diagonal terms are less than 12%, and therefore the C_ℓ estimates can be considered as roughly uncorrelated across bins on multipole space.

4.2. ARCHEOPS temperature angular power spectrum using SMICA

To apply the SMICA method to the ARCHEOPS data we choose to estimate two components (number required by the data: see Fig. 9 and related comments) corresponding to the CMB anisotropies and to unidentified residuals from foregrounds. The mixing matrix is simultaneously estimated allowing for recalibration of individual detectors against the most sensitive photometric pixel at 143 GHz.

We find that CMB anisotropies are clearly detected for all the bolometers. A second component, much weaker in amplitude, is significant only in the 217 GHz maps. This component is thought to be a weak residual of foreground subtraction (see Sect. 5.3, for a more detailed discussion). Figure 8 shows in red the estimated CMB power spectrum with SMICA assuming two components.

To assess the impact of the second component, we run SMICA assuming a single physical component in the ARCHEOPS maps, meant to be the CMB anisotropies. For this second analysis, we fix the CMB mixing parameters to the values derived from the dipole calibration, allowing the direct comparison with Xspect. Figure 8 shows in blue the CMB power spectrum obtained in this way.

The fit of the estimated model to the data is quantified by the lowest possible value $\phi(\widehat{\theta}) = \min_\theta \phi(\theta)$ of the spectral matching criterion Eq. (4). If the model of observations is correct (i.e. includes the probability distribution of the data), then $\phi(\widehat{\theta})$ should be statistically small. A finer picture is obtained by splitting the overall fit of $\phi(\widehat{\theta})$ into its components $w_q K(\widehat{R}_q, R_q(\widehat{\theta}))$ as a function of the multipole bin q. Figure 9 shows the spectral adjustment of the best one-component model and of the best two-component model. The adjustment is much better with two components than with a single component, indicating that a second component is required by the data.

Blind estimate for two components allows to separate systematic residuals in the two 217 GHz maps at the cost of some small increase in the CMB power spectrum error bars. The errors on the estimated CMB mixing parameters (bolometer intercalibration error) influence the error bars on the power spectrum estimate. The ratio between CMB power spectrum statistical error bars for the two and one component cases is about 20% at low ℓ and 10% at high ℓ.

5. Discussion

The CMB angular power spectrum measured by Archeops as computed using Xspect and SMICA extends to a larger multipole range the results presented in (Benoît et al. 2003a) and is in good agreement with them on the common multipole range reducing the error bars by a factor of three.

5.1. Consistency checks

Internal tests of consistency have been implemented in order to check the robustness of the results presented above. The ARCHEOPS CMB angular power spectrum has been computed for two different map resolutions ($nside = 512, 256$ corresponding to 7 and 14 arcmin pixels resp.) and we observe no significant differences between them. Furthermore, we have substantially varied the frequency intervals for the timeline

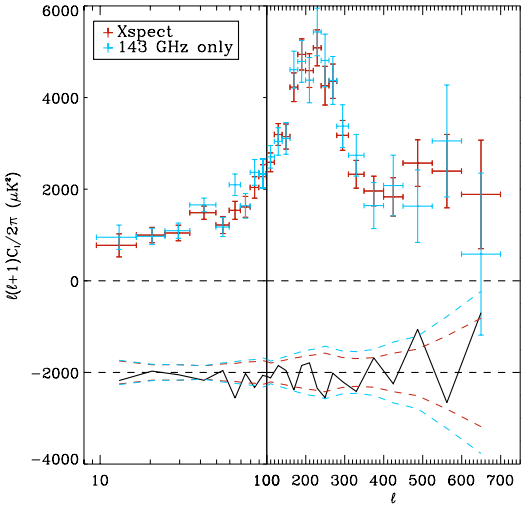

Fig. 10. Xspect angular power spectrum using six detectors (in red) compared to the one obtained using only the four 143 GHz detectors (in blue). The difference between the two power spectra is given in the bottom plot (shifted by 2000) and are compared to the error bars (black dotted line).

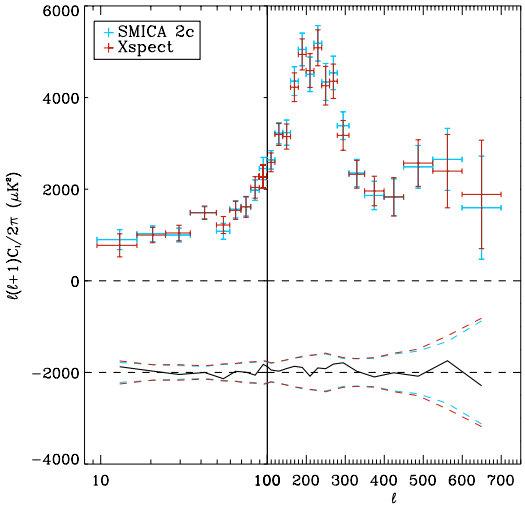

Fig. 11. ARCHEOPS angular power spectrum using Xspect (in red) and using SMICA (in blue). The difference between the two power spectra is given in the bottom plot (shifted by 2000) and are compared to the error bars (blue and red dotted line). See text for details.

bandpass filtering and no significant effect appears in the estimation of the angular power spectrum even at high multipoles. In addition, to check the consistency of the results between the two CMB channels (143 and 217 GHz) we have computed, using Xspect, the CMB angular power spectrum for only the four 143 GHz bolometers. Figure 10 shows this spectrum (in blue) compared to the one using the 6 most sensitive photometric pixels (in red). The spectra are in very good agreement, within the error bars, over the full multipole range. Using only the 143 GHz bolometers reduces significantly the sensitivity to the second acoustic peak but no systematic offsets are observed.

As an extra consistency check, we compare in Fig. 11 the ARCHEOPS angular power spectrum obtained using Xspect (in red) with the one computed with 2-components SMICA method (in blue). The difference between the two power spectra, given in the bottom plot, is well below the error bars (red and blue dotted line). Detailed discussion of this issue is presented in Sect. 5.3.

5.2. ARCHEOPS temperature angular power spectrum on the rings

We show in Fig. 12 the Fourier spectra obtained through the use of the two ring analysis methods described in Sect. 3.5 for the best ARCHEOPS bolometer at 143 GHz. These analyses are in agreement within the error bars and show a clear detection of the first acoustic peak. These results indicate that the processed timelines contain no obvious spurious feature at a particular time frequency.

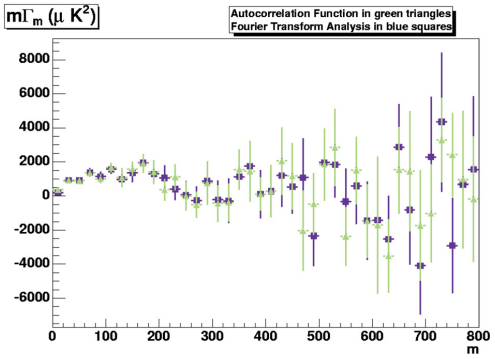

Fig. 12. Fourier spectra obtained through the use of the two methods described in Sect. 3.5 for the best ARCHEOPS bolometer at 143 GHz. These analyses are in agreement within the error bars.

5.3. Contamination from foregrounds

As any balloon-borne experiment, ARCHEOPS is exposed to the fluctuations of the atmospheric emission. Moreover the Galactic emission at 143 and particularly at 217 GHz is low but not negligible. Even if a careful decorrelation to suppress ozone and dust spurious emissions has been performed (see Sect. 2.2), the residuals from this decorrelation are a potential source of systematic errors in the determination of the CMB angular power spectrum.

The Galactic dust contribution must be much weaker at high Galactic latitudes. To assess the level of Galactic residuals, we have computed the angular power spectrum of the ARCHEOPS data using only the Northern part of the ARCHEOPS sky coverage. Figure 13 shows the estimate of the angular

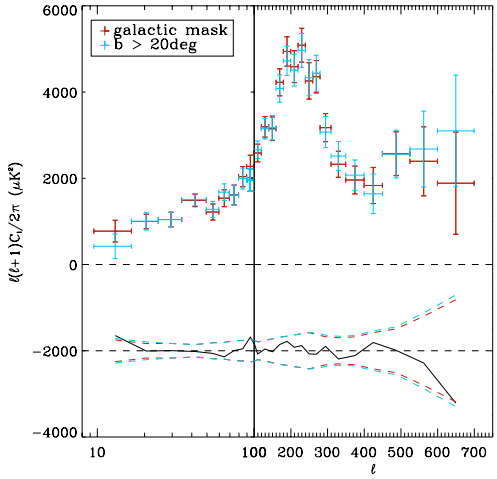

Fig. 13. Xspect ARCHEOPS power spectrum computed for the Galactic mask described in Sect. 2.2 (in red) and for $b > 20$ (in blue). The difference between the two estimates is given in the bottom plot (shifted by 2000) and compared to the error bars (blue and red dotted line).

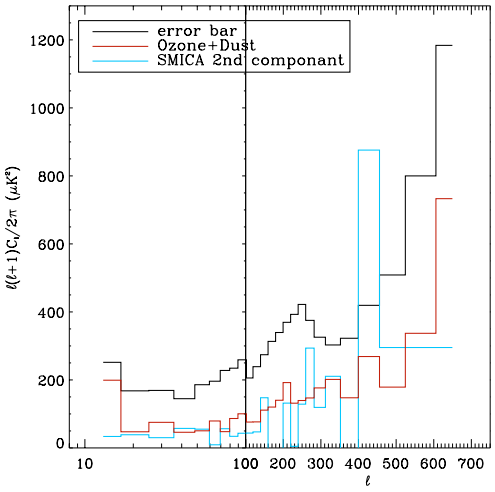

Fig. 14. Atmospheric and Galactic dust residual emissions on the ARCHEOPS 143 and 217 GHz maps. In red, the residual foreground emission computed by cross-correlating these maps with the 353 GHz maps using the Xspect method. In blue, the residual foreground emission obtained from the second component detected by the SMICA 2 components analysis of the ARCHEOPS data. In black, we plot for comparison the error bars of the ARCHEOPS CMB angular power spectrum.

power spectrum for the Galactic mask described in Sect. 2.2 (in red) and for high positive Galactic latitudes: $b > +20$ deg (in blue) using Xspect. The differences between the two power spectrum estimates, shown in the bottom plot, are significantly smaller than the error bars associated to them. We conclude from this that the residual dust emission in the CMB angular power spectrum obtained from the ARCHEOPS data is small compare to the statistical errors in the multipole range $17 \leq \ell < 700$. The multipole bin $10 \leq \ell < 17$ shows a more important contimation from dust residual emission but still at the levels of the statistical and systematic uncertainties. For $\ell < 10$ we found that the dust contamination was significant and therefore this multipole range was not included in this paper. The same test has been performed using SMICA and leads to identical conclusions.

To fully assess the residual contamination to the ARCHEOPS data from dust and atmospheric emissions we have performed two independent tests based on Xspect and SMICA respectively.

First, using the Xspect method we can cross-correlate the sky maps at 143 and 217 GHz used for the C_ℓ estimation with the sky maps of the 353 GHz ARCHEOPS detectors. The observed emission on the latter is dominated by dust and atmospheric emission and to first order we can neglect the CMB emission. Thus from this cross correlation, we can obtain an estimate of the residual foreground contribution to the ARCHEOPS CMB angular power spectrum computed with Xspect. The results from this analysis are shown in Fig. 14. The estimated contamination (in red) remains significantly below the statistical errors (in black) over the full multipole range except for the first multipole bin ($\ell = [10{-}17[$) for which the contamination is still smaller than the statistical error bar.

As discussed in Sect. 4.2 we have performed, using SMICA, a two component analysis of the ARCHEOPS six best photometric pixels. The first component on this analysis was identified as CMB emission whereas the second as the spurious residual foreground emission. This is significant only for the 217 GHz bolometer maps. This component is mainly due to residual atmospheric emission left behind after the linear decorrelation. This estimation is represented in Fig. 14, in blue, and can be compared to the foreground residual contamination estimated with Xspect at high multipoles. The SMICA estimate is of the same of order of magnitude and oscillates for $\ell > 200$. These oscillations come from the uncertainties on the estimation of the second component which are well reflected on the error bars obtained for it. This could be due to correlated noise between the 217 GHz maps which would not be present in the residual foreground estimate obtained using Xspect. Further, this conclusion is reinforced by the fact that this contribution does not seem to be fully additive as expected from the SMICA model.

From the above results we can conclude that the ARCHEOPS CMB angular power spectra obtained using Xspect and SMICA are fully compatible if we take into account the residual atmospheric contamination which is in any case well below the statistical error bars as shown in Fig. 15. We have plotted the differences between the ARCHEOPS CMB angular power spectra computed with SMICA 1 and 2 component (in blue), SMICA 1 component and Xspect (in black), and SMICA 2 components and Xspect (in red). For comparison the statistical error bars are shown (black dashed line). This figure visually confirms the fact that the contamination from foregrounds

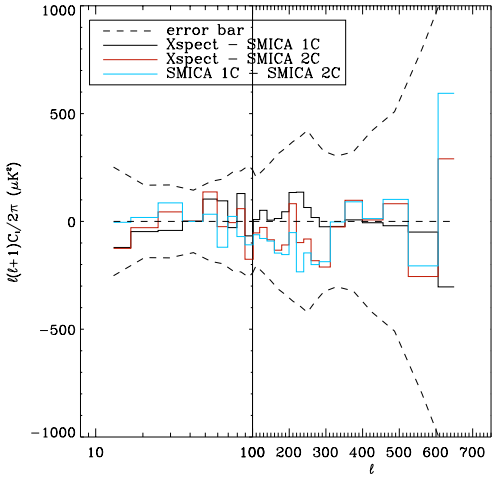

Fig. 15. Differences between the ARCHEOPS CMB angular power spectra computed with SMICA 1 and 2 component (in blue), SMICA 1 component and Xspect (in black), and SMICA 2 components and Xspect (in red). For comparison the statistical error bars are shown (black dashed line).

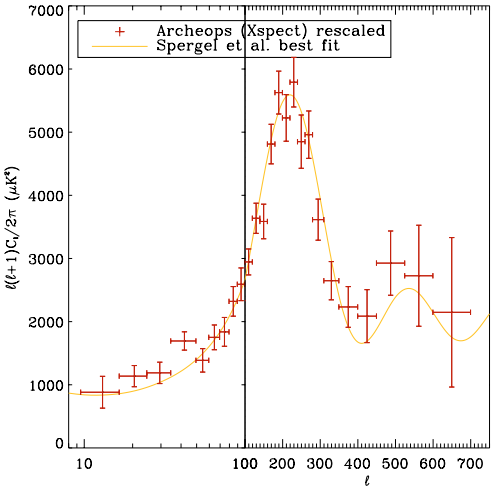

Fig. 16. The ARCHEOPS temperature angular power spectrum rescaled by a factor 1.07 in temperature superimposed on the Λ-CDM best-fit model by the WMAP team and presented in Spergel et al. (2003).

on the ARCHEOPS CMB angular power spectrum is well below the error bars. This analysis of the foreground contamination validates our choice of the galactic mask described in Sect. 2.2.

Finally, the contribution from point sources is negligible in the multipole range considered here (see Paper I).

5.4. Comparison to the standard Λ-CDM cosmological model

To check the validity of our results and their agreement with previous cosmological observations we have compared the CMB angular power spectrum measured by ARCHEOPS to the best-fit Λ-CDM cosmological model presented in (Spergel et al. 2003). This model was derived from a combination of the WMAP data with other finer scale CMB experiments, ACBAR and CBI and is defined by $h = 0.71992$, $\Omega_b h^2 = 0.02238$, $\Omega_m h^2 = 0.11061$, $\tau = 0.11026$, constant $n_s\,(0.05\ \mathrm{Mpc})^{-1} = 0.95820$ and normalization amplitude $A\,(0.05\ \mathrm{Mpc}) = 0.73935$.

In Fig. 16 we present the best-fit Λ-CDM cosmological model described above superimposed on the ARCHEOPS CMB angular power spectrum which is rescaled by a factor 1.07 in temperature (1.14 in C_ℓ). This factor has been computed by assuming that the differences between the ARCHEOPS data and the model are due to a global scaling factor for all angular scales which has been fitted to 1.07 ± 0.02 with χ^2 of 27/24 and probability $Q = 0.72$. For this fit we have only considered the statistical error bars on the angular power spectrum.

We observe that the agreement between the rescaled ARCHEOPS data and the model is very good. Here the model can be thought of as a guideline summarising other CMB experiments at different frequencies, in order to show the overall consistency across the electromagnetic spectrum. The scaling factor can be explained by the uncertainties on the absolute calibration of the ARCHEOPS data which are 6% in temperature (12% in C_ℓ). A more detailed analysis of this issue is reported to a forthcoming paper including the determination of cosmological parameters from the ARCHEOPS data as well as a comparison to other CMB observations at the map level.

6. Conclusion

ARCHEOPS was designed as a test-bench for PLANCK-HFI[3] in terms of detectors, electronics, cryogenics and data processing. ARCHEOPS has demonstrated the validity of these technical choices two years ago by determining, for the first time and in a single balloon flight, the temperature angular power spectrum of the CMB from the Sachs-Wolfe plateau to the first acoustic peak ($15 \leq \ell \leq 350$) using only two detectors.

In this paper we present an improved analysis of the ARCHEOPS data using the six most sensitive detectors and 20% of the sky, mostly clear of foregrounds. ARCHEOPS has measured the CMB angular power spectrum in the multipole range from $\ell = 10$ to $\ell = 700$ with 25 bins, confirming strong evidence for a plateau at large angular scales followed by two acoustic peaks centered around $\ell = 220$ and $\ell = 550$ respectively.

The ARCHEOPS CMB angular power spectrum has been determined using two different statistical methods, Xspect and SMICA. The results from these two methods are in very good agreement with differences between them well below the statistical error bars. Furthermore, they allow a detailed analysis of the residual foreground contribution which is mainly due to atmospheric and Galactic dust emissions. The residual

[3] www.planck-hfi.org

foreground emission on the ARCHEOPS data is small with respect to the error bars at all multipoles.

Finally, we have compared the ARCHEOPS CMB angular power spectrum to the best-fit Λ-CDM cosmological model presented in (Spergel et al. 2003) derived from a combination of the WMAP data with other smaller scale CMB experiments (ACBAR and CBI). We find that the ARCHEOPS data are in very good agreement with this model considering a rescaling factor to account for uncertainties on the absolute calibration.

A more detailed analysis for the determination of cosmological parameter with ARCHEOPS and other cosmological datasets will be discussed in a forthcoming paper. Furthermore, a comparison of the maps from ARCHEOPS, WMAP and other CMB datasets will be used to study the primordial nature of the measured CMB anisotropies from their electromagnetic spectrum.

All methods developed for this analysis will be implemented for the PLANCK-HFI data analysis. Even if PLANCK is less prone to systematic effects due to its space environment, the know-how acquired on ARCHEOPS data should prove useful in order to assess PLANCK final power spectrum.

Acknowledgements. We would like to pay tribute to the memory of Pierre Faucon who led the CNES team on this successful flight. The HEALPix package was used throughout the data analysis (Gorski et al. 1999).

References

Amblard, A., & Hamilton, J. C., 2004, A&A, 417, 1189
Ansari, R., Bargot, S., Bourrachot, A., et al. 2003, MNRAS, 343, 552
Barkats, D., Bischoff, C., Farese, P., et al., 2005, ApJ, 619, L127
Bennett, C. L., Halpern, M., Hinshaw, G., et al., 2003, ApJ, 148, 1
Benoît, A., Ade, P., Amblard, A., et al., 2003a, A&A, 399, L19
Benoît, A., Ade, P., Amblard, A., et al., 2003b, A&A, 399, L25
de Bernardis, P., Ade, P. A. R., Bock, J. J., et al., 2000, Nature, 404, 955
Douspis, M., Riazuelo, A., Zolnierowski, Y., & Blanchard, A., 2003, New Astron. Rev., 47, 755
Bourrachot, A., 2004, Ph.D. Thesis, Université Paris Sud Orsay
Cardoso, J.-F., Snoussi, H., Delabrouille, J., & Patanchon, G., 2002, EUSIPCO02 Conf. [arXiv:astro-ph/0209466]
Delabrouille, J., Gorski, K. M., & Hivon, E., 1998, MNRAS, 298, 445
Delabrouille, J., Cardoso, J. F., & Patanchon, G., 2003, MNRAS, 346, 1089
Finkbeiner, D., Davis, M., & Schlegel, D., 1999, ApJ, 524, 867
Fixsen, D. J., Cheng, E. S., Cottingham, D. A., et al., 1994, ApJ, 420, 445
Fosalba, P., Doré, O., & Bouchet, F. R., 2002, Phys. Rev. D, 65, 63003
Gorski K. M., Hivon E., & Wandelt B. D., 1999, in Proc. MPA/ESO Cosmology Conf., Evolution of Large-Scale Structure, ed. A. J. Banday, R. S. Sheth & L. Da Costa, PrintPartners Ipskamp, NL, 37 (also [arXiv:astro-ph/9812350])
Halverson, N. W., Leitch, E. M., Pryke, C., et al., 2002, ApJ, 568, 38
Hanany, S., Ade, P., Balbi, A., et al., 2000, ApJ, 545, L5
Hinshaw, G., Spergel, D. N., Verde, L., et al., 2003, ApJ, 148, 135
Hivon, E., Gorski, K. M., Netterfield, C. B., et al., 2002, ApJ, 567, 2
Lamarre, J. M., Puget, J. L., Bouchet, F., et al., 2003, NewAR, 47, 1017L
Lee, A. T., Ade, P., Balbi, A., et al., 2001, ApJ, 561, L1
Leitch, E., Kovac, J., Halverson, N., et al., ApJ, submitted [arXiv:astro-ph/0409357]
Lineweaver, C. H., Barbosa, D., Blanchard, A., et al., 1997, A&A, 322, 365
Macías-Pérez, J. F., Helbig, P., Quast, R., et al., 2000, A&A, 353, 419
Macías-Pérez, J. F., Bourrachot, A., Lagache, G., et al., 2005, in preparation
Madet, K., Maffei, B., Bock, J. J., et al., 2004, in preparation
Miller, A. D., Caldwell, R., Devlin, M. J., et al., 1999, ApJ, 524, L1
Netterfield, C. B., Devlin, M. J., Jarolik, N., et al., 1997, ApJ, 474, 47
Netterfield, C. B., Ade, P. A. R., Bock, J. J., et al., 2002, ApJ, 571, 604
Patanchon G., 2003, New Astron. Rev., 47, 871
Peebles P. J. E., & Hauser M. G., 1974, ApJS, 28, 19.
Peebles P. J. E., 1973, ApJ, 185, 431
Plaszczynski S., & Couchot F., 2003, MNRAS, submitted [arXiv:astro-ph/0309526]
Readhead, A., Myers, S., Pearson, T., et al., Science, 306, 836 [arXiv:astro-ph/0409569]
Rubino-Martin J. A., Rebolo, R., Carreira, P., et al., 2003, MNRAS, 341, 1084
Schlegel, D., Finkbeiner, D., & Davis, M., 1998, ApJ, 500, 525
Sievers, J. L., Bond, J. R., Cartwright, J. K., et al., 2003, ApJ, 591, 599
Spergel, D. N., Verde, L., Peiris, H. V., et al., 2003, ApJ, 148, 175
Szapudi, I., Prunet, S., Pogosyan, D., et al., 2001, ApJ, 548, L115
Tristram, M., Hamilton, J.-Ch., Macías-Peréz, J. F., et al., 2004, Phys. Rev. D, 69, 123008
Tristram, M., Macías-Peréz, J. F., Renault, C., et al., 2005, MNRAS, 358, 833
Yvon, D., & Mayet, F., 2004, A&A, in press [arXiv:astro-ph/0401505]

A&A 399, L25–L30 (2003)
DOI: 10.1051/0004-6361:20021722

Astronomy & Astrophysics

Cosmological constraints from Archeops

A. Benoît[1], P. Ade[2], A. Amblard[3,24], R. Ansari[4], É. Aubourg[5,24], S. Bargot[4], J. G. Bartlett[3,24], J.–Ph. Bernard[7,16], R. S. Bhatia[8], A. Blanchard[6], J. J. Bock[8,9], A. Boscaleri[10], F. R. Bouchet[11], A. Bourrachot[4], P. Camus[1], F. Couchot[4], P. de Bernardis[12], J. Delabrouille[3,24], F.–X. Désert[13], O. Doré[11], M. Douspis[6,14], L. Dumoulin[15], X. Dupac[16], P. Filliatre[17], P. Fosalba[11], K. Ganga[18], F. Gannaway[2], B. Gautier[1], M. Giard[16], Y. Giraud–Héraud[3,24], R. Gispert[7†,⋆], L. Guglielmi[3,24], J.–Ch. Hamilton[3,17], S. Hanany[19], S. Henrot–Versillé[4], J. Kaplan[3,24], G. Lagache[7], J.–M. Lamarre[7,25], A. E. Lange[8], J. F. Macías–Pérez[17], K. Madet[1], B. Maffei[2], Ch. Magneville[5,24], D. P. Marrone[19], S. Masi[12], F. Mayet[5], A. Murphy[20], F. Naraghi[17], F. Nati[12], G. Patanchon[3,24], G. Perrin[17], M. Piat[7], N. Ponthieu[17], S. Prunet[11], J.–L. Puget[7], C. Renault[17], C. Rosset[3,24], D. Santos[17], A. Starobinsky[21], I. Strukov[22], R. V. Sudiwala[2], R. Teyssier[11,23], M. Tristram[17], C. Tucker[2], J.–C. Vanel[3,24], D. Vibert[11], E. Wakui[2], and D. Yvon[5,24]

[1] Centre de Recherche sur les Très Basses Températures, BP 166, 38042 Grenoble Cedex 9, France
[2] Cardiff University, Physics Department, PO Box 913, 5, The Parade, Cardiff, CF24 3YB, UK
[3] Physique Corpusculaire et Cosmologie, Collège de France, 11 Pl. M. Berthelot, 75231 Paris Cedex 5, France
[4] Laboratoire de l'Accélérateur Linéaire, BP 34, Campus Orsay, 91898 Orsay Cedex, France
[5] CEA-CE Saclay, DAPNIA, Service de Physique des Particules, Bât. 141, 91191 Gif-sur-Yvette Cedex, France
[6] Laboratoire d'Astrophysique de l'Obs. Midi-Pyrénées, 14 avenue E. Belin, 31400 Toulouse, France
[7] Institut d'Astrophysique Spatiale, Bât. 121, Université Paris XI, 91405 Orsay Cedex, France
[8] California Institute of Technology, 105-24 Caltech, 1201 East California Blvd, Pasadena CA 91125, USA
[9] Jet Propulsion Laboratory, 4800 Oak Grove Drive, Pasadena, California 91109, USA
[10] IROE–CNR, Via Panciatichi, 64, 50127 Firenze, Italy
[11] Institut d'Astrophysique de Paris, 98bis boulevard Arago, 75014 Paris, France
[12] Gruppo di Cosmologia Sperimentale, Dipart. di Fisica, Univ. "La Sapienza", P. A. Moro, 2, 00185 Roma, Italy
[13] Laboratoire d'Astrophysique, Obs. de Grenoble, BP 53, 38041 Grenoble Cedex 9, France
[14] Nuclear and Astrophysics Laboratory, Keble Road, Oxford, OX1 3RH, UK
[15] CSNSM–IN2P3, Bât. 108, Campus Orsay, 91405 Orsay Cedex, France
[16] Centre d'Étude Spatiale des Rayonnements, BP 4346, 31028 Toulouse Cedex 4, France
[17] Institut des Sciences Nucléaires, 53 avenue des Martyrs, 38026 Grenoble Cedex, France
[18] Infrared Processing and Analysis Center, Caltech, 770 South Wilson Avenue, Pasadena, CA 91125, USA
[19] School of Physics and Astronomy, 116 Church St. S.E., University of Minnesota, Minneapolis MN 55455, USA
[20] Experimental Physics, National University of Ireland, Maynooth, Ireland
[21] Landau Institute for Theoretical Physics, 119334 Moscow, Russia
[22] Space Research Institute, Profsoyuznaya St. 84/32, Moscow, Russia
[23] CEA-CE Saclay, DAPNIA, Service d'Astrophysique, Bât. 709, 91191 Gif-sur-Yvette Cedex, France
[24] Fédération de Recherche APC, Université Paris 7, Paris, France
[25] LERMA, Observatoire de Paris, 61 Av. de l'Observatoire, 75014 Paris, France

Received 16 October 2002 / Accepted 22 November 2002

Abstract. We analyze the cosmological constraints that Archeops (Benoît et al. 2003) places on adiabatic cold dark matter models with passive power-law initial fluctuations. Because its angular power spectrum has small bins in ℓ and large ℓ coverage down to COBE scales, Archeops provides a precise determination of the first acoustic peak in terms of position at multipole $l_{\rm peak} = 220 \pm 6$, height and width. An analysis of Archeops data in combination with other CMB datasets constrains the baryon content of the Universe, $\Omega_{\rm b}h^2 = 0.022^{+0.003}_{-0.004}$, compatible with Big-Bang nucleosynthesis and with a similar accuracy. Using cosmological priors obtained from recent non–CMB data leads to yet tighter constraints on the total density, e.g. $\Omega_{\rm tot} = 1.00^{+0.03}_{-0.02}$ using the HST determination of the Hubble constant. An excellent absolute calibration consistency is found between Archeops and other CMB experiments, as well as with the previously quoted best fit model. The spectral index n is measured to be $1.04^{+0.10}_{-0.12}$ when the optical depth to reionization, τ, is allowed to vary as a free parameter, and $0.96^{+0.03}_{-0.04}$ when τ is fixed to zero, both in good agreement with inflation.

Key words. cosmic microwave background – cosmological parameters – early Universe – large–scale structure of the Universe

1. Introduction

A determination of the amplitude of the fluctuations of the cosmic microwave background (CMB) is one of the most

Send offprint requests to: A. Benoît,
e-mail: benoit@grenoble.cnrs.fr

⋆ Richard Gispert passed away few weeks after his return from the early mission to Trapani.

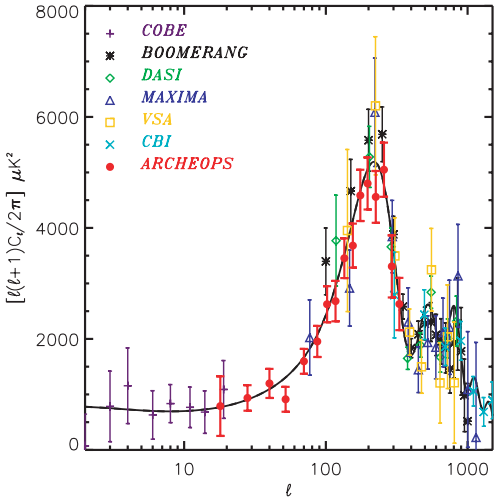

Fig. 1. Measurements of the CMB angular power spectrum by Archeops (in red dots) compared with CBDMVC datasets. A ΛCDM model (see text for parameters) is overplotted and appears to be in good agreement with all the data.

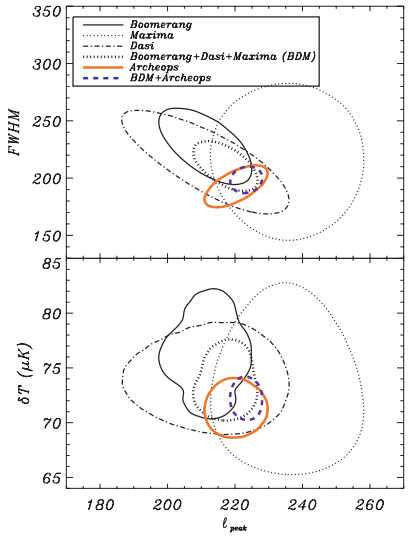

Fig. 2. Gaussian fitting of the first acoustic peak using Archeops and other CMB experiments ($\ell \leq 390$). *Top panel*: 68% CL likelihood contours in the first peak position and FWHM ($\ell_{\rm peak}, FWHM$) plane; *Bottom panel*: 68% CL likelihood contours in the first peak position and height ($\ell_{\rm peak}, \delta T_{\rm peak}$) plane for different CMB experiments and combinations. The width of the peak is constrained differently by Archeops and BDM experiments, so that the intersection lies on relatively large $\ell_{\rm peak}$. Hence, the BDM + Archeops zone is skewed to the right in the bottom panel.

promising techniques to overcome a long standing problem in cosmology – setting constraints on the values of the cosmological parameters. Early detection of a peak in the region of the so-called first acoustic peak ($\ell \approx 200$) by the Saskatoon experiment (Netterfield et al. 1997), as well as the availability of fast codes to compute theoretical amplitudes (Seljak et al. 1996) has provided a first constraint on the geometry of the Universe (Lineweaver et al. 1997; Hancock et al. 1998). The spectacular results of Boomerang and Maxima have firmly established the fact that the geometry of the Universe is very close to flat (de Bernardis et al. 2000; Hanany et al. 2000; Lange et al. 2001; Balbi et al. 2000). Tight constraints on most cosmological parameters are anticipated from the Map (Bennett et al. 1997) and Planck (Tauber et al. 2000) satellite experiments. Although experiments have already provided accurate measurements over a wide range of ℓ, degeneracies prevent a precise determination of some parameters using CMB data alone. For example, the matter content $\Omega_{\rm m}$ cannot be obtained independently of the Hubble constant. Therefore, combinations with other cosmological measurements (such as supernovæ, Hubble constant, and light element fractions) are used to break these degeneracies. Multiple constraints can be obtained on any given parameter by combining CMB data with anyone of these other measurements. It is also of interest to check the consistency between these multiple constraints. In this letter, we derive constraints on a number of cosmological parameters using the measurement of CMB anisotropy by the Archeops experiment (Benoît et al. 2003). This measurement provides the most accurate determination presently available of the angular power spectrum at angular scales of the first acoustic peak and larger.

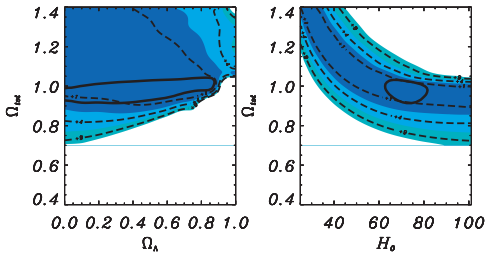

Fig. 3. Likelihood contours in the $(\Omega_\Lambda, \Omega_{\rm tot})$ (left) and $(H_0, \Omega_{\rm tot})$ (right) planes using the Archeops dataset; the three colored regions (three contour lines) correspond to resp. 68, 95 and 99% confidence levels for 2-parameters (1-parameter) estimates. Black solid line is given by the combination Archeops + HST, see text.

2. Archeops angular power spectrum

The first results of the February 2002 flight of Archeops are detailed in Benoît et al. (2003). The band powers used in this analysis are plotted in Fig. 1 together with those of other experiments (CBDMVC for COBE, Boomerang, Dasi, Maxima, VSA, and CBI; Tegmark et al. 1996; Netterfield et al. 2002; Halverson et al. 2002; Lee et al. 2001; Scott et al. 2002; Pearson et al. 2002). Also plotted is a ΛCDM model (computed using CAMB, 2000), with the following

Table 1. The grid of points in the 7 dimensional space of cosmological models that was used to set constraint on the cosmological parameters. * For h we adopt a logarithmic binning: $h(i+1) = 1.15 \cdot h(i)$; Q is in μK.

	$\Omega_{\rm tot}$	Ω_Λ	$\Omega_{\rm b}h^2$	h	n	Q	τ
Min.	0.7	0.0	0.00915	0.25	0.650	11	0.0
Max.	1.40	1.0	0.0347	1.01	1.445	27	1.0
Step	0.05	0.1	0.00366	*1.15	0.015	0.2	0.1

cosmological parameters: $\Theta = (\Omega_{\rm tot}, \Omega_\Lambda, \Omega_{\rm b}h^2, h, n, Q, \tau) = (1.00, 0.7, 0.02, 0.70, 1.00, 18\,\mu K, 0.)$ where the parameters are the total energy density, the energy density of a cosmological constant, the baryon density, the normalized Hubble constant ($H_0 = 100\,h$ km s^{-1} Mpc^{-1}), the spectral index of the scalar primordial fluctuations, the normalization of the power spectrum and the optical depth to reionization, respectively. The predictions of inflationary motivated adiabatic fluctuations, a plateau in the power spectrum at large angular scales followed by a first acoustic peak, are in agreement with the results from Archeops and from the other experiments. Moreover, the data from Archeops alone provides a detailed description of the power spectrum around the first peak. The parameters of the peak can be studied without a cosmological prejudice (Knox et al. 2000; Douspis & Ferreira 2002) by fitting a constant term, here fixed to match COBE amplitude, and a Gaussian function of ℓ. Following this procedure and using the Archeops and COBE data only, we find (Fig. 2) for the location of the peak $\ell_{\rm peak} = 220 \pm 6$, for its width $FWHM = 192 \pm 12$, and for its amplitude $\delta T = 71.5 \pm 2.0\,\mu$K (error bars are smaller than the calibration uncertainty from Archeops only, because COBE amplitude is used for the constant term in the fit). This is the best determination of the parameters of the first peak to date, yet still compatible with other CMB experiments.

3. Model grid and likelihood method

To constrain cosmological models we constructed a $4.5{\times}10^8$ C_ℓ database. Only inflationary motivated models with adiabatic fluctuations are being used. The ratio of tensor to scalar modes is also set to zero. As the hot dark matter component modifies mostly large ℓ values of the power spectrum, this effect is neglected in the following. Table 1 describes the corresponding gridding used for the database. The models including reionization have been computed with an analytical approximation (Griffiths et al. 1999).

Cosmological parameter estimation relies upon the knowledge of the likelihood function $\mathcal{L}$ of each band power estimate. Current Monte Carlo methods for the extraction of the C_ℓ naturally provide the distribution function $\mathcal{D}$ of these power estimates. The analytical approach described in Douspis et al. (2003) and Bartlett et al. (2000) allows to construct the needed $\mathcal{L}$ in an analytical form from $\mathcal{D}$. Using such an approach was proven to be equivalent to performing a full likelihood analysis on the maps. Furthermore, this leads to unbiased estimates of the cosmological parameters (Wandelt et al. 2001; Bond et al. 2000; Douspis et al. 2001a), unlike other commonly used χ^2 methods. In these methods, $\mathcal{L}$ is also assumed to be Gaussian. However this hypothesis is not valid, especially for the smaller modes covered by Archeops. The difference between our well–motivated shape and the Gaussian approximation induces a 10% error in width for large–scale bins. The parameters of the analytical form of the band power likelihoods $\mathcal{L}$ have been computed from the distribution functions of the band powers listed in Table 1 of Benoît et al. (2003). Using $\mathcal{L}$, we calculate the likelihood of any of the cosmological models in the database and maximize the likelihood over the 7% calibration uncertainty. We include the calibration uncertainty of each experiment as extra parameters in our analysis. The prior on these parameters are taken as Gaussians centered on unity, with a standard deviation corresponding to the quoted calibration uncertainty of each dataset. The effect of Archeops beam width uncertainty, which leads to less than 5% uncertainty on the C_ℓ's at $\ell \leq 350$, is neglected.

A numerical compilation of all the results is given in Table 2. Some of the results are also presented as 2D contour plots, showing in shades of blue the regions where the likelihood function for a combination of any two parameters drops to 68%, 95%, and 99% of its initial value. These levels are computed from the minimum of the negative of the log likelihood plus $\Delta = 2.3,\ 6.17$ and 11.8. They would correspond to 1, 2, 3 σ respectively if the likelihood function was Gaussian. Black contours mark the limits to be projected if confidence intervals are sought for any one of the parameters. To calculate either 1– or 2–D confidence intervals, the likelihood function is maximized over the remaining parameters. All single parameter confidence intervals that are quoted in the text are 1 σ unless otherwise stated, and we use the notation $\chi^2_{\rm gen} = m/n$ to mean that the generalized χ^2 has a value m with n degrees of freedom. In all cases described below we find models that do fit the data and therefore confidence levels have a well defined statistical interpretation. Douspis et al. (2003) describes how to evaluate the goodness of fit and Table 2 gives the various χ^2 values. When we use external non–CMB priors on some of the cosmological parameters, the analysis is done by multiplying our CMB likelihood hypercube by Gaussian shaped priors with mean and width according to the published values.

4. Cosmological parameter constraints

4.1. Archeops

We first find constraints on the cosmological parameters using the Archeops data alone. The cosmological model that presents the best fit to the data has a $\chi^2_{\rm gen} = 6/9$. Figure 3 gives confidence intervals on different pairs of parameters. The Archeops data constrain the total mass and energy density of the Universe ($\Omega_{\rm tot}$) to be greater than 0.90, but it does not provide strong limits on closed Universe models. Figure 3 also shows that $\Omega_{\rm tot}$ and h are highly correlated (Douspis et al. 2001b). Adding the HST constraint for the Hubble constant, $H_0 = 72 \pm 8$ km s^{-1} Mpc^{-1} (68% CL, Freedman et al. 2001), leads to the tight constraint $\Omega_{\rm tot} = 0.96^{+0.09}_{-0.04}$ (full line in Fig. 3), indicating that the Universe is flat.

Using Archeops data alone we can set significant constraints neither on the spectral index n nor on the baryon content $\Omega_{\rm b}h^2$ because of lack of information on fluctuations at small angular scales.

Fig. 4. Likelihood contours for (COBE + Archeops + CBI) in the $(\Omega_\Lambda, \Omega_{\rm tot})$, $(H_0, \Omega_{\rm tot})$, $(\Omega_{\rm tot}, n)$ and $(\Omega_{\rm b}h^2, n)$ planes.

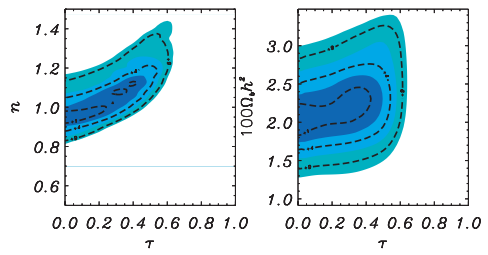

Fig. 5. Likelihood contours in the (τ, n) and $(\tau, \Omega_{\rm b}h^2)$ planes using Archeops + CBDMVC datasets.

4.2. COBE, Archeops, CBI

We first combine only COBE/DMR, CBI and Archeops so as to include information over a broad range of angular scales, $2 \leq \ell \leq 1500$, with a minimal number of experiments[1]. The results are shown in Fig. 4, with a best model $\chi^2_{\rm gen} = 9/20$. The constraint on open models is stronger than previously, with a total density $\Omega_{\rm tot} = 1.16^{+0.24}_{-0.20}$ at 68% CL and $\Omega_{\rm tot} > 0.90$ at 95% CL. The inclusion of information about small scale fluctuations provides a constraint on the baryon content, $\Omega_{\rm b}h^2 = 0.019^{+0.006}_{-0.007}$ in good agreement with the results from BBN (O'Meara et al. 2001: $\Omega_{\rm b}h^2 = 0.0205 \pm 0.0018$). The spectral index $n = 1.06^{+0.11}_{-0.14}$ is compatible with a scale invariant Harrison–Zel'dovich power spectrum.

[1] For CBI data, we used only the joint mosaic band powers and restrict ourselves to $\ell \leq 1500$.

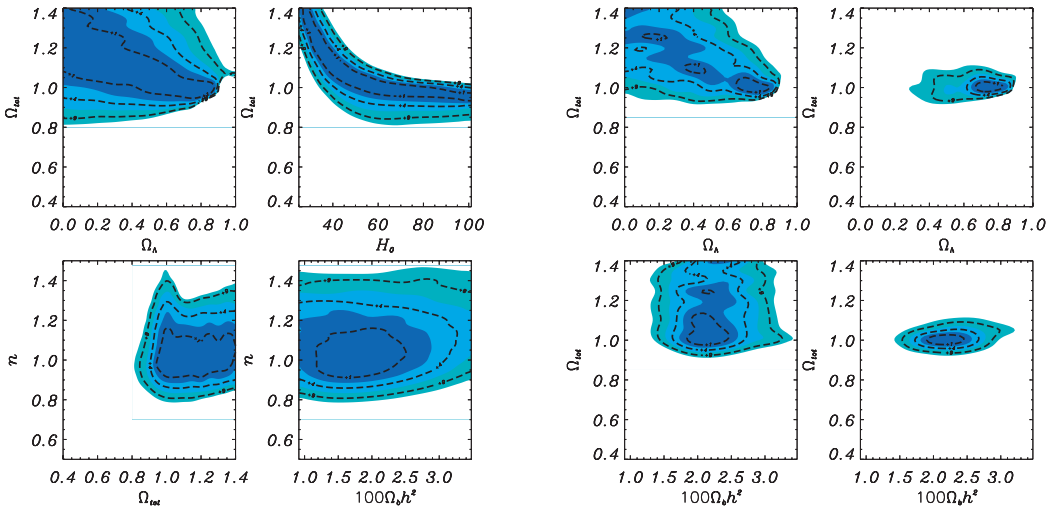

Fig. 6. Likelihood contours in the $(\Omega_{\rm tot}, \Omega_\Lambda)$ and $(\Omega_{\rm tot}, \Omega_{\rm b}h^2)$ planes. Left: constraints using Archeops+CBDMVC datasets. Right: adding HST prior for H_0.

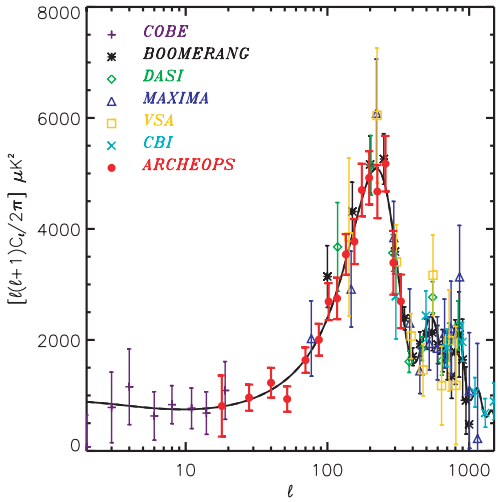

Fig. 7. Best model obtained from the Archeops + CBDMVC + HST analysis with recalibrated actual datasets. The fitting allowed the gain of each experiment to vary within their quoted absolute uncertainties. Recalibration factors, in temperature, which are applied in this figure, are 1.00, 0.96, 0.99, 1.00, 0.99, 1.00, and 1.01, for COBE, Boomerang, Dasi, Maxima, VSA, CBI and Archeops respectively, well within 1 σ of the quoted absolute uncertainties (<1, 10, 4, 4, 3.5, 5 and 7%).

4.3. Archeops and other CMB experiments

By adding the experiments listed in Fig. 1 we now provide the best current estimate of the cosmological parameters using CMB data only. The constraints are shown in Figs. 5 and 6 (left). The combination of all CMB experiments provides

Table 2. Cosmological parameter constraints from combined datasets. Upper and lower limits are given for 68% CL. See text for details on priors. The central values are given by the mean of the likelihood. The quoted error bars are at times smaller than the parameter grid spacing, and are thus in fact determined by an interpolation of the likelihood function between adjacent grid points.

Data	$\Omega_{\rm tot}$	$n_{\rm s}$	$\Omega_{\rm b}h^2$	h	Ω_Λ	τ	$\chi^2_{\rm gen}$/d.o.f.
Archeops	>0.90	$1.15^{+0.30}_{-0.40}$	–	–	<0.9	<0.45	6/9
Archeops + COBE + CBI	$1.16^{+0.24}_{-0.20}$	$1.06^{+0.11}_{-0.14}$	$0.019^{+0.006}_{-0.007}$	>0.25	<0.85	<0.45	9/20
CMB	$1.18^{+0.22}_{-0.20}$	$1.06^{+0.14}_{-0.20}$	$0.024^{+0.003}_{-0.005}$	$0.51^{+0.30}_{-0.30}$	<0.85	<0.55	37/52
Archeops + CMB	$1.15^{+0.12}_{-0.17}$	$1.04^{+0.10}_{-0.12}$	$0.022^{+0.003}_{-0.004}$	$0.53^{+0.25}_{-0.13}$	<0.85	<0.4	41/67
Archeops + CMB + $\tau = 0$	$1.13^{+0.12}_{-0.15}$	$0.96^{+0.03}_{-0.04}$	$0.021^{+0.002}_{-0.003}$	$0.52^{+0.20}_{-0.12}$	<0.80	0.0	41/68
Archeops + CMB + $\Omega_{\rm tot} = 1$	1.00	$1.04^{+0.10}_{-0.12}$	$0.021^{+0.004}_{-0.003}$	$0.70^{+0.08}_{-0.08}$	$0.70^{+0.10}_{-0.10}$	<0.40	41/68
Archeops + CMB + HST	$1.00^{+0.03}_{-0.02}$	$1.04^{+0.10}_{-0.08}$	$0.022^{+0.003}_{-0.002}$	$0.69^{+0.08}_{-0.06}$	$0.73^{+0.09}_{-0.07}$	<0.42	41/68
Archeops + CMB + HST + $\tau = 0$	$1.00^{+0.03}_{-0.02}$	$0.96^{+0.02}_{-0.04}$	$0.021^{+0.001}_{-0.003}$	$0.69^{+0.06}_{-0.06}$	$0.72^{+0.08}_{-0.06}$	0.0	41/69
Archeops + CMB + SN1a	$1.04^{+0.02}_{-0.04}$	$1.04^{+0.10}_{-0.12}$	$0.022^{+0.003}_{-0.004}$	$0.60^{+0.10}_{-0.07}$	$0.67^{+0.11}_{-0.03}$	<0.40	41/69
Archeops + CMB + BBN	$1.12^{+0.13}_{-0.14}$	$1.04^{+0.10}_{-0.12}$	$0.020^{+0.002}_{-0.002}$	$0.50^{+0.15}_{-0.10}$	<0.80	<0.25	41/68
Archeops + CMB + BF(H)	$1.11^{+0.12}_{-0.11}$	$1.03^{+0.12}_{-0.14}$	$0.022^{+0.004}_{-0.004}$	$0.46^{+0.09}_{-0.11}$	$0.45^{+0.10}_{-0.10}$	<0.40	43/69
Archeops + CMB + BF(L)	$1.22^{+0.18}_{-0.12}$	$1.03^{+0.07}_{-0.13}$	$0.021^{+0.003}_{-0.004}$	<0.40	<0.3	<0.40	45/69

∼10% errors on the total density, the spectral index and the baryon content respectively: $\Omega_{\rm tot} = 1.15^{+0.12}_{-0.17}$, $n = 1.04^{+0.10}_{-0.12}$ and $\Omega_{\rm b}h^2 = 0.022^{+0.003}_{-0.004}$. These results are in good agreement with recent analyses performed by other teams (Netterfield et al. 2002; Pryke et al. 2002; Rubino-Martin et al. 2002; Sievers et al. 2002; Wang et al. 2002). One can also note that the parameters of the ΛCDM model shown in Fig. 1 are included in the 68% CL contours of Fig. 6 (right).

As shown in Fig. 5 the spectral index and the optical depth are degenerate. Fixing the latter to its best fit value, $\tau = 0$, leads to stronger constraints on both n and $\Omega_{\rm b}h^2$. With this constraint, the prefered value of n becomes slightly lower than 1, $n = 0.96^{+0.03}_{-0.04}$, and the constraint on $\Omega_{\rm b}h^2$ from CMB alone is not only in perfect agreement with BBN determination but also has similar error bars, $\Omega_{\rm b}h^2_{\rm (CMB)} = 0.021^{+0.002}_{-0.003}$. It is important to note that many inflationary models (and most of the simplest of them) predict a value for n that is slightly less than unity (see, e.g., Linde 1990; Lyth & Riotto 1999 for a recent review).

4.4. Adding non–CMB priors

In order to break some degeneracies in the determination of cosmological parameters with CMB data alone, priors coming from other cosmological observations are now added. First we consider priors based on stellar candles like HST determination of the Hubble constant (Freedman et al. 2001) and supernovæ determination of $\Omega_{\rm m}$ and Λ (Perlmutter et al. 1999). We also consider non stellar cosmological priors like BBN determination of the baryon content, (O'Meara et al. 2001), and baryon fraction determination from X-ray clusters (Roussel et al. 2000; Sadat & Blanchard 2001). For the baryon fraction we use a low value, BF(L), $f_{\rm b} = 0.031h^{-3/2} + 0.012$ (±10%), and a high value, BF(H), $f_{\rm b} = 0.048h^{-3/2} + 0.014$ (±10%) (Douspis et al. 2001b and references therein). The results with the HST prior are shown in Fig. 6 (right). Considering the particular combination Archeops + CBDMVC + HST, the best fit model, within the Table 1 gridding, is $(\Omega_{\rm tot}, \Omega_\Lambda, \Omega_{\rm b}h^2, h, n, Q, \tau) = (1.00, 0.7, 0.02, 0.665, 0.945, 19.2\mu{\rm K}, 0.)$ with a $\chi^2_{\rm gen} = 41/68$. The model is shown in Fig. 7 with the data scaled by their best–fit calibration factors which were simultaneously computed in the likelihood fitting process. The constraints on h break the degeneracy between the total matter content of the Universe and the amount of dark energy as discussed in Sect. 4.1. The constraints are then tighter as shown in Fig. 6 (right), leading to a value of $\Omega_\Lambda = 0.73^{+0.09}_{-0.07}$ for the dark energy content, in agreement with supernovæ measurements if a flat Universe is assumed. Table 2 also shows that Archeops + CBDMVC cosmological parameter determinations assuming either $\Omega_{\rm tot} = 1$ or the HST prior on h are equivalent at the 68% CL.

5. Conclusion

Constraints on various cosmological parameters have been derived by using the Archeops data alone and in combination with other measurements. The measured power at low ℓ is in agreement with the COBE data, providing for the first time a direct link between the Sachs–Wolfe plateau and the first acoustic peak. The Archeops data give a high signal-to-noise ratio determination of the parameters of the first acoustic peak and of the power spectrum down to COBE scales ($\ell = 15$), because of the large sky coverage that greatly reduces the sample variance. The measured spectrum is in good agreement with that predicted by simple inflation models of scale–free adiabatic peturbations. Archeops on its own also sets a constraint on open models, $\Omega_{\rm tot} > 0.90$ (68% CL). In combination with CBDMVC experiments, tight constraints are shown on cosmological parameters like the total density, the spectral index and the baryon content, with values of $\Omega_{\rm tot} = 1.13^{+0.12}_{-0.15}$, $n = 0.96^{+0.03}_{-0.04}$ and $\Omega_{\rm b}h^2 = 0.021^{+0.002}_{-0.003}$ respectively, all at 68% CL and assuming $\tau = 0$. These results lend support to the inflationary paradigm. The addition of non–CMB constraints removes degeneracies between different parameters and allows to achieve a 10% precision on $\Omega_{\rm b}h^2$ and Ω_Λ and better than 5% precision on $\Omega_{\rm tot}$

Letter to the Editor

and n. Flatness of the Universe is confirmed with a high degree of precision: $\Omega_{\rm tot} = 1.00^{+0.03}_{-0.02}$ (Archeops + CMB + HST).

Acknowledgements. The authors would like to thank the following institutes for funding and balloon launching capabilities: CNES (French space agency), PNC (French Cosmology Program), ASI (Italian Space Agency), PPARC, NASA, the University of Minnesota, the American Astronomical Society and a CMBNet Research Fellowship from the European Commission.

References

Balbi, A., Ade, P., Bock, J., et al. 2000, ApJ, 545, L1
Bartlett, J. G., Douspis, M., Blanchard, A., & Le Dour, M. 2000, A&AS, 146, 507
Bennett, C. L., Halpern, M., Hinshaw, G., et al. 1997, 191st AAS Meet., 29, 1353
Benoît, A., Ade, P., Amblard, A., et al. 2003, A&A, 399, L19
Bond, J. R., Jaffe, A. H., & Knox, L. 2000, ApJ, 533, 19
de Bernardis, P., Ade, P. A. R., Bock, J. J., et al. 2000, Nature, 404, 955
Douspis, M., Bartlett, J. G., Blanchard, A., & Le Dour, M. 2001a, A&A, 368, 1
Douspis, M., Blanchard, A., Sadat, R., et al. 2001b, A&A, 379, 1
Douspis, M., & Ferreira, P. 2002, Phys. Rev. D, 65, 87302
Douspis, M., Bartlett, J. G., & Blanchard, A. 2003, A&A, submitted
Freedman, W. L., Madore, B. F., Gibson, B. K., et al. 2001, ApJ, 553, 47
Griffiths, L. M., Barbosa, D., & Liddle, A. R. 1999, MNRAS, 308, 854
Halverson, N. W., Leitch, E. M., Pryke, C., et al. 2002, MNRAS, 568, 38
Hanany, S., Ade, P., Balbi, A., et al. 2000, ApJ, 545, L5
Hancock, S., Rocha, G., Lasenby, A. N., & Gutierrez, C. M. 1999, MNRAS, 294, L1
Knox, L., & Page, L. 2000, Phys. Rev. Lett., 85, 1366
Lange, A. E., Ade, P. A., Bock, J. J., et al. 2001, Phys. Rev. D, 63, 4, 042001
Lee, A. T., Ade, P., Balbi, A., et al. 2001, ApJ, 561, L1
Lewis, A., Challinor, A., & Lasenby, A. 2000, ApJ, 538, 473
Linde, A. D., 1990, Particle Physics and Inflationary Cosmology (Harwood Academic, N.Y., 1990)
Lineweaver, C. H., Barbosa, D., Blanchard, A., & Bartlett, J. G. 1997, A&A, 322, 365
Lyth, D. H., & Riotto, A. 1999, Phys. Rep., 314, 1
Netterfield, C. B., Devlin, M. J., Jarolik, N., et al. 1997, ApJ, 474, 47
Netterfield, C. B., Ade, P. A. R., Bock, J. J., et al. 2002, ApJ, 571, 604
O'Meara, J. M.; Tytler, D., Kirkman, D., et al. 2001, ApJ, 552, 718
Pearson, T. J., Mason, B. S., Readhead, A. C. S., et al. 2002, ApJ, submitted [astro-ph/0205388]
Perlmutter, S., Aldering, G., Goldhaber, G., et al. 1999, ApJ, 517, 565, http://www-supernova.lbl.gov
Pryke, C., Halverson, N. W., Leitch, E. M., et al. 2002, ApJ, 568, 46
Roussel, H., Sadat, R., & Blanchard, A. 2000, A&A, 361, 429
Rubino-Martin, J. A., Rebolo, R., Carreira, P., et al. 2002, [astro-ph/0205367]
Sadat, R., & Blanchard, A. 2001, A&A, 371, 19
Scott, P. F., Carreira, P., Cleary, K., et al. 2002, MNRAS, submitted [astro-ph/0205380]
Seljak, U., & Zaldarriaga, M. 1996, ApJ, 469, 437
Sievers J. L., Bond, J. R., Cartwright, J. K., et al. 2002, ApJ, submitted [astro-ph/0205387]
Tauber, J. A., et al. 2000, IAU Symp. 204, ed. M. Harwit & M. G. Hauser
Tegmark, M. 1996, ApJ, 464, L35
Wandelt, B. D., Hivon, E., & Górski, K. M. 2001, Phys. Rev. D, 64, 83003
Wang, X., Tegmark, M., & Zaldarriaga, M. 2002, Phys. Rev. D, 65, 123001

Diffuse source separation in CMB observations

J. Delabrouille[1] and J.-F. Cardoso[2]

[1] APC, 11 place Marcelin Berthelot, F75231 Paris Cedex 05
delabrouille@apc.univ-paris7.fr
[2] LTCI, 46 rue Barrault, F75634 Paris Cedex 13 and
APC, 11 place Marcelin Berthelot, F75231 Paris Cedex 05
cardoso@enst.fr

1 Introduction

Spectacular advances in the understanding of the Big-Bang model of cosmology have been due to increasingly accurate observations of the properties of the Cosmic Microwave Background (CMB). The detector sensitivities of modern experiments have permitted to measure fluctuations of the CMB temperature with such a sensitivity that the contamination of the data by astrophysical foreground radiations, rather than by instrumental noise, is becoming the major source of limitation. This will be the case, in particular, for the upcoming observations by the Planck mission, to be launched by ESA in 2008 [Lamarre et al. (2003), Mandolesi et al. (2000), Lamarre et al. (2000)], as well as for next generation instruments dedicated to the observation of CMB polarisation.

In this context, the development of data analysis methods dedicated to identifying and separating foreground contamination from CMB observations is of the utmost importance for future CMB experiments. In many astrophysical observations indeed, and in particular in the context of CMB experiments, signals and images contain contributions from several components or *sources*. Some of these sources may be of particular interest (CMB or other astrophysical emission), some may be unwanted (noise).

Obviously, components cannot be properly studied in data sets in which they appear only as a mixture. Component separation consists, for each of them, in isolating the emission from all the other components present in the data, in the best possible way.

It should be noted that what "best" means depends on what the isolated data will be used for. Very often, one tries to obtain, for each component, an estimated map (or a set of maps at different frequencies) minimising the total error variance, i.e. minimising

$$\chi^2 = \sum_p |\widehat{s}(p) - s(p)|^2 \tag{1}$$

where $s(p)$ is the true component emission, and $\widehat{s}(p)$ its estimated value. p indexes the space of interest for the component, typically a set of pixels

(θ_p, ϕ_p), or modes (ℓ, m) of a spherical harmonic decomposition of a full sky map, or a set of Fourier modes (k_x, k_y)...

More generally, the objective of component separation is to estimate a *set of parameters* which describes the component of interest. In the simplest case, this set of parameters may be emission in pixels, but it may also be instead parameters describing statistical properties such as power spectra, spectral indices, etc... Since the set of parameters depends on the model assumed for the components, this model is of the utmost importance for efficient component separation. In the following, a significant part of the discussion will thus be dedicated to a summary of existing knowledge and of component modeling issues.

In the following, it is assumed that we are given a set of observations $y_i(p)$, where i, ranging from 1 to $N_{\rm chann}$, indexes the observation frequency. The observed emission in each of the frequency bands is supposed to result from a mixture of several astrophysical components, with additional instrumental noise.

In this review paper, we discuss in some detail the problem of diffuse component separation. The paper is organised as follows: in the next section, we review the principles and implementation of the ILC, a very simple method to average the measurements obtained at different frequencies; section 3 reviews the known properties of diffuse sky emissions, useful to model the observations and put priors on component parameters; section 4 discusses observation and data reduction strategies to minimize the impact of foregrounds on CMB measurements, based on physical assumptions about the various emissions; section 5 discusses the model of a linear mixture, and various options for its linear inversion to separate astrophysical components; section 6 discusses a non linear solution for inverting a linear mixture, based on a maximum entropy method; section 7 presents the general ideas behind Blind Source Separation (BSS) and Independent Component Analysis (ICA); section 8 discusses a particular method, the Spectral Matching ICA (SMICA); section 10 concludes with a summary, hints about recent and future developments, open issues, and a prospective.

Let the reader be warned beforehand that this review may not do full justice to much of the work having been done on this very exciting topic. The discussion may be somewhat partial, although not intentionally. It has not been possible to the authors to review completely and compare all of the relevant work, partly for lack of time, and partly for lack of details in the published papers. As much as possible, we have nonetheless tried to mention all of the existing work, to comment the ideas behind the methods, and to quote most of the interesting and classical papers.

2 ILC: Internal Linear Combination

The Internal Linear Combination (ILC) component separation method assumes very little about the components. One of them (e.g. the CMB) is considered to be the only emission of interest, all the other being unwanted foregrounds.

It is assumed that the template of emission of the component of interest is the same at all frequencies of observation, and that the observations are calibrated with respect to this component, so that for each frequency channel i we have:

$$y_i(p) = s(p) + f_i(p) + n_i(p) \tag{2}$$

where $f_i(p)$ and $n_i(p)$ are foregrounds and noise contributions respectively in channel i.

A very natural idea, since all the observations actually measure $s(p)$ with some error $f_i(p) + n_i(p)$, consists in averaging all these measurements, giving a specific weight w_i to each of them. Then, we look for a solution of the form:

$$\widehat{s}(p) = \sum_i w_i(p) y_i(p) \tag{3}$$

where the weights $w_i(p)$ are chosen to maximize some criterion about the reconstructed estimate $\widehat{s}(p)$ of $s(p)$, while keeping the component of interest unchanged. This requires in particular that for all p, the sum of the coefficients $w_i(p)$ should be equal to 1.

2.1 Simple ILC

The simplest version of the ILC consists in minimising the variance σ^2 of the map $\widehat{s}(p)$ using weights independent of p (so that $w_i(p) = w_i$ independent of p), with $\sum w_i = 1$. In this case, the estimated component is

$$\begin{aligned} \widehat{s}(p) &= \sum_i w_i y_i(p) \\ &= s(p) + \sum_i w_i f_i(p) + \sum_i w_i n_i(p). \end{aligned} \tag{4}$$

Hence, under the assumption of de-correlation between $s(p)$ and all foregrounds, and between $s(p)$ and all noises, the variance of the error is minimum when the variance of the ILC map itself is minimum.

2.2 ILC implementation

We now outline a practical implementation of the ILC method. For definiteness (and simplicity), we will assume here that the data is in the form of harmonic coefficients $s(\ell, m)$. The variance of the ILC map is:

$$\sigma^2 = \sum_{\ell \geq 1} \sum_{m=-\ell}^{\ell} \boldsymbol{w}^\dagger \, \mathbf{C}(\ell, m) \, \boldsymbol{w} = \boldsymbol{w}^\dagger \, \mathbf{C} \, \boldsymbol{w} \tag{5}$$

where $\mathbf{C}(\ell, m) = \langle \boldsymbol{y}(\ell, m) \boldsymbol{y}^\dagger(\ell, m) \rangle$ is the covariance matrix of the observations in mode (ℓ, m), and $\mathbf{C}$ is the covariance summed over all modes except $\ell = 0$. $\boldsymbol{y}(\ell, m)$ and $\boldsymbol{w}$ stand for the vectors of generic element $y_i(\ell, m)$ and w_i respectively. The minimum, under the constraint of $\sum w_i = 1$, is obtained, using the Lagrange multiplier method, by solving the linear system

$$\begin{aligned} \forall i, \qquad \frac{\partial}{\partial w_i} \left[\sigma^2 + \lambda \left(1 - \sum w_i \right) \right] &= 0 \\ \sum_i w_i &= 1 \end{aligned} \tag{6}$$

Straightforward linear algebra gives the solution

$$w_i = \frac{\sum_j \left[\mathbf{C}^{-1} \right]_{ij}}{\sum_{ij} \left[\mathbf{C}^{-1} \right]_{ij}} \tag{7}$$

Note that if the template of emission of the component of interest is the same at all frequencies of observation, but the observations are *not* calibrated with respect to this component, equation 2 becomes:

$$y_i(p) = a_i s(p) + f_i(p) + n_i(p) \tag{8}$$

In this case, it is still possible to implement an ILC. The solution is

$$\boldsymbol{w} = \frac{\boldsymbol{A}^T \mathbf{C}^{-1}}{\boldsymbol{A}^T \mathbf{C}^{-1} \boldsymbol{A}} \tag{9}$$

where $\boldsymbol{A}$ is the vector of recalibration coefficients a_i. This solution of equation 9 is equivalent to first changing the units in all the observations to make the response 1 in all channels, and then implementing the solution of equation 7.

2.3 Examples of ILC separation: particular cases

This idea of ILC is quite natural. It has, however, several unpleasant features, which makes it non-optimal in most real-case situations. Before discussing this, let us examine now what happens in two simple particular cases.

Case 1: Noisy observations with no foreground

If there are no foregrounds, and the observations are simply noisy maps of $s(p)$, with independent noise for all channels of observation, the ILC solution should lead to a noise-weighted average of the measurements.

Let us assume for simplicity that we have two noisy observations, y_1 and y_2, with $y_i = s + n_i$. In the limit of very large maps, so that cross correlations

between s, n_1 and n_2 vanish, the covariance matrix of the observations takes the form:

$$\mathbf{C} = \begin{bmatrix} S+N_1 & S \\ S & S+N_2 \end{bmatrix}$$

where S is the variance of the signal (map) of interest, and N_1 and N_2 the noise variances for the two channels. The inverse of $\mathbf{C}$ is:

$$\mathbf{C}^{-1} = \frac{1}{\det(\mathbf{C})} \begin{bmatrix} S+N_2 & -S \\ -S & S+N_1 \end{bmatrix}$$

and applying equation 7, we get $w_1 = N_2/(N_1+N_2)$ and $w_2 = N_1/(N_1+N_2)$. This is the same solution as weighting each map i proportionally to $1/N_i$.

Case 2: Noiseless observations with foregrounds

Let us now examine the opposite extreme, where observations are noiseless linear mixtures of several astrophysical components. Consider the case of two components, with two observations. We can write the observations as $\boldsymbol{y} = \mathbf{A}\boldsymbol{s}$, where $\mathbf{A}$ is the so-called "mixing matrix", and $\boldsymbol{s} = (s_1, s_2)^\dagger$ the vector of sources.
The covariance of the observations is

$$\mathbf{C} = \boldsymbol{y}\boldsymbol{y}^\dagger = \mathbf{A}\,\boldsymbol{s}\boldsymbol{s}^\dagger\mathbf{A}^\dagger$$

and its inverse is

$$\mathbf{C}^{-1} = [\mathbf{A}^\dagger]^{-1}\,[\boldsymbol{s}\boldsymbol{s}^\dagger]^{-1}\mathbf{A}^{-1} \tag{10}$$

Let us assume that we are interested in the first source. The data are then calibrated so that the mixing matrix $\mathbf{A}$ and its inverse are of the form

$$\mathbf{A} = \begin{bmatrix} 1 & a_{12} \\ 1 & a_{22} \end{bmatrix} \quad \text{and} \quad \mathbf{A}^{-1} = \frac{1}{\det(\mathbf{A})} \begin{bmatrix} a_{22} & -a_{12} \\ -1 & 1 \end{bmatrix}$$

Then, if we assume that components 1 and 2 are uncorrelated, equation 10 yields

$$\mathbf{C}^{-1} = \frac{1}{(\det(\mathbf{A}))^2} \begin{bmatrix} a_{22} & -1 \\ -a_{12} & 1 \end{bmatrix} \begin{bmatrix} S_1^{-1} & 0 \\ 0 & S_2^{-1} \end{bmatrix} \begin{bmatrix} a_{22} & -a_{12} \\ -1 & 1 \end{bmatrix} \tag{11}$$

where S_1 and S_2 are the variances of components 1 and 2 respectively. After expansion of the matrix product, we get:

$$\mathbf{C}^{-1} = \frac{1}{(\det(\mathbf{A}))^2} \begin{bmatrix} (a_{22}^2 S_1^{-1} + S_2^{-1}) & (-a_{22}a_{12}S_1^{-1} - S_2^{-1}) \\ (-a_{22}a_{12}S_1^{-1} - S_2^{-1}) & (a_{12}^2 S_1^{-1} + S_2^{-1}) \end{bmatrix} \tag{12}$$

and using equation 7, we get

$$\boldsymbol{w} = \frac{1}{(a_{22} - a_{12})} \begin{bmatrix} a_{22} \\ -a_{12} \end{bmatrix} \tag{13}$$

which is the transpose of the first line of matrix $\mathbf{A}^{-1}$, so that $\widehat{s}_1 = \boldsymbol{w}.\boldsymbol{y} = s_1$. As expected, *if the covariance of the two components vanishes*, the ILC solution is equivalent, for the component of interest, to what is obtained by inversion of the mixing matrix.

What happens now if the two components are correlated? Instead of the diagonal form $\mathrm{diag}(S_1, S_2)$, the covariance matrix of the sources contains an off-diagonal term S_{12}, so that equation 11 becomes:

$$\mathbf{C}^{-1} = \frac{1}{(\det(\mathbf{A}))^2} \frac{1}{(S_1 S_2 - S_{12}^2)} \begin{bmatrix} a_{22} & -1 \\ -a_{12} & 1 \end{bmatrix} \begin{bmatrix} S_2 & S_{12} \\ S_{12} & S_1 \end{bmatrix} \begin{bmatrix} a_{22} & -a_{12} \\ -1 & 1 \end{bmatrix} \quad (14)$$

which yields the solution

$$\boldsymbol{w} = \frac{1}{(a_{22} - a_{12})} \begin{bmatrix} a_{22} + S_{12}/S_2 \\ -a_{12} - S_{12}/S_2 \end{bmatrix} \quad (15)$$

The ILC is not equivalent anymore to the inversion of the mixing matrix $\mathbf{A}$. Instead, the estimate $\widehat{s}_1$ of s_1 is:

$$\widehat{s}_1 = \boldsymbol{w}.\boldsymbol{y} = s_1 - \frac{S_{12}}{S_2} s_2 \quad (16)$$

The ILC result is biased, giving a solution in which a fraction of s_2 is subtracted erroneously, in proportion to the correlation between s_1 and s_2, to lower as much as possible the variance of the output map. The implication of this is discussed in paragraph 2.6.

2.4 Improving the ILC method

With the exception of the CMB, diffuse sky emissions are known to be very non stationnary (e.g. galactic foregrounds are strongly concentrated in the galactic plane). In addition, most of the power is concentrated on large scales (the emissions are strongly correlated spatially). As the ILC method minimizes the total variance of the ILC map (the integrated power from all scales, as can be seen in equation 5), the weights w_i are strongly constrained essentially by regions of the sky close to the galactic plane, where the emission is strong, and by large scales, which contain most of the power. In addition, the ILC method finds weights resulting from a compromise between reducing astrophysical foreground contamination, and reducing the noise contribution. In other words, for a smaller variance of the output map, it pays off more to reduce the galactic contamination in the galactic plane and on large scales, where it is strong, rather than at high galactic latitude and on small scales, where there is little power anyway. This particularity of the ILC when implemented globally is quite annoying for CMB studies, for which all scales are interesting, and essentially the high galactic latitude data is useful.

Away from the galactic plane and on small scales, the best linar combination for cleaning the CMB from foregrounds and noise may be very different

from what it is close to the galactic plane and on large scales. A very natural idea to improve on the ILC is to decompose sky maps in several regions and/or scales, and apply an ILC independently to all these maps. The final map is obtained by adding-up all the ILC maps obtained independently in various regions and at different scales. Applications of these ideas are discussed in the next paragraph.

2.5 ILC-based foreground-cleaned CMB map from WMAP data

A map of CMB anisotropies has been obtained using the ILC method [Bennett et al. (2003)] on first year data from the WMAP mission, and has been released to the scientific community as part of the first year WMAP data products.

The input data is the set of five all sky, band averaged maps for the K, Ka, Q, V and W frequency bands, all of which smoothed to the same 1 degree resolution for convenience. The ILC is performed independently in 12 regions, 11 of which being in the WMAP kp2 mask at low galactic latitudes, designed to mask out regions of the sky highly contaminated by galactic foregrounds. This division into twelve regions is justified by the poor performance of the ILC on the full sky, interpreted as due to varying spectral indices of the astrophysical foregrounds. Discontinuities between the regions are reduced by using smooth transitions between the regions.

Little detail is provided on the actual implementation of the ILC by the WMAP team. Apparently, a non-linear iterative minimization algorithm was used, instead of the linear solution outlined in paragraph 2.2. Although there does not seem to be any particular reason for this choice, in principle the particular method chosen to minimize the variance does not matter, as long as it finds the minimum efficiently. There seem to be, however, indications that the convergence was not perfect, as discussed by Eriksen and collaborators in a paper discussing the ILC and comparing the results of the several of its implementations on WMAP data [Eriksen et al. (2004)]. Caution should probably be taken when using the WMAP ILC map for any purpose other than a visual impression of the CMB.

Tegmark and collaborators have improved the ILC method in several respects, and provide an independent CMB map obtained from WMAP data by ILC [Tegmark et al. (2003)]. Their implementation allows the weights to depend not only on the region of the sky, but also on angular scale, as discussed in paragraph 2.4. In addition, they partially deconvolve the WMAP maps in harmonic space to put them all to the angular resolution of the channel with the smallest beam, rather than smoothing all maps to put them all to the angular resolution of the channel with the largest beam. As a result, their ILC map has better angular resolution, but higher total noise. The high resolution map, however, can be filtered using a Wiener filter for minimal variance of the error. The Wiener-filtered map is obtained by multiplying each $a_{\ell m}$ mode of the map by a factor

$$W(\ell, m) = C_\ell / S_\ell$$

where C_ℓ is the estimated CMB power spectrum (computed for the cosmological model fitting best the WMAP data estimate), and S_ℓ is the estimated power spectrum of the noisy CMB map obtained by the authors using their ILC method.

The CMB map obtained by the WMAP team from first year data is shown in figure 1. For comparison, the map obtained by Tegmark et al. is shown in figure 2. Both give a good visual perception of what the CMB field looks like.

2.6 Comments about the ILC

The ILC has been used essentially to obtain a clean map of CMB emission. In principle, nothing prevents using it also for obtaining cleaned maps of other emissions, with the caveats that

- The data must be calibrated with respect to the emission of interest, so that the data takes the form of equation 2. This implies that the template of emission of the component of interest should not change significantly with the frequency-band of observation. This is the case for the CMB (temperature and polarisation), or for the SZ effect (to first order at least... more on this later).
- The component of interest should not be correlated with other components. Galactic components, being all strongly concentrated in the galactic plane, can thus not be recovered reliably with the ILC.

This issue of decorrelation of the component of interest $s(p)$ and the foregrounds can also generate problems in cases where the empirical correlation between the components does not vanish. As demonstrated in 2.3, the ILC method will not work properly (biasing the result) if the assumption the component of interest $s(p)$ are correlated for whatever reason. In particular, small data sets, even if they are realisations of actually uncorrelated random processes, are always empirically correlated to some level. For this reason, the ILC should not be implemented independently on too small subsets of the original data (very small regions, very few modes).

Finally, whereas the ILC is a powerful tool when nothing is known about the data, it is certainly non optimal when prior information is available. Foreground emissions are discussed in some detail in following section.

3 Sky emission model: components

"Know your enemy"... This statement, borrowed from elementary military wisdom, applies equally well in the fight against foreground contamination. Prior knowledge about astrophysical components indeed has been widely used in all practical CMB data analyses. Methods can then be specifically tailored

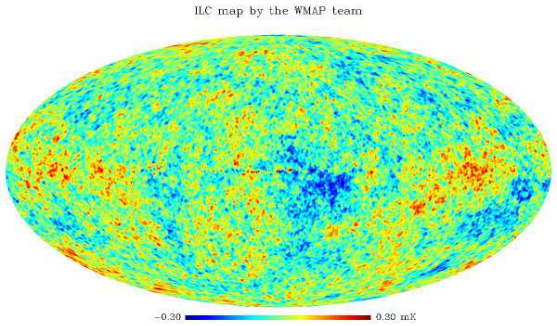

Fig. 1. The ILC map of the CMB obtained by the WMAP team (one year data). Residuals of galactic emission are clearly visible in the center of the map. The color scale spans a range of -300 to +300 μK thermodynamic, although localised residuals exceed these values.

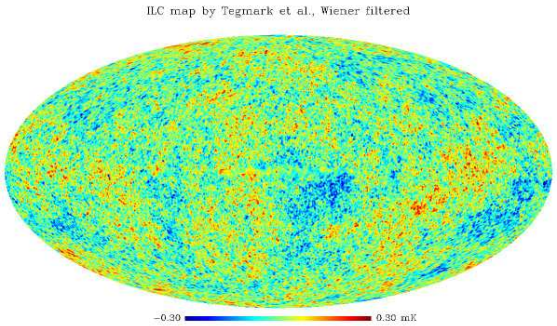

Fig. 2. The foreground-cleaned CMB map of Tegmark et al., obtained by the ILC method described in [Tegmark et al. (2003)], after Wiener filtering. The effect of the region and scale-dependent weighting can be seen in the center of the map (galactic center) where the map looks smoother and flatter than elsewhere. The color scale spans a range of -300 to +300 μK, although localised residuals exceed these values, as in figure 1. The superior angular resolution can clearly be seen.

to remove foregrounds based on their physical properties, in particular their morphology, their localisation, and their frequency scaling based on the physical understanding of their emission mechanisms.

In addition to knowledge about the unwanted foregrounds, prior knowledge about the component of interest is of the utmost importance for its identification and separation in observations. In the ILC method discussed above, for instance, the prior knowledge of the emission law of the CMB (derivative of a blackbody) is specifically used.

3.1 The various astrophysical emissions

Astrophysical emissions relevant to the framework of CMB observations can be classified in three large categories (in addition to the CMB itself). Diffuse galactic emission, extragalactic emission, and solar system emission.

Diffuse galactic emissions originate from the local interstellar medium (ISM) in our own galaxy. The ISM is constituted of cold clouds of molecular or atomic gas, of an intercloud medium which can be partly ionised, and of hot ionized regions presumably formed by supernovae. These different media are strongly concentrated in the galactic plane. The intensity of corresponding emissions decreases with galactic latitude with a cosecant law behaviour (the optical depth of the emitting material scales proportionnally to $1/\sin b$). Energetic free electrons spiralling in the galactic magnetic field generate synchrotron emission, which is the major foreground at low frequencies (below a few tens of GHz). Warm ionised material emits free-free (Bremstrahlung) emission, due to the interaction of free electrons with positively charged nuclei. Small particles of matter (dust grains and macromolecules) emit radiation as well, through thermal greybody emission, and possibly through other mechanisms.

Extragalactic emissions arise from a large background of resolved and unresolved radio and infrared galaxies, as well as clusters of galaxies. The thermal and kinetic Sunyaev-Zel'dovich effects, due to the inverse Compton scattering of CMB photons off hot electron gas in ionized media, are of special interest for cosmology. These effects occur, in particular, towards clusters of galaxies, which are known to comprise a hot (few keV) electron gas. Infrared and radiogalaxies emit also significant radiation in the frequency domain of interest for CMB observations, and contribute both point source emission from nearby bright objects, and a diffuse background due to the integrated emission of a large number of unresolved sources, too faint to be detected individually, but which contribute sky background inhomogeneities which may pollute CMB observations.

Solar system emission comprises emissions from the planets, their satellites, and a large number of small objects (asteroids). In addition to those, there is diffuse emission due to dust particles and grains in the ecliptic plane (zodiacal light). The latter is significant essentially at the highest frequencies of an instrument like the Planck HFI [Maris et al. (2006)].

In the rest of this section, we briefly outline the general properties of these components and the modeling of their emission in the centimetre to sub-millimetre wavelength range.

3.2 The Cosmic Microwave Background

The cosmic microwave background, relic radiation from the hot big bang emitted at the time of decoupling when the Universe was about 370,000 years old, is usually thought of (by cosmologists) as the component of interest in the sky emission mixture. Millimetre and submillimetre wave observations, however, sometimes aim not only at measuring CMB anisotropies, but also other emissions. In this case, the CMB becomes a noxious background which has to be subtracted out of the observations, just as any other.

The CMB emission is relatively well known already. The main theoretical framework of CMB emission can be found in any modern textbook on cosmology, as well as in several reviews [Hu & Dodelson (2002), White & Cohn (2002)]. The achievement of local thermal equilibrium in the primordial plasma before decoupling, together with the very low level of the perturbations, guaranties that CMB anisotropies are properly described as the product of a spatial template $\Delta T(p) = T_{\rm CMB}(p) - \overline{T}_{\rm CMB}$, and a function of ν (frequency scaling) which is the derivative of a blackbody with respect to temperature:

$$\Delta I_\nu(p) = \Delta T_{\rm CMB}(p) \left[\frac{\partial B_\nu(T)}{\partial T}\right]_{T=\overline{T}_{\rm CMB}\simeq 2.726\,{\rm K}} \tag{17}$$

In the standard cosmological model, the CMB temperature fluctuation map $\Delta T(p)$ is expected to be a realisation of a stationary Gaussian random field, with a power spectrum C_ℓ displaying a series of peaks and troughs (the acoustic peaks), the location and relative size of which are determined by a few free parameters of the cosmological model.[3]

Good maps of sky emission at a resolution of about 15 arcminutes, obtained from WMAP data in the frequency range 20–90 GHz, clearly comprise at high galactic latitude an astrophysical component compatible with all these predictions. The power spectrum is measured with excellent accuracy by WMAP up to the second Doppler peak, while complementary balloon–borne and ground–based experiments yield additional measurements at higher ℓ (smaller scales).

Efficient diffuse component separation methods should make use of this current status of knowledge about the CMB:

[3] The power spectrum C_ℓ is defined as the set of variances of the coefficients $a_{\ell m}$ of the expansion of the random field representing CMB relative temperature fluctuations $\Delta T(p)/\overline{T}_{\rm CMB}$ onto the basis of spherical harmonics on the sphere $Y_{\ell m}(\theta, \phi)$. The stationarity and isotropy of the random field guarantees that the variance of $a_{\ell m}$ (coefficients C_ℓ) is independent of m.

– Law of emission, known to a high level of precision to be the derivative of a blackbody with respect to temperature, as expected theoretically and checked experimentally with the Boomerang [de Bernardis et al. (2000)] and Archeops [Tristram et al. (2005)] multifrequency data sets, as well as with the WMAP data [Bennett et al. (2003), Patanchon et al. (2005)]
– Stationnarity and gaussianity to a high level of accuracy, as expected theoretically and checked on WMAP data [Komatsu et al. (2003)]
– Good cosmological prior on the power spectrum of the fluctuations, validated experimentally with several data sets [Netterfield et al. (2002), Hinshaw et al. (2006)]

A good visual impression of all-sky CMB emission is given in figures 1 and 2. The present status of knowledge of the power spectrum C_ℓ is shown in figure 3.

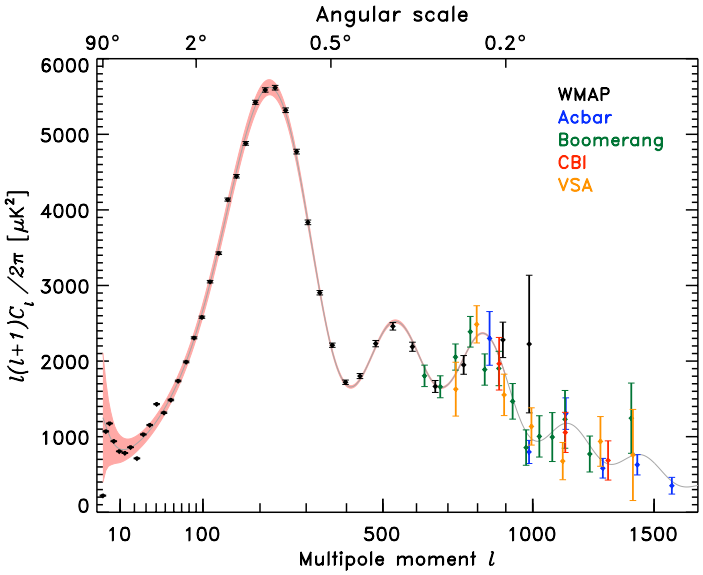

Fig. 3. Present-day best constraints of the CMB temperature power spectrum (from [Hinshaw et al. (2006)]). Data sets in addition to WMAP 3–year data are from [Jones et al. (2005), Kuo et al. (2004), Readhead et al. (2004), Dickinson et al. (2004)]

The extraction of CMB emission from a set of multifrequency observations may be done with the following objectives in mind (at least):

- Get the best possible map of the CMB (in terms of total least square error, from noise and foregrounds together);
- Get the CMB map with the least possible foreground contamination;
- Get the CMB map for which spurious non-gaussianity from foregrounds, noise and systematic effects is minimal;
- Get the best possible estimate of the CMB angular power spectrum...

Obviously, the best component separation method for extracting the CMB will depend on which of the above is the primary objective of component separation.

3.3 Emissions from the diffuse interstellar medium

Synchrotron emission

Synchrotron emission arises from energetic charged particles spiralling in a magnetic field. In our galaxy, such magnetic fields extend outside the galactic plane. Energetic electrons originating from supernovae shocks, spiraling in this field, can depart the galactic plane and generate emission even at high galactic latitudes. For this reason, synchrotron emission is less concentrated in the galactic plane than free-free and dust.

The frequency scaling of synchrotron emission is a function of the distribution of the energies of the radiating electrons. For number density distributions $N(E) \propto E^{-\gamma}$, the flux emission is also in the form of a power law, $I_\nu \propto \nu^{-\alpha}$, with $\alpha = (\gamma - 1)/2$. In Rayleigh-Jeans (RJ) temperature $\Delta T \propto \nu^{-\beta}$ with $\beta = \alpha + 2$. Typically, β ranges from 2.5 to 3.1, and is somewhat variable across the sky.

In spite of a moderate sensitivity for current standards, the 408 MHz all sky map [Haslam et al. (1981)], dominated by synchrotron emission, gives a good visual impression of the distribution of synchrotron over the sky.

In principle, synchrotron emission can be highly polarised, up to 50-70%

Free-Free emission

Free-free emission is the least well known observationally of the three major emissions originating from the galactic interstellar medium in the millimetre and centimetre wavelength range. This emission arises from the interaction of free electrons with ions in ionised media, and is called "free-free" because of the unbound state of the incoming and outgoing electron. Alternatively, free-free is called "Bremsstrahlung" emission ("braking radiation" in German), because photons are emitted while electrons loose energy by interaction with the heavy ions.

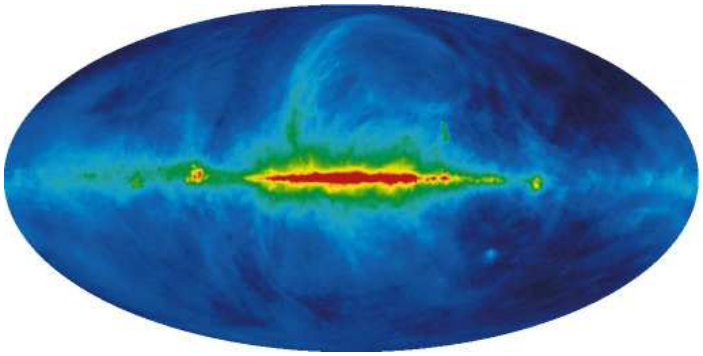

Fig. 4. The 408 MHz all-sky synchrotron map [Haslam et al. (1981)]. Data and images are available on the NASA Lambda web site.

Theoretical calculations of free-free emission in an electrically neutral medium consisting of ions and electrons gives an estimate of the brightness temperature at frequency ν for free-free emission of the form:

$$T_{\rm ff} \simeq 0.08235\, T_e^{-0.35}\, \nu^{-\beta} \int_{\rm l.o.s.} N_e N_i dl \qquad (18)$$

where T_e is in Kelvin, ν is in GHz and the line of sight integral of electron and ion density in cm^{-6}pc [Smoot (1998)]. Theoretical estimates of the spectral index, β, range from about 2.1 to 2.15, with errors of ± 0.03.

While free-free emission is not observed directly, as it never dominates over other astrophysical emissions, the source of its emission (mainly ionised hydrogen clouds) can be traced with hydrogen recombination emission lines, and particularly Hα emission. The connection between Hα and free-free has been discussed extensively by a number of authors [Smoot (1998), Valls-Gabaud (1998), McCullough et al. (1999)]. We have:

$$\frac{T_{\rm ff}[{\rm mK}]}{I_\alpha[{\rm R}]} \simeq 10.4\, \nu^{-2.14}\, T_4^{0.527}\, 10^{0.029/T_4}\, (1 + 0.08) \qquad (19)$$

Where $T_{\rm ff}$[mK] is the free-free brightness temperature in mK, I_α[R] the Hα surface brightness in Rayleigh, ν the frequency, and T_4 the temperature of the ionized medium in units of 10^4 K. The Rayleigh (R) is defined as 1 R = $(10^6/4\pi)$ photons/cm^2/s/sr.

Free-free emission, being due to incoherent emissions from individual electrons scattered by nuclei in a partially ionised medium, is not polarised (to first order at least).

Thermal emission of galactic dust

The present knowledge of interstellar dust is based on extinction observations from the near infrared to the UV domain, and on observations of its emission from radio frequencies to the infrared domain.

Dust consists in small particles of various materials, essentially silicate and carbonaceous grains of various sizes and shapes, in amorphous or crystalline form, sometimes in aggregates or composites. Dust is thought to comprise also large molecules of polycyclic aromatic hydrocarbon (PAH). The sizes of the grains range from few nanometers for the smallest, to micrometers for the largest. They can emit through a variety of mechanisms. The most important for CMB observations is greybody emission in the far infrared, at wavelengths ranging from few hundreds of microns to few millimeters. The greybody emission is typically characterised by a temperature $T_{\rm dust}$ and by an emissivity proportional to a power of the frequency ν:

$$I_\nu \propto \nu^\beta B_\nu(T_{\rm dust}) \tag{20}$$

where $B_\nu(T)$ is the usual blackbody emission

$$B_\nu(T) = \frac{2h\nu^3}{c^2}\frac{1}{e^{h\nu/kT}-1} \tag{21}$$

This law is essentially empirical. In practice, dust clouds along the line of sight can have different temperatures and different compositions: bigger or smaller grains, different materials. They can thus have different emissivities as well. Temperatures for interstellar dust are expected to range from about 5 Kelvin to more than 30 Kelvin, depending on the heating of the medium by radiation from nearby stars, with typical values of 16-18 K for emissivity indices $\beta \simeq 2$.

In principle, thermal emission from galactic dust should not be strongly polarised, unless dust particles are significantly asymmetric (oblate or prolate), and there exists an efficient process for aligning the dust grains in order to create a significant statistical asymmetry. Preliminary dust observations with the Archeops instrument [Benoît et al. (2004), Ponthieu et al. (2005)] seems to indicate polarisation levels of the order of few per cent, and as high as 15-20 per cent in a few specific regions.

Spinning dust or anomalous dust emission

In the last years, increasing evidence for dust-correlated emissions at frequencies below 30 GHz, in excess to expectations from synchrotron and free-free, has aroused interest in possible non-thermal emissions from galactic dust [Kogut et al. (1996), Leitch et al. (1997)]. Among the possible non-thermal emission mechanisms, spinning dust grains offer an interesting option [Draine & Lazarian (1998)].

At present, there still is some controversy on whether the evidence for non-thermal dust emission is robust enough for an unambiguous statement. Observations of different sky regions, indeed, yield somewhat different results [Dickinson et al. (2006), Fernández-Cerezo et al. (2006)], which may be due either to varying dust cloud properties, or to differences in the analyses and interpretations, or both. Certainly, investigating this question is an objective of primary interest for diffuse component separation methods (especially blind ones) in the near future.

3.4 The SZ effect

The Sunyaev Zel'dovich (SZ) effect [Sunyaev & Zeldovich (1972)] is the inverse Compton scattering of CMB photons on free electrons in ionised media. In this process, the electron gives a fraction of its energy to the scattered CMB photon. There are, in fact, several SZ effects: The thermal SZ effect is due to the scattering of photons on a high temperature electron gas, such as can be found in clusters of galaxies. The kinetic SZ effect is due to the scattering on a number of electrons with a global radial bulk motion with respect to the cosmic background. Finally, the polarised SZ effect is a second order effect due to the kinematic quadrupole of the CMB in the frame of an ensemble of electrons with a global transverse bulk motion with respect to the CMB.

SZ effects are not necessarily linked to clusters of galaxies. Any large body with hot ionised gas can generate significant effects. It has been proposed that signatures of inhomogeneous reionisation can be found via the kinetic and thermal SZ effect [Aghanim et al. (1996), Gruzinov & Hu (1998), Yamada et al. (1999)]. However, the largest expected SZ signatures originate from ionised intra-cluster medium.

Clusters of galaxies

Clusters of galaxies, the largest known massive structures in the Universe, form by gravitational collapse of matter density inhomogeneities on large scales (comoving scales of few Mpc). They can be detected either optically from concentrations of galaxies at the same redshift, or in the submillimeter by their thermal SZ emission, or by the effect of their gravitational mass in weak shear maps, or in X-ray. The hot intracluster baryonic gas can be observed through its X–ray emission due to Bremsstrahlung (free-free) emission of the electrons on the nuclei, which permits to measure the electron temperature (typically a few keV). On the sky, typical cluster angular sizes range from about one arcminute to about one degree. Clusters are scattered over the whole sky, although this distribution follows the repartition of structure on the largest scales in the universe. Large scale SZ effect observations may be also used to survey the distribution of hot gas on these very large scales, although such SZ emission, from filaments and pancakes in the distribution, is

expected to be at least an order of magnitude lower in intensity than thermal SZ emission from the clusters themselves.

Each cluster of galaxies has its own thermal, kinetic and polarised SZ emission. These various emissions and their impact on CMB observations and for cosmology have been studied by a variety of authors. Useful reviews have been made by Birkinshaw [Birkinshaw (1999)] and Rephaeli [Rephaeli (2002)], for instance.

Thermal SZ

The thermal SZ effect generated by a gas of electrons at temperature T_e is, in fact, a spectral distortion of the CMB emission law. It is common to consider as the effect the difference $\Delta I_\nu = I_\nu - B_\nu(T_{\rm CMB})$ between the distorted CMB photon distribution I_ν and the original one $B_\nu(T_{\rm CMB})$. In the non-relativistic limit (when T_e is lower than about 5 keV, which is the case for most clusters), the shape of the spectral distortion does not depend on the temperature. The change in intensity due to the thermal SZ effect is:

$$\Delta I_\nu = y \frac{x e^x}{(e^x - 1)} \left[\frac{x(e^x + 1)}{(e^x - 1)} - 4 \right] B_\nu(T_{\rm CMB}) \tag{22}$$

where $B_\nu(T_{\rm CMB})$ is the Planck blackbody emission law at CMB temperature

$$B_\nu(T_{\rm CMB}) = \frac{2h\nu^3}{c^2} \frac{1}{e^x - 1}$$

and $x = h\nu / kT_{\rm CMB}$. The dimensionless parameter y (Comptonisation parameter) is proportional to the integral of the electron pressure along the line of sight:

$$y = \int_{\rm los} \frac{kT_e}{m_e c^2} n_e \sigma_{\rm thomson} dl$$

where T_e is the electron temperature, m_e the electron mass, c the speed of light, n_e the electron density, and $\sigma_{\rm thomson}$ the Thomson cross section.

Kinetic SZ

The kinetic SZ effect is generated by the scattering of CMB photons off an electron gas in motion with respect to the CMB. This motion generates spectral distortions with the same frequency scaling as CMB temperature fluctuations, and are directly proportionnal to the velocity of the electrons along the line of sight. As the effect has the same frequency scaling as CMB temperature fluctuations, it is, in principle, indistiguishable from primordial CMB. However, since the effect arises in clusters of galaxies with typical sizes 1 arcminute, it can be distinguished to some level from the primordial CMB by spatial filtering, especially if the location of the clusters most likely to generate the effect is known from other information (e.g. the detection of the clusters through the thermal SZ effect).

Polarised SZ

The polarised SZ effect arises from the polarisation dependence of the Thomson cross section:

$$\sigma_T \propto |\boldsymbol{e_1}.\boldsymbol{e_2}|^2$$

where $\boldsymbol{e_1}$ and $\boldsymbol{e_2}$ are the polarisation states of the incoming and outgoing photon respectively. A quadrupole moment in the CMB radiation illuminating the cluster electron gas generates a net polarisation, at a level typically two orders of magnitude lower than the kinetic SZ effect [Sunyaev & Zeldovich (1980), Audit & Simmons (1999), Sazonov & Sunyaev (1999)]. Therefore, the kinetic SZ effect has been proposed as a probe to investigate the dependence of the CMB quadrupole with position in space. Cluster transverse motions at relativistic speed, however, generate also such an effect from the kinematic quadrupole induced by the motion. Multiple scattering of CMB photons also generates a low-level polarisation signal towards clusters.

The polarised SZ effects has a distinctive frequency scaling, independent (to first order) to cluster parameters and to the amplitude of the effect. Amplitudes are proportionnal:

- to τ for the intrinsic CMB quadrupole effect,
- to $(v_t/c)^2\tau$ for the kinematic quadrupole effect
- to $(kT_e/m_ec^2)\tau^2$ and $(v_t/c)\tau^2$ for polarisation effects due to double scattering.

Here τ is the optical depth, v_t the transverse velocity, c the speed of light, k the Boltzmann constant, and T_e and m_e the electron temperature and mass.

As polarised effects arise essentially in galaxy clusters, they can be sought essentially in places where the much stronger thermal effect is detected, which will permit to improve the detection capability significantly. Polarised SZ emission, however, is weak enough that it is not expected to impact significantly the observation of any of the main polarised emissions.

Diffuse component or point source methods for SZ effect separation?

The SZ effect is particular in several respects. As most of the emission comes from compact regions towards clusters of galaxies (at arcminute scales), most of the present-day CMB experiments do not resolve clusters individually (apart for a few known extended clusters). For this reason, it seems natural to use point source detection methods for cluster detection (see review by Barreiro [Barreiro (2005)]). However, the very specific spectral signature, the presence of a possibly large background of clusters with emission too weak for individual cluster detection, and the interesting possibility to detect larger scale diffuse SZ emission, makes looking for SZ effect with diffuse component separation methods an interesting option.

3.5 The infrared background of unresolved sources

The added emissions from numerous unresolved infrared sources at high redshift make a diffuse infrared background, detected originally in the FIRAS and DIRBE data [Puget et al. (1996)]. Because each source has its specific emission law, and because this emission law is redshifted by the cosmological expansion, the background does not have a very well defined frequency scaling. It appears thus, in the observations at various frequencies, as an excess emission correlated between channels. The fluctuations of this background are expected to be significant at high galactic latitudes (where not masked by much stronger emissions from our own galaxy), and essentially at high frequencies (in the highest frequency channels of the Planck HFI.

3.6 Point sources

The "point sources" component comprises all emissions from astrophysical objects such as radio galaxies, infrared galaxies, quasars, which are not resolved by the instruments used in CMB observations. For such sources, the issues are both their detection and the estimation of parameters describing them (flux at various frequencies, location, polarisation...), and specific methods are devised for this purpose. For diffuse component separation, they constitute a source of trouble. Usually, pixels contaminated by significant point source emission are blanked for diffuse component separation.

4 Reduction of foreground contamination

The simplest way of avoiding foreground contamination consists in using prior information on emissions to reduce their impact on the data: by adequate selection of the region of observation, by masking some directions in the sky, by choosing the frequency bands of the instrument, or, finally, by subtracting an estimate of the contamination. All of these methods have been used widely in the context of CMB experiments.

4.1 Selection of the region of observation

Perhaps the most obvious solution to avoid contamination by foregrounds is to design the observations in such a way that the contamination is minimal. This sensible strategy has been adopted by ground–based and balloon–borne experiments observing only a part of the sky. In this case, CMB observations are made away from the galactic plane, in regions where foreground contamination from the galactic emissions is known to be small. The actual choice of regions of observation may be based on existing observations of dust and synchrotron emission at higher and lower frequencies, picking those regions where the emission of these foregrounds is known to be the lowest.

The drawback of this strategy is that the observations do not permit to estimate very well the level of contamination, nor the properties of the foregrounds.

4.2 Masking

For all-sky experiments, a strategy for keeping the contamination of CMB observations by foregrounds consists in masking regions suspected to comprise significant foreground emissions, and deriving CMB properties (in particular the CMB power spectrum) in the "clean" region. The drawback of this strategy is that sky maps are incomplete.

Typically, for CMB observations, pixels contaminated by strong point sources (radio and infrared galaxies) are blanked, as well as a region containing the galactic plane. Such masks have been used in the analysis of WMAP data.

4.3 Selection of the frequency bands of the instrument

Of course, the selection of the frequency of observation to minimize the overall foreground contamination is a sensible option. For this reason, many CMB experiments aim at observing the sky around 70–100 GHz. Ground-based observations, however, need to take into account the additionnal foreground of atmospheric emission, which leaves as best windows frequency bands around 30 GHz, 90 GHz, 150 GHz, and 240 GHz.

Figure 5 shows the expected typical frequency scalings for the major diffuse emission astrophysical components, including the CMB. For efficient component separation, CMB experiment, ideally, should comprise two or three channels around 70-100 GHz where CMB dominates, one channel around 217 GHz (the zero of the SZ effect), two channels at higher frequencies to monitor dust emission, and 3-4 channels at lower frequencies to monitor low frequency foregrounds.

Below 100 GHz, the present state of the art technology suggests the use of radiometers with high electron mobility transistor (HEMT) amplifiers, whereas above 100 GHz, low temperature bolometers provide a significantly better sensitivity that any other techniques. Typically, a single experiment uses one technology only. For Planck specifically, two different instruments have been designed to cover all the frequency range from 30 to 850 GHz.

4.4 Foreground cleaning

As a refinement to the above simple observational strategies, a first-order estimate of foreground contamination, based on observations made at low and high frequencies, can be subtracted from the observations. Depending on the accuracy of the model, the overall level of contamination can be reduced

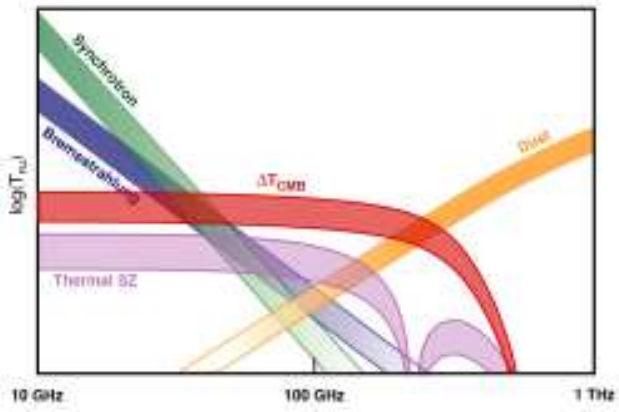

Fig. 5. The frequency scaling of CMB and most relevant diffuse foregrounds, in Rayleigh-Jeans temperature, between 10 GHz and 1 THz. Depending on the relative amplitude of synchrotron, bremsstrahlung and dust emissions, the minimum of galactic foregrounds is somewhat below 100 GHz. Free-free emission decreases roughly as $\nu^{-2.1}$ and synchrotron as ν^{-3}, while dust insreases as ν^2. The SZ effect is the major emission towards rich clusters, but is very localised. The thickness of the bands illustrates uncertainties as to the level of foregrounds, as well as uncertainties in the frequency scaling for synchrotron, free-free and dust emissions. Anomalous dust emission is not represented, due to our present lack of knowledge of the existence and nature of such a component.

by a factor of a few at least, which permits to reduce the amount of cut sky. This strategy, in particular, has been used by the WMAP team for the analysis of first year WMAP data [Bennett et al. (2003)].

Observations at low frequencies (10-40 GHz) can be used to map synchrotron emission and model its contribution in the 70-100 GHz range. Similar strategies can be used towards the high frequency side to model dust emission and subtract its contribution from CMB channels. For this purpose, models of emission as good as possible are needed, and the cleaning can be no better than the model used. There is always, therefore, a trade-off between a sophisticated model with simple correction methods (subtraction of an interpolation, simple decorrelation), and a simple model with sophisticated statistical treatments (multi-frequency filtering, independent component analysis). Which approach is best depends on a number of issues, and the answer is not completely clear yet.

5 The linear model and system inversion

The most popular model of the observations for source separation in the context of CMB observations probably is the linear mixture.

In this model, all components are assumed to have an emission which can be decomposed as the product of a spatial template independent of the frequency of observation, and of a spectral emission law which does not depend on the pixel. The total emission at frequency ν, in pixel p, of a particular emission process j is written as

$$x_j(\nu, p) = a(\nu) s_j(p)$$

or alternatively, in spherical harmonics space,

$$x_j(\nu, \ell m) = a(\nu) s_j(\ell m)$$

Forgetting for the moment annoying details concerning the response of the instrument (beams, frequency bands, etc...) the observation with a detector is then:

$$y_i(p) = \sum_j x_j(\nu_i, p) + n_i(p)$$

where $n_i(p)$ is the contribution of noise for detector i. For a set of detectors, this can be recast in a matrix–vector form as

$$\boldsymbol{y}(p) = \mathbf{A}\boldsymbol{s}(p) + \boldsymbol{n}(p) \tag{23}$$

Here, $\boldsymbol{y}(p)$ represent the set of maps observed with all detectors detector, and $\boldsymbol{s}(p)$ are the unobserved components (one template map per astrophysical component). The mixing matrix $\mathbf{A}$ which does not depend on the pixel for a simple linear mixture, has one column per astrophysical component, and one line per detector.

If the observations are given in CMB temperature for all detectors, and if the detectors are properly calibrated, each element of the column of the mixing matrix corresponding to CMB is equal to 1.

The problem of component separation consists in inverting the linear system of equation 23. Here we first concentrate on linear inversion, which consists in finding the "best" possible matrix $\mathbf{W}$ (such that $\widehat{\boldsymbol{s}} = \mathbf{W}\boldsymbol{y}$ is "as good an estimator of $\boldsymbol{s}$ as possible").

Covariances and multivariate power spectra

In the following, a lot of use will be made of second order statistics of various sorts of data. In general, for a collection of maps $\boldsymbol{x}(p) = \{x_i(p)\}$, the covariance will be noted as $\mathbf{R}_{\mathbf{x}}(p, p')$, the elements of which are:

$$R_{ij}(p, p') = \mathrm{cov}(x_i(p), x_j(p'))$$

Alternatively, in harmonic space, we denote as $\mathbf{R}_{\boldsymbol{x}}(\ell)$ the multivariate power spectrum of $\boldsymbol{x}$, i.e. the collection of matrices

$$\mathbf{R}_{\boldsymbol{x}}(\ell) = \langle \boldsymbol{x}(\ell, m)\boldsymbol{x}^{\dagger}(\ell, m)\rangle$$

where the brackets $\langle . \rangle$ denote ensemble average, and the dagger † denotes the transpose of the complex conjugate. Such a power spectrum is well defined only for stationary/isotropic random fields on the sphere for which $\langle \boldsymbol{x}(\ell, m)\boldsymbol{x}^{\dagger}(\ell, m)\rangle$ does not depend on m.

5.1 Simple inversion

If $\mathbf{A}$ is square and non singular, in absence of any additional information, then the inversion is obtained by

$$\mathbf{W} = \mathbf{A}^{-1} \tag{24}$$

and we have

$$\widehat{\boldsymbol{s}} = \mathbf{A}^{-1}\boldsymbol{y} = \boldsymbol{s} + \mathbf{A}^{-1}\boldsymbol{n} \tag{25}$$

Note that because of the remaining noise term, this inversion is not always the best solution in terms of residual error, in particular in the poor signal to noise regimes. For instance, if we have two measurements of a mixture of CMB + thermal dust in a clean region of the sky (low foregrounds), one of which, at 150 GHz, is relatively clean, and the other, at 350 GHz, quite poor because of high level noise, then it may be better to use the 150 GHz as the CMB template (even with some dust contamination), rather than to invert the system, subtracting little dust and adding a large amount of noise.

In terms of residual foreground contamination however (if the criterion is to reject astrophysical signals, whatever the price to pay in terms of noise), the only solution here is matrix inversion. The solution is unbiased, but may be noisy.

Note that an ILC method would produce a different solution, possibly slightly biased (as discussed in 2.6), but possibly better in terms of signal to noise ratio of the end product.

This solution can be applied if the full matrix $\mathbf{A}$ is known (not only the column of the component of interest, i.e. the CMB), without further prior knowledge of the data.

5.2 Inversion of a redundant system using the pseudo inverse

If there are more observations than components, but nothing is known about noise and signal levels, then the inversion is obtained by

$$\mathbf{W} = \left[\mathbf{A}^{\dagger}\mathbf{A}\right]^{-1}\mathbf{A}^{\dagger} \tag{26}$$

and we have

$$\widehat{\boldsymbol{s}} = \left[\mathbf{A}^\dagger\mathbf{A}\right]^{-1}\mathbf{A}^\dagger\boldsymbol{y} = \boldsymbol{s} + \left[\mathbf{A}^\dagger\mathbf{A}\right]^{-1}\mathbf{A}^\dagger\boldsymbol{n} \tag{27}$$

Again, this estimator is unbiased, but may contain a large amount of noise and may not be optimal in terms of signal to noise ratio. All the comments made in the previous paragraph hold as well for this solution.

Note that there is no noise-weighting here, so that one single very bad channel may contaminate significantly all the data after inversion. It is therefore not a very good idea to apply this estimator with no further thoughts.

Note that, again, this solution can be implemented without any further knowledge about signal and noise – only the entries of the mixing matrix for all components are needed.

5.3 A noise-weighted scheme: the Generalised Least-Square solution

Let us now assume that we know something additional about the noise, namely, its second order statistics. These are described by noise correlation matrices in real space, or alternatively by noise power spectra in Fourier (for small maps) or in harmonic (for all-sky maps) space.

We denote as $\mathbf{R_n}$ the noise correlation matrix and assume, for the time being, that the noise for each detector i is a realization of a random gaussian field, the generalised (or global) least square (GLS) solution of the system of equation 23 is:

$$\mathbf{W} = \left[\mathbf{A}^\dagger{\mathbf{R_n}}^{-1}\mathbf{A}\right]^{-1}\mathbf{A}^\dagger{\mathbf{R_n}}^{-1} \tag{28}$$

and we have

$$\widehat{\boldsymbol{s}} = \left[\mathbf{A}^\dagger{\mathbf{R_n}}^{-1}\mathbf{A}\right]^{-1}\mathbf{A}^\dagger{\mathbf{R_n}}^{-1}\boldsymbol{y} = \boldsymbol{s} + \left[\mathbf{A}^\dagger{\mathbf{R_n}}^{-1}\mathbf{A}\right]^{-1}\mathbf{A}^\dagger{\mathbf{R_n}}^{-1}\boldsymbol{n} \tag{29}$$

Again, the solution is unbiased. Altough there remains a noise contribution, this is the solution yielding the minimum variance error map for a deterministic signal (in contrast with the Wiener solution below, which optimises the variance of the error when the signal is stochastic, i.e. assumed to be a random field). It is also the best linear solution in the limit of large signal to noise ratio.

This solution is also theoretically better than the ILC when the model holds, but the price to pay is the need for more prior knowledge about the data (knowledge of the mixing matrix and of noise covariance matrices or power spectra). If that knowledge is unsufficient, one has to design methods to get it from the data itself. Such "model learning" methods will be discussed in section 7.

5.4 The Wiener solution

The Wiener filter [Wiener (1949)] has originally been designed to filter time series in order to suppress noise, but has been extended to a large variety

of applications since then. Wiener's solution requires additional information regarding the spectral content of the original signal and the noise. Wiener filters are characterized by the following:

- Both the noise and the signal are considered as stochastic processes with known spectral statistics (or correlation properties) – contrarily to the GLS method which considers the noise only to be stochastic, the signal being deterministic,
- The optimization criterion is the minimum least square error,
- The solution is linear.

In signal processing, a data stream $y(t) = s(t) + n(t)$ assumed to be a noisy measurement of a signal s can be filtered for denoising as follows: in Fourier space, each mode $y(f)$ of the data stream is weighted by a coefficient

$$W(f) = \frac{S(f)}{S(f) + N(f)}$$

where $S(f) = \langle |s(f)|^2 \rangle$ and $N(f) = \langle |n(f)|^2 \rangle$ are ensemble averages of the square moduli of the Fourier coefficients of the stochastic processes s and n.

In the limit of very small noise level $N(f) \ll S(f)$, the Wiener filter value is $W(f) = 1$, and the filter does not change the data. In the limit of very poor signal to noise $S(f) \ll N(f)$, the filter suppresses the data completely, because that mode adds noise to the total data stream, and nothing else.

It can be shown straightforwardly that the Wiener filter minimizes the variance of the error of the signal estimator $\widehat{s}(f) = W(f)y(f)$ (so that $\langle \int_f |\widehat{s}(f) - s(f)|^2 \mathrm{d}f \rangle$ is minimal).

The Wiener solution can be adapted for solving our component separation problem, provided the mixing matrix $\mathbf{A}$ and the second order statistics of the components and of the noise are known [Tegmark & Efstathiou (1996), Bouchet & Gispert (1999)] as:

$$\mathbf{W}^{(1)} = \left[\mathbf{A}^\dagger {\mathbf{R_n}}^{-1} \mathbf{A} + {\mathbf{R_s}}^{-1}\right]^{-1} \mathbf{A}^\dagger {\mathbf{R_n}}^{-1} \tag{30}$$

where $\mathbf{R_s}$ is the correlation matrix of the sources (or power spectra of the sources, in the Fourier or harmonic space), and $\mathbf{R_n}$ the correlation matrix of the noise. The superscript (1) is used to distinguish two forms of the Wiener filter (the second is given later in this section).

An interesting aspect of the Wiener filter is that:

$$\begin{aligned} \widehat{\boldsymbol{s}} &= \left[\mathbf{A}^\dagger {\mathbf{R_n}}^{-1} \mathbf{A} + {\mathbf{R_s}}^{-1}\right]^{-1} \mathbf{A}^\dagger {\mathbf{R_n}}^{-1} \boldsymbol{y} \\ &= \left[\mathbf{A}^\dagger {\mathbf{R_n}}^{-1} \mathbf{A} + {\mathbf{R_s}}^{-1}\right]^{-1} \mathbf{A}^\dagger {\mathbf{R_n}}^{-1} \mathbf{A} \boldsymbol{s} \\ &\quad + \left[\mathbf{A}^\dagger {\mathbf{R_n}}^{-1} \mathbf{A} + {\mathbf{R_s}}^{-1}\right]^{-1} \mathbf{A}^\dagger {\mathbf{R_n}}^{-1} \boldsymbol{n} \end{aligned} \tag{31}$$

The matrix in front of $\boldsymbol{s}$ is not the identity, and thus the Wiener filter does not give an unbiased estimate of the signals of interest. Diagonal terms can be

different from unity. In addition, non-diagonal terms may be non-zero, which means that the Wiener filter allows some residual foregrounds to be present in the final CMB map – the objective being to minimise the variance of the residuals, irrespective of whether these residuals originate from instrumental noise or from astrophysical foregrounds.

As noted in [Tegmark & Efstathiou (1996)], the Wiener solution can be "debiased" by multiplying the Wiener matrix by a diagonal matrix removing the impact of the filtering. The authors argue that for the CMB this debiasing is desirable for subsequent power spectrum estimation on the reconstructed CMB map. Each mode of a given component is divided by the diagonal element of the Wiener matrix for that component and that mode. This, however, destroys the minimal variance property of the Wiener solution, and can increase the noise very considerably. There is an incompatibility between the objective ofobtaining a minimum variance map, and the objective of obtaining an unbiased map which can be used directly to measure the power spectrum of the CMB. There is no unique method for both.

Before moving on, it is interesting to check that the matrix form of the Wiener filter given here reduces to the usual form when there is one signal only and when the matrix $\mathbf{A}$ reduces to a scalar equal to unity. In that case, the Wiener matrix $\mathbf{W}$ of equation 30 reduces to

$$W(f) = [1/S(f) + 1/N(f)]^{-1}/N(f) = S(f)/[N(f) + S(f)]$$

where S and N are the signal and noise power spectra, and we recover the classical Wiener formula.

Two forms of the Wiener Filter

In the literature, another form can be found for the Wiener filter matrix:

$$\mathbf{W}^{(2)} = \mathbf{R_s}\mathbf{A}^\dagger \left[\mathbf{R_n} + \mathbf{A}\mathbf{R_s}\mathbf{A}^\dagger\right]^{-1} \tag{32}$$

It can be shown straightforwardly that if the matrices

$$\mathbf{M}_1 = \left[\mathbf{A}^\dagger {\mathbf{R_n}}^{-1}\mathbf{A} + {\mathbf{R_s}}^{-1}\right]$$

and

$$\mathbf{M}_2 = \left[\mathbf{R_n} + \mathbf{A}\mathbf{R_s}\mathbf{A}^\dagger\right]$$

are regular, then the forms of equation 30 and 32 are equivalent (simply multiply both forms by $\mathbf{M}_1$ on the left and $\mathbf{M}_2$ on the right, and expand).

It may seem that the form of equation 32 is more convenient, as it requires only one matrix inversion instead of three. Each form, however, presents specific advantages or drawbacks, which appear clearly in the high signal to noise ratio (SNR) limit, and if power spectra of all signals are not known.

The high SNR limit

The two above forms of the Wiener filter are not equivalent in the high SNR limit. In this regime, equation 30 yields in the limit

$$\mathbf{W}_{\text{limit}}^{(1)} = \left[\mathbf{A}^\dagger {\mathbf{R_n}}^{-1} \mathbf{A}\right]^{-1} \mathbf{A}^\dagger {\mathbf{R_n}}^{-1}$$

which is the GLS solution of equation 28, and depends only on the noise covariance matrix, whereas equation 32 tends to

$$\mathbf{W}_{\text{limit}}^{(2)} = \mathbf{R_s}\mathbf{A}^\dagger \left[\mathbf{A}\mathbf{R_s}\mathbf{A}^\dagger\right]^{-1}$$

which depends only on the covariance of the signal. Therefore, some care should be taken when applying the Wiener filter in the high SNR ratio regime, when numerical roundup errors may cause problems.

Note that if $\left[\mathbf{A}^\dagger\mathbf{A}\right]$ is regular, then

$$\begin{aligned}
\mathbf{W}_{\text{limit}}^{(2)} &= \mathbf{R_s}\mathbf{A}^\dagger \left[\mathbf{A}\mathbf{R_s}\mathbf{A}^\dagger\right]^{-1} \\
&= \left[\mathbf{A}^\dagger\mathbf{A}\right]^{-1} \left[\mathbf{A}^\dagger\mathbf{A}\right] \mathbf{R_s}\mathbf{A}^\dagger \left[\mathbf{A}\mathbf{R_s}\mathbf{A}^\dagger\right]^{-1} \qquad (33) \\
&= \left[\mathbf{A}^\dagger\mathbf{A}\right]^{-1} \mathbf{A}^\dagger \qquad (34)
\end{aligned}$$

and the limit is simply the pseudo inverse of matrix $\mathbf{A}$, without any noise weighting. Of course, when there is no noise at all, $\mathbf{W}^{(1)}$ can not be implemented at all, and the Wiener solution is pointless anyway.

What if some covariances are not known?

It is interesting to note that even if the covariance matrix (or equivalently multivariate power spectrum) $\mathbf{R_s}$ of all sources is not known, it is still possible to implement an approximate Wiener solution if the maps of observations are large enough to allow a good estimate of the covariance matrix of the observations.

If $\boldsymbol{y} = \mathbf{A}\boldsymbol{s} + \boldsymbol{n}$ and if the noise and the components are independent, the covariance $\mathbf{R_y}$ of the observations is of the form:

$$\mathbf{R_y} = \mathbf{R_n} + \mathbf{A}\mathbf{R_s}\mathbf{A}^\dagger$$

Therefore, form 2 of the Wiener filter can be recast as:

$$\mathbf{W}^{(2)} = \mathbf{R_s}\mathbf{A}^\dagger \left[\mathbf{R_y}\right]^{-1} \qquad (35)$$

If all components are decorrelated, the matrix $\mathbf{R_s}$ is diagonal. For the implementation of a Wiener solution for one single component (e.g. CMB), only the diagonal element corresponding to the CMB (i.e. the power spectrum C_ℓ of the CMB) is needed, in addition to the multivariate power spectrum of the observations $\mathbf{R_y}$. The latter can be estimated directly using the observations.

5.5 Comment on the various linear inversion solutions

The above four linear solutions to the inversion of the linear system of equation 23 have been presented by order of increasing generality, increasing complexity, and increasing necessary prior knowledge. The various solutions are summarised in table 1. Three comments are necessary.

Firstly, we note that the Wiener solutions require the prior knowledge of the covariance matrices (or equivalently power spectra) of both the noise and the signal. For CMB studies, however, the measurement of the power spectrum of the CMB field is precisely the objective of the observations. Then, the question of whether the choice of the prior on the CMB power spectrum biases the final result or not is certainly of much relevance. For instance, the prior assumption that the power spectrum of the CMB is small in some ℓ range will result in filtering the corresponding modes, and the visual impression of the recovered CMB will be that indeed there is little power at the corresponding scales. For power spectrum estimation on the maps, however, this effect can be (an should be) corrected, which is always possible as the effective filter induced by the Wiener solution is known (for an implementation in harmonic space, it is equal for each mode ℓm, for each component, to the corresponding term of the diagonal of $\mathbf{W}_{\ell m}\mathbf{A}$). In section 8, a solution will be proposed for estimating first on the data themselves all the relevant statistical information (covariance matrices and frequency scalings), and then using this information for recovering maps of the different components.

Secondly, we should emphasise that the choice of a linear solution should be made with a particular objective in mind. If the objective is to get the best possible map in terms of least square error, then the Wiener solution is the best solution if the components are Gaussian. The debiased Wiener is not really adapted to any objective in particular. The GLS solution is the best solution if the objective is an unbiased reconstruction with no filtering and no contamination. In practice, it should be noted that small uncertainties on $\mathbf{A}$ result in errors (biases and contamination) even for the GLS solution.

As a third point, we note that it can be shown straightforwardly that for Gaussian sources and noise, the Wiener solution maximises the posterior probability $P(\boldsymbol{s}|\boldsymbol{y})$ of the recovered sources given the data. From Bayes theorem, the posterior probability is the product of the likelihood $P(\boldsymbol{y}|\boldsymbol{s})$ and the prior $P(\boldsymbol{s})$, normalised by the evidence $P(\boldsymbol{y})$. The normalising factor does not depend on s. We can write:

$$\begin{aligned} P(\boldsymbol{s}|\boldsymbol{y}) &\propto \exp\left[-(\boldsymbol{y}-\mathbf{A}\boldsymbol{s})^\dagger {\mathbf{R}_\mathbf{n}}^{-1}(\boldsymbol{y}-\mathbf{A}\boldsymbol{s})\right] \exp\left[-\boldsymbol{s}^\dagger {\mathbf{R}_\mathbf{s}}^{-1}\boldsymbol{s}\right] \\ \log(P(\boldsymbol{s}|\boldsymbol{y})) &= -\left[(\boldsymbol{y}-\mathbf{A}\boldsymbol{s})^\dagger {\mathbf{R}_\mathbf{n}}^{-1}(\boldsymbol{y}-\mathbf{A}\boldsymbol{s})\right] - \left[\boldsymbol{s}^\dagger {\mathbf{R}_\mathbf{s}}^{-1}\boldsymbol{s}\right] + \text{const.} \quad (36) \end{aligned}$$

where $\exp\left[-\boldsymbol{s}^\dagger {\mathbf{R}_\mathbf{s}}^{-1}\boldsymbol{s}\right]$ is the Gaussian prior for s. The requirement that

$$\frac{\partial}{\partial \boldsymbol{s}} \log(P(\boldsymbol{s}|\boldsymbol{y})) = 0$$

implies

$$\begin{aligned} -\mathbf{A}^\dagger {\mathbf{R_n}}^{-1}(\boldsymbol{y} - \mathbf{A}\boldsymbol{s}) + {\mathbf{R_s}}^{-1}\boldsymbol{s} &= 0 \\ \mathbf{A}^\dagger {\mathbf{R_n}}^{-1}\mathbf{A}\boldsymbol{s} + {\mathbf{R_s}}^{-1}\boldsymbol{s} &= \mathbf{A}^\dagger {\mathbf{R_n}}^{-1}\boldsymbol{y} \\ \left[\mathbf{A}^\dagger {\mathbf{R_n}}^{-1}\mathbf{A} + {\mathbf{R_s}}^{-1}\right]\boldsymbol{s} &= \mathbf{A}^\dagger {\mathbf{R_n}}^{-1}\boldsymbol{y} \end{aligned} \tag{37}$$

and thus we get the solution $\mathbf{W}^{(1)}$. In section 6, we will dicuss the case where the Gaussian prior is replaced by an entropic prior, yielding yet another solution for s.

5.6 Pixels, harmonic space, or wavelets?

The simple inversion of $\mathbf{A}$ using the inverse or pseudo-inverse can be implemented equivalently with any representations of the maps, in pixel domain, harmonic space, or on any decomposition of the observations on a set of functions as, e.g., wavelet decompositions [Moudden et al. (2005)]. The result in terms of separation is independent of this choice, as far as the representation arises from a linear transformation.

If all sources and signals are Gaussian random fields, the same is true for GLS or Wiener inversions, provided all the second order statistics are properly described by the covariance matrices $\mathbf{R_n}$ and $\mathbf{R_s}$.

These covariance matrices, in pixel space, take the form of the set of covariances:

$$\mathbf{R_n} = \{R_{n_i n_j}(p_i, p_j)\}$$

where

$$R_{n_i n_j}(p_i, p_j) = \langle n_i(p_i) n_j(p_j)\rangle$$

Similarly, in harmonic space, we have:

$$\mathbf{R_n} = \{R_{n_i n_j}(\ell_i, m_i, \ell_j, m_j)\}$$

where

$$R_{n_i n_j}(\ell_i, m_i, \ell_j, m_j) = \langle n_i(\ell_i, m_i) n_j(\ell_j, m_j)\rangle$$

If the number of pixels is large, if we deal with several sources and many channels at the same time (tens today, thousands in a few years), the implementation of the GLS or Wiener solution may be quite demanding in terms of computing. For this reason, it is desirable to implement the solution in the space where matrices are the most easy to invert.

For stationnary Gaussian random fields, harmonic space implementations are much easier then direct space implementations, because the covariance between distinct modes vanish, so that

$$R_{n_i n_j}(\ell_i, m_i, \ell_j, m_j) = \langle n_i(\ell_i, m_i) n_j(\ell_i, m_i)\rangle \delta_{\ell_i \ell_j} \delta_{m_i m_j}$$

The full covariance matrix consists in a set of independent covariance matrices (one for each mode), each of which is a small matrix of size $N_{\text{channels}} \times N_{\text{channels}}$ for $\mathbf{R_n}$, and of size $N_{\text{sources}} \times N_{\text{sources}}$ for $\mathbf{R_s}$.

Solution	$\mathbf{W} =$	Required prior knowledge	Comments
Inverse	$\mathbf{A}^{-1}$	$\mathbf{A}$	When there are as many channels of observation as components. Unbiased, contamination free.
Pseudo–inverse	$\left[\mathbf{A}^\dagger\mathbf{A}\right]^{-1}\mathbf{A}^\dagger$	$\mathbf{A}$	When there are more channels of observation than components. Unbiased, contamination free.
GLS	$\left[\mathbf{A}^\dagger{\mathbf{R_n}}^{-1}\mathbf{A}\right]^{-1}\mathbf{A}^\dagger{\mathbf{R_n}}^{-1}$	$\mathbf{A}$ and $\mathbf{R_n}$	Minimises the variance of the error for deterministic signals. Unbiased, contamination free.
Wiener 1	$\left[\mathbf{A}^\dagger{\mathbf{R_n}}^{-1}\mathbf{A}+{\mathbf{R_s}}^{-1}\right]^{-1}\mathbf{A}^\dagger{\mathbf{R_n}}^{-1}$	$\mathbf{A}$, $\mathbf{R_n}$ and $\mathbf{R_s}$	Minimises the variance of the error for stochastic signals. Biased, not free of contamination. Tends to the GLS solution in the limit of high SNR.
Wiener 2	$\mathbf{R_s}\mathbf{A}^\dagger\left[\mathbf{R_n}+\mathbf{A}\mathbf{R_s}\mathbf{A}^\dagger\right]^{-1}$	$\mathbf{A}$, $\mathbf{R_n}$ and $\mathbf{R_s}$	Equivalent to Wiener 1. Tends to the pseudo inverse in the limit of high SNR.
Debiased Wiener	$\Lambda\mathbf{R_s}\mathbf{A}^\dagger\left[\mathbf{R_n}+\mathbf{A}\mathbf{R_s}\mathbf{A}^\dagger\right]^{-1}$	$\mathbf{A}$, $\mathbf{R_n}$ and $\mathbf{R_s}$	The diagonal matrix Λ, inverse of the diagonal of $\mathbf{WA}$ where $\mathbf{W}$ is the Wiener solution, removes for each mode the filtering effect of the Wiener filter. Unbiased, but not contamination free.

Table 1. Summary of linear solutions to component separation when the mixing matrix $\mathbf{A}$ is known.

5.7 Annoying details

Under the assumption that the response of each detector i in the instrument can itself be decomposed in the product of a spectral response $h_i(\nu)$ and a frequency independent symmetrical beam B_i, the contribution of component j to the observation obtained with detector i is:

$$y_{ij}(\ell m) = \left[\int_\nu h_i(\nu) a(\nu) \mathrm{d}\nu\right] B_{i,\ell}\, s_j(\ell m)$$

where $B_{i,\ell}$ are the coefficients of the expansion of the symmetric beam of detector i on Legendre polynomials.

The mixing matrix of this new linear model is seen to include a band integration, assumed to first order to be independent of ℓ, a the effect of a beam, which depends on ℓ. Both can be taken into account in a linear inversion, if known a priori.

6 The Maximum Entropy Method

The Wiener filter provides the best (in terms of minimum-variance, or maximum likelihood) estimate of the component maps if two main asumptions hold. Firstly, the observations should be a linear mixture of distinct emissions. Secondly, the components and the noise should be (possibly correlated) Gaussian stationnary random processes.

Unfortunately, the sky is known to be neither Gaussian, nor stationnary, with the possible exception of the CMB itself. Is this critical?

The Maximum Entropy Method (MEM) of component separation is a method which inverts the same linear system of component mixtures, but assumes non-gaussian probability distributions [Hobson et al. (1998)].

6.1 Maximum Entropy

The concept of entropy in information theory has been introduced by Shannon in 1948 [Shannon (1948)]. The entropy of a discrete random variable X on a finite set of possible values $\{x_i\}$ with probability distribution function $p(x_i) = p(X = x_i)$, is defined as:

$$H(X) = -\sum_{i=1}^{N} p(x_i) \log p(x_i) \tag{38}$$

The principle of maximum entropy is based of the idea that whenever there is some choice to be made about the distribution function of the random variable X, one should choose the least informative option possible. Entropy measures the amount of information in a probability distribution, and entropy maximisation is a way of achieving this.

For instance, in the absence of any prior information, the probability distribution which maximises the entropy of equation 38 is a distribution with uniform probability, $p(x_i) = 1/N$, i.e. the least informative choice of a probability distribution on the finite set $\{x_i\}$, where all outcomes are equally likely. This is the most natural choice if nothing more is said about the probability distribution.

In the opposite, a most informative choice would be a probability which gives a certain result, (for instance always $X = x_1$). This is a probability distribution which minimizes entropy.

In the continuous case where X can achieve any real value x with probability density $p(x)$, entropy can be defined as:

$$H(X) = -\int_{-\infty}^{\infty} p(x) \log p(x)\, dx \tag{39}$$

Of course, maximum entropy becomes really useful when there is also additional information available. In this case, the entropy must be maximized within the constraints given by additional information.

For instance, the maximum entropy distribution of a real random variable of mean μ and variance σ^2 is the normal (Gaussian) distribution :

$$p(x) = \frac{1}{2\pi\sigma} \exp\left[-\frac{(x-\mu)^2}{2\sigma^2}\right]$$

For this reason, in absence of additional information about the probability distribution of a random variable of known mean and variance, it is quite natural, according to the Maximum Entropy principle, to assume a Gaussian distribution – which maximises the entropy, and hence corresponds to the least informative choice possible.

An other useful example is the maximum entropy distribution of a real positive random variable of mean μ, which is the exponential distribution :

$$p(x) = \frac{1}{\mu} \exp(-x/\mu)$$

6.2 Relative entropy

In fact, the differential entropy of equation 39 has an unpleasant property. It is not invariant under coordinate transformations (on spaces with more than one dimension).

The definition of *relative entropy* (or Kullback-Leibler divergence) between two distributions solves the issue. It can be interpreted as a measure of the amount of additional information one gets from knowing the actual (true) probability distribution $p(x)$, instead of an imperfect model $m(x)$, and is given by:

$$D_{\mathrm{KL}}(p||m) = \int_{-\infty}^{\infty} p(x) \log \frac{p(x)}{m(x)}\, dx \tag{40}$$

Later in this paper (in section 8), we will make use of the Kullback-Leibler divergence for measuring the "mismatch" between two positive matrices $\mathbf{R_1}$ and $\mathbf{R_2}$. It will actually correspond to the KL divergence between two Gaussian distributions with covariance matrices $\mathbf{R_1}$ and $\mathbf{R_2}$.

The relative entropy is invariant under coordinate transformations (because both the ratio $p(x)/m(x)$ and $p(x)dx$ are invariant under coordinate transformations).

6.3 Component separation with the MEM

In principle, replacing the Gaussian prior by some other prior is perfectly legitimate. In practice, the choice of such a prior is not obvious, as the full statistical description of a complex astrophysical component is difficult to apprehend..

Following the maximum entropy principle, one may decide to use as a prior the distribution which maximises the entropy given a set of constraints. If the constraints are the value of the mean, and the variance, then the maximum entropy prior is the Gaussian prior.

Hobson and collaborators, in their MEM paper [Hobson et al. (1998)], argue that based on the maximum entropy principle, an appropriate prior for astrophysical components s is

$$p(s) = \exp\left[-\alpha S_c(\boldsymbol{s}, \boldsymbol{m}_u, \boldsymbol{m}_v)\right] \tag{41}$$

with

$$S_c(\boldsymbol{s}, \boldsymbol{m}_u, \boldsymbol{m}_v) = \sum_{j=1}^{L} \left\{ \psi_j - m_{uj} - m_{vj} - s_j \ln\left[\frac{\psi_j + s_j}{2m_{uj}}\right] \right\}$$

where $\psi_j = [{s_j}^2 + 4m_{uj}m_{vj}]^{1/2}$, and where $\boldsymbol{m}_u$ and $\boldsymbol{m}_v$ are models of two positive additive distributions (which are not clearly specified) used to represent the astrophysical components.

A derivation for this is given in [Hobson & Lasenby (1998)], but the connection to entropy is not direct. In particular, the definition of entropy does not require the *values* of the random variables to be positive, but their *probability densities*, which makes the discussion unconvincing.

Pragmatically, the choice for the prior of equation 41 seems to be validated a posteriori by the performance of the separation, which is not worse (and actually better for some of the components) than that obtained with the Wiener filter. It is not likely to be optimal, however, because the non-stationnarity of components implies correlations in the harmonic domain, which are not fully taken into account in the MEM implementation.

The maximisation of the posterior probability (and hence of the product of the likelihood and the prior), is done with a dedicated fast maximisation

algorithm. We refer the reader to the relevant papers for additional details [Hobson & Lasenby (1998), Stolyarov et al. (2002)].

This method has been applied to the separation of components in the COBE data [Barreiro et al. (2004)].

6.4 Comments about the MEM

Although entropy has a clear meaning in terms of information content in the discrete case (e.g. it defines the minimum number of bits necessary to represent a sequence), there is no such interpretation in the continuous case. Entropy maximisation, understood as minimising the amount of arbitrary information in the assumed distribution, hence, is not very clearly founded for continuous images.

The "principle" of maximum entropy, as the name indicates, is not a theorem, but a reasonable recipe which seems to work in practice. In the context of the CMB, there is no guarantee that it is optimal, among all non-linear solutions of the mixing system. MEM outperforms the Wiener filter solution for some components in particular because the entropic prior of Hobson and Lasenby allows heavier tails than the Gaussian prior. Other priors however, based on a physical model of the emissions, might well perform even better in some cases. This question remains as an open problem in the field.

7 ICA and Blind source separation

7.1 About blind separation

The term "blind separation" refers to a fascinating possibility: if the components of a linear mixture are *statistically independent*, they can be recovered even if the mixing matrix $\mathbf{A}$ is unknown *a priori*. In essence, this is possible because statistical independence is, at the same time, a strong mathematical property and, quite often, a physically plausible one.

There is an obvious and strong motivation for attempting blind component separation: allowing underlying components to be recovered blindly makes it possible to analyze multi-detector data with limited, imperfect, or even outright missing knowledge about the emission laws of the components. Even better, one can process data without knowing in advance which components might be "out there". Hence, the blind approach is particularly well suited for exploratory data analysis.

In the last fifteen years, blind component separation has been a very active area of research in the signal processing community where it goes by the names of "blind source separation" (BSS) and "independent component analysis" (ICA). This section outlines the principles underlying some of the best known approaches to blind source separation. There is not a single best approach because there is not a unique way in which to express statistical independence on the basis of a finite number of samples.

7.2 Statistical independence

This section explains why blind component separation is possible in the first place. For the sake of exposition, the main ideas are discussed in the simplest case: there is no observation noise and there are as many "channels" as underlying components. Thus the model reduces to

$$\mathbf{y}(p) = \mathbf{A}\mathbf{s}(p)$$

where $\mathbf{A}$ is an $n \times n$ matrix and we are looking for an $n \times n$ matrix "separating matrix" $\mathbf{W}$. Of course, if the mixing matrix $\mathbf{A}$ is known, there is little mystery about separation: one should take $\mathbf{W} = \mathbf{A}^{-1}$ and be done with it.

If nothing is known about $\mathbf{A}$ but the components are known (or assumed) to be statistically independent, the idea is to determine $\mathbf{W}$ in such a way that the entries of vector $\mathbf{W}\mathbf{y}$ are independent (or as independent as possible). In other words, the hope is that by restoring independence, one would restore the components themselves. Amazingly enough, this line of attack works. Even better, under various circumstances, it can be shown to correspond to maximum likelihood estimation and there is therefore some statistical optimality to it... provided the hypothesis of statistical independence is expressed vehemently enough.

Note however that no matter the amount of statistical ingenuity thrown at blind component separation, there is no hope to recover completely the mixing matrix (or equivalently: the components). This is because a scalar factor can always be exchanged between each entry of $\mathbf{s}$ and the corresponding column of $\mathbf{A}$ without changing what the model predicts (*i.e.* the value of the product $\mathbf{A}\mathbf{s}$) and without destroying the (hypothetical) independence between the entries of $\mathbf{s}$. The same is true of a renumbering of the columns of $\mathbf{A}$ and of the entries of $\mathbf{s}$. In other words, blind recovery is possible only up to rescaling and permutation of the components. In many applications, this will be "good enough". If these indeterminacies have to be fixed, it can be done only by imposing additional constraints or resorting to side information.

For any possible choice $\mathbf{W}$ of a candidate separating matrix, denote

$$\mathbf{x}(p) = \mathbf{W}\mathbf{y}(p)$$

the corresponding vector of candidate components. If $\mathbf{W} = \mathbf{A}^{-1}$ then the entries of $\mathbf{x}$ are independent (since, in this case $\mathbf{x}(p) = \mathbf{s}(p)$). Under which circumstances would the *converse* true? Whenever the converse is true, it will be possible to recover the sources by looking for the linear transform $\mathbf{W}$ which makes them independent. Hence, we have a blind separation principle: to separate components, make them independent.

7.3 Correlations

The main difficulty in blind source separation is to define a measure of independence. The problem is that the simple decorrelation condition[4] between any two candidate components:

$$\frac{1}{P}\sum_{p=1}^{P} x_i(p)x_j(p) = 0 \quad \text{for} \quad 1 \le i \ne j \le n. \tag{42}$$

does not cut it. This is in fact obvious from the fact that this decorrelation condition between x_i and x_j is *symmetric*. Hence decorrelation provides only $n(n-1)/2$ constraints while n^2 constraints are needed to determine $\mathbf{W}$ uniquely. Therefore, more expressive forms of independence must be used. Two main avenues are possible: non-linear correlations and localized correlations, as described next.

Non-linear correlations

The "historical approach" to blind separation has been to determine a separating matrix $\mathbf{W}$ in order to obtain "non-linear decorrelations" *i.e.*

$$\frac{1}{P}\sum_{p=1}^{P} \psi_i(x_i(p))\; x_j(p) = 0 \quad \text{for} \quad 1 \le i \ne j \le n \tag{43}$$

where functions $\psi_1, \ldots, \psi_n : R \mapsto R$ are *non-linear* functions (more about choosing them below). By using non-linear functions, symmetry is broken and the required number of constraints is obtained, namely $n(n-1)$ (with n additional arbitrary constraints, needed for fixing the scale of each component.

Localized correlations

Another approach is to look for "localized decorrelation" in the sense of solving

$$\frac{1}{P}\sum_{p=1}^{P} \frac{x_i(p)}{\sigma_{ip}^2} x_j(p) = 0 \quad \text{for} \quad 1 \le i \ne j \le n \tag{44}$$

where for each component i, a sequence $\{\sigma_{ip}\}_{p=1}^{P}$ of positive number must be defined (more about this soon). Again, blind identification is possible because symmetry is broken, provided no two sequences of σ's are proportional.

[4] Here, as in the rest of this section, all signals are assumed to have zero mean.

Maximum likelihood

Why using the particular proposals (43) or (44) as extended decorrelation conditions rather than any other form, possibly more complicated? One reason is that reasonable algorithms exist for computing the $\mathbf{W}$ such that $\mathbf{x} = \mathbf{W}\mathbf{y}$ is a solution of (43) or (44). Another, more important reason is that these two conditions actually characterize the maximum likelihood estimate of $\mathbf{W}$ in simple and well understood models. Because of this, we can understand what the algorithm does and we have guidance for choosing the non-linear functions ψ_i in condition (43) or the varying variance profiles σ_{iq}^2 in condition (44) as stated next.

Non linear correlations. Assume that each component $\{s_i(p)\}$ is modeled as having all pixels independently and identically distributed according to some probability density p_i. In this model, the most likely value of $\mathbf{A}$ given the observations has for inverse a matrix $\mathbf{W}$ such that condition (43) holds with $\psi_i = -p_i'/p_i$. Hence, if the model is true (or approximately true), the non linear-function appearing in condition (43) should be taken as minus the derivative of the log-density of $s_i(p)$. For a Gaussian distribution p_i, the corresponding function ψ_i is linear: here, the necessary non-linearity of ψ_i corresponds to the non Gaussianity of the corresponding component.

Localized correlations. Alternatively, one may model each component $\{s_i(p)\}$ as having all pixels independently and *normally* distributed with zero-mean and "local" variance σ_{ip}^2. Then, in this model, the likeliest value of A given the observations has for inverse a matrix $\mathbf{W}$ such that $\mathbf{x} = \mathbf{W}\mathbf{y}$ satisfies condition (44).

7.4 ICA in practice

For the simple noise-free setting under consideration (the noisy case is addressed in next section), the algorithmic solutions depend on the type of decorrelation one decides to use.

Non linear decorrelation

Two popular ICA algorithms based on non-linear decorrelation (hence exploiting non Gaussianity) are JADE [Cardoso (1999)] and FastICA [Hyvärinen (1999)]. In practice however, these algorithms do not exactly solve an equation in the form (43). Rather, for algorithmic efficiency, they try to solve it under the additional constraint that the components are uncorrelated *i.e.* that condition (42) is satisfied exactly. The underlying optimization engine is a joint diagonalization algorithm for JADE and a fixed point technique for FastICA.

Localized decorrelation

Efficient algorithms for solving the localized decorrelation conditions (44) are based on assuming some regularity in the variance profiles: the sequences

$\{\sigma_{ip}^2\}$ are approximated as being constant over small domains. Hence, the global set $[1, P]$ is partitioned into Q subsets $\mathcal{I}_1, \ldots, \mathcal{I}_Q$, each containing a number P_q of points (so that $P = \sum_{q=1}^{Q} P_q$). In practice, these pixel subsets are (well chosen) spatial regions. With a slight abuse of notation, we write $\sigma_{ip}^2 = \sigma_{iq}^2$ if $p \in \mathcal{I}_q$. Then, a small amount of maths turns the decorrelation conditions (44) into

$$\left[\sum_{q=1}^{Q} P_q \mathbf{\Sigma}_q^{-1} \mathbf{W} \widehat{\mathbf{R}}_q \mathbf{W}^\dagger\right]_{ij} = 0 \quad \text{for} \quad 1 \le i \ne j \le n \tag{45}$$

where $\widehat{\mathbf{R}}_q$ is a localized covariance matrix

$$\widehat{\mathbf{R}}_q = \frac{1}{P_q} \sum_{p \in q} \mathbf{y}(p)\mathbf{y}(p)^\dagger \quad \text{and} \quad \mathbf{\Sigma}_q = \mathrm{diag}(\sigma_{1q}^2, \ldots, \sigma_{nq}^2). \tag{46}$$

An important point here is that by assuming piecewise constant variance profiles, the localized decorrelation condition can be expressed entirely in terms of the localized covariance matrices $\widehat{\mathbf{R}}_q$. Hence the localized covariance matrices appear as *sufficient statistics* in this model. Even better, the likelihood of $\mathbf{A}$ can be understood as a mismatch between these statistics and their predicted form, namely $\mathbf{R}_q = \mathbf{A}\mathbf{\Sigma}_q\mathbf{A}^\dagger$. Specifically, in this model the probability $p(\mathbf{y}(1), \ldots \mathbf{y}(P)|\mathbf{A}, \mathbf{\Sigma})$ of the data given $\mathbf{A}$ and the set $\mathbf{\Sigma} = \{\mathbf{\Sigma}_1, \ldots, \mathbf{\Sigma}_Q\}$ of covariance matrices is given by

$$\log p(\mathbf{y}(1), \ldots \mathbf{y}(P)|\mathbf{A}, \mathbf{\Sigma}) = -\phi(\mathbf{A}, \mathbf{\Sigma}) + \mathrm{cst}$$

where function ϕ is defined as

$$\phi(\mathbf{A}, \mathbf{\Sigma}) = \sum_q P_q K(\widehat{\mathbf{R}}_q, \mathbf{A}\mathbf{\Sigma}_q\mathbf{A}^\dagger) \tag{47}$$

and where $K(\cdot, \cdot)$ is a measure of divergence between two matrices defined as

$$K(\mathbf{R}_1, \mathbf{R}_2) = \frac{1}{2}\left(\mathrm{trace}(\mathbf{R}_1\mathbf{R}_2^{-1}) - \log\det(\mathbf{R}_1\mathbf{R}_2^{-1}) - n\right) \tag{48}$$

This shows that maximum likelihood estimation of $\mathbf{A}$ amounts to the minimization of the weighted mismatch (47) between the set of localized covariance matrices $\widehat{\mathbf{R}}_q$ (computed from the data) and their expected value $\mathbf{R}_q = \mathbf{A}\mathbf{\Sigma}_q\mathbf{A}^\dagger$ (predicted by the model).

In the noise-free case considered here, it turns out that there is a simple and very efficient algorithm (due to D.T. Pham) for minimizing the spectral mismatch.

8 SMICA

We have developed a component separation technique dubbed SMICA for 'spectral matching ICA' which is based on the ideas sketched at previous section but improves on them in several ways.

In its simplest form, SMICA is based on *spectral* statistics, that is, on statistics which are localized not in space but in frequency. These statistics are binned auto- and cross-spectra of the channels. More specifically, for a given set of $N_{\rm chann}$ multi-channels maps $\{y_i(p)\}$, we form for each (ℓ, m) the $N_{\rm chann} \times 1$ vector $\mathbf{y}(\ell, m)$ of their harmonic coefficients and define

$$\widehat{\mathbf{R}}(\ell) = \frac{1}{2\ell+1} \sum_{m=-\ell}^{m=+\ell} \mathbf{y}(\ell, m)\mathbf{y}(\ell, m)^\dagger$$

These empirical spectral covariance matrices are then binned. In the simplest case, we define Q top-hat bins, with the q-th frequency bin contains all frequencies ℓ between $\ell_q^{\rm min}$ and $\ell_q^{\rm max}$. We consider the binned spectra:

$$\widehat{\mathbf{R}}_q = \frac{1}{P_q} \sum_{\ell=\ell_q^{\rm min}}^{\ell=\ell_q^{\rm max}} (2\ell+1)\widehat{\mathbf{R}}(\ell) \quad \text{where} \quad P_q = \sum_{\ell=\ell_q^{\rm min}}^{\ell=\ell_q^{\rm max}} (2\ell+1).$$

Here P_q is the number of Fourier modes summed together in a single estimate $\widehat{\mathbf{R}}_q$.

The mixture model $\mathbf{y} = \mathbf{A}\mathbf{s} + \mathbf{n}$ predicts that the empirical spectra $\mathbf{R}_q$ have an expected value

$$\mathbf{R}_q = \langle \widehat{\mathbf{R}}_q \rangle = \mathbf{A}\mathbf{\Sigma}_q\mathbf{A}^\dagger + \mathbf{N}_q$$

where $\mathbf{\Sigma}_q$ are the binned spectral covariance matrix for the components in bin q and $\mathbf{N}_q$ is the same for noise, assumed to be uncorrelated from the components. The unknown parameters can be collected in a big vector θ:

$$\theta = \{\mathbf{A}, \{\mathbf{\Sigma}_q\}, \{\mathbf{N}_q\}\}$$

but in practice we will not fit such a large model. Many constraints can be imposed on θ. A typical choice is to assume that the components are uncorrelated between themselves and that the noise also is uncorrelated between channels. Such a choice would result in a smaller parameter set

$$\theta = \{\mathbf{A}, \{\mathrm{diag}\mathbf{\Sigma}_q\}, \{\mathrm{diag}\mathbf{N}_q\}\}$$

but infinitely many other options are possible, both more stringent (like assuming that the noise in each channel is a smooth function of the bin index q) or less stringent (like assuming that some components may not be uncorrelated). In the following, we do not assume a specific parametrization of

the binned spectral covariance matrices. Rather, we denote where θ is some parameter set which uniquely determines the values of $\mathbf{A}$ and each $\mathbf{R}_q$ and $\mathbf{N}_q$:

$$\{\mathbf{R}_q\} = \{\mathbf{R}_q(\theta)\} = \{\mathbf{A}(\theta)\mathbf{\Sigma}_q(\theta)\mathbf{A}(\theta)^\dagger + \mathbf{N}_q(\theta)\}$$

SMICA determines the set θ of unknown parameters by fitting the empirical spectral covariance matrices to whichever structure is predicted by the model. Specifically, the unknown parameters are found by minimizing the "spectral mismatch"

$$\phi(\theta) = \sum_q P_q \, K(\widehat{\mathbf{R}}_q, \mathbf{R}_q(\theta)) \tag{49}$$

averaged across bins. Some comments are in order regarding the matching criterion, the issue of non stationarity and practical implementation.

Matching criterion

The reason for choosing this particular form of mismatch between data and model is that minimizing (49) is identical to maximizing the likelihood of the data in a model where all components are 1) Gaussian 2) stationary and 3) have harmonic spectra which are constant over bins. Of course, these assumptions are not met in practice so one could choose a different criterion for matching $\widehat{\mathbf{R}}_q$ to $\mathbf{R}_q(\theta)$ but we have little statistical guidance for picking up an alternate matching measure. Furthermore, the assumptions 1) and 2) are met by the CMB and 3) is approximately correct for narrow bins. In addition, the failure of stationarity can be alleviated by using localized statistics (see below).

Non stationarity and localization

The spectral approach to building a likelihood function has some benefits, in particular the fact that it is perfectly suited to describing the statistical properties of the CMB. Another beneficial side effect is that it makes it easy to deal with varying resolution from channel to channel as long as the beam can be considered to be symmetrical

However, going straight away to harmonic space seems unreasonable to deal with highly non stationary components such as the galactic components. This issue can be addressed to some extent by resorting to localized spectral statistics. It is a simple matter to use spatial window functions to partition the sky into spatial domains [Cardoso et al. (2005)]. Although not a perfect solution, it certainly allows to capture a good deal of the non stationary features of the galactic sky.

Implementation

The definition of the spectral matching criterion (49) encapsulates all of the statistical modeling but leaves open the separate and possibly tricky issue

of minimizing $\phi(\theta)$.[5] Because the criterion is a likelihood in disguise, it is possible to use the EM algorithm for its minimization, with the components taken as latent variables. However, EM is often not fast enough and also is not able to deal with arbitrary parametrization of $\mathbf{\Sigma}_q(\theta)$ and $\mathbf{N}_q(\theta)$. It has been found necessary to use general optimization techniques. A conjugate gradient algorithm can be implemented because a reasonably tractable expression for the gradient of the criterion is available as:

$$\frac{\partial \phi}{\partial \theta} = \sum_q P_q \,\mathrm{trace}\left(\mathbf{R}_q(\theta)^{-1}(\mathbf{R}_q(\theta) - \widehat{\mathbf{R}}_q)\mathbf{R}_q(\theta)^{-1}\frac{\partial \mathbf{R}_q(\theta)}{\partial \theta}\right)$$

However, in our context, the conjugate gradient algorithm also requires preconditioning. A preconditioner can be classically obtained as the inverse of the Fisher information matrix $\mathrm{FIM}(\theta)$ which is taken as an approximation to the Hessian of $\phi(\theta)$:

$$\frac{\partial^2 \phi}{\partial \theta^2} \approx \mathrm{FIM}(\theta) = \sum_q P_q \,\mathrm{trace}\left(\mathbf{R}_q(\theta)^{-1}\frac{\partial \mathbf{R}_q(\theta)}{\partial \theta}\mathbf{R}_q(\theta)^{-1}\frac{\partial \mathbf{R}_q(\theta)}{\partial \theta}\right)$$

Mismatch control and error bars

A benefit of the SMICA approach is that it comes with a built-in measure of the quality of the model. Indeed, if we properly fit all the auto-cross spectra, then $\phi(\theta)$ should be 'statistically small'. Visual control of the quality of the spectral matching is obtained by plotting $\phi_q = P_q\, K(\widehat{\mathbf{R}}_q, \mathbf{R}_q(\hat{\theta}))$ versus q where $\hat{\theta}$ is the minimizer of $\phi(\theta)$. This quantity should be understood as a χ^2. If the model holds (Gaussian stationary components and noise) and when all spectral parameters are freely estimated ϕ_q behaves approximately as a χ^2 with a number of degrees of freedom equal to $N_1 - N_2$ where $N_1 = N_{\mathrm{chann}}(N_{\mathrm{chann}} + 1)/2$ is the number of degrees of freedom for an sample covariance matrix of size N_{chann} and where $N_2 = N_{\mathrm{comp}} + N_{\mathrm{chann}}$ is the number of adjustable spectral parameters (the variances of each components and noise levels in a given frequency bin).

9 Other blind, semi-blind, or model learning methods

This paper would not be complete without a quick review of some of the recent work. We quote here a few papers which we think deserve reading for

[5] We note in passing that some authors seem to make a confusion between the objective function (the criterion which has to be minimised, which derives from a statistical model) and the algorithm used for minimization. For instance, some authors use the terms "EM method", or "MCMC method", to design a method in which they use the EM algorithm, or Monte-Carlo Markov Chains. This is rather infortunate, and contributes to a certain level of confusion.

further exploration of component separation issues and methods. Although unevenly mature, these methods provide complementary approaches, with advantages ad drawbacks which deserve to be investigated.

9.1 FastICA

A blind component separation based on the FastICA method has been developed for CMB data reduction by Baccigalupi et al [Baccigalupi et al.(2000)], with an extension to the full sky by Maino et al [Maino et al.(2002)]. This blind approach uses, as "engine" for component separation, a measure of independence based on non-Gaussianity. Therefore, it is essentially equivalent to finding components which cancel non-linear correlations in the sense of equation 43.

For CMB applications, characterizing independence via non linear correlations of the form 43 has some limitations. Firstly, theory shows that this characterization allow for the separation of at most one Gaussian component [Cardoso (1998)]. The Gaussian component is somehow found "by default", as the particular component which is orthogonal to (uncorrelated with) all other non Gaussian components. This is a concern for component separation performed with the CMB as the main target. Secondly, the non-linear decorrelation conditions do not take the noise into account. Even though this can be fixed in some ad hoc fashion, it is computationally demanding to do it in maximum likelihood sense. Finally, pixel space implementations cannot easily handle channel-dependent beams (unless explicit beam deconvolution is performed). If, to circumvent this problem, one considers harmonic space implementation, performance suffers from the fact that Fourier tend to be more Gaussian than the original, pixel-domain maps.

FastICA, however, can outperform other component separation methods for some applications. Spectral based methods (like SMICA) cannot blindly separate two components if their angular power spectra are proportional. FastICA does not suffer from this limitation and therefore has an edge for separating galactic components. If all galactic components have similar power spectra (say, proportional to ℓ^{-3}) then SMICA is expected to perform poorly without prior information.

Although both FastICA and SMICA are blind methods entering in the general class of "independent component analysis", it should thus be stressed that they are conceptually very different. Performance, therefore, is expected to be very different also, and to depend on the actual properties of the data sets.

FastICA has been used on COBE and on WMAP data [Maino et al.(2003), Maino et al.(2007)].

9.2 Other recent developments

A "semi-blind" approach to component separation has been proposed by Tegmark and collaborators in a work where they model the foreground emissions using a number of physical parameters, which they estimate directly in the data sets [Tegmark et al.(2000)]. They estimate the impact of estimating these extra parameters in terms of accuracy loss on parameters of interest for CMB science. This paper was the first to address seriously the problem of component spectral indices varying over the sky.

Martinez-Gonzalez and collaborators have proposed a method for the extraction of the CMB specifically and for the estimation of its power spectrum [Martínez-González et al.(2003)]. The EM algorithm is the main tool of the implementation.

Eriksen and collaborators have developed a method based on a refined modeling of the astrophysical components, and fitting this model to the data to obtained estimates of foreground parameters [Eriksen et al. (2006)]. The fit of the parameters is made pixel by pixel at low-resolution using a MCMC techinque for exploring the likelihood. After this first "model learning" step, the parameters obtained are used to estimate high resolution component maps.

Recently, Hansen and collaborators have proposed a CMB cleaning method based on a wavelet fit of component emissions obtained by differencing observations in different channels, and subtraction of the fit from observations made at frequencies where the CMB dominates [Hansen et al.(2006)].

Bonaldi and collaborators have recently published a paper for estimating parameters of emission of astrophysical components (emission laws, described by spectral indices). The statistics used are based on estimations of the correlations of the observations using a subset of points on the sphere [Bonaldi et al.(2006)].

An alternate way of performing component separation has been proposed by Bobin and collaborators, based on sparse representations of the various emissions [Bobin (2006)]. The basic principle of this method consists in decomposing the observations in a set of (redundant) dictionnaries chosen so that each component can be represented sparsely in one of the dictionnaries. Separation is achieved by minimizing the number of coefficients required to represent the data set.

A comparison of these different methods on a common data set, for investigating their strengths and weaknesses and evaluating their relative performance for various objectives would be an interesting work to improve the quality of component separation with the data set of upcoming space missions.

10 Conclusion and prospects

With improving data quality and increasingly demanding performance in component characterisation, component separation will play an important role in the analysis of CMB data sets in the next decade.

In this paper, we have reviewed the main issues for component separation, concentrating on diffuse components specifically.

Although substantial work has been performed, open questions remain. Polarisation, for instance, is one of the next major objectives of CMB science, for which much better sensitivities are required, and for which foreground emission is poorly known... Time varying sources, as the emission due to zodiacal light (modulated by the trajectory of the instrument in the ecliptic), as solar system objects in general, and as intrinsically time-varying radio sources, require specific methods tailored for their extraction.

The upcoming Planck data set, expected to become available to the Planck consortium in 2008, will provide a fantastic and challenging data set for extracting the emission from all astrophysical processes emitting in the millimeter range.

References

[Aghanim et al. (1996)] Aghanim, N., Desert, F. X., Puget, J. L., & Gispert, R. 1996, *Ionization by early quasars and cosmic microwave background anisotropies*, Astronomy and Astrophysics, 311, 1

[Audit & Simmons (1999)] Audit, E., & Simmons, J. F. L. 1999, *The kinematic Sunyaev-Zel'dovich effect and transverse cluster velocities*, MNRAS, 305, L27

[Baccigalupi et al.(2000)] Baccigalupi, C., et al. 2000, *Neural networks and the separation of cosmic microwave background and astrophysical signals in sky maps*, MNRAS, 318, 769

[Barreiro (2005)] Barreiro, R. B. 2006, *Techniques for compact source extraction on CMB maps*, to appear in "Data Analysis in Cosmology", Springer-Verlag Lecture Notes in Physics. Valencia, 6-10 September 2004 (ArXiv Astrophysics e-prints, arXiv:astro-ph/0512538)

[Barreiro et al. (2004)] Barreiro, R. B., Hobson, M. P., Banday, A. J., Lasenby, A. N., Stolyarov, V., Vielva, P., & Górski, K. M. 2004, *Foreground separation using a flexible maximum-entropy algorithm: an application to COBE data*, MNRAS, 351, 515

[Bennett et al. (2003)] Bennett, C. L., et al. 2003, *First-Year Wilkinson Microwave Anisotropy Probe (WMAP) Observations: Preliminary Maps and Basic Results*, ApJ Supplement Series, 148, 1

[Bennett et al. (2003)] Bennett, C. L., et al. 2003, *First year Wilkinson Microwave Anisotropy Probe (WMAP) observations: foreground emission*, ApJ Supplement Series, 148, 97

[Benoît et al. (2004)] Benoît, A., et al. 2004, *First detection of polarization of the submillimetre diffuse galactic dust emission by Archeops*, Astronomy and Astrophysics, 424, 571

[Birkinshaw (1999)] Birkinshaw, M. 1999, *The Sunyaev Zel'dovich effect* Physics Reports, 310, 97

[Bobin (2006)] Bobin, J., Moudden, Y., Starck, J.-L. and Elad, M. 2006, *Morphological Diversity and Source Separation* IEEE Transaction on Signal Processing, in press.

[Bonaldi et al.(2006)] Bonaldi, A., Bedini, L., Salerno, E., Baccigalupi, C., & de Zotti, G. 2006, *Estimating the spectral indices of correlated astrophysical foregrounds by a second-order statistical approach*, MNRAS, 373, 271

[Bouchet & Gispert (1999)] Bouchet, F. R., & Gispert, R. 1999, *Foregrounds and CMB experiments I. Semi-analytical estimates of contamination*, New Astronomy, 4, 443

[Cardoso (1998)] Cardoso, J.-F. 1998, *Blind signal separation: statistical principles*, Proceedings of the IEEE. Special issue on blind identification and estimation, vol. 9, no 10, pp. 2009-2025

[Cardoso (1999)] Cardoso, J.-F. 1999, *High-order contrasts for independent component analysis*, Neural Computation, vol. 11, no 1, pp. 157-192

[Cardoso et al. (2005)] Cardoso, J.-F., et al. 2005, *Statistiques direction-multipôle pour la séparation de composantes dans le fonds de rayonnement cosmologique*, Actes du GRETSI, Louvain-la-Neuve, Belgique

[de Bernardis et al. (2000)] de Bernardis, P., et al. 2000, *A flat Universe from high-resolution maps of the cosmic microwave background radiation*, Nature, 404, 955

[Delabrouille et al. (2003)] Delabrouille, J., Cardoso J.-F. and Patanchon, G. 2003, *Multi-detector multi-component spectral matching and application for CMB data analysis*, MNRAS, vol. 346, no 4, pp. 1089-1102

[Dickinson et al. (2004)] Dickinson, C., et al. 2004, *High-sensitivity measurements of the cosmic microwave background power spectrum with the extended Very Small Array*, MNRAS, 353, 732

[Dickinson et al. (2006)] Dickinson, C., Casassus, S., Pineda, J. L., Pearson, T. J., Readhead, A. C. S., & Davies, R. D. 2006, *An Upper Limit on Anomalous Dust Emission at 31 GHz in the Diffuse Cloud [LPH96] 201.663+1.643*, Astrophysical Journal Letters, 643, L111

[Draine & Lazarian (1998)] Draine, B. T., & Lazarian, A. 1998, *Diffuse Galactic Emission from Spinning Dust Grains*, Astrophysical Journal Letters, 494, L19

[Eriksen et al. (2004)] Eriksen, H. K., Banday, A. J., Górski, K. M., & Lilje, P. B. 2004, *On foreground removal from the WMAP data by an ILC method: limitations and implications*, ApJ, 612, 633

[Eriksen et al. (2006)] Eriksen, H. K., et al. 2006, *Cosmic Microwave Background Component Separation by Parameter Estimation*, ApJ, 641, 665

[Fernández-Cerezo et al. (2006)] Fernández-Cerezo, S., et al. 2006, *Observations of the cosmic microwave background and galactic foregrounds at 12-17GHz with the COSMOSOMAS experiment*, MNRAS, 370, 15

[Gruzinov & Hu (1998)] Gruzinov, A., & Hu, W. 1998, *Secondary Cosmic Microwave Background Anisotropies in a Universe Reionized in Patches*, The Astrophysical Journal, 508, 435

[Hansen et al.(2006)] Hansen, F. K., Banday, A. J., Eriksen, H. K., Górski, K. M., & Lilje, P. B. 2006, *Foreground Subtraction of Cosmic Microwave Background Maps Using WI-FIT (Wavelet-Based High-Resolution Fitting of Internal Templates)*, ApJ, 648, 784

[Haslam et al. (1981)] Haslam, C. G. T., Klein, U., Salter, C. J., Stoffel, H., Wilson, W. E., Cleary, M. N., Cooke, D. J., & Thomasson, P. 1981, *A 408 MHz all-sky continuum survey. I - Observations at southern declinations and for the North Polar region*, Astronomy and Astrophysics, 100, 209

[Hinshaw et al. (2006)] Hinshaw, G., et al. 2006, *Three-Year Wilkinson Microwave Anisotropy Probe (WMAP) Observations: Temperature Analysis*, ArXiv Astrophysics e-prints, arXiv:astro-ph/0603451

[Hobson & Lasenby (1998)] Hobson, M. P., & Lasenby, A. N. 1998, *The entropic prior for distributions with positive and negative values*, MNRAS, 298, 905

[Hobson et al. (1998)] Hobson, M. P., Jones, A. W., Lasenby, A. N., & Bouchet, F. R. 1998, *Foreground separation methods for satellite observations of the cosmic microwave background*, MNRAS, 300, 1

[Hu & Dodelson (2002)] Hu, W., & Dodelson, S. 2002, *Cosmic Microwave Background Anisotropies*, Annual Review of Astronomy and Astrophysics, 40, 171

[Hyvärinen (1999)] Hyvvärinen, A. 1999, *Fast and Robust Fixed-Point Algorithms for Independent Component Analysis*, IEEE Transactions on Neural Networks 10(3):626-634

[Jones et al. (2005)] Jones, W. C., et al. 2005, *A Measurement of the Angular Power Spectrum of the CMB Temperature Anisotropy from the 2003 Flight of Boomerang*, ArXiv Astrophysics e-prints, arXiv:astro-ph/0507494

[Kogut et al. (1996)] Kogut, A., Banday, A. J., Bennett, C. L., Gorski, K. M., Hinshaw, G., & Reach, W. T. 1996, *High-Latitude Galactic Emission in the COBE Differential Microwave Radiometer 2 Year Sky Maps*, The Astrophysical Journal, 460, 1

[Komatsu et al. (2003)] Komatsu, E., et al. 2003, *First-Year Wilkinson Microwave Anisotropy Probe (WMAP) Observations: Tests of Gaussianity*, ApJ Supplement Series, 148, 119

[Kuo et al. (2004)] Kuo, C. L., et al. 2004, *High-Resolution Observations of the Cosmic Microwave Background Power Spectrum with ACBAR*, The Astrophysical Journal, 600, 32

[Lamarre et al. (2000)] Lamarre, J. M., et al. 2000, *The High Frequency Instrument of Planck: Design and Performances*, Astrophysical Letters Communications, 37, 161

[Lamarre et al. (2003)] Lamarre, J. M., et al. 2003, *The Planck High Frequency Instrument, a third generation CMB experiment, and a full sky submillimeter survey*, New Astronomy Review, 47, 1017

[Leitch et al. (1997)] Leitch, E. M., Readhead, A. C. S., Pearson, T. J., & Myers, S. T. 1997, *An Anomalous Component of Galactic Emission*, Astrophysical Journal Letters, 486, L23

[Maino et al.(2002)] Maino, D., et al. 2002, *All-sky astrophysical component separation with Fast Independent Component Analysis (FASTICA)*, MNRAS, 334, 53

[Maino et al.(2003)] Maino, D., Banday, A. J., Baccigalupi, C., Perrotta, F., & Górski, K. M. 2003, *Astrophysical component separation of COBE-DMR 4-yr data with FASTICA*, MNRAS, 344, 544

[Maino et al.(2007)] Maino, D., Donzelli, S., Banday, A. J., Stivoli, F., & Baccigalupi, C. 2007, *Cosmic microwave background signal in Wilkinson Microwave Anisotropy Probe three-year data with FASTICA* MNRAS, 374, 1207

[Mandolesi et al. (2000)] Mandolesi, N., Bersanelli, M., Burigana, C., & Villa, F. 2000, *The Planck Low Frequency Instrument*, Astrophysical Letters Communications, 37, 151

[Maris et al. (2006)] Maris, M., Burigana, C., & Fogliani, S. 2006, Astronomy and Astrophysics, 452, 685

[Martínez-González et al.(2003)] Martínez-González, E., Diego, J. M., Vielva, P., & Silk, J. 2003, *Cosmic microwave background power spectrum estimation and map reconstruction with the expectation-maximization algorithm*, MNRAS, 345, 1101

[McCullough et al. (1999)] McCullough, P. R., & et al. 1999, *Implications of Halpha Observations for Studies of the CMB*, ASP Conf. Ser. 181: Microwave Foregrounds, 181, 253

[Moudden et al. (2005)] Moudden, Y., Cardoso, J.-F., Starck, J.-L., Delabrouille, J. 2005, *Blind Component Separation in Wavelet Space: Application to CMB Analysis*, Eurasip Journal on Applied Signal Processing , 2005, 15 pp 2437-2454

[Netterfield et al. (2002)] Netterfield, C. B., et al. 2002, *A Measurement by BOOMERANG of Multiple Peaks in the Angular Power Spectrum of the Cosmic Microwave Background*, The Astrophysical Journal, 571, 604

[Patanchon et al. (2005)] Patanchon, G., Cardoso, J.-F., Delabrouille, J., & Vielva, P. 2005, *Cosmic microwave background and foregrounds in Wilkinson Microwave Anisotropy Probe first-year data*, MNRAS, 364, 1185

[Ponthieu et al. (2005)] Ponthieu, N., et al. 2005, *Temperature and polarization angular power spectra of Galactic dust radiation at 353 GHz as measured by Archeops*, Astronomy and Astrophysics, 444, 327

[Puget et al. (1996)] Puget, J.-L., Abergel, A., Bernard, J.-P., Boulanger, F., Burton, W. B., Desert, F.-X., & Hartmann, D. 1996, *Tentative detection of a cosmic far-infrared background with COBE*, Astronomy and Astrophysics, 308, L5

[Readhead et al. (2004)] Readhead, A. C. S., et al. 2004, *Extended Mosaic Observations with the Cosmic Background Imager*, The Astrophysical Journal, 609, 498

[Rephaeli (2002)] Rephaeli, Y. 2002, *The Sunyaev-Zeldovich effect: Recent progress and future prospects*, AIP Conf. Proc. 616: Experimental Cosmology at Millimetre Wavelengths, 616, 309

[Sazonov & Sunyaev (1999)] Sazonov, S. Y., & Sunyaev, R. A. 1999, *Microwave polarization in the direction of galaxy clusters induced by the CMB quadrupole anisotropy* MNRAS, 310, 765

[Shannon (1948)] Shannon, 1948, *A Mathematical Theory of Communication* Bell System Technical Journal, vol. 27, pp. 379-423, 623-656, July, October, 1948

[Smoot (1998)] Smoot, G. F. 1998, emphGalactic Free-Free and H-alpha emission, ArXiv Astrophysics e-prints, arXiv:astro-ph/9801121

[Stolyarov et al. (2002)] Stolyarov, V., Hobson, M. P., Ashdown, M. A. J., & Lasenby, A. N. 2002, *All-sky component separation for the Planck mission*, MNRAS, 336, 97

[Sunyaev & Zeldovich (1972)] Sunyaev, R. A., & Zeldovich, Y. B. 1972, *The Observations of Relic Radiation as a Test of the Nature of X-Ray Radiation from the Clusters of Galaxies* Comments on Astrophysics and Space Physics, 4, 173

[Sunyaev & Zeldovich (1980)] Sunyaev, R. A., & Zeldovich, I. B. 1980, *The velocity of clusters of galaxies relative to the microwave background - The possibility of its measurement* MNRAS, 190, 413

[Tegmark & Efstathiou (1996)] Tegmark, M., & Efstathiou, G. 1996, *A method for subtracting foregrounds from multifrequency CMB sky maps*, MNRAS, 281, 1297

[Tegmark et al.(2000)] Tegmark, M., Eisenstein, D. J., Hu, W., & de Oliveira-Costa, A. 2000, *Foregrounds and Forecasts for the Cosmic Microwave Background*, The Astrophysical Journal, 530, 133

[Tegmark et al. (2003)] Tegmark, M., de Oliveira-Costa, A., & Hamilton, A. J. 2003, *High resolution foreground cleaned CMB map from WMAP* Phys. Rev. D., 68, 123523

[Tristram et al. (2005)] Tristram, M., et al. 2005, *The CMB temperature power spectrum from an improved analysis of the Archeops data*, Astronomy and Astrophysics, 436, 785

[Valls-Gabaud (1998)] Valls-Gabaud, D. 1998, *Cosmological applications of H-alpha surveys*, Publications of the Astronomical Society of Australia, 15, 111

[White & Cohn (2002)] White, M., & Cohn, J. D. 2002, *The theory of anisotropies in the cosmic microwave background*, American Journal of Physics, 70, 106

[Wiener (1949)] Wiener, N. 1949, *Extrapolation, Interpolation, and Smoothing of Stationary Time Series*. New York: Wiley. ISBN 0262730057

[Yamada et al. (1999)] Yamada, M., Sugiyama, N., & Silk, J. 1999, *The Sunyaev-Zeldovich Effect by Cocoons of Radio Galaxies*, The Astrophysical Journal, 522, 66

A&A 491, 597–615 (2008)
DOI: 10.1051/0004-6361:200810116

Astronomy & Astrophysics

Component separation methods for the PLANCK mission

S. M. Leach[1,2], J.-F. Cardoso[3,4], C. Baccigalupi[1,2], R. B. Barreiro[5], M. Betoule[3], J. Bobin[6], A. Bonaldi[7,8], J. Delabrouille[3], G. de Zotti[1,7], C. Dickinson[9], H. K. Eriksen[10,11], J. González-Nuevo[1], F. K. Hansen[10,11], D. Herranz[5], M. Le Jeune[3], M. López-Caniego[12], E. Martínez-González[5], M. Massardi[1], J.-B. Melin[13], M.-A. Miville-Deschênes[14], G. Patanchon[3], S. Prunet[15], S. Ricciardi[7,16], E. Salerno[17], J. L. Sanz[5], J.-L. Starck[6], F. Stivoli[1,2], V. Stolyarov[12], R. Stompor[3], and P. Vielva[5]

[1] SISSA - ISAS, Astrophysics Sector, via Beirut 4, 34014 Trieste, Italy
e-mail: leach@sissa.it
[2] INFN, Sezione di Trieste, via Valerio 2, 34014 Trieste, Italy
[3] CNRS & Université Paris 7, Laboratoire APC, 10 rue A. Domon et L. Duquet, 75205 Paris Cedex 13, France
[4] Laboratoire de Traitement et Communication de l'Information (CNRS and Telecom ParisTech), 46, rue Barrault, 75634 Paris, France
[5] Instituto de Física de Cantabria (CSIC-UC), Avda. de los Castros s/n, 39005 Santander, Spain
[6] CEA - Saclay, SEDI/Service d'Astrophysique, 91191 Gif-Sur-Yvette, France
[7] INAF - Osservatorio Astronomico di Padova, vicolo dell'Osservatorio 5, 35122 Padova, Italy
[8] Dipartimento di Astronomia, vicolo dell'Osservatorio 5, 35122 Padova, Italy
[9] Infrared Processing and Analysis Center, California Institute of Technology, M/S 220-6, 1200 E. California Blvd, Pasadena, 91125, USA
[10] Institute of Theoretical Astrophysics, University of Oslo, PO Box 1029 Blindern, 0315 Oslo, Norway
[11] Centre of Mathematics for Applications, University of Oslo, PO Box 1053 Blindern, 0316 Oslo, Norway
[12] Astrophysics Group, Cavendish Laboratory, J J Thomson Avenue, Cambridge CB3 0HE, UK
[13] DSM/Irfu/SPP, CEA/Saclay, 91191 Gif-sur-Yvette Cedex, France
[14] Institut d'Astrophysique Spatiale, Bâtiment 121, 91405 Orsay, France
[15] Institut d'Astrophysique de Paris, 98 bis Boulevard Arago, 75014 Paris, France
[16] Space Sciences Laboratory, University of California Berkeley, Computational Cosmology Center, Lawrence Berkeley National Laboratory, CA 94720, USA
[17] Istituto di Scienza e Technologie dell'Informazione, CNR, Area della ricerca di Pisa, via G. Moruzzi 1, 56124 Pisa, Italy

Received 2 May 2008 / Accepted 17 September 2008

ABSTRACT

Context. The satellite will map the full sky at nine frequencies from 30 to 857 GHz. The CMB intensity and polarization that are its prime targets are contaminated by foreground emission.
Aims. The goal of this paper is to compare proposed methods for separating CMB from foregrounds based on their different spectral and spatial characteristics, and to separate the foregrounds into "components" with different physical origins (Galactic synchrotron, free-free and dust emissions; extra-galactic and far-IR point sources; Sunyaev-Zeldovich effect, etc.).
Methods. A component separation challenge has been organised, based on a set of realistically complex simulations of sky emission. Several methods including those based on internal template subtraction, maximum entropy method, parametric method, spatial and harmonic cross correlation methods, and independent component analysis have been tested.
Results. Different methods proved to be effective in cleaning the CMB maps of foreground contamination, in reconstructing maps of diffuse Galactic emissions, and in detecting point sources and thermal Sunyaev-Zeldovich signals. The power spectrum of the residuals is, on the largest scales, four orders of magnitude lower than the input Galaxy power spectrum at the foreground minimum. The CMB power spectrum was accurately recovered up to the sixth acoustic peak. The point source detection limit reaches 100 mJy, and about 2300 clusters are detected via the thermal SZ effect on two thirds of the sky. We have found that no single method performs best for all scientific objectives.
Conclusions. We foresee that the final component separation pipeline for will involve a combination of methods and iterations between processing steps targeted at different objectives such as diffuse component separation, spectral estimation, and compact source extraction.

Key words. cosmology: cosmic microwave background – methods: data analysis

1. Introduction

is a European Space Agency space mission whose main objective is to measure the cosmic microwave background (CMB) temperature and polarization anisotropies with high accuracy, high angular resolution and with unprecedented frequency coverage (The Planck Collaboration 2005). In anticipation of the launch, is stimulating much research and development into data processing methods that are capable of addressing the ambitious science programme enabled by these multi-frequency observations. It is expected that will break new ground in studies of the CMB, of the interstellar

Article published by EDP Sciences

medium and Galactic emission mechanisms on scales down to a few arcminutes, as well as of the emission from many extragalactic objects.

The processing of such multi-frequency data depends on both the science goals, as well as on the signal to noise regime and on the overall level and complexity of foreground contamination. This observation is borne out by a brief historical perspective on CMB data processing.

An example of the low foreground level and complexity regime is provided by the observations made by Boomerang at 145, 245 and 345 GHz (Masi et al. 2006), which targeted a region of sky with low emission from a single dust foreground. Here the two higher frequency channels acted as foreground monitors for the 145 GHz CMB deep survey, and were used to estimate that the foreground contamination at 145 GHz was at an rms level of less than 10 μK on angular scales of 11.5′ (Table 10, Masi et al. 2006). The 145 GHz CMB maps were then used for the purpose of power spectrum estimation in both temperature and polarization, after masking away a handful of compact sources (Jones et al. 2006). Masi et al. (2006) estimate that the cleanest 40% of the sky have a level of dust brightness fluctuations similar to those of the Boomerang observations, and that the cleanest 75% of the sky have brightness fluctuations less than three times larger.

An example of the high foreground level and complexity regime is available with the all-sky observations of the mission in five frequency channels from 23 to 94 GHz (Bennett et al. 2003a; Hinshaw et al. 2008). In this frequency range, the emission from at least three Galactic components (synchrotron, free-free and dust), as well as contamination by unresolved point sources must be contended with. also gives a clear example of science goal dependent data processing: CMB maps for use in non-Gaussianity tests are obtained from a noise-weighted sum of frequency maps at differing angular resolution, for which the regions most contaminated by foregrounds are masked (Komatsu et al. 2003); The analysis leading to the cosmological parameter estimation involves foreground cleaning by template subtraction, masking of the most contaminated 15% of sky, and subtracting a model of the contribution of unresolved point sources from the CMB cross power spectra (Hinshaw et al. 2003, 2007). For an improved understanding of galactic emission, the WMAP team have used a number of methods including template fits, internal linear combination (ILC), the maximum entropy method, and the direct pixel-by-pixel fitting of an emission model (Gold et al. 2008; Dunkley et al. 2008).

1.1. Component separation

Component separation is a catch-all term encompassing any data processing that exploits correlations in observations made at separate frequencies, as well as external constraints and physical modeling, as a means of distinguishing between different physical sources of emission.

has a number of different scientific objectives: the primary goal is a cosmological analysis of the CMB, but important secondary goals include obtaining a better understanding of the interstellar medium and Galactic emission, measurement of extragalactic sources of emission and the generation of a Sunyaev-Zeldovich (SZ) cluster catalogue. These planned objectives will lead to a set of data products which the consortium is committed to delivering to the wider community some time after the completion of the survey. These data products include maps of the main diffuse emissions and catalogues of extragalactic sources, such as galaxies and clusters of galaxies.

In this context, it is worth remembering that is designed to recover the CMB signal at the level of a few microkelvin per resolution element of 5′ (and less than one microkelvin per square degree). Numbers to keep in mind are the rms of CMB smoothed with a beam of 45′ *FWHM*, which is around 70 μK, while the rms of white noise at the same scale is around 0.7 μK. This level of sensitivity sets the ultimate goals for data processing – and component separation in particular – if the full scientific potential of is to be realised. However, less stringent requirements may be acceptable for statistical analyses such as power spectrum estimation, in particular on large scales where cosmic variance dominates the error of total intensity observations.

1.2. WG2

is designed to surpass previous CMB experiments in almost every respect. Therefore, a complete and timely exploitation of the data will require methods that improve upon foreground removal via template subtraction and masking. The development and assessment of such methods is coordinated within the "Component Separation Working Group" (WG2). Another working group in the collaboration, the C_ℓ temperature and polarization working group (WG3 or "CTP"), investigates other critical data analysis steps, in particular, map-making (Poutanen et al. 2006; Ashdown et al. 2007) and power spectrum estimation.

The present paper reports the results of the WG2 activity in the framework of a *component separation challenge* using a common set of simulated data.[1] In turn, this exercise provides valuable feedback and validation during the development of the Sky Model.

This is the first time, within the collaboration, that an extensive comparison of component separation methods has been attempted on simulated data based on models of sky emissions of representative complexity. As will be seen and emphasised throughout this paper, this aspect is critical for a meaningful evaluation of the performance of any separation method. In this respect, the present work significantly improves on the semi-analytical estimates of foreground contamination obtained by Bouchet & Gispert (1999) for the phase A study, as well as on previous work by Tegmark et al. (2000) .

The paper is organised as follows: In Sect. 2 we describe the sky emission model and simulations that were used, and describe the methodology of the Challenge. In Sect. 3 we give an overview of the methods that have been implemented and took part in the analysis. In Sect. 4 we describe the results obtained for CMB component separation and power spectrum estimation. The results for point sources, SZ and Galactic components are described in Sects. 5 and 6 we present our summary and conclusions. In Appendix A we provide a more detailed description of the methods, their implementation details and their strengths and weaknesses.

2. The challenge

The objective of the component separation challenge discussed herein is to assess the readiness of the collaboration to

[1] A similar data challenge has been undertaken in the past in the context of simulated and sub-orbital CMB data (the WOMBAT challenge; Gawiser et al. 1998).

tackle component separation, based on the analysis of realistically complex simulations. It offers an opportunity for comparing the results from different methods and groups, as well as to develop the expertise, codes, organisation and infrastructure necessary for this task.

This component separation challenge is designed so as to test on realistic simulated data sets, component separation methods and algorithms in a situation as close as possible to what is expected when actual data will be analysed. Hence, we assume the availability of a number of ancillary data sets. In particular, we assumed that six-year observations will be available. Although is significantly less sensitive than , it provides very useful complementary information for the separation of low-frequency Galactic components. This section describes our simulations, the challenge setup, and the evaluation methodology.

2.1. Sky emission

Our sky simulations are based on an early development version of the Sky Model (PSM, in preparation), a flexible software package developed by WG2 for making predictions, simulations and constrained realisations of the microwave sky.

The CMB sky is based on the observed multipoles up to $\ell = 70$, and on a Gaussian realisation assuming the best-fit C_ℓ at higher multipoles. It is the same CMB map used by Ashdown et al. (2007).

The Galactic interstellar emission is described by a three component model of the interstellar medium comprising of free-free, synchrotron and dust emissions. The predictions are based on a number of sky templates which have different angular resolution. In order to simulate the sky at resolution we have added small scale fluctuations to some of the templates. The procedure used is the one presented in Miville-Deschênes et al. (2007) which allows to increase the fluctuation level as a function of the local brightness and therefore reproduce the non-Gaussian properties of the interstellar emission.

Free-free emission is based on the model of Dickinson et al. (2003) assuming an electronic temperature of 7000 K. The spatial structure of the emission is estimated using a Hα template corrected for dust extinction. The Hα map is a combination of the Southern H-Alpha Sky Survey Atlas (SHASSA) and the Wisconsin H-Alpha Mapper (WHAM). The combined map was smoothed to obtain a uniform angular resolution of 1°. For the extinction map we use the $E(B-V)$ all-sky map of Schlegel et al. (1998) which is a combination of a smoothed IRAS 100 μm map (with resolution of 6.1′) and a map at a few degrees resolution made from DIRBE data to estimate dust temperature and transform the infrared emission in extinction. As mentioned earlier, small scales were added in both templates to match the resolution.

Synchrotron emission is based on an extrapolation of the 408 MHz map of Haslam et al. (1982) from which an estimate of the free-free emission was removed. The spectral emission law of the synchrotron is assumed to follow a perfect power law, $T_b^{\rm sync} \propto \nu^\beta$. We use a pixel-dependent spectral index β derived from the ratio of the 408 MHz map and the estimate of the synchrotron emission at 23 GHz in the data obtained by Bennett et al. (2003b) using a Maximum Entropy Method technique. A limitation of this approach is that this synchrotron model also contains any "anomalous" dust correlated emission seen by at 2 GHz.

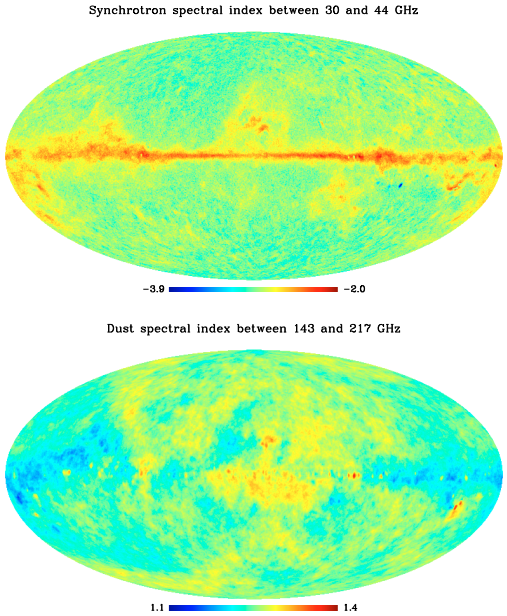

Fig. 1. Synchrotron and dust (effective powerlaw) spectral indices evaluated between 30 and 44 GHz, and 143 and 217 GHz respectively (in μK_{RJ}). A spatially varying spectral index corresponds to a foreground morphology that varies with frequency.

The thermal emission from interstellar dust is estimated using model 7 of Finkbeiner et al. (1999). This model, fitted to the FIRAS data (7° resolution), makes the hypothesis that each line of sight can be modelled by the sum of the emission from two dust populations, one cold and one hot. Each grain population is in thermal equilibrium with the radiation field and thus has a grey-body spectrum, so that the total dust emission is modelled as

$$I_\nu \propto \sum_{i=1}^{2} f_i \nu^{\beta_i} B_\nu(T_i) \qquad (1)$$

where $B_\nu(T_i)$ is the Planck function at temperature T_i. In model 7 the emissivity indices are $\beta_1 = 1.5$, $\beta_2 = 2.6$, and $f_1 = 0.0309$ and $f_2 = 0.9691$. Once these values are fixed, the dust temperature of the two components is determined using only the ratio of the observations at two wavelengths, 100 μm and 240 μm. For this purpose, we use the 100/240 μm map ratio published by Finkbeiner et al. (1999). Knowing the temperature and β of each dust component at a given position on the sky, we use the 100 μm brightness at that position to scale the emission at any frequency using Eq. (1). We emphasise that the emission laws of the latter two components, synchrotron and dust, vary across the sky as shown in Fig. 1. The spectral index of free-free is taken to be uniform on the sky since it only depends on the electronic temperature, taken as a constant here.

Point sources are modelled with two main categories: radio and infra-red. Simulated radio sources are based on the NVSS or SUMSS and GB6 or PMN catalogues. Measured fluxes at 1 and/or 4.85 GHz are extrapolated to frequencies assuming a distribution in flat and steep populations. For

Table 1. Characteristics of one year simulations (*upper*) and six year simulations (*lower*). and hit counts correspond to 1.7′ (Healpix $n_{\rm side}$ = 2048) and 6.8′ ($n_{\rm side}$ = 512) pixels respectively. N_ℓ is the white noise level calculated from the inhomogeneous distribution of hits.

Channel	30 GHz	44 GHz	70 GHz	100 GHz	143 GHz	217 GHz	353 GHz	545 GHz	857 GHz
FWHM [arcmin]	33	24	14	10	7.1	5	5	5	5
$\sigma_{\rm hit}$ [μK$_{\rm RJ}$]	1030	1430.	2380	1250	754	610	425	155	72
$\sigma_{\rm hit}$ [μK$_{\rm CMB}$]	1050	1510	2700	1600	1250	1820	5470	24 700	1 130 000
Mean; Median hits per pixel	82; 64	170; 134	579; 455	1010; 790	2260; 1790	2010; 1580	2010; 1580	503; 396	503; 396
$N_\ell^{1/2}$ [μK$_{\rm CMB}$]	0.066	0.065	0.063	0.028	0.015	0.023	0.068	0.62	28.4

Channel	23 GHz (K)	33 GHz (Ka)	41 GHz (Q)	61 GHz (V)	94 GHz (W)
FWHM [arcmin]	52.8	39.6	30.6	21	13.2
$\sigma_{\rm hit}$ [μK$_{\rm RJ}$]	1420	1420	2100	2840	5210
$\sigma_{\rm hit}$ [μK$_{\rm CMB}$]	1440	1460	2190	3120	6500
Mean; Median hits per pixel	878; 792	878; 790	2198; 1889	2956; 2577	8873; 7714
$N_\ell^{1/2}$ [μK$_{\rm CMB}$]	0.10	0.10	0.10	0.12	0.14

each of these two populations, the spectral index is randomly drawn from within a set of values compatible with the typically observed mean and dispersion. Infrared sources are based on the catalogue, and modelled as dusty galaxies (Serjeant & Harrison 2005). IRAS coverage gaps were filled by adding simulated sources with a flux distribution consistent with the mean counts. Fainter sources were assumed to be mostly sub-millimeter bright galaxies, such as those detected by SCUBA surveys. These were modelled following Granato et al. (2004) and assumed to be strongly clustered, with a comoving clustering radius $r_0 \simeq 8\ h^{-1}$ Mpc. Since such sources have a very high areal density, they are not simulated individually but make up the sub-mm background.

We also include in the model a map of thermal SZ spectral distortions from galaxy clusters, based on a simulated cluster catalogue drawn from a mass-function compatible with present-day observations and with ΛCDM parameters $\Omega_{\rm m} = 0.3$, $h = 0.7$ and $\sigma_8 = 0.9$ (Colafrancesco et al. 1997; de Zotti et al. 2005).

Component maps are produced at all and central frequencies. They are then co-added and smoothed with Gaussian beams as indicated in Table 1. A total of fourteen monochromatic maps have been simulated.

Finally, inhomogeneous noise is obtained by simulating the hit counts corresponding to one year of continuous observations by , using the Level-S simulations tool (Reinecke et al. 2006). An example of a hit count map is shown in the upper panel of Fig. 2. six year hit counts, obtained from scaling up the observed three year hit count patterns, are used to generate inhomogeneous noise in the simulated observations. The rms noise level per hit for both experiments is given in Table 1.

2.2. Challenge setup

The simulated data sets were complemented by a set of ancillary data including hitmaps and noise levels, IRAS, 408 MHz, and Hα templates, as well as catalogues of known clusters from ROSAT and of known point sources from NVSS, SUMSS, GB6, PMN and IRAS.

The Challenge proceeded first with a blind phase lasting around four months between August and November 2006, when neither the exact prescription used to simulate sky emission from these ancillary data sets, nor maps of each of the input components, were communicated to challenge participants.

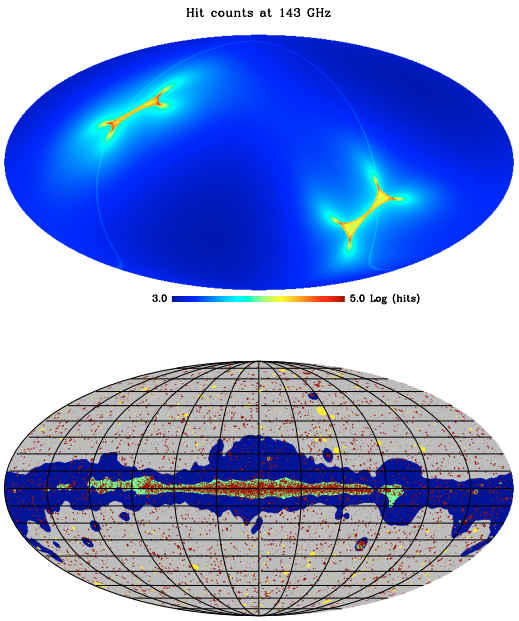

Fig. 2. *Upper panel*: hit counts for the 143 GHz channel. The inhomogeneities at the ecliptic poles are characteristic of 's cycloidal scanning strategy. *Lower panel*: the masking scheme separating the sky in three regions of different foreground contamination. The grey region at high Galactic latitudes is Zone 1, covering $f_{\rm sky} = 74\%$. The darker region at lower Galactic latitudes is Zone 2 and covers $f_{\rm sky} = 22\%$. The remaining region (green) along the Galactic ridge is Zone 3. The point source mask (red) covers 4% of Zone 1. The SZ mask (yellow) cuts detected SZ clusters at Galactic latitudes above 20 degrees, covering 1.4% of sky.

After this phase and an initial review of the results at the WG2 meeting in Catania in January 2007, the Challenge moved to an open phase lasting from January to June 2007. In this phase the input data-CMB maps and power spectrum, Galactic emission maps, SZ Compton y parameter map, point source

catalogues and maps, noise realisations – were made available to the participating groups.

All of the results presented here have been obtained after several iterations and improvements of the methods, both during the comparison of the results obtained independently by the various teams, and after the input data was disclosed. Hence, the challenge has permitted significant improvement of most of the methods and algorithms developed within the collaboration. The analysis of the Challenge results was led by the simulations team, with involvement and discussion from all participating groups.

Deliverables

A set of standard deliverables were defined. These included: a CMB map with 1.7′ pixels (Healpix $N_{\rm side} = 2048$) together with a corresponding map of estimated errors; the effective beam F_ℓ, which describes the total smoothing of the recovered CMB map due to a combination of instrumental beams and the filtering induced by the component separation process; a set of binned CMB power spectrum estimates (band averages of $\ell(\ell+1)C_\ell$) and error bars; maps of all the diffuse components identified in the data; catalogues of the infrared and radio sources, and SZ clusters; a map of the SZ Compton y parameter.

Masks

Different separation methods are likely to perform differently in either foreground-dominated or noise-dominated observations. Also, they may be more or less sensitive to different types of foregrounds. Since the level of foreground contamination varies strongly across the sky, we used a set of standard masks throughout this work, and they are shown in the lower panel of Fig. 2.

The sky is split into three distinct Galactic "Zones": Zone 1 is at high Galactic latitudes and covers 74% of sky, similar to the WMAP Kp0 mask with smoother edges and small extensions. Zone 2 is at lower Galactic latitudes and covers 22% of sky. The remaining 4% of sky is covered by Zone 3, which is similar to the WMAP Kp12 mask.

The point source mask is the product of nine masks, each constructed by excluding a two *FWHM* region around every source with a flux greater than 200 mJy at the corresponding frequency channel. This point source mask covers 4% of sky in Zone 1. For comparison, the point source masks of Bennett et al. (2003b) excludes a radius of 0.7° around almost 700 sources with fluxes greater than 500 mJy, covering a total of 2% of sky.

The SZ mask is constructed by blanking out small circular regions centered on 1625 SZ clusters detected with the needlet-ILC + matched filter method (see Sect. 5.2). For each of them, the diameter of the cut is equal to the virial radius of the corresponding cluster.

2.3. Comments about the sky emission simulations

A note of caution about these simulations of sky emission is in order. Although the PSM, as described above, has a considerable amount of sophistication, it still makes some simplifying assumptions – and cannot be expected to describe the full complexity of the real sky. This is a critical issue, as component separation methods are very sensitive to these details. We mention four of them.

First, Galactic emission is modelled with only three components, with no anomalous emission at low frequencies. This affects the spectral behaviour of components in the lower frequency bands below 60 GHz where the anomalous emission is thought to be dominant (Davies et al. 2006; Bonaldi et al. 2007; Miville-Deschênes et al. 2008).

Second, even though variable spectral emission laws are used for synchrotron and dust emission, this is still an idealisation: for the synchrotron, the emission law in each pixel is described by a single spectral index without any steepening. For dust, the emission is modelled as a superposition of two populations, with distinct but fixed temperature and emissivity. These approximations impact component separation, since almost perfect estimation of the relevant parameters of a given foreground emission is possible at frequencies where this foreground dominates, thereby allowing perfect subtraction in the cosmological channels.

Third, it is worth mentioning that only low resolution (∼1°) templates are available for synchrotron and free-free emissions. Hence, addition of small-scale power is critical: if such scales were absent from the simulations, but actually significant in the real sky, one might get a false impression that no component separation is needed on small scales. Also, the detection of point sources as well as galaxy clusters would be significantly easier, hence not representative of the actual problem. Here, missing small scale features are simulated using a non-stationary coloured Gaussian random field. Although quite sophisticated, this process can not generate for instance, filamentary or patchy structures known to exist in the real sky.

Fourth, our simulations are somewhat idealised in the sense that we use perfect Gaussian beams, assume no systematic effects, and assume that the noise is uncorrelated from pixel to pixel and from channel to channel. Also, the effect of the finite bandpass of the frequency channels is not taken into account, and we assume that the calibration and zero levels of each channel is perfectly known.

In spite of these simplifications, component separation remains a difficult task with our simulated data because of pixel-dependent spectral emission laws for dust and synchrotron, and of the presence of more than a million point sources with different emission laws, of hundreds of thousands of unresolved or extended SZ clusters, and of significant emission from a complex IR background. It is fair to say that this simulated sky is far more complex than anything ever used in similar investigations.

In closing this Section, we show in Fig. 3 the angular power spectra of the basic components for the 70 and 100 GHz channels, close to the foreground emission minimum. The spectra of CMB, noise and thermal SZ are compared to the spectra of the total Galactic emission evaluated at high and low Galactic latitudes, on Zone 1 and 2 respectively. The point source spectra are evaluated in Zone 1, both with and without the brightest sources above 200 mJy masked. Figure 3 shows the obvious impact on CMB studies of masking the most foreground-contaminated regions. It also indicates that there is a significant region of sky, Zone 2, for which Galactic emission and CMB power are comparable. In the following sections, results are evaluated independently in both Zones 1 and 2.

3. Outline of the methods

In this section we present a brief overview of the methods that have been used in this challenge. The section is divided in three parts, one for diffuse component separation methods, one for point source extraction, and one for SZ cluster extraction.

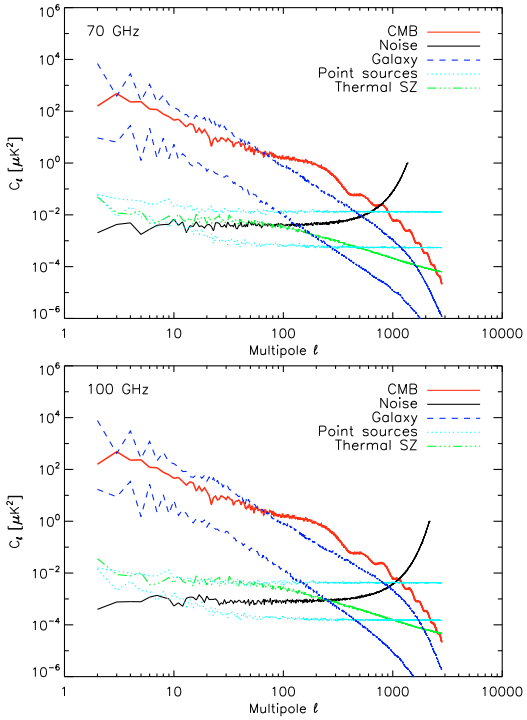

Fig. 3. Spectra of the simulated microwave sky components near the foreground minimum. CMB, noise with the effect of beam deconvolution, and the thermal SZ effect are evaluated on the full sky; point source power is evaluated on Zone 1 + 2 both with and without sources above 200 mJy masked; the galaxy power spectra are evaluated on Zone 1 and on Zone 2. The well-known importance of masking is evident, as is the fact that there is a significant proportion of sky (Zone 2, $f_{\rm sky} = 22\%$) for which Galactic emission is comparable to CMB power.

3.1. Diffuse component separation

The spirit of each method tested on the challenge data is outlined here. A more detailed description, including some details of their implementations and a discussion of their strengths and weaknesses is presented in Appendix A.

First we define some relevant terminology. The data model for a given channel ν is

$$d_\nu = b_\nu * x_\nu + n_\nu \tag{2}$$

where d_ν, x_ν, n_ν are respectively the observation map, the sky emission map and the noise map at frequency ν while b_ν is the instrumental beam of channel ν, assumed to be Gaussian symmetric, and $*$ denotes convolution on the sphere. The sky emission itself, x_ν, is a superposition of components. Most methods assume (implicitly or explicitly), that it can be written as a linear mixture

$$x_\nu = \sum_c A_{\nu c} s_c \tag{3}$$

where the sum runs over the components. In matrix-vector format, this reads $\boldsymbol{x} = \mathsf{A}\boldsymbol{s}$ where A is referred to as the "mixing matrix". Vector $\boldsymbol{s}$ is the vector of components. Vectors $\boldsymbol{d}$ and $\boldsymbol{n}$ are defined similarly. When this model holds, Eq. (2) becomes

$$d_\nu = b_\nu * \left(\sum_c A_{\nu c} s_c \right) + n_\nu. \tag{4}$$

In simple models, matrix A is constant over the sky; in more complex models, it varies over patches or even from pixel to pixel.

We now briefly describe each of the methods that performed component separation of the CMB (and possibly other diffuse components), and also mention how the CMB angular power spectrum is estimated.

- **Gibbs sampling** (Commander; Eriksen et al. 2008). The approach of Commander is to fit directly an explicit parametric model of CMB, foregrounds and noise to the antenna temperature of low-resolution map pixels. For the Challenge, Commander was used to analyse the data smoothed to 3° resolution at each channel with a pixel size of 54′ (Healpix $N_{\rm side} = 64$). For a given foreground model, Commander provides an exact foreground-marginalised CMB C_ℓ distributions using the Gibbs (conditional) sampling approach.
- **Correlated component analysis** (CCA; Bedini et al. 2005). The CCA approach starts with an estimation of the mixing matrix on patches of sky by exploiting spatial correlations in the data, supplemented by constraints from external templates and foreground scaling modeling. The estimated parameters are then used to reconstruct the components by Wiener filtering in the harmonic domain. The C_ℓ are estimated from the recovered CMB map.
- **Independent component analysis** (FastICA; Maino et al. 2002). The FastICA method is a popular approach to blind component separation. No assumptions are made about the frequency scaling or mixing matrix. Instead, assuming statistical independence between CMB and foregrounds, the mixing matrix is estimated by maximizing the non-gaussianity of the 1-point distribution function of linear combinations of input data. The inferred mixing matrix is used to invert the linear system of Eq. (4). The C_ℓ's are estimated from the recovered CMB map.
- **Harmonic-space maximum entropy method** (FastMEM; Hobson et al. 1998; Stolyarov et al. 2002). The FastMEM method estimates component maps given frequency scaling models and external foreground power spectra (and cross-power spectra) with adjustable prior weight. It is a non-blind, non-linear approach to inverting Eq. (4), which assumes a maximum-entropy prior probability distribution for the underlying components. The C_ℓ's are estimated from the recovered CMB component.
- **Generalised morphological component analysis** (GMCA; Bobin et al. 2007). Generalised Morphological Component Analysis is a semi-blind source separation method which disentangles the components by assuming that each of them is sparse in a fixed appropriate waveform dictionary such as wavelets. For the Challenge two variants of GMCA were applied: GMCA-blind was optimised for separation of the CMB component, and GMCA-model was optimised for separation of galactic components. The C_ℓ's are estimated from the recovered CMB map from the GMCA-blind method.
- **Spectral estimation via expectation maximisation** (SEVEM; Martínez-González et al. 2003). SEVEM performs component separation in three steps. In a first step, an internal template subtraction is performed in order to obtain foreground-reduced CMB maps in three centre channels

Table 2. Some characteristics of the diffuse component separation methods used in the challenge.

	Channels used	Components modelled	Resources and runtime
COMMANDER	, 30–353 GHz,	CMB, dust, sync, FF, mono-,dipoles	1000 CPU h, 2 day
CCA	, Haslam 408 MHz	CMB, dust, sync, FF	70 CPU h, 1.5 day
GMCA	, Haslam 408 MHz	CMB, SZ, sync., FF	1200 CPU h, 6 day
FastICA	143–353 GHz	Two components (CMB and dust)	21 CPU min, 20 s
FastMEM		CMB, SZ, dust, sync, FF	256 CPU h, 8 h
SEVEM		CMB	30 CPU h, 30 h
SMICA	,	CMB, SZ, dust, total galaxy	8 CPU h, 4 h
WI-FIT	70–217 GHz	CMB	400 CPU h, 8 h

(100–217 GHz). Then the CMB power spectrum is estimated from these maps, via the EM algorithm, assuming a signal plus (correlated) noise model. A final CMB map is obtained using a harmonic Wiener filter on the foreground-reduced maps.

– **Spectral matching independent component analysis** (SMICA; Delabrouille et al. 2003; Cardoso et al. 2008). The SMICA method estimates model parameters using observation correlations in the harmonic domain (auto- and cross-spectra). The estimated parameters are typically some mixing coefficients and the power spectra of independent components. For the challenge, the correlations between Galactic components are taken into account. The estimated parameters are then used to Wiener-filter the observations to obtain component maps. At small scales the C_ℓ's are one of the estimated parameters. At large scales $\ell \leq 100$ the C_ℓ's are estimated from a CMB map obtained using the ILC method.
– **Wavelet based high resolution fitting of internal templates** (WI-FIT; Hansen et al. 2006). The WI-FIT method computes CMB-free foreground plus noise templates from differences of the observations in different channels, and uses those to fit and subtract foregrounds from the CMB dominated channels in wavelet space. The C_ℓ's are estimated from the recovered CMB map.

Some characteristics of these methods are summarised in Table 2, which shows the data used, the components modelled and a rough indication of the computational resources required.

Note that many different approaches to diffuse component separation are represented here: blind, non-blind, semi-blind; methods based on linear combinations for foreground extraction; likelihood based methods which estimate parameters of a model of the foregrounds and the CMB; a maximum entropy method; methods based on cross correlations; a method based on sparsity. They also rely on very diverse assumptions and models.

3.2. Point source extraction

In the present challenge, point sources are detected in all channels independently. Two methods are used, the first based on a new implementation of matched filtering, and the second using the second member of the Mexican Hat Wavelet Family of filters (González-Nuevo et al. 2006). Point sources are detected by thresholding on the filtered maps.

This corresponds to a first step for effective point source detection. It does not exploit any prior information on the position of candidate sources; Such information can be obtained from external catalogues as in López-Caniego et al. (2007), or from detections in other channels. Neither does this approach exploit the coherence of the contaminants throughout frequencies, nor try to detect point sources *jointly* in more than one channel. Hence, there is margin for improvement.

– **Matched Filter** (MF): the high spatial variability of noise and foreground emission suggests using local filters (for instance on small patches). The sky is divided into 496 overlapping circular regions 12 degrees in diameter. Matched filtering is applied on each patch independently. A local estimate of the power spectrum of the background is obtained from the data themselves by averaging the power in circular frequency bins. A first pass is performed to detect and remove the brightest sources (above 20σ), in order to reduce the bias in background power estimation and to reduce possible artifacts in the filtered maps. Having removed these bright sources, the 5σ level catalogue is obtained by a second application of the whole procedure.
– **Mexican Hat Wavelet (MHW2)**: in a similar way, the sky is divided into 371 square patches. The size of each patch is 14.65×14.65 square degrees, with a 3 degree overlap among patches. Each patch is then individually filtered with the MHW2. For each patch, the optimal scale of the wavelet is obtained by means of a fast maximization of the wavelet gain factor. This step requires only a straightforward estimation of the variance of the patch, excluding the border and masking any sources above 30σ. A 5σ level catalogue is obtained by simple thresholding in a single step.

3.3. SZ cluster extraction

In the present data challenge, we address both the question of building an SZ catalogue, and of making a map of thermal SZ emission.

SZ map: three methods successfully produced SZ maps: ILC in harmonic space, ILC on a needlet frame, and SMICA. For ILC methods, the data are modelled as $\boldsymbol{d} = \boldsymbol{a}s + \boldsymbol{n}$ where $\boldsymbol{d}$ is the vector of observations (nine maps here, using data only), $\boldsymbol{a}$ is the SZ spectral signature at all frequencies (a vector with nine entries), s is the component amplitude and $\boldsymbol{n}$ is the noise. The ILC provides an estimator $\widehat{s}_{\rm ILC}$ of s using

$$\widehat{s}_{\rm ILC} = \frac{\boldsymbol{a}^t\, \widehat{\mathsf{R}}^{-1}}{\boldsymbol{a}^t\, \widehat{\mathsf{R}}^{-1}\, \boldsymbol{a}}\, \boldsymbol{d} \qquad (5)$$

where $\widehat{\mathsf{R}}$ is the empirical correlation of the observations, i.e. a 9×9 matrix, with entries $R_{\nu\nu'}$. In practice, the filter is implemented in bands of ℓ (ILC in harmonic space) or on subsets of needlet coefficients (ILC in needlet space). The needlet-ILC adapts to the local background to recover the SZ sky.

SZ catalogue: three main methods were used to obtain the cluster catalogue:

– the first one uses a single frequency matched filter (Melin et al. 2006) to extract clusters from the needlet-ILC map;

– the second one uses SExtractor (Bertin & Arnouts 1996) to extract clusters from the needlet-ILC map. Then, a single frequency matched filter is used to estimate cluster fluxes;
– the third is a Matched MultiFilter (Herranz et al. 2002), which implements cluster detection using the full set of input observations rather than from an intermediate SZ map. This third method is implemented independently in Saclay and in Santander.

The performance of these four methods is detailed in Table 4. The comparison is done at the same contamination level (∼10%), which corresponds to $S/N > 4.7$ for the needlet-ILC + MF catalogue, $S/N > 3.8$ for the needlet-ILC + SExtractor catalogue, $S/N > 4.3$ for the Matched Multifilter (MMF) Saclay catalogue and $S/N > 4.6$ for the MMF Santander catalogue.

This comparison is being extended to other cluster extraction methods in collaboration with the "Clusters and Secondary Anisotropies" working group (WG5). Some improvements are obtained using SExtractor as the extraction tool after the component separation step. There is still some margin for other improvements by increasing the studied area to include lower Galactic latitudes and by combining the SZ extraction methods with CMB and Galactic extraction methods more intimately.

4. Results for CMB

We now turn to the presentation and discussion of the results of the challenge, starting with the CMB component. We evaluate performance based on residual errors at the map and spectral level, and on residual errors at the power spectrum estimation level.

The first point to be made is that all methods have produced CMB maps in Zones 1 and 2. Foreground contamination is barely visible. A small patch representative of CMB reconstruction at intermediate Galactic latitude, is shown in Fig. 9. In the following, we focus on the analysis of the reconstruction error (or residual).

Since each method produces a CMB map at a different resolution, the recovered CMB maps are compared both against the input CMB sky smoothed only by the 1.7′ pixels, and against a 45′ smoothed version, in order to the emphasise errors at large scales.

4.1. Map-level residual errors

Maps of the CMB reconstruction error, with all maps smoothed to a common 45′ resolution, are shown in Fig. 5 for all of the methods (excluding Commander, which produced maps at 3° resolution). The remaining Galactic contamination is now visible at various levels for most methods, and in particular close to regions with the strongest levels of free-free emission. There is also evidence of contamination by SZ cluster decrements, which are visible as distinct negative sources away from the Galactic plane. As can be seen, significant differences between methods exist.

– At high Galactic latitudes, at this 45′ scale, the lowest contamination is achieved by SMICA, GMCA-BLIND and FastICA.
– In Zone 2, CCA, GMCA-MODEL, and FastMEM seem to filter out Galactic emission best while FastICA and WI-FIT are strongly contaminated.

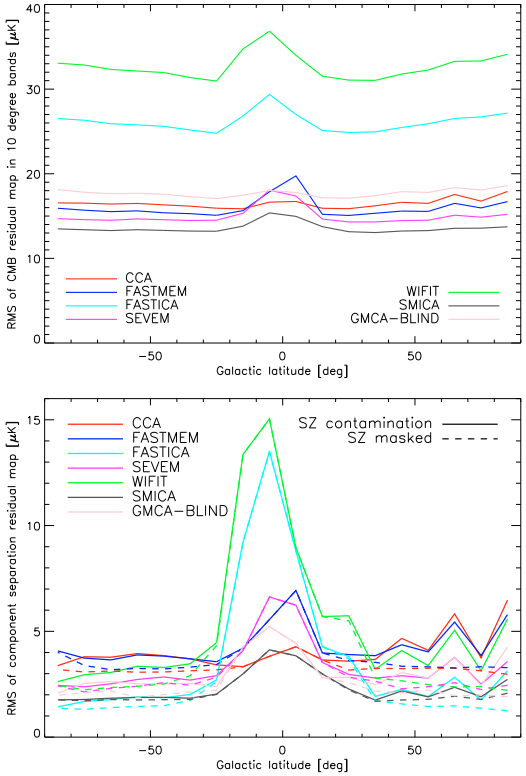

Fig. 4. *Upper*: rms of the residual error of the CMB map, calculated for each of 18 bands of 10 degrees width in Galactic latitude. For comparison, $\sigma_{\rm CMB} = 104.5\ \mu$K and $\sigma_{\rm noise} = 29.3\ \mu$K, for the 143 GHz channel alone (1.7′ pixels). *Lower*: rms of this residual map calculated at 45′ resolution. For comparison, $\sigma_{\rm CMB}(45') = 69.8\ \mu$K and $\sigma_{\rm noise}(45') = 0.7\ \mu$K for the 143 GHz channel. The corresponding residual maps are shown in Fig. 5.

A quantitative measure of the raw residual of the CMB map (reconstructed CMB minus unsmoothed input CMB) is provided by its rms, calculated for 18 zonal bands, each 10 degrees wide in Galactic latitude, excluding pixels in Zone 3 and from the point source mask. The results are shown in the upper panel of Fig. 4. This quantity, denoted $\sigma_{\Delta\rm CMB}$, gives a measure of the sum of the errors due to residual foreground contamination, noise, as well as from residual CMB (due to non unit response on small scales, for instance). For orientation, we can see that the ensemble of methods span the range $13\ \mu{\rm K} < \sigma_{\Delta\rm CMB} < 35\ \mu$K, which can be compared with $\sigma_{\rm CMB} = 104.5\ \mu$K and $\sigma_{\rm noise} = 29.3\ \mu$K, for the 143 GHz channel.

Similarly, the lower panel of Fig. 4 shows the rms of the smoothed residual errors shown in Fig. 5. Depending on the method, the typical level of foreground contamination (plus noise) has an rms from 2 to 5 μK on this smoothing scale. For comparison, $\sigma_{\rm CMB}(45') = 69.8\ \mu$K and $\sigma_{\rm noise}(45') = 0.7\ \mu$K for the 143 GHz channel.

4.2. Spectral residual errors

Next we calculate the spectra of the CMB raw residual maps, both on Zone 1 and Zone 2 (high and low Galactic latitudes),

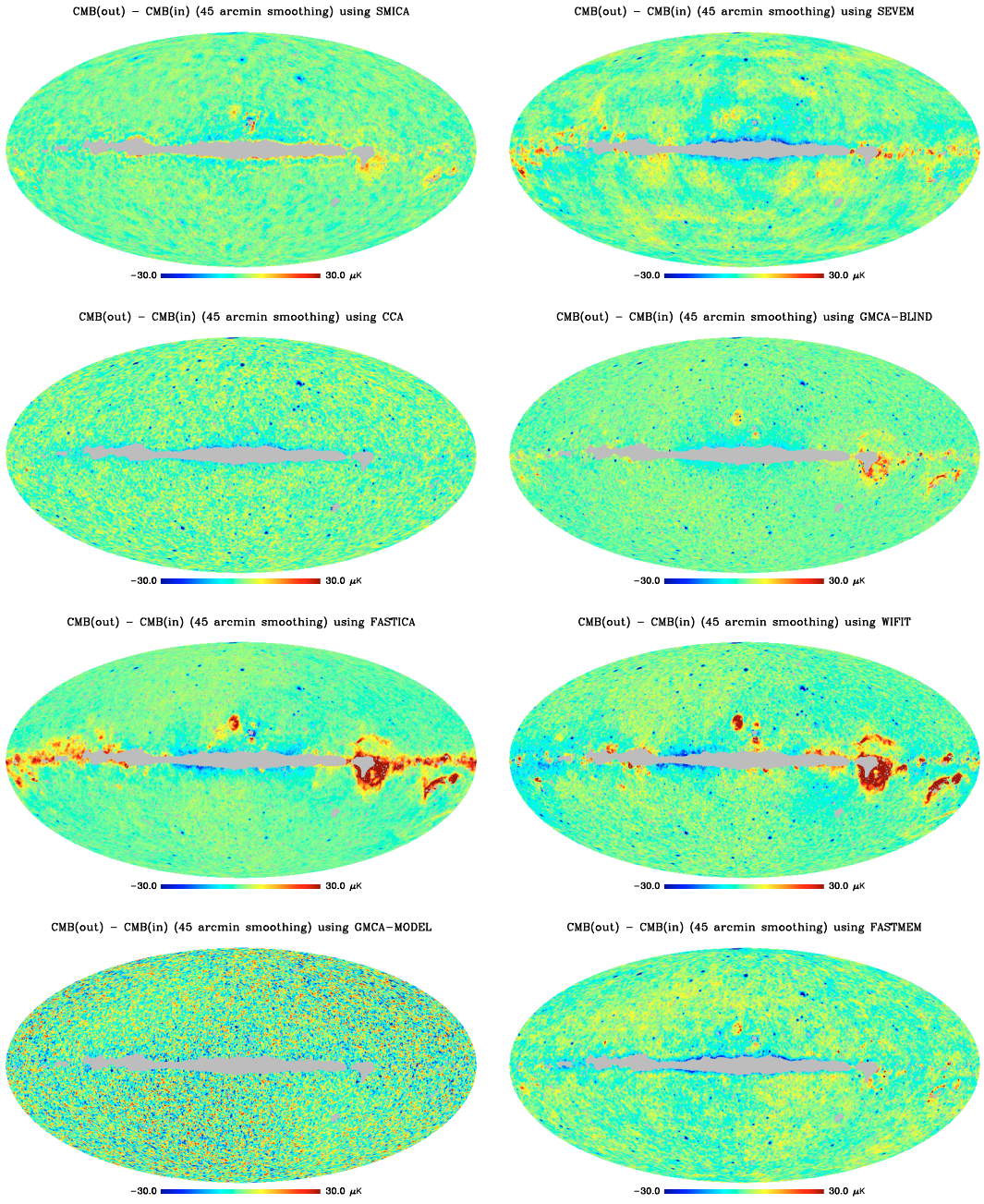

Fig. 5. CMB reconstruction error smoothed at 45′ resolution. These maps are described in Sect. 4.1, and their rms in Galactic latitude strips of 10° are shown in Fig. 4. Over a large fraction of sky, the typical rms of the residual error is between 2 and 5 μK, which can be compared with $\sigma_{\rm CMB}(45') = 69.8\ \mu$K and $\sigma_{\rm noise}(45') = 0.7\ \mu$K for the 143 GHz channel. Some contamination from the galactic components and bright clusters remains.

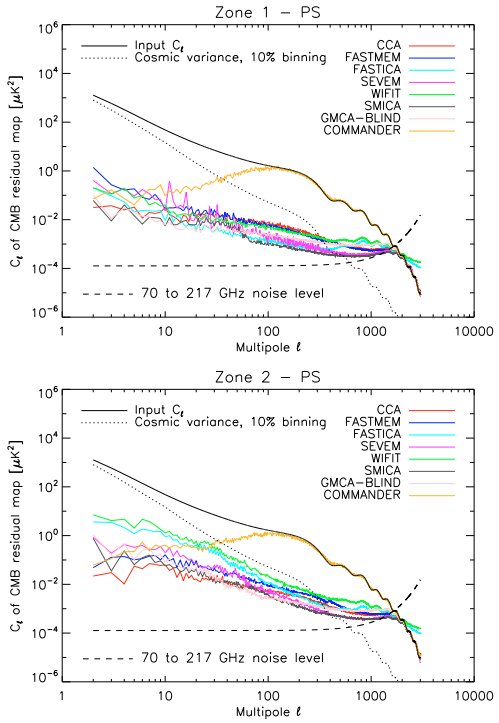

Fig. 6. Spectra of the CMB residual maps, evaluated on Zone 1 (*high Galactic latitudes*) and Zone 2 (*low Galactic latitudes*), both regions with point sources masked. Comparison with Fig. 3 shows the extent to which the Galactic contamination has been removed from the CMB on large angular scales.

with the brightest point sources masked. The results are shown in Fig. 6.

By comparing the spectra of the residuals with the original level of diffuse foreground contamination shown in Fig. 3, we can see that a considerable degree of diffuse foreground cleaning has been attained. There seems however to be a "floor" approached by the ensemble of methods, with a spread of about a factor of ten indicating differences in performance. This floor appears to be mostly free of residual CMB signal which would be visible as acoustic oscillations.

Its overall shape is not white: at high Galactic latitudes the residual spectra bottom out at very roughly $A = 0.015 \times \ell^{-0.7}\,\mu\mathrm{K}^2$, while a low Galactic latitudes the spectra bottom out at $A = 0.02 \times \ell^{-0.9}\,\mu\mathrm{K}^2$. This limit to the level of residuals is considerably higher than the "foreground-free" noise limit displayed as a dashed line.

It is, however, also significantly lower than the CMB cosmic variance, even with 10% binning in ℓ. This comforts us in the impression that component separation is effective enough for CMB power spectrum estimation (discussed next in this paper), although it may remain a limiting issue for other type of CMB science. In particular, it suggests that the component separation residuals, with these channels and the present methods, will dominate the error in CMB maps.

Recently Huffenberger et al. (2007) performed a reanalysis of the impact of unresolved point source power in the three-year data. They found that cosmological parameter constraints are sensitive to the treatment of the unresolved point source power spectrum beyond $\ell = 200$ characterised by a white noise level of $A = 0.015 \pm 0.005\,\mu\mathrm{K}^2$. By comparison, the residual foreground contamination obtained in our simulations is as low as $4 \times 10^{-4}\,\mu\mathrm{K}^2$ at $\ell = 200$.

4.3. Power spectrum estimation errors

Although not the main focus of effort for the Challenge, each group provided their own bandpower estimates of the CMB power spectrum, which in many cases showed obvious acoustic structure out to the sixth or seventh acoustic peak at $\ell \sim 2000$. As an illustration of this result, we show in the upper and middle panels of Fig. 7 the power spectrum estimates from the Commander and SMICA methods respectively.

To make a quantitative estimate of the accuracy of the power spectrum estimates D_ℓ of $\ell(\ell+1)C_\ell$, we calculate the quantity

$$\mathrm{FoM} = \frac{\Delta D_\ell / D_\ell}{\Delta C_\ell / C_\ell} \tag{6}$$

where ΔD_ℓ is the bias in the PSE compared to the PSE derived from the input CMB sky, and where $\Delta C_\ell / C_\ell$ is the expected accuracy of , obtained from Eq. (7) below. This figure of merit penalises biases in the power spectrum estimates without taking into account the error bars claimed by each group.

In the absence of foregrounds, an approximate lower bound on the relative standard deviation in estimating the power spectrum is given by

$$\frac{\Delta C_\ell}{C_\ell} \simeq \sqrt{\frac{2}{N_{\mathrm{modes}}}}\left(1 + \frac{\bar{N}_\ell}{C_\ell}\right), \tag{7}$$

where the number N_{modes} of available modes is

$$N_{\mathrm{modes}} = f_{\mathrm{sky}} \sum_{\ell=\ell_{\mathrm{min}}}^{\ell_{\mathrm{max}}} (2\ell + 1) \tag{8}$$

where f_{sky} denotes the fraction of sky coverage. The average noise power spectrum, $\bar{N}_\ell$, is obtained from the noise power spectra of the different channels

$$\bar{N}_\ell = \left(\sum_{\nu=1}^{N_{\mathrm{chan}}} \frac{B_{\nu\ell}^2}{N_{\nu\ell}} \right)^{-1}, \tag{9}$$

$$N_{\nu\ell} = \frac{4\pi\sigma_{\mathrm{hit}}^2}{n_{\mathrm{pix}}^2} \sum_p \frac{1}{n_{\mathrm{hit}}(p)}, \tag{10}$$

where $B_{\nu\ell}$ is the beam window function for channel ν, and using the calculated values of $N_{\nu\ell}$ given in Table 1. This theoretical limit Eq. (7) is used below to assess the impact of foregrounds on power spectrum estimation, taking the 70 to 217 GHz channels and assuming the noise levels from Table 1 together with an $f_{\mathrm{sky}} = 0.8$.

Ideally, the figure of merit given by Eq. (6) should be much less than one in the cosmic-variance limited regime (i.e. for $\ell \leq 500$ according to Fig. 6). Significant deviations from zero at low ℓ and over ± 1 at high ℓ are indications of significant departures from optimality. We display the FoM Eq. (6), calculated for the PSE of each method in the range $2 < \ell < 1000$, in the lower panel of Fig. 7.

Focusing first on the range $\ell < 20$ we can discern the best performance from Commander, which models the spatial variation of the foreground spectral indices, thus improving the subtraction of foregrounds on large scales. In the range

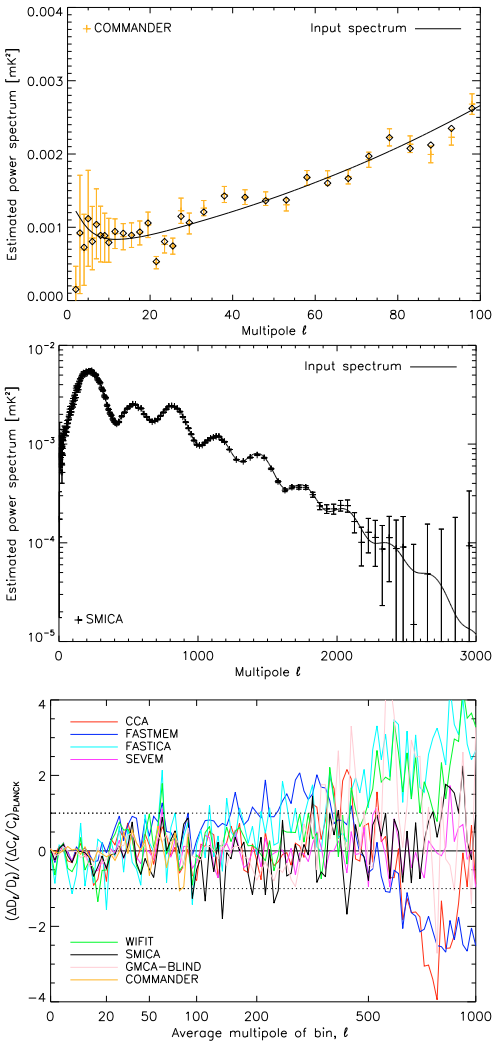

Fig. 7. *Upper*: power spectrum estimates (PSE) using Commander on large angular scales. The diamonds show the C_ℓ of the input CMB realisation. *Middle*: PSE of the recovered CMB map using the SMICA method. *Lower*: PSE compared with the estimates derived from the input CMB C_ℓ, and with the expected sensitivity, assuming $f_{\rm sky} = 0.8$. Beyond $\ell = 500$ biases in the PSE set in in some of the methods.

$20 < \ell < 500$, SEVEM, specifically designed for an estimate of the CMB power spectrum, performs best among the methods tested on this challenge. Beyond $\ell = 500$ we see the best performance from SEVEM and SMICA.

At best, it seems that obtaining PSE with FoM < 1 is achievable for the multipole range $2 < \ell < 1000$. Overall though, complete convergence between the results from different methods was not yet achieved.

4.4. Discussion

In closing this section on the results for the CMB component, we make some general observations, and attempt to explain some of the differences in these results, as shown in Fig. 5, and with reference to the characteristics of the analyses as detailed in Table 2.

The most significant foreground contamination, where it exists, is associated with regions where free-free emission is most intense, such as the Gum nebula and Orion A and B, and this is most easily visible in the residual maps of FastICA and WIFIT (which also suffers from some dust contamination). Possibly this can be explained by the more limited frequency range of data exploited in these two analyses.

The WMAP data were used in the separation only by Commander and SMICA. In the Commander case, the inclusion of additional low frequency channels (in particular the 23 GHz band) helps to recover the low frequency foregrounds. For SMICA, the use of the WMAP channels was not really mandatory for extracting the CMB, rather they have been used with the objective of developing a pipeline which uses all observations available. WMAP maps are expected to be useful for the extraction of low frequency galactic components. This specific aspect was not investigated further in the present work, as the simulations used here (which do not include any anomalous dust emission) are not really adequate to address this problem meaningfully.

5. Results for other components

5.1. Point sources

Additional efforts have been directed towards producing a catalogue of point sources, a catalogue of SZ clusters and maps of the thermal SZ effect and Galactic components.

The detection of point sources is both an objective of component separation (for the production of the early release compact source catalogue (ERCSC) and of the final point source catalogue), and also a necessity for CMB science, to evaluate and subtract the contamination of CMB maps and power spectra by this population of astrophysical objects (Wright et al. 2008; González-Nuevo et al. 2008).

The matched filter and the Mexican hat wavelet 2 have advantages and drawbacks. In principle, the matched filter is the optimal linear filter. However, it often suffers from inaccurate estimation of the required correlation matrix of the contaminants, and from the difficulty to adapt the filter to the local contamination conditions. On the data from the present challenge, this resulted in excessive contamination of the point source catalogue by small scale Galactic emission, mainly dust at high frequencies.

Table 3 summarises the PS detection achieved by these methods. We found that the Mexican hat wavelet 2 and the matched filter performed similarly in most of the frequency channels, and complement each other in the others. Performance depends on the implementation details, and on properties of the other foregrounds.

It should be noted that, for all channels, the 5σ detection limit is somewhat above what would be expected from (unfiltered) noise alone (by a factor 1.33 for the best case, 44 GHz, to 4.8 for the worst case, 857 GHz). This is essentially due to the impact of other foregrounds and the CMB, as well as confusion with other sources. In particular, this effect is more evident at 545 and 857 GHz, due to high dust contamination but also due to the confusion with the highly correlated population of SCUBA

Table 3. Results of point source detection on the present data challenge.

Channel	30 GHz	44 GHz	70 GHz	100 GHz	143 GHz	217 GHz	353 GHz	545 GHz	857 GHz
MF: flux limit [mJy] (5% cont.)	420	430	360	220	130	100	190	890	2490
Detections	655	591	623	1103	2264	2597	1994	1200	1132
MHW2: flux limit [mJy] (5% cont.)	395	450	380	250	140	120	230	430	2160
Detections	762	621	599	1065	2072	2203	1650	1832	1259

Table 4. Performance of the SZ cluster detection methods. The table gives the absolute number of detection for $|b| > 20°$.

Method	Detections	False	Reliability
Needlet-ILC + SExt.	2564	225	91%
Needlet-ILC + MF	1804	179	90%
MMF Saclay	1803	178	90%
MMF IFCA	1535	144	91%

sources (Granato et al. 2004; Negrello et al. 2004), which constitute a contaminant whose impact on point source detection was until now somewhat underestimated.

The number of detections for each frequency channel in Table 3 has been compared to the predictions made by López-Caniego et al. (2006), properly rescaled for our sky coverage. In general, there is a good agreement between the predictions and the results of this exercise, except for the 857 GHz channel, where the number of detections is roughly half the predicted one. Again, the difference may be due to the confusion of correlated infrared sources, that are now present in the PSM but were not considered by López-Caniego et al. (2006).

5.2. SZ effect

The recovery of an SZ map from the challenge data is illustrated in Fig. 8. The recovered full sky SZ is obtained by Wiener-filtering in harmonic space the needlet-ILC map of the SZ y parameter. Wiener filtering enhances the visibility of SZ clusters. We clearly identify by eye the brightest clusters in the map.

One of the main results of this study is the recovery of around 2300 clusters. This is significantly lower than the performance one could expect if the main limitation was the nominal noise, and if most detectable clusters were unresolved. Many of the recovered clusters are in fact resolved, and thus emit on scales where the contamination from CMB is not negligible. Small scale Galactic emission and the background of extragalactic sources, now included in the simulations, further complicate the detection. Further study is necessary to find the exact origin of the lack of performance, and improve the detection methods accordingly.

Actual detection performance, limited to 67% of the sky at Galactic latitudes above 20 degrees, is shown in Table 4. The ILC + SExtractor method gives the best result. The ILC+MF approach performs as well as the matched multifilter here. The two implementations of the MMF perform similarly. The difference in the number of detections achieved (about 13.5%), however, suggests that implementation details are important for this task.

Using the detected cluster catalogue obtained with the MMF, we have produced a mask of the detected SZ clusters. For each of the 1625 clusters we masked a region whose radius is given by the corresponding input cluster virial radius (ten times the core radius here).

5.3. Galactic components

For the Challenge, a number of methods were applied for separating out Galactic components. Table 2 lists which Galactic components were obtained by the different methods. Five groups have attempted to separate a high frequency dust-like component. Four groups have attempted separation of synchrotron and free-free at low frequencies.

We compared the reconstructed component maps with their counterpart input maps, both in terms of the absolute residual error and in terms of the relative error. Both these measures are computed after removing the best-fit monopole and dipole from the residual error map (fitted when excluding a region ±30° in Galactic latitude). We then defined a figure of merit $f_{20\%}$, which corresponds to the fraction of sky where the foreground amplitude is reconstructed with a relative error of less than 20%.

The main results can be summarised as follows: The dust component was the best reconstructed component with an $f_{20\%} \simeq 0.7$ for all methods. The relative error typically becomes largest at the higher galactic latitudes where the dust emission is faintest. The synchrotron component was reconstructed with an $f_{20\%} \simeq 0.3$–0.5, with Commander achieving the best results at 3° resolution, but with noticeable errors along the galactic ridge where, in our simulations, the synchrotron spectral index flattens off. Free-free emission is detected and identified in regions such as the Gum Nebula, Orion A and B, and the Ophiucus complex. However, the reconstruction of the free-free emission at low Galactic latitudes needs improving. On the other hand, the *total* Galactic emission (free-free plus synchrotron) at low-frequencies is better reconstructed, with $f_{20\%} \simeq 0.5$–0.8, with the best results from Commander.

In Fig. 9, we show for illustration the recovered total Galactic emission at 23 GHz from Commander, the dust emission at 143GHz from FastICA and, for comparison, the recovered CMB from SMICA on the same patch.

6. Summary and conclusions

In this paper we have described a CMB component separation Challenge based on a set of realistic simulations of the satellite mission. The simulated data were based on a development version of the Sky Model, and included the foreground emission from a three component Galactic model of free-free, synchrotron and dust, as well as radio and infra-red sources, the infra-red background, the SZ effect and -like inhomogeneous noise. We have cautioned that the simulations, while complex, still relied on some simplifying assumptions, as discussed in Sect. 2.3. Thus, there is no guarantee that the priors and data models that yielded the best separation on simulations will work equally well on the dataset. While this may seem to undercut the main purpose of this paper, we are simply acknowledging that we cannot anticipate in full detail what the component separation pipeline will look like and how effective it will be, based on an analysis of present-day simulations. In spite of this, it is clear that methods performing better on the simulated data have in general better chances to work better on the real sky.

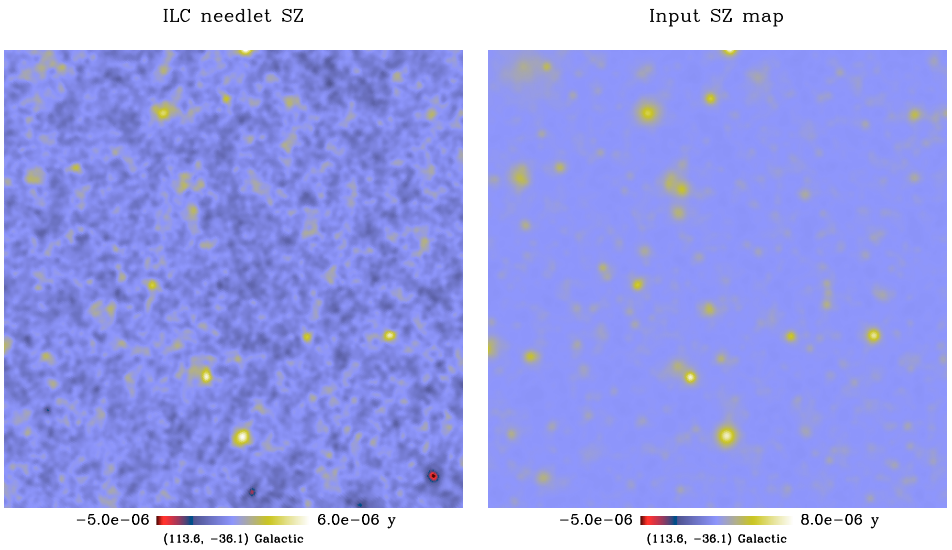

Fig. 8. Patch of the recovered needlet-ILC SZ map and input SZ map. For easier comparison of the two maps (12.5 × 12.5 deg), the input SZ map has been filtered to the same resolution as the output.

As a combined set of tools, the component separation methods developed and tested in this work offer very different ways to address the component separation problem and so comparable performance between different tools, when achieved, provides confidence in the conclusions of this work against some of the simplifications used in the model for simulating the sky emission.

We found that the recovered CMB maps were clean on large scales, in the sense that the rms of the residual contamination was much less than the cosmic variance: at best the rms residual of the cleaned CMB maps was of the order of 2 μK across the sky on a smoothing scale of 45′, with a spectral distribution described by $A = 0.015 \times \ell^{-0.7} \mu\mathrm{K}^2$ and $A = 0.02 \times \ell^{-0.9}\ \mu\mathrm{K}^2$ at high and low Galactic latitudes respectively. The effectiveness of the foreground removal is illustrated by comparing the input foreground power spectra of Fig. 3 with the residuals shown in Fig. 6. The two panels of the latter figure show that, with few exceptions, the methods manage to clean the low Galactic latitude Zone 2, where the foreground contamination is high, almost as well as they do for the high Galactic latitude Zone 1, where the CMB dominates at the frequencies near the foreground minimum. The amplitude of the power spectrum of residuals is, on the largest scales, four orders of magnitude lower than that of the input Galaxy power spectrum at the foreground minimum. This means that the CMB map could be recovered, at least by some methods, over the whole sky except for a sky cut at the 5 percent level (see Fig. 4). The CMB power spectrum was accurately recovered up to the sixth peak.

As detailed in Table 2, the outputs of the methods were diverse. While all have produced a CMB map, only a subset of them were used to obtain maps of individual diffuse Galactic emissions. Five (Commander, CCA, FastICA, FastMEM, SMICA) reconstructed thermal dust emission maps at high frequencies, and another five (Commander, CCA, FastMEM, GMCA, SMICA) yielded a map of the low-frequency Galactic emissions (synchrotron and free-free).

It is not surprising that the dust component was more easily reconstructed because it is mapped over a larger frequency range, and benefits from observations at high frequencies where it dominates over all other emissions, except the IR background at high Galactic latitudes. Moreover at high frequencies the noise level is lower and the angular resolution is better. Low frequency Galactic foregrounds suffer from more confusion, with a mixture of several components observed in only few channels, at lower resolution.

The relative errors of the reconstructed foreground maps are larger at high Galactic latitudes where the foregrounds are fainter. We have defined a figure of merit $f_{20\%}$, which corresponds to the fraction of sky where the amplitude of each galactic component has been reconstructed with a relative error of less than 20%. For most methods, $f_{20\%} \simeq 70\%$ was achieved for the dust component, while $f_{20\%} \simeq 50\%$ was achieved for the radio emission, increasing to 80% if component separation is performed at a relatively low resolution of 3°. Clearly, there is ample room and need for improvement in this area.

The flux limits for extragalactic point source detection are minimum at 143 and 217 GHz, where they reach ≃100 mJy. About 1000 radio sources and about 2600 far-IR sources are detected over about 67% of the sky ($|b| > 20°$). Over the same region of the sky, the best methods recover about 2300 clusters.

In closing, we list areas where work is in progress and improvements are expected: The sky model is being upgraded to include the anomalous emission component and polarization. We are in the process of integrating point source and SZ extraction algorithms together with the diffuse component separation algorithms into a single component separation pipeline. This is expected, on one side, to decrease the contamination of CMB maps on small angular scales, where point and compact sources (including SZ effects) dominate and, on the other side,

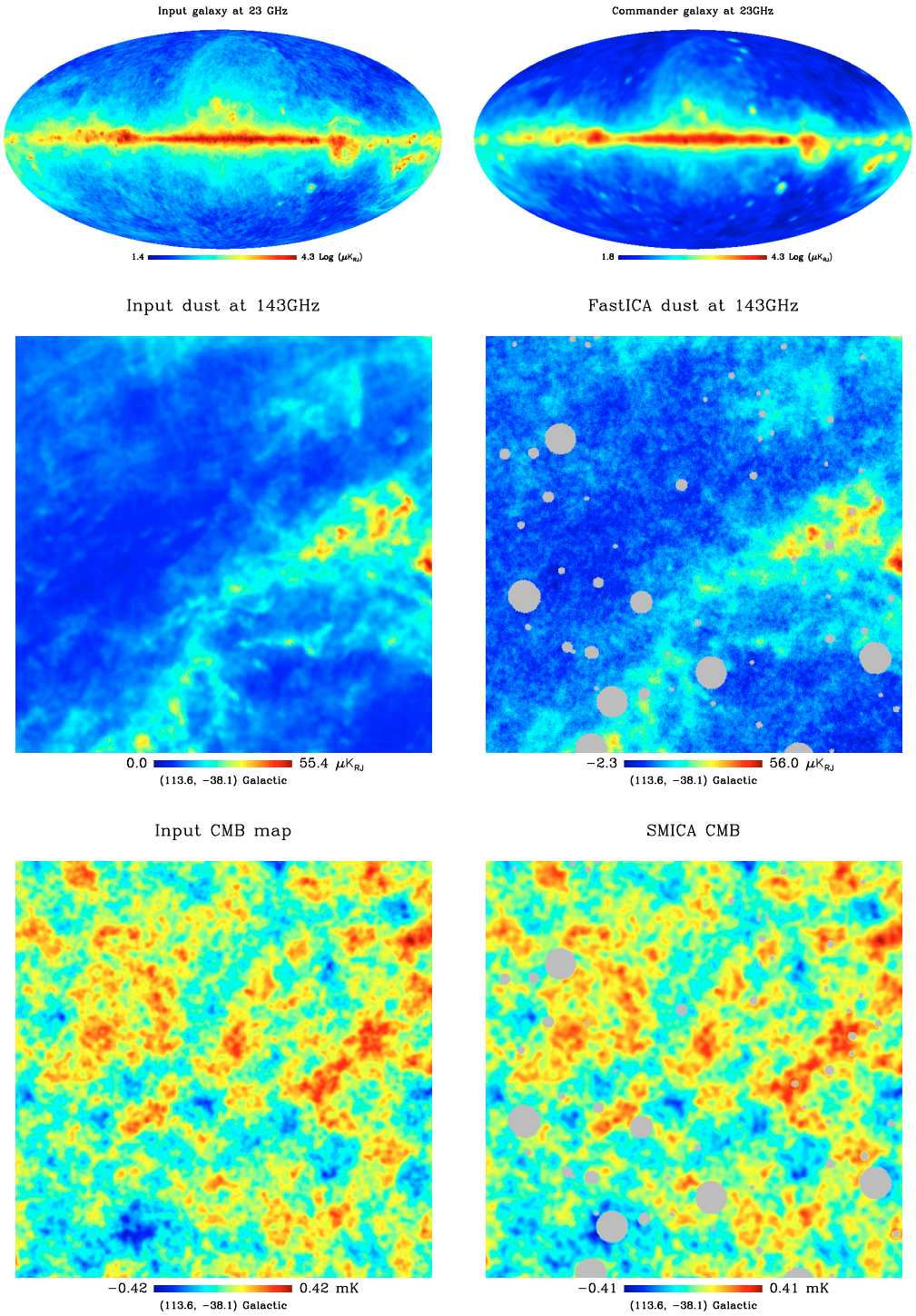

Fig. 9. Example input and recovered total galaxy emission at 23 GHz, dust at 143 GHz and CMB components.

to achieve a more efficient point and compact source extraction. Assessing this in more detail is part of WG2 work plans for the near future. The SEVEM foreground cleaning step now operates in wavelet space which allows for improved, scale-by-scale removal of foregrounds. In addition the recovery of the power spectrum estimates and error bars at the highest multipoles has been improved by reducing the cross-correlation between modes through the use of an apodised mask. For Commander, work is currently ongoing to extend the foreground sampler to multi-resolution experiments. CCA is being upgraded to fully exploit the estimated spatially-varying spectral indices in the source reconstruction step; SMICA is being improved to model unresolved point source power. The FastICA algorithm is being improved to handle data with a wider frequency coverage. The GMCA framework is being extended to perform a joint separation and deconvolution of the components.

Acknowledgements. The work reported in this paper was carried out by Working Group 2 of the Collaboration. is a mission of the European Space Agency. The Italian group were supported in part by ASI (contract Planck LFI Phase E2 Activity). The US Project is supported by the NASA Science Mission Directorate. The ADAMIS team at APC has been partly supported by the Astro-Map and Cosmostat ACI grants of the French ministry of research, for the development of innovative CMB data analysis methods. The IFCA team acknowledges partial financial support from the Spanish project AYA2007-68058-C03-02. This research used resources of the National Energy Research Scientific Computing Center, which is supported by the Office of Science of the US Department of Energy under Contract No. DE-AC02-05CH11231. D.H., J.L.S. and E.S. would like to acknowledge partial financial support from joint CNR-CSIC research project 2006-IT-0037. R.S. acknowledges support of the E.C. Marie Curie IR Grant (mirg-ct-2006-036614). C.B. was partly supported by the NASA LTSA Grant NNG04CG90G. S.M.L. would like to thank the kind hospitality of the APC, Paris for a research visit where part of this work was completed. We thank Carlo Burigana for a careful reading of the manuscript. We acknowledge the use of the Legacy Archive for Microwave Background Data Analysis (LAMBDA). Support for LAMBDA is provided by the NASA Office of Space Science. The results in this paper have been derived using the HEALPix package (Górski et al. 2005).

Appendix A: Description of methods

A.1. Commander

"Commander" is an implementation of the CMB and foregrounds Gibbs sampler most recently described by Eriksen et al. (2008); This algorithm maps out the joint CMB-foreground probability distribution, or "posterior distribution", by sampling. The target posterior distribution may be written in terms of the likelihood and prior using Bayes' theorem,

$$\Pr(\boldsymbol{s}, C_\ell, \theta_{\rm fg}|\boldsymbol{d}) = \mathcal{L}(\boldsymbol{d}|\boldsymbol{s}, \theta_{\rm fg}) \Pr(\boldsymbol{s}|C_\ell) \Pr(C_\ell) \Pr(\theta_{\rm fg}). \quad \text{(A.1)}$$

Here $\theta_{\rm fg}$ is the collection of all parameters required to describe the non-cosmological foregrounds. Since the noise is assumed to be Gaussian, the likelihood is simply given by the χ^2.

In the current analysis, the foregrounds are modelled by a sum of synchrotron, free-free and thermal dust emission, and free monopole and dipoles at each frequency band. The thermal dust component is approximated by a single-component modified blackbody with a fixed dust temperature $T_{\rm d} = 21$ K. Thus, the total foreground model reads

$$\begin{aligned} s_{\rm fg}(\nu, p) &= A_s(p) g(\nu) \left(\frac{\nu}{\nu_s}\right)^{\beta_s(p)} + A_f(p) g(\nu) \left(\frac{\nu}{\nu_f}\right)^{-2.15} \\ &+ A_{\rm d}(p) g(\nu) \frac{e^{h\nu_{\rm d}/kT_{\rm d}} - 1}{e^{h\nu/kT_{\rm d}} - 1} \left(\frac{\nu}{\nu_{\rm d}}\right)^{\beta_{\rm d}(p)+1} \\ &+ m_\nu^0 + \sum_{i=1}^{3} m_\nu^i (\hat{\boldsymbol{n}}(p) \cdot \hat{\boldsymbol{e}}_i), \end{aligned} \quad \text{(A.2)}$$

where $g(\nu)$ is the conversion factor between antenna and thermodynamic temperatures, and $\hat{\boldsymbol{n}}$ is the unit vector of pixel p. The free parameters are thus the foreground amplitudes, $A_{\rm s}$, A_f and $A_{\rm d}$, and spectral indices, $\beta_{\rm s}$ and $\beta_{\rm d}$, for each pixel, and the overall monopole, m_ν^0, and dipole amplitudes, m_ν^i, for each band. For priors, we adopt the product of the Jeffreys' ignorance prior and an informative Gaussian prior ($\beta_s = -3 \pm 0.3$ for synchrotron and $\beta_{\rm d} = 1.5 \pm 0.3$ for dust) for the spectral indices, while no constraints are imposed on the amplitudes.

Using the Gibbs (conditional) sampling technique, a set of samples drawn from the posterior distribution. From these samples the marginal posterior mean and rms component maps are derived, as well as the marginal CMB power spectrum posterior distribution.

The code assumes identical beams at all frequencies, and it is therefore necessary to smooth the data to a common resolution, limiting the analysis to large angular scales. For this particular data set, we have chosen a common resolution of $3^\circ FWHM$, with $54'$ pixels (Healpix $N_{\rm side} = 64$) and with $\ell_{\rm max} = 150$. For more details on the degradation process, see Eriksen et al. (2008). At this resolution, the CPU time for producing one sample is around one wall-clock minute. A total of 5400 samples were produced over four independent Markov chains, of which the first 2400 were rejected due to burn-in. Twelve frequency bands (covering frequencies between 23 and 353 GHz) were included, for a total cost of around 1000 CPU h.

The main advantage of this approach is simply that it provides us with the exact joint CMB and foreground posterior distribution for very general foreground models. From this joint posterior distribution, it is trivial to obtain the exact marginal CMB power spectrum and sky signal posterior distributions. Second, since any parametric foreground model may be included in the analysis, the method is very general and flexible. It also provides maps of the posterior means for individual components, and is therefore a true component separation method, and not only a foreground removal tool.

Currently, the main disadvantage of the approach is the assumption of identical beam profiles at each frequency. This strictly limits the analysis to the lowest resolution of a particular data set. However, this is a limitation of the current implementation, and not of the method as such.

A.2. Correlated component analysis (CCA)

CCA (Bedini et al. 2005) is a semi-blind approach that relies on the second-order statistics of the data to estimate the mixing matrix on sub-patches of the sky. CCA assumes the data model given by Eq. (4), and makes no assumptions about the independence or lack of correlations between pairs of radiation sources. The method exploits the spatial structure of the individual source maps and adopts commonly accepted models for source frequency scalings in order to reduce the number of free parameters to be estimated.

The spatial structures of the maps are accounted for through the covariance matrices at different shifts. From the data model adopted, the data covariance matrices at shifts (τ, ψ) are given by

$$\begin{aligned} \boldsymbol{C}_{\rm d}(\tau, \psi) &= \left\langle [\boldsymbol{d}(\theta, \phi) - \mu_{\rm d}] [\boldsymbol{d}(\theta + \tau, \phi + \psi) - \mu_{\rm d}]^{\rm t} \right\rangle \\ &= \boldsymbol{A} \boldsymbol{C}_{\rm s}(\tau, \psi) \boldsymbol{A}^{\rm t} + \boldsymbol{C}_{\rm n}(\tau, \psi) , \end{aligned} \quad \text{(A.3)}$$

where $\mu_{\rm d}$ is the mean data vector, and (θ, ϕ) is the generic pixel index pair. The matrices $\boldsymbol{C}_{\rm d}(\tau, \psi)$ can be estimated from the data, and the noise covariance matrices $\boldsymbol{C}_{\rm n}(\tau, \psi)$ are derived from the map-making noise estimations. From Eq. (A.3), we can estimate

the mixing matrix and free parameters of the source covariance matrices by matching the known quantities to the unknowns, that is by minimizing the following function for $\boldsymbol{A}$ and $\boldsymbol{C}_{\rm s}(\tau,\psi)$

$$\sum_{\tau,\psi} \|\boldsymbol{A}\boldsymbol{C}_{\rm s}(\tau,\psi)\boldsymbol{A}^{\rm t} - [\boldsymbol{C}_{\rm d}(\tau,\psi) - \boldsymbol{C}_{\rm n}(\tau,\psi)]\|, \quad \text{(A.4)}$$

where the Frobenius norm is used and the summation is taken over the set of shift pairs (τ,ψ) for which data covariances are non-zero. Given an estimate of $\boldsymbol{C}_{\rm s}$ and $\boldsymbol{C}_{\rm n}$, Eq. (4) can be inverted and component maps obtained via the standard inversion techniques of Wiener filtering or generalised least square inversion. For the Challenge, harmonic space Wiener filtering was applied, using a mixing matrix obtained by averaging the mixing matrices of different patches. More details on the method can be found in Bonaldi et al. (2006, 2007).

CCA can treat the variability of the spectral properties of each component with the direction of observation by working on sufficiently small sky patches, which must however be large enough to have sufficient constraining power; typically the number of pixels per patch must be around 10^5. To obtain a continuous distribution of the free parameters of the mixing matrix, CCA is applied to a large number of partially overlapping patches.

A drawback of the present version of CCA is common to many pixel-domain approaches to separation: the data must be smoothed to a common resolution. A Fourier-domain implementation of CCA (Bedini & Salerno 2007) would be able to cope with this problem. Alternatively for the pixel-domain version, the mixing matrix could be estimated from the smoothed maps and then used to separate the sources using the full resolution data.

A.3. Generalised morphological component analysis (GMCA)

GMCA (Bobin et al. 2007) is a blind source separation method devised for separating sources from instantaneous linear mixtures using the model given by Eq. (4). The components $\boldsymbol{s}$ are assumed to be sparsely represented (i.e. have a few significant samples in a specific basis) in a so-called sparse representation $\boldsymbol{\Phi}$ (typically wavelets). Assuming that the components have a sparse representation in the wavelet domain is equivalent to assuming that most components have a certain spatial regularity. These components and their spectral signatures are then recovered by minimizing the number of significant coefficients in $\boldsymbol{\Phi}$:

$$\min_{\{\boldsymbol{a},s\}} \lambda \left\|\boldsymbol{s}\boldsymbol{\Phi}^T\right\| + \frac{1}{2}\|\boldsymbol{d} - \boldsymbol{a}s\|_2^2. \quad \text{(A.5)}$$

In Bobin et al. (2007), it was shown that sparsity enhances the diversity between the components thus improving the separation quality. The spectral signatures of CMB and SZ are assumed to be known. The spectral signature of the free-free component is approximately known up to a multiplicative constant (power law with fixed spectral index). The synchrotron component is estimated via a separable linear model: $\boldsymbol{d}_{\rm sync} = a_{\rm sync}s_{\rm sync}$ where $a_{\rm sync}$ is parameterised by a spectral index $\beta_{\rm sync}$. This spectral index is estimated by solving the following problem:

$$\min_{\beta} \|\boldsymbol{r}_{\rm sync} - a_{\rm sync}(\beta)s_{\rm Haslam}\|_2^2 \quad \text{(A.6)}$$

where $\boldsymbol{r}_{\rm sync}$ is the residual obtained by extracting the contribution of all the components from the data $\boldsymbol{d}$ except synchrotron. $s_{\rm Haslam}$ is the Haslam synchrotron map; $a_{\rm sync}(\beta)$ is the spectral signature of synchrotron emission (power law). More precisely, β is estimated such that the Haslam multiplied by $a_{\rm sync}(\beta)$ matches the residual term $\boldsymbol{r}_{\rm sync}$.

A Wiener filter is applied to provide the denoised CMB estimate. The main advantage of GMCA is its ability to blindly extract strong galactic emission. Indeed, most galactic emission is well represented in a wavelet basis. The main disadvantage is that it relies on the way the deconvolution of the data is performed: an effective beam is used to account for the convolution.

A.4. Independent component analysis (FastICA)

Independent Component Analysis is an approach to component separation, looking for the components which maximise some measure of the statistical independence (Hyvarinen 1999). The FastICA algorithm presented here exploits the fact that non-Gaussianity is usually a convenient and robust measure of the statistical independence and therefore it searches for linear combinations $\boldsymbol{y}$ of the input multi-frequency data, which maximise some measure of the non-Gaussianity. In the specific implementation of the idea, employed here, the non-Gaussianity is quantified by the *neg-entropy*. Denoting by $H(\boldsymbol{y}) = -\int p(\boldsymbol{y})\log p(\boldsymbol{y})d\boldsymbol{y}$ the entropy associated with the distribution p, we define the neg-entropy as,

$$\text{neg-entropy}(\boldsymbol{y}) = H(\boldsymbol{y}_G) - H(\boldsymbol{y})\,, \quad \text{(A.7)}$$

where $\boldsymbol{y}_G$ is a Gaussian variable with the same covariance matrix as $\boldsymbol{y}$. The search for the maxima of the neg-entropy is usually aided by enhancing the role of the higher order moments of $\boldsymbol{y}$, which is achieved by means of a non-linear mapping. In the present implementation, the FastICA finds the extrema of the neg-entropy approximation given by $|E[g(\boldsymbol{y})] - E[g(\boldsymbol{y}_{\rm G})]|^2$, where E means the average over the pixels, and g represents the non-linear mapping of the data, which may be a power law in the simplest case. The algorithm is straightforwardly implemented in real space, and requires the same angular resolution for all channels. Note that for an experiment like where the resolution varies with frequency, this requires smoothing the input data to the lowest resolution before processing. The use of an efficient minimization procedure, with a required number of floating point operations scaling linearly with the size of the data set, makes the computational requirements essentially dominated by memory needed to be allocated to quickly access the multi-frequency data.

The algorithm has been tested so far as a CMB cleaning procedure, because the hypothesis of statistical independence is expected to be verified at least between CMB and diffuse foregrounds. It produced results on real (BEAST, COBE, WMAP) and simulated total intensity data, as well as on polarization simulations, on patches as well as all sky (see Maino et al. 2007, and references therein). The performance is made possible by two contingencies, i.e. the validity of the assumption of statistical independence for CMB and foregrounds, as well as the high resolution of the present CMB observations, which provides enough of statistical realizations (pixels) for the method to decompose the data into the independent components.

A.5. Harmonic-space maximum entropy method (FastMEM)

The Maximum Entropy Method (MEM) can be used to separate the CMB signal from astrophysical foregrounds including Galactic synchrotron, dust and free-free emission as well as SZ effects. The particular implementation of MEM used here

works in the spherical harmonic domain. The separation is performed mode-by-mode allowing a huge optimisation problem to be split into a number of smaller problems. The solution can thus be obtained more rapidly, giving this implementation its name: FastMEM. This approach is described by Hobson et al. (1998, 1999) for Fourier modes on flat patches of the sky and by Stolyarov et al. (2002, 2005) for the full-sky case.

If we have a model (or hypothesis) H in which the measured data $\boldsymbol{d}$ is a function of an underlying signal $\boldsymbol{s}$, then Bayes' theorem tells us that the posterior probability $\Pr(s|d, H)$ is the product of the likelihood $\Pr(\boldsymbol{d}|\boldsymbol{s}, H)$ and the prior probability $\Pr(\boldsymbol{s}, H)$, divided by the evidence $\Pr(\boldsymbol{d}, H)$,

$$\Pr(\boldsymbol{s}|\boldsymbol{d}, H) = \frac{\Pr(\boldsymbol{d}|\boldsymbol{s}, H)\Pr(\boldsymbol{s}|H)}{\Pr(\boldsymbol{d}|H)}. \quad \text{(A.8)}$$

The objective here is to maximise the posterior probability of the signal given the data. Since the evidence in Bayes' theorem is merely a normalisation constant we maximise the product of the likelihood and the prior

$$\Pr(\boldsymbol{s}|\boldsymbol{d}, H) \propto \Pr(\boldsymbol{d}|\boldsymbol{s}, H)\Pr(\boldsymbol{s}, H). \quad \text{(A.9)}$$

We assume that the instrumental noise in each frequency channel is Gaussian-distributed, so that the log-likelihood has a form of a χ^2 misfit statistic. We make the assumption that the noise is uncorrelated between spherical harmonic modes. We also assume that the beams are azimuthally symmetric, so that they are fully described by the beam transfer function B_ℓ in harmonic space. For mode (ℓ, m), the log-likelihood is

$$\chi^2(\boldsymbol{s}_{\ell m}) = (\boldsymbol{d}_{\ell m} - B_\ell \boldsymbol{A}\boldsymbol{s}_{\ell m})^T N_{\ell m}^{-1}(\boldsymbol{d}_{\ell m} - B_\ell \boldsymbol{A}\boldsymbol{s}_{\ell m}) \quad \text{(A.10)}$$

where $\boldsymbol{A}$ is the fixed frequency conversion matrix which describes how the components are mixed to form the data, and $N_{\ell m}^{-1}$ is the inverse noise covariance matrix for this mode. If the instrumental noise is uncorrelated between channels, then this matrix is diagonal. However, unresolved point sources can be modelled as a correlated noise component.

The prior can be Gaussian, and in this case we recover the Wiener filter with the well-known analytical solution for the signal s. However, the astrophysical components have strongly non-Gaussian distribution, especially in the Galactic plane. Therefore Hobson et al. (1998) suggested that an entropic prior be used instead. In this case, maximising the posterior probability is equivalent to the minimising the following functional for each spherical harmonic mode

$$\Phi_{\rm MEM}(\boldsymbol{s}_{\ell m}) = \chi^2(\boldsymbol{s}_{\ell m}) - \alpha S(\boldsymbol{s}_{\ell m}) \quad \text{(A.11)}$$

where $S(\boldsymbol{s})$ is the entropic term, and α is the regularisation parameter. The minimisation can be done numerically using one of a number of algorithms (Press et al. 1992).

FastMEM is a non-blind method, so the spectral behaviour of the components must be known in advance. Since $\boldsymbol{A}$ is fixed, the spectral properties of the components must be the same everywhere on the sky. However, small variations in the spectral properties, for example, dust temperature, synchrotron spectral index or SZ cluster electron temperature, can be accounted for by introducing additional components. These additional components correspond to terms in the Taylor expansion of the frequency spectrum with respect to the relevant parameter.

The initial priors on the components are quite flexible and they can be updated by iterating the component separation, especially if the signal-to-noise is high enough.

It is not necessary for all of the input maps to be at the same resolution since FastMEM solves for the most probable solution for unsmoothed signal, deconvolving and denoising maps simultaneously. It is flexible enough to include any datasets with known window function and noise properties. A mask can easily be applied to the input data (the same mask for all frequency channels) and this does not cause problems with the separation.

Since FastMEM uses priors on the signals, the solution for the signals is biased. This is especially evident if the signal-to-noise ratio is low. It is possible to de-bias the power spectrum statistically, knowing the priors and the FastMEM separation errors per mode. However, one can not de-bias the recovered maps since the errors are quadratic and de-biasing will introduce phase errors in the harmonics.

No information about the input components was used in the separation, and the prior power spectra were based solely on the physical properties of the components and templates available in the literature. The prior on the CMB component was set using the best-fit theoretical spectrum, instead of a WMAP-constrained realisation. This has a significant effect at low multipoles.

A.6. Spectral estimation via expectation-maximization (SEVEM)

SEVEM (Martínez-González et al. 2003) tries to recover only the CMB signal, treating the rest of the emissions as a generalised noise. As a first step, the cosmological frequency maps, 100, 143 and 217 GHz, are foreground cleaned using an internal template fitting technique. Four templates are obtained from the difference of two consecutive frequency channels, which are smoothed down to the same resolution if necessary, to avoid the presence of CMB signal in the templates. In particular, we construct maps of (30–44), (44–70), (545–353) and (857–545) differences. The central frequency channels are then cleaned by subtracting a linear combination of these templates. The coefficients of this combination are obtained minimising the variance of the final clean map outside the considered mask. The second step consists of estimating the power spectrum of the CMB from the three cleaned maps using the method (based on the Expectation-Maximization algorithm) described in Martínez-González et al. (2003), which has been adapted to deal with spherical data. Using simulations of CMB plus noise, processed in the same way as the Challenge data, we obtain the bias and statistical error of the estimated power spectrum and construct an unbiased version of the C_ℓ's of the CMB. This unbiased power spectrum is used to recover the CMB map from the three clean channels through Wiener filter in harmonic space. Finally, we estimate the noise per pixel of the reconstructed map using CMB plus noise simulations.

One of the advantages of SEVEM is that it does not need any external data set or need to make any assumptions about the frequency dependence or the power spectra of the foregrounds, other than the fact that they are the dominant contribution at the lowest and highest frequency channels. This makes the method very robust and, therefore, it is expected to perform well for real data. Moreover, SEVEM provides a good recovery of the power spectrum up to relatively hig ℓ and a small error in the CMB map reconstruction. In addition the method is very fast, which allows one to characterise the errors of the CMB power spectrum and map using simulations. The cleaning of the data takes around 20 mn, while the estimation of the power spectrum and map requires around 15 and 30 mn respectively. In fact, the whole process described, including producing simulations to

estimate the bias and errors, takes around 30 h on one single CPU. Regarding weak points, the method reconstructs only the CMB and does not try to recover any other component of the microwave sky although it could be generalised to reconstruct simultaneously the both the CMB and the thermal SZ effect. Also, the reconstructed CMB map is not full-sky, since the method does not aim to remove the strong contamination at the centre of the Galactic plane or at the point source positions. In any case, the masked region excluded for the analysis is relatively small.

A.7. Spectral matching independent component analysis (SMICA)

The principle of SMICA can be summarised in three steps: 1) compute spectral statistics; 2) fit a component-based model to them; 3) use the result to implement a Wiener filter in harmonic space. More specifically, an idealised operation goes as follows. Denote $\boldsymbol{d}(\xi)$ the column vector whose ith entry contains the observation in direction ξ for the i-th channel and denote $\boldsymbol{d}_{\ell m}$ the vector of same size (the number of frequency channels) in harmonic space. This is modelled as the superposition of C components $\boldsymbol{d}_{\ell m} = \sum_{c=1}^{C} \boldsymbol{d}^c_{\ell m}$. In Step 1), we compute spectral matrices $\widehat{\boldsymbol{C}}_\ell = \frac{1}{2\ell+1} \sum_m \boldsymbol{d}_{\ell m} \boldsymbol{d}^{\mathrm{T}}_{\ell m}$. In Step 2) we model the ensemble-averaged spectral matrix $\boldsymbol{C}_\ell = \langle \widehat{\boldsymbol{C}}_\ell \rangle$ as the superposition of C uncorrelated components: $\boldsymbol{C}_\ell = \sum_{c=1}^{C} \boldsymbol{C}^c_\ell$ and, for each component, we postulate a parametric model, that is, we let the matrix set $\{\boldsymbol{C}^c_\ell\}_{\ell=0}^{\ell_{\max}}$ be a function of a parameter vector θ^c. This parameterization embodies our prior knowledge about a given component. For instance, for the CMB component, we take $[\boldsymbol{C}^{\mathrm{cmb}}_\ell]_{ij} = e_i e_j c_\ell$ where e_i is the known CMB emmission coefficient for channel i and c_ℓ is the unknown angular power spectrum at frequency ℓ. The parameter vector for CMB would then be $\theta^{\mathrm{cmb}} = \{c_\ell\}_{\ell=0}^{\ell_{\max}}$. All unknown parameters for all components are then estimated by fitting the model to the spectral statistics, i.e. by solving $\min_{\theta^1,\ldots,\theta^C} \sum_{\ell=0}^{\ell_{\max}} (2\ell+1)\, K[\, \widehat{\boldsymbol{C}}_\ell \mid \sum_{c=0}^{C} \boldsymbol{C}^c_\ell(\theta^c)\,]$ where $K[\boldsymbol{C}_1|\boldsymbol{C}_2]$ is a measure of mismatch between two covariance matrices $\boldsymbol{C}_1$ and $\boldsymbol{C}_2$. The resulting values $\hat{\theta}^1, \ldots, \hat{\theta}^C$ provide estimates $\boldsymbol{C}^c_\ell(\hat{\theta}^c)$ of $\boldsymbol{C}^c_\ell$. The Wiener filter estimate of $\boldsymbol{d}^c_{\ell m}$ can be expressed as $\hat{\boldsymbol{d}}^c_{\ell m} = \boldsymbol{C}^c_\ell \boldsymbol{C}_\ell^{-1} \boldsymbol{d}_{\ell m}$. In practice, we use the fitted spectral matrices estimated at the previous step: component c is estimated as

$$\hat{\boldsymbol{d}}^c_{\ell m} = \boldsymbol{C}^c_\ell(\hat{\theta}^c) \boldsymbol{C}_\ell(\hat{\theta})^{-1} \boldsymbol{d}_{\ell m} \tag{A.12}$$

and the maps of each component in each channel are finally computed by inverse spherical harmonic transforms.

For processing the current data set, we have used a model containing four components: the CMB, the SZ component, a 4-dimensional Galactic component and a noise component.

The actual processing includes several modifications with respect to this outline: a) beam correction applied to each spectral matrix $\widehat{\boldsymbol{C}}_\ell$; b) spectral binning by which the (beam corrected) spectral matrices are averaged over bins of increasing lengths; c) localization implemented via aopdised masks, by which the SMICA process is conducted independently over two different sky zones.

Strengths: a) no prior information used regarding Galactic emission; b) accurate recovery of the CMB via Wiener filtering; c) it is a relatively fast algorithm; d) built-in goodness of fit.

Weaknesses: a) the results reported here do not account for the contribution of point sources for which a convenient model is lacking; b) localization in two zones is probably too crude; c) no separation of Galactic components.

A.8. Wavelet-based high-resolution fitting of internal templates (WI-FIT)

WI-FIT (Hansen et al. 2006) is based on fitting and subtraction of internal templates. Regular (external) template fitting uses external templates of Galactic components based on observations at frequencies different from the ones used to study the CMB. These templates are fitted to CMB data, the best fit coefficients for each component are found and the templates are subtracted from the map using these coefficients in order to obtain a clean CMB map. WI-FIT differs from this procedure in two respects: (1) it does not rely on external observations of the galaxy but forms templates by taking the difference of CMB maps at different channels. The CMB temperature is equal at different frequencies whereas the Galactic components are not. For this reason, the difference maps contain only a sum of Galactic components. A set of templates are constructed from difference maps based on different combinations of channels; (2) the fitting of the templates are done in wavelet space where the uncertainty on the foreground coefficients is much lower than a similar pixel based approach (in the pixel based approach, no pixel-pixel correlations are taken into account since the correlation matrix will become to large for -like data sets. In the wavelet based approach, a large part of these correlations are taken into account in scale-scale covariance matrices).

For calibration purposes, a set of 500 simulated CMB maps need to be produced and the full wavelet fitting procedure applied to all maps. This is where most CPU time goes. For resolution maps, around 1 Gb of memory is necessary to apply WI-FIT and a total of around 400 CPU h are required.

The strength of WI-FIT is that it relies on very few assumptions about the Galactic components. WI-FIT does however assume that the spectral indices do not vary strongly from pixel to pixel within the frequency range used in the analysis. If this assumption is wrong then WI-FIT leaves residuals in the areas where there are strongly varying spectral indices.

Another advantage of WI-FIT is that it is easy to apply and is completely linear, i.e. the resulting map is a linear combination of frequency channels with well known noise and beam properties. This will in general result in increased noise variance in the cleaned map. In order to avoid this, we smooth the internal templates in order to make the noise at small scales negligable and at the same time not make significant changes to the shape of the diffuse foregrounds. If the diffuse foregrounds turn out to be important at small scales $l > 300$, the smoothing of the internal templates will significantly reduce the ability of WI-FIT to perform foreground cleaning at these scales. Tests on the data have shown that diffuse foregrounds do not seem to play an important role at such small scales. This is valid for the frequency range observed by (i.e. at LFI-frequencies), similar tests will need to be made for the HFI data.

Finally, WI-FIT does not do anything to the point sources, which need to be masked.

References

Ashdown, M. A. J., Baccigalupi, C., Balbi, A., et al. 2007, A&A, 467, 761
Bedini, L., & Salerno, E. 2007, Lect. Notes Artif. Intell., 4694, 9
Bedini, L., Herranz, D., Salerno, E., et al. 2005, EURASIP J. Appl. Sig. Proc., 15, 2400
Bennett, C. L., Halpern, M., Hinshaw, G., et al. 2003a, ApJS, 148, 1
Bennett, C. L., Hill, R. S., Hinshaw, G., et al. 2003b, ApJS, 148, 97
Bertin, E., & Arnouts, S. 1996, A&AS, 117, 393
Bobin, J., Starck, J.-L., Fadili, J., & Moudden, Y. 2007, IEEE Trans. Image Processing, 16, 2662

Bonaldi, A., Bedini, L., Salerno, E., Baccigalupi, C., & de Zotti, G. 2006, MNRAS, 373, 271
Bonaldi, A., Ricciardi, S., Leach, S., et al. 2007, MNRAS, 382, 1791
Bouchet, F. R., & Gispert, R. 1999, New Astron., 4, 443
Cardoso, J.-F., Martin, M., Delabrouille, J., Betoule, M., & Patanchon, G. 2008, [arXiv:0803.1814]
Colafrancesco, S., Mazzotta, P., Rephaeli, Y., & Vittorio, N. 1997, ApJ, 479, 1
Davies, R. D., Dickinson, C., Banday, A. J., et al. 2006, MNRAS, 370, 1125
de Zotti, G., Ricci, R., Mesa, D., et al. 2005, A&A, 431, 893
Delabrouille, J., Cardoso, J.-F., & Patanchon, G. 2003, MNRAS, 346, 1089
Dickinson, C., Davies, R. D., & Davis, R. J. 2003, MNRAS, 341, 369
Dunkley, J., Komatsu, E., Nolta, M. R., et al. 2008 [arXiv:0803.0586]
Eriksen, H. K., Jewell, J. B., Dickinson, C., et al. 2008, ApJ, 676, 10
Finkbeiner, D. P., Davis, M., & Schlegel, D. J. 1999, ApJ, 524, 867
Gawiser, E., Finkbeiner, D., Jaffe, A., et al. 1998, [arXiv:astro-ph/9812237]
Gold, B., Bennett, C. L., Hill, R. S., et al. 2008, [arXiv:0803.0715]
González-Nuevo, J., Argüeso, F., López-Caniego, M., et al. 2006, MNRAS, 369, 1603
González-Nuevo, J., Massardi, M., Argüeso, F., et al. 2008, MNRAS, 384, 711
Górski, K. M., Hivon, E., Banday, A. J., et al. 2005, ApJ, 622, 759
Granato, G. L., De Zotti, G., Silva, L., Bressan, A., & Danese, L. 2004, ApJ, 600, 580
Hansen, F. K., Banday, A. J., Eriksen, H. K., Gorski, K. M., & Lilje, P. B. 2006, Astrophys. J., 648, 784
Haslam, C. G. T., Salter, C. J., Stoffel, H., & Wilson, W. E. 1982, A&AS, 47, 1
Herranz, D., Sanz, J. L., Hobson, M. P., et al. 2002, MNRAS, 336, 1057
Hinshaw, G., Spergel, D. N., Verde, L., et al. 2003, ApJS, 148, 135
Hinshaw, G., Nolta, M. R., Bennett, C. L., et al. 2007, ApJS, 170, 288
Hinshaw, G., Weiland, J. L., Hill, R. S., et al. 2008, [arXiv:0803.0732]
Hobson, M. P., Jones, A. W., Lasenby, A. N., & Bouchet, F. R. 1998, MNRAS, 300, 1
Hobson, M. P., Barreiro, R. B., Toffolatti, L., et al. 1999, MNRAS, 306, 232
Huffenberger, K. M., Eriksen, H. K., Hansen, F. K., Banday, A. J., & Gorski, K. M. 2007
Hyvarinen, A. 1999, IEEE Signal Proc. Lett. 6, 6, 145
Jones, W. C., Ade, P. A. R., Bock, J. J., et al. 2006, ApJ, 647, 823
Komatsu, E., Kogut, A., Nolta, M. R., et al. 2003, ApJS, 148, 119
López-Caniego, M., Herranz, D., González-Nuevo, J., et al. 2006, MNRAS, 370, 2047
López-Caniego, M., González-Nuevo, J., Herranz, D., et al. 2007, ApJS, 170, 108
Maino, D., Farusi, A., Baccigalupi, C., et al. 2002, MNRAS, 334, 53
Maino, D., Donzelli, S., Banday, A. J., Stivoli, F., & Baccigalupi, C. 2007, MNRAS, 374, 1207
Martínez-González, E., Diego, J. M., Vielva, P., & Silk, J. 2003, MNRAS, 345, 1101
Masi, S., Ade, P. A. R., Bock, J. J., et al. 2006, A&A, 458, 687
Melin, J.-B., Bartlett, J. G., & Delabrouille, J. 2006, A&A, 459, 341
Miville-Deschênes, M.-A., Lagache, G., Boulanger, F., & Puget, J.-L. 2007, A&A, 469, 595
Miville-Deschênes, M., Ysard, N., Lavabre, A., et al. 2008, ArXiv e-prints, 802
Negrello, M., Magliocchetti, M., Moscardini, L., et al. 2004, MNRAS, 352, 493
Poutanen, T., de Gasperis, G., Hivon, E., et al. 2006, A&A, 449, 1311
Press, W. H., Teukolsky, S. A., Vetterling, W. T., & Flannery, B. P. 1992, Numerical recipes in FORTRAN. The art of scientific computing (Cambridge: University Press), 2nd edn.
Reinecke, M., Dolag, K., Hell, R., Bartelmann, M., & Enßlin, T. A. 2006, A&A, 445, 373
Schlegel, D. J., Finkbeiner, D. P., & Davis, M. 1998, ApJ, 500, 525
Serjeant, S., & Harrison, D. 2005, MNRAS, 356, 192
Stolyarov, V., Hobson, M. P., Ashdown, M. A. J., & Lasenby, A. N. 2002, MNRAS, 336, 97
Stolyarov, V., Hobson, M. P., Lasenby, A. N., & Barreiro, R. B. 2005, MNRAS, 357, 145
Tegmark, M., Eisenstein, D. J., Hu, W., & de Oliveira-Costa, A. 2000, ApJ, 530, 133
The Planck Collaboration 2005, ESA-SCI(2005), [arXiv:astro-ph/0604069]
Wright, E. L., Chen, X., Odegard, N., et al. 2008, [arXiv:0803.0507]

A&A 493, 835–857 (2009)
DOI: 10.1051/0004-6361:200810514

Astronomy & Astrophysics

A full sky, low foreground, high resolution CMB map from WMAP

J. Delabrouille[1], J.-F. Cardoso[1,2], M. Le Jeune[1], M. Betoule[1], G. Fay[1,3], and F. Guilloux[1,4,5]

[1] Laboratoire AstroParticule et Cosmologie (APC), CNRS: UMR 7164, Université Paris Diderot – Paris 7, 10 rue A. Domon et L. Duquet, 75205 Paris Cedex 13, France
e-mail: delabrouille@apc.univ-paris7.fr
[2] Laboratoire de Traitement et Communication de l'Information (LTCI), CNRS: UMR 5141, Télécom ParisTech, 46 rue Barrault, 75634 Paris Cedex, France
[3] Laboratoire Paul Painlevé, CNRS: UMR 8524, Université Lille 1, 59655 Villeneuve d'Ascq Cedex, France
[4] Modélisation Aléatoire de Paris X (MODAL'X), Université Paris Ouest – Nanterre-la-Défense, 200 avenue de la République, 92001 Nanterre Cedex, France
[5] Laboratoire de Probabilités et Modèles Aléatoires (LPMA), CNRS: UMR 7599, Université Paris Diderot – Paris 7, 175 rue du Chevaleret, 75013 Paris, France

Received 3 July 2008 / Accepted 18 October 2008

ABSTRACT

Context. The WMAP satellite has made available high quality maps of the sky in five frequency bands ranging from 22 to 94 GHz, with the main scientific objective of studying the anisotropies of the Cosmic Microwave Background (CMB). These maps, however, contain a mixture of emission from various astrophysical origin, superimposed on CMB emission.
Aims. The objective of the present work is to make a high resolution CMB map in which contamination by such galactic and extra-galactic foreground emissions, as well as by instrumental noise, is as low as possible.
Methods. The method used is an implementation of a constrained linear combination of the channels with minimum error variance, and of Wiener filtering, on a frame of spherical wavelets called needlets, allowing localised filtering in both pixel space and harmonic space.
Results. We obtain a low contamination low noise CMB map at the resolution of the WMAP W channel, which can be used for a range of scientific studies. We obtain also a Wiener-filtered version with minimal integrated error.
Conclusions. The resulting CMB maps offer significantly better rejection of galactic foreground than previous CMB maps from WMAP data. They can be considered as the most precise full-sky CMB temperature maps to date.

Key words. cosmology: cosmic microwave background – methods: data analysis

1. Introduction

The WMAP satellite is one of the most successful experiments dedicated to mapping the Cosmic Microwave Background (CMB). The all-sky maps obtained in the WMAP five frequency bands, in temperature and polarisation, offer the best data set to date for making a sensitive all-sky map of the CMB anisotropies.

The CMB, however, is not the only source of emission at WMAP frequencies. Diffuse galactic emission from several processes contaminates the maps with an amplitude roughly proportional to the cosecant of the galactic latitude, compromising the observation of the CMB close to the galactic plane. In addition, a background of radio and infrared compact sources, galactic or extra-galactic, contributes to the total emission even at high galactic latitudes. Component separation consists of separating one or more of these sources of emission from the others in the data.

One of the main objectives of CMB experiments is the measurement of the CMB angular power spectrum C_ℓ which, with the assumption of statistical isotropy, describes the second order distribution of the CMB and can be estimated on a fraction of the sky. For this reason, many ground-based and balloon-borne experiments have concentrated their observations in "clean" regions of the sky, where galactic emission is low enough to negligibly impact the observations. For power spectrum estimation from full-sky observations, a safe approach consists of masking regions at low galactic latitude, and estimating power spectra on the cleanest regions of the sky. The impact of extragalactic point sources (evenly spread on the sky) on power spectrum estimates can be evaluated and corrected for using ancillary data (catalogues of known point sources and priors on the statistical distribution of sources).

Besides the power spectrum, the CMB map itself is interesting for several additional purposes:

- as a CMB template, to be subtracted from millimetre-wave observations when the scientific focus is on other emissions, or to be used for the calibration of other instruments;
- to assess the statistical isotropy of the CMB and check the homogeneity and isotropy of the Universe on the largest scales;
- to search for signatures of non-trivial topology, such as that of a multi-connected universe (Aurich et al. 2006; Caillerie et al. 2007; Niarchou & Jaffe 2007);
- to search for correlations of the CMB map with other emissions (Nolta et al. 2004; Fosalba & Gaztañaga 2004; Cabré et al. 2006; Cao et al. 2006; Pietrobon et al. 2006; McEwen et al. 2007; Rassat et al. 2007);
- to search for signatures of a non Gaussian distribution in the CMB (Mukherjee & Wang 2004; Vielva et al. 2004; Cayón et al. 2005; Cabella et al. 2006; McEwen et al. 2006b;

Article published by EDP Sciences

Tojeiro et al. 2006; McEwen et al. 2006a; Wiaux et al. 2007; Yadav & Wandelt 2007).

Several CMB maps obtained with the WMAP data are available for such research projects. The WMAP team has released part-sky foreground-reduced maps in the Q, V and W bands, and maps obtained by an Internal Linear Combination (ILC) of all WMAP channels (Hinshaw et al. 2007; Gold et al. 2008). Tegmark et al. (2003) have produced CMB maps with WMAP one year data, and subsequently with three year data, based on a harmonic space ILC method. Eriksen et al. (2004) presented an alternate version of the ILC CMB map at 1 degree resolution on one year data. Eriksen et al. (2007) used a Gibbs sampler to draw 100 realisations of the CMB under the posterior likelihood of a model of CMB and foregrounds; their estimated CMB map is the average of these realisations for three year data. On three year data again, Park et al. (2007) use an ILC technique on 400 different pixel ensembles, selected by the spectral index of the foreground emission as estimated by the WMAP team using a Maximum Entropy Method (MEM). More authors have addressed component separation on WMAP three year data and produced versions of a "clean" CMB map (Maino et al. 2007; Saha et al. 2007; Bonaldi et al. 2007). More recently, Kim et al. (2008) produced a CMB map from WMAP five year data.

All available maps suffer from limitations, some of which result from specific choices in the way the CMB map is produced. Several of these maps, for instance, do not fully exploit the resolution of the original observations. Some focus on cleaning the CMB of foreground at high galactic latitude, and are significantly contaminated by foreground in the galactic plane. Some are not full sky CMB maps. Finally, not all of the available maps have well characterised noise and effective beam. All these limitations impact on their usefulness for accurate CMB science.

In this paper, we address the problem of making a CMB temperature map which has the following properties:

- full sky coverage;
- being as close as possible to the true CMB (minimum variance of the error) everywhere on the sky, and on all scales;
- having the best resolution possible;
- having a well-characterised beam and noise.

In the following, we review these requirements and their impact on a CMB cleaning strategy (Sect. 2). We then review and compare available maps in Sect. 3. In Sect. 4, we describe and explain our ILC needlet method. The approach is tested and validated on realistic simulated data sets (Sect. 5) before applying it to WMAP data (Sect. 6). We then compare our CMB maps to the other existing maps, discuss the results, and conclude.

This paper considers only *temperature* maps.

2. General considerations

2.1. Requirements

We start with a review of the requirements above, and on the implication on the method to be used.

2.1.1. Full sky?

WMAP data are full sky. We wish to devise a method which allows recovery of an estimate of CMB emission everywhere, including in the galactic plane, and even (as much as possible) in the galactic centre as well as in pixels strongly contaminated by compact sources.

The large scale correlation properties of the CMB make it possible to estimate the CMB emission even in unobserved regions, by some kind of interpolation. This is what is also obtained with the Gibbs sampling technique of Eriksen et al. (2007). Equivalent in spirit although quite different in implementation is the use of an "inpainting" method such as that of Elad et al. (2005) and Abrial et al. (2008). Such interpolation methods alone are not fully satisfactory, as they discard information. In particular they do not allow the recovery of small scale CMB features in the mask. This is obvious, for instance, in the Gibbs-sampling average map of Eriksen et al. (2007).

At the opposite extreme, one may try to separate components in the galactic plane independently of what is done at higher galactic latitudes, since levels and properties of foreground emission depend strongly on sky direction. Hinshaw et al. (2007) and Tegmark et al. (2003) divide the sky into several independent regions, perform component separation independently in these regions, and then make a composite map by stitching together these independent solutions. Such approaches discard information (zone-to-zone correlations) and require careful treatment at the zone borders to avoid discontinuities and ringing.

A good method should perform well on both counts: localised processing and full exploitation of large scale correlations of the CMB and of galactic foreground emissions. This can be achieved with a spherical wavelet or *needlet* analysis of the maps (using the tools developed in Marinucci et al. 2008 and Guilloux et al. 2008), which is our approach in the present work.

2.1.2. Minimum variance?

Recovery of a CMB map can be conducted following various objectives, quantified by different "figures of merit". In this work, we choose, as do most authors, to minimise the variance of the difference between true and recovered CMB (this is the *overall* error; it includes additive noise, foreground emissions, and even multiplicative errors affecting the CMB itself).

This choice alone does not fully characterise the method to be used. The best theoretical solution also depends on the model of the data. An overview of existing methods can be found in the review by Delabrouille & Cardoso (2007).

In this paper, contrarily to other approaches which rely heavily on the structure of the data as described by a model, for instance a noisy linear mixture of independent components (Delabrouille et al. 2003), we assume as little as possible about the foreground emissions and the noise. In fact, we assume nothing except the following:

- the WMAP data are well calibrated, and have a known beam in each channel;
- the instrumental noise in all WMAP maps is close to being Gaussian and uncorrelated; its pixel-dependent level is approximately known;
- the CMB anisotropy emission law is known to be the derivative with respect to temperature of a $T = 2.725$ K blackbody;
- to first order, the template of CMB anisotropies is well represented by a Gaussian stationary random field, the spectrum of which is given by the WMAP best fit (as will be seen later, this last assumption is needed only to derive the Wiener filter; it is not necessary for our needlet ILC map).

These assumptions lead us to consider an "Internal Linear Combination" (ILC) method, followed by a Wiener filter to minimise the error integrated over all scales.

2.1.3. Best resolution?

The WMAP data comes in five frequency channels with varying resolution. To make the best of the data, we need a method which uses the smallest scale information from the *W* band, and information from additional bands (V, then Q, then Ka, and finally K) at increasingly larger scales. Multi-scale tools are well suited for this purpose.

The "best possible resolution" is not a well defined concept (and not necessarily the resolution of the *W* band). Indeed, there is a conflict between best possible resolution and minimum variance, as one can smooth or deconvolve a map arbitrarily in harmonic space, reducing or increasing the total noise variance in the process. Here, we make a map at the resolution of the W channel over the full sky, leaving open the option to filter this map if needed to reduce the noise – or deconvolve it for better angular resolution. Note that additional global filtering or deconvolution does not change the signal to noise per mode (only the integrated S/N).

The minimum variance map is obtained with a Wiener filter, which smoothes the map depending on the signal to noise ratio. As the noise and the contaminants are inhomogeneous, there is a strong motivation for the smoothing to depend on the location on the sky (the optimal solution to the resolution-variance tradeoff depending on the contamination level, which is local). If we relax the constraint about beam homogeneity, again, spherical needlets offer a natural way to obtain such location-dependent smoothing. In the present, however, in order to preserve the constancy of the effective beam over the sky, we implement the Wiener filter in harmonic space.

2.1.4. Accurate characterisation?

A fully accurate characterisation of the beam and noise is not straightforward, in particular because of the limited knowledge about the original frequency maps, which automatically propagates into the final CMB map. This work makes several approximations about beams and noise. Beams are assumed to be symmetric and therefore described by the b_ℓ transfer functions provided by the WMAP team. The instrumental noise is assumed uncorrelated, although non stationary. Analyses and Monte-Carlo simulations are used to characterise the residual noise of the final map, as well as to estimate the contribution of residual foregrounds, and biases if any. This is detailed further below.

2.1.5. Noise

Throughout this paper, the term "noise" refers to all sources of additive error, i.e. instrumental noise *and* foreground emissions.

2.2. Evaluation and comparison of reconstructed CMB temperature

We briefly discuss here the tools used for characterising and comparing CMB temperature maps.

2.2.1. Map description

A pixelised map is fully characterised by the specification of:

- a set of temperature values y_p in a number of pixels (here indexed by p);
- the effective beam at each pixel p, which in the most general case is a function $b_{p,p'}$;
- the noise n_p, the statistical properties of which, in the Gaussian case, are fully described by a noise covariance matrix $N_{p,p'}$.

The map value y_p is then linked to the true signal value s_p by:

$$y_p = \sum_{p'} b_{p,p'} s_{p'} + n_p. \quad (1)$$

The full characterisation of a given CMB map requires the specification of the additive noise n_p and of the response $b_{p,p'}$. When the beam is stationary over the sky and symmetric, which we assume in this work, it is fully specified by the coefficients b_ℓ of the expansion of the beam in Legendre polynomials.

2.2.2. Assumptions

Throughout this paper, the beam is assumed symmetric. Although this is an approximation, most pixels of the WMAP map are "visited" by any particular detector through a wide range of intersecting scans. The average beam in that pixel then is an average of the physical beam over many orientations, which makes the symmetry assumption reasonable.

In addition, in the absence of any specific localised processing, the beam is assumed to be invariant over the sky.

With the above two assumptions, the effect of beam convolution is best represented in harmonic space, with a multiplicative coefficient b_ℓ, independent of m, applied to the harmonic coefficients $a_{\ell m}$ of the map. We assume perfect beam knowledge as well as perfect calibration, so that no multiplicative uncertainty is attached to the map description (the beam integral, approximated as $\sum_{p'} b_{p,p'}$, is equal to unity independently of p, or, equivalently, the value of b_ℓ for $\ell = 0$ is assumed to be exactly unity).

The noise n_p of the original WMAP maps, for each frequency channel and each differencing assembly, is assumed uncorrelated from pixel to pixel, i.e. $N_{p,p'} = \langle n_p n_{p'} \rangle = \delta_{pp'} \sigma_p^2$. The variance σ_p^2 is pixel dependent because of uneven sky coverage. Noise is non-stationary, but assumed to be Gaussian distributed.

2.2.3. Comparison of maps at different resolution

The comparison of CMB maps is meaningful only if the maps are at the same resolution. As long as the beam transfer function does not vanish at any useful ℓ (which is always the case for Gaussian beams), the resolution of any map can be changed to anything else by harmonic transform and multiplication by the ratio of the beam transfer functions. In the present work, we approximate WMAP beams by their symmetric fit (i.e. azimuthally averaged beams), which is justified by the large range of scanning directions at any point in the sky.

This convolution – deconvolution property is widely used throughout this paper.

2.2.4. Masking

We define "tapered" regions of the sky for map comparison at varying galactic latitude. In particular, we define a Low Galactic Latitude (LGL) region and a complementary High Galactic Latitude (HGL) region. The LGL region, used to evaluate results in the galactic plane, completely excludes all data above 30 degrees galactic latitude (and below −30 degrees), and has a

15 degree transition zone with a cosine square shape. All pixels at absolute galactic latitudes below 15 degrees are kept with a coefficient of 1. The HGL region is the complementary, i.e. HGL = 1 – LGL. These "tapered" regions allow the computation of local power spectra with negligible spectral leakage of large scale power into small scales.

2.2.5. Power spectra comparison

For a given beam (i.e. multiplicative response as a function of ℓ), the comparison of the total map power as a function of ℓ (i.e. of the power spectra of the maps) is a direct figure of merit. The lower the power spectrum, the better the map.

Indeed, for fixed b_ℓ, two distinct maps contain the exact same contribution from CMB, but different noise levels. CMB and noise being assumed to be uncorrelated, power spectra are the sum of a CMB term ($b_\ell^2 C_\ell$) and a noise term (N_ℓ). The CMB term being the same for both spectra, any difference in total power spectrum can be interpreted as a difference in noise level.

Power spectra are computed independently for different regions of the sky (e.g. inside or outside the galactic plane). To minimise aliasing due to sharp cuts, we use masks with smooth transitions, defining the LGL and HGL regions described above.

The power spectrum of a map is evaluated as:

$$\widehat{C}_\ell = \frac{1}{(2\ell+1)\alpha} \sum_{m=-\ell}^{\ell} |a_{\ell m}|^2; \tag{2}$$

α is a normalising factor computed as the average value of the squared masking coefficients[1].

Power spectra estimated directly in this way from a masked sky are unreliable for modes corresponding to angular sizes larger than the typical size of the zone of the sky retained for computation.

2.3. Methods

We now give a brief introduction to the two main methods used in this paper (ILC and Wiener filtering). Many other methods exist for CMB cleaning (or component separation in general), which assume varying degrees of prior knowledge about sky emission, and model the data in different ways. These methods are not discussed nor used in this paper. For a review, see Delabrouille & Cardoso (2007).

2.3.1. The ILC

The data are modelled as

$$\boldsymbol{x} = \boldsymbol{a}s + \boldsymbol{n} \tag{3}$$

where $\boldsymbol{x}$ is the vector of observations (e.g. five maps), $\boldsymbol{a}$ is the response to the CMB for all observations (e.g. a vector with 5 entries equal to 1 if WMAP data only are considered) and $\boldsymbol{n}$ is the noise. Here it is assumed that all observations are at the same resolution.

The ILC provides an estimator $\hat{s}_{\rm ILC}$ of s as follows:

$$\hat{s}_{\rm ILC} = \frac{\boldsymbol{a}^t \widehat{\mathsf{R}}^{-1}}{\boldsymbol{a}^t \widehat{\mathsf{R}}^{-1} \boldsymbol{a}} \boldsymbol{x} \tag{4}$$

[1] The masking coefficient is simply 1 in regions kept for power spectrum computations, 0 in regions masked, and between 0 and 1 in the transitions.

where $\widehat{\mathsf{R}}$ is the empirical covariance matrix of the observations (e.g., a 5×5 matrix when 5 channels are considered). The biggest concern with the ILC (and the source of all problems of bias) is that this empirical covariance matrix has to be estimated on the data themselves. This will be discussed further in Sect. 4.

Note that the ILC solution of Eq. (4) is the linear filter which minimises the total variance of the output map, under the condition that the filter has unit response to the signal of interest (the signal with the emission law given by vector $\boldsymbol{a}$).

The details of the method for its implementation in the context of this work are further discussed in Sect. 4.

2.3.2. Wiener filtering

Given a single CMB map of known beam (assumed to be constant over the sky), it is possible to minimise the contamination by noise and foreground by (one-dimensional) Wiener filtering. The data is modelled as $x = s + n$, where now x is a single map, s the true CMB and n the noise. The Wiener filter gives to individual "modes" a weight proportional to the fraction of signal power in that mode, i.e.

$$\hat{s}_{\ell m} = \frac{b_\ell^2 C_\ell}{b_\ell^2 C_\ell + N_\ell} x_{\ell m} \tag{5}$$

where $b_\ell^2 C_\ell$ and N_ℓ are the power spectra of the (smoothed) CMB and of the noise (including smoothed foreground or foreground residuals) respectively, and $x_{\ell m}$ is the original noisy CMB map. It should be noted that if the CMB and the noise are uncorrelated, then $b_\ell^2 C_\ell + N_\ell = X_\ell$ is the power spectrum of the map $x_{\ell m}$, and the Wiener filter can be estimated directly using only a prior on the CMB power spectrum (assuming C_ℓ is known), and estimating X_ℓ on the map itself.

Wiener filtering in harmonic space minimises the variance of the error in the map if signal and noise are Gaussian and stationary. For non-stationary contaminants, the Wiener filter (5) is still meaningful, but is no longer optimal. Here, the Wiener filtering is applied after the ILC. Foreground contamination, strongly reduced by the ILC, is no longer dominant. Instead, instrumental noise is the major source of error on all scales where the Wiener filter is useful (departs from 1). A harmonic space implementation of the Wiener filter disregards this non-stationarity, applying the same coefficient to a given scale, whether it is in a region of deeper integration or not.

Better efficiency may be obtained by an implementation in another domain than the harmonic space (e.g. needlets), but this is not investigated further in this paper, as the consequence is a non stationary equivalent beam.

3. Evaluation and comparison of available maps

Before describing how to make yet another CMB map from WMAP data, we review the existing maps and evaluate in what respects they can be improved.

We start with a discussion of the existing methods, identifying for each of them the strengths and weaknesses of the approach, and their foreseeable consequences. Available CMB maps obtained from WMAP data are compared in terms of resolution, of the estimated contamination by foreground emission, and of noise level. In the absence of an absolute reference, discrepancies between available maps are also evaluated. This comparison permits an estimate of typical uncertainties, and to outline the "difficult regions" for CMB cleaning (which, unsurprisingly, are mostly located close to the galactic plane). We also

look specifically for residuals of galactic contamination by comparing the power spectrum of the reconstructed CMB map at high and at low galactic latitudes. Significant discrepancies between the two are interpreted as indicative of a residue of foreground emission.

3.1. Available maps

3.1.1. The WMAP ILC

The ILC maps obtained by the WMAP team (denoted as WILC1, WILC3 and WILC5 hereafter, depending on whether they are obtained using one year, three year or five year data) are described in Bennett et al. (2003), Hinshaw et al. (2007), and Gold et al. (2008) respectively.

For the three year and five year maps, the original frequency maps are smoothed to a common resolution of one degree. The sky is subdivided into 12 regions. One large region covers most of the sky at moderate to high galactic latitudes. The rest of the sky, concentrated around the galactic plane, is divided into 11 regions of varying galactic emission properties (amplitude and colour). An internal linear combination (ILC) is performed independently in each of these regions. A full sky composite map is obtained by co-adding the maps of the individual regions (with a $\simeq$1 degree transition between the zones to avoid sharp edge effects). Finally, a bias (inevitable consequence of empirical CMB-foreground correlation) is estimated by Monte-Carlo simulations, and subtracted from the composite map, to yield the final CMB map.

The three year and five year ILC maps differ from the one year map in several respects. The most significant is the recognition of the existence of a bias, and the attempt at correcting it using simulations. The limitations of the maps include their resolution (one degree), and the use of small regions in the ILC, which is bound to cause more bias than necessary on large scales (comparable to patch sizes)[2], as well as edge effects. This results in discontinuities between regions, obvious for instance in the estimated bias map shown in Hinshaw et al. (2007).

In the method used by the WMAP team, the coefficients of the linear combination used over most of the sky (region 0, which corresponds to the largest part of the sky at high galactic latitudes and a few low galactic latitude patches, and region 1, in the galactic plane but away from the galactic center) are set using only a small subset of the data inside the Kp2 cut (where the galactic emission is the strongest). This choice favours the rejection of galactic contamination, at the price of sub-optimal weighting of the observations in regions where the error is dominated by noise. It also assumes that the emission laws and relative power of the different foregrounds are the same in these regions, which is a strong (and probably wrong) assumption.

Furthermore, the ILC weights are set by minimising the variance of the map at one degree resolution. Modes at higher ℓ get very sub-optimal weighting, as they do not contribute significantly to the total variance of the one degree map. The K and Ka bands, in particular, contribute respectively about 0.156 and -0.086 to region 0 (the largest one) for WILC3. As a consequence, the final ILC map cannot be meaningfully deconvolved to better resolution than about 1 degree (because this would amplify dramatically small scale noise coming from the lowest frequency channels).

[2] Small patches contain few modes, hence empirical correlations are stronger, as discussed in Appendix A.

Finally, there is also an unsatisfactory degree of arbitrariness in the choice of the regions, which depend on priors about foreground emission, and are somewhat elongated across the galactic plane for no particular reason. Although none of these choices is unreasonable, the impact of this arbitrariness on the final map is difficult to evaluate.

For all these reasons, the WILC maps leave considerable margin for improvement. We aim, in particular, at obtaining a CMB map with better angular resolution, and with a better handling of non-stationarity and scale dependence of the contamination (foregrounds and noise).

3.1.2. The WMAP foreground-reduced maps

For temperature power spectrum analysis, the WMAP team has used part-sky foreground-reduced maps. The processing for foreground removal for the three year and five year releases is described in Hinshaw et al. (2007). Model templates for galactic emission are fitted to the Q, V and W WMAP channels outside of the Kp2 mask. A linear combination of synchrotron, free-free and dust, based on this fit, is then subtracted from the full sky Q, V, W maps.

In this procedure, a first galactic template, supposed to correspond to a linear combination of synchrotron and free-free emission, is obtained from the difference between the K and Ka bands. This template is produced at one degree resolution. An additional free-free template is obtained from Hα emission (Finkbeiner 2003) corrected for dust extinction (Bennett et al. 2003). A dust template is obtained from model 8 of Finkbeiner et al. (1999). "Clean" Q, V and W maps are obtained by decorrelation of these templates from the original Q, V and W observations.

The main limitation of this approach is that the model used is insufficient to guarantee a good fit of the total foreground emission simultaneously inside and outside of the Kp2 mask. As a consequence, the maps produced are heavily contaminated by foreground emissions in the galactic plane, the priority being given to higher galactic latitudes, with the objective of obtaining a part-sky high quality map on which high multipole CMB power spectra could be estimated reliably.

In addition, the maps are likely to depend significantly on the prior model assumed. Here, the WMAP team chooses dust model number 8 of Finkbeiner et al. (1999), and also ignores the plausible existence of anomalous dust emission. The exact impact of these a priori decisions is difficult to evaluate. Anomalous dust emission will come into the foreground reduced maps chiefly as a contaminant in the K-Ka synchrotron template, and hence lead to an erroneous extrapolation of this template to higher frequencies. Assumptions about the emission laws of the template correlated to H-alpha, and of the dust template, if inaccurate, will also result in inaccurate subtraction of free-free and dust. These errors in the estimate of foregrounds are bound to leave, after template subtraction, foreground residuals in the foreground reduced maps.

As an additional drawback, we note that the method generates correlated noise in the foreground-reduced maps, originating either from K and Ka channel noise or from a background of radio sources (see, e.g., Huffenberger et al. 2007; and Wright et al. 2008, for discussions on radio sources in WMAP data and their impact on the analysis of CMB observations with WMAP). Finally, on supra degree scales, the K and Ka bands, which are the most sensitive ones, are used only to subtract foreground emissions, whereas in the cleanest regions of the sky they would be more usefully used to estimate the CMB emission.

For all these reasons, WMAP foreground-reduced maps are not good CMB maps according to the criteria listed in the introduction.

3.1.3. The ILC by Eriksen et al.

Eriksen et al. (2004) have obtained a CMB map at 1 degree resolution with another implementation of the ILC. The map, denoted here EILC1, uses only one year data.

An interesting remark from Eriksen et al. is that the amount of residual dust is high in the ILC maps – the method being able to subtract only about half of the dust present in the W band. At scales larger than 1 degree, this lack of performance is likely to be due to the part of dust emission uncorrelated to low frequency galactic foreground. On the smallest scales, the situation is worse, as the low frequency WMAP channels do not have the resolution to help remove small scale dust emission from W band observations.

For this reason, in the present work, we improve on dust removal by using, as an additional measurement, the IRIS 100 micron dust template obtained from a combination of DIRBE and IRAS maps (Miville-Deschênes & Lagache 2005). As compared to the map of Eriksen et al., we also aim at better angular resolution – and, obviously, better sensitivity, achieved by using five year data sets.

3.1.4. The Gibbs-sampling map by Eriksen et al.

Recently, Eriksen et al. (2007) have produced a low resolution (3 degree) CMB map from WMAP three year data, using a Gibbs sampling technique to explore the likelihood of a parametric model of CMB and foreground emissions. A CMB map is obtained as the average of 100 sample CMB maps each drawn at random according to the posterior distribution of the model parameters given the observations.

The free parameters in the model are spherical harmonic coefficients $a_{\ell m}$ of the CMB map, the CMB harmonic power spectrum C_ℓ, monopole and dipole amplitudes in each WMAP band, the amplitude $a(\nu)$ of a dust template in each band, and amplitudes $f(p)$ and spectral indices $\beta(p)$ of a low-frequency foreground component, for each map pixel p.

The model is constrained by fixing the dust template at 94 GHz according to Finkbeiner et al. (1999), by a prior on the low-frequency foreground spectral index, assumed to be close to that of synchrotron radiation (-3 ± 0.3), and by the constraint that the monopole and dipole coefficients are orthogonal to the (noise-weighted) pixel-averaged foreground spectrum.

In spite of a good fit of the assumed model to the data at high galactic latitudes, there are some strong limitations to the resulting CMB map, and hence to its usage:

- the result of the sampling is obtained assuming a parametric model of foreground emission. There is no possible way of validating the systematic errors due to mismodelling, except marginalising over all possible model skies. This would require a Monte-Carlo simulation which takes into account all uncertainties in the modelling, not only values of the parameters for a given parametric model, but also the choice of the parameter set to be used to model the foreground emissions (varying the dust template according to uncertainties, assuming a different foreground model, etc.). This is not presently available;
- the resulting map is at 3 degree resolution and HEALPix nside = 64, considerably worse than WMAP can do;
- the data sets are cut with the Kp2 mask. Although a CMB is recovered in the mask by the average of the sample maps, the effective resolution inside the mask is lower than in the rest of the sky. In some sense, the Gibbs sampling technique (as implemented here) allows us to recover in the mask what is predictable from the outside map (assuming stationarity of the CMB anisotropy field). It allows only for a limited prediction of the CMB signal in the masked zone.

For all of these reasons, the Gibbs-sampling map of Eriksen et al. (hereafter EGS3) is not a good "best CMB" map according to our criteria.

3.1.5. The ILC by Park et al.

Park et al. (2007) provide their own version (hereafter the PILC3 map) of a one degree resolution CMB map obtained by an ILC on WMAP three year data. The originality of their approach lies in the fact that they cut the sky into 400 pixel ensembles, selected from a prior on their spectral properties. The 400 ensembles are defined from 20×20 spectral index bins (20 for K-V spectral index, and 20 for V-W). This approach is motivated by the fact that ILC weights are expected to vary with varying foreground properties.

There is a weak point to this approach. The authors use, to define their pixel "bins", the MEM solution derived by the WMAP team. If the MEM solution is wrong for a given pixel, that pixel will automatically be classified in the wrong pixel ensemble, and be weighted using the weights of the wrong population of pixels. To some extent then, this binning forces the result of the ILC to match the prior assumptions given by the MEM results. In turn, the MEM solution uses as a prior the result of the WMAP ILC, which is subtracted from the WMAP observations prior to using the MEM method to separate galactic foreground emissions.

As a consequence, the connection of the CMB map of Park et al. to the original WMAP data is far from direct. The map is bound to bear the signature of any arbitrary choice made before, in particular the choice of WMAP ILC regions, the 3-component model for galactic emission, and the MEM priors. For instance, discontinuities at the boundaries between the 12 regions of the WMAP ILC are clearly visible in the map of K-V spectral index used by the authors, as well as their group index (see Figs. 3a and 4a of their paper).

Park et al. then investigate the error in their reconstructed map by Monte-Carlo simulations. However, they use as an input galactic emission template the very model obtained by the MEM. This means that in the simulations, the spectral index maps are "exact". Therefore, the simulations accurately investigate the errors only if the MEM solution is correct, which is not likely to be the case – at least not to the level of precision required to produce a CMB map useful for precision cosmology.

Our method described in Sect. 4 uses as little prior information as possible, and aims at better angular resolution than 1 degree.

3.1.6. The "clean" map of Tegmark et al.

The approach of Tegmark et al. (2003), on both one year and three year data, is the only work to date which aims at producing a CMB map with both full sky coverage and best possible resolution.

Tegmark et al. (2003) have performed a foreground analysis of the WMAP one year maps, producing two high resolution

Table 1. Available CMB maps.

Name	resolution	data used	Reference	URL
WILC1	1°	1-yr	Bennett et al. (2003)	http://lambda.gsfc.nasa.gov/product/map/dr1/imaps_ILC.cfm
TILC1	W channel	1-yr	Tegmark et al. (2003)	http://space.mit.edu/home/tegmark/wmap/cleaned_map.fits
EILC1	1°	1-yr	Eriksen et al. (2004)	http://www.astro.uio.no/~hke/cmbdata/WMAP_ILC_lagrange.fits
WILC3	1°	3-yr	Hinshaw et al. (2007)	http://lambda.gsfc.nasa.gov/product/map/dr2/ilc_map_get.cfm
EGS3	3°	3-yr	Eriksen et al. (2007)	http://www.astro.uio.no/~hke/gibbs_data/cmb_mean_stddev_WMAP3_n64_3deg.fits
PILC3	1°	3-yr	Park et al. (2007)	http://newton.kias.re.kr/~parkc/CMB/SILC400/SILC400_bc.fits
TILC3	W channel	3-yr		http://space.mit.edu/home/tegmark/wmap/cleaned3yr_map.fits
WILC5	1°	5-yr	Gold et al. (2008)	http://lambda.gsfc.nasa.gov/product/map/dr3/ilc_map_get.cfm
KILC5	1°	5-yr	Kim et al. (2008)	http://www.nbi.dk/~jkim/hilc/

maps of the CMB. The first one, the "clean" map (hereafter TILC1), is obtained by a variant of the ILC in which weights are allowed to vary as a function of ℓ, and are computed independently in nine independent regions. The second, the "Wiener" map, is a Wiener-filtered version of the same map, in which the Wiener filter is applied in harmonic space, but independently in each zone.

This work by Tegmark et al. is an early attempt at finding linear combinations of the WMAP data which vary both in harmonic space and in pixel space. The pixel variation of the weights is made using zones which are defined according to the level of contamination by foreground emission, as computed from WMAP map differences W-V, V-Q, Q-K and K-Ka. The authors do not specify exactly how the frequency range is divided into ℓ-bands. While the text seems to indicate that weights are computed independently for each ℓ, figures hint that the weights are actually band-averaged, in 50 logarithmic bands subdividing the multipole range. It makes a difference for the ILC bias. For an ILC implemented ℓ by ℓ, the number of modes at a given ℓ is $2\ell + 1$, and thus remains small for most of the useful range of scales, yielding significant bias (of the order of 10% at $\ell = 25$, and 1% at $\ell = 250$, for a full sky ILC; for a part sky ILC, the bias is multiplied by a factor of the order of the inverse of the sky fraction). For band averages, the effect would be less dramatic, because of the higher number of modes per individual ILC.

In the end, the authors obtain a CMB "clean" map with a "beam corresponding to the highest-resolution map band", i.e. the beam of the W band.

The original paper describes the work done on the one year WMAP data. However maps for three year data are available on Max Tegmark's web site (see Table 1). We use the three year map (TILC3) for comparison with our own solution.

Although the approach of Tegmark and collaborators is quite good at high galactic latitudes, we can see in Fig. 1 that it performs poorly in the galactic plane. Also, the authors have not removed detected point sources from the WMAP data before making the ILC. As a result, their CMB map contains obvious point source residuals, for instance around galactic longitude 305° and latitude 57°, where a 5 mK peak can be seen.

Our method, although bearing some similarity to that of Tegmark and collaborators, aims at significantly improving the error characterisation, as well as the quality of foreground cleaning in the galactic plane.

3.1.7. The "Wiener" map of Tegmark et al.

In addition to their TILC map, Tegmark et al. (2003) publish a Wiener map (hereafter TW map), obtained from the TILC map by independent Wiener filtering in the 9 regions. This results in reduced integrated error in all regions, at the price of pixel-dependent extra smoothing. The consequence of this filtering is an effective zone-dependent beam.

Because of this extra smoothing, it is difficult to compare the TW map with other maps. The most meaningful figure of merit for the Wiener map, though, is the actual power of the error (output map minus true CMB). This is unavailable for any useful up-to-date real data set. Additional discussion about Wiener-filtered maps is deferred to Sect. 6.

3.1.8. The ILC map of Kim et al.

More recently, Kim et al. (2008) have made a CMB map from WMAP five year data, using a "harmonic" ILC method (KILC5 hereafter). Their method performs an ILC in the pixel domain but with pixel-dependent weights. The ILC weights are not constant over predefined zones on the sky but are computed as smooth weight maps defined in terms of a harmonic decomposition (hence the qualification of the method). More specifically, the weight maps are determined by minimising the total output CMB map variance with the constraint that these maps have no multipoles higher than $\ell_{\rm cutoff}$. For stability reasons, the KILC5 map is obtained with $\ell_{\rm cutoff} = 7$. Prior to computing ILC weights, all maps are deconvolved from their beam (effectively blowing up noise on small scales, in particular for the lowest frequency channels). Then, the channels are combined using map modes for $\ell < 300$.

With the above choices, the reconstructed map cannot be good on small scales. As the authors notice themselves, using small scale modes results in minimisation of noise rather than foreground (and, obviously, rejecting the low-frequency observations, which are the noisiest on small scales after deconvolution from the beam). Better results could probably be obtained by estimating weight maps for different bands of ℓ. In essence, this is what our needlet ILC method permits us to achieve.

Limiting the number of modes of the weight maps to $\ell \leq 7$, apparently for reasons of singularity of the system to be solved, results in spatial coherence of the weights on scales of about 35 degrees. The galactic ridge, however, is about 1 degree thick. Hence, the spatial variability of the ILC weights achieved by Kim et al. (2008) is not quite adapted to the actual scale of foreground variation. The needlet ILC method presented in our paper, as will be seen later on, solves this issue in a very natural way.

3.1.9. Other maps

Other authors have performed various foreground cleaning processes in the WMAP observations, producing a number of CMB maps for several different models of the foreground emission. Bonaldi et al. (2007) perform component separation on WMAP data using the CCA method described in

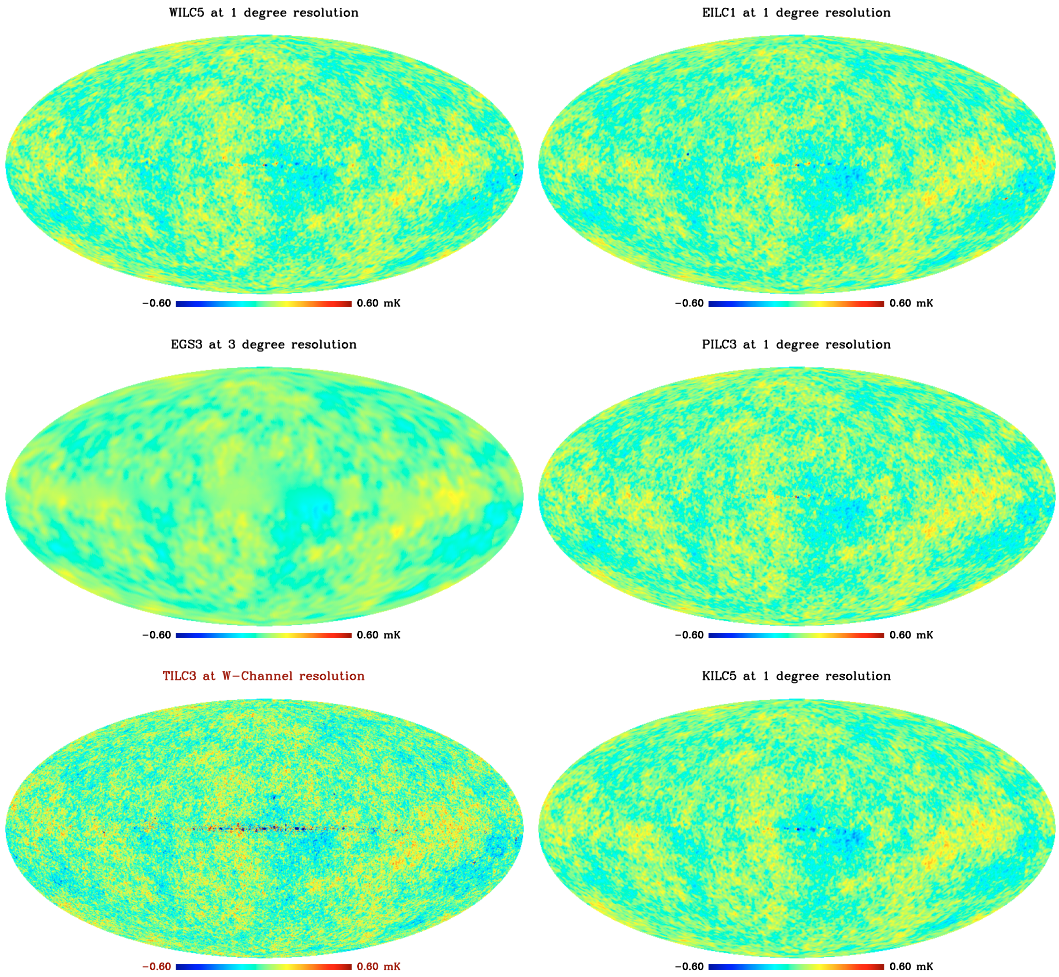

Fig. 1. A selection of presently available CMB maps from WMAP data. Contamination by galactic emission is visible in all of them at various levels, except for the 3-degree resolution EGS3 map (for which a galactic cut was applied and then filled by a plausible CMB extrapolated from higher galactic latitude data).

Bonaldi et al. (2006). Maino et al. (2007) obtain also several CMB maps, using the FastICA method (Maino et al. 2002). None of the CMB maps obtained is full sky, nor publicly available yet. They are not considered further in this analysis.

Finally, some foreground cleaning has also been performed by Saha et al. (2007). Their paper also includes an interesting analysis of the ILC bias. The primary goal of that work, however, is to compute the CMB power spectrum, rather than producing a CMB map.

3.1.10. Existing map summary

Figure 1 shows six available maps, all displayed on the same colour scale. It illustrates the resolution and foreground contamination of the various maps. Table 1 summarises the main properties of the maps. Only the TILC1 and TILC3 maps are high resolution attempts at component separation everywhere, including the galactic plane, combining all WMAP observations. All other maps (WILC maps, EILC1, EGS3, PILC3, KILC5) are at reduced resolution.

3.2. Map comparison

CMB maps produced from WMAP one year data have been compared by Eriksen et al. (2004), showing quite large differences, ranging from −100 to 100 μK. Similarly, Park et al. (2007) compare their PILC3 map with the WILC3 and TILC3 maps at 1.4 degree resolution, showing differences in excess of 40 μK. In the following, discrepancies between these various solutions are further investigated.

As a first step, we evaluate by how much the various maps at one degree resolution disagree over the full sky. The top panel

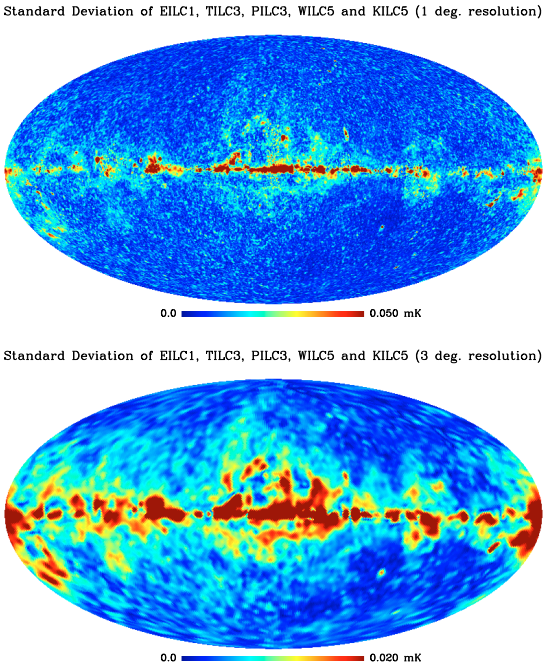

Fig. 2. *Top*: the standard deviation, per pixel for nside = 512, of the EILC1, TILC3, PILC3, WILC5 and KILC5 maps, at 1° resolution. *Bottom*: same at 3° resolution. Note the different color scales for the two panels.

of Fig. 2 shows the pixel based standard deviation of five such maps. In this evaluation, we exclude the EGS3 map (which is at 3 degree resolution, and is the source of additional variance in the Kp2 sky mask, where the CMB is estimated at even lower resolution).

All maps are obtained from observation of the same sky (sometimes starting from the same data set) and are smoothed to the same resolution (one degree) where noise is small. Discrepancies originate essentially from systematic differences in the methods. In the central regions of the galactic plane, discrepancies are significantly higher than 50 μK (with bright spots above 90 μK). In other sky regions, they are typically in the 10–20 μK range, except on compact spots again, where they are above 50 μK. The latter are probably due to residuals of the emission from strong compact sources. The discrepancy between the maps is greater in the ecliptic plane, which is a signature of the impact of the instrumental noise, uneven because of the WMAP scanning strategy. This is due to the different attention given to minimising the contribution of instrumental noise on small scales (rather than foreground emissions) in the final map (and to a much lesser extent to the difference of noise level between the various WMAP releases).

The bottom panel of Fig. 2 focuses the comparison to larger scales (3 degree beam). At high galactic latitudes, the discrepancies are below 10 μK except for a few localised regions (LMC, Ophiuchus complex) where they reach about 30 μK. Differences in the North Polar Spur, at the level of 10–15 μK, are also clearly visible. Close to and inside the galactic plane, systematic discrepancies significantly exceed 30 μK.

Including the EGS3 map in the comparison at high galactic latitudes does not change these conclusions. Pairwise comparisons of the available maps typically show the same level of discrepancies, which indicates that the variance of the solutions is not due to one single map being in strong disagreement with the others.

The conclusion of this comparison is that foreground residuals exist in the published CMB maps at the level of about 50 to 100 μK in the galactic ridge, 20 to 50 μK at low galactic latitudes, and 10 to 20 μK at higher galactic latitudes (above 30 degrees).

This observation calls for localised weightings, adapted to local properties of the foreground and the noise. This, however, is not easily compatible with the recovery of the largest modes of the CMB map, as pointed out before by Eriksen et al. (2004), and as demonstrated by the discontinuities observed between the CMB solutions in the different regions when the sky is cut, as in the TILC, EILC1, and WILC maps.

Our approach, then, will be to vary the relative weightings on small scales for small scale CMB reconstruction, and keep the weighting uniform over large regions of the sky for the recovery of the largest scales. This can be achieved quite straightforwardly by using the spherical needlets discussed in Sect. 4.

4. The ILC needlet method

4.1. The choice of the ILC

It is striking that all the presently available full sky CMB maps derived from an analysis of the WMAP data have been obtained by an implementation of the ILC method.

The ILC, indeed, has many advantages:

- the method relies only on two very safe assumptions: the CMB emission law, and the fact that the CMB template is not correlated to foreground emission[3];
- under these assumptions, the method minimises the empirical variance of the reconstruction error;
- the ILC is very simple in implementation.

The ILC has two major drawbacks.

- As noted for instance by Hinshaw et al. (2007), Delabrouille & Cardoso (2007), Saha et al. (2007), empirical correlations between the CMB and the source of contamination results in a bias; this bias is discussed in more detail below;
- In the absence of a model of the contaminants (foregrounds and noise), it is not possible to predict the reconstruction errors, which somewhat annihilates the benefit of making very safe assumptions about the properties of the data set.

4.2. The ILC bias

The existence of a "bias" in maps obtained by an ILC method is a well established fact. The derivation of this bias (which is, in fact, the systematic cancelling of a fraction of the projection of the CMB map onto the vector space spanned by the noise realisations for all the considered input maps), is given in the Appendix.

The order of magnitude to keep in mind is that about (m – 1) "modes" of the original CMB, out of N_p, are cancelled by

[3] In reality, it is likely that the CMB map actually *is* somewhat correlated to the foreground emissions (extragalactic point sources and SZ effect), because of the ISW effect. The implication of this is not studied further in the present paper.

the ILC, where m is the number of channels used, and N_p the number of independent pixels or modes in the regions for which the ILC is implemented independently. Note however that when the signal is strongly correlated between pixels, the bias can be significantly larger – see the appendix for details.

The practical consequences are:

- a loss of CMB power, which has to be taken into account for power spectrum estimation;
- an anti-correlation of the map reconstruction error with the real CMB sky.

The level of the bias induced by our method is investigated both theoretically (Appendix A), and through Monte-Carlo simulations.

4.3. Needlets

A *frame* is a collection of functions with properties close to those of a basis. *Tight frames* share many properties with orthonormal bases, but are redundant (see Daubechies 1992, for details).

Needlets were introduced by Narcowich et al. (2006) as a particular construction of a wavelet frame on the sphere. They have been studied in a statistical context (e.g. Baldi et al. 2008; Baldi et al. 2007) and have also been used recently for cosmological data analysis problems (e.g. Pietrobon et al. 2006). The most distinctive property of the needlets is their simultaneous perfect localisation in the spherical harmonic domain (actually they are spherical polynomials) and potentially excellent localisation in the spatial domain.

We recall here the definition and practical implementation of the needlet coefficents, following the generalised formulation by Guilloux et al. (2008). Let $h_\ell^{(j)}$, $j \in \mathcal{J}$ be a collection of window functions in the multipole domain, indexed by j. Suppose that for each scale j, $\xi_k^{(j)}$ is a grid of points (indexed by $k \in K^{(j)}$) which satisfies an exact[4] quadrature condition with weights $\lambda_k^{(j)}$. The needlets are axisymmetric functions defined by

$$\psi_k^{(j)}(\xi) = \sqrt{\lambda_k^{(j)}} \sum_{\ell=0}^{\ell_{\max}} h_\ell^{(j)} L_\ell\left(\xi \cdot \xi_k^{(j)}\right), \tag{6}$$

where the functions L_ℓ denote the Legendre polynomials.

Any square integrable function f on the sphere can be analysed by the scalar products $\beta_k^{(j)} := \langle f, \psi_k^{(j)} \rangle$ of the function f with *analysis needlets*. All the needlet coefficients of scale j are advantageously computed in the spherical harmonic domain, as the evaluation at points $\xi_k^{(j)}$ of a function whose multipole moment are simply $h_\ell^{(j)} a_{\ell m}$. These needlet coefficients, denoted $\gamma_k^{(j)}$, are given by:

$$\gamma_k^{(j)} = \sqrt{\lambda_k^{(j)}}\, \beta_k^{(j)}.$$

Each field of needlet coefficients can in turn be convolved with some *synthesis needlets*

$$\tilde{\psi}_k^{(j)}(\xi) = \sqrt{\lambda_k^{(j)}} \sum_{\ell=0}^{\ell_{\max}} \tilde{h}_\ell^{(j)} L_\ell\left(\xi \cdot \xi_k^{(j)}\right), \tag{7}$$

using the same procedure and leading to the map $X^{(j)}$ whose multipole moments are $h_\ell^{(j)} \tilde{h}_\ell^{(j)} a_{\ell m}$. The analysis and synthesis operations are summed up as: *Analysis*:

$$X \overset{\text{SHT}}{\longrightarrow} a_{\ell m} \overset{\times}{\longrightarrow} h_\ell^{(j)} a_{\ell m} \overset{\text{SHT}^{-1}}{\Longrightarrow} \gamma_k^{(j)}.$$

[4] Or almost exact, for all practical purposes.

Synthesis:

$$\gamma_k^{(j)} \overset{\text{SHT}^{-1}}{\Longrightarrow} h_\ell^{(j)} a_{\ell m} \overset{\times}{\longrightarrow} \tilde{h}_\ell^{(j)} h_\ell^{(j)} a_{\ell m} \overset{\text{SHT}}{\Longrightarrow} X^{(j)}.$$

Double arrows denote as many transforms as scales in $\mathcal{J}$. If X is band-limited to $\ell \le \ell_{\max}$ and if the reconstruction condition $\sum_j h_\ell^{(j)} \tilde{h}_\ell^{(j)} = 1$ holds for all $\ell \le \ell_{\max}$, then the complete process yields a decomposition of X in smooth maps, namely

$$\forall \xi, \quad X(\xi) = \sum_j X^{(j)}(\xi). \tag{8}$$

Note that the existence of a fast inverse spherical harmonic transform using the quadrature points $\xi_k^{(j)}$ is required in practice, and that HEALPix pixels and weights fulfil the quadrature condition only approximately. Further details can be found in Guilloux et al. (2008), with an extensive discussion on the choice of the spectral window functions.

A key feature of the needlet decomposition follows from the localisation of the analysis functions which allows for localised processing (such as denoising, signal enhancement, masking etc.) in the needlet coefficient domain, i.e. applying some non-uniform transforms to the coefficients $\gamma_k^{(j)}$. Other types of wavelets (for instance, the steerable wavelets of Wiaux et al. 2008, or the wavelets, ridgelets and curvelets of Starck et al. 2006) could also be used for localised processing on the sphere, although the quality of the localisation depends much on the details of the wavelet design. Needlets are compactly supported in the multipole domain and can be further designed to be well localised in the direct domain according to various criteria. This permits one to work on full sky data without real need for masking the galactic ridge.

4.4. The method

The method implemented in this work, and applied both to simulations and to the real WMAP data sets (for all releases), consists of the following steps:

- we start with the data set consisting of band-averaged temperature maps from WMAP (simulated or real data), to which we add the IRIS 100 micron map;
- WMAP-detected point sources are subtracted from the WMAP maps;
- we apply a preprocessing mask, in which a very small number of very bright compact regions are blanked (see Table 2); blanked regions are filled-in by interpolation; this is done only on the real WMAP data (not on simulations);
- all maps are deconvolved to the same resolution (that of the W channel[5].); this operation is performed in harmonic space;
- maps are analysed into a set of needlet coefficients $\gamma_k^{(j)}$ following the method described in 4.3;
- for each scale, the covariance matrix $\widehat{R}$ of the observations is computed locally (using an average of 32×32 needlet coefficients);
- the ILC solution is implemented for each scale in local patches;
- an output CMB map is reconstructed from the ILC filtered needlet coefficients; this map constitutes our main CMB product;

[5] A noise weighted average beam is obtained from the W1 W2 W3 W4 beam coefficients provided by the WMAP team.

– that map is Wiener-filtered in harmonic space, to make an alternate CMB map with lower integrated error (our best guess CMB map);
– in parallel, the actual ILC filter used on the analysed data set is applied to 100 different simulations of the WMAP noise, to estimate the noise contribution to the final map;
– the level of the biasing, which depends on the geometry and not much on the actual templates of CMB and foreground and noise, is estimated on a set of fully simulated data.

Each of these steps is described in more detail below.

4.5. Point source subtraction

Strong point sources in the input data set typically leave detectable residuals in the output ILC map, and modify at the same time the estimation of the background, leading to less rejection of other contaminants. On the other hand, their specific shape usually allows effective estimation and removal by other methods. For the purpose of this study we used information from the WMAP source catalogue (Hinshaw et al. 2007) which provides characterisation for all point sources detected above a 5σ threshold away from the galactic plane.

For all sources identified, we subtract from the input maps a Gaussian profile at the given position and with the given flux. Conversion factors between flux density and Gaussian amplitude, as well as the FWHM of the Gaussian profile are taken from Table 5 of Page et al. (2003) for one year data, and corresponding updates for the more recent releases.

For the simulated data set, the subtraction of detected point sources is mimicked by removing from the simulation all sources above 1 Jy (independently in all channels).

4.6. Blanking of compact regions

In addition to the point sources subtracted above, some compact regions of strong emission (mostly in the galactic plane) exceed the rejection capabilities of the method used in this analysis, because they are too local and/or too specific. Their contribution in the wings of the needlets also contaminates the solution far from the centre of the sources. Those sources cannot be satisfactorily subtracted in the same way as the previous ones, either because they are not strictly speaking point-like, or because they are bright enough that small departures of actual beam shapes from the Gaussian model used in the subtraction step leave significant residuals. As they represent only a very tiny fraction of the sky (we single out eleven such sources), we blank out these regions in all WMAP channels, cutting out circular patches adapted to the size of the beam and of the source. Table 2 gives the list of those regions with their main characteristics.

To reduce local pollution of the needlet coefficients by the sharp cut, the small blanked regions are filled in by a smooth interpolation, so that fluctuations at a larger scale than the hole size are at least coarsely reconstructed. More precisely, interpolation is made by diffusion of the boundary values inside the hole.

Although this masking and interpolation has no reason to be optimal, it is an efficient way of reducing the impact of very strong sources on their environment. The CMB inside the masked patches is recovered (to some extent) both by the interpolation of original maps (which avoids sharp discontinuities) and by the needlet decomposition and ILC reconstruction. The masked region is tiny: 0.058% of the sky in the K channel (the most affected).

Table 2. List of compact regions blanked in the pre-processing step.

Name	Galactic coordinates	Type
Crab neb	184.5575 –05.7843	SNR
sgr A	000.064 +00.147	Radio-Source
sgr B	000.599 +00.002	Radio-Source
sgr C	359.4288 –00.0898	HII region
sgr D	001.131 –00.106	Molecular cloud
Orion A	209.0137 –19.3816	HII region
Orion B	206.5345 –16.3539	Molecular cloud
Omega neb	015.051 –00.674	HII region
Cen A	309.5159 +19.4173	QSO
Cas A	111.735 –02.130	SNR
Carina neb	287.6099 –00.8542	HII region

A circular patch centered on the source, of radius 75, 55, 45, 45, 34 and 35 arcmin for the K, Ka, Q, V, W and IRIS 100 μm bands respectively, is masked. The masked regions are then filled with an extrapolation of edge values.

Table 3. Spectral bands used for the needlet decomposition in this analysis.

Band (j)	$\ell_{\rm min}$	$\ell_{\rm max}$	nside(j)
1	0	15	8
2	9	31	16
3	17	63	32
4	33	127	64
5	65	255	128
6	129	511	256
7	257	767	512
8	513	1023	512
9	769	1199	512

Needlet coefficient maps are made at different values of `nside`, given in the last column.

4.7. Needlet decomposition

The original observations (WMAP and IRIS) are decomposed into a set of filtered maps represented by their spherical harmonic coefficients:

$$a^{(j)}_{\ell m} = h^{(j)}_{\ell} a_{\ell m} \tag{9}$$

where $a_{\ell m}$ are the spherical harmonic coefficients of the original map, and $a^{(j)}_{\ell m}$ those of the same map filtered by the window function j. Needlet coefficients $\gamma^{(j)}_k$ are obtained as the value of the filtered map at points ξ_k.

For each scale j, the coefficients $\gamma^{(j)}_k$ are computed on a HEALPix grid at some value of `nside`, compatible with the maximum value of ℓ of band j. We use for `nside`(j) the smallest power of 2 larger than $l_{\rm max}/2$, with a maximum of 512. Details about the bands used are given in Table 3 and Fig. 3.

4.8. ILC implementation on needlet coefficients

The general idea is to independently implement the ILC on subsets of the needlet coefficients $\gamma^{(j)}_k$. For a given scale, these coefficients come in the format of a set of HEALPix maps (one per frequency channel). The ILC is implemented locally in space and locally in ℓ as follows.

Covariance matrices $\mathsf{R}^{(j)}_k = \langle \boldsymbol{\gamma}^{(j)}_k \boldsymbol{\gamma}^{(j)T}_k \rangle$ for scale j at pixel k are estimated as the average of the product of the computed needlet coefficients over some space domain $\mathcal{D}_k$. Because of this, there is a trade-off between localisation and accuracy of estimation. A better estimate of the true covariance is obtained by

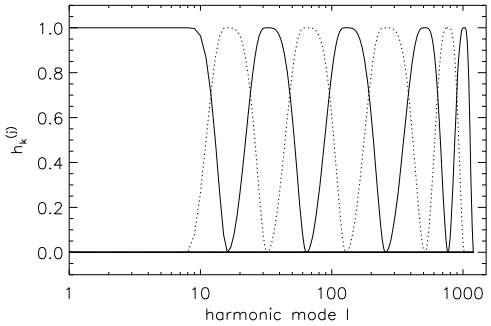

Fig. 3. The spectral bands used in this work for the definition of the needlets.

averaging the products of needlet coefficients between all pairs of maps over a large area, but this provides an estimate of the average covariance over that area. In practice, for the present analysis, we make use of the hierarchical property of the HEALPix pixelisation, and compute covariance matrices as the average in larger pixels, corresponding to a HEALPix pixelisation with `nside` = `nside`(j)/32. This provides a computation of the statistics by averaging $32^2 = 1024$ samples, which results in a precision of the order of 3 per cent for all entries of the $\mathsf{R}_k^{(j)}$ matrix. It implies an ILC bias of order 5/1024 (for $m = 6$ channels and $N_p = 1024$ coefficients per domain on which the ILC filter is estimated independently (see Appendix for details). Choosing a smaller area results in excessive error in the covariance estimates, and hence excessive bias. Choosing a larger area results in less localisation, and hence some loss of efficiency of the needlet approach.

We denote as $\widehat{\mathsf{R}}^{(j)}_{k'\in\mathcal{D}_k}$ the estimate of $\mathsf{R}_k^{(j)}$ obtained by averaging the value of $\boldsymbol{\gamma}_{k'}^{(j)}\boldsymbol{\gamma}_{k'}^{(j)^T}$ in domain $\mathcal{D}_k$.

On the largest scales ($\ell \le 50$), the typical angular extent of a needlet is larger than 5 degrees, and the value of `nside` for the map of needlet coefficients is less than 32. Covariance matrices are then computed on the full sky rather than on the largest possible HEALPix grid, i.e. $\mathcal{D}_k$ is the complete sky, rather than one of the 12 basis Healpix pixels.

Using these covariance matrices, the ILC is implemented using Eq. (4) for each domain. The estimated CMB needlet coefficients are:

$$\left[\widehat{\gamma}_k^{(j)}\right]_{\rm CMB} = \frac{\boldsymbol{a}^T\left[\widehat{\mathsf{R}}^{(j)}_{k'\in\mathcal{D}_k}\right]^{-1}}{\boldsymbol{a}^T\left[\widehat{\mathsf{R}}^{(j)}_{k'\in\mathcal{D}_k}\right]^{-1}\boldsymbol{a}}\,\boldsymbol{\gamma}_k^{(j)}. \tag{10}$$

4.9. Full map reconstruction

The full CMB map reconstructed from this set of needlet coefficients is our basic needlet ILC (NILC) CMB map.

4.10. Final Wiener filtering

For a number of purposes, in particular subtraction of an estimate of the CMB to study other emissions, it is interesting to use, instead of our ILC map at the resolution of the WMAP W channel, a map with minimal error. Such a map is obtained from the ILC map by one-dimensional Wiener filtering.

As a last processing step towards a minimum variance CMB map, we thus Wiener-filter our CMB map, to get rid of the large noise contamination at high ℓ. The Wiener filter is performed in harmonic space as described in 2.3.2.

The harmonic Wiener filter is given by formula 5, i.e. $w_\ell = b_\ell^2 C_\ell/(b_\ell^2 C_\ell + N_\ell)$. For its implementation, we need to know the relative power of CMB and noise. We assume that the best fit CMB power spectrum of the WMAP team is correct, hence C_ℓ is known. The beam factor b_ℓ is assumed perfectly known as well. The denominator $b_\ell^2 C_\ell + N_\ell$ can be estimated directly as the power spectrum of our output needlet ILC map.

In practice, we smooth the power spectra with $\delta\ell/\ell = 0.1$ to lower the variance of the power spectrum estimator on the output needlet ILC map. Even with this, the filter is poorly estimated for low modes, because of the large cosmic variance. As can be seen in Fig. 5, the signal to noise ratio of our reconstructed map is expected to be quite high at low ℓ. Therefore, the Wiener filter for low modes is expected to be very close to 1. For this reason, we set $w_\ell = 1$ for $\ell < 200$, and use a linear interpolation between $\ell = 200$ and $\ell = 250$.

4.11. Noise level estimate

The level of noise contamination (variance per pixel, and average power spectrum) in the output map is estimated by Monte-Carlo simulations, using the average of 100 realisations of the WMAP noise maps. For each initial set (i) of five noise maps (one noise map per WMAP channel), a single output noise map $n_p^{(i)}$ is obtained by performing the needlet decomposition of the initial noise maps, and filtering needlet coefficient maps with the same filter as that used on the single full simulated data set.

Denoting as $n_p^{(i)}$ and $n_{\ell m}^{(i)}$ respectively the pixel value and the harmonic space value of the noise map number i, we compute:

$$\sigma_p^2 = \frac{1}{N_i}\sum_i \left(n_p^{(i)}\right)^2 \tag{11}$$

and

$$\sigma_\ell^2 = \frac{1}{N_i(2\ell+1)}\sum_i\sum_m \left(n_{\ell m}^{(i)}\right)^2. \tag{12}$$

These are respectively estimates of the noise pixel variance and of the noise power spectrum of our final map.

4.12. Bias estimates

The impact of the ILC bias is estimated by Monte-Carlo simulations on simulated data sets. The corresponding error is of the order of 2% of the CMB.

4.13. Practical implementation

The practical implementation of this processing pipeline is made essentially using the `octave` language (the free software version of Matlab). The analysis is done in the framework of the pipeline tool developed by the ADAMIS team at the APC laboratory. This tool provides a flexible and convenient web interface for running our data analysis on simulations or real data with easy handling and tracing of the various pipeline options[6]. Single runs of the full pipeline require less than half an hour on a single processor

[6] See `http://www.apc.univ-paris7.fr/APC_CS/Recherche/Adamis/` in the "outreach" section.

of a standard desktop computer (dominated by harmonic transforms), whereas numerous pipelines on simulated data sets for Monte-Carlo are run on the ADAMIS 88-processor cluster, optimised for efficient I/O.

5. Simulations

5.1. The simulated data

We start with a validation of our method on simulated data sets. For this experiment, synthetic observations of the sky emission are generated using the Planck Sky Model (PSM). The PSM is a flexible software library, designed for simulating the total sky emission in the 10–1000 GHz frequency range, and developed as part of the foreground modelling activities of the Planck working group on component separation (Planck WG2). Sky emission comprises galactic components of four origins (free-free, synchrotron, thermal dust, and spinning dust, with spectral emission laws for dust and synchrotron varying from pixel to pixel), CMB, kinetic and thermal SZ effects, and the emission from a population of galactic and extragalactic point sources which includes radio sources, infrared sources, and an infrared background. Although not perfect, the model sky is thought to be sufficiently representative of the complexity of the real sky emission for our simulations to be meaningful.

Sky maps are produced at WMAP central frequencies for the K, Ka, Q, V and W band, and convolved in harmonic space with approximate WMAP instrumental beams (Gaussian symmetric beams are used for these simulations). Uncorrelated, non-stationary Gaussian noise is added, with a pixel variance deduced from the WMAP sensitivity per channel and effective hit count. To mimic the subtraction of the brightest point sources detected by WMAP, we remove from the model sky, at each frequency, all sources with flux above 1 Jy (assuming they would have been detected, and can be subtracted from the data set). The 11 compact regions listed in Table 2 however, being specific to the real sky, are not blanked for the simulations.

Although these simulations provide only an approximation of the real WMAP data sets, they are representative enough that the simulated data offer a component separation challenge close to that of the real data set. The IRIS map is used as part of the full set of data for the ILC implementation on simulations.

5.2. Results

Figure 4 shows the input simulated CMB, the output CMB, and the difference of the two for one particular simulation. The reconstruction is visually good except in regions of local strong galactic emission (in the galactic ridge, for example). This is to be expected: not only can the method not remove foreground emission perfectly, but in addition the price to pay to remove the foreground (even imperfectly) is more noise (because of sub-optimal weighting of the observations as far as noise contamination is concerned).

A more quantitative estimate of the level of contamination of the CMB map by foreground emissions and noise is obtained by looking at power spectra. Figure 5 shows the input simulated CMB power spectrum (dotted line), the spectrum of the output CMB (solid black line), and the spectrum of the map of residuals (difference between output and input, dashed line), both full sky (top panel) and in the HGL region (bottom panel). The angular power spectrum of the residual map is seen to be small compared to the CMB power on large scales, the two being comparable at $\ell \simeq 500$. Noise dominates on smaller scales.

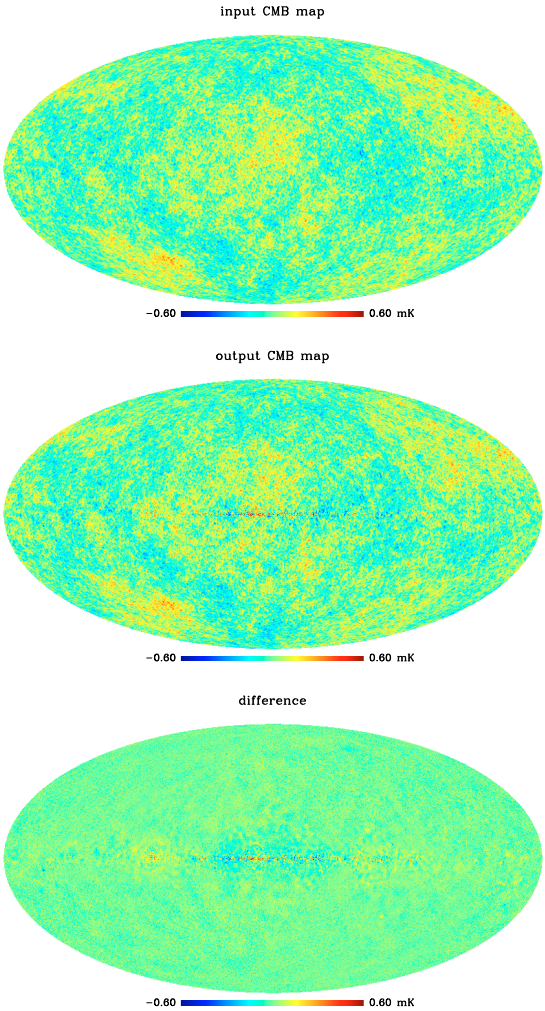

Fig. 4. *Top*: the simulated input CMB map. *Middle*: the reconstructed CMB. *Bottom*: the difference (output-input), displaying the residuals left by the method. All three maps share the same colour scale, and are at the resolution of the WMAP W channel.

The residuals due to the presence of galactic emission are seen to contribute power essentially below $\ell = 400$, where the power of the difference map is seen to be slightly higher in the full sky power spectrum than in the HGL power spectrum (this is visible, in particular, at the top of the first acoustic peak).

5.3. Bias

As discussed in 4.2, we expect a (small) bias in the ILC map, due to empirical correlations between the CMB emission and contaminants (including noise and foreground emission). This is not particular to our approach, and is expected for any ILC method. For better characterisation of our output map, we evaluate the effect both theoretically (in the Appendix) and numerically.

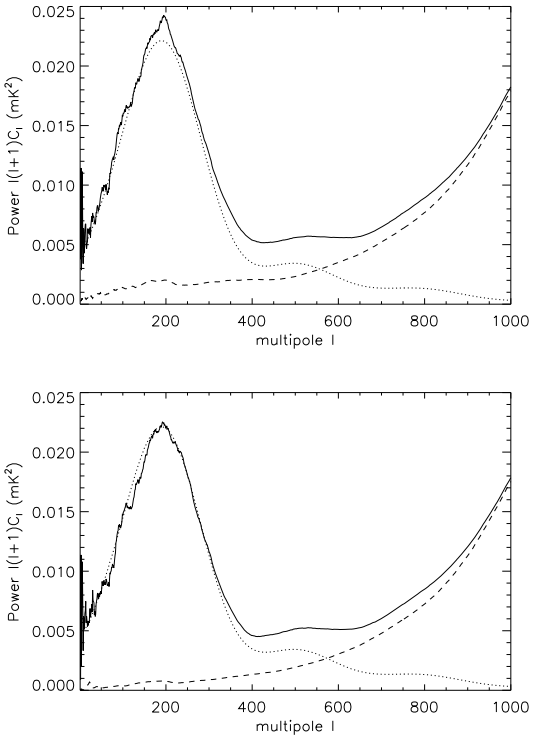

Fig. 5. *Top*: for simulated data sets, full sky power spectra of the output CMB map (plain line), and the difference map (dashed line). The CMB model used in the simulation is over-plotted as a dotted line. *Bottom*: same at high galactic latitude only (HGL region).

Although a general analytic estimate of the bias is complicated, Appendix A shows that (to first order at least and for reasonable assumptions about the CMB, foreground emissions, and noise) the amplitude of the effect does not depend much on what the actual foreground emissions are in detail, but is set essentially by the geometry of the domains considered (through a number of effective modes). It is then possible to estimate the amplitude of the effect by Monte-Carlo simulations on synthetic data sets resembling the actual WMAP observations.

Figure 6 illustrates an estimate of the bias $b(\ell)$ as a function of the harmonic mode, computed as a fractional error:

$$b(\ell) = \frac{\sum_m (\widehat{a}_{\ell m} - a_{\ell m})\, a^*_{\ell m}}{\sum_m |a_{\ell m}|^2} \qquad (13)$$

where $a_{\ell m}$ are the harmonic modes of the input CMB map, and $\widehat{a}_{\ell m}$ the harmonic modes of the output CMB map. The numerator in this equation computes the covariance of the residual map and the input map as a function of ℓ, and the denominator is a normalisation factor. For an error uncorrelated with the input, $b(\ell)$ should be close to 0 on average. Analytical estimates of the effect (see Appendix) suggest a bias of the order of 2% for our implementation (taking into account mode correlation). The numerical estimate of Fig. 6, obtained as the average bias for 500 simulated data sets, is in good agreement with this prediction, with slight variations due to varying numbers of effective modes for

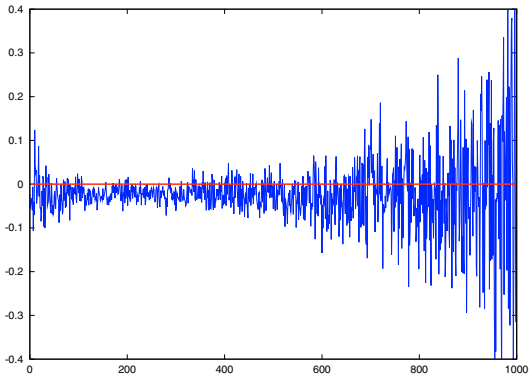

Fig. 6. The fractional bias in the ILC map as a function of ℓ, for one single simulation. This figure is illustrative both of the amplitude of the effect, and on its variance for one single realisation. Bias, and standard deviation of the bias, are of the same order of magnitude for most of the ℓ range.

different needlet scales. The average value of $b(\ell)$ between $\ell = 2$ and 1000 in that simulation is about -2.2%.

6. Application to WMAP data

6.1. ILC result

We now turn to the description of the results obtained on the real WMAP data sets. In order to facilitate the comparison with existing maps, we process independently one year, three year and five year data, to obtain three CMB maps (hereafter NILC1, NILC3 and NILC5). For each year, we use the beam estimates, noise level, and point source catalogue provided with the corresponding release.

The improvement of CMB reconstruction with consecutive data releases is illustrated in Fig. 7, which shows the full sky power spectra of the NILC CMB maps obtained with one year, three year, and five year WMAP data. The power spectra displayed are the raw power spectra of the output map, computed for the full sky, and smoothed with a variable window in ℓ of 10% width. While the lower part of the spectrum, cosmic variance limited and CMB dominated, does not change much, the high ℓ spectrum of the map, dominated by noise, decreases substantially with increasing observation time – as expected. The excellent agreement at low ℓ (up to $\ell \simeq 300$) between the power spectra and the model is striking. The bumps in the spectrum due to the first and second acoustic peaks are clearly visible on the five year map spectrum.

Our full-sky reconstructed CMB map for the five year observations, at the resolution of the W-channel, is displayed in the top panel of Fig. 8.

7. Discussion

7.1. Comparison with other maps

A full comparison of our needlet ILC maps (for all data releases) with all the other available maps would be too long for the present discussion. Rather, we decide to compare our five year result only with the TILC3 map on small scales (choice is motivated by the fact that the TILC is the only other full sky high resolution map available), and with the EGS3 map on large scales.

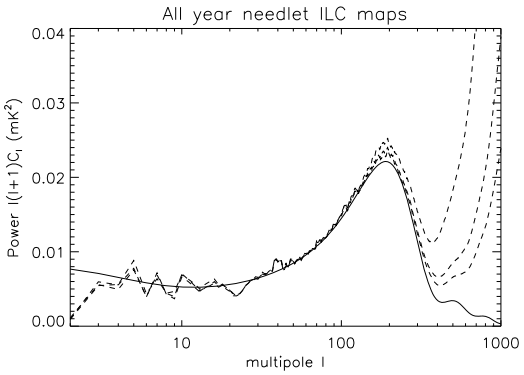

Fig. 7. Power spectra of the NILC map for one year, three year, and five year WMAP data.

This is of particular interest, as the EGS3 is the only map obtained with a method not based on the ILC, and also is a method specifically implemented for the recovery of the largest scales.

7.1.1. Comparison at the pixel level – small scales

On the smallest scales, we compare our needlet ILC map with the TILC and with the WMAP foreground-reduced W band. Figure 10 shows local regions of the foreground-reduced map, the NILC5 map, and the TILC3 map, in the galactic plane and at the galactic pole. Our needlet map is clearly less contaminated by galactic emission than the other two. At high galactic latitude, the NILC5 and TILC3 are visually comparable, while the foreground-reduced map appears to be more noisy, as expected.

The power spectrum of the output map for the five year data (NILC5 map), for three different sky coverages, is shown in the bottom panel of Fig. 9. On the same panel, we plot the angular power spectrum C_ℓ corresponding to the WMAP best fit model, corrected for the W-channel beam. On the top panel of the same figure, we show the same power spectrum estimates for the TILC3 map. This shows the improvement achieved by our method close to the galactic plane. This improvement is due both to the needlet approach and to the use of the IRIS map to help with dust subtraction. As seen in Fig. 7, the difference in quality between NILC5 and TILC3 cannot be explained solely by reduced noise (NILC5 and NILC3 being very close in quality for all scales except the smallest ones).

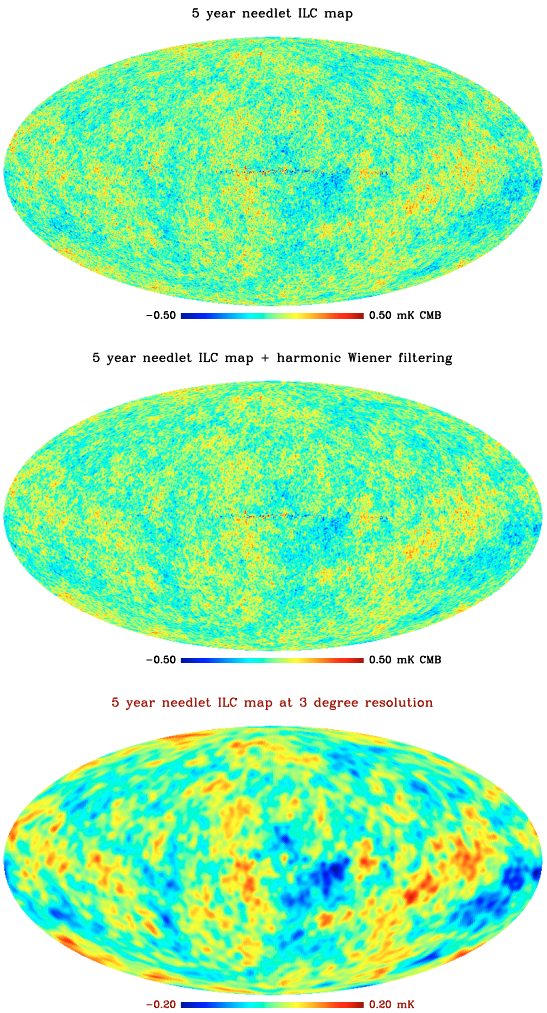

Fig. 8. *Top*: the NILC5 reconstructed WMAP CMB at the resolution of the W channel. *Middle*: the harmonic Wiener NILC5 CMB map. *Bottom*: the NILC5 CMB map at 3 degree resolution.

7.1.2. Comparison at the pixel level – large scales

Figure 11 gives a visual comparison of NILC5 (this work) and the EGS3 (Eriksen et al. 2007), as well as of NILC5 and KILC5 (Kim et al. 2008). In the top row, we display the EGS3 and KILC5 at a resolution of 3 degrees, and degraded to `nside` = 64. The bottom row shows the difference between our needlet ILC solution (displayed on the bottom panel of Fig. 8) and these two maps.

The most striking difference between the five year needlet ILC map and the EGS3 is in the galactic plane, where the EGS3 does not recover the intermediate angular scales. The difference, however, shows no particular clear structure, as expected if it is the random realisation of a Gaussian random field. It is thus probably essentially due to the difference between our CMB reconstruction on scales larger than 3 degrees, and the CMB on larger scales that can be inferred from the CMB reconstructed by Eriksen et al. outside of their galactic mask. At higher galactic latitude, the two maps are in good agreement, with no obvious feature which could be correlated to foreground emissions or to the CMB itself, with the exception of a hot spot in the large Magellanic cloud (which might be residual emission of the LMC in our map, as Eriksen et al. (2007) actually mask the centre of the LMC and obtain a solution in the direction of the LMC by extrapolation from nearby pixels). Above 30 degree absolute galactic latitude, the rms of the difference between our 3 degree map and the EGS3 map is 5.7 μK. The two maps are in much better agreement than the EGS3 and the WMAP MEM model maps (see Fig. 3 in Eriksen et al.). Note however that theoretically, if there were no foreground in the WMAP data, the noise standard

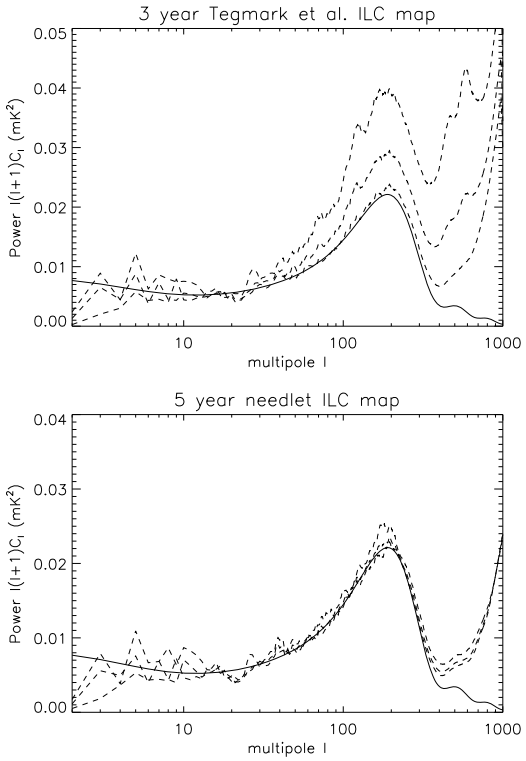

Fig. 9. Power spectrum of the reconstructed WMAP CMB map. For each of the two panels, the CMB best fit model is shown as a solid black line, and power spectra computed at low galactic latitudes (using the LGL mask), on the full sky (no mask), and at high galactic latitudes only (HGL mask) are displayed as dashed lines. Note that the map spectra plotted here are directly those of the maps, without any correction for the beam. *Top panel*: ILC map of (Tegmark et al. 2003, TILC3). *Bottom panel*: this work, with five year WMAP data. The power spectrum of the needlet ILC CMB is significantly more homogeneous than the power spectrum of the TILC3 map. We interpret this difference as an indication that the TILC3 map is significantly more contaminated by residuals of galactic emission. Note the different scales of the y-axis, and the improvement on small scales, with a noise power of about 0.024 mK^2 at $\ell = 1000$ for the NILC5 map at high galactic latitude, instead of about 0.040 mK^2 for TILC3. As indicated by Fig. 7, this is due essentially to the better quality of the five year release, since the NILC3 map also has a noise power spectrum of about 0.040 mK^2 at $\ell = 1000$.

deviation σ_n on a 3 degree map obtained by noise-weighted averaging using all WMAP channels would be about 3.2 μK for three year data. If instead we assumed that only the three highest frequency channels are free of foreground contamination, σ_n would be 4.4 μK.

The difference between our map and the KILC5 map is more systematic with, in particular, stronger differences in the galactic plane, in spite of the fact that the two methods work on the same input data set. A careful visual inspection of the CMB maps themselves gives the impression that the KILC5 map is probably systematically negative towards the galactic central regions. There is, however, no secure way to be certain which map is best.

7.2. Map characterisation

7.2.1. Beam

The effective beams of the reconstructed maps are plotted in Fig. 12, for both the full resolution five year needlet ILC map, and for the Wiener-filtered version. The map has been reconstructed for the range $0 \leq \ell \leq 1200$, with a smooth transition of the response, between ℓ of 1024 and 1200, from the nominal W band beam value to 0. This smooth transition allows us to avoid ringing effects which happen in the case of a sharp cut-off in ℓ. The ratio of the Wiener beam (dashed line) and ILC beam (solid line) gives a measure of the signal to noise ratio in each mode.

7.2.2. Instrumental noise

Given the ILC filter computed on the real data set, the level and properties of the instrumental noise can be straightforwardly computed by applying the *same* filter to simulated WMAP noise maps. From 100 noise realisations, we compute the average full-sky noise power spectrum (Fig. 13), as well as the noise standard deviation per pixel (Fig. 14). Noise properties are not as simple as one may wish: the noise is non stationary, because of both the uneven sky coverage and of the localised processing. It is also somewhat correlated pixel-to-pixel, in particular close to the galactic plane. This is unavoidable, but fortunately our pipeline allows us to make as many Monte-Carlo realisations of the instrumental noise as needed for any scientific study made using our needlet ILC map. One hundred such simulations are made available as part of our main data products.

7.2.3. Foreground residuals

More problematic is the evaluation of the contamination of the CMB map by foreground residuals. It requires prior information about the foregrounds, which the ILC method avoids using. An indication of the level of systematic uncertainty is obtained from the comparison of the various solutions (Fig. 2). An other option consists of checking the contamination on simulations. Figures 4 and 5 give an idea of the expected contamination from such simulations. This, however, is good only as long as the simulations are representative enough.

The comparison of the power spectrum of the output CMB map computed at high and low galactic latitude (Fig. 9), and a visualisation of the output CMP map at high and low galactic latitude (Fig. 10) also give an idea of the amount of galactic residuals, but none of these estimates is fully satisfactory for careful CMB science. This is, however, not particular to our map. No published CMB map is available with a good estimate of foreground contamination. Although this, clearly, is not fully satisfactory, we leave further investigations on this question for future work.

7.3. Final comments

7.3.1. Is our map optimal?

In the present work, we have obtained a CMB map which has been shown to be significantly less contaminated by foreground and noise than the other existing maps obtained from WMAP data. A natural question is whether we can do even better.

In the following, we outline where there is margin for improvement, and explain why we have stopped the analysis at its present state.

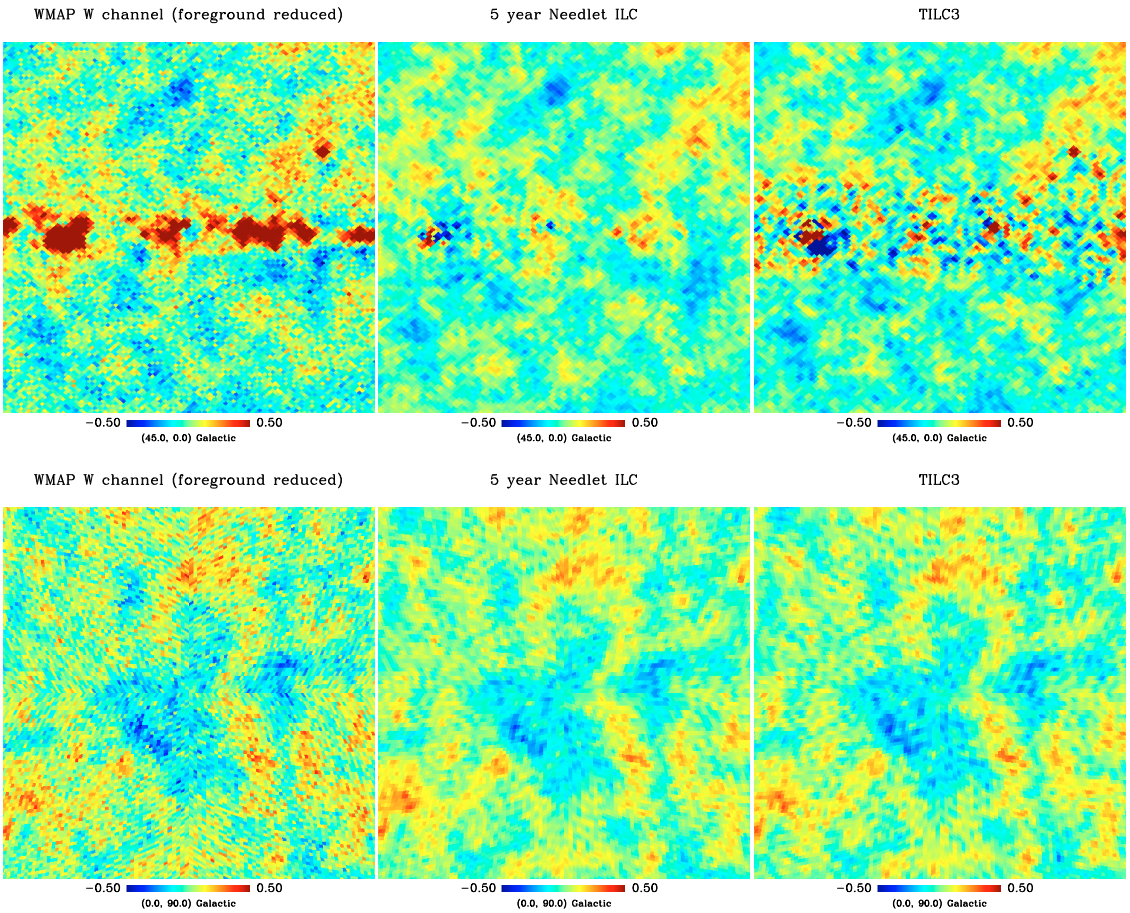

Fig. 10. CMB maps from WMAP three year data obtained with three techniques: *left column*: WMAP foreground reduced, W channel; *middle column*: our needlet ILC map; *right column*: the TILC map. The top line corresponds to a patch located in the galactic plane, centred around coordinates $(l, b) = (45°, 0°)$. The bottom line shows the recovered CMB around the North Galactic Pole.

First, the present analysis uses only limited external information and data sets: WMAP point source detections, and the IRIS 100 micron map. It is likely that something could be gained by using additional observations to help constrain the galactic emission.

Second, there is a trade-off between localisation of the estimation of covariance matrices, and bias in the ILC. The estimation of covariance matrices R_x over sets of $N_p = 32 \times 32$ needlet coefficents results from a compromise which has been made based on varying N_p in simulations, but has not been optimised in any way. In addition, the optimal solution is probably different at high galactic latitudes, where weights given to different channels probably do not vary much and thus require less localisation, and at low galactic latitudes, where the complexity of galactic emission calls for more localisation. We have tried to use $N_p = 16 \times 16$ (more localised ILC filters, but more bias) and $N_p = 64 \times 64$ (less localised ILC filters, but less bias). Our choice of $N_p = 32 \times 32$ seems, in simulations, not worse than anything else (nor much better either). The bias error has been verified to remain below the reconstruction error due to the contribution of the noise for small scales, and below cosmic variance uncertainty for large scales (see Fig. 13), and remains below an acceptable level of a few percent.

Similarly, the choice of the spectral window functions used on this data set has not been the object of specific optimisation. At low ℓ, we follow a "dyadic" scheme, where each window reaches an $\ell_{\rm max}$ of about twice the previous one. Wide spectral window functions allow for more localisation in pixel space, but narrow window functions allow for more accuracy in the harmonic domain. At high ℓ, because of the variation of the beams with ℓ, the relative noise levels of the different channels change quite fast with ℓ, which calls for more localisation in ℓ space. Here again, the optimal window functions are probably not the same at high and at low galactic latitudes. In practice, we chose a small number of bands to limit the number of harmonic transforms in the pipeline and allow reasonable localisation of the analysis.

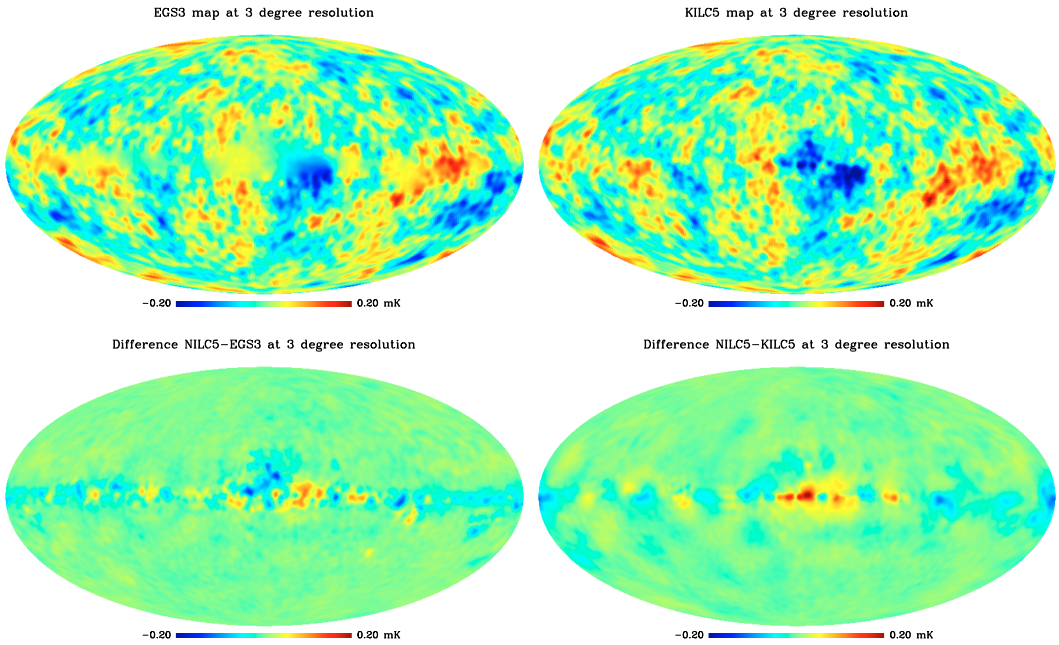

Fig. 11. *Top left*: the EGS3 map. *Top right*: The KILC5 map, smoothed at 3 degree resolution. *Bottom left*: the difference NILC5-EGS3; we see is a clear difference in the galactic plane with no particular structure, compatible with a smooth Gaussian field, where the EGS3 solution poorly estimates intermediate scales; a patch in the difference map at the location of the Large Magellanic Cloud is clearly visible also. *Bottom left*: the difference NILC5-KILC5; a clear structure aligned with the galactic plane is clearly visible, with a large difference towards the galactic center.

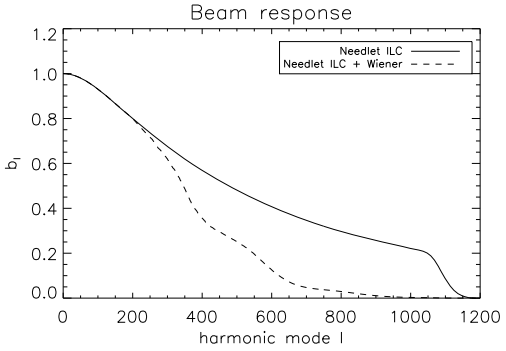

Fig. 12. Harmonic response of the beam of the NILC5 CMB map and of the Wiener-filtered version.

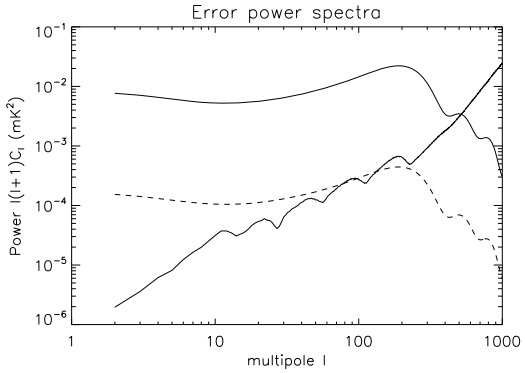

Fig. 13. Plot of the power spectrum of the noise (solid line). The spectrum for the WMAP best fit model is shown as a solid line, for comparison. The dashed line is 2% of the WMAP best fit C_ℓ, indicative of the level of the expected ILC bias. The bias is seen to dominate on large scales. There is, however, little margin for improvement, as few independent modes (or needlet coefficients) are available on the largest scales.

The choice we have made results from the principle of simplicity. We have tried to devise a pipeline which depends as little as possible on external data, on priors, or on fine tuning. A very simple scheme has permitted us to obtain a CMB map convincingly better than other maps available. This does not preclude any attempt at more optimisation for future work if needed.

7.3.2. Why ILC and not ICA?

It is certainly possible to tune our pipeline, changing some of its parameters. It would be possible also to use methods other than an ILC, for instance Independent Component Analysis (ICA) methods such as SMICA (Delabrouille et al. 2003; Cardoso et al. 2008), or more generally maximum likelihood methods fitting parametric models of the foreground emissions in the data sets. Such methods extract information about the foreground from the

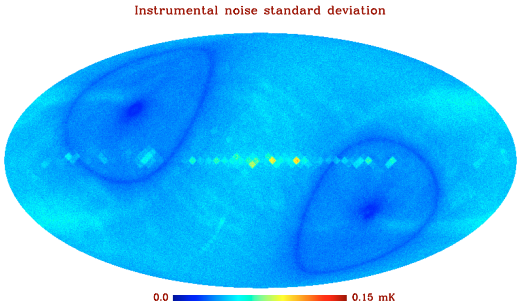

Fig. 14. Map of the standard deviation of the noise, per pixel at `nside` = 512, for the five year needlet ILC map at the resolution of the W channel. The adaptation of the filter to local contamination is obvious from the uniform noise level in large healpix pixels, in particular in the galactic plane. These large healpix pixels correspond to `nside` = 16, which is the size used to compute the average filter for the smallest scales. This illustrates the impact of the compromise between subtracting foreground emissions and increasing the noise with the use of the lower frequency channels, which have poor sensitivity on small scales.

data directly, possibly with the help of ancillary data sets, and use this information to clean the observations in some way.

In the present case however, it is not very likely that such attempts would give much better results than what is obtained here, unless one uses a very significant number of additional data sets and safe prior information. Indeed, the WMAP data consists of five channels only, from which a component separation method based on a meaningful model of foreground emission needs to extract CMB, synchrotron, free-free, spinning dust, thermal dust (i.e. five templates), and possibly also point sources, and variations of the spectral indices of some of the components – not to mention special regions of galactic emission such as cold cores and H-II regions, nor particular objects such as nearby resolved galaxies or galaxy clusters. Any component separation method based on the estimation of parameters for such a rich model would almost certainly be confronted with indeterminacy issues. Methods based on a precise model are expected to be effective when the data are very redundant as compared with the number of "parameters" of the emission model, which would not be the case here. Hence, the ILC is probably one of the best approaches for performing component separation on WMAP data. It is not surprising, then, that all methods producing full sky CMB maps from WMAP, or nearly so, implement some variant of the ILC.

Incidentally, ICA methods could benefit from the needlet framework.

8. Conclusions

In this paper, we have described a new approach to implement CMB extraction in WMAP data, using the ILC method on a needlet frame. Tests on simulations show excellent performance of the method, thanks to localisation both in pixel space and in harmonic space. Localisation in pixel space allows the ILC weights to adapt themselves to local conditions of foreground contamination and instrumental noise (this is essentially the reason why the NILC performs better than the TILC, in particular in the vicinity of the galactic plane). Localisation in harmonic space allows us to favour foreground rejection on large scales (where foreground emissions dominate the total error) and instrumental noise rejection on small scales (where foreground emissions are negligible but where, after beam deconvolution, the relative noise level between the various WMAP channels varies a lot as a function of scale). Needlets permit us to vary the weights smoothly on large scales, and rapidly on small scales, which is not possible by dividing the sky in zones prior to any processing.

As a further improvement on previous work on WMAP data, we include a dust template in the set of analysed observations. This is motivated by the fact that on the smallest scales, observed with reasonable signal to noise ratio by the W channel only, dust emission contributes a significant fraction of the total reconstruction of the map. Using the IRIS 100 micron map as an additional observation enables the ILC to reduce the final contamination by dust –thanks to correlations of dust emission between the W channel and the 100 micron map. Special care was also taken to subtract a number of strong point sources from the data prior to the ILC.

As discussed at length in the main text and in the Appendix, the implementation of a filter (the ILC) based on empirical estimates of covariance matrices leads to a bias. This is not particular to our map, but is the case for any ILC map. We have estimated the level of this systematic effect, both analytically and numerically, to be at the level of a few per cent on all scales. Our simulation tool allows us to make accurate estimates of the amplitude of the effect, if needed for any scientific exploitation of the NILC5 map.

The application of the method to WMAP one year and three year data (in addition to five year data) allows us to compare the needlet ILC solution to previous work. Our map is seen to be at least as good as others on large scales, while being significantly less contaminated by residual foreground and noise than others on small scales, in particular in the vicinity of the galactic plane. The application of the method to WMAP five year data yields a CMB map which we believe to be the cleanest full sky map of the CMB to date. Contamination by noise, and the power loss due to the use of the ILC method, are characterised by means of Monte Carlo simulations. The map is available for download on the ADAMIS web site[7], and can be used for a variety of science projects relying on accurate maps of the CMB.

Acknowledgements. The ADAMIS team at APC has been partly supported by the Astro-Map and Cosmostat ACI grants of the French ministry of research, for the development of innovative CMB data analysis methods. We acknowledge the use of the Legacy Archive for Microwave Background Data Analysis (LAMBDA). Support for LAMBDA is provided by the NASA Office of Space Science. The results in this paper have been derived using the HEALPix package (Górski et al. 2005). The authors acknowledge the use of the Planck Sky Model[8], developed by the Planck working group on component separation, for making the simulations used in this work. Our pipeline is mostly implemented in octave (`http://www.octave.org`).

Appendix A: Derivation of the ILC bias

In this appendix, we compute the error made after CMB reconstruction with the ILC and some of its statistical properties. In particular, we derive the correlation of the error with the true CMB signal, which yields a non unit effective "response" of the ILC filter – and hence a *bias* in the reconstructed map and in the CMB power spectrum computed from it. This bias has to

[7] `http://www.apc.univ-paris7.fr/APC_CS/Recherche/Adamis/cmb_wmap-en.php`
[8] `http://www.apc.univ-paris7.fr/APC_CS/Recherche/Adamis/PSM/psky-en.php`

be accounted for properly for further use of the reconstructed CMB map.

We model the data as:

$$\boldsymbol{x}_p = \boldsymbol{a} s_p + \boldsymbol{n}_p \tag{A.1}$$

where s_p are the coefficients of the map of interest over some domain $\mathcal{D}$ (e.g. needlet coefficients of the CMB map for a given scale and a given patch of the sky, or pixel values in a certain region of the sky, or values of the harmonic coefficients in some band of ℓ). p indexes the coefficient (i.e. pixel, or harmonic mode, or needlet coefficient). $\boldsymbol{x}_p$ are the observations of coefficient p for the set of available observed maps, and $\boldsymbol{n}_p$ the corresponding "noise" terms (including foreground contaminants).

The ILC is best applied over domains of p where all coefficients have (near) uniform expected signal and noise properties, so that the ILC weights are optimal simultaneously for all p. In particular, the rms values of all maps do not depend (much) on p in a given domain. Hence, we concentrate on one given domain of p for which we assume that the sequences s_p and $\boldsymbol{n}_p$ are independent, Gaussian random variables with distribution $\mathcal{N}(0, \sigma_s^2)$ and $\mathcal{N}(0, \mathsf{R}_n)$, with σ_s^2 the variance of s_p (the CMB) and R_n the covariance matrix of the noise (including foreground emissions).

The ILC estimate of s_p in domain $\mathcal{D}$ is given, for all p, by

$$\hat{s}_p = \frac{\boldsymbol{a}^t \widehat{\mathsf{R}}_x^{-1}}{\boldsymbol{a}^t \widehat{\mathsf{R}}_x^{-1} \boldsymbol{a}} \boldsymbol{x}_p \tag{A.2}$$

where $\widehat{\mathsf{R}}_x$ is an estimate of the covariance matrix of the observations, obtained as:

$$\begin{aligned} \widehat{\mathsf{R}}_x &= \frac{1}{N_p} \sum_p \boldsymbol{x}_p \boldsymbol{x}_p^t \\ &= \frac{1}{N_p} \sum_p (\boldsymbol{a} s_p + \boldsymbol{n}_p)(\boldsymbol{a} s_p + \boldsymbol{n}_p)^t \end{aligned} \tag{A.3}$$

with N_p the number of coefficients in domain $\mathcal{D}$. In the limit of large N_p, $\widehat{\mathsf{R}}_x$ approaches its expectation (ensemble average) value $E(\widehat{\mathsf{R}}_x) = \mathsf{R}_x$. For finite N_p, we have instead

$$\widehat{\mathsf{R}}_x = \mathsf{R}_x + \Delta_x \tag{A.4}$$

where Δ_x is a correction term corresponding to the departure of the empirical correlation from its ensemble average due to the finite sample size N_p. From now on, we assume that N_p is large enough that this correction is small: we investigate effects at first order in $1/N_p$.

A.1. First order expansion of the reconstruction error

We are interested in the reconstruction error:

$$d_p = \hat{s}_p - s_p \,. \tag{A.5}$$

The first and second moments of d_p, i.e. the mean value $E(d_p)$ of the reconstruction error, as well as its variance $E(d_p^2)$, are of particular interest for the interpretation of the reconstructed map. In particular, we have

$$E(\hat{s}_p^2) = E(s_p^2) + E(d_p^2) + 2E(s_p d_p). \tag{A.6}$$

In our case, $E(\hat{s}_p^2)$ can be used to estimate $E(s_p^2)$. In the case where domain $\mathcal{D}$ is a harmonic domain, p indexes harmonic modes (ℓ, m), and $E(s_p^2)$ is a term of the CMB power spectrum. In our needlet approach, $E(s_p^2)$ is also directly connected to the CMB power spectrum. For this reason, it is important to characterise in the best way we can the "noise bias" $E(d_p^2)$ and the covariance of the error with the CMB, $E(s_p d_p)$.

The ILC being constructed so that the response to the signal of interest is unity, only the filtered noise term contributes to the error d_p, which can then be written as:

$$d_p = \frac{\boldsymbol{a}^t \widehat{\mathsf{R}}_x^{-1}}{\boldsymbol{a}^t \widehat{\mathsf{R}}_x^{-1} \boldsymbol{a}} \boldsymbol{n}_p \tag{A.7}$$

$$= \frac{\boldsymbol{a}^t \left[\mathsf{R}_x + \Delta_x\right]^{-1}}{\boldsymbol{a}^t \left[\mathsf{R}_x + \Delta_x\right]^{-1} \boldsymbol{a}} \boldsymbol{n}_p \tag{A.8}$$

where Δ_x is a small perturbation to R_x. We use the first order expansion:

$$\left[\mathsf{R} + \Delta_x\right]^{-1} \simeq \mathsf{R}^{-1} - \mathsf{R}^{-1} \Delta_x \mathsf{R}^{-1} \tag{A.9}$$

which yields

$$d_p = \frac{\boldsymbol{a}^t \left[\mathsf{R}_x^{-1} - \mathsf{R}_x^{-1} \Delta_x \mathsf{R}_x^{-1}\right] \boldsymbol{n}_p}{\boldsymbol{a}^t \left[\mathsf{R}_x^{-1} - \mathsf{R}_x^{-1} \Delta_x \mathsf{R}_x^{-1}\right] \boldsymbol{a}} \,. \tag{A.10}$$

Writing:

$$\begin{aligned} \frac{1}{\boldsymbol{a}^t \left[\mathsf{R}_x^{-1} - \mathsf{R}_x^{-1} \Delta_x \mathsf{R}_x^{-1}\right] \boldsymbol{a}} &= \frac{1}{\boldsymbol{a}^t \mathsf{R}_x^{-1} \boldsymbol{a}} \frac{1}{(1-\epsilon)} \\ &\simeq \frac{1}{\boldsymbol{a}^t \mathsf{R}_x^{-1} \boldsymbol{a}} (1+\epsilon) \end{aligned}$$

where ϵ is

$$\epsilon = \frac{\boldsymbol{a}^t \mathsf{R}_x^{-1} \Delta_x \mathsf{R}_x^{-1} \boldsymbol{a}}{\boldsymbol{a}^t \mathsf{R}_x^{-1} \boldsymbol{a}} \tag{A.11}$$

we get

$$d_p \simeq \frac{\boldsymbol{a}^t \left[\mathsf{R}_x^{-1} - \mathsf{R}_x^{-1} \Delta_x \mathsf{R}_x^{-1}\right] \boldsymbol{n}_p}{\boldsymbol{a}^t \mathsf{R}_x^{-1} \boldsymbol{a}} (1+\epsilon) \,. \tag{A.12}$$

Keeping only first order terms in (Δ_x) yields:

$$\begin{aligned} d_p &= \frac{\boldsymbol{a}^t \mathsf{R}_x^{-1} \boldsymbol{n}_p}{\boldsymbol{a}^t \mathsf{R}_x^{-1} \boldsymbol{a}} - \frac{\boldsymbol{a}^t \mathsf{R}_x^{-1} \Delta_x \mathsf{R}_x^{-1} \boldsymbol{n}_p}{\boldsymbol{a}^t \mathsf{R}_x^{-1} \boldsymbol{a}} \\ &\quad + \frac{\left[\boldsymbol{a}^t \mathsf{R}_x^{-1} \boldsymbol{n}_p\right] \left[\boldsymbol{a}^t \mathsf{R}_x^{-1} \Delta_x \mathsf{R}_x^{-1} \boldsymbol{a}\right]}{\left[\boldsymbol{a}^t \mathsf{R}_x^{-1} \boldsymbol{a}\right]^2} . \end{aligned} \tag{A.13}$$

The first term on the right hand side, proportional to $\boldsymbol{n}$, is the "ideal" ILC error, i.e. the error we would get if we knew perfectly the "true" covariance matrix R_x of the observations. The second and third terms, proportional to Δ_x, are corrections due to the fact that this covariance matrix is actually obtained empirically from the observations themselves.

From Eqs. (A.3) and (A.4), we can write Δ_x in the form:

$$\Delta_x = \delta_s \boldsymbol{a}\boldsymbol{a}^t + \Delta_n + \widehat{\mathsf{C}} \tag{A.14}$$

where

$$\delta_s = \widehat{\sigma}_s^2 - \sigma_s^2 \tag{A.15}$$

$$\Delta_n = \widehat{\mathsf{R}}_n - \mathsf{R}_n \tag{A.16}$$

$$\widehat{\mathsf{C}} = \frac{1}{N_p} \sum_q \left(\boldsymbol{n}_q s_q \boldsymbol{a}^t + \boldsymbol{a} s_q \boldsymbol{n}_q^t\right). \tag{A.17}$$

These three quantities correspond respectively, in pixel (or mode, or needlet coefficient) p, to the uncertainty in CMB variance estimates due to "cosmic" (or sample) variance, to the error in the estimation of the "noise" covariance matrix alone (if maps of noise + foreground alone were available), and to a cross term, originating from the empirical covariance between CMB and noise due the finite sample size N_p.

The two last terms (small correction terms) in Eq. (A.13), being proportional to Δ_x, can be decomposed each into the sum of three terms, proportional to $(\delta_s \boldsymbol{a}\boldsymbol{a}^t)$, Δ_n, and $\widehat{\mathsf{C}}$ respectively. The signal and noise realisations enter the $(\delta_s \boldsymbol{a}\boldsymbol{a}^t)$ term as products of terms of the form $(\boldsymbol{a}\boldsymbol{a}^t s_q s_q \boldsymbol{n}_p)$ only, the Δ_n term as products of terms of the form $(\boldsymbol{n}_q \boldsymbol{n}_q^t \boldsymbol{n}_p)$. On the contrary, signal and noise realisations enter the $\widehat{\mathsf{C}}$ term as the product of terms in the form $(\boldsymbol{a} s_q \boldsymbol{n}_q^t \boldsymbol{n}_p)$, i.e. products of s and the second power of $\boldsymbol{n}$. Index q runs over domain $\mathcal{D}$.

Assuming that s and $\boldsymbol{n}$ are centred variables, the mean value of the error is immediately seen to vanish:

$$E(d_p) = 0. \tag{A.18}$$

The main contribution to the variance comes from the first term on the right hand side of Eq. (A.13). The second and third terms are small corrections to this variance estimate, so that to first order, we get:

$$E(d_p^2) \simeq \frac{\boldsymbol{a}^t \mathsf{R}_x^{-1} \mathsf{R}_n \mathsf{R}_x^{-1} \boldsymbol{a}}{\left[\boldsymbol{a}^t \mathsf{R}_x^{-1} \boldsymbol{a}\right]^2} \cdot \tag{A.19}$$

Recalling that $\mathsf{R}_x = \mathsf{R}_n + \sigma^2 \boldsymbol{a}\boldsymbol{a}^t$, where σ^2 is the variance of the CMB, and making use of the inversion formula:

$$\left[\mathsf{R}_n + \sigma^2 \boldsymbol{a}\boldsymbol{a}^t\right]^{-1} = \mathsf{R}_n^{-1} - \sigma^2 \frac{\mathsf{R}_n^{-1} \boldsymbol{a}\boldsymbol{a}^t \mathsf{R}_n^{-1}}{1 + \sigma^2 \boldsymbol{a}^t \mathsf{R}_n^{-1} \boldsymbol{a}} \tag{A.20}$$

we finally obtain:

$$E(d_p^2) \simeq \frac{1}{\left[\boldsymbol{a}^t \mathsf{R}_n^{-1} \boldsymbol{a}\right]} \cdot \tag{A.21}$$

The most interesting terms are those connecting the error to the signal of interest, $E(s_p d_p)$, which is necessary to compute the power spectrum of the output map according to A.6[9].

As mentioned previously, under the assumption that the signal of interest is not correlated to the noise and the foregrounds, the first term (main term) of the r.h.s. of Eq. (A.13) does not give rise to multiplicative errors (or correlation of d_p with s_p). Similarly, the corrective term proportional to $\delta_s \boldsymbol{a}\boldsymbol{a}^t + \Delta_n$, multiplied by s, gives terms which contain an odd power of s and an odd power of $\boldsymbol{n}$, and does not give rise to correlations. This assumption is correct, to excellent accuracy, when the signal of interest is CMB anisotropies[10]. We are left with:

$$\begin{aligned} E(s_p d_p) &= E\left(\sum_q \frac{s_p s_q}{N_p} \frac{\left[\boldsymbol{a}^t \mathsf{R}_x^{-1} \boldsymbol{n}_p\right]\left[\boldsymbol{a}^t \mathsf{R}_x^{-1} (\boldsymbol{n}_q \boldsymbol{a}^t + \boldsymbol{a}\boldsymbol{n}_q^t) \mathsf{R}_x^{-1} \boldsymbol{a}\right]}{\left[\boldsymbol{a}^t \mathsf{R}_x^{-1} \boldsymbol{a}\right]^2}\right) \\ &\quad - E\left(\sum_q \frac{s_p s_q}{N_p} \frac{\boldsymbol{a}^t \mathsf{R}_x^{-1} (\boldsymbol{n}_q \boldsymbol{a}^t + \boldsymbol{a}\boldsymbol{n}_q^t) \mathsf{R}_x^{-1} \boldsymbol{n}_p}{\boldsymbol{a}^t \mathsf{R}_x^{-1} \boldsymbol{a}}\right) \cdot \end{aligned} \tag{A.22}$$

[9] We warn the reader that some authors fail to make a clear distinction between the statistical (ensemble average) correlation, which is a deterministic quantity, and the "empirical correlations" computed, assuming some kind of ergodicity, as averages over finite sets of samples as in Eq. (A.3).

[10] Certainly the CMB is not correlated to galactic components. Small correlations with large scale structure, and hence with SZ effect and emission from outer galaxies, may exist because of the integrated Sachs-Wolfe effect. We neglect this effect in the present discussion.

Multiplying the numerator and denominator of the second term by $\boldsymbol{a}^t \mathsf{R}_x^{-1} \boldsymbol{a}$ and expanding numerators, two terms cancel and two remain. If we assume in addition that signal and/or noise coefficients are independent, i.e. $E(s_p s_q) = \sigma_s^2 \delta_{qp}$ and/or $E(\boldsymbol{n}_p \boldsymbol{n}_q^t) = \mathsf{R}_n \delta_{qp}$, only the pp term is non vanishing, and we get

$$E(s_p d_p) = \frac{\sigma_s^2}{N_p} \left(\frac{E\left((\boldsymbol{a}^t \mathsf{R}_x^{-1} \boldsymbol{n}_p)^2\right) - (\boldsymbol{a}^t \mathsf{R}_x^{-1} \boldsymbol{a})\, E\left(\boldsymbol{n}_p^t \mathsf{R}_x^{-1} \boldsymbol{n}_p\right)}{\left[\boldsymbol{a}^t \mathsf{R}_x^{-1} \boldsymbol{a}\right]} \right) \cdot \tag{A.23}$$

We compute

$$\begin{aligned} E\left(\left(\boldsymbol{a}^t \mathsf{R}_x^{-1} \boldsymbol{n}_p\right)^2\right) &= \boldsymbol{a}^t \mathsf{R}_x^{-1} \mathsf{R}_n \mathsf{R}_x^{-1} \boldsymbol{a} \\ &= \boldsymbol{a}^t \mathsf{R}_x^{-1} \left[\mathsf{R}_x - \sigma_s^2 \boldsymbol{a}\boldsymbol{a}^t\right] \mathsf{R}_x^{-1} \boldsymbol{a} \\ &= \left[\boldsymbol{a}^t \mathsf{R}_x^{-1} \boldsymbol{a}\right]\left[1 - \sigma_s^2\, \boldsymbol{a}^t \mathsf{R}_x^{-1} \boldsymbol{a}\right] \end{aligned} \tag{A.24}$$

and

$$\begin{aligned} E\left(\boldsymbol{n}_p^t \mathsf{R}_x^{-1} \boldsymbol{n}_p\right) &= \mathrm{Tr}\left(\mathsf{R}_x^{-1} \mathsf{R}_n\right) \\ &= \mathrm{Tr}\left(\mathsf{R}_x^{-1} \left[\mathsf{R}_x - \sigma_s^2 \boldsymbol{a}\boldsymbol{a}^t\right]\right) \\ &= \mathrm{Tr}\,(\mathsf{Id}) - \sigma_s^2\, \mathrm{Tr}\left(\mathsf{R}_x^{-1} \boldsymbol{a}\boldsymbol{a}^t\right) \\ &= m - \sigma_s^2 \left(\boldsymbol{a}^t \mathsf{R}_x^{-1} \boldsymbol{a}\right) \end{aligned} \tag{A.25}$$

where m is the number of channels used for the ILC (here, 5 WMAP channels + 1 IRIS map, for a total of 6). Substituting the results of Eqs. (A.24) and (A.25) into Eq. (A.23), we get the simple final result:

$$E(s_p d_p) = \frac{\sigma_s^2 (1 - m)}{N_p} \cdot \tag{A.26}$$

The error in the reconstructed CMB map comprises a term proportional (on average) to the CMB. In our application, $m = 6$ and $N_p = 1024$, so that if indeed all needlet coefficients were independent, the amplitude of the effect should be $E(s_p d_p) \simeq 5 \times 10^{-3} \sigma_s^2$, i.e. a bias of about half a percent in the CMB reconstruction.

A.2. A geometric interpretation

Although allowing the statistical derivation of the (anti-) correlation of the reconstruction error with the original CMB, the above derivation is not very illuminating about the mechanism giving rise to this CMB power loss. A geometrical reasoning gives better insight into what is actually going on.

For a given data set, the ILC works on one single realisation of all random fields. For an independent implementation of the ILC on N_p pixels (or modes, or needlet coefficients) of the observations, each data set is represented by a vector in an N_p-dimensional vector space W. The CMB $\boldsymbol{s}$, the observation $\boldsymbol{x}_i$ for each channel i, and each of the noise realisations $\boldsymbol{n}_i$ (including foreground emissions) are elements of W.

The collection of vectors $\boldsymbol{n}_i$ defines an m-dimensional subspace V of W. This is true irrespective of the nature of the foreground contaminants: indeed, although in principle vectors $\boldsymbol{n}_i$ could be linearly dependent, this happens in practice with vanishing probability (in particular if the observations are noisy).

Vector space W can thus be decomposed in two orthogonal subspaces, U and V, where V is the m-dimensional sub-space spanned by all vectors $\boldsymbol{n}_i$, and $U = V^\perp$ is a $(N_p - m)$ dimensional

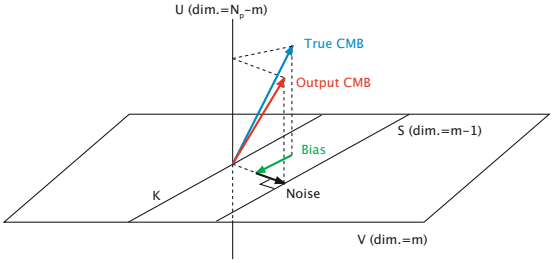

Fig. A.1. Geometric illustration of the ILC bias. The true CMB (blue) and the output CMB (red) are elements of $W = U \oplus V$. The difference between the two can be decomposed into the sum of two elements of V: a bias (green), which is an element of K, and a noise contribution (black), which is an element of H, the orthogonal of K in V.

vector space. The CMB itself can be decomposed into two components, one in U, and one in V:

$$\boldsymbol{s} = \boldsymbol{s}_U + \boldsymbol{s}_V \tag{A.27}$$

where $\boldsymbol{s}_U$ is the orthogonal projection of $\boldsymbol{s}$ onto U, and $\boldsymbol{s}_V$ its orthogonal projection onto V.

What happens when the ILC is made is the following: we look for weights w_i for all channels, that minimise the variance of the reconstructed map, i.e. minimise the norm of vector $\widehat{\boldsymbol{s}} = \sum_i w_i \boldsymbol{x}_i$, under the constraint that $\sum_i w_i = 1$. We have:

$$\begin{aligned}\widehat{\boldsymbol{s}} &= \boldsymbol{s}_U + \left(\boldsymbol{s}_V + \sum_i w_i \boldsymbol{n}_i\right) \\ &= \widehat{\boldsymbol{s}}_U + \widehat{\boldsymbol{s}}_V\end{aligned} \tag{A.28}$$

where the first term is a vector of U and the second term a vector of V, and the second line of the equation defines $\widehat{\boldsymbol{s}}_U$ and $\widehat{\boldsymbol{s}}_V$. Since these two subspaces of W are orthogonal, the norm of $\widehat{\boldsymbol{s}}$ is the sum of the norms of the two vectors $\widehat{\boldsymbol{s}}_U$ and $\widehat{\boldsymbol{s}}_V$. The norm of $\widehat{\boldsymbol{s}}$ thus depends on w_i only through the norm of the projection of $\widehat{\boldsymbol{s}}$ on subspace V.

The noise contribution to $\widehat{\boldsymbol{s}}$ appears as a linear combination of vectors $\boldsymbol{n}_i$. For varying values of w_i such that $\sum_i w_i = 1$, this linear combination spans an *affine* subspace S of V. S is of dimension $m - 1$ (an hyperplane). Defining K as the vector subspace of V spanned by linear combinations $\sum_i w_i \boldsymbol{x}_i$ such that $\sum_i w_i = 0$, we obtain S as:

$$S = \boldsymbol{p} + K \tag{A.29}$$

where $\boldsymbol{p}$ is any element of S.

We note that the vector subspace K *depends only on noise realisations, and not on* $\boldsymbol{s}$ *nor on the final ILC weights* (the latter only defining a single point on S – and on K by orthogonal projection). Hence, the direction of the one-dimensional vector subspace H of V orthogonal to K is also independent of $\boldsymbol{s}$ and of the final ILC weights.

For any element $\widehat{\boldsymbol{s}}_V = \boldsymbol{s}_V + \sum_i w_i \boldsymbol{n}_i$ of affine space S the norm of $\widehat{\boldsymbol{s}}_V$ is the sum of the norms of its projections onto K and H. Allowing weights w_i to vary, vector $\widehat{\boldsymbol{s}}_V$ spans S, and hence only the norm of the projection of $\widehat{\boldsymbol{s}}_V$ onto K varies (and not its projection on H). The minimum is reached when the projection of of $\widehat{\boldsymbol{s}}_V$ onto K vanishes. When this happens, the ILC has cancelled completely the linear combination of projections of $\boldsymbol{s}$ and $\boldsymbol{n}_i$ onto the $m - 1$-dimensional space K, and left untouched the projections of $\boldsymbol{s}$ and $\boldsymbol{n}_i$ onto the $N_p - m + 1$ dimensional vector space $U \oplus H$.

Assuming the CMB to be Gaussian and statistically isotropic, its coefficients in any orthogonal basis are Gaussian distributed random variables with variance σ^2/N_p (since the sum must have total variance σ^2). It follows straightforwardly that the correlation of the recovered CMB map with the input CMB map is $(N_p - m + 1)/N_p$, and that the "bias" is due to the loss of $m - 1$ modes of the original CMB, which have been unlucky enough to "live" in the $(m - 1)$ dimensional space K.

A.3. Comment on coefficient independence

The above derivation in Sect. A.1 assumes the independence of coefficients $\boldsymbol{n}_p$ and/or of coefficients s_p, i.e. $E(\boldsymbol{n}_p \boldsymbol{n}_q^t) = \mathsf{R}_n \delta_{qp}$ and/or $E(s_p s_q) = \sigma_s^2 \delta_{qp}$. When this assumption does not hold, we have:

$$\begin{aligned}E(s_p d_p) &= \frac{1}{N_p} \sum_q E\left(s_p s_q \frac{(\boldsymbol{a}^t \mathsf{R}_x^{-1} \boldsymbol{n}_p)(\boldsymbol{a}^t \mathsf{R}_x^{-1} \boldsymbol{n}_q)}{[\boldsymbol{a}^t \mathsf{R}_x^{-1} \boldsymbol{a}]}\right) \\ &\quad - \frac{1}{N_p} \sum_q E\left(s_p s_q \left(\boldsymbol{n}_p^t \mathsf{R}_x^{-1} \boldsymbol{n}_q\right)\right).\end{aligned} \tag{A.30}$$

Assuming that the noise and the CMB are independent, we have:

$$\begin{aligned}E(s_p d_p) &= \frac{1}{N_p} \sum_q E\left(s_p s_q\right) \frac{E\left((\boldsymbol{a}^t \mathsf{R}_x^{-1} \boldsymbol{n}_p)(\boldsymbol{a}^t \mathsf{R}_x^{-1} \boldsymbol{n}_q)\right)}{[\boldsymbol{a}^t \mathsf{R}_x^{-1} \boldsymbol{a}]} \\ &\quad - \frac{1}{N_p} \sum_q E\left(s_p s_q\right) E\left(\boldsymbol{n}_p^t \mathsf{R}_x^{-1} \boldsymbol{n}_q\right)\end{aligned} \tag{A.31}$$

where

$$E\left((\boldsymbol{a}^t \mathsf{R}_x^{-1} \boldsymbol{n}_p)(\boldsymbol{a}^t \mathsf{R}_x^{-1} \boldsymbol{n}_q)\right) = \boldsymbol{a}^t \mathsf{R}_x^{-1} E\left(\boldsymbol{n}_p \boldsymbol{n}_q^t\right) \mathsf{R}_x^{-1} \boldsymbol{a} \tag{A.32}$$

and

$$E\left(\boldsymbol{n}_p^t \mathsf{R}_x^{-1} \boldsymbol{n}_q\right) = \mathrm{Tr}\left(\mathsf{R}_x^{-1} E\left(\boldsymbol{n}_p \boldsymbol{n}_q^t\right)\right). \tag{A.33}$$

When p and q index needlet coefficients as in the present work, we have:

$$E\left(s_p s_q\right) = \sum_\ell \frac{2\ell + 1}{N_{\rm tot}} h_\ell^2 C_\ell P_\ell(\cos\theta_{qp}) \tag{A.34}$$

where s_p and s_q are needlet coefficients of the CMB map, evaluated at two different points p and q, C_ℓ is the angular power spectrum of the CMB, θ_{qp} is the angle between q and p, and $N_{\rm tot}$ is the total number of pixels of the needlet coefficient map. For noise maps (including foreground emissions), which are not stationary Gaussian random fields on the sphere, the analogous formula is just an approximation, which can be written as:

$$E\left(\boldsymbol{n}_p \boldsymbol{n}_q^t\right) \simeq \sum_\ell \frac{2\ell + 1}{N_{\rm tot}} h_\ell^2 \mathsf{R}_n(\ell)\, P_\ell(\cos\theta_{qp}) \tag{A.35}$$

where $\boldsymbol{n}_p$ and $\boldsymbol{n}_q$ are needlet coefficients of all noise maps, evaluated at two different points p and q, $\mathsf{R}_n(\ell)$ is the covariance of the noise needlet coefficients (an $m \times m$ matrix for each ℓ), and θ_{qp} and $N_{\rm tot}$ are defined as above.

Assuming that neither the noise level nor the CMB power vary much over the spectral window h_ℓ, $\mathsf{R}_n(\ell)$ and C_ℓ are approximately independent of ℓ, and can be taken out of the integral. We get:

$$E\left(s_p s_q\right) = C_\ell\, k(\theta_{qp}) \tag{A.36}$$

and

$$E\left(\boldsymbol{n}_p \boldsymbol{n}_q^t\right) = \mathsf{R}_n\, k(\theta_{qp}) \tag{A.37}$$

with

$$k(\theta_{qp}) = \sum_\ell \frac{2\ell+1}{N_{\rm tot}} h_\ell^2 P_\ell(\cos\theta_{qp}). \tag{A.38}$$

Hence, plugging this result, together with Eqs. (A.32) and (A.33), into Eq. (A.31) we get:

$$E(s_p d_p) = \frac{(1-m)}{N_p}\, C_\ell \sum_q k^2(\theta_{qp}). \tag{A.39}$$

Finally, noting that $\sigma_s^2 = C_\ell k(0)$, we get

$$E(s_p d_p) = \frac{(1-m)}{N_p}\, \frac{\sigma_s^2}{k(0)} \sum_q k^2(\theta_{qp}). \tag{A.40}$$

Equation (A.40) is the same as Eq. (A.26), except for a coefficient, which measures the correlation between signal and noise coefficients p and coefficients q in domain $\mathcal{D}$. In particular, the result is, again, independent of R_n.

Hence, we define an *effective number of modes*, $N_p^{\rm eff} = N_p/\alpha$, where

$$\alpha = \frac{\sum_q k^2(\theta_{qp})}{k(0)} \tag{A.41}$$

and we get

$$E(d_p s_p) = \frac{\sigma_p^2 (1-m)}{N_p^{\rm eff}}\,. \tag{A.42}$$

An approximation (and upper bound) for α is easily obtained in the special case where h_ℓ is a square spectral window, and when domains $\mathcal{D}$ over which the ILC is implemented are small regions of the sky, so that $h_\ell^2 = 1$, and $P_\ell(\cos\theta_{qp}) \simeq 1$. In this case, we have:

$$k(\theta_{qp}) \simeq \frac{1}{N_{\rm tot}} \left((\ell_{\rm max}+1)^2 - \ell_{\rm min}^2\right) \tag{A.43}$$

and we have

$$N_p^{\rm eff} \simeq \frac{N_p}{N_{\rm tot}} \left((\ell_{\rm max}+1)^2 - \ell_{\rm min}^2\right). \tag{A.44}$$

We note that $\left((\ell_{\rm max}+1)^2 - \ell_{\rm min}^2\right)$ simply is the number of harmonic coefficients selected by the spectral window h_ℓ, and that $N_p/N_{\rm tot} = f_{\rm sky}$ is a coefficient which takes into account the effect of partial sky coverage for the (local) calculation of the statistics of the data set, well in line with $N_p^{\rm eff}$ being understood as an effective number of modes.

References

Abrial, P., Moudden, Y., Starck, J.-L., et al. 2008, Statistical Methodology, 5, 289
Aurich, R., Lustig, S., & Steiner, F. 2006, MNRAS, 369, 240
Baldi, P., Kerkyacharian, G., Marinucci, D., & Picard, D. 2007, ArXiv e-prints, 706
Baldi, P., Kerkyacharian, G., Marinucci, D., & Picard, D. 2008, Annals of Statistics, in press [arXiv.org: math.ST/0606599]
Bennett, C. L., Hill, R. S., Hinshaw, G., et al. 2003, ApJS, 148, 97
Bonaldi, A., Bedini, L., Salerno, E., Baccigalupi, C., & de Zotti, G. 2006, MNRAS, 373, 271
Bonaldi, A., Ricciardi, S., Leach, S., et al. 2007, ArXiv e-prints, 707
Cabella, P., Hansen, F. K., Liguori, M., et al. 2006, MNRAS, 369, 819
Cabré, A., Gaztañaga, E., Manera, M., Fosalba, P., & Castander, F. 2006, MNRAS, 372, L23
Caillerie, S., Lachièze-Rey, M., Luminet, J.-P., et al. 2007, A&A, 476, 691
Cao, L., Chu, Y.-Q., & Fang, L.-Z. 2006, MNRAS, 369, 645
Cardoso, J.-F., Martin, M., Delabrouille, J., Betoule, M., & Patanchon, G. 2008, ArXiv e-prints, 803
Cayón, L., Jin, J., & Treaster, A. 2005, MNRAS, 362, 826
Daubechies, I. 1992, CBMS-NSF Regional Conference Series in Applied Mathematics, Ten lectures on wavelets (Philadelphia, PA: Society for Industrial and Applied Mathematics (SIAM)), Vol. 61
Delabrouille, J., & Cardoso, J. F. 2007, ArXiv Astrophysics e-prints
Delabrouille, J., Cardoso, J.-F., & Patanchon, G. 2003, MNRAS, 346, 1089
Elad, M., Starck, J. L., Donoho, D., & Querre, P. 2005, Applied and Computational Harmonic Analysis, 19, 340
Eriksen, H. K., Banday, A. J., Górski, K. M., & Lilje, P. B. 2004, ApJ, 612, 633
Eriksen, H. K., Dickinson, C., Jewell, J. B., et al. 2007, ArXiv e-prints, 709
Finkbeiner, D. P. 2003, ApJS, 146, 407
Finkbeiner, D. P., Davis, M., & Schlegel, D. J. 1999, ApJ, 524, 867
Fosalba, P., & Gaztañaga, E. 2004, MNRAS, 350, L37
Gold, B., Bennett, C. L., Hill, R. S., et al. 2008, ArXiv e-prints, 803
Górski, K. M., Hivon, E., Banday, A. J., et al. 2005, ApJ, 622, 759
Guilloux, F., Fay, G., & Cardoso, J.-F. 2008, Applied and Computational Harmonic Analysis, in press [arXiv:0706.2598]
Hinshaw, G., Nolta, M. R., Bennett, C. L., et al. 2007, ApJS, 170, 288
Huffenberger, K. M., Eriksen, H. K., Hansen, F. K., Banday, A. J., & Gorski, K. M. 2007, ArXiv e-prints
Kim, J., Naselsky, P., & Christensen, P. R. 2008, ArXiv e-prints, 803
Maino, D., Farusi, A., Baccigalupi, C., et al. 2002, MNRAS, 334, 53
Maino, D., Donzelli, S., Banday, A. J., Stivoli, F., & Baccigalupi, C. 2007, MNRAS, 374, 1207
Marinucci, D., Pietrobon, D., Balbi, A., et al. 2008, MNRAS, 383, 539
McEwen, J. D., Hobson, M. P., Lasenby, A. N., & Mortlock, D. J. 2006a, MNRAS, 371, L50
McEwen, J. D., Hobson, M. P., Lasenby, A. N., & Mortlock, D. J. 2006b, MNRAS, 369, 1858
McEwen, J. D., Wiaux, Y., Hobson, M. P., Vandergheynst, P., & Lasenby, A. N. 2007, ArXiv e-prints, 704
Miville-Deschênes, M.-A., & Lagache, G. 2005, ApJS, 157, 302
Mukherjee, P., & Wang, Y. 2004, ApJ, 613, 51
Narcowich, F., Petrushev, P., & Ward, J. 2006, SIAM J. Math. Anal., 38, 574
Niarchou, A., & Jaffe, A. 2007, Phys. Rev. Lett., 99, 081302
Nolta, M. R., Wright, E. L., Page, L., et al. 2004, ApJ, 608, 10
Page, L., Barnes, C., Hinshaw, G., et al. 2003, ApJS, 148, 39
Park, C.-G., Park, C., & Gott, J. R. I. 2007, ApJ, 660, 959
Pietrobon, D., Balbi, A., & Marinucci, D. 2006, Phys. Rev. D, 74, 043524
Rassat, A., Land, K., Lahav, O., & Abdalla, F. B. 2007, MNRAS, 377, 1085
Saha, R., Prunet, S., Jain, P., & Souradeep, T. 2007, ArXiv e-prints, 706
Starck, J.-L., Moudden, Y., Abrial, P., & Nguyen, M. 2006, A&A, 446, 1191
Tegmark, M., de Oliveira-Costa, A., & Hamilton, A. J. 2003, Phys. Rev. D, 68, 123523
Tojeiro, R., Castro, P. G., Heavens, A. F., & Gupta, S. 2006, MNRAS, 365, 265
Vielva, P., Martínez-González, E., Barreiro, R. B., Sanz, J. L., & Cayón, L. 2004, ApJ, 609, 22
Wiaux, Y., Vielva, P., Barreiro, R. B., Martinez-Gonzalez, E., & Vandergheynst, P. 2007, ArXiv e-prints, 706
Wiaux, Y., McEwen, J. D., Vandergheynst, P., & Blanc, O. 2008, MNRAS, 388, 770
Wright, E. L., Chen, X., Odegard, N., et al. 2008, ArXiv e-prints
Yadav, A. P. S., & Wandelt, B. D. 2007, ArXiv e-prints, 712

Monthly Notices of the ROYAL ASTRONOMICAL SOCIETY

Mon. Not. R. Astron. Soc. **401,** 1602–1612 (2010) doi:10.1111/j.1365-2966.2009.15798.x

Impact of calibration errors on CMB component separation using FastICA and ILC

Jason Dick,[1⋆] Mathieu Remazeilles[2,3⋆] and Jacques Delabrouille[2⋆]

[1] *SISSA via Beirut, 2-4, 34014 Trieste, Italy*
[2] *APC 10, rue Alice Domon et Léonie Duquet, 75205 Paris Cedex 13, France*
[3] *Laboratoire de Physique Théorique, Université Paris-Sud, 91405 Orsay, France*

Accepted 2009 September 25. Received 2009 September 8; in original form 2009 July 17

ABSTRACT

The separation of emissions from different astrophysical processes is an important step towards the understanding of observational data. This topic of component separation is of particular importance in the observation of the relic cosmic microwave background (CMB) radiation, as performed by the *Wilkinson Microwave Anisotropy Probe* satellite and the more recent *Planck* mission, launched on 2009 May 14 from Kourou and currently taking data. When performing any sort of component separation, some assumptions about the components must be used. One assumption that many techniques typically use is knowledge of the frequency scaling of one or more components. This assumption may be broken in the presence of calibration errors. Here we compare, in the context of imperfect calibration, the recovery of a clean map of emission of the CMB from observational data with two methods: FastICA (which makes no assumption of the frequency scaling of the components) and an 'Internal Linear Combination' (ILC), which explicitly extracts a component with a given frequency scaling. We find that even in the presence of small calibration errors (less than 1 per cent) with a *Planck*-style mission, the ILC method can lead to inaccurate CMB reconstruction in the high signal-to-noise ratio regime, because of partial cancellation of the CMB emission in the recovered map. While there is no indication that the failure of the ILC will translate to other foreground cleaning or component separation techniques, we propose that all methods which assume knowledge of the frequency scaling of one or more components be careful to estimate the effects of calibration errors.

Key words: cosmology: observations – cosmology: theory.

1 INTRODUCTION

Precise observation of the cosmic microwave background (CMB), as planned with the *Planck* space mission (Lamarre et al. 2003; Mennella et al. 2004; Tauber 2004), is of the utmost importance for better understanding, and confronting with precise observational data, the hot big bang model and its theoretical predictions. In this theoretical framework, such observations also permit constraining the parameters of the model, as is currently done to a lesser extent by a number of previous experiments, such as *COBE* (Bennett et al. 1996), *Wilkinson Microwave Anisotropy Probe* (*WMAP*; Komatsu et al. 2009), ACBAR (Reichardt et al. 2009), Archeops (Benoît et al. 2003; Tristram et al. 2005), *BOOMERanG* (MacTavish et al. 2006), CBI (Sievers et al. 2009), QUaD (QUaD collaboration: C. Pryke et al. 2008) and VSA (Rebolo et al. 2004).

⋆E-mail: dick@sissa.it (JD); remazeil@apc.univ-paris7.fr (MR); delabrouille@apc.univ-paris7.fr (JD)

With ever more sensitive instruments, the main source of uncertainty in CMB observations, rather than being instrumental noise, is the contamination of the observation by foreground emission. Astrophysical foregrounds comprise millimetre wave emission from the interstellar medium in our own Galaxy, as well as emission from compact extragalactic sources.

Component separation methods make use of the different emission laws of different astrophysical components to separate them through joint analysis of observations made at different wavelengths (Delabrouille & Cardoso 2007). Among those methods, the so-called Internal Linear Combination (ILC), which makes few assumptions about the physical properties of the CMB and the foregrounds, has been widely used for the analysis of *WMAP* data (Tegmark, de Oliveira-Costa & Hamilton 2003; Eriksen et al. 2004; Delabrouille et al. 2009; Kim, Naselsky & Christensen 2009). An important assumption of the ILC is that the frequency scaling of the CMB is assumed to be known. This is, in principle, a safe assumption, as small temperature fluctuations ΔT of the CMB generate brightness fluctuations proportional to ΔT, which scale in

frequency like the derivative of a blackbody spectrum with respect to the temperature, at the well-measured CMB temperature of $T = 2.728$ K. Deviation of the CMB from a blackbody spectrum at this temperature was tightly constrained by the Far Infrared Absolute Spectrophotometer (FIRAS) (Fixsen et al. 1996), with the relationship between the temperature fluctuations and the overall CMB spectrum verified by comparing FIRAS and DMR data (Fixsen et al. 1997). However, calibration coefficients for each channel, which are a multiplicative factor for each frequency, introduce an uncertainty in the frequency scalings of the CMB component in the presence of calibration errors. For space-based missions, these uncertainties are typically small (well below 1 per cent for the *WMAP* or *Planck*).

More sophisticated methods for component separation have been extensively studied in the community of statistical signal processing for a variety of applications. These methods are part of a field of activity generically designated as blind source separation (BSS), or equivalently independent component analysis (ICA). ICA methods perform separation on the basis of the assumption that each of the available observations is a different linear mixture of a well-defined number of statistically independent components. Such methods generically rely on no prior assumption on the scaling coefficients of the components in the different available observations (i.e. on the coefficients of each component in the 'mixtures'). In fact, recovering these coefficients (the so-called 'mixing matrix') is precisely the primary target of BSS. ICA methods, thus, do not typically assume perfect knowledge of the response of each channel to the CMB – nor that the CMB contribution is the same in all channels. For CMB studies particularly, this type of approach has led to the development of a large variety of methods, including CCA (Bedini et al. 2005; Bonaldi et al. 2006), FastICA (Baccigalupi et al. 2000; Maino et al. 2002), SMICA (Delabrouille, Cardoso & Patanchon 2003; Cardoso et al. 2008) and GMCA (Bobin et al. 2008). These methods have been used on real observational data in a variety of contexts (Patanchon et al. 2005; Maino et al. 2006; Bonaldi et al. 2007), and compared extensively on simulated data sets (Leach et al. 2008).

Both FastICA and ILC are methods which compose the extracted signal as a linear sum of the data channels. Because of this, they both require that each data component be convolved to the same resolution. The two main differences between the ILC and ICA methods are the following:

(i) Whereas ICA is designed to extract the scaling coefficients of each of the identified components from the data themselves, the ILC assumes perfect knowledge of the scaling coefficients for the component of interest (CMB).

(ii) The ILC does not make any assumption about the properties of foreground contamination, whereas ICA assumes that the data are satisfactorily described by a (noisy) linear mixture of independent components.

Clearly, these methods are bound to be more or less adapted to component separation, depending upon the actual properties of the data set and on the science objectives pursued. In the following, we propose to investigate, using realistic simulations of sky emission and of observational data for the *WMAP* and *Planck*, the relative performance of FastICA and ILC in the presence of calibration errors. Such calibration errors result in the violation of one of the assumptions of the ILC (the prior knowledge of the exact scaling coefficients of the CMB in the observations). By contrast, blind component separation methods are designed from first principles to estimate the scaling coefficients from the data, and in principle should not suffer much from calibration uncertainties.

The rest of this paper is organized as follows. In Section 2, we describe the ILC and ICA component separation methods. We describe our methodology for comparing the methods in Section 3. In Section 4, we present the results of our analysis, followed by our conclusions in Section 5. We also provide a detailed calculation of the effect of calibration errors on the ILC in Appendix A.

2 ILC AND ICA

In the following, we assume that the available data (maps $x_i(p)$ of observed sky) can be written as

$$x_i(p) = a_i s(p) + n_i(p), \tag{1}$$

where $s(p)$ is the map of the component of interest (the CMB), p indexes pixels in the map and $n_i(p)$ is the contribution from foregrounds and instrumental noise to the map $x_i(p)$. The coefficients a_i scale the relative amplitude of the CMB map in the different available observations. For observations in thermodynamic units, and perfect calibration, we have $\forall i$, $a_i = 1$.

2.1 The ILC

The philosophy behind the ILC is to find the linear combination of the available maps x_i which has minimal variance while retaining unit response to the CMB map. This linear combination, $\sum_i w_i x_i(p)$, is then an estimate $\hat{s}(p)$ of the true CMB map $s(p)$. The ILC weights w_i are found by solving the problem of minimizing $\mathrm{var}\sum_i w_i x_i(p)$ under the constraint $\sum_i w_i = 1$. In principle, this last constraint guarantees unit response to the CMB, as we have

$$\begin{aligned}\hat{s}(p) &= \sum_i w_i x_i(p) \\ &= s(p) + \sum_i w_i n_i(p).\end{aligned} \tag{2}$$

In the presence of foregrounds, which induce correlated errors from channel to channel, the ILC weights adjust themselves so that the linear combination cancels out as much of the foregrounds as possible. The actual weights, however, result from a trade-off between cancelling foregrounds and allowing errors due to instrumental noise in the final map.

The constrained minimization problem can be solved in a straightforward manner using a Lagrange multiplier method to impose $\sum_i w_i = 1$. The resulting weights are found to be

$$\boldsymbol{w} = \frac{\widehat{\mathbf{R}}^{-1}\boldsymbol{a}}{\boldsymbol{a}^t\,\widehat{\mathbf{R}}^{-1}\boldsymbol{a}}, \tag{3}$$

where $\widehat{\mathbf{R}}$ is the empirical covariance matrix of the observations. Note that we have used bold font to denote vectors, and have omitted the reference to the pixel value. From here on, this notation will be used. The ILC estimator of the CMB map $s(p)$ can be written as

$$\hat{s}_{\mathrm{ILC}} = \boldsymbol{w}^t\boldsymbol{x} = \frac{\boldsymbol{a}^t\,\widehat{\mathbf{R}}^{-1}}{\boldsymbol{a}^t\,\widehat{\mathbf{R}}^{-1}\boldsymbol{a}}\,\boldsymbol{x}. \tag{4}$$

The ILC weights, obviously, depend upon the assumed scaling coefficients a_i for the component of interest. It is then clear that an error in the assumed scalings changes the ILC performance, but by how much? As the ILC attempts to minimize the total variance of the output map, the constraint that $\sum w_i a_i = 1$ plays a critical role in guaranteeing that the linear combination does not adjust its coefficients to cancel the CMB as well as foregrounds. It is foreseeable,

then, that calibration errors could, in some cases, impact the performance of ILC more severely than just a small overall calibration error on the final output map.

2.2 FastICA

There is a wide choice of possible ICA methods to extract the CMB from multifrequency observations. In this paper, we make use of the standard FastICA algorithm as described in Hyvärinen (1999), with a few minor changes.

(i) We subtract an estimate of the instrument noise covariance matrix from the empirical covariance matrix of the data.

(ii) Instead of leaving the estimated signal as being unit variance, we set the CMB scaling to be such that the sum of the weights is equal to one, mirroring the ILC method to ensure unit response to the CMB.

FastICA is based on the general principle that a sum of two different independent probability distributions will always tend to be more Gaussian than either of the distributions are independently. We can thus extract N independent sources from N channels of data by forming the linear combination of the N channels which maximizes the non-Gaussianity of the extracted sources. A measure of the non-Gaussianity of each source is performed using functions such as

$$Y(x) \propto [E\{G(x)\} - E\{G(y)\}]^2 . \quad (5)$$

where x are data that have unit variance and y is a random variable drawn from a unit-variance Gaussian distribution. Here, $E\{\}$ is the expectation value of the data set or probability distribution enclosed and $G(x)$ is some non-linear function. Popular choices include a Gaussian, a polynomial or the logarithm of the hyperbolic cosine. Which specific choice is best depends upon precisely how the distribution of x differs from a Gaussian, though it is clear that for any choice of $G(x)$, $Y(x)$ will be zero if x is Gaussian-distributed, and positive definite otherwise. In this paper, we use $G(x) = x^4$.

FastICA assumes a model of the data of the form

$$\boldsymbol{x} = \mathbf{A}\boldsymbol{s} + \boldsymbol{n}, \quad (6)$$

where now vector $\boldsymbol{s}$ comprises all 'sources' (CMB + foregrounds) and $\boldsymbol{n}$ is instrumental noise only (for all channels). The objective of the method is to evaluate the mixing matrix $\mathbf{A}$, and then use this estimate to invert the linear system.

In order to optimize estimation of the mixing matrix that determines the linear combination of x which represents the individual sources, FastICA also performs a pre-whitening step. This pre-whitening step exploits the assumption of statistical independence to perform a linear transformation on the data, which sets its covariance matrix to the identity by multiplying the data by the inverse square root of its covariance. The mixing matrix then becomes a simple rotation matrix which, with its smaller number of degrees of freedom, is easier to estimate.

For generating the pre-whitening matrix, we do not make direct use of the covariance matrix of the data, as with basic FastICA, but instead use the estimated covariance matrix of the signal as in Maino et al. (2002). This can be understood simply by our modelling of the data (equation 6). Given this data model, the covariance of the observations is

$$\mathbf{R}_x = \langle (\mathbf{A}\boldsymbol{s} + \boldsymbol{n})(\mathbf{A}\boldsymbol{s} + \boldsymbol{n})^t \rangle,$$
$$\mathbf{R}_x = \mathbf{A}\mathbf{R}_s\mathbf{A}^t + \mathbf{R}_n. \quad (7)$$

Here the correct covariance matrix to use to whiten the signal is $\mathbf{A}\mathbf{R}_s\mathbf{A}^t$, which we estimate as $\mathbf{R}_x - \mathbf{R}_n$. The channel–channel noise covariance $\mathbf{R}_n$ is taken as diagonal with the diagonal elements estimated from our knowledge of the per-pixel noise in each map combined with how much each map was smoothed. The effect of the smoothing on the noise was estimated from noise-only Monte Carlo simulations. We have assumed that the signal and noise are uncorrelated in the above derivation.

Having performed the pre-whitening, all extracted sources have unit variance and are uncorrelated. To determine the overall CMB scaling, we first determine which of the sources is the CMB, then use the ILC strategy of setting the sum of the CMB weights equal to one. This ensures that the level of the CMB in the output is, at least in the case of no calibration error, equal to the level of the CMB in the maps.

3 METHOD

We now turn to the investigation of the impact of calibration errors on component separation with the ILC and FastICA. The approach of this investigation consists of generating simulated 'observations', with varying calibration errors, noise levels and frequency channels, and compares the performance of ILC and FastICA at recovering the CMB map.

Performance is measured in several ways, based on the measurement of reconstruction errors of different types.

Denoting as $s(p)$ the (beam-smoothed) CMB map used in the simulation, and as $\hat{s}(p)$ the CMB map obtained from processing the simulated data, the reconstruction error is $\hat{s}(p) - s(p)$.

This reconstruction error arises from two terms. A multiplicative term (i.e. a global calibration error) and an additive term. We have

$$\hat{s}(p) = \alpha s(p) + c(p),$$

where α is the global calibration coefficient and $c(p)$ is the additive contamination by foregrounds and noise. Ideally, we aim at $\alpha = 1$ and $c(p) = 0$.

In practice, in both ILC and ICA methods, the final map is reconstructed as a linear combination $\sum w_i x_i(p)$ of the input maps $x_i(p)$. Hence, for simulated data, one can compute easily $\alpha = \sum w_i a_i$ and $c(p) = \sum w_i n_i(p)$, where $n_i(p)$ are maps of the sum noise and foregrounds in channel i.

The comparison of the variance of the reconstruction error, of the overall response α and of the contamination $c(p)$ for ILC and ICA gives insight on the relative performance of the two, and of the main origin of error, in the presence of calibration uncertainties.

3.1 Simulations

In preparation for the forthcoming *Planck* space mission, simulations for the nine *Planck* frequency channels, from 30 to 857 GHz, as described in the Planck 'Bluebook',[1] are made. We also consider simulations in the *WMAP* frequency channels, between 23 and 94 GHz. Sky simulations are performed using the Planck Sky Model (PSM) package, version 1.6.3[2] and using the HEALPIX[3] pixelization. In the simulated observations, we introduce a small calibration error, so that each of the sky maps is multiplied by a calibration coefficient. We consider calibration errors $\delta a/a$ of 0.1, 0.2, 0.5 and 1 per cent,

[1] http://www.rssd.esa.int/SA/PLANCK/docs/Bluebook-ESA-SCI(2005)1_V2.pdf
[2] http://www.apc.univ-paris7.fr/APC_CS/Recherche/Adamis/PSM/psky-en.php
[3] http://healpix.jpl.nasa.gov

which implies calibration coefficients typically somewhere between 0.99 and 1.01.[4] We then add uniform white noise to the maps at a level given by the Planck Bluebook for each channel. Finally, all of the maps are smoothed to the resolution of the lowest frequency channel in our simulations, i.e. 33 arcmin beams for *Planck* and 54 arcmin beams for the *WMAP*.

3.1.1 Planck Sky Model

Sky maps are generated using a four-component model of galactic emission which includes free–free, synchrotron, thermal dust and spinning dust diffuse components. We also add emission from several populations of compact sources, which comprise ultracompact galactic H II regions, infrared and radio sources (both galactic and extragalactic), a far-infrared background emission and thermal Sunyaev–Zel'dovich (SZ) effect from a simulated distribution of galaxy clusters. For our *Planck* simulations, maps are generated at 30, 44, 70, 100, 143, 217, 353, 545 and 857 GHz, each at nside = 1024 (pixel diameter about 4 arcmin). For *WMAP* simulations, maps are generated at 23, 33, 41, 61 and 94 GHz, each at nside = 512 (pixel diameter about 8 arcmin). Maps are simulated using Gaussian symmetric beams. Only temperature maps are generated.

3.1.2 Post-processing of PSM *Outputs*

Instrumental noise is added separately after the sky is simulated with the PSM. For the *Planck*, we assume uniform sky coverage, with noise level corresponding to what is given in the Planck 'Bluebook'. Since the FastICA and ILC methods require maps that are at the same resolution, we then smooth all maps to the resolution of the 30 GHz channel, which has a Gaussian beam full width at half-maximum of 33 arcmin. As we use a relatively low-resolution beam, all maps are set to nside = 512 after smoothing.

After adding noise and smoothing maps to the same resolution, we simulate the calibration error by drawing a zero-mean Gaussian random variable x with rms equal to the desired calibration error (e.g. $\sigma = 0.002$ for 0.2 per cent error). We then multiply the map by $1 + x$. This is repeated for each frequency channel, with the same calibration rms error but a different realization of x for each.

While it makes no difference whether the calibration error simulation is performed before or after smoothing, we note that it is correct to add the calibration error after the noise, as the overall estimated noise level also depends upon the calibration of the instrument. As we make use of the estimated noise covariance between the channels, the estimated noise level after smoothing is also computed here.

3.2 Masking

For better performance of the FastICA or ILC component separation algorithms, it is safer to mask out particularly bright sources as well as those with strongly varying spectral properties. The mask is determined making use of a simple magnitude-based algorithm. First, we produce a theoretical estimate of the expected CMB rms based upon the *WMAP* power spectrum. We then generate a mask that removes all pixels which contain a value larger than four times the CMB rms.

[4] The calibration error expected for *Planck* is less than 1 per cent up to the 353 GHz channel, as given by the Planck 'Bluebook'.

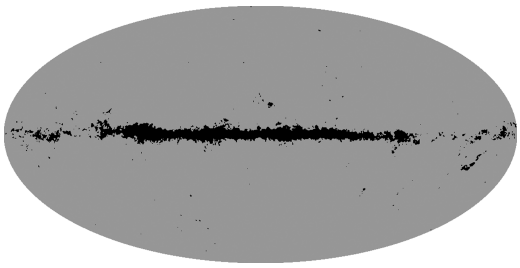

Figure 1. Mask that removes the brightest pixels from the 70 and 100 GHz channels.

For our maps, the mask used is a union of the masks computed as above from the 70 and 100 GHz channels. We make use of the mask as generated from the first realization with no calibration error, and do not recompute the mask between runs. The resultant mask is shown in Fig. 1. It is possible that we could obtain better component separation performance through more precise masking, but this is not expected to have any impact on the overall results of this paper. The study could have been performed with any arbitrary mask, as long as the average CMB to foreground ratio is not changed significantly.

3.3 Monte Carlo

In order to investigate both the average of the reconstruction error and its dispersion, we individually execute each of the above steps many times for each chosen set of parameters, the exact number depending upon the test. Summary statistics are then computed across the runs. When comparing different component separation techniques, the exact same set of realizations is used. Different choices of the calibration error level also make use of the same input sky maps.

For these simulations, CMB and noise are generated from their statistical properties separately in each simulation. The CMB is a Gaussian realization assuming, for all simulations, the same power spectrum, compatible with the *WMAP* best-fitting model, but new phases for each realization. Similarly, all realizations of noise are independent.

Other components are not fully independent from realization to realization. Galactic components, the model of which is heavily constrained by *WMAP* observations, do not change much. The SZ map is fixed (i.e. the same SZ template map is used in all simulations). A fraction of point sources remain similar (they are based on the positions of real sources) although their spectral emission law depends on the realization. An additional population of point sources, generated to correct for the sky coverage of point source surveys to homogenize the point source distribution, is generated independently for each sky realization.

4 RESULTS

In this section, we present both analytical and numerical results obtained after including the presence of calibration errors in the ILC and ICA component separation methods. The success or the failure of a method will be evaluated as follows. We construct the output CMB map estimates by ILC or ICA as well as the residual map, which is the difference map between the estimated output CMB

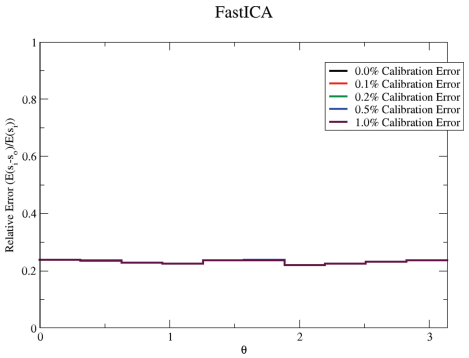

Figure 2. Plot of the relative error of FastICA as a function of the galactic latitude. Generated using 128 simulations for each case. As expected, the relative error of FastICA has very little dependence upon the calibration error.

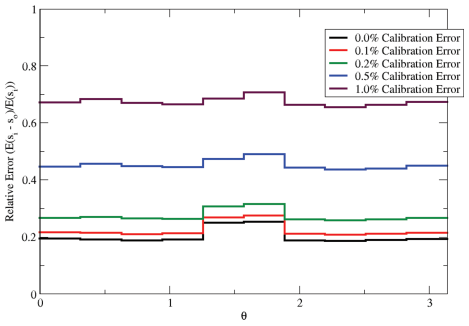

Figure 3. Plot of the relative error of ILC as a function of the galactic latitude. Generated using 128 simulations for each case. Unlike FastICA, ILC shows tremendous sensitivity to the calibration error, causing a notable reduction in the quality of the extraction of the CMB even at the optimistic 0.1 per cent calibration error level.

map and the simulated input CMB map. We compute the rms value of each of these maps and compare them. We also evaluate both the multiplicative factor α and the additive error $c(p)$ (introduced in Section 3), characterizing the reconstruction errors.

4.1 Compared reconstruction error

The average rms of the reconstruction error $\hat{s} - s$, over all simulations for the *Planck* experiment, is computed in 10 bands of varying galactic latitude. The relative error, $r = E(s - \hat{s})/E(s)$, for both FastICA and the ILC, is plotted in Figs 2 and 3.

As we expected, FastICA is almost completely unaffected by calibration errors. Because no assumption on the relative calibration is used, the overall calibration error just adds some small extra variance on the overall level of the extracted CMB.

The ILC, however, is not so well behaved as FastICA. While the ILC is somewhat better than FastICA at extracting the CMB when calibration is perfect, it quickly becomes worse as calibration errors of increasing magnitude are applied. Fig. 4 shows the output of a particular realization at 1 per cent calibration error where the ILC

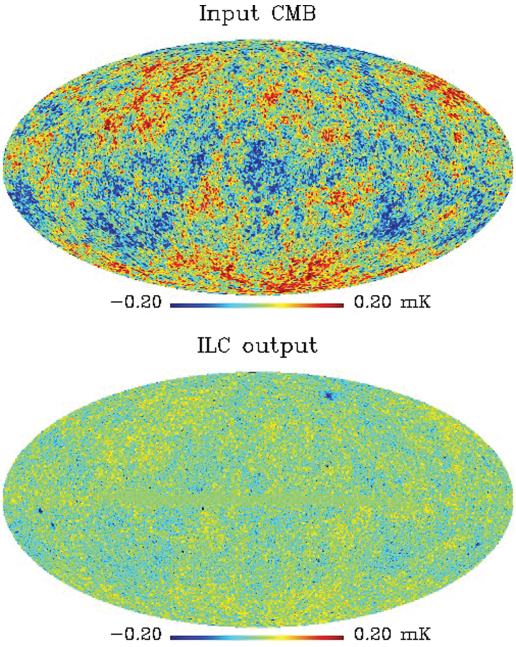

Figure 4. Input CMB- and ILC-estimated CMB plotted on a 0.2 mK scale for one realization at 1 per cent calibration error with particularly bad output (relative error near 1.0). Note that the variance of the ILC output is far below the input CMB, indicating that the input CMB was largely cancelled.

performed especially poorly, compared with the input CMB plotted on the same scale. The variance of the ILC output is much lower than the true CMB, and CMB features are strongly suppressed. As the ILC attempts to find the minimum-variance output, it finds that with calibration errors it is possible to partially cancel the CMB to get the lowest possible variance output.

4.2 Interpretation of the ILC failure

The impact of calibration errors on ILC weights, and on the output CMB map, is analytically explored in Appendix A. Here, we highlight that the signal-to-noise ratio plays a decisive role on this impact.

The ILC method is a linear combination of the maps observed in different frequency channels, $\hat{s} = \sum_i w_i x_i$. The ILC combination has minimum variance under the constraint

$$\sum_i w_i a_i = 1. \tag{8}$$

The constraint in principle guarantees the CMB conservation, otherwise $w_i = 0$ for all i would minimize the variance. If the calibration a_i is wrong, then the CMB conservation is no longer guaranteed. In some cases, when the signal-to-noise ratio is large enough, it can be dramatic for the CMB extraction (see Section 4.3).

As discussed above, the reconstruction error arises from two terms. A multiplicative term, i.e. a global calibration error term, and an additive contamination term. We can write the estimated

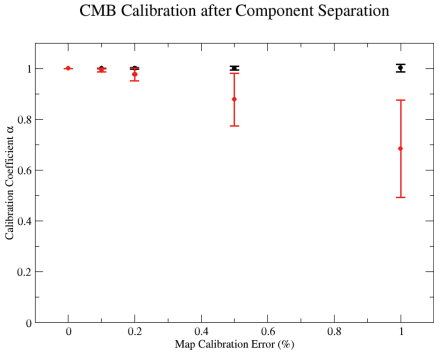

Figure 5. This figure shows the overall calibration coefficient of the output CMB map, computed from the known calibration errors in the inputs and the weights applied to obtain the output. The error bars represent the rms of α among the 128 realizations. For FastICA, the calibration coefficient is centred very near one, with an rms of approximately 1.5 times the map calibration error. By contrast, ILC has a CMB calibration that is perfect if the map calibration is perfect, but this quickly turns into a significant bias with large uncertainties as to the final calibration value.

CMB map as a function of the true CMB map as

$$\hat{s}(p) = \alpha s(p) + c(p),$$

where α is the global calibration coefficient and $c(p)$ is the contamination by foregrounds and noise. Fig. 5 shows this parameter α versus the input map calibration error. The presence of calibration errors δ_{a_i} modifies the calibration coefficients in each channel as $a_i \rightarrow a_i + \delta_{a_i}$, where $\delta_{a_i} \ll a_i$. We may explicitly expand the multiplicative error and the additive error in terms of the calibration errors δ_{a_i} and the ILC weights w_i:

$$\begin{aligned}\hat{s}(p) &= \sum_i w_i x_i(p) \\ &= \sum_i w_i (a_i + \delta_{a_i}) s(p) + \sum_i w_i n_i(p) \\ &= \left(1 + \sum_i w_i \delta_{a_i}\right) s(p) + \sum_i w_i n_i(p), \end{aligned} \quad (9)$$

where the ILC weights w_i satisfy the constraint $\sum_i w_i a_i = 1$. Thus, we have

$$c(p) = \sum_i w_i n_i(p), \quad (10)$$

$$\alpha = 1 + \sum_i w_i \delta_{a_i}. \quad (11)$$

The additive error term $c(p) = \sum_i w_i n_i(p)$ is responsible for a bias in the CMB estimation because of foreground and noise contaminations even in the absence of calibration errors. Delabrouille et al. (2009) have explored the impact of this term on the ILC estimation of the CMB and have found that, in addition to the standard reconstruction error due to foreground and noise contamination, there is a bias, $E[s(\hat{s} - s)]$, due to the estimation of second-order statistics on samples of finite size. Both errors contribute to the variance of the output CMB map as

$$E(\hat{s}^2) = E(s^2) + E[(\hat{s} - s)^2] + 2E[s(\hat{s} - s)].$$

The multiplicative error term $\alpha = 1 + \sum_i w_i \delta_i$ becomes non-trivial in the presence of calibration errors because the ILC weights w_i, as derived in equation (A6) of Appendix A, do not depend only on the calibration errors δ_{a_i} but also on the signal-to-noise ratio $\sigma^2 \mathbf{R}_n^{-1}{}_{ij}$, where $\sigma^2 = E(s^2)$ and $(\mathbf{R}_n)_{ij} = E(n_i n_j)$ denote, respectively, the variance of the CMB signal and the covariance matrix of the noise (including foregrounds).

4.3 Importance of the signal-to-noise ratio

From the exact expression (A6) of the weights, we may write the multiplicative factor $\alpha = 1 + \boldsymbol{w}^t \boldsymbol{\delta_a}$ as

$$\alpha = \frac{\boldsymbol{a}^t \mathbf{R}_n^{-1} \boldsymbol{a} + \boldsymbol{a}^t \mathbf{R}_n^{-1} \boldsymbol{\delta_a}}{\boldsymbol{a}^t \mathbf{R}_n^{-1} \boldsymbol{a} + \sigma^2 \left[\left(\boldsymbol{a}^t \mathbf{R}_n^{-1} \boldsymbol{a}\right) \left(\boldsymbol{\delta}_a^t \mathbf{R}_n^{-1} \boldsymbol{\delta_a}\right) - \left(\boldsymbol{a}^t \mathbf{R}_n^{-1} \boldsymbol{\delta_a}\right)^2 \right]}. \quad (12)$$

The immediate consequence of equation (12) is the existence of two regimes.

If the signal-to-noise ratio is small enough compared to the inverse of the calibration error, typically,

$$\text{if} \quad \sigma^2 \boldsymbol{\delta}_a^t \mathbf{R}_n^{-1} \boldsymbol{\delta}_a \ll 1, \quad \text{then} \quad \alpha \approx 1 + \mathcal{O}(|\boldsymbol{\delta_a}|/|\boldsymbol{a}|),$$

because the expression proportional to σ^2 becomes negligible in (12). So we tend to recover the almost perfect CMB reconstruction close to the case of no calibration error ($\boldsymbol{\delta_a} = 0$).

If the signal-to-noise ratio becomes large enough, then the reconstruction of the CMB signal may be dramatically damaged. This is the main result of this paper. Typically,

$$\text{if} \quad \sigma^2 \boldsymbol{\delta}_a^t \mathbf{R}_n^{-1} \boldsymbol{\delta}_a \gg 1, \quad \text{then} \quad \alpha \approx 0,$$

the multiplicative factor goes to zero since the expression proportional to σ^2 dominates all the other terms in (12), in which case the ILC estimation completely 'kills' the expected CMB signal, $\hat{s}(p) \approx c(p)$.

Let us complete the discussion by relating the first and second moments of the output CMB $\hat{s}$ and the reconstruction error $\hat{s} - s$ to the multiplicative and the additive errors. Considering that the CMB and the noise (including foregrounds) are independent random signals, $E(n_i s) = 0$, and assuming that $E(n_i) = 0$, we get

$$\begin{aligned} E(\hat{s} - s) &= (\alpha - 1) E(s), \\ E\left[s\,(\hat{s} - s)\right] &= (\alpha - 1) E(s^2), \\ E[(\hat{s} - s)^2] &= (\alpha - 1)^2 E(s^2) + E[c(p)^2], \end{aligned} \quad (13)$$

where $E[c(p)^2] = \boldsymbol{w}^t \mathbf{R}_n \boldsymbol{w}$. The detailed expression of these moments in terms of the calibration errors and the signal-to-noise ratio is derived in Appendix A. From (13), once again, if the signal-to-noise ratio is large enough, then the reconstruction of the CMB is biased since α moves away from one to reach zero.

4.4 A simple example

Here, we show a schematic description of the process using a simple example. We consider a two-channel case:

$$\begin{aligned} x_1 &= 0.99 s + n_1 \\ x_2 &= s + n_2, \end{aligned} \quad (14)$$

where s is the CMB, x_i is the i th channel of the data and n_i is the foregrounds plus instrument noise. The calibration coefficients are equal to one and a calibration error of 1 per cent has been considered in the first channel. If the signal-to-noise ratio is large enough, for example $n_i/s \ll 0.99$, then the noise is negligible in the observed maps

$$\begin{aligned} x_1 &\approx 0.99 s \\ x_2 &\approx s. \end{aligned} \quad (15)$$

Table 1. ILC reconstruction errors for *Planck* in the presence of 1, 0.5 and 0.1 per cent calibration errors.

Planck	1 per cent	0.5 per cent	0.1 per cent
Mult. factor α	0.665 00	0.852 58	0.992 37
Add. error $E[c(p)]$ (mK)	6.208e−2	3.455e−2	1.845e−2
$E[c(p)^2]$ (mK^2)	1.231e−2	3.46e−3	5.6e−4
$E[(\hat{s}-s)^2]$ (mK^2)	4.26e−3	1.91e−3	5.5e−4
$E[s(\hat{s}-s)]$ (mK^2)	−3.26e−3	−1.18e−3	−1.3e−4
$E(s^2)$ (mK^2)	7.42e−3	7.42e−3	7.42e−3
$E(\hat{s}^2)$ (mK^2)	5.16e−3	6.99e−3	7.71e−3

Table 2. ILC reconstruction errors for the *WMAP* in the presence of 1 per cent calibration errors.

WMAP	1 per cent
Mult. factor α	0.987 09
Add. error $E[c(p)]$ (mK)	1.129e−2
$E[c(p)^2]$ (mK^2)	6.9e−4
$E[(\hat{s}-s)^2]$ (mK^2)	6.5e−4
$E[s(\hat{s}-s)]$ (mK^2)	−2.4e−4
$E(s^2)$ (mK^2)	5.15e−3
$E(\hat{s}^2)$ (mK^2)	5.33e−3

The ILC estimate of the CMB thus reduces in that case to

$$\hat{s} \approx 100x_1 - 99x_2, \tag{16}$$

where the weights satisfy the constraint $100 - 99 = 1$, which would guarantee the CMB conservation if the calibration was correctly estimated. Consequently, the CMB estimate is of minimum variance since $E(\hat{s}^2) \approx 0$, but of course completely removes the expected input CMB, rendering the ILC totally irrelevant.

We may explain the process as follows. In the presence of a calibration error in one channel, the ILC algorithm minimizes the variance of

$$\hat{s} = (0.99w_1 + w_2)s + w_1n_1 + w_2n_2. \tag{17}$$

We can contrast this what we would get without calibration errors,

$$\hat{s} = (w_1 + w_2)s + w_1n_1 + w_2n_2. \tag{18}$$

With the constraint that $w_1 + w_2 = 1$, the contribution of the CMB signal to $\hat{s}$ is always s. This indicates that the weights will take whatever values they need to take to minimize the contribution of the noise.

However, in the presence of calibration errors, it becomes possible for the contribution of s to $\hat{s}$ to vary depending upon the choice of weights, indicating that a minimization of the variance of $\hat{s}$ will introduce some competition between minimizing $(0.99w_1 + w_2)s$ and minimizing $w_1n_1 + w_2n_2$. For the following weights

$$\begin{aligned} w_1 &= 100, \\ w_2 &= -99, \end{aligned} \tag{19}$$

the contribution of the CMB to $\hat{s}$ will be identically zero. This is what the ILC produces in the limit of the signal-to-noise ratio becoming very large with respect to the calibration error. In the opposite limit, that of small signal-to-noise ratio, it is the minimization of the second term, $w_1n_1 + w_2n_2$, that drives the minimization of $\hat{s}$, which mimics the behaviour under the assumption of no calibration error.

4.5 The case of *Planck*

In Table 1, we present the results of 10 simulations of the sky with an ILC estimation of the CMB in the presence of 0.1, 0.5 and 1 per cent calibration errors for the *Planck* experiment (nine frequency channels).

For 1 per cent, we observe a significant bias affecting the CMB reconstruction by the ILC. The multiplicative factor $\alpha = 0.665$ (Table 1) indicates that the CMB estimate eliminates roughly 33 per cent of the input CMB. The high sensitivity of *Planck* means a large signal-to-noise ratio, comparable to the inverse of the calibration error, which leads to a poor extraction of the CMB by ILC, as expected from formula (12). For 0.5 per cent calibration errors, 15 per cent of CMB is eliminated by the ILC estimation. Finally for 0.1 per cent calibration errors, 1 per cent of CMB is eliminated by the ILC estimation, which is nevertheless 10 times the calibration error – and clearly not acceptable for precision cosmology with *Planck*.

4.6 The case of *WMAP*

In Table 2, we present the results of 10 simulations of the sky with an ILC estimation of the CMB in the presence of 1 per cent calibration errors for the *WMAP* experiment. We observe a negligible bias affecting the CMB reconstruction by ILC. The multiplicative factor $\alpha \approx 0.99$ (Table 2) indicates that the percentage of eliminated input CMB by ILC is for the *WMAP* of the order of the calibration error, i.e. 1 per cent, as expected from formula (12) when the signal-to-noise ratio is small enough. The sensitivity of *WMAP* is small enough to render the ILC estimation of the CMB insensitive to calibration errors.

4.7 Actual *WMAP* ILC

The above result for the *WMAP* was obtained assuming that the ILC is performed on the masked sky of Fig. 1. In fact, ILC weights used by the *WMAP* team have been computed in a different way, by subdividing the sky into 12 regions. Since the values of their weights are known, as well as the mean calibration error, we may easily evaluate the error of the reconstruction performed by the *WMAP* team.

The order of magnitude of the ILC weights w_i^{WMAP} computed by the *WMAP* team is comprised between 10^{-2} and 3 (Hinshaw et al. 2007) and the relative calibration errors have been estimated by the *WMAP* team to be of the order of $\delta_{a,i} \sim 0.2$ per cent.

In the subdivision of the sky by the *WMAP* team, the region zero (Hinshaw et al. 2007) corresponds to the part of the sky outside the Galaxy and thus dominated by the CMB signal. A priori, since the signal-to-noise ratio is the highest in that high galactic latitude region, one might expect the effect of the calibration errors to be large. However, this is not the case.

We may estimate the maximum percentage of eliminated CMB in the region zero as follows:

$$\begin{aligned} |1-\alpha| &= \left| \sum_i w_i^{WMAP} \delta_{a_i} \right| \\ &\leq 0.002 \sum_i \left| w_i^{WMAP} \right| \\ &\leq 7 \times 10^{-3} = 0.7 \text{ per cent}, \end{aligned} \tag{20}$$

where w_i^{WMAP} are the ILC weights computed by the *WMAP* team in the region zero (Hinshaw et al. 2007). Therefore, the maximum percentage of eliminated CMB has the order of magnitude of the calibration error, i.e. few $\times\ 10^{-1}$ per cent, which is small.[5] So the multiplicative factor for the actual *WMAP* ILC in the presence of 0.2 per cent calibration errors is close to one, with a minor loss of CMB power:

$$\alpha \geq 0.993.$$

Interestingly, the ILC weights used at high galactic latitude by the *WMAP* team (Hinshaw et al. 2007) have been computed in a low galactic latitude region of the sky, where the signal-to-noise ratio is sufficiently small. This certainly explains why the ILC weights are close to those expected with no calibration errors and why the multiplicative factor is close to one. Therefore, the calibration uncertainties do not have a strong impact on the ILC weights computed in the *WMAP* third year data release. The bias due to calibration errors is negligible.

The price paid for this, as emphasized by Delabrouille et al. (2009), is that at high galactic latitude the *WMAP* weights are chosen to cancel galactic foregrounds rather than instrumental noise, a suboptimal choice away from the Galaxy, particularly for small scales.

4.8 Other ILC performed on *WMAP*

Several authors have used a version of the ILC to analyze *WMAP* data. This paper warns the users of the corresponding data sets that in the presence of calibration errors, some CMB power may be lost in the maps obtained. Further investigation would be needed to evaluate the exact impact for each individual recovered CMB map.

4.9 Debiasing

A natural question to ask is whether, since the effect of calibration errors is to introduce a loss of CMB power, it would not be possible to correct from this effect and 'recalibrate' a posteriori in some way.

First of all, this cannot be the optimal solution, as the noise contribution to the total error would be increased accordingly. The proper solution would be to get the right calibration beforehand. As we can see from Fig. 5 that the variance of α seems to be of the order of $1 - \alpha$. This indicates that the maximum improvement on the level of the CMB is to reduce the expectation value of $|1 - \alpha|$ by around a factor of 2. As $1 - \alpha$ becomes very large very quickly, this will not help when the calibration is not already very good compared to the signal-to-noise ratio.

Finally, even the knowledge of the expectation value of α is not very easy to get. Simulations give an estimate of its amplitude, but the actual value may depend on details, for which simulations are not guaranteed to be representative.

Hence, we leave this question open for further investigations.

4.10 Impact of the number of channels

Tests performed varying the number of channels used to perform the ILC with *Planck* data show that the ILC does better with calibration errors if fewer channels are used. To add new data, but end up with worse estimation of the desired products, indicates that the new data are not being used effectively, to say the least.

The reason for this degradation of the performance of the ILC when more channels are added is easy to understand. As discussed in Section 4.3, the ILC can erroneously cancel out part of the CMB if the signal-to-noise ratio is larger than the inverse of the calibration error, i.e. if

$$\sigma^2 \boldsymbol{\delta}_{\boldsymbol{a}}^t \mathbf{R}_n^{-1} \boldsymbol{\delta}_{\boldsymbol{a}} \gg 1. \tag{21}$$

As $\mathbf{R}_n^{-1}$ and $\mathbf{R}_n$ are symmetric matrices, they can be diagonalized, and we can write

$$\mathbf{R}_n^{-1} = \mathbf{O}^t \mathbf{D}_n^{-1} \mathbf{O},$$

where $\mathbf{O}$ is an orthonormal matrix and $\mathbf{D}_n^{-1}$ is a diagonal matrix. The condition of equation (21) then becomes

$$\sigma^2 (\mathbf{O}\boldsymbol{\delta}_{\boldsymbol{a}})^t \mathbf{D}_n^{-1} (\mathbf{O}\boldsymbol{\delta}_{\boldsymbol{a}}) \gg 1. \tag{22}$$

Matrix $\mathbf{O}$ preserves the norm, and thus elements of $\mathbf{O}\boldsymbol{\delta}_a$ are of the same order as those of $\boldsymbol{\delta}_{\boldsymbol{a}}$. It then suffices that one of the eigenvalues of $\mathbf{D}_n$ be small for $\sigma^2 \boldsymbol{\delta}_{\boldsymbol{a}}^t \mathbf{R}_n^{-1} \boldsymbol{\delta}_{\boldsymbol{a}}$ to be large, causing the CMB power loss discussed in this paper.

Now recalling that $\mathbf{R}_n$ is the covariance matrix of noise + foregrounds, it is easy to understand why more channels cause more problems with *Planck*. Foregrounds are significantly brighter than the noise, and comparable in amplitude to the CMB over a fraction of the sky. If they span a space of dimension equal or greater than the number of channels, matrix $\mathbf{D}_n$ will have no small eigenvalue. If, on the other hand, they span a space of dimension less than the number of channels, matrix $\mathbf{D}_n$ will have at least one small eigenvalue, generating the 'CMB loss' problem.

Physically, this is understood in the following way: if there are few channels, the minimization of the variance of the ILC linear combination will be achieved by cancelling foregrounds primarily. If however there are additional channels which are not needed to cancel out the foregrounds, the extra channels leave more freedom for the ILC weights to adjust themselves so as to cancel part of the CMB as well.

4.11 Extensions for real data sets

Our analysis addresses the simplest approach to the problem. There are some immediate avenues for research into the full impact of this bias on real data. For instance, with real data, we do not necessarily expect to have uniform calibration across the entire sky. More realistically, we can expect the calibration error to vary slowly over the sky. In this case, a straightforward extension of our analysis would be to investigate the impact of these errors on component separation made by patches.

The extreme case would be to consider the multiplicative calibration errors across the sky as being modelled as one overall calibration error plus a per-pixel component, not correlated from pixel to pixel. In this case, we can approximate the per-pixel calibration errors as an added (inhomogeneous) noise component.

Another extension of our analysis to real data would be to pay attention to the fact that the calibration error is likely to vary significantly from channel to channel in real data. Here, we would simply point out that it is only those few channels with the brightest CMB where we feel the calibration error is likely to be important. For space missions as the *WMAP* or *Planck*, where CMB channels are calibrated on the CMB dipole, a constant calibration error is likely to be a good approximation. Any analysis of how this bias

[5] It should be noted that this bound is a rough estimation, since we do not have access to the real value of the calibration error for each frequency channel.

effects real data would naturally have to take into account the precise calibration error for each channel in order to be applicable.

5 CONCLUSION

The primary conclusion of our work is that some care is required for performing component separation in the presence of calibration errors, in particular for sensitive multichannel instruments such as *Planck*. We have shown that two different component separation algorithms, FastICA and ILC, behave very differently in the presence of calibration errors. FastICA is completely unaffected, while the ILC can become biased by a significant amount with even small calibration errors. We propose that those attempting to make use of these or other component separation techniques pay close attention to how calibration errors affect their results. Some techniques will doubtlessly be completely unaffected, as FastICA was, while others may be very sensitive like ILC.

We also note that due to the fact that ILC in the presence of sufficient calibration errors biases the variance of the CMB low, and because we have a lower limit upon the variance of the CMB from the *WMAP*, through its measurement of the CMB power spectrum up to about $\ell = 900$, the variance of the ILC output may prove a useful diagnostic test if the calibration of *Planck* was performed well. The ability to use this as a cross-check on calibration also indicates that for a *Planck*-style mission we expect to recover, at a minimum, around 0.1–0.2 per cent relative calibration error. The reasoning for this is that if the calibration error is worse, then the ILC will produce a CMB map that is of lower variance than a similar map from the *WMAP*, which, in turn, tells us that the calibration was not very good. If we have information that the calibration was not as good as it could have been, then it is reasonable to expect that it is possible to improve said calibration.

Note that even though FastICA is not biased where ILC is, it is not clear that FastICA is better. The ILC does seem to produce lower errors in extracting the CMB, as seen in Figs 2 and 3. The biasing is troubling, but ILC retains lower extraction error up to somewhere between 0.1 and 0.2 per cent calibration error, at least at high galactic latitudes. If the calibration error is good enough, then we still expect ILC to remain a very useful method for extracting the CMB.

ACKNOWLEDGMENTS

We would like to thank Carlo Baccigalupi, Jean-François Cardoso, Maude Le Jeune and Radek Stompor for useful conversations related to this work. Some of the results in this paper have been derived using the HEALPIX (Górski et al. 2005) package. We also acknowledge the use of the PSM, developed by the Component Separation Working Group (WG2) of the Planck Collaboration.

REFERENCES

Baccigalupi C. et al., 2000, MNRAS, 318, 769
Bedini L., Herranz D., Salerno E., Baccigalupi C., Kuruouglu E. E., Tonazzini A., 2005, EURASIP J. Advances Signal Processing, 15, 2400
Bennett C. L. et al., 1996, ApJ, 464, L1
Benoît A. et al., 2003, A&A, 399, L25
Bobin J., Moudden Y., Starck J.-L., Fadili J., Aghanim N., 2008, Stat. Methodol., 5, 307
Bonaldi A., Bedini L., Salerno E., Baccigalupi C., de Zotti G., 2006, MNRAS, 373, 271
Bonaldi A., Ricciardi S., Leach S., Stivoli F., Baccigalupi C., de Zotti G., 2007, MNRAS, 382, 1791
Cardoso J.-F., Le Jeune M., Delabrouille J., Betoule M., Patanchon G., 2008, IEEE J. Selected Topics Signal Processing, Vol. 2, p. 735–746
Delabrouille J., Cardoso J.-F., 2007, preprint (arXiv:astro-ph/0702198)
Delabrouille J., Cardoso J.-F., Patanchon G., 2003, MNRAS, 346, 1089
Delabrouille J., Cardoso J.-F., Le Jeune M., Betoule M., Fay G., Guilloux F., 2009, A&A, 493, 835
Eriksen H. K., Banday A. J., Górski K. M., Lilje P. B., 2004, ApJ, 612, 633
Fixsen D. J., Cheng E. S., Gales J. M., Mather J. C., Shafer R. A., Wright E. L., 1996, ApJ, 473, 576
Fixsen D. J., Hinshaw G., Bennett C. L., Mather J. C., 1997, ApJ, 486, 623
Górski K. M., Hivon E., Banday A. J., Wandelt B. D., Hansen F. K., Reinecke M., Bartelmann M., 2005, ApJ, 622, 759
Hinshaw G. et al., 2007, ApJS, 170, 288
Hyvärinen A., 1999, IEEE Transactions on Neural Networks, 10, 626
Kim J., Naselsky P., Christensen P. R., 2009, Phys. Rev. D, 79, 023003
Komatsu E. et al., 2009, ApJS, 180, 330
Lamarre J. M. et al., 2003, New Astron. Rev., 47, 1017
Leach S. M. et al., 2008, A&A, 491, 597
MacTavish C. J. et al., 2006, ApJ, 647, 799
Maino D. et al., 2002, MNRAS, 334, 53
Maino D., Donzelli S., Banday A. J., Stivoli F., Baccigalupi C., 2006, preprint (arXiv:astro-ph/0609228)
Mennella A. et al., 2004, in Bertin G., Farina D., Pozzoli R., eds, AIP Conf. Ser. Vol. 703, Plasmas in the Laboratory and in the Universe: New Insights and New Challenges. Am. Inst. Phys., Melville, p. 401
Patanchon G., Cardoso J.-F., Delabrouille J., Vielva P., 2005, MNRAS, 364, 1185
QUaD collaboration: C. Pryke et al., 2008, preprint (arXiv:0805.1944)
Rebolo R. et al., 2004, MNRAS, 353, 747
Reichardt C. L. et al., 2009, ApJ, 694, 1200
Sievers J. L. et al., 2009, preprint (arXiv:0901.4540)
Tauber J. A., 2004, Adv. Space Res., 34, 491
Tegmark M., de Oliveira-Costa A., Hamilton A. J., 2003, Phys. Rev. D, 68, 123523
Tristram M. et al., 2005, A&A, 436, 785

APPENDIX A: ANALYTIC ANALYSIS OF ILC

In this appendix, we analytically derive the bias of the ILC estimator generated by calibration errors, and look at the impact of the signal-to-noise ratio on this bias. In particular, we show that, even in the presence of small calibration errors, the ILC tends to poorly extract the CMB if the signal-to-noise ratio is large.

A1 Review of ILC

We model the data as

$$\boldsymbol{x}(p) = \boldsymbol{a}s(p) + \boldsymbol{n}(p), \tag{A1}$$

where $\boldsymbol{x}(p)$ is the vector of the observed data at the pixel (or harmonic mode or needlet coefficient) p for the set of frequency channels, $s(p)$ is the CMB signal and $\boldsymbol{n}(p)$ is the vector of corresponding noise (including both foregrounds contaminants and instrumental noise) for the set of frequency channels. $\boldsymbol{a}$ is a vector which contains the frequency scaling of the component, so that in the case of CMB with no calibration errors one has $\boldsymbol{a} = (1, 1, \ldots, 1)$. In the following, we omit the index p.

We use σ^2 and $\mathbf{R}_n$, respectively, to denote the variance of the CMB signal s and the covariance matrix of the noise $\boldsymbol{n}$ (including foregrounds), and assume that s and $\boldsymbol{n}$ are independent such that the covariance matrix of the observed maps is $\mathbf{R}_x = (\mathbf{R}_n + \sigma^2 \boldsymbol{a}\boldsymbol{a}^t)$. The ILC implements an approximation of the ideal filter

$$\hat{s} = \frac{\boldsymbol{a}^t \mathbf{R}_x^{-1} \boldsymbol{x}}{\boldsymbol{a}^t \mathbf{R}_x^{-1} \boldsymbol{a}}, \tag{A2}$$

which is an unbiased minimum-variance estimate of s. In practice, the covariance $\mathbf{R}_x$ used in the ILC is an empirical estimate on a sample of finite size, and thus slightly differs from its ensemble average ($\hat{R}_x = \mathbf{R}_x + \Delta_x$). This induces a bias in the variance of the ILC, as shown by Delabrouille et al. (2009). In this appendix, we assume $\hat{R}_x = \mathbf{R}_x$ to investigate the bias that stems from errors in calibration alone ($\hat{\boldsymbol{a}} = \boldsymbol{a} + \boldsymbol{\delta}_a$).

A2 Bias due to calibration errors

An imperfectly estimated frequency scaling vector $\boldsymbol{a}$ includes calibration errors $\boldsymbol{\delta}_a$ which introduce a discrepancy between the observed data and the ILC weights that are used to reconstruct the CMB. This discrepancy is expected to be responsible for a bias in the reconstruction. Due to calibration errors $\boldsymbol{\delta}_a$, the observed map is modified as

$$\begin{aligned} \boldsymbol{x} &= (\boldsymbol{a} + \boldsymbol{\delta}_a)s + \boldsymbol{n}, \\ \mathbf{R}_x &= \mathbf{R}_n + \sigma^2 (\boldsymbol{a} + \boldsymbol{\delta}_a)(\boldsymbol{a} + \boldsymbol{\delta}_a)^t, \end{aligned} \tag{A3}$$

such that the ILC estimate becomes[6]

$$\hat{s} = \frac{\boldsymbol{a}^t \left[\mathbf{R}_n + \sigma^2 (\boldsymbol{a} + \boldsymbol{\delta}_a)(\boldsymbol{a} + \boldsymbol{\delta}_a)^t\right]^{-1}}{\boldsymbol{a}^t \left[\mathbf{R}_n + \sigma^2 (\boldsymbol{a} + \boldsymbol{\delta}_a)(\boldsymbol{a} + \boldsymbol{\delta}_a)^t\right]^{-1} \boldsymbol{a}} \left[(\boldsymbol{a} + \boldsymbol{\delta}_a)s + \boldsymbol{n}\right]. \tag{A4}$$

Making use of the inversion formula

$$\mathbf{R}_x^{-1} = \left[\mathbf{R}_n + \sigma^2 (\boldsymbol{a} + \boldsymbol{\delta}_a)(\boldsymbol{a} + \boldsymbol{\delta}_a)^t\right]^{-1} = \mathbf{R}_n^{-1} - \sigma^2 \frac{\mathbf{R}_n^{-1} (\boldsymbol{a} + \boldsymbol{\delta}_a)(\boldsymbol{a} + \boldsymbol{\delta}_a)^t \mathbf{R}_n^{-1}}{1 + \sigma^2 (\boldsymbol{a} + \boldsymbol{\delta}_a)^t \mathbf{R}_n^{-1} (\boldsymbol{a} + \boldsymbol{\delta}_a)}, \tag{A5}$$

we obtain the weights $\boldsymbol{w}$ of the ILC ($\hat{s} = \boldsymbol{w}^t \boldsymbol{x}$) as

$$\boldsymbol{w}^t = \frac{\boldsymbol{a}^t \mathbf{R}_n^{-1} + \sigma^2 \boldsymbol{a}^t \mathbf{R}_n^{-1} \left(\boldsymbol{a}^t \mathbf{R}_n^{-1} \boldsymbol{\delta}_a + \boldsymbol{\delta}_a^t \mathbf{R}_n^{-1} \boldsymbol{\delta}_a\right) - \sigma^2 \boldsymbol{\delta}_a^t \mathbf{R}_n^{-1} \left(\boldsymbol{a}^t \mathbf{R}_n^{-1} \boldsymbol{a} + \boldsymbol{a}^t \mathbf{R}_n^{-1} \boldsymbol{\delta}_a\right)}{\boldsymbol{a}^t \mathbf{R}_n^{-1} \boldsymbol{a} + \sigma^2 \left(\boldsymbol{a}^t \mathbf{R}_n^{-1} \boldsymbol{a}\right) \left(\boldsymbol{\delta}_a^t \mathbf{R}_n^{-1} \boldsymbol{\delta}_a\right) - \sigma^2 \left(\boldsymbol{a}^t \mathbf{R}_n^{-1} \boldsymbol{\delta}_a\right)^2}. \tag{A6}$$

In the absence of calibration errors ($\boldsymbol{\delta}_a = 0$), we recover the standard ILC weights

$$\boldsymbol{w}^t|_{\boldsymbol{\delta}_a = 0} = \frac{\boldsymbol{a}^t \mathbf{R}_n^{-1}}{\boldsymbol{a}^t \mathbf{R}_n^{-1} \boldsymbol{a}} = \frac{\boldsymbol{a}^t \mathbf{R}_x^{-1}}{\boldsymbol{a}^t \mathbf{R}_x^{-1} \boldsymbol{a}}, \tag{A7}$$

where the second equality[7] comes from the inversion formula (A5). We see that the presence of calibration errors induces a departure from the standard ILC weights through correction terms which explicitly depend on the signal-to-noise ratio $\sigma^2 \mathbf{R}_n^{-1}$. Typically if the signal-to-noise ratio is much smaller than the inverse of the calibration error squared (e.g. $\boldsymbol{\delta}_a^t \sigma^2 \mathbf{R}_n^{-1} \boldsymbol{\delta}_a \ll 1$) then the calibration errors will have little impact and the standard ILC weights are relevant. Else if the signal-to-noise ratio becomes comparable to the inverse of the calibration error squared, then the impact of calibration errors may be more dramatic on the CMB reconstruction since the variance of the ILC may be much lower than the true CMB. In the exact expression (A.6), we intentionally conserved second-order terms in $\boldsymbol{\delta}_a$ because they play a role of regularization terms when the signal-to-noise ratio $\sigma^2 \mathbf{R}_n^{-1}$ goes to infinity.

As a simple illustration let us apply the above result to the following example with two frequency channels and a diagonal noise covariance matrix:

$$\begin{aligned} x_1 &= 0.99s + n_1 \\ x_2 &= s + n_2. \end{aligned} \tag{A8}$$

Here the calibration error is 1 per cent. We note $\sigma^2 = E(s^2)$, $\mathbf{R}_n = \mathrm{diag}[\sigma_1^2, \sigma_2^2]$, where $\sigma_i^2 = E(n_i^2)$. In this example, $\boldsymbol{a}^t = (1, 1)$ and $\boldsymbol{\delta}_a^t = (-0.01, 0)$ so that the expression (A6) of $\boldsymbol{w}^t = (w_1, w_2)$ reduces to

$$w_1 = \frac{\frac{\sigma_2^2}{\sigma^2} - \delta_{a1}}{\frac{\sigma_1^2 + \sigma_2^2}{\sigma^2} + \delta_{a1}^2}, \tag{A9}$$

[6] It should be noted that the derivation would have been of course completely equivalent if we had considered calibration errors into the ILC weights instead of into the data.

[7] In practice, we have only access to the covariance matrix $\mathbf{R}_x$ of the observed maps but not to the noise covariance matrix $\mathbf{R}_n$ (including foregrounds) for constructing the ILC estimate. But theoretically, both the representations of the ILC estimate are identical.

$$w_2 = \frac{\frac{\sigma_1^2}{\sigma_2^2} + (1+\delta_{a1})\delta_{a1}}{\frac{\sigma_1^2+\sigma_2^2}{\sigma^2} + \delta_{a1}^2}. \tag{A10}$$

If the signal-to-noise ratio becomes very large (i.e. $\sigma_i^2/\sigma^2 \to 0$), then $w_1 \approx -1/\delta_{a1} = 100$ and $w_2 \approx (1+\delta_{a1})/\delta_{a1} = -99$, so that the output CMB vanishes $\hat{s} \approx 100x_1 - 99x_2 \approx 100n_1 - 99n_2 \approx 0$ when the noise is negligible. If the signal-to-noise ratio becomes very small, then $w_1 \approx \sigma_2^2/(\sigma_1^2+\sigma_2^2)$ and $w_2 \approx \sigma_1^2/(\sigma_1^2+\sigma_2^2)$, which is the standard least mean square solution.

The ILC estimate is given by

$$\hat{s} = \boldsymbol{w}^t(\boldsymbol{a}+\boldsymbol{\delta_a})s + \boldsymbol{w}^t\boldsymbol{n},$$

$$\hat{s} = \frac{\boldsymbol{a}^t\mathbf{R}_n^{-1}\boldsymbol{a} + \boldsymbol{a}^t\mathbf{R}_n^{-1}\boldsymbol{\delta_a}}{\boldsymbol{a}^t\mathbf{R}_n^{-1}\boldsymbol{a} + \sigma^2(\boldsymbol{a}^t\mathbf{R}_n^{-1}\boldsymbol{a})(\boldsymbol{\delta}_a^t\mathbf{R}_n^{-1}\boldsymbol{\delta_a}) - \sigma^2(\boldsymbol{a}^t\mathbf{R}_n^{-1}\boldsymbol{\delta_a})^2} s + \boldsymbol{w}^t\boldsymbol{n}. \tag{A11}$$

We assume $E(\boldsymbol{n}) = 0$, the ILC estimate is thus biased as

$$E(\hat{s}) = \frac{\boldsymbol{a}^t\mathbf{R}_n^{-1}\boldsymbol{a} + \boldsymbol{a}^t\mathbf{R}_n^{-1}\boldsymbol{\delta_a}}{\boldsymbol{a}^t\mathbf{R}_n^{-1}\boldsymbol{a} + \sigma^2(\boldsymbol{a}^t\mathbf{R}_n^{-1}\boldsymbol{a})(\boldsymbol{\delta}_a^t\mathbf{R}_n^{-1}\boldsymbol{\delta_a}) - \sigma^2(\boldsymbol{a}^t\mathbf{R}_n^{-1}\boldsymbol{\delta_a})^2} E(s). \tag{A12}$$

We see that in the limit of small signal-to-noise ratio, $\sigma^2(\mathbf{R}_n^{-1})_{ij} \ll 1$, the bias is of the order of magnitude of the calibration error: $E(s)\boldsymbol{a}^t\mathbf{R}_n^{-1}\boldsymbol{\delta_a}/\boldsymbol{a}^t\mathbf{R}_n^{-1}\boldsymbol{a}$. Whereas if $\sigma^2(\mathbf{R}_n^{-1})_{ij} \gg 1$, then the bias is accentuated since $E(\hat{s}) \to 0$.

Let us compute the mean value of the error $d = \hat{s} - s$ [assuming $E(\boldsymbol{n}) = 0$]:

$$\begin{aligned} E(d) &= E[\boldsymbol{w}^t(\boldsymbol{a}+\boldsymbol{\delta_a})s - s] \\ &= \frac{\boldsymbol{a}^t\mathbf{R}_n^{-1}\boldsymbol{\delta_a} - \sigma^2\left[(\boldsymbol{a}^t\mathbf{R}_n^{-1}\boldsymbol{a})(\boldsymbol{\delta}_a^t\mathbf{R}_n^{-1}\boldsymbol{\delta_a}) - (\boldsymbol{a}^t\mathbf{R}_n^{-1}\boldsymbol{\delta_a})^2\right]}{\boldsymbol{a}^t\mathbf{R}_n^{-1}\boldsymbol{a} + \sigma^2\left[(\boldsymbol{a}^t\mathbf{R}_n^{-1}\boldsymbol{a})(\boldsymbol{\delta}_a^t\mathbf{R}_n^{-1}\boldsymbol{\delta_a}) - (\boldsymbol{a}^t\mathbf{R}_n^{-1}\boldsymbol{\delta_a})^2\right]} E(s), \end{aligned} \tag{A13}$$

so that $E(d) \to -\mathrm{E(s)}$ when $\sigma^2(\mathbf{R}_n^{-1})_{ij} \gg 1$, and $E(d) \to 0$ when $\sigma^2(\mathbf{R}_n^{-1})_{ij} \ll 1$ and $\boldsymbol{\delta_a} \ll \boldsymbol{a}$.

In the same way, the cross correlation $E(sd)$ of the error of the reconstruction with the CMB signal

$$E(s\,d) = \frac{\boldsymbol{a}^t\mathbf{R}_n^{-1}\boldsymbol{\delta_a} - \sigma^2\left[(\boldsymbol{a}^t\mathbf{R}_n^{-1}\boldsymbol{a})(\boldsymbol{\delta}_a^t\mathbf{R}_n^{-1}\boldsymbol{\delta_a}) - (\boldsymbol{a}^t\mathbf{R}_n^{-1}\boldsymbol{\delta_a})^2\right]}{\boldsymbol{a}^t\mathbf{R}_n^{-1}\boldsymbol{a} + \sigma^2\left[(\boldsymbol{a}^t\mathbf{R}_n^{-1}\boldsymbol{a})(\boldsymbol{\delta}_a^t\mathbf{R}_n^{-1}\boldsymbol{\delta_a}) - (\boldsymbol{a}^t\mathbf{R}_n^{-1}\boldsymbol{\delta_a})^2\right]}\sigma^2 \tag{A14}$$

may vanish only if $\sigma^2(\mathbf{R}_n^{-1})_{ij} \ll 1$. If the signal-to-noise ratio becomes large enough, then $E(s\,d) \to -\sigma^2$, giving evidence of the cancellation of the CMB output.

We may also compute the variance of the error. Since the CMB and the noise are uncorrelated, we get

$$\begin{aligned} E(d^2) &= \left(\boldsymbol{w}^t\boldsymbol{\delta_a}\right)^2\sigma^2 + \boldsymbol{w}^t R_n \boldsymbol{w} \\ &\approx \left\{\frac{\boldsymbol{a}^t\mathbf{R}_n^{-1}\boldsymbol{\delta_a} - \sigma^2\left[(\boldsymbol{a}^t\mathbf{R}_n^{-1}\boldsymbol{a})(\boldsymbol{\delta}_a^t\mathbf{R}_n^{-1}\boldsymbol{\delta_a}) - (\boldsymbol{a}^t\mathbf{R}_n^{-1}\boldsymbol{\delta_a})^2\right]}{\boldsymbol{a}^t\mathbf{R}_n^{-1}\boldsymbol{a} + \sigma^2\left[(\boldsymbol{a}^t\mathbf{R}_n^{-1}\boldsymbol{a})(\boldsymbol{\delta}_a^t\mathbf{R}_n^{-1}\boldsymbol{\delta_a}) - (\boldsymbol{a}^t\mathbf{R}_n^{-1}\boldsymbol{\delta_a})^2\right]}\right\}^2\sigma^2 \\ &\quad + \frac{\boldsymbol{a}^t\mathbf{R}_n^{-1}\boldsymbol{a} + \sigma^2\left(2+\sigma^2\boldsymbol{a}^t\mathbf{R}_n^{-1}\boldsymbol{a}\right)\left[(\boldsymbol{a}^t\mathbf{R}_n^{-1}\boldsymbol{a})(\boldsymbol{\delta}_a^t\mathbf{R}_n^{-1}\boldsymbol{\delta_a}) - (\boldsymbol{a}^t\mathbf{R}_n^{-1}\boldsymbol{\delta_a})^2\right]}{\left\{\boldsymbol{a}^t\mathbf{R}_n^{-1}\boldsymbol{a} + \sigma^2\left[(\boldsymbol{a}^t\mathbf{R}_n^{-1}\boldsymbol{a})(\boldsymbol{\delta}_a^t\mathbf{R}_n^{-1}\boldsymbol{\delta_a}) - (\boldsymbol{a}^t\mathbf{R}_n^{-1}\boldsymbol{\delta_a})^2\right]\right\}^2}. \end{aligned} \tag{A15}$$

Note that the second term has been truncated at second order in $\boldsymbol{\delta_a}$. If $\sigma^2(\mathbf{R}_n^{-1})_{ij} \ll 1$, then we recover the standard reconstruction error with no calibration error: $E(d^2) \approx 1/(\boldsymbol{a}^t\mathbf{R}_n^{-1}\boldsymbol{a})$, as computed by Delabrouille et al. (2009). If the signal-to-noise ratio becomes large enough, then $\boldsymbol{w}^t R_n \boldsymbol{w}$ becomes negligible compared to the first term $(\boldsymbol{w}^t\boldsymbol{\delta_a})^2\sigma^2$ such that $E(d^2) \approx \sigma^2$, again giving evidence of the cancellation of the CMB output.

This paper has been typeset from a TEX/LATEX file prepared by the author.

Monthly Notices
of the
ROYAL ASTRONOMICAL SOCIETY

Mon. Not. R. Astron. Soc. (2010) doi:10.1111/j.1365-2966.2010.17624.x

CMB and SZ effect separation with constrained Internal Linear Combinations

Mathieu Remazeilles⋆ Jacques Delabrouille⋆ and Jean-François Cardoso⋆

APC 10, rue Alice Domon et Léonie Duquet, 75205 Paris Cedex 13, France

Accepted 2010 August 31. Received 2010 August 27; in original form 2010 June 29

ABSTRACT

The 'Internal Linear Combination' (ILC) component separation method has been extensively used on the data of the *Wilkinson Microwave Anisotropy Probe* (*WMAP*) space mission, to extract a single component, the cosmic microwave background (CMB), from the *WMAP* multifrequency data. We extend the ILC approach for reconstructing millimetre astrophysical emissions beyond the CMB alone. In particular, we construct a *constrained* ILC to extract maps of both the CMB and the thermal Sunyaev–Zeldovich (SZ) effect, with vanishing contamination from the other. The performance of the constrained ILC is tested on simulations of *Planck* mission observations, for which we successfully reconstruct independent estimates of the CMB and of the thermal SZ.

Key words: methods: data analysis – cosmic background radiation.

1 INTRODUCTION

The separation of components in observations of the cosmic microwave background (CMB) is an important part of the processing and analysis of such observational data. Various *component separation* methods have been developed to extract the emission of a single component (or of several of them) out of multifrequency observations (see e.g. Delabrouille & Cardoso 2009 for a review).

Often, such methods assume that the observations are a linear mixture of unknown components (or *sources*), in which case the data are modelled as

$$x_i(p) = \sum_j A_{ij} s_j(p) + n_i(p) \quad (1)$$

where $x_i(p)$ are $N_{\rm obs}$ observed maps (p indexing the pixel), $s_j(p)$ are $N_{\rm comp}$ templates for unknown components of interest and $n_i(p)$ are maps of noise for the observations. In matrix-vector format, equation (1) writes

$$\boldsymbol{x}(p) = \mathbf{A}\boldsymbol{s}(p) + \boldsymbol{n}(p), \quad (2)$$

The coefficients A_{ij} define the *mixing matrix* $\mathbf{A}$, which tells how much of each component $s_j(p)$ is present in each observation $x_i(p)$.

Blind component separation methods such as SMICA (Delabrouille, Cardoso & Patanchon 2003; Cardoso et al. 2008), FastICA (Hyvarinen 1999; Maino et al. 2002), JADE (Cardoso 1998), CCA (Bonaldi et al. 2006) or GMCA (Bobin et al. 2008) are primarily designed to solve the problem of estimating the sources s_i, separated from one another, in the case where the observations can be modelled as in equation (1) with the matrix $\mathbf{A}$ unknown. In practice, the first (and the most difficult) task is to estimate $\mathbf{A}$.

Then, if/when matrix $\mathbf{A}$ is known (either a priori, or after it has been determined using one of the forementioned blind component separation methods), the actual component separation is solved by inversion of the linear system of equation (1). Methods for doing so in the presence of instrumental noise have been investigated by a number of authors: Tegmark & Efstathiou (1996), Bouchet & Gispert (1999), Hobson et al. (1998) and Delabrouille, Patanchon & Audit (2002).

In CMB observations, in practice, at least one of the columns of the mixing matrix is usually known (i.e. one *mixing vector*) – that of the CMB because the spectrum is known. On the other hand, some components cannot be modelled as a single template which is simply scaled by mixing coefficients [e.g. emissions from the Galactic interstellar medium (ISM)] because their spectrum varies as a function of position on the sky. Then, the data model of equation (1) fails, and one has to resort to other approaches. For these reasons, the so-called 'Internal Linear Combination' or ILC, which does not assume any particular parametrization for foreground emission, has been extensively used in the analysis of the maps obtained by the *Wilkinson Microwave Anisotropy Probe* (*WMAP*) satellite to extract a CMB map (Bennett et al. 2003; Eriksen et al. 2004; Park, Park & Gott 2007; Kim, Naselsky & Christensen 2008; Delabrouille et al. 2009).

The *Planck* mission (Tauber 2004), launched on 2009 May 14, is a third-generation CMB experiment. It observes the sky in nine frequency channels ranging from 30 to 857 GHz. The high-frequency instrument of *Planck* (Lamarre et al. 2000, 2003), in particular, has been designed with bands centred at the minimum, the zero and the maximum of the thermal Sunyaev–Zeldovich (SZ) emission. The extraction of clean CMB and SZ maps, of a catalogue of galaxy

⋆E-mail: remazeil@apc.univ-paris7.fr (MR); delabrouille@apc.univ-paris7.fr (JD); cardoso@enst.fr (J-FC)

clusters selected by their thermal SZ effect and the investigation of bulk flows in the large-scale velocity field from kinetic SZ effect towards galaxy clusters are part of the scientific programme of *Planck*.

For these projects, accurate separation of CMB (and kinetic SZ) from thermal SZ is important (Aghanim, Górski & Puget 2001; Aghanim et al. 2003). In particular, residuals from thermal SZ in the CMB maps can be 'mistaken' for detectable kinetic SZ. They can also bias the estimation of cosmological parameters, in particular those which depend strongly on the small-scale CMB power spectrum, such as the scalar spectral index and the reionization optical depth (Taburet et al. 2009).

In the present paper, we address the problem of extending the ILC method to separate several components of interest with known 'mixing vector' in multifrequency observations such as those of *Planck*. The method, denoted as *constrained ILC*, is of interest for separation of CMB and thermal SZ components with vanishing residual contamination of one by the other.

2 ILC ESTIMATION OF CMB AND SZ

2.1 Astrophysical components

Astrophysical components can be separated into two broad categories: diffuse components and point sources.

Point sources (i.e. unresolved objects) are typically detected and identified with specific methods, based on spatial filtering (see e.g. Barreiro 2009 for a review). Such methods are effective when detectable sources are isolated. Experiments also observe a background of faint sources which, due to limited sensitivity and resolution, cannot be detected individually. Such a background is treated as a diffuse component.

Other diffuse components of interest comprise the CMB and diffuse emission from the ISM. SZ effects, thermal and kinetic (Sunyaev & Zeldovich 1972), can be considered either as point sources or as diffuse components, depending on the resolution, sensitivity and frequency coverage of the experiment considered. With *Planck*, a number of observable clusters will actually be resolved, and we will consider here the thermal SZ as a diffuse component.

The emission of the ISM is complex, as it involves several processes of emission which are not fully independent. The ISM is a tenuous medium comprising ordinary matter (in the form of atomic and molecular gas, and of matter aggregates), magnetic fields and cosmic rays (see e.g. Ferrière 2001 for a review). Hot gas emits through synchrotron radiation, warm gas by free–free emission, cold dust by greybody emission and plausibly by dipole emission from rotating dust grains. Molecules emit through molecular transitions and can contribute to the diffuse emission. The dependence of these emissions with frequency is a function of additional parameters which vary over the regions of emission, e.g. electron temperature for free–free, distribution of cosmic ray electrons as a function of energy for the synchrotron, composition and temperature of molecular clouds for molecular line emission.... In addition, as all the ISM is concentrated towards the Galactic plane, all of these processes do not result in independent, nor even simply uncorrelated, emissions.

2.2 The ILC method

The standard ILC assumes very little about the model of the data. It simply assumes that all available maps ($N_{\rm obs}$ maps, indexed by i) can be written, for all pixels p of the observed maps, as

$$x_i(p) = a_i s(p) + n_i(p), \tag{3}$$

which can be recast as

$$\boldsymbol{x}(p) = \boldsymbol{a} s(p) + \boldsymbol{n}(p), \tag{4}$$

where $\boldsymbol{x}(p)$ is the vector of observations ($N_{\rm obs}$ maps), $s(p)$ a single map of a component of interest, $\boldsymbol{a}$ is a known mixing vector which does not depend on p, with as many entries as there are channels of observation, and $\boldsymbol{n}$ includes instrument noise as well as all other astrophysical emissions. For all channels ($N_{\rm obs}$ maps), it is assumed that all observations are at the same resolution, although a harmonic or needlet space implementation of the ILC permits to deal with channel-dependent resolution in a simple way (assuming symmetric beams).

The ILC provides an estimator $\hat{s}_{\rm ILC}$ of s by forming the linear combination $\hat{s}(p) = \boldsymbol{w}^t \boldsymbol{x}(p)$ of the observed maps which has unit response to the component of interest (i.e. $\boldsymbol{w}^t \boldsymbol{a} = 1$) and has minimum variance. Straightforward algebra leads to ILC coefficients such that $\hat{s}_{\rm ILC}$ of s is given by

$$\hat{s}_{\rm ILC} = \frac{\boldsymbol{a}^t \widehat{\mathbf{R}}^{-1}}{\boldsymbol{a}^t \widehat{\mathbf{R}}^{-1} \boldsymbol{a}} \boldsymbol{x}, \tag{5}$$

where $\widehat{\mathbf{R}}$ is the empirical covariance matrix of the observations (Eriksen et al. 2004).

The ILC component separation method has advantages and drawbacks. The main advantage is that it does not assume a model for the components we are *not* interested in, i.e. all the components whose contributions are collected into a single nuisance term $\boldsymbol{n}(p)$. Drawbacks include the existence of a bias induced by any empirical correlation between the component of interest and the nuisance term, as described in the appendix of Delabrouille et al. (2009), and the need to know the coefficients a_i with some accuracy, especially for sensitive experiments (Dick, Remazeilles & Delabrouille 2010).

Note that the ILC relies on the component of interest to be uncorrelated with the contaminants, i.e. $\langle s(p) n_i(p) \rangle = 0$ for all channels of observation i.

In its simplest implementation, the ILC is performed on the complete maps, and one single global matrix $\widehat{\mathbf{R}}$ is used. It is possible, however, to decompose the original maps as sums of different data subsets, covering each of a different region in pixel space (Eriksen et al. 2004) or in harmonic space (Tegmark et al. 2003), to apply independent versions of the ILC to the different data subsets, and then to recompose a map from all these independent results. In the present paper, all the experiments done on simulated maps are performed in harmonic space. We have $\widehat{\mathbf{R}} = \widehat{\mathbf{R}}(\ell)$, and each such covariance matrix is estimated as

$$\widehat{\mathbf{R}}_{ij}(\bar{\ell}) = \frac{1}{N_{\bar{\ell}}} \sum_{\bar{\ell}-\Delta\bar{\ell}}^{\bar{\ell}+\Delta\bar{\ell}} \sum_{m} x_{\ell m,i} x^*_{\ell m,j}, \tag{6}$$

where $x_{\ell m,i}$ are the spherical harmonic coefficients of map $x_i(p)$ and N_ℓ is the number of modes (ℓ, m) in the window $[\ell - \Delta\ell, \ell + \Delta\ell]$:

$$N_\ell = (\ell + \Delta\ell + 1)^2 - (\ell - \Delta\ell)^2 . \tag{7}$$

Each single $\widehat{\mathbf{R}}(\ell)$ is obtained as the average over a window in ℓ of width $\Delta\ell$.

2.3 ILC and the SZ effect

So far, the ILC has been used almost exclusively to extract a CMB map, but it can be used in a similar way to extract any single component which is described as a single template scaling with frequency,

provided that the appropriate column of the mixing matrix is known, and that this template is not correlated with other emissions present in the data set.

SZ emission, which can be observed towards clusters of galaxies at millimetre wavelengths, arises through inverse Compton scattering of CMB photons off hot electrons of the intra-cluster gas (see e.g. Birkinshaw 1999 or Carlstrom, Holder & Reese 2002 for a review).

The thermal SZ emission, in the non-relativistic approximation, is given by the product of a template map $y(p)$ (the map of the cluster Compton parameter, proportional to the integral over the line of sight of $n_e T_e$), and of a known emission law $f(\nu)$. The Compton parameter is given by

$$y = \int_{\text{l.o.s.}} \frac{kT_e}{m_e c^2}\, n_e \sigma_T\, dl, \tag{8}$$

where k is the Boltzmann constant, m_e the electron mass, c the speed of light, σ_T the Thomson cross-section, and n_e and T_e the electron density and temperature, respectively. The frequency dependence of the effect is

$$f(\nu) = x(\nu)\frac{e^{x(\nu)}+1}{e^{x(\nu)}-1} - 4 \tag{9}$$

with

$$x(\nu) = \frac{h\nu}{kT_{\text{CMB}}}.$$

The coefficients a_i of equation (3), for the thermal SZ, are the integral of the emission law $f(\nu)$ in the frequency bands of the instrument used to observe the sky.

Kinetic SZ emission has the same emission law as CMB anisotropies, and is proportional to the peculiar velocity of the scattering electron gas (i.e. of the cluster) along the line of sight. Although the kinetic and thermal SZ effects arise from the same set of galaxy clusters, their correlation vanishes because of the sign dependence of the thermal SZ temperature.

Hence, it is possible to extract a map of the thermal SZ effect from multifrequency observations with an ILC in the same way as is done for the CMB. This method has been implemented and tested in data challenges using simulated data sets, organized in the context of the preparation of the *Planck* mission (Leach et al. 2008; Melin et al. in preparation) and has been done as well (on simulations or on real data sets) in Cooray, Hu & Tegmark (2000) and Veneziani et al. (2009).

Note that on the other hand, a CMB map obtained by an ILC contains emission from *both* primary CMB anisotropies and kinetic SZ effect. The latter is typically very small compared to primary CMB anisotropies. For high-resolution, high-sensitivity maps, however, the kinetic SZ can be separated from the CMB by matched filtering, using the cluster profile estimated from the thermal SZ map.

2.4 A two-component model for the ILC

Without assuming much about the detailed properties of the emissions of other foregrounds, and supposing we are interested mostly in the CMB and the SZ, both thermal (tSZ) and kinetic (kSZ), the observational data can be modelled by an extension of equations (3) and (4), as

$$x_i(p) = a_i s(p) + b_i y(p) + n_i(p) \tag{10}$$

or as

$$\boldsymbol{x}(p) = \boldsymbol{a} s(p) + \boldsymbol{b} y(p) + \boldsymbol{n}(p) \tag{11}$$

where, as in equation (3), $s(p)$ is the CMB map (including kSZ), but where now $y(p)$ is the thermal SZ map and $\boldsymbol{n} = \{n_i(p)\}$ includes both instrumental noise and unmodelled astrophysical foregrounds (i.e. all sky components except CMB, kSZ and tSZ), in all frequency channels. Vector $\boldsymbol{a} = (1, 1, \ldots, 1)^t$ is the CMB mixing vector and $\boldsymbol{b}$ is the mixing vector of the thermal SZ, as derived from equation (9).

2.5 Independent ILC estimation of CMB and SZ

It is a straightforward process to reconstruct both a (CMB+kSZ) and a tSZ map independently by implementing two separate ILC steps, one for the (CMB+kSZ), and one for the tSZ. Standard ILC gives

$$\hat{s}(p) = \frac{\boldsymbol{a}^t \widehat{\mathbf{R}}^{-1}}{\boldsymbol{a}^t \widehat{\mathbf{R}}^{-1} \boldsymbol{a}}\, \boldsymbol{x}(p), \qquad \hat{y}(p) = \frac{\boldsymbol{b}^t \widehat{\mathbf{R}}^{-1}}{\boldsymbol{b}^t \widehat{\mathbf{R}}^{-1} \boldsymbol{b}}\, \boldsymbol{x}(p).$$

Those estimates, however, do not fully take into account the prior knowledge about the existence of two components entering in the observations as described by equation (10). In particular, the ILC weights used for CMB reconstruction do not guarantee that the reconstructed CMB contains no thermal SZ. Similarly, the weights used to reconstruct the thermal SZ do not guarantee that the reconstructed thermal SZ does not contain any CMB (and kinetic SZ). In fact, using the above solutions with the data model of equation (10), we have

$$\hat{s}(p) = s(p) + \frac{\boldsymbol{a}^t \widehat{\mathbf{R}}^{-1} \boldsymbol{b}}{\boldsymbol{a}^t \widehat{\mathbf{R}}^{-1} \boldsymbol{a}}\, y(p) + \frac{\boldsymbol{a}^t \widehat{\mathbf{R}}^{-1}}{\boldsymbol{a}^t \widehat{\mathbf{R}}^{-1} \boldsymbol{a}}\, \boldsymbol{n}(p).$$

The second term on the right-hand side is the contamination of the recovered (CMB+kSZ) by thermal SZ. Similarly, when one recovers a tSZ map, we get

$$\hat{y}(p) = y(p) + \frac{\boldsymbol{b}^t \widehat{\mathbf{R}}^{-1} \boldsymbol{a}}{\boldsymbol{b}^t \widehat{\mathbf{R}}^{-1} \boldsymbol{b}}\, s(p) + \frac{\boldsymbol{b}^t \widehat{\mathbf{R}}^{-1}}{\boldsymbol{b}^t \widehat{\mathbf{R}}^{-1} \boldsymbol{b}}\, \boldsymbol{n}(p).$$

These solutions minimize (by construction) the total variance of the reconstructed maps, but both maps contain contamination from the other component of interest. For certain applications, this contamination is not acceptable. For instance, significant thermal SZ leaking into the reconstructed CMB will make it difficult to extract any kinetic SZ information from the reconstructed (CMB+kSZ) map.

2.6 Constrained ILC estimation of CMB and SZ

Now assume that we want to ensure that each reconstructed map of interest contains no contamination from the other component, i.e. the CMB map contains no contribution from the thermal SZ, and the thermal SZ contains no contribution from the CMB (nor from kinetic SZ).

When the linear mixture model of equation (1) holds with as many components as observations, and when the mixing matrix $\mathbf{A}$ is fully known, it is straightforward to reject perfectly unwanted components using weights given, for each recovered component, by the appropriate line of any matrix of the type

$$\mathrm{M} = [\mathbf{A}^t \mathbf{K} \mathbf{A}]^{-1} \mathbf{A}^t \mathbf{K}, \tag{12}$$

where $\mathbf{K}$ can be any matrix which 'weighs' the observations. Minimum variance is obtained when $\mathbf{K} = \mathbf{R}^{-1}$ (or equivalently when $\mathbf{K}$ is the inverse of the noise covariance matrix, $\mathbf{K} = \mathbf{R}_n^{-1}$). This has been discussed extensively by Tegmark (1997) in the context of making sky maps from noisy time-ordered data, and is discussed

as well in Delabrouille & Cardoso (2009). More recently, Hurier, Hildebrandt & Macias-Perez (2010) also investigate the use of additional knowledge of A for minimizing the contamination of a component of interest by other sky emissions.

Here, we do not assume full knowledge of $\mathbf{A}$, nor prior knowledge of $\mathbf{R}$ or $\mathbf{R}_n$. In the spirit of the ILC, we look for a minimum variance estimate $\hat{s}$ of the CMB map[1] s as a linear combination of the frequency maps x_i:

$$\hat{s} = \boldsymbol{w}^t \boldsymbol{x},$$

where the weights w_i have to satisfy the constraints

$$\boldsymbol{w}^t \boldsymbol{a} = 1, \tag{13}$$

$$\boldsymbol{w}^t \boldsymbol{b} = 0, \tag{14}$$

so that we conserve the CMB signal (including kSZ) and completely eliminate the thermal SZ signal. The weights thus are solutions of

$$\frac{\partial}{\partial w_i}\left[\boldsymbol{w}^t \widehat{\mathbf{R}} \boldsymbol{w} + \lambda(1 - \boldsymbol{w}^t \boldsymbol{a}) - \mu \boldsymbol{w}^t \boldsymbol{b}\right] = 0$$

where $\widehat{\mathbf{R}}$ is the empirical covariance matrix of the observed maps and λ, μ are Lagrange multipliers. We find the solution

$$\boldsymbol{w} = \lambda \widehat{\mathbf{R}}^{-1} \boldsymbol{a} + \mu \widehat{\mathbf{R}}^{-1} \boldsymbol{b}. \tag{15}$$

Applying constraints (13) and (14) to the solution (15), we have to solve the system

$$\lambda \boldsymbol{a}^t \widehat{\mathbf{R}}^{-1} \boldsymbol{a} + \mu \boldsymbol{a}^t \widehat{\mathbf{R}}^{-1} \boldsymbol{b} = 1, \tag{16}$$

$$\lambda \boldsymbol{b}^t \widehat{\mathbf{R}}^{-1} \boldsymbol{a} + \mu \boldsymbol{b}^t \widehat{\mathbf{R}}^{-1} \boldsymbol{b} = 0. \tag{17}$$

If $\boldsymbol{b}$ is not proportional to $\boldsymbol{a}$ (which is guaranteed since the CMB and the thermal SZ do not have the same emission law), there is a unique solution to the system, for which the Lagrange multipliers are

$$\lambda = \frac{\boldsymbol{b}^t \widehat{\mathbf{R}}^{-1} \boldsymbol{b}}{(\boldsymbol{a}^t \widehat{\mathbf{R}}^{-1} \boldsymbol{a})(\boldsymbol{b}^t \widehat{\mathbf{R}}^{-1} \boldsymbol{b}) - (\boldsymbol{a}^t \widehat{\mathbf{R}}^{-1} \boldsymbol{b})^2}, \tag{18}$$

$$\mu = -\frac{\boldsymbol{a}^t \widehat{\mathbf{R}}^{-1} \boldsymbol{b}}{(\boldsymbol{a}^t \widehat{\mathbf{R}}^{-1} \boldsymbol{a})(\boldsymbol{b}^t \widehat{\mathbf{R}}^{-1} \boldsymbol{b}) - (\boldsymbol{a}^t \widehat{\mathbf{R}}^{-1} \boldsymbol{b})^2}. \tag{19}$$

The weights of the constrained ILC (for CMB+kSZ reconstruction) are given by

$$\boldsymbol{w}^t = \frac{(\boldsymbol{b}^t \widehat{\mathbf{R}}^{-1} \boldsymbol{b}) \boldsymbol{a}^t \widehat{\mathbf{R}}^{-1} - (\boldsymbol{a}^t \widehat{\mathbf{R}}^{-1} \boldsymbol{b}) \boldsymbol{b}^t \widehat{\mathbf{R}}^{-1}}{(\boldsymbol{a}^t \widehat{\mathbf{R}}^{-1} \boldsymbol{a})(\boldsymbol{b}^t \widehat{\mathbf{R}}^{-1} \boldsymbol{b}) - (\boldsymbol{a}^t \widehat{\mathbf{R}}^{-1} \boldsymbol{b})^2}. \tag{20}$$

A similar expression with the role of $\boldsymbol{a}$ and $\boldsymbol{b}$ exchanged holds for the weights to be used for estimating the thermal SZ map $y(p)$.

This is the generalization of the ILC component separation when two components are recovered, and when one imposes that there is no leakage of one component in the reconstructed map of the other.

2.7 Application to simulated *Planck* observations

We investigate the performance of standard ILC and constrained ILC for separating the CMB and the thermal SZ using observations such as those of the *Planck* mission.

[1] The same derivation can be performed for thermal SZ reconstruction by simple inversion of the roles of $\boldsymbol{a}$ and $\boldsymbol{b}$ and of s and y.

2.7.1 Simulations

Our investigations are carried out on sky simulations generated with the *Planck* Sky Model (PSM) version 1.6.3[2] for all *Planck* low frequency instruments (LFI) and high frequency instruments (HFI) channels. Sky simulations include Gaussian CMB generated assuming a C_ℓ model fitting the *WMAP* 5-year observations (Hinshaw et al. 2009), thermal and kinetic SZ effect, four components of Galactic ISM emission including thermal and spinning dust, synchrotron, and free–free, and emission from point sources (radio and infrared). The resolution and noise level of the observations correspond to nominal mission parameters as described in the *Planck* 'Blue Book'. Some details about PSM simulations can be found in Leach et al. (2008) and Betoule et al. (2009). Fig. 1 displays the simulated emission in a small patch centred around Galactic coordinates of $(l, b) = (33^\circ, 89^\circ)$; this region is selected, in our full sky maps, for the presence of a bright galaxy cluster at high Galactic latitude, where Galactic foregrounds are low, which permits to illustrate best the separation of CMB and SZ.

2.7.2 ILC results: the CMB

As a first step, we implement the usual single-component ILC (standard ILC) for both the CMB and the thermal SZ. For this particular application, a small Galactic mask is used to blank out the region of strongest Galactic emission, which permits to implement the ILC in harmonic space (i.e. priority is given to the localization of the filters in harmonic space, rather than pixel space). The spectral statistics $\widehat{\mathbf{R}}(\ell)$ are computed in windows of ℓ of width $\Delta\ell = 50$ at low ℓ (at $\ell < 2075$), and $\Delta\ell = 20$ for the highest multipoles (at $\ell \geq 2075$). The ILC is performed independently for each ℓ.

Fig. 2 displays the results of the reconstruction of the CMB. The left-hand panel shows the standard ILC reconstruction of the CMB map, which can hardly be distinguished from the left-hand panel of Fig. 1 (the reconstruction is visually excellent, albeit one may notice faint small-scale granularity caused by noise). The middle panel shows the error (difference input–output) map using a standard harmonic domain ILC. Negative patches, which were not obviously detectable by visual inspection in the reconstructed CMB map, are clearly seen in the direction of the brightest clusters; the standard ILC, clearly, does not perfectly reject the thermal SZ effect. The amplitude of the thermal SZ leaking into the map is of 0.1 mK (thermodynamic) for the brightest cluster in the field, about 2.5 times the kinetic SZ effect for that particular galaxy cluster (and well above the *Planck* noise level).

The right-hand panel shows the reconstruction error when the constrained ILC is used instead (the corresponding CMB map cannot be distinguished by visual inspection from what is obtained with the standard ILC, and is not displayed). As expected, there is no indication in the error map of leakage of thermal SZ into the reconstructed map of CMB + kinetic SZ. In the present case, the impact of the additional constraint of vanishing thermal SZ contribution in the CMB has negligible impact on the total noise level.

Our example demonstrates that with data sets such as those of *Planck*, constraining the ILC to reject the thermal SZ effect makes it possible to avoid contaminating the CMB with SZ, with very little impact on the overall level of noise in the reconstructed CMB. This statement, however, does not hold for any possible experiment.

[2] http://www.apc.univ-paris7.fr/APC_CS/Recherche/Adamis/PSM/psky-en.php

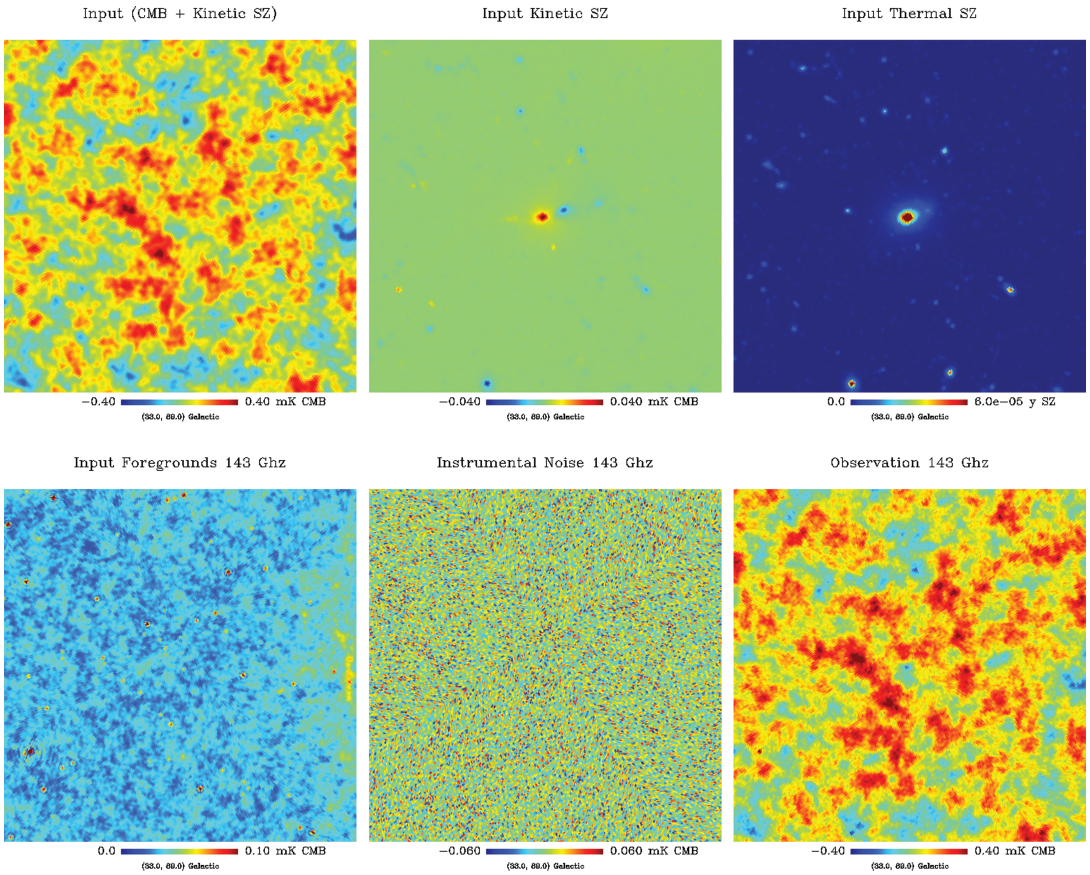

Figure 1. Simulated observations. A 12.°5 × 12.°5 patch of the simulated sky located at high Galactic latitude, around Galactic coordinates of $(l, b) = (33°, 89°)$. From top left to bottom right: CMB (including kinetic SZ), kinetic SZ, thermal SZ, other foregrounds (at 143 GHz), Noise of the 143 GHz channel. Total observed emission (including noise) at 143 GHz.

In the case of observations with more noise and less frequency channels, it may well be that constraining the ILC would actually result in significantly increased noise level, for negligible gain on the contamination by SZ.

2.7.3 ILC results: the SZ effect

Similarly, we show in Fig. 3 the reconstruction of thermal SZ effect by a standard ILC in that same area of the sky. Clusters are clearly visible, which confirms the sensitivity of *Planck* for detecting galaxy clusters and doing SZ science. It is clear that the very specific SZ emission law, with negative signal below 217 GHz and positive signal at higher frequencies, helps to separate it from other emissions effectively.

We compare the performance of the Standard ILC result (shown in Fig. 3), and a constrained ILC reconstruction (not shown), where the solution is constrained to perfectly reject components with the same colour as that of CMB anisotropies (i.e. both the CMB and the kinetic SZ). The result of the constrained ILC is not displayed since it is visually indistinguishable from the standard ILC result. Visual inspection of reconstruction errors (reconstructed thermal SZ minus true input thermal SZ at the same resolution) does not reveal any particular feature connected to any astrophysical component, in either reconstructed SZ map.

Hence, in the case of the reconstruction of the thermal SZ, the constrained ILC result is very similar to the standard one. The main reason for this lack of qualitative difference between the two filters is simple: as the CMB is seen by all channels with very good signal-to-noise ratio, the standard ILC always adjusts the ILC weights to null-out the CMB (or nearly so). Little is gained by imposing this constraint explicitly a priori.

3 CONCLUSION

In this article we have developed a *constrained ILC* method, and have shown how it can be used to reconstruct the CMB and the thermal SZ component with vanishing contamination of one by the other. We have applied the filters to simulations of *Planck*

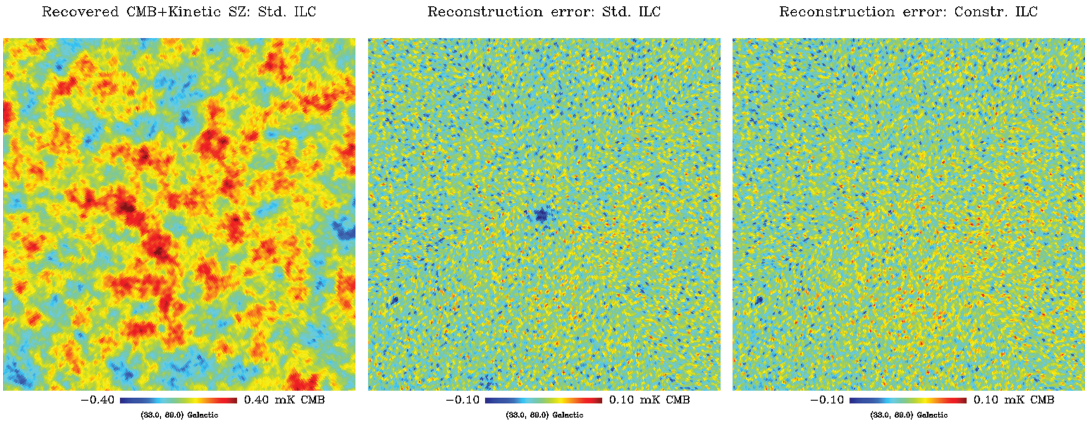

Figure 2. CMB extraction. Left-hand panel: the CMB reconstructed by standard ILC from simulated *Planck* observations (visualization of the small patch of Fig. 1). Middle panel: a detailed examination of the reconstruction error (recovered CMB minus input CMB, including the kSZ) reveals negative patches towards the direction of galaxy clusters. This is due to the leakage of thermal SZ into the reconstructed CMB. Right-hand panel: a constrained ILC guarantees the absence of contaminating tSZ in the reconstructed map, with minimal impact on the total error variance.

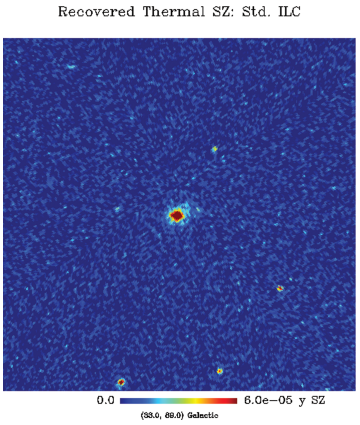

Figure 3. Thermal SZ standard ILC reconstruction centred around Galactic coordinates of $(l, b) = (33^\circ, 89^\circ)$ (5 arcmin resolution).

observations, and have shown that they permit to reconstruct both a CMB and a thermal SZ map with excellent performance.

ACKNOWLEDGEMENTS

Some of the results in this paper have been derived using the HEALPix package (Górski et al. 2005). We acknowledge the use of the PSM, developed by the Component Separation Working Group (WG2) of the *Planck* Collaboration.

REFERENCES

Aghanim N., Górski K. M., Puget J., 2001, A&A, 374, 1
Aghanim N., Hansen S. H., Pastor S., Semikoz D. V., 2003, J. Cosmol. Astro-Part. Phys., 5, 7
Barreiro R. B., 2009, in Martinez V. J., Saar E., Gonzales E. M., Pons-Borderia M. J., eds, Lecture Notes in Physics. Data Analysis in Cosmology, Vol. 665. Springer Verlag, Berlin, p. 207
Bennett C. L. et al., 2003, ApJS, 148, 97
Betoule M., Pierpaoli E., Delabrouille J., Le Jeune M., Cardoso J., 2009, A&A, 503, 691
Birkinshaw M., 1999, Phys. Rep., 310, 97
Bobin J., Moudden Y., Starck J., Fadili J., Aghanim N., 2008, Statistical Methodol., 5, 307
Bonaldi A., Bedini L., Salerno E., Baccigalupi C., de Zotti G., 2006, MNRAS, 373, 271
Bouchet F. R., Gispert R., 1999, New Astron., 4, 443
Cardoso J.-F., 1998, Proc. IEEE, 9, 2009
Cardoso J.-F., Le Jeune M., Delabrouille J., Betoule M., Patanchon G., 2008, IEEE J. Selected Topics Signal Processing, 2, 735
Carlstrom J. E., Holder G. P., Reese E. D., 2002, ARA&A, 40, 643
Cooray A., Hu W., Tegmark M., 2000, ApJ, 540, 1
Delabrouille J., Cardoso J., 2009, in Martinez V. J., Saar E., Gonzales E. M., Pons-Borderia M. J., eds, Lecture Notes in Physics, Vol. 665. Springer-Verlag, Berlin, p. 159
Delabrouille J., Cardoso J., Patanchon G., 2003, MNRAS, 346, 1089
Delabrouille J., Patanchon G., Audit E., 2002, MNRAS, 330, 807
Delabrouille J., Cardoso J., Le Jeune M., Betoule M., Fay G., Guilloux F., 2009, A&A, 493, 835
Dick J., Remazeilles M., Delabrouille J., 2010, MNRAS, 401, 1602
Eriksen H. K., Banday A. J., Górski K. M., Lilje P. B., 2004, ApJ, 612, 633
Ferrière K. M., 2001, Rev. Modern Phys., 73, 1031
Górski K. M., Hivon E., Banday A. J., Wandelt B. D., Hansen F. K., Reinecke M., Bartelmann M., 2005, ApJ, 622, 759
Hinshaw G. et al., 2009, ApJS, 180, 225
Hobson M. P., Jones A. W., Lasenby A. N., Bouchet F. R., 1998, MNRAS, 300, 1
Hurier G., Hildebrandt S. R., Macias-Perez J. F., 2010, (arXiv:1007.1149v2)
Hyvarinen A., 1999, IEEE Trans. Neural Networks, 10, 626
Kim J., Naselsky P., Christensen P. R., 2008, Phys. Rev. D, 77, 103002
Lamarre J.-M. et al., 2000, Astrophys. Lett. Commun., 37, 161
Lamarre J.-M. et al., 2003, New Astron. Rev., 47, 1017
Leach S. M. et al., 2008, A&A, 491, 597
Maino D. et al., 2002, MNRAS, 334, 53
Park C.-G., Park C., Gott J. R. I., 2007, ApJ, 660, 959

Sunyaev R. A., Zeldovich Y. B., 1972, Comments Astrophys. Space Phys., 4, 173
Taburet N., Aghanim N., Douspis M., Langer M., 2009, MNRAS, 392, 1153
Tauber J. A., 2004, Adv. Space Res., 34, 491
Tegmark M., 1997, ApJ, 480, L87
Tegmark M., Efstathiou G., 1996, MNRAS, 281, 1297
Tegmark M., de Oliveira-Costa A., Hamilton A. J., 2003, Phys. Rev. D, 68, 123523
Veneziani M. et al., 2009, ApJ, 702, 61

This paper has been typeset from a TEX/LATEX file prepared by the author.

Mon. Not. R. Astron. Soc. **346,** 1089–1102 (2003)

Multidetector multicomponent spectral matching and applications for cosmic microwave background data analysis

J. Delabrouille,[1]★ J.-F. Cardoso[2] and G. Patanchon[1]

[1]*PCC – Collège de France, 11, place Marcelin Berthelot, F-75231 Paris, France*
[2]*CNRS/ENST – 46, rue Barrault, 75634 Paris, France*

Accepted 2003 August 1. Received 2003 July 24; in original form 2002 December 12

ABSTRACT

We present a new method for analysing multidetector maps containing several astrophysical components. Our method, based on matching the data to a model in the spectral domain, permits us to estimate jointly the spatial power spectra of the components and of the noise, as well as their mixing coefficients. It is of particular relevance for analysis of millimetre-wave maps of cosmic microwave background (CMB) anisotropies.

Key words: methods: data analysis – cosmic microwave background – cosmology: observations.

1 INTRODUCTION

Mapping sky emissions at millimetre wavelengths, and in particular cosmic microwave background (CMB) anisotropies, is one of the main objectives of ongoing observational effort in millimetre-wave astronomy. Sensitive balloon-borne and space-borne missions such as *Archeops* (Benoît et al. 2002), *BOOMERanG* (de Bernardis et al. 2000), *MAXIMA* (Hanany et al. 2000) and *WMAP* (Bennett et al. 1997) are currently yielding a large quantity of multidetector and multifrequency measurements. Within a few years, the *Planck* mission (Lamarre et al. 2000; Bersanelli & Mandolesi 2000), to be launched by ESA in 2007, will observe the full sky with ∼100 detectors distributed in nine frequency bands ranging from 30 to 850 GHz. The main objective of these observations is the determination of the spatial power spectrum of CMB anisotropies. A secondary objective is identifying and mapping the emission from all contributing astrophysical processes.

The availability of several detectors operating in several bands makes it possible to devise new powerful data processing schemes. In particular, by combining data from several detectors, it is possible to substantially improve the signal-to-noise ratio (by weighted averaging) and to separate several foreground components (possibly of astrophysical interest in their own right) from the CMB by component separation methods. Component separation, however, typically requires good knowledge of the transfer function connecting a multicomponent sky to multidetector maps.

This paper proposes spectral matching as a new approach to processing multidetector, multicomponent (MDMC) data, in which all the information needed to estimate the spatial power spectra of components *and/or* to separate them is sought in the data structure itself. The method works with or without prior detector calibration and gives access to spatial power spectra in a straightforward way; it is statistically efficient (being a maximum likelihood technique) and computationally efficient (working with a small set of statistics rather than with original maps).

This paper is organized as follows. The idea of spectral estimation via multidetector multicomponent spectral matching is introduced in Section 2. Section 3 describes the technique in more detail, connects it to a maximum likelihood method, and discusses specific implementations. Section 4 is devoted to evaluating the performance of the method on synthetic *Planck* HFI observations. We discuss the method and some possible extensions in Section 5.

2 THE MULTIDETECTOR MULTICOMPONENT FRAMEWORK

Multidetector CMB measurements can be modelled as resulting from the superposition of multiple components. Statistically efficient data processing should coherently exploit this MDMC structure.

2.1 Data model

The sky emission at millimetre wavelengths is well modelled at first order by a linear superposition of the emissions of a few processes: CMB anisotropies, thermal dust emission, thermal Sunyaev–Zel'dovich (SZ) effect, synchrotron emission, etc. The observation of the sky with detector d is then a noisy linear mixture of N_c components:

$$y_d(\theta,\phi) = \sum_{j=1}^{N_c} A_{dj} s_j(\theta,\phi) + n_d(\theta,\phi), \quad (1)$$

where s_j is the emission template for the jth astrophysical process, hereafter referred to as a *source* or a *component*. The coefficients A_{dj} reflect emission laws and detector properties while n_d accounts

★E-mail: delabrouille@cdf.in2p3.fr

2003MNRAS.346.1089D

for noise. For simplicity, we neglect for the moment beam effects, postponing their discussion to Section 5.

Quantities of prime interest are spatial power spectra. For the jth component, at frequency ℓ, this is

$$C_j(\ell) = \langle\, |\, s_j(\ell)\,|^2 \rangle, \tag{2}$$

where $\langle\cdot\rangle$ denotes the expectation operator and ℓ indexes either a Fourier mode or an (ℓ, m) mode.

In practice, power spectra are estimated by averages over bins

$$C_j(q) = \frac{1}{n_q} \sum_{\ell \in \mathcal{D}_q} C_j(\ell), \tag{3}$$

where $q = 1, \ldots, Q$ is the spectral bin index, $\mathcal{D}_q$ is the set of frequencies contributing to bin q and n_q is the number of such frequencies.[1] Typical bins can be bands $\ell_{\min} \leqslant \ell < \ell_{\max}$ extending over a range of one to tens of ℓ values.

Multidetector power spectrum. Since we focus on jointly processing the maps from all detectors, it is convenient to stack $y_1, \ldots, y_{N_d}$ into a single $N_d \times 1$ vector Y. Then the set of equation (1) for all N_d detectors is more compactly written in matrix vector form as

$$\boldsymbol{Y}(\theta, \phi) = \mathbf{A}\boldsymbol{S}(\theta, \phi) + \boldsymbol{N}(\theta, \phi) \tag{4}$$

with a so called $N_d \times N_c$ 'mixing matrix' $\mathbf{A}$. In Fourier space, this equation reads

$$\boldsymbol{Y}(\ell) = \mathbf{A}\boldsymbol{S}(\ell) + \boldsymbol{N}(\ell). \tag{5}$$

The power spectrum of process $\boldsymbol{Y}$ is represented by the $N_d \times N_d$ spectral density matrix $\langle \boldsymbol{Y}(\ell)\boldsymbol{Y}(\ell)^\dagger \rangle$ where † denotes transpose conjugation. Its average over bins

$$\mathbf{R}_Y(q) = \frac{1}{n_q} \sum_{\ell \in \mathcal{D}_q} \langle \boldsymbol{Y}(\ell)\boldsymbol{Y}(\ell)^\dagger \rangle \quad (q = 1, \ldots, Q) \tag{6}$$

will also be referred to as a spectral density matrix. According to the linear model (1), it is structured as

$$\mathbf{R}_Y(q) = \mathbf{A}\mathbf{R}_S(q)\mathbf{A}^\dagger + \mathbf{R}_N(q) \quad (q = 1, \ldots, Q) \tag{7}$$

with $\mathbf{R}_S(q)$ and $\mathbf{R}_N(q)$ defined similarly to $\mathbf{R}_Y(q)$. Statistical independence between components implies

$$\mathbf{R}_S(q) = \mathrm{diag}(C_1(q), \ldots, C_{N_c}(q)). \tag{8}$$

For the sake of exposition, we assume that the noise is uncorrelated, both across detectors and in space, so that the noise structure is described by N_d parameters:

$$\mathbf{R}_N(q) = \mathrm{diag}\left(\sigma_1^2, \ldots, \sigma_{N_d}^2\right). \tag{9}$$

Parameter extraction by spectral matching. The MDMC model, as defined by equations (7–9), depends on a set $\{\mathbf{R}_Y(q)\}$ of Q spectral density matrices, which in turn depend on $\{\mathbf{A},\ C_j(q),\ \sigma_d^2)\}$, amounting to $N_d \times N_c + Q \times N_c + N_d$ scalar parameters. However, the number of independent correlations in Q spectral density matrices is $Q \times N_d(N_d + 1)/2$ (since each matrix is real symmetric). This latter number is (in general) higher than the former.

With this in mind, our proposal can be summarized as 'MDMC spectral matching', meaning: *estimate all (or parts of) the parameters* $\theta = \{\mathbf{A}, C_j(q), \sigma_d^2)\}$ *by finding the best match between* $\{\mathbf{R}_Y(q)\}$, *as specified by (7–9), and a set of* Q *'empirical spectral density matrices'* $\{\widehat{\mathbf{R}}_Y(q)\}$:

$$\widehat{\mathbf{R}}_Y(q) = \frac{1}{n_q} \sum_{\ell \in \mathcal{D}_q} \mathbf{Y}(\ell)\mathbf{Y}(\ell)^\dagger \quad (q = 1, \ldots, Q) \tag{10}$$

which are the natural non-parametric estimates of the corresponding $\mathbf{R}_Y(q)$.

2.2 Maximum likelihood spectral matching

Any reasonable measure of mismatch between the empirical density matrices $\{\widehat{\mathbf{R}}_Y(q)\}$ and their model counterparts $\{\widehat{\mathbf{R}}_Y(q;\theta)\}$ could be used to compute estimates of a θ parameter. In order to get good estimates, however, one should use a mismatch criterion derived from statistical principles. Such a derivation can be based on the statistical distribution of the Fourier coefficients of a stationary process which are (at least asymptotically in the data size) normally distributed, uncorrelated, with a variance proportional to the power spectrum (Whittle approximation, see Appendix B). Thus, the likelihood of the observations can be readily expressed in terms of spectral density matrices. Appendix B outlines how the (negative) log likelihood of the data then is (up to irrelevant factors and terms) equal to

$$\phi(\theta) = \sum_{q=1}^{Q} n_q D(\widehat{\mathbf{R}}_Y(q), \mathbf{R}_Y(q;\theta)) \tag{11}$$

where $D(\cdot, \cdot)$ is a measure of divergence between two positive $n \times n$ matrices defined by

$$D(\mathbf{R}_1, \mathbf{R}_2) = \mathrm{tr}\left(\mathbf{R}_1\mathbf{R}_2^{-1}\right) - \log\det(\mathbf{R}_1\mathbf{R}_2^{-1}) - n. \tag{12}$$

It can be seen[2] that $D(\mathbf{R}_1, \mathbf{R}_2) \geqslant 0$ with equality if and only if $\mathbf{R}_1 = \mathbf{R}_2$. Thus *spectral matching corresponds to maximum likelihood estimation in a stationary model*. The minimizer of $\phi(\theta)$ is then a maximum likelihood estimate, with the good statistical properties associated with it.

Only in an asymptotic framework can maximum likelihood procedures be proved to reach minimum estimation variance. This means that criteria which are equivalent to (11) are expected to have the same statistical quality as (11). In particular, criterion (11) can be replaced by a quadratic approximation: when each $\widehat{\mathbf{R}}_Y(q)$ is close to $\mathbf{R}_Y(q;\theta)$, a second-order expansion of $D(\widehat{\mathbf{R}}_Y, \mathbf{R}_Y)$ yields

$$D_2(\widehat{\mathbf{R}}_Y, \mathbf{R}_Y) = \mathrm{tr}\left(\widehat{\mathbf{R}}_Y^{-1}(\widehat{\mathbf{R}}_Y - \mathbf{R}_Y)\widehat{\mathbf{R}}_Y^{-1}(\widehat{\mathbf{R}}_Y - \mathbf{R}_Y)\right). \tag{13}$$

The resulting quadratic criterion is of particular interest when the unknown parameters enter *linearly* in $\mathbf{R}_Y(q;\theta)$ (for instance when $\mathbf{A}$ is known and θ only contains the binned power spectra of the components) since then criterion minimization becomes trivial. In this paper, however, we stick to using (11)–(12). Even though the divergence (12) may, in general, seem more difficult to deal with than its quadratic approximation (13), it actually lends itself to simple optimization via the EM algorithm (see Section 3.1) thanks to its connection to the likelihood.

2.3 Comments

Some preliminary comments about the MDMC spectral matching approach are in order.

[1] It is customary for CMB data analysis to weight the terms in sum 3 by $\ell(\ell + 1)$. For the sake of exposition, we use a flat weighting here (see Section 5 for weighted sums).

[2] For instance by expressing $D(\mathbf{R}_1, \mathbf{R}_2)$ in terms of the eigenvalues of $\mathbf{R}_2^{-1/2}\mathbf{R}_1\mathbf{R}_2^{-1/2}$.

Parameter choice. There is a lot of flexibility in the choice of parameters over which to minimize the spectral mismatch. By selecting different sets of parameters, different goals can be achieved. For instance, we may assume that matrix $\mathbf{A}$ and the noise spectrum $\mathbf{R}_N(q)$ are known so that the mismatch is minimized only with respect to the binned spectra $C_i(q)$ of all components: the method appears as a spectral estimation technique *which does not require the explicit separation of the observed maps into component maps*. Another important example, as illustrated in Section 4, consists of including matrix $\mathbf{A}$ among the free parameters. Then, the method works as the so-called 'blind techniques', and permits a determination of the emission law of the components, or the cross-calibration of detectors.

Degeneracies. A key issue in spectral matching is whether or not matrix $\mathbf{A}$ can be uniquely determined from the data only. When all parameters $\{\mathbf{A}, C_j(q), \sigma_d^2\}$ are allowed to vary, there are at least two obvious degeneracies. First, the *ordering* (or numbering) of the components in the model is immaterial: matrix $\mathbf{A}$ cannot be recovered to better than a column permutation on the sole basis of a spectral match. Second, a scalar factor can be exchanged, for each component j, between the jth column of $\mathbf{A}$ and $C_j(q)$. These scale factors cannot be determined from the data themselves.

Another trivial case of indetermination is when two columns of $\mathbf{A}$ corresponding to physically distinct components are proportional. In this case, the sum of the two appears in the model as one single component. The identifiability of the other components is not affected.

A more severe degeneracy occurs if any two components have proportional spectra. In this case, as is known from the noiseless case (Pham & Garat 1997), only the space spanned by the corresponding columns of $\mathbf{A}$ can be determined in a spectral match with $\mathbf{A}$ as a free parameter. In this case, however, the identifiability of the other components is unchanged, with no impact on the accuracy of component separation with a Wiener method (Section 5). The key point to remember is that spectral matching requires spectral diversity to separate components associated with unknown columns of $\mathbf{A}$.

Maximum likelihood. Section 2.2 explains why 'spectral matching' corresponds to maximum likelihood estimation. This occurs in a Gaussian stationary model with smooth (actually: constant over bins) spectra. In such a model the likelihood of the observations *is* a measure (11) of spectral matching. Since the likelihood then depends on the data *only* via the empirical spectral density matrices, the massive data reduction gained from replacing the observations by a (usually) much smaller set of statistics (the empirical spectral density matrices $\widehat{\mathbf{R}}_Y(q)$) is obtained without information loss.

Comparison with component separation. It is interesting to compare spectral matching with techniques based on prior explicit component separation.

Producing a CMB map as free as possible from foreground and noise contamination is the objective of the component separation step, in which maps obtained at different frequencies are combined to maximize the signal to noise ratio (where noise includes also foreground contamination).

The usual approach for taking advantage of multidetector measurements can be summarized as follows: first, form estimates $\widehat{s}_j(\ell)$ of component maps $s_j(\ell)$ (via component separation); secondly, estimate the spectrum of each component j by averaging within bins:

$$\widehat{C}_j(q) = \frac{1}{n_q} \sum_{\ell \in \mathcal{D}_q} |\widehat{s}_j(\ell)|^2, \tag{14}$$

with, possibly, some post-processing of the power spectrum estimates.

This method suffers from two difficulties. First, the best component separation methods typically require the prior knowledge of the statistical properties of the components (including the CMB power spectrum) and of the noise. Secondly, recovered maps contain residuals (including noise) which contribute to the total power, biasing the spectrum estimated on the map, unless the power spectrum of these residuals can be estimated accurately and subtracted.

In contrast our approach takes the reverse path. The first step is an estimation of the spectrum for the multidetector map (which takes the form of a sequence of spectral density matrices). This first step preserves all the joint correlation structure between maps. In essence, the second step (spectral matching) amounts to resolving the joint power spectrum into the spectra of individual components.

Hence, instead of first separating component *maps* and then computing power spectra, we first compute the multivariate power spectrum and then separate component *spectra*.

Applicability of spectral matching. The real sky emission is known to depart from the simple ideal model used for the development of the spectral matching method. It is important, then, to discuss how our method depends on some assumptions about the structure of the data.

In particular, the spectral adjustment is made under the following assumptions:

(i) the mixing matrix is position-independent,
(ii) the components are statistically independent,
(iii) noise is uncorrelated across detectors,
(iv) the components and the noise are normally distributed,
(v) the components and the noise are stationary,
(vi) the components and the noise are statistically isotropic,
(vii) their spectra are smooth functions of ℓ.

Assumptions i, ii, and iii are critical because they determine the structure (7) of the spectral matrices. Thus, matching estimates are no longer consistent if these assumptions are violated and for strong departures from the model, the spectral matching may fail completely. However, it is possible to refine the model as needed, for instance by including some correlation terms between components, by dividing the sky in patches where the mixing matrix may be assumed to be constant, by discarding regions of the sky where the emission is known to depart from the model (galactic regions of intense complex emission, strong point sources). The existence and applicability of such refined solutions depend on the exact sky emission model. If no structure can be assumed (for instance if the noise correlation matrix is completely arbitrary and unknown) there is not enough information to constrain the parameters uniquely.

Assumptions iv, v, vi and vii, in contrast, are not critical because they do not change the basic structure (7) of the spectral matrices and do not prevent the sample covariance matrices to converge to such a structure. Hence, violation of these assumptions only results in a loss of statistical efficiency with respect to techniques based on complex models. The Gaussianity assumption is not a requirement of the method because the sample covariance matrices (10) still have an expectation given by (7). If components or the noise are not Gaussian distributed, then some information is lost by only using second-order statistics (loss of efficiency), but consistency is preserved. Stationarity, isotropy, and spectral smoothness allow us to characterize in a meaningful way the distribution of a given component j via a simple smoothed spectrum $C_j(q)$. If they are violated then $C_j(q)$ may not have a meaningful statistical meaning; it is still

2003MNRAS.346.1089D

defined none the less and spectral matching will just produce an estimate of it. Again, the key point is that, regardless of the details of the distribution of $S_i(\ell)$, one can expect $\langle S_i(\ell)\bar{S}_j(\ell)\rangle = 0$ for $i \neq j$, that is, statistical independence is the true underlying inference engine. We also note that in the case of anisotropic spectra, it is always possible to use spectral domains $\mathcal{D}_q$ which are not ring-shaped.

Finally, spectral matching does not bias in any way the level of non-Gaussianity present in the CMB maps. Non Gaussian signals, even at low level, appear as an additional contribution to the CMB spectrum. They will show in maps as well, in a way depending on the method adopted to solve the linear system after the spectral matching step, once mixing coefficients and power spectra are known.

3 MDMC SPECTRAL MATCHING IN PRACTICE

The implementation of MDMC spectral matching will now be described in more detail; Section 3.1 describes the EM algorithm for its optimization; Section 3.2 describes a complementary technique for fast convergence.

3.1 The EM algorithm

The expectation maximization (EM) algorithm (Dempster, Laird & Rubin 1977) is a well-known technique for maximizing the likelihood of statistical models which include 'latent' or 'unobserved' variables. It is well suited to our purpose by taking the components as the latent variables. The EM algorithm is iterative: starting from an initial value of the parameters, it performs a sequence of parameter updates called 'EM steps'. Each step is guaranteed to increase the likelihood of the parameters.

The spectral matching criterion (11) actually being a likelihood function in disguise, the EM algorithm can be used for its minimization. Each EM step is guaranteed to improve the spectral fit by decreasing $\phi(\theta)$.

We consider the regular EM algorithm, based on the Gaussian likelihood described in Appendix B and taking as 'latent variables' the spectral modes $\mathbf{Y}(\ell)$. The form of the EM steps immediately follows, as sketched in Appendix C, and is summarized by the pseudo-code given in Table 1.

Table 1. The EM algorithm for minimizing the MDMC spectral mismatch $\phi(\theta)$ with respect to $\theta = \{\mathbf{A}, C_j(q), \sigma_d^2\}$.

Require: Spectral density matrices $\widehat{\mathbf{R}}_Y(1), \ldots, \widehat{\mathbf{R}}_Y(Q)$
Require: Initial value of $\theta = \{\mathbf{A}, C_j(q), \sigma_d^2\}$.
  Set $\widetilde{\mathbf{R}}_{yy}(q) = \widehat{\mathbf{R}}_Y(q)$ and $\widetilde{\mathbf{R}}_{yy} = \sum_q \frac{n_q}{n}\widetilde{\mathbf{R}}_{yy}(q)$.
  repeat
    {——— E-step. Compute conditional statistics:}
    Set $\mathbf{R}_S(q) = \mathrm{diag}(C_j(q))$ and $\mathbf{R}_N = \mathrm{diag}(\sigma_d^2)$
    for $q = 1$ to Q **do**
      $\mathbf{G}(q) = (\mathbf{A}^\dagger \mathbf{R}_N^{-1}\mathbf{A} + \mathbf{R}_S(q)^{-1})^{-1}$
      $\mathbf{W}(q) = \mathbf{G}(q)\mathbf{A}^\dagger\mathbf{R}_N^{-1}$
      $\widetilde{\mathbf{R}}_{ys}(q) = \mathbf{W}(q)\widehat{\mathbf{R}}_Y(q)\mathbf{W}(q)^\dagger + \mathbf{G}(q)$
      $\widetilde{\mathbf{R}}_{sy}(q) = \mathbf{W}(q)\widehat{\mathbf{R}}_Y(q)$
    end for
    $\widetilde{\mathbf{R}}_{ss} = \sum_{q=1}^{Q} \frac{n_q}{n}\widetilde{\mathbf{R}}_{ss}(q)$
    $\widetilde{\mathbf{R}}_{ys} = \sum_{q=1}^{Q} \frac{n_q}{n}\widetilde{\mathbf{R}}_{ys}(q)$
    {——— M-step. Update the parameters:}
    $\mathbf{A} = \widetilde{\mathbf{R}}_{ys}\widetilde{\mathbf{R}}_{ss}^{-1}$
    $C_i(q) = \left[\widetilde{\mathbf{R}}_{ss}(q)\right]_{ii}$
    $\sigma_d^2 = \left[\widetilde{\mathbf{R}}_{yy} - \widetilde{\mathbf{R}}_{sy}^\dagger\widetilde{\mathbf{R}}_{ss}^{-1}\widetilde{\mathbf{R}}_{sy}\right]_{dd}$
    Rescale the parameters (see text).
  until a convergence criterion is satisfied

It is worth mentioning that EM steps take such a regular structure when the parameters are $\theta = \{\mathbf{A}, C_j(q), \sigma_d^2\}$. A slightly different form would result from a more constrained parameter set.

Recall that, as previously noted, there is a scale indetermination on each component's spectrum when $\theta = \{\mathbf{A}, C_j(q), \sigma_d^2\}$. We have found that this inherent indetermination must be explicitly fixed in order for EM to converge (this is the rescaling step in the last line of the pseudo-code). Our strategy is, after each EM step, to fix the norm of each column of $\mathbf{A}$ to unity and to adjust the corresponding power spectra accordingly. This is an arbitrary choice which happens to work well in practice.

The algorithm is initialized as follows. We take $\mathbf{R}_n = \mathrm{diag}(\widehat{\mathbf{R}}_Y)$ where $\widehat{\mathbf{R}}_Y = \sum_q (n_q/n)\widehat{\mathbf{R}}_Y(q)$. This is a gross overestimation since it amounts to assume no signal and only noise. The initial value of $\mathbf{A}$ is obtained by using the N_c dominant eigenvectors of $\widehat{\mathbf{R}}_Y$ as the N_c columns of $\mathbf{A}$. Again, this is nothing like any real *estimate* of $\mathbf{A}$, but rather a vague guess in 'the right direction'. Finally, the spectra $P_i(q)$ are taken as to be the diagonal entries of $\mathbf{A}^\dagger\widehat{\mathbf{A}}$. This ad hoc initialization procedure seems satisfactory. Note that it is a common rule of thumb to initialize EM with overestimated noise power.

Regarding the stopping rule, there is little point in devising a sophisticated stopping strategy (in practice, the algorithm is run for a pre-specified number of steps based on a few preliminary experiments with the data) because EM is only used 'halfway': its output is further fed to a specialized optimization algorithm (described at next section).

3.2 Non-linear optimization

When applied to our data, the EM algorithm demonstrates rapid convergence at first, and then enters a second phase of slower convergence. This is due to the fact that some parameters (e.g. subdominant power spectra in some spectral domains) have a very small effect on the criterion. In order to reach the true minimum of $\phi(\theta)$, it appears necessary to complement EM with another minimization technique. The strategy is to use the straightforward EM algorithm to quickly get close to the minimum of $\phi(\theta)$ and then to complete the minimization using a dedicated minimization algorithm. This complementary algorithm can use a simple design thanks to the good starting point provided by EM.

The spectral mismatch criterion (11) can, in theory, be minimized by any optimization algorithm. However, the same effect that slows down EM in its final steps also makes the minimization of the mismatch criterion (11) difficult for *any* algorithm. In particular, simple gradient algorithms are unacceptably slow. Actually, we found that even conjugate gradient techniques cannot overcome this problem and had to resort to a quasi-Newton method. We have used the classic BFGS (Broyden–Fletcher–Goldfarb–Shapiro) algorithm (Luenberger 1973). This technique minimizes an objective function by successive one-dimensional minimization (line searches). At each step, the direction for the line search is the gradient 'rectified' by the inverse of Hessian matrix. The BFGS technique is a rule to update an estimate of the inverse Hessian matrix at low computational cost.

4 TESTING AND PERFORMANCE

We now turn to illustrating the applications and performance of our multidetector multicomponent spectral-matching method on a simple set of synthetic observations: three-component noisy linear mixtures featuring contributions from CMB anisotropies, dust

emission, and SZ thermal emission. Bias and statistical uncertainties are investigated by a Monte Carlo technique.

Five implementations of the method for different applications will be discussed:

(i) a multicomponent spatial power spectrum estimation assuming the mixing matrix is known,

(ii) a blind approach in which spatial power spectra, noise levels, and the emission laws of components are jointly estimated on the data,

(iii) a semi-blind approach where CMB and SZ emission laws are assumed to be known, and the emission law of the dust component (in addition to spatial power spectra and noise levels for all components) is estimated from the data,

(iv) an application for detector cross-calibration,

(v) a Wiener-filter component separation using parameters estimated via blind spectral matching.

Finite beam effects are neglected in the present work, although they are not a fundamental limitation for our method (see Section 5). For definiteness, we also assume here that the noise is white, although this assumption can also be relaxed if needed.

4.1 Simulated data

Synthetic observations in six frequency bands identical to those of the *Planck* HFI are generated on 300×300 pixel maps corresponding to a $12.^{\circ}5 \times 12.^{\circ}5$ field located at high galactic latitude. For each mixture realization, synthetic components and noise are obtained as follows.

(i) The CMB component is a *COBE*-normalized, randomly generated realization of CMB anisotropies obtained using the spatial power spectrum C_ℓ predicted by the CMBFAST software (Zaldarriaga & Seljak 2000) with $H_0 = 65$ km s^{-1} Mpc^{-1}, $\Omega_{\rm m} = 0.3$, $\Omega_{\rm b} = 0.045$, $\Lambda = 0.7$.

(ii) The galactic dust emission template is obtained from the 100-μm *IRAS* data in the sky region located around $\alpha = 204^{\circ}$ and $\delta = 11^{\circ}$. Bright stars are removed using a point source extracting algorithm. Residual stripes are cut out by setting to zero the contaminated Fourier coefficients. The Fourier modes suppressed in this way are randomly regenerated with a distribution obtained, for each mode, from the statistics of the other modes at the same scale in the *IRAS* map. This method preserves the (assumed) statistical azimuthal symmetry and general shape of the spatial spectrum.

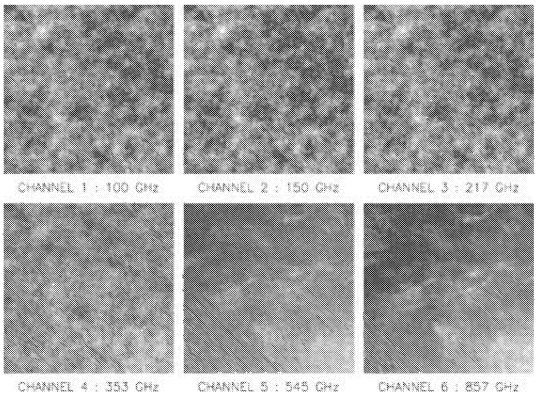

Figure 1. Simulated observations for six frequency bands. This figure can be seen in colour in the on-line version of the journal on *Synergy*.

Table 2. Fraction of the power in each of the components.

ν	100	143	217	353	545	857
CMB	0.889	0.926	0.896	0.275	0.0019	1.3×10^{-7}
dust	9×10^{-5}	6×10^{-4}	0.0082	0.215	0.687	0.938
SZ	0.0064	0.0032	2×10^{-7}	0.0044	0.00019	5.2×10^{-8}
noise	0.102	0.0727	0.108	0.536	0.320	0.0667

(iii) The thermal Sunyaev–Zel'dovich template is drawn at random from a set of 1500 SZ maps generated for this purpose using the software described in (Delabrouille, Melin & Bartlett 2002).

(iv) White noise at the level of the nominal per-channel *Planck* HFI values is added to the observations.

Synthetic observations are displayed in Fig. 1. The general common pattern which can be seen in the lowest frequency channels is simulated CMB anisotropies, whereas the pattern of emission of interstellar dust as observed with IRAS dominates our 857- and 545-GHz maps. The contribution of the SZ effect, very subdominant, is not obviously visible on these maps.

Table 2 gives, for each channel, the relative power of all components and of noise for a typical synthetic mixture (here, 'relative' means that the sum of all powers is normalized to unity). Typical input templates for the three components can be seen later (Fig. 6, left column).

4.2 Application 1: spectral estimation

The first application is the estimation of component spatial power spectra. It is assumed that the mixing matrix is known, but that the noise level for each map is not known precisely. The set of parameters to be estimated from the data then is $\theta = \{C_j(q), \sigma_d^2\}$.

Component spectra are estimated on 32 ring-shaped domains for 5000 different mixtures. The first 30 domains are equally spaced rings covering the lowest 60 per cent of the spatial frequencies ($0 < \ell/\ell_{\rm max} < 0.6$), and the remaining two cover respectively $0.6 < \ell/\ell_{\rm max} < 0.8$ and $0.8 < \ell/\ell_{\rm max} < 1$. This choice of spectral domains is adapted to the assumed azimuthal symmetry of the spectra by the choice of ring-shaped domains, and has a large number of rings in the region where the signal is strong and where information from source spectra is relevant.

The resulting estimation of the spatial power spectrum of the three components in the relevant frequency range is shown in Fig. 2. Errors on estimated spectra are obtained from the dispersion over the 5000 distinct simulated observations. For the SZ effect, the spatial power spectrum is averaged into larger bins after parameter estimation to reduce the scatter of the measurements. The figure shows that, as expected, a low-variance unbiased power spectrum is obtained for all components without explicit separation of the observations into component maps. For the CMB, the measurement is sample (cosmic) variance limited at small spatial frequencies. Such an effect does not appear on the dust spectrum estimate because we use only one dust map in the Monte Carlo simulation.

4.3 Application 2: blind parameter estimation

Let us now assume that the exact emission laws of all components are unknown. Then the full parameter set, to be estimated from the data, is $\theta = \{C_j(q), \sigma_d^2, \mathbf{A}\}$. Again, we estimate parameters on 5000 different simulated data sets. For each run, the scale freedom between mixing matrix columns and component power spectra is fixed by renormalizing to the true value of $\mathbf{A}$ at a single reference frequency

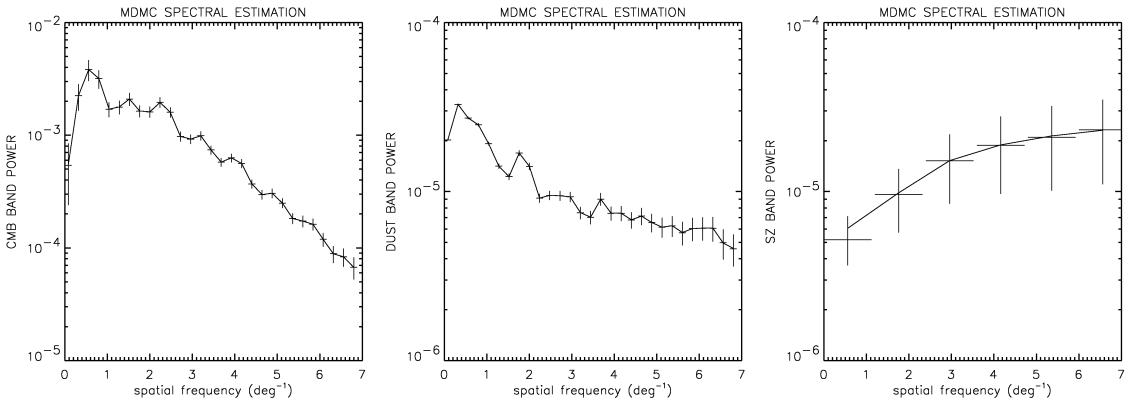

Figure 2. This figure shows the recovered spatial power spectrum $\ell^2 C_\ell$ (crosses) compared with the exact band-averaged spectra (solid lines) for CMB (left), dust (middle), and thermal SZ effect (right). These results correspond to a non-blind MDMC spectral estimation in which the mixing matrix **A** is known. Vertical bars show the 1σ errors, and horizontal bars the spatial frequency range of each bin.

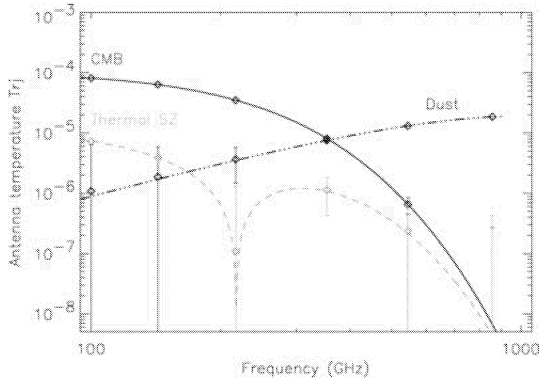

Figure 3. The figure shows the recovered emission laws of the components (diamonds) compared with the exact emission laws used in the simulations (solid lines). The errors are computed from the dispersion of the recovered values for 10 000 different synthetic mixtures.

(100 GHz for the CMB and thermal SZ effect, and 857 GHz for the dust). Error bars ($\pm 1\sigma$) for all parameters are computed from the distribution of the estimates over all simulated observations.

Fig. 3 displays recovered emission spectra (diamonds with 1σ error bars) as compared with exact emission spectra (lines). Emission laws of all components are recovered with no significant bias. The CMB emission law is recovered very accurately at all frequencies except 857 GHz. The dust emission law is recovered quite accurately at high frequencies, less accurately at frequencies where it is very subdominant. The SZ effect emission shape, subdominant at all frequencies, is recovered with larger relative error bars. Because of the renormalization, error bars for CMB and SZ vanish at 100 GHz, and the dust emission-law error bar vanishes at 857 GHz.

Spatial power spectra, in turn, are also estimated. As shown in Fig. 4, CMB and dust spatial power spectra are recovered with good accuracy and no significant bias, almost as well as for the non-blind spectral estimation. The SZ power spectrum is also significantly constrained, although error bars are significantly larger than in the non-blind spectral estimation.

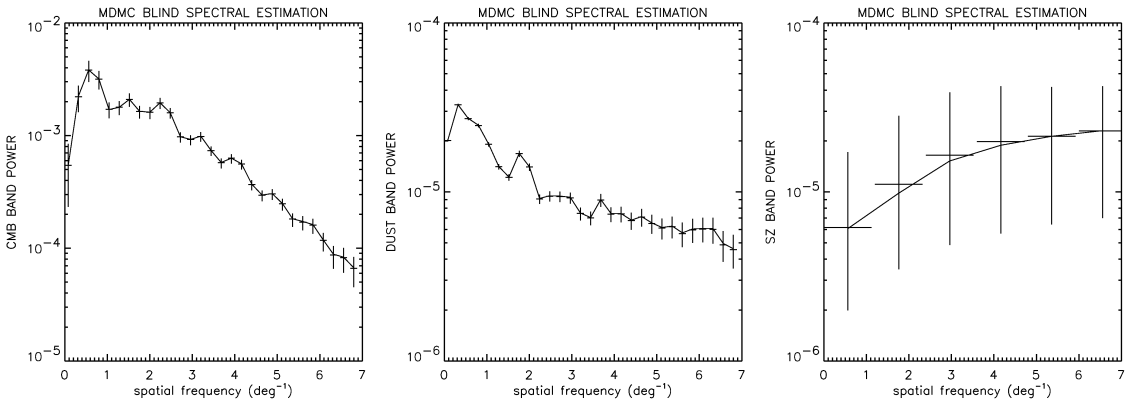

Figure 4. The figure – similar to Fig. 2 but for *blind* spectral matching – shows the recovered power spectra of the components compared to exact ones (solid lines). The errors are computed from the dispersion of the recovered values for 5000 different synthetic mixtures.

Table 3. Comparison of true and estimated noise levels (RMS). The errors are obtained from the dispersion of results obtained using 10 000 different mixtures.

Channel	100	143	217	353	545	857
RMS est. $\times 10^{-6}$	(29.1 ± 0.22)	(18.7 ± 0.13)	(12.85 ± 0.09)	(11.92 ± 0.07)	(8.98 ± 0.05)	(4.97 ± 0.06)
RMS true $\times 10^{-6}$	29.11	18.70	12.86	11.93	8.980	4.970

Table 4. Relative errors in dust emission-law estimation. In the first case, all the elements of the mixing matrix are estimated (blind approach). In the second case, the columns of the mixing matrix which corresponds to the CMB and the thermal SZ components are fixed (semi-blind approach). Although the semi-blind approach does not improve significantly the determination of the dust spectrum at 545 GHz, the improvement is very significant (factors of two to three) at other frequencies.

Channel	100	143	217	353	545	857
True dust em spectrum	0.3071	0.5902	1.2177	2.6106	4.5371	6.4288
Relative error, blind approach	6.229	2.469	0.634	0.0662	0.00790	No values
Relative error, semi-blind approach	2.623	1.056	0.285	0.0368	0.00725	No values

Finally, Table 3 shows the estimates of the noise RMS as compared to true levels. Relative errors are below 2.5 per cent for all channels.

4.4 Application 3: semi-blind parameter estimation

In our particular case, the emission laws of the CMB and of the SZ are known to almost perfect accuracy. Assume, however, that measuring the dust emission law is of particular interest. How much do we gain by forcing known emission laws to their true value, and estimating only the unknown dust emission spectrum?

We repeat the simulations described in 4.3, now fixing two columns of the mixing matrix, and estimating the third one (in addition to domain-averaged spatial spectra and noise levels). Table 4 compares quantitatively the relative errors on the resulting dust emission law. At low frequency (between 100 and 217 GHz), the accuracy of the estimation is improved by a factor of 2 to 3. At 353 GHz, the improvement is still noticeable, but at 545 GHz, where the dust emission begins to dominate, the blind and semi-blind approaches give similar errors. The use of partial prior information on the mixing matrix $\mathbf{A}$ is thus useful here to improve the estimation of the entries of $\mathbf{A}$ which contribute little relative power to the observations.

In addition to this substantial improvement in estimating the unknown 'dust column' of $\mathbf{A}$, the semi-blind approach is more efficient for estimating the SZ power spectrum than the full blind implementation. Fig. 5 shows the comparison of the quality of spectral estimation in the blind and semi-blind approaches relative to the non-blind. To the precision of our Monte Carlo tests (1–2 per cent level on error bars), the semi-blind result is as accurate for this particular mixture as the non-blind estimate, and significantly better than the blind result. As the semi-blind and the non-blind estimates give similar results, however, the actual enhancement in precision depends on details of the mixture and parametrization.

This comparison, however, shows that it is in general useful to exploit as much as possible reliable prior information. Our method is flexible enough to do so.

4.5 Application 4: detector calibration

The mixing matrix $\mathbf{A}$ depends not only on components (through emission spectra), but also on detectors (through frequency bands

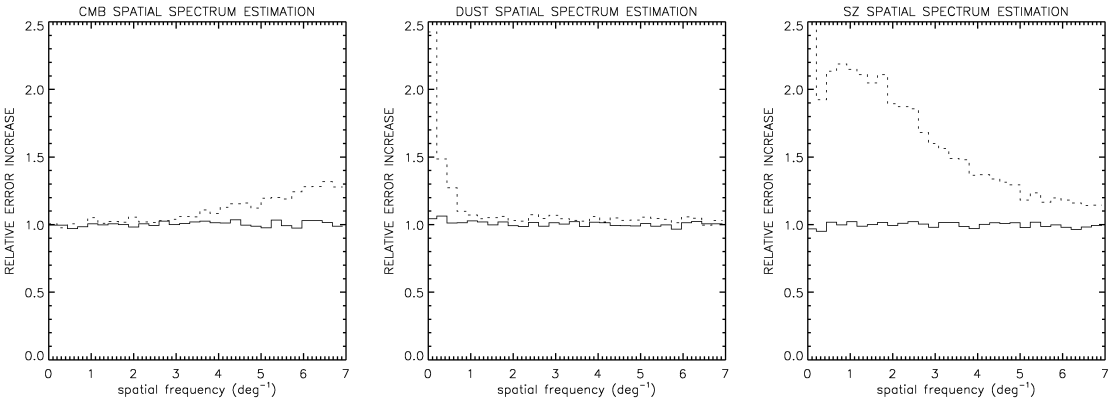

Figure 5. The figure shows the comparison of the quality of the blind and semi-blind power spectrum estimation of the components. The solid line displays the ratio between the size of the 1σ error in the semi-blind and in the non-blind spectral matching, showing that they are comparable to within simulation accuracy. In contrast, the dotted line shows the ratio between the size of the 1σ error in the blind and in the non-blind spectral matching, showing that some accuracy is lost when all components of the mixing matrix are adjusted as additional parameters.

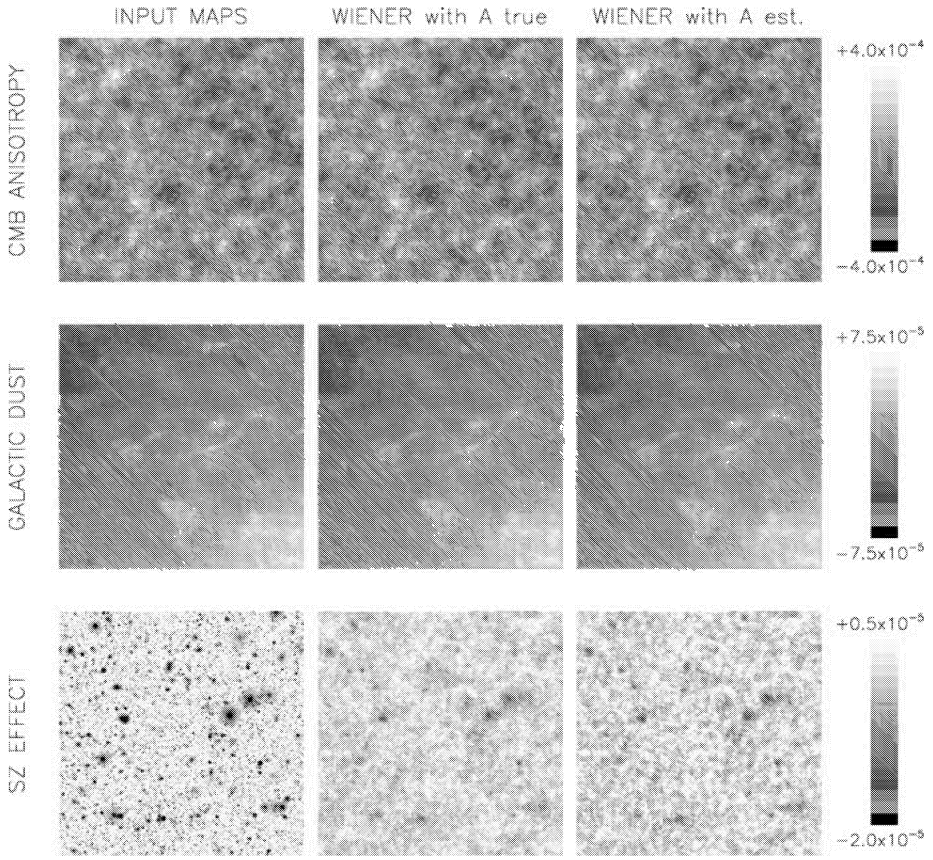

Figure 6. Left: true templates used as inputs. Middle: templates recovered using the 'true' Wiener filter. Right: templates recovered using the blind separation. This figure can be seen in colour in the on-line version of the journal on *Synergy*.

and optical efficiency). Mixing matrix coefficients A_{dj}, expressed in readout (rather than physical) units can be approximated by the product of a detector-dependent calibration coefficient α_d and an emission law $\epsilon_j(\nu)$:

$$A_{dj} \simeq \alpha_d \epsilon_j(\nu_d), \tag{15}$$

where ν_d is the central observing frequency of detector d. Used on a data set from detectors observing in the same frequency band, the estimation of $\mathbf{A}$ for any astrophysical component gives relative calibration coefficients between detectors. If in addition the emission law of at least one of the components is known (e.g. CMB anisotropies), the estimation of the mixing matrix provides a relative calibration across frequency bands. Finally, if among the components there is one with known emission spectrum and known amplitude (or known spatial power spectrum), absolute calibration can be obtained in the same way. For instance, it is not excluded that in the not-so-far future, a high-resolution experiment dedicated to a wide-field point source survey in the millimetre range can be calibrated on CMB anisotropies(!).

4.6 Application 5: component separation

The separation of astrophysical components by some kind of inversion of the linear system of equation (1) has been the object of extensive previous work. Popular linear methods are listed in Appendix **A**. In a Gaussian model, the best inversion is obtained by the Wiener filter. This filter, however, requires prior knowledge of the mixing matrix $\mathbf{A}$, component spatial power spectra, and noise power spectra. As discussed by Cardoso et al. (2002), our spectral-matching method yields all the parameters needed to implement a Wiener-based component separation *on maps*.

We compare the quality of component reconstruction using either the estimated parameter set $\theta = \{C_j(q), \sigma_d^2, \mathbf{A}\}$ or 'true' best-knowledge values.

Reconstructed maps. Fig. 6 illustrates the quality of map reconstruction by Wiener inversion. The first column displays the input components, the second column shows components recovered with the exact Wiener filter (computed from the true mixing matrix, ensemble averages of the noise, ensemble averages of CMB and SZ power spectra, and a k^{-3} fit of the spatial power spectrum of the dust template). The third column displays the components recovered by Wiener inversion using estimated parameters. In both cases, CMB and dust emissions are recovered satisfactorily, but the SZ effect – strongly peaked and hence poorly suited to processing in Fourier space – remains noisy. Visually, both methods perform about as well.

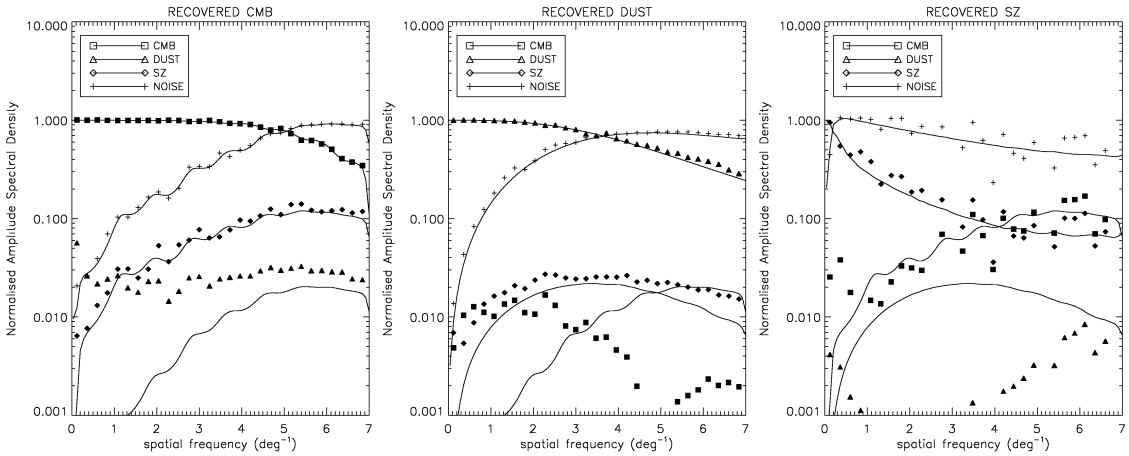

Figure 7. Contributions to the output map as a function of spatial frequency, relative to the true level of that component map. The left panel is for CMB, the middle panel for dust, and the right panel for the SZ effect. Results obtained with exact values of the mixing matrix, the spectra and noise levels are plotted as plain lines, and results obtained with the Wiener implementation using estimated parameters as diamonds.

Contamination levels. The quality of the separation can be assessed by a measure of contamination levels, i.e. how much of the other components get into a given component map after separation.

The Wiener matrix, $\mathbf{W} = [\mathbf{A}^t \mathbf{R}_N^{-1} \mathbf{A} + \mathbf{R}_S^{-1}]^{-1} \mathbf{A}^t \mathbf{R}_N^{-1}$, obtained with exact values of $\mathbf{A}$, $\mathbf{R}_N$ and $\mathbf{R}_S$, differs slightly from its estimate $\widehat{\mathbf{W}}$, computed with estimates $\widehat{\mathbf{A}}$, $\widehat{\mathbf{R}}_N$ and $\widehat{\mathbf{R}}_S(q)$.$\widehat{\mathbf{R}}_S(q)$ differs from $\mathbf{R}_S$ not only because it is an estimate, but also because it is a flat band-power approximation.

At each frequency, off-diagonal terms of $\widehat{\mathbf{W}}\mathbf{A}$ correspond to leakage of other components into a given component's estimate at spatial frequency k. Each panel of Fig. 7 refers to one component (CMB, dust and SZ), and shows the relative contribution of all components and of noise to the recovered map. Levels are relative to the true map, so that the contribution of a component to its own recovered map illustrates the spatial filtering induced by the Wiener inversion. The figure illustrates that the inversion done with blindly estimated parameters performs almost as well as the separation using exact values of the spectra and mixing matrix. Differences are typically much smaller than noise contamination, which is comparable with the blind and the non-blind approaches.

5 DISCUSSION

5.1 Related work on component separation

Explicit component separation was investigated first in CMB applications by Tegmark & Efstathiou (1996), Bouchet & Gispert (1999) and Hobson et al. (1998). In these applications, all the parameters of the model (mixing matrix, noise levels, statistics of the components, including the spatial power spectra) are assumed to be known.

Recent research has addressed the case of an imperfectly known mixing matrix. It is then necessary to estimate it (or at least some of its components) directly from the data. For instance, Tegmark et al. assume power-law emission spectra for all components except CMB and SZ, and fit spectral indices to the observations (Tegmark et al. 2000).

More recently, it has been proposed to resort to 'blind source separation' or 'independent component analysis' (ICA) methods. The work of Baccigalupi et al. (2000), further extended by Maino et al. (2002), implements a blind source separation method exploiting the non-Gaussianity of the sources for their separation. This infomax method, unfortunately, is not designed for noisy mixtures and cannot deal with a frequency-dependent beam.

The idea to use spectral diversity and an EM algorithm for the blind separation of components in CMB observations was proposed first by Snoussi et al. (2001). This approach exploits the spectral diversity of components as in our MDMC spectral matching, but assumes the prior knowledge of the spatial power spectra of the components. Our approach extends further on this idea, with significantly more flexibility, and the new point of view that spatial power spectra are actually the main unknown parameters of interest for CMB observations.

Other reports of blind component separation in Astronomical data include Nuzillard & Bijaoui (2000) and Funaro, Oja & Valpola (2001).

5.2 Comments on the spectral matching approach

Robustness. Our approach assumes that the data are collected in the form of a linear mixture of a known number of components that are independent, have different spatial power spectra, and different laws of emission as a function of frequency. These assumptions are valid in the three-component mixtures used in our simulations. Applying this method to real data obtained with the *Archeops* experiment (Benoît et al. 2003) gave us the opportunity to verify that the method is quite robust, with satisfactory performance even when the noise is neither white nor stationary, and when some residual systematic effects remain in the data. Of course, the exact impact of large departures from the model remains to be tested on a case by case basis.

Detector-dependent beams. It is quite usual in CMB observations that, because of the diffraction limit, the resolution of the available maps depends on frequency. For *Planck*, the resolution ranges from about 30 arcmin at 30 GHz to 4.5 arcmin at 350 GHz

2003MNRAS.346.1089D

and higher. It is mandatory that a method combining all observations benefit from the full resolution of the highest frequency channels. MDMC spectral matching, being implemented in Fourier (or spherical harmonics) space, permits one to take beam effects into account straightforwardly by including in the model the effect of a transfer function.

Identifying components. In practice, MDMC spectral matching runs with a fixed number of components. This number might not be well known (or even not very well defined), and must be guessed (or assumed). For CMB applications, an educated guess can be made (as usual for all component separation methods).

A practical way to handle this issue consists of applying the method several times with a increasing number of expected components. Comparing successive results permits one to identify 'stable' components, which remain essentially unchanged when more components are sought. Too few components result in unsatisfactory identification and poor adjustment of the model to the empirical spectrum. Too many components result in the separation of artificial components, either very weak or single-detector noise maps.

With this strategy, the method can be viewed as a component *discovery* tool, which can be useful in particular to uncover and separate out instrumental effects behaving as additional components.

Connected to the issue of component identification is the uniqueness (or identifiability) problem. As discussed above, MDMC spectral matching uses spectral diversity as the 'engine' of blind separation: components with proportional spatial power spectra (or nearly so) are not (or poorly) separated. In the current test, the three components are different enough that no such problem arises. In richer mixtures, containing contributions from several galactic components, it is quite possible that spectral diversity does not hold. If, for instance, several galactic components had a spatial power spectrum proportional to $1/k^3$, the method would satisfactorily estimate parameters relevant to the CMB and the SZ effect, but would be unable to un-mix Galactic contributions. A way out is to use a semi-blind approach in which some entries of the mixing matrix are forced to zero when the contribution of a particular component at a particular frequency is known to be negligible. This is the object of forthcoming research.

5.3 Comments on the Wiener inversion

After adjusting the parameters of the model to the data, the recovered mixing matrix, spectra, and noise levels can be used for component separation by Wiener inversion.

Quite interestingly, the Wiener filter can be implemented for identified components even if some sub-mixtures are not identified (for instance by lack of spectral diversity). It can be shown straightforwardly that the Wiener form

$$\mathbf{W} = \left[\mathbf{A}^\dagger \mathbf{R}_N^{-1} \mathbf{A} + \mathbf{R}_S^{-1}\right]^{-1} \mathbf{A}^\dagger \mathbf{R}_N^{-1} \tag{16}$$

can be rewritten equivalently as

$$\mathbf{W} = \mathbf{R}_S \mathbf{A}^\dagger [\mathbf{A}\mathbf{R}_S \mathbf{A}^\dagger + \mathbf{R}_N]^{-1} \tag{17}$$

or

$$\mathbf{W} = \mathbf{R}_S \mathbf{A}^\dagger \mathbf{R}_Y^{-1}. \tag{18}$$

Thus, the Wiener inversion for component j requires only an estimate of $\mathbf{R}_Y$ (readily available as $\widehat{\mathbf{R}}_Y$), of the spatial power spectrum of component j, and of the column of the mixing matrix $\mathbf{A}$ corresponding to component j. Therefore, *it is not necessary to identify all components, nor to know all spatial power spectra, nor to know noise levels, to separate the CMB from the other components*. We just need to know the CMB emission law (which we do) and its spatial power spectrum (which can be estimated blindly with our method).

As a final note, we stress that the Wiener method has the property of filtering the data spatially – an unpleasant fact when power spectra are estimated on separated maps. In contrast, MDMC spectral matching adjusts domain-averaged spatial power spectra on the data prior to component map separation (bypassing the need for power-spectrum estimation on output maps).

5.4 Comments on spectral estimation

In the above discussion, we have assumed for simplicity that the noise is spatially white for all detectors. This assumption, however, can be relaxed if needed, without (in general) loosing identifiability.

If the noise is uncorrelated between detectors, noise terms appear only on the diagonal of the multivariate power spectrum of the observations $\mathbf{R}_Y$. Off-diagonal terms contain only contributions from the off-diagonal terms of $\mathbf{A}\mathbf{R}_S\mathbf{A}^\dagger$. If noise power spectra are completely free, off-diagonal terms of $\widehat{\mathbf{R}}_Y$ constrain $\mathbf{A}\mathbf{R}_S\mathbf{A}^\dagger$, and diagonal terms serve to measure $\mathbf{R}_N$.

For instance, if the mixing matrix $\mathbf{A}$ is known, it is possible to adjust simultaneously the spatial power spectrum of the components and that of the noise on the data, as long as enough observations are available, which is generically the case.

If data from several experiments are analysed jointly, however, no correlated noise of instrumental origin is expected between data from detectors belonging to different experiments. This provides strong consistency checks, which ultimately provides an additional handle on the assessment of errors in the final results.

With a MDMC approach in Fourier (or spherical harmonic) space, data at different frequencies and with different beam sizes can be analysed jointly. This joint analysis can be done straightforwardly by stacking all observations from different instruments in the same vector of observations $\boldsymbol{Y}$, as long as they cover the same area of the sky. This is bound to become of major importance for the future scientific exploitation of multiscale and multifrequency data.

5.5 Using single-detector maps

For a well-calibrated instrument, the linear mixture model can be written in physical units, and the mixing matrix $\mathbf{A}$ depends only on the emission laws of components. Traditionally then, component separation is implemented on a set of maps per frequency channel (data from all detectors in each single frequency channel are combined into a single map). This approach should be preferred if good maps cannot be obtained independently for each detector (for sampling reasons, or because of striping...), and if all detector data at the same frequency can be combined (with some optimality) into one single map.

An alternate solution, when calibration coefficients and noise properties for individual detectors (levels, correlations between the noise of different detectors) are not known precisely, is to estimate parameters directly using single detector maps in readout units (e.g. microvolts), which can be done naturally with our spectral-matching method.

5.6 Comment on domain averaging

We have considered band-averaged spectra as in definition (3). In CMB studies, one may be more interested in quantities like $\ell(\ell+1)C_j(\ell)$ which are expected to vary more slowly than $C(\ell)$

itself. In this case, it may be more appropriate to perform bin averages as

$$\widetilde{\mathbf{R}}_Y(q) = \left(\sum_{\ell \in \mathcal{D}_q} \ell(\ell+1) \right)^{-1} \sum_{\ell \in \mathcal{D}_q} \ell(\ell+1)\, \mathbf{Y}(\boldsymbol{\ell}) \mathbf{Y}(\boldsymbol{\ell})^\dagger. \quad (19)$$

Spectral matching on such statistics would then yield estimates of

$$\widetilde{C}_j(q) = \left(\sum_{\ell \in \mathcal{D}_q} \ell(\ell+1) \right)^{-1} \sum_{\ell \in \mathcal{D}_q} \ell(\ell+1) C_j(\boldsymbol{\ell}). \quad (20)$$

This weighted band-averaging can be used in our MDMC spectral-matching method as well.

5.7 Extensions and application

The spectral matching method described in this paper resolves several problems relevant to the analysis of multidetector observations of noisy linear mixtures.

To a large extent, the efficiency of the method is due to the assumed structure of the data. In real observations, the model holds only approximately. For instance, some components may display anomalous behaviour in some regions of the sky. In this case, it may be worth cutting those regions out of the observations and treating them independently.

If the emission laws of some of the components vary slowly with position on the sky, then the method may be used on small maps rather than all-sky maps. A similar approach can be adopted in the case where spatial power spectra or noise levels are very dependent on sky coordinates.

Point sources induce correlated emissions across frequency channels, which cannot be modelled as a small set of additional components on the sky. One way to handle this problem is by detecting them with a matched filter, and blanking them out in the observations prior to applying the spectral matching.

To summarize, while MDMC spectral matching is a very powerful tool for CMB data analysis, it is not by itself a full reduction pipeline, and should be used for the most appropriate application, in conjunction with any other tool relevant to the problem at hand.

6 CONCLUSION

This paper describes a spectral matching method for blind source identification in noisy mixtures. The method adjusts a simple model of the data to the observations. We estimate a physically relevant set of parameters (fundamental parameters of the model: the mixing matrix, domain-averaged spatial power spectra of the sources and of noise) by maximum likelihood. Only unknown parameters are estimated, as the method lends itself easily to the modifications necessary to exploit partial prior information. Thanks to a Gaussian stationary model, the likelihood depends only on a reduced set of statistics (average spectral density matrices of the observations). An efficient, dedicated algorithm can adjust the parameters in just a few minutes on a modest workstation.

Our method is of particular relevance for CMB data analysis in a multidetector, multichannel mission such as *Planck*.

First, the method permits the blind separation of underlying components, hence, of emissions coming from different astrophysical sources. Obtaining clean maps of emissions resulting from distinct astrophysical processes is crucial to understanding their properties.

Secondly, the blind method permits one to estimate the number of components (by repeating the adjustment with a varying number of sources). This will be of utmost importance for analysing data from sensitive missions such as *Planck*, in particular for the identification and characterization of subdominant processes of foreground emission (e.g. free–free emission, non-thermal dust emission), or to track down systematic effects in the data.

Thirdly, the blind method can estimate the entries of the mixing matrix. This may be used, if needed, to constrain the emission law (electromagnetic spectrum) of the different components contributing to the mixture, which is essential for understanding their physical properties and possibly the emission processes.

Fourthly, if strong sources, for which the mixing matrix is well recovered, contribute to the mixture, the method can provide a useful tool for the intercalibration (or the absolute calibration) of the different detectors or of the different channels.

Fifthly, as our method is essentially a spectral matching method, which adjusts the spectra of a number of components to the observational data, it provides a direct measurement of the spatial power spectrum of the components in the mixture, of particular relevance for the CMB.

Sixthly, even though the above discussion assumed for simplicity a spatially white noise for all detectors, this assumption can be relaxed if needed, without (in general) loosing identifiability. The EM algorithm has to be adapted accordingly.

As a final word, let us emphasize that the method can be applied to sets of data from different experiments. As the MDMC spectral matching approach, implemented in Fourier space, straightforwardly accounts for beam effects, it can also be used for the blind, joint analysis of multiexperiment, multichannel, multidetector, multiresolution data as long as they cover the same area of the sky. The method may become an essential tool for mapping and analysing sources of emission observed with present and upcoming submillimetre experiments.

ACKNOWLEDGMENTS

We thank James G. Bartlett for a critical reading of the original manuscript. We acknowledge useful discussions with Mark Ashdown, Mike Hobson, Juan Macias, Ali Mohammad-Djafari, Hichem Snoussi, and the *Archeops* collaboration. This work was made possible by a grant from the French Ministère de la Recherche to stimulate interdisciplinary work for applying state-of-the-art signal and image processing techniques to CMB data analysis.

REFERENCES

Baccigalupi C. et al., 2000, MNRAS, 318, 769
Bennett C. L. et al., 1997, Am. Astron. Soc. Meeting, 191, 8701
Benoît A. et al., 2002, Astroparticle Phys., 17, 101
Benoît A. et al., 2003, A&A, 399, L23
Bersanelli M., Mandolesi R., 2000, Astrophys. Lett. Commun., 37, 171
Bouchet F. R., Gispert R., 1999, New Astron., 4, 443
Cardoso J.-F., Snoussi H., Delabrouille J., Patanchon G., 2002, in Proc. EUSIPCO Vol. 1, XI European Signal Processing Conf. Available online at http://www.carte-blanche.fr/~eusipco2002/, p. 561
de Bernardis P. et al., 2000, Nat, 404, 955
Delabrouille J., Melin J., Bartlett J., 2002, in Chen L., Ma C., Ng K., Pen U., eds, ASP Conf. Ser. Vol. 257, AMiBA 2001: High-Z Clusters, Missing Baryons, and CMB Polarization. Astron. Soc. Pac., San Francisco, p. 81
Dempster A., Laird N., Rubin D., 1977, J. R. Statistical Soc. B, 39, 1
Funaro M., Oja E., Valpola H., 2001, in Lee J., Makeig S., eds, Proc. ICA2001. 3rd Int. Conf. Independent Component Analysis and Blind Signal Separation. Available on-line at http://ica2001.ucsd.edu

Hanany S. et al., 2000, AJ, 545, L5
Hobson M. P., Jones A. W., Lasenby A. N., Bouchet F. R., 1998, MNRAS, 300, 1
Lamarre J.-M. et al., 2000, Astrophys. Lett. Commun., 37, 161
Luenberger D. G., 1973, Introduction to Linear and Nonlinear Programming. Addison-Wesley, Reading, MA
Maino D. et al., 2002, MNRAS, 334, 53
Nuzillard D., Bijaoui A., 2000, A&AS, 147, 129
Pham D.-T., Garat P., 1997, IEEE Tr. SP, 45, 1712
Snoussi H., Patanchon G., Maciaz-Perez J., Mohammad-Djafari A., Delabrouille J., 2001, in Fry R. L., ed., Proc. MAXENT Workshop, Bayesian Interference and Maximum Entropy Methods. AIP, New York, p. 125
Tegmark M., Efstathiou G., 1996, MNRAS, 281, 1297
Tegmark M., Eisenstein D. J., Hu W., de Oliveira-Costa A., 2000, ApJ, 530, 133
Zaldarriaga M., Seljak U., 2000, ApJS, 129, 431

APPENDIX A: LINEAR COMPONENT SEPARATION

The separation of astrophysical components relies on the key assumption that the total sky emission at frequency ν is a linear superposition of a number of components as in equation (1). In principle, then, the observation of the sky emission at several frequencies $(\nu_1, \nu_2, \ldots)$ recovers estimates $\widehat{\boldsymbol{S}}_j(\theta, \phi)$ of the component templates $\boldsymbol{S}_j(\theta, \phi)$ by inverting equation (1). There are several methods for a linear inversion of the system when the mixing matrix $\mathbf{A}$ is known.

(i) If there are as many noiseless observations as there are astrophysical components contributing to the total emission, by simple inversion of the square matrix $\mathbf{A}$, so that the recovered components, $\widehat{\boldsymbol{S}}$, are given by $\widehat{\boldsymbol{S}} = \mathbf{A}^{-1}\boldsymbol{Y}$.

(ii) If there are more observations than astrophysical components, the system can be inverted using the pseudo-inverse, $\widehat{\boldsymbol{S}} = [\mathbf{A}^\dagger\mathbf{A}]^{-1}\mathbf{A}^\dagger\boldsymbol{Y}$.

(iii) For optimal signal-to-noise ratio under Gaussian statistics, without other prior assumptions on the astrophysical components, one can use a generalized least-squares solution, $\widehat{\boldsymbol{S}} = [\mathbf{A}^\dagger\mathbf{R}_N^{-1}\mathbf{A}]^{-1}\mathbf{A}^\dagger\mathbf{R}_N^{-1}\boldsymbol{Y}$, where $\mathbf{R}_N$ is the noise correlation matrix.

(iv) The choice $\widehat{\boldsymbol{S}} = [\mathbf{A}^\dagger\mathbf{R}_N^{-1}\mathbf{A} + \mathbf{R}_S^{-1}]^{-1}\mathbf{A}^\dagger\mathbf{R}_N^{-1}\boldsymbol{Y} = \mathbf{W}\boldsymbol{Y}$ is the Wiener solution. It is the linear solution which minimizes the variance of the error, but requires knowledge of both the noise autocorrelation, $\mathbf{R}_N$, and of the component autocorrelation, $\mathbf{R}_S$. As $[\mathbf{WA}]_{ii} \leqslant 1$, this solution modifies the spatial spectra of the components since different weights are given to different spatial frequencies of a component map.

(v) The renormalized Wiener solution, $\widehat{\boldsymbol{S}} = \mathbf{\Lambda}\mathbf{W}\boldsymbol{Y}$, where $\mathbf{\Lambda} = [\mathrm{diag}(\mathbf{WA})]^{-1}$, is the Wiener solution under the constraint $[\mathbf{WA}]_{ii} = 1$. This solution renormalizes the Wiener solution at each spatial frequency, so that no spatial filtering is applied to the data.

In the above list, solution (i) is the special case of (ii) when $\mathbf{A}$ is square and regular; (ii) is the special case of 3 when the noise is white ($\mathbf{R}_N \propto \mathrm{Id}$); (iii) the special case of (iv) when the signal is much stronger than the noise; and (v) a constrained version of (iv) that does not modify the relative importance of different spatial frequencies in a component map after inversion. Depending on the chosen method, one or more of $\mathbf{A}$, $\mathbf{R}_N$ and $\mathbf{R}_S$ (which can be considered as parameters of the model) is needed to implement the inversion.

Realizing the fact that optimal component separation requires prior knowledge of a set of parameters of the model is one of the driving ideas behind our MDMC spectral-matching approach: we implement the *joint estimation* of all such parameters that are not necessarily known a priori.

APPENDIX B: SPECTRAL MATCHING AND LIKELIHOOD

This section shows that minimizing the spectral matching criterion (11) is equivalent to maximizing the likelihood of a simple model.

Gaussian likelihood and covariance matching. We first show how criterion (11) is related to a Gaussian likelihood. If y is a real $n \times 1$ zero mean Gaussian random vector with covariance matrix $\mathbf{R}$, then

$$-2\log p(\boldsymbol{y}) = \boldsymbol{y}^\dagger\mathbf{R}^{-1}\boldsymbol{y} + \log\det(2\pi\mathbf{R}). \tag{B1}$$

If $\mathbf{Y} = [\boldsymbol{y}_1, \ldots, \boldsymbol{y}_T]$ is an $n \times T$ matrix made of T such vectors, independent from each other, with $\mathrm{Cov}(\boldsymbol{y}_t) = \mathbf{R}_t$, then

$$-2\log p(\mathbf{Y}) = \sum_{t=1}^{T} \boldsymbol{y}_t^\dagger\mathbf{R}_t^{-1}\boldsymbol{y}_t + \log\det(2\pi\mathbf{R}_t). \tag{B2}$$

Assume further that the index set $[1, \ldots, T]$ can be decomposed in Q subsets $I_1, \ldots, I_Q$ such that R_t is constant with value $\mathbf{R}(q)$ over the qth subset, that is, $\mathbf{R}_t = \mathbf{R}(q)$ if $t \in I_q$. Then, equation (B12) can be rewritten, using $\boldsymbol{y}^\dagger\mathbf{R}^{-1}\boldsymbol{y} = \mathrm{tr}(\mathbf{R}^{-1}\boldsymbol{y}\boldsymbol{y}^\dagger)$, as

$$-2\log p(\mathbf{Y}) = \sum_{q=1}^{Q} n_q\left[\mathrm{tr}\widehat{\mathbf{R}}(q)(\mathbf{R}(q)^{-1}) + \log\det(\mathbf{R}(q))\right] + \text{constant}$$

where $\widehat{\mathbf{R}}(q) = \frac{1}{n_q}\sum_{t\in I_q}\boldsymbol{y}_t\boldsymbol{y}_t^\dagger$ and n_q is the number of indices in I_q. This last expression also reads

$$-2\log p(\mathbf{Y}) = \sum_{q=1}^{Q} n_q D(\widehat{\mathbf{R}}_y(q), \mathbf{R}_y(q)) + \text{constant} \tag{B3}$$

where the constant term is a function of the data Y via $\widehat{\mathbf{R}}_y(q)$ but not of any $\mathbf{R}(q)$. This form makes it clear that the mismatch (11) corresponds to the log-likelihood of a sequence of zero mean Gaussian vectors which are modelled as having blockwise identical covariance matrices.

Whittle approximation. The statistical distribution of the Fourier coefficients of a stationary time series is a well researched topic. If T samples $y(1), \ldots, y(T)$ of an n-variate discrete time series are available, the Fourier transform is:

$$\widetilde{y}(f) = \frac{1}{\sqrt{T}}\sum_{t=0}^{T-1} y(t)\exp -2\mathrm{i}\pi f t. \tag{B4}$$

For a stationary time series with spectral covariance matrix $R(f)$, simple asymptotic (for large T) results are available. In particular, the Whittle approximation consists of approximating the distribution of the Fourier transform $\widetilde{y}(f)$ at DFT points $f = q/T$ as follows.

(i) The real part and the imaginary part of $\widetilde{y}(f)$ are Gaussian, uncorrelated, with the same covariance matrix and $E\widetilde{y}(f)\widetilde{y}(f)^\dagger = R(f)$.

(ii) For $0 < p \neq p' < T/2$ (assuming T even and for p, p' integers), $\widetilde{y}(p/T)$ is uncorrelated with $\widetilde{y}(p'/T)$.

This is a standard approximation: it has been used for the blind separation of noise free mixtures of components by Pham & Garat

(1997) and in the context of astronomical component separation by e.g. Bouchet & Gispert (1999) and Tegmark & Efstathiou (1996).

Expression (B3) thus shows[3] that the minimization of (11) is equivalent to maximizing (the Whittle approximation to) the likelihood provided we model the spectra of the sources as being constant over spectral domains.

APPENDIX C: AN EM ALGORITHM IN THE SPECTRAL DOMAIN

The expectation maximization (EM) algorithm (Dempster et al. 1977) is a popular technique for computing maximum likelihood estimates. This section first briefly reviews the general mechanism of EM and then shows its specific form when applied to our model.

The EM algorithm. Consider a probability model $p(y, s \mid \theta)$ for a pair (y, s) of random variables with θ a parameter set. If the variable s is not observed, the log-likelihood of the observed y is

$$l(\theta) = \log p(y \mid \theta) = \log \int p(y, s \mid \theta)\, \mathrm{d}s. \tag{C1}$$

For some statistical models, the maximization of the log-likelihood $l(\theta)$ can be made easier by considering the EM functional:

$$l(\theta, \theta') = \int \log(p(y, s \mid \theta))\; p(s \mid y, \theta')\, \mathrm{d}s. \tag{C2}$$

The EM algorithm is an iterative method which computes a sequence of estimates according to

$$\theta^{(n)} \rightarrow \theta^{(n+1)} = \arg\max_{\theta} l\left(\theta, \theta^{(n)}\right). \tag{C3}$$

It can be shown that

$$l(\theta'', \theta') > l(\theta', \theta') \Rightarrow l(\theta'') > l(\theta'), \tag{C4}$$

meaning that every step of the algorithm can only increase the likelihood. Actually, a stationary point of the algorithm is also a stationary point of the likelihood since

$$\frac{\partial l(\theta)}{\partial \theta} = \left.\frac{\partial l(\theta, \theta')}{\partial \theta}\right|_{\theta'=\theta}. \tag{C5}$$

The EM algorithm is an interesting technique for maximizing the likelihood if (i) the computation of the conditional expectation in definition (C2) (E step) and (ii) the maximization (C3) of the functional (M step) are both computationally tractable.

Both the E step and the M step turn out to be straightforward because one elementary EM step amounts to solving

$$0 = \int \frac{\partial \log\left(p\left(y, s \,\middle|\, \theta^{(n+1)}\right)\right)}{\partial \theta}\, p\left(s \,\middle|\, y, \theta^{(n)}\right) \mathrm{d}s. \tag{C6}$$

In our model, the partial derivative in (C6) turns out to be a simple function of y and s, allowing the conditional expectation to be easily computed and equation (C6) to be easily solved. This is sketched in the following.

[3] Actually some care is required in dealing with the fact that the Fourier coefficients are complex-valued and that $\widetilde{y}(-f) = \widetilde{y}(f)^{\star}$. This introduces some minor complications in the computations, but does not affect the final result.

A single Gaussian vector. In order to introduce the necessary notations, we start by considering a simple case where $\boldsymbol{y} = \mathbf{A}\boldsymbol{s} + \boldsymbol{n}$ where $\boldsymbol{s}$ and $\boldsymbol{n}$ are independent Gaussian vectors with zero-mean and covariance matrices equal to $\mathbf{R}_s$ and $\mathbf{R}_n$ respectively. Then the parameter set is $\theta = (\mathbf{A}, \mathbf{R}_s, \mathbf{R}_n)$ and one has

$$-2\log p(\boldsymbol{y} \mid \boldsymbol{s}, \theta) = (\boldsymbol{y} - \mathbf{A}\boldsymbol{s})^{\dagger}\mathbf{R}_n^{-1}(\boldsymbol{y} - \mathbf{A}\boldsymbol{s}) + \log|\mathbf{R}_n| + \text{constant},$$

$$-2\log p(\boldsymbol{s} \mid \theta) \quad = \boldsymbol{s}^{\dagger}\mathbf{R}_s^{-1}\boldsymbol{s} + \log|\mathbf{R}_s| + \text{constant}.$$

Using $p(\boldsymbol{y}, \boldsymbol{s}) = p(\boldsymbol{y} \mid \boldsymbol{s})p(\boldsymbol{s})$, the log derivatives of the joint density with respect to the components of θ are

$$\frac{\partial \log p(\boldsymbol{y}, \boldsymbol{s} \mid \theta)}{\partial \mathbf{A}} = \mathbf{R}_n^{-1}\left[(\boldsymbol{y} - \mathbf{A}\boldsymbol{s})\boldsymbol{s}^{\dagger}\right], \tag{C7}$$

$$\frac{\partial \log p(\boldsymbol{y}, \boldsymbol{s} \mid \theta)}{\partial \mathbf{R}_n^{-1}} = -\frac{1}{2}\left[(\boldsymbol{y} - \mathbf{A}\boldsymbol{s})(\boldsymbol{y} - \mathbf{A}\boldsymbol{s})^{\dagger} - \mathbf{R}_n\right], \tag{C8}$$

$$\frac{\partial \log p(\boldsymbol{y}, \boldsymbol{s} \mid \theta)}{\partial \mathbf{R}_s^{-1}} = -\frac{1}{2}\left[\boldsymbol{s}\boldsymbol{s}^{\dagger} - \mathbf{R}_s\right]. \tag{C9}$$

Thus, in this simple model, computing the conditional expectations as in equation (C6) would boil down to evaluating the conditional expectations of the random variables $\boldsymbol{s}\boldsymbol{s}^{\dagger}$, $\boldsymbol{s}\boldsymbol{y}^{\dagger}$, $\boldsymbol{y}\boldsymbol{s}^{\dagger}$ and $\boldsymbol{y}\boldsymbol{y}^{\dagger}$. This is a routine matter in a Gaussian model $\boldsymbol{y} = \mathbf{A}\boldsymbol{s} + \boldsymbol{n}$ for which one finds

$$E(\boldsymbol{s}\boldsymbol{s}^{\dagger} \mid \boldsymbol{y}, \theta) = \mathbf{W}(\theta)\boldsymbol{y}\boldsymbol{y}^{\dagger}\mathbf{W}(\theta)^{\dagger} + \mathbf{C}(\theta), \tag{C10}$$

$$E(\boldsymbol{s}\boldsymbol{y}^{\dagger} \mid \boldsymbol{y}, \theta) = \mathbf{W}(\theta)\boldsymbol{y}\boldsymbol{y}^{\dagger}, \tag{C11}$$

$$E(\boldsymbol{y}\boldsymbol{s}^{\dagger} \mid \boldsymbol{y}, \theta) = \boldsymbol{y}\boldsymbol{y}^{\dagger}\mathbf{W}(\theta)^{\dagger}, \tag{C12}$$

$$E(\boldsymbol{y}\boldsymbol{y}^{\dagger} \mid \boldsymbol{y}, \theta) = \boldsymbol{y}\boldsymbol{y}^{\dagger}, \tag{C13}$$

with the following definitions for matrices $\mathbf{C}(\theta)$ and $\mathbf{W}(\theta)$:

$$\mathbf{C}(\theta) = \left(\mathbf{A}^{\dagger}\mathbf{R}_n^{-1}\mathbf{A} + \mathbf{R}_s^{-1}\right)^{-1}, \tag{C14}$$

$$\mathbf{W}(\theta) = \left(\mathbf{A}^{\dagger}\mathbf{R}_n^{-1}\mathbf{A} + \mathbf{R}_s^{-1}\right)^{-1}\mathbf{A}^{\dagger}\mathbf{R}_n^{-1}. \tag{C15}$$

Note that $\mathbf{C}(\theta) = \mathrm{Cov}(\boldsymbol{s} \mid \boldsymbol{y}, \theta)$ and that $\mathbf{W}(\theta)$ is the Wiener filter, that is $E(\boldsymbol{s} \mid \boldsymbol{y}, \theta) = \mathbf{W}(\theta)\boldsymbol{y}$.

The EM algorithm in the Whittle approximation. In our model, according to the Whittle approximation, the DFT points $y(k)$ are independent so that the EM functional (C2) for the whole data set simply is a sum over DFT frequencies of elementary functionals. Thus an EM step $\theta' \rightarrow \theta$ consists of solving

$$0 = \sum_k E\left\{\frac{\partial}{\partial\theta}\log p\left(\boldsymbol{y}(k), \boldsymbol{s}(k) \mid \theta\right) \mid \boldsymbol{y}(k), \theta'\right\}. \tag{C16}$$

To proceed further, equation (C16) is specialized to the case of interest by using two ingredients. First, we use the relation $y(k) = As(k) + n(k)$ and the Gaussianity of each pair $(y(k), s(k))$; this is expressed via equations (C7)–(C9). Secondly, we use the approximation that the power spectra are constant over each spectral domain. Combining these properties, the cancellation (C16) of the gradient with respect to $\mathbf{A}$, $\mathbf{R}_n$ and each $\mathbf{R}_s(q)$ yields

$$0 = \widetilde{\mathbf{R}}_{ys}(\theta') - \mathbf{A}(\theta)\widetilde{\mathbf{R}}_{ss}(\theta'), \tag{C17}$$

$$\begin{aligned} 0 = {} & \widetilde{\mathbf{R}}_{yy}(\theta') - \mathbf{A}(\theta)\widetilde{\mathbf{R}}_{sy}(\theta') - \widetilde{\mathbf{R}}_{ys}(\theta')\mathbf{A}(\theta)^{\dagger} \\ & + \mathbf{A}(\theta)\widetilde{\mathbf{R}}_{ss}(\theta')\mathbf{A}(\theta)^{\dagger} - \mathbf{R}_n, \end{aligned} \tag{C18}$$

$$0 = \widetilde{\mathbf{R}}_{ss}(\theta', q) - \mathbf{R}_s(\theta, q) \quad (q = 1, \ldots, Q), \tag{C19}$$

2003MNRAS.346.1089D

where we have defined the matrix

$$\widetilde{\mathbf{R}}_{ss}(\theta, q) = \frac{1}{n_q} \sum_{k \in \mathcal{D}_q} E\left(\boldsymbol{s}(k)\boldsymbol{s}(k)^\dagger \,|\, \boldsymbol{y}(k), \theta\right) \tag{C20}$$

and its weighted average over all domains

$$\widetilde{\mathbf{R}}_{ss}(\theta) = \sum_{q=1}^{Q} \frac{n_q}{n} \widetilde{\mathbf{R}}_{ss}(\theta, q). \tag{C21}$$

The same definitions hold for $\widetilde{\mathbf{R}}_{sy}(q, \theta)$ [resp. $\widetilde{\mathbf{R}}_{yy}(q, \theta)$] as an averaged conditional expectation of $\boldsymbol{s}(k)\boldsymbol{y}(k)^\dagger$ [resp. $\boldsymbol{y}(k)\boldsymbol{y}(k)^\dagger$] and $\widetilde{\mathbf{R}}_{sy}(\theta)$ [resp. $\widetilde{\mathbf{R}}_{yy}(\theta)$] as its weighted average over spectral domains.

Equations (C17)–(C19) are readily solved for unconstrained $\mathbf{A}$, $\mathbf{R}_n$ and $\mathbf{R}_s(q)$. Recall however that our model involves *diagonal* covariance matrices so that the actual parameter set is $(\mathbf{A}, C_j(q), \sigma_d^2))$. This constraint, however, preserves the simplicity of the solution of the M step since it suffices to use the diagonal parts of the solutions of (C17)–(C19). Thus, the M step boils down to

$$\mathbf{A} = \widetilde{\mathbf{R}}_{ys}(\theta')\widetilde{\mathbf{R}}_{ss}(\theta')^{-1}, \tag{C22}$$

$$\sigma_i^2 = \left[\widetilde{\mathbf{R}}_{yy}(\theta') - \widetilde{\mathbf{R}}_{ys}(\theta')\widetilde{\mathbf{R}}_{ss}(\theta')^{-1}\widetilde{\mathbf{R}}_{sy}(\theta')\right]_{ii}, \tag{C23}$$

$$P_i(q) = [\widetilde{\mathbf{R}}_{ss}(\theta', q)]_{ii}. \tag{C24}$$

The E-step of the algorithm essentially consists of computing the conditional covariance matrices $\widetilde{\mathbf{R}}_{\times\times}(q)$. In this step, the linearity and the Gaussianity of the model, together with the domain approximation, again provides us with significant computational savings. Indeed, matrices $\mathbf{C}$ and $\mathbf{W}$ defined at equations (C14) and (C15) are actually constant over each spectral domain so that the E-step is implemented by the following computations which directly stem from (C14)–(C15) and from equations (C10)–(C13):

$$\mathbf{C}(q) = \left(\mathbf{A}^\dagger \mathbf{R}_n^{-1} \mathbf{A} + \mathbf{R}_s(q)^{-1}\right)^{-1}, \tag{C25}$$

$$\mathbf{W}(q) = \left(\mathbf{A}^\dagger \mathbf{R}_n^{-1} \mathbf{A} + \mathbf{R}_s(q)^{-1}\right)^{-1} \mathbf{A}^\dagger \mathbf{R}_n^{-1}, \tag{C26}$$

$$\widetilde{\mathbf{R}}_{ss}(q) = \mathbf{W}(q)\widehat{\mathbf{R}}_y(q)\mathbf{W}(q)^\dagger + \mathbf{C}(q), \tag{C27}$$

$$\widetilde{\mathbf{R}}_{sy}(q) = \mathbf{W}(q)\widehat{\mathbf{R}}_y(q). \tag{C28}$$

From this, one easily reaches the EM algorithm as described at algorithm 1. The description of this procedure is completed by specifying the initialization, the rescaling of the parameters and the stopping rule, as briefly discussed next.

Some comments on EM implementation. Rescaling is required because, as noted above, the model is not completely identifiable: the spectral density matrices $\mathbf{R}_Y$ are unaffected by the exchange of a scalar factor between each column of $\mathbf{A}$ and each component's power spectrum. We have found that this inherent indetermination must be fixed in order for EM to converge. Our strategy is, after each EM step, to fix the norm of each column of $\mathbf{A}$ to unity and to adjust the corresponding power spectra accordingly. This is an arbitrary choice which happens to work well in practice.

The algorithm is initialized with the following parameters. We take $\mathbf{R}_n$ to be $\mathrm{diag}(\widehat{\mathbf{R}}_y)$ where $\widehat{\mathbf{R}}_y = \sum_q \frac{n_q}{n} \widehat{\mathbf{R}}_y(q)$. This is a gross overestimation since it amounts to assuming no signal and only noise. The initial value of $\mathbf{A}$ is obtained by using the N_c dominant eigenvectors of $\widehat{\mathbf{R}}_y$ as the N_c columns of $\mathbf{A}$. Again, this is nothing like any real *estimate* of $\mathbf{A}$, but rather a vague guess in 'the right direction'. Finally, the spectra $P_i(q)$ are taken as the diagonal entries of $\mathbf{A}^\dagger \widehat{\mathbf{R}}_y(q)\mathbf{A}$ which would be a correct estimate in the noise free case if $\mathbf{A}$ itself was. This ad hoc initialization procedure seems satisfactory. Note that it is a common rule of thumb to initialize EM with overestimated noise power.

Regarding the stopping rule, recall (from Section 3.2) that the EM algorithm is only used 'halfway' to the maximum of the likelihood and maximization is completed by a quasi-Newton technique. For this reason, there is little point in devising a sophisticated stopping strategy: in practice, the algorithm is run for a pre-specified number of steps (based on a few preliminary experiments with the data).

This paper has been typeset from a TEX/LATEX file prepared by the author.

Mon. Not. R. Astron. Soc. **364,** 1185–1194 (2005) doi:10.1111/j.1365-2966.2005.09380.x

Cosmic microwave background and foregrounds in *Wilkinson Microwave Anisotropy Probe* first-year data

G. Patanchon,[1⋆] J.-F. Cardoso,[2] J. Delabrouille[3] and P. Vielva[3,4]

[1] *Department of Physics & Astronomy, University of British Columbia, 6224 Agricultural Road, Vancouver, BC V6T 1Z1, Canada*
[2] *CNRS/ENST – 46, rue Barrault, 75634 Paris, France*
[3] *PCC – Collège de France, 11, place Marcelin Berthelot, F-75231 Paris, France*
[4] *Instituto de Física de Cantabria, Consejo Superior de Investigaciones Científicas – Universidad de Cantabria, Avda. Los Castros s/n, 39005 Santander, Spain*

Accepted 2005 June 28. Received 2005 June 23; in original form 2004 October 13

ABSTRACT

We perform a blind multicomponent analysis of the *Wilkinson Microwave Anisotropy Probe* (*WMAP*) 1-yr foreground-cleaned maps using Spectral Matching Independent Component Analysis (SMICA). We provide a new estimate of the cosmic microwave background (CMB) power spectrum as well as the amplitude of the CMB anisotropies across frequency channels. We show that the CMB anisotropies are compatible with temperature fluctuations as expected from the standard paradigm. The analysis also allows us to identify and separate a weak residual Galactic emission, present significantly in the Q band outside of the Kp2[1] mask limits, and mainly concentrated at low Galactic latitudes. We produce a map of this residual component by Wiener filtering using estimated parameters. The level of contamination of CMB data by this component is compatible with the *WMAP*-team estimation of foreground residual contamination. In addition, the multicomponent analysis allows us to estimate jointly the power spectrum of unresolved point-source emission.

Key words: methods: data analysis – cosmic microwave background – cosmology: observations.

1 INTRODUCTION

The cosmic microwave background (CMB) is one of the most powerful probes of modern cosmology. The shape of the spatial power spectrum of the small temperature fluctuations depends on the cosmological parameters describing, in the frame of the standard model, the matter content, the geometry and the evolution of the Universe (Jungman et al. 1996). Since the first detection of CMB anisotropies by the *Cosmic Background Explorer* (*COBE*) satellite in 1992 (Smoot et al. 1992), several ground-based and balloon-borne experiments have provided an accurate estimate of the power spectrum on a large range of angular scales. The recent *Wilkinson Microwave Anisotropy Probe* (*WMAP*) mission (Bennett et al. 2003a), after 1 yr of data acquisition, provided measurements of the power spectrum with unprecedented accuracy.

Measuring the CMB power spectrum is a difficult task. It requires a good characterization of noise contribution in the observations, as well as the subtraction of foreground astrophysical emission present at millimetre wavelengths (Bouchet & Gispert 1999). Both noise and foreground emissions can significantly bias CMB power-spectrum estimates if not well accounted for.

The *WMAP* data are the best presently available observation of the sky in the 20–90 GHz range. A careful separation of CMB from foregrounds, however, is required in order to make the best out of these observations. In particular, isolating CMB from foregrounds is of extreme importance for measuring accurately the angular power spectrum $\mathbf{C}(\ell)$ of CMB anisotropies and for cosmological interpretation.

The approach of the *WMAP* collaboration consists of cleaning observations from foreground contaminations for performing a CMB power-spectrum estimation on the cleaned maps. More specifically, Galactic foregrounds are subtracted using templates obtained from external data sets. In addition, strong known extragalactic point sources as well as the region of the Galactic plane are masked prior to the analysis. The CMB spectrum is estimated using a weighted average of the cross-power spectra of cleaned observation maps in the Q, V and W channels (Hinshaw et al. 2003). This avoids biases due to detector noise, assuming that the noise of different detectors is uncorrelated. This estimated spectrum is corrected for residual point-source contamination by subtracting an estimate of the contribution of the point sources in the cross-power spectra. The level of residual Galactic contaminations is estimated by cross-correlating the maps with the foreground templates.

A multicomponent approach of CMB spectral estimation has been proposed by Delabrouille, Cardoso & Patanchon (2003). Additional publications on the subject give variants and details (Cardoso et al.

⋆E-mail: patanch@physics.ubc.ca

[1] The Kp2 mask is provided by the *WMAP* team and is based on the K-band signal level to cancel strong galactic emissions.

2002; Patanchon et al. 2003). The method, called Spectral Matching Independent Component Analysis (SMICA), is based on matching the cross- and auto-power spectra of the observed maps to a parametric model described by the power spectra of all the astrophysical components, their relative amplitudes in the different channels and the noise power spectra. It is a very flexible approach: depending on available knowledge, most of the parameters may be either estimated from the data or kept at fixed values. In particular, emission laws for all or some of the components can be estimated.

There are several benefits of using SMICA in CMB analysis.

First, SMICA yields maximum-likelihood estimates of the CMB power spectrum for a model of linear mixture of Gaussian stationary components and noise. Therefore, if there are no foregrounds but only Gaussian CMB and noise, SMICA is expected to outperform quadratic estimates.

Secondly, SMICA allows to estimate jointly the spatial power spectra *and* the amplitude of the components in each channel (which are related to emission laws of components as well as calibration coefficients). In particular, the application on *WMAP* data allows us to check the following strong prediction of the standard model: CMB anisotropy should have a spectral emission law given, to first order, by a derivative (with respect to the temperature) of the blackbody law. Fixsen (2003) has measured the CMB anisotropy contribution in the *COBE* Far Infrared Absolute Spectrometer (FIRAS) data by looking for the *WMAP* anisotropy template in FIRAS. The author shows the compatibility of CMB anisotropy at large angular scales ($>5^\circ$) with temperature fluctuations in the Wien part of the spectrum. Our blind estimation of the component emission laws provides us with a unique tool for extending this result to frequencies covered by *WMAP* and to all measured angular scales (including the first acoustic peak) with a remarkable precision as shown below.

Finally, if there are foreground contributions in the observations, SMICA is designed to detect them and allows their separation. It permits indeed to jointly estimate power spectra of multiple components in the data, *to assess the significance of components*, and eventually to separate the effect of all the emissions.

In this paper, we investigate the existence of residual foreground emission in foreground-cleaned *WMAP* data. In particular, residual Galactic emission resulting from an error in the subtraction of Galactic templates can be present in the published maps. Such residuals may exist if external templates of Galactic emissions, extrapolated using a physical model to *WMAP* frequencies, are not quite representative of the actual Galactic components. Multicomponent analysis with SMICA allows to check for the existence of such a residual, and to quantify the level of contamination if any, without prior information on its power spectrum or on its amplitude across channels.

In addition, the *WMAP* collaboration has shown that unresolved point-source emissions have a non-negligible contribution to the data (Hinshaw et al. 2003; Komatsu et al. 2003). This result has been independently confirmed by Huffenberger, Seljak & Makarov (2004). As will be shown, SMICA also yields a coarse estimate of the level of point-source emission in *WMAP* data.

The paper is organized as follows. Section 2 introduces the data used for the analysis, the simulations performed in order to check our results and the model of the *WMAP* observations for SMICA. The method is described in Section 3. In Section 4, the results are presented. Finally, conclusions are provided in Section 5.

2 DATA

2.1 *WMAP* data and input maps for SMICA

The *WMAP* space probe, launched by National Aeronautics Space Agency (NASA) in 2001, is a large telescope for imaging the total emission of the sky at five different wavelengths (or frequency channels), with a resolution ranging from about 0.2° to 0.9° (limited by diffraction), and with full-sky coverage (Bennett et al. 2003a).

The data taken by *WMAP* have been made available to the scientific community after 1 yr of proprietary period, and is freely available on a dedicated NASA CMB web site.[2] The data consist of a set of 10 maps obtained by different detector pairs: four maps at 3.2 mm (*W* band at 94 GHz), two at each 4.9 and 7.3 mm (*V* band at 61 GHz and *Q* band at 41 GHz) and one at 9.1 and 13.0 mm (Ka band at 33 GHz and *K* band at 23 GHz). The data are provided in the HEALPix pixellization of the sphere[3] (Górski, Hivon & Wandelt 1998). Foreground-cleaned versions of the *Q*-, *V*- and *W*-band maps are also available. These maps have been used in the generation of the *WMAP* first-year CMB power spectrum by the *WMAP* team. The Galactic foreground signal, consisting of synchrotron, free–free and dust emission was removed using the three-band, five-parameter template-fitting method described in Bennett et al. (2003b). Galactic templates come from external data sets: the 408-MHz synchrotron map (Haslam et al. 1982), the predicted dust emission at 94 GHz using the Finkbeiner, Davis & Schlegel (1999) model, composite Hα map (Finkbeiner 2003) and the Galactic reddening $E(B-V)$ (Schlegel, Finkbeiner & Davis 1998).

For our analysis, we use the eight individual foreground-cleaned maps. We partially correct the maps from beam smoothing effects, so that every map gets the effective resolution of a reference map (we choose W3). We simply multiply the coefficients of the spherical harmonic decomposition by the inverse of beam transfer function ratio.

We consider two different sets of maps corresponding to different masking. For the first set (hereafter map set I), we apply the Kp2 Galactic mask provided by the *WMAP* collaboration, cancelling about 15 per cent of the pixels. For the second set (hereafter map set II), we mask the pixels corresponding to the Galactic latitudes lower than 40°. For both the sets, we mask the strongest point sources using the mask provided by the *WMAP* team. In all cases, masks are apodized for a smooth transition between 0 and 1 on a scale of 30 arcmin.

The prior correction of beam smoothing effects permits the application of SMICA using directly the pseudo cross- and auto-power spectra of observation (computed from partially covered maps). The true component power spectra can be obtained from these pseudo power spectra afterwards.

2.2 Simulations

In order to validate the method, assess error bars on the estimated parameters, and check for systematic errors in the analysis, we have generated 100 full-sky simulations of the *WMAP*-observed maps with 6.5-arcmin pixels (HEALPix $n_{\rm side}=512$). Each set of simulations consists of eight maps reproducing the observations in the *Q*, *V* and *W* bands. Maps contain synthetic CMB anisotropies degraded to the resolution of the detectors, assuming a symmetric beam pattern and using the transfer function published by *WMAP*. They contain

[2] http://lambda.gsfc.nasa.gov/
[3] http://www.eso.org/science/healpix/

anisotropic white noise at the expected level. CMB anisotropies are generated using the CMBFAST software (Zaldarriaga & Seljak 2000) with current 'concordance' cosmological parameters (Spergel et al. 2003). The simulated maps are partially deconvolved and the same mask as used for real data is applied.

No measurable bias has been observed in simulations. Error bars on all parameters (CMB power spectrum as well as mixing parameters) obtained from the dispersion over 100 independent simulations have been found to be in very good agreement (precision better than 10 per cent) with the closed form expression of equation (13), validating the use of the latter for final error bar estimates.

2.3 Model of the *WMAP* observations

The sky emission at *WMAP* frequencies is well described to first order by a linear superposition of the emissions of a few processes: CMB anisotropies, Galactic foregrounds (synchrotron, dust, free–free, ...), point-source emissions and Sunyaev Zel'dovich (SZ) effect. After subtraction of the Galactic foreground templates and masking, the *WMAP* data between 40 and 94 GHz can be modelled as noisy linear mixtures of CMB anisotropies, unresolved point sources and possibly small residual Galactic emissions [no significant SZ effect is expected to be present in *WMAP* observations (Bennett et al. 2003b), and Huffenberger et al. (2004) found no evidence of SZ effect using a multifrequency approach]. We assume that the emission laws of components are independent of the position (θ, ϕ) on the sky. Although this is only an approximation, it holds exactly for the CMB and for the Galactic residuals that are significant at one frequency band only. Thus, observation i is modelled as

$$x_i(\theta,\phi) = \sum_{c=1}^{N_c} \mathbf{A}_{ic} s_c(\theta,\phi) + n_i(\theta,\phi), \tag{1}$$

where s_c is the spatial distribution of the component c, n_i is the noise of the observation i and $\mathbf{A}_{ic}$ is the amplitude of the component c in map i given by

$$\mathbf{A}_{ic} = \int w_i(\nu)\, g_c(\nu)\, \mathrm{d}\nu, \tag{2}$$

where w_i is the spectral band of detector i and $g_c(\nu)$ is the emission law of component c. In matrix–vector format, model (1) reads

$$x(\theta,\phi) = \mathbf{A}s(\theta,\phi) + n(\theta,\phi) \tag{3}$$

with an $N_d \times N_c$ mixing matrix $\mathbf{A}$.

This simple model does not reflect the fact that resolution depends on the frequency band. In our analysis, this effect as well as the impact of the masks are accounted for in the spectral domain (see Section 3.4 for a sketch of the correction of beam and coverage effects).

On the statistical side, we will assume statistical independence between components, between the noise contaminations of different detectors and between the latter and all the components.

The standard model of cosmology predicts that CMB anisotropies are small temperature fluctuations of a pure blackbody spectrum. A first-order expansion around $T = 2.726$ K gives:

$$g_{\mathrm{CMB}}(\nu) \propto \left[\frac{\partial B_\nu(T)}{\partial T}\right]_{T=2.726\,\mathrm{K}}, \tag{4}$$

where $B_\nu(T)$ is the Planck law for the emission of a blackbody at temperature T.

Whereas the assumption that $\mathbf{A}_{ic}$ does not depend on the position is a good approximation to first order for Galactic components, it is not the case for point-source emissions. Nevertheless, since the brightest point sources are masked and since the frequency dependence of most of the contributing radio sources belongs to the flat population, their emission law can be roughly described as

$$g_{\mathrm{PS}}(\nu) \propto \left(\frac{\nu}{\nu_0}\right)^{\beta} \tag{5}$$

with $\beta \approx -2$ (Toffolatti et al. 1998). Note that unresolved point sources in the *WMAP* data have already been reported at a very low level (Hinshaw et al. 2003).

2.4 Spectral statistics

The spectra and cross-spectra at multipole ℓ of $x(\theta,\phi)$ (considered as an isotropic N_d-dimensional random field on the sphere) is the $N_d \times N_d$ spectral matrix $\mathbf{R}(\ell)$

$$\mathbf{R}(\ell) = \langle x(\ell,m)\, x(\ell,m)^\dagger \rangle, \tag{6}$$

where $\langle\cdot\rangle$ denotes an ensemble average, superscript dagger ($\dagger$) denotes transposition, and the $x(\ell,m)$ are the coefficients of the field on the basis of real spherical harmonics. This average value is independent of m because of isotropy.

In the linear model of equation (3), independence between components and noise implies that

$$\mathbf{R}(\ell) = \mathbf{A}\mathbf{C}(\ell)\mathbf{A}^\dagger + \mathbf{N}(\ell), \tag{7}$$

where $\mathbf{C}(\ell)$ and $\mathbf{N}(\ell)$ are the spectral matrices for the components and the noise, respectively. They are both diagonal matrices as a consequence of the independence assumption between components and between noise contaminations.

In practice, spectral matrices are estimated by averaging over multipole bins. Typically, one considers Q multipole bins with the qth bin ($1 \leqslant q \leqslant Q$) containing all harmonic modes (ℓ, m) such that $\ell_{\min}(q) \leqslant \ell \leqslant \ell_{\max}(q)$. If $n_q = \sum_{\ell=\ell_{\min}(q)}^{\ell_{\max}(q)} (2\ell+1)$ denotes the number of modes in the qth harmonic bin, then the empirical spectral matrix

$$\widehat{\mathbf{R}}_q = \frac{1}{n_q} \sum_{\ell=\ell_{\min}(q)}^{\ell_{\max}(q)} \sum_{m=-\ell}^{\ell} x(\ell,m) x(\ell,m)^\dagger \tag{8}$$

is the natural estimate of the average spectral matrix

$$\mathbf{R}_q = \frac{1}{n_q} \sum_{\ell=\ell_{\min}(q)}^{\ell_{\max}(q)} (2\ell+1)\mathbf{R}(\ell). \tag{9}$$

The latter inherits its structure from (7) as

$$\mathbf{R}_q = \mathbf{A}\mathbf{C}_q\mathbf{A}^\dagger + \mathbf{N}_q \tag{10}$$

with average spectral matrices $\mathbf{C}_q$ and $\mathbf{N}_q$ related to $\mathbf{C}(\ell)$ and $\mathbf{N}(\ell)$ as in definition (9).

3 SPECTRAL ESTIMATION AND COMPONENT SEPARATION WITH SMICA

The goal of our analysis is to identify and separate the components present in *WMAP* maps, to evaluate the amplitude of CMB anisotropies as a function of observation wavelength (as given by the corresponding column of $\mathbf{A}$), and to provide accurate estimates for power spectra of the CMB and other components. This section briefly describes a multidetector, multicomponent analysis method. It is a maximum-likelihood method based on a model of statistically independent components. Since it can be understood as a spectral matching technique, it is dubbed 'SMICA'. More details on SMICA can be found in Delabrouille et al. (2003).

3.1 Spectral matching

The SMICA analysis technique consists of minimizing a measure of the mismatch between the empirical covariance matrices $\widehat{\mathbf{R}}_q$ and their model counterparts $\mathbf{R}_q$. The minimization is conducted with respect to any relevant set of parameters describing the covariance matrices $\mathbf{R}_q$. The maximal parameter set is made of: the entries of the mixing matrix $\mathbf{A}$, the average power $[\mathbf{C}_q]_{cc}$ of the cth component in the qth multipole bin and the average power $[\mathbf{N}_q]_{ii}$ of the noise on the ith detector in the qth multipole bin.

One may choose to fix some of these quantities (prior knowledge) and to estimate the remaining ones, either freely or under some additional parametric constraints (see introduction to Section 4). In any case, denoting by θ a set of free parameters defining the values of $\mathbf{A}_{ic}$, $[\mathbf{C}_q]_{cc}$ and $[\mathbf{N}_q]_{ii}$, we obtain an estimate of θ by minimizing a joint spectral mismatch, quantified by a weighted sum

$$\Phi(\theta) = \sum_{q=1}^{Q} n_q \mathbf{D}(\widehat{\mathbf{R}}_q, \mathbf{R}_q(\theta)). \tag{11}$$

Any sensible measure $\mathbf{D}$ $(\ldots, \ldots)$ of matrix mismatch could be used to obtain a consistent estimate $\hat{\theta}$ of the θ parameter as $\hat{\theta} = \arg\min_\theta \Phi(\theta)$. We adopt

$$\mathbf{D}(\mathbf{R}_1, \mathbf{R}_2) = \frac{1}{2}\left[\mathrm{trace}\left(\mathbf{R}_1\mathbf{R}_2^{-1}\right) - \log\det\left(\mathbf{R}_1\mathbf{R}_2^{-1}\right) - N_d\right] \tag{12}$$

because then criterion (11) is, up to a constant, equal to minus the log likelihood of the data in a simple Gaussian isotropic model (see Delabrouille et al. 2003, for a derivation). Hence, minimizing criterion (11) is equivalent to maximizing the likelihood of this model. This fact guarantees good performance (at least for large n_q) when the data do come from an isotropic random field. Also, the connection with the likelihood criterion suggests a simple optimization strategy using the EXPECTATION-MAXIMIZATION (EM) algorithm. In practice, the minimization of the spectral mismatch (11) is achieved with the EM algorithm followed by a few steps of a descent method (the Broyden–Fletcher–Goldfarb–Shapiro algorithm) to speed-up the final convergence.

3.2 Error estimation

The SMICA estimator being a maximum-likelihood estimator, the asymptotic variance–covariance matrix of the estimates is given, when the model holds for some value θ_0 of the parameters, by

$$\mathrm{Cov}(\hat{\theta}) = \left\langle \left\{ (\hat{\theta} - \theta_0)(\hat{\theta} - \theta_0)^t \right\} \right\rangle \approx \mathbf{J}(\theta_0)^{-1}, \tag{13}$$

where the Fisher information matrix $\mathbf{J}(\theta_0)$ is, in our model,

$$[\mathbf{J}(\theta_0)]_{ij} = \frac{1}{2}\sum_q n_q \,\mathrm{trace}\left\{ \mathbf{R}_q^{-1}\frac{\partial \mathbf{R}_q}{\partial\theta_i}\mathbf{R}_q^{-1}\frac{\partial \mathbf{R}_q}{\partial\theta_j} \right\} \tag{14}$$

with all quantities evaluated at point θ_0. In practice, $\mathbf{J}(\theta_0)$ is approximated by $\mathbf{J}(\hat{\theta})$.

Departures from stationarity[4] and from Gaussianity do not bias the estimates of the spectral covariance matrices $\widehat{\mathbf{R}}_q$. Therefore, they do not introduce bias in the parameter estimates (at least at first order) even though they are likely to increase estimation error with respect to equations (13) and (14). The accuracy of the error bars prediction can be checked, thanks to simulations.

[4] In particular, as a consequence of *WMAP* scanning strategy, the noise variance per pixel on the observed maps is higher by a factor of the order of 4 around the ecliptic equator as compared to the polar regions.

The Galactic and point-source mask have the effect, to first order, of decreasing the effective number n_q of modes in each bin by a factor equal to the fraction of sky coverage. This is accounted for by multiplying every parameter error estimate by the inverse square root of this factor. This procedure has been validated with the help of numerous Monte Carlo simulations. We have found very good agreement even at low scales in spite of the fact that equations (13) and (14) are obtained in the asymptotic domain, that is, for large values of n_q.

3.3 Mismatch measure

The SMICA approach includes a built-in goodness of fit: the departure of the spectral statistics $\widehat{\mathbf{R}}_q$ from the best-fitting model of independent components is quantified by the divergence $\mathbf{D}(\widehat{\mathbf{R}}_q, \mathbf{R}_q(\hat{\theta}))$, which should be statistically small. For a known $N_d \times N_c$ mixing matrix, if the model of observations is correct, then $2n_q\mathbf{D}(\widehat{\mathbf{R}}_q, \mathbf{R}_q(\hat{\theta}))$ is asymptotically (i.e. for n_q large enough) distributed as a χ^2 with $N_d(N_d+1)/2 - (N_c + N_d)$ degrees of freedom. This value is obtained by subtracting the number of adjustable parameters per multipole bin (N_c auto-spectra plus N_d noise levels) from the $N_d(N_d+1)/2$ degrees of freedom of a symmetric matrix. In particular, for large enough n_q

$$\langle n_q \mathbf{D}(\widehat{\mathbf{R}}_q, \mathbf{R}_q(\hat{\theta}))\rangle = \frac{1}{2}\left[\frac{N_d(N_d+1)}{2} - (N_c + N_d)\right]. \tag{15}$$

3.4 Beam and coverage effects

We discuss the corrections needed to account for beam and coverage effects.

In the first approximation, if a mask covers a fraction α of the sky, an effective number αn_q should be used in place of n_q. However, since masking also introduces mode coupling, a better approximation is desired. We follow the Monte Carlo Apodised Spherical Transform Estimator (MASTER) formalism developed by Hivon et al. (2002). The idea is as follows: let $s(\theta, \phi)$ be an isotropic Gaussian random field with harmonic spectrum $c(\ell)$, of which only a masked version $\tilde{s}(\theta, \phi) = w(\theta, \phi)s(\theta, \phi)$ is observed. Denoting $\tilde{s}(\ell, m)$, the harmonic coefficients of $\tilde{s}(\theta, \phi)$, we have

$$\frac{1}{2\ell+1}\sum_{m=-\ell}^{m=\ell}\langle|\tilde{s}(\ell, m)|^2\rangle = \sum_{l'}\mathbf{M}_{\ell\ell'}c(\ell'), \tag{16}$$

where the coefficients $\mathbf{M}_{\ell\ell'}$ depend only on the mask (and thus can be computed independently of the data). Hence, if $\mathbf{M}_{\ell\ell'}$ is known, so is the bias introduced by the mask on the harmonic spectra.

In summary, we proceed as follows. In a first step, the input maps are masked, transformed to the spherical harmonic domain and brought to a common resolution (see Section 2.1). Next, bin-averaged empirical spectral matrices are computed according to equation (8) and a model of independent components is adjusted to them by minimizing (11). The resulting bin-averaged harmonic spectra of each component are then corrected by inverting the bin-averaged version of relation (16). This last stage also incorporates the correction of the common beam pattern.

3.5 Component map separation

Ideally, component maps would be estimated by applying a Wiener filter $\mathbf{W} = [\mathbf{A}^t\mathbf{N}^{-1}\mathbf{A} + \mathbf{C}^{-1}]^{-1}\mathbf{A}^t\mathbf{N}^{-1}$ to the observations. This solution maximizes the signal-to-noise ratio on each individual component map (here noise means detector noise plus other astrophysical

component emissions). In the limiting case, where noise is small as compared to component signals, $\mathbf{C}^{-1}$ is negligible and the Wiener filter yields unbiased (in the sense that $\mathbf{WA} = \mathbf{I}$) estimates of the maps. In poor signal-to-noise regimes, the signal is attenuated to suppress noise contamination in the reconstructed maps.

In practice, the Wiener filter is applied in the spherical harmonics space, using estimated values $\widehat{\mathbf{A}}$, $\widehat{\mathbf{N}}$ and $\widehat{\mathbf{C}}$ of the parameters. The harmonic coefficients of the estimated components are obtained as

$$\hat{s}(\ell, m) = \left[\widehat{\mathbf{A}}^{\mathrm{t}}\widehat{\mathbf{N}}_q^{-1}\widehat{\mathbf{A}} + \widehat{\mathbf{C}}_q^{-1}\right]^{-1}\widehat{\mathbf{A}}^{\mathrm{t}}\widehat{\mathbf{N}}_q^{-1}x(\ell, m) \qquad (17)$$

when $\ell_{\min}(q) \leqslant \ell \leqslant \ell_{\max}(q)$.

4 APPLICATION AND RESULTS

We now present a SMICA analysis of *WMAP* data. The two data sets described in Section 2.1 (map set I corresponding to sky regions outside of Kp2 mask, and map set II corresponding to Galactic latitudes higher than 40°, with the strongest point sources masked in both cases) are used for two independent analyses.

In a preliminary analysis (whose quantitative details are not reported here), we looked for the total number of components required by the map set I without imposing constraints either on the amplitude of the estimated components or on their spatial power spectra. In this totally blind analysis, we found two significant components. The first component, dominant in all the channels, is clearly identified as CMB. The second, weaker by several orders of magnitude and essentially significant in the Q band (it is detected to a lesser extent in the V and W bands) is thought to be a mixture of residual Galactic emissions and unresolved point sources. These last two processes cannot be reliably separated without introducing additional constraints because of nearly proportional mixing matrix columns (both components dominate in the Q band and are almost negligible in the others).

In order to differentiate between residual Galactic emission and point sources, we need to introduce some physical knowledge in the form of constraints on the system. Therefore, in most of the subsequent analyses, unless explicitly stated otherwise, we adjust a model with three components, one of them being strongly constrained to capture point-source contributions as follows. The emission spectrum of point sources is well described, at *WMAP* frequencies, by a power law with a spectral index $\beta \approx -2$ (Section 2.3) and their spatial power spectrum is expected to be almost flat since the effect of clustering is negligible in practice at radio frequencies (González-Nuevo, Toffolatti & Argüeso 2005). Hence, for one component, meant to be residual point-source emission, we fix the mixing parameters (the column of the mixing matrix) to $\mathbf{A}_{i,\mathrm{PS}} = (\nu_i/\nu_0)^{-2}$ in Rayleigh–Jeans (RJ) temperature units, and we constrain the harmonic power spectrum to be flat. Only one parameter, its amplitude, is left free to match the contribution of this component.

In summary, we match spectral matrices with three components. For two of them, meant to be CMB anisotropies and residual Galactic emission, no constraint on parameters is enforced (both the mixing parameters and the power spectra are determined exclusively from the data). The last component is constrained to have the emission law and spectral shape of point sources; only its amplitude is adjusted (but see Fig. 7 and the related comments). Finally, regarding noise, the average noise power is freely estimated in each map and each multipole bin.

The analysis is performed using the same multipole bins than those considered by the *WMAP* team, except for the first bin regrouping multipoles $\ell = 2$ and $\ell = 3$. We consider 37 bins in total, ranging from $\ell = 2$ to $\ell = 900$.

4.1 CMB anisotropies

Fig. 1 shows the estimated CMB power spectrum after correcting for partial coverage and beam and pixel transfer functions. It displays a peak around $\ell = 200$ (first acoustic peak) and a second peak around $\ell = 550$, both compatible with the measurement announced by the *WMAP* team.

SMICA and *WMAP*-team power-spectrum estimations show an excellent agreement for most multipoles. For multipoles between $\ell = 2$ and $\ell = 290$, the difference between the two power spectra is much smaller than the error bars (except for bins centred on $\ell = 190$ and $\ell = 210$ where the difference is of the order of the error bars), but is larger than statistical errors after removing cosmic variance contribution. This can be explained (at least partially) by the small differences in the sky coverage due to the apodization procedure we apply on the maps. For larger multipoles, the two estimates show somewhat larger differences which may be due, in part, to the two different weighting schemes used by the two methods for $\ell > 200$. For SMICA, no weighting of the pixels depending on the noise variance per pixel is applied prior to the analysis. On the contrary, the *WMAP* team applies different weighting schemes for $\ell > 200$ (a weighting proportional to 1/noise^2 for $\ell > 450$ and a transition weighting for $200 < \ell < 450$). Hence, discrepancies between the two estimates are expected to be larger for $\ell > 200$ since the two data sets are not quite identical. This may account for the small observed

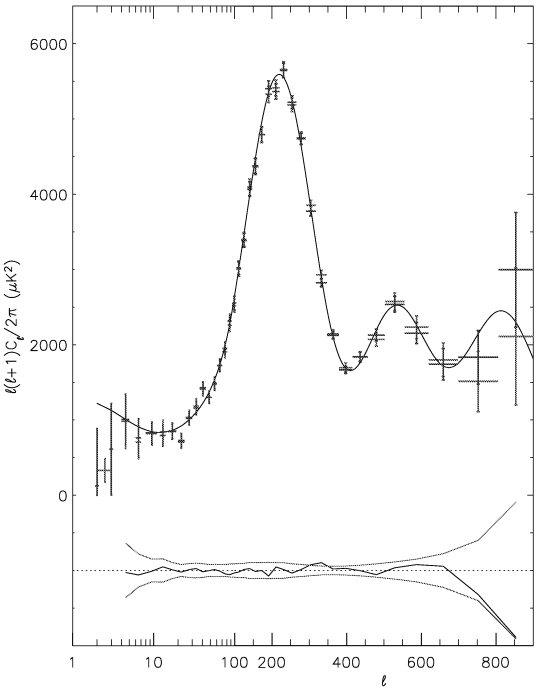

Figure 1. The CMB spatial power spectrum measured with SMICA (in red) as compared to the published *WMAP* 1-yr spectrum (in blue). The error bars from SMICA are computed from the Fisher information matrix using the estimated parameters (see Section 3.2). This explains the small error bar on the first bin of the SMICA estimate. We also plot the difference between power spectra for better comparison. The red curves correspond to $\pm 1\sigma$ error bars on the power spectrum obtained with SMICA.

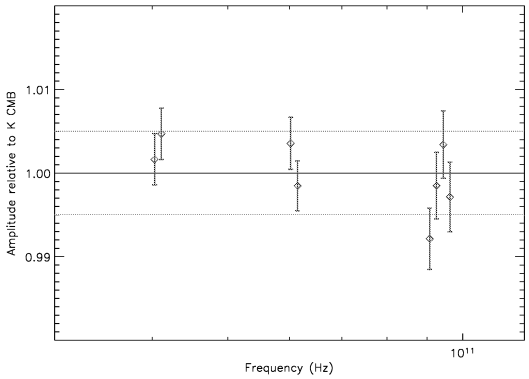

Figure 2. Measured amplitude of CMB fluctuations in each detector (in red) relative to temperature fluctuation units as given by the calibration on the dipole. The amplitude of the fluctuations is normalized to one on average. Data points at the same frequency band have been slightly offset in abscissa for readability. Blue lines delimit calibration 1σ errors provided by the *WMAP* team. The errors on estimated mixing parameters are statistical errors computed from the Fisher information matrix at convergence. In order to provide an error bar on every CMB mixing parameter, errors are not marginalized on CMB power-spectrum estimate (there is a degeneracy between power-spectrum amplitude and mixing parameters normalization).

differences. We note in the passing that the small dip at the top of the first acoustic peak in the *WMAP*-team estimate has disappeared in the SMICA estimate.

Fig. 2 shows the estimated amplitude of CMB anisotropies for all the observation channels, as given by the CMB column of the estimated mixing matrix $\hat{A}$. We find an emission law compatible with the expected derivative of a blackbody, to excellent accuracy. A fit of the form ν^α gives $\alpha = -0.0067 \pm 0.0058$ compatible with 0 at about 1.15σ. Refined calibration and systematics testing, as well as the second-year data, will reduce the error bar and clarify the significance of a possible deviation from the expected blackbody derivative. Note that, given the error bars, *the accuracy of the measurement of the CMB emission law is limited by detector calibration uncertainty rather than intrinsic statistical errors!* The present measurement shows that the emission law of the anisotropies is the same as that of the dipole, which is itself known (under the assumption that it is essentially due to a kinetic effect) to be the derivative with respect to the temperature of the CMB blackbody emission measured with FIRAS.

Fig. 3 displays a reconstruction of the CMB anisotropy map by Wiener filtering (equation 17) using the parameters estimated with SMICA. The now familiar CMB anisotropy pattern is clearly visible.

We have compared our recovered CMB map with other available CMB maps from *WMAP*: the Internal Linear Combination (ILC) map published by the *WMAP* team (Bennett et al. 2003b), the combined map used for non-Gaussianity analysis (e.g. Komatsu et al. 2003) and the two maps (*cleaned* and *Wiener filter*) obtained by Tegmark (Tegmark, de Oliveira-Costa & Hamilton 2003).

As seen in Fig. 4, we find very high correlation (≈99 per cent) with the two maps proposed by Tegmark as well as with the map used for non-Gaussianity studies up to $\ell \approx 200$. The correlation slightly decreases down to ≈95 per cent for multipoles larger than 200 (see Fig. 4). The cross-correlation with the ILC map is also around 99 per cent, but only up to multipoles $\ell \approx 20$. For smaller scales, the correlation with the ILC map decreases down to ≈60 per cent at $\ell \approx 200$ and then it increases up to ≈90 per cent at the smallest scales. The fact that the correlation with the ILC is smaller than with the other CMB maps is not surprising since, as explained by the *WMAP* team, the ILC was developed for foreground analyses and it is far from being the best CMB reconstruction (Bennett et al. 2003b).

We have also tested possible contamination caused by unsubtracted foreground emissions by cross-correlating our CMB reconstruction with templates of different Galactic emissions (synchrotron, thermal dust and free–free). We find no significant contamination: the correlation level is below the dispersion of the casual correlations between those templates and CMB Gaussian simulations (5–10 per cent).

4.2 Residual Galactic emission

Table 1 gives the emission law (the column of the mixing matrix) estimated for the second component in the map set I. Parameters are rescaled to normalize to unity in the Q1 band (where the component dominates) in order to fix the degeneracy between mixing parameter normalization and power-spectrum amplitude. Although much lower than the CMB, this second component is clearly detected in

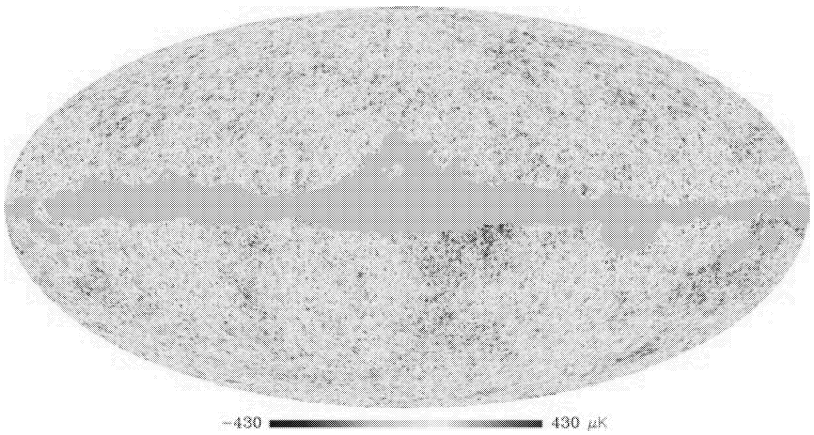

Figure 3. Map of CMB fluctuations obtained after Wiener filtering of the data using parameters estimated with SMICA.

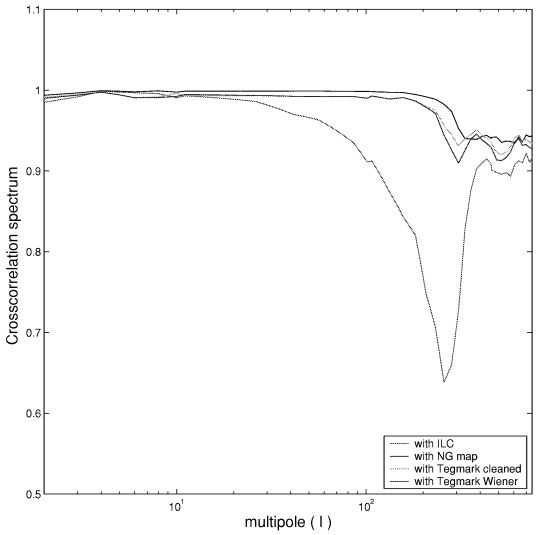

Figure 4. Cross-correlation spectra between our CMB map and other available CMB maps from the *WMAP* data: the ILC map published by the *WMAP* team (Bennett et al. 2003b), the combined map used for non-Gaussianity studies (e.g. Komatsu et al. 2003) and the two maps (*cleaned* and *Wiener filter*) obtained by Tegmark et al. (2003).

Table 1. Estimated relative amplitude of the second component in each of the observed maps in RJ temperature units and associated errors. The normalization of parameters is fixed with respect to Q1 map. Error on parameters is correlated at the 20-per cent level.

Detector	Q1	Q2	V1	V2	W1	W2	W3	W4
Amplitude (K/K)	1	0.85	0.04	0.02	−0.13	−0.27	−0.22	−0.16
Error (K/K)	0	0.08	0.07	0.07	0.08	0.09	0.09	0.09

the Q band (at about 10 standard deviations). Its mixing parameters are compatible with zero in V bands, and are systematically negative and detected at about two standard deviations on average, in each individual map of the W bands except W1. Mixing parameters for radiometers observing at the same frequency are compatible with a constant value, as expected for an astrophysical component. The amplitude of the component is at least 10 times larger in the Q band than in the V band (in RJ temperature units), and is larger in absolute value in the W band than in the V band. This behaviour is not a priori excluded if the component originates from residual Galactic emission (mainly synchrotron and dust correlated emission) after Galactic foreground removing operation by the *WMAP* team. In that case, mixing parameters of two different frequency bands may have opposite signs depending on the sign of the error on the parameters of the template fit.

Fig. 5 shows the map of the residual component obtained by Wiener filtering using estimated parameters. We can note a bright structure close to the Galactic Centre at the edges of the Galactic mask, which we identify as a residue from foreground subtraction in the *Ophiuchus complex*. Other residual structures associated to the *North polar spur*, the *Gum nebula*, the *Orion-Eridanus bubble* and the *Taurus* region can also be identified, suggesting that the emission of these regions does not perfectly match the model used by *WMAP* team.

We have found a significant correlation (≈40 per cent) between our second component and the *WMAP* synchrotron emission estimation at the Q band (using the Maximum Entropy Method, see Bennett et al. 2003b), which supports the Galactic origin of our second component.

As can be seen from the Wiener map (and as expected for Galactic emission), the component looks very non-stationary over the sky. As the stationarity of components is assumed in our model, errors on mixing parameters probably are somewhat underestimated but we do not expect this to change our interpretation.

Fig. 6 shows the estimated power spectra of the second component in both the map sets: map set I and map set II. For the estimation with the map set II, we have fixed the mixing parameters of the residual component, as well as the amplitude of point-source power spectrum to the values obtained with the map set I. This allows us

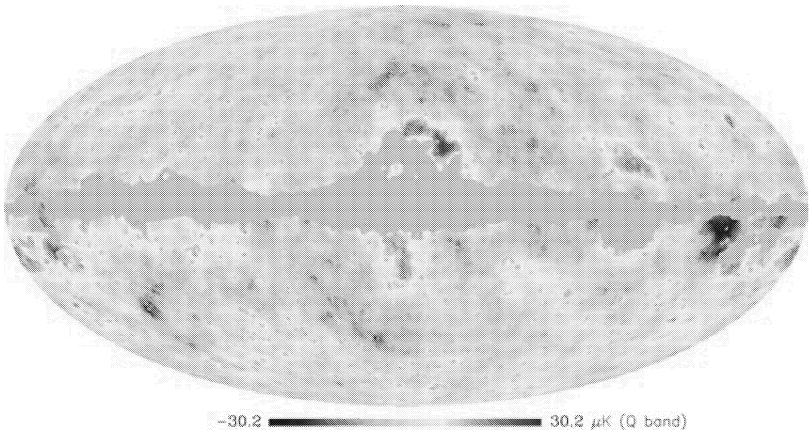

Figure 5. Map of the residual component as 'seen' in the Q band, obtained by Wiener filtering using estimated parameters.

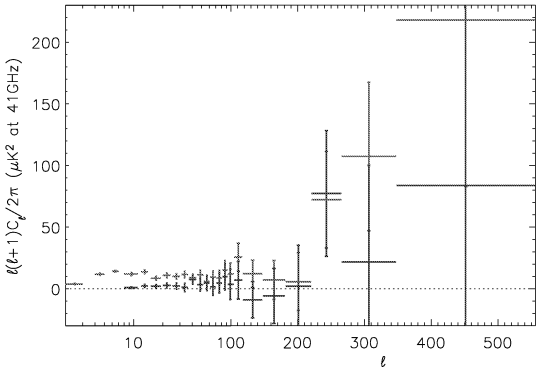

Figure 6. Estimated power spectrum of the second component from SMICA analysis in map set I (red ink) and comparison with the power spectrum estimated at Galactic latitudes higher than 40° (map set II, blue ink). Power spectra amplitudes are rescaled on the Q band. No positivity constraints are enforced for parameter estimates, making it easy to check their compatibility with zero. Cosmic variance, naturally included in error bar computation from the Fisher information matrix, has been removed afterwards from the error estimates. Estimated power spectra are rebinned for readability. Due to the lower-sky coverage fraction for map set II (30 per cent), the large angular scales are poorly constrained. We then restrained the analysis to multipoles $\ell > 10$ only.

to compare the two power-spectra estimates of a component with a fixed effective emission law. The estimated power spectrum of the residual component in map set I is measured with high significance for multipoles between $\ell = 2$ and $\ell \simeq 150$, and forms a plateau ($\ell^2 c(\ell) \approx$ constant) with an amplitude ≈10–12 μK^2 in the Q band. For higher multipoles, the beam transfer function of the Q-band detectors strongly suppresses the signal, and the sensitivity is not sufficient for accurate measurement of the component. Nevertheless, the last three bins show weak incompatibilities with 0 at (1.5–2)σ. Errors on those three parameters are strongly correlated (to ≈50 per cent due to the anticorrelation of those parameters with the amplitude of the point sources emission), so there is no clear evidence of detection for high multipoles.

The power of the residual component for angular scales larger than 1° to 2° is clearly reduced at Galactic latitude higher than 40°. It remains marginally detectable even though it is reduced by a factor greater than 4 for ℓ between 10 and 30.

We find that the power of the remaining Galactic foreground contamination in *WMAP* maps (outside of Kp2 mask) is about 1 per cent of the CMB anisotropy variance at large angular scales ($\ell < 100$) at 41 GHz. This result is in agreement with the *WMAP*-team estimate, based on correlation measurement using external foreground templates (Bennett et al. 2003b). The power of the residual component is less than 0.2 per cent of the CMB variance at 61 and 94 GHz.

4.3 Unresolved point-source emissions

In our analysis, the third component is rigidly constrained. As explained in the introduction to this section, the mixing parameters and the shape of the power spectrum are fixed to values expected for unresolved point-source emission, leaving only the overall amplitude to be determined from the data by spectral matching. We find $\mathbf{C}_{\rm PS}(\ell) = (9.2 \pm 5.0) \times 10^{-3}$ μK^2 at 41 GHz. This value is marginally compatible with the *WMAP*-team estimate (see Komatsu et al. 2003, for a discussion for the expected contribution of unresolved point sources to the CMB power spectrum, for different masks and flux limits) and model predictions (Argüeso et al. 2003): $(15.5 \pm 1.7) \times 10^{-3}$ μK^2.

The large error bar on our estimate is due to the difficulty of discriminating components with similar spectral characteristics. In this experiment, the residual Galactic component and the point-source component have similar effective emission laws (mixing matrix elements) and both components dominate in the Q band and can not be accurately estimated in V and W bands. So, some power for high multipoles can be exchanged between the second and the third components without significantly modifying the likelihood of the model.

We further investigate the distribution of the third component by performing two additional spectral matches on map set II. Neglecting residual Galactic emissions (we have seen in the previous section that residual Galactic emission is clearly reduced at high Galactic latitude), we now fit a two-component model (as opposed to previous matches, build with three components) with two different constraint sets. In a first match, all parameters related to point sources emission law and power spectra are fixed, except the amplitude, which is fitted. We find the amplitude of the power spectrum to be: $\mathbf{C}_{\rm PS}(\ell) = (11.3 \pm 3.5) \times 10^{-3}$ μK^2 at 41 GHz, in better agreement with the value already reported of $(15.5 \pm 1.7) \times 10^{-3}$ μK^2. In a second match, we relax all constraints on the shape of the power spectrum to obtain estimates of the power spectrum in every multipole bin. The resulting power spectrum of unresolved point sources is displayed in Fig. 7. Parameters are clearly incompatible with zero for most of the multipoles (assuming a priori a smooth power spectrum). A good compatibility with the model $\mathbf{C}_{\rm PS}(\ell) = 11.3 \times 10^{-3}$ μK^2 (41 GHz) is observed. If we readjust the model of the power spectrum to the estimated parameters using a simple χ^2, we obtain a similar value for the amplitude. Nevertheless, a weak excess of power can be seen for the lowest multipoles ($\ell < 50$) possibly due to a remaining Galactic contamination at high Galactic latitudes.

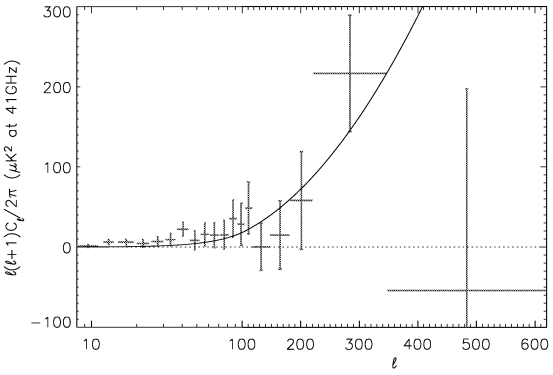

Figure 7. Power spectrum of unresolved point sources emission estimated with SMICA, assuming two components in the map set II (red). Mixing parameters of point-source emission has been fixed for the analysis. No constraint of positivity is given for parameter estimates allowing to check easily their compatibility with zero. Cosmic variance has been removed afterwards from the error estimates. Estimated power spectra are rebinned for readability. The black curve corresponds to the model of point-source power spectrum $\mathbf{C}_{\rm PS}(\ell) =$ constant with an amplitude estimated from the semiblind approach of 11.3×10^{-3} μK^2 (see text for details).

4.4 Goodness of fit

In this section, we briefly examine the fit of the best models to the data across multipole bins by plotting the weighted mismatch $n_q \mathbf{D}(\widehat{\mathbf{R}}_q, \mathbf{R}_q(\hat{\theta}))$ (see equations 11 and 12) against the bin index q. If the model of independent stationary component holds, the expected value of this measure of mismatch is given, for n_q large enough, by equation (15). In our plots, however, we use Monte Carlo simulations to have an estimate of the distribution of the mismatch, valid even in the non-asymptotic regime. We report goodness of fit of adjusted models in two cases: a one-component model and a three-component model.

Fig. 8 shows that the one-component model is clearly incompatible with the data for $\ell < 60$. It also shows that the fit obtained with three components is very satisfactory for most of the multipoles although small discrepancies remain, in particular for ℓ between 10 and 25. We interpret this as a clear indication that residual Galactic emission is present in the data for low multipoles.

We can investigate the origin of the remaining discrepancies by looking at the spectral mismatch between *pairs* of detectors. Fig. 9

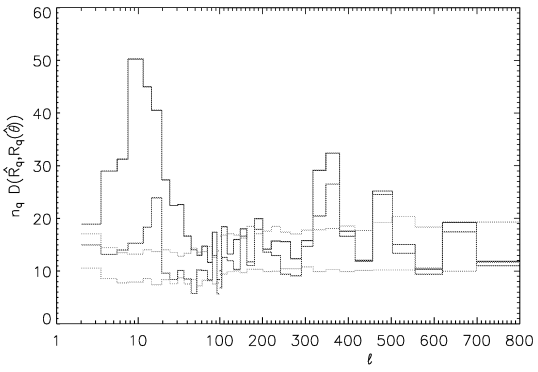

Figure 8. Spectral mismatch $n_q \mathbf{D}(\widehat{\mathbf{R}}_q, \mathbf{R}_q(\hat{\theta}))$ for map set I, with three components (red) and one component (blue). The green curves are the boundaries of the 68-per cent goodness of fit interval estimated using simulations. For three components, the fit is very satisfactory for most of the multipole bins (see text).

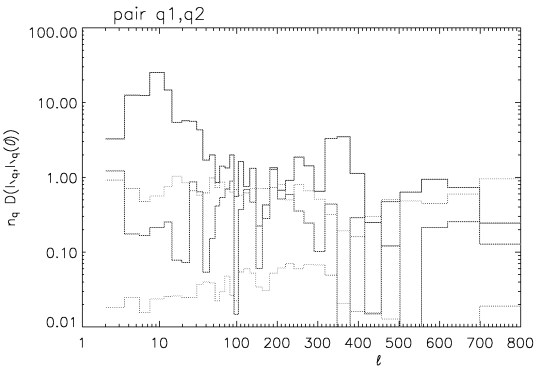

Figure 9. Spectral mismatch $n_q \mathbf{D}(\widehat{\mathbf{R}}_q, \mathbf{R}_q(\hat{\theta}))$ for the detector pair (Q1,Q2) only, with three components (red) and one component (blue). The green curves are the boundaries of the 68-per cent interval estimated using simulations. Note the logarithmic scale and thus the very significant reduction of the mismatch when three components are considered.

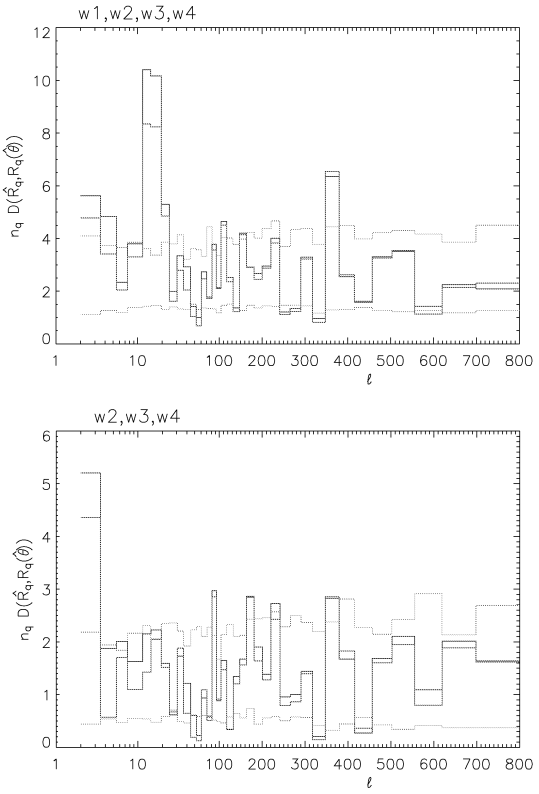

Figure 10. Spectral mismatch $n_q \mathbf{D}(\widehat{\mathbf{R}}_q, \mathbf{R}_q(\hat{\theta}))$ with three components (red) and one component (blue). Top: mismatch for all four *W*-band detectors; bottom: for the last three *W*-band detectors (W1 excluded).

shows the goodness of fit between the individual pair of detectors (Q1,Q2), assuming either one or three components. The misfit for the one-component model is now even more obvious (as compared to the global mismatch involving all detectors), as expected since the *Q* band is where the Galactic residual dominates.

As the second component is detected in the W channel as well, we also looked at the fit of one-component and three-component models for all W detectors together and for the set of W2, W3 and W4 (discarding W1). For both the figures, the goodness of fit is significantly better for three components than for a unique component for low multipoles.

A significant excess remains, which is probably due to the fine departure of the residual Galactic emission from the single template assumption. Fig. 10, however, rather points to remaining systematics in the W1 channels since the mismatch is significantly reduced when excluding the W1 detector.

This incompatibility, however, is small enough so that the CMB power spectrum is not affected because the errors for the lowest multipoles are dominated by cosmic variance.

5 CONCLUSIONS

We have performed blind and semiblind multicomponent analysis of the first-year *WMAP* data. We used the eight foreground-cleaned

high frequency maps (Q1 to W4) provided by the *WMAP* collaboration. Our analysis uses SMICA, a maximum-likelihood spectral matching method. Three significant astrophysical components (i) the CMB anisotropies, (ii) a residual Galactic emission and (iii) unresolved point-source emissions are jointly characterized in the foreground-cleaned maps after masking the strongest point sources and the Galactic plane using Kp2 mask. No significant thermal SZ emission is found with the present study, in agreement with the *WMAP* team (Bennett et al. 2003b) and Huffenberger et al. (2004).

Blind analysis allows us to estimate the power spectrum of CMB anisotropies as well as their amplitude across frequency channels confirming their cosmological nature. Our power-spectrum estimate is in excellent agreement with the *WMAP*-team estimate. We show that the measured emission law of CMB anisotropies at *WMAP* frequencies is compatible with the derivative of a blackbody, as expected for temperature fluctuations. The statistical errors on parameters related to the amplitude of the anisotropies are about 0.3 per cent, and are smaller than the calibration errors (0.5 per cent) on dipole modulation. Conversely, if CMB anisotropies are assumed to be pure temperature fluctuations, then the estimation of CMB amplitude across channels provides a relative calibration across frequency bands at a better precision than dipole calibration.

The second estimated component, corresponding to a weak residual Galactic emission, is mainly concentrated in Q-band maps outside of the Kp2 mask. We believe that this component results mainly from spatial variations of the difference between Haslam map (used as a synchrotron template for the subtraction) and synchrotron emission at *WMAP* frequencies. This component is weak compared to CMB anisotropies. The estimated power spectrum is about $\ell(\ell+1)\mathbf{C}(\ell)/2\pi \approx 10$–$12\ \mu\mathrm{K}^2$ for $\ell < 100$ in Q band and less than $2\ \mu\mathrm{K}^2$ in V and W band. Those estimates are compatible with *WMAP*-team estimates of foreground contamination. Finally, much of the power from this residual large-scale component disappears for Galactic latitude higher than 40°.

The third component corresponds to residual point sources emission. By fixing the parameters related to the emission law of point sources (we assume $(\nu/\nu_0)^{-2}$) and to the power spectrum (flat power spectrum), we estimate the amplitude of unresolved point-source power spectrum. We find at high Galactic latitude: $\mathbf{C}(\ell) = (11.3 \pm 3.7) \times 10^{-3}\ \mu\mathrm{K}^2$ at 41 GHz compatible with the *WMAP*-team estimation. We also provide an estimate of the power spectrum of the point sources at high Galactic latitude.

The goodness of fit of the three-component model is excellent, except for a very small discrepancy around $\ell \approx 20$, which is likely to be attributed to a systematic in W1. This inconsistency has no impact on the CMB power-spectrum estimate (because errors are dominated by cosmic variance), but could affect the estimates of weak components in data.

ACKNOWLEDGMENTS

This work was supported by the Canadian Natural Sciences and Engineering Research Council and by the French Ministry of Research. GP would like to thank Mark Halpern for useful discussions. JFC, JD and PV kindly thank financial support from a joint France–Spain project (Programmes d'Actions Intégrées Picasso, Acción Integrada HF03-163). We acknowledge the use of the Legacy Archive for Microwave Background data analysis (LAMBDA). Some results of this paper have been derived using the HEALPix (Górski et al. 1998) package. We acknowledge the use of the software package CMBFAST (http://www.cmbfast.org) developed by U. Seljak and M. Zaldarriaga.

REFERENCES

Argüeso F., González-Nuevo J., Toffolatti L., 2003, ApJ, 598, 86
Bennett C. L. et al., 2003a, ApJS, 148, 1
Bennett C. L. et al., 2003b, Wollack E., ApJS, 148, 97
Bouchet F. R., Gispert R., 1999, New Astron., 4, 443
Cardoso J.-F., Snoussi H., Delabrouille J., Patanchon G., 2002, EUSIPCO02 Conf. Proc., 1, 561
Delabrouille J., Cardoso J.-F., Patanchon G., 2003, MNRAS, 346, 1089
Finkbeiner D. P., 2003, ApJS, 146, 407
Finkbeiner D. P., Davis M., Schlegel D. J., 1999, ApJ, 524, 867
Fixsen D. J., 2003, ApJ, 594, L67
González-Nuevo J., Toffolatti L., Argüeso F., 2005, ApJ, 621, 1
Górski K. M., Hivon E., Wandelt B. D., 1998, in Banday A. J., Sheth R. S., Da Costa L., eds, Proc. MPA/ESO Cosmology Conf., Evolution of Large-Scale Structure. Print Partners Ipskamp, Enschede, p. 37
Haslam C. G. T., Stoffel H., Salter C. J., Wilson W. E., 1982, A&AS, 47, 1
Hinshaw G. et al., 2003, ApJS, 148, 135
Hivon E., Górski K. M., Netterfield C. B., Crill B. P., Prunet S., Hansen F., 2002, ApJ, 567, 2
Huffenberger K. M., Seljak U., Makarov A., 2004, Phys. Rev. D, 70, 063002
Jungman G., Kamionkowski M., Kosowsky A., Spergel D. N., 1996, Phys. Rev. D, 54, 1332
Komatsu E. et al., 2003, ApJS, 148, 119
Patanchon G., Snoussi H., Cardoso J.-F., Delabrouille J., 2003, PSIP03 Proc., 1, 17
Schlegel D. J., Finkbeiner D. P., Davis M., 1998, ApJ, 500, 525
Smoot G. F. et al., 1992, ApJ, 396, L1
Spergel D. N. et al., 2003, ApJS, 148, 175
Tegmark M., de Oliveira-Costa A., Hamilton A., 2003, PRD, 68, 123523
Toffolatti L., Argueso Gomez F., de Zotti G., Mazzei P., Franceschini A., Danese L., Burigana C., 1998, MNRAS, 297, 117
Zaldarriaga M., Seljak U., 2000, ApJS, 129, 431

This paper has been typeset from a TEX/LATEX file prepared by the author.

A&A 503, 691–706 (2009)
DOI: 10.1051/0004-6361/200911624

Astronomy & Astrophysics

Measuring the tensor to scalar ratio from CMB B-modes in the presence of foregrounds⋆

M. Betoule[1], E. Pierpaoli[2], J. Delabrouille[1], M. Le Jeune[1], and J.-F. Cardoso[1]

[1] AstroParticule et Cosmologie (APC), CNRS: UMR 7164, Université Denis Diderot, Paris 7, Observatoire de Paris, France
e-mail: betoule@apc.univ-paris7.fr
[2] University of Southern California, Los Angeles, CA 90089-0484, USA

Received 7 January 2009 / Accepted 7 May 2009

ABSTRACT

Aims. We investigate the impact of polarised foreground emission on the performances of future CMB experiments aiming to detect primordial tensor fluctuations in the early universe. In particular, we study the accuracy that can be achieved in measuring the tensor-to-scalar ratio r in the presence of foregrounds.
Methods. We designed a component separation pipeline, based on the S method, aimed at estimating r and the foreground contamination from the data with no prior assumption on the frequency dependence or spatial distribution of the foregrounds. We derived error bars accounting for the uncertainty on foreground contribution. We used the current knowledge of galactic and extra-galactic foregrounds as implemented in the Planck sky model (PSM) to build simulations of the sky emission. We applied the method to simulated observations of this modelled sky emission, for various experimental setups. Instrumental systematics are not considered in this study.
Results. Our method, with Planck data, permits us to detect $r = 0.1$ from B-modes only at more than 3σ. With a future dedicated space experiment, such as EPIC, we can measure $r = 0.001$ at $\sim 6\sigma$ for the most ambitious mission designs. Most of the sensitivity to r comes from scales $20 \leq \ell \leq 150$ for high r values, shifting to lower ℓ's for progressively smaller r. This shows that large-scale foreground emission does not prevent proper measurement of the reionisation bump for full sky experiments. We also investigate the observation of a small but clean part of the sky. We show that diffuse foregrounds remain a concern for a sensitive ground-based experiment with a limited frequency coverage when measuring $r < 0.1$. Using the Planck data as additional frequency channels to constrain the foregrounds in such ground–based observations reduces the error by a factor two but does not allow detection of $r = 0.01$. An alternate strategy, based on a deep field space mission with a wide frequency coverage, would allow us to deal with diffuse foregrounds efficiently, but is in return quite sensitive to lensing contamination. In contrast, we show that all-sky missions are nearly insensitive to small-scale contamination (point sources and lensing) if the statistical contribution of such foregrounds can be modelled accurately. Our results do not significantly depend on the overall level and frequency dependence of the diffused foreground model, when varied within the limits allowed by current observations.

Key words. cosmology: cosmic microwave background – cosmology: cosmological parameters – cosmology: observations

1. Introduction

After the success of the WMAP space mission in mapping the cosmic microwave background (CMB) temperature anisotropies, much attention now turns towards the challenge of measuring CMB polarisation, in particular pseudo-scalar polarisation modes (the B-modes) of primordial origin. These B-modes offer one of the best options for constraining inflationary models (Seljak & Zaldarriaga 1997; Hu & White 1997; Kamionkowski et al. 1997; Kamionkowski & Kosowsky 1998; Baumann & Peiris 2008).

First polarisation measurements have already been obtained by a number of instruments (Kovac et al. 2002; Sievers & CBI Collaboration 2005; Page et al. 2007), but no detection of B-modes has been claimed yet. While several ground-based and balloon-borne experiments are already operational, or under construction, no CMB-dedicated space-mission is planned after Planck at the present time: whether there should be one for CMB B-modes, and how it should be designed, are still open questions.

As CMB polarisation anisotropies are expected to be significantly smaller than temperature anisotropies (a few per cent at most), improving detector sensitivities is the first major challenge towards measuring CMB polarisation B-modes. It is not, however, the only one. Foreground emissions from the galactic interstellar medium (ISM) and from extra-galactic objects (galaxies and clusters of galaxies) superimpose to the CMB. Most foregrounds are expected to emit polarised light, with a polarisation fraction typically comparable to or larger than that of the CMB. Component separation (disentangling CMB emission from all these foregrounds) is needed to extract cosmological information from observed frequency maps. The situation is particularly severe for the B-modes of CMB polarisation, which will be, if measurable, subdominant on every scale and at every frequency.

The main objective of this paper is to evaluate the accuracy with which various upcoming or planned experiments can measure the tensor-scalar ratio r (see Peiris et al. (2003) for a precise definition) in the presence of foregrounds. This problem has been addressed before: Tucci et al. (2005) investigate the lower bound for r that can be achieved considering a simple foreground cleaning technique, based on the extrapolation of

⋆ Appendices are only available in electronic form at http://www.aanda.org

Article published by EDP Sciences

foreground templates and subtraction from a channel dedicated to CMB measurement; Verde et al. (2006) assume foreground residuals at a known level in a cleaned map, treat them as additional Gaussian noise, and compute the error on r due to such excess noise; Amblard et al. (2007) investigate how best to select the frequency bands of an instrument and how to distribute a fixed number of detectors among them, to maximally reject galactic foreground contamination. This analysis is based on an internal linear combination cleaning technique similar to the one of Tegmark et al. (2003) on WMAP temperature anisotropy data. The last two studies assume somehow that the residual contamination level is perfectly known – information that is used to derive error bars on r.

In this paper, we relax this assumption and propose a method for estimating the uncertainty on residual contamination from the data themselves, as would be the case for real data analysis. We test our method on semi-realistic simulated data sets, including CMB and realistic foreground emission, as well as simple instrumental noise. We study a variety of experimental designs and foreground mixtures. Alternative approaches to the same question are also presented in Dunkley et al. (2008a) and Baumann et al. (2008).

This paper is organised as follows: the next section (Sect. 2) deals with polarised foregrounds and presents the galactic emission model used in this work. In Sect. 3, we propose a method, using the most recent version of the S component separation framework (Cardoso et al. 2008), for providing measurements of the tensor to scalar ratio in the presence of foregrounds. In Sect. 4, we present the results obtained by applying the method to various experimental designs. Section 5 discusses the reliability of the method (and of our conclusions) against various issues, in particular modelling uncertainty. Main results are summarised in Sect. 6.

2. Modelling polarised sky emission

Several processes contribute to the total sky emission in the frequency range of interest for CMB observation (typically between 30 and 300 GHz). Foreground emission arises from the galactic interstellar medium (ISM), from extra-galactic objects, and from distortions of the CMB itself through its interaction with structures in the nearby universe. Although the physical processes involved and the general emission mechanisms are mostly understood, specifics of these polarised emissions in the millimetre range remain poorly known as few actual observations, on a significant enough part of the sky, have been made.

Diffuse emission from the ISM arises through synchrotron emission from energetic electrons, through free-free emission, and through grey-body emission of a population of dust grains. Small spinning dust grains with a dipole electric moment may also emit significantly in the radio domain (Draine & Lazarian 1998). Among those processes, dust and synchrotron emissions are thought to be significantly polarised. Galactic emission also includes contributions from compact regions such as supernovae remnants and molecular clouds, which have specific emission properties.

Extra-galactic objects emit via a number of different mechanisms, each of them having its own spectral energy distribution and polarisation properties.

Finally, the CMB polarisation spectra are modified by the interactions of the CMB photons on their way from the last scattering surface. Reionisation, in particular, re-injects power in polarisation on large scales by late-time scattering of CMB photons. This produces a distinctive feature, the reionisation bump, in the CMB B-mode spectrum at low ℓ. Other interactions with the latter universe, and in particular lensing, contribute to hinder the measurement of the primordial signal. The lensing effect is particularly important on smaller scales as it converts a part of the dominant E-mode power into B-mode.

In the following, we review the identified polarisation processes and detail the model used for the present work, with a special emphasis on B-modes. We also discuss main sources of uncertainty in the model, as a basis for evaluating their impact on the conclusions of this paper.

Our simulations[1] are based on the PSM, a sky emission simulation tool developed by the Planck collaboration for prelaunch preparation of Planck data analysis (Delabrouille et al. 2009). Figure 1 gives an overview of foregrounds as included in our baseline model. Diffuse galactic emission from synchrotron and dust dominates at all frequencies and on all scales, with a minimum (relative to CMB) between 60 and 80 GHz, depending on the galactic cut. Contaminations by lensing and a point source background are lower than primordial CMB for $r > 0.01$ and for $\ell < 100$, but should clearly be taken into account in attempts to measure $r < 0.01$.

2.1. Synchrotron

Cosmic ray electrons spiralling in the galactic magnetic field produce highly polarised synchrotron emission (e.g. Rybicki & Lightman 1979). This is the dominant contaminant of the polarised CMB signal at low frequency ($\lesssim$80 GHz), as can be seen in the right panel of Fig. 1. In the frequency range of interest for CMB observations, measurements of this emission have been provided, both in temperature and polarisation, by WMAP (Page et al. 2007; Gold et al. 2008). The intensity of the synchrotron emission depends on the cosmic ray density n_e, and on the strength of the magnetic field perpendicularly to the line of sight. Its frequency scaling and its intrinsic polarisation fraction f_s depend on the energy distribution of the cosmic rays.

2.1.1. Synchrotron emission law

For electron density following a power law of index p, $n_e(E) \propto E^{-p}$, the synchrotron frequency dependence is also a power law, of index $\beta_s = -(p+3)/2$. So, given the intensity of the synchrotron emission at a reference frequency ν_0, the intensity at the frequency ν reads:

$$S(\nu) = S(\nu_0)(\nu/\nu_0)^{\beta_s} \quad (1)$$

where the spectral index, β_s, is equal to -3 for a typical value $p = 3$.

The synchrotron spectral index depends significantly on cosmic ray properties. It varies with the direction of the sky, and possibly, with the frequency of observation (see e.g. Strong et al. 2007, for a review of propagation and interaction processes of cosmic rays in the galaxy). For a multi-channel experiment, the consequence of this is a decrease of the coherence of the synchrotron emission across channels, i.e. the correlation between the synchrotron emission in the various frequency bands of observation will be below unity.

Observational constraints have been put on the synchrotron emission law. A template of synchrotron emission intensity at 408 MHz has been provided by Haslam et al. (1982). Combining

[1] Foreground maps used specifically for this work are available at http://www.apc.univ-paris7.fr/~betoule/doku.php?id=bmodes

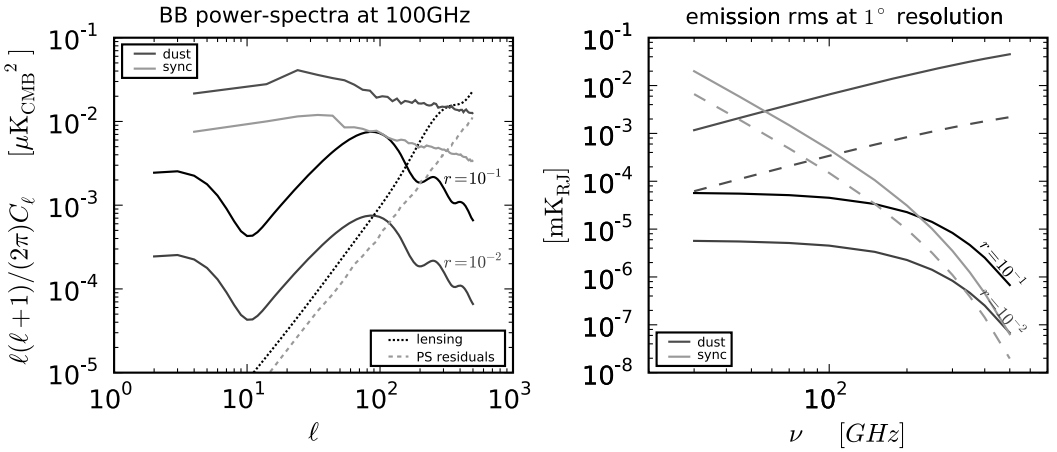

Fig. 1. Respective emission levels of the various components as predicted by the PSM. *Left*: predicted power spectra of the various components at 100 GHz, compared to CMB and lensing level for standard cosmology and various values of r ($\tau = 0.07$, and other cosmological parameters follow Dunkley et al. 2008b). The power spectra of diffuse galactic foregrounds are computed using the cleanest 55% of the polarised sky. The power spectrum from residual point sources is computed assuming that all sources brighter than 500 mJy (in temperature) in one of the Planck channels have been cut out. *Right*: typical frequency-dependence of the contributions to B-type polarisation of CMB, synchrotron and dust, at 1 degree resolution. The dashed lines correspond to the mean level of fluctuation as computed outside the mask used for the power spectra shown in *the left panel*.

this map with sky surveys at 1.4 GHz (Reich & Reich 1986) and 2.3 GHz (Jonas et al. 1998), Giardino et al. (2002) and Platania et al. (2003) have derived nearly full sky spectral index maps. Using the measurement from WMAP, Bennett et al. (2003) derived the spectral index between 408 MHz and 23 GHz. Compared to the former results, it showed a significant steepening toward $\beta_s = -3$ around 20 GHz, and a strong galactic plane feature with flatter spectral index. This feature was first interpreted as a flatter cosmic ray distribution in star forming regions. Recently, however, taking into account the presence, at 23 GHz, of additional contribution from a possible anomalous emission correlated with the dust column density, Miville-Deschênes et al. (2008) found no such pronounced galactic feature, in better agreement with lower frequency results. The spectral index map obtained in this way is consistent with $\beta_s = -3 \pm 0.06$. There is, hence, still significant uncertainty on the exact variability of the synchrotron spectral index, and in the amplitude of the steepening if any.

2.1.2. Synchrotron polarisation

If the electron density follows a power law of index p, the synchrotron polarisation fraction reads:

$$f_s = 3(p+1)/(3p+7). \quad (2)$$

For $p = 3$, we get $f_s = 0.75$, a polarisation fraction which varies slowly for small variations of p. Consequently, the intrinsic synchrotron polarisation fraction should be close to constant on the sky. However, geometric depolarisation arises due to variations of the polarisation angle along the line of sight, partial cancellation of polarisation occurring for superposition of emission with orthogonal polarisation directions. Current measurements show variations of the observed polarisation value from about 10% near the galactic plane, to 30–50% at intermediate to high galactic latitudes (Macellari et al. 2008).

2.1.3. Our model of synchrotron

In summary, the B-mode intensity of the synchrotron emission is modulated by the density of cosmic rays, the slope of their spectra, the intensity of the magnetic field, its orientation, and the coherence of the orientation along the line of sight. This makes the amplitude and frequency scaling of the polarised synchrotron signal dependant on the sky position in a rather complex way.

For the purpose of the present work, we use the synchrotron model proposed in Miville-Deschênes et al. (2008) (model 4). It relies on the synchrotron polarised template at 23 GHz measured by WMAP, and the computation of a spectral index map $\beta_s(\xi)$ used to extrapolate the template to other frequency following Eq. (1). This model also defines a pixel-dependent geometric depolarisation factor $g(\xi)$, computed as the ratio between the polarisation expected theoretically from Eq. (2), and the polarisation actually observed. This depolarisation, assumed to be due to varying orientations of the galactic magnetic field along the line of sight, is used also for modelling polarised dust emission (see below).

As an additional refinement, we also investigate the impact of a slightly modified frequency dependence with a running spectral index in Sect. 5. For this purpose, the synchrotron emission Stokes parameters ($S^X_\nu(\xi)$ for $X \in \{Q, U\}$), at frequency ν and in direction ξ on the sky, will be modelled instead as:

$$S^X_\nu(\xi) = S^X_{\nu_0}(\xi)\left(\frac{\nu}{\nu_0}\right)^{\beta_s(\xi)+C(\xi)\log(\nu/\nu_0)} \quad (3)$$

where $S^X_{\nu_0}(\xi)$ is the WMAP measurement at $\nu_0 = 23$ GHz, β_s the synchrotron spectral index map (Miville-Deschênes et al. 2008),

and $C(\xi)$ a synthetic template of the curvature of the synchrotron spectral index.

The reconstructed B-modes map of the synchrotron-dominated sky emission at 30 GHz is shown in Fig. 2 (synthesis of B-mode maps from Q/U maps is described further along with the pipeline presentation in Sect. 4.1).

2.2. Dust

The thermal emission from heated dust grains is the dominant galactic signal at frequencies higher than 100 GHz (Fig. 1). Polarisation of starlight by dust grains indicates partial alignment of elongated grains with the galactic magnetic field (see Lazarian (2007) for a review of possible alignment mechanisms). Partial alignment of grains should also result in polarisation of the far infrared dust emission.

Contributions from a wide range of grain sizes and compositions are required to explain the infrared spectrum of dust emission from 3 to 1000 μm (Désert et al. 1990; Li & Draine 2001). At long wavelengths of interest for CMB observations (above 100 μm), the emission from big grains, at equilibrium with the interstellar radiation field, should dominate.

2.2.1. Dust thermal emission law

There is no single theoretical emission law for dust, which is composed of many different populations of particles of matter. On average, an emission law can be fit to observational data. In the frequency range of interest for CMB observations, Finkbeiner et al. (1999) have shown that the dust emission in intensity is well modelled by emission from a two components mixture of silicate and carbon grains. For both components, the thermal emission spectrum is modelled as a modified grey-body emission, $D_\nu \sim B_\nu(T)\nu^\alpha$, with different emissivity spectral index α and different equilibrium temperature T.

2.2.2. Dust polarisation

So far, dust polarisation measurements have been mostly concentrated on specific regions of emission, with the exception of the Archeops balloon-borne experiment (Benoît et al. 2004), which has mapped the emission at 353 GHz on a significant part of the sky, showing a polarisation fraction around 4–5% and up to 10% in some clouds. This is in rough agreement with what could be expected from polarisation of starlight (Fosalba et al. 2002; Draine & Fraisse 2008). Macellari et al. (2008) show that dust fractional polarisation in WMAP5 data depends on both frequency and latitude, but is typically about 3% and anyway below 7%.

Draine & Fraisse (2008) have shown that for particular mixtures of dust grains, the intrinsic polarisation of the dust emission could vary significantly with frequency in the 100–800 GHz range. Geometrical depolarisation caused by integration along the line of sight also lowers the observed polarisation fraction.

2.2.3. Our model of dust

To summarise, dust produces polarised light depending on grains shape, size, composition, temperature and environment. The polarised light is then observed after integration along a line of sight. Hence, the observed polarisation fraction of dust depends on its three-dimensional distribution, and of the geometry of the galactic magnetic field. This produces a complex pattern which is likely to be only partially coherent from one channel to another.

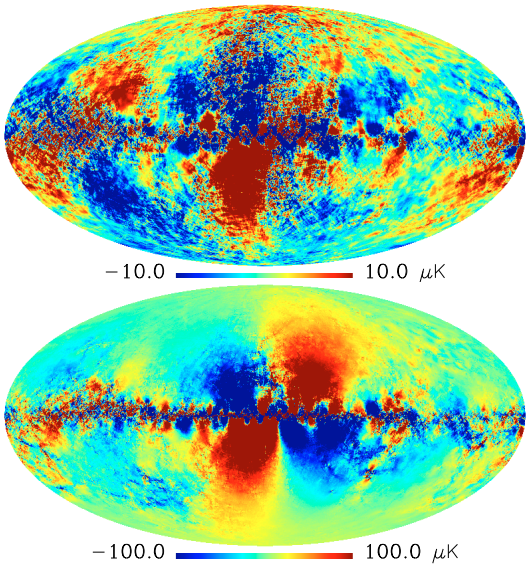

Fig. 2. B-modes of the galactic foreground maps (synchrotron + dust) as simulated using v1.6.4 of the PSM. *Top*: synchrotron-dominated emission at 30 GHz, *Bottom*: dust-dominated emission at 340 GHz.

Making use of the available data, the PSM models polarised thermal dust emission by extrapolating dust intensity to polarisation intensity assuming an intrinsic polarisation fraction f_d constant across frequencies. This value is set to $f_d = 0.12$ to be consistent with maximum values observed by Archeops (Benoît et al. 2004) and is in good agreement with the WMAP 94 GHz measurement. The dust intensity (D_ν^T), traced by the template map at 100 μm from Schlegel et al. (1998), is extrapolated using Finkbeiner et al. (1999, model #7) to frequencies of interest. The stokes Q and U parameters (respectively D^Q and D^U) are then obtained as:

$$D_\nu^Q(\xi) = f_d\, g(\xi)\, D_\nu^T(\xi)\, \cos(2\gamma(\xi)), \quad (4)$$

$$D_\nu^U(\xi) = f_d\, g(\xi)\, D_\nu^T(\xi)\, \sin(2\gamma(\xi)). \quad (5)$$

The geometric "depolarisation" factor g is a modified version of the synchrotron depolarisation factor (computed from WMAP measurements). Modifications account for differences of spatial distribution between dust grains and energetic electrons, and are computed using the magnetic field model presented in Miville-Deschênes et al. (2008). The polarisation angle γ is obtained from the magnetic field model on large scales and from synchrotron measurements in WMAP on scales smaller than 5 degrees. The maps $\gamma(\xi)$ and $g(\xi)$ are shown in Fig. 3. Figure 2 shows the B-modes of dust at 340 GHz using this model. In spite of the fact that the direction of polarisation of dust and synchrotron processes is determined by the same galactic magnetic field, differences in the 3-D distributions and in the depolarisation factors result in quite different B-mode polarisation patterns.

2.2.4. Anomalous dust

If the anomalous dust emission, which may account for a significant part of the intensity emission in the range 10–30 GHz

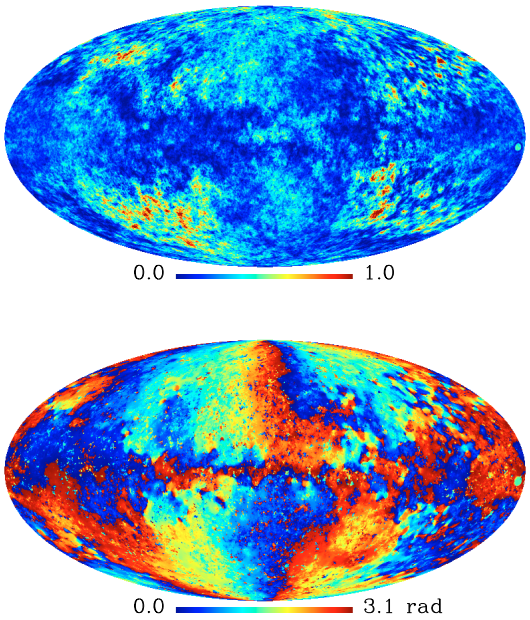

Fig. 3. Maps of the depolarisation factor g (*upper panel*) and polarisation angle γ (*lower panel*) entering in the model of dust polarised emission.

(Finkbeiner 2004; de Oliveira-Costa et al. 2004; Miville-Deschênes et al. 2008), can be interpreted as spinning dust grains emission (Draine & Lazarian 1998), it should be slightly polarised under 35 GHz (Battistelli et al. 2006), and only marginally polarised at higher frequencies (Lazarian & Finkbeiner 2003). For this reason, it is neglected (and not modelled) here. However, we should keep in mind that there exist other possible emission processes for dust, like the magneto-dipole mechanism, which can produce highly polarised radiation, and could thus contribute significantly to dust polarisation at low frequencies, even if subdominant in intensity (Lazarian & Finkbeiner 2003).

2.3. Other processes

The left panel in Fig. 1 presents the respective contribution from the various foregrounds as predicted by the PSM at 100 GHz. Synchrotron and dust polarised emission, being by far the strongest contaminants on large scales, are expected to be the main foregrounds for the measurement of primordial B-modes. In this work, we thus mainly focus on the separation from these two diffuse contaminants. However, other processes yielding polarised signals at levels comparable with either the signal of interest, or with the sensitivity of the instrument used for B-mode observation, have to be taken into account.

2.3.1. Free-free

Free-free emission is assumed unpolarised to first order (the emission process is not intrinsically linearly polarised), even if, in principle, low level polarisation by Compton scattering could exist at the edge of dense ionised regions. In WMAP data analysis, Macellari et al. (2008) find an upper limit of 1% for free–free polarisation. At this level, free-free would have to be taken into account for measuring CMB B-modes for low values of r. As this is just an upper limit however, no polarised free-free is considered for the present work.

2.3.2. Extra-galactic sources

Polarised emission from extra-galactic sources is expected to be faint below the degree scale. Tucci et al. (2005), however, estimate that radio sources become the major contaminant after subtraction of the galactic foregrounds. It is, hence, an important foreground at high galactic latitudes. In addition, the point source contribution involves a wide range of emission processes and superposition of emissions from several sources, which makes this foreground poorly coherent across frequencies, and hence difficult to subtract using methods relying on the extrapolation of template emission maps.

The PSM provides estimates of the point source polarised emission. Source counts are in agreement with the prediction of de Zotti et al. (2005), and with WMAP data. For radio-sources, the degree of polarisation for each source is randomly drawn from the observed distribution at 20 GHz (Ricci et al. 2004). For infrared sources, a distribution with mean polarisation degree of 0.01 is assumed. For both populations, polarisation angles are uniformly drawn in $[0 - 2\pi[$. The emission of a number of known galactic point sources is also included in PSM simulations.

2.3.3. Lensing

The last main contaminant to the primordial B-mode signal is lensing-induced B-type polarisation, the level of which should be of the same order as that of point sources (left panel of Fig. 1). For the present work, no sophisticated lensing cleaning method is used. Lensing effects are modelled and taken into account only at the power spectrum level and computed using the CAMB software package[2], based itself on the CMBFAST software (Zaldarriaga et al. 1998; Zaldarriaga & Seljak 2000).

2.3.4. Polarised Sunyaev-Zel'dovich effect

The polarised Sunyaev Zel'dovich effect (Sazonov & Sunyaev 1999; Audit & Simmons 1999; Seto & Pierpaoli 2005), is expected to be very subdominant and is neglected here.

2.4. Uncertainties on the foreground model

Due to the relative lack of experimental constraints from observation at millimetre wavelengths, uncertainties on the foreground model are large. The situation will not drastically improve before the Planck mission provides new observations of polarised foregrounds. It is thus very important to evaluate, at least qualitatively, the impact of such uncertainties on component separation errors for B-mode measurements.

We may distinguish two types of uncertainties, which impact differently the separation of CMB from foregrounds. One concerns the level of foreground emission, the other its complexity. Quite reliable constraints on the emission level of polarised synchrotron at 23 GHz are available with the WMAP

[2] http://camb.info

measurement, up to the few degrees scale. Extrapolation to other frequencies and smaller angular scales may be somewhat insecure, but uncertainties take place where this emission becomes weak and subdominant. The situation is worse for the polarised dust emission, which is only weakly constrained from WMAP and Archeops at 94 and 353 GHz. The overall level of polarisation is constrained only in the galactic plane, and its angular spectrum is only roughly estimated. In addition, variations of the polarisation fraction (Draine & Fraisse 2008) may introduce significant deviations to the frequency scaling of dust B-modes.

Several processes make the spectral indexes of dust and synchrotron vary both in space and frequency. Some of this complexity is included in our baseline model, but some aspects, like the dependence of the dust polarisation fraction with frequency and the steepening of the synchrotron spectral index, remain poorly known and are not modelled in our main set of simulations. In addition, uncharacterised emission processes have been neglected. This is the case for anomalous dust, or polarisation of the free-free emission through Compton scattering. If such additional processes for polarised emission exist, even at a low level, they would decrease the coherence of galactic foreground emission between frequency channels, and hence our ability to predict the emission in one channel knowing it in the others – a point of much importance for *any* component separation method based on the combination of multi-frequency observations.

The component separation as performed in this paper, hence, is obviously sensitive to these hypotheses. We will dedicate a part of the discussion to assess the impact of such modelling errors on our conclusions.

3. Estimating r with contaminants

Let us now turn to a presentation of the component separation (and parameter estimation) method used to derive forecasts on the tensor to scalar ratio measurements. Note that in principle, the best analysis of CMB observations should simultaneously exploit measurements of all fields (T, E, and B), as investigated already by Aumont & Macías-Pérez (2007). Their work, however, addresses an idealised problem. For component separation of temperature and polarisation together, the best approach is likely to depend on the detailed properties of the foregrounds (in particular on any differences, even small, between foreground emissions laws in temperature and in polarisation) and of the instrument (in particular noise correlations, and instrumental systematics). None of this is available for the present study. For this reason, we perform component separation in B-mode maps only. Additional issues such as disentangling E from B in cases of partial sky coverage for instance, or in the presence of instrumental systematic effects, are not investigated here either. Relevant work can be found in Kaplan & Delabrouille (2002); Challinor et al. (2003); Hu et al. (2003); Rosset et al. (2007); Smith & Zaldarriaga (2007).

For low values of tensor fluctuations, the constraint on r is expected to come primarily from the B-mode polarisation. B-modes indeed are not affected by the cosmic variance of the scalar perturbations, contrarily to E-modes and temperature anisotropies. In return, B-mode signal would be low and should bring little constraint on cosmological parameters other than r (and, possibly, the tensor spectral index n_t, although this additional parameter is not considered here). Decoupling the estimation of r (from B-modes only) from the estimation of other cosmological parameters (from temperature anisotropies, from E-modes, and from additional cosmological probes) thus becomes a reasonable hypothesis for small values of r. As we are primarily interested in accurate handling of the foreground emission, we will make the assumption that all cosmological parameters but r are perfectly known. Further investigation of the coupling between cosmological parameters can be found in Colombo et al. (2008) and Verde et al. (2006), and this question is discussed a bit further in Sect. 5.4.

3.1. Simplified approaches

3.1.1. Single noisy map

The first obstacle driving the performance of an experiment being the instrumental noise, it is interesting to recall the limit on r achievable in absence of foreground contamination in the observations. We thus consider first a single frequency observation of the CMB, contaminated by a noise term n:

$$x(\xi) = x^{\rm cmb}(\xi) + n(\xi) \tag{6}$$

where ξ denotes the direction in the sky. Assuming that n is uncorrelated with the CMB, the power spectra of the map reads:

$$C_\ell = r\mathcal{S}_\ell + \mathcal{N}_\ell$$

where $\mathcal{S}_\ell$ is the shape of the CMB power-spectrum (as set by other cosmological parameters), and $\mathcal{N}_\ell$ the power of the noise contamination. Neglecting mode to mode mixing effects from a mask (if any), or in general from incomplete sky coverage, and assuming that n can be modelled as a Gaussian process, the log-likelihood function for the measured angular power spectrum reads:

$$-2\ln\mathcal{L} = \sum_\ell (2\ell+1) f_{\rm sky}\left[\ln\left(\frac{C_\ell}{\hat{C}_\ell}\right) + \frac{\hat{C}_\ell}{C_\ell}\right] + \text{const.} \tag{7}$$

The smallest achievable variance σ_r^2 in estimating r is the inverse of the Fisher information $\mathcal{I} = -\boldsymbol{E}\left(\frac{\partial^2 \ln\mathcal{L}}{\partial r^2}\right)$ which takes the form:

$$\sigma_r^{-2} = \sum_{\ell=\ell_{\rm min}}^{\ell_{\rm max}} \frac{2\ell+1}{2} f_{\rm sky}\left(\frac{\mathcal{S}_\ell}{r\mathcal{S}_\ell + \mathcal{N}_\ell}\right)^2. \tag{8}$$

For a detector (or a set of detectors at the same frequency) of noise equivalent temperature s (in μK $\sqrt{s}$), and a mission duration of t_s seconds, the detector noise power spectrum is $\mathcal{N}_\ell = \frac{4\pi s^2}{B_\ell^2 t_s}\mu\text{K}^2$, with B_ℓ denoting the beam transfer function of the detector.

A similar approach to estimating σ_r is used in Verde et al. (2006) where a single "cleaned" map is considered. This map is obtained by optimal combination of the detectors with respect to the noise and cleaned from foregrounds up to a certain level of residuals, which are accounted for as an extra Gaussian noise.

3.1.2. Multi-map estimation

Alternatively, we may consider observations in F frequency bands, and form the $F\times 1$ vector of data $\boldsymbol{x}(\xi)$, assuming that each frequency is contaminated by $\boldsymbol{x}^{\rm cont}$. This term includes all contaminations (foregrounds, noise, etc.). In the harmonic domain, denoting $\boldsymbol{A}_{\rm cmb}$ the emission law of the CMB (the unit vector when working in thermodynamic units):

$$\boldsymbol{a}_{\ell m} = \boldsymbol{A}_{\rm cmb} a_{\ell m}^{\rm cmb} + \boldsymbol{a}_{\ell m}^{\rm cont}. \tag{9}$$

We then consider the $F \times F$ spectral covariance matrix R_ℓ containing auto and cross-spectra. The CMB signal being uncorrelated with the contaminants, one has:

$$\mathsf{R}_\ell = \mathsf{R}_\ell^{\rm cmb} + \mathsf{N}_\ell \tag{10}$$

with the CMB contribution modelled as

$$\mathsf{R}_\ell^{\rm cmb}(r) = r\mathcal{S}_\ell \boldsymbol{A}_{\rm cmb}\boldsymbol{A}_{\rm cmb}^\dagger \tag{11}$$

and all contaminations contributing a term N_ℓ to be discussed later. The dagger (†) denotes the conjugate transpose for complex vectors and matrices, and the transpose for real matrices (as $\boldsymbol{A}_{\rm cmb}$).

In the approximation that contaminants are Gaussian (and, here, stationary) but correlated, all the relevant information about the CMB is preserved by combining all the channels into a single filtered map. In the harmonic domain, the filtering operation reads:

$$\tilde{a}_{\ell m} = \boldsymbol{W}_\ell \boldsymbol{a}_{\ell m} = a_{\ell m}^{\rm cmb} + \boldsymbol{W}_\ell \boldsymbol{a}_{\ell m}^{\rm cont}$$

with

$$\boldsymbol{W}_\ell = \frac{\boldsymbol{A}_{\rm cmb}^\dagger \mathsf{N}_\ell^{-1}}{\boldsymbol{A}_{\rm cmb}^\dagger \mathsf{N}_\ell^{-1} \boldsymbol{A}_{\rm cmb}}\,. \tag{12}$$

We are back to the case of a single map contaminated by a characterised noise of spectrum:

$$\mathcal{N}_\ell = E|\boldsymbol{W}_\ell \boldsymbol{a}_{\ell m}^{\rm cont}|^2 = \left(\boldsymbol{A}_{\rm cmb}^\dagger \mathsf{N}_\ell^{-1} \boldsymbol{A}_{\rm cmb}\right)^{-1}. \tag{13}$$

If the residual $\boldsymbol{W}_\ell \boldsymbol{a}_{\ell m}^{\rm cont}$ is modelled as Gaussian, the single-map likelihood (7) can be used.

The same filter is used by Amblard et al. (2007). Assuming that the foreground contribution is perfectly known, the contaminant terms N_ℓ can be modelled as $\mathsf{N}_\ell = \mathsf{R}_\ell^{\rm noise} + \mathsf{R}_\ell^{\rm fg}$. This approach thus permits to derive the actual level of contamination of the map in the presence of known foregrounds, i.e. assuming that the covariance matrix of the foregrounds is known.

3.2. Estimating r in the presence of unknown foregrounds with SMICA

The two simplified approaches of Sects. 3.1.1 and 3.1.2 offer a way to estimate the impact of foregrounds in a given mission, by comparing the sensitivity on r obtained in absence of foregrounds (from Eq. (8) when $\mathcal{N}_\ell$ contains instrumental noise only), and the sensitivity achievable with known foregrounds (when $\mathcal{N}_\ell$ contains the contribution of residual contaminants as well, as obtained from Eq. (13) assuming that the foreground correlation matrix is known).

A key issue, however, is that the solution *and the error bar* require the covariance matrix of foregrounds and noise to be known[3]. Whereas the instrumental noise can be estimated accurately, assuming prior knowledge of the covariance of the foregrounds to the required precision is optimistic.

To deal with unknown foregrounds, we thus follow a different route which considers a multi-map likelihood (Delabrouille et al. 2003). If all processes are modelled as Gaussian isotropic, then standard computations yield:

$$-2\ln\mathcal{L} = \sum_\ell (2\ell+1) f_{\rm sky} K\left(\widehat{\mathsf{R}}_\ell, \mathsf{R}_\ell\right) + {\rm cst}. \tag{14}$$

[3] The actual knowledge of the contaminant term is not strictly required to build the filter. It is required, however, to derive the contamination level of the filtered map.

where $\widehat{\mathsf{R}}_\ell$ is the sample estimate of R_ℓ:

$$\widehat{\mathsf{R}}_\ell = \frac{1}{2\ell+1}\frac{1}{f_{\rm sky}} \sum_{m=-\ell}^{\ell} \boldsymbol{a}_{l,m}\boldsymbol{a}_{l,m}^\dagger \tag{15}$$

and where $K(\cdot,\cdot)$ is a measure of mismatch between two positive matrices given by:

$$K\left(\widehat{\mathsf{R}}, \mathsf{R}\right) = \frac{1}{2}\left[{\rm trace}(\mathsf{R}^{-1}\widehat{\mathsf{R}}) - \log\,\det(\mathsf{R}^{-1}\widehat{\mathsf{R}}) - F\right]. \tag{16}$$

Expression (14) is nothing but the multi-map extension of (7).

If N_ℓ is known and fixed, then the likelihood (Eq. (14)) depends only on the CMB angular spectrum and can be shown to be equal (up to a constant) to expression 7 with $C_\ell = rS_\ell$ and $\mathcal{N}_\ell$ given by Eq. (13). Thus this approach encompasses both the single map and filtered map approaches.

Unknown foreground contribution can be modelled as the mixed contribution of D correlated sources:

$$\mathsf{R}_\ell^{\rm fg} = \mathsf{A}\Sigma_\ell \mathsf{A}^\dagger \tag{17}$$

where A is a $F \times D$ mixing matrix and Σ_ℓ is the $D \times D$ spectral covariance matrix of the sources. The model of the spectral covariance matrix of the observations is then:

$$\mathsf{R}_\ell = r\mathcal{S}_\ell \boldsymbol{A}_{\rm cmb}\boldsymbol{A}_{\rm cmb}^\dagger + \mathsf{A}\Sigma_\ell\mathsf{A}^\dagger + \mathsf{R}_\ell^{\rm noise}.$$

We then maximise the likelihood (14) of the model with respect to r, A and Σ_ℓ.

We note that the foreground parameterisation in Eq. (17) is redundant, as an invertible matrix can be exchanged between A and Σ, without modifying the actual value of $\mathsf{R}^{\rm fg}$. The physical meaning of this is that the various foregrounds are not identified and extracted individually, only their mixed contribution is characterised. If we are interested in disentangling the foregrounds as well, e.g. to separate synchrotron emission from dust emission, this degeneracy can be lifted by making use of prior information to constrain, for example, the mixing matrix. Our multi-dimensional model offers, however, greater flexibility. Its main advantage is that no assumption is made about the foreground physics. It is not specifically tailored to perfectly match the model used in the simulation. Because of this, it is generic enough to absorb variations in the properties of the foregrounds, as will be seen later-on, but specific enough to preserve identifiability in the separation of CMB from foreground emission. A more complete discussion of the S method with flexible components can be found in Cardoso et al. (2008).

A couple last details on S and its practical implementation are of interest here. For numerical purposes, we actually divide the whole ℓ range into Q frequency bins $\mathcal{D}_q = \{\ell_q^{\rm min}, \cdots, \ell_q^{\rm max}\}$, and form the binned versions of the empirical and true cross power-spectra:

$$\begin{aligned}\widehat{\mathsf{R}}_q &= \frac{1}{w_q}\sum_{\ell\in\mathcal{D}_q}\sum_{m=-\ell}^{\ell} \boldsymbol{a}_{l,m}\boldsymbol{a}_{l,m}^\dagger \\ \mathsf{R}_q &= \frac{1}{w_q}\sum_{\ell\in\mathcal{D}_q}(2\ell+1)\mathsf{R}_\ell\end{aligned} \tag{18}$$

where w_q is the number of modes in $\mathcal{D}_q$. It is appropriate to select the domains so that we can reasonably assume for each $\ell \in \mathcal{D}_q, \mathsf{R}_\ell \approx \mathsf{R}_q$. This means that spectral bins should be small enough to capture the variations of the power spectra. In practice results are not too sensitive to the choice of the spectral bin

widths. Widths between 5 and 10 multipoles constitute a good tradeoff.

Finally, we compute the Fisher information matrix $\mathsf{I}_{i,j}(\boldsymbol{\theta})$ deriving from the maximised likelihood (14) for the parameter set $\boldsymbol{\theta} = (r, \mathsf{A}, \Sigma_1, \cdots, \Sigma_\mathsf{Q})$:

$$\mathsf{I}_{i,j}(\boldsymbol{\theta}) = \frac{1}{2}\sum_q w_q \mathrm{trace}\left(\frac{\partial \mathsf{R}_q(\boldsymbol{\theta})}{\partial\theta_i}\mathsf{R}_q^{-1}\frac{\partial \mathsf{R}_q(\boldsymbol{\theta})}{\partial\theta_j}\mathsf{R}_q^{-1}\right). \quad (19)$$

The lowest achievable variance of the r estimate is obtained as the entry of the inverse of the FIM corresponding to the parameter r:

$$\sigma_r^2 = \mathsf{I}^{-1}_{r,r}. \quad (20)$$

4. Predicted results for various experimental designs

We now turn to the numerical investigation of the impact of galactic foregrounds on the measurements of r with the following experimental designs:

- the P space mission, due for launch early 2009, which, although not originally planned for B-mode physics, could provide a first detection if the tensor to scalar ratio r is around 0.1;
- various versions of the EPIC space mission, either low cost and low resolution (EPIC-LC), or more ambitious versions (EPIC-CS and EPIC-2m);
- an ambitious (fictitious) ground-based experiment, based on the extrapolation of an existing design (the Cℓover experiment);
- an alternative space mission, with sensitivity performances similar to the EPIC-CS space mission, but mapping only a small (and clean) patch of the sky, and referred as the "deep field mission".

The characteristics of these instruments are summed-up in Table 1, and Fig. 4 illustrates their noise angular power spectra in polarisation.

4.1. Pipeline

For each of these experiments, we set up one or more simulation and analysis pipelines, which include, for each of them, the following main steps:

- simulation of the sky emission for a given value of r and a given foreground model, at the central frequencies and the resolution of the experiment;
- simulation of the experimental noise, assumed to be white, Gaussian and stationary;
- computation, for each of the resulting maps, of the coefficients of the spherical harmonic expansion of the B-modes $a^B_{\ell m}$;
- synthesis from those coefficients of maps of B-type signal only;
- for each experiment, a mask based on the B-modes level of the foregrounds is built to blank out the brightest features of the galactic emission (see Fig. 5). This mask is built with smooth edges to reduce mode-mixing in the pseudo-spectrum;
- statistics described in Eq. (18) are built from the masked B maps;

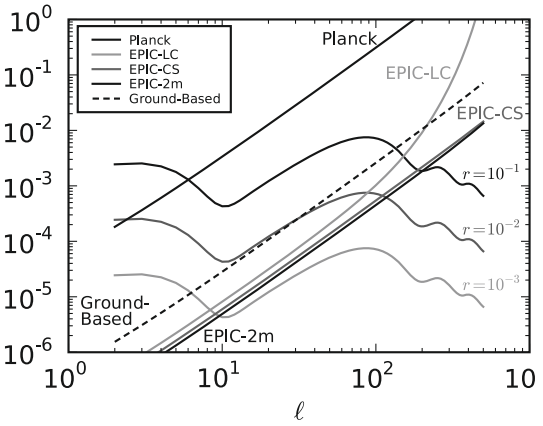

Fig. 4. Noise spectra of various experimental designs compared to B-modes levels for $r = 0.1$, 0.01 and 0.001. When computing the equivalent multipole noise level for an experiment, we assume that only the central frequency channels contribute to the CMB measurement and that external channels are dedicated to foreground characterisation.

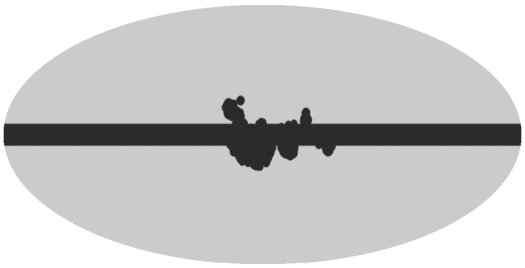

Fig. 5. Analysis mask for EPIC B maps, smoothed with a 1° apodisation window.

- the free parameters of the model described in Sect. 3.2 are adjusted to fit these statistics. The shape of the CMB pseudo-spectrum that enters in the model, is computed using the mode-mixing matrix of the mask (Hivon et al. 2002);
- Error bars are derived from the Fisher information matrix of the model.

We insist that step 3 and 4 of this pipeline can be conducted as proposed only for full sky experiments. Experiments with partial coverage would have to deal with E/B mixing effect. Formally, step 5 (masking) could not come after step 2 and 3 in the processing of real-life part-sky data. As our main concern in this work is foreground contamination, we neglect this problem in the following, but one has to remain aware of this simplification when analysing results of Sect. 4.4. Some tuning of the pipeline is necessary for satisfactory foreground separation. The three main free parameters are the multipole range $[\ell_{\min}, \ell_{\max}]$, the dimension D of the foreground component, and (for all-sky experiments) the size of the mask.

In practice we choose $\ell_{\min}$ according to the sky coverage and $\ell_{\max}$ according to the beam and the sensitivity. The value of D is selected by iterative increments until the goodness of fit (as measured from the S criterion on the data themselves, without knowledge of the input CMB and foregrounds) reaches its

Table 1. Summary of experimental designs.

Experiment	Frequency (GHz)	Beam FWHM (')	NET (μK $\sqrt{s}$)	$T_{\rm obs}$ (yr)	Sky coverage ($f_{\rm sky}$)
PLANCK	30, 44, 70	33, 24, 14	96, 97, 97	1.2	1
	100, 143, 217, 353	10, 7.1, 5, 5	41, 31, 51, 154		
EPIC-LC	30, 40, 60	155, 116, 77	28, 9.6, 5.3	2	1
	90, 135, 200, 300	52, 34, 23, 16	2.3, 2.2, 2.3, 3.8		
EPIC-CS	30, 45, 70, 100	15.5, 10.3, 6.6, 4.6	19, 8, 4.2, 3.2	4	1
	150, 220, 340, 500	3.1, 2.1, 1.4, 0.9	3.1, 5.2, 25, 210		
EPIC-2m	30, 45, 70, 100	26, 17, 11, 8	18, 7.6, 3.9, 3.0	4	1
	150, 220, 340, 500(,800)	5, 3.5, 2.3, 1.5(, 0.9)	2.8, 4.4, 20, 180(, 28k)		
Ground-Based	97, 150, 225	7.5, 5.5, 5.5	12, 18, 48	0.8	0.01
Deep field	30, 45, 70, 100	15.5, 10.3, 6.6, 4.6	19, 8, 4.2, 3.2	4	0.01
	150, 220, 340, 500	3.1, 2.1, 1.4, 0.9	3.1, 5.2, 25, 210		

expectation. The mask is chosen in accordance to maximise the sky coverage for the picked value of D (see Appendix A for further discussion of the procedure). The $f_{\rm sky} = 0.87$ mask in Fig. 5, used for EPIC analysis, is based on a 10 degrees cut of the galactic plane. An additional cut of brightest region on the B-modes map is built by applying a threshold on the emission level at the central frequency of the instrument. The threshold can be adjusted to obtain the suitable sky coverage. These two masks are combined and edges are smoothed by a 1-degree transition window[4]. For the Planck data analysis, the galactic plane cut is not necessary, and the emission level mask is used alone.

For each experimental design and fiducial value of r we compute three kinds of error estimates which are recalled in Table 2:

- knowing the noise level and resolution of the instrument, we first derive from Eq. (8) the error $\sigma_r^{\rm noise-only}$ set by the instrument sensitivity assuming no foreground contamination in the covered part of the sky. The global noise level of the instrument is given by $\mathcal{N}_\ell = \left(\boldsymbol{A}_{\rm cmb}^\dagger \mathsf{N}_\ell^{-1} \boldsymbol{A}_{\rm cmb}\right)^{-1}$, where the only contribution to N_ℓ comes from the instrumental noise: $\mathsf{N}_\ell = \mathsf{R}_\ell^{\rm noise} = {\rm diag}\left(\frac{4\pi s_\ell^2}{B_\ell^2 f^2 t_s}\right)$;
- in the same way, we also compute the error $\sigma_r^{\rm known-foreground}$ that would be obtained if foreground contribution $\mathsf{R}^{\rm fg}$ to the covariance of the observations was perfectly known, using $\mathsf{N}_\ell = \mathsf{R}_\ell^{\rm noise} + \mathsf{R}_\ell^{\rm fg}$. Here we assume that $\mathsf{R}^{\rm fg} = \widehat{\mathsf{R}}^{\rm fg}$ where $\widehat{\mathsf{R}}^{\rm fg}$ is the sample estimate of $\mathsf{R}^{\rm fg}$ computed from the simulated foreground maps;
- finally, we compute the error $\sigma_r^{\rm SMICA}$ given by the Fisher information matrix of the model (Eq. (20)).

In each case, we also decompose the FIM in the contribution from large-scale modes ($\ell \leq 20$) and the contribution from small scales ($\ell > 20$). We then compute error bars from these two separate contributions to give indications of the relative weight of the bump (due to reionisation) and the peak (at higher ℓ) in the constraint of r.

We may notice that in some favourable cases (at low ℓ, where the foregrounds dominate), the error estimate given by S can be slightly more optimistic than the estimate obtained using the actual empirical value of the correlation matrix $\widehat{\mathsf{R}}^{\rm fg}$. This reflects the fact that our modelling hypothesis, which imposes to $\mathsf{R}^{\rm fg}$ to be of rank smaller than D, is not perfectly verified in practice (see Appendix A for further discussion of this hypothesis). The (small) difference (an error on the estimation of σ_r when foregrounds are approximated by our model) has negligible impact on the conclusions of this work.

[4] The mask apodisation code can be downloaded from http://www.apc.univ-paris7.fr/~betoule/doku.php?id=software

4.2. Planck

The Planck space mission will be the first all-sky experiment to give sensitive measurements of the polarised sky in seven bands between 30 and 353 GHz. The noise level of this experiment being somewhat too high for precise measurement of low values of r, we run our pipeline for $r = 0.1$ and 0.3. We predict a possible 3-sigma measurement for $r = 0.1$ using S (first lines in Table 2). A comparison of the errors obtained from S , with the prediction in absence of foreground contamination, and with perfectly known foreground contribution, indicates that the error is dominated by cosmic variance and noise, foregrounds contributing to a degradation of the error of ∼30% and uncertainties on foregrounds for another increase around 30% (for $r = 0.1$).

Figure 4 hints that a good strategy to detect primordial B-modes with Planck consists in detecting the reionisation bump below $\ell = 10$, which requires the largest possible sky coverage. Even at high latitude, a model using $D = 2$ fails to fit the galactic emission, especially on large scales where the galactic signal is above the noise. Setting $D = 3$, however, gives a satisfactory fit (as measured by the mismatch criterion) on 95 percent of the sky. It is therefore our choice for Planck.

We also note that a significant part of the information is coming from the reionisation bump ($\ell \leq 20$). The relative importance of the bump increases for decreasing value of r, as a consequence of the cosmic variance reduction. For a signal–to–noise ratio corresponding roughly to the detection limit ($r = 0.1$), the stronger constraint is given by the bump (Appendix B gives further illustration of the relative contribution of each multipole). This has two direct consequences: the result is sensitive to the actual value of the reionisation optical depth and to reionisation history (as investigated by Colombo & Pierpaoli 2008), and the actual capability of Planck to measure r will depend on the level (and the knowledge of) instrumental systematics on large scales. Note that this numerical experiment estimates how well Planck can measure r in the presence of foregrounds *from B-modes only*.

4.3. EPIC

We perform a similar analysis for three possible designs of the EPIC probe (Bock et al. 2008). EPIC-LC and EPIC-CS correspond respectively to the low cost and comprehensive solutions. EPIC-2m is an alternate design which contains one extra high-frequency channel (not considered in this study) dedicated to

Table 2. Error prediction for various experimental designs, assumptions about foregrounds, and fiducial r values.

		Noise – only[a]			Known foregrounds[b]			S [c]					
Case	r	σ_r/r	$\sigma_r^{\ell\leq 20}/r$	$\sigma_r^{\ell>20}/r$	σ_r/r	$\sigma_r^{\ell\leq 20}/r$	$\sigma_r^{\ell>20}/r$	σ_r/r	$\sigma_r^{\ell\leq 20}/r$	$\sigma_r^{\ell>20}/r$	$r_{\rm est}$ [d]	$l_{\rm min}-l_{\rm max}$	$f_{\rm sky}$	D^e
PLANCK	0.3	0.075	0.17	0.084	0.1	0.2	0.12	0.15	0.22	0.2	**0.26**	2 - 130	0.95	3
	0.1	0.17	0.25	0.22	0.23	0.34	0.32	0.29	0.34	0.55	0.086			
EPIC-LC	0.01	0.019	0.084	0.019	0.05	0.18	0.053	0.079	0.18	0.1	**0.0098**	2–130	0.86	4
	0.001	0.059	0.15	0.064	0.27	0.4	0.38	0.37	0.43	0.82	0.00088			
EPIC-2m	0.01	0.016	0.083	0.016	0.027	0.12	0.027	0.032	0.11	0.036	**0.0096**	2–300	0.87	4
	0.001	0.051	0.14	0.055	0.14	0.25	0.16	0.16	0.24	0.24	**0.001**			
EPIC-CS	0.01	0.017	0.084	0.017	0.029	0.12	0.03	0.036	0.11	0.041	**0.0096**	2–300	0.87	4
	0.001	0.058	0.15	0.063	0.15	0.27	0.19	0.18	0.26	0.29	**0.00098**			
Ground-based	0.1	0.083	–	–	0.15	–	–	0.24	–	–	**0.11**	50–300	0.01	2
	0.01	0.18	–	–	0.8	–	–	1.6	–	–	0.018			
Grnd – based + Planck	0.01	0.18	–	–	0.51	–	–	0.69	–	–	0.0065	50–300	0.01	2
Deep field mission	0.001	0.082	–	–	0.1	–	–	0.13	–	–	**0.00092**	50–300	0.01	4

[a] Error bars derived assuming no foreground contamination i.e. using $\mathsf{N}_\ell = \mathsf{R}^{\rm noise}$ (see Eq. (8)). [b] Same as [a] but assuming perfectly known foreground contamination i.e. using $\mathsf{N}_\ell = \mathsf{R}^{\rm noise} + \mathsf{R}^{\rm fg}$. [c] Error bars obtained by the inversion of the FIM computed from the S model at the point of convergence of the algorithm (see Eq. (20)). [d] Estimated value at the convergence point in S ; detections at more than 4σ are bold-faced. [e] Size of the galactic component used in the model of S .

additional scientific purposes besides CMB polarisation. We consider two values of r, 0.01 and 0.001. For all these three experiments, the analysis requires $D = 4$ for a reasonable fit, which is obtained using about 87% of the sky.

The two high resolution experiments provide measurements of $r = 10^{-3}$ with a precision better than five sigma. For the lower values of r, the error is dominated by foregrounds and their presence degrades the sensitivity by a factor of 3, as witnessed by the difference between $\sigma_r^{\rm noise-only}$ and $\sigma_r^{\rm smica}$. However, while the difference between the noise-only and the S result is a factor 4-6 for EPIC-LC, it is only a factor about 2–3 for EPIC-CS and EPIC-2m. Increased instrumental performance (in terms of frequency channels and resolution) thus also allows for better subtraction of foreground contamination.

For all experiments considered, the constraining power moves from small scales to larger scale when r decreases down to the detection limit of the instrument. In all cases, no information for the CMB is coming from $\ell > 150$. Higher multipoles, however, are still giving constraints on the foreground parameters, effectively improving the component separation also on large scales.

4.4. Small area experiments

4.4.1. Ground-based

A different observation strategy for the measurement of B-modes is adopted for ground-based experiments that cannot benefit from the frequency and sky coverage of a space mission. Such experiments target the detection of the first peak around $\ell = 100$, by observing a small but clean area (typically 1000 square-degrees) in few frequency bands (2 or 3).

The test case we propose here is inspired from the announced performances of Cℓover (North et al. 2008). The selected sky coverage is a 10 degree radius area centred on lon $= 351°$, lat $= -56°$ in galactic coordinates. The region has been retained by the Cℓover team as a tradeoff between several issues including, in particular, foreground and atmospheric contamination. According to our polarised galactic foreground model, this also correspond to a reasonably clean part of the sky (within 30% of the cleanest).

The most interesting conclusion is that for $r = 0.01$, although the raw instrumental sensitivity (neglecting issues like E-B mixing due to partial sky coverage) would allow a more than five sigma detection, galactic foregrounds cannot be satisfactorily removed with the scheme adopted here.

An interesting option would be to complement the measurement obtained from the ground, with additional data such as that of Planck, and extract r in a joint analysis of the two data sets. To simply test this possibility here, we complement the ground data set with a simulation of the Planck measurements on the same area. This is equivalent to extend the frequency range of the ground experiment with less sensitive channels. We find a significant improvement of the error-bar from 1.6×10^{-2} to 0.69×10^{-2}, showing that a joint analysis can lead to improved component separation. The degradation of sensitivity due to foreground remains however higher than for a fully sensitive space mission (as witnessed by the following section). This last result is slightly pessimistic as we do not make use of the full Planck data set but use it only to constrain foregrounds in the small patch. However considering the ratio of sensitivity between the two experiments, it is likely that there is little to gain by pushing the joint analysis further.

4.4.2. Deep field space mission

We may also question the usefulness of a full-sky observation strategy for space-missions, and consider the possibility to spend the whole observation time mapping deeper a small but clean region. We investigate this alternative using an hypothetical experiment sharing the sensitivity and frequency coverage of the EPIC-CS design, and the sky coverage of the ground-based experiment. Although the absence of strong foreground emission may permit a design with a reduced frequency coverage, we keep a design similar to EPIC-CS to allow comparisons. In addition, the relative failure of the ground-based design to disentangle foregrounds indicates that the frequency coverage cannot be freely cut even when looking in the cleanest part of the sky. In the same way, to allow straightforward comparison with the ground-based case we stick to the same sky coverage, although in principle, without atmospheric constraints, slightly better sky areas could be selected.

In spite of the increased cosmic variance due to the small sky coverage, the smaller foreground contribution allows our harmonic-based foreground separation with S to achieve better results with the "deep field" mission than with the full sky experiment, when considering only diffuse galactic foreground. However, this conclusion does not hold if lensing is considered as will be seen in the following section.

We may also notice that, despite the lower level of foregrounds, the higher precision of the measurement requires the same model complexity ($D = 4$) as for the full sky experiment to obtain a good fit. We also recall that our processing pipeline does not exploit the spatial variation of foreground intensity, and is, in this sense, suboptimal, in particular for all-sky experiments. Thus, the results presented for the full-sky experiment are bound to be slightly pessimistic which tempers further the results of this comparison between deep field and full sky mission. This is further discussed below. Finally, note that here we also neglect issues related to partial sky coverage that would be unavoidable in this scheme.

4.5. Comparisons

4.5.1. Impact of foregrounds: the ideal case

As a first step, the impact of foregrounds on the capability to measure r with a given experiment, if foreground covariances are known, is a measure of the adequacy of the experiment to deal with foreground contamination. Figures for this comparison are computed using Eqs. (8) and (13), and are given in Table 2 (first two sets of three columns).

The comparison shows that for some experiments, σ_r/r in the "noise-only" and the "known foregrounds" cases are very close. This is the case for Planck and for the deep field mission. For these experiments, if the second order statistics of the foregrounds are known, galactic emission does not impact much the measurement. For other experiments, the "known foregrounds" case is considerably worse than the "noise-only" case. This happens, in particular, for a ground based experiment when $r = 0.01$, and for EPIC-LC.

If foreground contamination was Gaussian and stationary, and in absence of priors on the CMB power spectrum, the linear filter of Eq. (12) would be the optimal filter for CMB reconstruction. The difference between σ_r in the "noise-only" and the "known foregrounds" cases would be a good measure of how much the foregrounds hinder the measurement of r with the experiment considered. A large difference would indicate that the experimental design (number of frequency channels and sensitivity in each of them) is inadequate for "component separation".

However, since foregrounds are neither Gaussian nor stationary, the linear filter of Eq. (12) is not optimal. Even if we restrict ourselves to linear solutions, the linear weights given to the various channels should obviously depend on the local properties of the foregrounds. Hence, nothing guarantees that we can not deal better with the foregrounds than using a linear filter in harmonic space. Assuming that the covariance matrix of the foregrounds is known, the error in Eq. (8) with N_ℓ from Eq. (13) is a pessimistic bound on the error on r. The only conclusion that can be drawn is that the experiment does not allow effective component separation with the implementation of a linear filter in harmonic space. There is, however, no guarantee either that an other approach to component separation would yield better results. Hence, the comparison of the noise-only and known foregrounds cases shown here gives an upper limit of the impact of foregrounds, if they were known.

4.5.2. Effectiveness of the blind approach

Even if in some cases the linear filter of Eq. (12) may not be fully optimal, it is for each mode ℓ the best linear combination of observations in a set of frequency channels, to reject maximally contamination from foregrounds and noise, and minimise the error on r. Other popular methods as decorrelation in direct space, such as the so-called "internal linear combination", and other linear combinations cannot do better, unless they are implemented locally in both pixel and harmonic space simultaneously, using for instance spherical needlets as in Delabrouille et al. (2008). Such localisation is not considered in the present work.

Given this, the next question that arises is how well the spectral covariance of the foreground contamination can be actually constrained from the data, and how this uncertainty impact the measurement of r. The answer to this question is obtained by comparing the second and third sets of columns of Table 2.

In all cases, the difference between the results obtained assuming perfect knowledge of the foreground residuals, and those obtained after the blind estimation of the foreground covariances with S , are within a factor of 2. For EPIC-2m and the deep field mission, the difference between the two is small, which means that S allows for component separation very effectively. For a ground based experiment with three frequency channels, the difference is very significant, which means that the data does not allow a good blind component separation with S .

Comparing column set 1 (noise-only) and 3 (blind approach with S) gives the overall impact of unknown galactic foregrounds on the measurement of r from B-modes with the various instruments considered. For Planck, EPIC-2m, or a deep field mission with 8 frequency channels, the final error bar on r is within a factor of 2 of what would be achievable without foregrounds. For EPIC-LC, or even worse for a ground-based experiment, foregrounds are likely to impact the outcome of the experiment quite significantly. For this reason, EPIC-2m and the deep field mission seem to offer better perspectives for measuring r in the presence of foregrounds.

4.5.3. Full sky or deep field

The numerical investigations performed here allow –to some extent– to compare what can be achieved with our approach in two cases of sky observation strategies with the same instrument. For EPIC-CS, it has been assumed that the integration time is evenly spread on the entire sky, and that 87% of the sky is used to measure r. For the "deep field" mission, 1% of the sky only is observed with the same instrument, with much better sensitivity per pixel (by a factor of 10).

Comparing σ_r/r between the two in the noise-only case shows that the full sky mission should perform better (by a factor 1.4) if the impact of the foregrounds could be made to be negligible. This is to be expected, as the cosmic or "sample" variance of the measurement is smaller for larger sky coverage. After component separation however, the comparison is in favour of the deep field mission, which seems to perform better by a factor 1.4 also. The present work, however, does not permit to conclude on what is the best strategy for two reasons. First, this study concentrates on the impact of diffuse galactic foregrounds which are not expected to be the limiting issue of the deep field design. And secondly, in the case of a deep field, the properties of the (simulated) foreground emission are more homogeneous in the observed area, and thus the harmonic filter of Eq. (12) is close to optimal everywhere. For the full sky mission, however, the filter is obtained as a compromise minimising the overall

error ℓ by ℓ, which is not likely to be the best everywhere on the sky. Further work on component separation, making use of a localised version of S , is needed to conclude on this issue. A preliminary version of S in wavelet space is described in Moudden et al. (2004), but applications to CMB polarisation and full sky observations require specific developments.

5. Discussion

The results presented in the previous section have been obtained using a number of simplifying assumptions. First of all, only galactic foregrounds (synchrotron and dust) are considered. It has been assumed that other foregrounds (point sources, lensing) can be dealt with independently, and thus will not impact much the overall results. Second, it is quite clear that the results may depend on details of the galactic emission, which might be more complex than what has been used in our simulations. Third, most of our conclusions depend on the accuracy of the determination of the error bars from the Fisher information matrix. This method, however, only provides an approximation, strictly valid only in the case of Gaussian processes and noise. Finally, the measurement of r as performed here assumes a perfect prediction (from other sources of information) of the shape of the BB spectrum. In this section, we discuss and quantify the impact of these assumptions, in order to assess the robustness of our conclusions.

5.1. Small-scale contamination

5.1.1. Impact of lensing

Limitations on tensor mode detection due to lensing have been widely investigated in the literature, and cleaning methods, based on the reconstruction of the lensed B-modes from estimation of the lens potential and unlensed CMB E-modes, have been proposed (Knox & Song 2002; Hirata & Seljak 2003; Kesden et al. 2003; Lewis & Challinor 2006). However, limits on r achievable after such "delensing" (if any) are typically significantly lower than limits derived in Sect. 4, for which foregrounds and noise dominate the error.

In order to check whether the presence of lensing can significantly alter the detection limit, we proceed as follows: assuming no specific reconstruction of the lens potential, we include lensing effects in the simulation of the CMB (at the power spectrum level). The impact of this on the second order statistics of the CMB is an additional contribution to the CMB power spectrum. This extra term is taken into account on the CMB model used in S . For this, we de-bias the CMB S component from the (expectation value of) the lensing contribution to the power-spectrum. The cosmic variance of the lensed modes thus contributes as an extra "noise" which lowers the sensitivity to the primordial signal, and reduces the range of multipoles contributing significantly to the measurement. We run this lensing test case for the EPIC-CS and deep field mission. Table 3 shows a comparison of the constraints obtained with and without lensing in the simulation for a fiducial value of $r = 0.001$. On large scales for EPIC-CS, lensing has negligible impact on the measurement of r (the difference between the two cases is not significant on one single run of the component separation). On small scales, the difference becomes significant. Overall, σ_r/r changes from 0.18 to 0.21, which is not a very significant degradation of the measurement: lensing produces a 15% increase in the overall error estimate, the small-scale error (for $\ell > 20$) being most impacted. For the small coverage mission, however, the large cosmic variance of the lensing modes considerably hinder the detection.

Table 3. Comparison of the constraints on r with and without lensing (here $r = 0.001$).

	Nolensing			Lensing		
Experiment	σ_r/r	$\sigma_r^{\ell\leq 20}/r$	$\sigma_r^{\ell>20}/r$	σ_r/r	$\sigma_r^{\ell\leq 20}/r$	$\sigma_r^{\ell>20}/r$
EPIC − CS	0.18	0.26	0.29	0.21	0.26	0.38
Deepfield	0.13	–	–	1.1	–	–

Thus, at this level of r, if the reionisation bump is satisfactorily measured, the difference is perceptible but not very significant. Hence, lensing is not the major source of error for a full-sky experiment measuring r. It becomes however a potential problem for a small coverage experiment targeting the measurement of the recombination bump. Such a strategy would thus require efficient "delensing". Indications that "delensing" can be performed even in the presence of foregrounds in the case of a low noise and high resolution experiment can be found in Smith et al. (2008). However, a complete investigation of this case, accounting for all the complexity (diffuse foregrounds, point sources, lensing, modes-mixing effects), would be needed to conclude on the validity of a deep-field strategy.

5.1.2. Impact of extra-galactic sources

Although largely subdominant on scales larger than 1 degree, extra-galactic sources, in particular radio-sources, are expected to be the worst contaminant on small scales (see e.g. Tucci et al. 2004; Pierpaoli & Perna 2004). Obviously, the strongest point sources are known, or (for most of them) will be detected by Planck. Their polarisation can be measured either by the B-mode experiment itself, or by dedicated follow-up. We make the assumption that point sources brighter than 500 mJy in temperature (around 6000 sources) are detected, and that their polarised emission is subtracted from the polarisation observations. We stress that 500 mJy is a conservative assumption as Planck is expected to have better detection thresholds.

The present level of knowledge about point sources does not allow a very accurate modelling of the contribution to the power spectra of the remaining point sources (those not subtracted by the 500 mJy cut). For this reason we investigate their impact in two extreme cases: perfect modelling of their contribution to the power-spectra ("ideal" case), and no specific modelling at all ("no-model" case). Results of a S run for both assumptions are compared to what is obtained in total absence of point sources ("no-ps" case), and are summarised in Table 4.

The bottom line of this investigation is that modelling properly the point sources statistical contribution is necessary to measure $r = 0.001$. An insufficient model results in a biased estimator: for EPIC-CS the estimated r is two times larger than expected, with a difference incompatible with the error bar, in spite of an increased standard deviation (σ_r increased by +30% for $r = 0.001$). An ideal model restores the goodness of fit of the no-ps case and suppresses the bias of the estimator. Still, the presence of point sources increases the variance of the measurement of r. In our experiment, the effect is not truly significant (σ_r shifting from 1.84 to 1.91×10^{-4}).

Figure 6 shows the mismatch criterion (from Eq. (16), using covariance matrixes binned in ℓ) in the three cases. When no specific model of the point source contribution is used, some of their emission is nonetheless absorbed by the S "galactic" com-

Table 4. EPIC-CS measurement for three point sources cases.

r	$r^{\mathrm{no-ps}}$	r^{ideal}	$r^{\mathrm{no-model}}$	$\sigma_r^{\mathrm{no-ps}}$	$\sigma_r^{\mathrm{ideal}}$	$\sigma_r^{\mathrm{no-model}}$
0.001	1.07×10^{-3}	1.04×10^{-3}	2.00×10^{-3}	1.84×10^{-4}	1.91×10^{-4}	2.49×10^{-4}

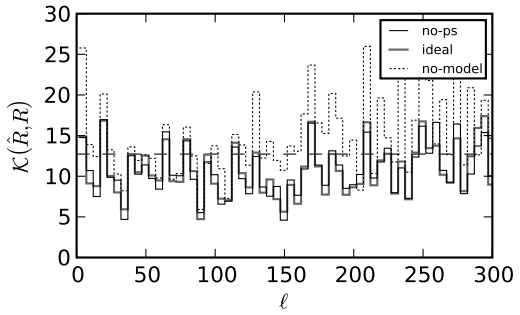

Fig. 6. Goodness-of-fit for the three point sources cases. For the reference case "no-ps", point sources have neither been including in the simulation, nor taken into account in the modelling. The mismatch criterion wander around its expectation value (horizontal dashed line). The "no-model" case is a pessimistic situation where no effort has been made to model the point sources contribution, yielding a net increase of the mismatch criterion. The "ideal" case presents an optimistic situation where the exact contribution of the simulated point sources has been used to build the model.

ponent, which adjusts itself (via the values of its maximum likelihood parameters) to represent best the total foreground emission. The remaining part is responsible for the increase of the mismatch at high ℓ. At the same time, the galactic estimation is twisted by the presence of point sources. This slightly increases the mismatch on large scales.

5.2. Galactic foregrounds uncertainties

We now investigate the impact on the above results of modifying somewhat the galactic emission. In particular, we check whether a space dependant curvature of the synchrotron spectral index, and modifications of the dust angular power spectrum, significantly change the error bars on r obtained in the previous section. Those two modifications reflect two of the main uncertainties on diffuse foregrounds modelling discussed in Sect. 2.4. Although it is quite expectable that substantial variations of dust emission law can occur, modifications of the model in this sense would remain purely speculative and we choose to stick with simple modification of the (poorly constrained) dust emission level. Those two points are also representative of two different kinds of modelling errors: the first modification impacts the coherence of the emission across channels, while the second one illustrates the effect of an overall increase of the contamination level.

5.2.1. Impact of synchrotron curvature

As mentioned earlier on, the synchrotron emission law may not be perfectly described as a single power law per pixel, with a constant spectral index across frequencies. Steepening of the spectral index is expected in the frequency range of interest. As this variation is related to the aging of cosmic rays, it should vary on the sky. Hence, the next level of sophistication in modelling synchrotron emission makes use of a (random) template map $C(\xi)$ to model the curvature of the synchrotron spectral index. We then produce simulated synchrotron maps as:

$$S_\nu^X(\xi) = S_{\nu_0}^X(\xi) \left(\frac{\nu}{\nu_0}\right)^{\beta_s(\xi)+\alpha C(\xi)\log(\nu/\nu_1)} \tag{21}$$

where α is a free parameter which allows to modulate the amplitude of the effect (as compared to Eq. (3)). The left panel of Fig. 7 illustrates the impact of the steepening on the synchrotron frequency scaling.

We now investigate whether such a modified synchrotron changes the accuracy with which r can be measured. We decide, for illustrative purposes, to perform the comparison for EPIC-2m, and for $r = 0.001$. Everything else, regarding the other emissions and the foreground model in S , remains unchanged. Table 5 shows the results of this study in terms of goodness of fit and influence on the r estimate. We observe no significant effect, which indicates that the foreground emission model of Eq. (17) is flexible enough to accommodate the variation of the synchrotron modelling. Even if we cannot test all possible deviation from the baseline PSM model, robustness against running of the spectral index remains a good indication that results are not overly model dependent.

Table 5. Influence of the running of the synchrotron spectral index on component separation in term of goodness of fit and r estimates for the EPIC-2m design.

r	σ_r	α	r_{est}	$-\ln \mathcal{L}$
		0	9.78×10^{-4}	11.6
0.001	1.8×10^{-4}	1	9.62×10^{-4}	11.5
		3	1.06×10^{-3}	11.7

Table 6. Influence of dust polarisation level on component separation.

Experiments	r	r^{origin}	r^{pessim}	$\sigma_r^{\mathrm{origin}}$	$\sigma_r^{\mathrm{pessim}}$
Ground – based	0.01	1.84×10^{-2}	1.69×10^{-2}	1.62×10^{-2}	1.62×10^{-2}
EPIC – 2m	0.001	8.77×10^{-4}	8.77×10^{-4}	3.68×10^{-4}	3.61×10^{-4}

5.2.2. Level and power spectrum of dust emission

Similarly, we now vary the model of dust emission and check how the main results of Sect. 4 are modified. Measurements give some constraints on dust emission on large scales, but smaller scales remain mostly unconstrained. Hence, we consider here a pessimistic extreme in which we multiply the large-scale level of the dust by a factor of two, and flatten the power spectrum from a nominal index of –2.5 to –1.9. The power spectra corresponding to these two cases are shown in Fig. 7 (right panel).

Running the same component separation pipeline for the ground based and the EPIC-2m experiments at their detection

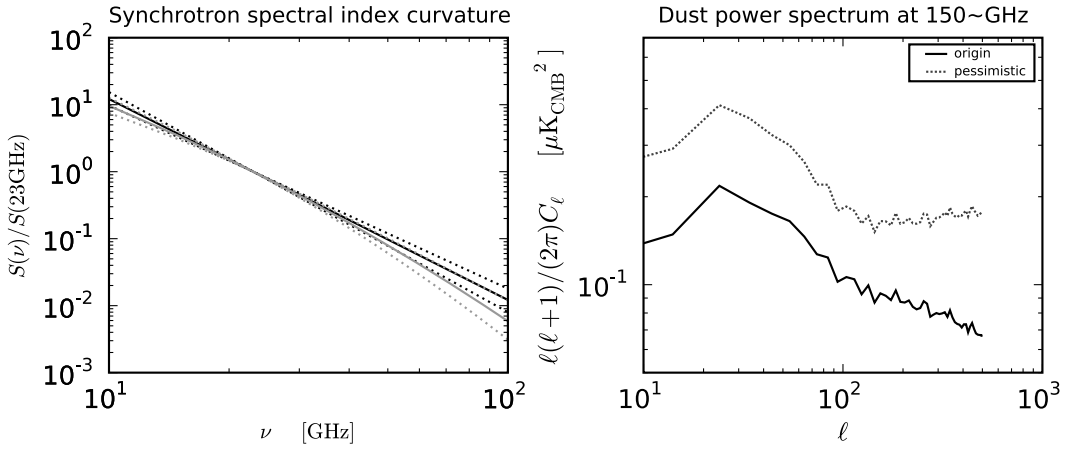

Fig. 7. Variations of the galactic foregrounds model. *The left panel* shows the dispersion of the synchrotron spectral index for the PSM model (in black) and the curved model (in gray). Solid lines present the frequency scaling for the mean values of the spectral index and dotted lines for its extremal values. The right panel shows the difference between the default power spectrum of dust polarisation B-modes at 150 GHz as modelled by the PSM (solid curve) and a model assuming pessimistic values for the overall level and power spectrum index (dotted curve).

limit, we find only marginal changes in the measured values of r (see Table 6). This result can be interpreted in the following way: as the noise of the experiment remains unchanged, the increased signal-to-noise ratio allows for a better constraint of the dust parameters. Component separation effectiveness depends mainly on the coherence of the component, rather than on its overall level.

Table 7. Comparaison of the predicted error bar and the root mean squared error measured on 100 Monte Carlo realisations of EPIC-CS observation.

r	$\langle r \rangle^a$	$\langle \sigma_r^{\mathrm{FISHER}} \rangle^a$	σ_r^{MC}
0.01	9.91×10^{-3}	3.59×10^{-4}	3.49×10^{-4}
0.001	1.05×10^{-3}	1.84×10^{-4}	1.84×10^{-4}

5.3. Error bar accuracy

Estimates of the error derived from the FIM (Eq. (20)) are expected to be meaningful only if the model leading to the likelihood (Eq. (14)) holds. In particular we assume that processes can be modelled as Gaussian.

We first note that the FIM errors are reasonably compatible with the difference between input and measured r values, which gives confidence that these error estimates are not obviously wrong. Nonetheless, we investigate this issue further, using Monte-Carlo studies to obtain comparative estimates of errors, with the EPIC-CS design. Table 7 gives, for two values of r and for 100 runs of the S pipeline in each case, the average recovered value of r, the average error as estimated from the Fisher matrix $\langle \sigma_r^{\mathrm{FISHER}} \rangle$, and the standard deviation σ_r^{MC} of the measured values of r. For each of the Monte-Carlo runs, a new realisation of CMB and noise is generated. Simulated galactic foregrounds, however, remain unchanged.

Results show that the FIM approximation give estimates of the error in very good agreement with the MC result. Hence, the FIM estimate looks good enough for the purpose of the present paper, given the number of other potential sources of error and the computational cost of Monte-Carlo studies.

The Monte-Carlo study also allows to investigate the existence of a bias. For an input tensor to scalar ratio of 0.01, we observe that the measured value of r seems to be systematically low, with an average of 9.91×10^{-3}. This we interpret as resulting from a slight over-fitting of the data. Still this small bias does not dominate the error and we are more interested in noise dominated regime. The overall conclusion of this investigation of error bars is that the errors estimated by the FIM are reasonably representative of the measurement error.

5.4. Other cosmological parameters

The main conclusions of this study are mostly independent of the value of all cosmological parameters except τ. Within present uncertainties indeed, only the value of the reionisation optical depth τ, which drives the amplitude and position of the reionisation bump, is critical for our estimations (Colombo et al. 2008). Lower τ means less accurate measurement of r, and higher τ better measurement of r. Here we choose a rather conservative value of $\tau = 0.07$ in agreement with the last measurements from WMAP (Dunkley et al. 2008b,c). The value of τ, however, should affect mainly low resolution and noisy experiments, for which most of the information comes from the lowest frequency "reionisation" bump in the B-mode spectrum.

Another issue is that we assume the value of τ and n_t (and, to a less extent, the value of all other cosmological parameters) to be perfectly known (setting the shape of the B-mode power spectrum). In fact, uncertainties on all cosmological parameters imply that the shape will be known only approximately, and within a certain framework. Such uncertainties will have to be taken into account in the analysis of a real-life data set. Our S pipeline can be adapted to do this, provided we know the uncertainties on the cosmological parameter set. A Monte-Carlo approach, in which we assume, for each S run, a B-mode power spectrum from one of the possible cosmological parameter sets, will permit to propagate the uncertainties onto the

measurement of r. We expect, however, that this additional error will be significantly smaller than that due to the experimental noise.

6. Conclusion

In this paper, we presented an investigation of the impact of foregrounds on the measurement of the tensor to scalar ratio of primordial perturbations. The measurement of r is based on the (simulated) observation of the B-mode polarisation of the cosmic microwave background by various instruments, either in preparation or planned for the future: the Planck space mission, a ground-based experiment of the type of Cℓover, and several versions of a possible dedicated space mission.

Foreground contamination is modelled and simulated using the present development version (v1.6.4) of the PSM. Our main analysis considers the contribution from diffuse polarised emission (from the galactic interstellar medium modelled as a mixture of synchrotron emission and thermal emission from dust) and from instrumental noise. The impact of more complicated galactic foreground emission, and of point sources and lensing, is investigated in a second step.

Our approach uses the S component separation method on maps of B-modes alone. The method is robust with respect to specifics of foreground emission, because it does not rely on an accurate representation of foreground properties. That last point is demonstrated by varying the input foreground sky, and comparing results obtained with different inputs, without changing the analysis pipeline.

It is shown that for r at the level of $r \simeq 0.1$, Planck could make a meaningful (3σ) detection from B-modes alone. The final sensitivity of Planck for measuring r may be better than what is achieved here, as a significant part of the constraining power on r should also come from EE/TE for high r. This has not been investigated in the present paper, which is more focussed on the measurement of low values of r (not achievable with Planck). With the various EPIC mission designs, one could achieve detections at levels of 4-8σ for $r = 10^{-3}$.

For full-sky, multi-frequency space missions, dealing with foregrounds in harmonic space results in a loss of sensitivity by a factor 3 to 4, as compared to what would be achievable without foregrounds, even if the covariance of foreground contaminants is known. The S pipeline allows to achieve performances almost as good (within a factor 1.5), which demonstrates the effectiveness of the blind approach, but is still significantly worse (factor 3–5) than if there were no foregrounds at all. The loss of sensitivity is probably due in part to insufficient localisation in pixel space, which results in suboptimality of the estimator. This could (at least in principle) be improved with a localised processing.

For the most ambitious EPIC space mission, we find that our main conclusions are not modified significantly when taking into account the contamination of primordial B-modes by extragalactic point sources, by gravitational lensing, or when simulating a more complicated galactic emission. In contrast, we find that the measurement of r from the ground with few frequency channels can be severely compromised by foregrounds, even in clean sky regions.

The joint analysis of such ground-based data together with those from less sensitive experiments covering a wider frequency range, such as the Planck data, permits to improve the constraints on r. Still, the result from a combined analysis of Planck and of a small patch observed from the ground at few frequencies cannot match what is obtained using sensitive measurements on the whole frequency range.

This makes a strong case for sensitive multi-frequency observations, and thus probably also for a space mission, as observations from the ground are severely limited (in frequency coverage) by atmospheric absorption and emission. This conclusion is further supported by the fact that a space mission mapping the same clean region (about 1% of the sky), but with the full frequency range allowed by the absence of atmosphere, makes it possible to deal with diffuse foregrounds very efficiently.

Such a deep field mission would, in that respect, outperform a comparable full-sky experiment. The results obtained in the present study, however, do not permit to conclude whether a full sky or a deep field mission would ultimately perform better. A strategy based on the observation of a small patch seems to offer better prospects for measuring r with an harmonic-space based version of S , but also seems to be more impacted by small-scale contamination than all-sky experiments, and is in particular quite sensitive to the lensing effect. Further developments of the component separation pipeline could improve the processing of both types of datasets.

As a final comment, we would like to emphasise that the present study designs, implements effectively, and tests thoroughly on numerous simulations a component separation method for measuring r with CMB B-modes which do not rely on a physical model of foreground emission. The method is shown to be robust against complicated foregrounds (pixel-dependent and running synchrotron spectral index, multi-template dust emission, polarised point sources and lensing). It is also shown to provide reliable errors bars on r by comparing analytical error bars (from the FIM) to estimates obtained from Monte-Carlo simulations. Although more work is needed for the optimal design of the next B-mode experiment, our results demonstrate that foregrounds can be handled quite effectively, making possible the measurement of r down to values of 0.001 or better, at the 5–6σ level.

Certainly, next steps will require fully taking into account small-scale contaminants, partial sky coverage effects, and probably some instrumental effects in addition to diffuse foregrounds. For this level of detail, however, it would be mandatory to refine as well the diffuse foreground model, using upcoming sensitive observations of the sky in the frequency range of interest and on both large and small scales. Such data will become available soon with the forthcoming Planck mission.

Acknowledgements. The authors acknowledge the use of the PSM, developed by the Component Separation Working Group (WG2) of the Planck Collaboration. The HEALPix package (Górski et al. 2005) was used for the derivation of some of the results presented in this paper. M.B. would like to thank USC for hospitality during the Spring 2008 and Marc-Antoine Miville-Deschênes for sharing his expertise on galactic foreground modelling. EP is an NSF–ADVANCE fellow (AST-0649899) also supported by NASA grant NNX07AH59G and Planck subcontract 1290790. J.D., J.F.C. and M.L.J. were partially supported by the ACI "Astro-Map" grant of the French ministry of research to develop the S component separation package used here.

Partial support for EP and MB in carrying out this research was provided by the Jet Propulsion Laboratory, California Institute of Technology, under a contract with the National Aeronautics and Space Administration and funded through the Director's Research and Development Fund Program. (SURP award 1314616)".

References

Amblard, A., Cooray, A., & Kaplinghat, M. 2007, Phys. Rev. D, 75, 083508
Audit, E., & Simmons, J. F. L. 1999, MNRAS, 305, L27
Aumont, J., & Macías-Pérez, J. F. 2007, MNRAS, 376, 739
Battistelli, E. S., Rebolo, R., Rubiño-Martín, J. A., et al. 2006, ApJ, 645, L141

Baumann, D., & Peiris, H. V. 2008, ArXiv e-prints
Baumann, D., Jackson, M. G., Adshead, P., et al. 2008, ArXiv e-prints
Bennett, C. L., Hill, R. S., Hinshaw, G., et al. 2003, ApJS, 148, 97
Benoît, A., Ade, P., Amblard, A., et al. 2004, A&A, 424, 571
Bock, J., Cooray, A., Hanany, S., et al. 2008, ArXiv e-prints
Cardoso, J.-F., Le Jeune, M., Delabrouille, J., Betoule, M., & Patanchon, G. 2008, ArXiv e-prints, 803
Challinor, A., Chon, G., Hivon, E., Prunet, S., & Szapudi, I. 2003, New Astron. Rev., 47, 995
Colombo, L. P. L., & Pierpaoli, E. 2008, ArXiv e-prints
Colombo, L. P. L., Pierpaoli, E., & Pritchard, J. R. 2008, ArXiv e-prints
de Oliveira-Costa, A., Tegmark, M., Davies, R. D., et al. 2004, ApJ, 606, L89
de Zotti, G., Ricci, R., Mesa, D., et al. 2005, A&A, 431, 893
Delabrouille, J., Cardoso, J.-F., & Patanchon, G. 2003, MNRAS, 346, 1089
Delabrouille, J., Cardoso, J., Le Jeune, M., et al. 2008, ArXiv e-prints
Delabrouille, et al. 2009, in preparation
Désert, F.-X., Boulanger, F., & Puget, J. L. 1990, A&A, 237, 215
Draine, B. T., & Fraisse, A. A. 2008, ArXiv e-prints
Draine, B. T., & Lazarian, A. 1998, ApJ, 508, 157
Dunkley, J., Amblard, A., Baccigalupi, C., et al. 2008a, ArXiv e-prints
Dunkley, J., Komatsu, E., Nolta, M. R., et al. 2008b, ArXiv e-prints, 803
Dunkley, J., Spergel, D. N., Komatsu, E., et al. 2008c, ArXiv e-prints
Finkbeiner, D. P. 2004, ApJ, 614, 186
Finkbeiner, D. P., Davis, M., & Schlegel, D. J. 1999, ApJ, 524, 867
Fosalba, P., Lazarian, A., Prunet, S., & Tauber, J. A. 2002, ApJ, 564, 762
Giardino, G., Banday, A. J., Górski, K. M., et al. 2002, A&A, 387, 82
Gold, B., Bennett, C. L., Hill, R. S., et al. 2008, ArXiv e-prints, 803
Górski, K. M., Hivon, E., Banday, A. J., et al. 2005, ApJ, 622, 759
Haslam, C. G. T., Salter, C. J., Stoffel, H., & Wilson, W. E. 1982, A&AS, 47, 1
Hirata, C. M., & Seljak, U. 2003, Phys. Rev. D, 67, 043001
Hivon, E., Górski, K. M., Netterfield, C. B., et al. 2002, ApJ, 567, 2
Hu, W., & White, M. 1997, New Astron., 2, 323
Hu, W., Hedman, M. M., & Zaldarriaga, M. 2003, Phys. Rev. D, 67, 043004
Jonas, J. L., Baart, E. E., & Nicolson, G. D. 1998, MNRAS, 297, 977
Kamionkowski, M., & Kosowsky, A. 1998, Phys. Rev. D, 57, 685
Kamionkowski, M., Kosowsky, A., & Stebbins, A. 1997, Phys. Rev. Lett., 78, 2058
Kaplan, J., & Delabrouille, J. 2002, in Astrophysical Polarized Backgrounds, ed. S. Cecchini, S. Cortiglioni, R. Sault, & C. Sbarra, AIP Conf. Ser., 609, 209
Kesden, M., Cooray, A., & Kamionkowski, M. 2003, Phys. Rev. D, 67, 123507
Knox, L., & Song, Y.-S. 2002, Phys. Rev. Lett., 89, 011303
Kovac, J. M., Leitch, E. M., Pryke, C., et al. 2002, Nature, 420, 772
Lazarian, A. 2007, J. Quant. Spec. Rad. Trans., 106, 225
Lazarian, A., & Finkbeiner, D. 2003, New Astron. Rev., 47, 1107
Lewis, A., & Challinor, A. 2006, Phys. Rep., 429, 1
Li, A., & Draine, B. T. 2001, ApJ, 554, 778
Macellari, N., Pierpaoli, E., Dickinson, C., & Vaillancourt, J. 2008, in prep.
Miville-Deschênes, M., Ysard, N., Lavabre, A., et al. 2008, ArXiv e-prints, 802
Moudden, Y., Cardoso, J., Starck, J., & Delabrouille, J. 2004, ArXiv Astrophysics e-prints
North, C. E., Johnson, B. R., Ade, P. A. R., et al. 2008, ArXiv e-prints
Page, L., Hinshaw, G., Komatsu, E., et al. 2007, ApJS, 170, 335
Peiris, H. V., Komatsu, E., Verde, L., et al. 2003, ApJS, 148, 213
Pierpaoli, E., & Perna, R. 2004, MNRAS, 354, 1005
Platania, P., Burigana, C., Maino, D., et al. 2003, A&A, 410, 847
Reich, P., & Reich, W. 1986, A&AS, 63, 205
Ricci, R., Prandoni, I., Gruppioni, C., Sault, R. J., & De Zotti, G. 2004, A&A, 415, 549
Rosset, C., Yurchenko, V. B., Delabrouille, J., et al. 2007, A&A, 464, 405
Rybicki, G. B., & Lightman, A. P. 1979, Radiative processes in astrophysics (New York: Wiley-Interscience), 393
Sazonov, S. Y., & Sunyaev, R. A. 1999, MNRAS, 310, 765
Schlegel, D. J., Finkbeiner, D. P., & Davis, M. 1998, ApJ, 500, 525
Seljak, U., & Zaldarriaga, M. 1997, Phys. Rev. Lett., 78, 2054
Seto, N., & Pierpaoli, E. 2005, Phys. Rev. Lett., 95, 101302
Sievers, J., & CBI Collaboration. 2005, in BAAS, 37, 1329
Smith, K. M., & Zaldarriaga, M. 2007, Phys. Rev. D, 76, 043001
Smith, K. M., Cooray, A., Das, S., et al. 2008, ArXiv e-prints
Strong, A. W., Moskalenko, I. V., & Ptuskin, V. S. 2007, Ann. Rev. Nucl. Part. Sci., 57, 285
Tegmark, M., de Oliveira-Costa, A., & Hamilton, A. J. 2003, Phys. Rev. D, 68, 123523
Tucci, M., Martínez-González, E., Toffolatti, L., González-Nuevo, J., & De Zotti, G. 2004, MNRAS, 349, 1267
Tucci, M., Martínez-González, E., Vielva, P., & Delabrouille, J. 2005, MNRAS, 360, 935
Verde, L., Peiris, H. V., & Jimenez, R. 2006, J. Cosmol. Astro-Part. Phys., 1, 19
Zaldarriaga, M., & Seljak, U. 2000, ApJS, 129, 431
Zaldarriaga, M., Seljak, U., & Bertschinger, E. 1998, ApJ, 494, 491

Appendix A: Parameterisation the foreground component and choice of a mask

In this appendix, we discuss in more detail the dimension D of matrix used to represent the covariance of the total galactic emission, and the choice of a mask to hide regions of strong galactic emission for the estimation of r with S .

A.1. Dimension D of the foreground component

First, we explain on a few examples the mechanisms which set the rank of the foreground covariance matrix, to give an intuitive understanding of how the dimension D of the foregrounds component used in S to obtain a good model of the data. Let us consider the case of a "perfectly coherent" physical process, for which the total emission, as a function of sky direction ξ and frequency ν, is well described by a spatial template multiplied by a pixel-independent power law frequency scaling:

$$S_\nu(\xi) = S_0(\xi)\left(\frac{\nu}{\nu_0}\right)^\beta \cdot \tag{A.1}$$

The covariance matrix of this foreground will be of rank one and $\mathsf{R}^{\mathrm{S}} = [\mathbf{A}\mathbf{A}^\dagger \mathrm{var}(S_0)]$, with $A_f = \left(\frac{\nu_f}{\nu_0}\right)^\beta$. Now, if the spectral index β fluctuates on the sky, $\beta(\xi) = \beta + \delta\beta(\xi)$, to first order, the emission at frequency ν around ν_0 can be written:

$$S_\nu(\xi) \approx S_0(\xi)\left(\frac{\nu}{\nu_0}\right)^\beta + S_0(\xi)\left(\frac{\nu}{\nu_0}\right)^\beta \delta\beta(\xi)\left(\frac{\nu-\nu_0}{\nu_0}\right)\cdot \tag{A.2}$$

This is not necessarily the best linear approximation of the emission, but supposing it holds, the covariance matrix of the foreground will be of rank two (as the sum of two correlated rank 1 processes). If the noise level is sufficiently low, the variation introduced by the first order term of Eq. (A.2) becomes truly significant, we can't model the emission by a mono-dimensional component as in Eq. (A.1).

In this work, we consider two processes, synchrotron and dust, which are expected to be correlated (at least by the galactic magnetic field and the general shape of the galaxy). Moreover, significant spatial variation of their emission law arises (due to cosmic aging, dust temperature variation ...), which makes their emission only partially coherent from one channel to another. Consequently, we expect that the required dimension D of the galactic foreground component will be at least 4 as soon as the noise level of the instrument is low enough.

The selection of the model can also be made on the basis of a statistical criterion. For example, Table A.1 shows the Bayesian information criterion (BIC) in the case of the EPIC-2m experiment ($r = 0.01$) for 3 consecutive values of D. The BIC is a decreasing function of the likelihood and of the number of parameter. Hence, lower BIC implies either fewer explanatory variables, better fit, or both. In our case the criterion reads:

$$BIC = -2\ln\mathcal{L} + k\ln\sum_q w_q$$

where k is the number of estimated parameters and w_q the effective number of modes in bin q. Taking into account the redundancy in the parameterisation, the actual number of free parameters in the model is $1 + F \times D + QD(D+1)/2 - D^2$. However, we usually prefer to rely on the inspection of the mismatch in every bin of ℓ, as some frequency specific features may be diluted in the global mismatch.

Table A.1. Bayesian information criterion of 3 models with increasing dimension of the galactic component for the EPIC-2m mission.

D	k	BIC
3	376	1.15×10^4
4	617	8.35×10^3
5	916	1.15×10^4

A.2. Masking influence

The noise level and the scanning strategy remaining fixed in the full-sky experiments, a larger coverage gives more information and should result in tighter constraints on both foreground and CMB. In practice, it is only the case up to a certain point, due to the non stationarity of the foreground emission. In the galactic plane, the emission is too strong and too complex to fit in the proposed model, and this region must be discarded to avoid contamination of the results. The main points governing the choice of an appropriate mask are the following:

- the covariance of the total galactic emission (synchrotron and dust polarised emissions), because of the variation of emission laws as a function of the direction on the sky, is never *exactly* modelled by a rank D matrix. However it is *satisfactorily* modelled in this way if the difference between the actual second order statistics of the foregrounds, and those of the rank D matrix model, are indistinguishable because of the noise level (or because of cosmic variance in the empirical statistics). The deviation from the model is more obvious in regions of strong galactic emission, hence the need for a galactic mask. The higher the noise, the smaller the required mask;
- S provides a built-in measure of the adequacy of the model, which is the value of the spectral mismatch. If too high, the model under-fits the data, and the dimension of the foreground model (or the size of the mask) should be increased. If too low, the model over-fits the data, and D should be decreased;
- near full sky coverage is better for measuring adequately the reionisation bump;
- the dimension of the foreground component must be smaller than the number of channels.

If the error variance is always dominated by noise and cosmic variance, the issue is solved: one should select the smaller mask that gives a good fit between the model and the data to minimise the mean squared error and keep the estimator unbiased.

If, on the other hand, the error seems dominated by the contribution of foregrounds, which is, for example, the case of the EPIC-2m experiment for $r = 0.001$, the tradeoff is unclear and it may happen that a better estimator is obtained with a stronger masking of the foreground contamination. We found that it is not the case. Table A.2 illustrates the case of the EPIC-2m experiment with the galactic cut used in Sect. 4 and a bigger cut. Although the reduction of sensitivity is slower in the presence of foreground than for the noise dominated case, the smaller mask still give the better results. We may also recall that the expression (7) of the likelihood is an approximation for partial sky coverage. The scheme presented here thus may not give fully reliable results when masking effects become important.

Table A.2. Estimation of the tensor to scalar ratio with two different galactic cuts in the EPIC-2m experiment.

r	$r^{\rm est}$	$\sigma_r^{\rm FISHER}$	$\sigma_r^{\rm no-fg}$	$f_{\rm sky}$
0.001	1.01×10^{-3}	1.60×10^{-4}	5.25×10^{-5}	0.87
0.001	1.01×10^{-3}	1.68×10^{-4}	5.72×10^{-5}	0.73

Appendix B: Spectral mismatch

Computed for each bin q of ℓ, the mismatch criterion, $w_q K\left(\widehat{\mathsf{R}}_q, \mathsf{R}_q(\theta^*)\right)$, between the best-fit model $\mathsf{R}_q(\theta^*)$ at the point of convergence θ^*, and the data $\widehat{\mathsf{R}}_q$, gives a picture of the goodness of fit as a function of the scale. Black curves in Figs. B.1 and B.2 show the mismatch criterion of the best fits for Planck and EPIC designs respectively. When the model holds, the value of the mismatch is expected to be around the number of degrees of freedom (horizontal black lines in the figures). We can also compute the mismatch for a model in which we discard the CMB contribution $w_q K\left(\widehat{\mathsf{R}}_q, \mathsf{R}_q(\theta^*) - \mathsf{R}_q^{\rm CMB}(r^*)\right)$. Gray curves in Figs. B.1 and B.2 show the mismatch for this modified model. The difference between the two curves illustrates the "weight" of the CMB component in the fit, as a function of the scale.

Figure B.1 shows the results for Planck for $r = 0.3$ and 0.1. The curves of the difference plotted in inclusion illustrate the predominance of the reionisation bump. In Fig. B.2, we plot the difference curve on the bottom panels for the three experiments for $r = 0.01$ and $r = 0.001$. They illustrate clearly the difference of sensitivity to the peak between the EPIC-LC design and the higher resolution experiments. In general it can be seen that no significant contribution to the CMB is coming from scales smaller than $\ell = 150$.

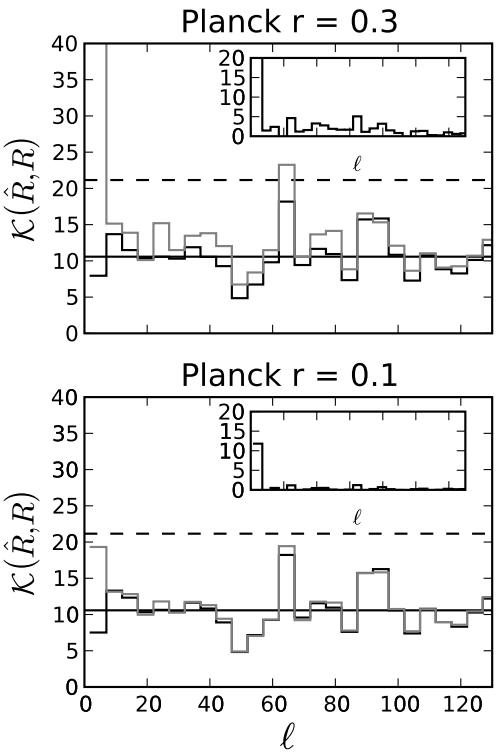

Fig. B.1. Those plots present the distribution in ℓ of the mismatch criterion between the model and the data for two values of r for P . On the grey curve, the mismatch has been computed discarding the CMB contribution from the S model. The difference between the two curves, plotted in inclusion, illustrates somehow the importance of the CMB contribution to the signal.

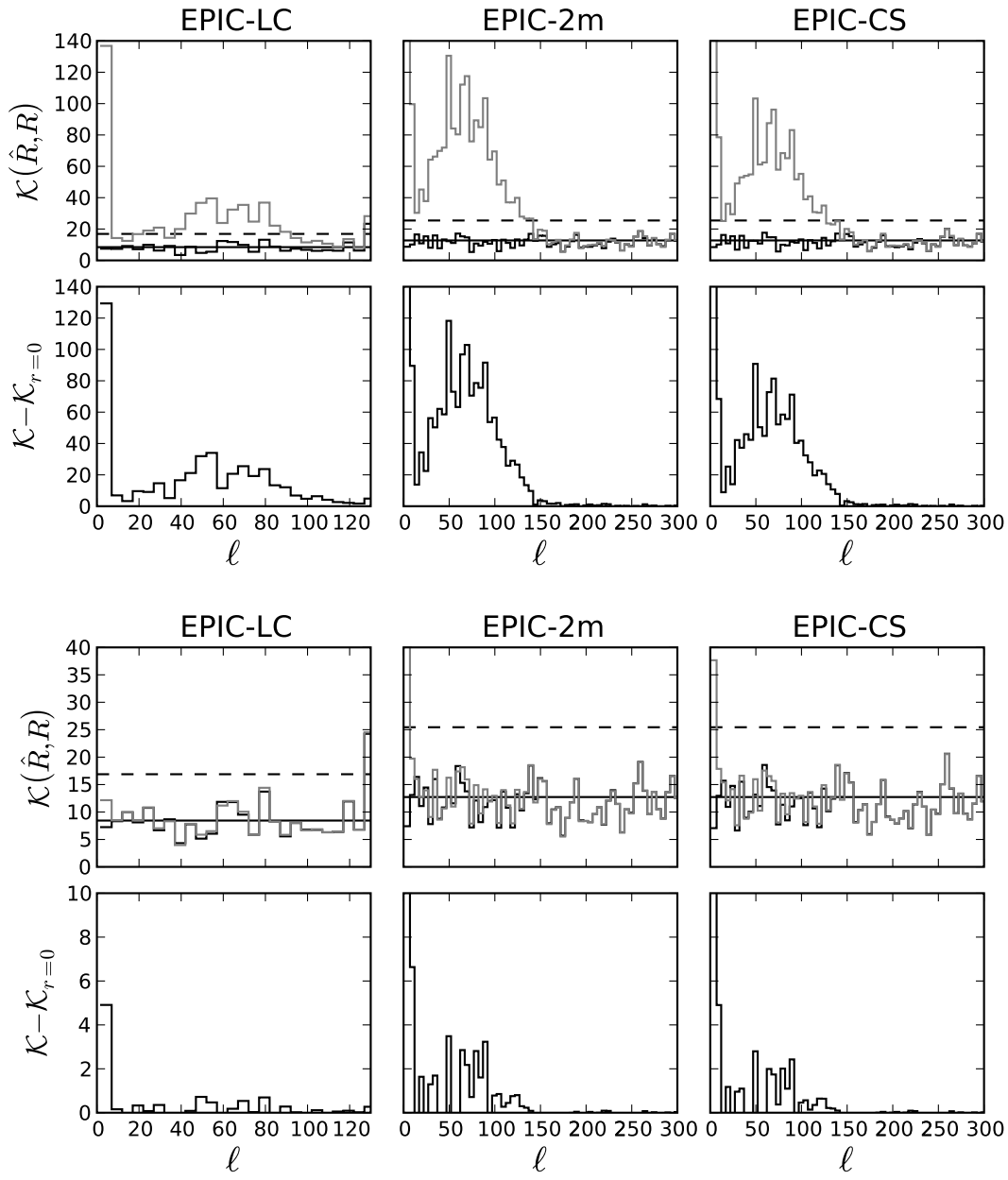

Fig. B.2. Mismatch criterion for $r = 0.01$ (*top*) and $r = 0.001$ (*bottom*). In each plot, the top panel shows the mismatch criterion between the best fit model and the data (black curve) and the best fit model deprived from the CMB contribution and the data (gray curve). Solid and dashed horizontal lines show respectively the mismatch expectation and 2 times the mismatch expectation. The difference between the gray and the black curve is plotted in the bottom panel and gives an idea of the significance of the CMB signal in each bin of ℓ.

PHYSICAL REVIEW D **78,** 083013 (2008)

CMB power spectrum estimation using wavelets

G. Faÿ,[*] F. Guilloux,[+] M. Betoule, J.-F. Cardoso,[‡] J. Delabrouille, and M. Le Jeune

Laboratoire AstroParticule et Cosmologie, UMR 7164, Université Paris 7—Denis Diderot and CNRS, 10, rue A. Domon et L. Duquet, 75205 Paris Cedex 13, France

(Received 8 July 2008; published 30 October 2008)

Observations of the cosmic microwave background (CMB) provide increasingly accurate information about the structure of the Universe at the recombination epoch. Most of this information is encoded in the angular power spectrum of the CMB. The aim of this work is to propose a versatile and powerful method for spectral estimation on the sphere which can easily deal with nonstationary uncorrelated noise and multiple experiments with various specifications. In this paper, we use needlets (wavelets) on the sphere to construct natural and efficient spectral estimators for partially observed and beamed CMB with nonstationary noise. In the case of a single experiment, we compare this method with pseudo-C_ℓ methods. The performance of the needlet spectral estimators (NSE) compares very favorably to the best pseudo-C_ℓ estimators, over the whole multipole range. On simulations with a simple model (CMB + uncorrelated noise with known variance per pixel + mask), they perform uniformly better. Their distinctive ability to aggregate many different experiments, to control the propagation of errors, and to produce a single wideband error bar is highlighted. The needlet spectral estimator is a powerful, tunable tool which is very well suited to the angular power spectrum estimation of spherical data such as incomplete and noisy CMB maps.

DOI: 10.1103/PhysRevD.78.083013 PACS numbers: 98.80.−k, 95.75.Pq, 98.80.Es

I. INTRODUCTION

The estimation of the temperature and polarization angular power spectra of the cosmic microwave background (CMB) is a key step for estimating the cosmological parameters. Cosmological information is encoded in the huge data sets (time order scanning data or high resolution maps) provided by ground-based, balloon-borne, or satellite experiments.

In the ideal case of noiseless and full-sky experiments, angular power spectrum estimation is a straightforward task. The empirical spectrum of the outcome of a Gaussian stationary field X, given by

$$\hat{C}_\ell = \frac{1}{2\ell+1} \sum_{m=-\ell}^{\ell} \langle X, Y_{\ell m}\rangle^2, \tag{1}$$

where $(Y_{\ell m})$ denote the usual spherical harmonics, also is the *maximum-likelihood* (ML) estimator of the power spectrum of X. It is efficient in the sense that its variance reaches the Cramér-Rao lower bound.

CMB maps are, however, more or less strongly contaminated by foregrounds and instrumental noises, depending on the wavelength, angular frequency ℓ, and the direction of observation. Ground-based experiments cover small parts of the sky while space missions (COBE, WMAP, and, in the near future, Planck) provide full-sky maps of the CMB, but still contaminated with galactic residuals. Then, the plain estimate (1) is no longer efficient nor even unbiased. To circumvent the nonstationarity of actual observations, the main ingredients for the spectral estimation used by, for instance, the WMAP collaboration [1] and also in most other analyses, are broadly the following ones. Usually, some part of the covered sky is blanked to remove the most emissive foregrounds or the most noisy measurements. This amounts to applying a *mask* or more generally a weight function to the sky. Most of the emissive foregrounds can be subtracted using some component separation procedure (see e.g. [2] for comparison methods with Planck-like simulated data). Even the best foreground-subtracted maps require masking a small fraction of the sky. Missing or masked data makes the optimal estimation of the power spectrum a much harder task. In particular, it breaks the diagonal structure of the covariance of the multipole moments $a_{\ell m} := \langle X, Y_{\ell m}\rangle$ of any stationary component. The maximum-likelihood estimation of the spectrum in the pixel domain has a numerical complexity that scales as N_{pix}^3 and requires the storage of N_{pix}^2 matrices. This is untractable for high resolution experiments such as WMAP or Planck ($N_{\mathrm{pix}} \simeq 13.10^6$). Nevertheless, for very low ℓ's ($\ell \leq 30$), ML estimation in the pixel domain can be performed on downgraded resolution maps; see [3,4], for instance. At higher ℓ's, a

[*]Laboratoire Paul Painlevé, UMR 8524, Université Lille 1 and CNRS, 59 655 Villeneuve d'Ascq Cedex, France; gilles.fay@univ-lille1.fr

[+]MODAL'X, Université Paris Ouest—Nanterre La Défense, 200 avenue de la République, 92001 Nanterre Cedex, France and Laboratoire de Probabilités et Modèles Aléatoires, UMR 7599, Université Paris 7—Denis Diderot and CNRS, 175 rue du Chevaleret, 75013 Paris, France.

[‡]Laboratoire de Traitement et Communication de l'Information, UMR 5141, Télécom ParisTech and CNRS, 46 rue Barrault, 75634 Paris Cedex, France.

suboptimal method based on the *Pseudo-C_ℓ* (PCL) gives quite satisfactory results in terms of complexity and accuracy [5]. It debiases the empirical or (pseudo) spectrum from the noise contribution and deconvolves it from the average mask effect. It works in the spherical harmonic domain, uses fast spherical harmonic transforms (SHT), and scales as $N_{\rm pix}^{3/2}$. The available pixels can be weighted according to the signal-to-noise ratio (SNR) at any given point. For signal-dominated frequencies (low ℓ's), the data are uniformly weighted; it yields the pseudo-C_ℓ estimator with uniform weights (PCLU). At noise-dominated frequencies (high ℓ's), each pixel is weighted by the inverse of the variance of the noise (PCLW estimator). The WMAP collaboration used uniform weights for $\ell \leq 500$, the inverse of the noise variance for $\ell > 500$ (see [1] Sec. 7.5) for its three-year release. Efstathiou [6] showed that the PCLW estimator is statistically equivalent to the ML estimator in the low SNR limit, which is usually the case at high ℓ's. In the same paper he proposed a hybrid method with a smooth transition between the two PCL regimes. Finally, when several maps are available, it is worth considering *cross-power spectra* between different channels since noise is usually uncorrelated from channel to channel (see [7] A1.1 or [8]).

Other estimation procedures do not fit in either of the two categories above. Among them, the spectral estimation from time ordered data by [9] or Gibbs sampling and Monte Carlo Markov chain methods such as MAGIC or Commander, see [10]. Those last methods try to estimate the complete posterior joint probability distribution of the power spectrum through sampling, which in turn can provide point estimates of the spectrum but also covariance estimates, etc. Recently, the multitaper approach has been imported from the time series literature to the field of spherical data by [11,12]. The goal of this approach is to provide an estimation of a localized power spectrum, under noiseless or stationary noise assumption.

In this paper, we focus on spectral estimation of the global power spectrum, in a frequentist framework. We consider spectral estimation at small angular scales, i.e. in the range of multipoles where the cost of ML estimation is prohibitive. We compare our method to PCL methods. We adopt somehow realistic models that include partial coverage of the sky, symmetric beam convolution, inhomogeneous and uncorrelated additive pixel noise, and multiple experiments.

Localized analysis functions such as wavelets are natural tools to tackle nonstationarity and missing data issues. There are different ways to define wavelets (in the broad sense of space-frequency objects) on the sphere, and our choice is to use the needlets, the statistical properties of which have received a recent rigorous treatment [13,14] and which have already been applied successfully to cosmology [15–17].

Needlets benefit from perfect (and freely adjustable) localization in the spherical harmonic domain, which enables their use for spectral estimation. Moreover, the correlation between needlet coefficients centered on two fixed directions of the sky vanishes as the scale goes to infinity, i.e. as the needlet concentrates around those points. The spatial localization is excellent. This property leads to several convergence results and motivates procedures based on the approximation of decorrelation between coefficients. In this contribution, we define and study a new angular power spectrum estimator that uses the property of localization of the wavelets in both spatial and frequency domains.

In the case of a single experiment with partial coverage and inhomogeneous noise, the needlet-based estimator deals straightforwardly with the variation of noise level over the sky, taking advantage of their localization in the pixel domain. Moreover, it allows a joint spectral estimation from multiple experiments with different coverages, different beams, and different noise levels. The proposed method mixes observations from all experiments with spatially varying weights to take into account the local noise levels. The resulting spectral estimator somehow mimics the maximum-likelihood estimator based on all the experiments.

The paper is organized as follows. In Sec. II, we present the observation model and recall the basics of needlet analysis and the properties of the needlet coefficients which are the most relevant for spectral estimation. In Sec. III, we define the needlet spectral estimators (NSE) in the single-map and multiple-maps frameworks. In Sec. IV, we present results of Monte Carlo experiments which demonstrate the effectiveness of our approach. In Sec. V, we summarize the strong and weak points of our method and outline the remaining difficulties.

II. FRAMEWORK

A. Observation model

Let T denote the temperature anisotropy of the CMB emission. For the sake of simplicity, we consider the following observation model:

$$X(\xi_k) = W(\xi_k)((B * T)(\xi_k) + \sigma(\xi_k)Z_k), \quad k = 1, \ldots, N_{\rm pix}, \tag{2}$$

where (ξ_k) is a collection of pixels on the sphere, W denotes a (0–1)-mask or any weight function $0 \leq W \leq 1$, B denotes the instrumental beam. An additive instrumental noise is modeled by the term $\sigma(\xi_k)Z_k$ with the assumption that (Z_k) is an independent standard Gaussian sequence. Further, we assume that σ, W, and B are known deterministic functions and that B is axisymmetric. Typically, the variance map σ^2 writes $\sigma^2(\xi_k) = \sigma_0^2/N_{\rm obs}(\xi_k)$, where $N_{\rm obs}$ is referred to as the *hit map*, that is, $N_{\rm obs}(\xi_k)$ is the number of times a pixel in direction ξ_k is seen by the instrument.

We assume that the observations have been cleaned from foreground emissions or that those emissions are present but negligible outside the masked region. When observations from several experiments are jointly considered, the model becomes

$$X_e(\xi_k) = W_e(\xi_k)((B_e * T)(\xi_k) + \sigma_e(\xi_k)Z_{k,e}), \quad k = 1, \ldots, N_{\text{pix}}, \qquad e = 1, \ldots, E, \tag{3}$$

where e indexes the experiment. The CMB sky temperature T is the same for all experiments but the instrumental characteristics (beam, coverage) differ (see, for example, Table II), and the respective noises can usually be considered as independent.

B. Definition and implementation of a needlet analysis

We recall here the construction and practical computation of the needlet coefficients. Details can be found in Refs. [18,19].

Needlets are based in a decomposition of the spectral domain in bands or "scales" which are traditionally indexed by an integer j. Let $b_\ell^{(j)}$ be a collection of window functions in the multipole domain, with maximal frequencies $\ell_{\text{max}}^{(j)}$ (see Fig. 1 below). Consider some pixelization points $\xi_k^{(j)}$, $k = 1, \ldots, N_{\text{pix}}^{(j)}$, associated with positive weights $\lambda_k^{(j)}$, $k = 1, \ldots, N_{\text{pix}}^{(j)}$ which enable exact discrete integration (quadrature) for spherical harmonics up to degree $2\ell_{\text{max}}^{(j)}$, that is, equality

$$\int_{\mathbb{S}} Y_{\ell m}(\xi)\mathrm{d}\xi = \sum_{k=1}^{N_{\text{pix}}^{(j)}} \lambda_k^{(j)} Y_{\ell m}(\xi_k^{(j)})$$

holds for any ℓ, m such that $\ell \le 2\ell_{\text{max}}^{(j)}$, $|m| \le \ell$. Needlets are the axisymmetric functions defined by

$$\psi_k^{(j)}(\xi) = \sqrt{\lambda_k^{(j)}} \sum_{\ell=0}^{\ell_{\text{max}}^{(j)}} b_\ell^{(j)} L_\ell(\xi \cdot \xi_k^{(j)}), \tag{4}$$

where L_ℓ denotes the Legendre polynomial of order ℓ normalized according to the condition $L_\ell(1) = \frac{2\ell+1}{4\pi}$. For proper choices of window functions $\{b_\ell^{(j)}\}_j$, the family $\{\psi_k^{(j)}\}_{k,j}$ is a *frame* on the Hilbert space of square-integrable functions on the sphere $\mathbb{S}$. In a B-adic scheme, it is even a *tight frame* [19]. Though redundant, tight frames are complete sets which have many properties reminiscent of orthonormal bases (see e.g. [20], chap. 3).

For any field X on the sphere, the coefficients $\gamma_k^{(j)} := (\lambda_k^{(j)})^{-1/2}\langle X, \psi_k^{(j)}\rangle$ are easily computed in the spherical harmonic domain as made explicit by the following diagram:

$$\begin{array}{ccc} \{X(\xi_k)\}_{k=1,\ldots,N_{\text{pix}}} & \xrightarrow{\text{SHT}} & a_{\ell m} \\ & & \Downarrow \times \\ \left\{\gamma_k^{(j)}\right\}_{k=1,\ldots,N_{\text{pix}}^{(j)}} & \xleftarrow{\text{SHT}^{-1}} & b_\ell^{(j)} a_{\ell m} \end{array} \tag{5}$$

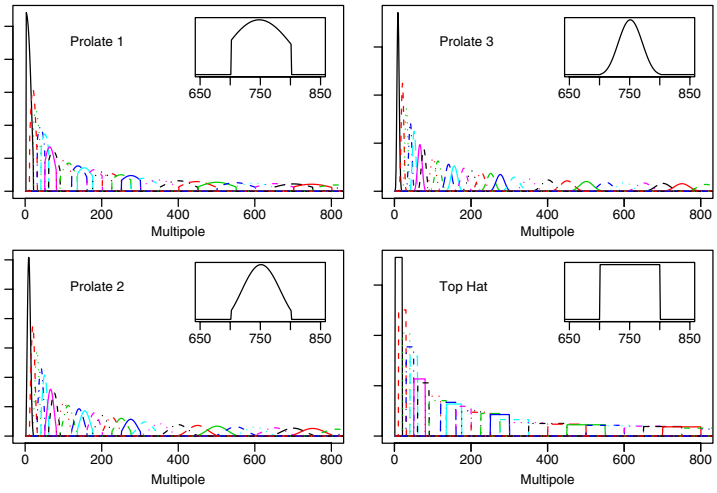

FIG. 1 (color online). Four families of window functions that are used for the NSE and compared numerically in Sec. IV A 2. There are three families of prolate spheroidal wave functions and one family of top-hat functions. All the families are defined on the same bands. Inset graphs show the window function in the 26th band. Each window function is normalized by the relation $(4\pi)^{-1} \times \sum(b_\ell^{(j)})^2(2\ell + 1) = 1$. Then, if the angular power spectrum is flat, $C_\ell \equiv C_0$, then $C^{(j)} \equiv C_0$ for all bands, according to (8).

Double arrows denote as many operations (e.g. spherical transforms) as bands. The initial resolution must be fine enough to allow an exact computation of the spherical harmonics transform up to degree $\ell_{\max}^{(j)}$. If, say, the HEALPix pixelization is used, the `nside` parameter of the original map determines the highest available multipole moments and, in turn, the highest available band j.

C. Distribution of the needlet coefficients

A square-integrable random process X on the sphere is said to be centered and stationary (or isotropic) if $\mathbb{E}(X(\xi)) = 0$, $\mathbb{E}(X(\xi)^2) < \infty$, and $\mathbb{E}(X(\xi)X(\xi')) = (4\pi)^{-1}\sum_\ell C_\ell L_\ell(\xi \cdot \xi')$, with C_ℓ referred to as the angular power spectrum of X. The next proposition summarizes the first and second order statistical properties of the needlet coefficients of such a process. They are the building blocks for any subsequent spectral analysis using needlets.

Proposition 1 Suppose that X is a stationary and centered random field with power spectrum C_ℓ. Then the needlet coefficients are centered random variables and, for any 4-tuple (j, j', k, k')

$$\mathrm{cov}[\gamma_k^{(j)}, \gamma_{k'}^{(j')}] = \sum_{\ell\geq 0} b_\ell^{(j)} b_\ell^{(j')} C_\ell L_\ell(\cos\theta), \tag{6}$$

where $\theta = \theta(j, k, j', k')$ is the angular distance between $\xi_k^{(j)}$ and $\xi_{k'}^{(j')}$. In particular

$$\mathrm{var}[\gamma_k^{(j)}] = C^{(j)}, \tag{7}$$

where

$$C^{(j)} := (4\pi)^{-1}\sum_{\ell\geq 0}(b_\ell^{(j)})^2(2\ell+1)C_\ell. \tag{8}$$

In other words, the variance of the coefficients $\gamma_k^{(j)}$ is the power spectrum of X properly integrated over the jth band.

Remark 1 It also follows from (6) that if the bands j and j' are nonoverlapping (this is the case for any nonconsecutive filters of Fig. 1), all the pairs of needlet coefficients $\gamma_k^{(j)}$ and $\gamma_{k'}^{(j')}$ are uncorrelated and then independent if the field is moreover Gaussian.

Suppose now that

$$X(\xi_k) = \sigma(\xi_k)Z_k, \qquad k = 1, \cdots, N_{\mathrm{pix}},$$

is a collection of independent random variables with zero mean and variance $\sigma^2(\xi_k)$, where σ is a band-limited function. This is a convenient and widely used model for residual instrumental noise (uncorrelated, but nonstationary). Needlet coefficients are centered and, moreover, if the quadrature weights are approximately uniform ($\lambda_k \simeq 4\pi/N_{\mathrm{pix}}$, as is the case of HEALPix) and σ is sufficiently smooth, then

$$\mathrm{cov}[\gamma_k^{(j)}, \gamma_{k'}^{(j')}] \simeq \int_{\mathbb{S}} \sigma^2(\xi)\psi_k^{(j)}(\xi)\psi_{k'}^{(j')}(\xi)\mathrm{d}\xi.$$

We denote

$$n_k^{(j)}(\sigma) := \left(\int_{\mathbb{S}} \sigma^2(\xi)|\psi_k^{(j)}(\xi)|^2\mathrm{d}\xi\right)^{1/2}, \tag{9}$$

the standard deviation of the needlet coefficient of scale j centered on ξ_k. When the noise is homogeneous (σ is constant), it reduces to $\frac{\sigma^2}{N_{\mathrm{pix}}}\sum_{\ell\geq 0}(2\ell+1)(b_\ell^{(j)})^2$.

D. Mask and beam effects

As already noticed in the introduction, missing or masked data makes the angular power spectrum estimation a nontrivial task. Simple operations in Fourier space such as debeaming become tricky. Needlets are also affected by both the mask and the beam. The effect on needlets of beam and mask can be approximated as described below. These approximations, which lead to simple implementations, are validated in numerical simulations in relatively realistic conditions in Sec. IV.

a. Mask. Recalling that the needlets are spatially localized, the needlet coefficients are expected to be insensitive to the application of a mask on the data if they are computed far away from its edges. Numerical and theoretical studies of this property can be found in [14,18]. In practice, we choose to quantify the effect of the mask on a single coefficient $\gamma_k^{(j)}$ by the loss induced on the $\mathbb{L}^2$-norm of the needlet $\psi_k^{(j)}$, i.e. a purely geometrical criterion. More specifically, needlet coefficients at scale j are deemed reliable [at level $t^{(j)}$] if they belong to the set

$$\mathcal{K}_{t^{(j)}}^{(j)} := \left\{k = 1, \ldots, N_{\mathrm{pix}}^{(j)} : \frac{\| W\psi_k^{(j)} \|_2^2}{\| \psi_k^{(j)} \|_2^2} \geq t^{(j)}\right\}. \tag{10}$$

Parameter $t^{(j)}$ is typically set to 0.99 or 0.95 for all bands. Note that $t \mapsto \mathcal{K}_t^{(j)}$ is decreasing, $\mathcal{K}_0^{(j)} = K^{(j)}$, and $\mathcal{K}_{1^+}^{(j)} = \varnothing$. In practice, this set is computed by thresholding the map obtained by the convolution of the mask with the axisymmetric kernel $\xi \mapsto (\sum_\ell b_\ell^{(j)} L_\ell(\cos\theta))^2$. This operation is easy to implement in the multipole domain.

b. Beam. Consider now the effect of the instrumental beam. Its transfer function B_ℓ is assumed smooth enough that it can be approximated in the band j by its mean value $B^{(j)}$ in this band, defined by

$$(B^{(j)})^2 := (4\pi)^{-1}\sum_{\ell\geq 0}(2\ell+1)(b_\ell^{(j)})^2 B_\ell^2. \tag{11}$$

In the following, the beam effect for spectral estimation is taken into account in each band. Indeed, with Definition (11), with no noise, no mask, and a smooth beam, Eq. (7) translates to

$$\mathrm{var}\left[\frac{\gamma_k^{(j)}}{B^{(j)}}\right] \simeq C^{(j)}, \qquad k = 1, \ldots, N_{\mathrm{pix}}^{(j)}. \tag{12}$$

In other words, thanks to the relative narrowness of the bands and to the smoothness of the beam and CMB spectrum, the attenuation induced by the beam can be approxi-

mated as acting uniformly in each band and not on individual multipoles. Numerically, with typical beam values from WMAP or ACBAR experiments (see Table II), the relative difference (statistical bias) between the goal quantity $C^{(j)}$ and the estimated one $\mathrm{var}(\gamma_k^{(j)})/(B^{(j)})^2$ remains under 1% for bands below $j = 27$ ($\ell_{\max} = 875$) for WMAP-W, and below $j = 39$ ($\ell_{\max} = 2000$) for ACBAR.

III. THE NEEDLET SPECTRAL ESTIMATORS (NSE)

A. Smooth spectral estimates from a single map

For any sequence of weights $w_k^{(j)}$ such that $\sum_{k=1}^{N_{\mathrm{pix}}^{(j)}} w_k^{(j)} = 1$ and for a clean (contamination-free), complete (full-sky), and nonconvolved (beam-free) observation of the CMB, the quantity

$$\hat{C}^{(j)} := \sum_{k=1}^{N_{\mathrm{pix}}^{(j)}} w_k^{(j)} (\gamma_k^{(j)})^2$$

is an unbiased estimate of $C^{(j)}$, a direct consequence of Proposition 1.

Remark 2 For uniform weights, this estimator is nothing but the estimator $\hat{C}_\ell$ from Eq. (1) binned by the window function $(b_\ell^{(j)})^2$. Indeed, (see diagram (5))

$$\hat{C}^{(j)} = (4\pi)^{-1} \sum_{\ell \geq 0} (b_\ell^{(j)})^2 \sum_{m=-\ell}^{\ell} a_{\ell m}^2 \tag{13}$$

$$= (4\pi)^{-1} \sum_{\ell \geq 0} (b_\ell^{(j)})^2 (2\ell + 1) \hat{C}_\ell. \tag{14}$$

This is the uniformly minimum variance unbiased estimator of $C^{(j)}$. The so-called *cosmic variance* is the Cramér-Rao lower bound for estimation of the parameter C_ℓ in the full-sky, noise-free case. Its expression simply is $2C_\ell^2/(2\ell + 1)$. Its counterpart for the binned estimator $C^{(j)}$ in this ideal context is

$$V_{\mathrm{cosmic}}^{(j)} = 2(4\pi)^{-2} \sum (b_\ell^{(j)})^4 (2\ell + 1) C_\ell^2. \tag{15}$$

Consider now the observation model (2). Up to the approximations of Sec. II D, one finds that

$$\hat{C}^{(j)} := \frac{1}{(B^{(j)})^2} \sum_{k \in \mathcal{K}_{t^{(j)}}^{(j)}} w_k^{(j)} \{(\gamma_k^{(j)})^2 - (n_k^{(j)})^2\} \tag{16}$$

is an unbiased estimate of $C^{(j)}$ as soon as

$$\sum_{k \in \mathcal{K}_{t^{(j)}}^{(j)}} w_k^{(j)} = 1. \tag{17}$$

The weights can further be chosen to minimize the mean-square error $\mathbb{E}(\hat{C}^{(j)} - C^{(j)})^2$, under the constraint (17). It amounts to setting the weights according to the local signal-to-noise ratio, which is nonconstant for nonstationary noise. This is a distinctive advantage of our method that it allows for such a weighting in a straightforward and natural manner. In the case of uncorrelated coefficients, this optimization problem is easy to solve (using Lagrange multipliers) and is equivalent to maximizing the likelihood under the approximation of independent coefficients (see Appendix C for details). It leads to the solution

$$w_k^{(j)}(\bar{C}) := (\bar{C} + (n_k^{(j)})^2)^{-2} \Big[\sum_{k' \in \mathcal{K}_{t^{(j)}}^{(j)}} (\bar{C} + (n_{k'}^{(j)})^2)^{-2} \Big]^{-1} \tag{18}$$

with $\bar{C} = C^{(j)}$. This is the unknown quantity to be estimated but it can be replaced by some preliminary estimate (for example, the spectral estimate of [1]). One can also iterate the estimation procedure from any starting point. The robustness of this method with respect to the prior spectrum is demonstrated in Sec. IV A 2 (see Fig. 6).

Those weights are derived under the simplifying assumption of independence of needlet coefficients. They can be used in practice because needlet coefficients are only weakly dependent. Precisely, for two fixed points on a increasingly fine grid ξ_k, $\xi_{k'}$ and well-chosen window functions, the needlets coefficients $(\gamma_k^{(j)}, \gamma_{k'}^{(j)})$ are asymptotically independent as $j \to \infty$ (see [14]). Note that this property is shared by well-known Mexican Hat wavelets, as proved in [21].

B. Smooth spectral estimates from multiple experiments

Consider now the observation model described by Eq. (3) with noise independence between experiments. Using the approximations of Sec. II D, Eq. (3) translates to

$$\frac{\gamma_{k,e}^{(j)}(X)}{B_e^{(j)}} = \gamma_k^{(j)}(T) + \frac{n_k^{(j)}(\sigma_e)}{B_e^{(j)}} Z_{k,e} \tag{19}$$

in the needlet domain, for indexes $k \in \mathcal{K}_{e,t^{(j)}}^{(j)}$, where $Z_{k,e}$ are standard Gaussian random variables which are correlated within the same experiment e but independent between experiments. As explained in the single-experiment case of Sec. III A, the coefficients are only slightly correlated. This justifies the use, in the angular power spectrum estimator, of the weights derived by the maximization of the likelihood with independent variables. The correlation between coefficients does not introduce any bias here but only causes loss of efficiency. As in the single-experiment case, only the coefficients sufficiently far away from the mask of at least one experiment are kept. Defining

$$\mathcal{K}^{(j)} = \cup_e \mathcal{K}_{e,t^{(j)}}^{(j)},$$

the aggregated estimator is implicitly defined (see Appendix C) by

$$\hat{C}^{ML,(j)} = \sum_{k\in\mathcal{K}^{(j)}} \tilde{w}_k^{(j)}(\hat{C}^{ML,(j)})\{(\tilde{\gamma}_k^{(j)})^2 - (\tilde{n}_k^{(j)})^2\} \quad (20)$$

with, for any k in $\mathcal{K}^{(j)}$

$$\tilde{\gamma}_k^{(j)} = \sum_e \omega_{k,e}^{(j)} \frac{\gamma_{k,e}^{(j)}}{B_e^{(j)}}, \quad (21)$$

$$\tilde{n}_k^{(j)} := \left[\sum_e \left(\frac{B_e^{(j)}}{n_k^{(j)}(\sigma_e)}\right)^2 \mathbf{1}_{k\in\mathcal{K}_{e,t^{(j)}}^{(j)}}\right]^{-1/2}, \quad (22)$$

$$w_{k,e}^{(j)} := \left(\frac{B_e^{(j)}}{n_k^{(j)}(\sigma_e)}\right)^2 \mathbf{1}_{k\in\mathcal{K}_{e,t^{(j)}}^{(j)}} (\tilde{n}_k^{(j)})^2 \quad (23)$$

and similarly to (18),

$$\tilde{w}_k^{(j)}(C) := (C + (\tilde{n}_k^{(j)})^2)^{-2}\left[\sum_{k'\in\mathcal{K}^{(j)}} (C + (\tilde{n}_{k'}^{(j)})^2)^{-2}\right]^{-1}. \quad (24)$$

Note that $\sum_e \omega_{k,e}^{(j)} = 1$ and $\sum_k \tilde{w}_k^{(j)} = 1$. An explicit estimator is obtained by plugging some previous, possibly rough, estimate $\bar{C}^{(j)}$ of $C^{(j)}$ in place of C of Eq. (24). Eventually, the aggregated angular power spectrum estimator is taken as

$$\hat{C}^{(j)} = \sum_{k\in\mathcal{K}^{(j)}} \tilde{w}_k^{(j)}(\bar{C}^{(j)})\{(\tilde{\gamma}_k^{(j)})^2 - (\tilde{n}_k^{(j)})^2\}. \quad (25)$$

This expression can be interpreted in the following way. For any pixel k in $\mathcal{K}^{(j)}$, that is for any pixel where the needlet coefficient is reasonably uncontaminated by the mask for at least one experiment, we compute an aggregated needlet coefficient $\tilde{\gamma}_k^{(j)}$ by the convex combination (21) of the debeamed needlet coefficients from all available experiments. Weights of the combination are computed according to the relative local signal-to-noise ratio (including the beam attenuation). Finally, a spectral estimation is performed on the single map of aggregated coefficients, in the same way as in Sec. III A. Those coefficients are squared and translated by $\tilde{n}_k^{(j)}$ to provide an unbiased estimate of $C^{(j)}$. Then all the available squared and debiased coefficients are linearly combined according to their relative reliability $\tilde{w}_k^{(j)}(C)$ which is proportional to $(C^{(j)} + (\tilde{n}_k^{(j)})^2)^{-1}$. Figures 13 and 14 display the values of those weights (maps) $\tilde{w}_k^{(j)}$ and $\omega_{k,e}^{(j)}$ for a particular mixing of experiments. See Sec. IV B for details.

C. Parameters of the method

In this section, we discuss various issues raised by the choice of the parameters of the NSE method. Those parameters are: the shape of the spectral window function $b_\ell^{(j)}$ in each band (or equivalently the shape of the needlet itself in the spatial domain), the bands themselves (i.e. the spectral support of each needlet), and the values of the thresholds $t^{(j)}$ that define the regions of the sky where needlets coefficients are trusted in each band; see Eq. (10). See Sec. IV A 2 for a numerical investigation.

1. Width and shape of the window functions

For spectral estimation, it is advisable to consider spectral window functions with relatively narrow spectral support, in order to reduce bias in the spectral estimation. The span of the summation in (4) can be fixed to some interval $[\ell_{\min}^{(j)}, \ell_{\max}^{(j)}]$. For our illustrations, the interval bands have been chosen to cover the range of available multipoles with more bands around the expected positions of the peaks of the CMB. The bands are described in Table I.

It is well known, however, that perfect spectral and spatial localization cannot be achieved simultaneously (call it the uncertainty principle). In order to reduce the effect of the mask, we have to check that the analysis kernels are well localized. This leads to the optimization of some localization criteria. If we retain the best $\mathbb{L}^2$ concentration in a polar cap $\Omega_{\theta^{(j)}} = \{\xi : \theta \le \theta^{(j)}\}$, namely

$$(b_\ell^{(j)})_{\ell=\ell_{\min},\cdots,\ell_{\max}} = \arg\max_{\mathsf{b}} \frac{\int_{\Omega_{\theta^{(j)}}} |\sum_{\ell=\ell_{\min}^{(j)}}^{\ell_{\max}^{(j)}} \mathsf{b}_\ell L_\ell(\xi)|^2 d\xi}{\int_{\mathbb{S}} |\sum_{\ell=\ell_{\min}^{(j)}}^{\ell_{\max}^{(j)}} \mathsf{b}_\ell L_\ell(\xi)|^2 d\xi}, \quad (26)$$

we obtain the analogous of the prolate spheroidal wave function (PSWF) thoroughly studied in e.g. Ref. [22] for the PSWF in $\mathbb{R}$ and [18,23] for PSWF on the sphere. In our simulations, we use PSWF needlets since they are well

TABLE I. Spectral bands used for the needlet decomposition in this analysis. Depending on $\ell_{\max}^{(j)}$, the needlet coefficient maps are computed using the HEALPix package, at different values of `nside`, given in the fourth line. The number $K^{(j)}$ of needlet coefficients in band j is then $12(\mathtt{nside}^{(j)})^2$. It is a kind of *decimated* implementation of the needlet transform. The last line gives the opening $\theta^{(j)}$ (in degrees) chosen in Eq. (26) to define the PSWF from the *Prolate 2* family (see Sec. IV A 2 for details).

Band (j)	1	2	3	4	5	⋯	20	21	22	23	24	25	26	27	28	29	⋯	35	36	37	38	39
$\ell_{\min}^{(j)}$	2	11	21	31	41	⋯	401	451	501	551	601	651	701	751	801	876	⋯	1326	1426	1501	1626	1751
$\ell_{\max}^{(j)}$	20	30	40	50	60		500	550	600	650	700	750	800	875	950	1025		1475	1625	1750	1875	2000
$\mathtt{nside}^{(j)}$	16	16	32	32	32	⋯	256	512	512	512	512	512	512	512	512	1024	⋯	1024	1024	1024	1024	1024
$\theta_0^{(j)}$	69	50	41	36	32	⋯	10.7	10.2	9.7	9.3	8.9	8.6	8.3	8.0	7.7	7.4	⋯	6.1	5.8	5.6	5.4	5.2

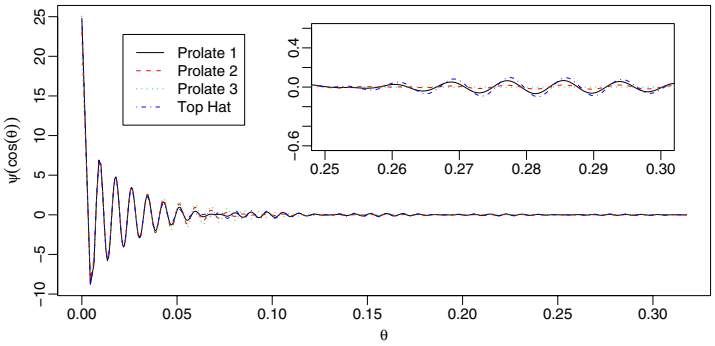

FIG. 2 (color online). Angular profile of the four needlets associated to the window functions at the 26th band ($701 \leq \ell \leq 800$) from the four families of Fig. 1. We have plotted the axisymmetric profile $\sum_\ell b_\ell L_\ell(\cos\theta)$ as a function of θ. Needlets with "smoother" associated window profile (such as Prolate 3) need more room to get well localized, but are less bouncing than needlets with abrupt window function (such as top-hat or Prolate 1).

localized and easy to compute. Other criteria and needlets can be investigated and optimized, at least numerically; see [18] for details. The choice of the optimal window function in a given band is a nontrivial problem which involves the spectrum itself, the characteristics of the noise and the geometry of the mask. Even if we restrict to PSWF as we do here, it is not clear how to choose the optimal opening $\theta^{(j)}$ for each band j. We can use several rules of thumb based on the approximate scaling relation between roughly B-adic bands and openings $\theta^{(j)}$ that preserve some Heisenberg product or Shannon number. Figure 1 represents three families of PSWF needlets that are numerically compared below. Their spatial concentration is illustrated by Fig. 2.

2. The choice of the needlets coefficients (mask)

Practically we want to keep as much information (i.e. as many needlet coefficients) as possible and minimize the effect of the mask. Using all the needlet coefficients regardless of the mask would lead to a biased estimate of the spectrum. It is still true if we keep all the coefficients outside but still close to the mask, keeping in mind that the needlets are not perfectly localized. On the other hand, getting rid of unreliable coefficients reduces the bias but increases the variance. This classical trade-off is taken by choosing the threshold level $t^{(j)}$ in Definition (10) of the excluding zones. For multiple experiments, a different selection rule can be applied to each experiment, according to the geometry of the mask and the characteristics of the beam and the noise.

IV. MONTE CARLO STUDIES

Recall that NSE spectral estimators are designed based on three approximations:

(i) one can neglect the impact of the mask on the needlet coefficients which are centered far enough from its edges;
(ii) one can neglect the variations of the beam and the CMB power spectrum over each band;
(iii) the weights, which are optimal under the simplifying assumption of independent needlet coefficients, still provide good estimates for the truly weakly correlated needlet coefficients.

We carry out Monte Carlo studies to investigate, first the actual performance of the method on realistic data, and second the sensitivity of the method with respect to its parameters. Stochastic convergence results under appropriate conditions is established in a companion paper [24].

A. Single map with a mask and inhomogeneous noise

In this section, we first consider model (2). According to Eqs. (12) and (16), any beam can be taken into account easily in the procedure. Without loss of generality, we suppose here that there is no beam (or B is the Dirac function). The case of different beams is addressed in Sec. IV B, see Table II.

The key elements for this numerical experiment are illustrated by Fig. 3. We simulate CMB from the spectrum C_ℓ given by the ΛCDM model that best fits the WMAP data. We use a Kp0 cut [25] for the mask and we take a simple nonhomogeneous noise standard deviation map (the SNR per pixel is 1.5 in two small circular patches and 0.4 elsewhere).

Using a mean-square error criterion, we first study the dependence of NSE performance on its free parameters. Then we compare NSE with methods based on spherical harmonic coefficients, known as pseudo-C_ℓ estimation and followed in [1]. For the reader's convenience, the PCL procedure is summarized in Appendix A.

TABLE II. Main parameters of the experiments to be aggregated. The beams are given in minutes of arc, `nside` refers to HEALPix resolution of the simulated maps, noise level is either a map computed from a hitmap and an overall noise level, or a uniform noise level per pixel (in μK CMB). Numbers quoted here are indicative of the typical characteristics of observations as those of WMAP, BOOMERanG, and ACBAR, and are used for illustrative purposes only.

Experiment	Beam	`nside`	Noise level	$f_{\rm sky}$
WMAP Q	31'	512	Given by the hit map	78.57%
WMAP V	21'	21'	Given by the hit map	78.57%
WMAP W	13'	13'	Given by the hit map	78.57%
BOOM-S	10'	1024	17.5 μK	2.80%
BOOM-D	10'	1024	5.2 μK	0.65%
ACBAR	5'	2048[a]	14.5 μK	1.62%

[a]We used `nside` = 1024 for our Monte Carlo simulations, as going to $\ell_{\rm max} \simeq 2000$ is enough to discuss all the features of our method.

1. Mean-square error

We shall measure the quality of any estimator $\hat{C}^{(j)}$ of $C^{(j)}$ by its mean-square error

$$\mathrm{MSE}\,(\hat{C}^{(j)}) = \mathbb{E}(\hat{C}^{(j)} - C^{(j)})^2.$$

This expectation is estimated using 400 Monte Carlo replications. Roughly speaking, the MSE decomposes as an average estimation error and a *sampling variance*. The estimation error term is intrinsic to the method. Ideally, it should be used to compare the relative efficiency of concurrent approaches. The sampling variance term is the so-called *cosmic variance*. It is given by the characteristic of the spectrum and coming from the fact that we only have one CMB sky, and thus $2\ell + 1$ $a_{\ell m}$'s to estimate one C_ℓ. It is increased by the negative influence of the noise and the mask. This gives an error term intrinsic to the whole experiment. When the sky is partially observed (let $f_{\rm sky}$ denote the fraction of available sky) and for high ℓ's (or j's), the cosmic variance must be divided by a factor $f_{\rm sky}$ leading to the following approximate Cramér-Rao lower bound at high frequencies:

$$V^{(j)}_{\rm sample} = f^{-1}_{\rm sky} V^{(j)}_{\rm cosmic}. \tag{27}$$

Including a homogeneous additive uncorrelated pixel noise with variance σ^2, the sample variance writes

$$2f^{-1}_{\rm sky}\sum_\ell (b^{(j)}_\ell)^4(2\ell+1)\left(C_\ell + \frac{4\pi}{N_{\rm pix}}\sigma^2\right)^2.$$

In a nonhomogeneous context, no close expression for the sampling variance is available: Eq. (27) will serve as one reference. When comparing different window functions in the same band, it must be kept in mind that different estimators do not estimate the same $C^{(j)}$ so that the sampling variances are not the same. In this case, we use the following normalized MSE

$$\frac{\mathrm{MSE}(\hat{C}^{(j)})}{f^{-1}_{\rm sky} V^{(j)}_{\rm cosmic}}. \tag{28}$$

2. Robustness with respect to parameter choice

This section looks into the robustness of NSE with respect to its free parameters.

First and as expected, the spectral estimation is very sensitive to the choice of the window functions. Even if we restrict to the PSWF, one has the freedom to choose a concentration radius $\theta^{(j)}$ for each band. We compare the mean-square error of the estimation for various choices of $\theta^{(j)}$ that lead to three of the window function families displayed in Fig. 1. The second prolate family is obtained using the "rule of thumb" relation $\theta^{(j)} = 2((\ell^{(j)}_{\rm min} + \ell^{(j)}_{\rm max})/2)^{-1/2}$. The values of those opening angles are in Table I. The first and third sequences of opening angles are the same with a multiplicative factor of 0.5 and 2, respectively. For the sake of comparison we also consider the top-hat window functions. Figure 4 shows the normalized MSE for those four "families" of needlets as a function of the band index. Notice the poor behavior of a nonoptimized window function and the far better performance of the second prolate family in comparison with top-hat and prolate 1 windows. Thus, in the following, we use this particular needlet family to study the sensitivity of the

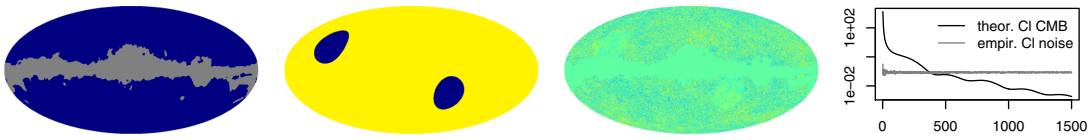

(a) Mask (b) Noise standard deviation (c) One simulated input map (d) Spectra

FIG. 3 (color online). Simplified model of partially covered sky and inhomogeneous additive noise. This model is used to compare numerically the NSE estimator with PCL estimators and to assess the robustness or the sensitivity of the method with respect to its parameters. The mask is kp0. In CMB μK units, the standard deviation of the uncorrelated pixel noise is 75 in the two small circular patches and 300 elsewhere.

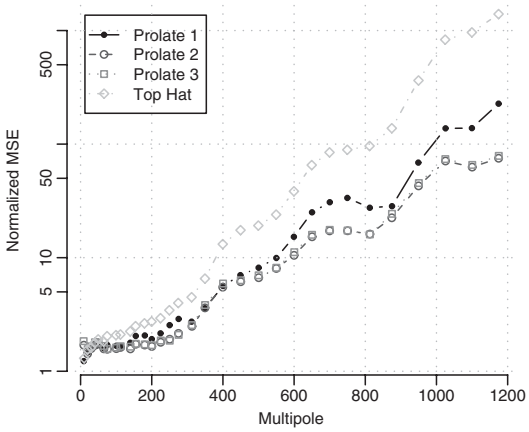

FIG. 4. Comparison of the normalized MSE (28) of the needlet spectral estimators for the four families of spectral window functions displayed in Fig. 1. The smoothness of the window function make the MSE smaller at high multipoles. At low multipoles, taking a too smooth function makes the needlet less localized and there is a loss of variance due to the smaller number $\mathcal{K}^{(j)}$ of needlet coefficients that are combined.

method with respect to the other parameters, and to compare NSE and PCL estimators.

Next, for the second family of PSWF, we compare the influence of the threshold value $t^{(j)} \equiv t$ for $t = 0.9, 0.95$, or 0.98. Figure 5 shows that this choice within reasonable values is not decisive in the results of the estimation procedure. For very low frequencies ($\ell \leq 100$), the conservative choice $t = 0.98$ increases the variance since many needlets are contaminated by the mask and discarded. Qualitatively, in such variance dominated regimes, taking more coefficients (e.g. $t = 0.9$) is adequate. However, we do not advocate the use of the NSE at low ℓ's where exact maximum-likelihood estimation is doable. At higher ℓ's, there is roughly no difference between the $t = 0.95$ and $t = 0.98$ thresholds.

Finally, we check the robustness of the method against an imprecise initial spectrum. We take $0.9C^{(j)}$ and $1.1C^{(j)}$ as initial values $\bar{C}^{(j)}$ and compare the results with the best possible initial value which is $C^{(j)}$ itself. The relative difference between the results, displayed in Fig. 6, does not exceed 1%.

3. Pseudo-C_ℓ versus needlet spectral estimator

We compare the NSE estimator given by Eq. (16) with an estimation based on the spherical harmonic coefficients of the uniformly weighted map and of the $1/\sigma^2$-weighted map. The result is displayed in Fig. 7.

As expected, at low multipoles, where the SNR is higher, the uniform pseudo-C_ℓ estimator performs better than the

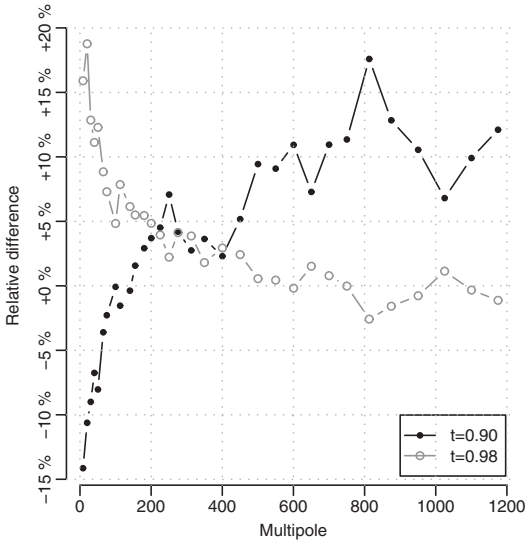

FIG. 5. Relative difference between the normalized MSE (28) of the needlet spectral estimation using thresholds 0.9 and 0.98, and the same with threshold 0.95. It highlights the fact that the estimation is not very sensitive to the value of this parameter, except at low ℓ's, where we do not advocate the use of the NSE. The window function family is "Prolate 2" from Fig. 1.

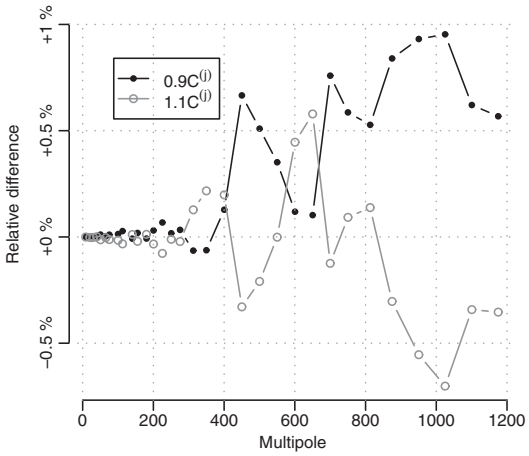

FIG. 6. Robustness of the NSE with respect to the initial value $\bar{C}^{(j)}$ given to the weights formula (18). We have performed the whole estimation with $\bar{C}^{(j)} = 0.9C^{(j)}$ and $\bar{C}^{(j)} = 1.1C^{(j)}$. This plot shows the relative difference between the normalized MSE under those initial values and the normalized MSE under the optimal initial value $\bar{C}^{(j)} = C^{(j)}$.

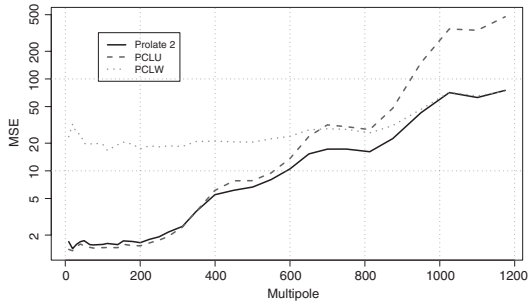

FIG. 7. Comparison of the relative MSE (28) of the two PCL estimators (PCLU for flat weights, PCLW for inverse variance weights) with the NSE, for Prolate family 2. For $300 \leq \ell \leq 1200$, the NSE is uniformly better than the best of the two PCL methods. It should be noted that the NSE may be improved again by optimizing the window profiles and the thresholds $t^{(j)}$ (e.g. by taking a lower threshold for low bands to reduce the variance, see Fig. 5).

weighted pseudo-C_ℓ estimator and, conversely, at high multipoles where the SNR is lower. Reference [6] proved that the equal-weights pseudo-C_ℓ estimator is asymptotically Fisher-efficient when ℓ goes to infinity. The behavior of the needlet estimator is excellent: its performance is comparable to the best of the two previous methods both at low and high multipoles. Thus, there is no need to choose arbitrary boundaries between frequencies for switching for one weighting to the other. The NSE estimator automatically implements a smooth transition between the two regimes and it does so quasioptimally according to noise and mask characteristics. At low ℓ's one should optimize the window function (the characteristic angle of opening of the prolates) to broaden the range of optimality of the NSE.

Providing a C_ℓ estimate with error bars is often not sufficient. Estimating the covariance matrix of the whole vector of spectral estimates is necessary for full error propagation towards, say, estimates of cosmological parameters. Figure 8 shows the values of the correlation matrix between the spectral estimates. In the idealistic case of a full-sky noiseless experiment, the theoretical correlation matrix is tridiagonal because window functions we have chosen only overlap with their left and right nearest neighbors. The mask induces a spectral leakage, which is, however, reduced for the smoothest window function. This leakage is, however, compensated for by the selection of coefficients in $\mathcal{K}^{(j)}_{i^{(j)}}$ [see Eq. (10)].

B. Aggregation of multiple experiments

Historically in CMB anisotropy observations, no single instrument provides the best measurement everywhere on the sky and for all possible scales. In the early 90's, the largest scales have been observed first by COBE-DMR, complemented by many ground-based and balloon-borne measurements at higher ℓ. Similarly, ten years later, WMAP full-sky observations on large and intermediate scales have been complemented by small scale, local observations of the sky as those of Boomerang, Maxima, ACBAR, or VSA.

The joint exploitation of such observations has been so far very basic. The best power spectrum is obtained by choosing, for each scale, the best measurement available, and discarding the others. One could, alternatively, average the measurements in some way, but the handling of errors is complicated in cases where a fraction of the sky is observed in common by more than one experiment.

Clearly, the data is best used if some method is devised that allows combining such complementary observations in an optimal way. In this section we present the results of a Monte Carlo study to illustrate the benefits of our method of an aggregated spectral estimator.

We simulate observations following the model (3), with $E = 6$ observed maps: 3 Kp0-masked maps with beams and noise-level maps according to the WMAP experiment in bands Q, V, and W respectively; 3 maps with uniform noise, observed in patches the size of which are equivalent

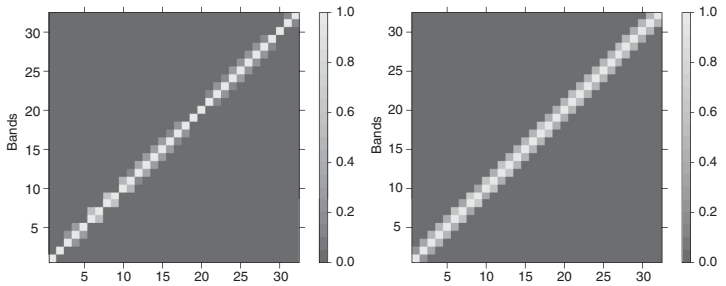

FIG. 8. Absolute value of the correlation matrix of vector $(\hat{C}^{(1)}, \ldots, \hat{C}^{(32)})$, whose entries are defined by Eq. (16). It has been estimated in the context of Fig. 3 using two different families of window functions and 400 Monte Carlo replicates. This shows the difference between a family of PSWF (left panel) and a family of top-hat windows (right panel).

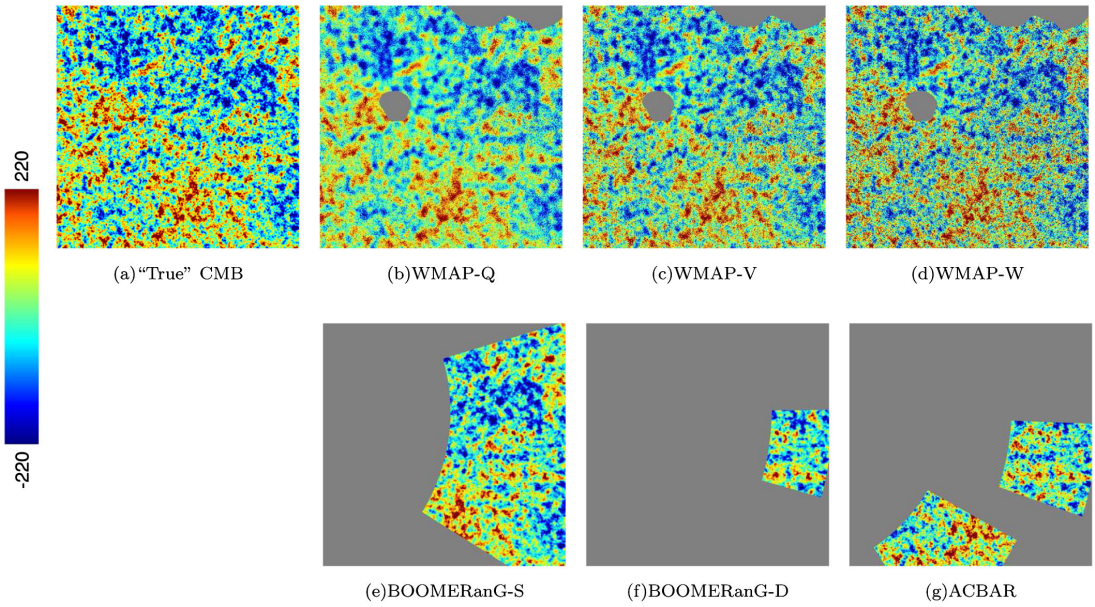

FIG. 9 (color online). Simulated observations from model (3) for the six experiments described in Table II, in a small patch around point $(-40, -90)$. The approximate size of the patch is 38×38 degrees.

to BOOMERanG-Shallow, BOOMERanG-Deep, and ACBAR observations, respectively, and noise levels representative of the sensitivities of those experiments. Table II gives the key features of these experiments. Further details can be found in [25,26] for WMAP, [27] for BOOMERanG, and [28,29] for ACBAR. However, we do not intend to produce fully-realistic simulations. Basically, no foregrounds are included in simulations (neither diffuse nor point sources); for ACBAR only the three sky fields of year 2002 are used; and for WMAP only one detector is used for each band.

Key elements for this numerical experiment are illustrated in Figs. 9–11, where we have displayed, respectively, one random outcome of each experiment according to

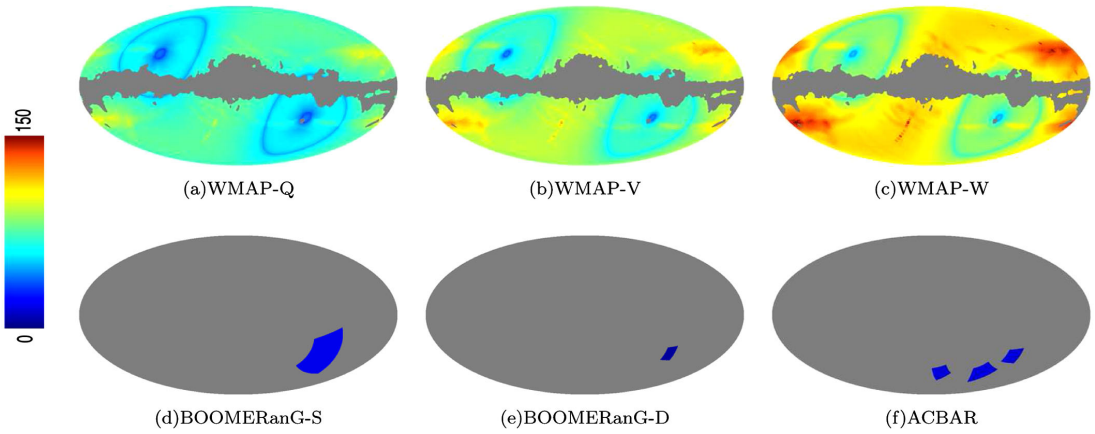

FIG. 10 (color online). Coverage and local pixel-noise levels of the six simple experiments described in Table II.

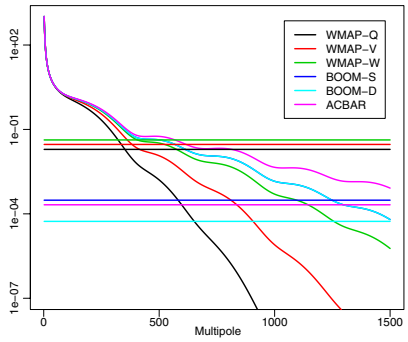

FIG. 11 (color online). Spectra of the beamed CMB (with the BOOMERanG lines overplotted) and noise levels (horizontal lines) seen by the six experiments, as if they were full sky (the f_{sky} effect is not taken into account).

those simplified models, the maps of local noise levels, and power spectra of the CMB and of the experiment's noise.

Figure 12 displays the maps of the weights $\omega_{k,e}^{(26)}$ (the 26th band is the multipole range $700 < \ell \leq 800$). According to Eq. (23), all those weights belong to [0,1] and for any fixed position, the sum of the weights over the six experiments is equal to one. Red regions indicate needlet coefficients which are far better observed in an experiment than in all others. The blue, light blue, and orange region are increasing but moderately low weights, showing that outside the small patches of BOOMERanG and ACBAR, most information on band 26 is provided by the channel W of WMAP. On the patches, needlet coefficients from WMAP are numerically neglected in the combination (21).

The debiased, squared, aggregated coefficients $(\tilde{\gamma}_k^{(26)})^2 - (\tilde{n}_k^{(26)})^2$ are displayed on the left map from Fig. 13. All those coefficients are approximately unbiased estimators of $C^{(26)}$. The map of weights $\tilde{w}_k^{(26)}$ is displayed on the right of Fig. 13. More weight is given to regions which are covered by lower noise experiments. The final estimate is obtained by averaging the pixelwise multiplication of these two maps.

Figures 14 and 15 show the benefit of the aggregation of different experiments, in comparison with separate estimations. In CMB literature, error bars from different experiments are usually plotted on a same graph with different colors. For easier reading, we plot the output of single-experiment NSE in separate panels (a, b, and c). Panel (d)

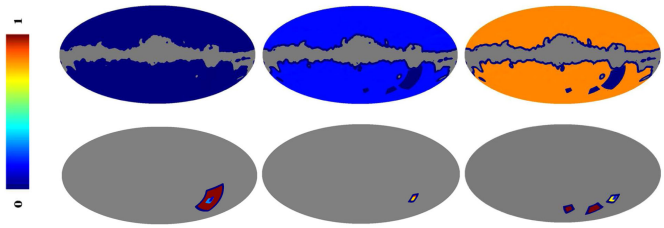

FIG. 12 (color online). Method for aggregating experiments: Weights $\omega_{k,e}^{(26)}$ for combining the needlet coefficients from the 26th band ($700 < \ell \leq 800$) and the six experiments. From left to right and top to bottom: WMAP-Q, WMAP-V, WMAP-W, BOOMERanG-S, BOOMERang-D, and ACBAR.

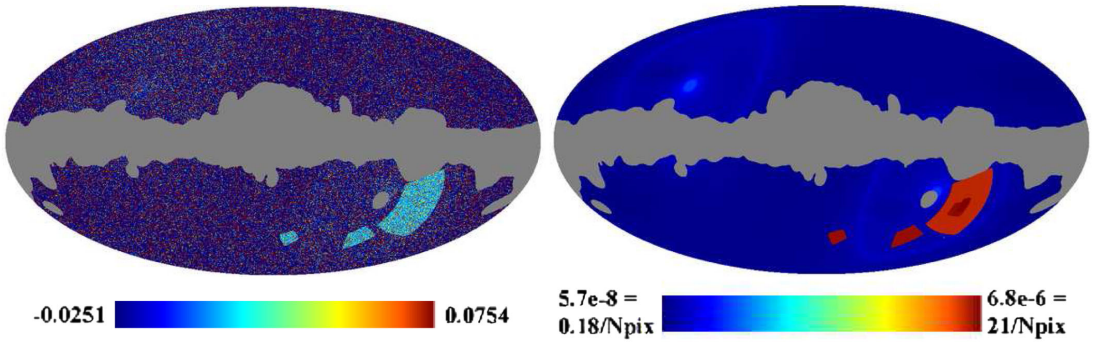

FIG. 13 (color online). Method for aggregating experiments: On the left, map of debiased squares of aggregated needlet coefficients, in the 26th band ($700 < \ell \leq 800$). On the right, map of the weights $w_k^{(j)}$ affected to those coefficients to estimate the power spectrum.

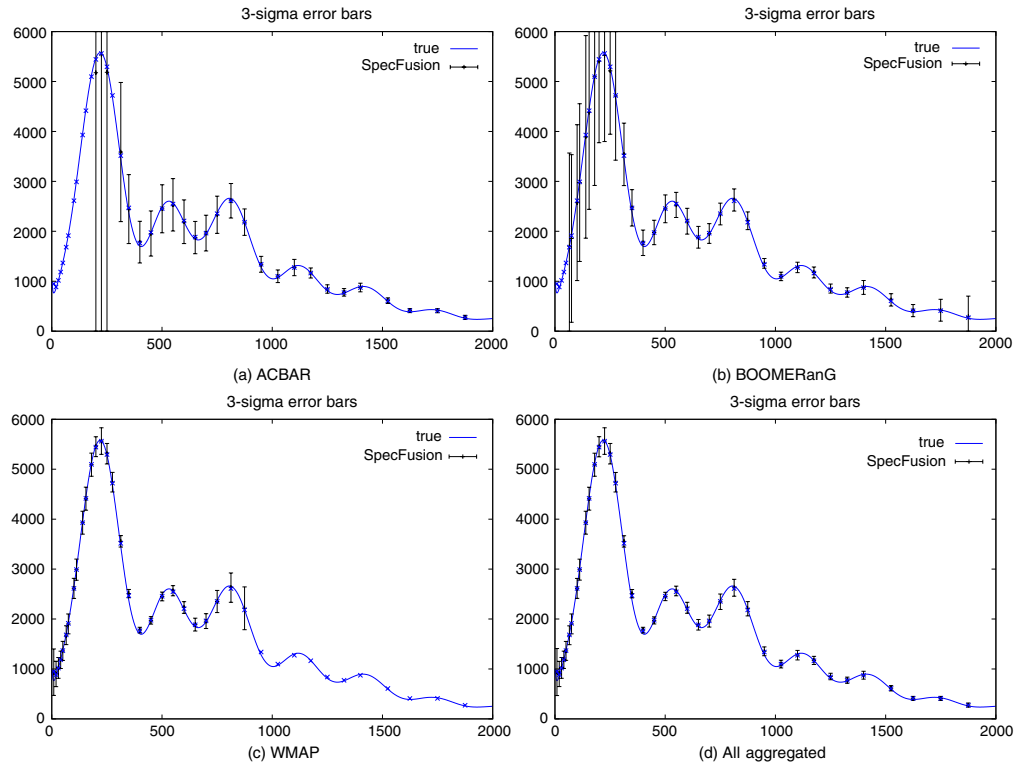

FIG. 14 (color online). Results for the aggregated NSE. Error bars are estimated by 100 Monte Carlo simulations. The ACBAR power spectrum is computed using the single-map needlet estimator described in Sec. III A, whereas the BOOMERanG and WMAP spectra are obtained using the aggregation of needlets coefficients from the two (BOOM-S and BOOM-D) and three (WMAP Q,V,W) maps, respectively. The final spectrum (d) is obtained by aggregating all available needlet coefficients from the six maps.

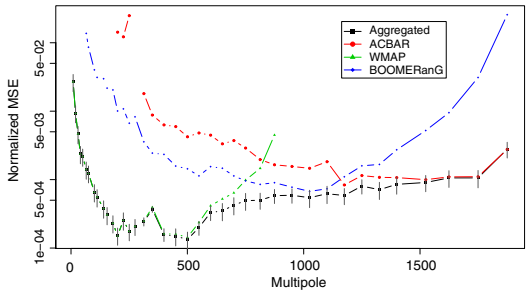

FIG. 15 (color online). Mean-square error of the three single experiment NSE estimators and of the aggregated NSE estimator. The 2-sigma error bars reflect the imprecision in the Monte Carlo estimation of the MSE of the aggregated NSE. Up to those uncertainties, the aggregated estimator is uniformly better than the best of all experiments. The improvement is decisive in "crossing" regions, where two experiments perform comparably. The normalized MSE here is $\mathbb{E}(\hat{C}^{(j)} - C^{(j)})^2/(C^{(j)})^2$.

shows the output of the aggregated NSE, which improves the best single experiment uniformly over the frequency

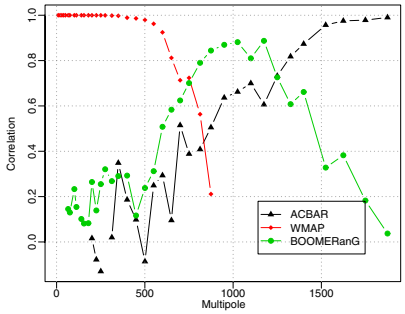

FIG. 16 (color online). Correlation between the aggregated estimator and single experiments estimators. This provides insight on the contribution of each experiment into the final aggregated single spectral estimate.

range, thanks to the locally adaptive combination of information from all expermiments.

Figure 16 highlights the cross-correlation between single-experiment estimators and the final aggregated estimator. It provides a complementary insight on the relative weight of each experiment in the spectral domain. The WMAP-like measures are decisive for lower bands, whereas BOOMERanG and ACBAR ones give estimators very much correlated to the aggregated one at higher bands. The aggregated NSE is eventually almost identical to the estimator obtained from ACBAR alone.

V. DISCUSSION

A. Complexity

According to (5), the calculation of all the needlet coefficients takes one SHT and $j_{\max}$ inverse SHT, where $j_{\max}$ is the number of bands. The weights $w_k^{(j)}$, $\tilde{w}_k^{(j)}$, and $\omega_{k,e}^{(j)}$ are obtained using simple operations on maps, so that the overall cost of the (aggregated) NSE scales as $N_{\rm pix}^{3/2}$ operations. This is comparable to the cost of the PCL methods.

B. Sensitivity to the noise knowledge

To be unbiased, the above described estimators require a perfect knowledge of the noise characteristics, as do pseudo-C_ℓ estimators. In both cases, the uncertainty on the noise can be tackled using cross-spectrum, that removes the noise on the average provided that the noises from each experiment are independent. Indeed, for any pixel k far enough from the masks of experiment e and e', $e \neq e'$, we have

$$\mathbb{E}[\gamma_{k,e}^{(j)}\gamma_{k,e'}^{(j)}] = B_e^{(j)}B_{e'}^{(j)}C^{(j)}.$$

Thus, an unbiased spectral estimator is given by

$$\bar{C}_{\rm cross}^{(j)} = \sum_{k\in\mathcal{K}^{(j)}} w_k^{(j)} \sum_{e\neq e'} (B_e^{(j)}B_{e'}^{(j)})^{-1}\gamma_{k,e}^{(j)}\gamma_{k,e'}^{(j)}, \qquad (29)$$

where the weights $w_k^{(j)}$ depend on a preliminary estimate of the spectrum and a possibly imprecise estimate of the local and aggregated noise levels that enter in the variance of $\gamma_{k,e}^{(j)}\gamma_{k,e'}^{(j)}$. This has not been investigated numerically yet but we can conjecture the qualitative results of this approach: more robustness with respect to noise misspecification but greater error bars than the NSE with perfectly known noise levels. Moreover, adapting the procedure described in [8], one can test for noise misspecification, and for the correct removal of the noise by considering the difference between the NSE $\hat{C}^{(j)}$ and cross-spectrum NSE $\hat{C}_{\rm cross}^{(j)}$.

VI. CONCLUSION

We have presented some potentialities of the needlets on the sphere for the angular power spectrum estimation. This tool is versatile and allows to treat consistently the estimation from a single map or from multiple maps. There remain many ways of improving or modifying the method described in Sec. III.

In the future, it is likely that again complementary data sets will coexist. This is the case, in particular, for polarization, for which Planck will measure the large scale CMB power on large scales with moderate sensitivity, while ground-based experiments will measure very accurately polarization on smaller scales. Extensions to polarization of the approach presented here will likely be important for the best exploitation of such observations.

ACKNOWLEDGMENTS

The ADAMIS team at APC has been partly supported by the Astro-Map and Cosmostat ACI grants of the French ministry of research, for the development of innovative CMB data analysis methods. The results in this paper have been derived using the HEALPix package [31]. Our pipeline is mostly implemented in octave (www.octave.org).

APPENDIX A: PSEUDO-C_ℓ ESTIMATORS

Let T be a stationary process with power spectrum $(C_\ell)_{\ell\geq 0}$, $\mathcal{W}$ an arbitrary weight function (or mask), and

$$\tilde{C}_\ell(\mathcal{W}) = \frac{1}{2\ell+1}\sum_{m=-\ell}^{\ell} |\langle Y_{\ell m}, \mathcal{W}T\rangle|^2$$

the so-called *pseudo-power spectrum* of T with mask $\mathcal{W}$. The ensemble average of this quantity is related to the true power spectrum by the formula

$$\mathbb{E}(\tilde{C}_\ell) = \mathcal{M}_{\ell\ell'}(\mathcal{W})C_{\ell'},$$

where $\mathcal{M}_{\ell\ell'}(\mathcal{W})$ is the doubly infinite coupling matrix associated with $\mathcal{W}$, see [5,30]. If U is a unit variance white pixel noise, denote by $V_\ell \equiv 4\pi\sigma^2/N_{\rm pix}$ its "spectrum" (see Appendix B). Consider now the model $X = \mathcal{W}_1 T + \mathcal{W}_2 U$. Then, if $\mathcal{M}_{\ell\ell'}(\mathcal{W}_1)$ is full rank,

$$(\mathcal{M}_{\ell\ell'}(\mathcal{W}_1))^{-1}\{\tilde{C}_\ell(\mathcal{W}_1) - \mathcal{M}_{\ell\ell'}(\mathcal{W}_2)V_{\ell'}\}$$

is an unbiased estimator of $C_{\ell'}$. It is obtained by deconvolving and debiasing the empirical spectrum. The observation model (2) with no beam coincides with the preceding framework with $\mathcal{W}_1 = W$ and $\mathcal{W}_2 = \sigma W$. This leads to the PCLU. One can also divide all the observations by σ^2, yielding to a similar scheme with $\mathcal{W}_1 = \sigma^{-2}W$ and $\mathcal{W}_2 = \sigma^{-1}W$. This is the PCLW. Both are used by the WMAP collaboration [1]. The uniform weights lead to better estimates in the high SNR regime (low ℓ's) whereas the flat weights perform better at low SNR (high ℓ's). Reference [6] showed that the pseudo-C_ℓ estimator is statistically equivalent to the maximum-likelihood estimator asymptotically as ℓ goes

to infinity. He also proposed an implementation of a smooth transition between those two regimes.

APPENDIX B: WHAT "NOISE SPECTRUM" MEANS

Let ν denote the noise. It is defined on pixels and supposed centered, Gaussian, independent from pixel to pixel, and of variance $\sigma^2(\xi)$, i.e.

$$\nu_k = \sigma(\xi_k)U_k, \qquad k = 1, \dots N_{\text{pix}},$$

with $U_1, \dots, U_{N_{\text{pix}}} \sim^{\text{i.i.d}} \mathcal{N}(0,1)$. Define $\nu_{\ell m} := \sum_k \lambda_k \nu_k Y_{\ell m}(\xi_k)$, and call them (abusively) the "discretized" multipole moments of the noise, which do not have any continuous counterpart because ν is not defined on the whole sphere. Define the corresponding discretized empirical spectrum $\tilde{N}_\ell := \frac{1}{2\ell+1}\sum_m \nu_{\ell m}^2$, then

$$\mathbb{E}(\nu_{\ell m}\nu_{\ell' m'}) = \sum_k \lambda_k^2 \sigma^2(\xi_k) Y_{\ell m}(\xi_k) Y_{\ell' m'}(\xi_k),$$

$$\tilde{N}_\ell = \frac{1}{2\ell+1}\sum_{k,k'} \lambda_k \lambda_{k'} \sigma(\xi_k)\sigma(\xi_{k'}) U_k U_{k'} L_\ell(\langle \xi_k, \xi_{k'}\rangle),$$

$$\text{and } \mathbb{E}(\tilde{N}_\ell) = \frac{1}{4\pi}\sum_k \lambda_k^2 \sigma^2(\xi_k) =: N_\ell.$$

This sequence N_ℓ can be thought of as the pixel-noise spectrum. Note that if $\lambda_k = \frac{4\pi}{N_{\text{pix}}}$, $k = 1, \dots, N_{\text{pix}}$, then $N_\ell = \frac{1}{N_{\text{pix}}}\int \sigma^2(\xi) \mathrm{d}\xi$. If the noise is moreover homogeneous, $\sigma(\xi) \equiv \sigma$, then $\mathbb{E}(\nu_{\ell m}\nu_{\ell' m'}) = \frac{4\pi\sigma^2}{N_{\text{pix}}}\delta_{\ell,\ell'}\delta_{m,m'}$.

APPENDIX C: VARIANCE ESTIMATION BY AGGREGATION OF EXPERIMENTS WITH INDEPENDENT HETEROSCEDASTIC NOISE

Consider the model

$$Y_{k,e} = X_k + n_{k,e} Z_{k,e},$$

where $\mathbf{X} := [X_k]_{k\in[1,N_{\text{pix}}]}$ and $\mathbf{Z} := [Z_{k,e}]_{(k,e)\in[1,N_{\text{pix}}]\times[1,E]}$ are independent, $X_k \sim^{\text{i.i.d}} \mathcal{N}(0, C)$, $Z_{k,e} \sim^{\text{i.i.d}} \mathcal{N}(0,1)$, and the noise standard deviations $n_{k,e}$ are known. This corresponds to the observation of the same signal $\mathbf{X}$ by E independent experiments, the observations being tainted by independent but heteroscedastic errors. Let $\mathbf{Y}_k := [Y_{k,e}]_{(e\in[1,E]}$ be the vector of observations at point (or index in a general framework) k, and let $\mathbf{Y} := ([\mathbf{Y}_k^T]_{k\in[1,N_{\text{pix}}]})^T$ be the full vector of observations. The covariance matrix of $\mathbf{Y}_k$ is $\mathbf{R}_k := \mathbf{1}\mathbf{1}^T C + \mathbf{N}_k$ where $\mathbf{N}_k := \text{diag}(n_{k,e}^2)_{e\in[1,E]}$ and $\mathbf{1}$ is the $E \times 1$ vector of ones. By independence of the $\mathbf{Y}_k$'s, the negative log-likelihood of C given $\mathbf{Y}$ thus writes

$$\mathcal{L}(C) := -2\log(P(\mathbf{Y}|C)) = -2\sum_k \log(P(\mathbf{Y}_k|C))$$

$$= \sum_k \mathbf{Y}_k{}^T \mathbf{R}_k^{-1} \mathbf{Y}_k + \log\det \mathbf{R}_k.$$

Denote

$$\tilde{n}_k := (\mathbf{1}^T \mathbf{N}_k^{-1}\mathbf{1})^{-1/2} = (\sum_e (n_{k,e})^{-2})^{-1/2}. \tag{C1}$$

It is immediate to check the following identity which will be used below:

$$\mathbf{R}_k{}^{-1}\mathbf{1} = \frac{\mathbf{N}_k^{-1}\mathbf{1}}{1 + C\tilde{n}_k^2}.$$

Define $\hat{\mathbf{R}}_k := \mathbf{Y}_k \mathbf{Y}_k{}^T$. The derivative of the negative log-likelihood writes

$$\begin{aligned}
\mathcal{L}'(C) &= \sum_k -\mathbf{Y}_k{}^T \mathbf{R}_k^{-1} \frac{\partial \mathbf{R}_k}{\partial C} \mathbf{R}_k^{-1}\mathbf{Y}_k + \text{tr}\left(\mathbf{R}_k^{-1}\frac{\partial \mathbf{R}_k}{\partial C}\right) \\
&= \sum_k \text{tr}(\mathbf{Y}_k{}^T \mathbf{R}_k^{-1}\mathbf{1}\mathbf{1}^T\mathbf{R}_k^{-1}\mathbf{Y}_k) + \text{tr}(\mathbf{R}_k^{-1}\mathbf{1}\mathbf{1}^T) \\
&= \sum_k \mathbf{1}^T\mathbf{R}_k^{-1}(\mathbf{R}_k - \hat{\mathbf{R}}_k)\mathbf{R}_k^{-1}\mathbf{1} \\
&= \sum_k \frac{\mathbf{1}^T\mathbf{N}_k^{-1}(\mathbf{R}_k - \hat{\mathbf{R}}_k)\mathbf{N}_k^{-1}\mathbf{1}}{(1 + C\tilde{n}_k^2)^2} \\
&= C\sum_k \frac{(\mathbf{1}^T\mathbf{N}_k^{-1}\mathbf{1})^2}{(1 + C\tilde{n}_k^2)^2} - \sum_k \frac{(\mathbf{1}^T\mathbf{N}_k^{-1}\mathbf{Y}_k)^2 - \mathbf{1}^T\mathbf{N}_k^{-1}\mathbf{1}}{(1 + C\tilde{n}_k^2)^2} \\
&= C\sum_k (C + \tilde{n}_k^2)^{-2} - \sum_k \frac{(\tilde{n}_k^2\mathbf{1}^T\mathbf{N}_k^{-1}\mathbf{Y}_k)^2 - \tilde{n}_k^2}{(C + \tilde{n}_k^2)^2}.
\end{aligned}$$

It follows that the likelihood is maximized for

$$C = \hat{C}(w) := \sum_k w_k(C, \mathbf{N})[(\tilde{n}_k^2\mathbf{1}^T\mathbf{N}_k^{-1}\mathbf{Y}_k)^2 - \tilde{n}_k^2]$$

with

$$w_k(C, \mathbf{N}) := (C + \tilde{n}_k^2)^{-2}\left[\sum_i (C + \tilde{n}_i^2)^{-2}\right]^{-1}. \tag{C2}$$

As the optimal weights depend on C, this only defines implicitly the ML estimator. For some approximate spectrum C^0, the proposed explicit NSE is given by $\hat{C}(\hat{w}_k)$ with $\hat{w}_k = w_k(C^0, \mathbf{N})$.

Particular case of a single experiment

In the particular case of a single experiment ($E = 1$) with heteroscedastic noise, following the model

$$Y_k = X_k + n_k Z_k,$$

the likelihood is maximized for

$$C = \hat{C}(w) := \sum_k w_k(C, \mathbf{N})(Y_k^2 - n_k^2) \tag{C3}$$

with $w_k(C, \mathbf{N})$ defined by Eq. (C2), and again, assuming that w_k is poorly sensitive to C, the NSE is $\hat{C}(\hat{w}_k(C^0))$ for some approximate spectrum C^0.

[1] G. Hinshaw, M. Nolta, C. Bennett, R. Bean, O. Dore, M. Greason, M. Halpern, R. Hill, N. Jarosik, A. Kogut, E. Komatsu, M. Limon, N. Odegard, S. Meyer, L. Page, H. Peiris, D. Spergel, G. Tucker, L. Verde, J. Weiland, E. Wollack, and E. Wright, Astrophys. J. Suppl. Ser. **170**, 288 (2007).

[2] S. M. Leach, J. Cardoso, C. Baccigalupi, R. B. Barreiro, M. Betoule, J. Bobin, A. Bonaldi, G. de Zotti, J. Delabrouille, C. Dickinson, H. K. Eriksen, J. González-Nuevo, F. K. Hansen, D. Herranz, M. LeJeune, M. López-Caniego, E. Martinez-González, M. Massardi, J. Melin, M. Miville-Deschênes, G. Patanchon, S. Prunet, S. Ricciardi, E. Salerno, J. L. Sanz, J. Starck, F. Stivoli, V. Stolyarov, R. Stompor, and P. Vielva, Component Separation Methods for the Planck Mission.

[3] J. R. Bond, A. H. Jaffe, and L. Knox, Phys. Rev. D **57** (4), 2117 (1998).

[4] M. Tegmark, Phys. Rev. D **55** (10), 5895 (1997).

[5] E. Hivon, K. M. Górski, C. B. Netterfield, B. P. Crill, S. Prunet, and F. Hansen, Astrophys. J. **567**, 2 (2002).

[6] G. Efstathiou, Mon. Not. R. Astron. Soc. **349** (2), 603 (2004).

[7] G. Hinshaw, D. N. Spergel, L. Verde, R. S. Hill, S. S. Meyer, C. Barnes, C. L. Bennett, M. Halpern, N. Jarosik, A. Kogut, E. Komatsu, M. Limon, L. Page, G. S. Tucker, J. L. Weiland, E. Wollack, and E. L. Wright, Astrophys. J. **148**, 135 (2003).

[8] G. Polenta, D. Marinucci, A. Balbi, P. de Bernardis, E. Hivon, S. Masi, P. Natoli, and N. Vittorio, J. Cosmol. Astropart. Phys. 11 (2005) 001.

[9] B. D. Wandelt, D. L. Larson, and A. Lakshminarayanan, Phys. Rev. D **70** (8), 083511 (2004).

[10] H. K. Eriksen *et al.*, Astrophys. J. Suppl. Ser. **155**, 227 (2004).

[11] F. A. Dahlen and F. J. Simons, Geophys. J. Int. **174**, 774 (2008).

[12] M. A. Wieczorek and F. J. Simons, J. Fourier Anal. Appl. **13** (6), 665 (2007).

[13] P. Baldi, G. Kerkyacharian, D. Marinucci, and D. Picard, arXiv:0706.4169v1.

[14] P. Baldi, G. Kerkyacharian, D. Marinucci, and D. Picard, arXiv:math/0606599v1.

[15] J. Delabrouille, J.-F. Cardoso, M. Le Jeune, M. Betoule, G. Faÿ, and F. Guilloux, arXiv:astro-ph/0807.0773.

[16] D. Marinucci, D. Pietrobon, A. Balbi, P. Baldi, P. Cabella, G. Kerkyacharian, P. Natoli, D. Picard, and N. Vittorio, Mon. Not. R. Astron. Soc. **383** (2), 539 (2008).

[17] D. Pietrobon, A. Balbi, and D. Marinucci, Phys. Rev. D **74**, 043524 (2006).

[18] F. Guilloux, G. Faÿ, and J.-F. Cardoso, Appl. Comput. Harmon. Anal. (to be published), http://dx.doi.org/10.1016/j.acha.2008.03.003.

[19] F. Narcowich, P. Petrushev, and J. Ward, SIAM J. Math. Anal. **38** (2), 574 (2006).

[20] I. Daubechies, *Ten Lectures on Wavelets*, CBMS-NSF Regional Conference Series in Applied Mathematics Vol. 61 (Society for Industrial and Applied Mathematics (SIAM), Philadelphia, PA, 1992).

[21] A. Mayeli, arXiv:0806.3009v1.

[22] D. Slepian and H. Pollak, Bell Syst. Tech. J. **40** (1), 43 (1961).

[23] F. J. Simons, F. A. Dahlen, and M. A. Wieczorek, SIAM Rev. **48**, 504 (2006).

[24] G. Faÿ and F. Guilloux, arXiv:0807.2162v1.

[25] C. L. Bennett, M. Halpern, G. Hinshaw, N. Jarosik, A. Kogut, M. Limon, S. S. Meyer, L. Page, D. N. Spergel, G. S. Tucker, E. Wollack, E. L. Wright, C. Barnes, M. R. Greason, R. S. Hill, E. Komatsu, M. R. Nolta, N. Odegard, H. V. Peiris, L. Verde, and J. L. Weiland, Astrophys. J. Suppl. Ser. **148**, 1 (2003).

[26] G. Hinshaw, J. L. Weiland, R. S. Hill, N. Odegard, D. Larson, C. L. Bennett, J. Dunkley, B. Gold, M. R. Greason, N. Jarosik, E. Komatsu, M. R. Nolta, L. Page, D. N. Spergel, E. Wollack, M. Halpern, A. Kogut, M. Limon, S. S. Meyer, G. S. Tucker, and E. L. Wright, Phys. Rev. Lett. **100**, 181301 (2008).

[27] S. Masi, P. A. R. Ade, J. J. Bock, J. R. Bond, J. Borrill, A. Boscaleri, P. Cabella, C. R. Contaldi, B. P. Crill, P. de Bernardis, G. de Gasperis, A. de Oliveira-Costa, G. de Troia, G. di Stefano, P. Ehlers, E. Hivon, V. Hristov, A. Iacoangeli, A. H. Jaffe, W. C. Jones, T. S. Kisner, A. E. Lange, C. J. MacTavish, C. Marini Bettolo, P. Mason, P. D. Mauskopf, T. E. Montroy, F. Nati, L. Nati, P. Natoli, C. B. Netterfield, E. Pascale, F. Piacentini, D. Pogosyan, G. Polenta, S. Prunet, S. Ricciardi, G. Romeo, J. E. Ruhl, P. Santini, M. Tegmark, E. Torbet, M. Veneziani, and N. Vittorio, Astron. Astrophys. **458**, 687 (2006).

[28] C. L. Reichardt, P. A. R. Ade, J. J. Bock, J. R. Bond, J A. Brevik, C. R. Contaldi, M. D. Daub, J. T. Dempsey, J. H. Goldstein, W. L. Holzapfel, C. L. Kuo, A. E. Lange, M. Lueker, M. Newcomb, J. B. Peterson, J. Ruhl, M. C. Runyan, and Z. Staniszewski, High resolution CMB power spectrum from the complete ACBAR data set.

[29] M. C. Runyan, P. A. R. Ade, R. S. Bhatia, J. J. Bock, M. D. Daub, J. H. Goldstein, C. V. Haynes, W. L. Holzapfel, C. L. Kuo, A. E. Lange, J. Leong, M. Lueker, M. Newcomb, J. B. Peterson, C. Reichardt, J. Ruhl, G. Sirbi, E. Torbet, C. Tucker, A. D. Turner, and D. Woolsey, Astrophys. J. Suppl. Ser. **149**, 265 (2003).

[30] P. J. E. Peebles, Astrophys. J. **185**, 413 (1973).

[31] K. Górski, E. Hivon, A. Banday, B. Wandelt, F. Hansen, M. Reinecke, and M. Bartelmann, Astrophys. J. **622**, 759 (2005), Package available at http://healpix.jpl.nasa.gov.

Annexe B

Résumé sur l'originalité des recherches présentées

Effet Sunyaev-Zel'dovich dans les amas de galaxies

L'effet Sunzaev-Zel'dovich, ou effet SZ, a été prédit théoriquement au début des années 1970 mais, comme noté par les auteurs de la première publication sur le sujet, les perspectives de détection étaient alors assez peu encourageantes. Pourtant, cet effet présente un intérêt de tout premier ordre pour la cosmologie à plusieurs titres (voir Chapitre 2). C'est pourquoi après les observations dans le domaine de longueur d'onde optique, puis X, la mesure de l'effet SZ dans le domaine millimétrique devient un domaine privilégié pour la recherche d'amas et l'étude de leurs propriétés physiques.

Entre 1996 et 2000, j'ai participé à l'observation de l'effet Sunyaev-Zel'dovich dans les amas de galaxies avec l'expérience Diabolo (Benoît et al. 2000; Désert et al. 2002), notamment à l'antenne de 30 m de l'IRAM à Pico Veleta. Les observations que nous avons effectuées avec Diabolo (Désert et al. 1998; Pointecouteau et al. 1999) figurent parmi les premières observations de l'effet SZ. Elles nous ont permis de mesurer la masse de gaz de plusieurs amas brillants, et de contraindre la température du gaz ainsi que la fraction de gaz (ce qui confirme, indépendamment des autres mesures cosmologiques, la présence de matière noire dans les amas).

J'ai continué mon travail sur les amas de galaxies avec la mise au point d'une méthode rapide de simulation de cartes d'effet SZ (Delabrouille et al. 2002), méthode qui a ensuite été développée et adaptée pour être incluse dans le Planck Sky Model dont il est question au Chapitre 6. J'ai encadré sur ce sujet le stage de DEA, puis la thèse de Jean-Baptiste Melin, de 2001 à 2004. Dans le cadre de cette thèse, j'ai également contribué à développer les méthodes requises pour la mesure et l'analyse de l'effet SZ dans les données d'expériences futures, notamment pour l'analyse des données Planck. Ceci a abouti à l'étude de la fonction de sélection des amas (Melin et al. 2005), d'une importance capitale pour l'interprétation cosmologique des observations, ainsi qu'à une méthode de détection d'amas sur la base d'un filtre adapté multi fréquence (Melin et al. 2006).

J'ai par la suite travaillé à développer une méthode de fabrication de cartes d'effet SZ à partir d'observations multi fréquence. Cette méthode a été utilisée avec succès dans le cadre d'un "data challenge" de Planck pour la constitution d'un catalogue d'amas de galaxies. Cette méthode, basée sur une minimisation contrainte de la variance de combinaisons linéaires des observations sur des domaines d'un frame d'ondelettes sur la sphère, semble prometteuse pour l'analyse future des données de Planck, puisqu'elle a obtenu, de façon cohérente, les meilleurs taux de détections sur les différents jeux de données simulées analysés. La méthode est décrite dans (Leach et al. 2008) et dans une publication en préparation spécifiquement dédiée au "challenge SZ".

Résumé sur l'originalité des recherches présentées

Mission Planck et "Planck Sky Model"

La mission spatiale Planck est une mission de troisième génération (après COBE et WMAP) dédiée à l'observation du fond de rayonnement cosmologique fossile. Planck observe le ciel dans 9 bandes de fréquence, avec une sensibilité intégrée environ 20 fois supérieure à WMAP, et une résolution angulaire trois fois meilleure. Planck est aujourd'hui la mission spatiale la plus importante pour la cosmologie et l'observation des émissions astrophysiques dans le domaine submillimétrique. En témoigne l'importance de la collaboration Planck (plus de 400 scientifiques à travers le monde, spécialisés dans des domaines divers).

De 1994 à 2008, j'ai participé à la définition et à la préparation de cette mission. Depuis le lancement le 14 mai 2008, je m'investis dans l'analyse scientifique des données (notamment des données de l'instrument HFI).

Dans le cadre de la préparation de la mission, j'ai démontré, au cours de l'étude de phase A, la faisabilité de la mesure en puissance totale (contrairement aux mesures différentielles de COBE et WMAP, qui nécessitent de dupliquer le système optique). Ceci a permis de valider le concept de la mesure avec Planck, et a conduit à la conception de la première mission spatiale pour la mesure des anisotropies en puissance totale, et à l'optimisation (dans la limite des contraintes opérationnelles) de la stratégie de balayage de Planck avec redondances. J'ai développé le concept de la méthode de fabrication de cartes par déstriage utilisée actuellement dans le DPC de Planck HFI. Cette stratégie de fabrication de cartes divise le problème en deux étapes : tout d'abord la construction de cercles (Delabrouille et al. 1998a), puis la fabrication de cartes à partir d'une collection de cercles (Delabrouille 1998a; Revenu et al. 2000). La stratégie de balayage de Planck, dont je discute les contraintes et l'optimisation dans une publication dédiée (Delabrouille et al. 1998b), est l'une des options que j'ai présentées dans ma thèse (Delabrouille 1998b). Elle a fait toutefois l'objet récemment d'une optimisation de la phase de la trajectoire de l'axe de spin du satellite.

J'ai également calculé l'impact de la lumière parasite en provenance des lobes lointains du diagramme d'antenne, et démontré que ces effets de lobes lointains pouvaient être corrigés au premier ordre lors d'une phase d'analyse de données. Cette étude a été prise en compte pour l'optimisation du compromis entre résolution angulaire et niveau de lumière parasite. Ces travaux sont présentés dans ma thèse (Delabrouille 1998b), et leur extension a fait l'objet d'un stage ingénieur que j'ai encadré en 2001.

J'ai travaillé sur le problème de la mesure de la polarisation avec Planck. La mission spatiale, à l'origine, était conçue surtout pour la mesure des anisotropies de température. J'ai contribué à proposer une configuration de détecteurs optimisée pour la mesure de la polarisation (Couchot et al. 1999). Cette configuration a été adoptée pour l'instrument HFI. Pendant plusieurs années, j'ai coordonné les activités relevant de l'étude des effets systématiques polarisés avec Planck. Ces travaux dédiés à la polarisation du fond cosmologique dans le contexte de la préparation de la mission Planck ont fait l'objet de plusieurs publications (Delabrouille & Kaplan 2002; Kaplan & Delabrouille 2002; Kaplan et al. 2003; Delabrouille et al. 2003b; Delabrouille 2004; Rosset et al. 2007).

Depuis 2005, je coordonne par ailleurs les activités du groupe de séparation de composantes (WG2) de Planck pour l'instrument HFI. L'objectif de ce groupe est de mettre au point et d'évaluer des méthodes permettant d'isoler, à partir de données multi fréquence et éventuellement d'observations externes, les différentes émissions astrophysiques contribuant au signal observé (fond cosmologique, émissions galactiques, émissions d'objets extragalactiques...). J'ai joué un rôle leader dans l'organisation de "data challenges" pour la séparation de composantes (Leach et al. 2008) et la mise au point d'un logiciel de modélisation de l'émission du ciel millimétrique, le Planck Sky Model ou "PSM", utilisé au sein de la collaboration Planck, et plus largement dans la communauté scientifique, pour simuler l'émission du ciel millimétrique.

Séparation de composantes et d'estimation spectrale

La contamination des observations du CMB par les émissions d'avant plan est une source potentielle d'erreur lors de l'observation des anisotropies de température ou de polarisation du fond cosmologique. Les premières observations du CMB sont marquées du questionnement récurrent de l'origine des anisotropies observées : anisotropies primordiales, ou émissions d'avant-plan ? Mais le problème de la séparation de composantes est aussi probablement le problème "ultime" pour l'analyse des données à venir, puisque dès lors que le bruit instrumental devient négligeable, c'est la confusion astrophysique qui constitue la principale source d'erreur dans l'interprétation des mesures.

J'ai consacré une fraction notable de mon temps de recherche depuis 2000 à l'étude de ce problème et à la mise au point de méthodes pour séparer au mieux les composantes astrophysiques présentes dans des données multi fréquence et multi résolution telles celles de Planck. J'ai notamment contribué à développer et étudier en détail deux méthodes maintenant largement utilisées dans la communauté et en particulier pour Planck, la méthode SMICA et la méthode d'ILC.

SMICA (Delabrouille et al. 2003a; Cardoso et al. 2008) est une méthode d'estimation spectrale multi composantes à partir de données multi fréquences (ou multi détecteurs). Elle permet de mesurer directement le spectre de puissance des différentes composantes présentes dans les données (et, notamment, du fond cosmologique) ainsi que le niveau de contribution de ces émissions dans les différents détecteurs. Il s'agit d'une méthode aveugle, qui n'utilise aucune information a priori sur les composantes présentes, à l'exception de leur indépendance statistique. Elle a été utilisée pour l'analyse des données d'Archeops (Tristram et al. 2005) et de WMAP (Patanchon et al. 2005), est actuellement utilisée pour l'analyse des données de Planck, et a été utilisée pour préparer une future mission de mesure de polarisation du fond cosmologique (Betoule et al. 2009; Dunkley et al. 2009a).

La méthode d'ILC quant à elle est une méthode connue depuis longtemps car très simple conceptuellement et d'implémentation aisée. Elle a été utilisée très largement par de nombreux auteurs, notamment pour l'analyse des données de la mission spatiale WMAP. J'ai proposé une implémentation sur des domaines d'une décomposition redondante en ondelettes sur la sphère. Une implémentation sur les données de WMAP a permis d'obtenir une carte du fond cosmologique sensiblement moins contaminée par les émissions d'avant plan que les autres cartes obtenues par ailleurs (Delabrouille et al. 2009). La méthode d'ILC toutefois ne permet que l'extraction d'une composante unique, dont la loi d'émission est connue. Elle est par ailleurs sujette à des biais assez subtils. J'ai travaillé récemment à la caractérisation détaillée de ces biais (Delabrouille et al. 2009; Dick et al. 2010) et à l'extension de la méthode pour l'extraction de composantes multiples (Remazeilles et al. 2010) ou complexes. J'encadre actuellement les activités d'un post doctorant (Mathieu Remazeilles) sur ce thème.

J'ai rédigé la majeure partie d'un article de synthèse du problème de la séparation de composantes en support d'un cours sur l'analyse de données en cosmologie (Delabrouille & Cardoso 2009).

Enfin, le développement de l'outil needlets (un type d'ondelettes sur la sphère), utilisé pour la séparation de composantes, permet aussi de mettre au point une méthode d'estimation spectrale en présence de contaminations et de résolution instrumentale non stationnaire sur le ciel. J'ai contribué à mettre au point une telle méthode (Faÿ et al. 2008). Une application aux données de la mission WMAP est en cours.

Expérience Archeops

J'ai participé aux différentes campagnes d'observation avec l'expérience ballon Archéops, depuis Trapani en Sicile en 1999, et depuis Kiruna en Suède entre 2001 et 2003. J'ai participé à la récupération de la nacelle en Russie après les vols de janvier 2001 et février 2003. J'ai contribué à l'analyse des

données des différents vols, notamment en encadrant le travail de thèse de Guillaume Patanchon sur l'application de la méthode SMICA aux données du vol scientifique de 2003 (Tristram et al. 2005), mais aussi en développant une partie des logiciels de traitement des données. J'ai joué un rôle important dans la définition, l'organisation et la mise en place d'une chaîne commune de traitement des données sous CVS à l'IAP. Les logiciels ainsi gérés ont servi de base aux développements ultérieurs mis en place dans le Data Processing Center de l'instrument Planck HFI.

L'expérience Archeops (Benoît et al. 2002) a servi de banc test pour la préparation de l'instrument Planck HFI. Elle a aussi permis de mesurer pour la première fois (avant WMAP) les anisotropies du fond cosmologique sur une gamme d'échelles angulaires couvrant la totalité du premier pic acoustique, depuis les grandes échelles observées par COBE jusqu'aux petites anisotropies observées par différentes expériences au sol et en ballon (Benoît et al. 2003a,b). Elle a également conduit à l'une des premières mesures du taux de polarisation de l'émission des poussières galactiques à 350 GHz (Benoît et al. 2004).

Équipe ADAMIS

J'ai assuré, entre 2005 et 2010, la mise en place et l'animation scientifique de l'équipe ADAMIS au laboratoire APC. Ce groupe de recherche est conçu comme un lieu de convergence interdisciplinaire, où se rassemblent les compétences d'astrophysiciens, de mathématiciens, de spécialistes de traitement statistique de l'information et d'ingénieurs informaticiens, pour résoudre par des méthodes novatrices les problèmes les plus complexes auxquels se heurte l'analyse de données dans les domaines de l'astrophysique et de l'astroparticule. L'équipe ADAMIS travaille sur le traitement de données en cosmologie, mais aussi sur la détection d'ondes gravitationnelles, les cosmiques de ultra haute énergie, et la simulation et modélisation numérique (notamment le développement du Planck Sky Model, et la simulation de disques d'accrétion et de formation de jets). Parmi les réussites de cette interdisciplinarité, notons la mise au point de méthodes d'analyse de données performantes, notamment (pour ce qui concerne ma propre recherche) le développement de méthodes de séparation de composantes, d'outils logiciels de traitement de données, et d'outils mathématiques d'analyse multi résolution sur la sphère.

Analyse des données de la mission WMAP

Je me suis impliqué dans plusieurs projets d'analyse des données de la mission spatiale WMAP, mises à la disposition de la communauté scientifique à partir de 2003. J'ai notamment travaillé à la séparation de composantes (Patanchon et al. 2005; Delabrouille et al. 2009; Ghosh et al. 2010), à la recherche de la signature de l'effet SZ et la contrainte des lois d'échelle des amas de galaxie par une analyse jointe des données de WMAP et de ROSAT (Melin et al. 2010), à la recherche de signatures non gaussiennes (Raeth et al. 2010), et à la mesure du spectre de puissance de température et de polarisation des anisotropies du fond cosmologique (Samal et al. 2010).

Polarisation du fond cosmologique

Au delà des études de la mesure de la polarisation du fond cosmologique avec Planck, déjà mentionnées plus haut, je m'investis dans la préparation d'une future mission spatiale pour la mesure de la polarisation du ciel millimétrique. J'ai notamment travaillé sur le problème des émissions d'avant plan polarisées (Tucci et al. 2005; Betoule et al. 2009; Dunkley et al. 2009a). J'encadre actuellement un post doctorant (Soumen Basak) sur le même sujet. J'ai participé activement à la préparation de la proposition de mission COrE en réponse à l'appel à idées de l'ESA dans le cadre du programme "Cosmic Vision" 2015-2025. J'ai notamment proposé de concevoir une mission avec un grand nombre

de bandes de fréquence distinctes. Ceci est, de mon point de vue, crucial pour permettre d'affranchir la mesure de la contamination par les avant plans, et isoler sans équivoque possible la contribution de modes de polarisation d'origine inflationnaire dans le fond de rayonnement cosmologique.

Annexe C

Liste des activités d'encadrement

Stages de Licence

- Ludovik LACROIX, Licence en Services et Technologies de l'Information et de la Communication, Université de Marne la Vallée, 1er juin – 31 août 2003 : *Participation à la définition et la mise en place des moyens matériel et logiciel pour l'équipe ADAMIS*
- Delphine DERYNG, 1ère année de Magistère de Physique, Université de Paris 7, 21 juin – 6 août 2004 : *Restauration de données détériorées et application au CMB*

Stages ingénieurs

- Anne-Laure PHILIPPOT, Institut National des Télécommunications, 2 avril – 31 août 2001 : *Correction d'effets de lobe par déconvolution semi-aveugle pour la mesure des fluctuations du fond de rayonnement cosmologique* Julien LARENA, Ecole Nationale Supérieure des Techniques Avancées, 3 mars – 12 septembre 2003 : *Cartographie pour l'analyse des anisotropies du fond diffus cosmologique*
- Dimitri DRUELLE, École Polytechnique, 10 avril – 1er septembre 2005 : *Développement d'un outil de simulation pour le traitement des données du satellite européen Planck*
- Guillaume BORDIER, 1ère année de l'ENSEA, 21 juin – 31 août 2007 : *Création du site web de l'équipe ADAMIS*

Stages de DEA ou Master

- Stéphane PAULIN-HENRIKSSON, DEA Modélisation et Instrumentation en Physique, Université de Paris 7, 1 mars –31 mai 1999 : *Observation des anisotropies du fond cosmologique avec le photomètre Diabolo*
- Guillaume PATANCHON, DEA Méthodes Instrumentales en Astrophysique et leurs applications spatiales, Université de Paris 6, 15 mars – 25 juin 2000 : *Simulation d'observations et séparation de composantes pour la mesure des fluctuations du fond de rayonnement cosmologique*
- Jean-Baptiste MELIN, DEA Astrophysique, Planétologie, Sciences et Techniques Spatiales, Université de Toulouse, 26 mars – 29 juin 2001 : *Simulation de cartes d'effet Sunyaev-Zel'dovich*
- Laurence PEROTTO, DEA Champs, Particules, Matière, juin 2002 : *Simulation de cartes de polarisation du fond de rayonnement cosmologique*
- Marc BETOULE, Master 2 recherche Astronomie et Astrophysique de Toulouse, 27 avril – 27 juin 2006 : *Analyse jointe de l'observation du fond diffus cosmologique : WMAP et Archeops*
- Guillaume CASTEX, Master 2 Noyaux, Particules, Astrophysique et Cosmologie de Paris 7, juin – juillet 2009 : *Le "Planck Sky Model"*

– Antoine DUVAL, Master 1 Ecole Normale Supérieure, cursus Maths – Physique, juillet 2010 : *Etude statistique de la distribution des rayons cosmiques de hautes énergies*

Thèses de Doctorat

Les cinq thèses suivantes ont été ou sont préparées sous ma direction ou co-direction :

– Guillaume PATANCHON, 2000 – 2003 : *Analyse multi-composantes d'observations du fond diffus cosmologique*
– Jean-Baptiste MELIN, 2001 – 2004 : *Amas de galaxies et effet Sunyaev-Zel'dovich : Observations et étude des effets de sélection des sondages*
– Marc BETOULE, 2006 – 2009 : *Analyse jointe multifréquence d'observations de température et de polarisation du fond cosmologique*
– Pietro PROCOPIO, 2007 – 2010 (en cotutelle internationale) : *Foreground implications in the scientific exploitation of CMB data*
– Guillaume CASTEX, 2009 – 2012 : *Le "Planck Sky Model" (Thèse en cours)*

Je me suis par ailleurs fortement impliqué dans l'encadrement d'une partie des travaux présentés dans les six thèses suivantes :

– Benoît REVENU (Thèse dirigée par Jean Kaplan, PCC), 1997 – 2000 : *Anisotropies de température et polarisation du rayonnement fossile : méthodes de détection et traitement de données*
– Cyrille ROSSET (Thèse dirigée par Thomas Patzak, PCC), 2000 – 2003 : *Contribution à la mesure de la polarisation du fond diffus cosmologique dans le cadre des programmes Archeops et Planck*
– Hichem SNOUSSI (Thèse dirigée par Ali Mohammad-Djafari, Supélec), 2000 – 2003 : *Approche Bayésienne en séparation de sources. Applications en imagerie*
– Svitlana ZINGER (Thèse dirigée par Henri Maître, Télécom-Paris), 2001 – 2004 : *Interpolation and resampling of three-dimensional data and its application for urban cartography and for determination of Cosmic Microwave Background*
– Silvia FERNANDEZ-CEREZO (Thèse dirigée par Rafael Rebolo, IAC), 2001 – 2005 : *Emisión galáctica difusa y medida de anisotropías en la radiación cósmica de microondas en escalas angulares intermedias*
– Tuhin GHOSH (Thèse dirigée par Tarun Souradeep, Inter-University Centre for Astronomy and Astrophysics – IUCAA, Pune, Inde) *Extraction de cartes d'émissions d'avant-plans dans les données WMAP (Thèse en cours)*

Post-Doctorants

– Juan MACIAS-PEREZ, pendant 6 mois en 2001 : *Travaux sur la séparation de composantes à partir d'observations multifréquences du CMB*
– Patricio VIELVA, décembre 2003 – janvier 2005 : *Travaux sur la détection de sources ponctuelles dans les observations millimétriques, sur l'analyse multicomposantes et sur les tests de non-gaussianité des fluctuations de température du fond cosmologique observées par WMAP*
– Mathieu REMAZEILLES, depuis mars 2009 : *Travaux sur la séparation de composantes dans le cadre de l'analyse des données de la mission Planck*
– Soumen BASAK, depuis décembre 2009 : *Travaux sur la séparation de composantes dans le cadre de la mesure de la polarisation du fond cosmologique*

Encadrement scientifique de groupes de travail au sein du consortium Planck

- Groupe d'étude des effets systématiques polarisés (WG 1.5)
- Groupe de mise en place de la chaîne de traitement des données polarisées (GPH 425)
- Groupe de travail séparation de composantes et modélisation de l'émission du ciel (WG 2)

Animation scientifique d'un groupe thématique du laboratoire APC

J'ai assuré, de 2003 à 2005 au sein de la fédération de recherche APC, puis de 2005 à 2010 dans le laboratoire APC, la mise en place et l'animation scientifique de l'équipe ADAMIS, une équipe interdisciplinaire pour l'analyse de données et les simulations numériques en astroparticule et cosmologie.

Annexe D

Curiculum Vitae

Jacques DELABROUILLE

42 ans, marié, trois enfants
16, avenue d'Orsay
91120 Palaiseau, France

e-mail: delabrouille@apc.univ-paris7.fr
tél domicile : +33 1 60 14 77 15
tél bureau : +33 1 44 27 99 43
mobile : +33 6 72 91 19 54

ÉDUCATION

1998 — **PhD en Physique**, The University of Chicago.
Doctorat Astrophysique et Techniques Spatiales, Paris XI, avec les félicitations du Jury

1994 — **Master of Science**, The University of Chicago.
Lauréat d'une bourse Lavoisier du Ministère des Affaires Étrangères.

1991 — **Diplôme d'ingénieur**, Télécom Paris
Spécialisation en Télécommunications et systèmes aérospatiaux.

EXPÉRIENCE PROFESSIONNELLE

2004-2010 — **CHARGE DE RECHERCHES CNRS LABORATOIRE APC (PARIS, FRANCE)**
Responsable du groupe d'analyse de données et simulations. Responsable d'une ACI du MERT (ACI « Masses de Données » Astro-Map). Responsable du groupe de travail « séparation de composantes » de la mission PLANCK.

1999-2003 — **CHARGE DE RECHERCHES CNRS AU COLLEGE DE FRANCE (PARIS, FRANCE)**
Préparation de la mission spatiale PLANCK et participation à l'expérience ballon ARCHEOPS.
Responsable d'une Action Concertée Incitative "Jeunes Chercheurs" du MERT. Membre du conseil de laboratoire et du conseil scientifique du PCC.

1994-1998 — **DOCTORAT ET ATER A L'IAS D'ORSAY (CO-TUTELLE ORSAY ET CHICAGO)**
Préparation de la mission spatiale PLANCK, observation de l'effet Sunyaev-Zel'dovich dans les amas de galaxies avec l'expérience DIABOLO.
Directeurs de thèse : Pr. Jean-Loup Puget et Pr. David N. Schramm

ASTRONOMY AND ASTROPHYSICS CENTER, EFI (CHICAGO, USA)
Recherche sur le fond de rayonnement cosmologique

1993-1994 — **HIGH ENERGY PHYSICS CENTER, EFI (CHICAGO, USA)**
Détection des grandes gerbes atmosphériques avec l'expérience CASA-MIA.

1992-1993 — **UNIVERSITY OF CHICAGO (USA)**
Assistant d'enseignement (300 heures d'enseignement en physique et électronique).

1992 (6 mois) — **STAGE DE DEA, CEA, CENTRE D'ETUDES NUCLEAIRES (SACLAY, FRANCE)**
Simulation Monte-Carlo de l'annihilation des positrons galactiques dans les nuages interstellaires

1991 (3 mois) : — **STAGE INGENIEUR AU FERMILAB (ILLINOIS, USA)**
Développement d'un préamplificateur faible bruit pour un prototype de calorimètre à Argon solide

1991 (3 mois) : — **STAGE INGENIEUR A L'ONERA (CHATILLON, FRANCE)**
Conception d'un filtre interpolateur pour détection radar bi-statique.

INTÉRETS PERSONNELS

Langues — **Français**, **Polonais**: langues maternelles;
Anglais: 12 années d'études, plusieurs années de pratique aux USA.
Allemand : 7 années d'études.
Russe : 2 années d'étude, séjours de plusieurs semaines en Russie et en Asie centrale
Espagnol : 2 années d'étude, séjours de plusieurs semaines en Espagne et Amérique Latine

Personnel — Musique (10 années d'étude du piano au Conservatoire National de Région de Bordeaux)
Plongée sous-marine (plongeur autonome niveau III)
Trekking et alpinisme (participation au Festival d'Alpinisme Khan-Tengri 2000 au Kazakhstan)
Voyages culturels ou sportifs

Bibliographie

Abazajian, K. N., Adelman-McCarthy, J. K., Agüeros, M. A., et al. 2009, ApJS, 182, 543

Ahmed, B., Alner, G. J., Araujo, H., et al. 2003, Astroparticle Physics, 19, 691

Akerib, D. S., Armel-Funkhouser, M. S., Attisha, M. J., et al. 2005, Phys.Rev.D, 72, 052009

Alcock, C., Allsman, R. A., Alves, D., et al. 1998, ApJ, 499, L9+

Alcock, C., Allsman, R. A., Alves, D. R., et al. 2000, ApJ, 542, 281

Alcock, C. & Paczynski, B. 1979, Nature, 281, 358

Allen, S. W., Schmidt, R. W., & Fabian, A. C. 2002, MNRAS, 335, 256

Alner, G. J., Araujo, H., Bewick, A., et al. 2005, Nuclear Instruments and Methods in Physics Research A, 555, 173

Alnes, H., Amarzguioui, M., & Grøn, Ø. 2006, Phys.Rev.D, 73, 083519

Alpher, R. A., Bethe, H., & Gamow, G. 1948, Physical Review, 73, 803

Andriamonje, S., Aune, S., Autiero, D., et al. 2007, JCAP, 4, 10

Armitage, C. & Wandelt, B. D. 2004, Phys.Rev.D, 70, 123007

Arnaud, M., Pointecouteau, E., & Pratt, G. W. 2007, A&A, 474, L37

Arnaud, M., Pratt, G. W., Piffaretti, R., et al. 2010, A&A, 517, A92+

Ashdown, M. A. J., Baccigalupi, C., Balbi, A., et al. 2007, A&A, 467, 761

Ashdown, M. A. J., Baccigalupi, C., Bartlett, J. G., et al. 2009, A&A, 493, 753

Astier, P., Guy, J., Regnault, N., et al. 2006, A&A, 447, 31

Asztalos, S. J., Carosi, G., Hagmann, C., et al. 2010, Physical Review Letters, 104, 041301

Audit, E. & Simmons, J. F. L. 1999, MNRAS, 305, L27

Basak, S., Prunet, S., & Benabed, K. 2009, A&A, 508, 53

Bennett, C. L., Hill, R. S., Hinshaw, G., et al. 2003, ApJS, 148, 97

Benoît, A., Ade, P., Amblard, A., et al. 2003a, A&A, 399, L19

Benoît, A., Ade, P., Amblard, A., et al. 2003b, A&A, 399, L25

Benoît, A., Ade, P., Amblard, A., et al. 2004, A&A, 424, 571

Benoît, A., Ade, P., Amblard, A., et al. 2002, Astroparticle Physics, 17, 101

Benoît, A., Zagury, F., Coron, N., et al. 2000, A&AS, 141, 523

Bernabei, R., Belli, P., Cerulli, R., et al. 2000, Physics Letters B, 480, 23

Bertin, E. & Arnouts, S. 1996, A&AS, 117, 393

Bertone, G., Hooper, D., & Silk, J. 2005, Physics Reports, 405, 279

Bertschinger, E. 1995, ArXiv Astrophysics e-prints

Betoule, M., Pierpaoli, E., Delabrouille, J., Le Jeune, M., & Cardoso, J. 2009, A&A, 503, 691

Bevis, N., Hindmarsh, M., & Kunz, M. 2004, Phys.Rev.D, 70, 043508

Birkinshaw, M. 1999, Physics Reports, 310, 97

Birkinshaw, M., Gull, S. F., & Hardebeck, H. 1984, Nature, 309, 34

Birkinshaw, M. & Hughes, J. P. 1994, ApJ, 420, 33

Birkinshaw, M., Hughes, J. P., & Arnaud, K. A. 1991, ApJ, 379, 466

Böhringer, H., Schuecker, P., Guzzo, L., et al. 2004, A&A, 425, 367

Böhringer, H., Voges, W., Huchra, J. P., et al. 2000, ApJS, 129, 435

Bouchet, F. R. & Gispert, R. 1999, New Astronomy, 4, 443

Bouchet, F. R., Prunet, S., & Sethi, S. K. 1999, MNRAS, 302, 663

Brown, M. L., Ade, P., Bock, J., et al. 2009, ApJ, 705, 978

Buchert, T. 2008, General Relativity and Gravitation, 40, 467

Cantalupo, C. M., Borrill, J. D., Jaffe, A. H., Kisner, T. S., & Stompor, R. 2009, ArXiv e-prints

Cardoso, J., Le Jeune, M., Delabrouille, J., Betoule, M., & Patanchon, G. 2008, IEEE Journal of Selected Topics in Signal Processing, vol. 2, issue 5, pp. 735-746, 2, 735

Carlstrom, J. E., Ade, P. A. R., Aird, K. A., et al. 2009, ArXiv e-prints

Carlstrom, J. E., Holder, G. P., & Reese, E. D. 2002, ARA&A, 40, 643

Carlstrom, J. E., Joy, M., & Grego, L. 1996, ApJ, 456, L75+

Cen, R. & Ostriker, J. P. 1999, ApJ, 514, 1

Challinor, A. & Lasenby, A. 1998, ApJ, 499, 1

Challinor, A. D., Mortlock, D. J., van Leeuwen, F., et al. 2002, MNRAS, 331, 994

Chiang, C., Ade, P. A. R., Barkats, D., et al. 2009, in American Astronomical Society Meeting Abstracts, Vol. 41, American Astronomical Society Meeting Abstracts, 754

Chuss, D. T., Ade, P. A. R., Benford, D. J., et al. 2010, in Society of Photo-Optical Instrumentation Engineers (SPIE) Conference Series, Vol. 7741, Society of Photo-Optical Instrumentation Engineers (SPIE) Conference Series

Coles, P. & Lucchin, F. 2002, Cosmology : The Origin and Evolution of Cosmic Structure, Second Edition, ed. Coles, P. & Lucchin, F.

Combes, F. 2002, New Astronomy Reviews, 46, 755

Condon, J. J., Cotton, W. D., Greisen, E. W., et al. 1998, AJ, 115, 1693

Cooray, A. & Baumann, D. 2003, Phys.Rev.D, 67, 063505

Couchot, F., Delabrouille, J., Kaplan, J., & Revenu, B. 1999, A&AS, 135, 579

Crill, B. P., Ade, P. A. R., Battistelli, E. S., et al. 2008, in Society of Photo-Optical Instrumentation Engineers (SPIE) Conference Series, Vol. 7010, Society of Photo-Optical Instrumentation Engineers (SPIE) Conference Series

Crittenden, R. G. & Turok, N. 1995, Physical Review Letters, 75, 2642

Crittenden, R. G. & Turok, N. 1996, Physical Review Letters, 76, 575

da Silva, A. C., Kay, S. T., Liddle, A. R., & Thomas, P. A. 2004, MNRAS, 348, 1401

Davis, Jr., L. & Greenstein, J. L. 1951, ApJ, 114, 206

de Oliveira-Costa, A., Tegmark, M., Gaensler, B. M., et al. 2008, MNRAS, 388, 247

de Oliveira-Costa, A., Tegmark, M., Gutierrez, C. M., et al. 1999, ApJ, 527, L9

Delabrouille, J. 1998a, A&AS, 127, 555

Delabrouille, J. 2001, New Astronomy Review, 45, 313

Delabrouille, J. 2004, Ap&SS, 290, 87

Delabrouille, J. & Cardoso, J. 2009, in Lecture Notes in Physics, Berlin Springer Verlag, Vol. 665, Lecture Notes in Physics, Berlin Springer Verlag, ed. V. J. Martinez, E. Saar, E. M. Gonzales, & M. J. Pons-Borderia , 159

Delabrouille, J., Cardoso, J., Le Jeune, M., et al. 2009, A&A, 493, 835

Delabrouille, J., Cardoso, J., & Patanchon, G. 2003a, MNRAS, 346, 1089

Delabrouille, J. & Filliatre, P. 2004, Ap&SS, 290, 119

Delabrouille, J., Górski, K. M., & Hivon, E. 1998a, MNRAS, 298, 445

Delabrouille, J. & Kaplan, J. 2002, in American Institute of Physics Conference Series, Vol. 609, Astrophysical Polarized Backgrounds, ed. S. Cecchini, S. Cortiglioni, R. Sault, & C. Sbarra, 135–143

Delabrouille, J., Kaplan, J., Piat, M., & Rosset, C. 2003b, Comptes Rendus Physique, 4, 925

Delabrouille, J., Melin, J., & Bartlett, J. G. 2002, in Astronomical Society of the Pacific Conference Series, Vol. 257, AMiBA 2001 : High-Z Clusters, Missing Baryons, and CMB Polarization, ed. L.-W. Chen, C.-P. Ma, K.-W. Ng, & U.-L. Pen, 81

Delabrouille, J., Puget, J., Gispert, R., & Lamarre, J. 1998b, ArXiv Astrophysics e-prints

Delabrouille, J. H. 1998b, PhD thesis, THE UNIVERSITY OF CHICAGO

Désert, F., Benoît, A., Camus, P., et al. 2002, in American Institute of Physics Conference Series, Vol. 616, Experimental Cosmology at Millimetre Wavelengths, ed. M. de Petris & M. Gervasi, 116–122

Désert, F., Benoît, A., Gaertner, S., et al. 1998, New Astronomy, 3, 655

Désert, F., Boulanger, F., & Puget, J. L. 1990, A&A, 237, 215

Désert, F., Macías-Pérez, J. F., Mayet, F., et al. 2008, A&A, 481, 411

Dick, J., Remazeilles, M., & Delabrouille, J. 2010, MNRAS, 401, 1602

Dicke, R. H., Peebles, P. J. E., Roll, P. G., & Wilkinson, D. T. 1965, ApJ, 142, 414

Dickinson, C., Davies, R. D., & Davis, R. J. 2003, MNRAS, 341, 369

Diego, J. M., Hansen, S. H., & Silk, J. 2003, MNRAS, 338, 796

Dobler, G. & Finkbeiner, D. P. 2008, ApJ, 680, 1235

Dodelson, S. 2003, Modern cosmology, ed. Dodelson, S.

Doran, M. 2005, JCAP, 10, 11

Draine, B. T. & Lazarian, A. 1998, ApJ, 508, 157

Dunkley, J., Amblard, A., Baccigalupi, C., et al. 2009a, in American Institute of Physics Conference Series, Vol. 1141, American Institute of Physics Conference Series, ed. S. Dodelson, D. Baumann, A. Cooray, J. Dunkley, A. Fraisse, M. G. Jackson, A. Kogut, L. Krauss, M. Zaldarriaga, & K. Smith, 222–264

Dunkley, J., Komatsu, E., Nolta, M. R., et al. 2009b, ApJS, 180, 306

Dupac, X. & Giard, M. 2002, MNRAS, 330, 497

EDELWEISS Collaboration. 2009, Physics Letters B, 681, 305

Elsner, F. & Wandelt, B. D. 2009, ApJS, 184, 264

Fabbri, R. 1981, Ap&SS, 77, 529

Faÿ, G., Guilloux, F., Betoule, M., et al. 2008, Phys.Rev.D, 78, 083013

Ferrière, K. M. 2001, Reviews of Modern Physics, 73, 1031

Finkbeiner, D. P. 2003, ApJS, 146, 407

Finkbeiner, D. P., Davis, M., & Schlegel, D. J. 1999, ApJ, 524, 867

Finkbeiner, D. P., Langston, G. I., & Minter, A. H. 2004, ApJ, 617, 350

Finkbeiner, D. P., Schlegel, D. J., Frank, C., & Heiles, C. 2002, ApJ, 566, 898

Fixsen, D. J., Cheng, E. S., Gales, J. M., et al. 1996, ApJ, 473, 576

Freedman, W. L., Madore, B. F., Gibson, B. K., et al. 2001, ApJ, 553, 47

Garcia-Bellido, J., Durrer, R., Fenu, E., Figueroa, D. G., & Kunz, M. 2010, ArXiv e-prints

Ghosh, T., Delabrouille, J., Remazeilles, M., Cardoso, J., & Souradeep, T. 2010, ArXiv e-prints

Gitti, M. & Schindler, S. 2004, A&A, 427, L9

Gold, B., Odegard, N., Weiland, J. L., et al. 2010, ArXiv e-prints

González-Nuevo, J., Toffolatti, L., & Argüeso, F. 2005, ApJ, 621, 1

Górski, K. M., Hivon, E., Banday, A. J., et al. 2005, ApJ, 622, 759

Grainge, K., Grainger, W. F., Jones, M. E., et al. 2002, MNRAS, 329, 890

Grainge, K., Jones, M., Pooley, G., Saunders, R., & Edge, A. 1993, MNRAS, 265, L57+

Gregory, P. C., Scott, W. K., Douglas, K., & Condon, J. J. 1996, ApJS, 103, 427

Gregory, P. C., Vavasour, J. D., Scott, W. K., & Condon, J. J. 1994, ApJS, 90, 173

Gunn, J. E. & Peterson, B. A. 1965, ApJ, 142, 1633

Guy, J., Sullivan, M., Conley, A., et al. 2010, A&A, 523, A7+

Harrison, E. 2000, Cosmology, ed. Harrison, E.

Haslam, C. G. T., Klein, U., Salter, C. J., et al. 1981, A&A, 100, 209

Haslam, C. G. T., Salter, C. J., Stoffel, H., & Wilson, W. E. 1982, A&AS, 47, 1

Herbig, T., Lawrence, C. R., Readhead, A. C. S., & Gulkis, S. 1995, ApJ, 449, L5+

Herranz, D., Sanz, J. L., Barreiro, R. B., & López-Caniego, M. 2005, MNRAS, 356, 944

Herranz, D., Sanz, J. L., Hobson, M. P., et al. 2002, MNRAS, 336, 1057

Hinderks, J. R., Ade, P., Bock, J., et al. 2009, ApJ, 692, 1221

Hinshaw, G., Nolta, M. R., Bennett, C. L., et al. 2007, ApJS, 170, 288

Hinshaw, G., Weiland, J. L., Hill, R. S., et al. 2009, ApJS, 180, 225

Hoang, T., Draine, B. T., & Lazarian, A. 2010, ApJ, 715, 1462

Hobson, M. P., Jones, A. W., Lasenby, A. N., & Bouchet, F. R. 1998, MNRAS, 300, 1

Holzapfel, W. L., Arnaud, M., Ade, P. A. R., et al. 1997a, ApJ, 480, 449

Holzapfel, W. L., Wilbanks, T. M., Ade, P. A. R., et al. 1997b, ApJ, 479, 17

Hubble, E. 1929, Proceedings of the National Academy of Science, 15, 168

Hubble, E. & Humason, M. L. 1931, Contributions from the Mount Wilson Observatory / Carnegie Institution of Washington, 427, 1

Iocco, F., Mangano, G., Miele, G., Pisanti, O., & Serpico, P. D. 2009, Physics Reports, 472, 1

Jaffe, A. H., Gawiser, E., Finkbeiner, D., et al. 1999, in Astronomical Society of the Pacific Conference Series, Vol. 181, Microwave Foregrounds, ed. A. de Oliveira-Costa & M. Tegmark, 367–+

Jarosik, N., Bennett, C. L., Dunkley, J., et al. 2010, ArXiv e-prints

Jenkins, A., Frenk, C. S., White, S. D. M., et al. 2001, MNRAS, 321, 372

Joint Iras Science, W. G. 1994, VizieR Online Data Catalog, 2125, 0

Jones, M., Saunders, R., Alexander, P., et al. 1993, Nature, 365, 320

Jungman, G., Kamionkowski, M., Kosowsky, A., & Spergel, D. N. 1996, Phys.Rev.D, 54, 1332

Kaiser, N. & Stebbins, A. 1984, Nature, 310, 391

Kaplan, J. & Delabrouille, J. 2002, in American Institute of Physics Conference Series, Vol. 609, Astrophysical Polarized Backgrounds, ed. S. Cecchini, S. Cortiglioni, R. Sault, & C. Sbarra, 209–214

Kaplan, J., Delabrouille, J., Fosalba, P., & Rosset, C. 2003, Comptes Rendus Physique, 4, 917

Kaplinghat, M., Chu, M., Haiman, Z., et al. 2003, ApJ, 583, 24

Katz, N., Weinberg, D. H., & Hernquist, L. 1996, ApJS, 105, 19

Keihänen, E., Keskitalo, R., Kurki-Suonio, H., Poutanen, T., & Sirvio, A. 2009, ArXiv e-prints

Keihänen, E., Kurki-Suonio, H., & Poutanen, T. 2005, MNRAS, 360, 390

Keihänen, E., Kurki-Suonio, H., Poutanen, T., Maino, D., & Burigana, C. 2004, A&A, 428, 287

Kitayama, T., Komatsu, E., Ota, N., et al. 2004, Publ. of the Astronomical Society of Japan, 56, 17

Knight, P. A. & Ponman, T. J. 1997, MNRAS, 289, 955

Knox, L. 1995, Phys.Rev.D, 52, 4307

Kofman, L. A. & Starobinskii, A. A. 1985, Soviet Astronomy Letters, 11, 271

Kolb, E. W., Matarrese, S., & Riotto, A. 2006, New Journal of Physics, 8, 322

Kolb, E. W. & Turner, M. S. 1990, The early universe, ed. Kolb, E. W. & Turner, M. S.

Komatsu, E., Smith, K. M., Dunkley, J., et al. 2010, ArXiv e-prints

Komatsu, E., Spergel, D. N., & Wandelt, B. D. 2005, ApJ, 634, 14

Kosowsky, A. 2003, New Astronomy Review, 47, 939

Kovac, J. M., Leitch, E. M., Pryke, C., et al. 2002, Nature, 420, 772

Kravtsov, A. V., Klypin, A. A., & Khokhlov, A. M. 1997, ApJS, 111, 73

Kurki-Suonio, H., Keihänen, E., Keskitalo, R., et al. 2009, A&A, 506, 1511

Lagache, G., Puget, J., & Dole, H. 2005, ARA&A, 43, 727

Lamarre, J., Puget, J., Ade, P. A. R., et al. 2010, A&A, 520, A9+

Lasserre, T., Afonso, C., Albert, J. N., et al. 2000, A&A, 355, L39

Leach, S. M., Cardoso, J., Baccigalupi, C., et al. 2008, A&A, 491, 597

Lewis, A., Challinor, A., & Lasenby, A. 2000, ApJ, 538, 473

Liddle, A. 2003, An Introduction to Modern Cosmology, Second Edition, ed. Liddle, A.

Liddle, A. R. & Lyth, D. H. 2000, Cosmological Inflation and Large-Scale Structure, ed. Liddle, A. R. & Lyth, D. H.

Lieu, R., Mittaz, J. P. D., & Zhang, S. 2006, ApJ, 648, 176

Liguori, M., Matarrese, S., & Moscardini, L. 2003, ApJ, 597, 57

Liu, G., da Silva, A., & Aghanim, N. 2005, ApJ, 621, 15

Macías-Pérez, J. F., Lagache, G., Maffei, B., et al. 2007, A&A, 467, 1313

Maiani, L., Petronzio, R., & Zavattini, E. 1986, Physics Letters B, 175, 359

Maino, D., Burigana, C., Górski, K. M., Mandolesi, N., & Bersanelli, M. 2002, A&A, 387, 356

Markevitch, M. & Vikhlinin, A. 2001, ApJ, 563, 95

Mason, B. S., Dicker, S. R., Korngut, P. M., et al. 2009, ArXiv e-prints

Mather, J. C., Fixsen, D. J., Shafer, R. A., Mosier, C., & Wilkinson, D. T. 1999, ApJ, 512, 511

Mauch, T., Murphy, T., Buttery, H. J., et al. 2003, MNRAS, 342, 1117

McMahon, J. J., Aird, K. A., Benson, B. A., et al. 2009, in American Institute of Physics Conference Series, Vol. 1185, American Institute of Physics Conference Series, ed. B. Young, B. Cabrera, & A. Miller, 511–514

Melin, J., Bartlett, J. G., & Delabrouille, J. 2005, A&A, 429, 417

Melin, J., Bartlett, J. G., & Delabrouille, J. 2006, A&A, 459, 341

Melin, J., Bartlett, J. G., Delabrouille, J., et al. 2010, ArXiv e-prints

Miville-Deschênes, M., Ysard, N., Lavabre, A., et al. 2008, A&A, 490, 1093

Narlikar, J. V. 2002, An introduction to cosmology, ed. Narlikar, J. V.

Natoli, P., de Gasperis, G., Gheller, C., & Vittorio, N. 2001, A&A, 372, 346

Navarro, J. F., Frenk, C. S., & White, S. D. M. 1995, MNRAS, 275, 720

Niemack, M. D., Ade, P. A. R., Aguirre, J., et al. 2010, in Society of Photo-Optical Instrumentation Engineers (SPIE) Conference Series, Vol. 7741, Society of Photo-Optical Instrumentation Engineers (SPIE) Conference Series

Norman, M. L. 2010, ArXiv e-prints

Paczynski, B. 1986, ApJ, 304, 1

Page, L., Hinshaw, G., Komatsu, E., et al. 2007, ApJS, 170, 335

Palanque-Delabrouille, N., Afonso, C., Albert, J. N., et al. 1998, A&A, 332, 1

Patanchon, G., Ade, P. A. R., Bock, J. J., et al. 2008, ApJ, 681, 708

Patanchon, G., Cardoso, J., Delabrouille, J., & Vielva, P. 2005, MNRAS, 364, 1185

Peacock, J. A. 1999, Cosmological Physics, ed. Peacock, J. A.

Peacock, J. A. & Dodds, S. J. 1994, MNRAS, 267, 1020

Peccei, R. D. & Quinn, H. R. 1977, Physical Review Letters, 38, 1440

Peebles, P. J. E. 1993, Principles of physical cosmology, ed. Peebles, P. J. E.

Peebles, P. J. E. & Yu, J. T. 1970, ApJ, 162, 815

Penzias, A. A. & Wilson, R. W. 1965, ApJ, 142, 419

Perlmutter, S., Aldering, G., Goldhaber, G., et al. 1999, ApJ, 517, 565

Pointecouteau, E., Arnaud, M., & Pratt, G. W. 2005, A&A, 435, 1

Pointecouteau, E., Giard, M., & Barret, D. 1998, A&A, 336, 44

Pointecouteau, E., Giard, M., Benoit, A., et al. 1999, ApJ, 519, L115

Ponthieu, N., Macías-Pérez, J. F., Tristram, M., et al. 2005, A&A, 444, 327

Poutanen, T., de Gasperis, G., Hivon, E., et al. 2006, A&A, 449, 1311

Pratt, G. W., Croston, J. H., Arnaud, M., & Böhringer, H. 2009, A&A, 498, 361

Preskill, J., Wise, M. B., & Wilczek, F. 1983, Physics Letters B, 120, 127

Press, W. H. & Schechter, P. 1974, ApJ, 187, 425

Puget, J., Abergel, A., Bernard, J., et al. 1996, A&A, 308, L5+

Quilis, V., Bower, R. G., & Balogh, M. L. 2001, MNRAS, 328, 1091

Raeth, C., Banday, A. J., Rossmanith, G., et al. 2010, ArXiv e-prints

Rees, M. J. & Sciama, D. W. 1968, Nature, 217, 511

Reese, E. D., Mohr, J. J., Carlstrom, J. E., et al. 2000, ApJ, 533, 38

Reichborn-Kjennerud, B., Aboobaker, A. M., Ade, P., et al. 2010, in Society of Photo-Optical Instrumentation Engineers (SPIE) Conference Series, Vol. 7741, Society of Photo-Optical Instrumentation Engineers (SPIE) Conference Series

Reinecke, M., Dolag, K., Hell, R., Bartelmann, M., & Enßlin, T. A. 2006, A&A, 445, 373

Remazeilles, M., Delabrouille, J., & Cardoso, J. 2010, MNRAS, 1769

Revenu, B., Kim, A., Ansari, R., et al. 2000, A&AS, 142, 499

Ricci, R., Prandoni, I., Gruppioni, C., Sault, R. J., & de Zotti, G. 2006, A&A, 445, 465

Ricci, R., Sadler, E. M., Ekers, R. D., et al. 2004, MNRAS, 354, 305

Rich, J. 2010, Fundamentals of Cosmology, ed. Rich, J.

Rosset, C., Yurchenko, V. B., Delabrouille, J., et al. 2007, A&A, 464, 405

Rubin, V. C., Ford, W. K. J., & . Thonnard, N. 1980, ApJ, 238, 471

Ruhl, J., Ade, P. A. R., Carlstrom, J. E., et al. 2004, in SPIE Conference Series, Vol. 5498, Millimeter and Submillimeter Detectors for Astronomy II., ed. C. M. Bradford, P. A. R. Ade, J. E. Aguirre, J. J. Bock, M. Dragovan, L. Duband, L. Earle, J. Glenn, H. Matsuhara, B. J. Naylor, H. T. Nguyen, M. Yun, & J. Zmuidzinas, 11–29

Sachs, R. K. & Wolfe, A. M. 1967, ApJ, 147, 73

Sadat, R. & Blanchard, A. 2001, A&A, 371, 19

Saha, R., Prunet, S., Jain, P., & Souradeep, T. 2008, Phys.Rev.D, 78, 023003

Samal, P. K., Saha, R., Delabrouille, J., et al. 2010, ApJ, 714, 840

Savage, C., Gelmini, G., Gondolo, P., & Freese, K. 2009, JCAP, 4, 10

Sazonov, S. Y. & Sunyaev, R. A. 1999, MNRAS, 310, 765

Sbarra, C., Carretti, E., Cortiglioni, S., et al. 2003, A&A, 401, 1215

Schindler, S., Hattori, M., Neumann, D. M., & Boehringer, H. 1997, A&A, 317, 646

Sehgal, N., Bode, P., Das, S., et al. 2010, ApJ, 709, 920

Seljak, U. 1996, ApJ, 463, 1

Seljak, U. & Zaldarriaga, M. 1996, ApJ, 469, 437

Sheth, R. K., Mo, H. J., & Tormen, G. 2001, MNRAS, 323, 1

Shimon, M., Rephaeli, Y., Sadeh, S., & Keating, B. 2009, MNRAS, 399, 2088

Sikivie, P. 2008, in Lecture Notes in Physics, Berlin Springer Verlag, Vol. 741, Axions, ed. M. Kuster, G. Raffelt, & B. Beltrán, 19–+

Silk, J. 1968, ApJ, 151, 459

Smoot, G. F., Bennett, C. L., Kogut, A., et al. 1992, ApJ, 396, L1

Sofue, Y. & Rubin, V. 2001, ARA&A, 39, 137

Springel, V., White, M., & Hernquist, L. 2001, ApJ, 549, 681

Springel, V., White, S. D. M., Jenkins, A., et al. 2005, Nature, 435, 629

Stolyarov, V., Hobson, M. P., Lasenby, A. N., & Barreiro, R. B. 2005, MNRAS, 357, 145

Stompor, R., Balbi, A., Borrill, J. D., et al. 2002, Phys.Rev.D, 65, 022003

Sugiyama, N., Silk, J., & Vittorio, N. 1993, ApJ, 419, L1+

Sunyaev, R. A. & Zeldovich, I. B. 1980, MNRAS, 190, 413

Sunyaev, R. A. & Zeldovich, Y. B. 1972, Comments on Astrophysics and Space Physics, 4, 173

Sutton, D., Johnson, B. R., Brown, M. L., et al. 2009a, MNRAS, 393, 894

Sutton, D., Zuntz, J. A., Ferreira, P. G., et al. 2009b, ArXiv e-prints

Swetz, D. S., Ade, P. A. R., Amiri, M., et al. 2010, ArXiv e-prints

Tauber, J. A., Mandolesi, N., Puget, J., et al. 2010, A&A, 520, A1+

Tegmark, M. 1997, ApJ, 480, L87+

Tegmark, M. & Efstathiou, G. 1996, MNRAS, 281, 1297

Tegmark, M., Eisenstein, D. J., Hu, W., & de Oliveira-Costa, A. 2000, ApJ, 530, 133

Teyssier, R. 2002, A&A, 385, 337

The CDMS Collaboration. 2009, ArXiv e-prints

The QUBIC collaboration, Battistelli, E., Baù, A., et al. 2010, ArXiv e-prints

Tibbs, C. T., Watson, R. A., Dickinson, C., et al. 2010, MNRAS, 402, 1969

Tristram, M., Patanchon, G., Macías-Pérez, J. F., et al. 2005, A&A, 436, 785

Tsuboi, M., Miyazaki, A., Kasuga, T., Matsuo, H., & Kuno, N. 1998, Publ. of the Astronomical Society of Japan, 50, 169

Tucci, M., Martínez-González, E., Vielva, P., & Delabrouille, J. 2005, MNRAS, 360, 935

Volders, L. M. J. S. 1959, Bulletin of the Astronomical Institutes of the Netherlands, 14, 323

Waelkens, A., Jaffe, T., Reinecke, M., Kitaura, F. S., & Enßlin, T. A. 2009, A&A, 495, 697

Wagoner, R. V., Fowler, W. A., & Hoyle, F. 1967, ApJ, 148, 3

Wandelt, B. D. & Górski, K. M. 2001, Phys.Rev.D, 63, 123002

Watson, R. A., Rebolo, R., Rubiño-Martín, J. A., et al. 2005, ApJ, 624, L89

Weinberg, S. 1978, Physical Review Letters, 40, 223

Weinberg, S. 2008, Cosmology, ed. Weinberg, S. (Oxford University Press)

White, S. D. M., Navarro, J. F., Evrard, A. E., & Frenk, C. S. 1993, Nature, 366, 429

Worrall, D. M. & Birkinshaw, M. 2003, MNRAS, 340, 1261

Wright, E. L., Chen, X., Odegard, N., et al. 2009, ApJS, 180, 283

Yvon, D. & Mayet, F. 2005, A&A, 436, 729

Zaldarriaga, M. 1997, Phys.Rev.D, 55, 1822

Zavattini, E., Zavattini, G., Ruoso, G., et al. 2008, Phys.Rev.D, 77, 032006

Zwart, J. T. L., Barker, R. W., Biddulph, P., et al. 2008, MNRAS, 391, 1545

Zwicky, F. 1933, Helvetica Physica Acta, 6, 110